TU Delft

Delft University of Technology

Proceedings of the 5th Symposium on the Dynamics and Control of Single-track Vehicles Bicycle and Motorcycle Dynamics 2023, October 18-20, Delft, The Netherlands

Moore, J.K.; de Vries, E.; Dressel, A.; Alizadehsaravi, L.

DOI
10.59490/mg.121

Publication date
2024

Document Version
Final published version

Citation (APA)
Moore, J. K., de Vries, E., Dressel, A., & Alizadehsaravi, L. (Eds.) (2024). *Proceedings of the 5th Symposium on the Dynamics and Control of Single-track Vehicles: Bicycle and Motorcycle Dynamics 2023, October 18-20, Delft, The Netherlands* . (The Evolving Scholar; Vol. 3). TU Delft OPEN Publishing. https://doi.org/10.59490/mg.121

Important note
To cite this publication, please use the final published version (if applicable).
Please check the document version above.

Copyright
Other than for strictly personal use, it is not permitted to download, forward or distribute the text or part of it, without the consent of the author(s) and/or copyright holder(s), unless the work is under an open content license such as Creative Commons.

Takedown policy
Please contact us and provide details if you believe this document breaches copyrights.
We will remove access to the work immediately and investigate your claim.

This work is downloaded from Delft University of Technology.
For technical reasons the number of authors shown on this cover page is limited to a maximum of 10.



Proceedings of the 5th Symposium on the Dynamics and Control of Single-Track Vehicles

Bicycle and Motorcycle Dynamics 2023, October 18-20, Delft, The Netherlands

Jason K. Moore, Edwin de Vries, Andrew Dressel, Leila Alizadehsaravi

TU Delft

TU Delft OPEN

Proceedings of the 5th Symposium on the Dynamics and Control of Single-Track Vehicles

Bicycle and Motorcycle Dynamics 2023, October 18-20, Delft, The Netherlands

Published by:

TU Delft OPEN Publishing



Editors:

Jason K. Moore[1]
Edwin de Vries[2]
Andrew Dressel[3]
Leila Alizadehsaravi[4]



DOI:

https://doi.org/10.59490/mg.121

ISBN 978-94-6366-958-0

Cover:

Rixt Tuinstra, TU Delft Media

Jason K. Moore[1]
Edwin de Vries[2]
Andrew Dressel[3]
Leila Alizadehsaravi[4]

Contact:

[1] Delft University of Technology

j.k.moore@tudelft.nl
orcid: 0000-0002-8698-6243

[2] Cruden B.V.

[3] University of Wisconsin-Milwaukee

orcid: 0000-0003-0322-9815

[4] Delft University of Technology

orcid: 0000-0002-9654-7064



This work is licensed under a Creative Commons Attribution 4.0 International (CC BY 4.0) licence © 2024 published by TU Delft OPEN Publishing on behalf of the authors.

Design & layout:

Afra Knaap, Rixt Tuinstra

Citation:

Moore, J.K., Vries, E. de, Dressel, A., & Alizadehsaravi, L. (Eds.). (2024). *Proceedings of the 5th Symposium on the Dynamics and Control of Single-Track Vehicles: Bicycle and Motorcycle Dynamics 2023, October 18-20, Delft, The Netherlands*. BMD. TU Delft OPEN Publishing.

Keywords:

bicyle, motorcycle, single-track vehicle, dynamics, control

Conflict of Interest

Editorial decisions on papers where an author was a proceedings editor were made by editors that did not author the paper. Reviewers were assigned abstracts and papers from different institutions and to non-collaborators to minimize conflicts of interest. Reviewers are kept anonymous to avoid authors influencing the review outcomes. Any conflicts of interest of the authors are stated in their abstract or paper.

Data Access Statement

Data supporting the findings is available upon request to the author, at the authors' discretion. No data availability requirements were imposed on the authors.

Use of AI

No restrictions or reporting of the use of artificial intelligence in the creation of the abstracts and articles was imposed. Listed abstract and paper authors are accountable for the accuracy and integrity of their work.

Peer Review

The papers in this conference book have been peer-reviewed, with open peer review reports and anonymous reviewers. The editors and the publisher would like to thank reviewers for their time and effort.

Disclaimer

Every attempt has been made to ensure the correct source of images and other potentially copyrighted material was ascertained, and that all materials included in this book have been attributed and used according to their license. If you believe that a portion of the material infringes someone else's copyright, please contact j.k.moore@tudelft.nl.

Foreword

Jason K. Moore, Edwin de Vries, Andrew Dressel, & Leila Alizadehsaravi

Dear Readers,

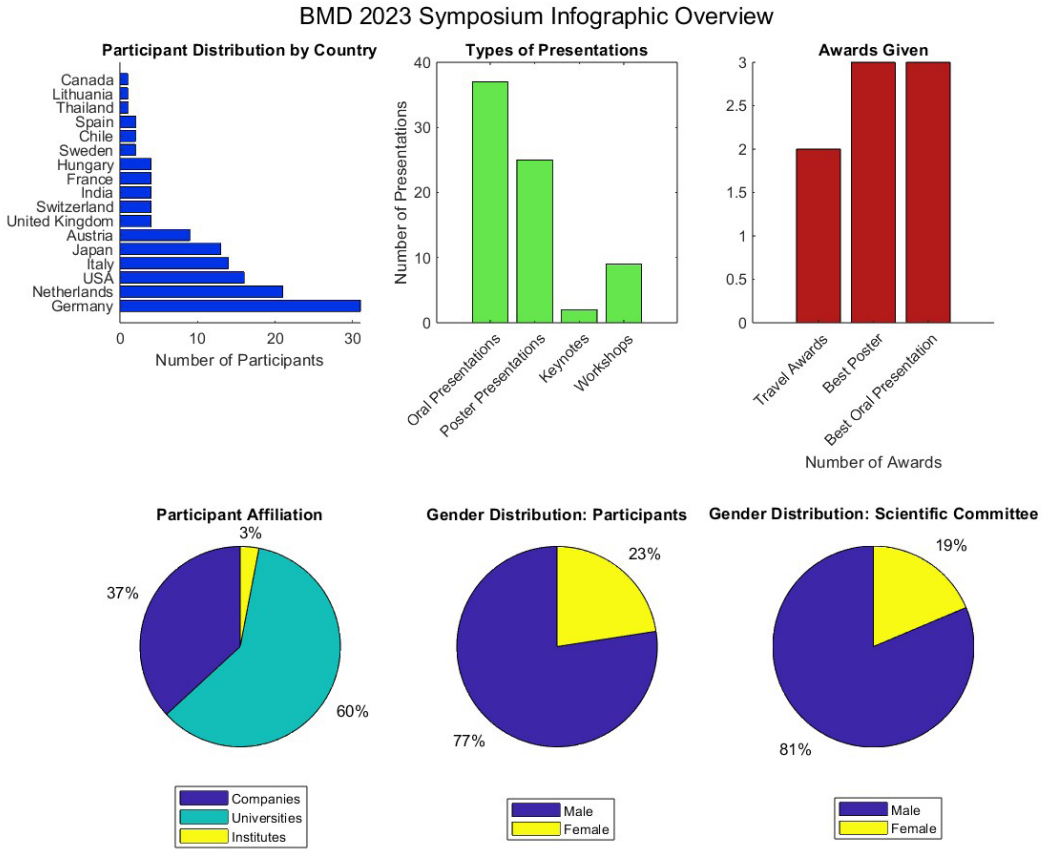
The first Bicycle and Motorcycle Dynamics conference was held in Delft, The Netherlands in the fall of 2010. The conference was initiated by Dr. Arend Schwab and Dr. Jaap Meijaard as a way to both connect and reconnect researchers who had interests in the dynamics and control of single-track vehicles. In 2023, the conference returned to Delft after a decade of successful and growing prior instances in Narashino, Japan (2013), Milwaukee, USA (2016), and Padua, Italy (2019). At each conference, we ask the accepted presenters to draft a paper for sharing among the conference attendees. We did this, in part, to reflect tradition from similar historical conferences in the field, but those pre-internet conferences also printed a physical bound book of the proceedings for permanent record keeping. We never created a book, but instead provided these papers on a CD or thumb drive for in-conference circulation. Our thumb drive approach meant the papers would unlikely be seen by the wider world and that they could be lost to history. In 2016 and 2019, we partnered with Figshare to host author-consented papers digitally. These are available for anyone to download and are archived permanently, but still did not provide a full record of the conference due to the opt-in nature of the arrangement. For 2023, we partnered with the Delft University of Technology Library's publisher TU Delft OPEN to revive the nature of a true conference proceedings, but with a modern and open twist. All extended abstracts were reviewed by the scientific committee and the accepted abstracts are available digitally on the

online Orvium publishing platform. The abstracts also make up the first chapter of this proceedings book as a complete record of the presented works in 2023. The second chapter of this book contains the submitted and peer-reviewed conference papers. Each paper went through an open peer review process on the Orvium platform under the banner of TU Delft OPEN's "Evolving Scholar" publication. This is the first time we have peer-reviewed and formally published the papers from the conference. Those papers that completed the peer review are included here in full. Prior versions of each paper with the public reviews can be viewed on Orvium. Any rejected abstracts and papers were removed from Orvium and are not included in this book. The Delft University of Technology Library published the proceedings as a digital print-on-demand book and archived the works permanently. All of this required a large effort from many people: library employees, student assistants, reviewers, Orvium developers, and us editors, and we are proud of the result. We hope that you are too and that what you learn from these papers will help forward our science and engineering work into the future.

Sincerely,

The BMD 2023 Editors: Jason K. Moore, Edwin de Vries, Andrew Dressel, and Leila Alizadehsaravi

The following infographic visualizes the participation at the 2023 conference.



List of Contributors

Organizing Committee

- Jason K. Moore [TU Delft]
- Leila Alizadehsaravi [TU Delft]
- Andrew Dressel [University of Wisconsin, Madison]
- Edwin de Vries [Cruden B.V.]

Organizing Volunteers

We thank all of the volunteers who helped before, during, and after the conference.

- Christoph Schmidt [TU Delft]
- Gabriele Dell'Orto [TU Delft]
- Jan Groenhuis [TU Delft]
- Jules Ronné [Uni. Gustave Eiffel]
- Julie van Vlerken [TU Delft]
- Kirsten Dijkman [TU Delft]
- Linda van der Spaa [TU Delft]
- Marten Haitjema [TU Delft]
- Ragnhild Maarleveld [TU Delft]
- Riender Happee [TU Delft]
- Thomas Habing [TU Delft]
- Tim Reuscher [RWTH Aachen]
- Yumiko Henneberry [TU Delft]

Publishing Support

We thank TU Delft OPEN and Orvium for bringing the proceedings publication to life and providing a platform for reviewing and digital sharing.

- Nicoleta Nastase [TU Delft OPEN]
- Joke Dales [TU Delft OPEN]
- Animesh Sahoo [TU Delft OPEN]
- Frederique Belliard [TU Delft OPEN]
- Antonio Romero [Orvium]
- Roberto Rabasco [Orvium]

Scientific Committee

We thank the scientific committee for reviewing all of the abstract submissions and also to those who participated in the paper reviews.

- Alberto Doria [University of Padua]
- Alejandra Polanco [University Gustave Eiffel]
- Alessandro Beghi [University of Padua]
- Alka Gupta [Harley Davidson]
- Arend Schwab [Delft University of Technology]
- Arno Stienen [Delft University of Technology]
- Atanas Popov [University of Nottingham]
- Eric Maris [Radboud University]
- Gianpiero Mastinu [Polytechnic University of Milan]
- Ichiro Kageyama [Nihon University]
- Jaap Meijaard [Delft University of Technology]
- James Sadauckas [Trek Bicycle Corporation]
- Jim Brendelson [Cycle Scientific LLC]
- Jodi Kooijman [Swugo B.V.]
- Jürgen Wrede [Pforzheim University]
- Linda van der Spaa [Delft University of Technology]
- Manfred Plöchl [TU Wien]
- Marco Dozza [Chalmers University of Technology]
- Marco Pezzola [MUNER, Alma Mater Studiorum – Università di Bologna]
- Matteo Corno [Polytechnic University of Milan]
- Matteo Massaro [University of Padua]
- Mattia Bruschetta [University of Padua]
- Michael Taylor [Harley Davidson]
- Mont Hubbard [University of California, Davis]
- Nicolay Ruffo [VI-grade Srl]
- Riender Happee [Delft University of Technology]
- Roberto Lot [University of Padua]
- Sam Brockie [Delft University of Technology]
- Simos Evangelou [Imperial College London]

- Siri Berge [Delft University of Technology]
- Stephen Cain [West Virginia University]
- Tomoya Kitani [Shizuoka University]

Sponsors

We thank all of the conference sponsors for financial, material, and labor support.

- Department of Biomechanical Engineering, Delft University of Technology [Institutional]
- TU Delft OPEN Publishing [Institutional]
- Dynamotion [Silver]
- Cycle Scientific LLC [Bronze]
- UWM Bicycle and Motorcycle Engineering Research Lab [Bronze]
- Abeona Cycling
- Bosch eBike Systems
- Ligfiets.net
- Piet Noordzij
- Pforzheim University of Applied Sciences: Institute for Smart Bicycle Technology

Content

Chapter 1: Extended Abstracts 24-148

O01 Identification and Modeling of a Mountain Bike Front Suspension Subsystem Equipped with a Telescopic Fork and Tire Damping 26
Noah Schoeneck, James Sadauckas, and Mark Nagurka

O02 Improvement of Cycling Efficiency for Drivetrains with Elasticity 29
W. den Boer

O03 Bicycle fork longitudinal vibrations induced by front braking 31
Matteo Formentini, Enrico Giolo, Edoardo Marconi, and Alessandro Rovarin

O04 Balancing Standstill Motorcycles by Steering Control with Feedback Delay 33
Hanna Zsofia Horvath and Denes Takacs

O05 On the Development of a Path Tracking Controller by combining Optimal Preview 35
David Gabriel, Daniel Baumgärtner, and Daniel Görges

O06 A self-stable remote control bicycle design and implementation as a teaching project 37
Álvaro Varela, Pablo Rubial, Eduardo Sobrino, Urbano Lugrís, and Emilio Sanjurjo

O07 Using a steer-into-the-fall based control law to stabilize a pedelec 39
Yannick Hanakam, Jürgen Wrede, Martin Pfeiffer, and Stefan Hillenbrand

O08 Instrumented Bicycle for Experimental Investigation of Braking Dynamics including Front Brake induced Rear Wheel Lift Up 41
J. Skatulla, O. Maier, and S. Schmidt

O09 Development of a Hardware-in-the-Loop Test Bench for Validation of an ABS System on an e-Bike 43
N. Ramosaj, C. Fusco, and E. Viennet

O10 Enhanced Braking of E-Scooters 45
F. Klinger, J. Edelmann, and M. Plöchl

O11 A Review on Test Method Development for Motorcycle Autonomous Emergency Braking Systems 47
Nora Leona Merkel

O12 Essential Bicycle Dynamics for Microscopic Traffic Simulation: An Example Using the Social Force Model 50
Christoph M. Schmidt, Azita Dabiri, Frederik Schulte, Riender Happee, and Jason K. Moore

O13 Investigation of the Applicability of a Motorcyclist Model for Trajectory Prediction in Real Traffic 51
F. Scherer and M. Eschinger

O14 Trajectory Prediction for Powered Two Wheelers with Deep Learning 53
Karl Ludwig Stolle, Anja Wahl, and Stephan Schmidt

O15 A mobile recording system featuring high-precision time synchronization 55
Takuro Sone, Takehuro Maeda, and Tomoya Kitani

O16 Data Collection for Learning the Dynamics and Control of an Electric Unicycle 57
Levente Mihályi, Xunbi A. Ji, Gábor Orosz, and Dénes Takács

O17 Dynamics of a Manual Wheelchair and User During Propulsion 59
Kathylee Pinnock Bradford, Meegan G. Van Straaten, Omid Jahanian, Melissa M.B. Morrow, and Stephan M. Cain

O18 Experimental assessment of the effect of cyclist's posture on comfort during time-trial events on road cycling 61
A. Polanco, D. Suarez, A. Doria, and L. Munoz

Content

O19 Evaluation of Lane Change Maneuvers on a Dynamic Motorcycle Riding Simulator Utilizing a Rider Learning Input 63
Raphael Pleß, Sebastian Will, and Nora Leona Merkel

O20 Can a bicycle be balanced using an optimal feedback control mechanism that ignores the sensorimotor delay? 65
Glykeria Sdoukopoulou and Eric Maris

O21 Planar Dynamics of a Motorcycle: Parameter Sensitivity of Ride Comfort to Engine Mounting System Nonlinearities..... 67
Sudhir Kaul

O22 Theoretical and experimental findings for an tyre-road friction potential estimator for motorcycles 69
C. Ott, F. Klinger, and M. Plöchl

O23 Indoor measurement of the lateral characteristics of a cargo bicycle tire..... 71
G. Dell'Orto, F.M. Ballo, G. Mastinu, R. Happee, and J.K. Moore

O24 Thermal model for bicycle tire internal temperature evaluation in various contact conditions 73
F. Farroni, G. Napolitano Dell'Annunziata, M. Ruffini, G. Dell'Orto, and G. Mastinu

O25 Radial Stiffness and Damping of Mountain Bike Tires Subject to Impact Determined Using the Coefficient of Restitution 75
J. Sadauckas, N. Schoeneck, and M. Nagurka

O26 Measuring vertical tyre stiffness of bicycle tires 78
M. Rothhämel

O27 Experimental assessment of SST evaluation as handling quality indicator 80
Jules Ronné, Laura Dubuis, and Thomas Robert

O28 Adapting a variable stability mechanism for a tilting tricycle from the delta to the tadpole wheel configuration 82
Andrew Dressel and Jason Moore

O29 Objective evaluation of handling and stability of a bicycle 85
Marcel Keyser, Edoardo Marconi, Matteo Formentini, and Enrico Giolo

O30 Modeling of a Bicycle Cargo Trailer with Magic Formula Tire model for Vehicle Dynamics 87
Marius Miller, Markus Pfeil, Ralph Kennel, and Raphael Murri

O31 Lap Time Sensitivity Analyses in High-Powered Electric Motorcycles 89
Louis Flanagan and Atanas A. Popov

O32 Validation of a bicycle simulator based on objective criteria 91
Donaji Martinez Garcia, Kilian Gröne, Martin Fischer, Min Zhao, and Melina Bergen

O33 Towards Black-Box Dynamic Modelling within Learning-based Nonlinear Model 93
Francesco Bianchin, Enrico Picotti, and Mattia Bruschetta

O34 Evaluating bicycle frame loads through semi-analytical multibody simulation methods 95
J. Bolk and B. Corves

O35 Parameterized and validated equations of motion for a tadpole style cargo tricycle..... 97
Clemens Groß and Steffen Müller

O36 BRiM: A Modular and Extensible Open Source Framework for Creating Bicyle-Rider Models.... 99
Timo J. Stienstra, Samuel G. Borckie, and Jason K. Moore

O37 On the fundamental dynamics of rolling wheels: an Appellian approach..... 101
Máté B. Vizi, Gábor Orosz, Dénes Takács, Gábor Stépán

Content

P01 A bicycle can be balanced by stochastic optimal feedback control but only accurate speed estimates 104

Eric Maris

P02 Position Measuring System for a Motorcycle Using Quad Omnidirectional Cameras..... 106

Junji Hirasawa

P03 OMS: A Software Package for the Minimum-Time Optimal-Control Simulation of Motorcycles . 108

Edoardo Marconi, Matteo Formentini, and Enrico Giolo

P04 Bicycle handling quality perception: mixed effect of stability and manoeuvrability 110

Jules Ronné, Laura Dubuis, and Thomas Robert

P05 Motion cueing utilizing gravity 112

Christian G. Bäverstrand

P06 Modelling Braking and Steering Avoidance Maneuvers for Micromobility..... 114

Tianyou Li, Frederik Bruzelins, and Marco Dozza

P07 Evaluating the handling of a titling tricycle with variable stability..... 116

Floris van Willigen, Andrew Dressel, and Jason Moore

P09 Simulation validation - a new methodological approach applied to motorcycle riding simulators 118

Sebastrian Will, Thomas Hammer, Raphael Pleß, Nora Leona Merkel, and Alexandra Neukum

P10 A Vector-Loop Analysis Approach to Kinematics of Bicycle Steering Geometry 120

A. Suresh, M. Barath, and A. do Rego

P11 A Study of Suspension Geometry for Personal Mobility Vehicles (PMVs) with Inward Tilt Mechanism 121
Tetsunori Haraguchi and Tetsuya Kaneko

P12 Analysis of stopping behaviour of cyclists at a traffic light-controlled intersection using trajectory data 123
Claudia Leschik, Meng Zhang, and Kay Gimm

P13 Analytical expression to calculate the suspension sag of vehicles..... 125
F. Vasquez

P14 Application of tire multiphysical modeling methodologies for the preliminary definition of a racing motorcycle setup 127
M. Ruffini, F. Alberti, D. Andrea, F. Farroni, G. Napolitano Dell'Annunziata, G. Risitano, and D. Milone

P15 Experimental Identification of the Lateral Dynamics of a Steering-assisted Two-wheeled Vehicle 129
Stefano Lovato, Matteo Massaro, and Roberto Lot

P16 Modeling and Implementation of a Reaction Wheel Stabilization System for Low Speed Balance of a Cargo Bicycle 131
Jason K. Moore, Jeswin Koshy Cherian, Björn Andersson, Oliver Lee, and Anders Ranheim

P18 Influence of aerodynamic lift and centre of pressure position in motorcycle stability 133
Benjamin E. Gonzalez T. and Felipe A. Vasquez S.

P19 Balancing Control of a Unicycle Robot with Double Flywheels 135
M. Parnichkun and S. Chantarachit

Content

P20 Influence of Rear Wheel Vertical Displacement and Target Sag on Suspension Performance of a Cruiser Motorcycle 138
K. Peck and J. Sadauckas

P21 2-Skate-Single-Track-Vehicle without Fork-Angle, Trail or Power: Tested for Rideability, Phase-Lag and Steady-State-Lean-Angles 140
Pierre M. Ethier

P23 New design approach for leaf-springs in motorcycles 142
Hannes Fellner

P24 Racebike Dynamics: The Dynamic Racebike State Plot 144
C. One Feichtinger

P25 From Theory to practice: monotoring mechanical power output during wheelchair field and court sports using intertial measurement units 146
Marit P. van Dijk, Marco J.M. Hoozemans, Monique A.M. Berger, and DirkJan H.E.J. Veeger

Chapter 2: Papers 149-464

A mobile recording system featuring high-precision time synchronization 151
Takuro Sone, Takehiro Maeda, and Tomoya Kitani

A Review on the Development of a Test Method for Motorcycle Autonomous Emergency Braking Systems 162
Nora L. Merkel

Adapting a variable stability mechanism for a tilting tricycle from the delta to the tadpole wheel configuration 174
Andrew Dressel and Jason Moore

Analysis of stopping behaviour of cyclists at a traffic light-controlled intersection using trajectory data 183
Claudia Leschik, Meng Zhang, and Kay Gimm

Analytical expression to calculate the suspension stroke and sag of vehicles..... 193
F. Vasquez

Application of tire multi-physical modeling methodologies for the prelimenary definition of a racing motorcycle setup 204
Flavio Farroni, Guido Napolitano Dell'Annunziata, Marco Ruffini, Fabio Alberti, Danilo D'Andrea, Giacomo Risitano, and Dario Milone

Assessment of bicycle experimental objective handling quality indicators 216
Jules Ronné, Laura Dubuis, and Thomas Robert

Bicycle frame load estimation using semi-analytical multi-body simulation methods..... 227
Johannes Bolk and Burkhard Corves

BRiM: A Modular Bicycle-Rider Modeling Framework 237
Timótheüs J. Stienstra, Samuel G. Brockie, and Jason K. Moore

Development of a Hardware-in-the-Loop Test Bench for Validation of an Anti-lock Braking System on an e-Bike 249
N. Ramosaj, C. Fusco, and E. Viennet

Essential Bicycle Dynamics for Microscopic Traffic Simulation: An Example Using the Social Force Model 262
Christoph M. Schmidt, Azita Dabiri, Frederik Schulte, Riender Happee, and Jason K. Moore

Evaluation of Lane Change Maneuvers on a Dynamic Motorcycle Riding Simulator Utilizing a Rider Leaning Input 274
Raphael Pleß, Sebastian Will, Nora L. Merkel, and Alexandra Neukum

Content

Identification and Modeling of a Mountain Bike Front Suspension Subsystem Equipped with a Telescopic Fork and Tire Damping 286
Noah Schoeneck, James Sadauckas, and Mark Nagurka

Improvement of Cycling Efficiency for Drivetrains with Elasticity 298
Willem den Boer

Influence of aerodynamic lift and centre of pressure position in motorcycle stability 309
Benjamin E. Gonzalez and Felipe A. Vasquez

Influence of Available Rear Wheel Travel and Target Sag on Suspension Performance of a Cruiser Motorcycle 319
K. Peck and J. Sadauckas

Instrumented Bicycle for Experimental Investigation of Braking Dynamics including Front Brake induced Rear Wheel Lift Up 332
J. Skatulla, O. Maier, and S. Schmidt

Investigation of the Applicability of a Motorcyclist Model for Trajectory Prediction in Real Traffic 344
F. Scherer and M. Eschinger

Measuring vertical tyre stiffness of bicycle tyres 357
Malte Rothhämel

Modeling of a Bicycle Cargo Trailer with Magic Formula Tire Model for Vehicle Dynamics Simulation 366
Marius Miller, Markus Pfeil, Ralph Kennel, and Raphael Murri

Modelling, parameterizing and validating the motion of a tadpole style cargo tricycle with real world experiments 378
Clemens Groß and Steffen Müller

On the Development of a Path Tracking Controller by combining Optimal Preview Control and Pursuit Control Methods 388
David Gabriel, Daniel Baumgärtner, and Daniel Görges

Position Measuring System for a Motorcycle Using Quad Omnidirectional Cameras 400
Junji Hirasawa

Simulator validation - a new methodological approach applied to motorcycle riding simulators 407
Sebastian Will, Thomas Hammer, Raphael Pleß, Nora Leona Merkel, and Alexandra Neukum

Systematic Literature Review: Motorcycle Simulators 416
Dorothea Wildner and Frank Diermeyer

The History of Two-wheeled Vehicle Dynamics in Japan and Subsequent Trends 428
Ichiro Kageyama

Trajectory Forecasting for Powered Two Wheelers by Roll Angle Prediction with an LSTM Network 441
Karl Ludwig Stolle, Anja Wahl, and Stephan Schmidt

Validation of a bicycle simulator based on objective criteria 453
Donaji Martinez Garcia, Kilian Gröne, Martin Fischer, Min Zhao, and Melina Bergen

Chapter 1:

Extended Abstracts

The Evolving Scholar (2023)

https://doi.org/10.24404/63fbcb2b97997d1e1509baff

Bicycle and Motorcycle Dynamics 2023
Symposium on the Dynamics and Control of Single Track Vehicles
18 – 20 October 2023, Delft University of Technology, The Netherlands

Type of the Paper: Extended Abstract

Identification and Modeling of a Mountain Bike Front Suspension Subsystem Equipped with a Telescopic Fork and Tire Damping

Noah Schoeneck[1*], James Sadauckas[2], and Mark Nagurka[3]

[1]Vehicle Measurements Group, Harley-Davidson Motor Company, Yucca AZ 86438, USA; noah.schoeneck@harley-davidson.com
[2]Trek Performance Research, Trek Bicycle Corporation, Waterloo, WI, 53594, USA; jim_sadauckas@trekbikes.com; ORCID 0000-0002-6055-9047;
[3]Professor Emeritus, Department of Mechanical Engineering, Marquette University, Milwaukee, WI 53233, USA; mark.nagurka@marquette.edu
*corresponding author.

Name of Editor: Jason Moore
Submitted: 26/04/2023
Accepted: 13/04/2023
Published: 26/04/2023
Citation: Schoeneck, N., Sadauckas, J. & Nagurka, M. (2023). Identification and Modeling of a Mountain Bike Front Suspension Subsystem Equipped with a Telescopic Fork and Tire Damping. The Evolving Scholar - BMD 2023, 5th Edition.
This work is licensed under a Creative Commons Attribution License (CC-BY).

Abstract:

A key component in the mountain bike industry is the telescopic front suspension, which offers the advantage of improved performance when traversing obstacles and rough terrain and during high impact landings. Over the last three decades these suspensions have become more widely adopted and more complex in design. Despite their popularity, there has been limited reported literature focused on the behavior of the telescopic front suspension as a dynamic subsystem in models commonly used in both the motorcycle and automotive industries, e.g., half moto and quarter car models. This paper presents a system identification and modeling approach that promises a deeper understanding of the dynamic behavior of vehicles with telescopic front suspensions.

The quarter car model suspension consists of a set of springs and dampers that act between the body and the wheel as well as another set that acts between the wheel and ground. To reflect the common airborne event that occurs with a mountain bike front suspension subsystem, the half moto model has been modified to explore post-impact behavior. This approach is distinct from the more traditional approach in the literature with the tire starting at rest on the ground.

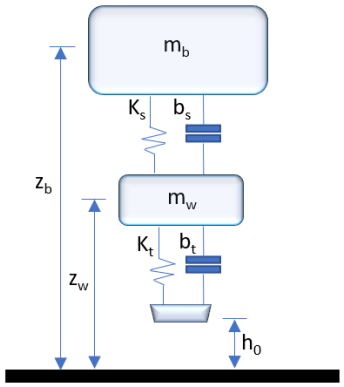


Figure 1. Half moto free body diagram

Figure 1 shows the free body diagram for a half moto impact model, where m_b is the mass of the body, m_w is the mass of the wheel assembly, k_s and b_s are the stiffness and damping coefficients of the suspension, k_t and b_t are the stiffness and damping coefficients

© 2023 Schoeneck, N., Sadauckas, J. & Nagurka, M. published by TU Delft OPEN on behalf of the authors.
ISSN: 2667-2812

of the tire, z_w is wheel displacement, z_b is the body displacement, and h_0 is the initial height for impact. This height is used to calculate the velocity at impact, v_i, an initial velocity condition for z_b and z_w of the model.

$$v_i = \sqrt{2gh_0} \tag{1}$$

The equations of motion for the model of Figure 1 are

$$m_b\ddot{z}_b = k_s(z_w - z_b) + b_s(\dot{z}_w - \dot{z}_b) - m_b g \tag{2}$$

$$m_w\ddot{z}_w = -k_s(z_w - z_b) - b_s(\dot{z}_w - \dot{z}_b) + k_t z_w + b_t\dot{z}_w - m_w g \tag{3}$$

To capture the flight, impact, and landing event routinely seen by a mountain bike front-end, a vertical drop test was utilized. The tire starts the test airborne, i.e., above the ground by an appreciable amount (roughly pedestrian curb height). This leads to relatively higher initial impact than the small perturbations, often forced sinusoids, more commonly seen in quarter car literature. Subsequently, depending on the system parameters, the system may actually bounce and leave the ground again before eventually settling into damped oscillation and decay. A vertical drop test sled fixture was developed and fitted with a telescopic mountain bike front suspension and mountain bike tire. Additional weight was added to the fixture sled to approximate the loading of a mountain bike front end with a rider seated on the vehicle.

Measuring and quantifying individual component parameters is a necessary step before a subsystem model can be developed. A mountain bike front end consists primarily of two components – the tire and the front suspension. Measuring tire parameters can be difficult. Because of that, this work builds on previous work by the authors to quantify the tire parameters obtained by a coefficient of restitution approach. The telescopic front suspension stiffness and damping parameters were found utilizing a shock dynamometer.

Eleven simulations were performed to gain a deeper understanding of each parameter's contribution to the overall system. The parameters were varied between linear, bi-linear, non-linear or the parameter was eliminated completely from the model to quantify its effects. The peak sled, suspension, and tire displacements from the simulation were compared to the results obtained from the test fixture. The results show that a purely linear model of the front subsystem can lead to suspension displacement errors on the first peak following impact of 13.1 mm (14%) and 14.2 mm (21%) error on the second peak when compared to the measured data on the test fixture. In addition to large peak displacement errors, the linear system does not accurately predict that the subsystem will come to rest but exhibits an underdamped behavior. A bi-linear simulation produces clear improvements of the signature shape of the curve and no longer acts as an underdamped system. Suspension displacement error of the first impact event matches the error seen in the linear model, but the second peak has an improvement seeing 6.6 mm (10%) of error. Tire displacement has very little error on the first impact event, but under predicts the last two peaks. The non-linear model produces suspension and sled displacements that closely match the test data for the first two peaks. The suspension displacement error of the first peak is 2.5 mm (3%) and 1.5 mm (2%) for the second peak. However, the nonlinear simulation exhibits comparable error to the final valley and peaks in the bi-linear system.

A set of simulations was created to explore the effects of tire damping. There is a differing opinion in the literature if it is appropriate to exclude tire damping in the half moto model because the influence of tire damping on the subsystem is presumed small compared to the suspension. Tire damping provided a modest improvement in peak displacement for both the sled and suspension displacements. The quality of the results and stability of the simulation were improved with the incorporation of tire damping. Suspension velocity and tire displacement both displayed unrealistic ringing if tire damping was excluded from the model.

Comparison of the results from the test fixture and modified half moto model provides a systematic process of testing and validating a mountain bike front subsystem equipped with a telescopic front suspension and damped tire. The drop test used here with an appreciable (curb) drop height has added benefits to other small displacement and/or forced perturbation test fixtures often used in aerospace and agriculture applications in that it has the ability to capture impact routinely encountered in mountain bike riding conditions. The fixture under the test conditions described is able to stroke the suspension to 90% of available fork travel and achieve stroking velocities in excess of 1.5 m/s, which captures fork damping dynamics beyond common dynamometer limits.

References

Arrieta Castro, A. & Rill, G. (2020). *Road Vehicle Dynamics.* Boca Raton: CRC Press.

Carabias Acosta, E., Castillo Aguilar, J.J., Cabrera Carrillo, J. A., Velasco Garcia, J.M., Fernandez, J.P., & Alcazar Vargas, M.G. (2020, June 18). Modeling of Tire Vertical Behavior Using a Test Bench. *IEEE Access, 8*, pp. 106531-106541.

Dixon, J.C. & Mech, F.I. (2007). *The Shock Absorber Handbook.* West Sussex: John Wiley & Sons, Ltd.

© 2023 Schoeneck, N., Sadauckas, J. & Nagurka, M. published by TU Delft OPEN on behalf of the authors.
ISSN: 2667-2812

Huaitao, W., Wu, D., & Feng, W. (2017, May 2). A New Method for Determining Horizontal Impact Load Based on Rotational Speed of Aircraft Wheel in Landing Gear Drop Test. *MATEC Web of Conferences*. doi:10.1051/matecconf/201711403004

Klug, S., Moia, A., & Schnabel, F. (2019). Influence of damper control on traction and wheelie of a full suspension eBike with anti-squat geometry. *Bicycle and Motorcycle Dynamics.* Padova.

Levitt, J.A., & Zorka, N.G. (1991). The Influence of Tire Damping in Quarter Car Active Suspension Models. *Journal of Dynamic Systems, Measurement, and Control*, 134-137.

Maher, D. & Young, P. (2011, March). An insight into linear quarter car model accuracy. *Vehicle System Dynamics, 49*(3), pp. 463-480.

Sadauckas, J., Schoeneck, N., & Nagurka, M. (2023) Radial Stiffness and Damping of Mountain Bike Tires Subject to Impact Determined Using the Coefficient of Restitution. Manuscript submitted for publication.

© 2023 Schoeneck, N., Sadauckas, J. & Nagurka, M. published by TU Delft OPEN on behalf of the authors.
ISSN: 2667-2812

The Evolving Scholar (2023)
https://doi.org/10.24404/63f61b6e019e65a57e5c2066
Bicycle and Motorcycle Dynamics 2023
Symposium on the Dynamics and Control of Single Track Vehicles
18 – 20 October 2023, Delft University of Technology, The Netherlands

Type of the Paper: Extended Abstract

Improvement of Cycling Efficiency for Drivetrains with Elasticity

W. den Boer

Huron Cycling LLC; willem@huroncycling.com

Name of Editor: Jason Moore
Submitted: 28/02/2023
Accepted: 13/04/2023
Published: 26/04/2023
Citation: den Boer, W. (2023). Improvement of Cycling Efficiency for Drivetrains with Elasticity. The Evolving Scholar - BMD 2023, 5th Edition.
This work is licensed under a Creative Commons Attribution License (CC-BY).

Abstract:

Test and modeling results are presented on a bicycle crankset with limited elasticity. Figure 1 depicts the operation principle and photograph of the cranksets. Like record-breaking running shoes, the crankset has spring action, which mitigates the effect of the dead zone during the pedal stroke. Fiber composite leaf springs are inserted inside the hollow carbon crank arms. The crank arms are not directly attached to the crank axle. Instead, sleeve bearings allow the crank arms to rotate by up to about five degrees relative to the crank axle. The rotation is counteracted by the springs and is proportional to applied torque at the pedals.

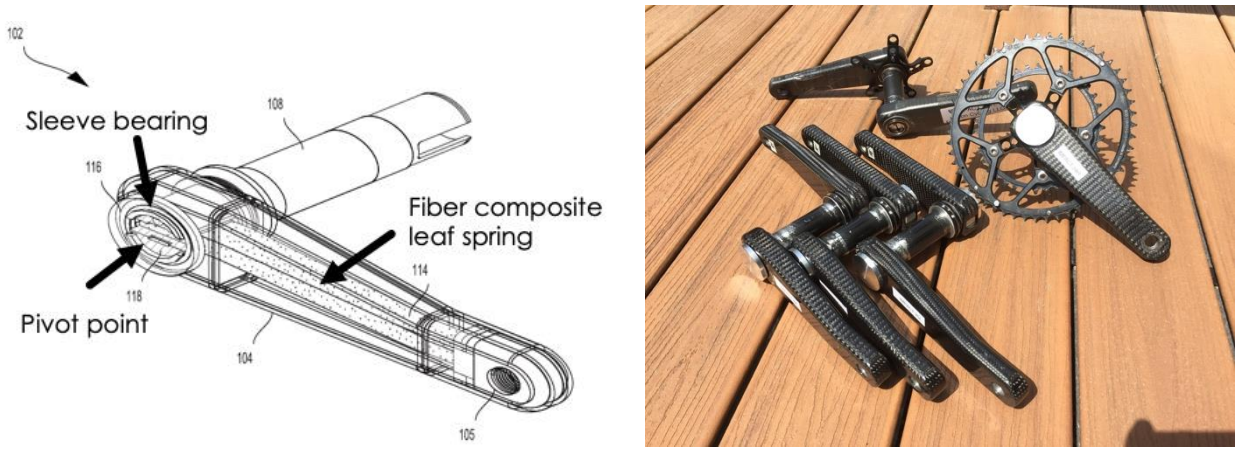


Figure 1. Solidworks drawing and photograph of cranksets with elasticity.

The angle of rotation θ at the crank arms relative to the crank axle is given by:

$$\theta = \frac{\tau}{k} = \frac{P}{\omega k} \quad (1)$$

where τ is the torque from the tangential force F applied at the pedals ($\tau = F*r$ with r the crank length of 175 mm). P is the applied power and ω is the angular velocity of the crank arms. k is a constant representing the degree of elasticity by bending of the leaf spring. For conventional cranksets without intentional elasticity the k value is high (Fairwheel Bikes, 2021), typically > 5000 Nm, so that θ is small. In our novel crankset k = 1000 Nm, resulting in θ = 0.07 rad (4 degrees) and a deflection at the pedals $D = \theta*r$ = 12.25 mm (0.48 inch) for a tangential force of 400 N (90 pounds). Leaf springs with different k values can be used depending on the power and skill of the cyclist.

© 2023 den Boer, W. published by TU Delft OPEN on behalf of the authors.
ISSN: 2667-2812

The novel crankset was installed on a carbon frame bicycle and compared with a conventional crankset with forged aluminum crank arms, while keeping the gear ratio constant at 36/17. To eliminate wind drag factors and changing conditions the testing was performed indoors on a Tacx Neo smart trainer with a slope setting of 3 %. Two power meters were used:

1. A Powertap P1 pedal power meter at left and right pedals to measure input power

2. The internal power meter of the Tacx Neo to measure effective speed

The ratio of effective speed to input power is used as a measure of cycling efficiency. Depending on the maximum torque during the downstroke this ratio is typically a few percent higher than for the conventional crankset (Bastianelli et al., 2019, Den Boer, 2019-1). Details of multiple tests which show consistently improvement of around 2 % at constant power levels of 200 W and cadence of 71 rpm will be presented. Other implementations of elastic drivetrains have also demonstrated improvements in cycling efficiency (Hamamoto, 2019).

To understand the test results computer modeling of bicycle speed and crank arm angular velocity vs. time was performed for different values of k, input power and cadence. The power P applied to the crank arms was assumed to vary sinusoidally from a maximum during the downstroke to a minimum close to zero in the dead spot, in agreement with our measurements of the rotation angle θ vs. time for left and right crank arms.

It is difficult to explain the observed improvement in cycling efficiency from just the dependence of force and angular velocity profiles on k. The improvement is attributed instead to the conversion of irreversible energy losses from twisting in conventional crank arms (Fairwheel Bikes, 2021, ACT Lab 2016) and flexing of the frame (ACT Lab, 2017) under load to reversible energy losses (energy return) with the leaf springs in our crankset. The strain energy losses in the crank arms of conventional cranksets can be 1.6 % at a cadence of 100 rpm (Fairwheel Bikes, 2021) and even higher at lower rpm for the same power input. Energy return from the elastic leaf springs, contributing to torque, provides a qualitative explanation of the observed improvement in efficiency. It depends not only on the k value of the novel crankset, but also on the stiffness of the frame and the conventional crankset used in the comparison. The modeling shows that the expected efficiency improvement with the novel crankset is proportional to τ_0/k, where τ_0 is the maximum torque applied to the pedals during the downstroke. According to equation (1) the improvement is therefore also proportional to P and inversely proportional to ω (i.e. cadence).

In addition to energy return there is another potential benefit of a degree of elasticity in the crank arms: It may reduce the onset of muscle fatigue (Hamamoto, 2019) by reducing the force on the pedals during the first part of the downstroke.

Our measurement of deflection angle θ with rotation sensors has been used to determine the torque profile vs. time. In combination with angular velocity measurement it is therefore a method to measure power at left and right pedals (Den Boer, 2019-2) without relying on strain gauges.

References

ACT Lab (2016), Crank Fatigue Test, https://www.youtube.com/watch?v=7rZ1L6brkNE
ACT Lab (2017), Frame Fatigue with Pedalling Forces Test, https://www.youtube.com/watch?v=8blo6O_KIAs
Bastianelli, B. M., Workman, A. & McGregor, S. (2019, June), Novel Crank with Elastomer Spring Improves Effective Power in Trained Cyclists and Triathletes, *Medicine & Science in Sports & Exercise*, Chicago, 2019, 51(6S):p 942-943, June 2019.
Den Boer, W. (2019-1), US Patent 11,142,281, Cycle Crank Assembly, www.huroncycling.com
Den Boer, W. (2019-2),White Paper IMPACT power meter August 2019: www.huroncycling.com
Fairwheel Bikes (2021), https://blog.fairwheelbikes.com/reviews-and-testing/road-bike-crank-testing/
Hamamoto, Y. (2019), US Patent 10,450,030, Rotational Apparatus and Bicycle provided with same, www.free-power.jp

© 2023 den Boer, W. published by TU Delft OPEN on behalf of the authors.
ISSN: 2667-2812

The Evolving Scholar (2023)

http://dx.doi.org/10.59490/6489dba0d56c14e8d00e85c3

Bicycle and Motorcycle Dynamics 2023
Symposium on the Dynamics and Control of Single Track Vehicles
18–20 October 2023, Delft University of Technology, The Netherlands

Type of the Paper: Extended Abstract

Bicycle fork longitudinal vibrations induced by front braking

Matteo Formentini [1,*], Enrico Giolo [1], Edoardo Marconi [1], Alessandro Rovarin [1]

[1] Dynamotion s.r.l., Italy; matteo.formentini@dynamotion.it; enrico.giolo@dynamotion.it; edoardo.marconi@dynamotion.it, ORCID 0000-0001-8221-4472; alessandro.rovarin@dynamotion.it

[*] corresponding author

Name of Editor: Jason Moore
Submitted: 14/06/2023
Accepted: 26/06/2023
Published: 26/06/2023
Citation: Formentini, M., Marconi, E., Giolo, E. & Rovarin, A. (2023). Bicycle fork longitudinal vibrations induced by front braking. The Evolving Scholar - BMD 2023, 5th Edition. This work is licensed under a Creative Commons Attribution License (CC-BY).

Abstract:

This work deals with the longitudinal vibrations of the front fork of a bicycle that may originate under front braking, reporting novel experimental evidence and proposing interpretative models to gain insights into the possible causes. This phenomenon constitutes a fairly recent problem compared to the century-long history of the bicycle, as it appears linked to the application of disk brakes, and the scientific literature reports a very limited number of studies concerning this topic. (Klug et al., 2021) considers this phenomenon focusing on its implications on brake control, linked to altered system dynamics and estimation problems on the relevant variables. However, fork vibrations also have other negative implications such as reduced rider confidence and comfort, which encourage further investigations. (Skatulla et al., 2022) attempts to identify the cause of these vibrations with a multibody model, and ascribes the problem to a wheel hopping motion. The model indicates that, in the presence of fork vibrations, the average braking force is 33% lower compared to the non-oscillating case, which highlights the importance of a careful study of the phenomenon.

In order to acquire experimental evidence of the phenomenon under study, specific road tests were conducted on a steel-frame carbon-fork bicycle equipped with disk brakes. The bicycle was ridden down a slope and the front brake was applied at speeds between 20 and 10 km/h. The vibrations of the fork were measured using a piezoelectric accelerometer placed in the proximity of the front wheel axle. With the aim of investigating the influence of different components on the onset of the fork vibrations, two

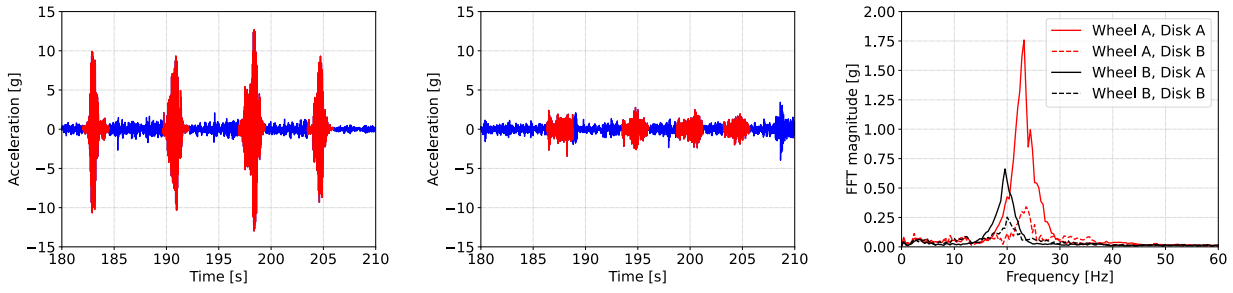


Figure 1: Results of road tests: time-domain acceleration signal measured with wheel A combined with disks A (a) and B (b), and mean Fourier transform of fork longitudinal acceleration in the braking events with the four components sets tested (c).

©2023 Formentini, M., Giolo, E., Marconi, E., & Rovarin, A. published by TU Delft OPEN on behalf of the authors.
ISSN: 2667-2812

 http://dx.doi.org/10.59490/6489dba0d56c14e8d00e85c3



Figure 2: Laboratory set-up for the modal analysis. Green arrow: direction of hammer excitation; red arrows: direction of measured accelerations.

front wheels and two disk brakes were tested, for a total of four different combinations. The main results are reported in Figure 1. Figure 1a and Figure 1b show the longitudinal acceleration measured with one wheel and two different brake disks, braking events are highlighted in red. Figure 1c depicts the mean magnitude of the Fourier transforms of the braking events. Both time- and frequency-domain plots emphasize high-amplitude vibrations when disk A in employed, with maximum FFT magnitude increasing by 3 to 5 times compared with the use of disk B. This suggests an influence of the brake's friction materials on the generation of fork vibrations. Indeed, stick-slip between pads and rotors was already identified as a notable cause of vibrations in bicycles in (Redfield, 2008, 2014). It is also noted that, while the simulations in (Skatulla et al., 2022) show that fork vibrations arise when the braking torque is applied in a step from zero to the maximum torque allowed by tire friction, but do not appear when the braking torque is applied following a lower step or a ramp, the experiments carried out within the present study indicate vibrations are generated even if the brake is applied gradually and up to a moderate degree (far from 'stoppie' or tire-friction limits).

As noted in (Redfield, 2008, 2014), different structural properties of components can act to promote or prevent the occurrence of stick-slip and consequent vibrations. Building upon this observation, a four-degree-of-freedom lumped-element model was devised with the aim of seeking a set of structural parameters that can reduce the sensitivity of the vehicle to different combinations of brake friction materials. In general, stiffer and more damped components mitigate the problem. A modal analysis was performed employing the experimental set-up shown in Figure 2 to investigate the dynamic properties of the front-end components of the bicycle involved in the vibrations observed on the road and estimate the parameters necessary to populate the lumped-element model. This test identified the longitudinal bending mode of the fork at a frequency of about 26 Hz for wheel A and 24 Hz for wheel B. This result is consistent with results reported in the literature for different types of bicycles (Champoux et al., 2007; Doria and Formentini, 2011; Doria et al., 2019) and correlates well with the vibration frequency measured on the road.

References

Champoux, Y., Richard, S., and Drouet, J.-M. (2007). Bicycle structural dynamics. *Sound and vibration*, 41(7):16–25.

Doria, A. and Formentini, M. (2011). Identification of the structural modes of high performance bicycles in the perspective of wobble control. In *2011 ASME International Design Engineering Technical Conferences and Computers and Information in Engineering Conference*.

Doria, A., Marconi, E., and Cialoni, P. (2019). Modal analysis of a utility bicycle from the perspective of riding comfort. In *2019 ASME International Design Engineering Technical Conferences and Computers and Information in Engineering Conference*. American Society of Mechanical Engineers.

Klug, S., Moia, A., Verhagen, A., Görges, D., and Savaresi, S. (2021). The influence of bicycle fork bending on brake control. *Vehicle System Dynamics*, 59(3):375–395.

Redfield, R. (2008). Brake induced vibration in mountain bikes. *Proceeding of the Engineering of Sport, 7th International Sports Engineering Association (ISEA) Conference*.

Redfield, R. (2014). Bike braking vibration modelling and measurement. *Procedia engineering*, 72:471–476.

Skatulla, J., Maier, O., and Schmidt, S. (2022). Fork bending self-oscillation on bicycles influencing braking performance. In *10th Annual International Cycling Safety Conference (ICSC2022)*.

©2023 Formentini, M., Giolo, E., Marconi, E., & Rovarin, A. published by TU Delft OPEN on behalf of the authors.
ISSN: 2667-2812

The Evolving Scholar (2023)

http://dx.doi.org10.59490/647daeb569d559aa327d02f6

Bicycle and Motorcycle Dynamics 2023
Symposium on the Dynamics and Control of Single Track Vehicles
18–20 October 2023, Delft University of Technology, The Netherlands

Type of the Paper: Extended Abstract

Balancing Standstill Motorcycles by Steering Control with Feedback Delay

Hanna Zsofia Horvath [1,*], Denes Takacs [1,2]

[1] Department of Applied Mechanics, Faculty of Mechanical Engineering, Budapest University of Technology and Economics, Budapest, Hungary; hanna.horvath@mm.bme.hu, ORCID 0000-0002-9427-3565, takacs@mm.bme.hu, ORCID 0000-0003-1226-8613
[2] ELKH-BME Dynamics of Machines Research Group, Budapest, Hungary;
[*] corresponding author

Name of Editor: Jason Moore
Submitted: 05/06/2023
Accepted: 05/06/2023
Published: 21/06/2023
Citation: Horvath, H. & Takacs, D. (2023). Balancing Standstill Motorcycles by Steering Control with Feedback Delay. The Evolving Scholar - BMD 2023, 5th Edition.
This work is licensed under a Creative Commons Attribution License (CC-BY).

Abstract:

In the development of autonomous vehicles, engineers are facing fascinating but complex tasks. The motion control of vehicles provides many challenges, even in the case of cars, but these challenges are more complicated for motorcycles. For example, balancing single-track vehicles is not straightforward at zero longitudinal speed; many exercises are also needed for humans to learn the so-called track-stand trick.

In this study, we focus on the linear stability of a riderless self-driving motorcycle, considering zero longitudinal speed. We design a linear state feedback steering controller to stabilize the motorcycle in the vertical position. For this, we use a spatial mechanical model that is based on the Whipple bicycle model (Whipple, 1899). This spatial mechanical model consists of four rigid bodies: the chassis, the fork, the front and the rear wheels, see Figure 1(a).

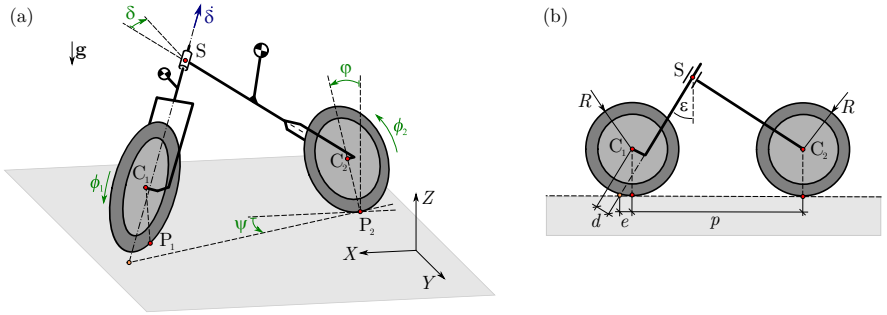


Figure 1. (a) Mechanical model of the motorcycle, (b) relevant geometric parameters in side view ($\psi = 0$, $\varphi = 0$ and $\delta = 0$).

To describe the configurational space, one has to choose seven generalized coordinates. Let us choose X and Y as the coordinates of the center point C_2 of the rear wheel, ψ as the yaw angle, φ as the lean angle, δ as the steering angle, ϕ_1 and ϕ_2 as the rotational angles of the front and the rear wheels around their own axes. In this study, we focus on the steering geometry; hence, the trail e, the rake angle ε and the fork offset d play key roles in the analysis, see Figure 1(b).

©2023 Horvath, H. Z. & Takacs, D. published by TU Delft OPEN on behalf of the authors.
ISSN: 2667-2812

Considering the pure rolling of the wheels, four scalar kinematic constraining equations can be formulated. Since our goal is to stabilize the motorcycle for zero longitudinal speed, the rotational speed of the rear wheel is also considered to be zero: $\dot{\phi}_2 = 0$. The governing equations are derived with Kane's method (Kane, 1985) for which we choose the lean rate and the steering rate as pseudovelocities (i.e., $\sigma_1 = \dot{\varphi}$ and $\sigma_2 = \dot{\delta}$). For zero longitudinal speed, the linearized equations of motion can be written as $\mathbf{M}\ddot{\mathbf{x}} + \mathbf{K}\mathbf{x} = \mathbf{Q}$, where $\mathbf{M}$ is the mass matrix, $\mathbf{K}$ is the stiffness matrix, $\mathbf{x} = [\varphi \quad \delta]^{\mathrm{T}}$ and $\mathbf{Q} = [0 \quad M^{\mathrm{s}}]^{\mathrm{T}}$ with internal steering torque M^{s}. The above described governing equations agree with the literature (Meijaard, 2007). As a first step, we use a simple linear state feedback controller with feedback delay τ:

$$M^{\mathrm{s}}(t,\tau) = -P^{\mathrm{s}}_{\varphi}\varphi(t-\tau) - P^{\mathrm{s}}_{\delta}\delta(t-\tau) - D^{\mathrm{s}}_{\varphi}\dot{\varphi}(t-\tau) - D^{\mathrm{s}}_{\delta}\dot{\delta}(t-\tau)\,, \tag{1}$$

where P^{s}_{φ} and P^{s}_{δ} are proportional control gains for the lean and the steering angles, D^{s}_{φ} and D^{s}_{δ} are derivative control gains for the lean and the steering rates, respectively.

By considering zero feedback delay, i.e., $\tau = 0$, the stability boundaries can be analyzed analytically. We substitute $M^{\mathrm{s}}(t,0)$ into the equations of motion and derive the characteristic equation in the polynomial form of $b_0\lambda^4 + b_1\lambda^3 + b_2\lambda^2 + b_3\lambda + b_4 = 0$. According to the Routh-Hurwitz stability criteria, all coefficients of the characteristic equation and the third principal matrix of the Hurwitz matrix H_3 have to be positive. In Figure 2(a), the analytically obtained stability boundaries and the stable region are plotted in the plane of control gains P^{s}_{φ} and D^{s}_{φ}. The other two control gains are fixed, i.e., $P^{\mathrm{s}}_{\delta} = 100\,\mathrm{Nm}$ and $D^{\mathrm{s}}_{\delta} = 10\,\mathrm{Nms}$ and geometric parameters are based on a small-scale experimental rig (Szabo, 2021).

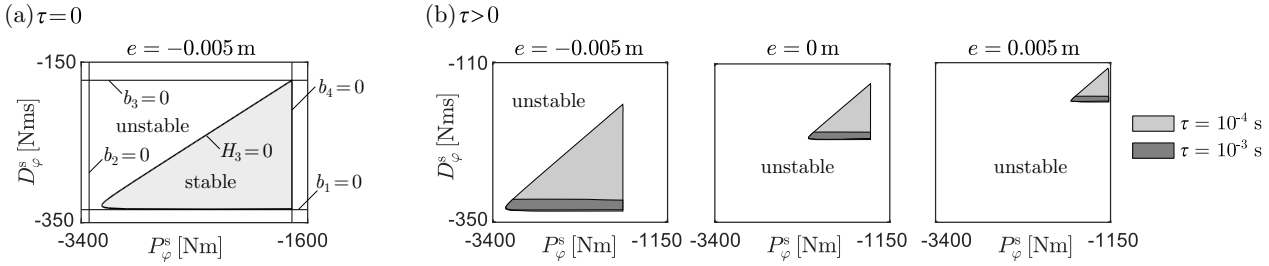


Figure 2. (a) Stability boundaries for $\tau = 0$ and $e = -0.005\,\mathrm{m}$, (b) stability charts for $\tau > 0$ and for different trail values.

When the time delay is taken into account, i.e., $\tau > 0$, the stability charts can be constructed with the help of semi-discretization (Insperger, 2011). The stable domains are shaded by gray in Figure 2(b) for $\tau > 0$ and for negative, zero and positive trail values, respectively. It is shown that the presence of a small time delay already restricts the stable domain of the control gains significantly. More importantly, having a negative trail increases the stable domain. Namely, in contrast to the requirements of the high speed stability of the motorcycle, the negative trail is beneficial for the balancing task. The experimental validation of the theoretical results is a future task, as like as the nonlinear analysis of the motorcycle balancing task.

Acknowledgments: The research is supported by the National Research, Development and Innovation Office under grant no. NKFI-128422, 2020-1.2.4-TET-IPARI-2021-00012 and partly supported by the Janos Bolyai Research Scholarship of the Hungarian Academy of Sciences. Supported by the UNKP-22-5-BME-314, UNKP-22-3-II-BME-101 New National Excellence Program of the Ministry for Innovation and Technology from the source of the National Research, Development and Innovation Fund.

References

Kane, T. R., & Levinson, D. A., (1985). *Dynamics: Theory and Applications*. McGraw-Hill.

Meijaard, J. P., Papadopoulos, J. M., Ruina, A. & Schwab, A. L. (2007). Linearized Dynamics Equations for the Balance and Steer of a Bicycle: A Benchmark and Review. *Proc. of Royal Society A*, 1955–1982.

Insperger, T. & Stepan, G., (2011). *Semi-discretization for Time-Delay Systems*. Springer, New York.

Szabo, A., Horvath, H. Z., & Takacs, D. (2021, December 12-15). Simplified mechanical model for balancing a motorbike with steering at zero speed. *ECCOMAS Thematic Conference on Multibody Dynamics*, Budapest, Hungary.

Whipple, F. J. W. (1899). The Stability of the Motion of a Bicycle. *Quart. J. Pure Appl. Math.*, 312–348.

©2023 Horvath, H. Z. & Takacs, D. published by TU Delft OPEN on behalf of the authors.
ISSN: 2667-2812

The Evolving Scholar (2023)

http://dx.doi.org/10.24404/63fc7fe222b9278b7d0866f9

Bicycle and Motorcycle Dynamics 2023
Symposium on the Dynamics and Control of Single Track Vehicles
18–20 October 2023, Delft University of Technology, The Netherlands

Type of the Paper: Extended Abstract

On the Development of a Path Tracking Controller by combining Optimal Preview Control and Pursuit Control Methods

David Gabriel [1,*], Daniel Baumgärtner [1], Daniel Görges [2]

[1] Bosch eBike Systems, Robert Bosch GmbH, Gerlingen-Schillerhöhe, Germany; david.gabriel@de.bosch.com
[2] Department of Electrical & Computer Engineering, University of Kaiserslautern, Kaiserlautern, Germany;
[*] corresponding author

Name of Editor: Jason Moore
Submitted: 27/02/2023
Accepted: 20/04/2023
Published: 26/04/2023
Citation: Gabriel, D., Baumgärtner, D. & Görges, D. (2023). On the Development of a Path Tracking Controller by combining Optimal Preview Control and Pursuit Control Methods. The Evolving Scholar - BMD 2023, 5th Edition.
This work is licensed under a Creative Commons Attribution License (CC-BY).

Abstract:

In the development of advanced rider assistance systems, a self-driving bicycle or motorcycle can be very helpful. Such a system is not only able to perform more reproducible measurements than a human but can also be used for safety-critical maneuvers. An important aspect when developing a self-driving single-track vehicle is the development of a controller that can stabilize the vehicle and can follow a desired roll angle, steer angle or yaw rate. When such a controller has been implemented, the next step is to develop a path tracking controller so that the vehicle can not only be operated remotely but can also follow a predefined path (important for reproducible measurements).

A simplified cascaded control loop is shown in Fig. 1. For that control loop it is assumed, that the bicycle travels at a constant speed and that the bicycle states are measurable or that an observer exists, which estimates the bicycle state vector from the measured signals.

When using a cascaded controller, the inner loop should be at least 3-4 times faster than the outer loop. Otherwise, performance problems and instabilities of the whole system can occur. As a result, with a slow lateral-dynamics controller, the path-tracking controller must be even slower. In (Gabriel et al., 2022) a lateral dynamics controller was presented, which is able to stabilize the

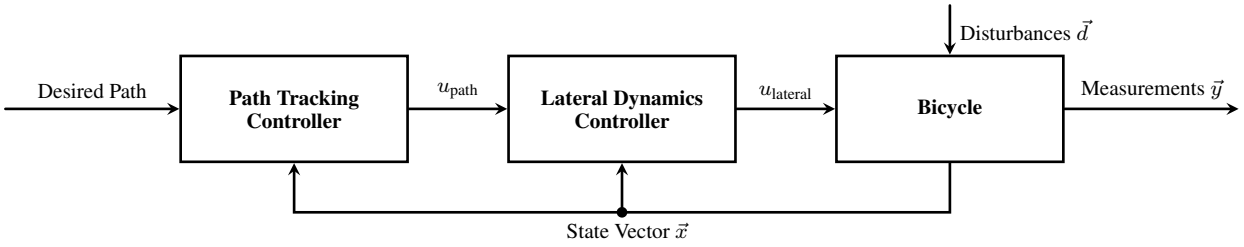


Figure 1. Cascaded control loop for combined stabilization and path tracking control.

©2023 Gabriel, D., Baumgärtner D. & Görges, D. published by TU Delft OPEN on behalf of the authors.
ISSN: 2667-2812

 http://dx.doi.org/10.24404/63fc7fe222b9278b7d0866f9

bicycle and track a desired yaw rate of the bicycle. That controller has a time constant of $\tau \approx 1.5s$, therefore the outer control loop must have a time constant of at least $4.5s$.

Various path-tracking controllers can be found in literature. They can be divided into two groups: On the one hand, there are geometric path tracking controllers such as the "Pure Pursuit Controller" and the "Staneley Controller", which completely neglect the dynamical behavior of the underlying system. Hence, it is important that the cascaded-control loop rule is followed, otherwise the whole system can become unstable (Heredia et al., 2007). On the other hand, there are linear and nonlinear model-based controllers that take the system dynamics into account and usually combine the path-tracking controller and the lateral-dynamics controller in a single controller.

We have several requirements on the path-tracking controller, which none of the existing approaches can fulfill:

- The controller should ensure good tracking behavior despite the relatively slow steering dynamics of the lateral-dynamics controller.
- Tight corners should not be cut. In particular, curves with a minimum radius associated with a bicycle roll angle of $15 - 20°$, should be possible.
- The controller has to use little computing power so that it can be implemented on a microcontroller.

The problem with the geometric controllers is, that they would require huge look-ahead distances to be stable. That would lead to cutting corners. The nonlinear model-based approaches cannot be used because the algorithms usually require a lot of computing power. The linear model-based approaches such as in (Sharp et al., 2001) are very promising, but cannot be used due to the linear path model, which does not allow directional changes of $> 90°$ within the preview distance.

To fulfill all our requirements, methods of the model-based controllers and the geometric controllers must be combined:
Instead of using the Linear Quadratic Integral controller which was proposed in (Gabriel et al., 2022), an Optimal Preview controller (similar to the one in (Sharp et al., 2001)) is used as lateral-dynamics controller. This controller not only receives a reference yaw rate for the current time step but also a reference yaw rate trajectory for a specific preview time. By using a controller with preview, the inner loop becomes faster since it can react to setpoint changes in advance.
The reference yaw rate trajectory must be generated by the path-tracking controller in the outer loop. Therefore, the path-tracking controller must first find an intermediate path which guides the bicycle from the current position back to a target point on the reference path. A reference yaw rate trajectory can be generated from that intermediate path. When the intermediate path is calculated it is important to ensure that the resulting reference yaw rate trajectory is realizable (no jumps in the reference yaw rate) and that the target point is reached with the correct conditions for the following path. Therefore, not only the current position and the target position, but also the current yaw angle and yaw rate as well as the target yaw angle and yaw rate are taken into account when calculating the intermediate path. To calculate an intermediate path with the required boundary conditions quintic polynomials can be used.

The developed path-tracking controller was tested in simulations and experiments. Very good results were achieved, the requirements are fully satisfied, and the bicycle was able to follow specified paths with minimum radii smaller than $2m$.

References

Gabriel, D. Baumgärtner, D., Görges, D. (2022, November), Development and Validation of a Remote-Controlled Test Platform. *International Cycling Safety Conference 2022*.

Heredia, G., Ollero, A. (2007), Stability of autonomous vehicle path tracking with pure delays in the control loop. *Advanced Robotics*, 21(1-2), 23-50

Sharp, R. S., Valtetsiotis (2001), Optimal Preview Car Steering Control. *Vehicle System Dynamics*, 35, 101-117

©2023 Gabriel, D., Baumgärtner D. & Görges, D. published by TU Delft OPEN on behalf of the authors.
ISSN: 2667-2812

The Evolving Scholar (2023)

http://dx.doi.org/10.24404/63fcdab29ec79b6496a2a385

Bicycle and Motorcycle Dynamics 2023
Symposium on the Dynamics and Control of Single Track Vehicles
18–20 October 2023, Delft University of Technology, The Netherlands

Type of the Paper: Extended Abstract

A self-stable remote control bicycle design and implementation as a teaching project

Álvaro Varela [1], Pablo Rubial [1], Eduardo Sobrino [1], Urbano Lugrís [2], Emilio Sanjurjo [2,*]

[1] University of A Coruña, Ferrol, 15403, A Coruña, Spain; alvaro.varela2@udc.es, p.rubialy@udc.es, e.scortes@udc.es
[2] Laboratorio de Ingeniería Mecánica, Campus Industrial de Ferrol, CITENI, University of A Coruña, Ferrol, 15403, A Coruña, Spain; urbano.lugris@udc.es, ORCID 0000-0002-3537-9597; emilio.sanjurjo@udc.es, ORCID 0000-0002-3024-911X
[*] corresponding author

Name of Editor: Jason Moore
Submitted: 27/02/2023
Accepted: 13/04/2023
Published: 26/04/2023
Citation: Varela, Á., Rubial, P., Sobrino, E., Lugrís, U. & Sanjurjo, E. (2023). A self-stable remote control bicycle design and implementation as a teaching project. The Evolving Scholar - BMD 2023, 5th Edition.
This work is licensed under a Creative Commons Attribution License (CC-BY).

Abstract:

The Polytechnic School of Engineering of Ferrol, from the University of A Coruña, has been increasing the amount of practical teaching for their engineering students. Within this framework, an optional course, called Interdisciplinary Project, started in the academic year 2019-2020. In this course, which lasts two semesters on the last year of the degree, the students have to address an engineering problem, starting from a theoretical study, and finishing with a solution to the problem.

During the 2021-2022 academic year, the topic consisted in the development of a remote control bicycle. From the teaching viewpoint, the project included several interesting topics, such as mechanical design, control theory, estimation theory, manufacturing, etc. In addition, the problem is interesting due to its possible applications, such as autonomous motorcycles, or steer-controlled narrow-track tilting vehicles, to name a few.

The main aim for this course was the development of a remote control bicycle, using exclusively the steering to keep the balance. The idea is that the bicycle could be controlled with two signals: one would provide the longitudinal control (i.e.: increasing or reducing the speed), and the other would provide the heading control. In order to fulfill this, the main challenge is to achieve the lateral stability of the vehicle.

The project started from a Littium Ibiza Dogma electric bicycle, which was lent for one year by Ciclos Roca, a local bicycle shop. This is a conventional pedal-assist e-bike, but it has a manual throttle, which enables for an easy way to control the longitudinal speed of the bicycle when it is transformed into a remote control vehicle. A Futaba 3-channel surface radio system was already available at the beginning of the project.

From the starting point, the students developed the control system, designed the mechanical modifications to be made to the bicycle, and implemented the whole prototype. Since the bicycle was initially lent for one year, no permanent modifications were allowed, and every modification should be reversible. Moreover, since this is "just" a teaching project, the budget should be kept as low as possible.

The design of the control algorithm was inspired in the one used in Maceira et al. (2021), where a linearized Whipple model (see Meijaard et al. (2007)) is combined with an LQR controller. However, in Maceira et al. (2021), the control input was the steering torque, while in this project, the steering angular rate was used instead. This design removed the need for a precisely characterized steering torque model or a steering torque measurement, but it required an additional PI controller instead, in order to achieve the

©2023 Varela, Á., Rubial, P., Sobrino,E., Lugrís, U., & Sanjurjo, E. published by TU Delft OPEN on behalf of the authors.
ISSN: 2667-2812

 http://dx.doi.org/10.24404/63fcdab29ec79b6496a2a385

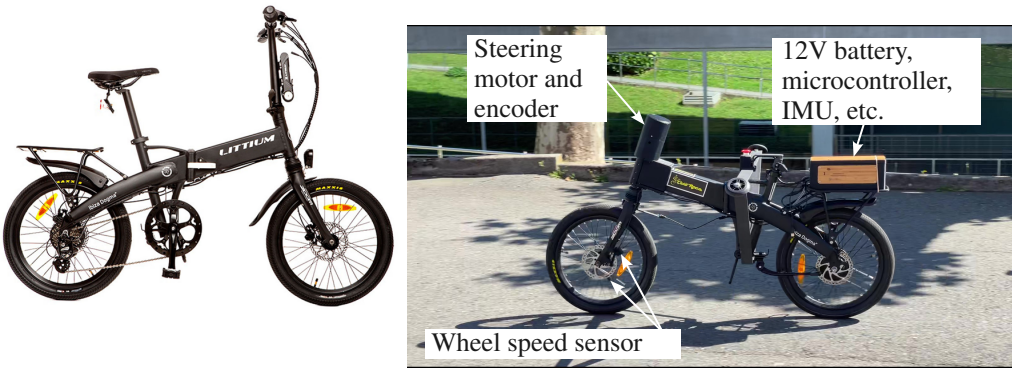


Figure 1. Left: the bicycle in its original state. Right: the remote control bicycle prototype.

proper input speed required by the LQR control. The output of the control system is the roll angle, and the roll angle reference is set by the user through the remote control.

In order to implement this controller, some measurements are required, namely, the longitudinal speed, the roll angle, the roll rate, the steering angle, and the steering rate.

The speed measurement was implemented using a Sharp GP1A57HRJ00F photointerrupter and a small 3d printed flap attached to the front disk brake, which interrupts the sensor beam once per wheel turn. The time between consecutive interruptions provides a good approximation of the longitudinal speed. In order to measure the steering angle and the steering rate, the motor employed to act the steering included an incremental encoder. In this case, a Pololu 37Dx73L 12V DC motor with a gear reduction of 150:1 was selected.

Finally, the main board of the system is an Arduino Uno Wifi rev. 2. This board was selected because, in addition to the microcontroller, it includes an IMU, which is used to measure the roll rate, and it is also employed by the roll angle estimator.

The original bicycle and the final result after the transformation can be seen in Figure 1. Without taking into account the original bicycle (lent for this first year of the project), and the remote control system, the cost of the whole project was kept below 500 euros.

In upcoming years, it is expected to improve steering system by means of a more powerful motor, and a drive with less backlash and capable of handling a greater torque. Also, a braking system will be added. After these improvements are made, it is also expected to add more autonomous capabilities to the vehicle, with automatic obstacle avoidance, or even autonomous driving.

References

Maceira, D., Luaces, A., Lugrís, U., Naya, M. A., and Sanjurjo, E. (2021). Roll angle estimation of a motorcycle through inertial measurements. *Sensors*, 21(19).

Meijaard, J., Papadopoulos, J. M., Ruina, A., and Schwab, A. L. (2007). Linearized dynamics equations for the balance and steer of a bicycle: a benchmark and review. *Proceedings of the Royal Society A: Mathematical, Physical and Engineering Sciences*, 463:1955–1982.

©2023 Varela, Á., Rubial, P., Sobrino,E., Lugrís, U., & Sanjurjo, E. published by TU Delft OPEN on behalf of the authors.
ISSN: 2667-2812

The Evolving Scholar (2023)
https://doi.org/10.59490/6482e9b4d8611d76b7ba3369
Bicycle and Motorcycle Dynamics 2023
Symposium on the Dynamics and Control of Single Track Vehicles
18 – 20 October 2023, Delft University of Technology, The Netherlands

Type of the Paper: Extended Abstract

Using a steer-into-the-fall based control law to stabilize a pedelec

Yannick Hanakam[1,*], Jürgen Wrede[2], Martin Pfeiffer[3], Stefan Hillenbrand[4]

[1]Institute for Smart Bicycle Technology, Pforzheim University; y.hanakam@outlook.de (0009-0004-5246-8980)
[2]Institute for Smart Bicycle Technology, Pforzheim University; juergen.wrede@hs-pforzheim.de
[3]Institute for Smart Bicycle Technology, Pforzheim University; martin.pfeiffer@hs-pforzheim.de
[4]Institute for Smart Bicycle Technology, Pforzheim University; stefan.hillenbrand@hs-pforzheim.de
*corresponding author.

Name of Editor: Jason Moore
Submitted: 09/06/2023
Accepted: 26/06/2023
Published: 26/06/2023
Citation: Hanakam, Y., Wrede, J., Pfeiffer, M. & Hillenbrand, S. (2023). Using a steer-into-the-fall based control law to stabilize a pedelec. The Evolving Scholar - BMD 2023, 5th Edition. This work is licensed under a Creative Commons Attribution License (CC-BY).

Abstract

Despite having complex dynamics, a bicycle can be stabilized easily by steering into the direction the bicycle leans, also known as *steer-into-the-fall*. Although this can be a difficult task for the cyclist, this basic control law can easily be implemented by a technical system to help the cyclist to stabilize the bicycle. As several studies on bicycle dynamics show, at least theoretically in simulations, a proportional controller based on the *steer-into-the-fall* principle is sufficient to stabilize a bicycle (Åström et al., 2005; Schwab et al., 2008). A steering assistance system consisting of a proportional controller and an electric motor applying torque to the handlebars can provide steering assistance and thus help stabilizing the bicycle. However, the design of a proportional controller working in parallel with the rider can be tricky. To prevent the cyclist from being irritated, the natural steering behavior of the bicycle must be affected as little as possible by the steering interventions. In addition, the cyclist always must be in control of the handlebars.
In this study, we propose a control strategy based on a proportional controller that is designed using classical control engineering methods. Used in a pedelec with a prototype steering assistance system, this study investigates the effect of the controller on the stability of the pedelec and the impact of the steering interventions on the cyclist's riding experience.

The present study

The study presented in this paper is part of the "BikeAssist" project at the Institute for Smart Bicycle Technology at Pforzheim University (Germany), in which a steering assistance system for pedelecs is developed. This system is designed to provide additional steering torque to assist the cyclist in maintaining balance on the pedelec at low speed. BikeAssist is sponsored by the German Federal Ministry of Education and Research (contract number 13FH533IX6).
A controller designed according to the *steer-into-the-fall* concept applies additional steering torque. In (Schwab et al., 2008), this control concept is called *intuitive control* as it adopts the same stabilization strategy that is intuitively used by the cyclist.
The expected benefit of this concept is that the steering interventions by the controller should be perceived as "natural" by the cyclist. In its simplest form, this stabilization principle can be implemented as a proportional controller, as shown by (Åström et al., 2005) and (Schwab et al., 2008). The controller is designed to generate a steering torque proportional to the roll rate of the bicycle. In this study, three different controller configurations were used:

- C0: no control intervention.
- C1: low feedback gain resulting in lower level of intervention.
- C1: higher feedback gain resulting in more significant control interventions.

The study presented in this paper examines the influence of the supplemental interventions of a steering assistance system on the stability of the bicycle. A test group of 60 riders (30 men and 30 women, between 59 and 84 years of age) carried out a riding task in a test environment using an instrumented pedelec with a steering assistance system.

© 2023 Yannick Hanakam, Jürgen Wrede, Martin Pfeiffer, Stefan Hillenbrand. published by TU Delft OPEN on behalf of the authors.
ISSN: 2667-2812

The riding task, which was repeated nine times, consisted of three sections:

1. The cyclist had to ride straight ahead at 5 km/h,
2. turn around in a curve,
3. then ride back straight ahead at 6.5 km/h.

The control configuration was modified between test runs while riders were unaware of the actual set up. Measurements of the bicycle motion are used to evaluate the objective stability of the bicycle and interviews with the riders give a measure for the perceived stability.

Results

The objective stability of the pedelec can be evaluated by using the rectified roll rate, calculated separately for the sections at 5 km/h and at 6.5 km/h for each test run, as shown in Figure 1.

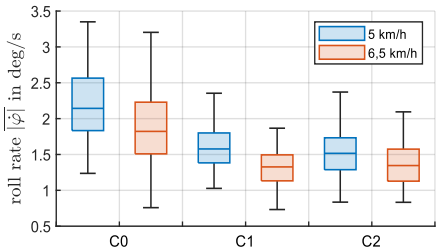


Figure 1: Comparison of the rectified roll rates for riding in straight line at two different velocities (5 km/h and 6,5 km/h).

Figure 1 shows, that in both configurations C1 and C2 and for both velocities the roll rate decreases compared to the test runs with the deactivated system C0. Using a one-way analysis of variance for each velocity variant to assess the effect of the steering assistance on the stability of the pedelec, measured by the rectified roll rate, the roll rate differed statistically significant for the different configurations. Post-hoc analysis revealed a significant difference ($p < 0.001$) between configuration C0 and C1 as well as between C0 and C2 both for 5 km/h and for 6,5 km/h. Between C1 and C2 no significant difference could be found (p=0,382 for 5 km/h and p=0,978 for 6,5 km/h).

Conclusion

The results of this study show, that providing steering assistance to the cyclist based on a proportional controller can significantly increase the measurable stability. However, higher feedback gains do not result in better stability. This may be caused by the cyclists. The interventions of the system are unfamiliar and may be perceived as being too strong resulting in the rider counteracting the controller. Thus, the stabilizing effect of the steering interventions is reduced. Although the objective stability of the bicycle is improved by the steering assist system, the subjective evaluation yielded mixed results.

References

Åström, K. J., Klein, R. E., & Lennartsson, A. (2005). Bicycle dynamics and control: adapted bicycles for education and research. *IEEE Control Systems Magazine*, *25*(4), 26–47. https://doi.org/10.1109/MCS.2005.1499389

Schwab, A. L., Kooijman, J. D. G., & Meijaard, J. P. (Eds.) (2008). *Some recent developments in bicycle dynamics and control*.

© 2023 Yannick Hanakam, Jürgen Wrede, Martin Pfeiffer, Stefan Hillenbrand. published by TU Delft OPEN on behalf of the authors.
ISSN: 2667-2812

The Evolving Scholar (2023)
https://doi.org/10.24404/63fe5c46c9d7c3ebc76e944b
Bicycle and Motorcycle Dynamics 2023
Symposium on the Dynamics and Control of Single Track Vehicles
18 – 20 October 2023, Delft University of Technology, The Netherlands

Type of the Paper: Extended Abstract

Instrumented Bicycle for Experimental Investigation of Braking Dynamics including Front Brake induced Rear Wheel Lift Up

J. Skatulla[1,2,*], O. Maier[1], and S. Schmidt[2]

[1]Robert Bosch GmbH
[2]Otto von Guericke University Magdeburg
*corresponding author: Johann Skatulla, johann.skatulla@de.bosch.com

Name of Editor: Jason Moore
Submitted: 28/02/2023
Accepted: 14/04/2023
Published: 26/04/2023
Citation: Skatulla, J., Maier, O. & Schmidt, S. (2023). Instrumented Bicycle for Experimental Investigation of Braking Dynamics including Front Brake induced Rear Wheel Lift Up. The Evolving Scholar - BMD 2023, 5th Edition.
This work is licensed under a Creative Commons Attribution License (CC-BY).

Abstract:

An instrumented bicycle equipped with sensors measuring variables of motion including absolute over ground velocity and attitude is presented. Relevant design parameters are measured including geometric parameters, inertia values, suspension parameters, and tire characteristics. A multibody simulation is set up and validated. The bicycle is used to investigate brake induced pitch-over motion in detail. Robust indicators of rear wheel ground contact loss are identified.

Instrumented bicycles (IB) are a critical tool to understand the dynamics involved as well as to validate simulation models. Using them for transportation-related research has increased in popularity recently, a majority of the publications focus on behavioral and safety related studies (Gadsby & Watkins, 2020). But little work can be found on detailed analysis of pitch-over motion. Bretting et al. (2010) crash tested bicycles in a controlled environment observing the motion extrinsically and Maier et al. (2016b) presented an IB for manned and unmanned road test of eBike ABS.

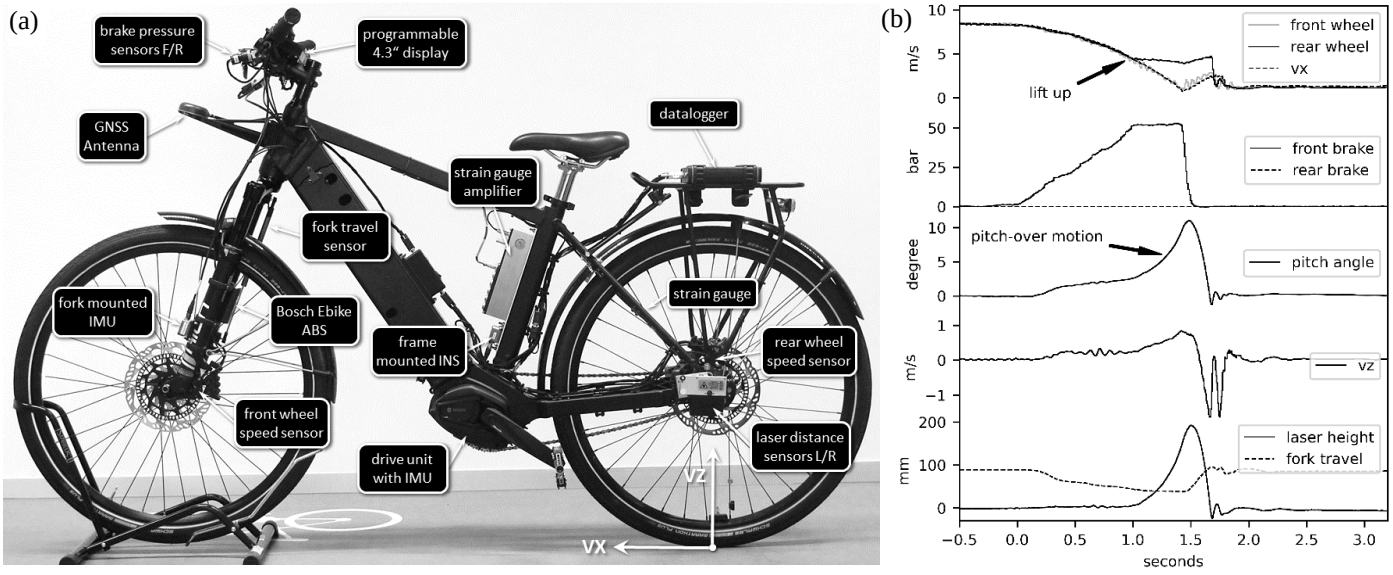


Figure 1. Details of the instrumented bicycle. (a) Bicycle equipped with sensors. Frame mounted INS measures body velocities with respect to rear wheel contact point. (b) Measurement record of brake maneuver including lift up and pitch-over motion.

© 2023 Skatulla, J., Maier, O., & Schmidt, S. published by TU Delft OPEN on behalf of the authors.
ISSN: 2667-2812

Bicycles exhibit complex dynamics that can be divided in two groups. Longitudinal and vertical dynamics describe motions in the central plane of symmetry including rolling forward, stoppies, wheelies, and suspension activities. Lateral dynamics take place out of the central plane of symmetry including balancing, leaning, steering, and turning. Using the bicycles brake system can cause multiple motions. First and foremost, the bicycle is decelerated longitudinally when the brake is applied. If applied to strong on a low grip surface the wheels can start to skid, causing an out-of-plane slide sideways. Applying the front brake to strong on a high grip surface can excessively shift the wheel loads towards the front, causing the rear wheel load to become zero. Thus, the wheel lifts up. This scenario represents the beginning of an in-plane pitch-over motion. The minimum deceleration to start a lift up for a given pitch angle is called critical deceleration. Maier et al. (2016a) showed: The critical deceleration decreases with increasing pitch angle. Once started, the pitch-over motion is self-amplified for a constant break input. If not acted upon swiftly, pitch angle and pitch rate increase until a point of no return is surpassed. Then even completely releasing the brake can no longer prevent a fall over the handlebars.

Figure 1 shows the IB, it is an eBike equipped with Bosch drive unit and battery. It has a trekking bike frame geometry with front suspension only. There are 6D inertial measurement units (IMU) mounted in various locations: on the fork, inside the drive unit, and on the seat tube. The latter one is part of an inertial navigation system (INS) whose GNSS antenna is mounted on the head tube. The INS provides high accuracy measurements of absolute over ground velocity and attitude (roll, pitch, and yaw angle) with an accuracy of 0.05 m/s and 0.1 degree respectively. It also provides body velocities in a local coordinate system attached to the rear wheel contact point, as seen in Figure 1. Pressure sensors near the handlebars measure front and rear master cylinder pressure of the hydraulic disk brakes. Furthermore, a Bosch eBike ABS is mounted. It can modulate the pressure at the front brake caliper and measures front and rear wheel speed. Also, the travel of the front suspension is measured by a displacement transducer. The distance from the rear axle to the rear wheels contact patch is measured with two laser sensors mounted on the left and right side of the bicycle. Additionally, a strain gauge was applied at the rear chain stay to measure the normal contact force of the rear wheel. The drive unit measures motor and rider torque as well as cadence information. All signals are logged with a sampling frequency of 500 Hz by the datalogger and stored on a SD card. A programmable 4.3-inch display is mounted on the handlebars. It displays live data to the rider, allowing an immediate check of the riding maneuver and compare it to maneuver specification.

In order to allow modelling and simulation of the IB, relevant design parameters needed to be obtained. Photogrammetry provided geometric parameters. The wheels and frames mass and moment of inertia was measured. Stiffness and dampening of the fork in compression and bending direction was also measured. Additionally, the rider's mass was measured. The friction coefficient of the brake was identified from measurements as well as the tire road contact (Pacejka model, asphalt, and gravel). An existing multibody simulation was parameterized and validated against measurements with a good alignment.

The IB is used to investigate lift up dynamics, Figure 1 shows selected signals from a measurement record of such a situation. The rider increases the front brake pressure gradually, the load is shifted towards the front compressing the suspension fork. After one second critical brake pressure of 50 bar is reached. A pitch-over motion starts, brake pressure is held constant. Pitch angle and rear wheel height increase progressively (due to self-amplification) until 10 ° and 200 mm is reached respectively. At t = 1.5 s the brake is released. Afterwards the bike starts to come down again, impacting on the surface followed by brief bouncing.

A ground truth signal for rear wheel lift up can be obtained from the IB's sensors in various ways: Lift up height and rear wheel normal load can be observed directly. Additionally, rear wheel speed is a very good indication for lift up. When the rear wheel is not braked, it conserves the rotational energy and spins freely when lifted of the ground. Also pitch angle and normal velocity vz give clear indication of lift up, for instance by applying threshold-based detection.

The presented IB enables in depth study of lift up scenarios and flip-over motion. Its capability of providing a ground truth will be used in future work. New lift up detection algorithms using a subset of the available sensors can be tested and evaluated. And new control algorithms to mitigate flip-over motion using pressure modulation can be tried.

References

Bretting, G. P., Jansen, H. P., Callahan, M., Bogler, J., & Prunckle, J. (2010). Analysis of Bicycle Pitch-Over in a Controlled Environment. *SAE International Journal of Passenger Cars - Mechanical Systems*, 3(1), 57–71. https://doi.org/10.4271/2010-01-0064

Gadsby, A., & Watkins, K. (2020). Instrumented bikes and their use in studies on transportation behaviour, safety, and maintenance. *Transport Reviews*, 40(6), 774–795. https://doi.org/10.1080/01441647.2020.1769227

Maier, O., Pfeiffer, M., Scharpf, S., & Wrede, J. (2016a). Conditions for nose-over and front wheel lockup of electric bicycles (pp. 219–224). *11th France-Japan & 9th Europe-Asia Congress on Mechatronics (MECATRONICS) /17th International Conference on Research and Education in Mechatronics (REM), IEEE*. https://doi.org/10.1109/MECATRONICS.2016.7547145

Maier, O., Pfeiffer, M., & Wrede, J. (2016b). Development of a Braking Dynamics Assistance System for Electric Bicycles: Design, Implementation, and Evaluation of Road Tests. *IEEE/ASME Transactions on Mechatronics*, 21(3), 1671–1679. https://doi.org/10.1109/TMECH.2015.2505186

SBG Systems SAS. (2020, November). *ELLIPSE SERIES High Performance, Miniature Inertial Sensors* [Hardware Manual]. https://support.sbg-systems.com/sc/el/files/latest/11240254/17990941/1/1617893855126/Ellipse+3+-+Hardware+Manual.pdf

© 2023 Skatulla, J., Maier, O., & Schmidt, S. published by TU Delft OPEN on behalf of the authors.
ISSN: 2667-2812

The Evolving Scholar (2023)

https://doi.org/10.59490/649d9ceb4adb98a3b887079f

Bicycle and Motorcycle Dynamics 2023
Symposium on the Dynamics and Control of Single Track Vehicles
18 – 20 October 2023, Delft University of Technology, The Netherlands

Type of the Paper: Extended Abstract

Development of a Hardware-in-the-Loop Test Bench for Validation of an ABS System on an e-Bike

N. Ramosaj[1], C. Fusco[1,2], E. Viennet[1,*]

[1]School of Engineering and Architecture of Fribourg, HES-SO University of Applied Sciences and Arts Western Switzerland; nicolas.ramosaj@hefr.ch; christia.fusco@hes-so.ch; emmanuel.viennet@hefr.ch ORCID 0009-0004-0922-2934
[2]Dipartimento di Ingegneria Meccanica e Aerospaziale, Politecnico di Torino, Italy
*corresponding author.

Name of Editor: Jason Moore
Submitted: 30/06/2023
Accepted: 03/07/2023
Published: 03/07/2023
Citation: Ramosaj, N., Fusco, C. & Viennet, E. (2023). Development of a Hardware-in-the-Loop Test Bench for Validation of an ABS System on an e-Bike. The Evolving Scholar - BMD 2023, 5th Edition.
This work is licensed under a Creative Commons Attribution License (CC-BY).

Abstract:

Electrically assisted bicycles (e-bikes) have become increasingly popular and may facilitate active commuting. But this comes at the price of safety since e-bikers have a higher risk of traffic accidents than conventional cyclists (Haufe et al. 2022). However, the availability of electric energy onboard allows the emergence of active safety systems like antilock braking systems (ABS) that could help reduce the accident rate in the same way it was observed in the last decades for cars and motorcycles (Maier, 2018). ABS is a mechatronic device involving multi-domain expertise (electronics, mechanics, software) and conflicting objectives (cost, performance, perceived quality, safety of operation, safety of testing). This makes a model-based system engineering (MBSE) methodology a well-suited approach to develop such a device. In the MBSE context, simulation models are deployed all along the development cycle, from requirements down to testing phases (both verification and validation).

This paper presents the development of a test-bench that can be leveraged to validate an e-bike ABS for multiple bicycle geometry, loading and test scenarios. The approach consists in reproducing the dynamics of an e-bike thanks to a simulation model and interfacing it with a physical brake and the ABS hardware under test, thus obtaining a hardware in the loop (HiL) test bench as mentioned in (Heidrich et al., 2013) and (Pfeiffer et al., 2019). Figure 1 presents an overview of the installation whose core part is the real-time target machine running the virtual bike model. This setup allows the test engineer to first test and evaluate the ABS behavior in a safe place, before starting tests on the track.

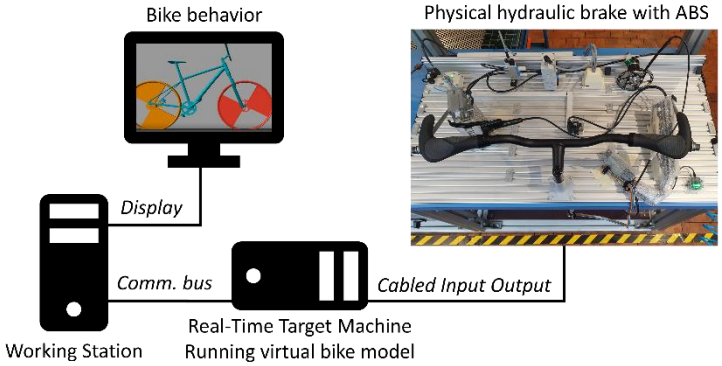


Figure 1. Concept of the developed hardware-in-the-loop test-bench. The ABS hardware under test is interfaced to the real-time target machine that runs the virtual bike model.

The developed dynamic model represents an e-bike with a semi-rigid frame (front suspension only). The simulation model considers 6 degrees of freedom: longitudinal, vertical and pitch motion of the bike frame; front and rear wheel rotation; front suspension travel. The parameters of the model are either directly measured when feasible or reproduced from literature or

© 2023 Ramosaj N., Fusco C. & Viennet, E. published by TU Delft OPEN on behalf of the authors.
ISSN: 2667-2812

identified indirectly from bicycle measurements. A fixed step solver is used for numerical integration with a time step of 1.0 ms, allowing the model to communicate real-time with the ABS and its control unit.

The fidelity of the model is assessed by comparing its results against measurements conducted on a physical test bike. The test bike is a Flyer Goroc 2 instrumented with various sensors including force at front brake lever, longitudinal and vertical acceleration (X axis and Z axis), pitch rate (Y axis), front and rear wheel speeds, suspension travel.

Figure 2 shows preliminary results obtained with the developed HiL test-bench where a physical ABS is interfaced to a virtual bike model running on a real-time target machine. The tested scenario is a hard front braking maneuver with an initial velocity of approx. 10 m/s, a soft front suspension and a flat road with low grip. When a slip condition is detected at the front wheel, the ABS triggers a release of the pressure in the hydraulic brake circuit, thus lowering the actual force measured at the front brake pad. When the front wheel does not slip anymore, the pressure in the hydraulic brake circuit rises again thanks to the pump integrated in the ABS system.

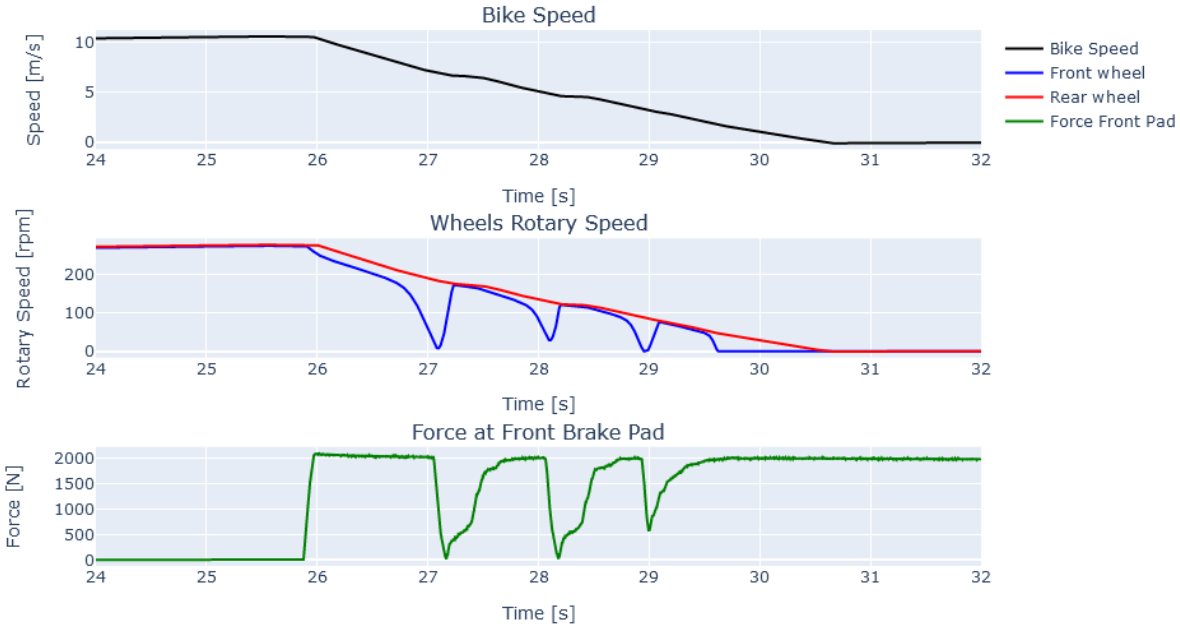


Figure 2. Preliminary set of results obtained with the HiL test-bench. Test scenario shows that ABS triggers a decrease of effective force at front brake when a slip condition is detected at the front wheel.

Further work investigates the impact of some bike parameters like geometry, loading, suspension stiffness and tire grip on the braking performance with the tested ABS.

References

Haufe S, Boeck HT, Häckl S, et al., (2022), Impact of electrically assisted bicycles on physical activity and traffic accident risk: a prospective observational study. *BMJ Open Sport & Exercise Medicine 2022.*

Heidrich L. et al., (2013), Hardware-in-the-loop test rig for integrated vehicle control systems, *IFAC Proceedings Volumes, 46, 21, 683-688*.

Maier, O. (2018), *Modellbasierte Entwicklung eines aktiven Sicherheitssystems für elektrifizierte Fahrräder*, PhD Thesis, Otto-von-Guericke-Universität Magdeburg.

Pfeiffer, M., Wrede, J., Steeb, S., (2020), Validation of a Dynamics Assistance System Using Hardware-in-the-Loop Simulation. *Symposium on the Dynamics and Control of Single Track Vehicles*.

© 2023 Ramosaj N., Fusco C. & Viennet, E. published by TU Delft OPEN on behalf of the authors.
ISSN: 2667-2812

The Evolving Scholar (2023)
https://doi.org/10.24404/63fe21fc458ade05d08303fc
Bicycle and Motorcycle Dynamics 2023
Symposium on the Dynamics and Control of Single Track Vehicles
18 – 20 October 2023, Delft University of Technology, The Netherlands

Type of the Paper: Extended Abstract

Enhanced Braking of E-Scooters

F. Klinger*, J. Edelmann, and M. Plöchl

Institute of Mechanics and Mechatronics, TU Wien, Austria; florian.klinger@tuwien.ac.at
*corresponding author.

Name of Editor: Jason Moore
Submitted: 28/02/2023
Accepted: 11/04/2023
Published: 26/04/2023
Citation: Klinger, F., Edelmann, J. & Plöchl, M. (2023). Enhanced Braking of E-Scooters. The Evolving Scholar - BMD 2023, 5th Edition.
This work is licensed under a Creative Commons Attribution License (CC-BY).

Abstract:

Electric scooters, termed e-scooters in the following, appeared in traffic some years ago and became increasingly popular since then. Little weight, small dimensions and a comfortable propulsion system add up to an attractive means of transportation, especially for urban areas. The trend towards e-scooters is likely to increase for both, vehicles in private ownership as well as offered by respective sharing companies. The growing popularity of this new type of vehicles is unfortunately accompanied by an increasing number of accidents and injuries, which are frequently reported in media as well as in scientific literature. One might think of numerous causes for e-scooter accidents, ranging from the vehicle itself (e.g. small wheels, unfamiliar handling dynamics), to the rider (e.g. lack of attention, disregard of traffic rules), to the traffic environment (e.g. darkness, interaction with other traffic participants). In particular, however, rider of e-scooters frequently report of problems related to the braking behaviour of e-scooter in ordinary every-day traffic scenarios: low braking deceleration, sudden skidding of the tyres on wet surfaces, complicated and unfamiliar operation of the (electric and/or friction) braking system for the front and rear wheel, misjudgement of achievable decelerations, road grip, etc. These and similar difficulties especially related to the braking behaviour are reported in several actual studies on the driving safety behaviour of e-scooters, see e.g. (Siebert et al., 2021).

To overcome above problems, an intelligent braking system which assists the rider to properly apply the front and rear brakes of the e-scooter, depending on the actual driving condition, might be helpful. Similar Advanced Driver Assistance Systems (ADAS), such as variable brake force distribution, anti-lock braking systems, wheel lift-off prevention etc., are well-known for passenger cars and motorcycles, as well as bicycles, (Pretagostini et al., 2020; Savino et al., 2020; Corno et al., 2018). However, braking (control) strategies devised for these vehicles are not directly applicable to e-scooters, since there are distinctive differences from a vehicle dynamics point of view. These differences concern the vehicle itself (small wheels with little inertia, unknown tyre behaviour, combined electric and friction brakes), as well as in particular the human rider: note that the mass of the rider body by far exceeds the mass of the e-scooter, and that the position of the human rider standing on the footboard is less restricted compared to the sitting position on bicycles and motorcycles; resulting effects on the lateral and longitudinal dynamics behaviour will be discussed in the present study, along with their consequences for control strategies for a combined actuation of the front and rear braking forces for enhanced braking of e-scooters.

A basic model of a motorcycle (Cossalter et al., 2004) was shown in a precedent study of the authors (Klinger et al., 2021) to be suitable for e-scooters as well to cope effects of load transfers and different standing positions of the rider on the braking performance. Based on this model, ideal distributions of the braking forces $S_{1,2}$ to front and rear tyre for different constant decelerations $-\ddot{x}$ (black dotted lines) and different rider positions (green lines) are shown in Fig. 1 (left). Ideal in this case refers to the utilisation of the same braking force coefficient, i.e. the ratio of longitudinal force over actual normal force, at each tyre. It becomes obvious that the composition of ideal braking forces depends non-linearly on the selected deceleration or friction potential, respectively, as well as on the standing position of the rider. These effects can be attributed to the high centre of gravity of the combined vehicle–rider system in relation to the wheelbase, and make it particularly difficult for the rider to apply the right amount of braking force at each tyre to fully utilize the tyre-road friction potential on one hand, and to avoid skidding on the other hand; this in turn makes the idea of an assistance systems very appealing in order to improve the vehicle safety of e-scooters. The latter especially holds true for shared/rental e-scooter, where the riders are typically less familiar with the behaviour of the vehicle.

© 2023 Klinger, F., Edelmann, J., & Plöchl, M. published by TU Delft OPEN on behalf of the authors.
ISSN: 2667-2812

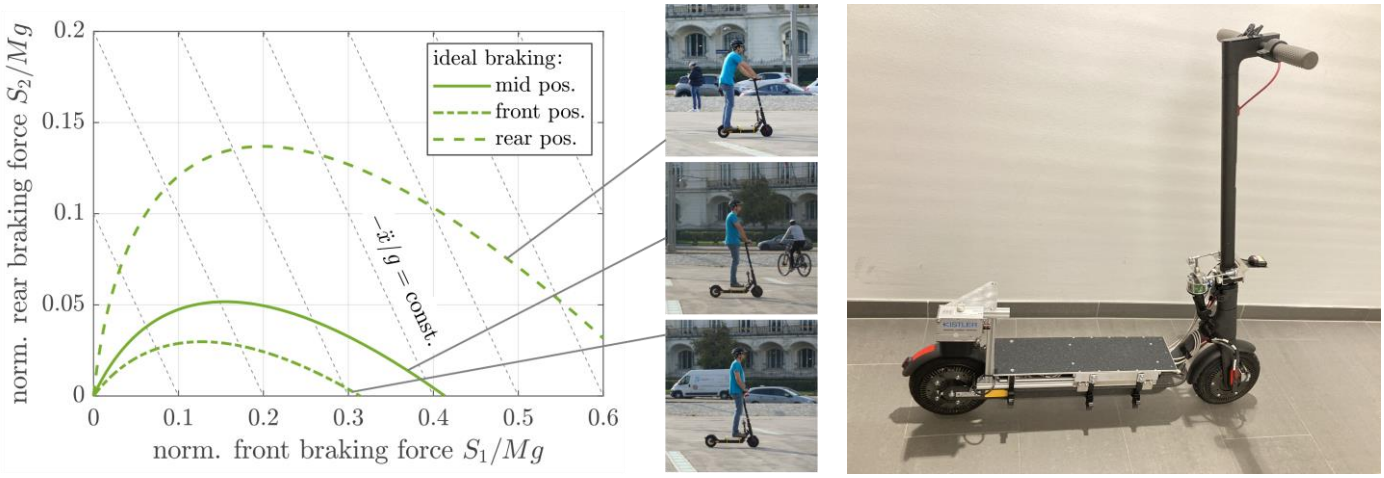


Figure 1. Left: Ideal brake force distribution for an e-scooter model for different decelerations and different positions of the rider along the footboard (left). Right: E-scooter equipped with measurement devices used in the present study.

In the present study, a simulation model of e-scooter and rider is used, which takes a limited friction potential between the tyres and the road into account, as well as inertial properties of the human rider body. Based on these quantities, strategies especially for emergency braking manoeuvres will be discussed, aiming to assist the rider to provide a suitable total braking force as well as its distribution on the front and rear tyre. Thereby, two goals need to be strived for: (i) to achieve maximal decelerations/minimal stopping distance, (ii) to simultaneously maintain a stable driving condition. The latter involves to prevent a lift-off of the rear wheel, a locking of front or rear wheel, and – more elaborate – to ensure, that the side forces of front and rear tyre necessary to remain in a stable upright position may be transmitted between the tyres and the road. Both, tyre–road friction potential and inertial properties of the vehicle–rider system are presumed to be known at first, and are then gradually replaced by respective values derived by parameter estimation methods.

Model parameter of the simulation model and input signals for the estimation methods are derived from an actual e-scooter, see Fig. 1 (right), equipped with several measurement devices to capture: the steering angle, actual position and velocity via GPS, accelerations and angular rotation rates via an IMU positioned in the aluminium box at the footboard, as well as the rotational speeds of front and rear wheel via hall-sensors and toothed discs. In addition, a Correvit system is used to measure velocities in longitudinal and lateral direction, and in this way to identify the slip quantities of front and rear tyre therefrom. The parameters of a tyre model in longitudinal direction to account for larger slip values at braking manoeuvres will be identified and presented.

References

Corno, M., D' Avico, L., & M., S. S. (2018, August 21–24). An Anti-Lock Braking System for Bicycles. *2018 IEEE Conference on Control Technology and Applications (CCTA)*, Copenhagen, Denmark, 834–839.

Cossalter, V., Lot, R., & Maggio, F. (2004). On the Braking Behavior of Motorcycles. *SAE Transactions* 113(6), 1274–1280.

Klinger, F., Klinger, M., Edelmann J, Plöchl, M. (2021, August 17–19). Electric Scooter Dynamics – From a Vehicle Safety Perspective. In A. Orlova, & D. Cole (Eds.), *Advances in Dynamics of Vehicles on Roads and Tracks II*, *IAVSD 2021*, Lecture Notes in Mechanical Engineering. Springer, Cham, 11.

Pretagostini, F., Ferranti, L., Berardo, G., Ivanov, V., & Shyrokau, B. (2020). Survey on Wheel Slip Control Design Strategies, Evaluation and Application to Antilock Braking Systems. *IEEE Access*, 8, 10951-10970.

Savino, G., Lot, R., Massaro, M., Rizzi, M., Symeonidis, I., Will, S., & Brown, J. (2020). Active safety systems for powered two-wheelers: A systematic review. *Traffic Injury Prevention*, 21(1), 78-86.

Siebert, F.W., Ringhand, M., Englert, F., et al. (2021). Braking bad – Ergonomic design and implications for the safe use of shared E-scooters. *Safety Science* 140, 13.

© 2023 Klinger, F., Edelmann, J., & Plöchl, M. published by TU Delft OPEN on behalf of the authors.
ISSN: 2667-2812

The Evolving Scholar (2023)
https://doi.org/10.24404/63fe629a71c23925f1d87627
Bicycle and Motorcycle Dynamics 2023
Symposium on the Dynamics and Control of Single Track Vehicles
18 – 20 October 2023, Delft University of Technology, The Netherlands

Type of the Paper: Extended Abstract

A Review on Test Method Development for Motorcycle Autonomous Emergency Braking Systems

Nora Leona Merkel[1]*

[1] Würzburger Institut für Verkehrswissenschaften (WIVW GmbH); merkel@wivw.de, https://orcid.org/0000-0002-4865-368X
*corresponding author.

Name of Editor: Jason Moore
Submitted: 28/02/2023
Accepted: 14/04/2023
Published: 26/04/2023
Citation: Merkel, N. (2023). A Review on Test Method Development for Motorcycle Autonomous Emergency Braking Systems. The Evolving Scholar - BMD 2023, 5th Edition.
This work is licensed under a Creative Commons Attribution License (CC-BY).

Abstract:

In the passenger car and truck sector, assistance systems that intervene in emergency situations and thus help to improve vehicle safety have already been successfully used for many years. One common example for this are autonomous emergency braking systems (AEB). These are already standard equipment in many passenger cars or even legally required in trucks in the European Union.

Although motorcyclists are subject to a high risk of suffering severe or fatal injuries in road traffic, systems that actively intervene in emergency situations are not yet available in the motorcycle sector. One reason for this is that passenger car systems cannot easily be adapted due to the motorcycle specific single-track vehicle dynamics. There are characteristic challenges that set limits to the possible application of actively intervening assistance systems. Exceeding these limits when applying a system like AEB on a motorcycle could result in the occurrence of new critical situations that are no longer controllable for the rider.
Still, previous research comes to the conclusion that assistance systems for motorcycles have the potential to increase riding safety and identifies autonomous emergency braking systems for motorcycles (MAEB) as one of the most promising technologies (Savino et al., 2013).

One major challenge in MAEB studies is the conflict of goals between the aim to optimize the effectiveness of MAEB by identifying maximum possible decelerations that can be applied in a safe way and the wish to evaluate ‘natural’ rider reactions to an autonomous braking intervention. For the latter, riders should not anticipate the manoeuvre. They are supposed to be surprised by the autonomous deceleration in order to achieve unbiased results.
Obviously, it is ethically unacceptable to determine feasible deceleration limits with unprepared study participants. Approaching these limits carries the risk of provoking critical situations. During the research described in the paper at hand, a multi-phase approach was developed, in order to overcome the trade-off between achieving maximum effectiveness of braking interventions by identifying maximum feasible decelerations on the one hand and on the other hand evaluating unbiased reactions of unprepared riders.
While other research groups focus on urban riding scenarios at velocities up to 50 km/h in their MAEB research (e.g., Lucci et al., 2021), the investigations described here concentrate on higher velocities as they occur in rural scenarios.

The method starts with a determination of controllability limits during the first phase. In this stage of the investigations, the test persons are expert riders. These experts are experienced professional riding instructors and trainers. They are assumed to be particularly suitable to assessing the skills of unexperienced riders. The experts evaluate different levels of autonomous decelerations concerning their feasibility for unprofessional motorcyclists.

In the second step, the method includes a potential analysis with the aim to compare various intervention strategies (in terms of deceleration profiles) in order to prioritise the most promising approach(es). The potential analysis includes the evaluation of physical rider reactions that influence the potential velocity reduction as well as an assessment of the acceptance of the autonomous interventions. This investigation is conducted as a participant study with unprofessional riders.

© 2023 Merkel, N.L. published by TU Delft OPEN on behalf of the authors.
ISSN: 2667-2812

In the third phase, which is again conducted as participant study with unprofessional riders, the method intends to analyse the reactions of riders to unexpected braking interventions in a more detailed way. The focus of this study part is on the relative movements between the riders and the motorcycle. This includes, e.g., upper body and head displacement as well as support forces on the handlebar. A main focus is on the identification of characteristic behaviour and timing. This helps to gain further knowledge about the requirements for the design of autonomous emergency braking interventions that result from characteristic rider behaviour.

The three phases of the investigation method are shown in Figure 1.

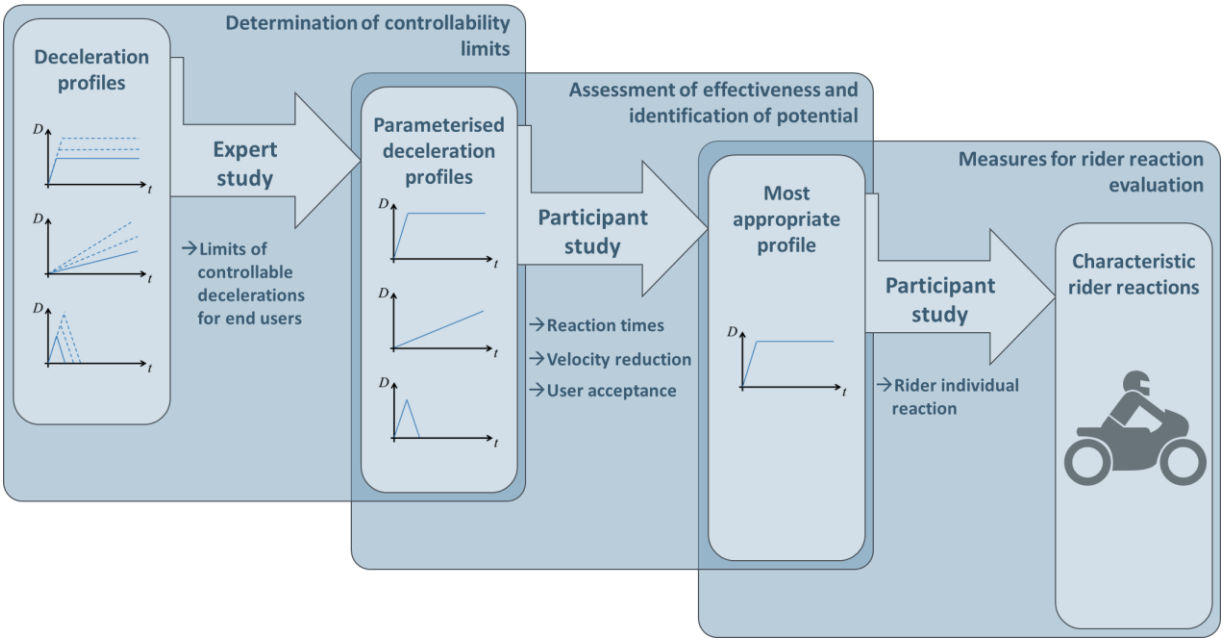


Figure 1. Three phases of the investigation method (Merkel, 2022).

Throughout the research described in this paper, the developed investigation method was exemplarily applied to a prototype MAEB system. The paper provides an overview of the major results of all three phases of MAEB assessment.
The method proves to be appropriate and delivers promising results regarding the applicability of autonomous emergency braking systems for motorcycles in the evaluated scenarios. The reproducibility of the measured rider reactions creates confidence that the corresponding effects are predictable, which means that the rider behaviour does not represent a completely incalculable safety-critical factor for the application of MAEB.

The successful application of the method leads to the conclusion that it can serve as a basis for the release of systems that intervene in the longitudinal dynamics. It gives manufacturers and system suppliers the opportunity to systematically prove that their systems are controllable for end users and can be applied without causing additional risks. Thus, the method can contribute to the future use of safety-enhancing assistance systems for motorcycles.

Acknowledgements

The described research was conducted during my time as a research associate and doctoral candidate at the Institute of Automotive Engineering (FZD) at Technische Universität Darmstadt. I would like to express my gratitude to my supervisor Prof. Dr. rer. nat. Hermann Winner for giving me the opportunity to work on this topic and for providing me with advice and support at all times.

References

Lucci, C., Marra, M., Huertas-Leyva, P. Baldanzini, N. & Savino, G. (2021). Investigating the feasibility of Motorcycle Autonomous Emergency Braking (MAEB): design criteria for new experiments to field test automatic braking. *MethodsX*. DOI: https://doi.org/10.1016/j.mex.2021.101225.

Merkel, N. L. (2022). *Untersuchungen zur Anwendbarkeit Automatischer Notbremssysteme für Motorräder*. Dissertation, Technische Universität Darmstadt, Darmstadt, Germany. DOI: https://doi.org/10.26083/tuprints-00021096

Savino, G, Giovannini, F, Baldanzini, N, Pierini, M. & Rizzi, M. (2013). Assessing the potential benefits of the motorcycle autonomous emergency braking using detailed crash reconstructions. *Traffic injury prevention*, 14, 40–49. DOI: https://doi.org/10.1080/15389588.2013.803280

© 2023 Merkel, N.L. published by TU Delft OPEN on behalf of the authors.
ISSN: 2667-2812

The Evolving Scholar (2023)

http://dx.doi.org/10.59490/649d4037c2c818c6824899bd

BICYCLE & MOTORCYCLE DYNAMICS 2023

TU Delft OPEN

Bicycle and Motorcycle Dynamics 2023
Symposium on the Dynamics and Control of Single Track Vehicles
18–20 October 2023, Delft University of Technology, The Netherlands

Type of the Paper: Extended Abstract

Essential Bicycle Dynamics for Microscopic Traffic Simulation: An Example Using the Social Force Model

Christoph M. Schmidt [1,*], Azita Dabiri [1], Frederik Schulte [1], Riender Happee [1], Jason K. Moore [1]

[1] Delft University of Technology, The Netherlands; c.m.schmidt@tudelft.nl, ORCID 0000-0002-9405-6384, a.dabiri@tudelft.nl, ORCID 0000-0002-1296-7580, f.schulte@tudelft.nl, ORCID 0000-0003-3159-4393, r.happee@tudelft.nl, ORCID 0000-0001-5878-3472, j.k.moore@tu-delft.nl, ORCID 0000-0002-8698-6143
[*] corresponding author

Name of Editor: Jason Moore
Submitted: 29/06/2023
Accepted: 29/06/2023
Published: 29/06/2023
Citation: Schmidt, C., Dabiri, A., Schulte, F., Happee, R. & Moore, J. (2023). Essential Bicycle Dynamics for Microscopic Traffic Simulation: An Example Using the Social Force Model. The Evolving Scholar - BMD 2023, 5th Edition.
This work is licensed under a Creative Commons Attribution License (CC-BY).

Abstract:

Microscopic traffic simulation is a popular tool in traffic research and planning. It enables the evaluation of interventions in a traffic system based on the movement of individual simulated agents. These can be for example infrastructural changes or the introduction of new road users like automated vehicles. Historically, this focused exclusively on car traffic. For heterogeneous settings with different kinds of road users, the original simulation concepts have to be adapted. Car-focused simulations often model vehicle dynamics as a combination of longitudinal movement along a prescribed lane and discrete lane change. However, road users like cyclists and pedestrians can operate more freely around the road infrastructure and hence their behavior is difficult to capture with current lane-based models (Twaddle et al., 2014). We propose a microscopic model describing bicycle interaction using the social force paradigm (Helbing and Molnár, 1995). Here we take into account bicycle kinematics, to create realistic bicycle paths. Qualitative evaluation shows simulated interactions with plausible cyclist trajectories. Inspired by particle physics, Helbing and Molnár (1995) introduced the social force model to simulate pedestrian movement. They assume that the movement of a single pedestrian in a crowd is governed by attractive and repulsive effects exerted on the individual by their intentions, other people, and infrastructure. The social force $\boldsymbol{F}(t) := \frac{\mathrm{d}\boldsymbol{v}(t)}{dt}$ describes this relationship. The overall social force is the sum of the effects on a person a in their environment defined as follows.

$$\boldsymbol{F}_a = \boldsymbol{F}_a^0 + \sum_b \boldsymbol{F}_{a,b} + \sum_B \boldsymbol{F}_{a,B} + \sum_i \boldsymbol{F}_{a,i} \tag{1}$$

$\boldsymbol{F}_a^0$ is a social force towards the destination based on the difference between the current and desired speed in the direction of the destination. $\boldsymbol{F}_{a,b}$ is a repulsive social force between persons a and b which prevents approaching closely. $\boldsymbol{F}_{a,B}$ are repulsive forces of delimiting infrastructure and $\boldsymbol{F}_{a,i}$ are attractive forces between persons that lead to group formation. Each of these forces can be calculated as the negative gradient of a potential $W(\boldsymbol{x}, \boldsymbol{y})$. The acceleration $\frac{\mathrm{d}\boldsymbol{v}}{dt}$ caused by the resulting force then leads to a simulation of 2D movement. To use social forces with cars and bicycles, researchers separate the lateral and longitudinal components of the resulting force and control the respective movements of the pedestrian model (Kaths, 2017) or the steer and acceleration of a two-wheeled kinematic vehicle model considering wheel slip (Huang et al., 2011; Schönauer et al., 2012). Schönauer et al. (2012) conclude that dedicated bicycle kinematics are needed to generate accurate cyclist path simulations.

$$\frac{\mathrm{d}}{\mathrm{d}t}\begin{bmatrix} x \\ y \\ \varphi \\ v \\ \delta \end{bmatrix} = \begin{bmatrix} v\cos\varphi \\ v\sin\varphi \\ \frac{v}{l}\tan\delta \\ a \\ \omega_\delta \end{bmatrix} \tag{2}$$

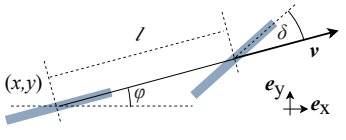


Figure 1: Geometry of the kinematic bicycle model.

©2023 Schmidt, C. M., Dabiri, A., Schulte, F., Happee, R. & Moore, J. K. published by TU Delft OPEN on behalf of the authors.
ISSN: 2667-2812

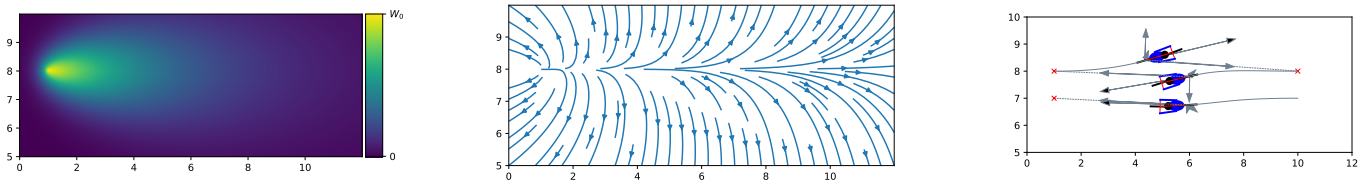
 http://dx.doi.org/10.59490/649d4037c2c818c6824899bd

This work pairs an adapted social force paradigm with the kinematic bicycle model. Centering on the rear wheel axis (Figure 1), Equation 2 describes the kinematic bicycle model (Corke, 2017, p. 101). x, y are the bicycle position in cartesian coordinates, θ is its orientation, v and a are its longitudinal velocity and acceleration, and δ and ω_δ are the steering angle and steering rate respectively. l is the distance between the rear and front wheels. Other than the pedestrian model (Helbing and Molnár, 1995), the bicycle model constrains lateral movement. Hence, the original definition of the social force, which causes instantaneous motion in the direction of the force, can't be applied directly. Rather, the resulting social force should cause the cyclist to apply a control input to the dynamic system. Hence, we redefine the social force as $\boldsymbol{F} := \boldsymbol{v}$. This cyclist social force becomes a vector field of preferred velocities under social and environmental influences. Through the steer rate ω_δ and acceleration a, a cyclist tries to align the movement of the bicycle with the direction and magnitude of the social force vectors. We use two proportional controllers with the gains $K_{\mathrm{p},1}$ and $K_{\mathrm{p},2}$ to emulate this control effort.

$$a = K_{\mathrm{p},1}(\|\boldsymbol{F}\| - v) \tag{3}$$

$$\omega_\delta = K_{\mathrm{p},2}\left(\arctan\frac{F_\mathrm{y}}{F_\mathrm{x}} - \varphi - \delta\right) \tag{4}$$

Following Helbing and Molnár (1995) and Huang et al. (2011), we use elliptic potentials with exponential decay and speed-dependent excentricity to calculate repulsive forces. Figure 2 exemplarily shows an elliptic potential (Figure 2a) and the corresponding force field derived from its gradient (Figure 2b) of the left cyclists at the beginning of the simulated evasive maneuver of Figure 2c. In this scenario, three originally opposing cyclists take appropriate and realistic action to evade each other, controlled solely by the social force model. Grey arrows show the individual forces and black arrows show the resulting force.



(a) Potential of the left cyclist (b) Repulsive force field of the left cyclist (c) Evasive maneuver

Figure 2: Simulation of a conflict scenario with the bicycle social force model

Continuing with our project, we aim to gradually integrate more complex bicycle models with the social force concept to introduce other effects that constrain bicycle movement into microscopic traffic simulation. For example, the inverted pendulum model includes the bicycle lean angle and the stabilization task (Karnopp, 2013, p. 146). This requires to countersteer and hence influences simulated cyclist trajectories and their capability to realistically react to their environment. We hypothesize, that these effects will lead to a more accurate simulation of road user conflicts which is vital for robust estimation of traffic safety and efficiency within traffic simulation. Going forward, we will use real-world data to develop and validate this model.

References

Corke, P. (2017). *Robotics, Vision and Control: Fundamental Algorithms In MATLAB®*, volume 118 of *Springer Tracts in Advanced Robotics*. Springer, Cham, 2nd edition.

Helbing, D. and Molnár, P. (1995). Social force model for pedestrian dynamics. *Physical Review E*, 51(5):4282–4286.

Huang, W., Schönauer, R., and Fellendorf, M. (2011). *Social Force Based Vehicle Model for Two-Dimensional Spaces*. [Paper Presentation]. Transportation Research Board 91st Annual Meeting, Washington D.C.

Karnopp, D. (2013). *Vehicle Dynamics, Stability and Control*. Mechanical Engineering. CRC Press, Boca Raton, 2nd edition.

Kaths, H. (2017). *Development of Tactical and Operational Behaviour Models for Bicyclists Based on Automated Video Data Analysis*. [Doctoral dissertation, Technische Universität München]. mediaTUM. https://mediatum.ub.tum.de/?id=1366878.

Schönauer, R., Stubenschrott, M., Huang, W., Rudloff, C., and Fellendorf, M. (2012). Modeling Concepts for Mixed Traffic: Steps toward a Microscopic Simulation Tool for Shared Space Zones. *Transportation Research Record*, 2316(1):114–121.

Twaddle, H., Schendzielorz, T., and Fakler, O. (2014). Bicycles in Urban Areas: Review of Existing Methods for Modeling Behavior. *Transportation Research Record*, 2434(1):140–146.

©2023 Schmidt, C. M., Dabiri, A., Schulte, F., Happee, R. & Moore, J. K. published by TU Delft OPEN on behalf of the authors.
ISSN: 2667-2812

The Evolving Scholar (2023)

https://doi.org/10.24404/63fe57dc0f4c41fd7083b6df

Bicycle and Motorcycle Dynamics 2023
Symposium on the Dynamics and Control of Single Track Vehicles
18 – 20 October 2023, Delft University of Technology, The Netherlands

Type of the Paper: Extended Abstract

Investigation of the Applicability of a Motorcyclist Model for Trajectory Prediction in Real Traffic

Scherer, F.[1]* and Eschinger, M.[2]

[1]Technical University Darmstadt; florian.scherer@tu-darmstadt.de, https://orcid.org/0009-0007-8234-3347
[2]Technical University Darmstadt, maximilian.eschinger@web.de
*corresponding author.

Name of Editor: Jason Moore
Submitted: 28/02/2023
Accepted: 30/03/2023
Published: 26/04/2023
Citation: Scherer, F. & Eschinger, M. (2023). Investigation of the Applicability of a Motorcyclist Model for Trajectory Prediction in Real Traffic. The Evolving Scholar - BMD 2023, 5th Edition.
This work is licensed under a Creative Commons Attribution License (CC-BY).

Abstract:

For the development of new types of assistance systems for motorbikes, the focus is increasingly on the rider himself. Warning functions or interventions into the current trajectory to avoid accidents require, in addition to the consideration of driving dynamic limits, an exact description of the riding abilities of the respective person, or the typical behaviour of the rider (Prokop, 2017). In Scherer et al (Scherer, 2022), a model for the prediction of motorbike driving dynamics data taking into account rider influence is presented on the basis of measurement data on a closed-off test track. The modelling assumes neither rider nor vehicle specific parameters to be known. For the modelling, parameterisable mathematical functions are used to describe the speed- and roll angle progression. Significant differences between different riders are thus visible in the test track investigations. In contrast to previous scientific approaches with stochastic evaluation of riding ability f.e. in (Magiera, 2020), with the model from (Scherer, 2022) it is possible to interpret measurement data using clear rider-specific parameters, to approximate their course and to compare them across riders. Example parameters are correction amplitudes, trends and limit values. Furthermore, the parameters enable a reliable identification of critical manoeuvres. Based on the describable roll angle and speed, an approach for calculating the future vehicle position was developed in (Scherer, 2022). The calculation is based on quasi-stationary cornering, which is extended by dynamic domains through correction factors. Furthermore, the correction factors allow an estimation of the riding style and additionally represent the individuality of the rider.

In the current paper, the applicability of this rider model to real traffic data is investigated. For this purpose, individual so-called evaluation curves are defined as examples, which are located on typical motorbike routes in Germany. Selected riders ride the same route several times, taking into account as constant as possible environmental conditions. Individuals repeat this investigation several times at intervals of several months and with different vehicles in order to make influences due to so-called seasonal effects or vehicle-specific behaviour investigable. In this paper, initial findings are presented regarding the influence on, or change in, riders' behaviour due to the choice of vehicle or the time of the measurement. An assessment is given of the extent to which the model of rider behaviour developed under laboratory conditions (Scherer, 2022) can be transferred to real traffic situations.

© 2023 Scherer, F. & Eschinger, M. published by TU Delft OPEN on behalf of the authors.
ISSN: 2667-2812

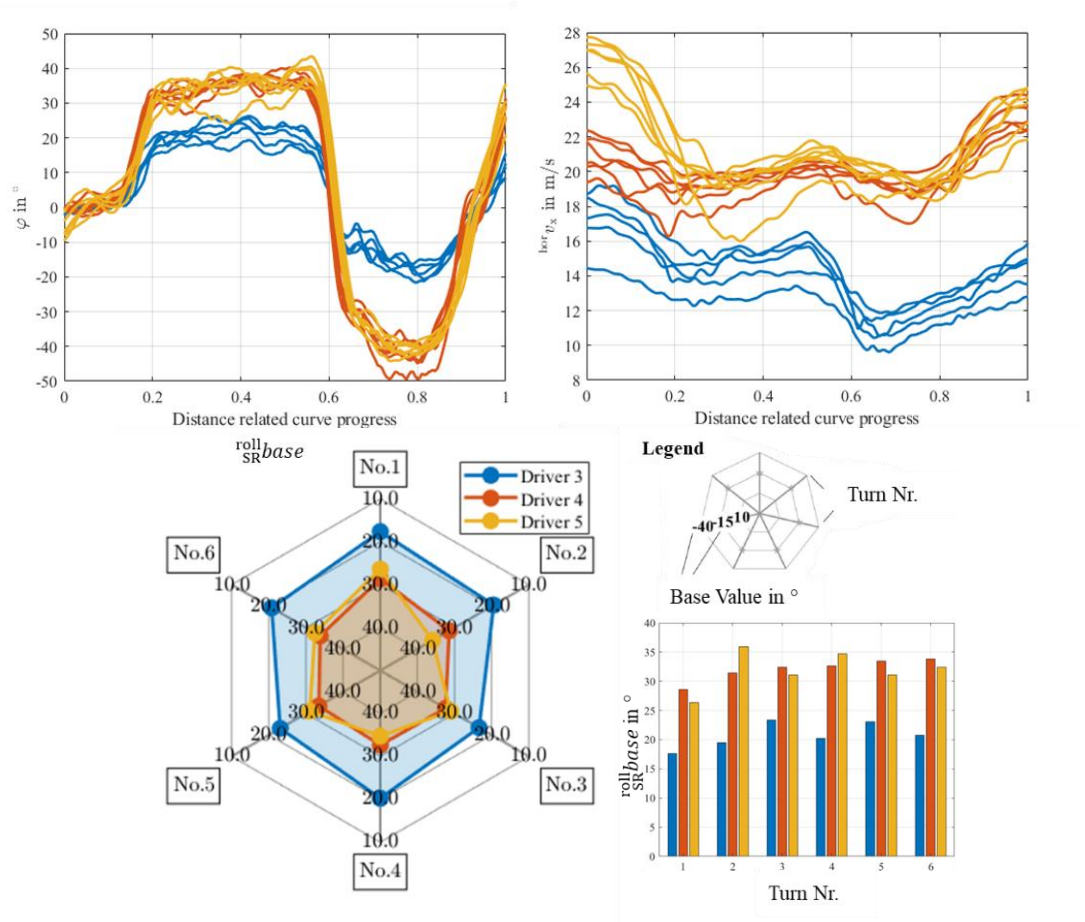


Figure 1: above: roll angle and velocity over distance related curve progress of three rider in an evaluation curve, down: corresponding rider parameters

This results in an estimation of the expected accuracy of the trajectory prediction under real conditions. As a result of this investigation, the applicability of the rider model to real traffic data is shown. **Figure 1** (above) shows an example of the roll angles and speed curves of three different riders passing through an evaluation curve six times repeatedly with the same vehicle. Here, the repeatability of one person's riding style can already be seen, as well as differences from other riders. **Figure 1** (down) shows the parameterisation generated from the measurement data shown. Here, as well, a rider specificity is visible in the coefficients of the parameterisation functions. In particular, rider and curve specific influences are evident in the roll angle coefficients. The application of the model to estimate the future position shows that an application to real driving data is possible. As a quality criterion for the evaluation of the overall accuracy, the lateral offset between the calculated and the measured trajectory is considered as a function of the distance travelled. The overall error between the measured data investigated in this paper and the position resulting from the estimation is in more than 85 % of the manoeuvres with a maximum lateral deviation of less than 2 %. Compared to the results presented in (Scherer, 2022) based on the measurement data from the test person study on closed terrain with an error of less than 1.5 %, this paper provides evidence of the applicability of the trajectory prediction under real conditions.

With the model presented here, rider-dependent trajectory predictions through a section of road ahead, taking into account an uncertainty interval, will also be possible in real traffic situations in the future.

References

Magiera, N, (2020) Identifikation des Fahrfertigkeitsniveaus von Motorradfahrern in Kurvenfahrt im Realverkehr, *Dissertation*, TU Darmstadt, Germany

Prokop, G., Hannawald, L., Köbe, M. (2017, April), Szenarien-basierte Plattform zur Inspektion automatisierter Fahrfunktionen - Eine Bewertungsmethodik zur Inspektion automatisierter Fahrfunktionen. *Proceedings, Symposium für Unfallforschung und Sicherheit im Straßenverkehr der ADAC Stiftung*, Munich, Germany, 115-127

Scherer, F., Basten, T. (2022, October 03-04), Development of a motorcyclist model for trajectory prediction. *Proceedings, 14th International Motorcycle Conference 2022*, Cologne, Germany, 265-299

© 2023 Scherer, F. & Eschinger, M published by TU Delft OPEN on behalf of the authors.
ISSN: 2667-2812

The Evolving Scholar (2023)

https://doi.org/10.24404/63fdc49b743b257fd7f65c53

Bicycle and Motorcycle Dynamics 2023
Symposium on the Dynamics and Control of Single Track Vehicles
18 – 20 October 2023, Delft University of Technology, The Netherlands

Type of the Paper: Extended Abstract

Trajectory Prediction for Powered Two Wheelers with Deep Learning

Karl Ludwig Stolle[1,*], Anja Wahl[1], and Stephan Schmidt[2]

[1]Robert Bosch GmbH; karlludwig.stolle@bosch.com, https://orcid.org/0000-0002-6535-1894; anja.wahl@bosch.com
[2]University of Applied Science Merseburg
*corresponding author.

Name of Editor: Jason Moore
Submitted: 28/02/2023
Accepted: 16/04/2023
Published: 26/04/2023
Citation: Stolle, K., Wahl, A. & Schmidt, S. (2023). Trajectory Prediction for Powered Two Wheelers with Deep Learning. The Evolving Scholar - BMD 2023, 5th Edition.
This work is licensed under a Creative Commons Attribution License (CC-BY).

Abstract:

The development of active safety systems for powered two wheelers (PTW) plays an important role to reduce the number of accidents involving PTW. Three quarter of PTW accidents in Europe are non-single accidents (Brown et al., 2021), in which riders are prone to heavy injuries or fatalities due to inherently low passive safety of PTW. The Connected Motorcycle Consortium (CMC) investigates the use of vehicle-to-X (V2X) communication to avoid collisions by warning the rider and drivers of surrounding vehicles in case of an imminent risk of collision (Connected Motorcycle Consortium, n.d.). Beside collisions, single vehicle accidents make up of 25 % of PTW accidents with fatalities or serious injured riders, 64 % of them occur during cornering (Brown et al., 2021). The majority of single accidents are primarily caused by rider error and could therefore be avoided (Biral et al., 2014). Future Advanced Rider Assistance Systems (ARAS) addressing either the V2X or the single vehicle accident domain will require information about the riding intention. The calculation of a trajectory in the upcoming seconds of the ride is one way to describe this intention. The presented work pursues the prediction of the PTW lateral dynamic state by means of a roll angle trajectory over the upcoming 4 s of riding. Inputs for the prediction model are PTW internal signals only, that are measurements of vehicle dynamics, rider inputs, and rider behavior.

Making a prediction based on any physical model of a PTW is limited to the time constant between rider inputs and the dynamic states. A previous study of the authors revealed that the time delay between the first steer torque input and the roll angle state ranges between 0.45 s and 2 s for the given test motorcycle, dependent on velocity (Stolle et al., 2022). Consequently, empirical methods need to be applied to achieve further predictions. Scherer and Basten (2022) present a parameterizable mathematical model for the prediction rider-individual and curve-individual roll angle trajectories. Upon reviewing the on-road riding data to be used in this work, it became apparent that the effort required to develop a heuristic model for the prediction is unforeseeable high, coupled with uncertain chances of success. Therefore, it was decided to use the exploratory capability of a deep learning (DL) model to investigate the possibilities in predicting the PTW roll angle state based on the given riding data. An ablation study is realized to understand the feature importance of the non-common measurement signals of rider steering inputs and rider behavior.

On-road data of more than 70 h ridden by 21 riders on an equipped test motorcycle is available for the development of the DL model. It contains a broad variety of routes from all over Southwest Germany with a focus on rural roads. Only riding with a velocity > 30 km/h is regarded for the prediction task to ensure the motorcycle is in the stable regime: this leaves ~ 65 h of data remaining. Beside filtering of signals, the riding data needs further preparation. Removing the bias from an outweighing share of straight riding condenses the overall data to ~ 28 h used for training, validation, and test.

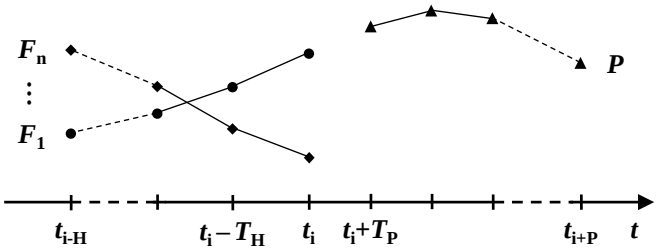


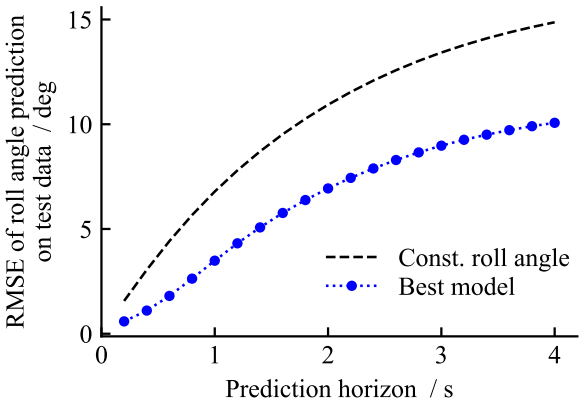
Figure 1. Drawing of the DL model's time-series prediction task: multiple features F are used to predict P at current time t_i

© 2023 One, A. B., Two, A. C., & Three, A. D. published by TU Delft OPEN on behalf of the authors.
ISSN: 2667-2812

Concrete task of the DL model is the prediction of future roll angle values P from the current point in time t_i up to a certain maximum preview time t_{i+P} at multiple discrete points that are evenly spaced with T_P – this prediction vector will be referred to as prediction horizon. Input to the model is a set of n features F, all time-series data, from t_{i-H} in the past up to the current point in time t_i at discrete points sampled with T_H. The prediction task described is visualized schematically in Figure 1. The DL model consists of one long short-term memory (LSTM) layer that is followed by a multilayer perceptron (MLP), which is a common neural network architecture for time-series prediction (Altche & De La Fortelle, 2017). Hyperparameter optimization is done on the network's size, training parameters, and sampling T_H and history length t_{i-H} of the input features.

The prediction performance of the optimized DL model on test data is presented as "best model" in Figure 2, where the left graph shows the root mean square error (RMSE) of the roll angle prediction for each point along the 4 s prediction horizon separately. This DL model uses a set of 16 features including non-common sensors for steering torque, rate & angle ("steering system") as well as for rider upper body lean & offset and rider head yaw angle ("rider behavior"). A basic prediction approach assuming constant roll angle over the prediction horizon is evaluated on the same test data and presented in the left graph of Figure 2 to contextualize the DL model's performance; its overall RMSE is 54 % higher, as shown in the table on the right of Figure 2.

Furthermore, a detailed ablation study on the importance of the non-common input features is carried out. Its condensed results are presented in the table on the right of Figure 2 as the change in overall RMSE loss compared to the best model for two different input configurations. Removing the rider behavior features in the "standard + steering system" configuration increases the error by 5 %. Additionally removing the steering system features leaves only common measurement signals in the "standard" configuration behind and leads the RMSE to increase by 7 % over the full "standard + steering system + rider behavior" model.



Prediction model configurations	Relative change of overall RMSE on test data
Standard + steering system + rider behavior	Best model (reference)
Standard + steering system	+ 5 %
Standard	+ 7 %
Basic prediction: constant roll angle assumption	+ 54 %

Figure 2. RMSE of the roll angle prediction evaluated at each point of the prediction horizon on test data (left). Relative change of overall RMSE loss on test data compared to the best model for different prediction model configurations (right).

In summary, the LSTM based DL model predicting a roll angle trajectory is a promising approach for the detection of the riding intention regarding lateral dynamics. The method demonstrates that there is information in the history of the time-series measurement signals of a PTW that is valuable for the prediction of future roll angles. The results of an ablation study reveal the importance of different input features and thus highlight the positive effect of non-common measurement signals, as the removal of both steering system and rider behavior measurements decreases the overall prediction performance. Future work will investigate how maneuvers and riding styles affect the prediction.

References

Altche, F., & De La Fortelle, A. (2017). An LSTM network for highway trajectory prediction. In *IEEE 20th International Conference on Intelligent Transportation Systems (ITSC)* (pp. 353–359). IEEE.

Biral, F., Bosetti, P., & Lot, R. (2014). Experimental evaluation of a system for assisting motorcyclists to safely ride road bends. *European Transport Research Review*, *6*(4), 411–423. https://doi.org/10.1007/s12544-014-0140-6

Brown, L., Morris, A., Thomas, P., Ekambaram, K., Margaritis, D., Davidse, R., Usami, D. S., Robibaro, M., Persia, L., Buttler, I., Ziakopoulos, A., Theofilatos, A., Yannis, G., Martin, A., & Wadji, F. (2021). Investigation of accidents involving powered two wheelers and bicycles - A European in-depth study. *Journal of Safety Research*, *76*, 135–145. https://doi.org/10.1016/j.jsr.2020.12.015

Connected Motorcycle Consortium. (n.d.). *Applications to improve rider safety*. Retrieved February 3, 2023, from https://www.cmc-info.net/applications.html

Scherer, F., & Basten, T. (2022). Entwicklung eines Motorradfahrendenmodells zur Trajektorienprädiktion. In Insitut für Zweiradsicherheit (ifz) e.V. (Ed.), *ifz-Research Publication Series: Nr. 20, Sicherheit - Umwelt - Zukunft XIV: Tagungsband der 14. Internationalen Motorradkonferenz 2022* (pp. 265–299). Institut für Zweiradsicherheit.

Stolle, K. L., Wahl, A., & Schmidt, S. (2022). Importance of motorcycle rider upper body movement for rider intention detection and motorcycle state prediction. In Insitut für Zweiradsicherheit (ifz) e.V. (Ed.), *ifz-Research Publication Series: Nr. 20, Sicherheit - Umwelt - Zukunft XIV: Tagungsband der 14. Internationalen Motorradkonferenz 2022* (pp. 32–41). Institut für Zweiradsicherheit.

© 2023 One, A. B., Two, A. C., & Three, A. D. published by TU Delft OPEN on behalf of the authors.
ISSN: 2667-2812

The Evolving Scholar (2023)

http://dx.doi.org/10.59490/649f22789bdaf83436b1087a

Bicycle and Motorcycle Dynamics 2023
Symposium on the Dynamics and Control of Single Track Vehicles
18–20 October 2023, Delft University of Technology, The Netherlands

Type of the Paper: Extended Abstract

A mobile recording system featuring high-precision time synchronization

Takuro Sone [1,*], Takehiro Maeda [2], Tomoya Kitani [1]

[1] Graduate School of Science and Technology, Shizuoka University, Japan; t-sone@kitanilab.org, ORCID 0000-0002-2648-9057; t-kitani@inf.shizuoka.ac.jp, ORCID 0000-0002-1723-6197
[2] Graduate School of Integrated Science and Technology, Shizuoka University, Japan;
[*] corresponding author

Name of Editor: Firstname Lastname
Submitted: 30/06/2023
Accepted: 03/07/2023
Published: 03/07/2023
Citation: Sone, T., Maeda, T. & Kitani, T. (2023). A mobile recording system featuring high-precision time synchronization. The Evolving Scholar - BMD 2023, 5th Edition. This work is licensed under a Creative Commons Attribution License (CC-BY).

Abstract:

In order to analyze the motion of motorcycles and other vehicles, it is desirable to measure and record data using a combination of data loggers and video and audio recording devices and accurately integrate the collected data. For this purpose, it is necessary to be able to record the position and time at which data was recorded with sufficient accuracy. In recent years, it has become relatively easy to determine the recorded position with an accuracy on the order of cm by using high-precision satellite positioning such as RTK-GNSS. On the other hand, determining the position of a moving object from data timestamps with an accuracy of cm order often requires a time accuracy of 1 millisecond or better.

The time stamps used in conventional data loggers, general video cameras, smartphones, and other motion sensors and video recording functions cannot easily achieve a time accuracy of 1 millisecond due to limitations such as the accuracy of the built-in clock generator and the effects of communication delays related to synchronization. The accuracy of the built-in clock generators of consumer-use equipment may have an error on the order of 100 ppm due to various factors. This error cannot be ignored, as even a recording of only 10 seconds cannot guarantee a time accuracy of 1 millisecond. The problem is further complicated when software is involved. In particular, there is a video camera in which the video frame interval fluctuates on the order of several tens of percent due to load fluctuations in the video encoding. A calibration signal for synchronization is used to guarantee the time accuracy of data loggers. In professional equipment, high-precision time management is performed by SMPTE timecode (SMPTE12M-1, 2008) and IEEE1588[1], etc. However, it is not common in consumer equipment. In general, synchronizing data loggers in remote locations or between different media, such as inertial motion and video/audio recording, is not easy.

This paper proposes a method and system for time synchronization between independent data loggers, motion sensors, and different media, such as video and audio, within a 1-millisecond error. The proposed method takes advantage of the fact that the one-second timing pulses (PPS signals) generated by typical GNSS receivers have accuracy on the order of 100 nanoseconds for synchronization purposes. The proposed system achieves synchronization by embedding PPS signals in an inertial measurement unit (IMU) and by displaying LEDs synchronized with PPS signals in the camera images.

Figure 1 shows a block diagram of the main parts of the prototype experimental system with the motorcycle. A logger collects observation data from GNSS, IMU, and vehicle information, and a video camera records video images. The GNSS receiver connected to the logger receives correction information via a server from the electronic reference point. It performs satellite positioning with centimeter-level positional accuracy and nanosecond-level time accuracy using the RTK method.

The IMU device [2] used in the proposed system, simultaneously records PPS signals at the sampling timing and can identify the time

[1] https://standards.ieee.org/ieee/1588/4355/
[2] InvenSence™MPU9250

©2023 Sone, T., Maeda, T., & Kitani, T. published by TU Delft OPEN on behalf of the authors.
ISSN: 2667-2812

 http://dx.doi.org/10.59490/649f22789bdaf83436b1087a

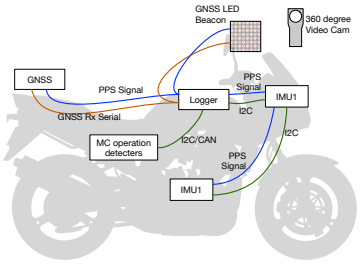


Figure 1. Experimental system overview



Figure 2. GNSS LED Beacon

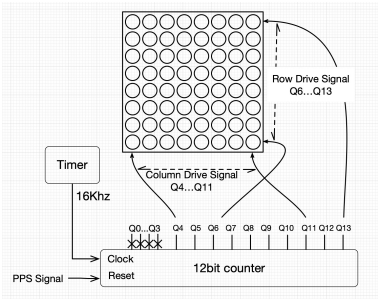


Figure 3. LED matrix driver circuit outline



Figure 4. MC video recording scene



Figure 5. Visualization in GoogleEarth

with the accuracy of the IMU sampling frequency. Using our team's previous work (Ando et al., 2020), we can also identify the time with even higher accuracy by analyzing the IMU data over a longer period. This method takes advantage of the stable and constant interval nature of IMU sampling. In the data evaluation with a sampling frequency of 1 kHz, the time was identified with an average error of 0.136 milliseconds. Although some video cameras can input an electrical signal for time synchronization, the timing of data encoding and the computational load may cause a discrepancy with the recorded time. Therefore, the proposed method employs a method in which a synchronizing LED is projected in the actual video image. Suppose the frame rate during video recording is stable and constant. In that case, the shooting time can be accurately determined by analyzing the image of a single LED lit by the PPS signal using the same method as in the IMU case described above. In our evaluation using an action camera with a frame rate of 240 fps and a shutter speed of 1/3840 seconds, we have confirmed that the time is determined with an accuracy of about 0.4 milliseconds. In the proposed system, the GNSS LED Beacon shown in Figure 2 was developed with multiple LEDs to enable highly accurate time synchronization even with video cameras whose frame rate is not stable. Figure 3 shows the outline of the LED matrix drive circuit. The 8x8 LED matrix is lit by a combination of time signals (10 bits) in 1-millisecond increments generated by resetting a counter with a PPS signal, which is fed by a 16 kHz asynchronous clock input. It is possible to read the time with up to 1 millisecond accuracy directly from the video image taken by the GNSS LED beacon. The time can be read directly from the video image of the GNSS LED beacon with an accuracy of up to 1 millisecond.

The snapshot in Figure 4 shows the GNSS LED Beacon attached to the handlebars of the motorcycle and the 360° camera capturing driving images. Figure 5 is a screenshot of the operation logs of the brake (red) and turn signal (yellow) as the trajectories shifted 30 cm above and to the left and right sides of the motorcycle's travel path and displayed on GoogleEarth.

References

ST 12-1:2008 - SMPTE Standard - For Television - Time and Control Code, *ST 12-1:2008* pp. 1–40, 7 Feb. 2008, doi: 10.5594/SMPTE.ST12-1.2008.

Ando, T., and Kitani, T. (2020), A Time Alignment Method for Multiple Sensing Systems with GNSS Timing and IMUs with Frame-Sync Input, *Proceedings, 2020 IEEE International Conference on Pervasive Computing and Communications Workshops (PerCom Workshops)*, pp. 1–6, Austin, TX, USA, doi: 10.1109/PerComWorkshops48775.2020.9156099.

©2023 Sone, T., Maeda, T., & Kitani, T. published by TU Delft OPEN on behalf of the authors.
ISSN: 2667-2812

The Evolving Scholar (2023)

http://dx.doi.org/10.59490/64676f9c81cd4f660eed285e

Bicycle and Motorcycle Dynamics 2023
Symposium on the Dynamics and Control of Single Track Vehicles
18–20 October 2023, Delft University of Technology, The Netherlands

Type of the Paper: Extended Abstract

Data Collection for Learning the Dynamics and Control of an Electric Unicycle

Levente Mihályi [1,*], Xunbi A. Ji [2], Gábor Orosz [2,3], Dénes Takács [1,4]

[1] Department of Applied Mechanics, Faculty of Mechanical Engineering, Budapest University of Technology and Economics, Budapest, Hungary; mihalyi@mm.bme.hu, ORCID 0009-0007-5901-0624; takacs@mm.bme.hu, ORCID 0000-0003-1226-8613
[2] Department of Mechanical Engineering, University of Michigan, Ann Arbor, MI 48109, USA; xunbij@umich.edu, ORCID 0000-0002-7024-2959; orosz@umich.edu, ORCID 0000-0002-9000-3736
[3] Department of Civil and Environmental Engineering, University of Michigan, Ann Arbor, MI 48109, USA;
[4] ELKH-BME Dynamics of Machines Research Group, Budapest, Hungary;
[*] corresponding author

Name of Editor: Jason Moore
Submitted: 19/05/2023
Accepted: 21/06/2023
Published: 29/06/2023
Citation: Mihályi, L., Ji, X., Orosz, G. & Takács, D. (2023). Data Collection for Learning the Dynamics and Control of an Electric Unicycle. The Evolving Scholar - BMD 2023, 5th Edition.
This work is licensed under a Creative Commons Attribution License (CC-BY).

Abstract:

The spreading of micromobility devices in road transportation systems can open many possibilities. Balance assisted single-wheel vehicles (also called electric unicycles or EUCs) can solve transportation problems in unique ways. Due to their design, they can fit into tight spaces, they do not have significant weight, and their acquisition and maintenance costs are relatively low. For personal travel and for carrying small packages unicycles offer a competitive alternative in urban transportation. In addition, performing delivery tasks in driverless mode may also be feasible considering the simplicity of such mobile robots and their resemblance of human delivery personnel. However, the upright position of such micromobility vehicles is typically unstable. This provide unicycles with high level of maneuverability, but at the same time, they require skilled riders (or high performance controllers) to ensure safe operation (Sheng and Yamafuji, 1995).

In this paper, an experimental method suitable for analyzing the motion of an electric unicycle and its rider is introduced. The main motivation behind the experiment is to learn how humans balance and maneuver while riding the EUC. This may help us in evaluating the safety of human rider, design balance-assist features and/or self-driving functionalities. Our results provide data for later analysis of a human-ridden electric unicycle for a variety maneuvers.

Specifically, we collected data for 34 runs of 7 different maneuvers using 2 riders of different levels of balancing skills. An *OptiTrack* motion tracking system with 12 cameras covering a volume of approximately $4 \times 6 \times 2$ meters was utilized (Molnár et al., 2021). These sensors provide high-precision position and orientation data for each body part defined by a set of markers as shown in Fig. 1. From the *OptiTrack* system, the (x, y, z) coordinates of a predefined pivot point and the orientation angles (yaw, tilt and pitch) are obtained for each body part. The pivot points are mostly set to be human joints and they are shown in white circle where the axis located at each rigid body in Fig. 1(c).

The data collected via the *OptiTrack* system for the EUC and helmet are presented in Fig. 2. These graphs represent a figure-8 maneuver, which is a complex motion because it can be accomplished by turning in relatively large angles around all the three axes. Panel (a) shows the trajectory of the helmet (red line) and the EUC (blue line) in 3D space while making a full figure-8 pattern. It can be seen in panels (b)–(d) that the orientation of the head differ from the orientation of the EUC. This can be explained by the fact that the local coordinate system of the helmet follows the direction the rider is looking at. Using numerical differentiation and data smoothing techniques, the velocity, acceleration, angular velocity and angular acceleration of each rigid body can be obtained from

©2023 Mihályi, L., Ji, X. A., Orosz, G. & Takács D. published by TU Delft OPEN on behalf of the authors.
ISSN: 2667-2812

http://dx.doi.org/10.59490/64676f9c81cd4f660eed285e

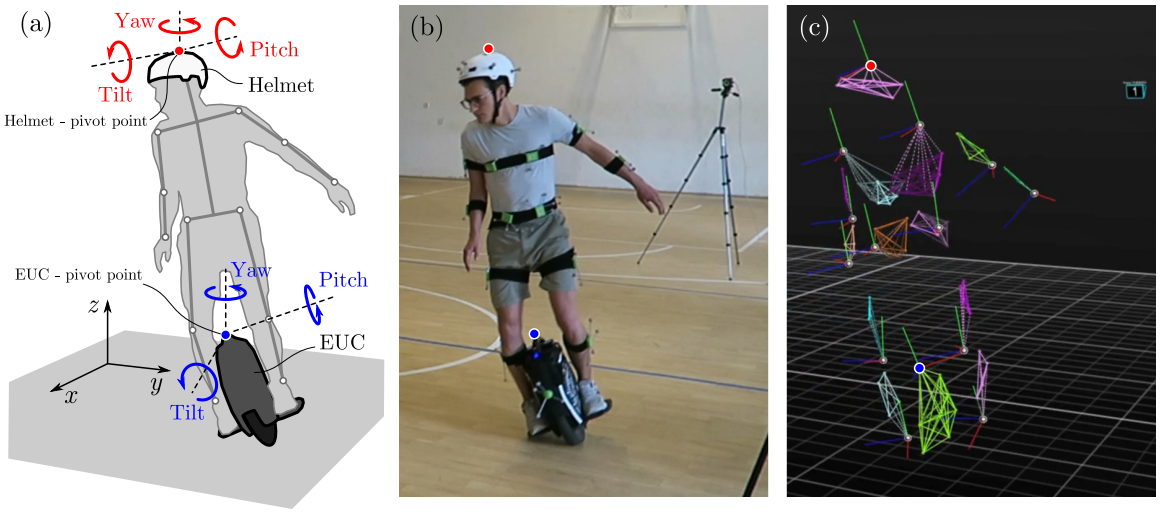


Figure 1. (a) Simplified skeleton model of the human rider on the EUC with the definitions of the pivot points, yaw, tilt and pitch angles. Turning maneuver with the reflective markers in normal camera view (b), and OptiTrack view (c) displaying the corresponding body segments as rigid bodies with the pivot points.

data. As a next step, we will use the measured data to predict the acceleration and angular acceleration. Neural delay differential equations with trainable delay (Ji et al., 2021) will be utilized for learning to capture the reaction time delay (Insperger and John, 2021) of the human rider. These will be combined with a principle model to predict the torque component applied on the EUC by the rider.

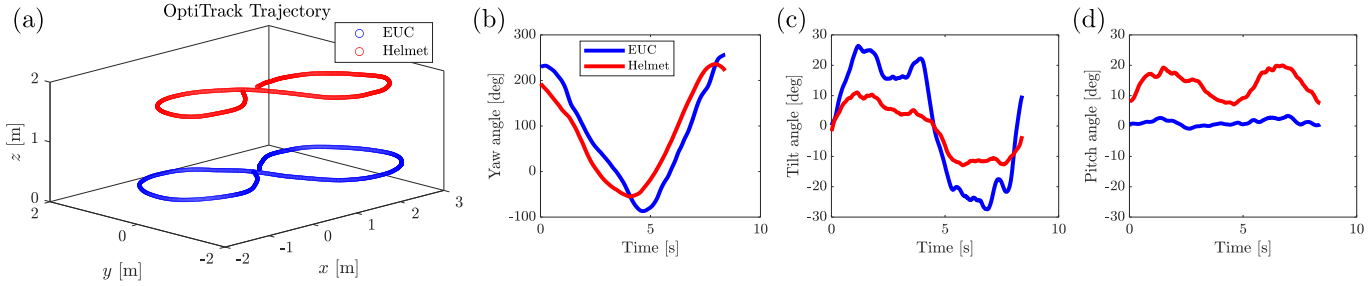


Figure 2. Data obtained from OptiTrack related to figure-8 maneuver: trajectories of two specific rigid bodies (a), and their time series of angles to determine the orientation (b)–(d).

References

Insperger, T. and John, M. (2021). *Delay and Uncertainty in Human Balancing Tasks*. Springer Cham.

Ji, X. A., Molnár, T. G., Avedisov, S. S., and Orosz, G. (2021). Learning the dynamics of time delay systems with trainable delays. In *Proceedings of the 3rd Conference on Learning for Dynamics and Control*, volume 144, pages 930–942. PMLR.

Molnár, Cs., A., Zelei, A., and Insperger, T. (2021). Rolling balance board of adjustable geometry as a tool to assess balancing skill and to estimate reaction time delay. *Journal of the Royal Society Interface. 18: 20200956*.

Sheng, Z. and Yamafuji, K. (1995). Study on the stability and motion control of a unicycle: Part I: Dynamics of a human riding a unicycle and its modeling by link mechanisms. *JSME International Journal, Series C*, 38(2):249–259.

©2023 Mihályi, L., Ji, X. A., Orosz, G. & Takács D. published by TU Delft OPEN on behalf of the authors.
ISSN: 2667-2812

The Evolving Scholar (2023)
https://doi.org/10.24404/63fe188ab0aa2217597e8751
Bicycle and Motorcycle Dynamics 2023
Symposium on the Dynamics and Control of Single Track Vehicles
18 – 20 October 2023, Delft University of Technology, The Netherlands

Type of the Paper: Extended Abstract

Dynamics of a Manual Wheelchair and User During Propulsion

Kathylee Pinnock Branford[1], Meegan G. Van Straaten[2], Omid Jahanian[2], Melissa M. B. Morrow[3], and Stephen M. Cain[1*]

[1]West Virginia University, Morgantown, WV, USA; kp0107@mix.wvu.edu, 0009-0002-2991-7384; stephen.cain@mail.wvu.edu, 0000-0003-1961-4195
[2]Mayo Clinic, Rochester, MN, USA; VanStraaten.Meegan@mayo.edu, 0000-0002-8954-5415; Jahanian.Omid@mayo.edu, 0000-0002-5379-1462
[3]University of Texas Medical Branch, Galveston, TX, USA; memorrow@utmb.edu, 0000-0002-6500-6572
*corresponding author

Name of Editor: Jason Moore
Submitted: 28/02/2023
Accepted: 18/04/2023
Published: 26/04/2023
Citation: Pinnock Branford, K., Van Straaten, M., Jahanian, O., Morrow, M. & Cain, S. (2023). Dynamics of a Manual Wheelchair and User During Propulsion. The Evolving Scholar - BMD 2023, 5th Edition.
This work is licensed under a Creative Commons Attribution License (CC-BY).

Abstract:

Aging causes shoulder tendons to deteriorate for all people, but for people with spinal cord injuries who use a manual wheelchair (MWC) shoulder tendons will tear and cause pain at a younger age and higher rate than people without physical disabilities, (Jahanian et al., 2022). Improved understanding of the daily arm use of MWC users is critical to finding modifiable factors that can decelerate the progression of shoulder pathology. One of the most studied MWC tasks is wheelchair propulsion, as it is the primary mode of mobility and is biomechanically demanding for the upper extremities. Prior studies of overground MWC propulsion have utilized instrumented push rims, which measure triaxial forces and moments exerted by the hand on the push rim during the push phase of propulsion (Cooper, 2009). However, the instrumented push rim is heavier than users' wheel and has limitations for long-term collection during daily life. In contrast, MEMS inertial sensors, which enable continuous measurements of linear acceleration and angular rate in the free-living environment, are lightweight, small, and can be easily attached to a MWC user's wheelchair with minimal impact on wheelchair dynamics. Therefore, our goal is to develop an approach to quantify external forces during MWC propulsion using MWC-mounted inertial sensors, which will enable estimates of upper extremity loading in non-laboratory environments without burdensome instrumentation. In this study, our aim was to evaluate whether acceleration of the system (MWC user and MWC) and center of mass (COM) could be accurately measured using only MWC-mounted inertial sensors.

We utilized a total of 20 inertial sensors (MTw, Xsens/Movella; mass = 16g, acceleration range = ± 160m/s^2, angular rate range = ± 2000deg/s, sampling frequency = 180Hz); one was placed on each wheel hub, one was secured to the MWC frame, and 17 were secured to the participants' body segments (feet, shanks, thighs, pelvis, thorax, upper arms, forearms, hands, and head). An instrumented treadmill (Bertec Corporation; Columbus, Ohio; sampling rate = 1000Hz) recorded ground reaction forces and moments. In this pilot study, data was collected from one able-bodied individual propelling a MWC (TiLite ZR) on the instrumented treadmill at a speed of 1.2m/s. Using the known user and MWC mass, we calculated the acceleration of the user/MWC system COM in the direction of travel from the measured ground reaction force. We also measured the acceleration of the MWC in the direction of travel using two different approaches: 1) by differentiating MWC speed calculated from measured wheel rotation rate and 2) from direct measurements of linear acceleration captured by the frame-mounted sensor. Accelerations of individual body segments were captured from the body-mounted sensors.

Contrary to our expectations, the acceleration of the MWC was notably different from the acceleration of the user/MWC system COM (Figure 1A; RMS difference = 0.32m/s^2, R^2 = 0.29). In contrast, the directly measured acceleration of the MWC was in close agreement with the acceleration of the MWC calculated from wheel rotation rate (Figure 1A; RMS difference = 0.13m/s^2, R^2 = 0.90), confirming that the observed fluctuations in MWC accelerations are true fluctuations and are not measurement noise. Many studies of MWC dynamics assume a MWC user rigidly attached to the wheelchair with rigid upper body dynamics (Johnson & Aylor, 1985; Teran & Ueda, 2017). However, studies have demonstrated that overground wheelchair propulsion and upper body movement cause intra-cycle velocities variations that are often neglected (Chénier et al., 2016). Equation (1) can be used to calculate the acceleration of the user/MWC system COM (a_{system}) if the masses ($m_{segment\ i}$) and accelerations ($a_{segment\ i}$) of all body segments are known. Because the acceleration of the MWC (a_{MWC}) is significantly different from the acceleration of the user/MWC system COM, the accelerations of the body segments of the MWC user are not negligible (Figure 1B).

© 2023 Pinnock Branford, K., Van Straaten, M. G., Jahanian, O., Morrow, M. M. B., & Cain, S. M. published by TU Delft OPEN on behalf of the authors.
ISSN: 2667-2812

$$a_{system} = \left(\frac{1}{m_{total}}\right) * \left(m_{MWC} * a_{MWC} + \sum_{i=1}^{n} (m_{segment\ i} * a_{segment\ i})\right) \quad (1)$$

Figure 1B illustrates the distribution of linear accelerations of each body segment in the direction of travel measured during propulsion. While small in mass, the upper extremities (hand, forearm, and upper arm) experience large accelerations during MWC propulsion, suggesting that the dynamic movements of the upper extremities have a significant impact on the MWC/user system COM acceleration. In comparison, the lower extremities (feet, shanks, thighs, and pelvis) have acceleration distributions similar to the MWC. Body movements of an MWC user (accelerations) can significantly impact the dynamics of the vehicle, especially when the mass of the user is large relative to the mass of the vehicle. The results here are not unlike research demonstrating the importance of bicycle rider COM movements when balancing a bicycle (Cain et al., 2016). Therefore, including the dynamics of the MWC user may be important to include in models of wheelchair dynamics. Future work will aim to accurately estimate MWC/user system COM acceleration using a minimal set of inertial sensors by modelling the movement of the MWC user during propulsion.

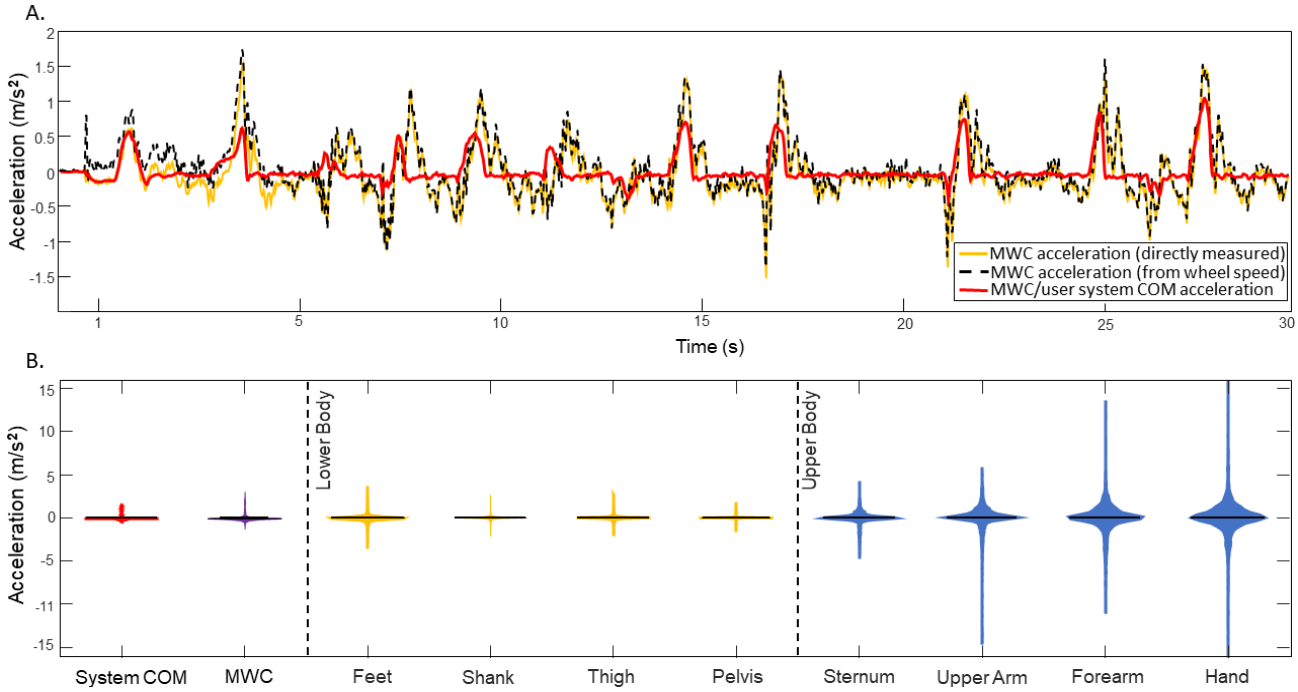


Figure 1. (A) Acceleration of the MWC/user system COM and acceleration of the MWC versus time for one trial (speed = 1.2m/s). MWC acceleration was considerably different than the system COM acceleration. Directly measured acceleration of the MWC was in close agreement with the acceleration of the MWC calculated from wheel rotation rate. **(B)** Distributions of the linear acceleration of the system COM, the MWC, and body segments in the direction of travel for one trial (speed = 1.2m/s). The upper extremities experience larger accelerations than the lower body segments, which are more similar to the acceleration of the MWC alone.

References

Cain, S. M., Ashton-Miller, J. A., & Perkins, N. C. (2016). On the skill of balancing while riding a bicycle. *PLoS one*, 11(2), e0149340.

Chénier, F., Gagnon, D.H., Blouin, M., & Aissaoui, R. (2016). A Simplified Upper-Body Model to Improve the External Validity of Wheelchair Simulators. *IEEE/ASME Transactions on Mechatronics*, 21, 1641-1649.

Cooper R. A. (2009). SMARTWheel: From concept to clinical practice. *Prosthetics and orthotics international*, 33(3), 198–209. https://doi.org/10.1080/03093640903082126

Jahanian, O., Van Straaten, M. G., Barlow, J. D., Murthy, N. S., & Morrow, M. M. B. (2022). Progression of rotator cuff tendon pathology in manual wheelchair users with spinal cord injury: A 1-year longitudinal study. *The journal of spinal cord medicine*, 1–11. Advance online publication. https://doi.org/10.1080/10790268.2022.2057720

Johnson, B.W., & Aylor, J.H. (1985). Dynamic Modeling of an Electric Wheelchair. *IEEE Transactions on Industry Applications*, IA-21, 1284-1293.

Teran, E., & Ueda, J. (2017). Influence of rolling resistance on manual wheelchair dynamics and mechanical efficiency. International *Journal of Intelligent Robotics and Applications*, 1, 55-7

© 2023 Pinnock Branford, K., Van Straaten, M. G., Jahanian, O., Morrow, M. M. B., & Cain, S. M. published by TU Delft OPEN on behalf of the authors.
ISSN: 2667-2812

The Evolving Scholar (2023)
https://doi.org/10.24404/63fe5b20b42c25c6cb80a1b5
Bicycle and Motorcycle Dynamics 2023
Symposium on the Dynamics and Control of Single Track Vehicles
18 – 20 October 2023, Delft University of Technology, The Netherlands

Type of the Paper: Extended Abstract

Experimental assessment of the effect of cyclist's posture on comfort during time-trial events on road cycling

A. Polanco[1,2,*], D. Suarez[2], A. Doria[3] and L.Munoz[4]

[1]Université Gustave Eiffel, France; alejandra.polanco@univ-eiffel.fr, ORCID 0000-0002-9561-6443
[2]Pontificia Universidad Javeriana, Colombia; d-suarez@javeriana.edu.co, ORCID 0000-0001-6264-2250
[3]University of Padova, Italy; alberto.doria@unipd.it, ORCID 0000-0003-0896-7796
[4]Universidad de los Andes, Colombia; lui-muno@uniandes.edu.co, ORCID 0000-0002-7402-1862
*corresponding author.

Name of Editor: Jason Moore
Submitted: 28/02/2023
Accepted: 14/04/2023
Published: 26/04/2023
Citation: Polanco, A., Suarez, D., Doria, A. & Munoz, L. (2023). Experimental assessment of the effect of cyclist's posture on comfort during time-trial events on road cycling. The Evolving Scholar - BMD 2023, 5th Edition.
This work is licensed under a Creative Commons Attribution License (CC-BY).

Abstract:

During cycling, road irregularities are transmitted to the rider through the bicycle in terms of vibrations. The contact areas between the bicycle and the cyclist are the buttocks, hands, and feet, and in the cases in which aerobars are used, the elbows. The relevance of the quantification of vibrations transmitted to cyclists lies in their relationship with comfort (Doria, 2020) and potential health risks. The effect of vibrations on human activities depends on their magnitudes and the time of exposure. For this reason, in this study, the magnitudes of vibrations transmitted to cyclists while riding in different postures were quantified and the time of exposure to such vibrations during cycling was analyzed. This work presents the results obtained from implementing a pilot methodology to assess the effect of the change of cyclists' posture on the vibrations' transmission. The posture variation was performed by modifying the aerobars height considering a time-trial cycling scenario. The magnitudes of vibrations transmitted through the seat post and steering tube were quantified in terms of vibration total values. In addition, an analysis of the implications of the time of exposure to vibrations in cycling was performed based on thresholds of exposure increasing health risks.

Five recreational cyclists voluntarily participated in the tests after signing an informed consent form (mass: 73.8±11.8 kg, height: 1.75±0.06 m, age: 35±7 years). The riders used their own bicycles and standard cycling clothes. The tests were performed on aerobars postures varying the height of the elbow pads using spacers on the steering tube or the aerobars support. The height was set to the maximum (ABhigh) and minimum (ABlow) allowed by each bicycle settings.



Figure 1. Left, set up for the vibrations' transmission measurement. Right, acceleration orientations analyzed in the study.

The vibrations were measured during outdoor tests while the riders pedaled on a testing route at a constant speed. The accelerations along three directions were registered on the seat post and steering tube with accelerometers. The tests consisted of traveling three times at a constant speed of 25 km/h on a 400 m straight route with smooth asphalt. Wireless triaxial accelerometers with a sampling frequency of 5000 Hz (SlamStick LOG-0002-025G-PC, MIDE, USA) were placed on the bicycles

© 2023 Polanco, A., Suarez, D., Doria, A. & Munoz, L. published by TU Delft OPEN on behalf of the authors.
ISSN: 2667-2812

using clamp supports, as presented in Fig 1. A GPS (Forerunner 910, GARMIN, USA) and a speed sensor (Speed sensor 2, GARMIN, USA) were used to register and display the speed to the rider in real time.

The vibrations were computed in terms of vibration total values (a_v) combining the rms accelerations on three orthogonal coordinates and considering the human sensitivity according to ISO2631 (ISO, 1997) for the seat post and ISO5349 (ISO, 2001) for the steering tube. It is worth highlighting that a_v and comfort are inversely related. The thresholds of exposure increasing health risks were assessed considering the curves of health guidance caution zones for whole-body vibration presented in ISO 2631 and the threshold for an increased probability of presenting the hand-arm vibration syndrome presented in ISO 5349. Considering the equivalency between vibration exposures, it is possible to estimate acceptable values of exposure to vibrations (a_a) for given exposure times (t_e) for the accelerations on the seat post and stem, as expressed in Equations (1) and (2), respectively.

$$a_{a,seatpost} = 1.2\sqrt{4/t_e} \quad (1)$$

$$a_{a,steeringtube} = 2\sqrt{8/t_e} \quad (2)$$

The magnitudes of vibrations transmitted to the cyclists through the seat post and steering tube are graphically presented in Figure 2. A one-way ANOVA was performed using a significance level of 0.05 to verify the differences in the a_v between postures. Regarding the seat post, it was obtained that for all the riders, the vibrations increased when changing from ABhigh to ABlow (between 3% and 12%). Nevertheless, only for cyclists 2 and 3, the difference was statistically significant. Regarding the steering tube, a significant difference was found only for cyclist 5, whose acceleration index decreased by 21% when changing from ABhigh to ABlow. The results show that the magnitude of the difference in the a_v of the seat post and the steering tube between the postures changes for each cyclist. The results indicate that for some cyclists, ABlow is less comfortable in the saddle and more comfortable in the steering tube than ABhigh.

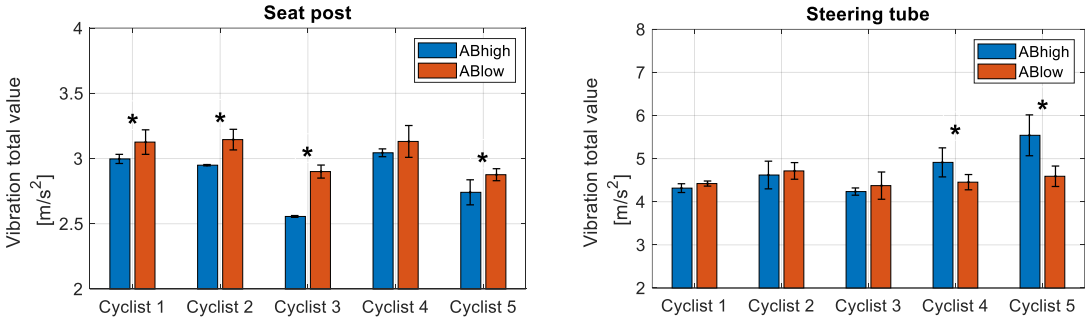


Figure 2. Vibration total values. Left, results for the seat post. Right, results for the steering tube (Asterisks used for pointing out statistically significant differences between postures).

By analyzing the acceleration magnitude ranges registered in this study in the seat post and the stem with respect to the acceptable values of exposure to vibrations, it was observed that the exposure duration to enter a zone of health caution varies between 30 minutes and 2 hours. These time ranges are commonly exceeded in cycling during training and competition, reflecting potential adverse effects on the riders' health due to the prolonged and continuous interaction with the bicycle.

In conclusion, the implementation of an outdoor methodology for assessing the vibrations transmitted to the rider while cycling permitted identifying differences in the vibrations due to changes in the riders' posture. It was observed that for some riders reducing the height of aerobars improved the comfort in the elbows while worsening the comfort on the buttocks. It was also concluded that the exposure to vibrations during cycling should be evaluated in reference to the duration of the riding sessions to reduce possible scenarios of health risk. It is expected to perform the experimental assessment of the effect of cyclist's posture on comfort for a larger group of cyclists to confirm the findings.

References

Doria, A., Marconi, E., Munoz, L., Polanco, A. & Suarez, D. (2020). An experimental-numerical method for the prediction of on-road comfort of city bicycles. *Vehicle system dynamics*, 59(9), 1376-1396.

International Organization for Standardization. (1997). *ISO 2631-1 Mechanical vibration and shock - Evaluation of human exposure to whole-body vibration*.

International Organization for Standardization. (2001). *ISO 5349-1 Mechanical vibration -- Measurement and evaluation of human exposure to hand-transmitted vibration*.

© 2023 Polanco, A., Suarez, D., Doria, A. & Munoz, L. published by TU Delft OPEN on behalf of the authors.
ISSN: 2667-2812

The Evolving Scholar (2023)
https://doi.org/10.24404/63fce42a602ce6dccb0620d0
Bicycle and Motorcycle Dynamics 2023
Symposium on the Dynamics and Control of Single Track Vehicles
18 – 20 October 2023, Delft University of Technology, The Netherlands

Type of the Paper: Extended Abstract

Evaluation of Lane Change Maneuvers on a Dynamic Motorcycle Riding Simulator Utilizing a Rider Leaning Input

Raphael Pleß[1,*], Sebastian Will[1], and Nora Leona Merkel[1]

[1]Würzburger Institut für Verkehrswissenschaften GmbH; pless@wivw.de, https://orcid.org/0009-0006-5984-6723; will@wivw.de, https://orcid.org/0000-0003-0098-6212; merkel@wivw.de, https://orcid.org/0000-0002-4865-368X
*corresponding author.

Name of Editor: Jason Moore
Submitted: 28/02/2023
Accepted: 13/04/2023
Published: 26/04/2023
Citation: Pleß, R. (2023). Evaluation of Lane Change Maneuvers on a Dynamic Motorcycle Riding Simulator Utilizing a Rider Leaning Input. The Evolving Scholar - BMD 2023, 5th Edition.
This work is licensed under a Creative Commons Attribution License (CC-BY).

Abstract:

Up until today, high fidelity dynamic motorcycle riding simulators (DMRS) lack behind the rideability and accessibility of real motorcycles. This is a limiting factor, when it comes to the applicability of such simulators in the development processes of motorcycle manufacturers, suppliers and research institutes. Extensive training of the study participants enables valid studies, but decreases the test efficiency and weakens the trust of managers and decision makers into the results gained on the simulator.

One approach to increase the rideability of DMRS is to introduce technology, that allows utilizing rider motion as an input to the simulation, instead of only implementing a steering input. This approach is called “Dual Loop Rider Control” (DLRC) and is realized on the DESMORI Simulator by means of a roll torque measurement that takes any coupling torque between the rider and

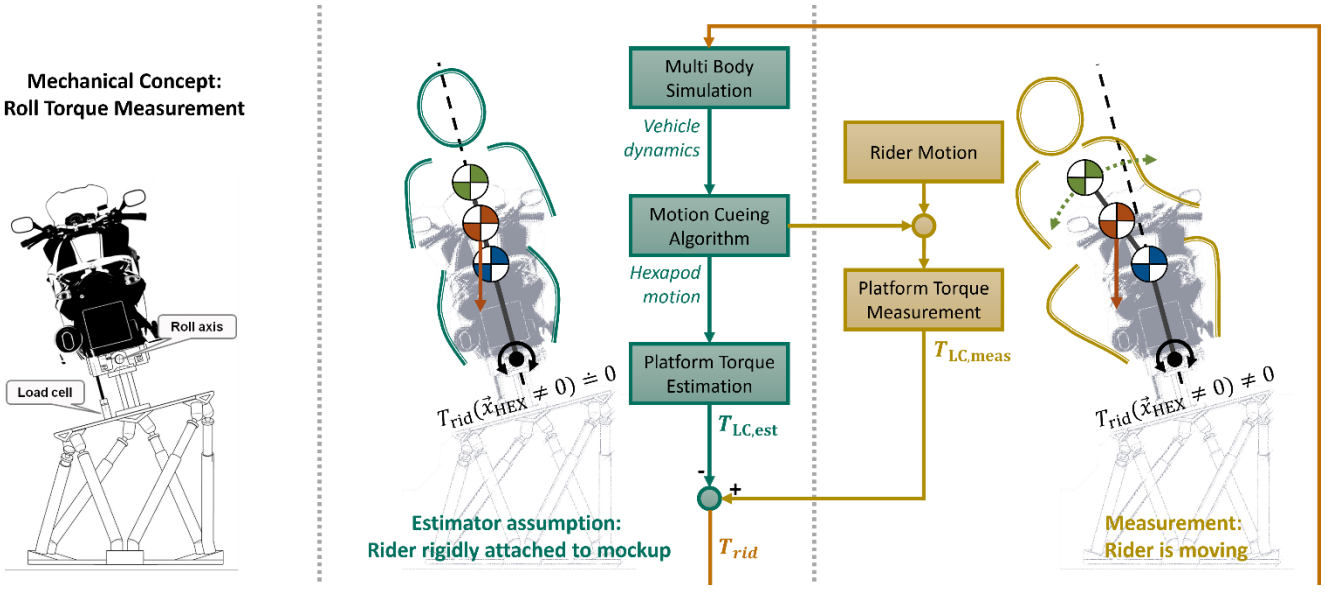


Figure 1: Determination of the rider induced roll torque T_{rid} on the DESMORI Motorcycle Riding Simulator

the motorcycle frame around the vehicle’s longitudinal axis into account. (Pleß, 2016)
The mechatronic concept is depicted in **Figure 1**. The system is affecting the steady state equilibrium of the motorcycle during cornering, e.g., reducing the motorcycle roll angle and steer torque, when a rider is performing a lean-in motion.

© 2023 Pleß, R., Will, S., & Merkel, N. published by TU Delft OPEN on behalf of the authors.
ISSN: 2667-2812

The objective of the paper at hand is to discuss, if and how the applicability and performance of DLRC in dynamic riding maneuvers can be rated. Scales and ratings known from literature, that are for example applied for the analysis of motorcycle handling, are not sufficient for this purpose. For instance, the Lane-Change-Roll Index will decrease when implementing DLRC and utilizing lean-in (vs. riding with steering input only). Typically, the lower steer torque efforts would indicate improved handling ratings. But ultimately, they have no relevance in terms of rideability, accessibility and realism of the simulator, as these don't just correlate with lower steering efforts. Therefore, new performance measures are needed.

It is hypothesized, that an increased rideability of the simulator is observable in a higher precision and repeatability when performing a certain maneuver. A set of characteristic values describing the lance change maneuver is presented, that allows to rate the performance of the simulator. The values result from a curve fitting of the vehicle trajectory to a hyperbolic tangent function. In order to investigate the effects of DLRC on these characteristic values, the lane change maneuver is tested at velocities between 30 km/h and 100 km/h in three different configurations:

- Configuration 1: The maneuvers are performed without activation of the rider leaning input.
  (i.e. representing the state-of-the-art simulators that utilize pure steering control.)
- Configuration 2: The maneuvers are performed with activated rider leaning input
  (i.e., riding without hands.)
- Configuration 3: The maneuvers are performed using both steering and leaning input.
  (i.e. with DLRC)

The data collected in the lane-change maneuvers shows, that the leaning input results in plausible dynamic vehicle responses, when riding without hands. The developed characteristic values indicate slight improvements by the use of DLRC compared to the state-of-the-art configuration. **Figure 2** exemplarily shows a representation of the characteristic values resulting from the lane-change *tanh*-fitting. An activated DLRC (red circles) results in slightly smoother lane transitions compared to the pure steering control (blue circles). The lateral change rate decreases slightly, as does the root mean square error between the measured trajectory and the reference *tanh*-curve.

It is concluded, that the use of DLRC is beneficial in dynamic scenarios. However, just like on real motorcycles, the simulator handling is still dominated by the steering controls and imperfections in that domain cannot be compensated by DLRC.

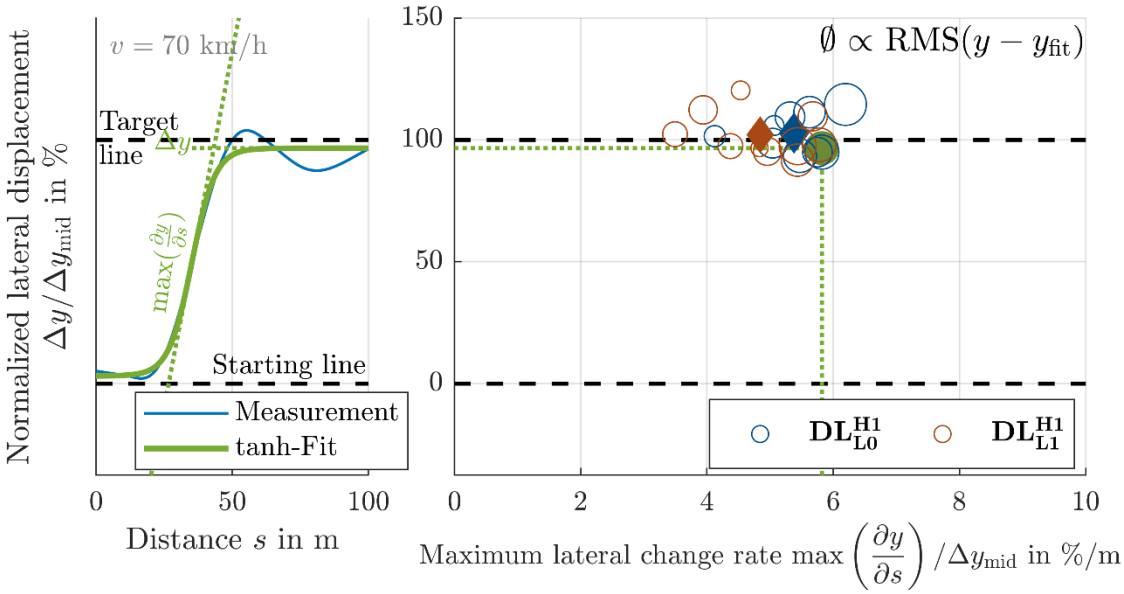


Figure 2: Circle-cluster showing the characteristic values resulting from a lane-change maneuver at 70 km/h.

References

Pleß, R. (2016). Approach to a holistic input determination for a motorcycle riding simulator. *Proceedings of the Bicycle & Motorcycle Dynamics Symposium, Milwaukee, 2016*

© 2023 Pleß, R., Will, S., & Merkel, N. published by TU Delft OPEN on behalf of the authors.
ISSN: 2667-2812

The Evolving Scholar (2023)

http://dx.doi.org/10.24404/6400d2243b869d7aadef8d38

Bicycle and Motorcycle Dynamics 2023
Symposium on the Dynamics and Control of Single Track Vehicles
18–20 October 2023, Delft University of Technology, The Netherlands

Type of the Paper: Extended Abstract

Can a bicycle be balanced using an optimal feedback control mechanism that ignores the sensorimotor delay?

Glykeria Sdoukopoulou [1], Eric Maris [2]

[1] Donders Institute for Brain, Cognition and Behaviour, Radboud University, Nijmegen, The Netherlands; glykeria.sdoukopoulou@ru.nl
[2] Donders Institute for Brain, Cognition and Behaviour, Radboud University, Nijmegen, The Netherlands; eric.maris@donders.ru.nl, ORCID 0000-0001-5166-1800
* corresponding author

Name of Editor: Jason Moore
Submitted: 02/03/2023
Accepted: 26/04/2023
Published: 28/04/2023
Citation: Sdoukopoulou, G. & Maris, E. (2023). Can a bicycle be balanced using an optimal feedback control mechanism that ignores the sensorimotor delay? The Evolving Scholar - BMD 2023, 5th Edition.
This work is licensed under a Creative Commons Attribution License (CC-BY).

Abstract:

A rider balances her bicycle by means of control actions computed by the central nervous system (CNS) and executes these actions via her body's neuromuscular system. A biologically realistic model for bicycle balance control must take into account the biological constraints of the neuromuscular system. In the present study, we focus on the sensorimotor delay (SMD), which is the time between the registration of sensory feedback and the delivery of the control action (Crevecoeur and Gevers (2019)). From empirical studies (Scott (2016)) we know that the SMD is between 60 and 100 ms. This study has two objectives: (1) to investigate the biological plausibility of a model of bicycle balance control with respect to SMD and, (2) to formulate a prediction component (implemented in the CNS) and evaluate whether it successfully deals with bicycle imbalance caused by a SMD that is too long.

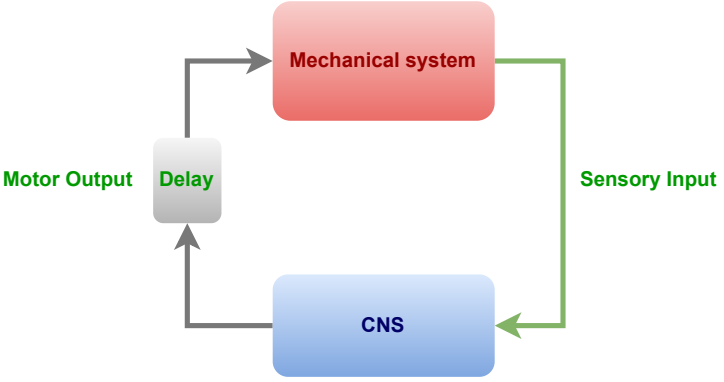


Figure 1. Framework of the bicycle balance control enhanced by the SMD. The mechanical system (in red) is controlled by the computational system, CNS, (in blue). The CNS receives the sensory information (in green) and in response generates optimal motor control actions (in black). The motor control actions are delayed by a shift register.

©2023 Sdoukopoulou, Glykeria, Maris, Eric published by TU Delft OPEN on behalf of the authors.
ISSN: 2667-2812

The biological plausibility of the bicycle balance control with respect to the SMD (see Fig. 1) was investigated in the context of the stochastic optimal feedback control (OFC). Concretely, we exploited the framework of bicycle balance control derived in Maris (2022). The balance control comprises two components, the mechanical and the cognitive. The former one consists of the plant, the bicycle and the rider's body, and obeys the laws of mechanics. The cognitive component refers to the biological mechanisms that the central nervous system (CNS) exploits to respond to the physical principles. The CNS uses an internal forward model to control the mechanical system. It receives the sensory information and in response generates two optimal motor control actions: (1) steering and (2) leaning the upper body. Both the sensory input and the motor output were corrupted by noise. The SMD was simulated by a shift register and it could be introduced either on the motor output or the sensory input. In this study, we introduced the delay in the motor output and we assumed an optimal CNS. All simulations were performed using the benchmark double pendulum (BDP) for studying the bicycle's passive dynamics and the double pendulum as described by Meijaard et al. (2007). Regarding the bicycle's passive dynamics, the linearized EOM are derived for a bicycle and a rider with no upper body. On the other hand, the linearized EOM of the double compound pendulum model the interactions between the upper body and the rear frame, including the lower body.

For evaluating the biological plausibility of a model of bicycle balance control, we must take into account that, even while cycling without external perturbations, there is variation in the lean and steering angles. This variation reflects the inevitable sensorimotor noise (SMN) and the control actions dealing with its consequences (Maris (2022)). Every realistic model therefore must have a random component that produces lean and steering angle variation that approximates the variation observed during actual cycling in a perturbation free environment. In our simulation study, we independently manipulated SMD and SMN amplitude (SMNA) and evaluated whether there are (SMD,SMNA) pairs that produce realistic lean and steering angles. In this way, we determined the maximum SMD that produces realistic steering and lean angles, and we observed that this exceeded the minimum SMD measured in humans.

We next investigated whether SMD-induced stabilization failure could be repaired by adding a prediction component to the CNS. There are several ways to build such a prediction component (Crevecoeur and Gevers (2019)), and in our simulation study we focused on linear prediction (Makhoul (1975)) using the CNS's internal model. We will compare the performance of the different prediction components with respect to how well they can stabilize the bicycle for a wide range of SMDs and SMN characteristics.

References

Crevecoeur, F. and Gevers, M. (2019). Filtering compensation for delays and prediction errors during sensorimotor control. *Neural computation*, 31(4):738–764.

Makhoul, J. (1975). Linear prediction: A tutorial review. *Proceedings of the IEEE*, 63(4):561–580.

Maris, E. (2022). A bicycle can be balanced by stochastic optimal feedback control. *arXiv preprint arXiv:2202.11480*.

Meijaard, J. P., Papadopoulos, J. M., Ruina, A., and Schwab, A. L. (2007). Linearized dynamics equations for the balance and steer of a bicycle: a benchmark and review. *Proceedings of the Royal society A: mathematical, physical and engineering sciences*, 463(2084):1955–1982.

Scott, S. H. (2016). A functional taxonomy of bottom-up sensory feedback processing for motor actions. *Trends in neurosciences*, 39(8):512–526.

©2023 One, A. B., Two, A. C., & Three, A. D. published by TU Delft OPEN on behalf of the authors.
ISSN: 2667-2812

The Evolving Scholar (2023)

https://doi.org/10.59490/645b85b32e41cde9599a9048

Bicycle and Motorcycle Dynamics 2023
Symposium on the Dynamics and Control of Single Track Vehicles
18 – 20 October 2023, Delft University of Technology, The Netherlands

Type of the Paper: Extended Abstract

Planar Dynamics of a Motorcycle: Parameter Sensitivity of Ride Comfort to Engine Mounting System Nonlinearities

Sudhir Kaul[1]

[1]School of Engineering and Technology, Western Carolina University; skaul@wcu.edu, ORCID: 0000-0003-4696-1571

Name of Editor: Jason Moore
Submitted: 02/06/2023
Accepted: 02/06/2023
Published: 21/06/2023
Citation: Kaul, S. (2023). Planar Dynamics of a Motorcycle: Parameter Sensitivity of Ride Comfort to Engine Mounting System Nonlinearities. The Evolving Scholar - BMD 2023, 5th Edition.
This work is licensed under a Creative Commons Attribution License (CC-BY).

Abstract:

This paper examines the influence of several nonlinearities of an engine mounting system on the planar (in-plane) dynamics of a motorcycle. While the primary aim of the engine mounting system is to enhance ride comfort, some of the nonlinearities associated with the system can influence handling in a motorcycle due to the coupled dynamics of the rear unsprung mass and the swing arm. The use of engine mounts is not common in motorcycle powertrains except for a few commercial manufacturers who use isolators to mitigate shaking forces produced by the engine, or to isolate the frame from torque recoil, or to provide isolation at idling.

A planar model of a motorcycle with eight degrees-of-freedom has been used for this study. This model incorporates a multi-axial nonlinear model of the engine mounting system. The nonlinearities investigated in this study are limited to stiffness and damping characteristics of the engine mounting system. However, other nonlinearities can also be investigated through this model. The statistical linearization method has been used in this study to derive an equivalent linear model, this method has shown reasonable accuracy when the excitation input is stationary and Gaussian, and even for non-stationary inputs in some cases (Ricardo, 2013). The governing equation of motion (EOM) of the eight degree-of-freedom system with stiffness and damping nonlinearities of the engine mounting system can be expressed as follows in Equation (1):

$$M\ddot{Y} + \mathrm{C}\dot{Y} + KY + f(Y,\dot{Y}) = \tilde{K}X + \tilde{C}\dot{X} \tag{1}$$

where $\boldsymbol{f(Y,\dot{Y})}$ is an 8×1 matrix consisting of all the terms associated with the nonlinearities of the mounting system while $\boldsymbol{M}$, $\boldsymbol{C}$, and $\boldsymbol{K}$ are the 8×8 mass, damping, and stiffness matrices respectively. Furthermore, $\boldsymbol{Y}$ is the 8×1 matrix consisting of all the degrees-of-freedom of the model while $\widetilde{\boldsymbol{K}} = \begin{bmatrix} 0 & 0 & k_{pf} & 0 & 0 & 0 & 0 & 0 \\ 0 & 0 & 0 & 0 & k_{pr} & 0 & 0 & 0 \end{bmatrix}^T$ and $\widetilde{\boldsymbol{C}} = \begin{bmatrix} 0 & 0 & c_{pf} & 0 & 0 & 0 & 0 & 0 \\ 0 & 0 & 0 & 0 & c_{pr} & 0 & 0 & 0 \end{bmatrix}^T$, where $\boldsymbol{k_{pf}}$ and $\boldsymbol{c_{pf}}$ are the stiffness and damping constants of the front tire while $\boldsymbol{k_{pr}}$ and $\boldsymbol{c_{pr}}$ are the stiffness and damping constants of the rear tire; and $\boldsymbol{X}$ represents the road excitation input at the front and rear tires with $\boldsymbol{X} = \left[y_f(t) \quad y_f\left(t - \frac{p}{V}\right)\right]^T$, where $\boldsymbol{y_f}$ is the vertical displacement input at the front tire due to the irregularity of the road surface, $\boldsymbol{p}$ is the wheelbase of the motorcycle, and $\boldsymbol{V}$ is the constant velocity at which the motorcycle is traveling in a straight line. Such a representation of the road excitation input accounts for wheelbase filtering due to a lag between the front tire and the rear tire as the motorcycle travels at a constant velocity in a straight line and has been used in other studies on ride comfort (Cossalter, 2006; Cossalter et al., 2006). The detailed derivation of the general model used for this study can be found in the existing literature (Kaul, 2020) and a layout of the model can be seen in Figure 1.

The equivalent linear model for the nonlinear model in Equation (1) has been derived by using the statistical linearization method, and is expressed in Equation (2) as:

$$M\ddot{Y} + (C + C_e)\dot{Y} + (K + K_e)Y = \tilde{K}X + \tilde{C}\dot{X} \tag{2}$$

© 2023 Kaul, S. published by TU Delft OPEN on behalf of the authors.
ISSN: 2667-2812

where $\boldsymbol{C_e}$ and $\boldsymbol{K_e}$ are the equivalent damping and stiffness matrices that have been derived to account for nonlinearities of the engine mounting system. This equivalent linear model is used to determine the power spectral density (PSD) of acceleration of each degree-of-freedom as well as the time domain and frequency domain response of the system.

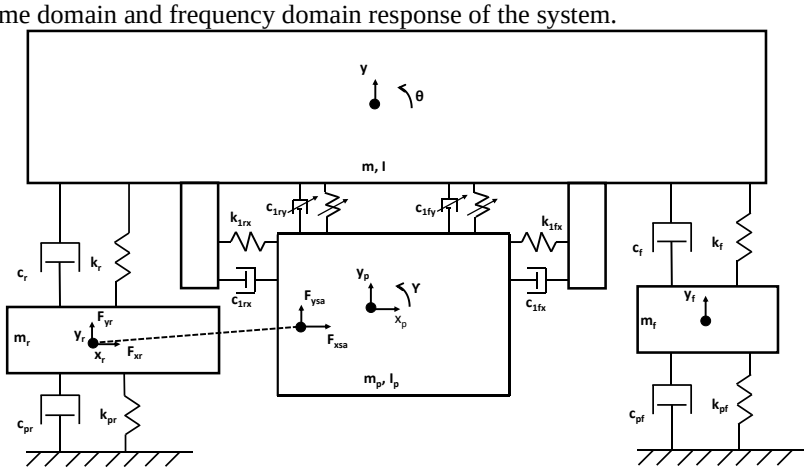


Figure 1. Planar model with engine mounting system nonlinearities.

The parameters used for this study have been adapted from existing literature (Cossalter, 2006; Kaul, 2020) and are listed as follows: $\boldsymbol{p = 1.4\ \text{m}}$, $\boldsymbol{b = 0.7\ \text{m}}$, $\boldsymbol{m = 200\ \text{kg}}$, $\boldsymbol{I = 40\ \text{kg m}^2}$, $\boldsymbol{k_f = 15\ \text{kN/m}}$, $\boldsymbol{k_r = 25\ \text{kN/m}}$, $\boldsymbol{k_{pf} = 180\ \text{kN/m}}$, $\boldsymbol{k_{pr} = 180\ \text{kN/m}}$, $\boldsymbol{m_f = 15\ \text{kg}}$, $\boldsymbol{m_r = 20\ \text{kg}}$, $\boldsymbol{m_p = 100\ \text{kg}}$, $\boldsymbol{I_p = 10\ \text{kg m}^2}$, $\boldsymbol{x_{r1} = 320\ \text{mm}}$, $\boldsymbol{y_{r1} = 55\ \text{mm}}$, $\boldsymbol{x_{f1} = 325\ \text{mm}}$, $\boldsymbol{y_{f1} = 20\ \text{mm}}$.

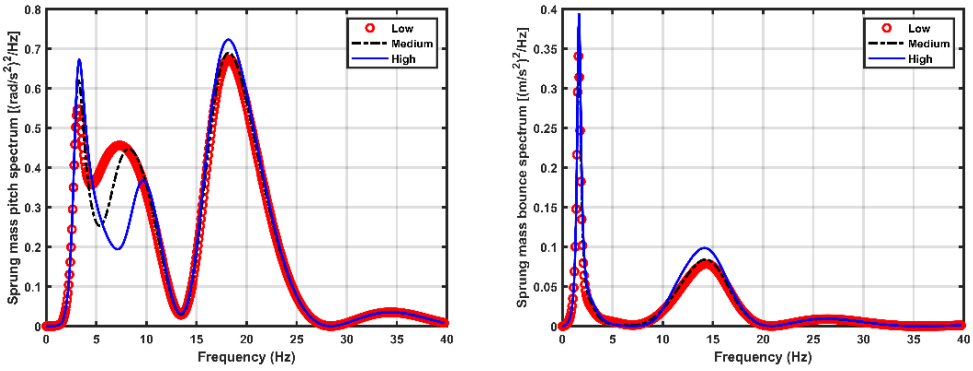


Figure 2. Acceleration spectrum of sprung mass (a) pitch (b) bounce – stiffness nonlinearity.

Three cases of stiffness nonlinearity summarized in the results in Figure 2 indicate varying levels of progressive increase in the effective vertical stiffness of the mounting system (listed as low, medium, and high) with increasing displacement of the powertrain when the motorcycle is traveling in a straight line with a constant velocity of 20 m/s (72 kph) over an asphalted road surface with a bumpy profile. Progressive increase in stiffness is a common design requirement for engine mounting systems in motorcycles due to limited space around the powertrain. As seen from the results in Figure 2, the peaks of both spectra are influenced to varying levels by different configurations of stiffness nonlinearity while the root mean square of acceleration is significantly influenced by the stiffness nonlinearity, particularly for the pitch spectrum.

The nonlinear model provides an analytical insight that can be useful during the early stages of development. Suspension system nonlinearities can be incorporated into the model for a holistic determination of ride comfort from the planar model. Some experimental correlation will be needed in the future for model validation.

References

Cossalter, V. (2006). *Motorcycle Dynamics*. Second Edition, Lulu, Morrisville, NC, USA.
Cossalter, V., Doria, A., Garbin, S., & Lot, R. (2006). Frequency-domain method for evaluating the ride comfort of a motorcycle. *Vehicle System Dynamics*, 44, 339–355.
Kaul, S. (2020). Planar Dynamics of a Motorcycle: Influence of Vibration Isolation System Nonlinearity. *International Journal of Acoustics and Vibration*, 25, 597–608.
Ricardo, L.A.R. (2013). *Nonlinear Stochastic Analysis of Motorcycle Dynamics*. PhD Thesis, Rice University, Houston, TX, USA.

© 2023 Kaul, S. published by TU Delft OPEN on behalf of the authors.
ISSN: 2667-2812

The Evolving Scholar (2023)

http://dx.doi.org/10.24404/63fdc1dae801a6f1332c92a1

Bicycle and Motorcycle Dynamics 2023
Symposium on the Dynamics and Control of Single Track Vehicles
18–20 October 2023, Delft University of Technology, The Netherlands

Type of the Paper: Extended Abstract

Theoretical and experimental findings for an tyre-road friction potential estimator for motorcycles

Ott C. [1,*], Klinger F. [1], Edelmann J. [1], Plöchl M. [1]

[1] Institute of Mechanics and Mechatronics, Vehicle System Dynamics Research Group, TU Wien, Austria; christoph.ott@tuwien.ac.at; florian.klinger@tuwien.ac.at; johannes.edelmann@tuwien.ac.at; manfred.ploechl@tuwien.ac.at

[*] corresponding author

Name of Editor: Jason Moore
Submitted: 28/02/2023
Accepted: 13/04/2023
Published: 26/04/2023
Citation: Ott, C., Klinger, F., Edelmann, J. & Plöchl, M. (2023). Theoretical and experimental findings for an tyre-road friction potential estimator for motorcycles. The Evolving Scholar - BMD 2023, 5th Edition.

This work is licensed under a Creative Commons Attribution License (CC-BY).

Abstract:

The tyre-road contact is the only connection of a motorcycle with the ground and has therefore a decisive influence on its longitudinal and lateral dynamics. Due to this fact, knowledge of the tyre-road friction potential can contribute to performance improvements of current motorcycle systems as Anti-Lock Braking System (ABS), Traction Control System (TCS), Stability Control System and may also be required for the development of further functions of an Advanced Driver Assistance System (ADAS).
Basically, the road-grip estimation methods can be classified into *cause-based* and *effect-based* identification methods. Former are based on the identified environmental conditions such as the temperature, rain detection, and water or snow detection on the roadway to infer a change of the grip conditions. This can also be done predictively within certain limits, but usually only allows the classification of the grip conditions. The latter uses the effects of the current tyre-road contact conditions on the tyre/motorcycle dynamic behaviour to estimate the maximum friction potential. In this case, real-time capable models are required, which represent, in addition to the dynamic behaviour of the motorcycle, also the tyre forces and torques appropriately.

Although this research topic has been covered extensively, they refer exclusively to two-track vehicles. A relevant exception to this is the publication of Savino et al. (2013). This article, based on an estimation method proposed by Tanelli et al. (2009), addresses the road-grip potential estimation of a motorcycle during a braking manoeuvre along a straight path with a linear basis function for the tyre characteristics. A comprehensive review of effect-based friction estimation methods can be found in Acosta et al. (2018).
In cause of this work, the potential of the grip estimation will be discussed based on the required excitation level and estimation time. Idealised conditions, with added white noise to the signals, are considered. Estimating the tyre-road friction potential requires an excitation above the linear tire behaviour within the transient region of the tyre characteristics. It is reasonable to assume that the excitation level in the longitudinal direction is higher than in the lateral direction for an everyday use case. Therefore the chosen driving manoeuvre is similar to that used by Savino et al. (2013).

A rigid two-wheel motorcycle model, consisting of the motorcycle's longitudinal equation of motion (EOM) and a rotational EOM for each wheel, combined with a simplified magic formula (MF) tyre model is used to describe the system in a simple way. Lateral slip and roll (camber) angle are not considered within this idealized environment. The estimation algorithm with this non-linear system description is based on a discrete extended Kalman-Filter (EKF) (Simon, 2006). Since the wheel dynamic is much faster than the longitudinal dynamics of the motorcycle, it is favourable to approximate the related discretized system equation by a truncated Taylor expansion, according to Rill (2006).

Under the premise that a wide range of the tyre characteristic curve is reached by the applied torques, a sawtooth profile was selected for the drive torque at the rear wheel and the brake torque at the front wheel. A previously defined maximum excitation level (μ/μ_{max}) is reached by selecting the torque amplitudes accordingly, provided this is possible without lifting a wheel.

©2023 O. C., K. F., E. J, & P. M. published by TU Delft OPEN on behalf of the authors.
ISSN: 2667-2812

 http://dx.doi.org/10.24404/63fdc1dae801a6f1332c92a1

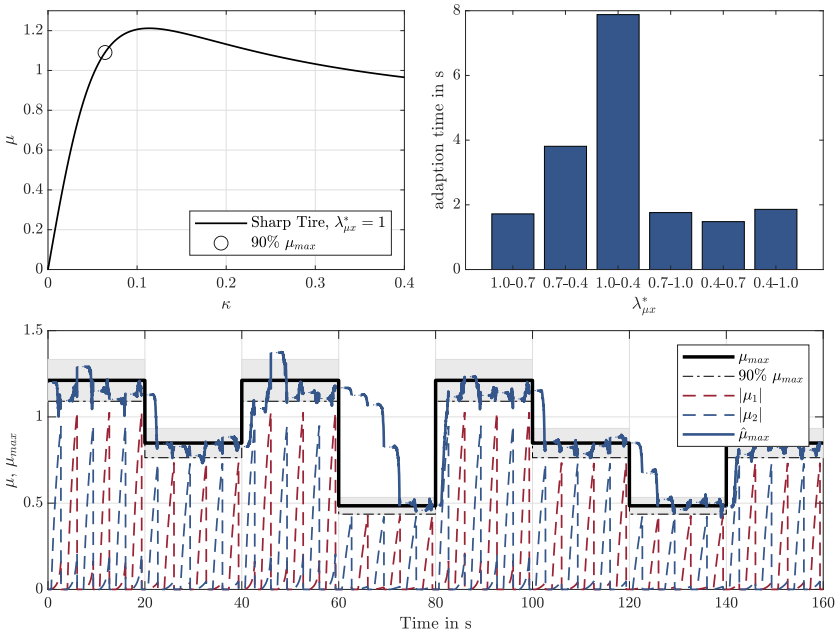


Figure 1. Tyre characteristics with indicated maximum excitation of $90\%\ \mu_{max}$ (top left); required adaption time for changes of the friction scaling factor $\lambda^*_{\mu x}$ (top right); tyre-road friction potential estimation at changing friction scaling factor with an maximum excitation of $90\%\ \mu_{max}$ (bottom)

The tyre MF parameters used for the simulation are from Sharp et al. (2004), and the characteristics is shown in the top left diagram of figure 1. In addition, the chosen maximum excitation level is marked by the circle. The progress of the estimated tyre-road friction potential $\hat{\mu}_{max}$ is compared with the actual value μ_{max} in the lower diagram. Changes in the grip conditions are realized with the related MF scaling factor $\lambda^*_{\mu x}$.
Based on these estimations with idealised conditions, the required excitation level, as well as the minimum adaption time for the implemented algorithm could be shown. These findings will be verified with actual test runs by this year's summer. Another objective of these tests is to determine the tyre characteristics for different road conditions, as the chosen estimation method relies on a pronounced transient region of the motorcycle tyre. With the new data, it will be possible to evaluate the potential of an friction potential estimator with longitudinal excitation. It may be advisable to use the slip stiffness as an estimation variable.

References

Acosta, M., Kanarachos, S., and Blundell, M. (2018). Virtual tyre force sensors: An overview of tyre model-based and tyre model-less state estimation techniques. *Proceedings of the Institution of Mechanical Engineers, Part D: Journal of Automobile Engineering*, 232(14):1883–1930.

Rill, G. (2006). A modified implicit euler algorithm for solving vehicle dynamic equations. *Multibody System Dynamics*, 15:1–24.

Savino, G., Giovannini, F., Baldanzini, N., and Pierini, M. (2013). Real-time estimation of road–tyre adherence for motorcycles. *Vehicle System Dynamics*, 51(12):1839–1852.

Sharp, R., Evangelou, S., and Limebeer, D. J. (2004). Advances in the modelling of motorcycle dynamics. *Multibody system dynamics*, 12:251–283.

Simon, D. (2006). *Optimal State Estimation: Kalman, H infinity, and Nonlinear Approaches*. John Wiley & Sons, Inc.

Tanelli, M., Piroddi, L., and Savaresi, S. M. (2009). Real-time identification of tire–road friction conditions. *IET control theory & applications*, 3(7):891–906.

©2023 O. C., K. F., E. J, & P. M. published by TU Delft OPEN on behalf of the authors.
ISSN: 2667-2812

The Evolving Scholar (2023)
https://doi.org/10.24404/644ba1e13c57633bb23a9dc6
Bicycle and Motorcycle Dynamics 2023
Symposium on the Dynamics and Control of Single Track Vehicles
18 – 20 October 2023, Delft University of Technology, The Netherlands

Type of the Paper: Extended Abstract

Indoor measurement of the lateral characteristics of a cargo bicycle tyre

G. Dell'Orto[1,2,*], F. M. Ballo[1], G. Mastinu[1] , R. Happee[2], J.K. Moore[2]

[1]Politecnico di Milano, Italy; [2]Delft University of Technology, The Netherlands;
gabriele.dellorto@polimi.it, ORCID 0000-0001-6186-6869;
federicomaria.ballo@polimi.it, ORCID 0000-0002-0557-9889; gianpiero.mastinu@polimi.it, ORCID 0000-0001-5601-9059; r.Happee@tudelft.nl, ORCID 0000-0001-5878-3472; j.k.moore@tudelft.nl
*corresponding author.

Name of Editor: Edwin de Vries
Submitted: 18/05/2023
Accepted: 18/05/2023
Published: 26/06/2023
Citation: Dell'Orto, G., Ballo, F., Mastinu, G., Happee, R. & Moore, J. (2023). Indoor measurement of the lateral characteristics of a cargo bicycle tyre. The Evolving Scholar - BMD 2023, 5th Edition.
This work is licensed under a Creative Commons Attribution License (CC-BY).

Abstract:

The use of bicycles as a cheap and healthy way to travel the "last mile" is spreading widely in the cities. This new way of dealing with short trips, known as "micro-mobility", is also fostered by the new awareness of the global impact of ICE vehicles and rising fuel costs. In recent years, also cargo bikes are knowing a large use, both for families with children and for delivery purposes. They are commonly configured as two-wheeled vehicles with extended wheelbase to carry loads in front the rider (known as "front-loader" bicycles), or behind the rider (models known as "longtail"). This requires fairly skilled riders to deal with driving dynamics, different from the common bicycle we are used to (Miller, M., 2023). They can easily reach a speed of 25 km/h (according to the regulations in most EU countries) being usually pedal-assisted.
Tyre characteristics may strongly affect bicycle dynamics (Bulsink, V., 2015). This applies even more for cargo bikes as they are featured by remarkable load variation (load/unload configuration), relatively high speed and torque applied to the tyres, both during acceleration and braking phases. In this context, it is important to have a good understanding of tyre characteristics. With the aim of designing safer and higher performing bicycles, numerical models are required. Furthermore, existing mechanical models of bicycles mostly ignore tyre dynamics and need to be updated with realistic tyre models (Dell'Orto, G., 2022).



Figure 1. Test-rig *VeTyT* with the cargo bicycle tyre mounted on. The device was designed to ensure the proper alignment and provide an accurate measurement.



Figure 2. New steel plates for *VeTyT*. To accomplish with the specific dimensions of cargo bicycle wheel, new steel plates were designed and manufactured.

© 2023 Dell'Orto, G., Ballo, F. M., & Mastinu, G. published by TU Delft OPEN on behalf of the authors.
ISSN: 2667-2812

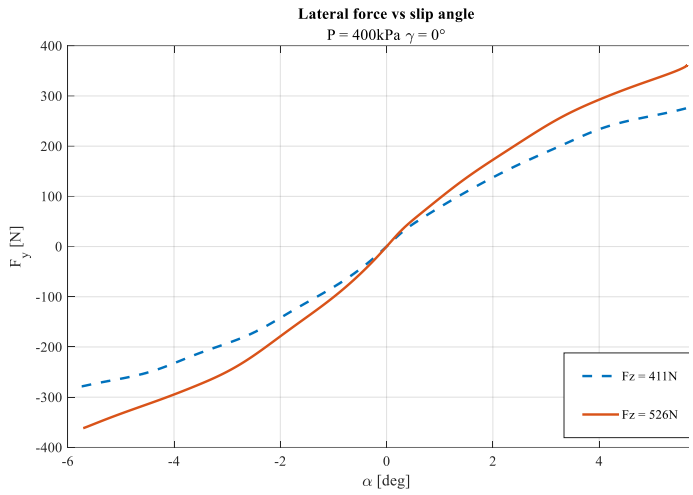


Figure 3. Lateral force $\boldsymbol{F_y}$ [N] as function of slip angle α [deg]. Results were experimentally obtained for inflation pressure of 400 kPa and camber angle equal to 0 deg.

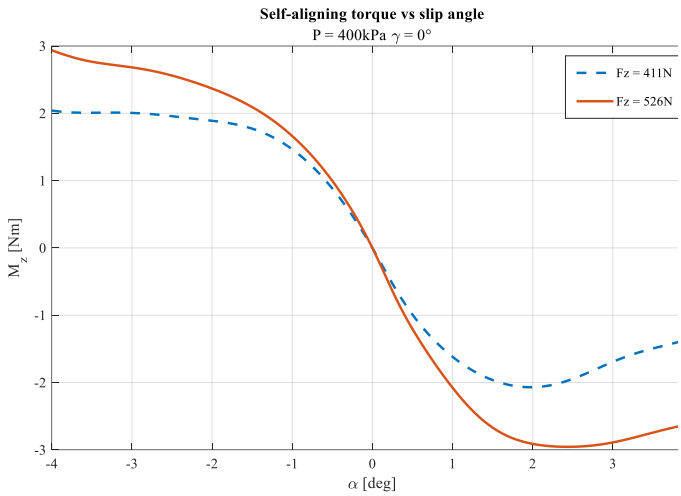


Figure 4. Self-aligning torque $\boldsymbol{M_z}$ [Nm] as function of slip angle α [deg]. Results were experimentally obtained for inflation pressure of 400 kPa and camber angle equal to 0 deg.

Measurements were performed with *VeTyT*, an indoor test-rig specific for bicycle tyres, designed at the Department of Mechanical engineering of Politecnico di Milano (Figure 1) (Dell'Orto, G., 2022). It is the only test-rig for bicycle tyres complying to the standard ISO 9001-2015, ensuring a certified procedure for testing. We can measure lateral force and self-aligning torque, as tyre parameters vary.
The tyre 20"x2,15 was mounted on a standard aluminum rim and tested on flat track. The specific dimensions of the cargo bicycle wheel forced us to update the test-rig, designing a new steel fork to ensure sufficient stiffness and new steel plates to carry the wheel on flat track (Figure 2). Inflation pressure was set to 400 kPa, as recommended by the manufacturer. Tests were performed applying a vertical load of 411 N and 526 N, according to the technical limits of the test-rig. The camber was set to 0 degree, as first stage of the study.
The lateral force and self-aligning torque as function of the slip angle are shown in Figure 3 and Figure 4, respectively. It is clear the difference in outcomes adjusting the vertical load. As the vertical load increases, both the lateral force and the self-aligning torque increase in magnitude. As expected, the tyre can generate higher forces with higher vertical load. It is worth noticing that the peak value of lateral force will be reached for very large slip angles (> |6| degrees, the maximum value tested in this study). Tyres for cargo bicycles are designed to carry large loads, therefore we expect to reach saturation conditions for higher vertical forces or, conversely, large slip angles. The cornering stiffnesses are reported in Table 1: for vertical load 526 N it is 24% higher than that found at 411 N.

Table 1. Cornering stiffness for different vertical loads. In the last column, the variation (in percentage) of cornering stiffness due to increasing vertical load.

Vertical load	Cornering stiffness	Variation %
411 N	*85.1 N/ °*	-
526 N	*105.5 N/ °*	*+24%*

This project was partly financed and supported by the TKI/ClickNL 'De Fiets van de Toekomst' grant and Royal Dutch Gazelle. Special thanks to Dr. Mario Pennati, Vincenzo Tartaglione and Isabel Pollini for their support during tyre testing.

References

Bulsink, V., Doria, A, van de Belt, D., Koopman, B. (2015). The effect of tyre and rider properties on the stability of a bicycle. *Advance in Mechanical Engineering 7(12)*. https://doi.org/10.1177/1687814015622596
Dell'Orto, G., Ballo, F. M., Mastinu, G., Gobbi, M. (2022). Bicycle tyres – development of a new test-rig to measure mechanical characteristics. *Measurement*, 202, 111813. https://doi.org/10.1016/j.measurement.2022.111813
Dell'Orto, G., Ballo, F. M., Mastinu, G. (2022). Experimental methods to measure the lateral characteristics of bicycle tyres – a review. *Vehicle System Dynamics*, 1–23. https://doi.org/10.1080/00423114.2022.2144388
Miller, M., Pfeil, M., Reick, B., Murri, R., Stetter, R., Kennel, R. (2023) Measurement and Modeling of a Cargo Bicycle Tire for Vehicle Dynamics Simulation. *Appl. Sci.*,13, 2542. https://doi.org/10.3390/app13042542

© 2023 Dell'Orto, G., Ballo, F. M., & Mastinu G. published by TU Delft OPEN on behalf of the authors.
ISSN: 2667-2812

The Evolving Scholar (2023)
https://doi.org/10.24404/63fe327a6cf80479c0db7f83
Bicycle and Motorcycle Dynamics 2023
Symposium on the Dynamics and Control of Single Track Vehicles
18 – 20 October 2023, Delft University of Technology, The Netherlands

Type of the Paper: Extended Abstract

Thermal model for bicycle tire internal temperature evaluation in various contact conditions

Farroni F.[1]*, Napolitano Dell'Annunziata G.[1], Ruffini M.[1], Dell'Orto G.[2], Mastinu G.[2]

[1]Università degli Studi di Napoli Federico II, Italy; flavio.farroni@unina.it, ORCID 0000-0001-8257-5534; guido.napolitanodellannunziata@unina.it, ORCID 0000-0002-7293-4975, marco.ruffini@unina.it
[2]Politecnico di Milano, Italy; gabriele.dellorto@polimi.it, ORCID 0000-0001-6186-6869; gianpiero.mastinu@polimi.it, ORCID 0000-0001-5601-9059
*corresponding author.

Name of Editor: Jason Moore
Submitted: 28/02/2023
Accepted: 13/04/2023
Published: 26/04/2023
Citation: Farroni, F., Napolitano Dell'Annunziata, G., Ruffini, M., Dell'Orto, G. & Mastinu, G. (2023). Thermal model for bicycle tire internal temperature evaluation in various contact conditions. The Evolving Scholar - BMD 2023, 5th Edition.
This work is licensed under a Creative Commons Attribution License (CC-BY).

Abstract:

Bicycle mobility has become increasingly popular as a sustainable and healthy means of transportation. Bicycles are not only a cost-effective mode of transportation but also help to reduce traffic congestion and air pollution. However, the efficiency and safety of bicycling largely depend on the optimization of bike components, such as the tires. The importance of bike tire optimization cannot be underestimated as it can affect both the bicycle dynamics and bicycle performance. In recent years, research has focused on improving the design and materials used in bike tires to enhance their efficiency and safety, mainly investing on empirical correlation activities (Steyn, 2014) and FEA models (Kumar, 2018).
Due to the lack of multi-physical mathematical models able to analyze and reproduce complex tire/road contact phenomena, useful to predict the wide range of working conditions, this research aims to the development of a bicycle tire thermal model. With the know-how gained in motorcycle applications (Farroni, 2020), the main outcome is to provide the full temperature local distribution inside the tire inner rubber layers and the inflation chamber. Such kind of information plays a fundamental role in the definition of the optimal adherence conditions, for both safety and performance maximization, and as an indicator of the proper tire design for various applications, each requiring specific heat generation and management.

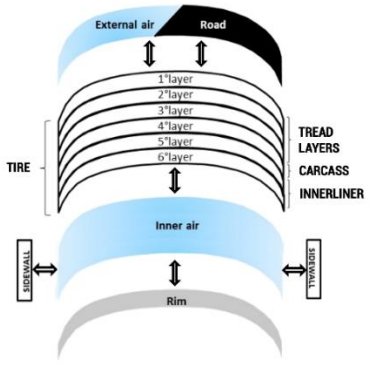


Figure 1. The conceptual scheme of the tire thermal model, and of its internal structure

The model, based on the thermodynamics Fourier Differential Equations applied to a three dimensional domain, has been parameterized measuring for a reference bicycle tire the variation of the footprint extension due to vertical load, camber and inflation pressure. Furthermore, the thermal conductivity and the specific heat of the various layers and materials constituting the tire was measured with a nondestructive procedure (Farroni, 2018). Data input and outputs are schematized in Figure 2.

© 2023 Farroni F., Napolitano Dell'Annunziata G., Ruffini M., Dell'Orto G., published by TU Delft OPEN on behalf of the authors.
ISSN: 2667-2812

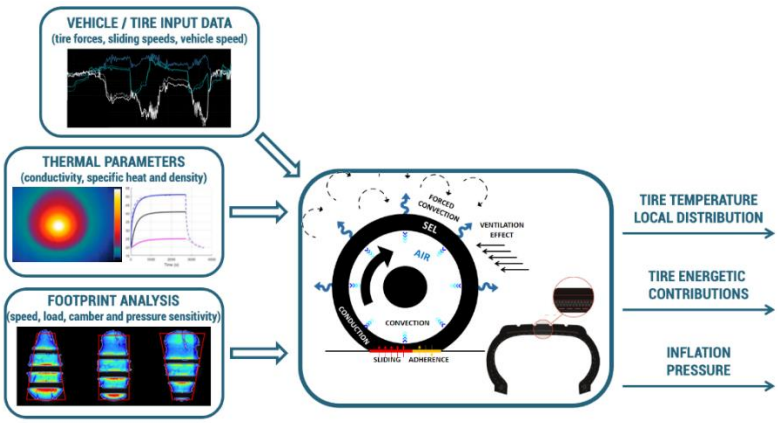


Figure 2. The tire thermal model parameterization principle and the input/output overview

The experimental validation has been carried out thanks to an innovative test-rig developed at Politecnico di Milano (Figure 3). It is the only test-rig for measuring the mechanical characteristics of bicycle tires complying to the standard ISO 9001-2015. It has been specifically instrumented for the activity, acquiring the external tire temperatures to be compared with the respective simulated ones, under various working conditions.

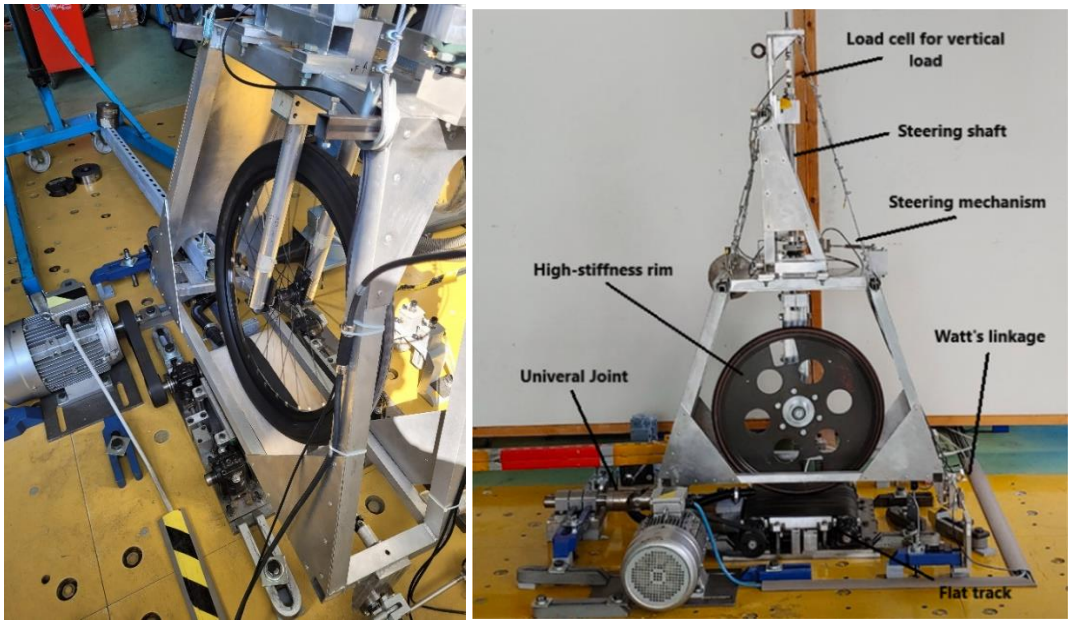


Figure 3. Test-rig used for the experimental validation of bicycle tyre thermal model (Dell'Orto, 2022).

References

Dell'Orto, G., Ballo, F. M., Mastinu, G., Gobbi, M. (2022). Bicycle tyres – development of a new test-rig to measure mechanical characteristics. *Measurement*, 202, 111813. https://doi.org/10.1016/j.measurement.2022.111813

Farroni, F., Lenzo, B., Mancinelli, N., Mercantini, M., Sakhnevych, A., Timpone, F. (2020), A real-time Thermal Model for the Analysis of Tire/Road Interaction in Motorcycle Applications. Symposium on the Dynamics and Control of Single Track Vehicles. A *Proceedings of the 2019 Bicycle and Motorcycle Dynamics Conference: A Symposium on the Dynamics and Control of Single Track Vehicles held in Padova, Italy September 9th through 11th in the year 2019.*

Farroni, F., Russo, M., Sakhnevych A., Timpone F. (2018), TRT EVO: Advances in real-time thermodynamic tire modeling for vehicle dynamics simulations, *Proc IMechE Part D: J Automobile Engineering, 233(1) 121–135.*

Kumar, M., Rajan, H. (2018), Finite Element Analysis of Bicycle Wheel, *International Research Journal of Engineering and Technology (IRJET), 5(6), 949-956.*

Steyn, W. J.vdM., Warnich, J. (2014), Comparison of tyre rolling resistance for different mountain bike tyre diameters and surface conditions, *South African Journal for Research in Sport, Physical Education and Recreation, 36(2), 179-193.*

© 2023 Farroni F., Napolitano Dell'Annunziata G., Ruffini M., Dell'Orto G., published by TU Delft OPEN on behalf of the authors.
ISSN: 2667-2812

The Evolving Scholar (2023)

https://doi.org/10.24404/63fd8435fca7904adf915064

Bicycle and Motorcycle Dynamics 2023
Symposium on the Dynamics and Control of Single Track Vehicles
18 – 20 October 2023, Delft University of Technology, The Netherlands

Type of the Paper: Extended Abstract

Radial Stiffness and Damping of Mountain Bike Tires Subject to Impact Determined Using the Coefficient of Restitution

J. Sadauckas[1,*], N. Schoeneck[2], and M. Nagurka[3]

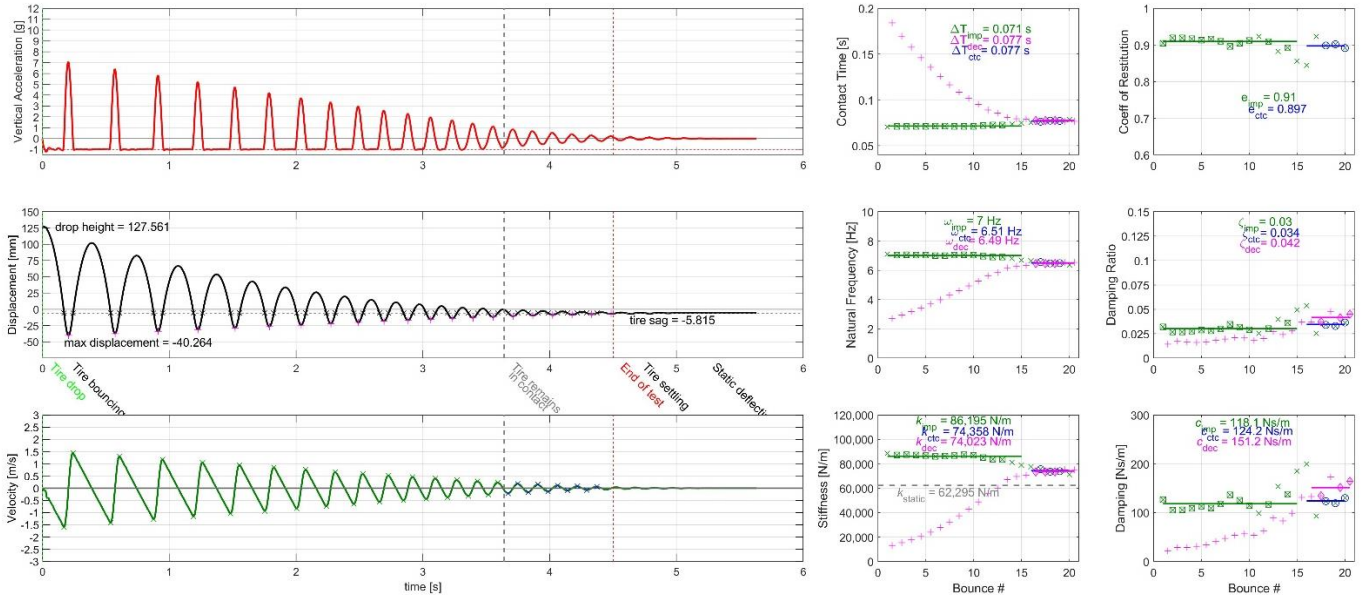
[1]Trek Performance Research, Trek Bicycle Corporation, Waterloo, WI, 53594, USA; jim_sadauckas@trekbikes.com; ORCID 0000-0002-6055-9047
[2]Vehicle Measurements Group, Harley-Davidson Motor Company, Yucca AZ 86438, USA; noah.schoeneck@harley-davidson.com
[3]Professor Emeritus, Dept of Mechanical Engineering, Marquette University, Milwaukee, WI 53233, USA; mark.nagurka@marquette.edu
*corresponding author.

Name of Editor: Jason Moore
Submitted: 28/02/2023
Accepted: 13/04/2023
Published: 26/04/2023
Citation: Sadauckas, J., Schoeneck, N. & Nagurka, M. (2023). Radial Stiffness and Damping of Mountain Bike Tires Subject to Impact Determined Using the Coefficient of Restitution. The Evolving Scholar - BMD 2023, 5th Edition.
This work is licensed under a Creative Commons Attribution License (CC-BY).

Abstract:

Mountain bikes are essentially ruggedized versions of a standard bicycle with geometry and features suited to off-road cycling. Their intended use case has them encountering jumps, bumps, drops, and impact. As such, their designs have evolved to include front and often rear suspension systems composed of springs and dampers in sometimes elaborate kinematic arrangements. Despite extensive design resources spent optimizing and tuning these suspension systems, very little has been published regarding the in-plane behavior of their tires or bicycle tires in general (Knuit, 2014). In this work, a drop test bench is utilized to measure the dynamic radial stiffness and damping of numerous mountain bike tires including four common sizes spanning 29er, plus-sized, and fat tire variants (Dressel, 2020), as well as various constructions ranging from trail, through enduro, and downhill. The tire is treated as a classical, lumped Kelvin-Voigt model with a parallel arrangement of a spring and damper (Acosta, 2020).

Identification of the system parameters is accomplished by treating the tire as a bouncing ball and using the coefficient of restitution from pre and post impact velocities to determine the dynamic stiffness and damping (Nagurka, 2006). The advantages of this approach in comparison to a classical logarithmic-decrement approach (Wong, 2001; Cuong, 2013) are discussed.



© 2023 Sadauckas, J. Schoeneck, N., & Nagurka, M. published by TU Delft OPEN on behalf of the authors.
ISSN: 2667-2812

Figure 1. Graphs of wheel acceleration, displacement, and velocity versus time (left) with system parameters derived per bounce (right) from coefficient of restitution during impact (green), contact (blue), and in contrast to log-decrement (magenta).

The coefficient of restitution ε_n at each tire bounce $\boldsymbol{n}$ is expressed as a velocity ratio:

$$\varepsilon_n = \left| \frac{\dot{x}_{n\,post}}{\dot{x}_{n\,pre}} \right| \tag{1}$$

where $\dot{x}_n$ is the sled velocity and the subscripts indicate the pre- and post-contact velocities separated by contact time ΔT. Stiffness $k_{\boldsymbol{n}}$ can be determined given sled mass $\boldsymbol{m}$:

$$k_n = m\left(\frac{\pi}{\Delta T_n}\right)^2 \left[1 + \left(\frac{ln\ \varepsilon_n}{\pi}\right)^2\right] \tag{2}$$

The damping ratio $\boldsymbol{\zeta_n}$ can be determined solely from the coefficient of restitution ε_n:

$$\zeta_n = \frac{-\ ln\ \varepsilon_n}{\pi} \left[1 + \left(\frac{ln\ \varepsilon_n}{\pi}\right)^2\right]^{-\frac{1}{2}} \tag{3}$$

Moreover, tire impact footprints are collected and compared to their much smaller static counterparts.



Figure 1. Tire impact footprints (black) for 29 × 2.3”, 27.5 × 2.8”, 29 × 3”, and 26 × 4” knobby tires with static footprints overlaid (color). Note “stadium” (rectangle with radiused corners) shape of former vs. more traditional ellipse of latter (1:5 scale).

Results suggest that due to its viscoelastic nature mountain bike tire dynamic radial stiffness is appreciably higher than its quasi-static value. Furthermore, although its damping is relatively low (spanning 2 to 5% of critical), it can affect subjective “trail feel” and can be perceptibly influenced by tire selection, size, construction, and inflation pressure. The measured dynamic radial stiffness and damping values are critical for subsequent numerical and multibody modeling of the tire’s contribution to the suspension system (Schoeneck, 2023) with the goal of improving performance, safety, comfort, and control of two-wheelers. Additional attempts to isolate the contribution of contact patch friction, or “scrub,” to the dynamic radial stiffness and damping using ice, gel, or other low friction material proved challenging and may be explored in future work. Further implications relating tire damping to rolling resistance (Ejsmont, 2019) may also be the subject of future work.

References

Acosta, E. & Castillo, J., Cabrera, J., Velasco García, J. M., Fernández, J. & Alcazar, M. (2020). Modeling of tire vertical behavior using a test bench. *IEEE Access*. PP. 1-1. 10.1109/ACCESS.2020.3000533.

Cuong, D., Zhu, S., Hung, D., & Ngoc, N. (2013). Study on the vertical stiffness and damping coefficient of tractor tire using semi-empirical model. *Hue University Journal of Science*. 83. 5-15. 10.26459/jard.v83i5.3071.

Dressel, A., & Sadauckas, J. (2020). Characterization and modeling of various sized mountain bike tires and the effects of tire tread knobs and inflation pressure. *Applied Sciences*, 10(9), 3156. https://doi.org/10.3390/app10093156.

Ejsmont, J. & Owczarzak, W. (2019). Engineering method of tire rolling resistance evaluation. *Measurement*. 145. 10.1016/j.measurement.2019.05.071

Knuit, J., De Kok, F., Raaphorst, P. & Van der Spek, A. (2014). Bicycle tire stiffness and damping. TU Delft. http://bicycle.tudelft.nl/tiretestingvertical/

© 2023 Sadauckas, J. Schoeneck, N., & Nagurka, M. published by TU Delft OPEN on behalf of the authors.
ISSN: 2667-2812

Nagurka, M.L., & Huang, S. (2006). A mass-spring-damper model of a bouncing ball. *International Journal of Engineering Education*, Vol. 22, No. 2, 393-401.

Schoeneck, N., Sadauckas, J., & Nagurka, M. (2023, Oct. 18-20). Identification and modeling of a mountain bike front suspension subsystem equipped with a telescopic fork and tire damping. *Abstract submitted, BMD2023*, Delft University, Netherlands.

Wong, J.Y. (1993). Theory of Ground Vehicles. John Wiley & Sons, New York, 2 ed.

© 2023 Sadauckas, J. Schoeneck, N., & Nagurka, M. published by TU Delft OPEN on behalf of the authors.
ISSN: 2667-2812

The Evolving Scholar (2023)

http://dx.doi.org/10.24404/63fd130ddf639dbecb55e672

Bicycle and Motorcycle Dynamics 2023
Symposium on the Dynamics and Control of Single Track Vehicles
18–20 October 2023, Delft University of Technology, The Netherlands

Type of the Paper: Extended Abstract

Measuring vertical tyre stiffness of bicycle tyres

M. Rothhämel [1,*]

[1] KTH Vehicle Dynamics & Center for ECO[2] Vehicle Design, Department of Engineering Mechanics, Royal Institute of Technology, Sweden; malter@kth.se, ORCID 0000-0002-2480-5554

[*] corresponding author

Name of Editor: Jason Moore
Submitted: 27/02/2023
Accepted: 14/04/2023
Published: 26/04/2023
Citation: Rothhämel, M. (2023). Measuring vertical tyre stiffness of bicycle tyres. The Evolving Scholar - BMD 2023, 5th Edition.
This work is licensed under a Creative Commons Attribution License (CC-BY).

Abstract:

This contribution presents an analysis of the vertical tyre stiffness of 20” bicycle tyres as usually mounted on bicycle carriers for the transport of children. The current research contributes to the science on bicycle comfort with the focus on the next generation cyclists with parameter variation in type of tyre, inflation pressure, pre-load and frequency.

Studying bicycle carrier comfort is an important research topic for at least three reasons. First, it is closely related to sustainable mobility, as the problem of low-emission and (sub-)urban daily mobility is often planned to be solved through an increased use of bicycles. Second, bicycle as mode of transportation is more and more in focus even for simulation tools supporting planning of infrastructure. So, there is need for empirical data for the simulation of bicycles as means of transport. Third, child transportation in bicycle carriers makes a significant fraction of child transportation by bike. Safety is often an argument for the carrier. However, there is lack of data about the vibration level.

Zegelaar (1998) made comprehensive measurements of automotive tyres. He found that the vertical stiffness of rolling tyres differed from the stiffness of non-rolling tyres when excited randomly but hardly when excited sinusoidally. On bicycles Lepine et al. (2016) measured in-situ two different wheel sets on system level and could distinguish the two wheel-sets. Doria et al. (2019) measured the static vertical tyre stiffness in a larger experiment around modal analysis of a utility bicycle. They found a certain non-linear behaviour at loads around 100 N but a quite linear behaviour at higher loads, however, no tyre modes were identified. In a later experiment Doria et al. (2021) tested a numerical method to predict the comfort of a city bike and identified most of the peaks in a frequency range larger than 20 Hz. In contrast, Rothhämel (2023) found when investigating the system comfort of bicycle carriers, next to a dependency of speed and inflation pressure, peaks at 3.3 Hz and higher.

In cycling there is a development to wider tyres, even in racing cycling. This contributes to a decrease of rolling resistance, however, an increase of comfort is always assumed but not yet shown systematically. Regarding bicycle carriers wider tyres (balloon tyres) are often used in combination with lower inflation pressure to increase comfort. In previous experiments lower tyre inflation pressure did not automatically correspond to decreased level of acceleration i. e. increased comfort.

In this investigation we tested the vertical tyre stiffness of two different types of tyres at different pre-load and inflation pressure over a frequency range of 1 Hz to 30 Hz. One tyre was a so called balloon tyre in the ERTRO dimension 60-406, the other tyre was a narrow foldable tyre in the ERTRO dimension 35-406. Figure 1 visualises the results summarised for the balloon tyre. The vertical tyre stiffness increases as expected with tyre inflation pressure. The increase of vertical tyre stiffness over vertical load is also inflation pressure dependent. At low pressure the vertical load hardly affects the stiffness, however, at higher inflation pressure, the influence of vertical force increases. In addition, the vertical tyre stiffness increases slightly but significant over frequency.

©2023 M. R. published by TU Delft OPEN on behalf of the authors.
ISSN: 2667-2812

 http://dx.doi.org/10.24404/63fd130ddf639dbecb55e672

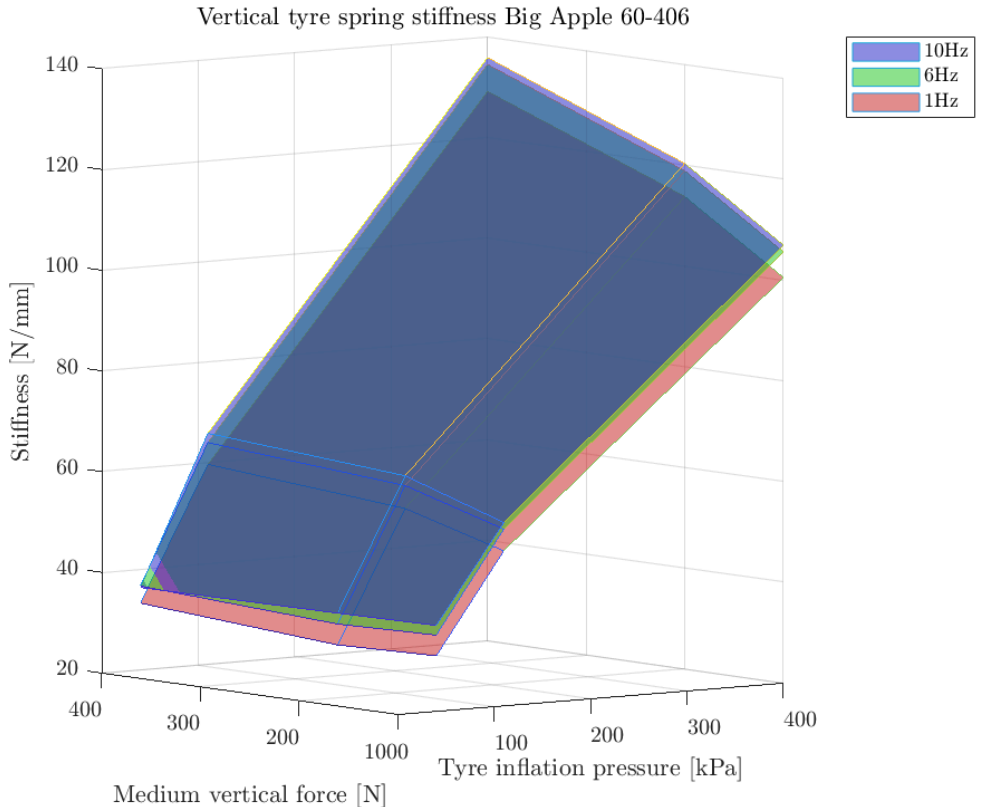


Figure 1. Vertical tyre stiffness over excitation force and tyre inflation pressure.

When comparing the two different tested tyres, the balloon tyre had about three times the air volume of the narrow tyre. Of course, these tyres will be operated at different inflation pressure in real life. Anyhow, to show the comparison of the stiffness at the same conditions (inflation pressure 100 kPa, vertical load 400+/-200 N, frequency 6 Hz), the balloon tyre shows a 20% higher stiffness than the narrow tyre.

The full paper will show the data for both of the tyres including the mapping of the frequency dependency. Static tyre stiffness results will complete the picture.

References

Doria, A., Marconi, E., and Cialoni, P. (2019). Modal analysis of a utility bicycle from the perspective of riding comfort. In *Proceedings of the ASME Design Engineering Technical Conference*, volume 3.

Doria, A., Marconi, E., Munoz, L., Polanco, A., and Suarez, D. (2021). An experimental-numerical method for the prediction of on-road comfort of city bicycles. *Vehicle system dynamics*, 59(9):1376–1396.

Lepine, J., Champoux, Y., and Drouet, J. (2016). Test protocol for in-situ bicycle wheel dynamic comfort comparison. *Procedia Engineering*, 147:568–572.

Rothhämel, M. (2023). Comfort and vibration level of children in cycle carriers (accepted for publication).

Zegelaar, P. (1998). The dynamic response of tyres to brake torque variations and road unevennesses, Ph.D. thesis, TU Delft.

©2023 M. R. published by TU Delft OPEN on behalf of the authors.
ISSN: 2667-2812

The Evolving Scholar (2023)

http://dx.doi.org/10.59490/649be2798f89e6e10a799ec2

Bicycle and Motorcycle Dynamics 2023
Symposium on the Dynamics and Control of Single Track Vehicles
18–20 October 2023, Delft University of Technology, The Netherlands

Type of the Paper: Extended Abstract

Experimental assessment of SST evaluation as handling quality indicator

Jules Ronné [1], Laura Dubuis [1], Thomas Robert [1,*]

[1] Univ Lyon, Univ Eiffel, Univ Claude Bernard Lyon 1, LBMC UMR_T 9406, F-69622 Lyon, France; jules.ronne@univ-lyon1.fr, ORCID 0000-0002-0867-6422; laura.dubuis@univ-lyon1.fr, ORCID 0000-0002-0851-0844; thomas.robert@univ-eiffel.fr, ORCID 0000-0002-6502-7082

[*] corresponding author

Name of Editor: Jason Moore
Submitted: 29/06/2023
Accepted: 30/06/2023
Published: 30/06/2023
Citation: Ronné, J., Dubuis, L. & Robert, T. (2023). Experimental assessment of SST evaluation as handling quality indicator. The Evolving Scholar - BMD 2023, 5th Edition.
This work is licensed under a Creative Commons Attribution License (CC-BY).

Abstract

The growth of urban bicycles, including cargo and foldable designs, has driven the evolution of bicycle design. In order to support this evolution, design rules that ensure good handling quality - the ease and precision with which a bike can be controlled - could be beneficial. However, despite extensive research in recent years, theoretical approaches to quantifying bicycle handling quality still have strong limitations and lack validity (Schwab & Meijaard, 2013). Moreover, subjective evaluations are subjected to large inter-individual / inter-session variability and require very carefully controlled experiments. Therefore, there is a need to find criteria, based on measures that can be easily obtained in an ecological setting, to objectify the bicycle's handling quality.

Numerous parameters have been proposed in the literature to characterise bicycle motion. However, there is no strong evidence for an effective indicator of handling quality. Recently, a new indicator called the SST evaluation (Singular Spectral Transformation) has been proposed (Takagi et al., 2022) to predict a combination of rider's subjective perceptions. This study aims to investigate the link between perceived handling quality and the SST evaluation on a larger sample of the population (only 3 riders in (Takagi et al., 2022)) .

Material and methods

This study included 30 adults participants who self-declared their riding proficiency as beginner to advanced. Participants were instructed to ride two commercially available bicycles (a Strida 5 foldable bike, and an Omnium Cargo V3 cargo bike) on a 130 m long track that was closed to traffic. The task was to maintain a constant speed and follow a path marked by a 9 cm wide white line on a flat and smooth tarmac. The path consisted of a straight line, a left turn, a slalom, and a right turn. Each participant completed three laps at three different speed instructions (S: "slowest possible," C: "comfort speed, which maximises the feeling of control," F: "faster than comfort speed") with both bicycles. The order in which the bikes and speed conditions were presented was randomised.

To assess the handling quality of the bicycles, participants were asked to rate their experience at the end of each lap using the Cranfield Aircraft Handling Qualities Rating Scale (CAHQRS, a 10 levels scale from 0 to 9). A higher score on the CAHQRS indicates that the bicycle is more difficult to control.

The bicycles were equipped with 3 XSens DOT sensors, which were placed on the rear wheel spokes, frame and handlebar. The sensors measured 3-axis accelerations, rate angles and magnetic field, at 120 Hz. Roll angle was obtained using the XSens DOT fusion algorithm.

SST evaluation is based on singular spectral transformation of linear regression residuals. The regression used is fitted between roll angle and handlebar angular velocity (Takagi et al., 2022). SST evaluation were calculated and averaged on each lap of the data-set.

©2023 Ronné, J., Dubuis, L., & Robert, T. published by TU Delft OPEN on behalf of the authors.
ISSN: 2667-2812

 http://dx.doi.org/10.59490/649be2798f89e6e10a799ec2

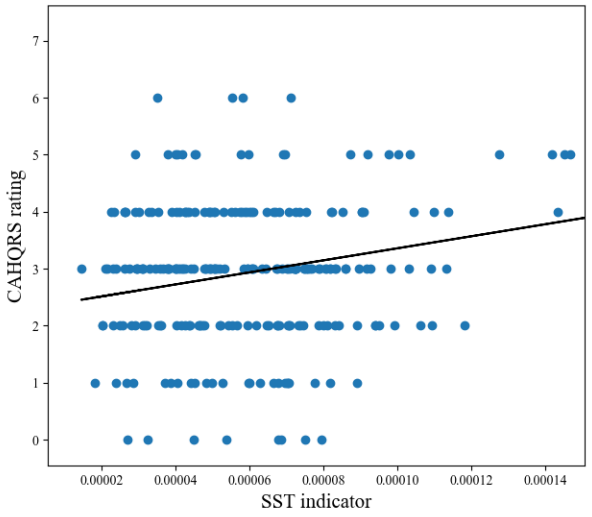


Figure 1. CAHQRS ratings against the mean value of SST evaluation for each lap of all participants

CAHQRS ratings were plotted against the mean value of SST evaluation on each lap. The link between perceived handling quality and SST evaluation were tested with a linear regression analysis.

Results and discussion

Regression analysis find out a statistically significant effect ($p < 0.05$) of SST evaluation on handling quality ratings. However, the fitted model explains poorly ratings variability ($r^2 = 0.047$). It could be that SST evaluation was initially assessed across a mixture of rider's perception (the first component of a PCA analysis over 10 different questions) and not only the difficulty to ride the bikes. Another possibility is the fact that handling quality results of a complex interaction between different characteristics. Indeed, an analysis of the rider's subjective perception for this experiment shows that handling quality is affected by stability (at low speed) and manoeuvrability (at high speed) (Ronné et al., 2023). Therefore, handling quality might be difficult to capture using a single criteria. This idea is also in line with the fact that, in the study by (Takagi et al., 2022), the effect of the SST evaluation on subjective ratings was not consistent across different experimental conditions.

This study fails to validate the SST evaluation as an objective indicator for the handling quality on a large sample of population. To date, such an indicator is still missing. Current work focuses building indicators of handling quality that take into account different bicycle characteristics such as the stability at low speeds and manoeuvrability at higher speeds.

References

Harris, D., Gautrey, J., Payne, K., & Bailey, R. (2000). The Cranfield aircraft handling qualities rating scale: A multidimensional approach to the assessment of aircraft handling qualities. *Aeronautical Journal*, 104(1034), 191-198.

Takagi, S., Oka, M., & Mori, H.(2022), Evaluation of Riding Instability of a Bicycle with Children as Passengers Using the Relationship Between Handlebar Angle and Roll Angle, *In: Yamamoto, S., Mori, H. (eds) Human Interface and the Management of Information: Applications in Complex Technological Environments. HCII 2022. Lecture Notes in Computer Science, vol 13306. Springer, Cham.*

Kooijman, J.D.G., Schwab, A.L. (2013). A review on bicycle dynamics and rider control. *Vehicle System Dynamics*, *51(11)*, 1722–1764.

Ronné, J. Dubuis, L., Robert, T. (2023). Bicycle handling quality perception: mixed effect of stability and manoeuvrability. Abstract submitted to the 2023 Bicycle Dynamics Conference.

©2023 Ronné, J., Dubuis, L., & Robert, T. published by TU Delft OPEN on behalf of the authors.
ISSN: 2667-2812

The Evolving Scholar (2023)

https://doi.org/10.24404/63fe2c902f198c184a58ee9b

Bicycle and Motorcycle Dynamics 2023
Symposium on the Dynamics and Control of Single Track Vehicles
18 – 20 October 2023, Delft University of Technology, The Netherlands

Type of the Paper: Extended Abstract

Adapting a variable stability mechanism for a tilting tricycle from the delta to the tadpole wheel configuration

Andrew Dressel[1]*, Jason Moore[2]

[1]TU Delft; AndrewDressel@hotmail.com, ORCID 0000-0003-0322-9815
[2]TU Delft; J.K.Moore@tudelft.nl, ORCID 0000-0002-8698-6143
*corresponding author.

Name of Editor: Christoph Schmidt
Submitted: 01/03/2023
Accepted: 20/03/2023
Published: 26/04/2023
Citation: Dressel, A. & Moore, J. (2023). Adapting a variable stability mechanism for a tilting tricycle from the delta to the tadpole wheel configuration. The Evolving Scholar - BMD 2023, 5th Edition.
This work is licensed under a Creative Commons Attribution License (CC-BY).

Abstract:

We previously presented a narrow-track tilting tricycle with a variable stability mechanism integrated between the swing arms that support a pair of rear wheels, in the so-called “delta” configuration. We now examine adopting that variable stability mechanism to work on a tricycle with a parallelogram linkage between a pair of front wheels, in the so-called “tadpole” configuration.

It was fairly straightforward to allow for varying the stability by splitting the parallelogram into two independent halves, each comprising two A-arms and a kingpin, and then controlling the motion of the two halves with a bell crank and two tie rods, just as we did with the swing arms of the previous vehicle.

We have also separated the two tasks of positioning the tie rod ends on the bell crank and enforcing symmetry of the tie rods. The former does not require much force and can be easily implemented with the same cables the rider uses to control the mechanism, but the latter does require large forces and is better implemented with a local linkage.

Implementing a decent Ackermann steering geometry, allowing for both large tilt and steer angles, and decoupling tilting from steering, however, proved to be quite a challenge, at least while we attempted to implement it with bar linkages. Fortunately, we discovered a 2006 paper by Prof Drstvenšek et al. describing a Bowden cable and cam system that looked promising.

© 2023 Dressel, A. & Moore, J. published by TU Delft OPEN on behalf of the authors.
ISSN: 2667-2812

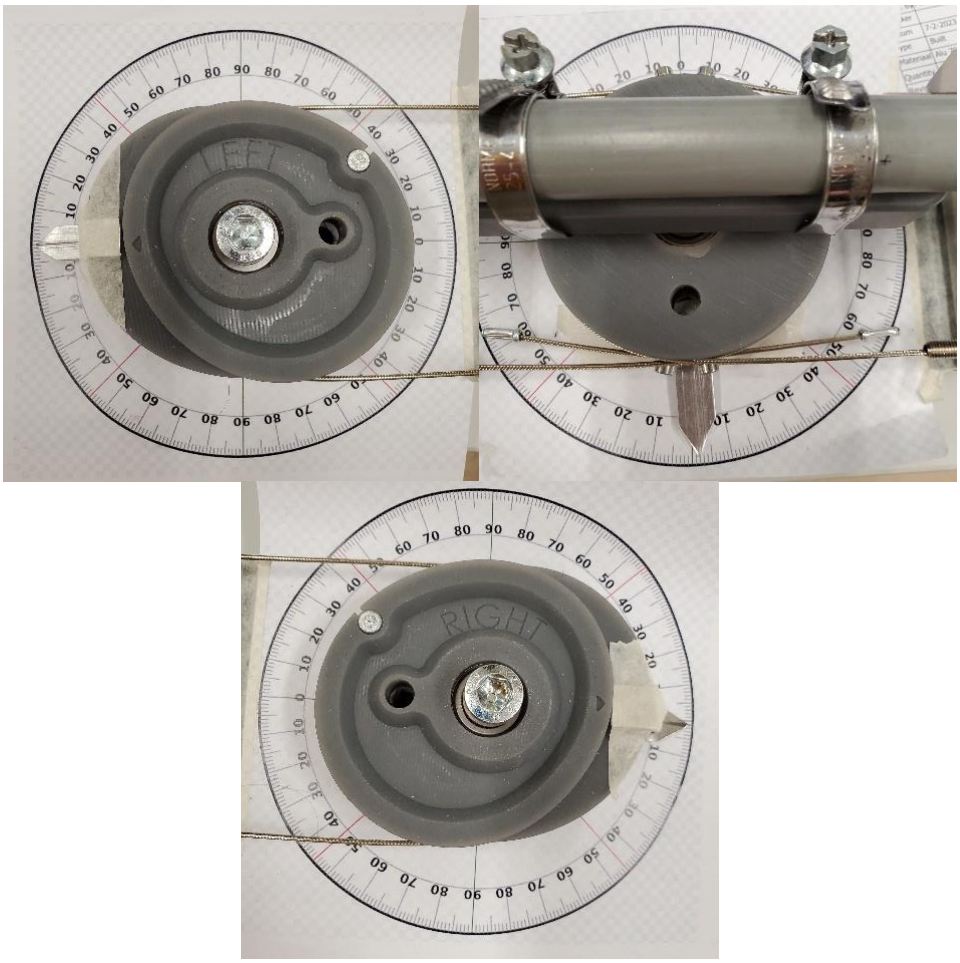


Figure 1. Images of the cable and cam steering system proof-of-concept prototype.

The system performed well in numerical simulations, but we were concerned that drag in the Bowden cables would interfere with the natural self-stability we hoped the vehicle would demonstrate. Thankfully, evaluations of several commercially available steer-by-cable cargo bikes and a couple of our own proof-of-concept prototypes proved that very low friction was possible.

Finally, we are building a working prototype of the complete vehicle and will evaluate its handling in a separate submission.

© 2023 Dressel, A. & Moore, J. published by TU Delft OPEN on behalf of the authors.
ISSN: 2667-2812

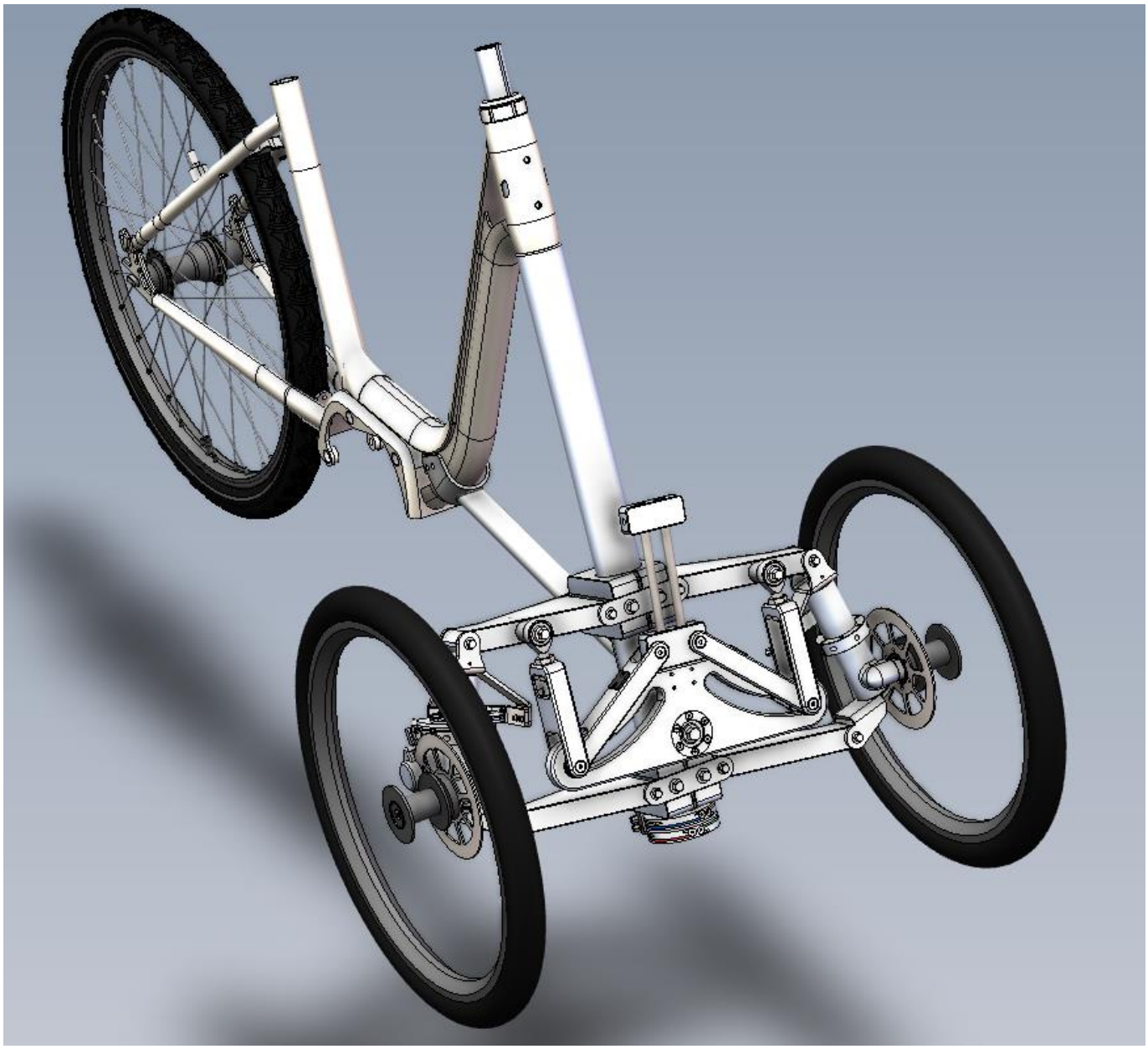


Figure 2. Final design solid model.

This project was financed and supported by the TKI/ClickNL 'De Fiets van de Toekomst' grant and Royal Dutch Gazelle.

References

Drstvenšek, I., Drstvenšek, S., Valentan, B., Balič, J. (2006, April 20-22), Mathematical Background of Development of Steering Mechanism for Human Powered Vehicle, *5th International DAAAM Baltic Conference "Industrial Engineering - Adding Innovation Capacity of Labour Force and Entrepreneurs"*, Tallinn, Estonia

Pierson, A. M., Shortreed, A. K., Van Asten, P. D., Dressel, A. E. (2020, August 17–19), A Narrow-Track Tilting Tricycle With Variable Stability That the Rider Can Control Manually, *Proceedings of the ASME 2020 International Design Engineering Technical Conferences and Computers and Information in Engineering Conference. Volume 4: 22nd International Conference on Advanced Vehicle Technologies*, Virtual, Online

© 2023 Dressel, A. & Moore, J. published by TU Delft OPEN on behalf of the authors.
ISSN: 2667-2812

The Evolving Scholar (2023)

http://dx.doi.org/10.59490/648fffb96b711301bfa9adfa

Bicycle and Motorcycle Dynamics 2023
Symposium on the Dynamics and Control of Single Track Vehicles
18–20 October 2023, Delft University of Technology, The Netherlands

Type of the Paper: Extended Abstract

Objective Evaluation of Handling and Stability of a Bicycle

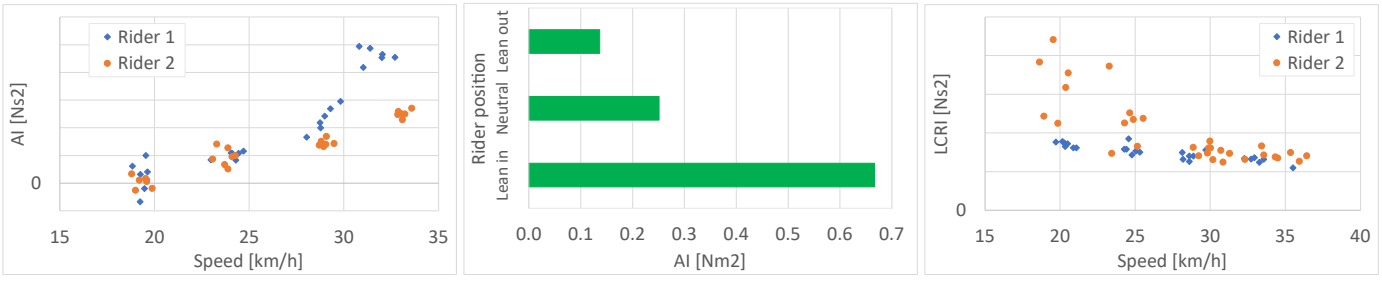
Marcel Keyser [1,*], Edoardo Marconi [2], Matteo Formentini [2], Enrico Giolo [2]

[1] Specialized Bicycle Components, Inc., U.S.A.; marcel.keyser@specialized.com, ORCID 0009-0003-5340-5925
[2] Dynamotion s.r.l., Italy; edoardo.marconi@dynamotion.it, ORCID 0000-0001-8221-4472; matteo.formentini@dynamotion.it; enrico.giolo@dynamotion.it
* corresponding author

Name of Editor: Jason Moore
Submitted: 19/06/2023
Accepted: 29/06/2023
Published: 29/06/2023
Citation: Keyser, M., Marconi, E., Formentini, M. & Giolo, E. (2023). Objective evaluation of handling and stability of a bicycle. The Evolving Scholar - BMD 2023, 5th Edition.
This work is licensed under a Creative Commons Attribution License (CC-BY).

Abstract:

This abstract deals with the objective evaluation of the dynamic behavior of a bicycle, with the aim of defining a testing and simulation protocol allowing the assessment of the vehicle's handling and stability characteristics. Quantifiable measures and repeatable testing procedures were developed within the body of research on motorcycle handling. As a result, a well-established procedure for the objective evaluation of motorcycle handling exists today. This methodology makes use of standard maneuvers and objective in-dices (Cossalter, 2006), allowing a straight-forward comparison between different vehicles, and can be used in product development based on both experimental tests and simulations. Similarly, the research on motorcycle stability suggests some relevant techniques to assess this dynamic property: tests such as constant-speed or coast-down runs are able to highlight weave and wobble respec-tively, and can be analyzed with different approaches, such as time-domain least-square fitting and stochastic subspace identification (Veneri et al., 2019). Similar procedures could be applied to other single-track vehicles, such as bicycles, but – to the best of the au-thors' knowledge – the literature reports no evidence of such usage of these techniques. According to the extensive literature review in (Schwab and Meijaard, 2013), no standard handling quality tests for bicycles have been developed, resulting in non-comparable results among different studies. More recent works propose a new handling index and employ it in numerical investigations – see, e.g., (Moore and Hubbard, 2019) – but do not discuss a standard experimental procedure. The stability of bicycle out-of-plane vibration modes has been the object of numerous numerical and analytical studies for decades, while experimental research on the topic is far more recent, see, e.g., (Magnani et al., 2013; Previati et al., 2019).



(a) (b) (c)

Figure 1: Example of handling test results: acceleration index from steady turning (a), effect of rider position on acceleration index (b), lane change roll index from lane change test (c).

©2023 Keyser, M., Marconi, E., Formentini, M., & Giolo, E. published by TU Delft OPEN on behalf of the authors.
ISSN: 2667-2812

 http://dx.doi.org/10.59490/648fffb96b711301bfa9adfa

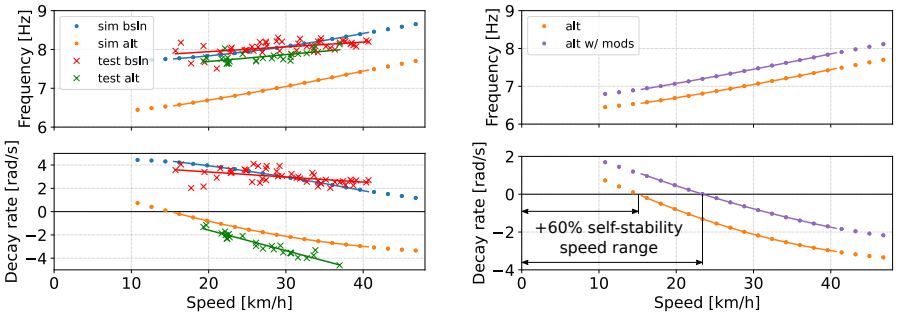


Figure 2: Wobble stability results: tests vs. simulations, baseline ('bsln') and alternative ('alt') configurations (a), simulations of unmodified vs. modified alternative configurations (b).

This work explores the application to an e-bike of a protocol derived from the one developed for motorcycles, emphasizing the adjustments required and the issues raised by the new use case. The same tests are also replicated in simulations performed using the multibody code *FastBike* (Cossalter et al., 2011), showing the potentiality of a virtual sensitivity analysis in product development. Different handling tests are performed by two riders, and each test is evaluated by computing the related standard index. Figure 1 reports some relevant results of the handling tests. Figure 1a shows the acceleration index as a function of vehicle speed for a steady turning maneuver with 15 m radius. A difference between the two riders appears at higher speeds, which is likely connected to a different attitude of the rider on the bicycle, as suggested by dedicated tests on the effect of the lean of the rider's upper body on the acceleration index, see Figure 1b. Figure 1c shows the lane change roll index as a function of vehicle speed for a lane change maneuver with 1.5 m lateral shift and 3 m transition distance. In this case, noticeable differences between the two riders appear at lower speeds, with the less experienced Rider 2 also showing a large scatter of results: this is likely due to the use of the upper-body lateral motion as an additional lateral input (in addition to steering torque). Compared to motorcycle testing, the higher rider-to-vehicle mass ratio makes these issues particularly relevant when testing bicycles, and must be accounted for when designing the testing protocol. In addition to handling characterization, coast-down tests are performed in order to assess the stability of the wobble mode in two configurations, i.e., the baseline vehicle and an alternative configuration with a different weight distribution. A numerical sensitivity analysis is also performed with the aim of improving the stability of the wobble mode in the alternative configuration. Figure 2a compares the test and simulation results: the simulation model is tuned and validated against the test results of the baseline and alternative configurations, respectively. The multibody model is then used to find a combination of feasible vehicle modifications (components' geometry, inertia and stiffness) that allow extending the self-stability speed range of the alternative configuration by 60%, see Figure 2b. In sum, this works traces guidelines and recommendations for the dynamic testing of bicycles, and shows that simulation tools borrowed from the motorcycle field are a valid means to drive product development.

References

Cossalter, V. (2006). *Motorcycle Dynamics*. Lulu.

Cossalter, V., Lot, R., and Massaro, M. (2011). An advanced multibody code for handling and stability analysis of motorcycles. *Meccanica*, 46:943–958.

Magnani, G., Ceriani, N. M., and Papadopoulos, J. (2013). On-road measurements of high speed bicycle shimmy, and comparison to structural resonance. In *2013 IEEE International Conference on Mechatronics (ICM)*, pages 400–405. IEEE.

Moore, J. K. and Hubbard, M. (2019). Expanded optimization for discovering optimal lateral handling bicycles. In *Proceedings of the 2019 Bicycle and Motorcycle Dynamics Conference*.

Previati, G., Mastinu, G., Magnani, G., et al. (2019). Analysis of bicycle shimmy and relevant bicycle compliances. In *Proceedings of the 2019 Bicycle and Motorcycle Dynamics Conference*.

Schwab, A. L. and Meijaard, J. P. (2013). A review on bicycle dynamics and rider control. *Vehicle system dynamics*, 51(7):1059–1090.

Veneri, M., Bova, M., Massaro, M., and Formentini, M. (2019). A tool for the automatic identification of weave and wobble. In *Proceedings of the 2019 Bicycle and Motorcycle Dynamics Conference*. Poster.

©2023 Keyser, M., Marconi, E., Formentini, M., & Giolo, E. published by TU Delft OPEN on behalf of the authors.
ISSN: 2667-2812

The Evolving Scholar (2023)

http://dx.doi.org/10.24404/63fe1d88598888792a7ec830

Bicycle and Motorcycle Dynamics 2023
Symposium on the Dynamics and Control of Single Track Vehicles
18–20 October 2023, Delft University of Technology, The Netherlands

Type of the Paper: Extended Abstract

Modeling of a Bicycle Cargo Trailer with Magic Formula Tire Model for Vehicle Dynamics Simulation

Marius Miller [1,*], Markus Pfeil [1], Ralph Kennel [2], Raphael Murri [3]

[1] Department of Electrical Engineering, Ravensburg-Weingarten University (RWU), Germany; marius.miller@rwu.de, ORCID 0000-0002-4574-608X; markus.pfeil@rwu.de
[2] School of Engineering and Design, Technical University of Munich (TUM), Germany; ralph.kennel@tum.de
[3] School of Engineering and Computer Science, Bern University of Applied Sciences (BFH), Switzerland; raphael.murri@bfh.ch
[*] corresponding author

Name of Editor: Jason Moore
Submitted: 02/03/2023
Accepted: 26/04/2023
Published: 28/04/2023
Citation: Miller, M., Pfeil, M., Kennel, R. & Murri, R. (2023). Modeling of a Bicycle Cargo Trailer with Magic Formula Tire Model for Vehicle Dynamics Simulation. The Evolving Scholar - BMD 2023, 5th Edition.
This work is licensed under a Creative Commons Attribution License (CC-BY).

Abstract:

Tomorrow's delivery transportation faces new challenges in order to meet its requirements under the aspect of sustainability. Especially in urban areas, this can lead to difficulties, as a large number of stores have to be supplied with a wide variety of goods. One solution to this problem is provided by systems according to Carla Cargo (2022); Nuewiel (2022) and Kyburz (2022), which are an extension of classic bicycle trailers for the transportation of heavy loads. In addition to conventional bicycle trailers these are equipped with a heavy-duty frame and an additional electric drive to support the user. While conventional bicycles together with their rider have a weight of approx. 100kg depending on the class of bicycle and user weight, cargo trailers can have a total weight of more than 250kg depending on the load and trailer configuration. The coupling of both systems therefore results in a major modification of the driving dynamics. For this reason, intelligent and safe control of the electric powertrain is essential. In this context, Korayem et al. (2022) refers to the phenomenon of snaking and jack-knifing of trailers, which is dependent on the load and its position on the trailer as well as on the transmissible force of the tire to the road. In order to control a complex tractor-trailer system, knowledge of the tire behavior is therefore required. Due to this fact, the tire behavior must be studied in particular, since tires for use in cargo trailers are driven with a camber angle $\gamma = 0°$ due to their suspension, unlike bicycles. Existing studies according to Doria (2012); Dressel (2013) and Dressel (2020), which deal with the modeling of bicycle tires, are not ideal to be used for this special application since their research includes $\gamma \neq 0°$ and smaller normal force $F_{N,z}$ values. For this reason, the presented research focuses on the measurement and modeling of a special tire for cargo applications under realistic conditions and the integration of the resulting tire model in a complete vehicle model. As part of the research, the mobile tire measurement laboratory (MoReLab) of the Bern University of Applied Sciences (BFH) is used to measure and characterize a Schwalbe "Pick-Up" tire in size 55-406 ETRO (20 x 2.15 in). The investigations are carried out with 3, 3.5 and 4 bar tire pressure p. Further, the measurements are performed at a speed of $v = 5.556\ \frac{m}{s}$ and $F_{N,z}$ of 625 N as well as 765 N. Since the test truck is designed for the automotive and truck sector, an adapter rim must be manufactured to connect bicycle tires to the system. By using the adapter rim, an unavoidable offset occurs, which places the center of the tire outside the center of the measurement hub. Due to this offset crosstalk occurs that leads to a strong drift of the aligning torque $T_{t,z}(\alpha)$. To compensate the crosstalk a matrix method according to Schrand (2007) is performed, which causes the measurement data to follow the base curve described by Pacejka & Besselink (2012). The crosstalk compensated data data is shown in Figure 1 for $p = 4$ bar and $F_{N,z} = 625$ N. In the framework of comprehensive vehicle dynamics investigations of cargo trailers, a model of the system is generated. For this reason, it is investigated whether a general magic formula (MF) model can be generated from the results of the tire measurements, which can then be integrated into the overall vehicle model. The resulting MF model for $F_{t,x}$,$F_{t,y}$ and $T_{t,z}$ is shown in Figure 1 as a dashed black line. With NRMSE values from 0.009 to 0.074 it can be

©2023 Miller, M., Pfeil, M., Kennel, R. & Murri R. published by TU Delft OPEN on behalf of the authors.
ISSN: 2667-2812

 http://dx.doi.org10.24404/63fe1d88598888792a7ec830

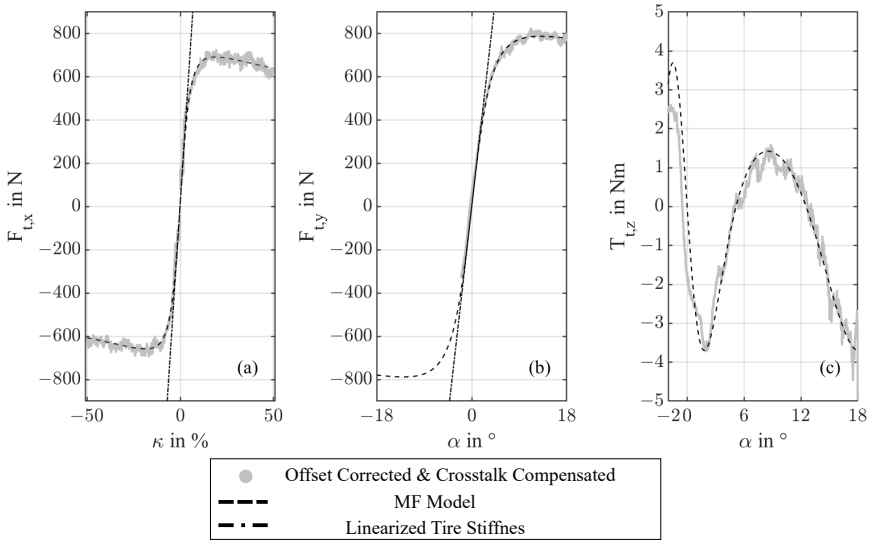


Figure 1. Measured longitudinal $F_{t,x}$ and lateral force $F_{t,y}$ and aligning torque $T_{t,z}$ as a function of tire slip κ or slip angle α with fitted MF Model curve.

shown that the general MF model used allows to represent the tire behavior of the tested tire with an good overall fit, so that it can be used for further complete vehicle simulation. Detailed information about the complete measurement and modeling proces can be found in Miller et al. (2023). In the context of complete vehicle modeling, the driving dynamics of a single-axle two wheeled bicycle trailer with the presented tire model will be further analyzed. Investigations regarding both steady-state cornering and short-term avoidance maneuver build the fundamental basis for the subsequent controller design of a new all-wheel drive trailer with torque distribution based on measurements of hitchforce F_h according to Miller et al. (2021) and hitchangle θ.

References

Alberto Doria, Mauro Tognazzo, Gianmaria Cusimano, Vera Bulsink, Adrian Cooke & Bart Koopman (2013) Identification of the mechanical properties of bicycle tyres for modelling of bicycle dynamics, Vehicle System Dynamics, 51:3, 405-420, DOI: 10.1080/00423114.2012.754048

Carla Cargo (2022). Products - eCarla. Available online: https://www.carlacargo.de/de/produkte/ecarla/ [14.07.2022].

Dressel, Andrew Erwin, "Measuring and Modeling the Mechanical Properties of Bicycle Tires" (2013). Theses and Dissertations. 386. https://dc.uwm.edu/etd/386

Dressel, A., & Sadauckas, J. (2020). Characterization and Modelling of Various Sized Mountain Bike Tires and the Effects of Tire Tread Knobs and Inflation Pressure. Applied Sciences, 10(9), 3156. https://doi.org/10.3390/app10093156

Korayem, A.H.; Khajepour, A.; Fidan B. (2022), "A Review on Vehicle-Trailer State and Parameter Estimation," in IEEE Transactions on Intelligent Transportation Systems, vol. 23, no. 7, pp. 5993-6010, July 2022, doi: 10.1109/TITS.2021.3074457

Kyburz (2022). Products - DXP. Available online: https://kyburz-switzerland.ch/en [14.07.2022].

Miller, M., Kaufmann, A., Reick, B., & Pfeil, M. (2021). Intelligente Anhängerdeichsel für verschiedene Zugfahrzeuge.

Miller, M., Pfeil, M., Reick, B., Murri, R., Stetter, R., & Kennel, R. (2023). Measurement and Modeling of a Cargo Bicycle Tire for Vehicle Dynamics Simulation. Applied Sciences, 13(4), 2542. https://doi.org/10.3390/app13042542

Nüwiel (2022). ProductP. Available online: https://www.nuwiel.com/etrailer/ [14.07.2022].

Pacejka, H.B., Besselink, I. (2012) *Tire and Vehicle Dynamics*, 3rd ed.; Butterworth-Heinemann: Oxford, UK.

Schrand, D. (2007). Cross-Talk Compensation Using Matrix Methods. *Sensors Transducers J.* 2007, *5*, 1157–1163.

©2023 Miller, M., Pfeil, M., Kennel, R. & Murri R. published by TU Delft OPEN on behalf of the authors.
ISSN: 2667-2812

The Evolving Scholar (2023)
https://doi.org/10.24404/63f9e69bdfe4d01fe0ab82bd
Bicycle and Motorcycle Dynamics 2023
Symposium on the Dynamics and Control of Single Track Vehicles
18 – 20 October 2023, Delft University of Technology, The Netherlands

Type of the Paper: Extended Abstract

Lap Time Sensitivity Analyses in High-Powered Electric Motorcycles

Louis Flanagan[1], and Atanas A. Popov[2,*]

[1]PhysicsX, U.K.; LouisFlanagan@hotmail.co.uk
[2]Faculty of Engineering, University of Nottingham, Nottingham NG7 2GX, U.K.; Atanas.Popov@nottingham.ac.uk, 0000-0002-3159-5647
*corresponding author.

Name of Editor: Jason Moore
Submitted: 27/02/2023
Accepted: 14/04/2023
Published: 26/04/2023
Citation: Flanagan, L. & Popov, A. (2023). Lap Time Sensitivity Analyses in High-Powered Electric Motorcycles. The Evolving Scholar - BMD 2023, 5th Edition.
This work is licensed under a Creative Commons Attribution License (CC-BY).

Abstract:

Electric vehicles and low carbon technology are currently at the forefront of research due to the need to rapidly reduce global carbon emissions. Significant effort has been invested into the improvement of electric cars but comparatively little for electric motorcycles, especially high-performance electric motorcycles. For achieving high-performance, it is important to capture relevant design trade-offs and plan for vehicle optimisation prior to starting detailed design. These design trade-offs typically involve optimal sizing of the vehicle battery, electric motor, and motor drive, as well as the determination of the optimum lift-to-drag ratio. A full vehicle analysis, including pertinent mechanical and electrical elements, is required to perform this properly, as the system is highly interdependent. Existing models are shown to be lacking in key areas, notably the integration of an appropriate battery model, a realistic electric motor model (reflecting modern high-performance electric motorcycle design practices), and an appropriate tyre model.

The work reported herewith is based on detailed research in electric motorcycles (Flanagan, 2022). A full vehicle model of a modern high-performance electric motorcycle was built and validated. Firstly, a rigid body dynamics motorcycle model that included a realistic tyre model, the effects of downforce, differing front and rear tyres, and front-wheel drive was developed. Further work increased the depth and suitability of the electric powertrain modelling for high-performance electric motorcycles. The battery thermal and electrical responses were modelled as well as the powertrain torque response, including saturation and loss modelling of the motor, motor drive and final drive. Motor dynamometer tests and battery cycle testing were performed to validate these models.

Having built the vehicle model, a lap simulation procedure was then developed, implemented, and validated. Validation used lap data acquired at several racing events, including the Isle of Man TT Zero, Pikes Peak International Hillclimb (PPHIC), and Elvington Airfield Land speed record attempts. The lap simulation was then extended to include the effects of energy deployment strategy on lap time. Energy deployment optimization is accomplished by computing the gradient of the energy deployment vs. lap time gain, for each deployment zone and by using this to identify areas of high lap time sensitivity per unit energy deployment. Deployment is then prioritized in these areas subject to sensible constraints for rider integration. An additional methodology was also developed for designs that were limited by the battery thermal performance, see Figure 1(a). The combined deployment strategy was shown to significantly affect lap time and has implications for full vehicle optimization, in particular powertrain development.

The work continued with lap time simulations of the Isle of Man TT Zero and PPHIC, investigating the respective influence of energy management on battery sizing, see Figure 1(b). This showed that it was important to include the energy management strategy into the design evaluation and that the energy management trade-offs were specific to each race event. Additionally, analysis showed that situations where battery temperature management strategies dominated should be avoided by the proper design of a battery cooling system. This is because the penalty associated with reducing battery temperature through power and velocity limitations is higher than that of including sufficient direct air cooling, despite the associated aerodynamic drag penalty.

Here, the aim is to use this advanced model to determine the main performance drivers for high-performance electric motorcycles. The practical goal is to identify the sensitivities to design parameters and to quantify their effect from a full vehicle perspective. This can then be used to guide the trade-offs and development pathways required for a full vehicle design optimization.

© 2023 Flanagan, L., & Popov A. A. published by TU Delft OPEN on behalf of the authors.
ISSN: 2667-2812

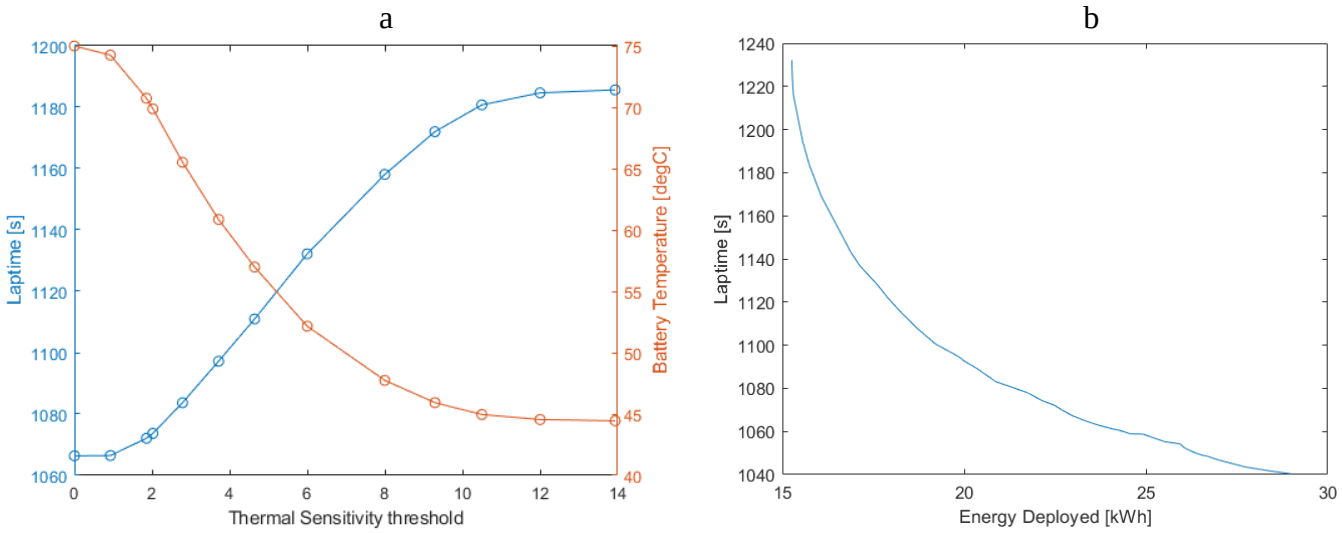


Figure 1. (a) Lap time obtained with differing battery limit temperatures and optimal deployment strategy. (b) Lap time obtained with differing total energy deployment limits and optimal deployment strategy.

As the battery is a significant performance differentiator, the mass sensitivity and energy sensitivity are determined, the resulting trade-off is then calculated when considering the TT drive cycle with the energy deployment strategy used. Further sensitivities including the minimum viable winglet lift to drag ratio, gearbox efficiency, electric motor construction choices, as well as switching module choices, are evaluated in the context of the TT Zero race.

By equating the relative lap time sensitivities to mass and additional energy it is shown that in most circumstances it is beneficial to increase the battery size up to a point where no energy management is required. However, in some scenarios even with unlimited battery choice, it can be advantageous to include some energy management as the lap time sensitivity to additional mass exceeds that of the additional energy gained from additional battery. Although caution is recommended here, as battery degradation will serve to reduce the available battery energy with multiple battery cycles.

As the design trade-offs can differ between events, a similar activity is undertaken for the Pikes Peak International Hillclimb (PPHIC). Here, it is seen that a sufficient size battery for maximal deployment at tyre limit is achievable leading to the reduced need for optimal energy deployment and a significant difference in the optimal winglet lift to drag ratio. This highlights the event specific nature of the vehicle optimization. It is worth noting however that the TT is more representative of the longer drive cycles expected for on road use.

A lap simulation tool for high-performance electric superbike evaluation has been developed, and a simplified energy and temperature management methodology implemented. For example, this tool has identified the fact that the University of Nottingham 2018 TT Zero contender was severely compromised by its choice to forgo battery cooling, as well as by the lack of energy deployment strategy.

Methods to overcome these issues have been implemented through design changes and/or deployment strategy changes. The use of targeted velocity and power limitations without design changes, results in 7 s of lap time improvement, when compared to the global power and velocity limitation strategy previously employed by (Blissett, 2019). The inclusion of battery air cooling is shown to result in a 30 s lap time reduction and the full deployment of the stored energy, despite the increased drag associated with air cooling. This lap time reduction is further improved by an additional 8 s by re-optimising the gear ratio for this higher deployment level and deployment strategy.

In summary, the lap simulation tool is shown to be extremely useful for the design and development of high-performance electric motorcycles, with sensitivity to many pertinent design parameters, from switching module choice to winglet target aerodynamic efficiencies. Further work to utilising multivariate optimisation would automate this performance discovery effort and lead to an accelerated and more refined design process, but this is beyond the scope of the present paper.

References

Blissett, J. (2019). *A Wholistic Motor Design Philosophy for Electric Motorcycles in Motorsport.* PhD thesis, University of Nottingham, U.K.
Flanagan, L. (2022). *High-Powered Electric Motorcycle Integrated Performance Studies.* PhD thesis, University of Nottingham, U.K.

© 2023 Flanagan, L., & Popov A. A. published by TU Delft OPEN on behalf of the authors.
ISSN: 2667-2812

The Evolving Scholar (2023)
https://doi.org/10.59490/64999cf248c7df442c1860e8
Bicycle and Motorcycle Dynamics 2023
Symposium on the Dynamics and Control of Single Track Vehicles
18 – 20 October 2023, Delft University of Technology, The Netherlands

Type of the Paper: Extended Abstract

Validation of a bicycle simulator based on objective criteria

Donaji Martinez Garcia[1]*, Kilian Gröne[1], Martin Fischer[1], Min Zhao[1] and Melina Bergen[1]

[1]German Aerospace Center - DLR; Donaji.MartinezGarcia@dlr.de, ORCID 0000-0002-0839-0627; Kilian.Groene@dlr.de, ORCID 0000-0001-9035-4440; Ma.Fischer@dlr.de, ORCID 0000-0001-8435-4321; Min.Zhao@dlr.de, ORCID 0000-0002-0485-5255 ; Melina.Bergen@dlr.de, ORCID 0009-0009-0727-0218
*corresponding author.

Name of Editor: Jason Moore
Submitted: 26/06/2023
Accepted: 27/06/2023
Published: 27/06/2023
Citation: Martinez Garcia, D., Gröne, K., Fischer, M. & Zhao, M. (2023). Validation of a bicycle simulator based on objective criteria. The Evolving Scholar - BMD 2023, 5th Edition.
This work is licensed under a Creative Commons Attribution License (CC-BY).

Introduction

The validation of simulators is very important, as it determines to which extent the results of a simulator study can be transferred to the real world. Simulator studies are valid when they provide results that can be generalized to real-world situations and the occurrence of unwanted symptoms such as simulator sickness doesn´t influence the results (Shoman und Imine 2021). The goal is to provoke a realistic riding behavior. Behavioral validity is a measure for how the participants feel and act while driving on the simulator. To evaluate behavioral validity, performance measures of a simulator can be compared with those of a real bicycle riding on-road (O'Hern et al. 2017). The aim of the study presented in this paper was to first evaluate a new control logic together with hardware changes done to the DLR bicycle simulator and identify in which areas it is possible to fine tune the simulator so that it allows for a more realistic behavior. For this purpose, two different versions of the simulator will be compared based on objective criteria first in a simulator study and then to data of an equipped research bicycle.

Method

For the simulation, a VR visualization based on real geographical data of the research intersection was created in Unreal Engine 4. Two different set-ups of the DLR bicycle simulator (Martinez Garcia et al. 2022; Fischer et al. 2022) were tested in different scenarios. For the longitudinal dynamics, the measurement of vehicle speed on V 2.0 and braking was performed with an incremental encoder that has higher resolution and lower latency than the bicycle trainer used in V 1.1. In addition, the wind simulator was configured to deliver wind dynamically (depending on cycling speed), whereas in V1.1 it was static and constantly delivered the same amount of air at the same speed. For the lateral dynamics on V1.1, the force feedback of the steering motor was calculated by a modified steering force simulation based on motorized vehicles, whereas on V 2.0 it was calculated based on the Whipple-bicycle physics model (Meijaard et al. 2007). The lean angle behavior was controlled either by the force of the body (V 1.1) or by the position of the steering angle (V 2.0). In the full paper, further details of the implementation will be provided.

The real-world study aims to gather validation data with the research bicycle BoBBi, which is equipped with a series of sensors such as a radar, lidar, steer angle sensor and an Inertial Measurement Unit (IMU). The study will take place in April at the research intersection in Braunschweig.

Experimental set-up

A within-subject study was designed in which both versions of the simulator were successfully tested by 27 participants (5 female, 22 male, mean age 29.4 years). 8 participants could not finish the study due to simulator sickness or not being able to control the simulator. After a training, 6 scenarios (4 at the intersection, a slalom and a turning head track) with different tasks were conducted. Beside questionnaires on simulator sickness and presence, simulation data on e.g. driving velocity, steer angle, and lean angle was collected in order to answer the following research questions: RQ1: Does the mechanical structure and control of the bicycle simulator allow the feeling of riding on a real bike? RQ2: Is the data collected from the bicycle simulator similar to the data of a real bicycle? To answer these questions, the following hypotheses were evaluated. H1: The mechanical and algorithmic changes will improve the steering behavior. H2: The mechanical algorithmic changes will improve the leaning behavior. H3: The cycling speed choice will be more realistic with V 2.0.

© 2023 Martinez Garcia, D., Gröne, K., Fischer, M., & Zhao, M. published by TU Delft OPEN on behalf of the authors.
ISSN: 2667-2812

Results

For the steering behavior (H1) no clear differences between the two versions could be seen. The analysis of the leaning angle (H2) shows a more controlled behavior with V 2.0 and a more even distribution of leaning angles (s. Figure 1).

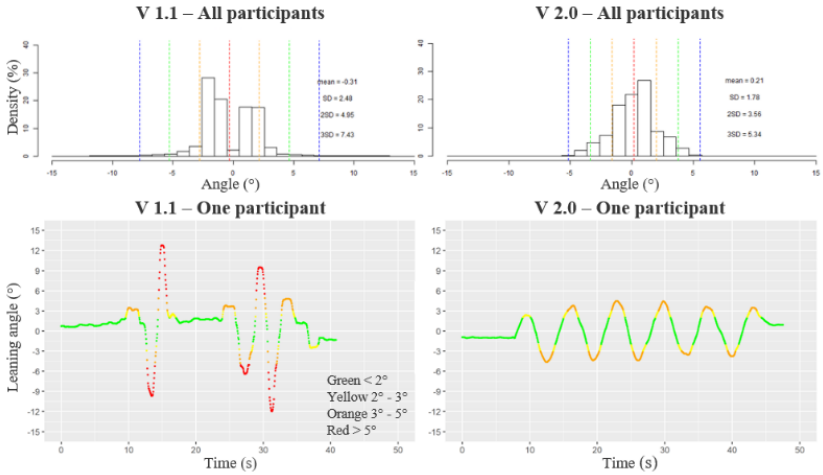


Figure 1. Leaning angle on a slalom course. Distribution for all participants (top) and a single participant (bottom)

The cycling speed of the participants was evaluated to solve H3. These analyses show that the braking behavior was influenced by the delays provoked by the bike trainer in version V 1.1, this means, that riders slowed their velocity earlier or drove slower in order to be able to brake on time. Furthermore, the speed choice behavior on V 2.0 was more continuous than on V 1.1. The subjective evaluation gave no clear result, but a distinct preference of V 2.0 for the longitudinal dynamics.

Discussion and conclusion

Some limitations of this study include that too many changes were performed on the simulator in parallel. Therefore, it is partly difficult to evaluate them individually. For this reason, more specific research will be performed on each feature which requires further fine-tuning. As the steering angle analysis gave no clear results, the steering angular velocity will be analyzed. In the full paper, the real-world statistical data obtained by utilizing the DLR research intersection and BoBBi will be analyzed and compared with the simulator data. This will provide insights in the behavioral validity of the different versions. The findings from these analyses will be incorporated into the further development of the simulator.

References

Fischer, M.; Temme, G.; Gröne, K.; Martinez Garcia, D.; Grolms, G.; Rehm, J. (2022): A VRU-simulator for the evaluation of pedestrian and cyclist-vehicle interaction – Design criteria and implementation. *Proceedings of the Driving Simulation Conference 2022 Europe*, Strasbourg, France, 153–159.

Martinez Garcia, D.; Gröne, K.; Quante, L.; Fischer, M.; Thal, S.; Henze, R. (2022): Parameter tuning of a bicycle simulator for a realistic riding behaviour and motion perception. *In: Product Solutions Book - Driving Simulation & Virtual Reality Conference & Exhibition 2022 Europe*, Strasbourg, France, 101–102.

Meijaard, J.P; Papadopoulos, Jim M.; Ruina, Andy; Schwab, A.L (2007): Linearized dynamics equations for the balance and steer of a bicycle: a benchmark and review. In: Proc. R. Soc. A. 463 (2084), 1955–1982. DOI: 10.1098/rspa.2007.1857.

O'Hern, Steve; Oxley, Jennie; Stevenson, Mark (2017): Validation of a bicycle simulator for road safety research. *Accident analysis and prevention* 100, 53–58. DOI: 10.1016/j.aap.2017.01.002.

Shoman, Murad M.; Imine, Hocine (2021): Bicycle Simulator Improvement and Validation. *IEEE Access* 9, 55063–55076. DOI: 10.1109/ACCESS.2021.3071214.

© 2023 Martinez Garcia, D., Gröne, K., Fischer, M., & Zhao, M. published by TU Delft OPEN on behalf of the authors.
ISSN: 2667-2812

The Evolving Scholar (2023)

http://dx.doi.org/10.59490/64664617311fc849d76663c1

Bicycle and Motorcycle Dynamics 2023
Symposium on the Dynamics and Control of Single Track Vehicles
18–20 October 2023, Delft University of Technology, The Netherlands

Type of the Paper: Extended Abstract

Towards Black-Box Dynamics Modelling within Learning-based Nonlinear Model Predictive Control for Virtual Motorcycles

Francesco Bianchin [1], Enrico Picotti [2,*], Mattia Bruschetta [2]

[1] TUM School of Computation, Information and Technology, Technical University of Munich; francesco.bianchin@tum.de, ORCID 0009-0004-7916-467X [2] Department of Information Engineering, University of Padova, Italy; ORCID 0000-0002-5356-610X; ORCID 0000-0003-0769-4191

[*] corresponding author

Name of Editor: Jason Moore
Submitted:18/05/2023
Accepted: 18/05/2023
Published: 26/06/2023
Citation: Bianchin, F., Picotti, E. & Bruschetta, M. (2023). Towards Black-Box Dynamics Modelling within Learning-based Nonlinear Model Predictive Control for Virtual Motorcycles. The Evolving Scholar - BMD 2023, 5th Edition.
This work is licensed under a Creative Commons Attribution License (CC-BY).

Abstract:

In recent years, both academic and industrial effort has been devoted to developing Virtual Riding (VR) strategies, in line with the attempts towards virtual prototyping in the automotive business. The advantages of virtual prototyping include reduced costs, time-to-market, and increased safety. Nonlinear Model Predictive Control (NMPC) schemes have been utilized to achieve high-performance real-time control of the motorcycle system, while emulating a realistic riding behavior, as described, e.g., in Massaro (2011); Bruschetta et al. (2021). To apply NMPC techniques, a detailed model of the plant is necessary, and different dynamics models have been proposed in literature. However, the accuracy of physics-based motorcycle models that grant real-time feasibility of the NMPC remained questionable when compared to a realistic system behavior. Besides, they require specific measurements and identification procedures to be applied. In this sense, Learning-based NMPC (LbNMPC) framework, described in Hewing et al. (2020), could be a promising new direction. LbMPC is a broad research field that generally refers to the implementation of learning techniques into NMPC control schemes. Specifically, the *learning dynamics* sub-field covers the data-based adaptation of the NMPC prediction model. In this context, Gaussian Process Regression (GPR) resulted very effective in applicative scenarios, as shown in Kabzan et al. (2019); Carron et al. (2019); Picotti et al. (2023).

We propose an LbNMPC controller for a virtual motorcycle based on black-box dynamics modeling, i.e. a purely obtained through the acquired data. Learning-based dynamics models of the accelerations have been obtained by GPR, where the targets are the yaw $\ddot{\psi}$ and roll $\ddot{\theta}$ accelerations in body frame, while longitudinal and lateral ones are computed by the nominal model described in Bruschetta et al. (2021). Two independent zero-mean GPs have been trained, defining the covariance matrix through the Squared Exponential kernel. To reduce the computational burden, a sparse GP approximation and a feature selection procedure have been applied. Regarding the former, the Variational Free Energy approach proposed in Titsias (2009) has been employed, while the latter has been implemented adapting the iterative incremental approach proposed in Rossi et al. (2006), using R^2 index to define the feature importance. The obtained black-box acceleration estimates are greatly consistent with the *real* ones, i.e. the simulated ones in the commercial high-fidelity simulation framework `VI-BikeRealTime`, as depicted in Fig. 1. The achieved R^2 values for yaw and roll are 0.82 and 0.90, respectively.

The LbNMPC obtained using the black-box model has been compared to the NMPC using the nominal physics-based model described in Bruschetta et al. (2021). The configuration of the controllers is the same, except for the prediction model within. The closed-loop behavior on a racetrack has been evaluated based on the tracking capabilities. In particular, lateral and angular displacement with respect to the given trajectory and the velocity error with respect to the given profile have been assessed. The LbNMPC achieved a significant reduction (between 48% and 83%) of all the indicators, as reported in Tab. 1 and depicted in Fig. 2, while involving an increase of 248% of the computational time. Indeed, the results demonstrate the benefits achievable by the LbNMPC approach, while still acknowledging the significant computational burden increment.

©2023 Bianchin, F., Picotti, E., & Bruschetta, M. published by TU Delft OPEN on behalf of the authors.
ISSN: 2667-2812

 http://dx.doi.org/10.59490/64664617311fc849d76663c1

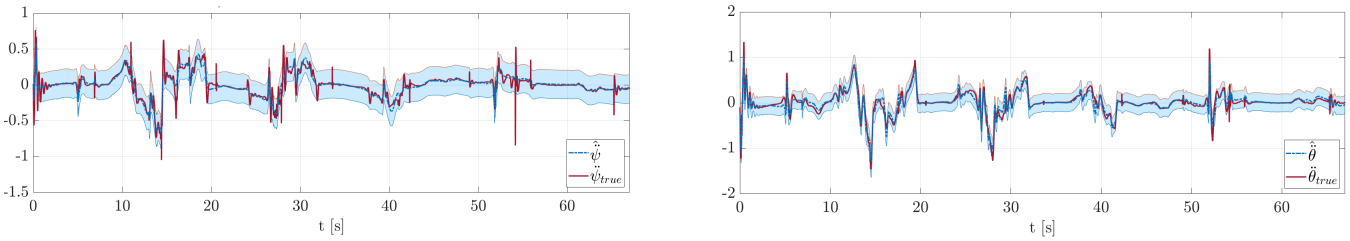


Figure 1. Black-box yaw and roll accelerations' estimation.

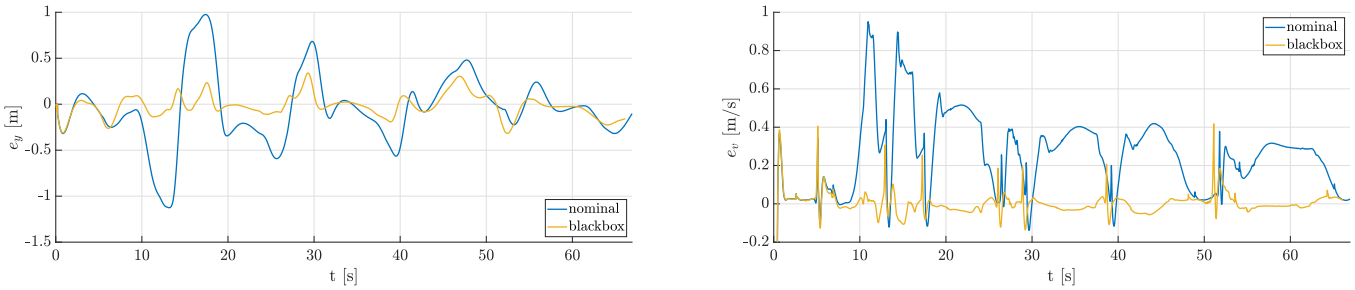


Figure 2. Lateral error w.r.t. trajectory and velocity error w.r.t. reference profile for nominal and black-box models.

References

Bruschetta, M., Picotti, E., De Simoi, A., Chen, Y., Beghi, A., Nishimura, M., Tezuka, Y., and Ambrogi, F. (2021). Real-time nonlinear model predictive control of a virtual motorcycle. *IEEE Transactions on Control Systems Technology*, 29(5):2214–2222.

Carron, A., Arcari, E., Wermelinger, M., Hewing, L., Hutter, M., and Zeilinger, M. N. (2019). Data-driven model predictive control for trajectory tracking with a robotic arm. *IEEE Robotics and Automation Letters*, 4(4):3758–3765.

Hewing, L., Wabersich, K. P., Menner, M., and Zeilinger, M. N. (2020). Learning-based model predictive control: Toward safe learning in control. *Annual Review of Control, Robotics, and Autonomous Systems*, 3(1):269–296.

Kabzan, J., Hewing, L., Liniger, A., and Zeilinger, M. N. (2019). Learning-based model predictive control for autonomous racing. *IEEE Robotics and Automation Letters*, 4(4):3363–3370.

Massaro, M. (2011). A nonlinear virtual rider for motorcycles. *Vehicle system dynamics*, 49(9):1477–1496.

Picotti, E., Mion, E., Libera, A. D., Pavlovic, J., Censi, A., Frazzoli, E., Beghi, A., and Bruschetta, M. (2023). A learning-based nonlinear model predictive controller for a real go-kart based on black-box dynamics modeling through gaussian processes. *IEEE Transactions on Control System Technology*. Accepted.

Rossi, F., Lendasse, A., Francois, D., Wertz, V., and Verleysen, M. (2006). Mutual information for the selection of relevant variables in spectrometric nonlinear modelling. *Chemometrics and Intelligent Laboratory Systems*, 80(2):215–226.

Titsias, M. (2009). Variational learning of inducing variables in sparse gaussian processes. In van Dyk, D. and Welling, M., editors, *Proceedings of the Twelth International Conference on Artificial Intelligence and Statistics*, volume 5 of *Proceedings of Machine Learning Research*, pages 567–574, Hilton Clearwater Beach Resort, Clearwater Beach, Florida USA. PMLR.

Table 1. Closed-loop results in terms of mean tracking performance and computational time.

	nominal	black-box
e_y $[m]$	0.277	0.0936 (-66.2%)
e_ψ $[deg]$	0.908	0.472 (-48.0%)
e_v $[m/s]$	0.268	0.0451 (-83.2%)
T_{solver} $[ms]$	6.57	22.84 (+248%)

©2023 Bianchin, F., Picotti, E., & Bruschetta, M. published by TU Delft OPEN on behalf of the authors.
ISSN: 2667-2812

The Evolving Scholar (2023)

https://doi.org/10.24404/63ee3d8af04524edcd2db287

Bicycle and Motorcycle Dynamics 2023
Symposium on the Dynamics and Control of Single Track Vehicles
18 – 20 October 2023, Delft University of Technology, The Netherlands

Type of the Paper: Extended Abstract

Evaluating bicycle frame loads through semi-analytical multibody simulation methods

Bolk J.[1]*, Corves B.[2]

[1] Institute of Mechanism Theory, Machine Dynamics and Robotics, RWTH Aachen University, Germany; Bolk@igmr.rwth-aachen.de; 0000-0002-8777-509X
[2] Institute of Mechanism Theory, Machine Dynamics and Robotics, RWTH Aachen University, Germany; Corves@igmr.rwth-aachen.de, 0000-0003-1824-3433
*corresponding author.

Name of Editor: Jason Moore
Submitted: 16/02/2023
Accepted: 13/04/2023
Published: 25/04/2023
Citation: Bolk, J. & Corves, B. (2023). Evaluating bicycle frame loads through semi-analytical multibody simulation methods. The Evolving Scholar - BMD 2023, 5th Edition.
This work is licensed under a Creative Commons Attribution License (CC-BY).

Abstract:

The transport industry is currently experiencing a revolution, as a result of which sales of bicycles are increasing worldwide. For bicycle manufacturers, it is necessary to solve the conflict of goals between a time- and cost-efficient design and an inexpensive, yet safe product. At the same time, the weight of the bicycle is playing an increasingly important role, which means that new lightweight designs have to be developed. In modern design processes the operating loads to which the system components are subjected, play an important role. However, determining these is a major challenge, since not all components are accessible to measurement technology and existing test specifications often do not correspond to the real load situations.

A popular approach is the use of fully analytical multi body simulation methods to recreate the loads of real world driving. The results form the basis for finite-element analyses with which the component stress can be determined (Johannesson, 2014). However, compared to other vehicle industries, bicycle development faces special challenges when it comes to the application of such simulation methods. To perform these fully analytical simulations, a numerical model of the driving route as well as the driver is required. Although there are many approaches on this subject, the models of driver and track are too inaccurate due to unavoidable simplifications in regards to the determination of quantitative loads (Bruni, 2020). This leads to an inadequate design foundation, which is especially true for the (mountain) sports sector, since both the complexity of the load scenarios and the load itself are extremely high.

A high potential to solve existing challenges offers the so-called semi-analytical approach (SAA). This simulation setup applies forces directly on the system in form of measured data (Tebbe, 2006). In this way, challenging modeling tasks such as driver and route can be circumvented. Several studies in the literature explore these methods for moving systems without common constraints to the environment (Tebbe, 2006; Joubert 2020). Whereby these publications only consider vehicles that have a much higher weight ratio between rider and vehicle and lower load variety compared to bicycles. To prevent the system in these moving, unconstraint systems from accelerating uncontrollably in the simulation, passive and active stabilization methods can be used. These can be represented in the form of artificial constraints in the system, with the goal of recreating the applied forces in form of reaction forces or by control loops, stopping the acceleration of the center of gravity (Tebbe, 2006; Joubert 2020). For the purpose of designing bicycles, it is necessary to use the simplest simulation and measurement method possible, while being able to calculate component loads based on loads applied to the system, without distorting them through the simulation process.

This paper aims to show the potential of the semi-analytical approach for the calculation of loads on bicycles through the evaluation of various existing methods. To achieve this goal, synthetic measurement data at load application points are generated through fully analytical multi body simulations using a full suspension bicycle. The simulation is excited by a passive driver model and various road models, shown in Figure 1a. The excitation investigates straight-line rides with periodic excitations and jump excitations by board stone crossings and jumps as they occur in mountain biking. These data are applied to passively and actively stabilized simulation setups in order to calculate component loads of the frame structure. For passive stabilization, the suitability of artificial constraints on various components such as the frame or wheel hubs is investigated, given the lack of clear constraints in the

© 2023 Bolk, J., & Corves, B. published by TU Delft OPEN on behalf of the authors.
ISSN: 2667-2812

environment of a bicycle, see Figure 1b. Furthermore, control loops are utilized to provide the stability, see Figure 1c. In order to evaluate the suitability of the different SAA, forces are compared at reference points with the forces from the fully analytical measurement run. The results generally show that systems such as bicycles, in which the critical loads are not applied by the system inertia itself but from outside, are particularly suitable for the application. Existing disadvantages such as the neglect of system inertia in some approaches thus only play a subordinate role. Furthermore, a good agreement between the component loads from the full-analytical simulation and the loads calculated from the SAA could be determined for the scenarios considered.

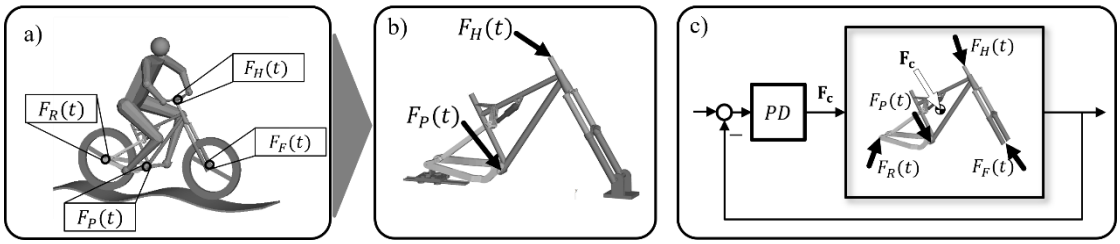


Figure 1. (a) Generation of synthetic measurement data. (b) passive semi analytical simulation setup. (c) active semi-analytical simulation setup.

References

Bruni, S.; Meijaard, J. P.; Rill, G.; Schwab, A. L.: State-of-the-art and challenges of railway and road vehicle dynamics with multibody dynamics approaches. *Multibody system dynamics*, 49 (2020)

Johannesson, P.; Speckert, M.: Guide to load analysis for durability in vehicle engineering. *Chichester West Sussex United Kingdom: Wiley* (2014)

Joubert, N.; Boisvert, M.; Blanchette, C.; St-Amant, Y.; Desrochers, A.; Rancourt, D.: Frame loads accuracy assessment of semianalytical multibody dynamic simulation methods of a recreational vehicle. *Multibody system dynamics*, 50 (2020)

Tebbe, J. C.; Chidambaram, V.; Kline, J. T.; Scime, S.; Shah, M. P.: Chassis loads prediction using measurements as input to an unconstrained multi-body dynamics model. *SAE 2006 World Congress and Exhibition*. Detroit: SAE International (2006)

© 2023 Bolk, J., & Corves, B. published by TU Delft OPEN on behalf of the authors.
ISSN: 2667-2812

The Evolving Scholar (2023)
https://doi.org/10.59490/6461fae57a7554ff28deada4
Bicycle and Motorcycle Dynamics 2023
Symposium on the Dynamics and Control of Single Track Vehicles
18 – 20 October 2023, Delft University of Technology, The Netherlands

Type of the Paper: Extended Abstract

Parameterized and validated equations of motion for a tadpole style cargo tricycle

Clemens Groß[1,*] and Steffen Müller[2]

[1]Chair of Automotive Engineering, Technische Universität Berlin; email gross.1@tu-berlin.de; ORCID: 0000-0002-1606-3845
[2]Chair of Automotive Engineering, Technische Universität Berlin; email steffen.mueller@tu-berlin.de
*corresponding author.

Name of Editor: Jason Moore
Submitted: 15/05/2023
Accepted: 15/05/2023
Published: 19/06/2023
Citation: Groß, C. & Müller, S. (2023). Parameterized and validated equations of motion for a tadpole style cargo tricycle. The Evolving Scholar - BMD 2023, 5th Edition.
This work is licensed under a Creative Commons Attribution License (CC-BY).

Abstract:

In the past years, cargo bicycles in different configurations have gained popularity for many use cases. Their configurations differ substantially. Single-track cargo bicycles and their kinematics are linked closely to conventional bicycles. The kinematics of inverted tricycles, so-called tadpole trikes, are very different. In the final paper, we will present a novel physical model of a tadpole style cargo tricycle for the mathematical description of the driving behavior, which can be used for applications such as stability analysis or motion prediction. We will furthermore present our instrumented tadpole cargo tricycle which is used to parametrize our kinematic model and used to validate the theoretically derived equations of motion.

Introduction and State of the Art

Dating as far back as 1899, bicycle dynamics have been of great interest in mechanical engineering. Models for the conventional concept of a two-wheeled bicycle are already available, just like for four-wheelers. Only a few works consider the specific needs of tricycles though. Even fewer studies focus on the specifics of so-called tadpole tricycles, which are used commonly for cargo bicycles. With the exception of the works of Sponziello et al. (2008), Bartolozzi et al. (2008), and Wibowo et al. (2017), little attention has been drawn towards this topic. Sponziello et al. (2008) presented a mathematical model of a tadpole-style motor scooter, respectively a MSC Adams model of it (Bartolozzi et al. 2008), and validated it against an instrumented scooter. Due to the differences in chassis design between this scooter and widespread concepts of cargo tricycles, their model cannot be used for the specifics of the latter. Wibowo et al. (2017) showed a simplified, two-dimensional model of another type of tadpole-style scooter and discussed controller design for this vehicle without quantifying errors arising from this simplification. A concise, parameterized, and validated model for cargo tricycles is missing yet – we aim at closing this gap.

Geometry and Model Assumptions

A sketch of the tadpole cargo tricycle model is shown in Figure 1. The model consists of five rigid bodies: the rear wheel (W), the rear frame (F), the front frame/cargo box assembly (B), as well as the front right (R) and front left (L) wheel.

Based on the Newtonian Frame $\boldsymbol{N}$, the rear-wheel contact point is located by the coordinates $\boldsymbol{x_w}$, $\boldsymbol{y_w}$ along the unit vectors $\boldsymbol{n_x}$ and $\boldsymbol{n_y}$ and may turn with $\boldsymbol{\psi}$ about $\boldsymbol{n_z}$. We introduce a contact point reference frame $\boldsymbol{C}$ in this very point. The rear wheel may rotate about its center axis $\boldsymbol{w_y}$ with $\boldsymbol{\alpha_w}$ and have a roll angle $\boldsymbol{\phi}$ about the ground plane. Since the rear wheel is only allowed to rotate around the shared axis in the rear frame, the roll and yaw angle of the rear frame are equal to those of the rear wheel. The front frame (B) may turn with an angle $\boldsymbol{\delta}$ around the revolute joint that connects F and B. This revolute joint is placed under an angle $\boldsymbol{\lambda}$ relative to the perpendicular axis. When comparing our cargo tricycle with conventional bicycles it is worth noting that the sign of $\boldsymbol{\lambda}$ differs. Turning the handlebars therefore also enforces a roll angle $\boldsymbol{\phi}$ on the rear frame (F), which depends on geometric parameters such as $\boldsymbol{\lambda}$ and the handlebar steering angle $\boldsymbol{\delta}$. Finally, R and L may turn about their center axes $\boldsymbol{r_y}$ and $\boldsymbol{l_y}$ through $\boldsymbol{\alpha_r}$ and $\boldsymbol{\alpha_l}$.

© 2023 Groß, C., Müller, S. published by TU Delft OPEN on behalf of the authors.
ISSN: 2667-2812

We assume that the wheels are flat, rolling discs. Furthermore, all three wheels are required to touch the ground plane at all times. In our finalized paper, we will show these equations of motions with respective constraints and discuss the implications made by geometrical parameter choice to the driving dynamics of the cargo bicycle.

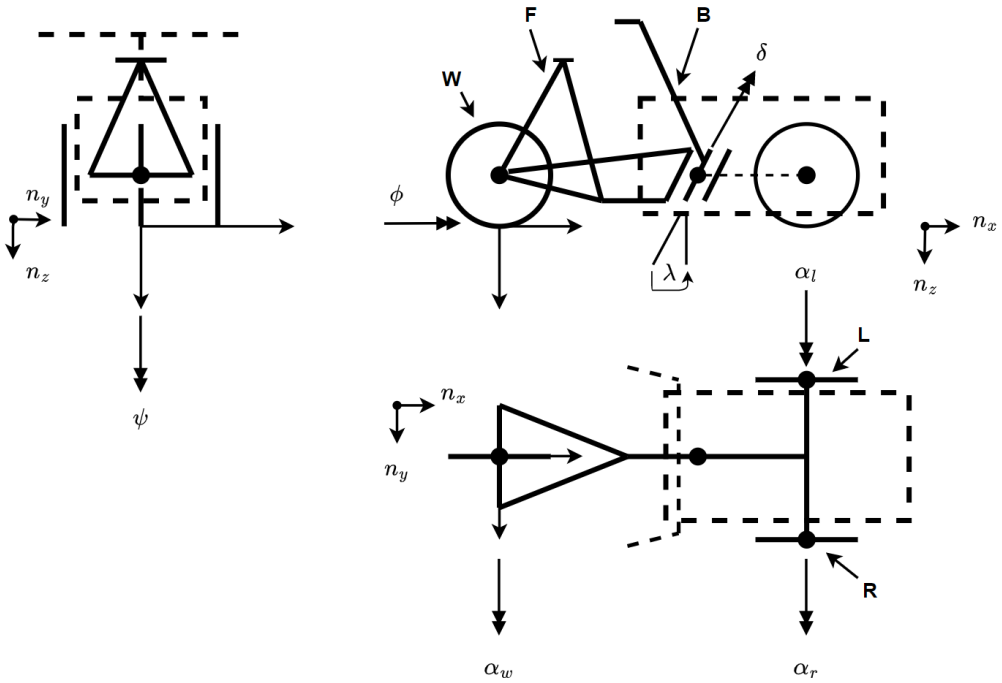


Figure 1. A schematic of the instrumented tadpole cargo tricycle.

Instrumented Cargo Tricycle

In order to validate the equations of motion, we will make use of an instrumented tadpole style cargo tricycle, which we have prepared at our department. To measure the steering angle, a resistive displacement sensor is used. This sensor is connected to the steering axle and thus measures the steering angle $\boldsymbol{\delta}$. The roll angle of the rear frame $\boldsymbol{\phi}$ is measured by the help of an IMU. We will also determine the relevant parameters (such as mass, center of gravity, inertia tensors) of the tricycle and its respective parts through experiments for this cargo tricycle.

Expected Outcome and Contribution

The paper will introduce a novel mathematical model for tadpole cargo tricycles and show how its parameters can be determined through experiments. Furthermore, experimental parameter designation will be discussed. The model will be validated against the instrumented cargo tricycle. We will discuss the influence of parameters on the driving dynamics of the tadpole tricycle.

References

Bartolozzi, R., Frendo, F., Giuggiano, M., & Sponziello A. (2008). Comparison between experimental and numerical handling tests for a three-wheeled motorcycle. S*AE Int. J. Engines* 1(1): 1389-1395, doi: 10.4271/2008-32-0061.

Sponziello, A., Frendo, F., & Giuggiano, M. (2008). Stability analysis of a three-wheeled motorcycle. S*AE Int. J. Engines* 1(1):1396-1401, doi: 10.4271/2008-32-0062.

Wibowo, Lambang, L., Pratama, G. & Surojo, E. (2017, October 5-6). Simulation and Analysis of Three Wheeled Reverse Trike Vehicles with PID Controller. In Suwarno, V. S. Djanali, B. Pramujati and V. A. Yartys (Eds.), *Proceedings of the 3rd International Conference on Mechanical Engineering (ICOME 2017),* Surabaya, Indonesia.

© 2023 Groß, C., Müller, S. published by TU Delft OPEN on behalf of the authors.
ISSN: 2667-2812

The Evolving Scholar (2023)

http://dx.doi.org/10.59490/64d0a280b2791c2b16b6b2ea

Bicycle and Motorcycle Dynamics 2023
Symposium on the Dynamics and Control of Single Track Vehicles
18–20 October 2023, Delft University of Technology, The Netherlands

Type of the Paper: Extended Abstract

BRiM: A Modular and Extensible Open-Source Framework for Creating Bicycle-Rider Models

Timo J. Stienstra [1,*], Samuel G. Brockie [1], Jason K. Moore [1]

[1] Faculty of Mechanical, Maritime and Materials Engineering (3mE), Delft University of Technology, The Netherlands; t.j.stienstra@student.tudelft.nl, ORCID 0000-0003-4600-515X

[*] corresponding author

Name of Editor: Edwin de Vries
Submitted: 07/08/2023
Accepted: 09/08/2023
Published: 09/08/2023
Citation: Stienstra, T., Brockie, S. & Moore, J. (2023). BRiM: A Modular and Extensible Open-Source Framework for Creating Bicycle-Rider Models. The Evolving Scholar - BMD 2023, 5th Edition.
This work is licensed under a Creative Commons Attribution License (CC-BY).

Abstract:

Bicycles have been modelled for more than 150 years of their 200 years of existence (Schwab and Meijaard, 2013). These mathematical models provide insights into how various factors affect the bicycle dynamics, such as the effects of velocity (Schwab and Meijaard, 2013) and rider control (Sharp, 2008) on stability. These insights in turn help in the development of bicycles with improved stability, handling, and comfort (Plöchl et al., 2012). Mathematical modelling is also powerful when used to investigate the human controller in bicycle-rider systems, particularly for experiments that would be difficult to conduct safely, such as investigating forces during bicycle crashes, or involve measurements that are difficult or could be unethical to make, such as in-vivo muscular re-cruitment. The motorcycle literature details the interaction between human and vehicle, but this is yet to be done for human-bicycle systems.

A commonality among investigations around bicycle dynamics is the reuse of the Whipple model, which has been linearised by Papadopoulos and Ruina (2007). Most researchers also extend this model. Examples include extension with tyre models (Schwab and Meijaard, 2013) or by attaching a rider (Moore, 2012). It would be useful if there existed a common framework for creating such models, within which extensions to the bicycle model, or biomechanical models of the rider, could easily be added. Such a framework would also enable models to be easily shared between researchers, helping with research dissemination and academic reproducibility. To address these needs, this work develops *BRiM*, a modular and extensible framework for creating *B*icycle-*Ri*der *M*odels.

At its core, *BRiM* facilitates the construction of a base bicycle model, which is compatible with modular modelling extensions. This model is also composable with other extensions, such as models of the rider. The base bicycle model can either be the Whipple bicycle (Whipple, 1899), useful in simulations that require the dynamics of the bicycle, or a stationary bicycle model, suitable for simulations that focus only on the rider's pedalling. The model is defined using a tree representation, where each model is composed of modular submodels, to which load groups can be attached. The submodels mainly alter the kinematic behaviour of the bicycle and are strongly coupled to the geometry of the bicycle model. Examples include toroidal shaped wheels, which include the crown curvature radius of the tyres, and a leaning rider model, which adds at least one extra degree of freedom. Load groups on the other hand define the forces and torques that act upon the system. The most common example is a simple driving torque acting on the rear wheel, but more complex loads are torsional spring-dampers. *BRiM* also supports biomechanical modelling of the rider. These can be torque- or muscle-driven, and can consist of pedalling lower limbs connected to the pedals, steering-capable upper bodies, or both combined. After composing a bicycle-rider model from *BRiM*'s library of components and extensions, the system's equations of motion can be formed automatically and used for simulation.

BRiM is developed as an open-source Python package. It leverages the open-source Python package *SymPy* (Meurer et al., 2017), a computer algebra system with a module, `sympy.physics.mechanics`, that allows dynamical systems to be defined and their

©2023 Stienstra, T. J. & Brockie, S. G. & Moore, J. K. published by TU Delft OPEN on behalf of the authors.
ISSN: 2667-2812

 http://dx.doi.org/10.59490/64d0a280b2791c2b16b6b2ea

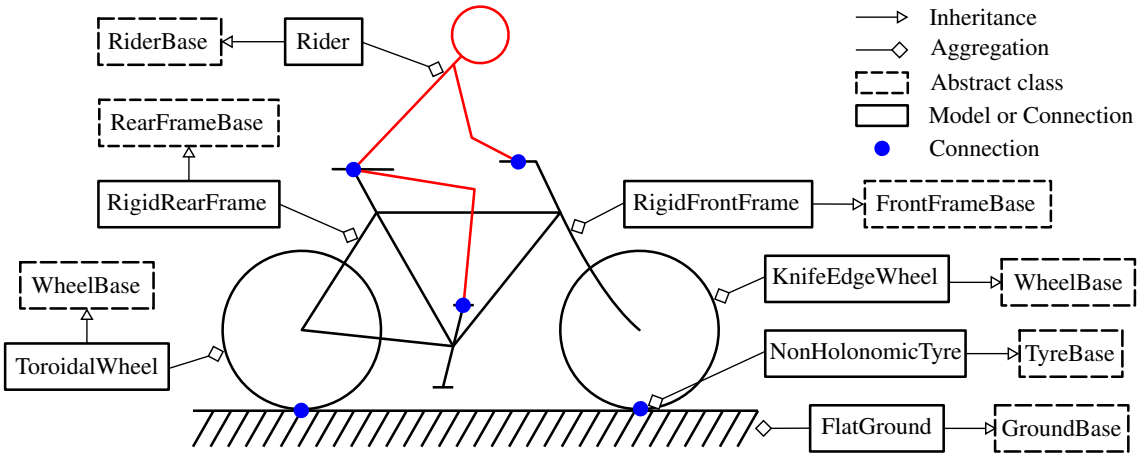


Figure 1. Simplified visualisation of the architecture used by *BRiM*. This example uses the Whipple model as a base and extends it with a rigid rear and front frame, while using two different types of wheel models and a custom rider, which is optional. Connections describe the interaction between two or more submodels.

equations of motion derived in symbolic form. Symbolic equations of motion were chosen because they are analytically exact, have the potential to be mathematically efficient, and can be used to generate high-performance numeric code, all of which lead to accurate and fast simulations.

The effectiveness of *BRiM* is demonstrated by solving trajectory tracking problems for a rolling disc, which will be extended to bicycle-rider models. A direct collocation algorithm implemented in *Pycollo* (Brockie, 2021) is used to find the control required to minimise the error between prescribed analytic paths and the simulated trajectories of models created using *BRiM*. This optimisation strategy showcases the effectiveness of *BRiM* as it allows the trajectory tracking problem to be solved easily for multiple different bicycle models of varying complexity. This indicates that researchers can use *BRiM* to solve other practical problems.

This project has been made possible in part by CZI grant CZIF2021-006198 and grant DOI https://doi.org/10.37921/240361looxoj from the Chan Zuckerberg Initiative Foundation (funder DOI 10.13039/100014989).

References

Brockie, S. G. (2021). *Predictive Simulation of Musculoskeletal Models Using Direct Collocation*. PhD thesis, University of Cambridge.

Meurer, A., Smith, C. P., Paprocki, M., Čertík, O., Kirpichev, S. B., Rocklin, M., Kumar, A., Ivanov, S., Moore, J. K., Singh, S., Rathnayake, T., Vig, S., Granger, B. E., Muller, R. P., Bonazzi, F., Gupta, H., Vats, S., Johansson, F., Pedregosa, F., Curry, M. J., Terrel, A. R., Roučka, v., Saboo, A., Fernando, I., Kulal, S., Cimrman, R., and Scopatz, A. (2017). SymPy: symbolic computing in python. *PeerJ Computer Science*, 3:e103.

Moore, J. K. (2012). *Human Control of a Bicycle*. PhD thesis, University of California, Davis.

Papadopoulos, J. M. and Ruina, A. (2007). Linearized dynamics equations for the balance and steer of a bicycle: a benchmark and review. *Proceedings of the Royal society A: mathematical, physical and engineering sciences*, 463(2084):1955–1982.

Plöchl, M., Edelmann, J., Angrosch, B., and Ott, C. (2012). On the wobble mode of a bicycle. *Vehicle System Dynamics*, 50(3):415–429. Publisher: Taylor & Francis _eprint: https://doi.org/10.1080/00423114.2011.594164.

Schwab, A. L. and Meijaard, J. P. (2013). A review on bicycle dynamics and rider control. *Vehicle System Dynamics*, 51(7):1059–1090.

Sharp, R. S. (2008). On the Stability and Control of the Bicycle. *Applied Mechanics Reviews*, 61(6).

Whipple, F. J. (1899). The stability of the motion of a bicycle. *Quarterly Journal of Pure and Applied Mathematics*, 30(120):312–348.

©2023 Stienstra, T. J. & Brockie, S. G. & Moore, J. K. published by TU Delft OPEN on behalf of the authors.
ISSN: 2667-2812

The Evolving Scholar (2023)

http://dx.doi.org/10.24404/63fdb252b7265d4b80e4078d

Bicycle and Motorcycle Dynamics 2023
Symposium on the Dynamics and Control of Single Track Vehicles
18–20 October 2023, Delft University of Technology, The Netherlands

Type of the Paper: Extended Abstract

On the fundamental dynamics of rolling wheels: an Appellian approach

Máté B. Vizi [1,2,*], Gábor Orosz [3,4], Dénes Takács [1,2], Gábor Stépán [1]

[1] Department of Applied Mechanics, Budapest University of Technology and Economics, Budapest, Hungary; vizi@mm.bme.hu, ORCID 0000-0001-7372-1296; takacs@mm.bme.hu, ORCID 0000-0003-1226-8613; stepan@mm.bme.hu, ORCID 0000-0003-0309-2409
[2] ELKH-BME Dynamics of Machines Research Group, Budapest, Hungary;
[3] Department of Mechanical Engineering, University of Michigan, Ann Arbor, MI 48109, USA; orosz@umich.edu, ORCID 0000-0002-9000-3736
[4] Department of Civil and Environmental Engineering, University of Michigan, Ann Arbor, MI 48109, USA;
[*] corresponding author

Name of Editor: Jason Moore
Submitted: 28/02/2023
Accepted: 31/03/2023
Published: 26/04/2023
Citation: Vizi, M., Orosz, G., Takács, D. & Stépán, G. (2023). On the fundamental dynamics of rolling wheels: an Appellian approach. The Evolving Scholar - BMD 2023, 5th Edition.
This work is licensed under a Creative Commons Attribution License (CC-BY).

Abstract:

The dynamical model of the rolling wheel serves as the basis for modeling autonomous unicycles such as presented in Naveh et al. (1999), Suzuki et al. (2014) and Cao et al. (2023). Based on the fundamental dynamics of the rolling wheel, one may get an insight about the physically feasible motions of unicycles and the stability properties of such motions. Moreover, novel control strategies can be developed based on this dynamical analysis.

The mechanical model of the rolling wheel consists of a disc of mass m and radius R as shown in the left panel of Figure 1. It is considered that the wheel rolls without slipping on the horizontal plane, this assumption gives $n_\mathrm{k} = 2$ kinematic and $n_\mathrm{g} = 1$ geometric constraining equations. Five generalized coordinates are needed to describe the system dynamics, these are chosen as follows: the disc's horizontal position is described by the center point planar coordinates x_G and y_G in ground-fixed reference frame F_0; the disc's orientation is represented by Euler angles using the yaw angle ψ, the tilt angle ϑ and the the pitch angle φ; see Fig. 1. Due to the two kinematic constraints, the rolling wheel is a nonholonomic mechanical system, so the equations of motion can be obtained by the Appellian approach (Appell, 1900); the required three pseudo velocities $\sigma_j,\ j = 1, \ldots, 3$ are chosen to be the angular velocity components in frame F_2 that is traveling with the wheel except the pitch rotation:

$$\boldsymbol{\omega} = \begin{bmatrix} \dot{\vartheta} & \dot{\psi}\sin\vartheta + \dot{\varphi} & \dot{\psi}\cos\vartheta \end{bmatrix}^\mathsf{T}_{\mathrm{F}_2} \quad \Rightarrow \quad \sigma_1 = \dot{\vartheta}\,,\ \ \sigma_2 = \dot{\psi}\sin\vartheta + \dot{\varphi}\,,\ \ \sigma_3 = \dot{\psi}\cos\vartheta\,. \tag{1}$$

This leads to the system of equations of motion of the rolling wheel:

$$\begin{cases} \dot{\sigma}_1 = \dfrac{6\sigma_2\sigma_3}{5} - \dfrac{\sigma_3^2\tan\vartheta}{5} + \dfrac{4g\sin\vartheta}{5R}\,, \\ \dot{\sigma}_2 = -\dfrac{2\sigma_1\sigma_3}{3}\,, \\ \dot{\sigma}_3 = -2\sigma_1\sigma_2 + \sigma_1\sigma_3\tan\vartheta\,, \\ \dot{\vartheta} = \sigma_1\,, \end{cases} \qquad \begin{cases} \dot{\psi} = \sigma_3\dfrac{1}{\cos\vartheta}\,, \\ \dot{\varphi} = \sigma_2 - \sigma_3\tan\vartheta\,, \\ \dot{x}_\mathrm{G} = \sigma_1 R\sin\psi\cos\vartheta + \sigma_2 R\cos\psi\,, \\ \dot{y}_\mathrm{G} = -\sigma_1 R\cos\psi\cos\vartheta + \sigma_2 R\sin\psi\,. \end{cases} \tag{2}$$

The rolling wheel can be interpreted as an $n = 6 - n_\mathrm{k}/2 - n_\mathrm{g} = 4$ degrees-of-freedom nonholonomic cyclic system: the first four equations of (2) are the so-called essential dynamics while the remaining four equations describe the so-called hidden dynamics.

©2023 Vizi, M. B., Orosz, G., Takács, D. & Stépán, G. published by TU Delft OPEN on behalf of the authors.
ISSN: 2667-2812

 http://dx.doi.org/10.24404/63fdb252b7265d4b80e4078d

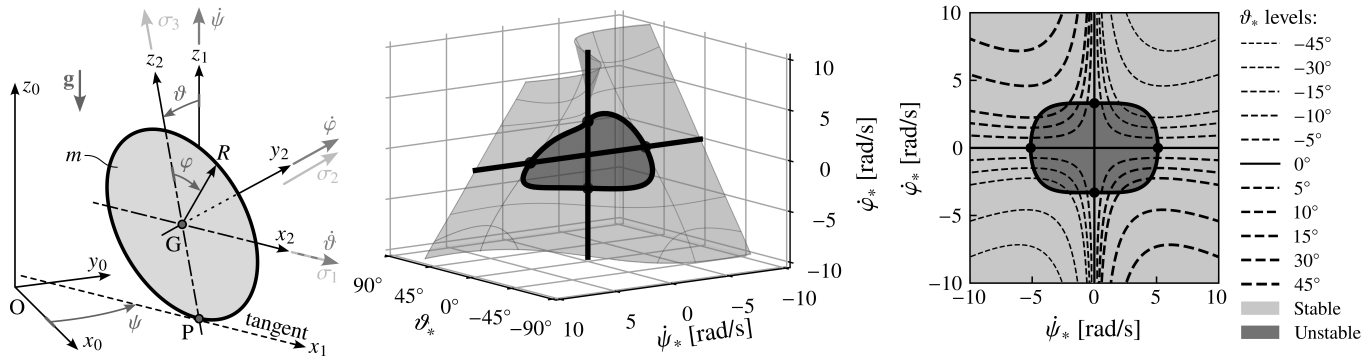


Figure 1. Mechanical model of the rolling wheel (left panel) and the steady state motions (middle and right panels)

The fixed-points of the essential dynamics correspond to the steady state motions. The rolling wheel has three different types of steady states: the straight rolling steady state (with $\vartheta_* = 0$ and $\dot\psi_* = 0$) when the wheel center G follows a straight path, the turning-rolling steady state when the wheel center G follows a circular path, and the spinning steady state (with $\vartheta_* = 0$ and $\dot\varphi_* = 0$) when the wheel center G remains still. While $\sigma_{1*} = 0$, the steady state pseudo velocities σ_{2*}, σ_{3*} and the steady state tilt angle ϑ_* are not independent of each other. The steady state pseudo velocities can be transformed back to the physically meaningful steady state yaw and pitch rates, $\dot\psi_*$ and $\dot\varphi_*$, respectively:

$$6\sigma_{2*}\sigma_{3*}R - \sigma_{3*}^2 R\tan\vartheta_* + 4g\sin\vartheta_* = 0 \quad \Rightarrow \quad 5\dot\psi_*^2 R\sin\vartheta_*\cos\vartheta_* + 6\dot\psi_*\dot\varphi_* R\cos\vartheta_* + 4g\sin\vartheta_* = 0\,. \tag{3}$$

This relation (3) is shown as surface in the middle panel of Figure 1. The stability of these steady state states are obtained by means of linear stability analysis. The essential dynamics linearized around a steady state (3) has the form of

$$\begin{bmatrix}\dot{\tilde\sigma}_1\\ \dot{\tilde\sigma}_2\\ \dot{\tilde\sigma}_3\\ \dot{\tilde\vartheta}\end{bmatrix} = \begin{bmatrix}0 & A_{12} & A_{13} & A_{14}\\ A_{21} & 0 & 0 & 0\\ A_{31} & 0 & 0 & 0\\ 1 & 0 & 0 & 0\end{bmatrix}\begin{bmatrix}\tilde\sigma_1\\ \tilde\sigma_2\\ \tilde\sigma_3\\ \tilde\vartheta\end{bmatrix}, \quad \begin{aligned} A_{12} &= \tfrac{6}{5}\dot\psi_*\cos\vartheta_*, & A_{21} &= -\tfrac{2}{3}\dot\psi_*\cos\vartheta_*,\\ A_{13} &= \tfrac{4}{5}\dot\psi_*\sin\vartheta_* + \tfrac{6}{5}\dot\varphi_*, & A_{31} &= -\dot\psi_*\sin\vartheta_* - 2\dot\varphi_*,\\ A_{14} &= -\tfrac{1}{5}\dot\psi_*^2 + \tfrac{4g}{5R}\cos\vartheta_*., \end{aligned} \tag{4}$$

where tilde refers to the perturbed state variables. Based on the eigenvalues of matrix $\mathbf{A}$, the stability of the steady state motions are shown in the middle and right panels of Figure 1, where the light gray and the dark gray areas represent the (neutrally) stable and unstable steady states, respectively. The upright static equilibrium and its' vicinity is unstable; perturbing such a steady state leads to deviating trajectories with large oscillations. However, large enough yaw and/or pitch rates result in a stable behavior of the rolling wheel: small perturbations yield only small oscillations around such a steady state. The critical pitch rate $\dot\varphi_{\rm crit}$ of straight rolling and the critical yaw rates $\dot\psi_{\rm crit}$ of spinning and turning-rolling are as follows:

$$\dot\varphi_{\rm crit} = \sqrt{\frac{g}{3R}}\,, \quad \dot\psi_{\rm crit} = \sqrt{\frac{4g}{5R}}\,, \quad \dot\psi_{\rm crit,1,2} = \sqrt{\frac{2g}{5R}}\sqrt{\frac{3 - 6\cos^2\vartheta_* \pm \sqrt{76\sin^4\vartheta_* - 96\sin^2\vartheta_* + 9}}{(2\sin^2\vartheta_* - 3)\cos\vartheta_*}}\,. \tag{5}$$

In the first two cases, having larger angular velocities than these critical ones yield stable steady state motions, while $|\dot\psi_*| < \dot\psi_{\rm crit,1}$ or $\dot\psi_{\rm crit,2} < |\dot\psi_*|$ result in stable turning-rolling steady states.

Novel control strategies can be developed for autonomous unicycles by extending this dynamical analysis for simple unicycle models. The straight rolling steady state can be used for a stabilizing controller which aims to stabilize even the relatively slow straight motions, also, simple trajectory tracking controllers can be built upon this. The turning-rolling steady states allow more advanced path planning for steering and maneuvering.

References

Appell, P. (1900). Sur une forme générale des équations de la dynamique (On a general form of the equations of dynamics). *Journal für die reine und angewandte Mathematik (Journal for Pure and Applied Mathematics)*, 121:310–319.

©2023 Vizi, M. B., Orosz, G., Takács, D. & Stépán, G. published by TU Delft OPEN on behalf of the authors.
ISSN: 2667-2812

http://dx.doi.org/10.24404/63fdb252b7265d4b80e4078d

Cao, X., Bui, D. C., Takács, D., and Orosz, G. (2023). Autonomous unicycle: Modeling, dynamics, and control. *submitted*.

Naveh, Y., Bar Yoseph, P., and Halevi, Y. (1999). Nonlinear modeling and control of a unicycle. *Dynamics and Control*, 9:279–296.

Suzuki, H., Moromugi, S., and Okura, T. (2014). Development of robotic unicycles. *Journal of Robotics and Mechatronics*, 26(5):540–549.

©2023 Vizi, M. B., Orosz, G., Takács, D. & Stépán, G. published by TU Delft OPEN on behalf of the authors.
ISSN: 2667-2812

The Evolving Scholar (2023)
https://doi.org/10.24404/63f649c20cea3689dfaed39e
Bicycle and Motorcycle Dynamics 2023
Symposium on the Dynamics and Control of Single Track Vehicles
18 – 20 October 2023, Delft University of Technology, The Netherlands

Type of the Paper: Extended Abstract

A bicycle can be balanced by stochastic optimal feedback control but only with accurate speed estimates

Eric Maris[1]

[1]Donders Institute for Brain, Cognition and Behaviour, Radboud University; eric.maris@donders.ru.nl, 0000-0001-5166-1800

Name of Editor: Jason Moore
Submitted: 22/02/2023
Accepted: 22/04/2023
Published: 25/04/2023
Citation: Maris, E. (2023). A bicycle can be balanced by stochastic optimal feedback control but only with accurate speed estimates. The Evolving Scholar - BMD 2023, 5th Edition.
This work is licensed under a Creative Commons Attribution License (CC-BY).

Abstract:

Balancing a bicycle is typical for the balance control humans perform as a part of a whole range of behaviours (walking, running, skating, skiing, etc.). I will present a general model of balance control (see Fig. 1) and apply it to the balancing of a bicycle. Balance control has both a physics (mechanics) and a neurobiological component. The physics component pertains to the laws that govern the movements of the rider and his bicycle, and the neurobiological component pertains to the mechanisms via which the central nervous system (CNS) uses these laws for balance control. I will present a computational model of this neurobiological component, based on the theory of stochastic optimal feedback control (OFC)(Todorov, 2004; Todorov & Jordan, 2002). The central concept in this model is a computational system, implemented in the CNS, that controls a mechanical system outside the CNS. This computational system uses an internal model to calculate optimal control actions as specified by the theory of stochastic OFC. For the computational model to be plausible, it must be robust to at least two inevitable inaccuracies: (1) model parameters that the CNS learns slowly from interactions with the CNS-attached body and bicycle (i.e., the internal noise covariance matrices), and (2) model parameters that depend on unreliable sensory input (i.e., movement speed). By means of simulations, I demonstrate that this model can balance a bicycle under realistic conditions and is robust to inaccuracies in the learned sensorimotor noise characteristics. However, the model is not robust to inaccuracies in the movement speed estimates.

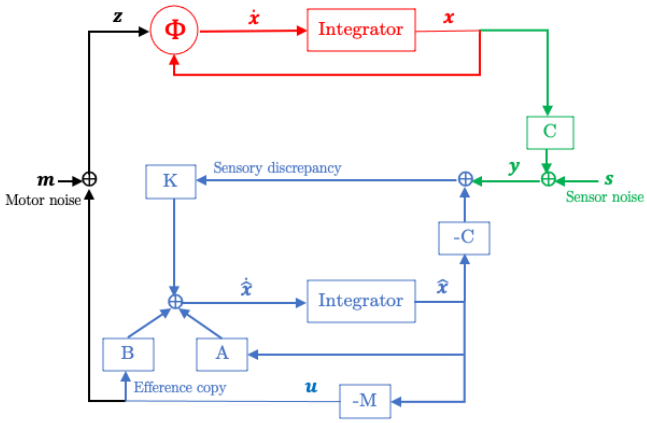


Fig 1. Sensorimotor control of a mechanical system (in red) by input from a computational system (in blue). The mechanical system is governed by the nonlinear differential equations $\dot{\boldsymbol{x}} = \boldsymbol{\Omega}(\boldsymbol{x}, \boldsymbol{z})$, and the computational system produces an optimal control action $\boldsymbol{u}$. The motor output system (in black) adds noise $\boldsymbol{m}$ to $\boldsymbol{u}$ and feeds this into the mechanical system. The sensory input system (in green) maps the state variables $\boldsymbol{x}$ to sensory variables, adds noise $\boldsymbol{s}$ and feeds the resulting sensory input $\boldsymbol{y}$ into the computational system. The

© 2023 Maris, E. published by TU Delft OPEN on behalf of the authors.
ISSN: 2667-2812

computational system calculates an optimal internal state estimate $\hat{\boldsymbol{x}}$ by integrating a linear differential equation (characterized by the matrices $\boldsymbol{A}$, $\boldsymbol{B}$, $\boldsymbol{C}$, and the Kalman gain $\boldsymbol{K}$) that takes the sensory feedback $\boldsymbol{y}$ as input. The optimal control action $\boldsymbol{u}$ is obtained from $\hat{\boldsymbol{x}}$ and the linear quadratic regulator (LQR) gain $-\boldsymbol{M}$.

All simulations were performed using two models of the rider-bicycle combination: the steered double pendulum (SDP) and the benchmark double pendulum (BDP). The SDP (see Fig. 2) contains ingredients of three familiar models: the double compound pendulum on a cart (Bogdanov, 2004), the Acrobot (Tedrake, 2021), and the torsional spring-mass-damper system. Roughly speaking, the SDP is a double compound pendulum of which the base can be steered by a wheel (instead of a cart) and the joint between the two rods (at the hips) can be actuated, as in the Acrobot. Both actuated joints, one at the handlebars and one at the hips, are modelled as a torsional spring-mass-damper system.

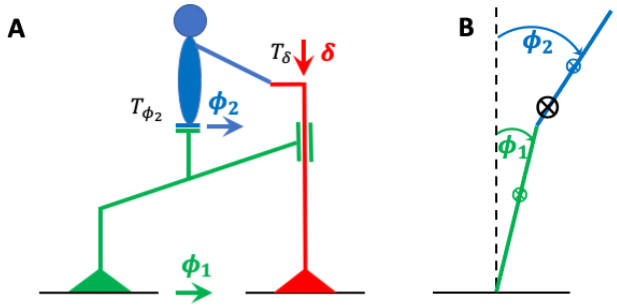


Fig 2. The steered double pendulum (SDP). (A) Side view. (B) Rear view.

The BDP (see Fig. 3) is a combination of an existing benchmark model for studying the passive dynamics of a bicycle (Meijaard et al., 2007) and the double pendulum. The BDP is based on two ideas. The first idea is to follow the approach of Meijaard et al. (2007) and derive linearized EoM for a bicycle with the rider's lower body rigidly attached to the rear frame and no upper body. These linearized EoM depend on a number of constants, and I chose these constants such that (1) the front frame is as similar as possible to the self-stable benchmark bicycle model described by Meijaard et al. (2007), and (2) the lengths and masses are as similar as possible to the SDP. The second idea is to model the interactions between the upper body and the rear frame (which includes the lower body) by the linearized EoM of the double compound pendulum.

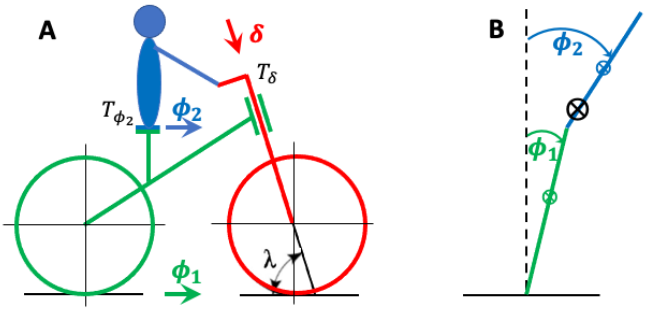


Fig 3. The benchmark double pendulum (SDP). (A) Side view. (B) Rear view.

References

Bogdanov, A. (2004). Optimal control of a double inverted pendulum on a cart. *Oregon Health and Science University, Tech. Rep. CSE-04-006, OGI School of Science and Engineering, Beaverton, OR*.

Meijaard, J. P., Papadopoulos, J. M., Ruina, A., & Schwab, A. L. (2007). Linearized dynamics equations for the balance and steer of a bicycle: a benchmark and review. Proceedings of the Royal Society of London A: Mathematical, Physical and Engineering Sciences,

Tedrake, R. (2021). Underactuated Robotics: Algorithms for Walking, Running, Swimming, Flying, and Manipulation (Course Notes for MIT 6.832). Downloaded on 20-08-2021 from http://underactuated.mit.edu/.

Todorov, E. (2004). Optimality principles in sensorimotor control. *Nature Neuroscience*, *7*(9), 907-915.

Todorov, E., & Jordan, M. I. (2002). Optimal feedback control as a theory of motor coordination. *Nature Neuroscience*, *5*(11), 1226-1235.

© 2023 Maris E. published by TU Delft OPEN on behalf of the authors.
ISSN: 2667-2812

The Evolving Scholar (2023)

https://doi.org/10.59490/6498e9850d5cf303b8bd2f90

Bicycle and Motorcycle Dynamics 2023
Symposium on the Dynamics and Control of Single Track Vehicles
18 – 20 October 2023, Delft University of Technology, The Netherlands

Type of the Paper: Extended Abstract

Position Measuring System for a Motorcycle Using Quad Omnidirectional Cameras

Junji Hirasawa[1,*]

[1]Ibaraki KOSEN, College of Technology; hirasawa@ss.ibaraki-ct.ac.jp, https://orcid.org/0000-0001-9213-5831
*corresponding author.

Name of Editor: Jason Moore
Submitted: 26/06/2023
Accepted: 26/06/2023
Published: 26/06/2023
Citation: Hirasawa, J. (2023). Position Measuring System for a Motorcycle Using Quad Omnidirectional Cameras. The Evolving Scholar - BMD 2023, 5th Edition. This work is licensed under a Creative Commons Attribution License (CC-BY).

Abstract:

In this article, improvement on a measurement system for position of a motorcycle is described. Position measurement of a running motorcycle is difficult problem because the loading of measuring equipments would cause changing the mass and the moment of inertia of the vehicle (Kageyama, 2017) (Waegli, 2008). Therefore author had proposed novel measuring method using omnidirectional cameras to get relative angles to fixed camera positions (Hirasawa, 2021) (Hirasawa, 2023). Results of the previous research show that the simple measuring method with image processing techniques could apply to position measurement of an 8-shape running motorcycle around 2 omnidirectional cameras. The weakness of the method using 2 omnidirectional cameras is large error nearby camera baseline (the line connecting 2 cameras) especially in the baseline direction.

To improve precision of position measurement, author had added 2 omnidirectional cameras to the system. Relative positions of quad omnidirectional cameras are shown in Figure 1. Camera 1 and Camera 2 are attached on green and red pylons respectively. Midpoint of 2 cameras is set as the original point of the coordinate X_0-Y_0-Z_0. Two dimensional position of the measuring point are calculated easily using relative angle from Camera 1 and Camera 2, similar to the principle of a stereo camera as Equation 1.

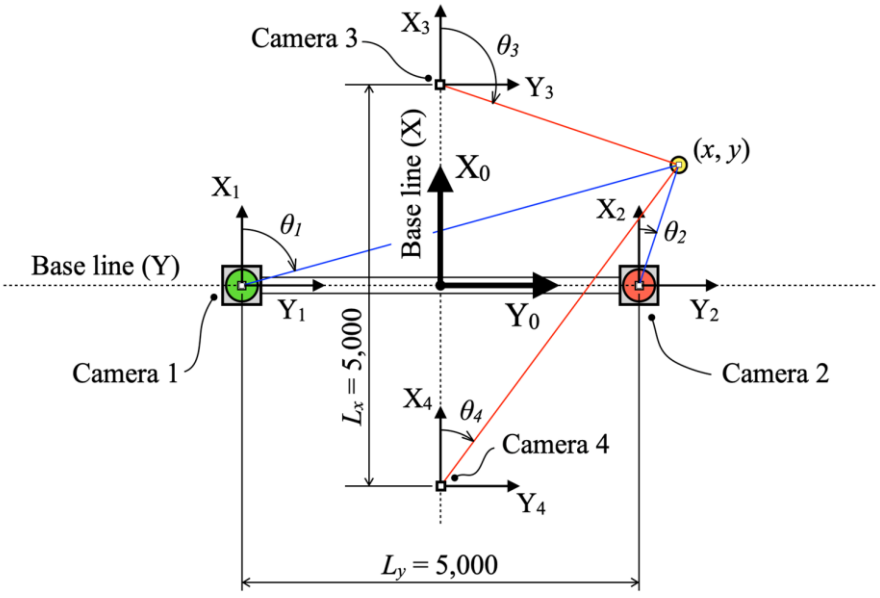


Figure 1. Disposition of quad omnidirectional cameras for position measuring system.

© 2023 Hirasawa, J. published by TU Delft OPEN on behalf of the authors.
ISSN: 2667-2812

Camera 3 and Camera 4 are set on the orthogonal direction to the baseline of Camera 1 and Camera 2. Position of the measuring point are calculated as Equation 2 using images from Camera 3 and Camera 4.

$$(x, y) = (L_y \frac{\cos\theta_1 \cos\theta_2}{\sin(\theta_1 - \theta_2)}, \frac{L_y}{2} \frac{\sin(\theta_1 + \theta_2)}{\sin(\theta_1 - \theta_2)}) \quad (1)$$

$$(x, y) = (\frac{L_x}{2} \frac{\sin(\theta_3 + \theta_4)}{\sin(\theta_3 - \theta_4)}, L_x \frac{\sin\theta_3 \sin\theta_4}{\sin(\theta_3 - \theta_4)}) \quad (2)$$

L_y is distance of Camera 1 to 2 on baseline(Y), L_x is distance of Camera 3 to 4 on baseline(X). θ_1, θ_2, θ_3 and θ_4 are relative angle from each camera shown in Figure 1.

Figure 2 shows the locus of a motorcycle that run around pylons with 8-shape course. Running test with a real motorcycle has executed on a paved area in the Shirosato test center of JARI(Japan Automobile Research Institute) in November 2022. Figure 2 shows 1 lap result of movement of the center of the helmet which was worn by the rider. The test vehicle is an electric scooter "e-Vino" that is produced by YAMAHA Motor Co., Ltd. Blue cross in Figure 2 are plotted on the position that is calculated using Equation 1 and 2 every 1 second. In case of nearby within 1[m] from baseline (Y), *x* and y that derived from Equation 2 (using θ_3 and θ_4) take priority. In contrast, in case of nearby within 1[m] from baseline (X), *x* and y that derived from Equation 1 (using θ_1 and θ_2) take priority. Black circle in Figure 2 are plotted on the position of omnidirectional cameras. The asymmetrical shape of the locus show a personal habit and the immaturity of the rider.

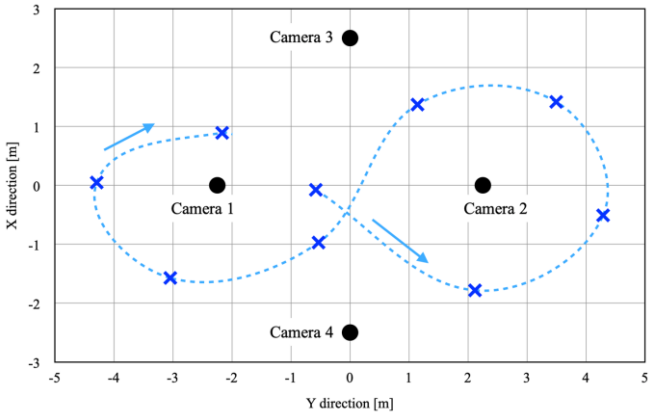


Figure 2. The locus of a motorcycle with 8-shape course.

It is confirmed that the proposed method using quad omnidirectional cameras obtain position data of a motorcycle in the constant precision. The weak point of the system is necessity to treat many image files generated from 4 cameras in offline. To develop sequential program which outputs position data automatically is an urgent issue.

References

Hirasawa, J. (2021). Research on Motion Measurement for a Motorcycle Using Image Processing. *Proceedings of JSME Transportation and Logistics*, No.21-72, PS2-10.

Hirasawa, J. (2023). Using Omnidirectional Cameras to Measure Position of a Motorcycle. *Transactions of Society of Automotive Engineers of Japan*, Vol.54, No.1, 21-28.

Kageyama, I., et al. (2017). Study on Influence of Tire Characteristics on Motorcycles Behavior. *Proceedings of JSAE Congress* (*Spring*), 20175091.

Waegli, A., Schorderet, A., Prongue, C. and Skaloud, J. (2008). Accurate Trajectory and Orientation of a Motorcycle derived from low-cost Satellite and Inertial Measurement Systems. *Proceedings of 7th ISEA conference, P42*, 1–6.

© 2023 Hirasawa, J. published by TU Delft OPEN on behalf of the authors.
ISSN: 2667-2812

The Evolving Scholar (2023)

http://dx.doi.org/10.59490/6489dcca9da9d2965b06242e

Bicycle and Motorcycle Dynamics 2023
Symposium on the Dynamics and Control of Single Track Vehicles
18–20 October 2023, Delft University of Technology, The Netherlands

Type of the Paper: Extended Abstract

OMS: A Software Package for the Minimum-Time Optimal-Control Simulation of Motorcycles

Edoardo Marconi [1], Matteo Formentini [1,*], Enrico Giolo [1]

[1] Dynamotion s.r.l., Italy; edoardo.marconi@dynamotion.it, ORCID 0000-0001-8221-4472; matteo.formentini@dynamotion.it; enrico.giolo@dynamotion.it
[*] corresponding author

Name of Editor: Jason Moore
Submitted: 14/06/2023
Accepted: 26/06/2023
Published: 26/06/2023
Citation: Marconi, E., Formentini, M. & Giolo, E. (2023). OMS: a software package for the minimum-time optimal-control simulation of motorcycles. The Evolving Scholar - BMD 2023, 5th Edition.
This work is licensed under a Creative Commons Attribution License (CC-BY).

Abstract:

A new software package for the minimum-time optimal-control simulation of motorcycles, named OMS (*Optimal Maneuver Simulation*), is presented. A renowned application of non-linear optimal control is the minimum-time simulation of racing vehicles. The objective is to find the control strategy that allows completing a maneuver (typically, a lap of a race track) in the minimum time, while complying with the equations of motions and a set of constraints (e.g., road borders, maximum tire friction, engine power). The tools necessary to perform this kind of simulations are a solver and appropriate models for the vehicle and road. Setting up a tool for minimum-time optimal-control simulations from scratch can be extremely time-consuming and complicated: consider, in particular, selecting or building an appropriate solver, and building and validating a vehicle model. OMS integrates a set of tried-and-tested components in a single software package, enabling users new to minimum-time simulation to kick-start this activity.

Various software tools for the solution of non-linear optimal-control problems are available today, even though many teams involved in top-class racing build their own software for exclusive internal use. The software package OMS employs the indirect collocation algorithm described in Bertolazzi et al. (2006). The vehicle model integrated into OMS is the one used in Marconi and Massaro (2020, 2022), developed building upon a multibody motorcycle model that was widely validated against experimental data logs, see, e.g., Cossalter et al. (2010, 2013). Figure 1 compares the speed and roll angle obtained from a simulation performed with OMS and the corresponding data log. For this example, simulated and logged lap times differ by 0.06%. The vehicle model was built using *MBSymba* (Lot and Massaro, 2017), a collection of methods and procedures for the automatic generation of the equations of motion of multibody systems. Tire forces and torques are computed using a linear saturated model with relaxation equations.

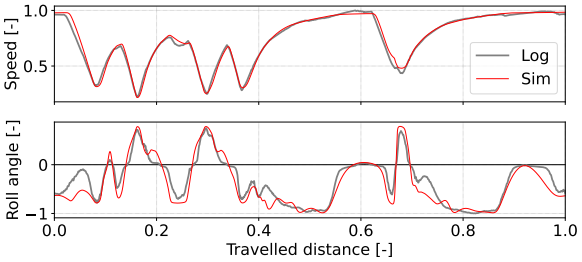
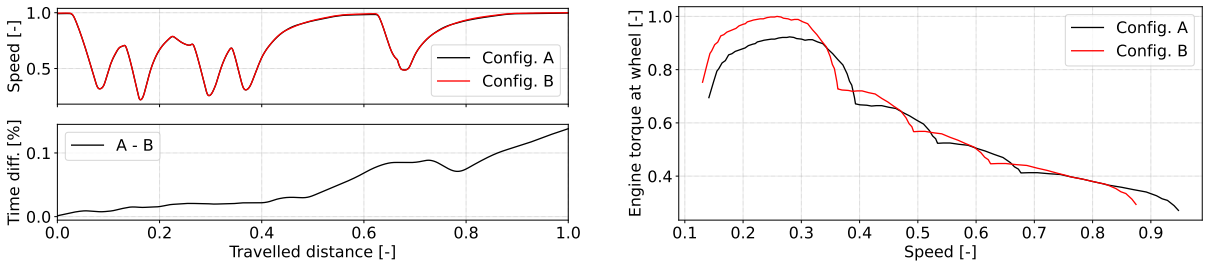


Figure 1: Example of log vs. simulation results from OMS.

©2023 Marconi, E., Formentini, M., & Giolo, E. published by TU Delft OPEN on behalf of the authors.
ISSN: 2667-2812

 http://dx.doi.org/10.59490/6489dcca9da9d2965b06242e



(a) (b)

Figure 2: Example of sensitivity analysis performed with OMS: speed and time difference between two vehicle variants (a), engine torque at the wheel for the two vehicle variants (b).

The typical suspension scheme of racing motorcycles (front telescopic fork and rear swingarm) is considered, with stiffness and damping modeled with polynomial functions. The track is described by a three-dimensional road model built following the approach presented in Limebeer and Massaro (2018); Massaro and Limebeer (2021). The controls of the vehicle model (optimized by the solver) are the steering torque and the front and rear tire longitudinal forces, while the outputs include, e.g., trajectory, speed, suspension travels, steering angle, roll angle and rate, tire loads and lateral forces.

OMS packs all aforementioned features in a software package that includes the binary files for the solver and motorcycle model, a set of scripts for user data, and a command line interface. In particular, the user scripts contain vehicle and road data, and can be visualized and modified with any text editing s oftware. Sample vehicle and track datasets are provided with the software, with comments guiding the user in modifying them to build their own. The vehicle, track, and other simulation options are selected through a main user file, which allows storing the settings for future u se. A typical use case of OMS is performing a sensitivity analysis on some vehicle parameters to assess the effect of different vehicle configurations on the lap-time performance on a given track. In carrying out this task, typical programming tools such as *if* statements – available in user files through *Ruby* syntax – can be exploited to build and select different vehicle variants. Examples of possible vehicle parameters that can be varied include the gearbox ratios, the final drive ratio, the engine torque curve, the position of the center of mass, the mass and moments of inertia, and the maximum lean angle. For instance, Figure 2a shows the comparison between two different final drive ratios, resulting in the different engine torque at the rear wheel reported in Figure 2b. This kind of analysis allows an objective evaluation of the performance advantage determined by various alternative vehicle configurations.

References

Bertolazzi, E., Biral, F., and Da Lio, M. (2006). Symbolic-numeric efficient solution of optimal control problems for multibody systems. *Journal of computational and applied mathematics*, 185(2):404–421.

Cossalter, V., Lot, R., and Tavernini, D. (2013). Optimization of the centre of mass position of a racing motorcycle in dry and wet track by means of the 'optimal maneuver method'. In *2013 IEEE International Conference on Mechatronics (ICM)*, pages 412–417. IEEE.

Cossalter, V., Peretto, M., and Bobbo, S. (2010). Investigation of the influences of tyre-road friction and engine power on motorcycle racing performance by means of the optimal manoeuvre method. *Proceedings of the Institution of Mechanical Engineers, Part D: Journal of Automobile Engineering*, 224(4):503–519.

Limebeer, D. J. and Massaro, M. (2018). *Dynamics and optimal control of road vehicles*. Oxford University Press.

Lot, R. and Massaro, M. (2017). A symbolic approach to the multibody modeling of road vehicles. *International Journal of Applied Mechanics*, 9(05):1750068.

Marconi, E. and Massaro, M. (2020). The effect of suspensions and racetrack three-dimensionality on the minimum lap time of motorcycles. In *Advances in Dynamics of Vehicles on Roads and Tracks: Proceedings of the 26th Symposium of the International Association of Vehicle System Dynamics, IAVSD 2019, August 12-16, 2019, Gothenburg, Sweden*, pages 1368–1377. Springer.

Marconi, E. and Massaro, M. (2022). Optimal recovery manoeuvres of racing motorcycles. *Meccanica*, 57(2):457–472.

Massaro, M. and Limebeer, D. (2021). Minimum-lap-time optimisation and simulation. *Vehicle System Dynamics*, 59(7):1069–1113.

©2023 Marconi, E., Formentini, M., & Giolo, E. published by TU Delft OPEN on behalf of the authors.
ISSN: 2667-2812

The Evolving Scholar (2023)

http://dx.doi.org/10.59490/648c083143b3bec00d30df9f

Bicycle and Motorcycle Dynamics 2023
Symposium on the Dynamics and Control of Single Track Vehicles
18–20 October 2023, Delft University of Technology, The Netherlands

Type of the Paper: Extended Abstract

Bicycle handling quality perception: mixed effect of stability and manoeuvrability

Jules Ronné [1], Laura Dubuis [1], Thomas Robert [1,*]

[1] Univ Lyon, Univ Eiffel, Univ Claude Bernard Lyon 1, LBMC UMR_T 9406, F-69622 Lyon, France; jules.ronne@univ-lyon1.fr, ORCID 0000-0002-0867-6422; laura.dubuis@univ-lyon1.fr, ORCID 0000-0002-0851-0844; thomas.robert@univ-eiffel.fr, ORCID 0000-0002-6502-7082

[*] corresponding author

Name of Editor: Jason Moore
Submitted: 30/06/2023
Accepted: 30/06/2023
Published: 30/06/2023
Citation: Ronné, J., Dubuis, L. & Robert, T. (2023). Bicycle handling quality perception: mixed effect of stability and manoeuvrability. The Evolving Scholar - BMD 2023, 5th Edition.
This work is licensed under a Creative Commons Attribution License (CC-BY).

Abstract

Growth of urban bicycles functions and expectations pushes designs to evolve. Design rules which guarantee good handling quality (the precision and perception of ease with which a human can complete a given tack) could benefit design e volutions. Although the link between bicycle design and its dynamics is well established, its impact on the handling quality remains poorly understood. Complex interactions between very different design parameters can lead to equivalent handling. Despite extensive research these last years, theoretical approaches to quantify the bicycle handling quality still have strong limitations and lack of validity (Schwab & Meijaard, 2013; Takagi et al., 2022), and experimental approaches remain necessary. Yet, there is no strong evidence of which experimental parameters could be used to characterise handling quality. Handling quality is suspected to result of a complex interaction between stability (the ability of bike-rider system to recover form a perturbation) and manoeuvrability (the best performance achievable by the vehicle for a given task, without taking into account the rider's control limits), which are both highly speed dependant. This study aims to investigate this link between handling quality, stability and manoeuvrability. We expect that handling quality perception is affected by a lack of stability at low speed and affected by poor manoeuvrability at higher speed.

Material and methods

Thirty adults (self declared as beginner to advanced riders) were asked to ride two different commercial bicycles on 130 m long track closed to traffic. Experimental bicycles were chosen to be uncommon and with extreme design parameters: Strida 5 (foldable bike) and Omnium Cargo V3 (cargo bike). The participants were asked to maintain a constant speed and to follow as much as they can a path painted on a flat and smooth t armac. The path was made of a 9 cm wide white line (one straight line, one left turn, a slalom and a right turn). Each participant rode 3 times at 3 different speed instructions (S: "slowest possible", C: "comfort speed, which maximise the feeling of control", F: "faster than comfort speed") with both bikes. Bikes and speed conditions were presented in a randomised order. At the end of each lap, the participants were asked to fill a questionnaire about their riding feelings made of 4 items (See Table 1). The fist item evaluates the Handling quality thanks to the Cranfield Aircraft Handling Qualities Rating Scale (CAHQRS, the higher the score, the harder to control the bicycle is.) (Harris et al., 2000). Remaining items are adapted from (Takagi et al., 2022) (the higher the score, the stronger the feeling is). Q1 describes the sensation of an oscillating movement of the handlebars induced or not by the rider. Q2 describes the sensation of losing balance on a turn, the definition of which is left to the discretion of the cyclist. Q3 describes the sensation of not following the task instructions (whatever the cause). Bicycles were equipped with 3 IMUs (XSens DOT) (rear wheel spokes, frame and handlebar), although these data will not be analysed in this first study. The effects of speed instruction ("S", "C", "F") and bicycle were statistically tested on the scores for each item score with a repeated measurement two-way ANOVA and post-hoc tests.

©2023 Ronné, J., Dubuis, L., & Robert, T. published by TU Delft OPEN on behalf of the authors.
ISSN: 2667-2812

 http://dx.doi.org/10.59490/648c083143b3bec00d30df9f

Table 1. Questionnaire about the riding feeling.

Item	Description	Scale
CAHQRS	Handling quality	0 to 9
Q1	Feeling the need to wobble the handlebar	1 to 5
Q2	Feeling instability during turns	1 to 5
Q3	Feeling the line is hard to follow	1 to 5

Results and discussion

Statistical test on CAHQRS ratings find out a significant effect of speed instructions ($p<0.001$) (figure 1). "Slow" and "Fast" laps are characterised by a poor handling quality compared to "Comfort" laps. A similar effect was found for the feeling of instability during turns (Q2) and the feeling of difficulty of the line following task (Q3). On the opposite, the feeling of "oscillating handlebar" (Q1) was higher for "Slow" laps than for "Comfort" and "Fast" laps (no difference between these last two conditions). The only difference found between the two bicycles was a higher difficulty of the line following task (Q3) for "Fast" laps for the cargo bike.

As expected, handling quality perception exhibit a statistically significant non-monotonic effect of speed instructions. "Low" speed have been characterised by oscillating handlebar feeling (Q1), which is consistent with the common weave mode instability at low speed. "Comfort" and "Higher" speeds distinguish themselves by the instability during turns feeling (Q2) which is also consistent with limited manoeuvrability at higher speed. Despite very different designs, few differences were observed between the two bikes. It could be explained by the fact both bikes are tried-and-tested designs. The only difference appears on "Fast" laps, where Omnium V5 bicycle were more difficult to ride probably caused by its large wheelbase (1.6 m versus 0.9 m for Strida bike).

Preliminary results confirm that handling quality is affected by stability and manoeuvrability. It suggests that describing a bicycle handling quality requires to characterise both of these characteristics across usage speed range. Future work will focus on handling quality perception prediction based on signals that have been collected by IMUs set on both bicycles. Objective indicators are expected to discriminate between bicycles better than subjective ratings.

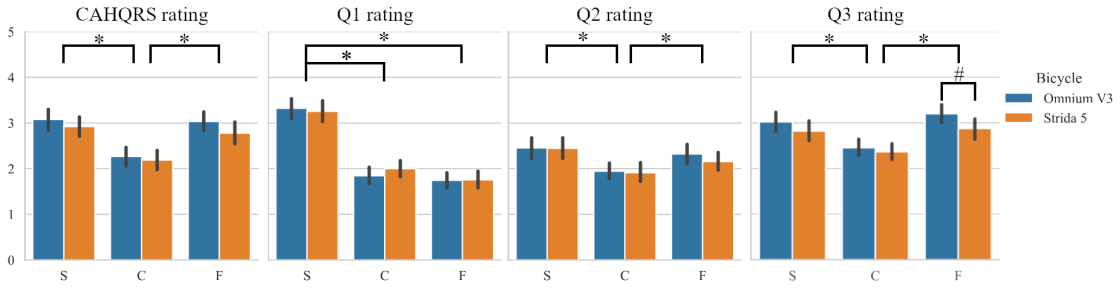


Figure 1. Mean and standard deviation across subjects of scores given to the questionnaire's items, spread by bicycle and speed instruction. * and # indicate a significant difference ($p<0.05$) between speed instructions or bicycles, respectively. Handling quality exhibit a non-monotonic effect of speed instructions.

References

Harris, D., Gautrey, J., Payne, K., & Bailey, R. (2000). The Cranfield aircraft handling qualities rating scale: A multidimensional approach to the assessment of aircraft handling qualities. *Aeronautical Journal*, 104(1034), 191-198.

Takagi, S., Oka, M., & Mori, H.(2022), Evaluation of Riding Instability of a Bicycle with Children as Passengers Using the Relationship Between Handlebar Angle and Roll Angle. , *In: Yamamoto, S., Mori, H. (eds) Human Interface and the Management of Information: Applications in Complex Technological Environments. HCII 2022. Lecture Notes in Computer Science, vol 13306. Springer, Cham.*

Kooijman, J.D.G., Schwab, A.L. (2013). A review on bicycle dynamics and rider control. *Vehicle System Dynamics*, *51(11)*, 1722–1764.

©2023 Ronné, J., Dubuis, L., & Robert, T. published by TU Delft OPEN on behalf of the authors.
ISSN: 2667-2812

The Evolving Scholar (2023)

https://doi.org/10.24404/63fc7436b2ed6687183b0d8b

Bicycle and Motorcycle Dynamics 2023
Symposium on the Dynamics and Control of Single Track Vehicles
18 – 20 October 2023, Delft University of Technology, The Netherlands

Type of the Paper: Extended Abstract

Motion cueing utilizing gravity

Christian G. Bäverstrand[1,2]

[1]Chalmers University of Technology; garfve@chalmers.se; https://orcid.org/0009-0008-0317-8505
[2]Tenstar Simulation AB; christian.baverstrand@tenstarsimulation.com

Name of Editor: Jason Moore
Submitted: 27/02/2023
Accepted: 12/04/2023
Published: 26/04/2023
Citation: Bäverstrand, C. (2023). Motion Cueing utilizing gravity. The Evolving Scholar - BMD 2023, 5th Edition.
This work is licensed under a Creative Commons Attribution License (CC-BY).

Abstract:

There are a few motorcycle simulators on the consumer market. Very few of them even remotely replicate the actual accelerations the rider is subjected to when riding a bike. The motion that is the very essence of a bike causes the most controversy, the leaning. Commercial simulators like MotoTrainer, DevotionSIM or Simumak's Simesbike focus on replicating the real-life lean angle rather than simulating the forces and accelerations the driver would feel while riding. The sway acceleration in the global reference system is effectively turned into heave in the local reference system of the motorcycle and rider when using a VR headset, making it much easier to replicate than for a car simulator. For a motorcycle we can utilize the only free of charge continuous acceleration, earth gravity, without having to use excessive roll motions.

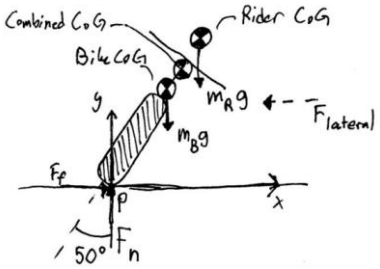


Figure 1. A simplified figure describing the forces acting on an upright motorcycle driver in a turn where the bike leans 50 degrees.

This means the hardware needed to tilt the rider and platform can be much smaller and use less power. Instead of leaning the platform +-60 degrees to simulate race lean, you need less than 10 degrees of lean to simulate cornering forces. We designed our motion platform to evaluate this. Since the motorcycle is in equilibrium in a turn, we can assume that the moment around P in figure 1 is zero, effectively pointing the resulting force of the combined masses toward the tire contact patch. Hence it would not be necessary to lean the simulation platform at all to accurately simulate the feeling of cornering if the rider sits upright. In racing however, it is very common that the rider leans off the motorcycle into the corner to shift the center of gravity in order to keep the bike more upright. In this case the motion platform would have to lean the opposite way of the turn to align the expected resulting force vector of the rider, bike and cornering forces with the gravitational force. The angle the motion platform would need to lean in order to simulate the right feeling for the rider would be angle alpha in figure 2 below. In doing so, the resulting force from the combined center of gravity of bike and rider and the lateral forces would become parallel to the earth gravity vector. Illustrated in figure 3.

© Christian G. Bäverstrand. published by TU Delft OPEN on behalf of the authors.
ISSN: 2667-2812

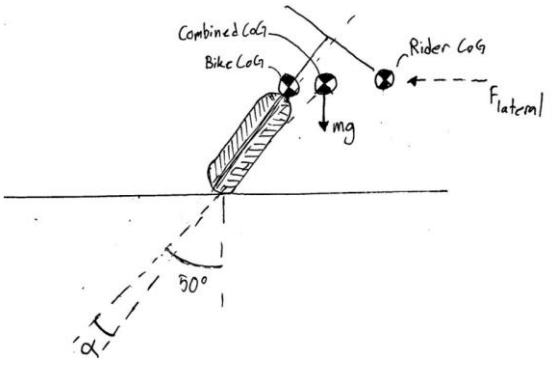


Figure 2. A figure showing the angle needed to simulate the direction of the cornering forces.

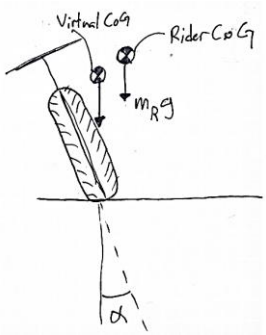


Figure 3. A figure showing the motion platforms actual lean angle compensating for rider displacement.

Our motion platform was built for movements around 12 degrees for roll and pitch, 5 degrees yaw around the virtual contact patch of the front wheel and 130mm heave. The simulator is mainly focused on handling in a race setting with the geometry and controls of a super sport motorcycle. For a road racing driver to train how to move around on the motorcycle it is important that the simulator correctly depicts how the forces will act on the driver in real life, which is the opposite of what simulators mentioned above do today. The simulator software used is GP-bikes, a road racing simulator developed by the one-man studio "PiBoSo". It is focused on accurately simulating the physics and outputs most necessary telemetry data including yaw, pitch, roll, heave, sway and surge. A plugin was written for the motion software SimTools 3 and the platform moves as expected.
Another important aspect of race simulation is the turning. A motorcycle is most efficiently turned by using so called counter steering. This means you apply force to the handlebars in the opposite direction of your turn, causing the bike to lean into the turn. The same can be done by shifting your body weight but it is much less efficient. To most people counter steering is counter intuitive which makes it very difficult to simulate so that it works with the instincts of most level of riders. We have chosen to put torque sensors in the handlebars of the simulator that read rider torque input in the front fork rotation axis. Using these forces together with throttle input and brake input lean angle output is approximated. The turning angle of the front fork is calculated by the simulator software and returned to the handlebar servos.



Figure 4. A picture of the finished motion platform with fairings and controls mounted.

Evaluation of the motion platform we built has been done mostly driving ourselves but also testing with experienced road racing drivers. Interesting results were observed including riders trying to jump off the rig when crashing.
Drivers equipped with VR headsets that hadn't seen the platform in motion before testing estimated the roll motion as much larger than it actually was and, in most cases, they thought it leaned the other way than it actually did.

© 2023 Christian G. Bäverstrand, published by TU Delft OPEN on behalf of the authors.
ISSN: 2667-2812

The Evolving Scholar (2023)
https://doi.org/10.24404/640f2c96371d6d7969826057
Bicycle and Motorcycle Dynamics 2023
Symposium on the Dynamics and Control of Single Track Vehicles
18 – 20 October 2023, Delft University of Technology, The Netherlands

Type of the Paper: Extended Abstract

Modelling Braking and Steering Avoidance Maneuvers for Micromobility

Tianyou Li[1,*], Fredrik Bruzelius[1], and Marco Dozza[1]

[1] Department of Mechanics and Maritime Sciences, Chalmers University of Technology; tianyou.li@chalmers.se; fredrik.bruzelius@chalmers.se; marco.dozza@chalmers.se
* Corresponding author.

Name of Editor: Jason Moore
Submitted: 13/03/2023
Accepted: 20/04/2023
Published: 26/04/2023
Citation: Li, T., Buzelius, F. & Dozza, M. (2023). Modelling Braking and Steering Avoidance Maneuvers for Micromobility. The Evolving Scholar - BMD 2023, 5th Edition.
This work is licensed under a Creative Commons Attribution License (CC-BY).

Abstract

Recent advancements in technology make it possible for advanced driving assistance systems (ADAS) to recognize micromobility vehicles (MMV) and include them in their threat assessment (Wachtel et al., 2022). However, today we lack the rider-vehicle models which are of great importance in understanding the interconnection between the MMV and its rider. These models may help ADAS predict micromobility kinematics and provide accurate threat assessments, especially when avoidance maneuvers from micromobility must be considered. In this study, we modelled avoidance maneuvers from micromobility vehicles to support ADAS threat assessment.

We compared traditional bicycles (with and without assistance) with e-scooters (a small personal scooter and a large scooter) in a field test, where 36 participants avoided a stationary obstacle by either braking or steering. Field data was collected from on-vehicle inertial measurement units and a stationary LiDAR next to the obstacle. Each participant performed four tasks on each of the four MMV (Fig. 1), including braking and steering maneuvers with different levels of urgency (comfortable or harsh). Every time before they started riding, the participants would be instructed in what the next task was. In the comfortable maneuvers, the participants were asked to brake and steer as comfortable as they would in real traffic, while in the harsh tasks, they were asked to brake and steer as late as possible. Kinematic data, such as acceleration, steering angle, and steering rate, were collected and analyzed.

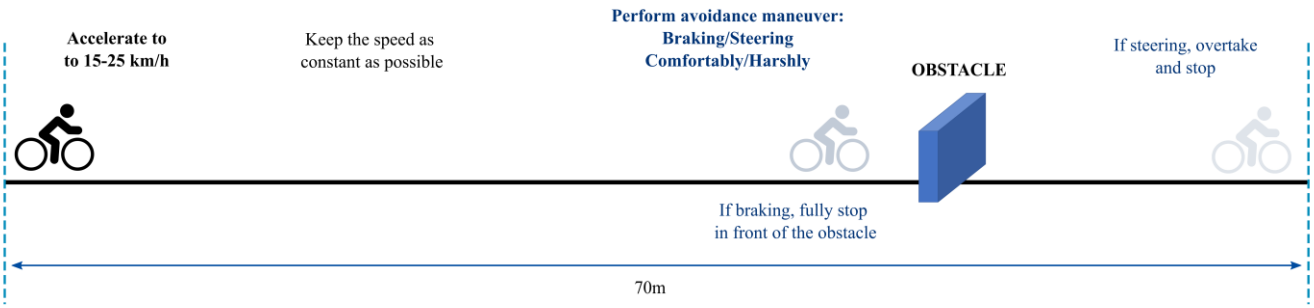


Figure 1. Riding tasks. Comfortable and harsh braking and steering maneuvers were randomized across each vehicle and participant.

The participants achieved statistically significantly larger longitudinal deceleration and jerk in harsh barking and shorter lateral distance to the obstacle in harsh steering, than they did in the comfortable maneuvers. Among all the vehicles, the small scooter exhibited the worst braking performance, and the two e-scooters achieved statistically significantly smaller steering rate than the bicycles. Figure 2 shows the distributions of time-to-collision (TTC) when the participants started the collision-avoidance

© 2023 Tianyou Li, Fredrik Bruzelius & Marco Dozza, published by TU Delft OPEN on behalf of the authors.
ISSN: 2667-2812

maneuvers. According to the result from a generalized linear mixed effects analysis, the TTC in harsh braking and steering was statistically significantly smaller than in comfortable maneuvers. In addition, the TTC when the participants started steering away was statistically significantly smaller and had a lower variance than the TTC at braking start. This was the case for both comfortable and harsh maneuvers.

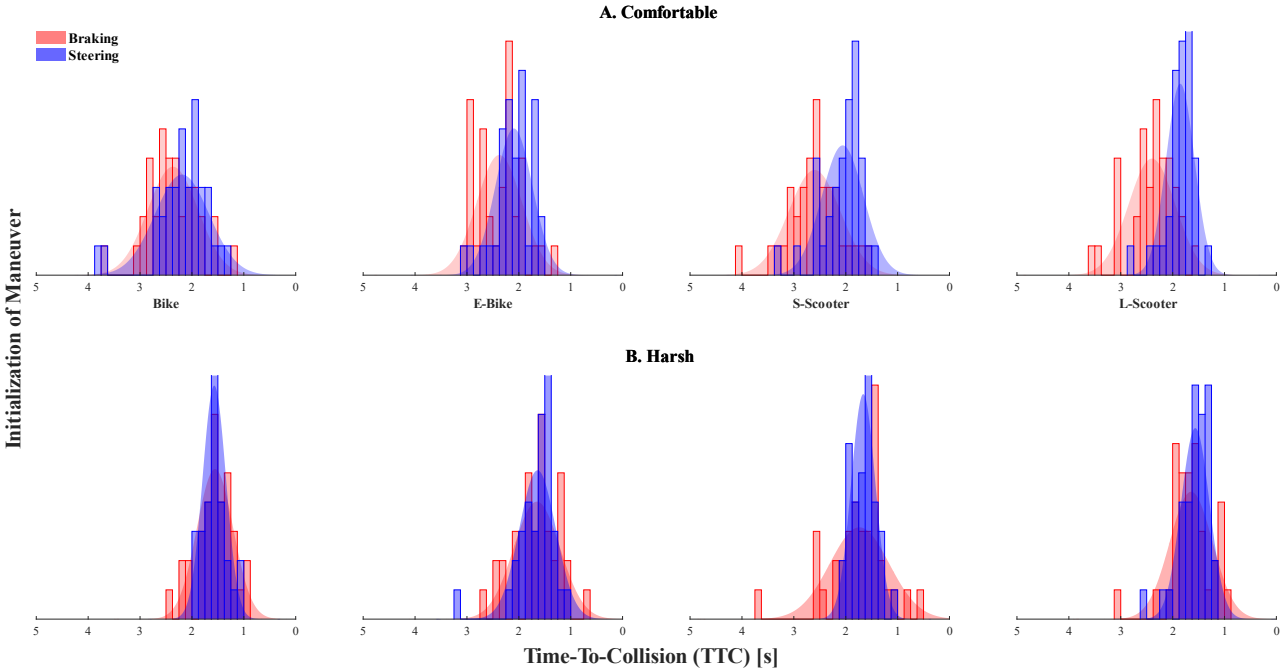


Figure 2. Histogram and Gaussian distributions of time-to-collision (TTC) when a maneuver was initialized.

The results from this study may inform the development and evaluation of ADAS. For instance, the models proposed by this study may support the threat assessment of ADAS by providing reasonable values for how rider behavior may influence micromobility kinematics in crash avoidance, similarly to what Brännström et al., 2014 proposed for car drivers. The findings of this study may also be beneficial for infrastructure designers in engineering adequate infrastructure that accommodates the new MMV (e.g., a wider cycle path with larger safety margin for overtaking and less sharp curves that supports smoother steering for the e-scooters). In addition, road policy makers may utilize the findings of this study to improve the regulations on new MMV (e.g., required education on riding MMV, speed limitations tailored for specific new MMV, etc.)

Future studies may include a broader range of MMV and test different speeds. Further, naturalistic data should be used to verify the ecological validity of the models proposed from field trials.

References

Brännström, M., Coelingh, E., & Sjöberg, J. (2014). Decision-making on when to brake and when to steer to avoid a collision. *International Journal of Vehicle Safety 1*, 7(1), 87-106.

Dozza, M., Li, T., Billstein, L., Svernlöv, C., & Rasch, A. (2022). How do different micro-mobility vehicles affect longitudinal control?
Results from a field experiment. *Journal of Safety Research.*

Wachtel, D., Edler, J., Schröder, S., Queiroz, S., & Huber, W. (2022, October). Convolutional Neural Network Classification of Vulnerable Road Users based on Micro-Doppler Signatures using an Automotive Radar. In *2022 IEEE 25th International Conference on Intelligent Transportation Systems (ITSC)* (pp. 866-872). IEEE.

© 2023 Tianyou Li, Fredrik Bruzelius & Marco Dozza, published by TU Delft OPEN on behalf of the authors.
ISSN: 2667-2812

The Evolving Scholar (2023)
https://doi.org/10.24404/63fe2e2127799c0b2d1600b8
Bicycle and Motorcycle Dynamics 2023
Symposium on the Dynamics and Control of Single Track Vehicles
18 – 20 October 2023, Delft University of Technology, The Netherlands

Type of the Paper: Extended Abstract

Evaluating the handling of a tilting tricycle with variable stability

Floris van Willigen[1], Andrew Dressel[2]*, Jason Moore[3]

[1]TU Delft; F.A.vanWilligen@student.tudelft.nl
[2]TU Delft; AndrewDressel@hotmail.com, ORCID 0000-0003-0322-9815
[3]TU Delft; J.K.Moore@tudelft.nl, ORCID 0000-0002-8698-6143
*corresponding author.

Name of Editor: Christoph Schmidt
Submitted: 01/03/2023
Accepted: 14/04/2023
Published: 26/04/2023
Citation: Dressel, A., van Willigen, F. & Moore, J. (2023). Evaluating the handling of a tilting tricycle with variable stability. The Evolving Scholar - BMD 2023, 5th Edition.
This work is licensed under a Creative Commons Attribution License (CC-BY).

Abstract:

To evaluate the handling of a tilting tricycle with variable stability and tadpole wheel configuration, described in detail in a separate submission, we select three handling metrics from the literature, develop a testing methodology, and combine the results into a single handling score. For simplicity of implementation and ease of transferring sensors from vehicle to vehicle, we choose metrics that only require kinematic data. Finally, we assess the handling only in low- and moderate-speed situations.

Here are the three metrics we select and the two maneuvers we perform to collect the data we use to calculate them:

1. The maximum value of the so-called yaw factor (yaw rate / steer rate).
   We compute this metric from the kinematic data recorded during a slalom maneuver.
   A low maximum yaw factor indicates smooth turning in the slalom maneuver which correlates with better handling.

2. The average magnitude of the steer angle.
   We compute this metric from the kinematic data recorded during a low speed line following maneuver.
   The magnitude of the steer angle is related to the difficulty of following the line correctly.
   A low steer angle correlates with a low effort and good handling.

3. The average time delay between the roll rate and the steer rate.
   We compute this metric from the kinematic data recorded during a low speed line following maneuver.
   A low time delay indicates a swift response to correct roll angle in low speed handling.

We combine the three metrics into a single handling performance score with a logarithmic scale to increase the influence of any single metric, as shown in equation (1). We also include scale factors to balance the values of each metric.

$$Score = \log(M_1 \cdot \alpha_1) + \log(M_2 \cdot \alpha_2) + \log(M_3 \cdot \alpha_3) \quad (1)$$

We tested this method on three reference bicycles: a Batavus Verona as it comes from the factory (stock), the same bike with the front fork rotated 180° to dramatically increase trail, and a Gazelle Ami C7 as it comes from the factory. The latter is also the bicycle that we describe converting into a tilting tricycle in a separate submission.

This method of calculating a single handling performance score successfully discriminates between the vehicles with significant results. Table 1. shows the means and standard deviations of the three metrics for each vehicle after several test runs, and Figure 1. shows the total handling score for each vehicle.

© 2023 Dressel, A., van Willigen, F. & Moore, J. published by TU Delft OPEN on behalf of the authors.
ISSN: 2667-2812

Table 1. The means and standard deviations calculated for each metric and the combined score for each vehicle.

Vehicle	Batavus Verona 7 – Stock		Batavus Verona 7 – Flipped		Gazelle Ami C7 - Stock	
Metric	Mean	Std Dev	Mean	Std Dev	Mean	Std Dev
Max yaw	3.60	0.31	4.25	0.48	4.09	0.251
Steer angle	3.66	0.39	7.28	0.88	3.94	0.59
Time delay	0.235	0.028	0.330	0.032	0.227	0.023
Score	1.51		0.987		1.43	

We also collect data from two other tilting tricycles, but not in time to include the results in this abstract.

Future experiments will show the handling performance of the tilting tricycle with the variable stability. The hypothesis is that we will see advantages of the tricycle and that we will find the configuration where the handling is equivalent to that of the reference bicycle.

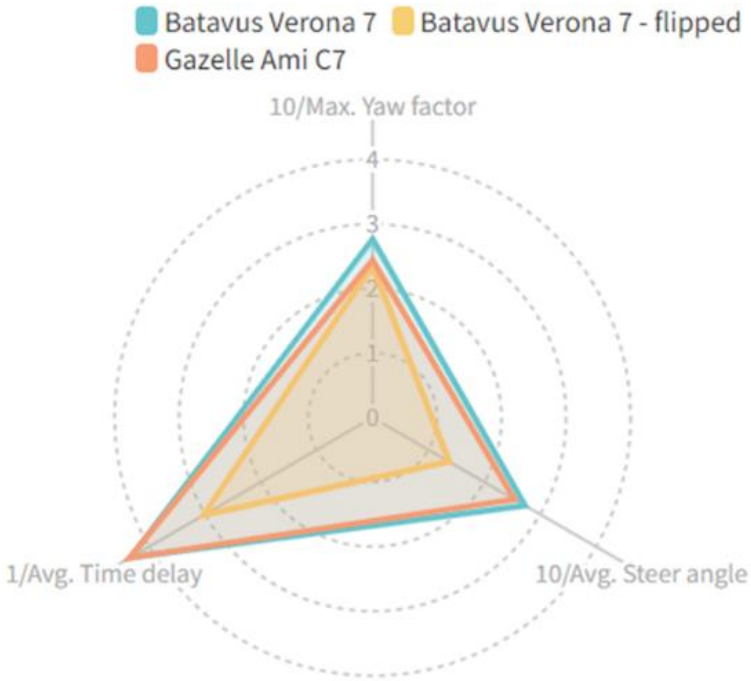


Figure 1. A radar chart showing the score of the three test vehicles with the scale factor for each score indicated at the vertex. The two bicycles as delivered from the factory have very similar performance, and the bicycle with the front fork reversed (flipped) has significantly worse handling performance.

This project was financed and supported by the TKI/ClickNL 'De Fiets van de Toekomst' grant and Royal Dutch Gazelle.

References

Cossalter, V., 2002. Motorcycle Dynamics. No. ISBN 09720514-0-6. Race Dynamics, Greendale, WI.

Cossalter, V., & Sadauckas, J. (2006). Elaboration and quantitative assessment of manoeuvrability for motorcycle lane change. Vehicle System Dynamics, 44(12), 903-920.

Kovácsová, N., de Winter, J. C. F., Schwab, A. L., Christoph, M., Twisk, D. A. M., & Hagenzieker, M. P. (2016). Riding performance on a conventional bicycle and a pedelec in low speed exercises: Objective and subjective evaluation of middle-aged and older persons. *Transportation Research. Part F: Traffic Psychology and Behaviour*, 42(Part 1), 28-43

McRuer DT, Jex HR. A review of quasi-linear pilot models. IEEE Trans Hum Factors Electron. 1967;HFE-8(3):231–249.

Pierson, A. M., Shortreed, A. K., Van Asten, P. D., Dressel, A. E. (2020, August 17–19), A Narrow-Track Tilting Tricycle With Variable Stability That the Rider Can Control Manually, *Proceedings of the ASME 2020 International Design Engineering Technical Conferences and Computers and Information in Engineering Conference. Volume 4: 22nd International Conference on Advanced Vehicle Technologies*, Virtual, Online

Schwab, A. L., & Meijaard, J. P. (2013). A review on bicycle dynamics and rider control. Vehicle system dynamics, 51(7), 1059-1090.

© 2023 Dressel, A., van Willigen, F. & Moore, J. published by TU Delft OPEN on behalf of the authors.
ISSN: 2667-2812

The Evolving Scholar (2023)

https://doi.org/10.59490/6454fe8ebbbd7753dc6d1d39

Bicycle and Motorcycle Dynamics 2023
Symposium on the Dynamics and Control of Single Track Vehicles
18 – 20 October 2023, Delft University of Technology, The Netherlands

Type of the Paper: Extended Abstract

Simulator validation – a new methodological approach applied to motorcycle riding simulators

Sebastian Will[1]*, Thomas Hammer[1], Raphael Pleß[1], Nora Leona Merkel[1], and Alexandra Neukum[1]

[1] Würzburger Institut für Verkehrswissenschaften (WIVW GmbH); will@wivw.de, https://orcid.org/0000-0003-0098-6212; hammer@wivw.de; pless@wivw.de; merkel@wivw.de, https://orcid.org/0000-0002-4865-368X; neukum@wivw.de
*corresponding author.

Name of Editor: Jason Moore
Submitted: 05/05/2023
Accepted: 05/05/2023
Published: 26/06/2023
Citation: Will, S., Hammer, T., Pleß, R., Merkel, N. & Neukum, A. (2023). Simulator validation – a new methodological approach applied to motorcycle riding simulators. The Evolving Scholar - BMD 2023, 5th Edition.
This work is licensed under a Creative Commons Attribution License (CC-BY).

Abstract:

Whenever driving simulators are used in research and development, to a certain extent the generalizability of the gained results is subject to discussion. Typically, a simulator gets validated in a rather effortful and complex process in order to prove the adequacy of the use of this specific simulator as research tool for a given research question. Since decades, there is plenty of research regarding the methods to validate simulators mainly from the automotive domain (e.g., Blaauw, 1982, Blana, 1996). Traditionally, there is a differentiation between a simulator's physical validity and its behavioral validity. Whilst the first focusses on the simulator's behavior and the presence of specific cues and operating elements, the latter focusses on the driver's perception and consequently behavior. Furthermore, the degree of accordance between vehicle and simulator forms a category of validity, namely, absolute and relative validity. Whilst absolute validity describes an absolute numerical accordance of measurable dimensions between vehicle and simulator (e.g., certain forces, accelerations), relative validity describes a correlational accordance. Independent of the addressed dimension, simulator validation is a highly complex process, which is specific to the respective research question for which the simulator gets validated. Regarding single-track vehicle simulator concepts for which there is less experience from previous research (e.g., Cossalter, Lot, Massaro & Sartori, 2011), a rather broad validation procedure could be a useful tool in order to assess a simulator's overall characteristics and therefore to assess its potential fields of application on a wider basis. This paper presents such a methodological validation approach applied to motorcycle riding simulators. The main assumption of the method is that complex riding tasks can be divided into smaller units that allow for discrimination of specific rider input characteristics, the so-called minimal-scenarios. These minimal-scenarios are riding tasks such as *'starting from standstill'* or *'initiating a curve at constant velocity'*. Furthermore, it is assumed that minimal-scenarios can be reorganized to more complex riding tasks. This is intended to describe the variety of potential applications with a necessary minimum of elementary tasks in order to reduce the validation effort for a global assessment of the simulator's capabilities (Hammer, Pleß, Will, Neukum & Merkel, 2021). This more generic result can also be regarded as a limitation.



Figure 1. Measurement motorcycle (left), dynamic motorcycle riding simulator DESMORI (center) and static motorcycle riding simulator (right) used for the validation study.

© 2023 Will, S., Hammer, T., Pleß, R.; Merkel, N. L., & Neukum, A. published by TU Delft OPEN on behalf of the authors.
ISSN: 2667-2812

In order to investigate the applicability of the developed validation concept, a series of experiments has been conducted. The data shown here comes from a study with N = 15 motorcyclists (aged m = 37 years, SD = 14), which compared motorcycling with a real vehicle on a test track and the riders' performance in a dynamic and a static motorcycle riding simulator (see Figure 1).

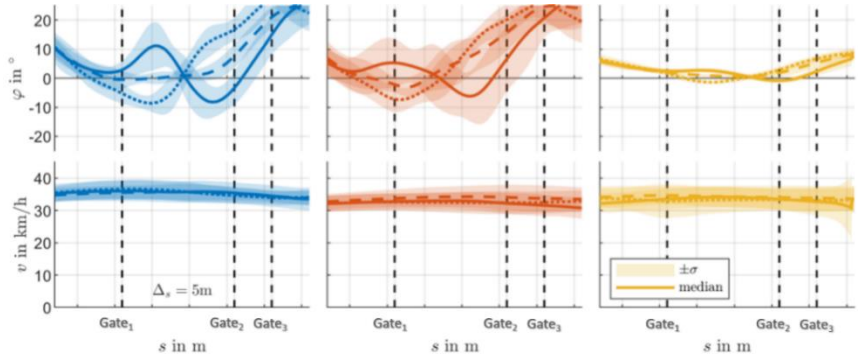


Figure 2. Roll angles and velocities for the avoidance maneuver in the environments test motorcycle (blue), dynamic motorcycle riding simulator (red) and static motorcycle riding simulator (yellow). The solid line indicates an avoidance maneuver to the left, the dotted line to the right and the dashed line shows the control maneuver going straight.

In all three test environments the motorcyclists were instructed to ride on an oval-shaped test course with a constant velocity of 35 km/h. A visual signal in the dashboard indicated at short notice whether to perform an avoidance maneuver to the left, to the right or whether to continue the oval-shaped course without avoidance maneuver. The different trajectories were marked using gates with traffic cones. Figure 2 shows exemplary vehicle dynamics data from this test sequence 'avoidance maneuver', which consisted of three previously defined minimal-scenarios 'constant riding', 'entering a turn (v = const.)' and 'exiting a turn (v = const.)'. Across all test environments, people manage to comparably follow the target speed instruction. The roll angle over time shows a higher accordance between real riding and the dynamic motorcycle riding simulator, while the implemented vehicle dynamics model of the static simulator is not capable of replicating real effects. Based on the specific research question and the resulting relevance of physical or behavioral validity, the tested sequence of minimal-scenarios can support the assumed simulator's validity for different research questions. For instance, the example given above aims at validating an avoidance maneuver existing of three different minimal-scenarios. If the results for the relevant concept of validity are positive, there is no need to conduct separate validation studies for different research questions involving the same relevant minimal-scenarios. In this case, an investigation of a warning assistance system, which aims at triggering an avoidance maneuver could be investigated likewise to a hazard perception training, which includes avoiding a suddenly appearing threat, on that same simulator.

In summary, the presented method does not try to substitute established methodologies in the field of driving simulator validation. The proposed approach shall provide a sound method for a justified global assessment of a simulator's potential fields of application including objective dynamics data as well as subjective assessments. This is done with a defined set of minimal-scenarios to which the established validation concepts shall be applied. This method was developed to be applied to single-track vehicle simulators as these simulators are in a rather early stage compared to well-established passenger car simulators and a wider overview about the simulator's validity could be more helpful than a statement about the simulator's validity for one specific research question. Yet, it is not limited to the field of single-track vehicles and may deliver interesting insights in potential down- and upsides of a simulator concept across all modes of transport.

Acknowledgements

This research was funded by the German Federal Highway Research Institute (Bundesanstalt für Straßenwesen, BASt) with the grant agreement number FE 82.0700/2017.

References

Blaauw, G. J. (1982). Driving experience and task demands in simulator and instrumented car: A validation study. *Human Factors*, 24 (4), 473-486, doi: https://doi.org/10.1177/001872088202400408.

Blana, E. (1996). Driving Simulator Validation Studies: A Literature Review. *Institute of Transport Studies, University of Leeds*, Working Paper 480. http://eprints.whiterose.ac.uk/2111

Cossalter, V., Lot, R., Massaro, M., & Sartori, R. (2011). Development and validation of an advanced motorcycle riding simulator. *Proceedings of the Institution of Mechanical Engineers, Part D: Journal of Automobile Engineering*, 225, 705-720. doi:10.1177/0954407010396006

Hammer, T., Pleß, R., Will, S., Neukum, A., & Merkel, N. L. (2021). *Anwendungsmöglichkeiten von Motorradsimulatoren* (Bundesanstalt für Straßenwesen Ed. Vol. M323). Carl Schünemann Verlag, Bremen.

© 2023 Will, S., Hammer, T., Pleß, R.; Merkel, N. L., & Neukum, A. published by TU Delft OPEN on behalf of the authors.
ISSN: 2667-2812

The Evolving Scholar (2023)

https://doi.org/10.24404/63fe214f40eead27b431c184

Bicycle and Motorcycle Dynamics 2023
Symposium on the Dynamics and Control of Single Track Vehicles
18 – 20 October 2023, Delft University of Technology, The Netherlands

Type of the Paper: Extended Abstract

A Vector-Loop Analysis Approach to Kinematics of Bicycle Steering Geometry

A. Suresh[1], M. Barath[2], and A. do Rego[2,*]

[1]TVS Motor Company Research and Development; anandhu.suresh@tvsmotor.com
[2] TVS Motor Company Research and Development; m.barath@tvsmotor.com; ashleyandrew.filipe@tvsmotor.com
*corresponding author.

Name of Editor: Jason Moore
Submitted: 28/02/2023
Accepted: 13/04/2023
Published: 26/04/2023
Citation: Suresh, A., Barath, M. & do Rego, A. (2023). A Vector-Loop Analysis Approach to Kinematics of Bicycle Steering Geometry. The Evolving Scholar - BMD 2023, 5th Edition.
This work is licensed under a Creative Commons Attribution License (CC-BY).

Abstract:

Kinematic analysis is an extremely important subject in various areas on engineering. By using input motion instead of input force, problems can be represented as algebraic instead of differential equations (Gibbs, 1928). Nearly all quantities involved in kinematic analysis are either vectors or magnitudes of vectors. Exceptions to this are angular quantities, however all orders of their derivatives are vectors. Kinematic analysis is carried out by formulating the problem as a set of simultaneous vector equations which can be solved using vector algebra (Vinogradov, 2020b) (Stanisic, 2014). Vector loop analysis can also be used to optimize the design of mechanisms (Tsai & Joshi, 2002). However, till today conventional vector analysis has not been used for kinematic analyses to the extent possible. Instead, other tools have become predominant, namely complex numbers, graphics, matrices and quaternion algebra.

Bicycle steering geometry kinematics is complex and difficult to visualize, predominantly due to the oblique rotation angle of steering (castor) and shape of tire profile. However, a kinematics model of bicycle finds application in many areas like deriving dynamics, building robust control and estimation systems for active stability control, stability analysis etc. The intent of this paper is to introduce an intuitive approach, which is easily visualizable for deriving bicycle kinematics. This paper explores use of vector loop analysis in kinematics of bicycle steering geometry. The change in vehicle states like yaw angle, tire patch position, front wheel orientation due to a static steering rotation for a fixed roll angle is included in this study. Although this paper primarily discusses rigid bodies, extending this approach to include suspension compressions and tire compressions is also discussed. This approach becomes further relevant with the advancements of symbolic math toolboxes available today as this method can be used along with these tools. This method is also scalable to induce further complexities into the model to closely mimic the real-world scenarios.

References

Vinogradov, O. (2020). *Fundamentals of Kinematics and Dynamics of Machines and Mechanisms*. CRC Press.

Stanisic, M. M. (2014). *Mechanisms and Machines: Kinematics, Dynamics, and Synthesis, SI Edition*. Cengage Learning.

Tsai, L., & Joshi, S. A. (2002). Kinematic Analysis of 3-DOF Position Mechanisms for Use in Hybrid Kinematic Machines. *Journal of Mechanical Design*, *124*(2), 245–253. https://doi.org/10.1115/1.1468860

Gibbs, J. W. (1928). *The Collected Works of J. Willard Gibbs: pt. 1. Elementary principles in statistical mechanics. pt. 2. Dynamics. Vector analysis and multiple algebra. Electromagnetic theory of light, etc.*

© 2023 Suresh, A., Barath, M., & do Rego, A. published by TU Delft OPEN on behalf of the authors.
ISSN: 2667-2812

The Evolving Scholar (2023)

https://doi.org/10.59490/647bd5221539af025bb4e5a2

Bicycle and Motorcycle Dynamics 2023
Symposium on the Dynamics and Control of Single Track Vehicles
18 – 20 October 2023, Delft University of Technology, The Netherlands

Type of the Paper: Extended Abstract

A Study of Suspension Geometry for Personal Mobility Vehicles (PMVs) with Inward Tilt Mechanism

Tetsunori Haraguchi[1,2,*], Tetsuya Kaneko[3]

[1]Institutes of Innovation for Future Society, Nagoya University; haraguchi@nagoya-u.jp; ORCID 0000-0003-4978-4005
[2]College of Industrial Technology, Nihon University; haraguchi.tetsunori@nihon-u.ac.jp
[3]Department of Mechanical Engineering for Transportation, Osaka Sangyo University; kaneko@ge.osaka-sandai.ac.jp
*corresponding author.

Name of Editor: Jason Moore
Submitted: 04/06/2023
Accepted: 26/06/2023
Published: 26/06/2023
Citation: Haraguchi, T. & Kaneko, T. (2023). A Study of Suspension Geometry for Personal Mobility Vehicles (PMVs) with Inward Tilt Mechanism. The Evolving Scholar - BMD 2023, 5th Edition.
This work is licensed under a Creative Commons Attribution License (CC-BY).

Abstract:

Personal Mobility Vehicles (PMVs) have a long history as compact and highly efficient vehicles, but in recent years, a completely new PMV concept, which tilts inward during turning, has attracted attention. The authors have been studying the social suitability of the two front wheels one rear wheel PMV with an active inward tilting mechanism.

Although, PMV that tilts inward during turning, may has a tendency for pitching during turning like automobiles depending on the roll axis arrangement, the suspension spring constants are not allowed to be set high like motorcycles, therefore it is difficult to suppress the pitching. For this reason, it is strongly required to suppress the pitching tendency with the suspension geometry itself. However, since the PMV that tilts inward during turning is a new concept, there are not such theoretical studies, previously.

If the aim is equalization the amount of sinking in the front and rear during turning, the requirements for the suspension geometry can be analyzed using the force balance model in the back view as shown in Figure 1, in which the vehicle mass is divided by the front and rear distribution.

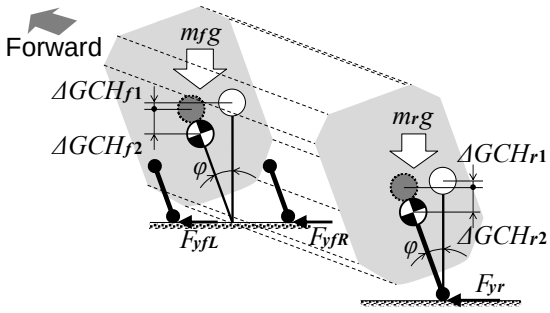


Figure 1. Balance model divided into front and rear.

Table 1. Vehicle specifications.

Item	Unit	Value	Item	Unit	Value
Total length (L)	m	2.645	Normalized camber stiffness (D_y)	10^{-2}/deg	1.49
Total width (W)	m	0.880	Front spring constant (k_f)	kN/m	7.20
Total height (H)	m	1.445	Rear spring constant (k_r)	kN/m	10.0
Wheel base (l)	m	2.020	Gravity center height (GCH)	m	0.358
Front tread (Tr)	m	0.807	Front mass distribution (m_f)	kg	222
Total mass (m)	kg	370	Rear mass distribution (m_r)	kg	148

In a PMV with two front wheels and one rear wheel, there are various types of suspensions for the front, such as a double wishbone type and a telescopic type, but for the rear, there is essentially only a full trailing arm (swing arm) type similar to a motorcycle. Therefore, the pitching will be suppressed by a method of matching the front amount of sinking during turning with the rear amount of sinking of the full trailing arm type.

First, Figure 2 shows the state of force balance during turning of the full trailing arm rear suspension. Since the reaction force that supports the tire lateral force generated during turning occurs only in the axial direction of the virtual suspension arm, the force in the direction that causes the vehicle body to sink remains. Using the spring constants of the rear suspension in Table 1, the relationship between the turning lateral acceleration (a) and the amount of vehicle body sinking in the vertical direction is obtained as shown in Figure 3. It can be seen that this sinking amount (ΔGCH_{r2}) is strongly nonlinear comparing with the decrease in the center of gravity height (GCH) of the vehicle due to the inward tilt during turning (ΔGCH_{r1}). And then, the front amount of sinking will be adjusted to the rear amount of sinking by the front force balance during turning.

© 2023 Haraguchi, T., & Kaneko, T. published by TU Delft OPEN on behalf of the authors.
ISSN: 2667-2812

Next, Figure 4 shows the force balance when a double wishbone type is used for front suspension as in automobiles. The force (F_{Lift}) in the direction that lifts the vehicle body due to force balance is given by Equation (1). The relationship between lateral acceleration (a) and the amount of sinking of the vehicle is shown in Figure 5.

$$F_{Lift} = F^*_{zfR} + F^*_{zfL} = D_y\gamma_f \sin\alpha \left(\frac{F_{zfR}}{\cos\alpha\cos\varphi - \sin\alpha\sin\varphi} + \frac{F_{zfL}}{\cos\alpha\cos\varphi + \sin\alpha\sin\varphi}\right) \quad (1)$$

$$\alpha \text{ and } \varphi \text{ are small and if } F_{zfR} = F_{zfL}, \text{then } F_{Lift} \approx 0 \text{ regardless of the value of } \alpha$$

Figure 6 shows the relationship between α, R_α and lifting and sinking of the vehicle body. With respect to the diagonal or horizontal lines in the diagram showing the relationship between α and R_α when $\Delta GCH_{f2}=0$, the vehicle body sinks in the upper left area and lifts in the lower right area. When using a double wishbone type suspension, a compromise must be accepted between body pitching and road disturbance, because the sinking geometry on double wishbone is not easy.

And then, Figure 7 shows the force balance during turning using a telescopic type suspension commonly used in motorcycles. The mechanism of the vehicle body lifting and sinking (Equation (2)) is equivalently same as Figure 2. In a PMV that tilts inward during turning, there is no need for load transfer between the left and right wheels during a steady turn. Therefore, both the pitching suppression of the vehicle body and the requirement of free from the road disturbance are compatible.

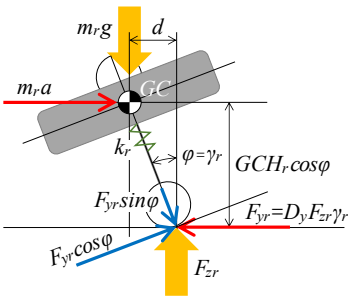


Figure 2. Full trailing arm rear suspension.

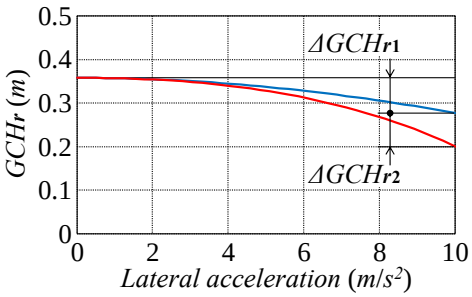


Figure 3. Rear body sinking.

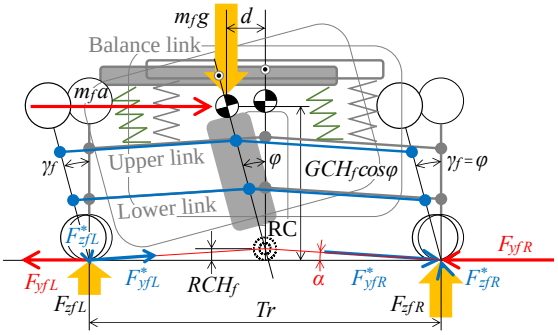


Figure 4. Double wishbone (D/W) front suspension.

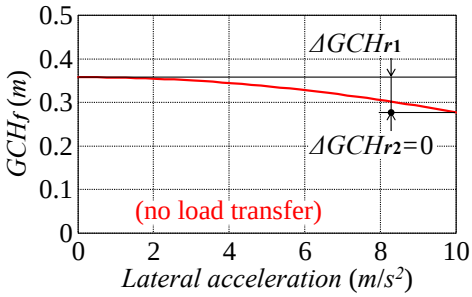


Figure 5. Front body sinking (D/W).

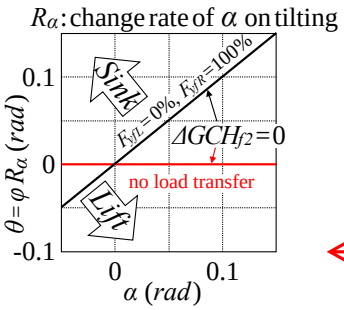


Figure 6. Lift and sinking (D/W).

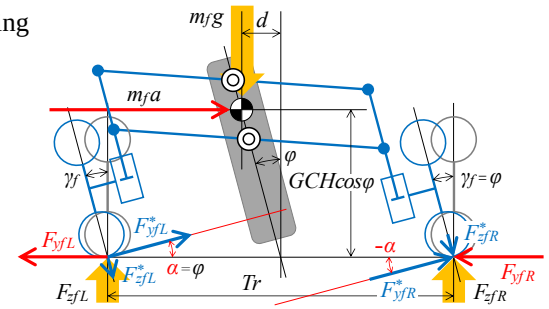


Figure 7. Telescopic front suspension.

Generally, in PID control for active inward tilt tracking, the actual tilt angle delays significantly with respect to the lateral acceleration (a) of the vehicle. If the inward tilt angle has not yet occurred at all, significant load transfer between the left and right wheels occurs as same as of automobiles. However, the front and rear body do not sink, and pitching does not occur, because α of front suspension is zero in case the telescopic type. When an inward tilt angle that is just in balance with the turning lateral acceleration (a) is generated, no load transfer occurs between the left and right wheels. Therefore, the front body sink as much as of the rear body, and pitching does not occur either. In other words, unlike the double wishbone type, the telescopic type almost satisfies the requirements of suppressing pitching of the vehicle body and the free from road disturbance.

The only cause of pitching in the telescopic type suspension that should be considered might be the time delay in load transfer due to the roll inertia (I_x) of the vehicle body given by Equation (3).

$$F_{Lift} = F^*_{zfR} + F^*_{zfL} = -D_y\gamma_f \sin\alpha \left(F_{zfR} + F_{zfL}\right) \quad (2)$$

$$I_x\ddot{\varphi} = F_{zfR} - F_{zfL} \quad (3)$$

References

Haraguchi, T. (2020). *4. Personal Mobility Vehicle (J)* (Mobility Service, Mobility Innovation Series, Vol. 1, pp. 92–123). Corona Publishing Co., Ltd., Tokyo, Japan. ISBN 978-4-339-02771-6.

Haraguchi, T., Kageyama, I., & Kaneko, T. (2019). Study of Personal Mobility Vehicle (PMV) with Active Inward Tilting Mechanism on Obstacle Avoidance and Energy Efficiency. *Applied Sciences, MDPI, 9*(4737). https://doi.org/10.3390/app9224737

Haraguchi, T., & Kaneko, T. (2023). Design Requirements for Personal Mobility Vehicle (PMV) with Inward Tilt Mechanism to Minimize Steering Disturbances Caused by Uneven Road Surface. *Inventions, MDPI, 8*(37). https://doi.org/10.3390/inventions8010037

© 2023 Haraguchi, T., & Kaneko, T. published by TU Delft OPEN on behalf of the authors.
ISSN: 2667-2812

The Evolving Scholar (2023)
https://doi.org/10.24404/63fe36f6fd33480b61c11947

Bicycle and Motorcycle Dynamics 2023
Symposium on the Dynamics and Control of Single Track Vehicles
18 – 20 October 2023, Delft University of Technology, The Netherlands

Type of the Paper: Extended Abstract

Analysis of stopping behaviour of cyclists at a traffic light-controlled intersection using trajectory data

Claudia Leschik[1*], Meng Zhang[2] and Kay Gimm[1]

[1]Institute of Transportation Systems, German Aerospace Center (DLR e. V.), Lilienthalplatz 7, 38108 Brunswick, Germany, Claudia.Leschik@dlr.de
[2]Institute of Transportation Systems, German Aerospace Center (DLR e. V.), Rutherfordstraße 2, 12489 Berlin, Germany, Meng.Zhang@dlr.de
*corresponding author.

Name of Editor: Jason Moore
Submitted: 28/02/2023
Accepted: 30/03/2023
Published: 26/04/2023
Citation: Leschik, C., Zhang, M. & Gimm, K. (2023). Analysis of stopping behaviour of cyclists at a traffic light-controlled intersection using trajectory data. The Evolving Scholar - BMD 2023, 5th Edition.
This work is licensed under a Creative Commons Attribution License (CC-BY).

Abstract:

Even if stop lines for vulnerable road users, foot paths and bicycle paths provide clear boundaries for stopping at traffic light-controlled intersections, this is not always the case in reality. In addition to poor infrastructure, such as potholes, puddles or high curbs, the presence of other road users and the further route choice can also affect the stopping point of vulnerable road users. Cyclists get in the way of others if they don't follow the stop line. Cyclists who are riding in the wrong direction also have to stop somewhere at the intersection. The aim of the study is to investigate cyclists' stopping behaviour (e.g., stopping position) at intersections with consideration of the impact of groups, wrong-way riding and road usage. The information can be used to improve models of bicyclist behaviour for example in application in simulations, in which cyclists only stop at clearly definable locations. Furthermore, the results of this study will provide clues in the application field for autonomous vehicles to correctly anticipate bicycle behaviour at intersections.

The traffic observation took place between March 11th and March 17th at the AIM Research Intersection in Brunswick, Germany. This large-scale research facility is part of the Application Platform for Intelligent Mobility (AIM) and records trajectory data with stereo-camera systems. The period from 6:15 a.m. to 6:30 p.m. was analyzed. The corresponding scene videos were recorded in reduced resolution, so that faces and license plates could not be recognized. The position, speed, acceleration and heading of detected and classified bicyclists were used to investigate the stopping behaviour. The AIM Research Intersection has a separate foot path and bicycle path, separate stop lines for foot paths and bicycle paths, and also separate crossings lanes for pedestrians and cyclists. Bicycles without the presence of other bicycles as well as bicycles with at least one other bicycle in the crossing area were analyzed. The stopping position was divided into different areas using previously defined polygons (stop line of foot or cycle path, at the stop line, behind the stop line). In the evaluation, a distinction was made between cyclists who stopped before crossing the intersection and cyclists who crossed through without stopping. For the analysis, single cyclists were considered, as well as several cyclists on one side of the intersection. Around 30%, of 1,411 detected single cyclists stopped on the foot or bicycle path. Around 79% (n=196) of the stopping single cyclists crossed the intersection in the correct direction. 68% of them stopped on the bicycle path. Only 18% stopped at the bicycle stop line. Wrong-way cyclists (n=63) stopped most frequently on the foot path (70%). In addition, it was examined where the intersection was crossed (foot path or bicycle path) and whether stopping beforehand lead to different results. Regardless of whether they stopped before crossing the intersection or not, cyclists used the bicycle path more often when they were in a group of bicyclists. Another subject of investigation was the speed and whether cyclists might drive slower and therefore more carefully if they do not use the cycle path. The speed of cyclists on the footpath is slightly lower.

In overall, it can be stated that stopping behaviour of bicyclists could be successfully modelled based on the conducted traffic observation. Parameter distributions are derived and in a next step ready for implementation for example in the microscopic simulation SUMO (Lopez et al., 2018).

© 2023 Leschik, A., Zhang, M. & Gimm K. published by TU Delft OPEN on behalf of the authors.
ISSN: 2667-2812

References

Lopez, P. A., Behrisch, M., Bieker-Walz, L., Erdmann, J., Flötteröd, Y. P., Hilbrich, R., Lücken, L., Rummel, J., Wagner, P. & Wießner, E. (2018, November). Microscopic traffic simulation using sumo. In 2018 21st international conference on intelligent transportation systems (ITSC) (pp. 2575-2582). IEEE.

© 2023 Leschik, A., Zhang, M. & Gimm K. published by TU Delft OPEN on behalf of the authors.
ISSN: 2667-2812

The Evolving Scholar (2023)

http://dx.doi.org/10.24404/63fe85b8dcf3bfbf73b5943b

Bicycle and Motorcycle Dynamics 2023
Symposium on the Dynamics and Control of Single Track Vehicles
18–20 October 2023, Delft University of Technology, The Netherlands

Type of the Paper: Extended Abstract

Analytical expression to calculate the suspension sag of vehicles.

Vasquez F. [1,*]

[1] Department of Mechanical Engineering, University of Concepcion, Chile; fevasquez@udec.cl, ORCID 0000-0002-6385-237X
[*] corresponding author

Name of Editor: Jason Moore
Submitted: 01/03/2023
Accepted: 13/04/2023
Published: 26/04/2023
Citation: Vasquez, F. (2023). Analytical expression to calculate the suspension sag of vehicles. The Evolving Scholar - BMD 2023, 5th Edition.
This work is licensed under a Creative Commons Attribution License (CC-BY).

Abstract:

The suspension system of a vehicle is essentially conceived with two objectives: to provide comfort to the passengers and maintain tires in contact with the ground (roadholding). Comfort is enhanced by reducing the transmission of road irregularities into the chassis and passenger, while roadholding, by allowing the tire to follow the road irregularities to reduce detachments. The typical suspension system achieves this by connecting each wheel to the chassis with a properly designed spring and damper. It is well known, however, that optimal comfort and roadholding cannot be achieved simultaneously since they require a different set of stiffness and damping. In order to alleviate this conflict, springs, and dampers are built with non-linear laws which are regularly evolving, particularly those of off-road bicycles and motorcycles.

In the preliminary design of a motorcycle suspension (and the whole motorcycle), simple equations are used since the first prototypes need to be conceived and evaluated in a short time (Lot, 2021). To this end, the half-motorcycle model is considered since it is the simplest model able to capture the effect of the suspension on the chassis and tires. Specifically, this model divides the motorcycle into the front and rear ends and captures the vertical motions of the chassis and wheel masses due to road input with two degrees of freedom. Additionally, the suspension elements are considered linear to further simplify the analysis. For this model, optimal stiffness and damping for comfort or roadholding can be calculated directly by algebraic expressions (Sheibe, 2009).

The use of the suspension stroke with the calculated stiffness needs to be revised for different load cases. Of particular importance is the spring deformation in static equilibrium, known as suspension sag. It determines the amount of suspension stroke that is available for transient compressions or extensions before reaching any of the ends. Reaching the compression end-stroke, due to a sufficiently large upward obstacle or landing, generates a sudden shock on the chassis and rider, which is highly detrimental to comfort. On the other hand, reaching the extension end-stroke, due to a large downward obstacle or rebound after landing, may cause the tire to detach from the ground, which is detrimental for roadholding. Therefore, the suspension sag needs to be rationally selected to minimize reaching any of the ends for the expected transients.

The common practice is to set the suspension sag on 33% of the suspension stroke (Thede, 2010), by adding an appropriate preload of the springs. In this way, two-thirds of the stroke are available for a transient compression from equilibrium, and one third for an extension. It is done since it is argued that avoiding shocks on the chassis is more important than avoiding detachments (Lot, 2021). Despite this reasonable argument, significantly different values are also recommended for specific disciplines such as 25% for motocross, 15% for cross-country bicycles, and 40% for downhill ones. Nonetheless, these are recommended as starting points to be subsequently adjusted by each rider according to the particular terrain and riding style. Determination of the specific sag value for a given application seems cumbersome in the non-academic literature, while no model or discussion is found in the academic one. Therefore, the aim of this paper is to propose a simple, yet general model to calculate the suspension sag needed for a specific situation or riding discipline, particularly for the preliminary design stage of motorcycles and bicycles.

©2023 F. V., published by TU Delft OPEN on behalf of the authors.
ISSN: 2667-2812

To achieve this, we calculate the expected suspension stroke needed for different road inputs with a simple model, from where we find the suspension sag. Specifically, we use the linear half-motorcycle model, and consider optimal stiffness and damping for comfort and road holding, separately. To further maintain simplicity, we only consider a continuous random road excitation defined according to ISO8608 (ISO, 2016) transited at different speeds, as input. Following (Lot, 2021) we calculate the power spectral density (PSD) response of the suspension stroke S_{ss} in the frequency domain ω with Equation (1):

$$S_{ss}(\omega) = |H_s(i\omega)|^2 S_{vv}, \tag{1}$$

where $H_s(i\omega)$ is the frequency response function of the suspension stroke, and S_{vv} is the velocity PSD of the road elevation. Then, we calculate the root-mean-square of the response by integrating the single-sided PSD, from where we estimate the amplitude of the suspension stroke. Lastly, by evaluating the required suspension stroke, we find a mathematical expression to determine the minimum sag required in terms of road class and longitudinal speed.

It is important to note that this result has been derived only for continuous excitation. Nonetheless, the response to an impulsive excitation such as an isolated bump or landing can be indirectly estimated under certain considerations. For example, the suspension requirement to an upward step of height h, can be approximated to the response to a road class with an equivalent rms road elevation. In the same way, the response to a landing at vertical velocity v_y, can also be associated with a certain road class with equivalent road elevation velocity. The proposed procedure is general, in the sense that it is not bounded to a specific discipline or driving style since the road input can be any continuous road. Nonetheless, the road class and longitudinal speed representative of each discipline and/or driving style still needs to be determined.

References

ISO 8608., (2016). *Mechanical Vibration - Road Surface Profiles*. Standard, International Organization for Standardization.

Lot, R., Sadauckas, J., (2021). *Motorcycle design: Vehicle Dynamics Concepts and Applications*. ISBN: 979-12-200-9852-6

Thede, P., Parks, L., (2010). *Race Tech's Motorcycle Suspension Bible*, Motorbooks.

Sheibe, F., Smith, M., (2009). Analytical solutions for optimal ride comfort and tyre grip for passive vehicle suspensions. *Vehicle System Dynamics*, *47*, 1229–1252.

©2023 F. V., published by TU Delft OPEN on behalf of the authors.
ISSN: 2667-2812

The Evolving Scholar (2023)
https://doi.org/10.24404/63fe3ff9d4edb555c192c537
Bicycle and Motorcycle Dynamics 2023
Symposium on the Dynamics and Control of Single Track Vehicles
18 – 20 October 2023, Delft University of Technology, The Netherlands

Type of the Paper: Extended Abstract

Application of tire multiphysical modeling methodologies for the preliminary definition of a racing motorcycle setup

Ruffini M.[1], Alberti F.[2], D'Andrea D.[2], Farroni F.[1]*, Napolitano Dell'Annunziata G.[1], Risitano G.[2], Milone D.[2]

[1]Università degli Studi di Napoli Federico II; flavio.farroni@unina.it, ORCID 0000-0001-8257-5534, guido.napolitanodellannunziata@unina.it, ORCID 0000-0002-7293-4975, marco.ruffini@unina.it
[2]Università degli Studi di Messina; grisitano@unime.it, ORCID 0000-0002-0506-8720, fabio.alberti@unime.it, danilo.dandrea@unime.it, dario.milone@unime.it
*corresponding author.

Name of Editor: Jason Moore
Submitted: 28/02/2023
Accepted: 10/04/2023
Published: 26/04/2023
Citation: Ruffini, M., Farroni, F., D'Andrea, D., Farroni, F., Napolitano Dell'Annunziata, G., Risitano, G. & Milone, D. (2023). Application of tire multiphysical modeling methodologies for the preliminary definition of a racing motorcycle setup. The Evolving Scholar - BMD 2023, 5th Edition.
This work is licensed under a Creative Commons Attribution License (CC-BY).

Abstract:

Optimizing the performance of racing motorcycles is a central goal for competition teams. The necessity to ensure driver stability and a good level of grip in the widest possible range of riding conditions makes it necessary for tires to work in the right temperature window, capable of ensuring the highest interaction force between tire and road (Farroni 2022). Indeed, the magnitude of the tire-road interaction forces of the motorcycle tackling a specific dynamic maneuver is strictly influenced by the tire structure and the tire compound viscoelastic characteristics, which in turn is strongly influenced by the tire's layers' temperatures (Farroni 2018). Specifically, the internal temperature of the tire is a parameter that can be difficult to measure and control but has a significant impact on motorcycle performance and, also, on driver stability. For this reason, deepening the knowledge of internal tire layers temperatures in racing motorcycles, could have an important impact and provide useful information to work on performance optimization on the track and to find the right motorcycle setup. With this aim, Farroni et al. introduced a motorcycle application of their physical thermal model thermoRIDE (Farroni 2020), derived from "Thermo Racing Tyre" (TRT), able to accurately reproduce the tire thermal dynamics in all the vehicle working conditions and to provide the full temperature local distribution inside the tire's inner rubber layers (Figure 1).



Figure 1. Example of thermoRIDE tire mesh configuration in motorcycle applications.

In this work, the introduced thermal model is adopted for an activity concerning the development of a moto-student vehicle, to predict the racing motorcycle setup allowing the tire to work in a thermal window that optimizes grip and maximizes tire life.

© 2023 Farroni F., Napolitano Dell'Annunziata G., Ruffini M., published by TU Delft OPEN on behalf of the authors.
ISSN: 2667-2812

More in detail, a focus has been placed on the effects of the motorcycle's wheelbase and pivot height variations on internal tire temperatures. Indeed, the stability and handling of the vehicle are highly dependent on the geometric properties of the chassis (Scappaticci 2017). Several values of such quantities have been tested in a properly implemented vehicle model developed in the "VI-BikeRealTime" environment, validated by outdoor tests, able to provide forces acting on the tires, slip indices, and speeds, needed by the thermal model as inputs (Figure 2). Since the thermoRIDE model relies on Fourier's law of conduction related to a three-dimensional body, it has been also required to identify the thermal diffusivity of each layer of interest employing an experimentally validated procedure (Allouis 2016) to ensure that the achieved results are reliable and consistent. Finally, the model in use needs one last input, which is the extension of contact patches under various load, pressure, and camber conditions. These have been obtained through indoor testing and another experimentally validated procedure. Through the analysis of the internal temperatures calculated by the model, reached by the various layers of the tire, it has been possible to investigate which of the simulated conditions cause a too fast thermal activation of the tire and which of them is able to avoid overheating and underheating phenomena. Furthermore, since having the tires working at the right temperature in the fastest possible time is crucial in a race, various tire warm-up levels via thermal blankets have been tried, to figure out at which temperature and for how long to use them to reach an optimal inner liner and tread core temperature.

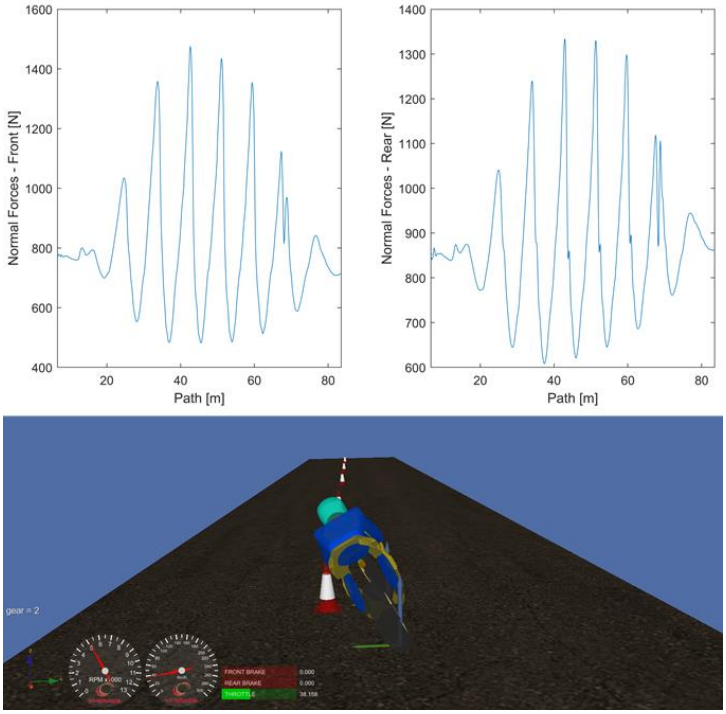


Figure 2. Normal tires forces evaluated from slalom test in VI-BikeRealTime® environment.

References

Allouis, C., Farroni, F., Sakhnevych, A., Timpone, F. (2016). Tire thermal characterization: test procedure and model parameters evaluation. *Proceedings of the 24th World Congress on engineering*, London, 2016.

Farroni, F. Sakhnevych, A. (2022) Tire multiphysical modeling for the analysis of thermal and wear sensitivity on vehicle objective dynamics and racing performances. In *Simulation Modelling Practice and Theory, vol. 117.*

Farroni, F., Lenzo, B., Mancinelli, N., Mercantini, M., Sakhnevych, A., Timpone, F. (2020). A real-time Thermal Model for the Analysis of Tire/Road Interaction in Motorcycle Applications. *Proceedings of the 2019 Bicycle and Motorcycle Dynamics Conference: A Symposium on the Dynamics and Control of Single Track Vehicles*, Padova, 2019.

Farroni, F., Russo, M., Sakhnevych A., Timpone F. (2018), TRT EVO: Advances in real-time thermodynamic tire modeling for vehicle dynamics simulations. *Proceedings of the IMechE, Part D, Journal of Automobile Engineering, 233(1), 121–135.*

Scappaticci, L., Bartolini, N., Guglielmino, E., Risitano, G. (2017), Structural optimization of a motorcycle chassis by pattern search Algorithm. In *Engineering Optimization, vol. 49.*

© 2023 Farroni F., Napolitano Dell'Annunziata G., Ruffini M., published by TU Delft OPEN on behalf of the authors.
ISSN: 2667-2812

The Evolving Scholar (2023)

http://dx.doi.org/10.24404/63f71f4dd1dc6fa8952ab120

Bicycle and Motorcycle Dynamics 2023
Symposium on the Dynamics and Control of Single Track Vehicles
18–20 October 2023, Delft University of Technology, The Netherlands

Type of the Paper: Extended Abstract

Experimental Investigation on the Lateral Dynamics of a Steering-assisted Two-wheeled Vehicle

Stefano Lovato [1], Matteo Massaro [1,*], Roberto Lot [1]

[1] Department of Industrial Engineering, University of Padova, Via Venezia 1, 35131 Padova, Italy ; stefano.lovato.1@phd.unipd.it, ORCID 0000-0003-3892-7816, matteo.massaro@unipd.it, ORCID 0000-0001-6256-3384, roberto.lot@unipd.it, ORCID 0000-0001-5022-5724

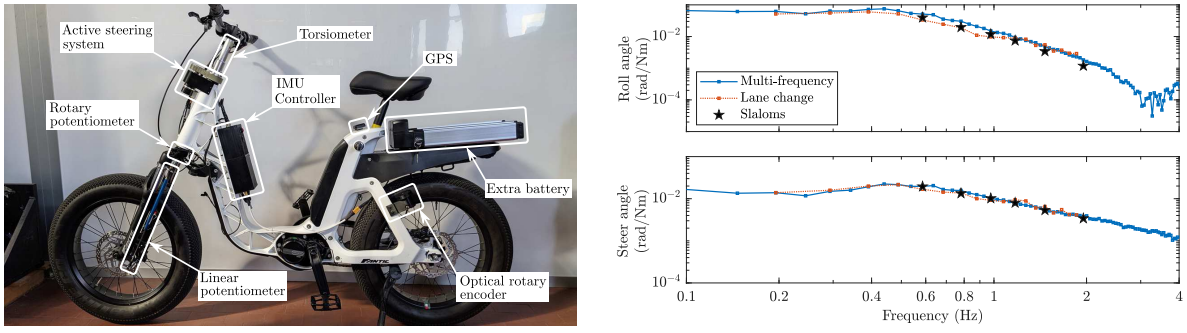
[*] corresponding author

Name of Editor: Jason Moore
Submitted: 23/02/2023
Accepted: 16/04/2023
Published: 26/04/2023
Citation: Lovato, S., Massaro, M. Lot, R. (2023). Experimental Identification of the Lateral Dynamics of a Steering-assisted Two-wheeled Vehicle. The Evolving Scholar - BMD 2023, 5th Edition.
This work is licensed under a Creative Commons Attribution License (CC-BY).

Abstract:

The demand of powered two-wheelers (PTW) for personal mobility is increasing, with more than 500 million of PTWs circulating worldwide (WHO, 2017). Compared to cars, PTWs have smaller costs, emissions and reduced traffic congestion. However, the intrinsic instability of PTWs rises serious concerns on the rider's safety. While several assistance systems have been proposed for cars, the application to PTW is still in its infancy, see for example (Dialynas et al., 2018; Lot and Fleming, 2020). Advanced riding assistance systems have the potential to reduce the number and severity of accidents, by stabilizing in scenarios such as low-speed riding and emergency braking.

The authors recently proposed in (Lovato et al., 2022a,b) an active steering assistant (ActiSA), which supports the rider in controlling the handlebar by applying a steering torque to the front assembly, while keeping the rigid connection between the handlebar and the

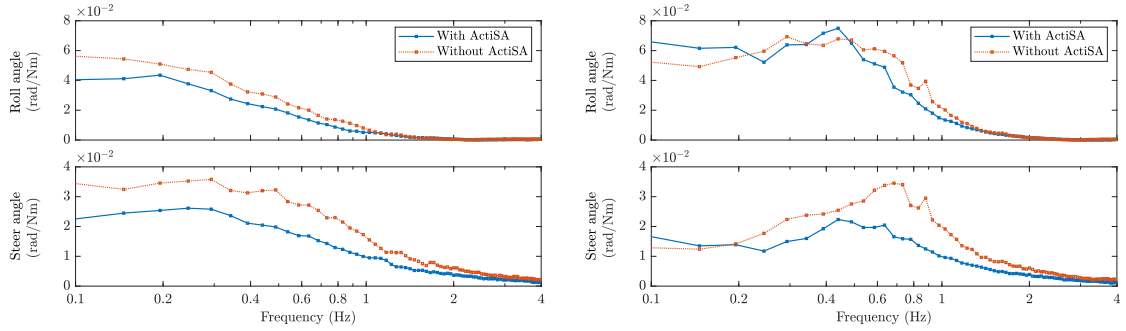


(a) (b)

Figure 1. (a) Layout of the ActiSA system, and (b) magnitude of the TFs of roll (top) and steer (bottom) angles with respect to the rider's steering torque at 20 kph and with the ActiSA connected.

©2023 Lovato, S., Massaro, M., & Lot, R. published by TU Delft OPEN on behalf of the authors.
ISSN: 2667-2812

 http://dx.doi.org/10.24404/63f71f4dd1dc6fa8952ab120



(a) 10 kph (b) 20 kph

Figure 2. Magnitude of the TFs of roll (top) and steer (bottom) angles with respect to the rider's torque.

front wheel for safety reason. The prototype is based upon on a urban e-bike, with a weight of 36 kg and a propulsion power of 250 W. The assistance steering torque is applied with a brushless electric motor connected to the steering shaft by a gearbox and a belt transmission. A number of sensors is employed to monitor the vehicle motion and the rider's steering torque, including an inertial measurement unit, a GPS, and a torsiometer. The system layout is illustrated in Figure 1(a).

While the ActiSA system is designed to support the rider in certain scenarios only, it remains inactive most of the time to minimise energy usage. This paper addresses the question of whether or not the mere presence of the inactive ActiSA system may negatively affects handling. In particular, we investigate how the ActiSA affects the vehicle lateral dynamics when the system is inactive. The frequency response functions (FRFs) of the steering torque to roll and steering are identified in two vehicle setups, namely with the ActiSA mechanically connected, but switched off, and mechanically disconnected to the steering system. Different types of manoeuvres are performed at nominal speeds 10 and 20 kph, namely 2×5 m lane-change, slaloms, and multi-frequency steering excitation, which consists of a driving session with the rider applying a steering excitation torque in the range 0.1–4.0 Hz. In each test the rider does not pedal and the propulsion power is provided by the e-bike motor, controlled to keep the speed constant. The time-domain signals are logged at 1 KHz. The data post-processing includes the filtering and decimation to give a final sampling rate of 100 Hz. The roll and steer FRF are computed using a H1 estimator, with a windowing depending on the manoeuvre. Figure 1(b) shows the magnitude of the roll and steer FRFs for the tests at 20 kph, with the ActiSA mechanically connected. The comparison of the experimental FRFs from the different approaches proves the reliability of the multi-frequency tests, which is less time consuming and allows a larger frequency content with respect to slalom and lane change. The impact of the ActiSA is investigated from the comparison of the FRFs identified with the multi-frequency excitation tests in the two vehicle setups. Figure 2 shows the roll and steer FRFs at 10 kph (a) and 20 kph (b) in both the vehicle setups. The ActiSA proves to have an impact on the steer FRF in the range 0.1–2.0 Hz, with a reduction factor in the magnitude of 0.5–0.7. The results obtained show that the ActiSA system has a visible effect on the FRFs, that was also perceived by the rider during the tests.

References

WHO (2017), Powered two- and three-wheeler safety: a road safety manual for decision-makers and practitioners. World Health Organization.

Dialynas, G., Schwab, A., Happee, R. (2018), Design and implementation of a steer-by-wire bicycle. In International Cycling Safety Conference.

Lot, R., Fleming, J. (2020), Active safety systems for powered two-wheelers: A systematic review. In Traffic Injury Prevention, vol. 21 (78–86).

Lovato, S., Bova, M., Massaro, M., Andriollo, M., Lot, R. (2022), Active Steering Assistant for Powered Two-Wheelers: Hardware Prototyping and Results. In Niola, V., Gasparetto, A., Quaglia, G., Carbone, G. (eds) Advances in Italian Mechanism Science. IFToMM Italy 2022. Mechanisms and Machine Science, vol.. 122. Springer.

Lovato, S., Bova, M., Massaro, M., Andriollo, M., Lot, R. (2022), An Active Steering Assistant System for Powered Two-Wheelers. In Lecture Notes in Engineering and Computer Science. World Congress on Engineering 2022, vol. 2244 (95–102).

©2023 Lovato, S., Massaro, M., & Lot, R. published by TU Delft OPEN on behalf of the authors.
ISSN: 2667-2812

The Evolving Scholar (2023)

http://dx.doi.org/10.59490/6450ba60ee29c320fcbe928a

Bicycle and Motorcycle Dynamics 2023
Symposium on the Dynamics and Control of Single Track Vehicles
18–20 October 2023, Delft University of Technology, The Netherlands

Type of the Paper: Extended Abstract

Modeling and Implementation of a Reaction Wheel Stabilization System for Low Speed Balance of a Cargo Bicycle

Jason K. Moore [1,*], Jeswin Koshy Cherian [1], Björn Andersson [2], Oliver Lee [2], Anders Ranheim [2]

[1] Delft University of Technology, The Netherlands ; j.kmoore@tudelft.nl, ORCID 0000-0002-8698-6143; j.koshycherian@student.tudelft.nl, ORCID 0009-0002-2264-8097;
[2] Ictech AB, Sweden ; bjorn.andersson@ictech.se; oliver.lee@ictech.se; anders.ranheim@ictech.se
[*] corresponding author

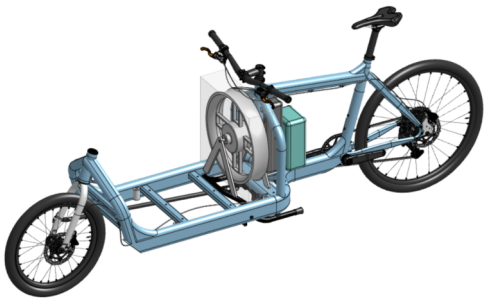
Name of Editor: Christoph Schmidt
Submitted: 01/07/2023 Accepted:
03/07/2023 Published: 03/07/2023

Citation: Moore, J., Koshy Cherian, J., Andersson, B., Lee, O. & Ranheim, A. (2023). Modeling and Implementation of a Reaction Wheel Stabilization System for Low Speed Balance of a Cargo Bicycle. The Evolving Scholar - BMD 2023, 5th Edition.
This work is licensed under a Creative Commons Attribution License (CC-BY).

Abstract:

Cargo bicycle use has grown over the last decade with electrification contributing to a rapid growth in the recent y ears. With the growth of safer bicycle infrastructure in many countries, these vehicles can be a greener, more energy efficient replacement for cars for a variety of short and medium distance activities, e.g. "last mile" delivery or transportation for families. One particular problem cargo two-wheelers face is that the vehicles are hard to balance and handle at low and near zero speeds. Delivery people need to quickly park their vehicle without the need for a bicycle storage rack or cumbersome kickstands for quick door calls. Similarly, parents need to seat and remove their children from the vehicle without worrying that it would fall. Also, both vehicles come to a stop in traffic many times throughout a trip. At every instance near zero speed, balance assistance would simplify vehicle operation for the rider; even enabling it as a new transportation mode for those with limited motor skills and coordination. Our goal was to develop and test the feasibility of robotically stabilizing a single track cargo bicycle at zero and near zero forward speeds.

There is a long history of efforts to robotically stabilize single track vehicles beginning with inventions like Brennan's monorail in the early 1900's (Barr, 1907), to the motorcycle steer motor control of (Ruijs and Pacejka, 1985), and a too long list of models



(a) CAD rendering of the envisioned reaction wheel on a common delivery bicycle model.



(b) Prototype vehicle with a Bafung motor driven at 48 V with a maximum power of 1500 W and added rim mass to maximize the rotational inertia.

Figure 1: Vehicle images.

©2023 Moore, J. K., Koshy Cherian, J., Andersson, B., Lee, O., & Ranheim, A. published by TU Delft OPEN on behalf of the authors.
ISSN: 2667-2812

 http://dx.doi.org/10.59490/6450ba60ee29c320fcbe928a

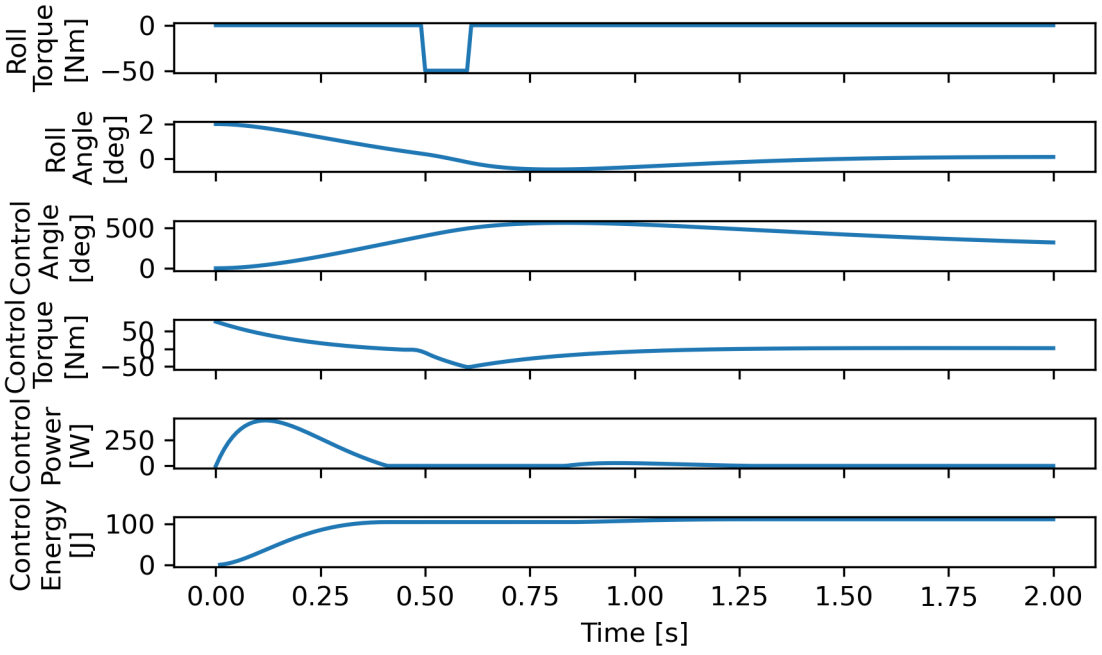


Figure 2: Roll stabilization results at zero speed from an initial roll angle of 2 ° and a pulse roll torque perturbation showing the reaction wheel controller behavior: angle, torque, power, and energy consumption.

and demonstrations of steer control, control moment gyroscopes, reaction wheels, inverted pendulums and the like. None of these solutions have become commercially viable, so our approach tries to focus on the narrow need of near zero speed stabilization. We chose a reaction wheel due to the low cost (<$500), ability to stabilize vehicle roll at any speed, and the possibility to fit the reaction wheel in a concealed manner in a small portion of the cargo space.

To that end, we have developed a compact reaction wheel that fits in the cargo space of a standard cargo bicycle. The reaction wheel is capable of applying roll torques up to 200 $\mathrm{N\,m}$ to the vehicle, see Figure 1a. This can stabilize the roll degree of freedom at zero speed for roll angles up to about 10 °. Figure 2 shows that the reaction wheel can stabilize the vehicle from a 2 ° and 50 $\mathrm{N\,m}$ disturbance within two seconds using about 100 J and 50 $\mathrm{N\,m}$ of peak torque. A modern e-bike battery has up to 4M joules of energy available for use so it is possible to dedicate a portion of the energy to stabilization during medium length trips. Minimizing the energy consumption from the reaction wheel while maximizing stability will be investigated further.

The reaction wheel has some disadvantages, including significantly increasing the mass of the vehicle as well as increasing the complexity and cost. The energy consumption can be large when the system is constantly managing large repeated disturbances, reducing the available range of an e-bike (possibly drastically and unexpectedly to the rider). The reaction wheel will generate pitching torques during rapid changes in heading (although we expect this to be negligible). These disadvantages can be overcome with system optimization.

In the paper and presentation, we will report on the model and simulation results that demonstrate the practicality of the design as well as its limits. We will also report on the performance of the prototype shown in Figure 1b in relation to the simulation results.

This research has been made possible with financial support from the Swedish Transport Authority ('Skyltfonden').

References

Barr, R. (1907). Louis Brennan's Gyro-mono-rail: An invention that is likely to revolutionise the traffic of the world. *The idler; an illustrated monthly magazine*, 31(60):650–657.

Ruijs, P. A. and Pacejka, H. B. (1985). Research in lateral dynamics of motorcycles. *Vehicle System Dynamics*, 14(1–3):149–152.

©2023 Moore, J. K., Koshy Cherian, J., Andersson, B., Lee, O., & Ranheim, A. published by TU Delft OPEN on behalf of the authors.
ISSN: 2667-2812

The Evolving Scholar (2023)

http://dx.doi.org/10.59490/649e491f3e542128d59873c2

Bicycle and Motorcycle Dynamics 2023
Symposium on the Dynamics and Control of Single Track Vehicles
18–20 October 2023, Delft University of Technology, The Netherlands

Type of the Paper: Extended Abstract

Influence of aerodynamic lift and centre of pressure position in motorcycle stability

Benjamin E. Gonzalez T. [1,*], Felipe A. Vasquez S. [2,]

[1] Department of Mechanical Engineering, University of Concepcion, Chile; bgonzalez2018@udec.cl, ORCID 0000-0001-6132-1367
[2] Department of Mechanical Engineering, University of Concepcion, Chile; fevasquez@udec.cl, ORCID 0000-0002-6385-237X
[*] corresponding author

Name of Editor: Firstname Lastname
Submitted: 30/06/2023
Accepted: 30/06/2023
Published: 30/06/2023
Citation: González, B. & Vasquez, F. (2023). Influence of aerodynamic lift and centre of pressure position in motorcycle stability. The Evolving Scholar - BMD 2023, 5th Edition.
This work is licensed under a Creative Commons Attribution License (CC-BY).

Abstract:

Motorcycles are systems with complex dynamic behaviour that can become unstable under certain driving conditions. The basic study of motorcycle stability considers four degrees of freedom (DoF) (Sharp, 1971), and demonstrates the three well-known modes of vibration of a motorcycle: weave, wobble and capsize (Lot, 2021). Capsize is a non-oscillatory roll motion of the chassis, similar to an inverted pendulum, which is typically stable within a certain range of longitudinal speed. Contrarily, wobble and weave are oscillatory modes, with motions mainly of the front and rear chassis respectively, that can become unstable above or below certain speeds, making them particularly dangerous. Additionally, the existence of instabilities makes the motorcycle difficult to handle since the behaviour is less predictable and the rider needs to introduce corrective measures to attenuate them. Avoiding such instabilities from the design stage is not trivial since they depend on various interrelated parameters, such as geometry, mass distribution, rider interaction, suspension system, and aerodynamics, among others.

Aerodynamic forces in a vehicle can be essentially described by its longitudinal and vertical components together with its point of application on the vehicle. The former are known as drag and lift forces respectively, while the latter as the centre of pressure (CoP). Several studies had shown that aerodynamic forces have an influence on stability. For example, (Cooper, 1983), indicates that introducing a fairing or windshield can significantly stabilise wobble from cross-winds. While, (Bridges et al., 1987), showed that the addition of a top box can excite the wobble mode. More extensively, (Meijaard et al., 2006) studied aerodynamic drag and suspension effects on the stability of a motorcycle in a straight line and steady cornering. They explain that drag influences stability through four mechanisms: dampening lateral motion, changing weight distribution, tire cornering stiffness, and rake geometry. They found that these mechanisms combined result in a tendency to stabilise wobble and destabilise weave. In general, aerodynamic forces can improve or worsen stability, therefore the introduction of aerodynamic devices needs to be judicious.

It is well known that in motorsport performance needs to be enhanced continuously and aerodynamics can be used to this end. During the last years, MotoGP motorcycles had been equipped with diverse aerodynamics devices such as front and rear winglets, and are in strong development. Aerodynamic specialists are taking advantage of the variable aerodynamics of two-wheeled vehicles due to leaning angle and changing rider position to introduce devices that are useful only in certain situations. These changes in motorcycle aerodynamics can be summarised as a moving CoP with variable force magnitude. Changing the CoP position and the addition of lift force certainly affect the four mechanisms described by (Meijaard et al., 2006), but their effect on stability had not been described in the literature. Therefore the aim of this research is to extend on (Meijaard et al., 2006) research, by analysing the influence of CoP position and aerodynamic lift in motorcycle stability in straight line and steady cornering.

To this end, we perform a stability analysis on a motorcycle with variable CoP and lift. Particularly, we use the 11 DoF motorcycle model described by (Meijaard et al., 2006), add various lift forces magntiudes, and consider the CoP, in various positions. In straight

©2023 González, B. & Vasquez, F. published by TU Delft OPEN on behalf of the authors.
ISSN: 2667-2812

line, we consider it ahead, aligned, and behind the motorcycle centre of mass, and in cornering we consider it on both sides of the symmetry plane of the motorcycle to account for rider lateral displacement. For these situations, we perform the bifurcation analysis to identify the influence on stability. The result contributes to the understanding of motorcycle aerodynamics providing new insights into how to use aerodynamics to enhance stability. The results apply directly to racing motorcycles, but can also be extended to road motorcycles to enhance safety. As in (Meijaard et al., 2006), the effect of the rider as a controller was neglected, and needs further study.

References

Briges, P., Russell, J., (1987). The Effect of Topboxes on Motorcycle Stability. *Vehicle System Dynamics, 16(5–6)*, 345–354.

Cooper, K., (1983). The effect of handlebar fairings on motorcycle aerodynamics. *SAE Technical Paper 830156, 1983*

Meijaard, J. P., Popov, A. A., (2006). Influences of aerodynamic drag, the suspension system and rider 's body position on instabilities in a modern motorcycle. *Vehicle System Dynamics, 44:sup1*, 690–697

Lot, R., Sadauckas, J., (2021). *Motorcycle design: Vehicle Dynamics Concepts and Applications*. ISBN: 979-12-200-9852-6

Sharp, R. S. (1971). The stability and control of motorcycles. *Proceedings of the IMechE, Part C, Journal of Mechanical Engineering Science*, *13*, 316–329.

©2023 González, B. & Vasquez, F. published by TU Delft OPEN on behalf of the authors.
ISSN: 2667-2812

The Evolving Scholar (2023)

https://doi.org/10.24404/63ce53a5c41c79b0ffd14020

Bicycle and Motorcycle Dynamics 2023
Symposium on the Dynamics and Control of Single Track Vehicles
18 – 20 October 2023, Delft University of Technology, The Netherlands

Type of the Paper: Extended Abstract

Balancing Control of a Unicycle Robot with Double Flywheels

Parnichkun, M.[1]*, Chantarachit, S.[2]

[1]Asian Institute of Technology; manukid@ait.ac.th; 0000-0002-1026-8030
[2]Rajamangala University of Technology Thanyaburi; surachat.chantarachit@gmail.com
*corresponding author.

Name of Editor: Jason Moore
Submitted: 23/01/2023
Accepted: 18/04/2023
Published: 25/04/2023
Citation: Parnichkun, M. & Chantarachit, S. (2023). Balancing Control of a Unicycle Robot with Double Flywheels. The Evolving Scholar - BMD 2023, 5th Edition.
This work is licensed under a Creative Commons Attribution License (CC-BY).

Abstract:

Balancing of unstable system is a challenging topic. Unicycle robot is the robot which has only one contact point with ground. This type of robot is unstable in both roll and pitch directions. The research on unicycle robot was introduced at Stanford University (Bryson et el**,** 1988). A unicycle robot which used a pair of gyroscopes controlled by Gain-Scheduled was proposed in 2005 by DAO (Dao et el, 2005). Majima in (Majima et el, 2005) and (Majima et el, 2006) proposed to balance a unicycle robot in roll direction by using angular momentum. Roll balancing by changing falling direction was proposed by Vos (Vos et el, 1990). In this research, a unicycle robot has been designed and developed as shown in Figure 1. A pair of gyroscopes installed on both sides of the frame is used to generate torque in roll direction. The unicycle wheel is used to generate torque in pitch direction. LQR is used to balance the unicycle robot both in roll and pitch directions.

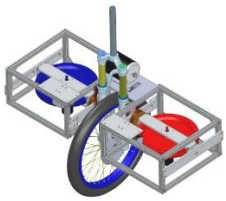


Figure 1. Unicycle robot

Dynamic model of the unicycle robot can be expressed in the non-linear dynamic equation as shown in Equation (1). *M* is inertia matrix. *C* is Coriolis matrix. *G* is gravity matrix, and *D* is disturbance matrix. The disturbance matrix combines the equivalent forces from external disturbances, friction, and parameter uncertainties. Coulomb friction is also considered in the disturbance matrix. Since the robot operates at low speed, the viscous friction is small and negligible. This term (*D* matrix) is considered separately from the robot dynamic model. And *F* is the input force matrix.

$$\boldsymbol{M(q)\ddot{q} + C(q,\dot{q}) + G(q) + D = F} \tag{1}$$

After linearization and conversion to state-space form, the model is expressed by

$$\boldsymbol{\dot{x} = Ax + Bu} \tag{2}$$

LQR is an optimal controller that optimally determines the gains by compromising the states and control input cost. The LQR cost function is expressed by

$$\boldsymbol{J = \int_0^\infty (x^T Q x + u^T R u)\, dt} \tag{3}$$

The *Q* and *R* matrices are the state and control weighting matrices, respectively. Each weighting element determines which state propriety is concerned. The control signal follows Equation (4).

© 2023 Parnichkun, M., Chantarachit, S.. published by TU Delft OPEN on behalf of the authors.
ISSN: 2667-2812

https://doi.org/10.24404/63ce53a5c41c79b0ffd14020

Bicycle and Motorcycle Dynamics 2023
Symposium on the Dynamics and Control of Single Track Vehicles
18 – 20 October 2023, Delft University of Technology, The Netherlands

$$\boldsymbol{u} = -\boldsymbol{K}\boldsymbol{x} \tag{4}$$

To eliminate steady-state error and improve the performance, the LQR+I controller is applied. The simulation and experimental results of the LQR+I controller, shows that the steady-state errors of roll, pith, yaw, and wheel angles are removed as shown in Figure 2.

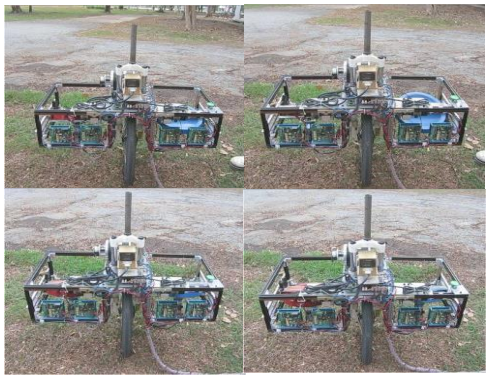


Figure 2. Unicycle robot balancing and control

The performance comparison between LQR and LQR+I summarized in Table 1 and Table 2 shows that the overshoot is reduced by 39.64% in roll angle and 250% in wheel position from the conventional LQR. This reveals that the introducing the integral action can reduce the overshoot and steady-state error.

Table 1. Simulation result of the robot using LQR

LQR	Roll	Yaw	Pitch	Wheel
Rise time (sec)	0.0622	0.0202	0.2674	3.76E-5
Settling time (sec)	4.2786	9.3275	3.8761	3.3021
Peak (rad)	0.2899	1.0447	0.0872	5.1475
Peak time (sec)	0.43	1.2611	0.0148	0.7713

Table 2. Simulation result of the robot using LQR+I

LQR+I	Roll	Yaw	Pitch	Wheel
Rise time (sec)	0.0732	0.0519	0.199	1.10E-5
Settling time (sec)	4.0617	16.484	10.0489	3.1448
Overshoot (%)	-39.64	-42.33	0	-252.69
Undershoot (%)	-142.84	-211.14	-20.38	48.44
Peak (rad)	0.2076	0.734	0.0872	1.4595
Peak time (sec)	0.7713	0.7713	0	0.5282

References

Bryson, A., Schoonwinkel, A. (1988), Design and test of a computer-stabilized unicycle, Engineering.

Dao, M.Q. and Liu, K.Z (2005), Gain-scheduled stabilization control of a unicycle robot, JSME International Journal Series C, Vol. 4, pp. 649-656.

Majima, S. and Kasai, T. and Kadohara, T. (2006), A Design of a Control Method for Changing Yaw Direction of an Underacuatted Unicycle Robot, TENCON 2006. 2006 IEEE Region 10 Conference, pp. 1-4.

Majima, S. and Kasai, T (2005), A controller for changing the yaw direction of an underactuated unicycle robot, International Conference on Technology and Automation, pp.77-88.

© 2023 Parnichkun, M., Chantarachit, S.. published by TU Delft OPEN on behalf of the authors.
ISSN: 2667-2812

https://doi.org/10.24404/63ce53a5c41c79b0ffd14020

Bicycle and Motorcycle Dynamics 2023
Symposium on the Dynamics and Control of Single Track Vehicles
18 – 20 October 2023, Delft University of Technology, The Netherlands

Vos, D.W. and Von Flotow, A.H.(1999), Dynamics and nonlinear adaptive control of an autonomous unicycle: theory and experiment, Decision and Control, 1990., Proceedings of the 29th IEEE, pp. 182-187.

© 2023 Parnichkun, M., Chantarachit, S.. published by TU Delft OPEN on behalf of the authors.
ISSN: 2667-2812

The Evolving Scholar (2023)
https://doi.org/10.59490/649dd1dceb4973f2ee0bd3e1
Bicycle and Motorcycle Dynamics 2023
Symposium on the Dynamics and Control of Single Track Vehicles
18 – 20 October 2023, Delft University of Technology, The Netherlands

Type of the Paper: Extended Abstract

Influence of Rear Wheel Vertical Displacement and Target Sag on Suspension Performance of a Cruiser Motorcycle

K. Peck[1,*], and J. Sadauckas[2]

[1] Vehicle Dynamics Group, Harley-Davidson Motor Company, Milwaukee, WI, 53222, USA; kasey.peck@harley-davidson.com; ORCID 0009-0004-8497-7691
[2] Trek Performance Research, Trek Bicycle Corporation, Waterloo, WI, 53594, USA; jim_sadauckas@trekbikes.com; ORCID 0000-0002-6055-9047
*corresponding author.

Name of Editor: Jason Moore
Submitted: 29/06/2023
Accepted: 15/08/2023
Published: 15/08/2023
Citation: Peck, K. & Sadauckas, J. (2023). Influence of Rear Wheel Vertical Displacement and Target Sag on Suspension Performance of a Cruiser Motorcycle. The Evolving Scholar - BMD 2023, 5th Edition.
This work is licensed under a Creative Commons Attribution License (CC-BY).

Abstract:

The design and optimization of two-wheel vehicle suspension provides an exciting design challenge due to the multitude of potential layouts and interrelated variables to consider. Balancing these design factors to achieve the desired *comfort* and *roadholding* performance (Lot, 2021) while also ensuring the vehicle achieves the desired trim state under the various operating conditions (Cossalter, 2006), termed *chassis control* for the purposes of this paper, requires a deep level of technical understanding to execute successfully. Consequently, a specific area of two-wheel vehicle suspension that has received little attention is defining the nominal vehicle trim state in terms of target sag and the associated proportion of vertical wheel displacement to be used in compression versus that available for rebound. For closed course racing vehicles, both on-road and off-road, the suspension displacement and target sag are determined experimentally based on testing and iteration to obtain the sole objective of minimum lap time. Conversely, for commercial on-road vehicles, suspension displacement and target sag are often constrained by numerous vehicle design requirements such as seat height and packaging limitations. These design constraints require production-intent suspension displacement and target sag to be determined early in the product development cycle. Until now, limited literature has been published regarding nominal target sag and how best to proportion suspension displacement between compression and extension, though a general guideline proposes ~33% target sag as the starting point (Thede, 2010). The intention of this paper is to provide a deeper technical understanding of suspension performance trade-offs between available suspension displacement and target sag using physical vehicle testing and multibody simulations.

In this paper, two rear suspension layouts have been tested with different suspension displacements and target sags while maintaining the same seat height and vehicle ride height. For all configurations both subjective rider feedback and objective data were collected over discrete negative (downward) and positive events. Qualitative suspension performance was captured by a professional motorcycle test rider, trained to articulate any tangible differences between the configurations on closed-course suspension events. Quantitative suspension data was simultaneously collected on the vehicle including front fork and rear shock displacement and stroking velocity, acceleration at the steer head and mid-frame, as well as vehicle pitch rate and pitch angle to correlate to subjective ride feel. The analysis of the qualitative and quantitative data yielded suspension performance metrics that were used to correlate to a multibody model. Simulation was conducted over various discrete negative and positive events of increasing size to quantify the influence of sag on suspension performance across a wider range of bump conditions.

© 2023 Peck, K., Sadauckas, J. published by TU Delft OPEN on behalf of the authors.
ISSN: 2667-2812

Table 1. Alternative rear suspension configurations compared during on-road testing

	Rear Layout #1	Rear Layout #2	Rear Layout #3
Rear Wheel Vertical Wheel Displacement [mm]	86	113	
Target Sag [% Stroke]	30%	46.7%	
Rear Wheel Rate [N/mm]	27.1	27.1	
Rebound Damper Spec.	A	A	B
Seat Height [mm]	655.3	655.3	
Compression Stroke [mm]	60.2	60.2	
Extension Stroke [mm]	25.8	52.8	

Results of the study show quantifiable improvements in both suspension *comfort* and *road holding* when using increased suspension displacements and increased sag (more available rebound stroke), though degradations to *chassis control* were noted during aggressive braking events. The increase in available extension displacement of rear suspension Layout #2 enabled a reduction in rear shock rebound damping (Layout#3) without increasing the occurrence of topping. This reduction in rear shock rebound damping improved *road holding* by allowing the rear tire to better follow the profile of negative road events and improved *comfort* through reduced forward pitching of the vehicle over discrete positive events (Cao, 2011). Additionally, the increase in available extension displacement reduced the spring preload force near full extension and enabled improved *comfort* by reducing the abruptness of discrete positive events encountered while at the extended portion of suspension stroke. Analysis of the measured vehicle data enabled the creation of objective suspension performance metrics and provided the necessary information to understand these alternative rear suspension layouts using multibody modeling. Simulation results further expanded on the performance trade-offs between the suspension displacement and target sag by enabling the analysis of additional bump configurations. Ultimately the study provided systematic guidance on the nominal suspension displacement and target sag for the specific road-going motorcycle studied and highlights sag as a critical tuning parameter often neglected in the literature.

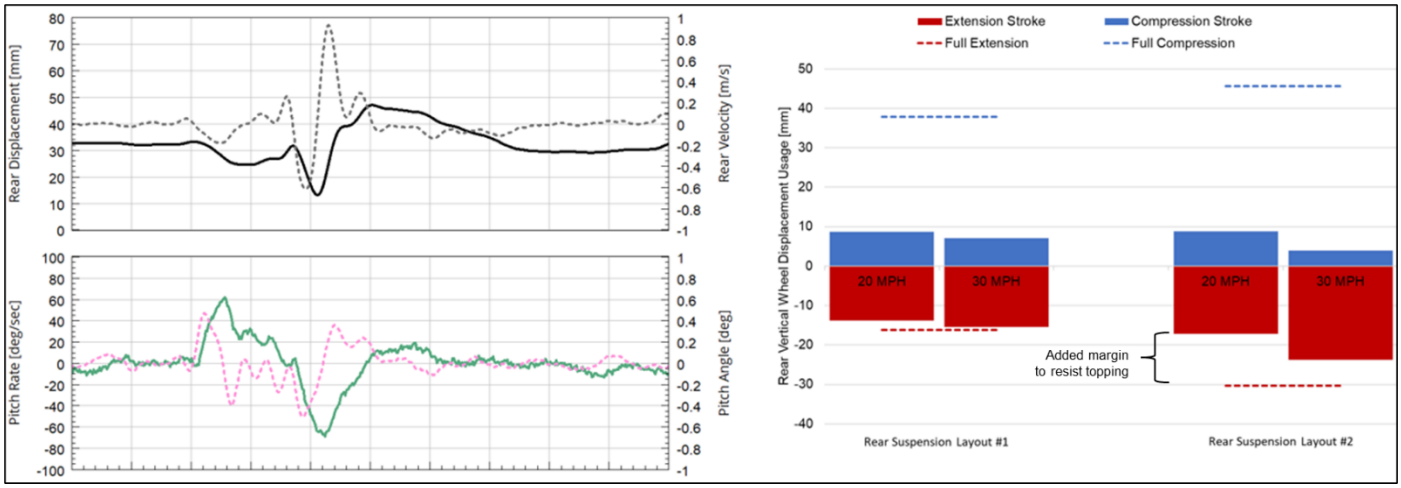


Figure 1. Left: Example of surrogate on-vehicle data over discrete negative event (step-down) including rear suspension displacement and velocity (solid black and grey dashed respectively) as well as pitch rate and pitch angle (solid green and magenta dotted). Right: Summary of compression and extension displacement usage over a discrete negative event (step-down) at both 20 and 30 mph comparing two surrogate rear suspension configurations differing in extension displacement and target sag.

References

Cao, D., Song, X., & Ahdmadian, M. (2011). Editors' perspectives: Road Vehicle Suspension Design, Dynamics, and Control. *Journal of Vehicle System Dynamics*. https://doi.org/10.1080/00423114.2010.532223.

Cossalter, V. (2006). *Motorcycle Dynamics* (2nd ed.). Lulu.com.

Lot, R., & Sadauckas, J. (2021). *Motorcycle Design: Vehicle Dynamics Concepts and Applications*. Lulu.com.

Thede, P., & Parks, L. (2010). *Race Tech's Motorcycle Suspension Bible*. Motorbooks.

© 2023 Peck, K., Sadauckas, J. published by TU Delft OPEN on behalf of the authors.
ISSN: 2667-2812

The Evolving Scholar (2023)
https://doi.org/10.59490/645be2c02d0b52c3ea6fba8d
Bicycle and Motorcycle Dynamics 2023
Symposium on the Dynamics and Control of Single Track Vehicles
18 – 20 October 2023, Delft University of Technology, The Netherlands

2-Skate-Single-Track-Vehicle without Fork-Angle, Trail or Power: Tested for Rideability, Phase-Lag and Steady-State-Lean-Angles

Author: Pierre M. Ethier[1]

[1]Independent; 26 Bérubé, St-Ferréol-les-Neiges, Québec, Canada, G0A 3R0; info@dynamik23.com; pierreethier123@gmail.com

Name of Editor: Jason Moore
Submitted: 10/05/2023
Accepted: 10/05/2023
Published: 19/06/2023
Citation: Ethier, P. (2023). 2-Skate Zero Wheel Fork-Angle Trail & Power Single-Track Vehicle tests by Many Riders for Rideability, Phase Lag and Steady-State Lean Angles. The Evolving Scholar - BMD 2023, 5th Edition.
This work is licensed under a Creative Commons Attribution License (CC-BY).

Abstract:

A 2-Skate, short for a Two-Inline-Ice-Skates-Single-Track-Vehicle, was built to show that without wheels, gyroscopic effects, fork angle, trail and power-to-the-wheels, a person could ride it. But the rider might have been a circus acrobat that can also sit backwards on his bicycle handlebar, and pedal while juggling and turning around in circle. So the present study aimed at determining if ordinary persons can ride the 2-Skate with confidence, with the same phase lag between torso and vehicle leaning when slaloming, and the same torso and vehicle lean angles in steady state curves as predicted. A protocol was designed and 12 riders tested the 2-Skates. With the exception of a 79 year old and on their first trial, they could ride it and go slaloming. Three did the phase lag and lean angle tests and obtained similar results, confirming the prediction of the Torso-Arms-Handlebar Steering Theory first presented by Ethier (1974), with differential non-holonomic and servomechanism system equations, and further explained on the web with access to recently revised equations. This confirmation (a) sheds light on how bicycles are steered, (b) clarifies that Countersteering is done automatically at low speeds, (c) supports and clarifies the way mountain bike steering is taught, (d) suggests a slight modification of the way motorcycle Countersteering is taught, (e) can be used to develop a different approach to 2-Wheeler simulators, (f) and can renew interest for motorcycles with seat belts and protective structure like the BMW-C1, and the closed-cabin electric motorcycles like the ultra-low drag and award winning Peraves e-Tracer.

Introduction: The rider of a single-track vehicle grips the handlebar, which constitutes the Torso-Arms-Handlebar or TAH mechanism. The torso leaning left of the vehicle chassis, naturally turns the handlebar to the right, due to the arms acting as links to the handlebar (Motorcycle and Bicycle Steering, retrieved February 26, 2023 https://dynamik23.com/home-2/2wheels/).



Figure 1. Rider leaning to his left naturally turns the handlebar to his right

This mechanism constitutes the detector between torso-angle and chassis-angle of a torso-chassis follower servomechanism: Above a minimal speed with the rider staying upright and the vehicle falling right, the handlebar thus naturally countersteers the handlebar to the right, generating a centrifugal force to the left, which brings it back to vertical. This explains the stability at slow speeds as soon as the hands are put on the handlebar: there is no need for gyroscopic reactions to build up with speed. And when the rider leans left to go left, the TAH mechanism naturally countersteers the handlebar to the right. The centrifugal force to the left leans the vehicle to the left, past the torso leaning, until the handlebar naturally countersteers to the left which steers the vehicle in the correct direction.

© 2023 Pierre M. Ethier published by TU Delft OPEN on behalf of the authors.
ISSN: 2667-2812

This natural control of the handlebar constitutes the TAH Steering Theory, first exposed by Ethier (1974),first published by Ethier (2000), and actually further explained on the web (Accessed February 28, https://dynamik23.com/home-2/2wheels/). Many other steering theories exist among which: (a) The Countersteering Theory itself, by which the rider voluntarily countersteers only above speeds of 19 KMH (12 MPH), says a Google Search with keywords "At what speed do you countersteer on a motorcycle". (b) Keeping balance with torso leaning right or left. (c) Gyroscopic reactions. (d) Front fork geometry, fork angle and trail. (e) "Follow your line" in mountain bike trails… But these theories fail to explain: (a) why there would be a minimal Countersteering speed, (b) why nobody in the road bicycle or the mountain bike communities ever teach or voluntarily applies Countersteering as is taught in the motorcycle community, (c) why the stable speeds with hands ON the handlebar is much lower than OFF the handlebar…

Around 2001, a 2-Skate (short for Two-Inline-Ice-Skates-Single-Track-Vehicle) was built to show that without the wheels, fork angle, trail and power to the wheels, such a vehicle was still rideable because the TAH mechanism was still present. Ethier's web site further shows that removing the mechanism leaves nothing to hold up the vehicle, which automatically falls (*2.7 Isolating factors affecting steering, using a 2-Skate*, accessed February 28, 2023 https://dynamik23.com/home-2/2wheels/proofs/#Isolating-factors-affecting-steering). But well trained circus acrobats can sit on their handlebar and pedal backwards while juggling with five balls. So perhaps Ethier is such an acrobat that can ride the 2-Skate, which cannot really be rideable by ordinary cyclists. Answering the question whether the 2-Skatre is rideable or not by cyclists, was the **objective** of the present study.



Figure 2. 2-Skate – Zero-Wheel Zero-Fork-Angle Zero-Trail and Zero-Power Single-Track Vehicle

Methodology: Equipped with a helmet and boot crampons, the rider sat on the 2-Skate. If feeling OK, he was pushed by someone else: (a) He only tried to stay up without forcing the handlebar, as he would do on a bicycle. (b) He was next asked to slalom through a line of four orange cones, each distanced 2 meters apart, to confirm his turning ability. (c) Then he was asked to do a constant slalom without the cones, left-right-left-right… towards a camera filming him. (d) He was finally asked to go straight, then do an 8 meter large right turn towards another camera, and keep on turning past it, so the camera could picture him in this large somewhat steady-state turn. Pictures, videos, personal information, and weather conditions were recorded.

Results: Twelve riders have tested the 2-Skate. A 79 year old only did the first part going straight. All others that were not acrobats but active cyclists, went riding it and slaloming as they would do on their bicycles. Constant slaloming tests clearly showed a phase lag between the rider torso lean angle to the vertical and the vehicle lean angle, as predicted by the TAH Theory and servomechanism theory. And vehicle lean angle being larger than torso lean angle was also clearly confirmed, also as predicted by the TAH Theory, further supporting it. For safety purposes, only Pierre Ethier demonstrated to them that removing the hands from the handlebar, simply let the 2-Skate keep on going and immediately fall, since nothing controlled the handlebar – or in servomechanism words: the feedback loop was removed.

Conclusions: Without wheels, fork angle, trail or motive power, the 2-Skate was easily rideable with the Torso-Arms-Handlebar or TAH mechanism present. Removing this mechanism immediately made the vehicle fall. This supports that the TAH Theory definitely explains part of what makes bicycles and motorcycles rideable and steerable. Thus this theory: (a) sheds light on how bicycles are steered, and it could be considered in any further single-track vehicle study, (b) clarifies that Countersteering is done automatically at low speeds, (c) supports and clarifies the way mountain bike steering is taught, (d) suggests a slight modification of the way motorcycle Countersteering is taught, with more emphasis on leaning towards where you want to go, (e) can be used to develop a different approach to 2-Wheeler simulators where torso lean angle would control front-wheel orientation, (f) and can be used to develop special steering means that could renew interest for development of motorcycles with seat belts and protective structure like the BMW-C1, and the closed-cabin electric motorcycles like the ultra-low drag and award winning Peraves e-Tracer.

References:

Ethier, P. M. *Dynamique des Véhicules à Deux Roues et Modifications les Rendant Plus Sécuritaires*, Master thesis in Mechanical Engineering, Laval University, Quebec, Canada, 1974, 109 pages. Access to thesis, erratum and Excel spreadsheet: Retrieved February 26, 2023 https://corpus.ulaval.ca/entities/publication/38f1aea6-fab0-4252-ae9d-d934dae1eeac

Ethier, P. M. (2000). *Motorcycle-Rider Servomechanism Steering Theory*. 2000-01-3565 Society of Automotive Engineers. 13 Pages. Retrieved February 26, 2023 https://www.sae.org/publications/technical-papers/content/2000-01-3565/

© 2023 Pierre M. Ethier published by TU Delft OPEN on behalf of the authors.
ISSN: 2667-2812

The Evolving Scholar (2023)
https://doi.org/10.24404/63fc6f89603785470204c0a6
Bicycle and Motorcycle Dynamics 2023
Symposium on the Dynamics and Control of Single Track Vehicles
18 – 20 October 2023, Delft University of Technology, The Netherlands

Type of the Paper: Extended Abstract

New design approach for leaf-springs in motorcycles

Author: Hannes Fellner[1]

E-mail: Hannes.Fellner@ktm.com[1]

Name of Editor: Jason Moore
Submitted: 27/02/2023
Accepted: 14/04/2023
Published: 26/04/2023
Citation: Fellner, H. (2023). New design approach for leaf-springs in motorcycles. The Evolving Scholar - BMD 2023, 5th Edition.
This work is licensed under a Creative Commons Attribution License (CC-BY).

Abstract:

A leaf spring is a very simple type of mechanical spring which is commonly used for heavy duty suspension systems. In single-track vehicles, such as motorcycles or bicycles, the coil and air spring are most widespread as well as current state of the art. However, the application of a leaf spring is nothing new on these types of vehicles. Various design approaches can be admired in museums. A century ago, it was even more common than the coil spring, but history shows us that this spring system has gradually been replaced due to its inherent disadvantages. In this document, we want to introduce an alternative leaf spring design and the associated benefits. One that at the core is old and simple in form but utilizes new approaches and technologies to meet the demands of modern motorcycle and improve riding behavior.

Usually, a leaf spring consists of one or more thin narrow plates that are located between the frame and axle. These are normally thicker in the middle and taper out towards the end to act as a three-point bending beam. The key point of our concept is the elimination of one connection point. Therefore, only two connection points are utilized and the spring with associated attachments is pivoted to the main frame at the upper end and to the swingarm at the lower end.

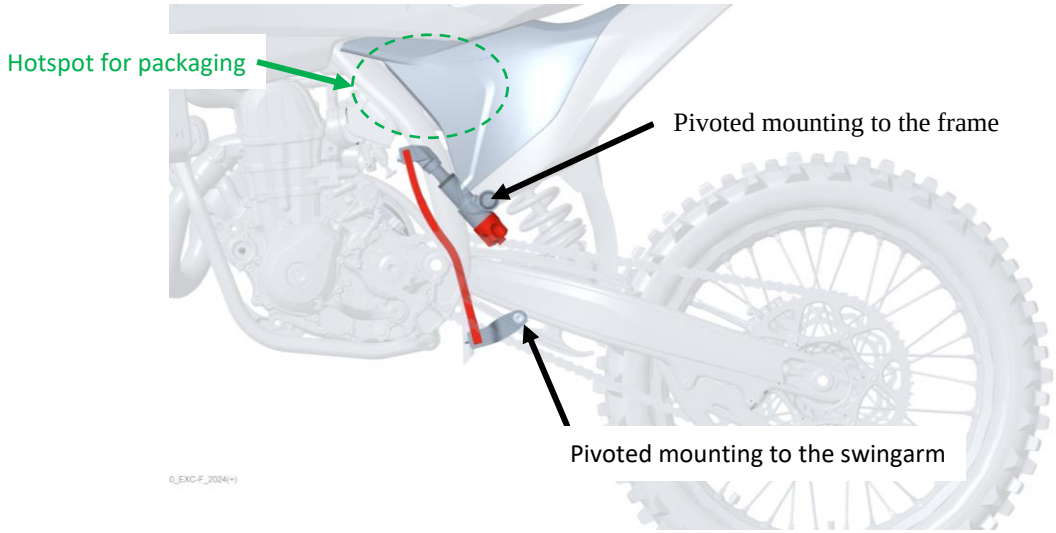


Figure 1. Positioning of the leaf spring in the motocross bike

At first glance this seems like a small step, but it fundamentally changes how the leaf spring is loaded and results in several advantages. In the following paragraphs we would like to explain a few of them in detail. The information is always presented relative to the currently standard coil spring and at the beginning of each topic the requirements of the modern offroad motorcycles are explained.

© 2023 Hannes Fellner published by TU Delft OPEN on behalf of the authors.
ISSN: 2667-2812

The first advantage is the spring material. The current coil spring is generally made from steel or titanium for motorsport applications. In contrast the leaf spring can be made from composite materials. For the sake of completeness, it must be mentioned that it is possible to have a composite coil spring, but they are very complex to produce, expensive and bigger in size. The leaf spring is comparatively easy to manufacture since it only consists of unidirectional layers. The composite material and its associated properties (high specific strength and high specific modulus) open the door for a lightweight product with small dimensions. The material properties along with the reduced unsprung mass improve comfort and NVH.

The second advantage is the spring characteristics. Demonstrated as the wheel force vs. wheel travel. A highly progressive spring characteristic is used to ensure good riding comfort at standard ride-height and sufficient suspension travel reserve in case of big suspension inputs. For motocross bikes this characteristic is typically generated by a special linkage. For the leaf spring concept, the linkage is not necessary because the progressive characteristic comes from the spring itself. Figure 2 shows the elastic deformation of the spring assembly at a fully compressed suspension condition. The rotation of the upper attachment point is essential for the increase in spring stiffness with increasing suspension travel. The amount of spring progression that is generated always depends on the spring geometry. For example, the spring design in Figure 2 more than doubles the spring rate during a full stroke (without any additional linkage).

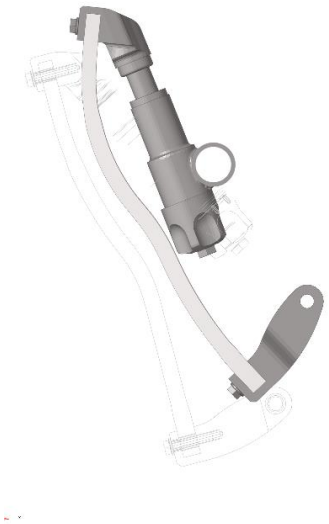


Figure 2. Unloaded spring condition (semi-transparent) and fully loaded condition

Although there are other interesting aspects to this spring concept, the last point is intended to explain the packaging advantages in terms of space requirements. The green dashed circle in Figure 1 shows a particular packaging hotspot on a modern motocross motorcycle. For the rider's ergonomics, it is particularly important that the bike is relatively slim in the area of the legs/footrests. If it is too broad, then the rider must spread his legs very wide while standing on the bike and this leads to an uncomfortable posture. At the same time packaging space must be available in that area for components such as, the air intake for the combustion engine, exhaust pipe and shock absorber. These two requirements normally contradict each other. Due to the fact that the leaf spring is placed in a different position we can improve that hotspot and generate free space which can then be used to optimize other components. While not explicitly related to the suspension, the leaf spring is a first step to improve different vehicle attributes. For example, engine performance because of the possibility to package a bigger air box.

References

-

© 2023 Hannes Fellner published by TU Delft OPEN on behalf of the authors.
ISSN: 2667-2812

The Evolving Scholar (2023)

http://dx.doi.org/10.24404/63f73e1389c3963515388e67

Bicycle and Motorcycle Dynamics 2023
Symposium on the Dynamics and Control of Single Track Vehicles
18–20 October 2023, Delft University of Technology, The Netherlands

Type of the Paper: Extended Abstract

Racebike Dynamics: The Dynamic Racebike State Plot

Feichtinger C. One [1]

[1] Institute of Automotive Engineering, Graz University of Technology; c.feichtinger@airdrop.at, ORCID 0000-0003-2082-0877
[*] corresponding author

Name of Editor: Jason Moore
Submitted: 27/02/2023
Accepted: 05/04/2023
Published: 26/04/2023
Citation: Feichtinger, C. (2023). Racebike Dynamics: The Dynamic Racebike State Plot. The Evolving Scholar - BMD 2023, 5th Edition.
This work is licensed under a Creative Commons Attribution License (CC-BY).

Abstract:

Riding a motorbike is characterised by permanent dynamics. In motorcycle racing the rider plays an important role in terms of its riding style – the relative position of the rider in different riding situations on the racetrack. From an engineering point of view the riding style has a huge impact on the center of gravity position of the overall racebike and rider system. The different rider positions also have a strong impact on the aerodynamics of the overall racebike and rider system. Additional changes during a race or test day due to external influences or internal signs of wear and tear must be considered – this applies to the rider as well as to components of the motorbike. This paper is based on the PhD thesis of Feichtinger (Feichtinger, 2021) and presents the **dynamic racebike state plot** as well as the derived quantity χ as representative caracteristic for the dyanmic of a racebike. This diagram was developed as a basis for all further analyses and investigations. It helps to identify and compare different motorbike variations and different rider types.

The dynamic racebike state plot The lean angle and the speed of the racebike are in general the leading quantities to describe the racebike state on a racetrack. Therefore, the speed – lean angle plot, or 'dynamic racebike state plot' is introduced here. Fig. 1 shows a generic, dynamic racebike state plot with the speed range of up to $300\,km/h$ for mid class racebikes. The plot contains the following information.

- **Maximum possible lean angle** ($\tan\varphi_{bike} = \mu_{lat}$) as limitation of the lateral tire friction coefficient – horizontal blue lines.
- **Design space limitation** for the lean angle – horizontal green lines. This is the mechanical limit where any part of the racebike is touching the ground. Usually this is the footrest or the lower part of the swingarm. The maximum lean angle from the design space limitation must be bigger than the maximum lean angle from the lateral tire friction coefficient. Only then, the racebike can be moved at the dynamic riding limit without touching the ground – which normally results in a crash.
- Iso-lines for **constant cornering radii** between $r_c = 10 \cdots 500\,m$ for a given, constant lateral tire friction coefficient of $\mu_{lat} = 1$. The Iso-lines are calculated using the simple relation between the lean angle and the racebike speed $tan\,\varphi_{bike} = v_{bike}^2/(r_c\,g)$. They show the maximum possible lean angle φ_{bike} for a given corner radius r_c and a given racebike speed v_{bike}.
- The **motion profile** of a track segment when the racebike is accelerating out of a left-hand corner onto a long straight is shown in the lower right corner of the plot – red line. The marked points A, B and C are also marked in the main plot. The motion profile shows the individual speed – lean angle states along this track segment.

©2023 One, F. C. published by TU Delft OPEN on behalf of the authors.
ISSN: 2667-2812

http://dx.doi.org/10.24404/63f73e1389c3963515388e67

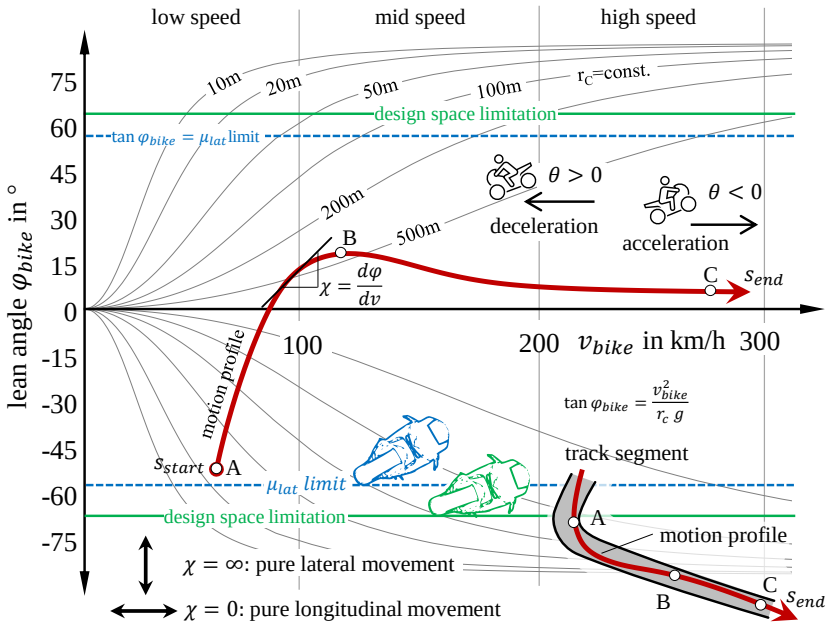


Figure 1. Dynamic Racebike State Plot (Speed – lean angle plot) with lean angle limits of the lateral tire friction and by the available design space. The diagram shows Iso–lines for a constant cornering radius relation between the lean angle and the racebike speed. The red line shows a typical motion profile on a track segment when accelerating out of a left-hand corner onto a long straight (by Christoph Feichtinger – own work).

- In the shown motion profile the racebike starts at a lean angle of $-55°$. In the first part the racebike is raised at moderate longitudinal speed changes. Then the racebike is rolling slightly in the opposite direction ($+20°$ point B), before bringing the racebike in the final upright position. The section between points B and C shows mainly a longitudinal acceleration with small lean angle changes.
- The derivative of the lean angle according to the speed, is defined here. It is denoted with the quantity chi χ, just that $\chi = d\varphi/dv$. The **new introduced derivative quantity** χ shows the slope of the motion profile in the speed – lean angle plot.
  - Chi values of $\chi = \pm\infty$ show a **pure lateral movement** of the racebike – Rolling of the racebike without any speed change.
  - Chi values of $\chi = 0$ show a **pure longitudinal movement** of the racebike – Accelerating or braking without any lean angle change.
- It is task of the rider to optimize chi χ, such that the combination of side forces and longitudinal forces on the grip level leads to a minimum lap time. The new quantity χ, combines the complete, complex dynamics of the motorbike in one size.

The dynamic racebike state plot is used for the assessment of characteristic riding situations. In the course of the work the racebike state plot and the derived quantites and riding situations are used for the assessment of the aerodynamic characteristics of a racebike on a racetrack using a motorbike mulitbody model using Jourdain's principle.

Furthermore, the dynamic racebike state plot supports the identification of riding style differences and performance relevant changes of the racebike and tires.

References

Feichtinger, C.S., (2021). *Racebike Dynamics, Aerodynamic Motorbike Model for the Dynamic Riding Limit on a Racetrack*. Monographic Series TU Graz, Graz.

©2023 One, F. C. published by TU Delft OPEN on behalf of the authors.
ISSN: 2667-2812

The Evolving Scholar (2023)

https://doi.org/10.59490/64ec6e78bc8ab0e973e0782b

Bicycle and Motorcycle Dynamics 2023
Symposium on the Dynamics and Control of Single Track Vehicles
18 – 20 October 2023, Delft University of Technology, The Netherlands

Type of the Paper: Extended Abstract

From Theory to practice: monitoring mechanical power output during wheelchair field and court sports using inertial measurement units

Marit P. van Dijk[1,*], Marco J. M. Hoozemans[2], Monique A. M. Berger[3], DirkJan H.E.J. Veeger[1]

[1]Department of Biomechanical Engineering, Delft University of Technology, Delft, The Netherlands; m.p.vandijk@tudelft.nl, 0000-0002-4900-8084; h.e.j.veeger@tudelft.nl, 0000-0003-0292-6520
[2]Department of Human Movement Sciences, Faculty of Behavioural and Movement Sciences, Vrije Universiteit Amsterdam, Amsterdam, The Netherlands; m.j.m.hoozemans@vu.nl, ORCID 0000-0001-7358-2601
[3]Centre of Expertise Health Innovation, The Hague University of Applied Sciences, The Hague, The Netherlands; m.a.m.berger@hhs.nl, 0000-0002-2014-8817
*corresponding author.

Name of Editor: Jason Moore
Submitted: 28/08/2023
Accepted: 30/08/2023
Published: 22/09/2023
Citation: Hoozemans, M., Berger, M. & Veeger, D. (2023). From Theory to practice: monitoring mechanical power output dur-ing wheelchair field and court sports using inertial measurement units. The Evolving Scholar - BMD 2023, 5th Edition.
This work is licensed under a Creative Commons Attribution License (CC-BY).

Abstract:

An important performance determinant in wheelchair sports is the power exchanged between the athlete-wheelchair combination and the environment, in short, mechanical power. To monitor the mechanical power during wheelchair sports practice, inertial measurement units (IMUs) might be used. However, a well-founded and unambiguous theoretical framework that follows the dynamics of manual wheelchair propulsion is required to validly apply IMUs for mechanical power assessment in wheelchair sports. Such a framework does not yet exist. Therefore, this research has two goals. First, to present a theoretical framework that supports the use of IMUs to estimate power output via power balance equations. Second, to create a set of guidelines on how to use IMUs to monitor mechanical power during wheelchair propulsion supported by experimental data.

Theoretical framework

To apply the mechanical power balance as defined by van Ingen-Schenau & Cavanagh (1990) to a wheelchair athlete, a suitable system must be defined. Two model options are proposed. The first, and simplest approach, is the athlete-wheelchair model (AW model), in which the athlete-wheelchair combination is modelled as a single rigid body (Eq. 1). The second model option is the wheelchair model (AW model), in which all forces, moments, and corresponding (angular) velocities, acting on the transportation object, in this case, the manual wheelchair (wc) are modeled (Eq. 2). This approach is often used in rowing and kayaking (de Vette et al., 2022). As the instantaneous power graphs of the two models differ from each other, but the models are essentially the same, both can be used to estimate the transferred mechanical power. Depending on the kinematics available, one may choose one or the other.

It follows from Eq. 1 and Eq. 2 that, to determine power output of the athlete-wheelchair combination, the following should be determined: 1) the acceleration and velocity of the COMAW (Eq. 1) or the acceleration and velocity of the wheelchair (Eq. 2), and 2) the external forces, i.e., rolling resistance, air resistance and gravity. However, measuring all variables with IMUs is not (yet) possible. To enable estimating power output from IMU data, three assumptions are proposed. Assumption 1: mean velocity and acceleration of the wheelchair are equal to mean velocity and acceleration of the COMAW over multiple propulsion cycles. Assumption 2: air resistance can be neglected during indoor wheelchair court sports. Assumption 3: the rolling resistance force during wheelchair propulsion can be determined by a ‘classic’ deceleration test.

Considering the assumptions for wheelchair propulsion, mean power that is exchanged between the athlete-wheelchair combination and the environment over multiple stroke cycles can be estimated using two IMUs on the wheelchair (van Dijk et al., 2022). The power balance resulting from these assumptions is given in Eq. 3. Here, *T* is the duration of one complete stroke cycle in seconds. If the assumptions are reasonable and the wheelchair is unmotorized, the mean power output derived from IMU data ($\overline{\boldsymbol{P_{IMU}}}$) is similar to the mean power from the athlete-wheelchair model ($\overline{\boldsymbol{P_{AW}}}$) and the wheelchair model ($\overline{\boldsymbol{P_W}}$), see Eq. 4.

$$P_{AW} = \boldsymbol{F}_{roll,COM} * \boldsymbol{v}_{COM} + \boldsymbol{F}_{air,COM} * \boldsymbol{v}_{COM} + \boldsymbol{F}_{g,COM} * \boldsymbol{v}_{COM} + m_{AW} * \boldsymbol{v}_{COM} * \boldsymbol{a}_{COM} \quad (1)$$

$$\boldsymbol{P_W} = \boldsymbol{F_{roll,wc}} * \boldsymbol{v_{wc}} + \boldsymbol{F_{air,wc}} * \boldsymbol{v_{wc}} + \boldsymbol{F_{g,wc}} * \boldsymbol{v_{wc}} + \boldsymbol{m_W} * \boldsymbol{v_{wc}} * \boldsymbol{a_{wc}} \quad (2)$$

© 2023 Dijk, M.P., Hoozemans, M.J.M., Berger, M.A.M., Veeger, H.E.J. published by TU Delft OPEN on behalf of the authors.
ISSN: 2667-2812

$$\overline{P_{IMU}} = (1/T) * \int_0^T (F_{drag} + F_{g,athlete+wc}) * v_{wc} + m_{athlete+wc} * v_{wc} * a_{wc} \quad (3)$$

$$\overline{P_{IMU}} \approx \overline{P_{AW}} = \overline{P_W} \quad (4)$$

Monitoring power using IMUs in practice

Methods: To determine the validity of the IMU model (i.e., Eq. 3) and underlying assumptions, power was estimated from IMU data during wheelchair propulsion and was subsequently compared to gold standard optical motion capture data (to obtain power values based on the P_{AW} model and P_W model). To this end, eleven participants (8 female, mean age=30±9 years, mean body mass=72±8 kg) without wheelchair experience propelled an all-court sports wheelchair on a large (3.0 x 5.0 m) treadmill at a constant velocity (1.2 m/s) and during an acceleration from 1.2 to 1.7 m/s. At the same time, kinematics were measured using two IMUs (one at the wheel axle and one at the wheelchair frame) and an optical motion capture system (with marker clusters on the wheelchair, sternum, head, upper arm and lower arm). Rolling resistance coefficients per wheel were determined from a set of drag tests according to Sauret et al. (2013). The normal forces and rolling resistance coefficients were used to determine the instantaneous rolling resistance according to Eq. 7. F_{drag} was determined by a drag test in upright position directly. Wheelchair velocity was determined from the angular velocity of the IMU on the wheel axis.

Results: Whereas the instantaneous power graphs of the three methods differ from each other, the results reveal no difference between gold standard cycle average power values and the proposed IMU-based cycle average power (1.8% mean difference, N.S.), which is constituted of the rolling resistance (estimated from drag tests) and estimated change in kinetic energy (based on wheelchair velocity and wheelchair acceleration). As the first assumption must be true over a longer time duration, kinetic energy differences between ($\overline{P_{IMU}}$) and ($\overline{P_{AW}}$) are expected to equal out. However, as the estimated rolling resistance shows a 0.9-1.7% underestimation, over time, IMU-based power is expected to be slightly underestimated as well.

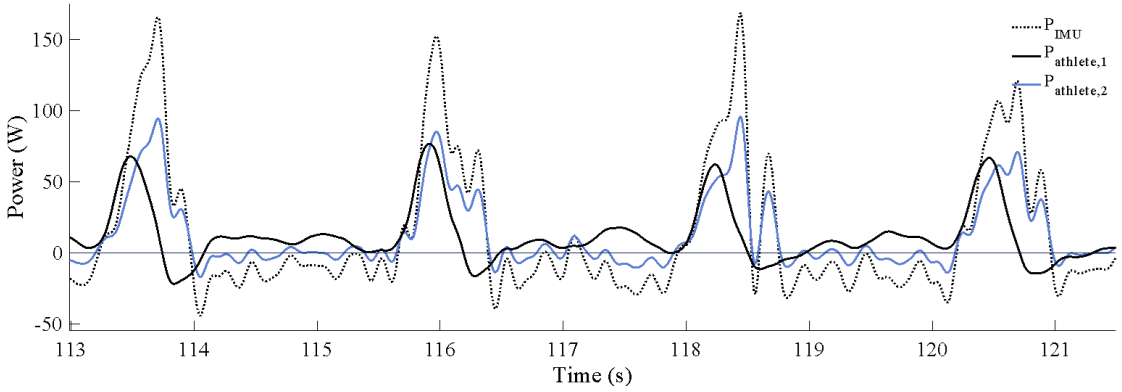


Table 3. Mean (S.D.) power and power differences per cycle averaged over three consecutive pushes

	Absolute power values in Watt			Power difference (AW model - IMU model)	
	IMU model	AW model	W model	in Watt	in % of P_{AW}
Steady state					
P	10.7 (1.0)	10.5 (0.9)	10.8 (0.9)	-.19 (.25)	-1.8%
Ekin	-0.1 (0.3)	-0.3 (0.3)	-0.2 (0.3)	-.41 (.30)*	-3.9%
Proll	10.4	10.6	10.6	.18 (.14)	1.7%
Accelerate					
P	16.4 (2.7)	15.7 (2.6)	13.9 (2.1)	-.71 (.76)	-4.5%
Ekin	4.1 (1.3)	3.3 (1.3)	1.5 (1.0)	-.81 (.73)*	-5.2%
Proll	12.3 (1.6)	12.4 (1.6)	12.4 (1.6)	.15 (.06)*	0.9%

* p-value < 0.05, ** p-value < 0.01

To conclude, with a proper drag or deceleration test, one IMU on the wheelchair frame and one IMU on the wheel axis, decent power estimations can be obtained in daily wheelchair (sports) practice. The theoretical framework and the resulting IMU-based power is thus well suitable to estimate mechanical power during straight-line wheelchair propulsion in wheelchair court sports and daily wheelchair practice, and it is an important first step towards feasible power estimations in all wheelchair (sports) situations.

References

de Vette, V. G., Veeger, D. (H. E. J.), and van Dijk, M. P. (2022). Using Wearable Sensors to Estimate Mechanical Power Output in Cyclical Sports Other than Cycling—A Review. Sensors, 23(1), 50. https://doi.org/10.3390/s23010050

Sauret, C., Vaslin, P., Dabonneville, M. and Cid, M. (2007). Drag force mechanical power during a propulsion cycle on a manual wheelchair. Computer methods in biomechanics and biomedical engineering, 10. doi.org/10.1080/10255840701478885

van Dijk, M. P., Hoozemans, M.J.M., Berger, Monique A.M. and Veeger, DirkJan H.E.J. (*under review*), From Theory to Practice: Monitoring Mechanical Power Output During Wheelchair Field and Court Sports Using IMUs. pre-print

© 2023 Dijk, M.P., Hoozemans, M.J.M., Berger, M.A.M., Veeger, H.E.J. published by TU Delft OPEN on behalf of the authors.
ISSN: 2667-2812

van Ingen-Schenau, G. J., & Cavanagh, P. R. (1990). Power equations in endurance sports. Journal of Biomechanics, 23(9). 865-81

© 2023 Dijk, M.P., Hoozemans, M.J.M., Berger, M.A.M., Veeger, H.E.J. published by TU Delft OPEN on behalf of the authors.
ISSN: 2667-2812

Chapter 2:

Papers

The Evolving Scholar Vol. 3, 2023

http://dx.doi.org/10.59490/65f84cf78af65ac695efa63b

Bicycle and Motorcycle Dynamics 2023
Symposium on the Dynamics and Control of Single Track Vehicles
18–20 October 2023, Delft University of Technology, The Netherlands

Type of the Paper: Conference Paper

Revised

A mobile recording system featuring high-precision time synchronization

[version 2; peer reviewed]

Takuro Sone[1,*], Takehiro Maeda[2], Tomoya Kitani[1]

[1] Graduate School of Science and Technology, Shizuoka University, Japan; t-sone@kitanilab.org, ORCID 0000-0002-2648-9057; t-kitani@inf.shizuoka.ac.jp, ORCID 0000-0002-1723-6197

[2] Graduate School of Integrated Science and Technology, Shizuoka University, Japan;

[*] corresponding author

Name of Editor: Jason Moore
First published: 26/09/2023
Last published: 13/05/2024
Citation: Sone, T., Maeda, T. & Kitani, T. (2024). A mobile recording system featuring high-precision time synchronization [version 2; peer reviewed]. The Evolving Scholar - BMD 2023, 5th Edition.

This work is licensed under a Creative Commons Attribution License (CC-BY).

Abstract:

In mobile environments where recording devices and subjects are in motion, integrating data collected from multiple devices requires precise location and time information. Given that high-precision satellite positioning technology provides centimeter-level accuracy and that movement speeds in mobile environments are around several 10 m/s, the required time accuracy is under 1 millisecond. However, achieving this time accuracy with commonly used devices is not typically feasible.

This paper describes a basic architecture to realize time synchronization with less than one millisecond error with an independent recorder using high-precision timing pulses (1-PPS signal) output by a GNSS receiver. Next, we propose a method to precisely identify the image capture time using an optical beacon combining multiple point light sources called GNSS Clock Beacon (GCB). The time of image capture can be determined from GCB images with an accuracy less than or equal to the exposure duration. Finally, we describe an example implementation of a mobile recording system that can be mounted on a motorcycle, which can record time-synchronized data and video with high accuracy using multiple data loggers and video equipment.

Keywords:

Motorcycle, Sensing System, Time Accuracy, Media System, Gnss

©2023 Sone, T., Maeda, T., & Kitani, T. published by TU Delft OPEN on behalf of the authors.
ISSN: 2667-2812

 http://dx.doi.org/10.59490/65f84cf78af65ac695efa63b

1 Introduction

In recent years, data collection in various application fields, such as vehicle operation records, motion analysis, 3D digital mapping, traffic monitoring, and disaster monitoring, has become active. This is due to the rapid development of equipment and analysis technologies used in various fields, such as trajectory and motion measurement of moving objects, various types of sensing, 3D shape measurement with MMS (Mobile Mapping System), video capture, and object recognition with in-vehicle cameras, and so on. As a result, it has become easier than ever to collect a large amount of diverse and high-quality data in a mobile environment. These applications share the common feature of using multiple types of equipment to record various data at various locations and times and then integrating these data to extract meaningful data. To integrate and analyze such data, it is necessary to identify both the data acquisition location and the recording time with sufficient accuracy. With the spread of high-precision satellite positioning technologies such as RTK GNSS, optaining positional accuracy on the order of centimeters outdoors. However, it is not easy to accurately determine the time to integrate data collected by commonly used equipment.

The general form of a data recorder or media recorder is a microprocessor system that reads observation data output from various input devices such as sensors, adds time information (time stamps), encodes the data, and outputs media data. Let us consider the case where multiple recording devices observe an observation target. If the observation target and recording devices are stationary and the recording devices are synchronized with each other, it is relatively easy to integrate and process the recorded data. However, in a mobile recording environment, the observation targets and recording devices are not stationary, and the recording devices generally operate asynchronously, so the recorded data cannot be integrated and processed as they are.

We will now discuss the time accuracy required when at least one of the measurement targets and the recording device is in motion. The movement speed in daily life is on the order of 10 m/s. For example, consider the case where a roadside video camera records a vehicle traveling at 36 km/h. Suppose that the video camera image can be analyzed to determine the vehicle's position in each captured frame with an accuracy of 1 cm. In this case, it is necessary to be able to determine the shooting time of each frame of the video camera with an accuracy of 1 ms to correlate the position of the vehicle measured by GNSS and the position of the vehicle identified from the image with an accuracy of 1 cm. As a similar example, to correlate the movement of a vehicle recorded by an Inertial Measurement Unit (IMU) attached to the vehicle with the movement trajectory of the vehicle with an accuracy of 1 cm, the recording time of the IMU must be known with a time accuracy of 1 ms.

For professional equipment such as video systems in broadcasting stations and audio equipment in recording studios, synchronization mechanisms such as SMPTE [1] and IEEE1588 [2] can be used to achieve high-precision time synchronization. However, these devices are usually expensive and large, and the synchronization signal must be wired to all devices. These features make them unsuitable for data collection in a mobile recording environment. Data loggers and video cameras commonly used in mobile recording environments do not have a high-precision time synchronization mechanism, making it difficult to record data with a time accuracy of 1 ms in most cases. Causes of inaccuracy of time information include the following.

1. Accuracy of the clock of the recording device
   The accuracy of the recording device's internal clock is generally insufficient. For example, it is difficult to achieve an accuracy of 1 ms using the NTP protocol [3][4][1] via a network in a mobile environment. In addition, the built-in clocks of devices that do not have network functions are generally accurate to the second and are not trustworthy at all if they are operated without being set to the correct time in the first place.

2. Stability of the built-in clock of the device
   Recording devices usually measure time-based on the built-in clock. The error of a crystal oscillator, commonly used as a built-in clock, is on the order of several 10 ppm. Therefore, an error of about one second per day may occur. For example, since the frame rate of a video camera depends on the crystal oscillator, the time on the order of 0.1 seconds is unreliable for a one-hour video recording.

3. Constraints of the media data format
   The EXIF[2] format is widely used for video and still image data, but sometimes the capture time is recorded in one-second increments, which may not be accurate enough. In addition, a mechanism for recording highly accurate position/time infor-

[1] RFC5905, https://datatracker.ietf.org/doc/html/rfc5905
[2] http://www.fifi.org/doc/jhead/exif-e.html

©2023 Sone, T., Maeda, T., & Kitani, T. published by TU Delft OPEN on behalf of the authors.
ISSN: 2667-2812

mation pairs in media data is necessary for highly accurate data integration processing. However, since there is no general standard for describing such metadata, the only way to do so is to use proprietary specifications at present.

This study will focus on synchronization mechanisms to compensate for clock setting errors and internal clock stability for consumer equipment and simple experimental devices. Since the details of the media data format problem are beyond the scope of this paper, we will only point out the problems and introduce the previous studies in Section 2.

The rest of this paper is organized as follows. First, in Section 2, standards and previous studies on time synchronization are introduced. In Section 3, the error factors affecting time synchronization are analyzed. Next, we explain a high-precision time recording method using a common data logger architecture as an example and propose a method to obtain the video capture time with high precision using an optical beacon driven by a 1-PPS signal. In Section 4, the prototype system is described and evaluated. Finally, in Section 5, we summarize the whole paper and discuss the prospects of this research.

2 Related Work

In professional broadcasting equipment, SMPTE Timecode [1] is used to synchronize video frames with high precision. In the digital audio network used in professional audio equipment, IEEE1588 [2] is used for high-precision audio sampling accuracy time management. These technologies are unsuitable for mobile recording because they require wired connections between devices, and the equipment is usually large and expensive.

Puttnies el al.'s survey paper [5] provides a survey of time synchronization studies and analyzes all techniques according to three criteria: estimation algorithms used, achievable synchronization accuracy, and experimental conditions. Zhou et al. conducted a detailed analysis of the accuracy and stability of quartz crystal oscillators in their study [6]. This study showed that the crystal oscillator's temperature dependence causes fluctuations on the order of tens of ppm.

Xinyu et al. show that time synchronization is one of the key points in decentralized real-time simulation systems and describe a time synchronization method using 1-PPS signals [7]. Siccardi et al. discuss the need to consider electrical characteristics when using the 1-PPS signal of the GNSS Receiver for precise timing systems [8]. Taufik et al. present an accuracy verification of the timing signals output by UBLOX's low-cost GNSS Receiver M8T [9]. Mengtong et al.'s paper [10] studies a system for precisely synchronizing multiple systems with a 1-PPS signal. In this study, the hardware is synchronized by 1-PPS signal without software intervention to realize a very accurate (about 50 ns) synchronization system. Guo et al. evaluated timing signals in a mixed system of GPS receivers and IEEE1588 devices to ensure the reliability of the $1\mu s$-accuracy timing clocks required in intelligent electronic devices (IEDs) used in transmission substations [11]. Lai et al. [12] describe a timing parameter calibration for Video Camera using 10×10 LED array. However, the details are not clear because we could not find any information on the specific method.

In a previous work of our research team (Ando et al. [13]), we proposed a method to determine the sampling time with high accuracy using an IMU device[3] that can record synchronous signals simultaneously with the measurements.

In Section 1, we discussed the lack of a standard mechanism for recording highly accurate location and time information in combination with media data. SDM Ontology [14] is the result of work done by another research team, including the first author, to address this issue. SDM Ontology is a spatio-temporal media ontology for comprehensively recording various metadata and media data.

3 Time Synchronization Method

The general form of a data recorder or media recorder is that the microprocessor system reads the observation data output from various input devices such as sensors, adds time information (time stamp), and then outputs the media data encoded with the observation data. Error factors in the time information added to media data can be roughly classified into two categories: those caused by the accuracy of the system's built-in clock and those caused by the system architecture.

The accuracy of the system's internal clock is a fundamental factor in discussing time synchronization. As mentioned earlier, it is difficult to synchronize an internal clock with an accuracy of 1 ms on a typical system. In the next subsection, we will introduce

[3] InvenSense™MPU9250 in [13]

©2023 Sone, T., Maeda, T., & Kitani, T. published by TU Delft OPEN on behalf of the authors.
ISSN: 2667-2812

 http://dx.doi.org/10.59490/65f84cf78af65ac695efa63b

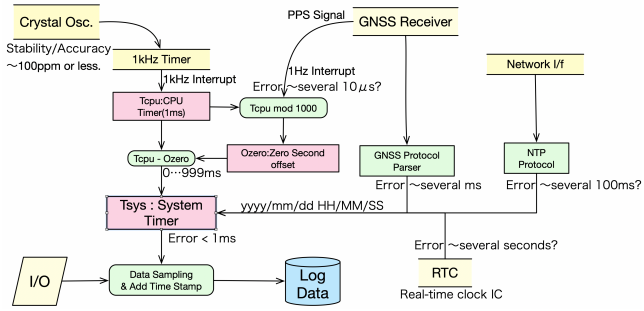


Figure 1: Typical data logger architecture

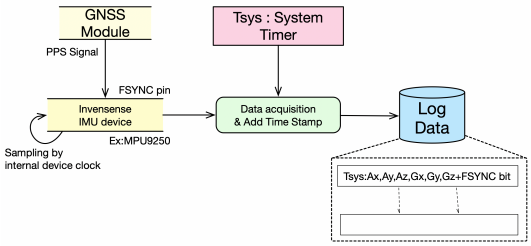


Figure 2: IMU logger architecture

a method to perform accurate time synchronization using very accurate 1-PPS signals output from a GNSS receiver based on the typical architecture of a data recorder.

Error factors attributable to the system architecture are errors caused by data processing and data transfer from the time of observation to the time-stamping process. This is rarely a problem for devices with long observation intervals or small data volumes, such as temperature and barometric pressure sensors. However, when the observation interval is short or the amount of data is large, data transfer within the device and buffering delays occur, which become error factors for specifying the observation time. In video devices, such problems are more pronounced because two-dimensional pixel data must be read out continuously at a constant frame rate. Software-induced delays can also occur, such as delays in the timing of microprocessor readout of data from input devices and the time required for data processing until time stamping is applied. In some cases, it is possible to reduce these error factors by optimizing the system hardware and software. However, when using off-the-shelf equipment or software, it is often difficult to control the time errors caused by these factors, or the amount of delay is not clearly defined.

To fundamentally eliminate the above-mentioned time synchronization error factors, capturing synchronization information at the same time as the observation of the target. Some sensor devices can record external input synchronization signals simultaneously as they read out sensor data. In the case of video cameras, this error factor can be removed by recording the optical synchronization signal as part of the image. Recording a synchronization signal superimposed on an audio signal is equally effective. In either case, the recorded data can be analyzed and the synchronization signal extracted to determine the recording time of the data with high accuracy. The details are described below.

3.1 Typical data logger time synchronization architecture

Figure 1 is an example of a typical data logger architecture in which the 1-PPS signal is input and the internal clock is synchronized by software. The basic operation of a data logger is to time-stamp data input from I/O devices and output Log Data. The System Timer (T_{sys}) in the figure is a clock managed by the system. T_{sys} is generally managed as a pair of a calendar time in seconds and a CPU timer ($Tcpu$ in the figure) with a resolution of about 1 ms. The logger CPU reads the calendar time from the real-time clock IC (RTC) at system startup. The calendar time accuracy of the RTC depends on the crystal oscillator built into the RTC, so it may contain an error of about 1 sec/day and is not reliable. After that, the time can be easily adjusted by using the data received from the GNSS receiver or the NTP protocol to ensure accuracy to the nearest second. A typical implementation is to update the $Tcpu$ value by counting the number of interrupts generated by a timer built into the CPU with a 1 ms cycle. It is also possible to implement this function by directly reading the register of the timer built into the CPU. By interrupting the CPU at the rising edge of the 1-PPS signal from the GNSS receiver and recording the value of $Tcpu$ at the timing when the interrupt occurs (O_{zero} in the figure), it is possible to make T_{sys} function as a clock synchronized with the 1-PPS signal. The accuracy of $Tcpu$ depends on the built-in crystal oscillator (Crystal Osc. in the figure) and has an error of several tens of ppm, so there is a possibility that a deviation of several tens of μs per second may occur. However, this error can be ignored since 1-PPS interrupts occur every second. On the other hand, 1-PPS interrupts may be delayed due to interrupt disable intervals and interrupt priority in the operating system (OS), device drivers, and user programs. Although both factors are implementation-dependent and the delay time cannot be guaranteed, in general, the interrupt delay time is smaller for Real-Time OS (RTOS, e.g., [15], [16]) and systems without OS compared to Linux-based OS and PC-based OS. A PC-based OS is unsuitable for this paper because there is no guarantee for response time. It has been reported [17] that the worst interrupt latency for a Linux-based OS is on the order of ms. On the other hand, empirically, a 32-bit CPU with RTOS

©2023 Sone, T., Maeda, T., & Kitani, T. published by TU Delft OPEN on behalf of the authors.
ISSN: 2667-2812

 http://dx.doi.org/10.59490/65f84cf78af65ac695efa63b

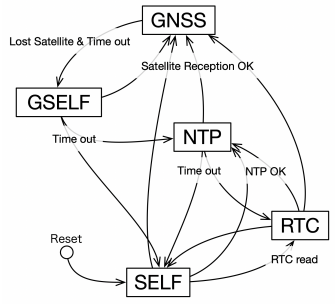


Figure 3: Timer States

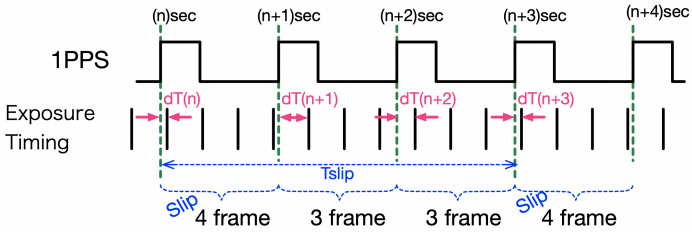


Figure 4: Time synchronization method concept

can be expected to have a delay time of less than the order of $100\,\mu s$. To achieve a time synchronization accuracy of 1 ms or less, using a system with an RTOS instead of a Linux-based OS. In any case, it is necessary to verify the system's performance by making measurements while the system is implemented to compensate for the system's time accuracy.

The accuracy of T_{sys} immediately after system startup depends on the RTC, and after the network connection is established, it depends on the accuracy of the NTP protocol. T_{sys} becomes sufficiently accurate only when the GNSS receiver can receive satellite signals. If the reception condition of the GNSS receiver deteriorates due to tunnels, the time accuracy of T_{sys} depends on the accuracy of the built-in crystal oscillator and the NTP protocol. Thus, the reliability of T_{sys} in the mobile recording environment changes with time, and the accuracy of the timestamps assigned to the Log Data also changes. Since the quality of data recorded with the low accuracy of timestamps can be regarded as deteriorated, it is necessary to take this into consideration when performing data integration processing. To take such considerations into account, it is desirable to record a reliability index for estimating the time accuracy of T_{sys} in the timestamps assigned to Log Data.

As an example of implementation, we introduce a method to manage a reliability index of clock accuracy (S_{tm}: Timer State) in pair with an internal clock (T_{sys}). S_{tm} is a state variable of a 5-state state machine with state transitions in Figure 3. Immediately after system startup, T_{sys} is uninitialized and running on its own internal clock (SELF-state), and the value of T_{sys} is not available. When the clocks are set by RTC, NTP, and GNSS, S_{tm} transitions to the RTC-state, NTP-state, and GNSS-state, respectively. The accuracy of T_{sys} is determined by these clock-setting factors. After a certain period of time without GNSS signal reception, S_{tm} times out and transitions to the GSELF-state. The reason for defining the GSELF-state is that after a loss of satellite signals, T_{sys} is driven by the internal crystal oscillator, and the accuracy of T_{sys} decreases with time so that the time accuracy of the GNSS state can no longer be guaranteed. As time passes, the accuracy of T_{sys} decreases further, and the GSELF-state transitions to the SELF-state upon another timeout. Similarly, when NTP communication is interrupted, or RTC readings fail, a timeout causes a transition to the SELF-state. The timestamp recorded by the Logger includes the current time of T_{sys} as well as S_{tm}. When integrating Log Data in post-processing, only data from the GNSS-state of S_{tm} should be used if highly accurate time synchronization is required. However, data recorded in other states are not necessarily useless, depending on the required time accuracy. The accuracy of the timestamp can be estimated from the S_{tm} value, so it is possible to judge whether the data is valid or not. From the above, it can be said that the method of recording time quality index (S_{tm}) along with timestamps (T_{sys}) is useful for controlling the time quality of logged data.

3.2 Time synchronization method for sensor devices with synchronous information

Our research team studied a method to obtain highly accurate data acquisition timing by inputting 1-PPS signals to a sensor device that can record synchronous signals simultaneously with data acquisition. The target sensor device was InvenSence™MPU9250, a 9-axis IMU device with an I2C bus connection that simultaneously records 1-PPS signals at the sampling timing. Figure 2 shows a schematic diagram of the data logger with this IMU. The MPU9250 can acquire sensor values at a specified sampling frequency f using its built-in timer. When the sampling frequency of the IMU device is set to f (For simplicity, f is assumed to be an integer), the time that data is observed immediately after the rising edge of the 1-PPS signal is in the range of $0 \sim \frac{1}{f}$ with respect to every second. If the data sampling timing of IMU is accurate, the number of samples per second is always f. However, if there is a small error in the built-in timer of IMU, the number of samples per second may be $f+1$ or $f-1$. In our study, we call such an event SLIP and show that the sampling timing can be determined by the error in $\frac{1}{f \times Tslip}$ by observing the interval $Tslip$ at which the SLIP

©2023 Sone, T., Maeda, T., & Kitani, T. published by TU Delft OPEN on behalf of the authors.
ISSN: 2667-2812

occurs. T_{sys} in Figure 2 is the time when the logger CPU reads the data from the IMU device, which is different from the sampling time of the IMU. By analyzing the synchronization signal (fsync bit) recorded in Log Data, the sampling time can be obtained with high accuracy.

Table 1 is the result of analyzing the mean and variance of the time error based on the actual measurement and is taken from [13].

Table 1: Example of Time Synchronization Error Analysis Results [13]

	without method	Proposal	
Sampling frequency (Hz)	Avg. (ms)	Avg. (ms)	Sd. (ms)
500	1.0	0.267	0.184
1000	0.5	0.136	0.101

3.3 Time synchronization of video recording devices

As mentioned earlier, it is often difficult for general image recording devices such as still cameras and video cameras to accurately record the time of image capture, but the method of synchronizing the synchronization signal to the captured image is effective in this case as well.

The simplest method is to use a video camera to capture a single LED driven by 1-PPS signal. We call this method the GNSS-1-LED method. The analysis method for time identification is exactly the same as that of the IMU logger described above. By measuring the interval of video frames when the LED synchronized with the 1-PPS signal lights up, the the capture time can be determined with high accuracy. Figure 4 shows a concept diagram of the GNSS-1-LED time identification method. The upper signal represents the 1-PPS signal, and the lower short vertical lines represent the timing of capturing video frames. For the sake of simplicity, the figure shows a frame rate f of about 3.3 fps. The number of frames captured per second can be measured based on the rising edge of the 1-PPS signal. The number of frames per second varies when the frame rate is not an integer value. In this figure, the number of frames per second is normally 3, but it can be read that the number of frames per second is 4 once every 3 seconds. In our previous study [13], we called this event SLIP. In this figure, the interval at which SLIP occurs ($Tslip$) is 3 seconds. The time difference between the rising edge of the 1-PPS and the frame immediately following it is the smallest when the SLIP occurs ($dT(n), dT(n+3)$). In our previous study, we found that $0 < dT(n), dT(n+3) < \frac{1}{3\times3}$. As a result, the time when each frame was taken can be specified with an accuracy of about 0.11 seconds.

The frame rate of a typical video camera is about 30 to 240 fps. If the frame rate is 240 fps and the SLIP interval is 10 seconds, the time accuracy can be estimated to be $\frac{1}{2400} = 417\mu$s. The average time error of the frames obtained by this method was 0.270 ms with a standard deviation of 0.147 ms, based on the LEDs driven by the 1-PPS signal at a frame rate of 240 fps on a GoPro HERO9. The frame shooting time identified using L-Beacon (see the next subsection) was the standard for verifying the time accuracy. If the internal clock of the video camera is sufficiently accurate, the time interval between the occurrence of SLIPs will be longer. If even one SLIP is successfully observed, the length of the interval before and after the SLIP can be regarded as the lower limit of the SLIP occurrence interval, which enables highly accurate time identification. If no SLIPs are observed, the time accuracy is $\frac{1}{f}$, which is the same as the case when the method of the previous study is not used.

The above is an explanation of analysis methods based on the assumption that a video camera with a stable and constant frame rate is used to capture sufficiently long videos. It is not suitable for the analysis of very short video or still camera images or for the analysis of video images with inconsistent frame rates or missing frames.

In the next subsection, we describe a method to identify the time of capture from a single image precisely by using multiple LEDs driven by a 1-PPS signal.

3.4 GNSS Clock Beacon

The purpose of using multiple LEDs is to represent the current time by the lighting pattern of the LEDs. The current time down to the second can be obtained in a known way as described in Section 3.1. The LED lighting pattern should represent the precise time information of less than one second of the current time. In this paper, devices that display precise current times based on GNSS

©2023 Sone, T., Maeda, T., & Kitani, T. published by TU Delft OPEN on behalf of the authors.
ISSN: 2667-2812

1-PPS signals are collectively called GNSS Clock Beacons (GCBs). There are various possible types of GCBs. The following sections describe the configuration and time reading performance of Linear GCBs and Matrix GCBs. These types of GCBs were selected based on the small number of LEDs used and the simplicity of the drive circuit. The number of LEDs required for each type of GCB depends on the desired time accuracy. The time precision targeted in this paper is about 1 ms, as described in Section 1. For the sake of simplicity, the following description is based on a GCB configuration that can represent time with an accuracy of about 1 ms, unless otherwise specified in advance.

1. Linear GCB
   Linear GCB is a type of GCB that represents the current time in milliseconds as a binary number. We have developed two types of Linear GCBs, L-Beacon and CL-Beacon.

   (a) L-Beacon (Linear Beacon)
   L-Beacon is the simplest Linear GCB that expresses the time in milliseconds in binary numbers using 10 LEDs. Figure 5a shows an example of L-Beacon circuit configuration, and Figure 7a shows the appearance of the prototype L-Beacon. The red LED represents the current time. The green LED is a marker to detect GCBs in the image. A 16 kHz clock signal generated by a timer is input to a 14-bit counter circuit, and the upper 10 bits of the counter are used to drive the 10 LEDs of the L-Beacon. By resetting the counter circuit on the rising edge of the 1-PPS signal, the 10 LEDs represent the current time in milliseconds as a binary number. The reason for using a 14-bit counter circuit is that the Clock signal and the 1-PPS signal are asynchronous. Using a 16 kHz Clock and ignoring the lower 4 bits of the counter, the L-Beacon is driven with an error of $-32\,\mu$s$\pm 32\,\mu$s. This error is negligible. If you use a GNSS receiver that can output multiple timing signals (e.g., ublox™M8T[4]), you can synchronize the Clock signal and 1-PPS signal. In this case, the Clock is set to 1 kHz, and a 10-bit counter can be driven to represent the current time without error.

   (b) CL-Beacon (Complemental Linear beacon)
   CL-Beacon is a GCB that expresses the current time with 21 LEDs by adding 10 inverted LEDs corresponding to each of the 10 LEDs of L-Beacon plus 1-PPS signal. Figure 5b is an example of the circuit configuration of CL-Beacon. In addition to the L-Beacon circuit, 10 LEDs with logic inversion are added. Figure 7b shows the appearance of the prototype CL-Beacon. The 10 LEDs in the bottom row are the same as those of L-Beacon, and the 10 LEDs in the top row are the logic-reversed ones. Green and blue LEDs are markers for position detection. The bottom center LED is for monitoring the 1-PPS signal. It is not used for time detection. The size of the prototype, excluding the GNSS antenna, is $105\,\mathrm{mm} \times 85\,\mathrm{mm} \times 70\,\mathrm{mm}$. The weight is about $250\,\mathrm{g}$.

2. Matrix GCB
   The Matrix GCB is a type of GCB that inputs the signals from the counter circuit included in the circuit of the Linear type GCB as drive signals for the rows and columns of the matrix LED and drives a 2-dimensional array of LED matrix. We have devised two types of Matrix GCBs, M-Beacon and CM-Beacon.

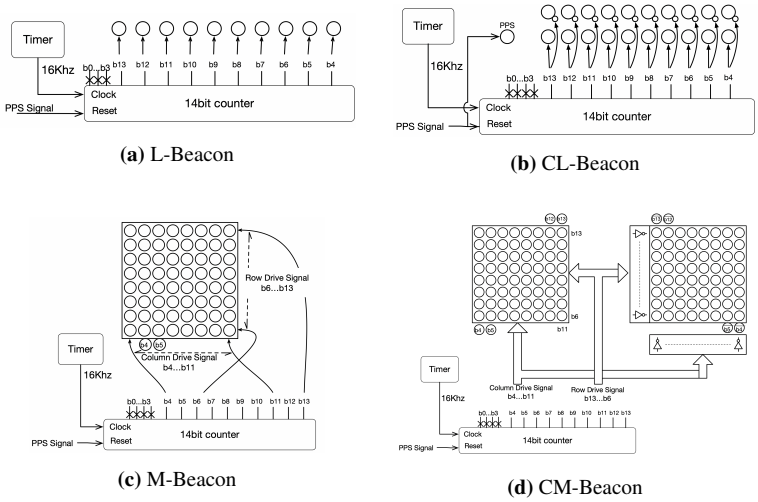
   (a) M-Beacon (Matrix Beacon)
   Figure 5c shows an example of M-Beacon circuit configuration. Figure 7c shows the appearance of the prototype M-Beacon. Since there are 10 signals from the counter circuit, it is necessary to use an LED matrix of 10×10. However, generally available LED matrix parts are limited to 8×8. To realize a 10×10 LED matrix, it is necessary to combine many discrete LEDs, and the circuit scale will become large. In this study, we prioritized the realization of GCB with the simplest circuit possible used 8×8 matrix LED parts and added the minimum necessary LEDs individually to make a prototype M-Beacon. LEDs in symmetrical positions relative to the diagonal of the 10 x 10 matrix blink in the same pattern, which is redundant for time recognition. However, removing them is difficult due to the matrix LED parts' structure, so the redundant LEDs are left as they are.

   The circuit up to the 14-bit counter is the same as that of L-Beacon. M-Beacon uses signals from the counter circuit as drive signals for rows and columns of matrix LED. The matrix LED turns on when the row and column drive signals are asserted together. As a result, the LEDs on the diagonal line of 10×10 matrix will light up in the same pattern as L-Beacon, but the other LEDs will light up in a complex pattern expressed as a product of the row and column signals. In the M-Beacon shown in this figure, b13 (pulse width 512 ms) to b6 (pulse width 4 ms) are input as row drive signals for matrix LEDs, and b11 (pulse width 128 ms) to b4 (pulse width 1 ms) as column drive signals. The positional relationship between 10×10 matrix and the LEDs implemented in M-Beacon is as shown in Figure 6. M-Beacon has independent LEDs for b4 (pulse width: 1 ms) and b5 (pulse width: 2 ms), which were not supported by 8×8 matrix. Due to an

[4]https://www.u-blox.com/en/product/neolea-m8t-series

©2023 Sone, T., Maeda, T., & Kitani, T. published by TU Delft OPEN on behalf of the authors.
ISSN: 2667-2812

 http://dx.doi.org/10.59490/65f84cf78af65ac695efa63b



(a) L-Beacon **(b)** CL-Beacon **(c)** M-Beacon **(d)** CM-Beacon

Figure 5: GCB block diagrams

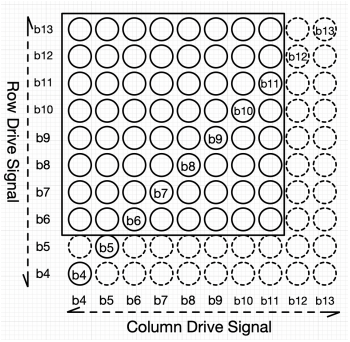
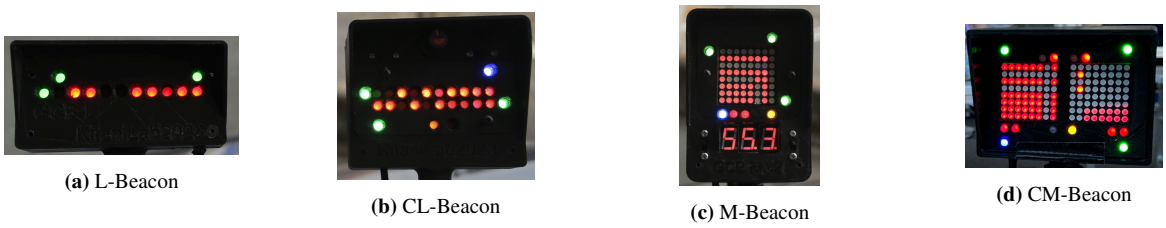


Figure 6: Location of M-Beacon LEDs in 10×10 matrix



(a) L-Beacon **(b)** CL-Beacon **(c)** M-Beacon **(d)** CM-Beacon

Figure 7: GCB prototypes

oversight at the start of the prototype, LEDs b12 (pulse width: 256 ms) and b13 (pulse width: 512 ms) are not mounted as they should be.

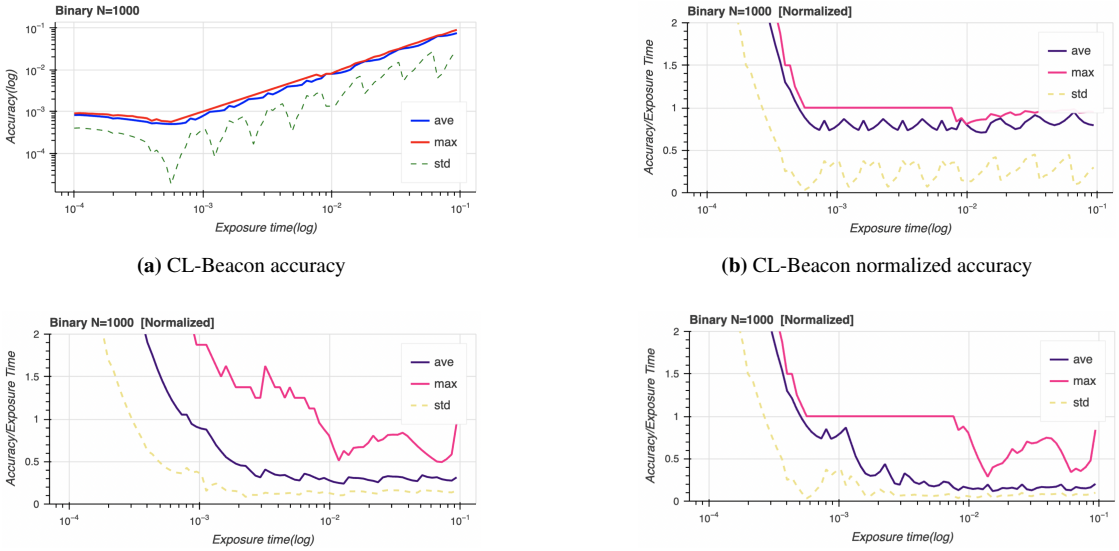
(b) CM-Beacon (Complemental Matrix Beacon)
CM-Beacon is a matrix-type beacon with an additional set of LEDs driven by inverting the LED drive signal of M-Beacon. Figure 5d is an example of CM-Beacon circuit configuration. Figure 7d shows the appearance of the prototype CM-Beacon. The left half of CM-Beacon in this figure is the same as M-Beacon, and the right half is a set of LEDs driven by a logic-reversed signal. Although the left and right LEDs are in a line-symmetrical relationship, the lighting pattern of the 8×8 matrix LEDs is not a simple inverted pattern. The size of the prototype, excluding the GNSS antenna, is $115\,\mathrm{mm} \times 85\,\mathrm{mm} \times 70\,\mathrm{mm}$. The weight is about $290\,\mathrm{g}$.

We developed a simulator and tested the accuracy of time reading from images taken by linear-type GCBs with exposure times ranging from 0.1 ms to 100 ms. As a result, it was found that the detection time may not be uniquely determined in the image taken by the L-Beacon. On the other hand, the time read from the image of CL-Beacon can always be uniquely determined, and the accuracy of the time read is less than or equal to the exposure time if the exposure time is 0.5 ms or longer. Figure 8a shows the maximum, mean, and standard deviation of the time accuracy read from the LED lighting pattern of the captured CL-Beacon image. The horizontal axis represents the exposure time when the image is taken, and the vertical axis represents the time accuracy. Figure 8b is a graph of the normalized value obtained by dividing the readable time accuracy by the exposure time. A value of 1 on the vertical axis indicates that the readable time accuracy is the same as the exposure time. This figure shows that the time accuracy of a CL-Beacon image is always equal to or lower than the exposure time if the exposure time is 0.5 ms or longer. The accuracy deteriorates at exposure times of 0.5 ms or less because the pulse width of the least significant bit of the LED is 1 ms. If the minimum pulse width is shortened by increasing the bit width of the counter, it will be possible to handle faster shutter speeds.

The Matrix-type GCBs were also analyzed in the simulator. As a result, it was found that, as in the case of linear type GCBs, M-Beacon sometimes does not have a unique time readable from the LED lighting pattern, but CM-Beacon always has a unique time readable from the LED lighting pattern. Figures 8c and 8d show the results of simulator analysis of normalized time accuracy read from the images of M-Beacon and CM-Beacon. This result shows that the matrix beacon can identify the shooting time with higher

©2023 Sone, T., Maeda, T., & Kitani, T. published by TU Delft OPEN on behalf of the authors.
ISSN: 2667-2812

 http://dx.doi.org/10.59490/65f84cf78af65ac695efa63b



(a) CL-Beacon accuracy

(b) CL-Beacon normalized accuracy

(c) M-Beacon normalized accuracy

(d) CM-Beacon normalized accuracy

Figure 8: Time accuracy analysis by Simulator

accuracy than the exposure time. In particular, the CM-Beacon clearly outperforms the CL-Beacon with an average time accuracy of about $\frac{1}{2}$ to $\frac{1}{5}$ with an exposure time of 1.5 ms or longer and a maximum value of about 1 to $\frac{1}{2}$. However, it has no clear advantage over CL-Beacon in the section where the exposure time is shorter than about 1.5 ms. M-Beacon performs worse than CL-Beacon in some sections where the maximum time accuracy exceeds the exposure time. There is also a problem that unique time may not be readable, so it can be said that there is little advantage to using M-Beacon.

To summarize the above results, we can say that CL-Beacon is superior under the condition where the exposure time is shorter than about 1.5 ms, and CM-Beacon is superior under the condition where the exposure time is longer. Therefore, a simple configuration of CL-Beacon is sufficient in conditions where the exposure time is shorter than 1.5 ms, such as daytime outdoor shooting. On the other hand, CM-Beacon is advantageous for indoor or nighttime shooting where the exposure time is longer.

4 Mobile Recording System

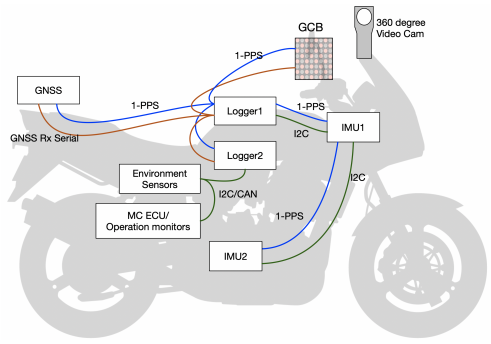


Figure 9: Motorcycle recording system overview

Figure 9 is an overview of the prototype system on a motorcycle that we have developed. Logger1 and Logger2 are data loggers. Both of them have a built-in M5Stack[5] and are capable of WiFi communication. M5Stack is a prototype microcomputer board with a 32-bit CPU and RTOS. Although not shown in Figure 9, M5Stack is connected to the Internet via a mobile router or smartphone.

[5]https://m5stack.com/

©2023 Sone, T., Maeda, T., & Kitani, T. published by TU Delft OPEN on behalf of the authors.
ISSN: 2667-2812

 http://dx.doi.org/10.59490/65f84cf78af65ac695efa63b

Logger1 and Logger2 receive serial data and 1-PPS signals from the GNSS receiver device[6] and synchronize their internal clocks with an accuracy of 1 ms. The GNSS receiver performs cm-accurate positioning 5 times per second with the built-in RTK positioning engine using the correction information obtained via the Internet. Logger1 is connected to two IMUs[7] via I2C. 1-PPS signals are also connected to the IMUs, and by embedding 1-PPS signals in some of the IMU device data, the sampling time of each IMU can be determined with high accuracy. Logger2 acquires the operation status of the motorcycle via I2C or CAN and records the time with an accuracy of 1 ms. The configuration of Logger1 and Logger2 is almost as described in Section 3.1.

By using a 360° video cam to capture images of a GCB attached to a motorcycle and analyzing the images in post-processing, it is possible to add a highly accurate time stamp to each video frame. Other video recording devices such as action cams, smartphones, and still cameras can also be used, and there are almost no restrictions on the equipment that can be used. Since GCB only identifies the time to less than 1 second, if you suspect that the internal clock of the camera equipment has an error of more than 1 second, it is recommended to add a current time display function like the M-Beacon in Figure 7c. While the accuracy of the internal clock is unlikely to be a problem for a smartphone or a video camera connected to a smartphone, the internal clock of stand-alone equipment is often unreliable in terms of time in seconds. The M-Beacon shown in Figure 7c has added hardware to display the digits of seconds of the current time on a 7-segment LEDs. By reading the 7-segment LED from the image, it is possible to determine the exact time of shooting even if the internal clock of the camera equipment has an error of ± 30 sec. If the 7-segment LED displaying the current time is driven by a dynamic lighting system, it will not be able to read the value when the exposure time is short, so it must be driven by a static lighting system. Also, care should be taken when installing the GCB on the motorcycle, since the GCB will not be readable if it is exposed to direct sunlight, if the image is missing a large portion, or if the image size is too small.

In this prototype system, two loggers and two IMUs were connected to one GNSS receiver in the motorcycle to collect data, and one video camera was used to record video. All the collected data and media data were recorded with an approximate time accuracy of 1 ms or less. To add a new logger, the 1-PPS signal from the GNSS receiver is simply shared to obtain synchronized data. It is also easy to add a video or still camera if the position allows GCBs to be captured in the image. Devices within direct range of the 1-PPS signal line can be synchronized using a single GNSS receiver. For recording devices located at a distance from each other, such as another vehicle or roadside, another GNSS receiver is required. But the time accuracy obtained is the same regardless of the location. This is the greatest advantage of using a 1-PPS signal for time synchronization.

5 Conclusion

In this paper, we focus on the increasing number of applications in which various data, such as observation data and video records collected by multiple equipment, are integrated and processed, and we discuss methods for acquiring data of the necessary quality.

Section 3 describes the basic architecture to specify the data recording time of data loggers and video recording devices with high accuracy by using the high time accuracy of the timing clock (1-PPS signal) output by GNSS receivers.

Next, the configuration and accuracy of the GNSS Clock Beacon (GCB), which is designed to determine the exposure time from an image accurately, are described and analyzed (Section 3.4). GCB is a generic term for optical beacons that use multiple LEDs driven by a 1-PPS signal to indicate the current time with an accuracy of 1 ms. At the time of writing this paper, we have analyzed four types of GCBs. Among them, CL-Beacon (Figures 5b and 7b) and CM-Beacon (Figures 5d and 7d) were found to have superior performance. Simulation-based analysis shows that CL-Beacon can identify the time with the same or lower accuracy than the exposure duration for exposure times longer than 0.5 ms. CL-Beacon is a GCB consisting of 21 LEDs with a 10-bit binary signal representing the current time (0–999 ms) in 1 ms increments and its inverted signal. The analysis of CM-Beacon using matrix LED shows that the average time accuracy is about $\frac{1}{2}$ to $\frac{1}{5}$ with an exposure duration of more than 1.5 ms. The maximum value is also about 1 to $\frac{1}{2}$, showing clearly better performance than CL-Beacon, but there is no difference in time accuracy below 1.5 ms.

Section 4 describes the configuration of a prototype system mounted on a MotorCycle as an example of a mobile recording system.

The analysis and validation work for GCB is not yet complete. We will publish more detailed results when they become available.

[6] ublox™F9P
[7] InvenSence™MPU9250

©2023 Sone, T., Maeda, T., & Kitani, T. published by TU Delft OPEN on behalf of the authors.
ISSN: 2667-2812

References

[1] SMPTE. ST 383:2008 - SMPTE standard - for television - material exchange format (MXF) - mapping DV-DIF data to the MXF generic container (standard). *ST 383:2008*, pages 1–24, 2008.

[2] IEEE. IEEE standard for a precision clock synchronization protocol for networked measurement and control systems - redline. *IEEE Std 1588-2008 (Revision of IEEE Std 1588-2002) - Redline*, pages 1–300, 2008.

[3] David L Mills. Network time protocol (NTP). Technical report, 1985.

[4] D.L. Mills. Internet time synchronization: the network time protocol. *IEEE Transactions on Communications*, 39(10):1482–1493, 1991.

[5] Henning Puttnies, Peter Danielis, Ali Rehan Sharif, and Dirk Timmermann. Estimators for time synchronization-survey, analysis, and outlook. *IoT*, 1(2):398–435, 2020.

[6] Hui Zhou, Charles Nicholls, Thomas Kunz, and Howard Schwartz. Frequency accuracy & stability dependencies of crystal oscillators. *Carleton University, Systems and Computer Engineering, Technical Report SCE-08-12*, 2008.

[7] Yao Xinyu. Time synchronization under 1PPS signal in distributed real-time simulation system. *International Journal of Intelligent Systems and Applications*, 2(2):48, 2010.

[8] Marco Siccardi, Daniele Rovera, and Stefania Romisch. Delay measurements of PPS signals in timing systems. In *2016 IEEE International Frequency Control Symposium (IFCS)*, pages 1–6, 2016.

[9] M Taufik, Yuwono, M N Cahyadi, and J R Putra. Analysis level of accuracy GNSS observation processing using u-blox as low-cost GPS and geodetic GPS (case study: M8T). *IOP Conference Series: Earth and Environmental Science*, 389(1):012041, nov 2019.

[10] Lv Mengtong and Tao Linwei. Synchronization technology and system based on 1 pulse per second signal. In *2021 IEEE International Conference on Signal Processing, Communications and Computing (ICSPCC)*, pages 1–5, 2021.

[11] Hao Guo and Peter Crossley. Design of a time synchronization system based on GPS and IEEE 1588 for transmission substations. *IEEE Transactions on Power Delivery*, 32(4):2091–2100, 2017.

[12] Hau Wah Lai, Cho Man Tsui, Kam Yuen Chan, and Aaron Yui Kuen Yan. Design of a synchronous counter with two-dimensional 10 x 10 LED array for calibration of timing parameters of video cameras. In *2019 URSI Asia-Pacific Radio Science Conference (AP-RASC)*, pages 1–1, 2019.

[13] Takashi Ando and Tomoya Kitani. A time alignment method for multiple sensing systems with GNSS timing and imus with frame-sync input. In *2020 IEEE International Conference on Pervasive Computing and Communications Workshops (PerCom Workshops)*, pages 1–6, 2020.

[14] Takuro Sone, Shin Kato, Ray Atarashi, Jin Nakazato, Manabu Tsukada, and Hiroshi Esaki. An ontology for spatio-temporal media management and an interactive application. *Future Internet*, 15(7), 2023.

[15] Fei Guan, Long Peng, Luc Perneel, and Martin Timmerman. Open source FreeRTOS as a case study in real-time operating system evolution. *Journal of Systems and Software*, 118:19–35, 2016.

[16] Masato Kamio, Keiichi Nakamura, Shinsuke Kobayashi, Noboru Koshizuka, and Ken Sakamura. Micro T-Kernel: A low power and small footprint RTOS for networked tiny devices. In *2009 Sixth International Conference on Information Technology: New Generations*, pages 587–594, 2009.

[17] Ken Watanabe. *Transister Technology*, chapter 9: Performance test! Output response speed when signal input or interrupt occurs (in Japanese), pages 98–104. CQ Publishing Co., March 2016. https://toragi.cqpub.co.jp/Portals/0/backnumber/2016/03/p098.pdf.

©2023 Sone, T., Maeda, T., & Kitani, T. published by TU Delft OPEN on behalf of the authors.
ISSN: 2667-2812

The Evolving Scholar Vol. 3, 2023 https://dx.doi.org/10.59490/65ba99129dca4c6d0c364a82

Bicycle and Motorcycle Dynamics 2023
Symposium on the Dynamics and Control of Single Track Vehicles
18 – 20 October 2023, Delft University of Technology, The Netherlands

Type of the Paper: Conference Paper

Revised

A Review on the Development of a Test Method for Motorcycle Autonomous Emergency Braking Systems [version 2; peer reviewed]

Nora L. Merkel[1,*]

[1] Würzburger Institut für Verkehrswissenschaften (WIVW GmbH), Germany; merkel@wivw.de, ORCID 0000-0002-4865-368X

*corresponding author

Name of Editor: Jason Moore
First published: 06/10/2023
Last published: 27/03/2024
Citation: Merkel, N. (2024). A Review on the Development of a Test Method for Motorcycle Autonomous Emergency Braking Systems [version 2; peer reviewed]. The Evolving Scholar - BMD 2023, 5th Edition. This work is licensed under a Creative Commons Attribution License (CC-BY).

Abstract:

In the passenger car and truck sector, assistance systems that intervene in emergency situations and thus help to improve vehicle safety have already been successfully used for many years. Although motorcyclists are subject to a high risk of suffering severe or fatal injuries in road traffic, systems that actively intervene in emergency situations are not yet available in the motorcycle sector. One reason for this is that passenger car systems cannot easily be adapted due to the motorcycle specific single-track vehicle dynamics. There are characteristic challenges that set limits to the possible application of actively intervening assistance systems. Exceeding these limits when applying an assistance system on a motorcycle could result in the occurrence of new critical situations that are no longer controllable for the rider. Still, previous research concludes that assistance systems for motorcycles have the potential to increase riding safety and identifies autonomous emergency braking systems for motorcycles (MAEB) as one of the most promising technologies (Savino et al., 2013).

One major challenge in MAEB studies is the conflict of goals between the aim to optimize the effectiveness of MAEB by identifying maximum possible decelerations that can be applied in a safe way and the wish to evaluate 'natural' rider reactions to an autonomous braking intervention. For the latter, riders should not anticipate the autonomous deceleration in order to achieve unbiased results. However, it is ethically unacceptable to determine feasible deceleration limits with unprepared study participants as approaching these limits carries the risk of provoking critical situations. During the research described in the paper at hand, a multi-phase approach was developed, in order to overcome the trade-off between achieving maximum effectiveness of braking interventions by identifying maximum feasible decelerations on the one hand and on the other hand evaluating unbiased reactions of unprepared riders. While other research groups focus on urban riding scenarios at velocities up to 50 km/h in their MAEB research (e.g., Lucci et al., 2021), the investigations described here concentrate on higher velocities as they occur in rural scenarios.

Throughout the research described in this paper, the developed investigation method was exemplarily applied to a prototype MAEB system. The paper provides an overview of the major results of all three phases of MAEB assessment. The method proves to be appropriate and delivers promising results regarding the applicability of autonomous emergency braking systems for motorcycles in the evaluated scenarios. The reproducibility of the measured rider reactions creates confidence that the corresponding effects are predictable, which means that the rider behavior does not represent a completely incalculable safety-critical factor for the application of MAEB. The successful application of the method leads to the conclusion that it can serve as a basis for the release of systems that intervene in the longitudinal dynamics. It gives manufacturers and system suppliers the opportunity to systematically prove that their systems are controllable for end users and can be applied without causing additional risks. Thus, the method can contribute to the future use of safety-enhancing assistance systems for motorcycles.

Keywords: Motorcycle Safety, Autonomous Emergency Braking, AEB, MAEB, Motorcycle, Rider Behavior, Rider State

©2023 Merkel, N.L. published by TU Delft OPEN on behalf of the authors.
ISSN: 2667-2812

Introduction

The objective of this paper is to summarize the research on MAEB that was conducted at the Institute of Automotive Engineering (FZD) at TU Darmstadt throughout since 2016. It describes the development of a multi-phase investigation method that allows to identify appropriate autonomous braking maneuvers that offer maximum effectiveness while not causing unreasonable additional risk in an already critical situation. The method consists of three phases. Each phase is represented by a study concept with a certain objective. These individual phases were developed, applied and evaluated in various research projects. As the single investigations focus on quite different aspects, they cannot stand for themselves when aiming for an evaluation of the applicability of a system. Only combined within the method described in the following, the investigations provide a comprehensive assessment of a particular MAEB.

An in-depth discourse of the contents of this paper and more details on the development and evaluation of the method can be found in the doctoral thesis *'Investigations on the Applicability of Autonomous Emergency Braking Systems for Motorcycles'* (Merkel, 2020).

Initial Situation[1]

A lot of important findings have already been generated from previous research in the field of MAEB. E.g., the potential of MAEB to increase safety for motorcyclists has been analyzed and proven based on a detailed evaluation of accident databases and simulations (Savino et al., 2013). In laboratory tests it was shown that riders are not significantly destabilized in their position on the vehicle by an unexpected deceleration and tolerate the maneuvers. Decelerations up to 3.5 m/s^2 were investigated (Symeonidis et al., 2012). However, these and other findings were gained under more or less artificial conditions, e.g., a laboratory test on sled construction (Symeonidis et al., 2012), deliberately riding towards a stationary obstacle (Savino et al., 2012), or automatic braking during free riding with no obstacle with riders informed about the purpose of the test (Savino et al., 2016). It remains to prove whether the results still apply under realistic conditions, i.e., if riders do not expect an emergency braking situation or an intervention.

Still, in terms of maximizing the effectiveness of MAEB, the finding that riders can control and accept rather low decelerations is not sufficient. It is essential to determine the limit to which autonomous emergency braking maneuvers are still controllable for motorcyclists in order to fully exploit the potential of MAEB to increase safety. Moreover, it must not only be investigated whether corresponding interventions are controllable for riders, but also if they are still accepted. Without the acceptance of the riders, the implementation of MAEB in the market cannot be realized successfully.

In order to obtain reasonable results concerning the feasibility and acceptance of MAEB, it is not sufficient to confront only prepared riders with autonomous braking maneuvers, as it is done in most of the known research. It is assumed that riders who expect the intervention (even if they do not know exactly when it will happen) will not react in the same way as those who experience the situation without any expectation. Thus, for investigating how motorcyclists handle an autonomous braking intervention and how they succeed to stabilize the vehicle, only test persons who are not informed about the aim of the experiment beforehand can be considered.

Identifying maximum controllable decelerations to achieve the greatest possible effectiveness of the intervention contradicts this desire to investigate natural rider reactions. The identification of controllability limits requires to increase interventions to critical ranges and thereby bears the risk of loss of control, i.e., destabilization of the vehicle, possibly even falls, and is consequently not justifiable from an ethical point of view.

It is therefore necessary to develop a suitable procedure that decouples the goals of *'identification of controllability limits'* and *'investigation of natural rider reactions'*. This enables both questions to be addressed without subjecting unprepared participants to an unjustifiable risk of injury and at the same time without participants' level of preparation biasing the results.

Test Method Development

The test method development is based on the assumption that for the application of an autonomous braking intervention at maximum deceleration, the rider needs to be in a so-called *ready-for-braking* state. This means that there is a certain amount of body tension

[1] This section represents the situation at the beginning of the here-described research in 2016. Up until today, various other research groups have of course also proceeded in their MAEB research. Examples for this are research on the detection of one-handed riding during the activation of automated braking (Wahl et al., 2019) and field testing of MAEB in urban riding scenarios Lucci et al. (2021).

©2023 Merkel, N.L. published by TU Delft OPEN on behalf of the authors.

ISSN: 2667-2812

 http://dx.doi.org/10.59490/65ba99129dca4c6d0c364a82

and both hands are at the handlebar in order to support initial forces and the rider is aware of the braking situation. In a situation that requires an autonomous braking intervention, these requirements are usually not fulfilled. I.e., the rider must be motivated to change from an arbitrary state to the ready-for-braking state by building up body tension, bringing the hands to the handlebar and developing situation awareness. In the following, this phase will be referred to as 'transition'. The described process is illustrated in Figure 1.

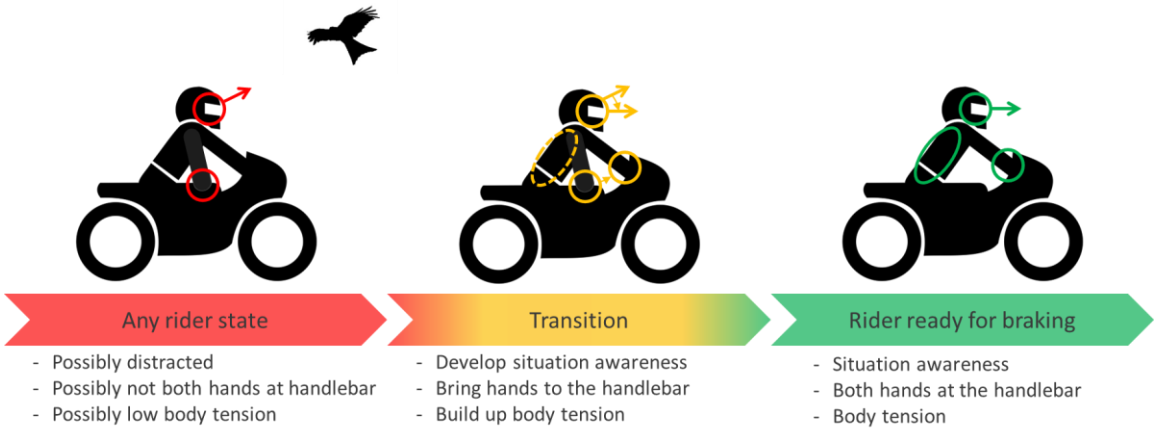


Figure 1. Phases of the rider state prior to a braking maneuver (Merkel, 2022).

Strategies to bring the rider to the ready-for-braking state before applying maximum automatic deceleration could for instance be acoustic, visual or haptic warnings. The approach chosen in the research described here is to apply a partial deceleration to initiate the transition phase. This is based on the assumption that a low-level deceleration will intuitively lead to situation awareness and causes body tension and a movement towards the handlebar automatically. The approach unites two advantages: on the one hand, there is no necessity to interpret a warning first, the transition is initiated automatically and on the other hand, velocity can already be reduced before the rider is ready for maximum deceleration and thus the effectiveness of the MAEB can be increased.

Consequently, the aim of the research is to find out how an automatic deceleration must be designed to achieve an effective initiation of the transition and which levels of deceleration are already applicable before the rider reaches the ready-for-braking state without causing a loss of control.

The method starts with a determination of controllability limits during the first phase. As stated before, an approximation to controllability limits must not be performed with unprepared participants. In this phase of the investigations, the test persons are expert riders. These experts are experienced professional riding instructors and trainers. They are assumed to be particularly suitable to assessing the skills of unexperienced riders.

To determine the most suitable design, three different deceleration profiles as illustrated in Figure 2 were investigated during the studies: a constant low-level deceleration ('block profile'), a slow buildup of deceleration ('ramp profile') and a short braking 'impulse'. The experts evaluate increasing levels of the autonomous decelerations concerning their feasibility for non-expert motorcyclists. Starting at a low level (3 m/s^2 for block and impulse, 3 m/s^3 for ramp), decelerations are increased for each intervention, until the experts assess the maneuver as no longer controllable for non-expert riders. This is repeated at various initial velocities, in order to identify possible velocity dependencies of the feasible deceleration level and for all three deceleration profiles.

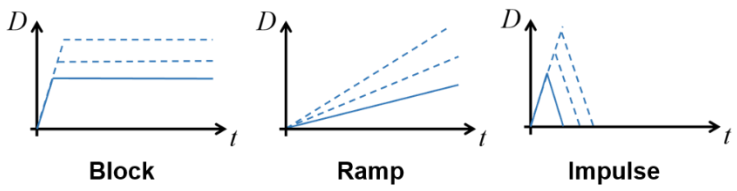


Figure 2. Braking profiles investigated during the expert study.

The parameters for controllable decelerations identified during the expert study build the basis for the second phase of the test method. In this phase, for the first time, unprepared participants (non-expert riders) experience autonomous braking interventions in a realistic emergency braking scenario (suddenly decelerating preceding vehicle). Based on reaction times, velocity reduction

©2023 Merkel, N.L. published by TU Delft OPEN on behalf of the authors.
ISSN: 2667-2812

 http://dx.doi.org/10.59490/65ba99129dca4c6d0c364a82

(compared to baseline experiments with no autonomous braking intervention) and user acceptance, the parameterized deceleration profiles are evaluated concerning their potential to increase safety for motorcyclists during emergency braking situations. This leads to the identification of the most appropriate intervention strategy.

In the third phase, which is again conducted as a participant study with non-expert riders, the method intends to analyze the reactions of riders to unexpected braking interventions in a more detailed way. It concentrates on the profile that was identified as most appropriate during the preceding first participant study. The focus of this third study is on the relative movements between the riders and the motorcycle. This includes, e.g., upper body and head displacement as well as support forces on the handlebar. A main focus is on the identification of characteristic behavior and timing. This helps to gain further knowledge about the requirements for the design of autonomous emergency braking interventions that result from characteristic rider behavior.

The three phases of the investigation method are summarized in Figure 3.

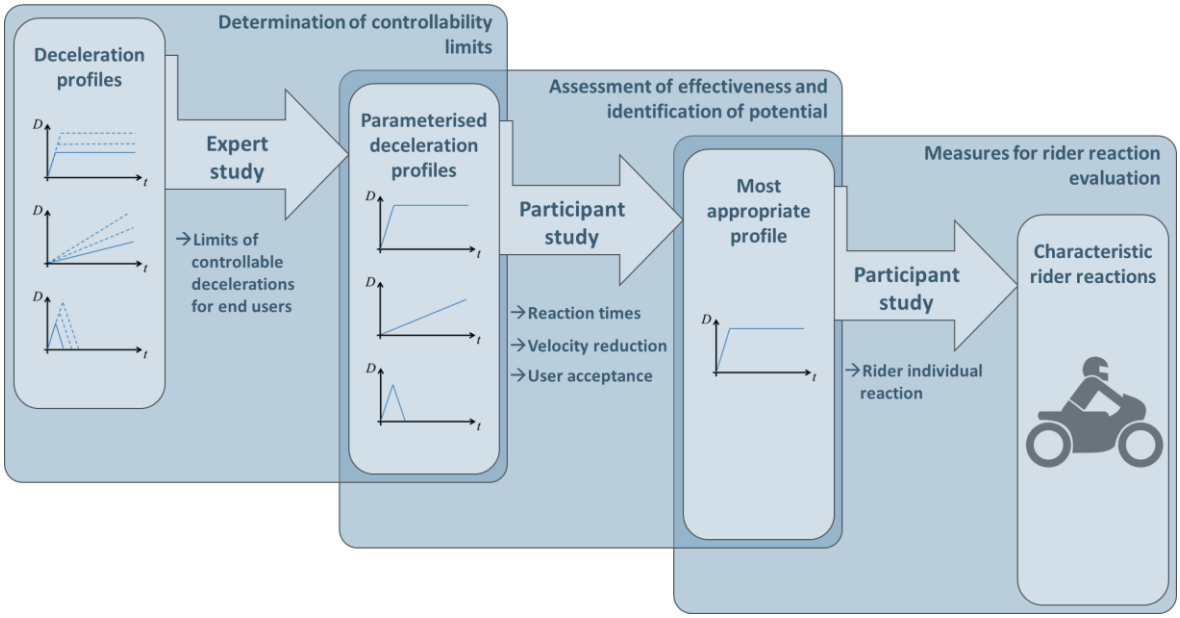


Figure 3. Three phases of the investigation method (Merkel, 2022).

Application of the Method and Results

Throughout the research described in this paper, the developed investigation method was exemplarily applied to a prototype MAEB system. All three study concepts described in the previous section were carried out on the August-Euler-Airfield in Griesheim near Darmstadt throughout various projects. The main results are summarized in the following.

Expert study – parameterization of deceleration profiles

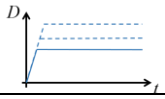
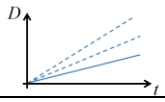
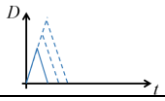
First of all, the expert study was performed with five riding trainers and instructors. While riding at a determined velocity on a straight and flat section of the test track on a measurement motorcycle, they were knowingly decelerated via remote control. The automatic braking interventions were triggered via remote control by the experiment supervisor. The experts evaluated the controllability of the three deceleration profiles at increasing levels. The determined parameters build the basis for the following participant studies. The feasible decelerations or deceleration gradients were mainly assessed for initiating the deceleration at 70 km/h, as this is the intended velocity for the participant studies (representing riding in rural scenarios). As it cannot be ruled out that the initial velocity influences the controllability of deceleration interventions, the determined limits only apply for this explicit velocity. First investigations on the velocity influence can be found in Merkel et al. (2018).

The controllability levels for unprepared non-expert riders at 70 km/h identified by the experts are shown in Table 1.

©2023 Merkel, N.L. published by TU Delft OPEN on behalf of the authors.
ISSN: 2667-2812

 http://dx.doi.org/10.59490/65ba99129dca4c6d0c364a82

Table 1. Results of the expert study (Merkel et al., 2018).

Braking profiles	Varied parameters		Determined controllability limit
Block	Level of deceleration		5 m/s^2
Ramp	Gradient		9.1 m/s^3
Impulse	Level of deceleration		4.7 m/s^2

First participant study – identification of most appropriate deceleration profile

With the knowledge on controllable deceleration (gradient) levels for non-expert riders, the first participant study was performed. The aim of this study was to examine to what extent the different deceleration profiles are suitable to assist riders in emergency braking situations and which increase of safety this can offer.

During the experiments, the riders followed a dummy target on the measurement motorcycle. At an appropriate instance (correct distance between the vehicles, correct velocity, enough straight track left), the deceleration was triggered by the experiment supervisor. Besides maneuvers with the three autonomous deceleration profiles, reference experiments without any intervention were performed in order to gain a ground truth by measuring unassisted reaction times. The study was carried out with 18 participants. With the aim of receiving unbiased assessments and to avoid habituation effects, only two braking maneuvers were performed per participant (36 runs in total). After elimination of the invalid runs, 19 braking maneuvers can be evaluated (5x block, 5x ramp, 5x impulse, 4x reference). (Merkel et al., 2019)

First of all, the reaction times to the autonomous deceleration were evaluated. During a braking maneuver, the deceleration of the vehicle causes a forward displacement of the rider's upper body relatively to the vehicle. Only when the rider adapts to the changing vehicle state, the full deceleration (not reduced by relative movement component) can also be found at the upper body. This causes a certain time lag between the vehicle deceleration and the deceleration of the rider body. This time lag represents the transition time that riders need to reach the ready-for-braking state. The upper body deceleration is measured by an acceleration sensor that is mounted to the riders' back. The additional measurements that were taken into account in order to evaluate the transition were the rising supporting force on the handlebar (time lag between rising deceleration and rising handlebar force) and reactions in terms of applying the brake or clutch levers (transition finished as soon as lever displacement is detected). These measures come directly from the measurement motorcycle. The transition times can be found in Table 2.

To evaluate the safety potential of the MAEB to increase safety for motorcyclists, the possible gain of velocity reduction during the reference reaction time was determined. The first pillar of this evaluation is the measured velocity reduction during the transition phase. The second pillar is based on a theoretical consideration: It is assumed that after the transition phase, it is possible to increase the autonomous deceleration to a maximum level. This means to determine the potential velocity reduction Δv_{Red} within the reference time T_{Ref} (reaction time from the reference experiments) for each braking profile, it is assumed that after the transition period T_{Trans}, the rest of the reference time span (1.65 s – 0.57 s) is used to decelerate at D_{max} = 7 m/s^2. The calculation is exemplarily shown for the block profile in (Equation 1). Within the transition time of 0.57 s, the velocity is reduced by 1.48 m/s (mean reduction determined during experiments). The rest of 1.08 s within the reference phase are used to decelerate at 7 m/s^2. This results in a total velocity reduction of 9.04 m/s. The results of this analysis are also shown in Table 2.

©2023 Merkel, N.L. published by TU Delft OPEN on behalf of the authors.

ISSN: 2667-2812

 http://dx.doi.org/10.59490/65ba99129dca4c6d0c364a82

$$\Delta v_{\mathrm{Red,Block}} = \Delta v_{\mathrm{Trans,Block}} + \left(T_{\mathrm{Ref}} - T_{\mathrm{Trans,Block}}\right) \cdot D_{\max} \quad (1)$$
$$= 1.48\ \frac{\mathrm{m}}{\mathrm{s}} + (1.65\ \mathrm{s} - 0.57\ \mathrm{s}) \cdot 7\ \frac{\mathrm{m}}{\mathrm{s}^2}$$
$$= 9.04\ \frac{\mathrm{m}}{\mathrm{s}}$$

Table 2. Potential velocity reduction of the deceleration profiles (Merkel et al., 2019).

Profile	Mean transition time T_{Trans} in s	Mean velocity reduction within transition period $\Delta v_{\mathrm{Trans}}$ in m/s	Potential velocity reduction within 1.65 s Δv_{Red} in m/s
Block	0.57	1.48	9.04
Ramp	1.04	1.69	5.96
Impulse	1.37	0.77	2.73
Reference	1.65	0.57	0.57

The results show that the block profile is the most appropriate strategy in order to apply a partial deceleration before riders reach the ready-for-braking state. With an average of 0.57 s, it generates the fastest transition and enables a comparatively large velocity reduction already during the transition phase due to the fast brake pressure build-up.

In addition to the analysis of the measurement data, the participants were interviewed concerning their subjective evaluation of the braking interventions. The evaluation was based on the controllability scale according to Neukum et al. (2008). Within this scale maneuvers are first rated as ‘noticeable’, disturbing’, ‘dangerous’ or ‘not controllable’. Within these categories the interventions are then classified on a finer numerical scale (see Figure 4).

Figure 4 shows the distributions of the ratings given for the different maneuvers. As expected, the reference scenarios are rated least critical. These maneuvers are mostly assigned to the lower end of the scale in the harmless range (noticeable, but not disturbing or dangerous). All but one of the block braking interventions are also rated as harmless. However, the average of 2.8 is slightly higher than for the reference braking (2.67).

On average, the ramp profile is also rated as harmless (3.4). However, the spread is larger, with several ratings in the ‘disturbing’ range. The impulse profile is rated most critically. The average rating is in the lower ‘disturbing’ range (4). But here, too, there is a scattering of ratings across the ‘noticeable’ and ‘disturbing’ ranges.

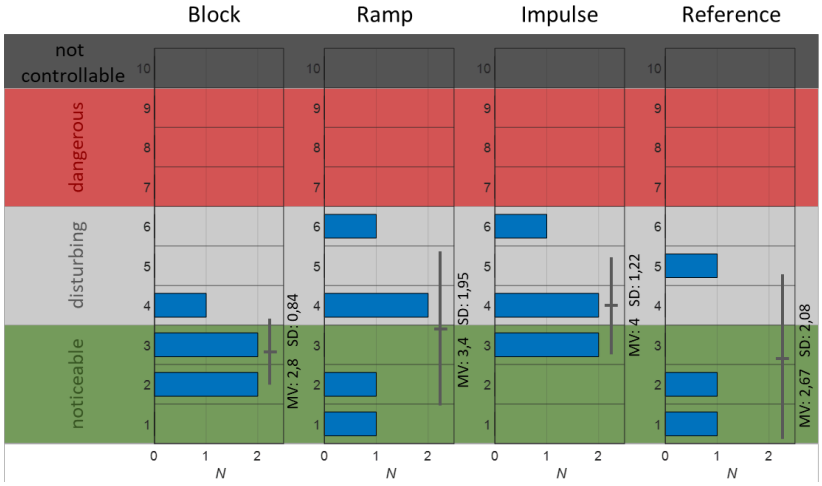


Figure 4. User acceptance of deceleration profiles (Merkel et al., 2022).

©2023 Merkel, N.L. published by TU Delft OPEN on behalf of the authors.
ISSN: 2667-2812

 http://dx.doi.org/10.59490/65ba99129dca4c6d0c364a82

Consequently, the block profile not only performs best in terms of transition time and velocity reduction (objective criteria), but also in the subjective assessment of controllability. For this reason, the second participant study concentrates on this profile.

Second participant study – analysis of characteristic rider reactions[2]

After the controllability limits for unintended decelerations and the most appropriate braking profile have been identified, the third phase (second participant study) has the aim to achieve a better understanding on how riders adapt to the changing vehicle state during a braking maneuver and thus identify characteristic behavior. In investigations on the identification of appropriate measures for such evaluations, the relative movements between the rider's upper body and the motorcycle were found to be suitable to describe the rider reactions to sudden unexpected changes of the vehicle state. Within the second participant study, these measures are used to analyze the reproducibility of the rider behavior during braking maneuvers, including a comparison of automatic braking interventions vs. maneuvers in which the riders had to apply the brakes themselves (Merkel & Winner, 2020). The upper body movements are measured by three wireless inertial measurement units that are attached to the rider's back and helmet as it is shown in Figure 5.

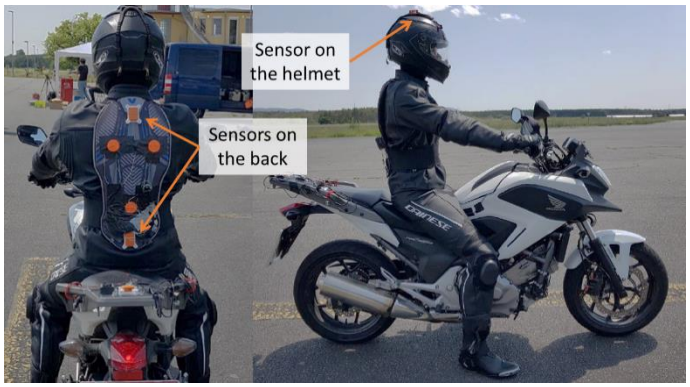


Figure 5. Sensor positions.

When the rider experiences an automatic braking intervention, due to inertial forces, the upper body moves forward. As the rider is connected to the motorcycle at the seat and the forward movement is limited by the fuel tank, this results in a pitch movement (see Figure 6) that can be measured at different points of the upper body and also at the head of the rider. We assume that the point at which the rider starts to work against the forward movement is represented by the maximum of the pitch rate. From this point the pitch is slowed down until the rider pushes him/herself back to the initial position (→ negative pitch rate).

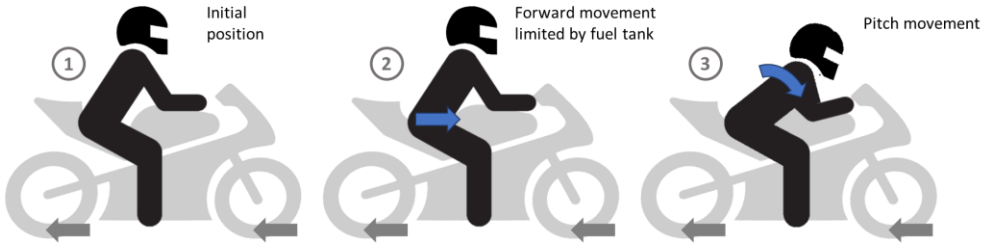


Figure 6. Relative movement of the rider during an autonomous braking intervention (Merkel, 2022).

In preparatory experiments (Merkel & Winner, 2019) the head movement appeared to be the most promising measurement to evaluate the rider adaption to the decelerating motorcycle. This assumption was based on the fact that the head movement was the best-suited measurement for the differentiation between autonomous and manual braking maneuvers (see Figure 7). However, this analysis was limited by the fact that it was based on data from only one rider.

[2] Large parts of the text in this section have already been published in Merkel & Winner (2020). Nevertheless, it is important to repeat it here, as the results are an integral part in the overall context of the here-described investigation method. Permission to use was granted by the editors.

©2023 Merkel, N.L. published by TU Delft OPEN on behalf of the authors.

ISSN: 2667-2812

 http://dx.doi.org/10.59490/65ba99129dca4c6d0c364a82

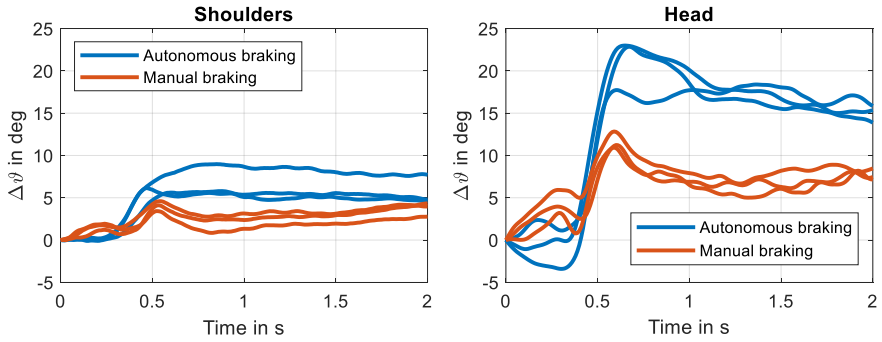


Figure 7. Pitch movement during braking maneuvers: shoulder vs. head (Merkel & Winner, 2020).

The actual second participant study was conducted with 14 participants (1 run per participant, 12 valid maneuvers). Assessing the data from these experiments, it turns out that comparing different riders, the reaction to an automatic braking intervention is very homogenous for the upper body (measured at the shoulder and lumbar spine level), whereas the head movement can differ significantly (Merkel & Winner, 2020, see Figure 8).

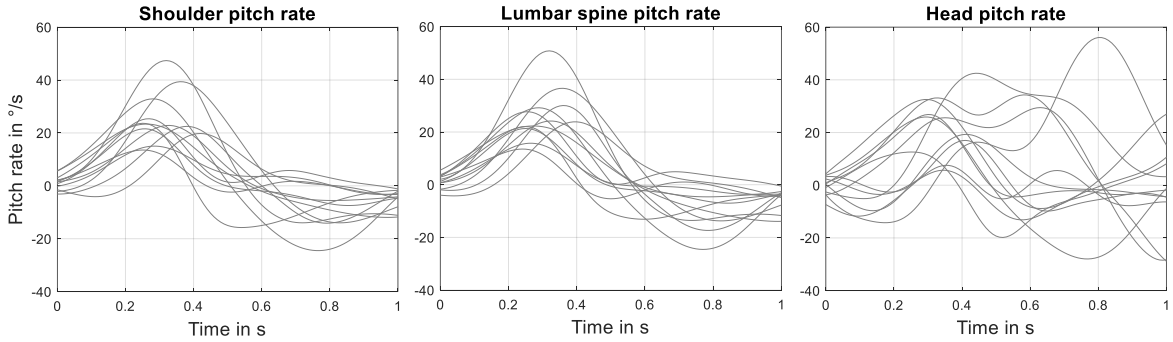


Figure 8. Body pitch rates for all participants after the beginning of an autonomous deceleration (Merkel & Winner, 2020).

The maximum of the pitch rate (rider starts counteracting the forward movement) was analyzed for shoulder, lumbar spine level and head for all riders. For the analysis, the time at which the maximum is reached is particularly interesting. The absolute maximum pitch rates are subject to a lot of influencing factors (e.g., body measurements of the rider), so they are barely comparable. Time $t = 0$ represents the beginning of the brake pressure increase.

As Figure 8 shows, the pitch rates at the shoulder and lumbar spine level follow a characteristic behavior, while the head movement can differ. This can be explained by the fact that the cervical spine is the most flexible part of the spine and the rider might for example raise or lower the head during the maneuver to get a better overview of the situation. This partially occurring difference between the back and the head movement can also be found by comparing the time of the maximum pitch rate over all 12 valid runs. While the mean time of the maximum pitch rate is still very close for shoulder, lumbar spine and head, the standard deviation is significantly higher for the head. It is about twice as high as for shoulder and lumbar spine (see Table 3).

Table 3. Mean time for maximum pitch rate over all riders in the AEB maneuvers (Merkel & Winner, 2020).

	Mean time of max. pitch rate & std. dev. in s	**Min. time** of max. pitch rate in s	**Max. time** of max. pitch rate in s
Shoulder	0.32 ± 0.06	0.26	0.43
Lumbar spine	0.31 ± 0.05	0.25	0.41
Head	0.33 ± 0.12	0.02	0.46

The homogeneity of the upper body movements in autonomous braking maneuvers cannot be retrieved in the maneuvers in which the riders had to apply the brakes themselves. In these cases, the pitch rate curves differ a lot between the riders. This can be

©2023 Merkel, N.L. published by TU Delft OPEN on behalf of the authors.

ISSN: 2667-2812

explained by the fact that in the manual maneuvers, the deceleration profiles vary significantly. For example, some riders build up brake pressure very fast as soon as they notice the deceleration of the target vehicle and then slowly release the brakes again, while others apply the brakes smoothly and observe the situation and increase the deceleration when they get quite close to the target vehicle. Furthermore, the body movement is not a pure reaction to the changing vehicle state anymore. The rider initiates the deceleration consciously and thus can prepare for it, e.g., by building up body tension prior to applying the brakes. Some riders even show a negative pitch rate while applying the brakes, i.e., they straighten up during the maneuver. The diagrams in Figure 9 show the body movements for all participants in the manual braking maneuvers.

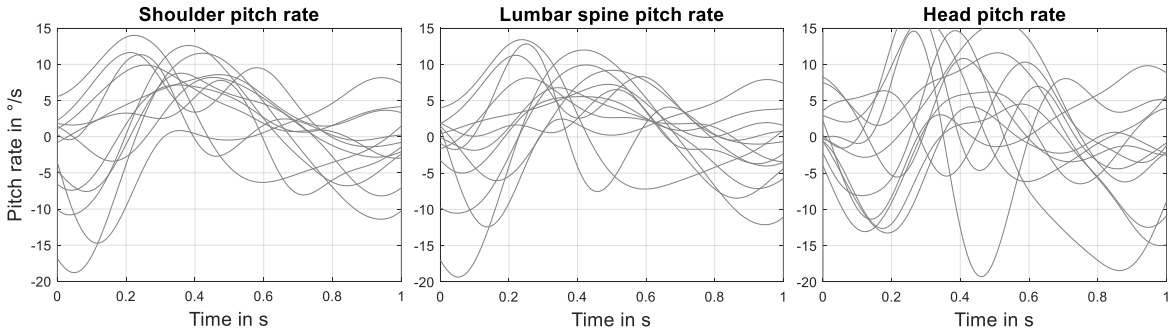


Figure 9. Body pitch rates for all participants in the manual braking maneuvers (Merkel & Winner, 2020).

The observations regarding the manual braking maneuvers allow the conclusion that the automatic braking interventions help to make the rider reaction 'controllable' or at least predictable. By provoking an unintentional rider reaction, influences of rider individual (conscious) behavior are interrupted and a characteristic process is initiated. The experiments show that while the rider behavior in rider-induced braking maneuvers is quite inhomogeneous, the unintentional reactions to automatic braking interventions follow a certain pattern. This creates confidence that it is possible to estimate rider reactions when designing automatic braking interventions and to use this knowledge to develop autonomous emergency braking systems that can be used at low risk.

While the head movement appeared promising in preparatory investigations as it showed the most significant differentiation between different maneuvers for one individual rider (Merkel & Winner, 2019), the experiments described in this paper show that this measure shows a clear weakness in terms of reliability and reproducibility when comparing various riders. Thus, the head movement cannot be seen as a reliable measure to evaluate if a rider has achieved the ready-for-braking state.

It has been shown that the pitch movement of the rider's upper body is a more reproducible measure to describe the rider reaction during automatic braking interventions. This measure stays within a slim corridor for all evaluated maneuvers and all riders. Due to the low flexibility of the spine between the lumbar spine level and the shoulder level, the pitch rates at both measuring points stay very close. For future studies this creates confidence that one single pitch rate sensor at the back might be sufficient.

An additional conclusion of the study is that the homogeneity of the rider reactions in autonomous braking scenarios is quite promising regarding the possibility to evaluate the controllability of MAEB systems in studies with relatively small numbers of participants and to transfer the results to a larger number of riders.

Summary of the study results

The multi-phase study concept developed as described at the beginning of this paper was completely run through during the here-described research within the framework of various projects. For a prototype system, controllable parameters for different deceleration profiles were determined in an expert study. Subsequently, the parameterized profiles were examined in a participant study with non-expert riders. In this study, the effectiveness and acceptance of the autonomous interventions were assessed. The prioritized (block) profile was applied in another participant study in order to generate a better understanding of the reaction of unprepared riders to unanticipated braking interventions in terms of characteristic patterns and reproducibility.

The controllability limits determined in the expert study were used to set the parameters of the deceleration profiles for the first participant study. Unprepared riders were confronted with the parameterized interventions and the effectiveness (measured by the possible velocity reduction) and acceptance of the interventions were examined. From the acceptance (interventions are never perceived as 'dangerous' in the subjective evaluation) and the absence of loss of control, it can be concluded that an early expert study is suitable for determining appropriate parameters for an automatic braking intervention. The experts' assessment of the controllability of the partial braking profiles is confirmed.

©2023 Merkel, N.L. published by TU Delft OPEN on behalf of the authors.

ISSN: 2667-2812

From the results of this first participant study, the deceleration profile ‘block’ emerges as the most promising design of autonomous deceleration during the transition phase. The clear benefit to the ramp profile in second place with regard to velocity reduction (32.5 km/h for block vs. 21.5 km/h for ramp within the reference period) allows all other profiles to be discarded and the block profile to be exclusively applied for further investigations.

The investigation of the riders’ individual reaction to the intervention in the second participant study shows that the involuntary physical reaction to an automatic braking intervention follows a characteristic pattern across all participants. The reactions stay in such a narrow corridor that the conclusion suggests that the automatic intervention even contributes to making the rider reaction ‘controllable’ or at least predictable. The homogeneous rider reactions observed in this part of the study create confidence that in the future, even small samples of test persons will be sufficient to obtain meaningful results for the investigation or release of MAEB.

The determination of the pitch rate maximum on the rider’s upper body as the peak of the almost symmetrical transition phase confirms the result of the first participant study for the block profile. The pitch rate maximum occurs after about half (0.32 ± 0.06 s) of the transition duration determined there (0.57 ± 0.1 s). However, due to the much smaller scatter in the timing, the pitch rate turns out to be a more reliable measure.

Review of the Method and Conclusion[3]

Motivated by the challenges described at the beginning of the paper regarding the investigation of active interventions by assistance systems on motorcycles, a method was developed that allows to determine controllability limits of a MAEB without exposing test subjects to an increased risk compared to everyday motorcycling. At the same time, the method allows to investigate natural reactions of unprepared riders that do not anticipate the emergency braking situation to occur.

The method was successfully applied to a prototypically implemented system (no environment detection, remote-controlled triggering of braking interventions) and proved to be practicable. It could be shown that automatic braking interventions on motorcycles are basically applicable and, within suitable limits, do not add unreasonable hazard (beyond the risk usually assumed for motorcycling) to the rider.

The development and validation of the method has the potential to contribute to the future release of autonomous emergency braking systems for motorcycles. It opens the opportunity to manufacturers to systematically demonstrate that their developed systems are controllable for users and can therefore be used without creating an additional hazard. From the third part of the study (second participant study) follows the assumption that the involuntary rider reaction is channeled into a controllable path by the unexpected intervention. With respect to this finding, it may be sufficient that a simplified participant study follows an expert study. If a certain braking profile has already been specified, the determination of the safety potential can be omitted in the second study. It then only serves to validate the controllability limits determined by the experts and allows to evaluate the acceptance. The controllability evaluation can be carried out, for example, according to the Response Code of Practice. According to this procedure, an 85 % controllability level is proven if in a study with unprepared participants, 20 out of 20 valid runs fulfil the ‘pass’ criteria (Brockmann, 2009).

False positive interventions can also be covered with a similar procedure. If it cannot be ruled out that a MAEB generates false positive interventions, it must be ensured that these are controllable. The determination of the basic controllability limits could also be realized with an expert study, while in the second phase, the controllability is assessed according to a procedure described by Neukum (2015).

The measures determined in the third part of the study to describe rider reaction first of all serve to prove that rider behavior during an automatic emergency braking intervention is reproducible. Once the controllability has been proven for a system, the rider's movement does not need to be permanently recorded. The parameterized deceleration profile can be applied to initiate the rider's transition to a ready-to-brake state, and after a conservatively estimated transition time, the deceleration can be increased to a maximum possible level. Nevertheless, it is conceivable that, in the future, interventions could even be adapted to the individual rider by means of real-time monitoring of the rider's state. For example, riders who show particularly short transition times could be given maximum deceleration earlier and an even greater velocity reduction could be achieved. However, it remains to be

[3] Contents of the review and limitations sections are translated from Merkel (2022). The source is licensed under the CC BY-SA 4.0 license.

©2023 Merkel, N.L. published by TU Delft OPEN on behalf of the authors.

ISSN: 2667-2812

discussed whether, with already very short transition times (well below 1 s), the additional effort for continuous recording and processing of the rider's state is justified.

Limitations and open research questions[3]

In the described research, all studies were performed with the same motorcycle. The extent to which the vehicle geometry influences the limits of controllability and the subjectively perceived criticality remains to be clarified in the future (e.g., touring motorbike with upright seating posture and high, wide handlebars vs. sports motorbike with crouched posture and low stub handlebars).

In the expert study, first impressions were gathered on the influence of the initial speed on controllability limits. However, further investigations are needed here with broader coverage of different speed ranges. Especially with regard to urban riding in the (unstable) low velocity range, further investigations are indispensable if a MAEB is also to be used in this area. The same applies to automatic deceleration during cornering. It can be assumed that in certain roll angle ranges automatic decelerations can no longer be controlled, which has already been indicated withing the expert study (Merkel et al., 2018). However, further investigations are necessary here.

In the described tests, the automatic decelerations were maintained in the safe test environment until the vehicle came to a standstill. Under real conditions (e.g., with following traffic), it can be assumed that automatic braking will be terminated at a certain point, e.g., when the risk of collision has been neutralized, or in order to let the rider take full control of the vehicle's longitudinal dynamics. Here, too, it is necessary to investigate how the deceleration is to be degraded. As with the buildup, involuntary rider reactions are to be expected when deceleration is released, which - just as the initiation of braking - must not destabilize the rider-vehicle system. The degradation is also particularly relevant when any cancellation criterion is reached, e.g., if the rider decides to perform an evasion maneuver during the deceleration and reaches a roll angle that is defined as an operational limit. Here, it must in any case be avoided that in an already critical situation (roll angle build-up during an automatic braking maneuver) an additional potential destabilization occurs due to an unsuitable degradation of the deceleration.

The ideal conditions given in the described studies (rider has both hands on the handlebars, attention is on the riding task) are not always given in real traffic. For example, operating navigation or communication systems can lead to one-handed or even freehand riding, the rider could take his eyes off the road or stand on the footrests instead of sitting in the saddle. It is precisely in such situations of distraction that the intervention of an assistance system may become necessary. If an automatic braking intervention is not ruled out by the system in such cases, the controllability must also be ensured in the event of such so-called misuse cases, and thus must be investigated.

In addition to cases of misuse, the rider reaction in cases of false positive interventions also must be considered. As described above, the first reaction to an automatic braking intervention is an involuntary effect following physical laws. Therefore, no difference in the rider reaction is to be expected in the first moment under the same riding conditions (apart from the lack of a potential collision partner). Nevertheless, it must be ensured that the rider does not subsequently take an undesirable action that leads to a critical condition due to a lack of understanding or misinterpretation of the situation. Thus, false positive interventions represent another future research question.

Beyond the investigation of MAEB, future research could deal with the transferability of the presented method to the investigation of other actively intervening assistance systems for motorcycles.

Ethics

Ethical approval for the participant studies was obtained from the Ethics Commission of the Technical University of Darmstadt under the references EK 32/2018 (first participant study) and EK 39/2019 (second participant study).

Acknowledgements

The described research was conducted during my time as a research associate and doctoral candidate at the Institute of Automotive Engineering (FZD) at the Technical University of Darmstadt. I would like to express my gratitude to my supervisor Prof. Dr. rer. nat. Hermann Winner for giving me the opportunity to work on this topic and for providing me with advice and support at all times.

©2023 Merkel, N.L. published by TU Delft OPEN on behalf of the authors.

ISSN: 2667-2812

References

Brockmann, M. (2009). Code of Practice for the Design and Evaluation of ADAS. http://www.acea.be/publications/article/code-of-practice-for-the-design-and-evaluation-of-adas, 2009. Access: 17-11-2021.

Lucci, C., Marra, M., Huertas-Leyva, P. Baldanzini, N. & Savino, G. (2021). Investigating the feasibility of Motorcycle Autonomous Emergency Braking (MAEB): design criteria for new experiments to field test automatic braking. *MethodsX*. Volume 8, DOI: https://doi.org/10.1016/j.mex.2021.101225.

Merkel, N. L. (2022). *Untersuchungen zur Anwendbarkeit Automatischer Notbremssysteme für Motorräder*. Dissertation, Technische Universität Darmstadt, Darmstadt, Germany. DOI: https://doi.org/10.26083/tuprints-00021096

Merkel, N. L., Pleß, R., Scheid, K., Winner, H. (2018, October 1-2). Einsatzgrenzen automatischer Notbrems-systeme für motorisierte Zweiräder – eine Expertenstudie. In Institute for Motorcycle Safety e.V. (Ed.), *Proceedings of the 12th International Motorcycle Conference 2018*, Cologne/Online, Germany, 2018.

Merkel, N. L., Pleß, R., Winner, H., Hammer, T., Schneider, N., Will, S. (2019, June 10-13). Tolerability of Unexpected Autonomous Emergency Braking Maneuvers on Motorcycles – A Method for Experimental Investigation, In: *Conference on the Enhances Safety of Vehicles (ESV)*, Eindhoven, Netherlands, 2019.

Merkel, N. L., Pleß, R.; Winner, H., Hammer, T., Schneider, N., Will, S. (2022). *Automatische Notbremssysteme für Motorräder - Abschlussbericht zum Projekt FE 82.0661/2015*. Berichte der Bundesanstalt für Straßenwesen, Reihe F: Fahrzeugtechnik (147), Fachverlag NW in der Carl Ed. Schünemann KG, Bremen, 2022.

Merkel, N. L., Winner, H. (2019, September 9-11). Measures for the Evaluation of Riders' Adaption to the Changing Vehicle State during Autonomous Emergency Braking Maneuvers on Motorcycles, In *Symposium on Bicycle and Motorcycle Dynamics*, Padua, Italy, 2019.

Merkel, N. L., Winner, H. (2020, September 1 - October 6). Characteristic Rider Reactions to Autonomous Emergency Braking Maneuvers on Motorcycles. In Institute for Motorcycle Safety e.V. (Ed.), *Proceedings of the 13th International Motorcycle Conference 2020*, Cologne/Online, Germany, 2020.

Neukum, A. (2015). Beherrschbarkeit fehlerhafter Eingriffe in die Fahrzeugquerdynamik. In Kompaß, K. (Ed.): *Fahrerassistenz und Aktive Sicherheit, Haus der Technik Fachbuch*. expert verlag, Renningen, 2015.

Neukum, A., Lübbeke, T., Krüger, H.-P., Mayser, C.. Steinle, J. (2008). ACC-Stop&Go: Fahrerverhalten an funktionalen Systemgrenzen. In Maurer, M.; Stiller, C. (Eds.): *5. Workshop Fahrerassistenzsysteme - FAS2008*. Karlsruhe, Germany, 2008.

Savino, G, Giovannini, F, Baldanzini, N, Pierini, M. & Rizzi, M. (2013). Assessing the potential benefits of the motorcycle autonomous emergency braking using detailed crash reconstructions. In *Traffic injury prevention*, 14, 40–49. DOI: https://doi.org/10.1080/15389588.2013.803280

Savino, G., Pierini, M., Thompson, J., Fitzharris, M., Lenne, M. G. (2016). Exploratory field trial of motorcycle autonomous emergency braking (MAEB). In *Traffic injury prevention (8)*, 17, 855–862, 2016.

Savino, G., Pierini, M., Baldanzini, N. (2012). Decision logic of an active braking system for powered two wheeler. In *Proceedings of the Institution of Mechanical Engineers, Part D: Journal of Automobile Engineering (8)*, 226, 1026–1036, 2012.

Symeonidis, I., Kavadarli, G., Schuller, E., Graw, M., Peldschus, S. (2012). Analysis of the stability of PTW riders in autonomous braking scenarios, In *Accident Analysis and prevention*,49, 212–222, 2012.

Wahl, A., Schmälzle, P., Klews, M., Henzler, M.. (2019, September 9-11). Detection of One-Handed Riding during Activation of Automated Braking, In *Symposium on Bicycle and Motorcycle Dynamics*, Padua, Italy, 2019.

©2023 Merkel, N.L. published by TU Delft OPEN on behalf of the authors.

ISSN: 2667-2812

The Evolving Scholar Vol. 3, 2023 https://dx.doi.org/10.59490/65c54c6425dcba41658e0df1

Bicycle and Motorcycle Dynamics 2023
Symposium on the Dynamics and Control of Single Track Vehicles
18 – 20 October 2023, Delft University of Technology, The Netherlands

Type of the Paper: Conference Paper

Revised

Adapting a variable stability mechanism for a tilting tricycle from the delta to the tadpole wheel configuration

[version 2; peer reviewed]

Andrew Dressel[1]*, Jason Moore[2]

[1]University of Wisconsin-Milwaukee; ADressel@uwm.edu, ORCID 0000-0003-0322-9815
[2]Delft University of Technology; J.K.Moore@tudelft.nl, ORCID 0000-0002-8698-6143

*corresponding author

Name of Editor: Edwin de Vries
First published: 03/10/2023
Last published: 27/02/2024
Citation: Dressel, A. & Moore, J. (2024). Adapting a variable stability mechanism for a tilting tricycle from the delta to the tadpole wheel configuration [version 2; peer reviewed]. The Evolving Scholar - BMD 2023, 5th Edition.
This work is licensed under a Creative Commons Attribution License (CC-BY).

Abstract:

We previously presented a narrow-track tilting tricycle with a variable stability mechanism integrated between the swing arms that support a pair of rear wheels, in the so-called “delta” configuration, and with recumbent seating. We now examine adopting that variable stability mechanism to work on a tricycle with a split-parallelogram linkage between a pair of front wheels, in the so-called “tadpole” configuration, and with upright seating.

It was fairly straightforward to allow for tilting by replacing the front wheel and fork with a split parallelogram comprising two paired A-arms and kingpins, controlling the motion of the two halves with a bell crank and two tie rods, and then varying the handling of the vehicle by moving the connection point of the tie rods on the bell crank, just as we did with the swing arms of the previous vehicle.

We have also separated the two tasks of positioning the tie rod ends on the bell crank and enforcing symmetry of the tie rods. The former does not require much force and can be easily implemented with Bowden cables, but the latter does require large forces and is better implemented with a local rigid-bar linkage.

Implementing decent Ackermann steering geometry, allowing for both large tilt and steer angles, and decoupling tilting from steering, however, proved to be quite a challenge, at least while we attempted to implement it with bar linkages. Fortunately, we discovered a 2006 paper by Prof Drstvenšek et al. describing a Bowden cable and cam system that looked promising.

Finally, the resulting vehicle handles very nicely. When in “full bicycle” mode, it handles quite similar to the original bicycle that we had converted into the tricycle. When in “rigid tricycle” mode, it keeps the rider upright when stationary or when riding at a walking pace. In between these two extremes, it handles even better than the original bicycle in a slalom course and when slowly following a straight line.

Keywords: Tilting Tricycle

©2023 Dressel, A. & Moore, J. published by TU Delft OPEN on behalf of the authors.
ISSN: 2667-2812

Introduction

Our motivation for implementing a tilting tricycle at all is not only to provide the best of both worlds: hold the rider upright when stopped or moving slowly, as a rigid tricycle does, and lean into turns when moving faster than walking speeds to allow a narrow axle track and normal seat height without danger of roll-over accidents, as a bicycle does. We also seek to help the rider maintain balance when riding between these two extreme modes.

We have previously explored a promising mechanism for achieving these three goals with a vehicle that has recumbent seating, the so-called delta wheel configuration, with one wheel in front and two wheels at the back, and front-wheel drive by means of a so-called “moving bottom bracket” with the crank mounted to and moving with the front fork.

When we proposed pursuing this work further to Royal Dutch Gazelle, a supporter of this project, they advised us that recumbent seating is not very popular with European riders and that delta wheel configurations are thought to look antiquated and geriatric. Thus, our goal was to recreate the functionality of the variable geometry tilt mechanism in a vehicle with upright seating and tadpole wheel configuration.

Since rear-wheel steering is problematic at best for tilting vehicles, the two wheels in front must be steered, and since bicycle wheels are not designed to withstand large side loads, the two wheels in front should tilt with the vehicle to keep the load they bare mostly in the plane of the wheel.

Finally, a visit to a cargo bike festival, at which we were able to test ride several prototype and commercially-available tilting tricycles, highlighted that the situations that arise when encountering the limits on steering or tilting angles were awkward at best, requiring the rider to put a foot down, or dangerous at worst, leading to a roll-over accident. Therefore, we strove to implement the largest steer and tilt angles that we could.

Methodology

It was straightforward to retrofit the variable-width bell crank and tie rods to the split-parallelogram tilting mechanism supporting the pair of front wheels. By mounting the bell crank low and connecting the tie rods to the upper A-arms, we were able to keep the tie rods in tension and avoid buckling issues.

We also improved the control mechanism for the variable-width bell crank. In the first vehicle, the two functions of positioning of the tie rod ends and enforcing the symmetry of that positioning were both implemented with the same Bowden cable system. This has proven problematic, however, because the enforcement of symmetry requires large forces when the bell crank rotates to enable tilting of the vehicle. These forces are related to the weight of the rider and beyond the capacity of the bicycle brake cables originally used to counter them. Therefore, we separated these two functions, and developed a rigid-bar linkage to enforce symmetry, which then left the relatively low-force task of positioning the tie rod ends to perfectly sufficient Bowden cables.

The rigid-bar linkage consists of two links and a slider on a rail. One end of each link is connected to one of the tie rod ends, and the other end of each link is connected to the slider, which is constrained to slide on a rail mounted orthogonally to the center of the bell crank. Thus, the tie rod ends are forced to maintain perfect symmetry about the center of the bell crank, and the rigid links easily handled the loads applied to them. These links, the slider, and the rail can all be seen mounted to the top edge of the bell crank in figures 7 and 8 below.

Finally, we needed a way to steer the two front wheels that would create correct Ackermann geometry, allow for large steer and tilt angles, and decouple steering from tilting to avoid bump steer. An investigation of steering systems implemented with rigid links, as on most automobiles, revealed that the goals of correct Ackermann and decoupled steering and tilting are incompatible. Plus, rigid links cannot provide a range of steering angles approaching 180° for danger of two links becoming colinear and thereby creating a mechanical singularity.

Fortunately, we discovered a 2006 paper by Prof. Drstvenšek et al. describing a Bowden cable and cam steering system for a human-powered vehicle that looked promising. We could not follow the published derivation of the kinematic relationship between steering angle and cam radius, so we derived our own, as shown below in Equation (1)

©2023 Dressel, A. & Moore, J. published by TU Delft OPEN on behalf of the authors.

ISSN: 2667-2812

$$r_\ell = r_c\theta_c/\theta_\ell = r_c\theta_c/\text{acot}(\cot\theta_c - \tfrac{1}{2}at/wb) \text{ and } \rightarrow r_r = r_c\theta_c/\theta_r = r_c\theta_c/\text{acot}(\cot\theta_c + \tfrac{1}{2}at/wb) \quad (1)$$

where

r_ℓ, r_c, and r_r are the radii of the left, center, and right cams, respectively.

θ_ℓ, θ_c, and θ_r are the rotation (steer) angles of the left, center, and right cams, respectively.

at is the distance between the two steered wheels, the "axle track"

wb is the distance between the front and rear axles, the "wheelbase"

These equations can be derived from Figure 1 as follows:

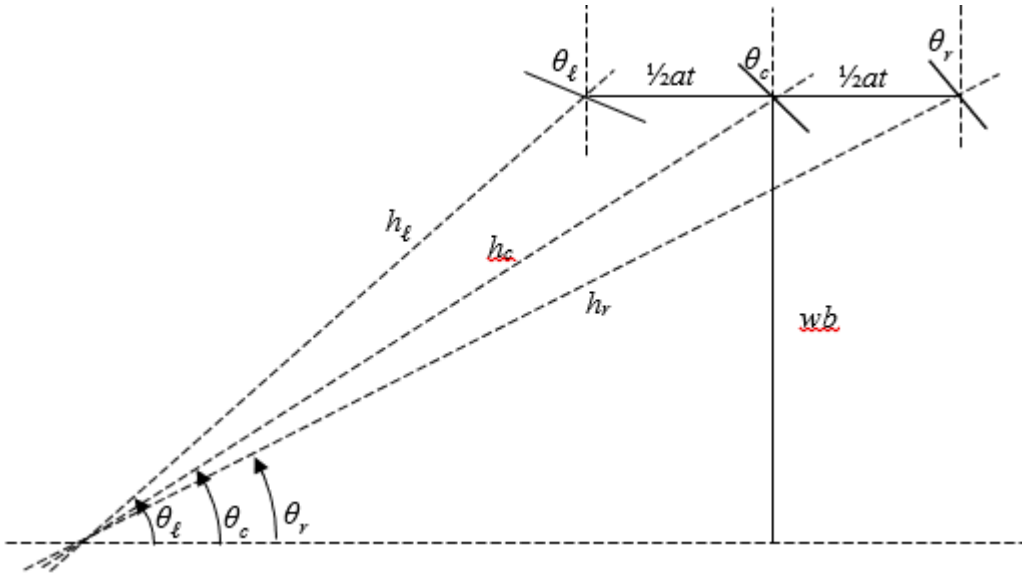


Figure 1. Ackermann steering geometry.

First, use the wheelbase, the rear wheel axel axis, and the front wheel axel axes to define right triangles that meet the Ackermann condition: the axel axes all intersect at one spot.

Then, relate the left, center, and right steer angles, θ_ℓ, θ_c, θ_r, by introducing and them eliminating the hypotenuses h_ℓ, h_c, h_r.

$h_c\sin\theta_c = wb \rightarrow h_c = wb/\sin\theta_c$
$h_\ell\sin\theta_\ell = wb \rightarrow h_\ell = wb/\sin\theta_\ell$
$h_\ell\cos\theta_\ell + \tfrac{1}{2}at = h_c\cos\theta_c$
$wb\cos\theta_\ell/\sin\theta_\ell + \tfrac{1}{2}at = wb\cos\theta_c/\sin\theta_c$
$wb\cot\theta_\ell + \tfrac{1}{2}at = wb\cot\theta_c$
$wb\cot\theta_\ell = wb\cot\theta_c - \tfrac{1}{2}at$
$\cot\theta_\ell = \cot\theta_c - \tfrac{1}{2}at/wb$
$\theta_\ell = \text{acot}(\cot\theta_c - \tfrac{1}{2}at/wb)$

$h_c\sin\theta_c = wb \rightarrow h_c = wb/\sin\theta_c$
$h_r\sin\theta_r = wb \rightarrow h_r = wb/\sin\theta_r$
$h_r\cos\theta_r - \tfrac{1}{2}at = h_c\cos\theta_c$
$wb\cos\theta_r/\sin\theta_r - \tfrac{1}{2}at = wb\cos\theta_c/\sin\theta_c$
$wb\cot\theta_r - \tfrac{1}{2}at = wb\cot\theta_c$
$wb\cot\theta_r = wb\cot\theta_c + \tfrac{1}{2}at$
$\cot\theta_r = \cot\theta_c + \tfrac{1}{2}at/wb$
$\theta_r = \text{acot}(\cot\theta_c + \tfrac{1}{2}at/wb)$

Finally relate the motion of the center, driving pulley, to the left and right cams by their radii:

$r_c\theta_c = r_\ell\theta_\ell = r_r\theta_r \rightarrow r_\ell = r_c\theta_c/\theta_\ell = r_c\theta_c/\text{acot}(\cot\theta_c - \tfrac{1}{2}at/wb)$ and $\rightarrow r_r = r_c\theta_c/\theta_r = r_c\theta_c/\text{acot}(\cot\theta_c + \tfrac{1}{2}at/wb)$, as above.

©2023 Dressel, A. & Moore, J. published by TU Delft OPEN on behalf of the authors.

ISSN: 2667-2812

These equations produce discontinuities, of course, when the argument to arccotangent() changes sign, but we handle this in the MATLAB implementation to generate the following smooth curves, as shown in Figure 2.

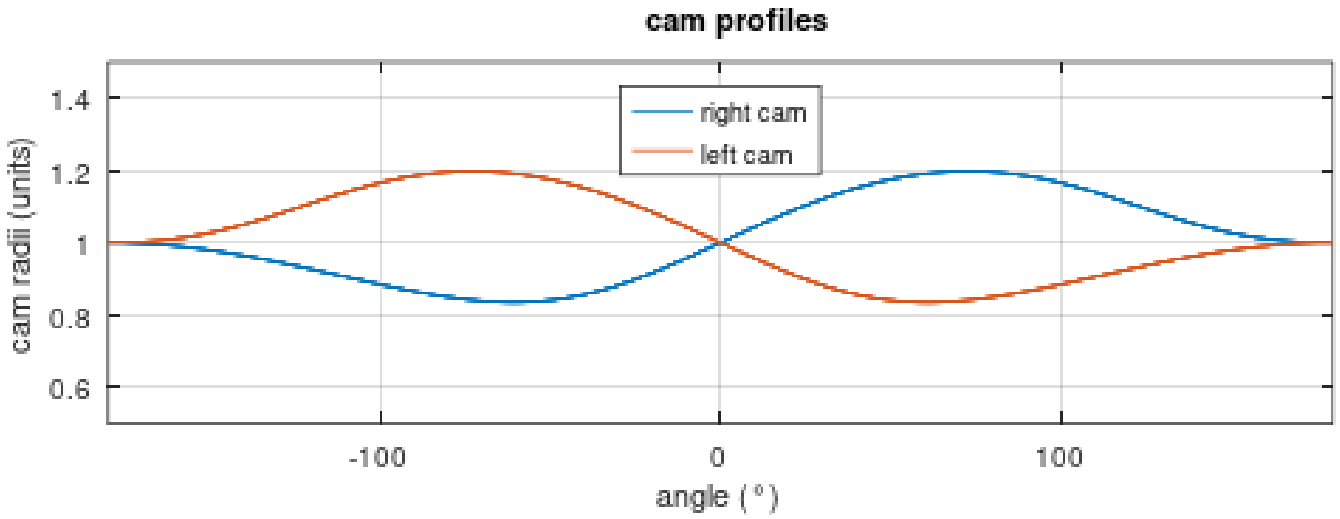


Figure 2. Steering cam profiles.

These cam radii generate the desired Ackermann steering angles, as shown in Figure 3, at least in theory.

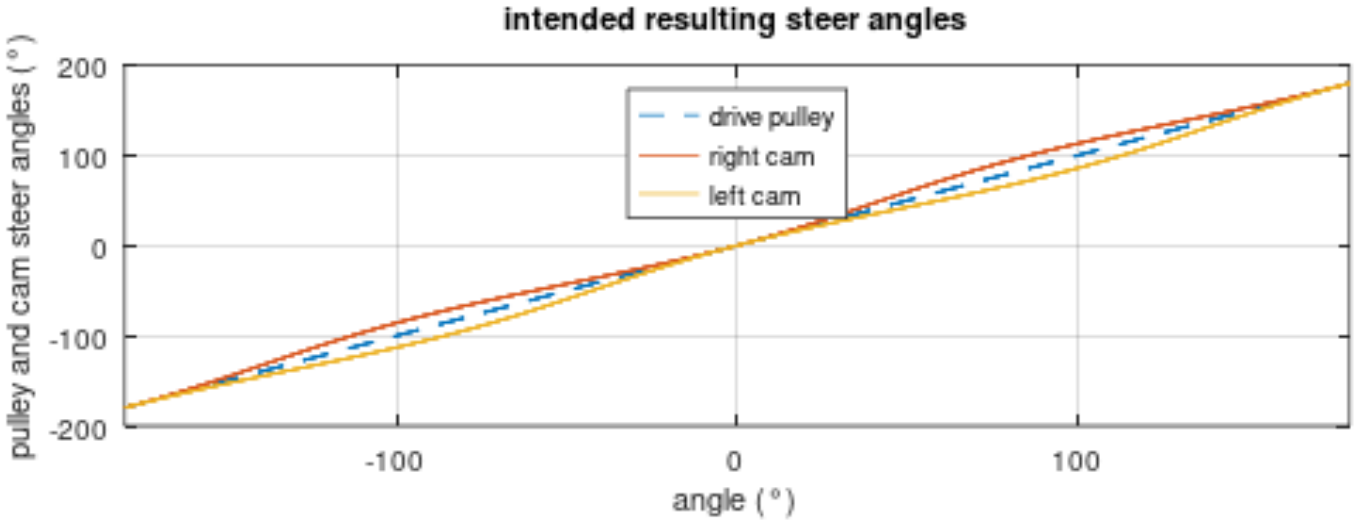


Figure 3. Resulting steer angles.

Figure 4, below, shows how the pulleys, cams, and cables may be arranged. In the actual, physical implementation on the protype tricycle, the left and right cams are separated and attached directly to the left and right kingpins, respectively, and the cables are routed through flexible Bowden cable housing from the centrally located drive and idler pulleys to the left and right wheels.

©2023 Dressel, A. & Moore, J. published by TU Delft OPEN on behalf of the authors.

ISSN: 2667-2812

 http://dx.doi.org/10.59490/65c54c6425dcba41658e0df1

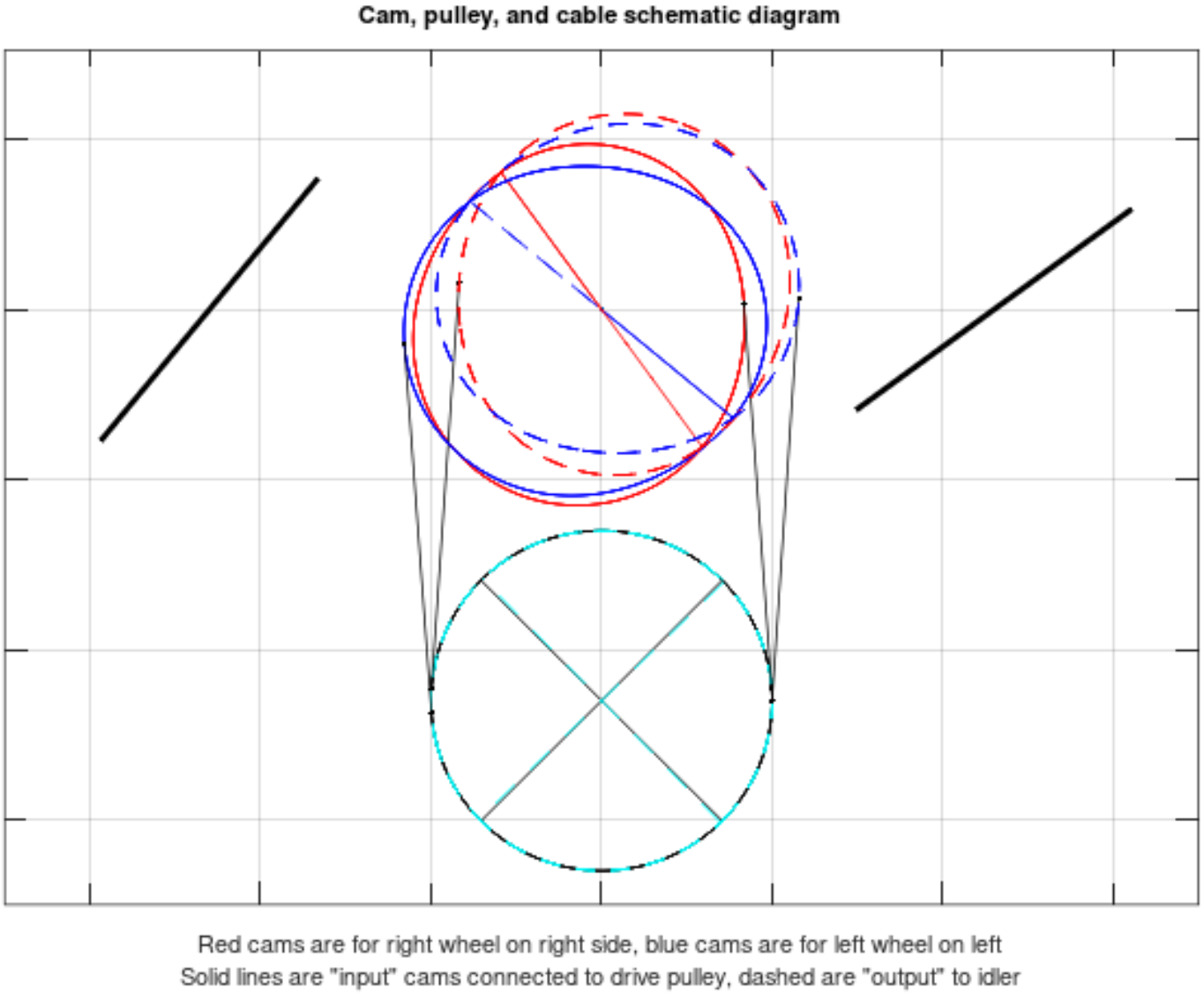


Figure 4. Schematic diagram of drive and idler pulleys at bottom, left and right input and output cams at top center, right steered wheel at top right, and left steered wheel at top left, steered to a 45° right turn.

An issue with this whole design, however, is that it ignores how the point at which the cable contacts the cam moves slightly around the cam as the cam radius changes, and so the cam at these nearby points does not have exactly the intended radius. This additional detail causes small errors in the resulting steer angles which we extract from a numerical simulation, as shown in Figure 5. It can also be seen that the differences are not perfectly symmetrical and that the left side follows a slightly different track when returning from the right-hand turn than it did as the turn was made. Thus, the blue line appears double between 25° and 50°.

Methods that we tried to correct for these small errors include: simply using the error calculated for the theoretically ideal cam profiles as a correction factor to reshape them, and forcing the cables to contact the cams at the 3 o'clock and 9 o'clock positions. Neither of these made a noticeable improvement, and we suspect that the issues are that the first does not take into account where the cable actually contacts the cam, and the second artificially distorts the length of the cable because it is no longer tangent to the cam at the point of contact.

©2023 Dressel, A. & Moore, J. published by TU Delft OPEN on behalf of the authors.
ISSN: 2667-2812

 http://dx.doi.org/10.59490/65c54c6425dcba41658e0df1

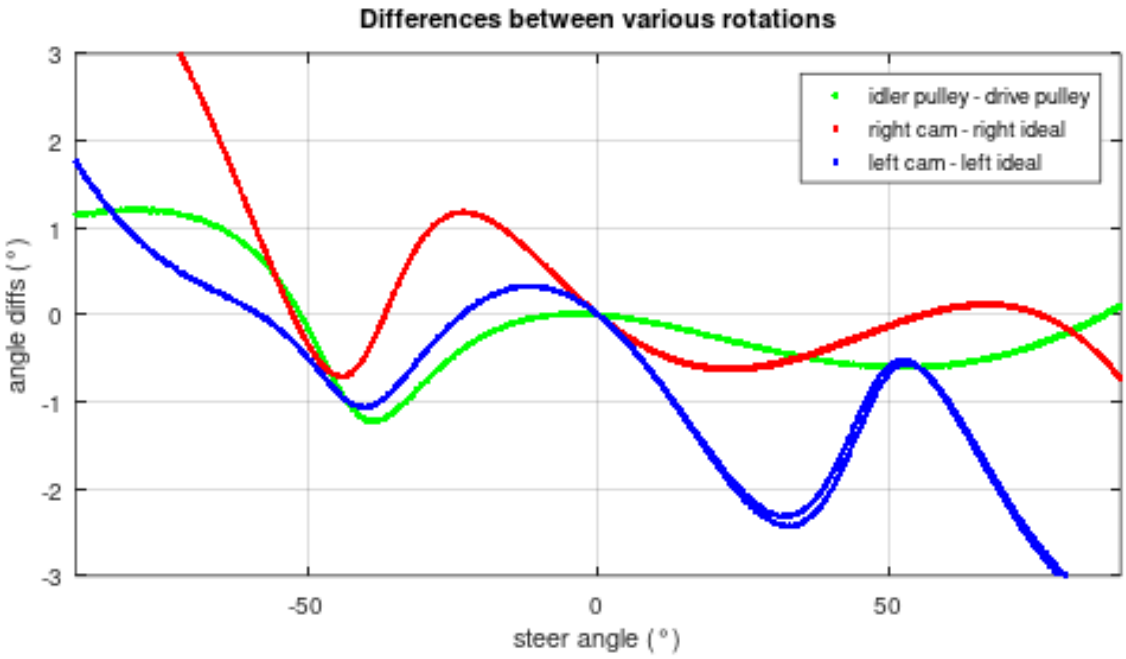


Figure 5. Differences between intended and actual angles, according to numerical simulation.

After trying to correct this error by several methods, without success, we were eventually forced to accept it due to the time-limited nature of the project and its funding.

We 3D printed prototype cams, as shown in Figure 6, to confirm that the system would work as designed and that the cables would generate sufficiently low friction, and it took us two tries to meet this goal. Our first attempt used generic bicycle brake cables and housing, which generated far too much friction. When we switched to high-end, coated cables and lined housing to eliminate metal-on-metal contact, the situation was greatly improved.

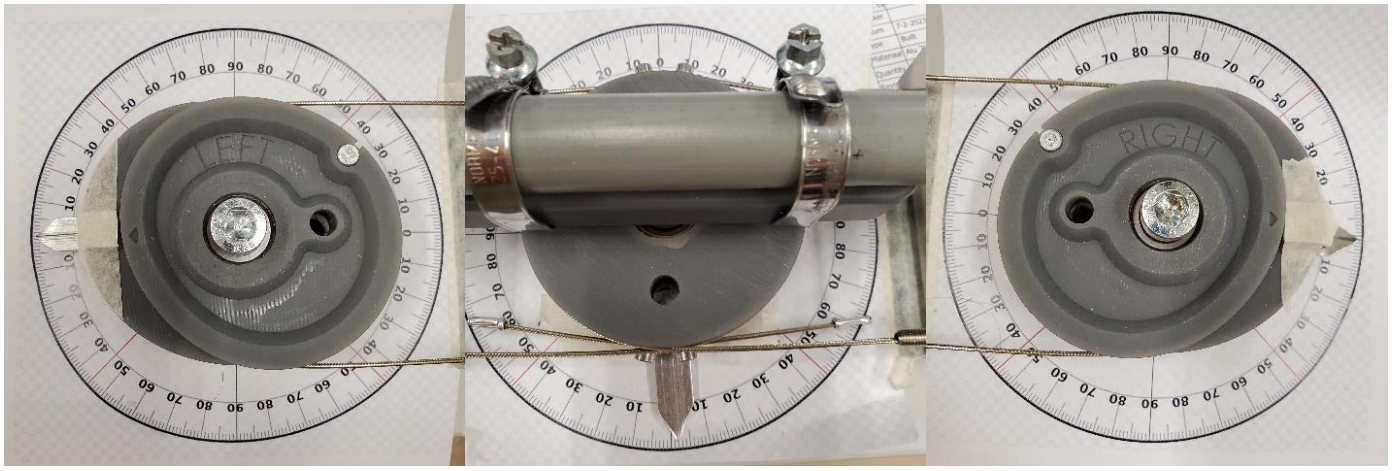


Figure 6. Images of the cable and cam steering system 3D-printed prototype.

These images of the 3D printed prototype cams also illustrate the error described above. If all the cams had constant radii, then the cable and the radial line at which it contacts the cam would be orthogonal. If the cams do not have constant radii, and the cam radius

©2023 Dressel, A. & Moore, J. published by TU Delft OPEN on behalf of the authors.

ISSN: 2667-2812

is changing rapidly enough in the vicinity of where the cable contacts the cam, the cable will contact the cam at a point to which the radial line is no longer orthogonal to the cable.

Nevertheless, we forged ahead to keep on our tight schedule, and the bicycle we chose to convert into a tilting tricycle is a Gazelle Ami C7, a modern take on the traditional Dutch city bike.

With the key objectives and components selected, the rest of the design consisted of many compromises to minimize axle track while maximizing tilt and steer angles. Figure 7 shows the resulting solid model, and Figure 8 shows the resulting physical vehicle, which has an axle track of 750 mm, a maximum tilt angle of 48°, and a maximum steer angle of 45°.

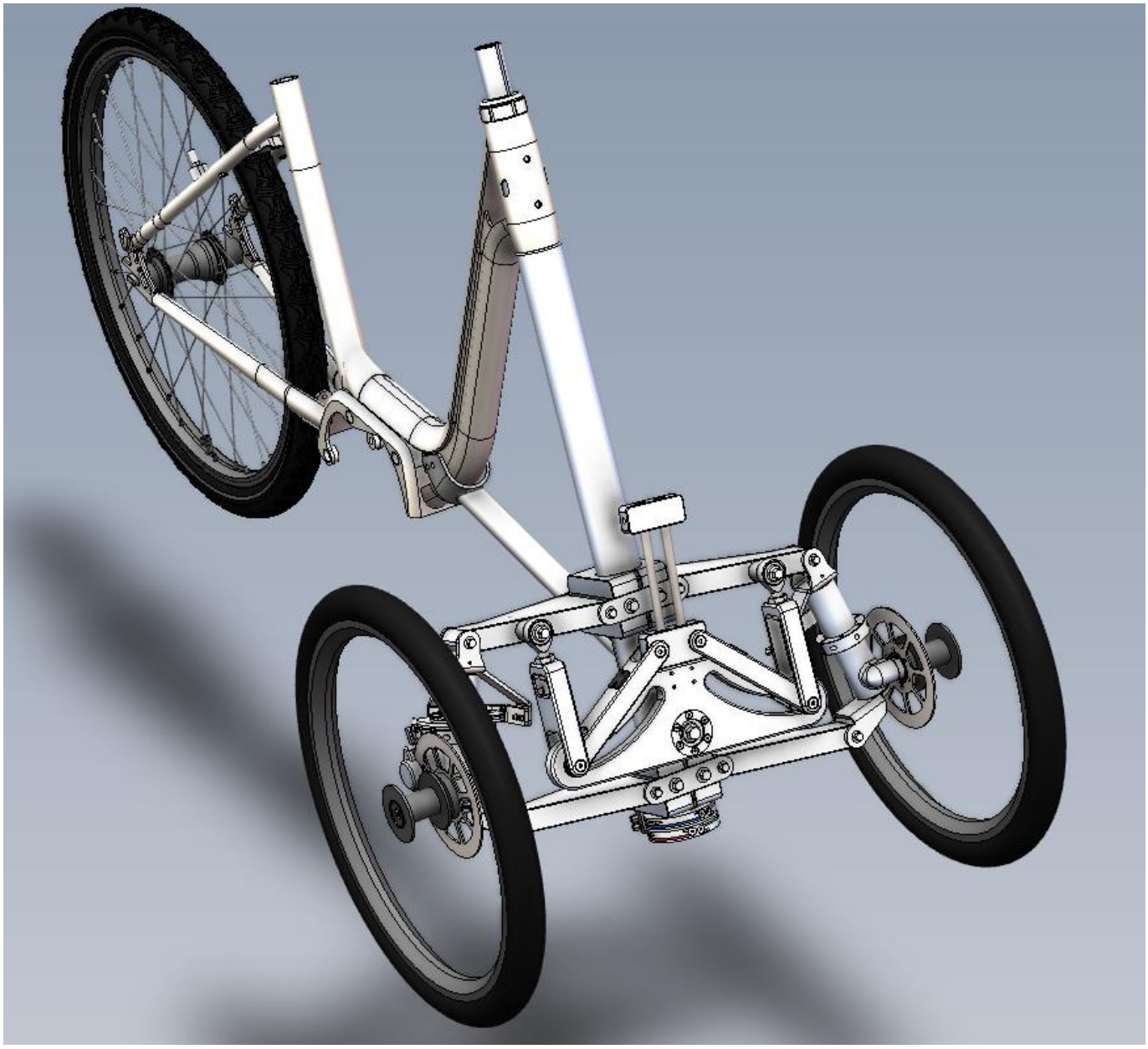


Figure 7. Final design solid model.

©2023 Dressel, A. & Moore, J. published by TU Delft OPEN on behalf of the authors.

ISSN: 2667-2812

The resulting physical prototype, when in the “bicycle” configuration, handles nearly as well as the original bicycle, and, when in the “rigid tricycle” configuration, keeps the rider upright without need for feet on the ground. When configured halfway between these two extremes, it handles better, based on a handling metric developed in a parallel project, than any other bicycle or tricycle we tested.

The handling metric mentioned above was developed by Floris van Willigen as part of his master’s thesis at TU Delft, and he finalized this metric before this tilting tricycle was available for testing. He focused specifically on commuting and so, from his review of the literature, he chose two riding tests to perform:

1. a slalom course ridden at a “moderate” speed
2. and following a straight line at a “slow” speed.

During these tests, IMUs rigidly attached to the front and rear frame record yaw and roll rates which he then integrated to calculate yaw and roll angles. From those values, Mr. van Willigen calculated three handling metrics:

1. maximum yaw factor, which is the yaw rate divided by the steer angle, a measure of the steer response of the vehicle,
2. the mean absolute steer angle, a measure of the low-speed balance of the vehicle,
3. and the time delay between the roll rate and steer rate, a measure of the responsiveness of the vehicle to rider inputs.

He collected data from multiple trials, rejected outliers, and performed a careful analysis to ensure that the results are statistically significant. Finally, he scaled the values and combined them into a single score.

He performed these tests on four bicycles and three other tilting tricycles, and when the tilting tricycle created for this project was configured halfway between a bicycle and a rigid tricycle, it produced the best score.

Conclusion

A tilting mechanism with variable geometry, which had previously been demonstrated on a tricycle with recumbent seating and delta wheel configuration, has been successfully adopted to a tricycle with upright seating and tadpole wheel configuration.

A steer-by-cable mechanism has been implemented to provide good Ackermann steering geometry, large tilt and steer angles, and decoupled tilting and steering to avoid bump steer.

The resulting physical prototype handles as hoped and scored well on a handling test that was developed before the physical prototype became available.

Acknowledgements

This project was financed and supported by the TKI/ClickNL 'De Fiets van de Toekomst' grant and Royal Dutch Gazelle.

Detailed design and construction were expertly performed at DEMO on the TU Delft campus by Frank Schilder under the sage supervision of Wouter Gregoor.

©2023 Dressel, A. & Moore, J. published by TU Delft OPEN on behalf of the authors.

ISSN: 2667-2812



Figure 8. Final physical prototype.

References

Drstvenšek, I., Drstvenšek, S., Valentan, B., Balič, J. (2006, April 20-22), Mathematical Background of Development of Steering Mechanism for Human Powered Vehicle, *5th International DAAAM Baltic Conference "Industrial Engineering - Adding Innovation Capacity of Labour Force and Entrepreneurs"*, Tallinn, Estonia

Pierson, A. M., Shortreed, A. K., Van Asten, P. D., Dressel, A. E. (2020, August 17–19), A Narrow-Track Tilting Tricycle with Variable Stability that the Rider can Control Manually, *Proceedings of the ASME 2020 International Design Engineering Technical Conferences and Computers and Information in Engineering Conference. Volume 4: 22nd International Conference on Advanced Vehicle Technologies*, Virtual, Online

van Willigen, F. (2023) Evaluation of the handling of a variable dynamics tilting tricycle: A novel handling assessment method, Master's thesis, Delft University of Technology

©2023 Dressel, A. & Moore, J. published by TU Delft OPEN on behalf of the authors.

ISSN: 2667-2812

The Evolving Scholar Vol. 3, 2023 https://dx.doi.org/10.59490/65e0736e3d3955984cdf53a6

Bicycle and Motorcycle Dynamics 2023
Symposium on the Dynamics and Control of Single Track Vehicles
18 – 20 October 2023, Delft University of Technology, The Netherlands

Type of the Paper: Conference Paper

Revised

Analysis of stopping behaviour of cyclists at a traffic light-controlled intersection using trajectory data

[version 2; peer reviewed]

Claudia Leschik[1]*, Meng Zhang[2] and Kay Gimm[1]

[1]Institute of Transportation Systems, German Aerospace Center (DLR e. V.), Lilienthalplatz 7, 38108 Brunswick, Germany, Claudia.Leschik@dlr.de
[2]Institute of Transportation Systems, German Aerospace Center (DLR e. V.), Rutherfordstraße 2, 12489 Berlin, Germany, Meng.Zhang@dlr.de

*corresponding author.

Name of Editor: Jason Moore
First published: 07/09/2023
Last published: 08/05/2024
Citation: Leschik, C., Zhang, M. & Gimm, K. (2024). Analysis of stopping behaviour of cyclists at a traffic light-controlled intersection using trajectory data [version 2; peer reviewed]. The Evolving Scholar - BMD 2023, 5th Edition.
This work is licensed under a Creative Commons Attribution License (CC-BY).

Abstract:

Cyclists have various route options to get to their destination. They can share lanes with vehicles, share lanes with pedestrians, or have their own lane. In Germany there are often marked lanes across intersections and stop lines in front of the crossing, guiding the cyclists their way. However, these markings are not always respected in the way they should be.

This study is intended to examine the stopping behaviour of cyclists at a traffic light-controlled intersection. A distinction was made between single cyclists (n = 1,411) and cyclist groups (more than one cyclist; n = 475). The stopping area was divided into polygons to understand where most people stop before an intersection. Furthermore, it was examined where people continued to ride after stopping (bicycle or pedestrian crossing) and this was compared with cyclists who did not stop.

The aim of this study is to investigate cyclists' stopping behaviour (e.g. stopping position) at intersections with consideration of the impact of groups, wrong-way cycling and road usage. It is to be investigated whether single cyclists behave differently than cyclist groups and whether there are differences in the two groups for wrong way cyclists. Both - single cyclists (69.38%) and cyclist groups (84.57%) - crossed the intersection more frequently without stopping within the observation period. In all cases, cyclists stopped mostly at the bicycle stopping line or used the bicycle crossing, thereby complying with the law. Most wrong way cyclists on the bicycle crossing were found for single cyclists with stopping (10%, n = 27) and cyclist groups with stopping (8%, n = 12). The speeds between single cyclists and cyclist groups differ slightly, and the stopping behaviour is very similar if the bicycle crossing is used after the stop.

The study shows that cyclists also stop far away from the intersection at unexpected positions that may not be in the field of vision of autonomous vehicles. Nevertheless, the cyclists still cross the intersection, partly also on the footpath, which is not rule compliant and unexpected. The information can be used to improve models of cyclists' behaviour, for example, in microscopic simulations, in which cyclists only stop at clearly defined locations. Knowledge about the stopping position and the further crossing of the intersection can help to make simulations more realistic, e.g. when planning or changing new infrastructure. Furthermore, the results of this study will provide further knowledge, which helps developing autonomous driving functions to correctly anticipate cycling behaviour at intersections.

Keywords: Stopping Behaviour, Trajectory Analysis, Cyclists, Road Usage, Wrong-way Cycling

©2023 Leschik, C., Zhang, M. & Gimm. K published by TU Delft OPEN on behalf of the authors.
ISSN: 2667-2812

Introduction

Infrastructure elements like stop lines, footpaths, and bicycle paths provide vulnerable road users (VRU) with clear guidance on where to stop, but actual stopping behaviour differs from the guidance. In addition to poor infrastructure, such as potholes, puddles or high curbs, the presence of other road users and the further route choice can also affect the stopping point of VRUs at intersections. Cyclists get in the way of others if they don't stop at the stop line. Cyclists who are riding in the wrong direction also have to stop somewhere at the intersection because there is no designated stop line in front of the crossing area, nor is there the necessary space to avoid blocking the bicycle path while stopping.

The stopping behaviour of vehicles has been well studied. This includes whether vehicles stop at stop signs or only coast (Darwish et al., 2022) and where they stop at the stop line at signals (Kim et al., 2008). Other studies often focus on the perception of speed and distance and whether it is still possible for a pedestrian to cross the street in front of a car (Sun et al., 2015), or the dilemma zone of whether vehicles should drive or stop at yellow traffic lights (Karri et al., 2021). A simulation study examined the influence of infrastructure, lane markings and speed for cyclists with cars turning right (Thorslund & Lindström, 2020).

Numerous studies have already examined the stopping behaviour of cyclists on the roadway with motorised traffic. The studies investigated how cyclists behave at stop signs. It was consistently found that cyclists rarely or never stop at stop signs (Ayres et al., 2015; Silva, 2015) In addition, various studies have shown how cyclists behave at the stop line when it is in front of the stop line of motorised traffic (Loskorn, 2010; Mangundu & Koorey, 2010). Bicycle boxes in front of or next to the stop line of motorised traffic can increase cyclists' sense of safety and cyclists are more visible to motorists.

The stopping behaviour on a bicycle infrastructure separated from the roadway has rarely been investigated. In a study at a “traffic playschool” 57 children cycling a route as instructed in Helsingborg, Sweden. Video observation showed that children prefer to stand directly at the stop line and wait for the green traffic light. When crossing the stop line a little (during red-light), it was corrected by rolling back. (Briem et al., 2004)

The size of cyclist group affects the cycling behaviour and could even affect the stopping behaviour of them. Studies on red-light violations have shown that the presence of other cyclists and/or motorists reduces the likelihood of a red-light violation being committed. Additionally, it increases the likelihood of other cyclists crossing the intersection when a cyclist was crossing the intersection at red-light. (Bureau Goudappel Coffeng, 1985; Fraboni et al., 2018; Johnson et al., 2011; Wu et al., 2012)

After stopping, cyclists continue to cross the intersection. There are already several studies that examine route selection. Studies show that cyclists often take the shortest route. Separating bicycle paths or reducing the speed of motorised traffic will increase cyclists’ perception of safety. (Van der Waerden et al., 2024; Guo et al., 2013)

In Germany, unless exceptionally signalled, riding in the opposite direction on the bicycle path is a criminal offence (§ 2 para. 4 StVO). This is also reflected in the design of the bicycle path infrastructure. The bicycle path often has a stop line in front of the crossing area with traffic lights, sometimes with a waiting area. Therefore, waiting cyclists cannot block other cyclists on the bicycle path. However, when riding on the bicycle path in the wrong direction, there is no stop line or waiting area and cyclists use the footpath as an alternative.

The stopping behaviour of cyclists on a separated bicycle path at an intersection with traffic lights has rarely been researched. For infrastructure design purposes it is important to understand where cyclists stop, where they continue their journey and whether they use the pedestrian crossing to avoid a detour via the bicycle crossing. It is also important to understand whether there are differences in the behaviour of cyclists riding alone or in groups. Information about cycling and stopping behaviour can be used to determine the space required for an infrastructure and can be mapped more realistically in simulations in order to redesign or reconstruct intersections. An analysis of the stopping behaviour can also help to improve simulation models because this is currently hardly considered and cyclists stop at an imaginary line. Parameter distributions can be used for implementation, for example, in the microscopic simulation SUMO (Lopez et al., 2018). Additionally, the analysis can point out further risks for autonomous driving. Unexpected or non-compliant behaviour can be a limitation for autonomous vehicles and must therefore be investigated.

The purpose of this study is to investigate the general stopping behaviour of cyclists at an urban intersection. The intersection has a separated bicycle- and footpath and has traffic lights. The aim is to determine whether cyclists stop at their stop line or prefer other locations. It is also to be examined whether the stopping behaviour differs when cyclists stop alone or as a group at the intersection.

©2023 Leschik, C., Zhang, M. & Gimm. K. published by TU Delft OPEN on behalf of the authors.

ISSN: 2667-2812

 http://dx.doi.org/10.59490/65e0736e3d3955984cdf53a6

Method

Trajectory data from traffic observations in Brunswick, Germany (e.g. route, speed, position) as well as video annotation for verification were used to analyse the stopping behaviour of cyclists at a traffic light-controlled intersection.

Traffic Observation

This large-scale research facility is part of the Application Platform for Intelligent Mobility (AIM) and records trajectory data with 20 Hz with 14 stereo-camera systems (Figure 1d). The data contained information about GNSS-based timestamp, location (UTM), velocity, acceleration, road user type (e.g. bicycle, car, motorcycle) and size of each detected road user (Knake-Langhorst, 2022). The image processing part to derive trajectory data is shortly described. The objects are captured using stereo video signal processing based on spatial correlation. This allows to determine distances in the image via the Hamming distance (disparity). Temporal correlation is also used, which involves linking identical pixels in successive images (optical flow). The linking of disparity measurements in consecutive images allows to measure the speed of pixels directly. Later on, position and speed of the traffic participants are derived. (Arndt, 2021; Talukder & Matthies, 2004) The accuracy is expected to be better than 25 cm of deviation in average per trajectory. In tests with vehicles with high precision positioning systems lateral deviation was partly one-digit in average. Figure 1a shows the AIM Research Intersection from above. Figure 1b and c show the video detection technology both on a traffic light-pole and on the ground for better detection of vulnerable road users. The respective field of view of the individual cameras is shown in Figure 1c. To illustrate which road users are recognised, Figure 1e shows an example plot of all road users detected in one hour.



Figure 1. Application Platform for Intelligent Mobility (AIM) Research Intersection in Brunswick, Germany. a: Satellite image, orientated north. b and c: Cameras on masts and on the ground. d: Cameras' field of view. e: Mapping of all trajectories in an hour. Orthophoto source: DLR e. V.

Real data were examined to investigate the stopping behaviour and the further choice of route of cyclists. The traffic observation took place between March 11th and March 17th 2019 at the AIM Research Intersection in Brunswick, Germany. The period of daytime from 6:30 a.m. to 6:30 p.m. was analysed – so between dawn and sunset. The weather during the measured week was mixed with clouds and partly rain. The corresponding scene videos were recorded in reduced resolution, so that faces and license plates could not be recognized, in accordance with the data protection concept. The position, average speed, acceleration and heading of detected cyclists were used to investigate the stopping behaviour. The intersection has separate footpaths and bicycle paths, separate stop lines for both, and also separate crossing lanes for pedestrians and cyclists, which guide them separately across the intersection (see Figure 2, left).

©2023 Leschik, C., Zhang, M. & Gimm. K. published by TU Delft OPEN on behalf of the authors.

ISSN: 2667-2812

http://dx.doi.org/10.59490/65e0736e3d3955984cdf53a6

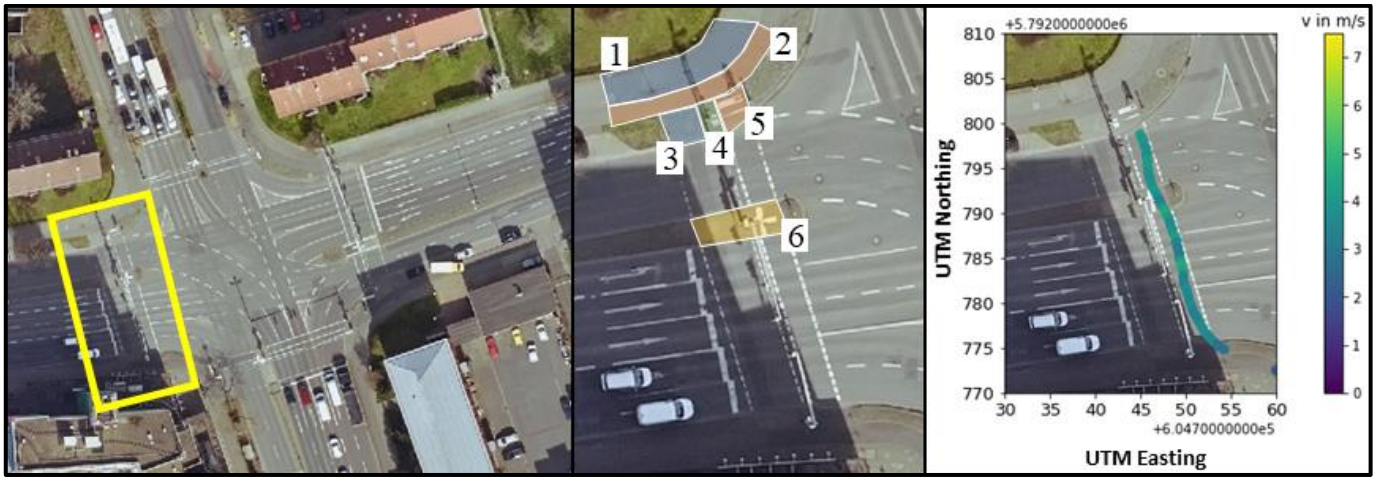


Figure 2. Overview of the AIM Research Intersection in Brunswick, Germany; orientated north. Left: Satellite image of AIM Research Intersection (yellow: area of interest for this analysis). Middle: Detailed view of the area of interest with example polygons (1: footpath, 2: bicycle path, 3: waiting area and stop line for pedestrians, 4: space between pedestrian and bicycle waiting areas and stop lines, 5: waiting area and stop line for cyclists, 6: crossing aid). Right: An example trajectory of a cyclist on the bicycle crossing in map projection system UTM 32U. Orthophoto source: DLR e. V.

Traffic Analysis

The recorded trajectories were filtered automatically by developed algorithms for cyclists. The whole process from data recording to analysis is shown in Figure 3.

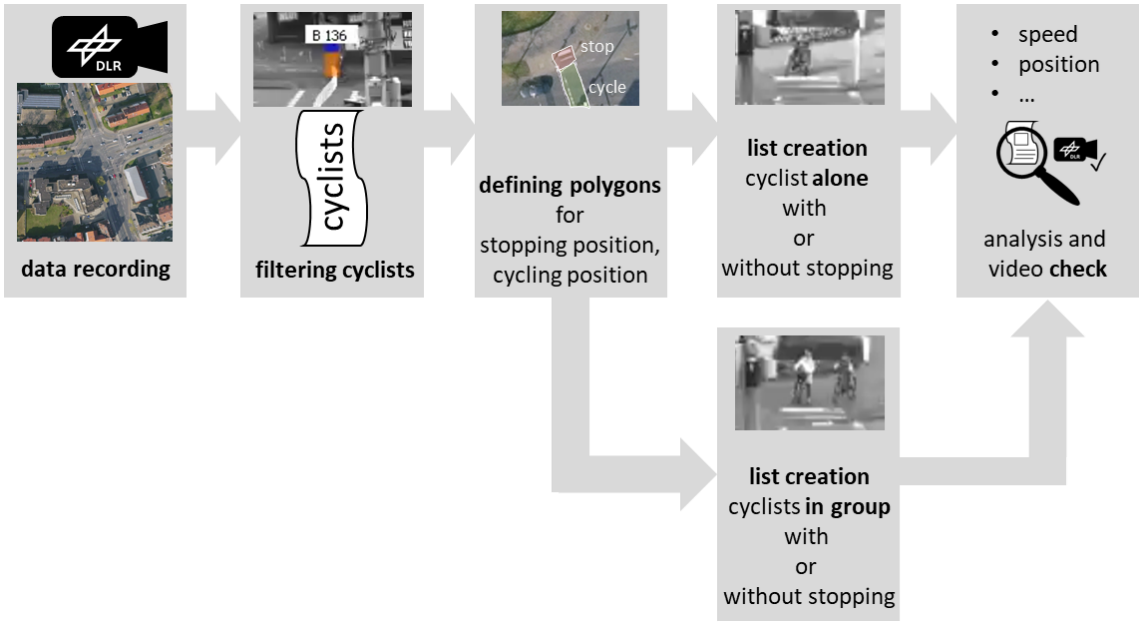


Figure 3. Outline of the analysis procedure from data recording to filtering and analysis.

The area of interest for this analysis was divided into different areas with the help of polygons (see Figure 2, middle). In this analysis, the polygons have the function of a virtual induction loop to detect the presence of a traffic participant. The polygons have a self-chosen shape and have been adapted to the interesting places of the infrastructure. A JavaScript-based tool was used to define the polygons and to obtain the corresponding GeoJSON file. This allows geographic data to be described and then processed in e.g. Python scripts. Areas covered by polygons can be checked for intersection trajectories these areas and whether the absolute

©2023 Leschik, C., Zhang, M. & Gimm. K. published by TU Delft OPEN on behalf of the authors.

ISSN: 2667-2812

 http://dx.doi.org/10.59490/65e0736e3d3955984cdf53a6

velocity is v_{abs} < 0.5 m/s for several time steps, which makes it possible to examine the position at which cyclists stopped at the intersection and how they continued their journey after stopping. Furthermore, it was investigated whether several cyclists were present at the same time within a radius of 20 m. Due to imprecise detection of groups of cyclists, these were not counted. In this study, a distinction is only made between single cyclist or cyclist groups (at least 2 or more). In the case of cyclist groups, they must be present in the area of the intersection.

In addition, the data set was divided into stopping and non-stopping cyclists. At the end, the behaviour of single cyclists or in a group when stopping or not stopping was compared. The videos were used to validate the results. It was checked whether it was actually cyclist groups or whether there were incorrectly detected objects.

Results

The paper addresses two main points – where do cyclists stop at a signalized crossing and how do cyclists continue their journey across the intersection (without analysing red-light violations).

Data Preparation

Cyclists without the presence of other cyclists (single cyclists) as well as cyclists with at least one other cyclist (cyclist groups) in the crossing area were analysed. The stopping behaviour of cyclists differs depending on whether the permitted direction of travel was used or not. Usually, the permitted direction of travel for cyclists is counterclockwise at an intersection in Germany. There is mostly a stop line for cyclists in the permitted direction of travel (see **Figure 4**, left) and no stop line in the direction of travel that is not permitted (see **Figure 4**, right).



Figure 4. Overview of the stopping area at the stop line for cyclists. Left: Bicycle path in the right direction of travel with a stop line next to the bicycle path (north to south). Right: Bicycle path in the not permitted direction of travel without a stop line next to the bicycle path (south to north).

The stop line is just outside the bicycle path and can be understood as a small waiting area. Behind the stop line, a dedicated pedestrian crossing (pedestrian crossing) and a dedicated bicycle crossing (bicycle crossing) lead across the intersection. **Figure 5** shows a schematic overview of Figure 4 for the right direction of travel. Single cyclists are shown on the left and cyclist groups is shown on the right. There is a stop line in front of bicycle crossing and pedestrian crossing (thick white line) and behind the view line (small white line), which is the last line before the roadway and which is the area where there is visibility into the intersection.

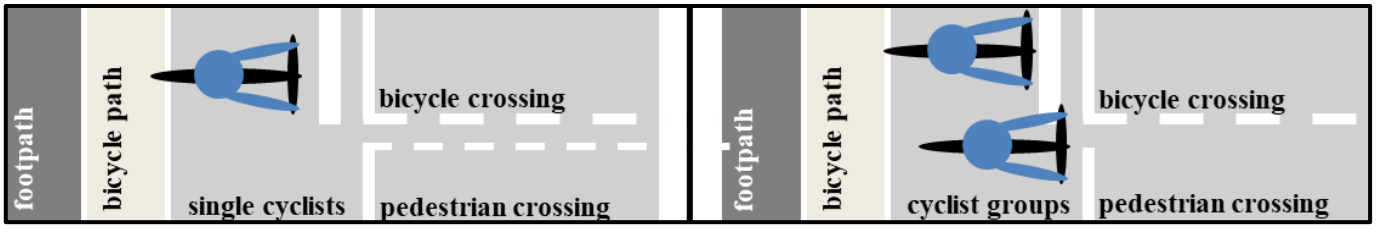


Figure 5. Sketched overview: single cyclists (left) and cyclist groups (right). Both variants can use the pedestrian crossing or bicycle crossing and can start in front of pedestrian crossing, bicycle crossing or on footpath (or bicycle path).

Behind the waiting area for cyclists with the stop line in front of bicycle crossing is the bicycle path and behind this exists a footpath. As already shown in Figure 2, all possible areas were examined as potential stopping areas. There were no stops in the bicycle

©2023 Leschik, C., Zhang, M. & Gimm. K. published by TU Delft OPEN on behalf of the authors.

ISSN: 2667-2812

crossing and pedestrian crossing areas (see Figure 4), which are on the roadway for motorized traffic. They are only used to describe the continuation of the journey.

Stopping Position

During the observation period, 1,886 cyclists (incl. wrong-way cyclists (WWC)) or pairs of cyclists were tracked and used for an analysis. There were 1,411 single cyclists and 475 cyclist groups at the intersection. Table 1 shows the different classes of both groups according to stopping or not stopping and where they stopped or rode. Both single cyclists (69.38%) and cyclist groups (84.57%) crossed the intersection more frequently without stopping within the observation period. In all cases, cyclists stopped mostly at the bicycle crossing or used the bicycle crossing, thereby complying with the law. Only 13.18% of the single cyclists and 1.19% of the cyclist groups stopped at the pedestrian crossing or drove on the pedestrian crossing without stopping. It is noticeable that the proportion of pedestrian crossing users is lower for cyclist groups than single cyclists.

WWC on the bicycle crossing were analysed and in the case of single cyclists without stopping, there were around 7% WWC (n = 41), in the case for single cyclists with stopping, there were around 10% WWC (n = 27). In the analysis of cyclist groups, the proportions are lower, although the number of cases is lower, too. For cyclist groups without stop there were around 5.5% (n = 13) and for cyclist groups with stop were around 8% WWC (n = 12). For further analyses a distinction was made between cyclists who stopped before crossing the intersection and those who crossed without stopping. For the analysis, single cyclists were considered, as well as cyclist groups at the intersection.

Table 1. Comparison of single cyclists and cyclist groups distinguishing whether the cyclists stopped or rode through (without stop) and if so, where the cyclists stopped or which lane the cyclists used (pedestrian crossing or bicycle crossing).

single cyclists (n = 1,411)	stop and ride	pedestrian crossing	n = 61
		bicycle crossing	n = 371
	ride without stop	pedestrian crossing	n = 125
		bicycle crossing	n = 854
cyclist groups (n = 337)	stop and ride	pedestrian crossing	n = 2
		bicycle crossing	n = 188
	ride without stop	pedestrian crossing	n = 2
		bicycle crossing	n = 283

Figure 6 shows the differences for single cyclists and cyclist groups and the difference whether bicycle crossing or pedestrian crossing was used afterwards. In addition, differences in stopping behaviour between cyclists riding in the direction of travel and cyclists riding in the wrong direction of travel are also shown.

The case of cyclist groups and pedestrian crossing is not shown, because there were only two pairs of cyclists from north to south (permitted direction of travel) who stopped in front of pedestrian crossing. Only data that could be assigned to a clear polygon and whose start was north or south of the intersection were used for this analysis. Cyclists who start in the north ride in the correct direction of travel. Cyclists starting in the south are WWC.

Single cyclists using bicycle crossing after the stop, stop most often on the bicycle path (57.27%) but wrong-way cyclists stop most often (84.62%) on the footpath (Figure 6, left and Figure 7a + d). It's not clear why cyclists don't stop at the stop line, but stop on the bicycle path. Possible reasons for this can be that the stop line is too close to the road, and it feels unsafe for the cyclists or that puddles have formed on the roadway due to the precipitation and the cyclists have taken more distance to the intersection. If cyclists used the pedestrian crossing after stopping, their previous stopping position were concentrated in front of the pedestrian crossing (61.54%), while the previous stopping position of WWC were mostly on the footpath (58.82%) (Figure 6, middle and Figure 7b + e). The distribution of stopping position for cyclist groups using bicycle crossing after the stop is similar to single cyclists using bicycle crossing after the stop. The most frequent stop is on the bicycle path and for WWC on the footpath (Figure 6, right and Figure **7**c + f). Overall, WWC mostly stop on the footpath, possibly to provide space for oncoming cyclists.

©2023 Leschik, C., Zhang, M. & Gimm. K. published by TU Delft OPEN on behalf of the authors.

ISSN: 2667-2812

http://dx.doi.org/10.59490/65e0736e3d3955984cdf53a6

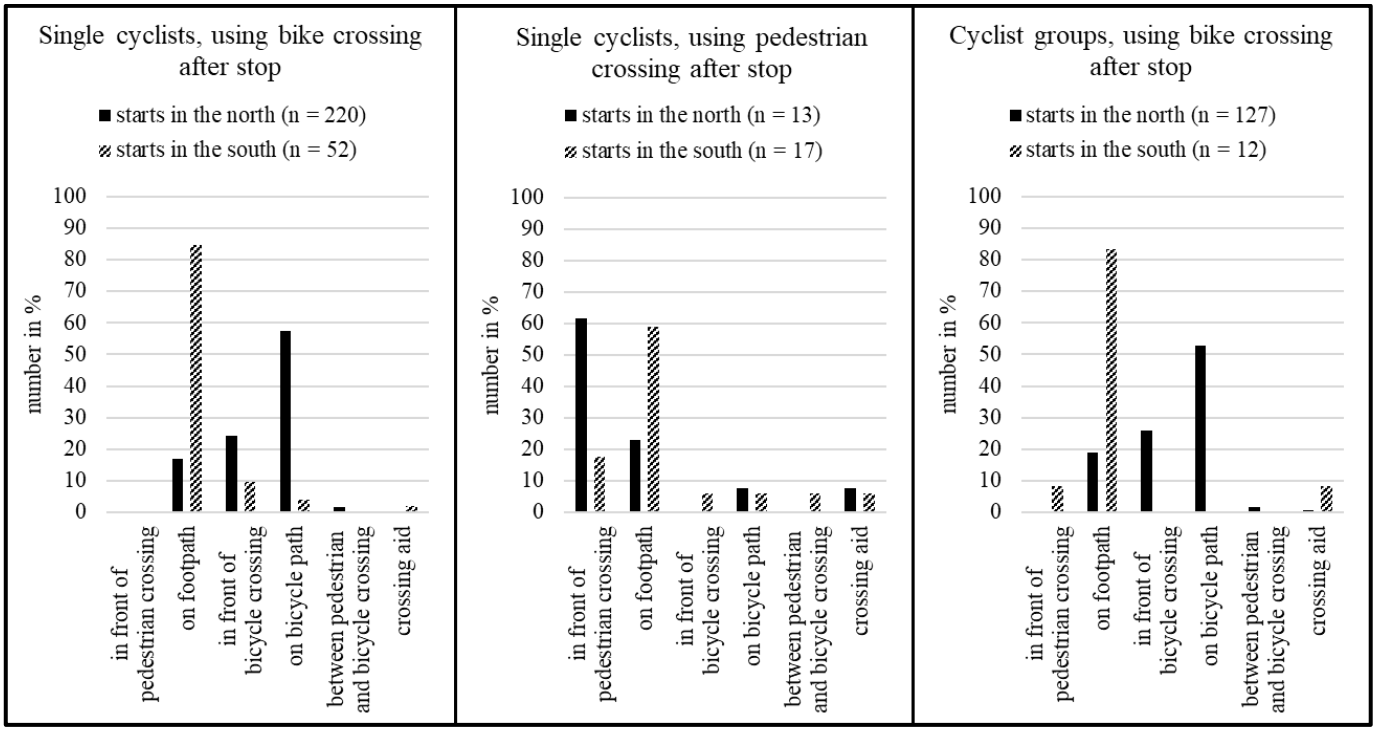


Figure 6. Comparison of stopping location. Left: single cyclists and using the bicycle crossing after stopping. Middle: single cyclists and using the pedestrian crossing after stopping. Right: cyclist groups and using bicycle crossing after stopping. cyclist groups using pedestrian crossing after stopping is not shown. “Starts in the south” are WWC.



Figure 7. Examples of different stopping behaviour. First row shows the correct direction of travel and second row shows the WWC. The images are sorted according to Figure 6: single cyclists, using bicycle crossing after stop (a+d), single cyclists, using pedestrian crossing after stop (b+e) and cyclist groups, using bicycle crossing after stop (c+f).

Speed while Crossing

Another subject of investigation was the speed and whether cyclists might ride slower if they do not use the bicycle path. Table 2 shows the different average speeds for single cyclists and cyclist groups for stopping and riding and riding without stopping.

©2023 Leschik, C., Zhang, M. & Gimm. K. published by TU Delft OPEN on behalf of the authors.

ISSN: 2667-2812

Table 2. Riding behaviour and use of the crossing with velocity. Only the riding speed (without stopping time) was considered for the speed calculation.

stop and ride / ride	speed in m/s for single cyclists	speed in m/s for cyclist groups
stop and ride (pedestrian crossing)	1.71 (n = 61)	1.19 (n = 2)
ride without stop (pedestrian crossing)	3.17 (n = 125)	3.60 (n = 2)
stop and ride (bicycle crossing)	2.34 (n = 371)	2.29 (n = 188)
ride without stop (bicycle crossing)	3.51 (n = 854)	3.23 (n = 283)
sum	3.46 (n = 1,411) | STD = 0.85	3.24 (n = 475) | STD = 0.63

The average velocity for single cyclists and cyclist groups is relatively low in all cases. Presumably because the crossing cannot be navigated straight ahead, but instead, due to the layout of the intersection, a slight curve has to be navigated beforehand. The average speed of the cyclists who stopped does not take the stopping time into account. The speeds of single cyclists and cyclist groups are quite similar. It can only be stated that the speed is lower for cyclists who have stopped. This is plausible since the distance examined is less than 25 m. The speed of single cyclists rides without stop (bicycle crossing) is slightly greater than for cyclist groups.

It was further analysed whether there is a relationship between the day of the week and the speed of cyclists. Given that the AIM research intersection is in an urban area, there is more traffic during weekdays in comparison to weekends. The intersection is used for commuting to work on the one hand and for travelling to the Technical University of Brunswick on the other. There is also a canteen of the University nearby. These could be reasons for the increased traffic volume during the week. The average speed in weekdays is consistent ($v_{mean} = 3.51 \pm 0.11$ m/s). A correlation analysis between the number of cyclists per day and the average speed shows a non-significant correlation ($r = 0.75$, $p = 0.15$) during weekdays. There seems to be no correlation between the number of cyclists and the travel speed. A correlation analysis over the entire week does not lead to a significant result ($r = 0.001$, $p = 0.998$).

Discussion

This study focused on the analysis of stopping behaviour and cycling route while crossing an intersection with traffic lights. A distinction was made between single cyclists and cyclist groups. Cyclist groups are defined as minimum of two cyclists travelling in the same direction. For this purpose, real trajectory data were recorded and analysed at an urban intersection.

There are various studies on whether the behaviour of people traveling alone differs from traveling behaviour in groups (Bureau Goudappel Coffeng, 1985; Fraboni et al., 2018; Johnson et al., 2011; Wu et al., 2012). The studies show that the presence of other road users increases the likelihood of complying with the rules (no red-light violation). The results are transferable with the result that cyclists in groups use the bicycle path more frequently (in accordance with the law). This study compared whether a cyclist was alone or more than one cyclist was cycling in the area of interest at the same time. In further analyses, the number of cyclist groups should be counted to determine further effects. This can be done automatically through precise detection of the objects or through manual video annotation. In addition, it could be interesting to investigate red-light violations and to check whether pedestrian crossing or bicycle crossing is used more frequently then. No information on traffic light control was available during the study period. This data is now directly available at AIM research intersection for future work. A generic option to identify the state of light would be image recognition.

More people stopped on the bicycle path than directly at the stop line (Figure 8). This requires further investigation as to whether the stop line is too close to the traffic and therefore conveys a lower sense of safety. There may be various reasons why cyclists do not stop at the stop line. The stop line could be too far away from the intersection or too close. Cyclists also stop close to the bicycle traffic lights, they hold on to the small mast and are therefore behind the stop line. A survey of cyclists could provide information as to whether the stop line is ignored because it is inconveniently located or is not used for other reasons. Puddles could not be detected due to the reduced video quality, but cannot be ruled out as a possible source of stopping and riding behaviour, as it was raining during the observation period. It can be assumed that weather has an impact on stopping behaviour and riding behaviour (clearing snow from the bicycle and footpaths, puddles on the road). This should be considered in further studies. It was observed,

©2023 Leschik, C., Zhang, M. & Gimm. K. published by TU Delft OPEN on behalf of the authors.

ISSN: 2667-2812

especially in the case for WWC, that cyclists stopped on the footpath because there was a small canopy to protect them from the rain.

The study does not differentiate between age or gender. Therefore, it cannot be ruled out that the stopping behaviour was independent of age or gender. Video annotation can be used in further studies to provide a rough estimate of age. However, gender is difficult to differentiate due to the low quality of the videos.

The infrastructure also plays a major role in stopping behaviour, as the stopping behaviour of WWC showed in this study. Transferability to other intersections should be checked. In this study, measurements were taken at an intersection with traffic lights. There was a separate footpath and bicycle path with bends in the roadway. The intersection is used for commuting to work and for travelling to the Technical University of Brunswick.

Furthermore, only times with daylight were examined. A day-night comparison could not be conducted. Future studies may consider extending the measurement period during the night. It can be assumed that there are fewer cyclists on the road in the dark, but no assumption can yet be made as to whether they behave differently (speed, stopping behaviour) than during the day.

Conclusion

The study explores the stopping behaviour of cyclists and shows where they stop at an intersection with separated foot- /bicycle path and traffic lights. It differentiates between whether cyclists waiting alone or in groups at the traffic lights. Furthermore, the study provides an insight into the further choice of route, including whether the footpath or bicycle path is used.

The majority of cyclists uses the bicycle crossing and rides in the right direction (69.38% for single cyclists riding without stop, 60.00% for cyclist groups riding without stop). The speeds between single cyclists and cyclist groups differ slightly, and the stopping behaviour is very similar if the bicycle crossing is used after the stop. The stopping behaviour changes when riding on the pedestrian crossing after the stop, but too few cases are known for cyclist groups. More people stopped on the bicycle path than directly at the stop line. Most WWC on bicycle crossing were found for single cyclists with stopping (10%, n = 27) and cyclist groups with stopping (8%, n = 12).

The study has shown that cyclists do not always stop at the stop line intended for them. They stop partly everywhere at different percentages, even if they use the bicycle crossing afterwards. Initial analysis also shows that people often stop in front of the pedestrian crossing or cycle on it when turning right (or the WWC turn left) at the end of the intersection. This could mean that cyclists want to save time when turning and do not want to take the detour via the bicycle crossing. This requires further analysis and can improve the prediction of cycling routes.

In overall, it can be stated that stopping behaviour of cyclists could be well described based on the conducted traffic observation. The next step is to check whether the individual parameter distributions (position, speed) have an influence on microscopic simulation and whether these can be modelled more realistically.

The study shows that cyclists do not always cycle in the right direction and that autonomous vehicles should consider that cyclists also do not follow the rules. They also use the footpath to cross. In addition, they do not stop at the stop line and thus possibly not in the field of vision of the autonomous vehicle.

References

Arndt, R. (2021). Stereo-Video-Sensortechnik - Detektion und Verfolgung von Verkehrsobjekten am Testfeld Niedersachsen. [Stereo video sensor technology - detection and tracking of traffic objects at the Test Bed Lower Saxony for automated and connected mobility] guest lecture at the DLR (online) on 26.04.2021. Unpublished manuscript.

Ayres, T. J., Kelkar, R., Kubose, T., & Shekhawat, V. (2015, September). Bicyclist behavior at stop signs. In Proceedings of the Human Factors and Ergonomics Society Annual Meeting (Vol. 59, No. 1, pp. 1616-1620). Sage CA: Los Angeles, CA: SAGE Publications.

Briem, V., Radeborg, K., Salo, I., & Bengtsson, H. (2004). Developmental aspects of children's behavior and safety while cycling. Journal of pediatric psychology, 29(5), 369-377.

©2023 Leschik, C., Zhang, M. & Gimm. K. published by TU Delft OPEN on behalf of the authors.

ISSN: 2667-2812

Coffeng, B. G. (1985). Roodlichtdiscipline van (brom) fietsers: een verkennend onderzoek. Opdracht van het Directoraat-Generaal Rijkswaterstaat, Dienst Verkeerkunde DVK, ed. Kenmerk RWD/752/18/Ht (Deventer: Bureau Goudappel Coffeng).

Darwish, W. (2022). FACTORS AFFECTING STOPPING BEHAVIOUR AT SUBURBAN INTERSECTIONS. Acta Logistica, 9(1), 109-114.

Fraboni, F., Puchades, V. M., De Angelis, M., Pietrantoni, L., & Prati, G. (2018). Red-light running behavior of cyclists in Italy: An observational study. Accident Analysis & Prevention, 120, 219-232.

Guo, H., Wang, W., Guo, W., & Zhao, F. (2013). Modeling lane-keeping behavior of bicyclists using survival analysis approach. Discrete dynamics in nature and society, 2013.

Johnson, M., Newstead, S., Charlton, J., & Oxley, J. (2011). Riding through red lights: The rate, characteristics and risk factors of non-compliant urban commuter cyclists. Accident Analysis & Prevention, 43(1), 323-328.

Karri, S. L., De Silva, L. C., Lai, D. T. C., & Yong, S. Y. (2021). Classification and prediction of driving behaviour at a traffic intersection using SVM and KNN. SN computer science, 2, 1-11.

Kim, W., Zhang, J., Fujiwara, A., Jang, T. Y., & Namgung, M. (2008). Analysis of stopping behavior at urban signalized intersections: Empirical study in South Korea. *Transportation research record*, *2080*(1), 84-91.

Knake-Langhorst, S. (2022), Generische Systemarchitektur für die Erhebung mikroskopischer Verkehrsdaten [Generic system architecture for the collection of microscopic traffic data], PhD thesis, Technische Universität Berlin, Germany, Fakultät V – Verkehrs- und Maschinensysteme, https://elib.dlr.de/186352/1/knake-langhorst_sascha.pdf.

Lopez, P. A., Behrisch, M., Bieker-Walz, L., Erdmann, J., Flötteröd, Y. P., Hilbrich, R., Lücken, L., Rummel, J., Wagner, P. & Wießner, E. (2018, November). Microscopic traffic simulation using sumo. In 2018 21st international conference on intelligent transportation systems (ITSC) (pp. 2575-2582). IEEE.

Loskorn, J., Mills, A., Brady, J., Duthie, J., Machemehl, R., Beaudet, A., ... & Fialkoff, J. (2010). Effects of bicycle boxes on bicyclist and motorist behavior at intersections. Austin, Texas: University of Texas at Austin.

Mangundu, E., & Koorey, G. (2010). Effects on Motor Vehicle Behavior of Color and Width of Bicycle Facilities at Signalized Intersections.

Silva, C. M. C. (2015). Bicyclists' Stopping Behaviors: An Observational Study of Bicyclists' Patterns and Practices (Doctoral dissertation).

Sun, R., Zhuang, X., Wu, C., Zhao, G., & Zhang, K. (2015). The estimation of vehicle speed and stopping distance by pedestrians crossing streets in a naturalistic traffic environment. *Transportation research part F: traffic psychology and behaviour*, *30*, 97-106.

Talukder, A., & Matthies, L. (2004, September). Real-time detection of moving objects from moving vehicles using dense stereo and optical flow. In *2004 IEEE/RSJ International Conference on Intelligent Robots and Systems (IROS)(IEEE Cat. No. 04CH37566)* (Vol. 4, pp. 3718-3725). IEEE.

Thorslund, B., & Lindström, A. (2020). Cyclist strategies and behaviour at intersections. Conscious and un-conscious strategies regarding positioning. *Transportation research part F: traffic psychology and behaviour*, *70*, 149-162.

Van der Waerden, P., Van der Waerden, J., & Gebhard, S. (2024). Intersection based innovations and cyclists' route choice decisions in urban areas. Transport policy, 146, 205-214.

Wu, C., Yao, L., & Zhang, K. (2012). The red-light running behavior of electric bike riders and cyclists at urban intersections in China: an observational study. Accident Analysis & Prevention, 49, 186-192.

©2023 Leschik, C., Zhang, M. & Gimm. K. published by TU Delft OPEN on behalf of the authors.

ISSN: 2667-2812

The Evolving Scholar Vol. 3, 2023

http://dx.doi.org/10.59490/65bb23b9a9e7b296b4866314

Bicycle and Motorcycle Dynamics 2023
Symposium on the Dynamics and Control of Single Track Vehicles
18–20 October 2023, Delft University of Technology, The Netherlands

Type of the Paper: Conference Paper

Revised

Analytical expression to calculate the suspension stroke and sag of vehicles

[version 2; peer reviewed]

Vasquez F. [1,*]

[1] Department of Mechanical Engineering, University of Concepcion, Chile; fevasquez@udec.cl, ORCID 0000-0002-6385-237X

[*] corresponding author

Name of Editor: Jason Moore
First published: 19/09/2023
Last published: 03/04/2024
Citation: Vasquez, F. (2024). Analytical expression to calculate the suspension stroke and sag of vehicles [version 2; peer reviewed]. The Evolving Scholar - BMD 2023, 5th Edition.

This work is licensed under a Creative Commons Attribution License (CC-BY).

Abstract:

Suspension stroke and sag are important to provide comfort to the passengers and to maintain contact of the tyres with the ground (road holding), nonetheless, they have not been extensively discussed in the literature. In this article, we aim to obtain elementary expressions to calculate the stroke and sag. To this end, we use the suspension displacement variance found in the literature, which has been derived for continuous road excitations, and by introducing a reliability interval, we are able to find the desired expressions. We extended the analysis to the case when the optimal suspensions are used, and furthermore, we simplified the expressions using two approximations. Lastly, a numerical example shows that the derived equations yield reasonable values for a first approximation, highlighting that they are valid for continuous excitations.

Keywords:

Suspension Design, Vehicle Dynamics, Optical Suspension

©2023 F. V., published by TU Delft OPEN on behalf of the authors.
ISSN: 2667-2812

 http://dx.doi.org/10.59490/65bb23b9a9e7b296b4866314

1 Introduction

A vehicle's suspension system is designed with two objectives: to provide comfort to the passengers and to maintain contact of the tyres with the ground (road holding). To enhance comfort, it reduces the transmission of road irregularities into the chassis, while, to improve road holding, it minimizes variations in tyre force at the contact point. A typical suspension system achieves these goals by connecting each wheel to the chassis with a properly designed spring and damper. However, it is widely recognized that optimal comfort and road holding cannot be simultaneously achieved, as they demand different stiffness and damping settings. Consequently, determining the appropriate setup poses a challenging task.

Simple models are employed to comprehend the variables involved and evaluate prototypes in a short time (Lot, 2021). The widely used half-motorcycle model (the quarter-car model in four-wheeled vehicles) is particularly effective. This model, dividing the motorcycle into front and rear ends, captures the vertical motions of the chassis and wheel masses due to road input with two degrees of freedom. Additionally, the suspension elements are considered linear to simplify the analysis further. While sacrificing precision, this model allows the derivation of several algebraic expressions that are not possible with more detailed models. For example, responses to random road inputs, including the variance of sprung mass acceleration, tyre force variation, and suspension displacement, can be calculated directly in terms of road characteristics, driving speed, vehicle masses, damping, and stiffness. Furthermore, specific values of stiffness and damping optimal for comfort or road holding can be directly calculated (Sheibe, 2009). These expressions provide preliminary values of stiffness and damping for the next design stage, where they are refined, and non-linearities are added to improve performance.

Concerning the required suspension stroke or space, it must accommodate displacements arising from at least three sources. Firstly, the displacement arising from spring deformation in the static condition, commonly known as suspension sag, establishes the operation point. This point changes with extra passengers or luggage and in quasi-static conditions of hard braking or acceleration (Lot, 2021). Around this operation point, the suspension continuously moves due to road irregularities. There is agreement that these oscillations can be treated as a random process, showing a normal distribution through measurements. (CITA) Lastly, additional transient displacements might be imposed over these, arising from isolated events such as potholes and bumps. If the suspension stroke is not large enough, or the static equilibrium position is set improperly, displacements might reach the suspension ends. Reaching the compression end-stroke during landings or due to a sufficiently large upward obstacle generates a sudden shock on the chassis and rider, which is highly detrimental to comfort. On the other hand, reaching the extension end-stroke due to a large downward obstacle or rebound after landing may cause the tyre to detach from the ground, which is detrimental to road holding. Therefore, defining the correct amount of suspension stroke and then the suspension sag allows minimizing reaching any ends, improving vehicle performance.

Suspension stroke is usually defined based on typical values for the corresponding vehicle segment (Lot, 2021). In contrast, suspension sag is usually set at 33% of the suspension stroke (Thede, 2010), which is achieved by adding an appropriate preload to the springs. In this way, two-thirds of the stroke is available for compressions from the operation point and one-third for an extension. This approach is justified by the argument that avoiding shocks on the chassis is more important than avoiding detachments (Lot, 2021). Despite this reasonable argument, significantly different values are also recommended for specific disciplines, such as 25% for motocross, 15% for cross-country bicycles, and 40% for downhill ones. Nonetheless, these are recommended as starting points to be subsequently adjusted by each rider according to the particular terrain and riding style. Determining the specific sag value for a given application seems cumbersome in the non-academic literature, while no model or discussion is found in the academic one.

In this article, we focus on the suspension stroke and sag required for continuous road excitations, as the suspension must always accommodate them. We leave the static and quasi-static displacement for future analysis since they mainly depend on external factors such as carrying load, suspension geometry and isolated events since their existence is not always assured. Therefore, this paper aims to analyze suspension stroke and sag and propose a simple yet general model to calculate them. To achieve this, first, we calculate the suspension stroke needed to accommodate the displacements arising from continuous road excitation using the displacement variance equation from the literature. Next, we introduce the expressions of optimal stiffness and damping for comfort and road holding and find the required stroke for these optimal conditions. We further introduce the first natural frequency of the system to derive even simpler expressions from which a relation between the stroke required in optimal comfort and road holding is proposed. Lastly, we present a numerical example to test the derived equations.

©2023 F. V., published by TU Delft OPEN on behalf of the authors.
ISSN: 2667-2812

2 Mathematical model of suspension displacements due to continuous excitation

This section briefly presents the derivation of the expression for the suspension displacement and sag, as shown in the literature. We focus on the main assumptions for deriving the suspension displacement variance as described in (Popp, 2010) and (Lot, 2021). Although the theory of random vibrations has been extensively described in specific literature, these authors clearly present the assumption that justifies its application to vehicle dynamics. They are relevant to us since they allow us to justify the expressions derived subsequently in Section 3. First, we present the description of the rough road as an stochastic process. Subsequently we apply this excitation to a linear half-motorcycle model to maintain simplicity and show three methods to find the suspension displacement.

2.1 Road description

Road unevenness can be categorized into individual and continuous (Popp, 2010). Individual or isolated events such as potholes, bumps and edges produce discrete or impulsive excitations (Lot, 2021) and essentially generate free vibrations in the vehicle (Popp, 2010). If the irregularity is large enough, it can cause safety-related incidents and usually require a non-linear approach (Limebeer, 2018). On the other hand, continuous road unevenness causes a continuous excitation, resulting in forced vibrations. Although less harmful than important isolated events, it occurs in everyday rides, so it is equally important (Limebeer, 2018). Although road roughness can be measured deterministically to study the response of the vehicle to that specific road, it is convenient to consider it as a stochastic process since it allows us to extend conclusions to other roads using statistics (Popp, 2010). Since we aim to obtain general conclusions, we consider stochastic continuous excitations.

These authors agree that a stochastic process can describe continuous road irregularities. This means a random variable $h(x)$ can be used to describe the road height h at a specific longitudinal distance x from a reference. Moreover, as explained by (Popp, 2010), several studies have shown that the process is stationary, normally distributed, and ergodic. The stationary random process means that the statistical properties are the same at all longitudinal positions, which is a feasible assumption for roads constructed with the same technology (Lot, 2021). Normal distribution, is a reasonable assumption as demonstrated by (Dodds, 1973) and means that the probability density function of the road height at each point p is given by the well-known Gauss function given by Equation (1):

$$p(h_i) = \frac{1}{\sigma_i\sqrt{2\pi}} exp\left[-\frac{(h_i - m_i)^2}{2\sigma_i^2}\right], \tag{1}$$

where m_i and σ_i are mean and standard deviation of the road height h_i at point x_i, respectively. From this Equation, reliability intervals can be derived, which indicate the probability of finding the random variable within the interval defined by the mean and k_r standard deviations to each side, i.e.

$$m - k_r\sigma < h_i < m + k_r\sigma, \quad k_r = 1, 2, 3, .. \tag{2}$$

In particular, for $k_r = 1, 2, 3$, the probabilities are $0.683, 0.955, 0.997$. By further defining the height reference in the mean value $m = 0$, the probability only depends on the standard deviation. This means, for example, that the probability that the road height is less than $\pm 2\sigma$ is 95%. Lastly, ergodic means that the statistical properties of each random variable h_i, obtained by considering several measurements or realisations of the road at position x_i, are the same statistical properties of each road measurement. It is also a feasible assumption according to (Popp, 2010).

The road height's single-sided power spectral density (PSD) Φ is widely used to describe roads. The simplest model, which is used by standard ISO 8608 (ISO, 2016) to classify roads, is given by Equation (3):

$$\Phi(\Omega) = \Phi_0(\Omega_0)\left(\frac{\Omega_0}{\Omega}\right)^2, \tag{3}$$

where, Φ_0 is the amplitude in m^2/(rad/m) at the reference circular frequency, which is usually considered as $\Omega_0 = 1$ rad/m. This function is a downward slope on a logarithmic scale and is valid for $0.063 \leq \Omega \leq 17.77$ rad/m. Essentially, the standard defines eight bands in this plot labelled from A to H, classifying smooth to very irregular roads, respectively. Each band is characterised by a central value Φ_0 at frequency Ω_0. The importance of the formulation with PSDs is that its integral is directly the variance of the random variable.

The vehicle response depends on the excitations in time rather than in space. Therefore, the road description given before is converted to the temporal domain. Following (Lot, 2021), first, the number of radians of oscillation per second received by the vehicle ω are

©2023 F. V., published by TU Delft OPEN on behalf of the authors.
ISSN: 2667-2812

 http://dx.doi.org/10.59490/65bb23b9a9e7b296b4866314

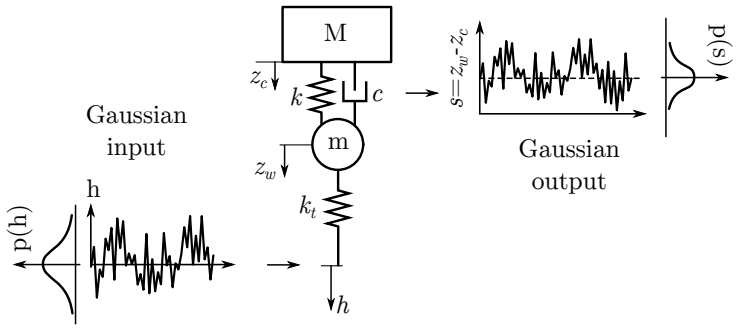


Figure 1. Half-motorcycle model consists on a sprung mass M (chassis) connected to the unsprung mass m (wheel) by linear spring and damper of constants k and c respectively. Road height $h(t)$ excites the system through the tyre which has a vertical stiffness k_t. The output of interest is the suspension displacement $s(t)$, positive in compression.

proportional to the number of radians of oscillation per meter Ω and the meters travelled per second by the vehicle V, i.e. $\omega = V\Omega$. Additionally, the variance of road height measured in time or space must be the same in a sufficiently long road, since its the same road seen at different speeds, Equation (4) must hold true.

$$\sigma_h^2 = \int \Phi(\Omega) d\Omega = \int \Phi(\omega) d\omega \tag{4}$$

Given that $d\omega = V d\Omega$, it can be shown that $\Phi(\omega) = \Phi(\Omega)/V$. In this way the road PSD in temporal domain is given by Equation (5):

$$\Phi(\omega) = \quad \frac{\Phi_0}{V} \left(\frac{\Omega_0 V}{\omega}\right)^2 = V\Phi_0 \left(\frac{\Omega_0}{\omega}\right)^2. \tag{5}$$

This means that the intensity with which the road excites the vehicle is proportional to the height of the road irregularities and the speed at which it is being driven over them.

The spectrum Φ_v of road height velocity $\dot{h}$, can be shown to be $\Phi(\omega)_v = \omega^2 \Phi(\omega)$. After some manipulation the road height velocity spectrum is given by Equation (6):

$$\Phi(\omega)_v = V\Phi_0\Omega_0^2, \tag{6}$$

which is a constant function. This means that the road velocity equally excites low and high frequencies, or the road velocity is a white-noise process. According to (Popp, 2010), the noise intensity q of a white-noise process is given by $q = \pi\Phi$. Then, considering Equation (6), the noise intensity of the road height velocity results in Equation (7):

$$q_v = \pi V \Phi_0 \Omega_0^2. \tag{7}$$

where Ω_0 can be dropped if it is considered to be 1 rad/m.

Thus, we have described road roughness as a stochastic process with three main characteristics: stationary, normally distributed, and ergodic. Next, by considering the driving speed, we convert the excitation from space into the temporal domain. Lastly, we show that the derivative of such excitation, namely, the road height velocity, has a constant spectrum, and we found an explicit expression for its intensity.

2.2 Suspension displacement on rough road

The road excitation creates a displacement in the suspension, which needs to be calculated. The simplest model able to capture the essential dynamics of the suspension is the well-known quarter-car model known as the half-motorcycle model (Lot, 2021) in two-wheeled vehicles. It consists of a sprung mass M (chassis) connected to the unsprung mass m (wheel) by linear spring and damper of constants k and c respectively, Figure 1. The road interacts with the wheel through the tyre, which has a vertical stiffness k_t. Vertical displacement of chassis $z_c(t)$ and wheels $z_w(t)$ are commonly used as the independent coordinates of the model, and

©2023 F. V., published by TU Delft OPEN on behalf of the authors.
ISSN: 2667-2812

the road vertical displacement is $h(t)$ is the input. (Limebeer, 2018), (Lot, 2021), (Popp, 2010) show that the equations of motion of this model are given by Equation (8):

$$\begin{bmatrix} M & 0 \\ 0 & m \end{bmatrix} \begin{bmatrix} \ddot{z}_c \\ \ddot{z}_w \end{bmatrix} + \begin{bmatrix} c & -c \\ -c & c \end{bmatrix} \begin{bmatrix} \dot{z}_c \\ \dot{z}_w \end{bmatrix} + \begin{bmatrix} k & -k \\ -k & k+k_t \end{bmatrix} \begin{bmatrix} z_c \\ z_w \end{bmatrix} = \begin{bmatrix} 0 \\ k_t \end{bmatrix} h(t) \tag{8}$$

Which can be written in compact form as on Equation (9):

$$\mathbf{M}\ddot{\mathbf{z}} + \mathbf{C}\dot{\mathbf{z}} + \mathbf{K}\mathbf{z} = \mathbf{H}h(t), \tag{9}$$

They can be rearranged in state-space form as on Equation (10):

$$\begin{bmatrix} \dot{\mathbf{z}} \\ \ddot{\mathbf{z}} \end{bmatrix} = \begin{bmatrix} \mathbf{0} & \mathbf{I} \\ -\mathbf{M^{-1}K} & -\mathbf{M^{-1}C} \end{bmatrix} \begin{bmatrix} \mathbf{z} \\ \dot{\mathbf{z}} \end{bmatrix} + \begin{bmatrix} \mathbf{0} \\ -\mathbf{M^{-1}H} \end{bmatrix} h(t) \tag{10}$$

and in compact form as on Equation (11):

$$\dot{\mathbf{x}} = \mathbf{A}\mathbf{x} + \mathbf{B}h(t). \tag{11}$$

where the state vector is $\mathbf{x} = [\mathbf{z}\ \dot{\mathbf{z}}]^{\mathbf{T}}$. Lastly, by further differentiating with respect to time, an expression for the response of the system with respect to road height velocity $\dot{h}(t)$ is obtained on Equation (12).

$$\ddot{\mathbf{x}} = \mathbf{A}\dot{\mathbf{x}} + \mathbf{B}\dot{h}(t). \tag{12}$$

Now, the suspension response to the road input can be obtained by at least three methods. A direct approach is to generate a road profile of a chosen class and integrate the Equation of motion (11) to obtain the system response $\mathbf{x}(t)$, from where the suspension stroke $s(t)$ can be calculated by Equation (13):

$$s(t) \quad = z_c(t) - z_w(t). \tag{13}$$

However, given that, strictly speaking, the solution obtained is for that particular road, it is not possible to generalize conclusions easily. Nonetheless, since the system is linear, frequency or covariance analysis can be used to obtain more general conclusions. For example, using a frequency analysis, the variance of the output process can be calculated directly from the input statistics. This is possible because of the system's linearity, which implies that if the input is a normally distributed random process, so will the output, recall Figure 1.

In particular, according to (Lot, 2021) the PSD of the suspension displacement Φ_s, is calculated using the suspension transfer function $H_s(i\omega)$, Equation (15), and road height velocity PSD Φ_v, Equation (6), as shown on Equation (14):

$$\Phi_s(i\omega) = |H_s(i\omega)|^2 \Phi_v. \tag{14}$$

$$H_s(i\omega) = \frac{z_c(i\omega) - z_w(i\omega)}{\dot{h}(i\omega)} = \frac{mk_t i\omega}{D(i\omega)} \tag{15}$$

where, $D(i\omega) = Mm(i\omega)^4 + (M+m)c(i\omega)^3 + [M(k+k_t) + mk](i\omega)^2 + ck_t i\omega + kk_t$.

Since the road height velocity PSD is a constant value, the suspension PSD is simply the transfer function scaled by $\Phi_v = V\Phi_0\Omega_0^2$. The variance of the suspension stroke is then given by Equation (16)

$$\sigma_s^2 = \int_0^\infty \Phi_s d\omega = V\Phi_0\Omega_0^2 \int_0^\infty |H_s(i\omega)|^2 d\omega. \tag{16}$$

Integration of this expression is cumbersome and it can be alleviated using symbolic algebra. Nonetheless, it can be avoided using a third approach, the covariance analysis, as described by Popp (2010). From Equation (8), it is possible to express the suspension displacement in terms of the derivatives of the state $\mathbf{x}$ as Equation (17):

$$s = z_c - z_w = \frac{-M\ddot{z}_c - c(\dot{z}_c - \dot{z}_w)}{k} = \begin{bmatrix} \frac{-c}{k} & \frac{c}{k} & \frac{-M}{k} & 0 \end{bmatrix} \dot{\mathbf{x}} = \mathbf{g}^{\mathbf{T}}\dot{\mathbf{x}}. \tag{17}$$

©2023 F. V., published by TU Delft OPEN on behalf of the authors.
ISSN: 2667-2812

Also, the stroke variance can be expressed as Equation (18):

$$\sigma_s^2 = \mathbf{g^T P g} \tag{18}$$

where $\mathbf{P}$ is the covariance matrix of $\dot{\mathbf{x}}$. Popp (2010) obtains this matrix by solving the Lyapunov matrix equation,

$$\mathbf{A P}_x + \mathbf{P}_x \mathbf{A}^T + \mathbf{B Q}_w \mathbf{B}^T = 0 \tag{19}$$

and after some manipulations, he shows that the suspension displacement variance is given by Equation (20)

$$\sigma_s^2 = \frac{q}{2} \frac{M+m}{c}. \tag{20}$$

Remarkably, this result agrees with the one obtained by Gobbi (2001) using frequency analysis.

In summary, we applied the stochastic road derived previously to a linear quarter car model to maintain simplicity. First, we showed the equations of motion of this vehicle, in general, and state-space forms, and we further showed an expression in terms of the road height velocity. Subsequently, we show three methods to calculate the suspension displacement for the stochastic road. We explain that temporal analysis is direct but not generalizable; frequency analysis is greatly simplified using road height velocity instead of road height since it is a constant input, nonetheless, it results in a cumbersome expression to integrate; and lastly, we consider the covariance analysis as explained by Popp (2010), to find the suspension displacement of a vehicle driving on a stochastic road. The main assumptions considered for the derivation are a linear vehicle and the stochastic road being stationary, normally distributed and ergodic.

3 Required suspension stroke

In this section, we present a method to find the size or stroke required by the suspension, together with the sag. In particular, we extend the results of the suspension displacement variance into a specific stroke value by defining a confidence interval. First, we derive an expression for the required suspension stroke with a general set of parameters. Subsequently, we derive the expression for the particular case of the optimal suspension parameters given by (Sheibe, 2009).

3.1 With general suspension parameters

The suspension displacement variance can be expressed explicitly in terms of the road and driving speed by substitution of the noise intensity, Equation (7), as in Equation (21):

$$\sigma_s^2 = \frac{\pi V \Phi_0}{2} \frac{M+m}{c}, \tag{21}$$

where Ω_0^2 has been ignored after considering $\Omega_0 = 1$ rad/m.

Since the suspension displacement is a random variable, the stroke required to accommodate *every* occurrence is infinite. Therefore, to materialize a suspension stroke, we need to define the amount of displacements we want to fit within the suspension stroke. This can be done by defining the reliability interval, with parameter k_r, and considering the standard deviation of the suspension displacement σ_s. As depicted in Figure (2), the suspension stroke is given by Equation (22):

$$l_{max} = 2 k_r \sigma_s \tag{22}$$

Which in explicit form is given by Equation (23):

$$l_{max} = 2 k_r \sqrt{\frac{\pi}{2} V \Phi_0 \frac{M+m}{c}}. \tag{23}$$

For example, by choosing $k_r = 3$, it can be determined that a suspension stroke of $l_{max} = 6\sigma_s$ will accommodate 99.7% of suspension displacements, Additionally, since the normal distribution is symmetric with respect to the mean value, which is the

©2023 F. V., published by TU Delft OPEN on behalf of the authors.
ISSN: 2667-2812

 http://dx.doi.org/10.59490/65bb23b9a9e7b296b4866314

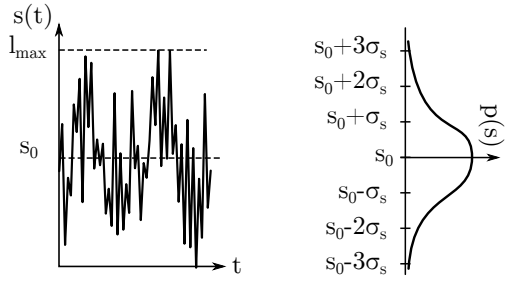


Figure 2. Suspension displacement $s(t)$ has a normal distribution around the operation point s_0. The suspension stroke required l_{max} is twice its standard deviation σ_s times the reliability parameter $k_r = 1, 2, 3, ...$

static equilibrium point, the compressions and extensions around the are equally expected, and the suspension sag s_0 needs to be half the size of the suspension stroke as given by Equation (24):

$$s_0 = k_r \sqrt{\frac{\pi}{2} V \Phi_0 \frac{M+m}{c}}. \tag{24}$$

In summary, a reliability interval must be introduced to calculate a required suspension stroke and sag since the displacement is random. After its definition and considering the standard deviation of the suspension displacement, an expression for the suspension stroke has been derived in terms of the excitation (road and driving speed) and vehicle masses and damping. Lastly, due to the symmetry of the response, the sag needs to be half of the stroke.

3.2 With optimal suspension parameters

Suspension stiffness and damping can be optimized for road holding or comfort and calculated with analytical expressions for the quarter car model as described in (Sheibe, 2009) and (Gobbi, 2001). With Equations (23, 24), we can now extend those results to calculate the suspension stroke and sag required for such optimal suspensions. For example, expressions for optimal stiffness and damping for road holding are given by (Lot, 2021) in terms of masses and tyre stiffness by Equations (25) and (26):

$$k_{rh} = \frac{M m k_t}{(M+m)^2} \tag{25}$$

$$c_{rh} = \sqrt{\frac{m M^3 k_t}{(M+m)^3}}. \tag{26}$$

Other authors such as (Guiggiani, 2018) recommend defining the suspension stiffness such that the first natural frequency is in a particular range. Combining both approaches, we can rewrite the optimal damping as Equations (27):

$$c_{rh} = M \sqrt{\frac{k_{rh}}{(M+m)}}, \tag{27}$$

where k_{rh} is calculated such that the desired first natural frequency is achieved, and tyre stiffness is obtained from Equation (25). Using this damping in Equation (23), we find that the required suspension stroke for optimal road holding is given by Equation (28):

$$l_{max,rh} = 2k_r \sqrt{\frac{\pi V \Phi_0}{2} \sqrt{\frac{(M+m)^3}{kM^2}}} \tag{28}$$

and suspension sag is half this value.

Furthermore, by taking into consideration that $M + m \approx M$ since usually the sprung mass M is about 8-10 times the unsprung mass (Lot, 2021) and that the first natural frequency is approximately $\omega_n = 2\pi f_n \approx \sqrt{k/M}$, we can find an approximation to the

©2023 F. V., published by TU Delft OPEN on behalf of the authors.
ISSN: 2667-2812

 http://dx.doi.org/10.59490/65bb23b9a9e7b296b4866314

Table 1. Parameters for the half-motorcycle model of Figure (1) for the rear axle of a sport-touring motorcycle,

M	113.8	kg
m	28	kg
k	21000	N/m
c	1300	Ns/m
k_t	150000	N/m

suspension stroke for road holding as Equation (29):

$$l_{max,rh} \approx \; k_r \sqrt{\frac{V\Phi_0}{f_n}}. \tag{29}$$

Regarding the optimal suspension for comfort, the expressions presented by (Lot, 2021) are given by by Equations (30) and (31):

$$k_c = 0 \tag{30}$$

$$c_c = k\sqrt{\frac{M+m}{k_t}}, \tag{31}$$

which is are feasible in practice since a non-zero stiffness is required to support vehicle weight. Therefore, non-optimal suspension and tyre stiffness must be imposed for practical purposes. Substituting this damping into Equation (23), we find the suspension stroke required for optimal comfort as Equation (32):

$$l_{max,c} = \; 2k_r \sqrt{\frac{\pi V\Phi_0}{2}\sqrt{(M+m)\frac{k_t}{k^2}}} \tag{32}$$

and the suspension sag is half this value. Using the same considerations for road holding, we can approximate the suspension stroke required for optimal comfort as Equation (33):

$$l_{max,c} \approx \; k_r \sqrt{\frac{V\Phi_0}{f_n}\sqrt{\frac{k_t}{k}}}. \tag{33}$$

Interestingly we can see that suspension stroke for optimal road holding and comfort are related according to Equation (34):

$$l_{max,c} \approx \; l_{max,rh} \left(\frac{k_t}{k}\right)^{1/4} \tag{34}$$

which means that if the suspension setting is changed from optimal road holding to optimal comfort, the suspension stroke (and suspension sag) needs to be increased by a factor of $\left(\frac{k_t}{k}\right)^{1/4}$ independently of the road, driving speed and vehicle mass and damping.

4 Numerical example: Suspension stroke required by a sport-touring motorcycle

In the following section, we provide a numerical example of the suspension stroke required for a sport-touring motorcycle to visualize the equations derived.

First, we consider the parameters of the sport-touring motorcycle described in Lot (2021), a 270 kg motorcycle with rider included, designed for a top speed of 60 m/s. After decomposing the motorcycle into the half-motorcycle model, the parameters for the rear axle are shown in Table (1). Next, according to its market segment, this motorcycle is expected to travel on regular asphalt roads. This corresponds to Class C Road, for which we consider $\Phi_0 = 16\ 10^{-6}$ m^2/(rad/m) that is the middle of this class interval. Lastly, we assume a reliability interval of $k_r = 3$ in order to get 99.7% of occurrences within the suspension stroke since we want to avoid reaching any of the suspension ends in most cases possible.

Using Equations (23) and (24) we find that the suspension stroke and sag required for these considerations are 0.077 m and 0.039 m, respectively. The motorcycle was actually designed with a suspension stroke of 0.14m and a 33% of sag, which is 0.046m. Figure

©2023 F. V., published by TU Delft OPEN on behalf of the authors.
ISSN: 2667-2812

 http://dx.doi.org/10.59490/65bb23b9a9e7b296b4866314

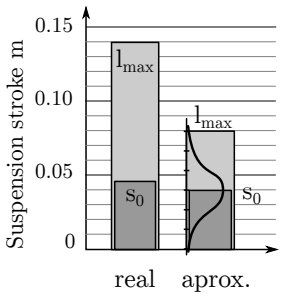


Figure 3. Suspension displacement $s(t)$ has a normal distribution around the operation point s_0. The suspension stroke required l_{max} is twice its standard deviation σ_s times the reliability parameter $k_r = 1, 2, 3, ...$

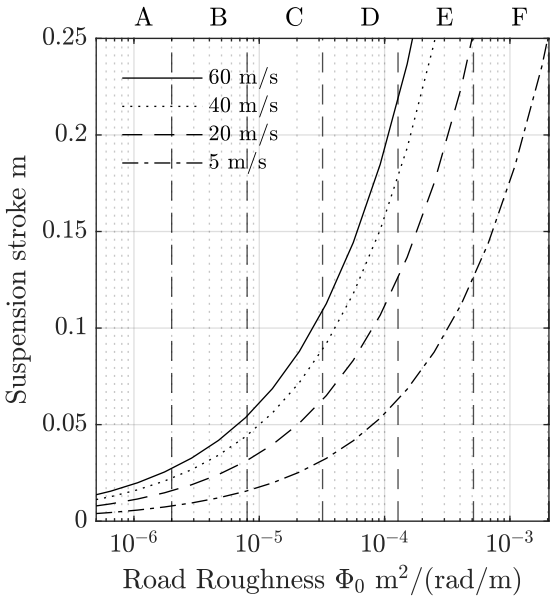


Figure 4. Suspension stroke required by the sport-touring motorcycle described in Table (1) to get 99.7% of occurrences within the stroke (i.e avoiding full extension or compression) for different driving speeds and road roughness.

(3) compares the real suspension and the one approximated by the derived Equations. It can be seen that sag is well approximated by the proposed expression, which means that the stroke left for extensions in a real motorcycle is mainly to accommodate road roughness. Conversely, the real suspension stroke is about 1.5 larger than predicted. This is likely because the real suspension needs to accommodate extra compressions arising from increased static equilibrium position and isolated bumps beyond compressions from road roughness.

Next, we calculate the suspension stroke required for several road classes and speeds to predict the motorcycle's performance in different conditions from the design case. As it can be seen in Figure (4), if the motorcycle uses the calculated stroke of 0.077m, it can also drive on poor roads, such as class D and E, but at top speeds of 15 m/s and 3.7 m/s, respectively. Differently using the real suspension of 0.14m, these roads could be driven faster, at 49.6 m/s and 12.4 m/s, respectively.

Now, if this motorcycle is designed with the optimal suspension for road holding and a natural frequency of 1.3 Hz, which is a typical value according to (Lot, 2021), the required suspension stroke would be 0.096 m. Similarly, using the simplified version in Equation (29), we obtain 0.087 m, meaning it is underestimated by 10% On the other hand, if the motorcycle is designed with optimal suspension for comfort, and considering the original suspension and tyre stiffness, the stroke needs to be $\left(\frac{150000}{21000}\right)^{1/4} = 1.63$ times larger than l_{rh}, which is 0.157 m.

©2023 F. V., published by TU Delft OPEN on behalf of the authors.
ISSN: 2667-2812

This example shows that the equations derived in this article provide a reasonable first approximation for the suspension stroke and sag required in a vehicle due to continuous road excitation. Furthermore, it can be used to evaluate the changes required in stroke to accommodate changes in stiffness or damping. The main advantage is that it has a simple formulation and requires few parameters, which is beneficial in the early design stages. Nonetheless, it must be pointed out that changes in loads, driving manoeuvres, and isolated events such as large potholes or bumps will generate displacements in the suspension beyond the stroke calculated here. Therefore, the values given by these equations must be taken as a starting point and not as final design parameters.

5 Conclusions

Analytical expressions were derived to calculate the suspension stroke and sag required for a continuous road excitation. To this end, first, we presented a review of the calculation of suspension displacement under continuous excitation, which is mainly based on random vibration theory. Here, we explained that road roughness is described as a random variable, being stationary, normally distributed, and ergodic. This process excites the vehicle represented by a linear half-motorcycle model, and the system response is derived. Next, we briefly described three methods to obtain the suspension displacement from the system response: temporal, frequency and covariance analysis. Due to linearity, the suspension displacement is also random, and the suspension displacement variance expression was presented according to (Popp, 2010).

Subsequently, we used this result to find an expression for the required suspension stroke. We found that since the displacement is random, a reliability interval needs to be introduced to convert the variance into a specific stroke. This means we must define the probability of a displacement within a specific interval. Particularly, we explain that the suspension stroke required is twice the standard deviation times the reliability parameter while the suspension sag is half this value. Substitution of the variance described in the literature into these expressions is the central idea and contribution of this article. To the best of the author's knowledge, this result has not been presented before in the literature.

Next, we extend this idea into the particular case of optimal suspensions described by (Sheibe, 2009). By introducing the algebraic expressions of stiffness and damping optimal for road holding or comfort, we derived the expressions for the suspension stroke and sag required for these two optimal situations. In the search for elementary expressions, we introduced an approximation for the first natural frequency of the system by ignoring the unsprung mass since it is several times smaller than the sprung mass. It resulted in simplified versions of the suspension stroke and sag required for both optimal situations. Interestingly, we found that the suspension stroke required for comfort is larger than for road holding by a factor that only depends on the ratio of tyre and suspension stiffness.

Lastly, with a numerical example on a sport-touring motorcycle, we showed that the derived expressions yield reasonable results and that they can be used to evaluate the performance of the motorcycle under different conditions (speed or road) and parameters (stiffness and damping). The example also helped to highlight the main assumptions of the derived equations. The most important is that the stroke and sag are calculated for rough road excitations, which means that the proposed equations ignore isolated events and changes in static operation point. Indeed, the real stroke was found to be 1.5 times larger than the calculated stroke for rough road excitations, showing the need for a larger stroke to accommodate the other excitations. Nonetheless, the suspension sag was predicted reasonably well, showing that isolated events and changes in static operation point primarily affect the suspension compressions rather than extensions. A second important assumption is the linear system. Increasing departures from linearity, such as non-linear damping or tyre-ground detachments, will result in larger differences in the use of suspension than predicted. A third important assumption to be considered is the single-slope PSD road roughness description. If the road is better described with a two-slope PSD as described by many authors, the proposed expressions will also differ from reality.

In this way, in this article we had derived a simple analytical expression for the required suspension stroke and sag of vehicles by using the suspension displacement variance found in the literature. We found that it yields reasonable results and is particularly well suited for early design stage of the suspension since it is limited to continuous road, linear vehicle and a simple road description.

References

Dodds, C.,& Robson, J. (1973) The description of road surface roughness. *J. Sound and Vibration*, *31*, 175–183

Gobbi, M. & Mastinu, G. (2001). Analytical Description and Optimization of the Dynamic Behaviour of Passively Suspended Road Vehicles. *J. Sound and Vibration*, *245*, 457–481.

Guiggiani, M.(2018). *The Science of Vehicle Dynamics*. Springer.

©2023 F. V., published by TU Delft OPEN on behalf of the authors.
ISSN: 2667-2812

ISO 8608., (2016). *Mechanical Vibration - Road Surface Profiles*. Standard, International Organization for Standardization.

Limebeer, D., Massaro, M., (2018). *Dynamics and Optimal Control of Road Vehicles*. Oxford University Press

Lot, R., Sadauckas, J., (2021). *Motorcycle Design: Vehicle Dynamics Concepts and Applications*.

Popp, K., Schiehlen, W., (2010). *Ground Vehicle Dynamics*. Springer.

Thede, P., Parks, L., (2010). *Race Tech's Motorcycle Suspension Bible*, Motorbooks.

Sheibe, F., Smith, M., (2009). Analytical Solutions for Optimal Ride Comfort and Tyre Grip for Passive Vehicle Suspensions. *Vehicle System Dynamics*, *47*, 1229–1252.

©2023 F. V., published by TU Delft OPEN on behalf of the authors.
ISSN: 2667-2812

The Evolving Scholar Vol. 3, 2023

http://dx.doi.org/10.59490/6617d703879b85da25b041a0

Bicycle and Motorcycle Dynamics 2023
Symposium on the Dynamics and Control of Single Track Vehicles
18–20 October 2023, Delft University of Technology, The Netherlands

Type of the Paper: Conference Paper

Revised

Application of tire multi-physical modeling methodologies for the preliminary definition of a racing motorcycle setup

[version 2; peer reviewed]

Flavio Farroni[1,*], Guido Napolitano Dell'Annunziata[1], Marco Ruffini[1], Fabio Alberti[2], Danilo D'Andrea[2], Giacomo Risitano[2], Dario Milone[2]

[1] Department of Industrial Engineering, Università degli Studi di Napoli Federico II, Italy; flavio.farroni@unina.it, ORCID 0000-0001-8257-5534
[2] Department of Engineering, Università degli Studi di Messina, Italy; grisitano@unime.it, ORCID 0000-0002-0506-8720
[*] corresponding author

Name of Editor: Jason Moore
First published: 14/02/2024
Last published: 12/04/2024
Citation: Farroni, F., Napolitano Dell'Annunziatta, G., Ruffini, M., Alberti, F., D'Andrea, D., Risitano, G. & Milone, D. (2024). Application of tire multi-physical modeling methodologies for the preliminary definition of a racing motorcycle setup [version 2; peer reviewed]. The Evolving Scholar - BMD 2023, 5th Edition.
This work is licensed under a Creative Commons Attribution License (CC-BY).

Abstract:

Optimizing the performance of racing motorcycles is a central goal for competition teams. The necessity to ensure driver stability and a good level of grip in the widest possible range of riding conditions makes it necessary for tires to work in the right temperature window, capable of ensuring the highest interaction force between tire and road. Specifically, the internal temperature of the tire is a parameter that can be difficult to measure and control but has a significant impact on motorcycle performance and, also, on driver stability. Deepening knowledge of internal tire temperature in racing motorcycles can improve performance optimization on the track and can aid in finding the right motorcycle setup. In this work, a physical thermal model is adopted for an activity concerning the development of a moto-student vehicle, to predict the racing motorcycle setup allowing the tire to work in a thermal window that optimizes grip and maximizes tire life. More in detail, a focus has been placed on the effects of the motorcycle's wheelbase and pivot height variations on internal tire temperatures. Indeed, the stability and handling of the vehicle are highly dependent on the geometric properties of the chassis. Several values of such quantities have been tested in a properly implemented vehicle model developed in the "VI-BikeRealTime" environment, validated by outdoor tests, able to provide forces acting on the tires, slip indices, and speeds, needed by the thermal model as inputs. Through the analysis of the internal temperatures calculated by the model, reached by the various layers of the tire, it has been possible to investigate which of the simulated conditions cause a too-fast thermal activation of the tire and which of them can avoid overheating and underheating phenomena. In addition, this research has delved into the correlation between motorcycle riders' paths and temperature fluctuations with the aim of comprehending how minor alterations in routine maneuvers may influence tire energy activation, particularly in the context of racing and qualifying conditions.

Keywords:

Automotive engineering, Motorcycle Thermal Model, Multi-physical Modeling, Motorcycle Setup Optimization, Tire Characterization

©2023 Farroni, F., Napolitano Dell'Annunziata, G., Ruffini M., Alberti F., D'Andrea D., Risitano G., & Milone, D. published by TU Delft OPEN on behalf of the authors.
ISSN: 2667-2812

 http://dx.doi.org/10.59490/6617d703879b85da25b041a0

Introduction

Racing teams that are in competition strive to maximize the performance of their motorcycles. The fundamental need to ensure rider stability and secure excellent grip across a wide spectrum of riding conditions necessitates that motorcycle tires work within an optimal temperature range [8, 18]. This temperature window is essential for attaining the highest possible interaction force between the tire and the road surface, a parameter that profoundly influences the vehicle's stability and handling characteristics [2, 12]. This need for tire optimization becomes particularly pronounced in the context of motorcycle racing, where high roll angles and rapid speeds amplify the tire's significance as the sole point of contact with the road [4]. The tire's capacity to deliver optimal performance hinges on its complex structure and viscoelastic characteristics, which are, in turn, significantly governed by the temperatures experienced by various layers within the tire [9, 10]. However, accurately measuring and controlling the internal temperature of a tire presents a formidable challenge. Despite these difficulties, it remains abundantly clear that tire temperature profoundly impacts motorcycle performance and rider stability on the track.

To address this critical challenge, our research harnesses a motorcycle-specific adaptation of the physical thermal model thermoRIDE [6]. This model has proven its mettle by faithfully replicating the thermal dynamics of motorcycle tires across diverse operational conditions. Notably, it empowers us with a temperature distribution map within the tire's inner rubber layers. By carefully analyzing the internal temperatures across various layers of the tire, it is possible to pinpoint the conditions that lead to rapid thermal activation, as well as those that prevent overheating or underheating phenomena. The study presented in this paper aims to exploit the capability of this cutting-edge thermal model to aid in the development of a racing motorcycle prototype. More in detail, our goal is to conduct a preliminary analysis to understand if this model can assist in identifying the best configuration for a racing motorcycle, which will allow the tire to operate at its optimal temperature, thus ensuring better traction and longevity [19]. The first area of focus is the analysis of how the fork angle and the swingarm length of a motorcycle impact the distribution of temperature in the tire. These key chassis components play a significant role in determining the motorcycle's overall stability and handling capabilities [20]. Additionally, we will explore how various driving patterns can affect the activation velocity of the tires' energy. Understanding this aspect is crucial for the driver to prepare for a qualifying lap or the start of the race. To conduct this research, we employ a calibrated vehicle model within the "VI-BikeRealTime" simulation environment. This model yields crucial inputs such as the forces acting on the tires, slip indices, and speeds, all of which are essential for the thermal model's operation. As part of the efforts to guarantee reliability and consistency and let the thermal model work, it is also necessary to identify the thermal diffusivity of each layer in the tire. This endeavor is realized through a procedure grounded in experimentation and validation [1]. Furthermore, there is a need to delve into the complexities of the contact patches between the tire and the road. These contact conditions prove to be dynamic and multifaceted, shifting with variations in load, pressure, and camber conditions [17]. Employing a combination of indoor testing and validated procedures, we scrutinize the contact patch extension. This research endeavor unfolds in the backdrop of a broader understanding - that the optimization of tire performance and the thermal conditions of these critical components hold the key to unlocking the full potential of racing motorcycles. Our work wants to contribute to this understanding by shedding light on the intricate interplay between motorcycle performance, tire temperatures, and vehicle setup. The insights deriving from this type of study can generate an important value for racing teams striving to achieve the perfect balance between tire performance and rider stability in the demanding and dynamic world of motorcycle racing. In the pursuit of this balance, this work embraces the challenge of translating scientific knowledge into practical racing solutions, with the ultimate goal of enhancing performance on the track.

1 Materials and Methods

1.1 Motorcycle dimensions

The model utilized in this context is exemplified by the motorcycle prototype that took part in the international Motostudent competition. To be more specific, the focus of our analysis was on a Pre-Moto3 motorcycle prototype. This model was designed to accommodate modifications in the fundamental dimensions of the motorcycle. Within this framework, it is possible to adjust critical components such as the positions of the steering joint, pivot, and stiffness for both suspensions. These alterations are undertaken with the primary objective of identifying and achieving the optimal configuration for the prototype. The general layout of this motorcycle prototype encompasses various key elements that play a crucial role in its performance and handling characteristics. These elements include the steering joint, pivot, and ride height, along with other essential design features and specifications. The chosen solution for the front suspension is the conventional upside-down telescopic design, whereas, for the rear suspension, a progressive-to-frame solution has been selected. The model encompasses the utilization of geometric dimensions, including the relative length and posi-

©2023 Farroni, F., Napolitano Dell'Annunziata, G., Ruffini M., Alberti F., D'Andrea D., Risitano G., & Milone, D. published by TU Delft OPEN on behalf of the authors.
ISSN: 2667-2812

 http://dx.doi.org/10.59490/6617d703879b85da25b041a0

tion of fundamental points such as the "steer joint" and "pivot," as well as the inertial properties such as weight, inertial matrices, and coordinates of the centroids of the vehicle to be simulated. The geometric dimensions were determined through prior analytical calculations, while the inertial properties were acquired using the CAD system. The geometric characteristics of the motorcycle are summarized in Table 1.

Table 1. Motorcycle Geometric Features

Geometric Feature	Value
Wheelbase	1290 ± 77 mm
Offset	30 mm
Swingarm Length	513 ± 7 mm
Fork Angle	$22° \pm 2°$
Motorcycle Mass	110 kg

1.2 Testing and simulations

In essence, the primary objective revolves around the analysis and refinement of the motorcycle prototype. The overarching goal is the improvement of design, performance, and overall functionality, particularly during open-loop maneuvers. This undertaking is fueled by the need to identify and understand the paramount factors that wield a significant thermal influence on motorcycle tires' performance, especially during intricate maneuvers like slaloms. To achieve this, the team embarked on a systematic series of simulations adjusting the parameters illustrated in Figure 1 [16].

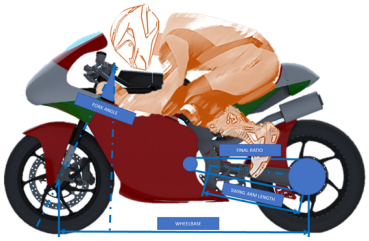


Figure 1. Fundamental Dimensions Considered during the Vehicle Performance Analysis.

Moreover, the inquiry extended beyond the mechanical aspects. The team ventured into the realm of the rider's driving style, conducting an exploration of the various trajectories adopted to successfully navigate the challenging slalom course. The rider's techniques and choices in maneuvering the motorcycle through this course offered invaluable insights into the interplay between the human and the vehicle. The conducted analyses have been divided into three steps. Specifically, variations of one parameter at a time were individually considered. The test groups considered are as follows:

1. TEST I: Variation in the rider's driving style. Trajectories taken by the rider during the slalom were altered;
2. TEST II: Variation in the length of the motorcycle's swingarm;
3. TEST III: Variation in the fork angle.

For each of these tests, the telemetry channels most related to the temperatures developed by the tires were considered so as to better understand as the mechanical parameter of the bike or riding style changed what was happening to the temperatures developed by the tires themself. More in detail, since the grip is closely related to the temperatures that develop in the inner layers of the tire, these analyses were done using a physical-analytical thermal model called the "thermoRIDE" model.

2 thermoRIDE Model

The thermoRIDE model is a physical-analytical tire model designed to comprehensively study and analyze the complex interactions between a tire, its external environment, and the inner wheel chamber as can be seen in Figure 2 [6]. It can be used to assist

©2023 Farroni, F., Napolitano Dell'Annunziata, G., Ruffini M., Alberti F., D'Andrea D., Risitano G., & Milone, D. published by TU Delft
OPEN on behalf of the authors.
ISSN: 2667-2812

 http://dx.doi.org/10.59490/6617d703879b85da25b041a0

in optimizing the motorcycle's performance by providing guidance on how to properly carry out the motorcycle setup in order to improve the tire behavior. Additionally, it offers valuable insights to help prevent potentially dangerous situations such as overheating or problems caused by tires that are too cold. This model is capable of simulating the temperature distribution in the tire layers and of relating this distribution to the heat exchange mechanisms. thermoRIDE model considers several critical heat-related phenomena, including heat generation and exchange processes within the tire structure and with the external environment [7]:

- ***Heat Generation Mechanisms***
  - *Friction Power:* Arising from the tire-road tangential interaction;
  - *Strain Energy Loss:* Resulting from cyclic deformations during tire rolling.
- ***Heat Exchange Processes***
  - *Tire-Road Thermal Conduction:* heat conduction between the tire tread and the road pavement;
  - *Internal Thermal Conduction:* heat conduction between different points within the tire structure due to temperature gradients;
  - *Tire-External Air Thermal Convection:* convection phenomena occurring at the tread surface with external air;
  - *Tire-Inner Air Thermal Convection:* convection phenomena occurring between the inner liner layer and the inner air.

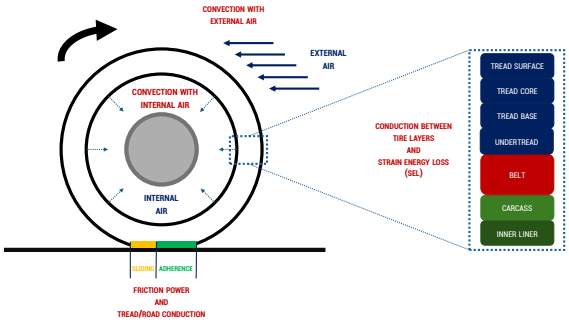


Figure 2. thermoRIDE Model Scheme.

2.1 Mathematical Model

The mathematical foundation of the presented model relies on Fourier's diffusion equation, applied to a three-dimensional domain. This equation describes the energy within the system, accounting for gains and losses. Fourier's law of heat conduction, a fundamental principle in thermodynamics, states that heat transfer is proportional to the temperature gradient and the thermal conductivity of the material [13]. Mathematically, this relationship is expressed as:

$$\vec{q} = -k\nabla T \tag{1}$$

Where:

- $\vec{q}$: Local heat flux density [W/m²]
- k: Material's conductivity [W·m/K]
- ∇T: Temperature gradient [K/m]

©2023 Farroni, F., Napolitano Dell'Annunziata, G., Ruffini M., Alberti F., D'Andrea D., Risitano G., & Milone, D. published by TU Delft OPEN on behalf of the authors.
ISSN: 2667-2812

It is possible to derive a parabolic partial differential equation from Fourier's law, suitable for numerical integration in transient thermal conditions [15]. To achieve that, an infinitesimal volume element $dV = dxdydz$ is considered. Since the change in the internal energy of a closed system is equal to the amount of heat supplied to the system, minus the amount of work done by the system on its surroundings, and the control volume is considered not deformable, the internal energy dU of the infinitesimal volume dV is given by the following expression:

$$dU = \rho \cdot dV \cdot c_v \cdot T \tag{2}$$

Here, ρ represents density, c_v denotes specific heat at constant volume, and T signifies temperature.

Since the volume dV is not able to do any work ($dL = 0$), the change in the internal energy dU is linked only to the amount of heat dQ added to the system. The term dQ encompasses two distinct contributions:

- *Heat exchanged through the outer surface of the volume dV:*

$$dQ_{EX} = -dt \cdot \oint dS \cdot \vec{q} \cdot \hat{n} \cdot dS = -dt \cdot \nabla \cdot (k \nabla T) \cdot dV \tag{3}$$

- *Heat generated within the volume dV:*

$$dQ_G = \dot{q}_G \cdot dV \cdot dt \tag{4}$$

Here, $\dot{q}_G$ represents the rate of heat generation per unit volume and unit time (in W/m$^3 \cdot$ s), and $\hat{n}$ denotes the normal unit vector to the faces of the volume element.

By combining equations 2, 3, and 4, the energy balance equation for the infinitesimal volume dV is derived:

$$\rho \, dV \, c_v \, dT = \dot{q}_G \, dV \, dt + dt \, \nabla \cdot (k \, \nabla T) \, dV \tag{5}$$

Equation 5, divided on both sides by the quantity $\rho \cdot dV \cdot c_v \cdot dt$, defines the Fourier heat equation:

$$\frac{\partial T}{\partial t} = \frac{\dot{q}_G}{\rho c_v} + \frac{\nabla \cdot (k \nabla T)}{\rho c_v} \tag{6}$$

Equation 6 enables the determination of the three-dimensional temperature distribution $T(x, y, z, t)$, contingent upon the specification of boundary conditions. It governs the temporal variation of temperature concerning a specific thermal gradient and elucidates how temperature evolves due to generative effects and heat transport phenomena.

The complexity of the phenomena to model and the degree of accuracy required for the applications towards which it is intended has made it necessary to take into account the dependence of the thermodynamic quantities and in particular of the thermal conductivity on the temperature. Furthermore, the non-homogeneity of the tire has also made it important to consider the variation of the above parameters along the thickness. Therefore, the Fourier equation takes the following state-space formulation:

$$\frac{\partial T}{\partial t} = \frac{\dot{q_G}}{\rho c_v} + \frac{1}{\rho c_v} \left(\frac{\partial^2 k(z,T) T}{\partial x^2} + \frac{\partial^2 k(z,T) T}{\partial y^2} + \frac{\partial^2 k(z,T) T}{\partial z^2} \right) \tag{7}$$

To solve Equation 7 by means of a numerical method and obtain the evolution of the temperature field over time, it is important to make an appropriate tire model, and correctly model the thermal phenomena introduced above.

2.2 Tire Structural Model

The tire is considered to be parallelepiped-shaped and it is discretized by means of a grid, whose nodes represent the points in which the temperature will be determined instant by instant thanks to the written Fourier Equation 7. The discretization of the tire,

©2023 Farroni, F., Napolitano Dell'Annunziata, G., Ruffini M., Alberti F., D'Andrea D., Risitano G., & Milone, D. published by TU Delft
OPEN on behalf of the authors.
ISSN: 2667-2812

 http://dx.doi.org/10.59490/6617d703879b85da25b041a0

which caters to its unique attributes such as dimensions, diffusivity, and inertia, can substantially vary. This variability is aimed at accurately representing the transient and steady-state thermal dynamics while upholding real-time requirements across diverse tire operational conditions. The default tire structure encompasses six layers along the radial direction:

- *Tread Surface:* the outermost part that is in contact with the road and external air;
- *Tread Core:* positioned just below the surface, directly tied to grip and also to tire stiffness;
- *Tread Base:* the deepest tread layer, whose temperature affects mostly the tire stiffness rather than the grip level;
- *Belt:* situated beneath the tread base and made of a series of wire cloths arranged with small angles, this layer is significantly linked to the strain energy loss phenomenon;
- *Body Plies:* layer composed by a series of mutually parallel cords of very durable and at the same time flexible material, surrounded by the vulcanized rubber compound; it is another important contributor to the SEL, because of the energy dissipated by the friction among different plies and within the plies;
- *Inner Liner:* last layer of the tire which is in contact with the inner air, not significantly influencing SEL, stiffness, or grip.

For what concerns the lateral discretization of the tire, the standard one is illustrated in Figure 3. However, for motorcycle tires, the discretization along the y direction can be customized with up to 16 ribs (Figure 3 showcases the default configuration). This customization is contingent upon the availability of pre-initialized boundary conditions maps specific to the analyzed tire [6].

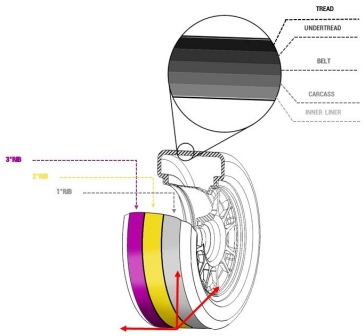


Figure 3. thermoRIDE Tire Mesh Scheme.

2.3 Heat Exchange and Heat Generation Mechanisms

The writing of the balance equations for each generic node requires the modeling of the heat exchange and heat generation mechanisms. In order to achieve that, there is a need to model the mechanisms of heat exchange and heat generation introduced at the beginning of the chapter.

2.3.1 Friction Power

Friction power (FP), is a heat generation mechanism connected with the thermal power produced at the tyre-road interface because of the tangential stresses that, in the sliding zone of the contact patch, work by dissipating heat [11]. In the balance equations writing, FP can be associated directly with the nodes involved in the contact with the ground. FP is calculated based on global force and sliding velocity values assumed to be equal throughout the contact patch:

$$FP = \frac{F_x {v_x}^s + F_y {v_y}^s}{A_{CP}} \tag{8}$$

©2023 Farroni, F., Napolitano Dell'Annunziata, G., Ruffini M., Alberti F., D'Andrea D., Risitano G., & Milone, D. published by TU Delft OPEN on behalf of the authors.
ISSN: 2667-2812

where F_x and F_y are the longitudinal and lateral interaction forces in [N]; ${v_x}^s$ and ${v_y}^s$ are the longitudinal and lateral sliding velocities in [m/s]; A_{CP} is the contact patch area in $[\mathrm{m}^2]$. Part of this thermal power is transferred to the tire, the remaining to the asphalt.

2.3.2 Strain Energy Loss

The energy dissipated by the tire as a result of cyclic deformations is called strain energy loss (SEL) [3]. This dissipation is due to a superposition of several phenomena: intra-plies friction, friction inside plies, and nonlinear viscoelastic behavior of all rubbery components. The cyclic deformations to which the system is subject occur with a frequency corresponding to the tire's rotational speed. During the rolling, indeed, portions of the tire, entering continuously in the contact area, are submitted to deformations which cause energy loss and then heat dissipation. The empirical SEL formulation is a function of the following parameters and it deeply depends on the tire characteristics [5]:

$$SEL = f(\overline{F}, \omega, \gamma, {p_{in}}^{air}) \tag{9}$$

where $\overline{F}$ is the average interaction force at the contact patch in [N], ω is the wheel rotation frequency [rad/s], γ is the wheel camber angle [rad] and, finally, ${p_{in}}^{air}$ represents the inflation pressure in the wheel chamber $[\mathrm{N/m}^2]$.

2.3.3 Heat Exchange with the Road

Thermal conduction between the tire's tread and the asphalt is modeled using Newton's formula, which employs an appropriate heat exchange coefficient. The heat exchange term (Q_C) for the i-th node is computed as follows:

$$Q_c = H_c(T_r - T_i)\Delta X \Delta Y \tag{10}$$

The terms of this expression can be described as follows:

- H_c is the equivalent conduction coefficient in $[\frac{\mathrm{W}}{\mathrm{m^2K}}]$
- T_r is the track temperature in [K];
- T_i is the temperature of the generic node in [K];

This heat exchange mechanism strongly concerns the tread surface layer.

2.3.4 Heat Exchange with the Outside/Inside Air

The intricate process of heat transfer between a surface and a fluid in motion at varying temperatures is elucidated by natural and forced convection equations. In detail, to describe the tire heat exchange with the external air it is necessary to consider the mechanism of forced convection, occurring when there is relative motion between the car and the air, and the mechanism of natural convection linked to situations of absent motion. Supposing the tire invested by the air similarly to a cylinder invested transversely from an air flux, the convection heat transfer can be modeled by Newton's law of cooling formulation [14]:

$$Q_{conv} = h_c(T_{air} - T_i)\Delta X \Delta Y \tag{11}$$

where T_{air} is the air temperature at the boundary tire layer in Kelvin and h_c is the convection coefficient. The determination of this last coefficient, both for forced and natural convection, is based on the classical approach of the dimensionless analysis.

Finally, it can be noted that the radiation heat transfer is neglected.

©2023 Farroni, F., Napolitano Dell'Annunziata, G., Ruffini M., Alberti F., D'Andrea D., Risitano G., & Milone, D. published by TU Delft
OPEN on behalf of the authors.
ISSN: 2667-2812

 http://dx.doi.org/10.59490/6617d703879b85da25b041a0

2.4 Contact Patch Evaluation

In order to model the thermal exchanges involving the tire, it is crucial, as observable from the above formulas, to have information about the size and shape of the contact zone between the tire itself and the road. The size and the shape of the contact areas are obtained by means of specifically developed test procedures, based on the use of a scanner and a special tool developed in Matlab. In these tests, the tires are scanned in different working conditions. In detail, tests are executed in different static conditions varying the vertical load F_z, the internal pressure ${p_{in}}^{air}$, and the wheel alignment configuration in terms of camber angle γ. In particular, because very high wheel camber angles are reached for motorcycles, in order to have robust information related to contact patches, it has been necessary to develop a special mechanical arm (Figure 4) that, integrated into the hydraulic press required to bring in the desired loads, allows very high angles of inclination to be reached for all load and pressure conditions.



Figure 4. Special Mechanical Arm Integrated into the Hydraulic Press.

An example of the obtained contact patch related to a vertical load of 1800N, an inflation pressure of 2.7 bar, and an inclination angle of 40 degrees, is shown in Figure 5. At this point, a set of four values is measured for each contact patch to characterize each of them. More in detail, the four values are related to the length of each side of the contact patch. Once the physical consistency has been verified based on the limit settings identified during experimental tests, the computed values are used as input for a tool that generates a map of the contact footprints based on the selected working conditions at any given time. Finally, it should be noted that static contact patches are acquired with this procedure. However, the instantaneous dynamic contact patch extension and shape can be quite different because of particular transient conditions of wheel loading, the centrifugal effect on the rolling tire, and viscoelastic tire intrinsic characteristics. To implement the contact patch dynamic characteristics MBD/FEA tire models, able to fit both static and dynamic experimental data, can constitute a valid instrument.



(a) 3D Tire Mesh. (b) Acquired Contact Patch.

Figure 5. Example of Measured Tire Contact Patch.

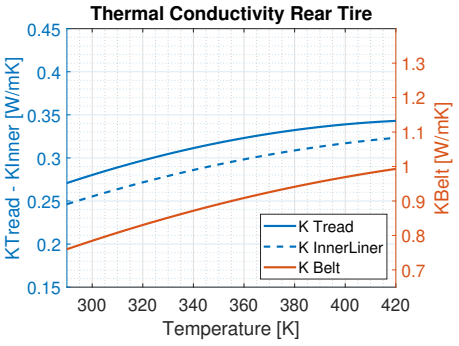
2.5 Tyre Thermal Characterization

The thermoRIDE model is designed to precisely simulate the thermal dynamics of vehicle tires under various working conditions. However, this model requires an accurate thermal characterization of all the tire layers involved. To achieve this, a non-destructive procedure has been proposed by C. Allouis et al., which can obtain the thermal diffusivity of each tire layer [1]. In this procedure, the tire tread surface is heated in a small spot employing a laser beam collimated with a lens, while the temperatures reached on an area located around the heated point (tread) and on the corresponding inner surface (inner liner) are acquired using two thermal cameras. Using the above instrumentation, the tire radial and circumferential temperature gradients are acquired. Then, these are employed in a model, known as "Thermo Racing Tyre Laboratory" model (TRTLab), to obtain the thermal diffusivity of the tire layers based on the use of Fourier's equation of diffusion applied to a three-dimensional domain. The heat generation term of the Fourier law, in

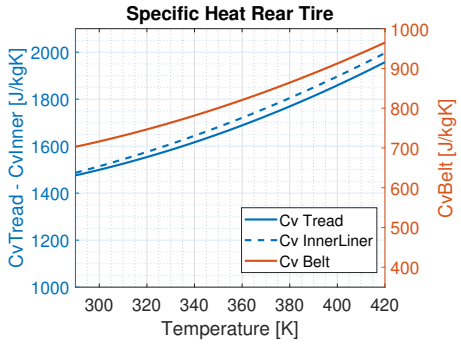
©2023 Farroni, F., Napolitano Dell'Annunziata, G., Ruffini M., Alberti F., D'Andrea D., Risitano G., & Milone, D. published by TU Delft
OPEN on behalf of the authors.
ISSN: 2667-2812

 http://dx.doi.org/10.59490/6617d703879b85da25b041a0

this case, is related to the laser thermal flux at the tread surface nodes. This heat generation term is assigned only to the tread nodes located within the laser spot area and the entire heating flux power is subdivided into singular nodes in relation to the laser spot area portion. The TRTLab Model is able to simulate the trend of the surface temperature and the inner temperature. So, knowing the data about these temperatures deriving from the experimental procedure explained above, a reverse engineering process is carried out by modifying the values of density, specific heat, and thermal conductivity until the simulated curves overlap with those acquired. When this happens the values of these quantities found for each layer are assumed as the physical parameters of the tire. For the rear tires of the motorcycle under consideration, the TRTLab model provided the results shown in Figure 6 for what concerns the thermal conductivity and the specific heat coefficient. The solid blue curve relates to the thermodynamic properties of the tread, the dashed blue curve to those of the inner liner, and the orange curve refers to the belt in which metal wires are present. From these curves, it can be seen that for this tire, the type of compound from which the tread is made conducts more heat than that from which the inner liner is made. Instead, these two compounds have very similar values of specific heat. As for the belt, it has completely different values because of the different material it is made of and, of course, it conducts heat much more than the rubber.



(a) Thermal Conductivity.



(b) Specific Heat Coefficient.

Figure 6. Rear Tire Thermal Properties.

2.6 Model Input/Output

The input data needed by the thermoRIDE consists of the telemetry channels, obtained using the "VI-BikeRealTime" environment, shown in Table 2. Instead, as for the output temperatures, they are summarized in the following Table 3.

Table 2. Model Input

Quantity	UOM	Description
F_z	[N]	Vertical interaction force
F_x	[N]	Longitudinal interaction force
F_y	[N]	Lateral interaction force
v_x	[m/s]	Wheel hub longitudinal velocity
v_y	[m/s]	Wheel hub lateral velocity
s_r	[-]	Slip ratio
s_a	[rad]	Slip angle
ω	[rad/s]	Wheel angular velocity
γ	[rad]	Inclination angle
T_{Air}	[°C]	Ambient air temperature
T_{Track}	[°C]	Road pavement temperature

Table 3. Model Output

Quantity	UOM	Description
$T_{\text{TreadSurf}}$	[°C]	Tread surface temperature
$T_{\text{TreadCore}}$	[°C]	Tread core temperature
$T_{\text{TreadBase}}$	[°C]	Tread base temperature
$T_{\text{InnerLiner}}$	[°C]	Inner liner temperature
T_{InnerAir}	[°C]	Internal air temperature
p_{InnerAir}	[bar]	Internal air pressure

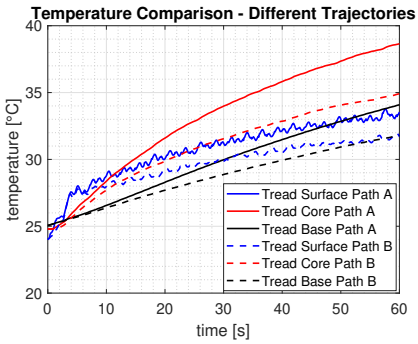
3 Results

This section presents the results of simulations conducted using the thermal model to understand the impact of certain changes in vehicle setup and driving style on temperatures. The focus is mainly on tread temperatures, which significantly affect grip. These results are related to slalom maneuvers performed in the VI-BikeRealTime virtual environment. This preliminary analysis aims to explore the potential use of thermoRIDE to enhance the performance of racing motorcycles. It is worth noting that this is an

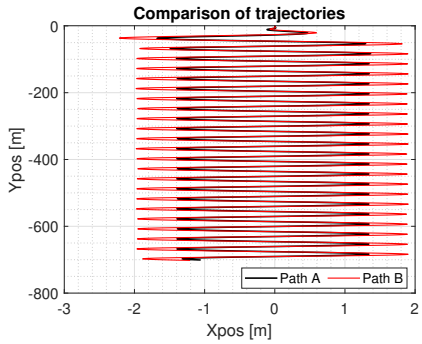
©2023 Farroni, F., Napolitano Dell'Annunziata, G., Ruffini M., Alberti F., D'Andrea D., Risitano G., & Milone, D. published by TU Delft
OPEN on behalf of the authors.
ISSN: 2667-2812

 http://dx.doi.org/10.59490/6617d703879b85da25b041a0

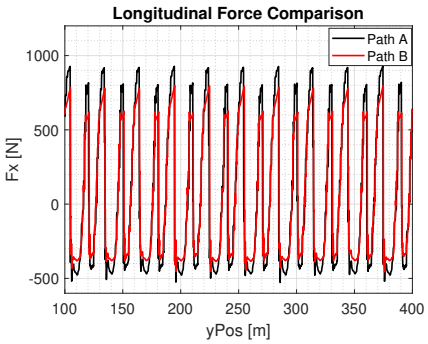
exploratory study to determine the model's reaction to various factors such as motorcycle setup or driving style. Therefore, it is advisable to focus on the qualitative patterns and fluctuations when executing even a basic maneuver such as the slalom, rather than giving excessive importance to precise temperature readings. In addition, it is specified that all results presented refer to the rear tire but, for this type of maneuver, similar considerations apply to the front tire. In Figure 7a, the thermoRIDE simulation results for two different trajectories followed by the virtual driver are shown. The trajectories were generated by changing in the VI-BikeRealTime virtual environment the radius of curvature with which the rider approaches the slalom. These two different paths both refer to setups having a fork angle of 19.8° and a swingarm length of 506 mm. First of all, it can be seen, in both cases, that for the slalom maneuver under exam, the temperature of the middle layer of the tread is the one that increases the most. This is related to the fact that no tire pre-heating was considered, so the tread surface starts from a low temperature and this does not rise much because this layer is most affected by the effect of convection with the outside air. In contrast, the tread core, not being subject to convection, retains some of the heat from friction power and also some of the heat from the inner layers. Finally, for this type of maneuver, the SEL generated is not much so the base tread (innermost layer of the tread), feeling less of the effects of friction power and having little heat coming from the tire carcass gets less warm. Clear differences can be highlighted by comparing the results of the two different trajectories. Specifically, the first one (path A), referred to by the continuous curves, is a narrower trajectory while the second one (path B) is more outward as can be seen in Figure 7b. As can be seen from Table 4 and in Figure 7c the innermost trajectory generates higher longitudinal forces, thus higher longitudinal friction powers. Instead, the lateral forces are only slightly higher in the case of the wider trajectory as shown in Figure 7d. So, Path A generates more friction power and raises tread temperatures higher than Path B. In addition, the narrower trajectory is traveled at a slightly higher speed and, therefore, there is somewhat higher SEL generation.



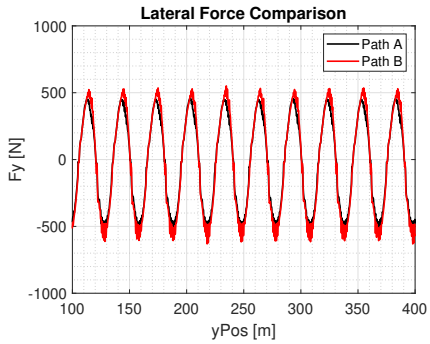
(a) thermoRIDE Results for Two Different Trajectories.



(b) Comparison of Trajectories.



(c) Longitudinal Force Comparison.



(d) Lateral Force Comparison.

Figure 7. thermoRIDE Results Analysis for Two Different Trajectories.

Table 4. Average Rear Forces and Longitudinal Velocities for Different Paths

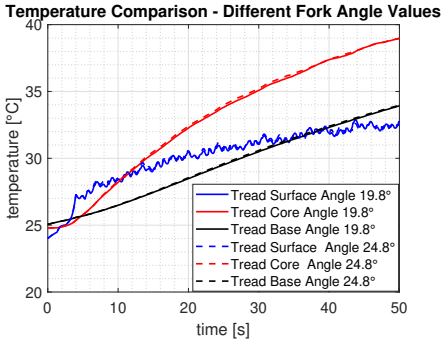
Path [m]	Average Longitudinal Force (N)	Average Lateral Force (N)	Average Longitudinal Velocity (m/s)
Path I	437.1	299.6	11.56
Path II	395.8	336.3	10.32

The analysis of temperature variations in the tread layers following setup changes are shown in Figure 8a and Figure 9a with their respective zooms in Figure 8b and 9b. More in detail, Figure 8a compares the temperatures for two different fork angle inclination values, 19.8° and 24.8°, when the swingarm length is set at 506mm; while Figure 9a shows the variation in temperature due to changes in swingarm length, 506 mm and 526 mm, when the fork angle is set at 19.8°. For all the cases, path A was referred to

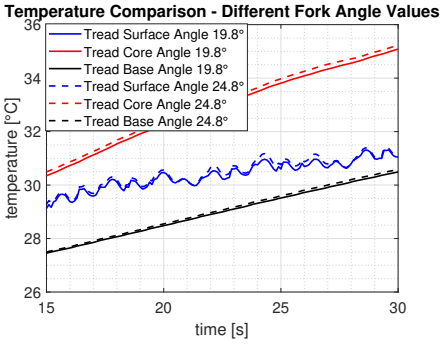
©2023 Farroni, F., Napolitano Dell'Annunziata, G., Ruffini M., Alberti F., D'Andrea D., Risitano G., & Milone, D. published by TU Delft
OPEN on behalf of the authors.
ISSN: 2667-2812

 http://dx.doi.org/10.59490/6617d703879b85da25b041a0

as the trajectory. In the first case, it can be seen that the model is sensitive even to a simple setup change such as the one under consideration and for a very trivial maneuver such as the slalom. In particular, from the zoom on the right, it is possible to note that when the fork angle value is higher there is a slight rise in all three tread layer temperatures. The clearest is observable for the tread core. Figures 9a and 9b demonstrate that extending the swingarm length leads to a decrease in tread temperatures across the board, with a more pronounced effect than previously observed. By implementing these adjustments and utilizing thermoRIDE to analyze their impact, there is the opportunity to acquire valuable intelligence on how to optimize tire thermal regulation.

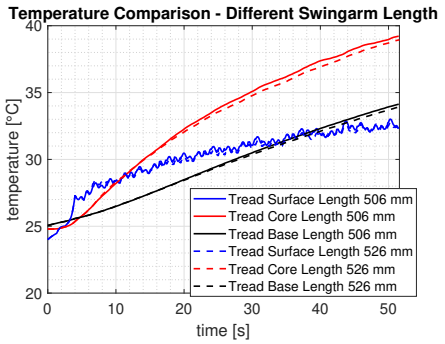


(a) thermoRIDE Results for Two Different Fork Angles.

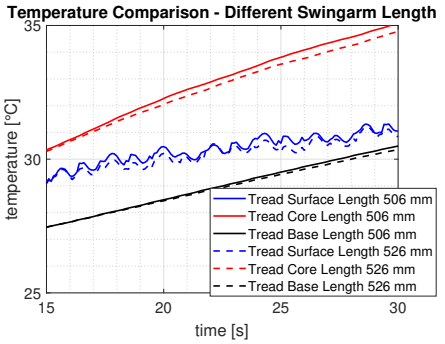


(b) Zoom of thermoRIDE Results for Two Different Fork Angles.

Figure 8. thermoRIDE Results Analysis for Two Different Fork Angle Values.



(a) thermoRIDE Results for Two Different Swingarm Lengths.



(b) Zoom of thermoRIDE Results for Two Different Swingarm Lengths.

Figure 9. thermoRIDE Results Analysis for Two Different Swingarm Lengths.

Conclusion

In this study, we conducted simulations using a physical-analytical thermal model to investigate the effects of various changes in vehicle setup and driver's driving style on tire temperatures, with a specific focus on tread temperatures, which significantly influence grip. The simulations were performed during slalom maneuvers within the VI-BikeRealTime virtual environment. The primary objective of this preliminary analysis was to assess the potential utility of the thermal model in enhancing the performance of racing motorcycles. It is important to emphasize that this study serves as an exploratory investigation, aiming to understand the model's responses to different factors related to motorcycle setup and rider behavior. Valuable preliminary insights were gained from the simulations conducted, revealing how the thermal model seems to be able to optimize racing motorcycle performance. The results indicated that different trajectories impact tire thermal histories. This information, provided by thermoRIDE, can be highly beneficial in assisting drivers to warm up their tires before a qualifying session or race. Additionally, the model can be important to carefully approach curves on certain circuits to avoid overheating that may lead to thermal degradation, causing faster wear and reduced performance during the race. Even though the effect of modifications in fork angle geometry and swingarm length on thermal model simulation outcomes might not be as considerable as the impact of trajectories, it is still detectable. The thermal model is very responsive to even the tiniest adjustments in maneuvers like the slalom, which is crucial to grasp how to handle the correct configuration and where to concentrate on enhancing motorcycle design. In the subsequent phase of our research, we intend to perform more complicated and extended maneuvers beyond the slaloms talked about in this article to fully comprehend the effect

©2023 Farroni, F., Napolitano Dell'Annunziata, G., Ruffini M., Alberti F., D'Andrea D., Risitano G., & Milone, D. published by TU Delft
OPEN on behalf of the authors.
ISSN: 2667-2812

of these modifications and observe more noticeable temperature changes. Furthermore, we plan to simulate single laps on the track with the same lap time but following different trajectories. This will highlight the usefulness of the model in preparing for qualifying sessions and races. Moreover, it is our intention to analyze different riding styles in terms of the rider's lateral movement to deepen their effect on the internal temperatures of the tire on a full race track simulation. In addition, similar analyses will be conducted not only using simulations in the virtual environment but also using telemetry acquired on the track appropriately. Finally, another focus point will be a more accurate definition of the SEL formulation for this type of application.

References

[1] Allouis, C., Farroni, F., Sakhnevych, A., and Timpone, F. (2016). Tire thermal characterization: test procedure and model parameters evaluation. In *Proceedings of the 24th World Congress on engineering*, London.

[2] Barbaro, M., Genovese, A., Timpone, F., and Sakhnevych, A. (2024). Extension of the multiphysical magic formula tire model for ride comfort applications. *Nonlinear Dynamics*.

[3] Brancati, R., Strano, S., and Timpone, F. (2011). An analytical model of dissipated viscous and hysteretic energy due to interaction forces in a pneumatic tire: Theory and experiments. *Mechanical Systems and Signal Processing*.

[4] Cossalter, V. and Doria, A. (2005). The relation between contact patch geometry and the mechanical properties of motorcycle tyres. *Vehicle System Dynamics*.

[5] Farroni, F., , Rocca, E., and Timpone, F. (2013). A full scale test rig to characterize pneumatic tyre mechanical behaviour. *International Review of Mechanical Engineering (IREME)*.

[6] Farroni, F., Mancinelli, N., and Timpone, F. (2020). A real-time thermal model for the analysis of tire/road interaction in motorcycle applications. *Applied Sciences*.

[7] Farroni, F., Russo, M., Sakhnevych, A., and Timpone, F. (2018). Trt evo: Advances in real-time thermodynamic tire modeling for vehicle dynamics simulations. *Journal of Automobile Engineering*.

[8] Farroni, F. and Sakhnevych, A. (2022). Tire multiphysical modeling for the analysis of thermal and wear sensitivity on vehicle objective dynamics and racing performances. *Simulation Modelling Practice and Theory*.

[9] Genovese, A., Maiorano, A., and Russo, R. (2022). A novel methodology for non-destructive characterization of polymers' viscoelastic properties. *International Journal of Applied Mechanics*.

[10] Genovese, A. and Pastore, S. R. (2021). Development of a portable instrument for non-destructive characterization of the polymers viscoelastic properties. *Mechanical Systems and Signal Processing*.

[11] Gent, A. N. and Walter, J. D. (2006). *Pneumatic tire*.

[12] Guiggiani, M. (2023). *The Science of Vehicle Dynamics*. Springer Cham.

[13] Kreith, F., Manglik, R. M., and Bohn, M. S. (2010). *Principles of Heat Transfer*. Brooks/Cole.

[14] Mavros, G. (2019). A thermo-frictional tyre model including the effect of flash temperature. *Vehicle System Dynamics*.

[15] Minkowycz, W. J., Sparrow, E., and Y., M. J. (2000). *Handbook of Numerical Heat Transfer*. John Wiley & Sons Inc.

[16] Risitano, G., Scappaticci, L., Grimaldi, C., and Mariani, F. (2012). Analysis of the structural behavior of racing motorcycle swingarms. Technical report, SAE Technical Paper.

[17] Romano, L., Timpone, F., Bruzelius, F., and Jacobson, B. (2022). Rolling, tilting and spinning spherical wheels: analytical results using the brush theory. *Mechanism and Machine Theory*, 173.

[18] Sakhnevych, A. (2022). Multiphysical mf-based tyre modelling and parametrisation for vehicle setup and control strategies optimisation. *Vehicle System Dynamics*.

[19] Sakhnevych, A. and Genovese, A. (2024). Tyre wear model: A fusion of rubber viscoelasticity, road roughness, and thermodynamic state. *Wear*.

[20] Scappaticci, L., Bartolini, N., Guglielmino, E., and Risitano, G. (2017). Structural optimization of a motorcycle chassis by pattern search algorithms. *Engineering Optimization*.

©2023 Farroni, F., Napolitano Dell'Annunziata, G., Ruffini M., Alberti F., D'Andrea D., Risitano G., & Milone, D. published by TU Delft
OPEN on behalf of the authors.
ISSN: 2667-2812

The Evolving Scholar Vol. 3, 2023

http://dx.doi.org/10.59490/65e718b10d45168c0b1a3a00

Bicycle and Motorcycle Dynamics 2023
Symposium on the Dynamics and Control of Single Track Vehicles
18–20 October 2023, Delft University of Technology, The Netherlands

Type of the Paper: Conference Paper

Revised

Assessment of bicycle experimental objective handling quality indicators
[version 2; peer reviewed]

Jules Ronné[1], Laura Dubuis[1], Thomas Robert[1,*]

[1] Univ Lyon, Univ Eiffel, Univ Claude Bernard Lyon 1, LBMC UMR_T 9406, F-69622 Lyon, France; jules.ronne@univ-lyon1.fr, ORCID 0000-0002-0867-6422; aura.dubuis@univ-lyon1.fr, ORCID 0000-0002-0851-0844; thomas.robert@univ-eiffel.fr, ORCID 0000-0002-6502-7082

[*] corresponding author

Name of Editor: Jason Moore
First published: 04/10/2023
Last published: 27/03/2024
Citation: Ronné, J., Dubuis, L. & Robert, T. (2024). Assessment of bicycle experimental objective handling quality indicators [version 2; peer reviewed]. The Evolving Scholar - BMD 2023, 5th Edition.
This work is licensed under a Creative Commons Attribution License (CC-BY).

Abstract:

Understanding and mastering handling quality is a critical concern for bicycle designers, as it directly impacts safety, comfort, and performance. However, this aspect has received limited attention to date. Existing literature offers experimental handling quality indicators based on bicycle kinematics, but their validity has yet to be established. This study aims to assess the predictive power of these indicators using experimental data derived from subjective assessments of handling quality. This data, obtained from a protocol involving 20 participants and 2 bicycles, enabling the testing 39 experimental indicators. The results indicate that certain vehicle kinematic quantities are indeed correlated with the perception of handling quality, but with low predictive power. Indicators based on handlebar movement are the most effective in explaining the sensation of handling quality. These indicators perform particularly well at low speeds, where physical and cognitive workload are associated with the quantity of control actions on the handlebars.

Keywords:

Bike, Kinematic, Subjective, Single-track Vehicle

©2023 Ronné, J., Dubuis, L., & Robert, T. published by TU Delft OPEN on behalf of the authors.
ISSN: 2667-2812

 http://dx.doi.org/10.59490/65e718b10d45168c0b1a3a00

1 Introduction

Context Cycling has become increasingly popular in urban areas in recent years. Its use is intensifying and diversifying. As well as being a recreational vehicle, bicycles are becoming (or re-emerging) as a means of transport (both personal and professional) in urban environments. The emergence of new uses, in particular cargo bicycles (for transporting people or goods), is driving changes in vehicles and practices. This wider use raises questions about the comfort, performance and safety of these vehicles. Mastering these characteristics will help facilitating the inclusive development of this low-carbon mobility, whatever the level of proficiency of users.

Given this context, it appears of primary importance to be able to characterise how well one can "handle" a given bicycle. Being able to experimentally evaluate the handling quality of a bike would be generally useful in a design process to quantify the performance of a design. This type of approach had already been proposed by Cain et al. (2012) for the development of stabilising wheels for children with learning disabilities.

Handling quality definition Handling quality is a 2-dimensional quantity defined by the ease and precision with which a pilot may complete a given task (Cooper and Harper, 1969). It describes the quality of the interaction between a cyclist and their bicycle. This concept is relatively consensual and is used in the automotive and aeronautical industries as well as for 2-wheeled vehicles (Cooper and Harper, 1969; Sugizaki and Hasegawa, 1988; Horiuchi and Yuhara, 1998; Kuroiwa et al., 1995; Weir and DiMarco, 1978; Hess, 2012).

Handling quality subjective assessment To date, the most promising approach for bicycle handling quality remains the subjective scale of Cooper-Harper (Hess, 2012) developed in the the aeronautic field (Cooper and Harper, 1969). It is interesting to note that this scale integrates both the cyclist's workload (which refers to ease) and performance (which refers to precision).

In similar fields (motorcycles and automotive), handling quality is mainly based on rider physical workload (omitting the performance component). The latter is often derived from steering torque measurement (Kuroiwa et al., 1995; Zellner and Weir, 1978; Cossalter and Sadauckas, 2006). But given the low torque needed to be controlled compared to a motorcycle, this approach is irrelevant for bicycles. Other objective measures of the physical and cognitive workload (using physiological approach, like fNRIS) remains complex and difficult to deploy in an ecological setting.

Finally, the most suitable approach for bicycle handling quality is the subjective rating scale developed by Cooper and Harper (1969). However, an objective approach to overcome data variability and methodological precautions inherent in the questionnaires is highly desirable. It would enable the handling quality evaluation of bicycles on larger scales and within an ecological setting. As highlighted by the review from Schwab and Meijaard (2013), this question is still a seldome addressed research issue. The authors also highlight the lack of standardised procedures for assessing the handling quality of a bicycle in a given experimental condition. Ideally, such indicators would be based solely on the vehicle kinematics or dynamics, that could be easily accessible.

Existing objective handling quality indicators To date, Takagi et al. (2022) are among the few to propose objective experimental indicators (SST evaluation and Handle Per Roll) based on vehicle kinematics, attempting to correlate them with cyclists' feeling (riding instability). This assessment methodology has not been addressed yet to bicycle handling quality.

The motorcycle, as a single-track vehicle, is probably the most similar vehicle for identifying handling quality indicators for bicycles. However, although both vehicles are primarily controlled through handlebar actions (Schwab and Meijaard, 2013), the forces involved are not of the same order of magnitude: a few N.m for bicycles (2.5 Nm maximum in Cain and Perkins (2010) experiment) compared to tens of N.m for motorcycles (20 to 100 Nm in Kuroiwa et al. (1995) experiment). Thus, motorcycle indicators based on steering torque will not be included in the study. However, motorcycle handling quality indicators based on kinematic quantities such as Yaw factor (Zellner and Weir, 1978) and Mozzi axis (Cossalter and Doria, 2004) are included. Indicators used to analyse bicycle movement in previous studies were also included. These indicators can be categorised into two approaches: variability of motion and quantification of *steer into the lean* strategy. In the variability approach, the variability of bicycle state variables (roll angle, yaw angle, and steering angle) and their derivatives are studied (Moore et al., 2010; Cain et al., 2016, 2012; Matsuzawa et al., 2009). The

©2023 Ronné, J., Dubuis, L., & Robert, T. published by TU Delft OPEN on behalf of the authors.
ISSN: 2667-2812

 http://dx.doi.org/10.59490/65e718b10d45168c0b1a3a00

quantification of *steer into the lean* strategy generally involves the analysis of correlations between bicycle state variables, such as roll rate/steer rate (Cain et al., 2016, 2012) and steer rate/roll angle (Takagi et al., 2022).

In the context of studying indicators solely based on vehicle kinematics, indicators based on the cyclist's torso lean will not be considered .

Objective and outline This article aims to assess the predictive power of 39 objective handling quality indicators. To do this, an experimental dataset was constructed by recruiting 20 cyclists who performed a line tracking task on a track using bikes equipped of IMUs. Participants subjectively rated the handling of the bicycles usingquestionnaires. This data have served as a reference for the assessment of handling quality indicators.

2 Material and methods

2.1 Cyclists

A sample of 20 cyclists (29 $\pm$ 6 years old) over the age of 18 who declared they knew how to ride a bicycle, were included in the study. Participants under 155 cm were excluded as they were outside the saddle adjustment range. These cyclists declared they had no balance problems and no particular physical disabilities.

2.2 Experimental bicycles

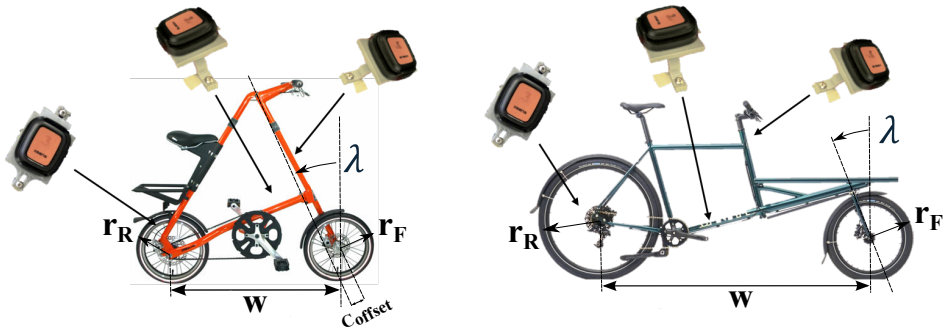


Figure 1. The experimental bicycles : foldable bicycle form Strida™ (left) and cargo bicycle (V3) from Omnium™ with their main geometric parameters

Bicycles setup Two commercially available urban bicycles were used for the experiment: a foldable bicycle from Strida™ and a cargo bicycle (V3) from Omnium™ (Figure 1). These two bicycles were chosen for their unusual design compared to the average city users' habits (see Table 1). More design parameters are available in the supplementary materials.

Parameter	Wheelbase	Caster offset	Steer axis tilt	Front wheel radius	Rear wheel radius
Symbol	w (m)	c_{offset} (m)	λ (°)	r_F (m)	r_R (m)
Omnium™cargo V3	1.59	0.0345	14	0.259	0.366
Strida™	0.89	0.055	24	0.196	0.196

Table 1. Geometric parameters of experimental bicycles

Bicycle motion is described by the following state vector: $(\delta, \phi, \psi, \dot{\delta}, \dot{\phi}, \dot{\psi}, u)$ as illustrated in Figure 2. Its components respectively describe: steering, roll and yaw angles and their time derivatives and the bicycle speed.

©2023 Ronné, J., Dubuis, L., & Robert, T. published by TU Delft OPEN on behalf of the authors.
ISSN: 2667-2812

 http://dx.doi.org/10.59490/65e718b10d45168c0b1a3a00

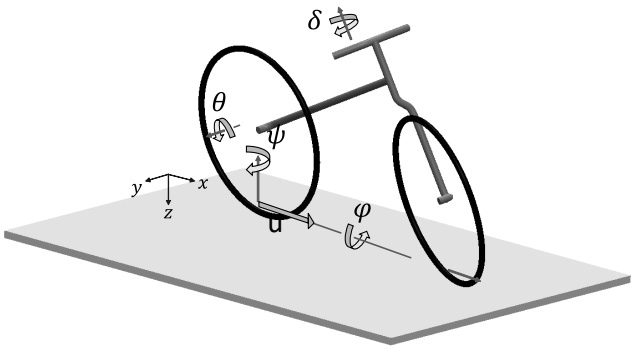


Figure 2. The experimental bicycles and their main geometric parameters definition

This state vector was estimated using three XSens DOT inertial sensors sampling at 60 Hz placed on the handlebar, frame, and rear wheel of each bicycle, as presented in Figure 1 . The sensors were synchronised so that the XSens fusion algorithm could be used to provide the orientation of each sensor relative to a global reference frame.

The rear wheel IMU was used to estimate the speed of the bicycle u from the rear wheel radius r_R and the wheel angular velocity $\dot{\theta}$. The other inertial units were used to measure angle and angle rates of the frame roll $(\phi, \dot{\phi})$ and yaw $(\psi, \dot{\psi})$, and the handlebar steering angle $(\delta, \dot{\delta})$.

2.3 Track

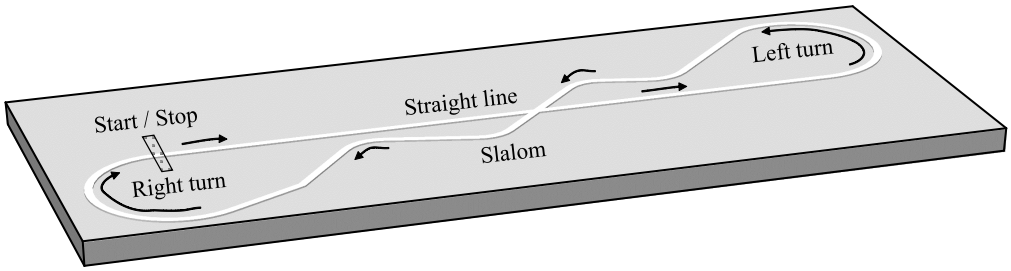


Figure 3. The track consists of a 130-meter-long white line painted on the ground, composed of a straight line, a slalom and two U-turns.

A path-tracking task was chosen so that a clear set of instructions could be defined and allowing self-assessment of the performance achieved. This task was chosen because it requires control qualities that are useful for mobility in an urban environment. Also, by its restrictive nature, this task seeks to exacerbate the participants' control difficulties.

Thus a 130 m long track was marked out on the ground of a flat tarmac car park closed to traffic. The circuit consists of a 10 cm wide line of white paint (see Figure 3).

The circuit is made up of a 43 m straight line, a circular left turn (5 m radius), a slalom (4 curves) and a circular right turn (5 m radius) . This track was designed as a mixed circuit, inspired by standard motorcycle manoeuvres, combining a straight, a slalom and two U-turns. The trajectories are deliberately demanding to create variations in difficulty.

©2023 Ronné, J., Dubuis, L., & Robert, T. published by TU Delft OPEN on behalf of the authors.
ISSN: 2667-2812

 http://dx.doi.org/10.59490/65e718b10d45168c0b1a3a00

2.4 Subjective assessment of handling quality

Among handling quality rating scales found in the literature, Cranfield Aircraft Handling Qualities Rating Scale (CAHQRS) from Harris et al. (2000) originally derived from the work of Cooper and Harper (1969) was chosen. This scale provides a discrete unidimensional measurement on 10 levels including performance and the load perceived by the cyclist. Its use for bicycle evaluation has already been suggested by Hess (2012). The CAHQRS was translated into French and adapted for use on bicycles. The scale used starts at level 0: "I achieved the task, extremely easily, I needed minimal compensation", and ends at level 9: "I failed in controlling the bike, I stopped, I needed maximal compensation".

2.5 Experimental procedure and conditions

The experiments were performed in two consecutive blocks, one per bicycle. The order of the blocks was randomised between subjects.

For each block, the bicycle saddle setup was adjusted to the participants, ensuring that they could at least touch the ground with the tip of their foot while sitting on the saddle. This position enabled them to stop easily and stabilise the bicycle with their feet.

The participants then had 5 minutes of training, during which they were free to test the circuit. The aim of this training was to allow the cyclists to familiarise them with the bikes ensuring they were comfortable at a variety of speeds.

At the end of this learning period, the participants were asked to perform laps of circuit at different speeds: as slowly as possible, at the optimal control speed, and faster than the optimal control speed. The optimal control speed is defined as the speed the cyclist self-estimated to be the best to control the bike on this specific task. A total of nine laps was performed per block (three per requested speed). The order of the requested speed was randomised, except the first lap that was always at the optimal control speed.

For each lap, the instructions given were: (1) Complete a single lap without breaking, (2) Try to keep the front wheel on the white line, (3) Try to maintain a constant speed.

2.6 Included Indicators

Yaw factor and derivatives In this paper, the Yaw factor (Y_F), initially utilised as a handling indicator in Zellner and Weir (1978), was subsequently chosen as variable of interest. This variable is a ratio that quantifies the amount of yaw rate per unite of steer angle. Unlike Zellner and Weir (1978) which uses a theoretical model to evaluate the experimental Yaw factor, Y_F was a variable used as a basis for calculating potential handling quality indicators. Three indicators are defined based on Y_F: its standard deviation, its mean value and its entropy. Using the same state variables ψ and δ (and their derivatives), additional indicators were constructed based on cross-correlation approach. Table 2 describes the 9 indicators derived form the Yaw factor and the additional indicators.

Variable(s)	Fomula	Indicator	Description
Y_F	$\frac{\dot{\psi}}{\delta}$	$\mu(Y_F)$	Mean value
		$\sigma(Y_F)$	Standard-deviation
		$H(Y_F)$	Average entropy over 10^3 draws, for samples of 10^3 points
(ψ,$\dot{\delta}$), ($\dot{\psi}$,δ), ($\dot{\psi}$,$\dot{\delta}$)		$\lvert R(.,.)\rvert$	Absolute value of cross-correlation maximum peak
		$\lvert \tau(.,.)\rvert$	Associated time lag to absolute value of cross-correlation maximum peak

Table 2. Indicators based on the Yaw factor

Mozzi axis The Mozzi Axis, or instantaneous screw axis, is a concept proposed by Cossalter and Doria (2004) to study arbitrary two-wheels manoeuvres. This approach is based on the idea that any manoeuvre is a generalised form of slalom where the spacing between the cones is not constant. The Mozzi axis is the velocity vector of the vehicle frame from which 2 variables are calculated: 1- the transverse coordinate of the intersection point between the instantaneous screw axis and the ground (noted y_M), 2- the angle of the instantaneous screw axis with respect to the horizontal (θ_M). In Cossalter and Doria (2004), a qualitative interpretation of the trajectory of y_M and θ_M highlights the importance of the peaks and discontinuities of these variables from a handling quality

©2023 Ronné, J., Dubuis, L., & Robert, T. published by TU Delft OPEN on behalf of the authors.
ISSN: 2667-2812

 http://dx.doi.org/10.59490/65e718b10d45168c0b1a3a00

perspective. Peaks and discontinuities in y_M and θ_M are, by definition, associated with the change in sign of roll and yaw rates, and therefore with the oscillation of the bicycle frame. The 7 indicators based on Mozzi axis are presented in Table 3.

Variables	Fomula	Indicators	Description
y_M	$\frac{\dot{\psi}V}{\dot{\psi}^2+\dot{\phi}^2}$	$\sigma(y_M)$	Standard-deviation of y_M
		$H(y_M)$	Average entropy over 10^3 draws, for samples of 10^3 points
		$N_{peaks}(y_M)/T$	Number of peaks per unit of time
		$\mu_{peaks}(y_{Mozzi})$	Mean value of peaks
		$max_{peaks}(y_M)$	Maximum value of peaks
θ_M	$\arctan(\frac{\dot{\psi}}{\dot{\phi}})$	$\sigma(\theta_M)$	Standard-deviation
		$H(\theta_M)$	Signal entropy

Table 3. Indicators based on the Mozzi axis

State variable variability Movement variability has been proposed several times as an approach to quantifying handling quality (Moore et al., 2010; Cain et al., 2016, 2012; Matsuzawa et al., 2009). This classic approach to human equilibrium is based on the principle of minimal actions (Todorov, 2004), which may imply that high variability in the amount of control action is synonymous with low handling quality. In this study, the variability (standard deviation and entropy) of the steering, roll and yaw angles and their time derivatives are candidates, which leads to 12 indicators.

Variables	Fomula	Indicator	Description
δ, $\dot{\delta}$		$\sigma(.)$	Standard deviation
		$H(.)$	Average entropy over 10^3 draws, for samples of 10^3 points
ϕ, $\dot{\phi}$		$\sigma(.)$	Standard deviation
		$H(.)$	Average entropy over 10^3 draws, for samples of 10^3 points
ψ, $\dot{\psi}$		$\sigma(.)$	Standard deviation
		$H(.)$	Average entropy over 10^3 draws, for samples of 10^3 points

Table 4. Indicators based on state variable variability

***Steer into the lean* strategy** In Cain et al. (2016, 2012), the authors studied the balance of the bicycle under the cyclist's control using approaches similar to those for standing balance. They are interested in the cyclist's ability to align the centre of pressure with the centre of mass of the system while riding straight (bicycle + cyclist). In the case of the bicycle, this balance strategy can be summed up in the notion of *steer into the lean*. Maintaining the bicycle's balance seems to be a prerequisite for carrying out any manoeuvre. This is why balance indicators are also candidates to explain part of the handling quality. Thus roll and steering angle (and their time derivatives) are two variables of interest in our study. Based on Cain et al. (2016, 2012); Takagi et al. (2022), 11 candidate indicators are presented in Table 5. Indicators based on an SST (Singular Spectral Transformation) approach are very sensitive to the analysis parameters. In this paper, the window width was 60 points and 2 components have been used.

Variables	Indicators	Description
ϕ, $\dot{\delta}$	$\mu(SST)$	Mean anormality degree
	$max(SST)$	Maximum anormality degree
	$\sigma(SST)$	Standard deviation of anomality degree
(δ,ϕ),(δ,$\dot{\phi}$), ($\dot{\delta}$,ϕ), ($\dot{\phi}$,$\dot{\delta}$)	$\lvert R(.,.)\rvert$	Absolute value of cross-correlation maximum peak
	$\lvert\tau(.,.)\rvert$	Associated time lag to absolute value of cross-correlation maximum peak

Table 5. *Steer into the lean* strategy derived indicators

©2023 Ronné, J., Dubuis, L., & Robert, T. published by TU Delft OPEN on behalf of the authors.
ISSN: 2667-2812

 http://dx.doi.org/10.59490/65e718b10d45168c0b1a3a00

2.7 Data analysis and statistical methods

As a reminder, the aim of this study was to evaluate a set of objective handling quality indicators based on kinematic variables analysing the movement of the bicycle. The evaluation was carried out by quantifying the capacity of the objective indicators to explain the subjective feeling measurements considered here as our reference data.

In order to remove the effects of drift associated with IMU measurements, a high-pass Butterworth filter was applied afterwards on the angle raw signals (5th order, cut-off frequencies of 0.05 Hz).

The acceleration and braking phases present over the complete laps and the initial (straight line) and final segments (right turn) have been cut to exclude the transient effects.

The handling ratings showed a break in monotony around 2.5 m/s (Ronné et al., 2023), therefore laps were grouped in two subsets based on their average speed: below (and respectively above) 2.5 m/s. A third group included all data regardless of speed. Analyses were performed either on the whole lap or on one of the 4 segments of the lap: straight line, left turn, slalom, right turn (see Figure 3). Segments were identified thanks to the estimation of the distance travelled obtained by integration of the speed vector.

Each indicator was evaluated by a univariate robust linear regression model (robust_linear_model.RLM from python statsmodels library). As explained in the supplementary material section, the code used to generate the results is supplied.

For each model, 2 criteria were calculated to evaluate the tested indicator: 1- the signed Pearson coefficient squared ($sign(R)R^2$), which gave the explanatory power of the indicator and the direction of the correlation, 2- the normalised root mean square error (NRMSE), which measured the prediction performance. The RMSE was normalised using the full amplitude of the handling quality scale.

Given the subdivision of the data (3 speed groups and 4+1 segments), the 39 indicators were evaluated in 15 statistical models each. Only those having a p-value greater than 0.05 are presented.

3 Results

3.1 General results

Our dataset included (before filtering) 386 laps. Subjective ratings of handling quality on CAHQRS were normally distributed with a mean of 2.9 (level 3 : " I achieved the task correctly, I needed medium compensation") and a standard deviation of 1.3 (see Figure 4) . As presented in Ronné et al. (2023) the CAHQRS ratings exhibited no significant effect of bicycle in this experiment. Except for one specific speed (faster than optimal speed) where the Omnium™cargo bicycle was significantly harder to control.

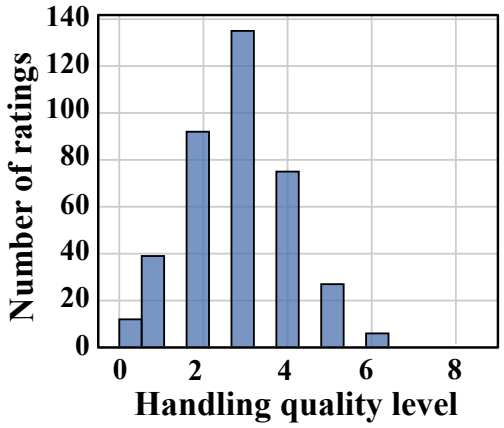


Figure 4. Distribution of the subjective handling quality ratings

©2023 Ronné, J., Dubuis, L., & Robert, T. published by TU Delft OPEN on behalf of the authors.
ISSN: 2667-2812

The results are presented by indicator family in bar charts showing the mean value $sign(R)R^2$ between the 5 segments considered. The error bars represent the standard deviation. The absence of a bar indicates that only one segment is statistically significant. Indicators are listed in descending order of R^2.

3.2 Yaw factor and derivatives

Among the Yaw factor indicators, 7 out of 9 showed a significant correlation on at least one of the 15 conditions (see Figure 5 (a)). On average, the explanatory power (R^2) of the models was less than 5%, while the root mean square error was around 12% of full scale. In general, the models showed very little explanatory power for speeds above 2.5 m/s. The $|R(\dot{\psi}, \dot{\delta})|$ indicator was the best overall, exhibiting the most versatile performance across speed groups in the family.

3.3 Mozzi axis

Among the Mozzi axis indicators, 4 out of 7 showed a significant correlation on at least one of the 15 conditions (see Figure 5 (b)). On average, the explanatory power of the models was less than 5%, as for the previous family of indicators. The mean square error was also of the order of 12% of full scale. The indicator $N_{peaks}(y_M)/T$ had the highest R^2 while the others based on y_M had very little explanatory power, as did the variability indicators. For this family too, the models with the highest R^2 were also the most versatile over all the segments, even if this family was less predictive than the previous one. Association between the indicators and the perceived handling quality appeared to be stronger for the lower speed group (v<2.5 m/s)

3.4 State variable variability

Among the state variable variability indicators, 9 out of 12 showed a significant correlation on at least one of the 15 conditions (see Figure 5 (c)). On average, the explanatory power of the models was less than 5%, as for the previous family of indicators. The mean square error was also of the order of 13% of full scale. The best model, based on $\sigma(\dot{\delta})$ reached 10% explanatory power for $v < 2.5$ m/s. Similar indicators: $H(\dot{\delta})$,$H(\delta)$,$\sigma(\delta)$, also based on steering motion, presented comparable trend results although they perform less well. Models based on the variability of other state variables performed even less well. Like in the previous family, the association between the indicators and the perceived handling quality seems stronger for the lower speed group (v<2.5 m/s).

3.5 *Steer into the lean* strategy

Among the *Steer into the lean* indicators, 11 out of 11 showed a significant correlation on at least one of the 15 conditions (see Figure 5 (d)). On average, the explanatory power of the models was less than 5%, as for the previous family of indicators. The mean square error was also of the order of 12% of full scale. The model based on $R(\dot{\delta}, \phi)$, reached about 9% of explanatory power, which was the best performance overall for $v > 2.5$ m/s.

4 Discussion

Most of the tested indicators demonstrated statistical significance (p<0.05) in at least one tested condition (segment and speed). The root mean square error was relatively independent of the tested models and was on the order of 12% of the full scale. However, the explanatory power of univariate models for handling quality remained low (13% at best). Although the measurement variability with the Cooper-Harper scale has never been studied in the field of cycling, it is highly likely that the inherent intra- and inter-individual variability associated with such a subjective measurement limits the predictability of the models.

The best results were obtained for speeds below 2.5 m/s using the indicators quantifying the amount of control actions on the handlebars ($\sigma(\dot{\delta})$, $H(\dot{\delta})$, $H(\delta)$, $\sigma(\delta)$). This supports the hypothesis of Ronné et al. (2023) that in this speed range, handling quality is related to a phenomenon of instability. Indeed, in this range, low handling quality is associated with a strong sense of balance loss and intense handlebar movements (Ronné et al. (2023)). Thus, the effectiveness of models based on the quantity of control actions on the handlebars can be explained by the fact that they capture some of the characteristics of bicycle motion associated with a balance-seeking situation. Hence, it is expected that indicators based on the *steer into the lean* strategy are also significant at low

©2023 Ronné, J., Dubuis, L., & Robert, T. published by TU Delft OPEN on behalf of the authors.
ISSN: 2667-2812

http://dx.doi.org/10.59490/65e718b10d45168c0b1a3a00

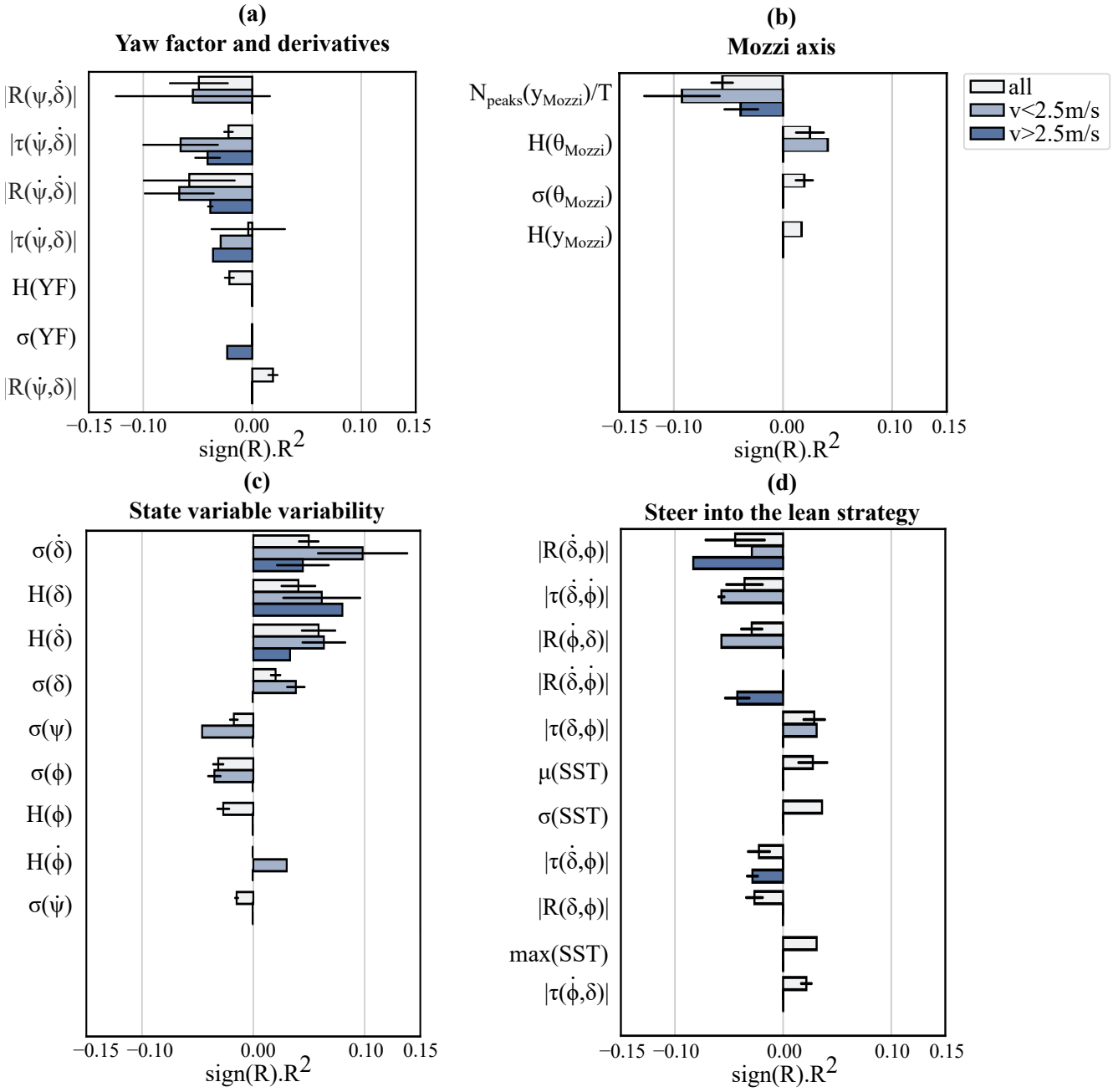


Figure 5. Significant (p<0.05) regression results for the 4 indicators family

©2023 Ronné, J., Dubuis, L., & Robert, T. published by TU Delft OPEN on behalf of the authors.
ISSN: 2667-2812

speeds. Above 2.5 m/s, the tested indicators no longer capture the movement-specific aspects associated with handling quality as effectively. The division of speeds does not prevent the same indicators from showing significant results above 2.5 m/s. However, these models are not very explanatory, which is likely due to the presence of a few instability situations in the data. This can also be explained by the fact that at higher speeds, performance deteriorates (and so do the ratings), even though this phenomenon is not captured by the kinematic indicators. A transition between the mechanisms governing the sensation of handling quality is very likely to occur around 2.5 m/s in our data. These conclusions would benefit from being extended to other bicycles and tasks.

Based on these results, the best univariate model, based on $\sigma(\dot{\delta})$, explains (at best) approximately 15% of the variability in the sensation of handling quality for speeds below 2.5 m/s. With an NRMSE of 12%, it does not allow differentiation of experimental conditions with precision below 2 units on the Cooper-Harper scale. Although it performs less well for speeds above 2.5 m/s, it is significant for all three speed groups tested. It is also significant for several segments of the circuit. Given its limited precision, it seems more relevant in the current state of knowledge to use it as a trend indicator rather than a direct predictor of the handling quality. This is especially true as the model adjustment likely incorporates a circuit-specific effect used in the experiment.

In cases where $\sigma(\dot{\delta})$ is used under similar conditions, lower variability in the steer rate indicates a lesser amount of control actions and, consequently, a lower physical and cognitive workload. However, since handling quality encompasses both ease and precision, the latter should not be overlooked. Indeed, one limitation of this indicator is that it does not control the actual performance achieved. In the case of a bicycle with a very stiff steering, $\sigma(\dot{\delta})$ could be low while the steering torque required is high and performance is compromised.

Conclusion

Handling quality is a desirable attribute for designing safe, comfortable, and high-performance bicycles. The literature presents various experimental indicators based on vehicle kinematics, the validity of which has not yet been evaluated. Our experimental dataset has allowed for the statistical assessment of these indicators, revealing that a significant portion of the sensation of handling quality can be explained. Consequently, indicators measuring the quantity of control actions on the handlebars performed the best, especially at lower speeds (<2.5 m/s). However, these indicators remain simplistic, and future research will aim to better define their scope of application and potential enhancements.

This study is not intended to propose a standardised methodology for assessing handling quality. However, our results do highlight certain points to be taken into account in the future development of such a methodology. The effect of speed on the predictive capacity of the indicators highlights the need to use indicators adapted to experimental conditions. The separation of the two speed groups we used in this study (2.5m/s) is dependent on the geometry of our circuit. The development of a standardised procedure must therefore take into account the match between speed, circuit specificity and the experimental indicators selected.

Acknowledgement

We would like to acknowledge the significant contribution of François May (MSc) to the experiments.

Supplementary materials

We provide the data table containing the calculated indicators and the subjective ratings. We also provide the full regression results table. The code for reproducing the results and displaying the figures is also provided. All there materials can be find here : RONNE, Jules; DUBUIS, Laura; ROBERT, Thomas, 2023, "Assessment of bicycle experimental objective handling quality indicators", https://doi.org/10.57745/TKPDBV, Recherche Data Gouv.

The complete parameters set of our two experimental bikes for the Carvallo-Whipple Model are available at the link below. They consist of two files: `"p_strida_foldable.npy"` and `p_omnium_cargobike.npy`. Ronné, Jules; Dubuis, Laura; Robert, Thomas, 2024, "Replication data for "Assessing the handling quality of bicycles : a review of current theoretical approaches", https://doi.org/10.57745/NH970D, Recherche Data Gouv, V1

©2023 Ronné, J., Dubuis, L., & Robert, T. published by TU Delft OPEN on behalf of the authors.
ISSN: 2667-2812

References

Cain, S. M., Ashton-Miller, J. A., and Perkins, N. C. (2016). On the Skill of Balancing While Riding a Bicycle. *PLOS ONE*, 11(2):e0149340. Publisher: Public Library of Science.

Cain, S. M. and Perkins, N. C. (2010). Comparison of a Bicycle Steady-State Turning Model to Experimental Data. page 21.

Cain, S. M., Ulrich, D. A., and Perkins, N. C. (2012). Using Measured Bicycle Kinematics to Quantify Increased Skill as a Rider Learns to Ride a Bicycle. pages 195–199. ASME.

Cooper, G. and Harper, R. (1969). The use of pilot ratings in evaluation of aircraft handling qualities. *NASA Ames Technical Report*.

Cossalter, V. and Doria, A. (2004). Analysis of motorcycle slalom manoeuvres using the Mozzi axis concept. *Vehicle System Dynamics*, 42(3):175–194.

Cossalter, V. and Sadauckas, J. (2006). Elaboration and quantitative assessment of manoeuvrability for motorcycle lane change. *Vehicle System Dynamics*, 44(12):903–920. Publisher: Taylor & Francis _eprint: https://doi.org/10.1080/00423110600742072.

Harris, D., Gautrey, J., Payne, K., and Bailey, R. (2000). The Cranfield aircraft handling qualities rating scale: a multidimensional approach to the assessment of aircraft handling qualities. *The Aeronautical Journal*, pages 191–198.

Hess, R. (2012). Modeling the Manually Controlled Bicycle. 42(3):13.

Horiuchi, S. and Yuhara, N. (1998). An Analytical Approach to the Prediction of Handling Qualities of Vehicles With Advanced Steering Control System Using Multi-Input Driver Model. *Journal of Dynamic Systems, Measurement, and Control*, 122(3):490–497.

Kuroiwa, O., Baba, M., and Nakata, N. (1995). Study of Motorcycle Handling Characteristics and Rider Feeling During Lane Change. page 950200. Conference Name: International Congress & Exposition.

Matsuzawa, S., Iwase, M., Sadahiro, T., and Hatakeyama, S. (2009). Motion analysis by experiment and simulation for riding bicycles with children. In *2009 IEEE International Conference on Systems, Man and Cybernetics*, pages 859–864, San Antonio, TX, USA. IEEE.

Moore, J. K., Hubbard, M., Schwab, A. L., Kooijman, J. D. G., and Peterson, D. L. (2010). Statistics of bicycle rider motion. *Procedia Engineering*, 2(2):2937–2942.

Ronné, J., Dubuis, L., and Robert, T. (2023). Bicycle handling quality perception: mixed effect of stability and manoeuvrability.

Schwab, A. L. and Meijaard, J. P. (2013). A review on bicycle dynamics and rider control. *Vehicle System Dynamics*, 51(7):1059–1090.

Sugizaki, M. and Hasegawa, A. (1988). Experimental Analysis of Transient Response in Motorcycle-Rider Systems. page 881783.

Takagi, S., Oka, M., and Mori, H. (2022). Evaluation of Riding Instability of a Bicycle with Children as Passengers Using the Relationship Between Handlebar Angle and Roll Angle. In Yamamoto, S. and Mori, H., editors, *Human Interface and the Management of Information: Applications in Complex Technological Environments*, Lecture Notes in Computer Science, pages 388–403, Cham. Springer International Publishing.

Todorov, E. (2004). Optimality principles in sensorimotor control. *Nature Neuroscience*, 7(9):907–915.

Weir, D. H. and DiMarco, R. J. (1978). Correlation and Evaluation of Driver/Vehicle Directional Handling Data. SAE Technical Paper 780010, SAE International, Warrendale, PA. ISSN: 0148-7191, 2688-3627.

Zellner, J. W. and Weir, D. H. (1978). Development of Handling Test Procedures for Motorcycles. page 780313.

©2023 Ronné, J., Dubuis, L., & Robert, T. published by TU Delft OPEN on behalf of the authors.
ISSN: 2667-2812

The Evolving Scholar Vol. 3, 2023

http://dx.doi.org/10.59490/6595820fa5398fcc65e8398a

Bicycle and Motorcycle Dynamics 2023
Symposium on the Dynamics and Control of Single Track Vehicles
18–20 October 2023, Delft University of Technology, The Netherlands

Type of the Paper: Conference Paper

Revised

Bicycle frame load estimation using semi-analytical multi-body simulation methods

[version 2; peer reviewed]

Johannes Bolk[1,*], Burkhard Corves[2]

[1] Institute of Mechanism Theory, Machine Dynamics and Robotics, RWTH Aachen University, Germany; Bolk@igmr.rwth-aachen.de, ORCID 0000-0002-8777-509X
[2] Institute of Mechanism Theory, Machine Dynamics and Robotics, RWTH Aachen University, Germany; Corves@igmr.rwth-aachen.de, ORCID 0000-0003-1824-3433
[*] corresponding author

Name of Editor: Jason Moore
First published: 25/09/2023
Last published: 27/03/2024
Citation: Bolk, J. & Corves, B. (2024). Bicycle frame load estimation using semi-analytical multi-body simulation methods [version 2; peer reviewed]. The Evolving Scholar - BMD 2023, 5th Edition.
This work is licensed under a Creative Commons Attribution License (CC-BY).

Abstract:

The design and dimensioning of bicycles have always been a challenging task. It is necessary to solve the conflict between a high level of safety against component failure and the demand for a lightweight and cost-efficient design. The operating loads to which the system components are subjected play a decisive role in this task. However, the determination of these loads is a crucial challenge. Besides the widespread use of multi-body simulation in other vehicle industries, in the design of bicycles, the potential has so far remained largely untapped. The main problems arise in modeling the complex driving tracks and the need for a driver model that accurately represents the complex human behavior.
Using a semi-analytical modeling approach, the system excitation is directly applied in the form of measured loads. This opens the possibility of representing the rider, track, and tire behavior in their full complexity within the numerical simulation, without making simplifications in the modeling process. However, replacing constraints between the bicycle and the environment with forces leads to an unconstrained system where imbalances can lead to instabilities in the form of uncontrolled accelerations, making the results unusable.
This paper presents and evaluates the accuracies of four simulation methods that allow a semi-analytical simulation of bicycles. These are defined by two variations of a locating-floating bearing of the wheel hubs, constraining at a static reference point and the constraining of the frame to a reference point guided along the original frame trajectory. The input of the semi-analytical simulation is based on synthetic measurement data, conducted in a fully analytical simulation with a passive driver model. In contrast to the previous applications of this approach, it was shown that for bicycles, highly accurate results can be calculated without taking the trajectory of the bicycle into account.

Keywords:

Multi-body Simulation, Operating Loads, Semi-analytical Approach, Hybrid Simulation Approach, Bicycle Loads, Bicycle Simulation

©2023 Bolk, J.& Corves, B published by TU Delft OPEN on behalf of the authors.
ISSN: 2667-2812

 http://dx.doi.org/10.59490/6595820fa5398fcc65e8398a

Introduction

The transport industry is currently experiencing a revolution, as a result, sales of bicycles are at a high level (German Bicycle Industry Association, 2023). The design and dimensioning of bicycles have always been a challenging task in the development process. While prototype tests established in bicycle development can ensure a minimum level of safety for strength verification, they are unable to represent the complexity and diversity of the loads occurring during operation (Köhler et al., 2012). Ensuring the safety of bicycles is particularly important because the failure of a critical component leaves the rider virtually unprotected in case of a fall. With the advent of more and more innovative bicycle kinematics such as full suspension bikes or structures such as cargo bikes, it is becoming increasingly difficult to design safe bicycles just based on experience and applicable testing standards.

In other vehicle industries the widespread use of multi-body simulation (MBS) allows for early statements of the loading and stress conditions in the development process. With the increased capabilities of computers and established tire and road models, a common approach is the use of fully analytical MBS methods to replicate loads of real-world driving. The results form the basis for finite-element analyses with which the component stress can be determined (Johannesson and Speckert, 2014). However, the potential of this process remains largely untapped in bicycle development. The reasons for this lie in the development of an analytical environment model that can accurately represent the actions of the rider and the wheel-road contact, even in demanding riding situations. There is extensive research for passive and active driver models in the area of vehicle dynamics evaluation and also investigations in track wheel contact (Bruni et al., 2020). However, these can only be transferred to a limited extent to highly complex driving scenarios with the aim of quantitatively representing the operating loads numerically. This leads to an inadequate design foundation, which is especially true for the sports sector since both the complexity of the load scenarios and the loads themselves are high.

An alternative modeling approach offers great potential for solving these problems. Instead of the classical "fully analytical" environment model, measurement data can be used at the system boundaries to excite the vehicle model (Tebbe et al., 2006). By using this "semi-analytical approach" (SAA), the analytical rider and track models are replaced by measured excitations at the system boundaries. Thus rider, track, and tire behavior are fully accounted for in their complexity within the simulation, without making simplifications in the modeling process. The measurement data allows for a comprehensive representation, ensuring a more accurate analysis and evaluation of the bicycle's performance. But when the measured loads are applied to unconstrained systems, it can lead to instabilities in the form of uncontrolled accelerations that do not occur in reality (Speckert et al., 2009; Tebbe et al., 2006). Accordingly, the simulation results become unusable due to motion induced forces. The reason for these unintended movements is the lack of constraints on the vehicle system. Replacing constraint of the track-wheel contact with measured forces at the wheel hub leads to a system where no constraints between the system and the environment reduce the degree of freedom (DOF), therefore leaving the system unconstrained. Even small load imbalances in the excitation can cause the system to accelerate uncontrolled.

The engineering challenge is to stabilize or constrain the simulation without affecting the system behavior and, consequently, the simulation results. The simulation can be considered successful when the determined system loads in the SAA correspond to the real driving scenario. Various stabilization approaches can be pursued for this purpose. Some methods are explored in literature for moving systems without common constraints to the environment (Blanchette et al., 2021; Joubert et al., 2020; Speckert et al., 2009; Tebbe et al., 2006). These approaches can be implemented in the form of artificial constraints at static or dynamic reference points in the system. Active control strategies can also be implemented, where combinations of P, I, and D Controls are used to calculate forces that counteract the unintended movement. Another challenge is the consideration of the inertia forces inside the system itself. In the mentioned applications critical loads on the components were caused by inertia loads inside the system itself in the form of inertia forces. Most of the methods suggest that these must also be taken into account in the application of the SAA. This is achieved by measuring the pose of the system as a function of time and by either directly constraining the system to the measured trajectory or by using it as a reference point for feedback control stabilization.

Previous publications have considered vehicles in which the mechanical structure itself was the prime source of critical loads, such as cars or motorized tricycles. In bicycle systems, however, the inertia forces of the system itself play a minor role compared to the inertia forces of the driver and active forces like pedaling induced by the driver. The driver's weight can easily surpass ten times that of the bicycle, thus resulting in significantly higher inertia forces. Therefore, exciting the model based on the loads originating from outside the system at the connection points to the wheels and the driver can be sufficient for the SAA of the loads during operation. The data required would thus be reduced by the center of gravity trajectories, only requiring the loads at the system boundaries. This is a great advantage, as the measurement of six-dimensional position data is demanding and cost-intensive, especially since driving routes can be located in rough terrain. As a result, stabilization approaches that were previously ruled out for systems with high inertia forces become interesting again. To that end, the scope of this paper is to evaluate the potential of the SAA for the application on bicycle simulation. In particular, stabilization approaches with artificial constraints were examined and re-evaluated with the background of the new system properties.

©2023 Bolk, J.& Corves, B published by TU Delft OPEN on behalf of the authors.
ISSN: 2667-2812

 http://dx.doi.org/10.59490/6595820fa5398fcc65e8398a

1 Methodology

To enable the use of MBS, it is necessary to determine a simple measurement and simulation method capable of calculating accurate component loads without distorting them in the simulation process itself. The bicycle model used in this study corresponds to a full-suspension mountain bike frame, presented in detail in subsection 1.1. Measurement data for the excitation and validation of the SAA is generated in terms of a fully analytical simulation with a passive driver model. In this way, any errors or deviations that occur can be directly attributed to the methodology and are not falsified by deviations in the modeling or measurement of the input data. The modeling of the simulation to obtain the synthetic measurement data is described in subsection 1.2. In order to test the suitability of SAA in general and different stabilization methods in particular, various simulation setups are implemented in an MBS environment and evaluated, see subsection 1.3. In order to prove the hypothesis of the admissible inertia neglect for bicycles, a setup in which the bicycle is guided along a measured trajectory is also considered. In order to compare the performance of the individual SAA with the reference runs, time-force curves are compared. Furthermore, two characteristic values are defined to evaluate the suitability of the simulations, see subsection 1.4.

1.1 Bike Model

The utilized bicycle model is shown in Figure 1. It consists of eight rigid bodies, a frame- and a fork suspension. The component properties, such as geometric connection points, mass, mass inertia tensor, and center of gravity, were experimentally determined and validated in research conducted by (Ingenlath, 2019). The total mass of the bicycle structure as shown in the Figure is $m_{\mathrm{bicycle}} = 15\,\mathrm{kg}$. The model incorporates linearized force element characteristics, which were also derived from the measurements presented in (Ingenlath, 2019). In order to validate the performance of the different SAA-setups, several points throughout the system are used to compare the recreated loads by the SAA with respect to the loads occurring in the reference drive, see Figure 1. Two of the validation points are in the connection between frame and fork. The fork bearing is modeled with two constraint points at the top and bottom. The bottom constraint is limiting axial (y-direction) and radial movement (x-direction), the top is only constraining radial movement. In this way, only forces in the connection of frame and fork need to be examined. Furthermore, the bearing between the frame and the chainstay is analyzed as well as the connection between the seat stay and leaver. The forces are measured in local coordinate systems, displayed in Figure 1. The exact same model is used in the reference drive as well as in the SAA-setups.

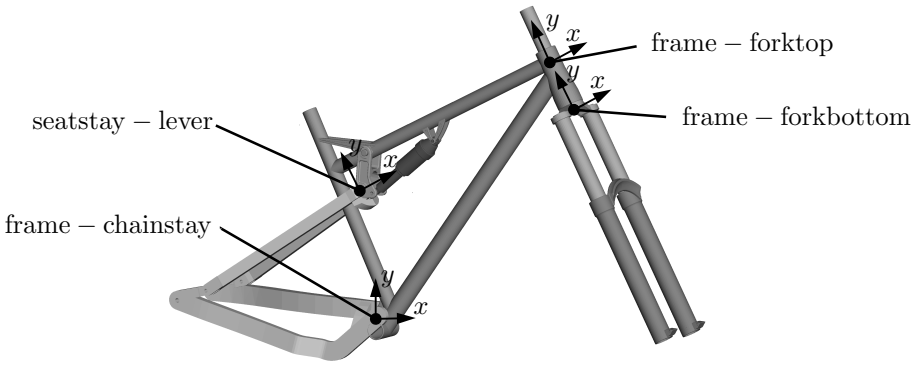


Figure 1: Representation of the bicycle model, consisting of eight rigid bodies and spring-damper suspensions in the frame and the fork. In addition, the validation points including the respective coordinate systems are shown.

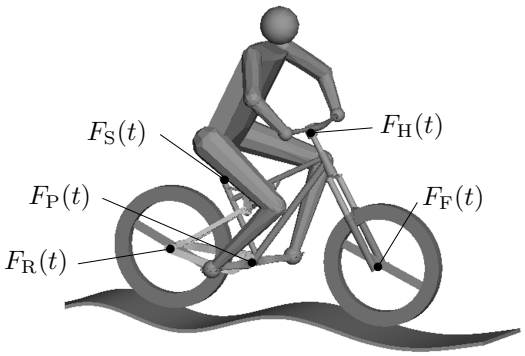
1.2 Reference Data

The reference drive, which is used to generate the synthetic input and to validate loads, is implemented as a full analytical MBS. In this way, errors originating from differences in the modeling of real-world components are eliminated. Consequently, any differences between the results obtained from the SAA and those of the reference run can be attributed to the simulation method itself. The simulations are performed with a passive rider model with a mass of $m_{\mathrm{driver}} = 80\,\mathrm{kg}$. The rider is connected to the bicycle model via handlebars, seat, and pedals. The rider is modeled with nine bodies that are movable relative to each other, see Figure 2a. The position and speed-dependent properties of the legs and arms are represented by force elements. The definition of the body properties and the force elements of the rider are taken from (Ingenlath, 2019). The wheel-track contact is executed via a one-sided constraint with spring and damper properties in the contact point. The wheel properties are also taken from (Ingenlath, 2019). The

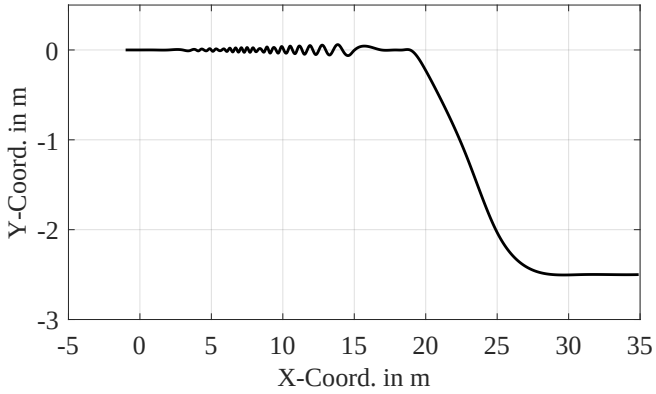
©2023 Bolk, J.& Corves, B published by TU Delft OPEN on behalf of the authors.
ISSN: 2667-2812

 http://dx.doi.org/10.59490/6595820fa5398fcc65e8398a

track model describes a periodically increasing excitation in frequency and amplitude, generating forces in the x- and y-directions. This is followed by a descent, at the end of which high accelerations in y direction occur, see Figure 2b.



(a) Representation of the passive driver model. The connection points between the system and the environment, where the measurement data for the SAA excitation is recorded, are marked.



(b) Representation of the test track: Following a transient phase, a periodic excitation with increasing amplitude and frequency is applied, resulting in vertical and horizontal excitation. This is followed by a downhill ride that leads to high vertical accelerations.

Figure 2: Model of the fully analytical simulation that is used to generate the synthetic measurement data as well as the validation data.

To compute the excitation and validation loads, the system, consisting of a human and a bike, travels along the track at an initial velocity of $v_{\mathrm{start}} = 5\,\mathrm{m/s}$. The drive is calculated over a period of $t_{\mathrm{drive}} = 5\,\mathrm{s}$ with a sample rate of $f = 1200\,\mathrm{Hz}$. The measured loads at the system boundary, which are further used in order to excite the semi-analytical simulations are defined as follows: Forces in the front (F_{F}) and rear hub (F_{R}), seat forces (F_{S}), forces between the fork and the handlebar (F_{H}) and forces between the bottom bracket and the frame (F_{P}). As the bicycle only moves on a vertical plane and no chain forces are considered in this work, no torques, rolling, and gearing motions need to be considered. Besides the forces, the position and orientation trajectory of the frame center of gravity are extracted from the simulation.

1.3 Semi-analytical Simulation Setup

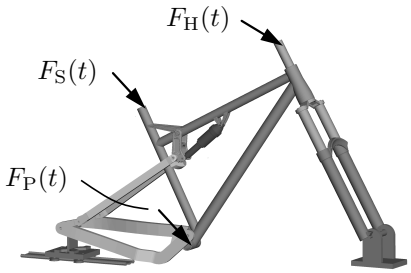
In addition to the suitability of SAA for bicycle simulation due to the possibility of overcoming complex modeling tasks, the bicycle system as such is particularly suited to the application of SAA of unconstrained systems. The reason for this lies in the possibility of computing accurate results without replicating the system inertia loads, see Introduction. To examine this thesis in more detail, three simulation setups with artificial constraints are introduced, in which the bicycle is hold on place. In addition, a fourth simulation setup is described where the system is moved along the trajectory of the bicycle measured in the reference drive. Since this enables the recreation of inertia forces within the system, conclusions about the need to account for these inertia forces can be drawn. Gravity is not considered in any of the semi-analytical simulations, since the simulation assumes static equilibrium.

Hub constraints

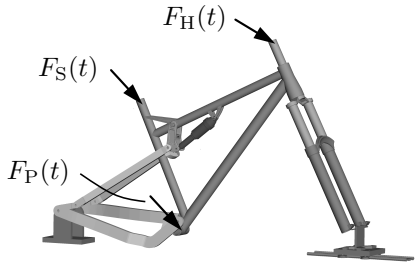
Based on the principles used in test stand models such as in DIN ISO 4210 (DIN Standards Committee, 2023), and also as a general intuitive way of constraining the bicycle system, a locating-floating bearing setup at the wheel hubs is investigated. Since the wheel loads can be considered as reaction loads resulting from the inertia- or active loads of the bicycle driver system, constraining them could generate reaction loads in the SAA model as well. The locating-floating bearing setup results in two simulation models. One setup with the locating bearing in the front hub, referred to as *fixed front hub*, see Figure 3a. Secondly, a setup with the locating bearing in the rear hub, referred to as *fixed rear hub*, see Figure 3b. The locating bearing is constraining all translational DOF and a floating bearing allows only horizontal movement. Both bearings allow a rotation of the hub axis, except for longitudinal rotations of the bicycle. As the hubs are constrained, the only excitation loads the setup requires are the loads induced by the driver. Thus, the hub forces are not required. This is beneficial as in real-world applications, the implementation of a wheel load transducer to measure the hub loads is far more complicated than the measurement setup for the driver loads.

©2023 Bolk, J.& Corves, B published by TU Delft OPEN on behalf of the authors.
ISSN: 2667-2812

 http://dx.doi.org/10.59490/6595820fa5398fcc65e8398a



(a) Simulation model of *fixed front hub* with the application points of the excitation forces

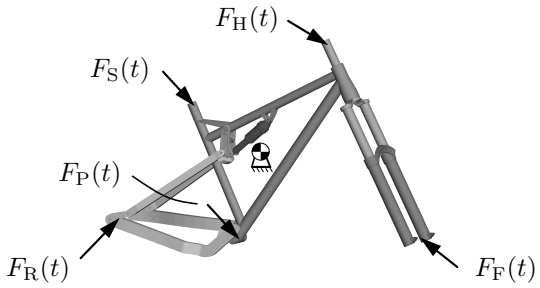


(b) Simulation model of *fixed rear hub* with the application points of the excitation forces.

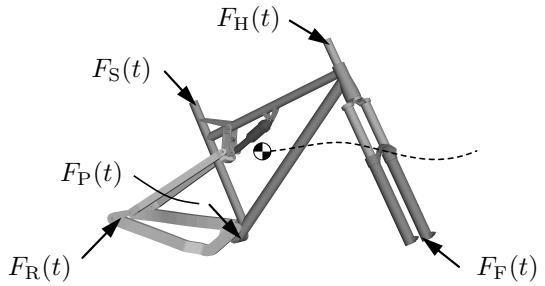
Figure 3: Semi-analytical simulation models with artificial hub constraints

Frame constraints

Furthermore, an artificial constraint setup is examined where all six DOF of the frame are constrained to a fixed point, see Figure 4a. This allows for an excitation with all five input loads, measured in the reference run. This setup is referred to as *fixed frame*. Finally, in the *guided frame* setup, the frame is constrained with all DOF to a fixed point that is driven along the pose trajectory recorded in the reference drive, see Figure 4b. This setup aims to reproduce some of the inertia loads of the multi-body system with the goal of increasing the accuracy of the results.



(a) Simulation model of *fixed frame* with the application points of the excitation forces.



(b) Simulation model of *guided frame* with the application points of the excitation forces. The frame trajectory along which the fixed point is guided as indicated by the dashed line.

Figure 4: Semi-analytical simulation models with artificial frame constraints

1.4 Evaluation Methods

The objective of this study is to identify a model that can accurately replicate the entire course of the internal loads. The evaluation is partially based on a visual comparison of the force-time diagrams at validation points in the bicycle system. In order to make more precise statements and to be able to effectively compare the curves with each other, three characteristic values are introduced. On the one hand, the root-mean-square error (RMSE) between the force-time curve of the fully analytical reference run (Ref) and the semi-analytical approach (SAA) is calculated at the validation points, see Equation (1). To ensure comparability between different datasets the (RMSE)-value is normalized with a range between the maximum and minimum values of the reference data, see (NRMSE) defined in Equation (2).

$$\mathrm{RMSE} = \sqrt{\frac{1}{n}\sum_{i=1}^{n}(\mathrm{SAA}_i - \mathrm{Ref}_i)^2} \tag{1}$$

$$\mathrm{NRMSE} = \frac{\mathrm{RMSE}}{\mathrm{Ref}_{max} - \mathrm{Ref}_{min}} \cdot 100 \tag{2}$$

©2023 Bolk, J.& Corves, B published by TU Delft OPEN on behalf of the authors.
ISSN: 2667-2812

 http://dx.doi.org/10.59490/6595820fa5398fcc65e8398a

On the other hand, the coefficient of determination R^2 is used. This coefficient is often used in the evaluation of regressions and shows the correlation between the regression and data points in relation to the x-axis. Applied to the comparison of two force-time curves, the coefficient provides information about the similarity of the course or the correlation of deflections in the loads of the SAA and the reference run (Ref) in relation to the simulation time. Values of this parameter are between zero and one where one corresponds to an exact similarity, see Equation (3).

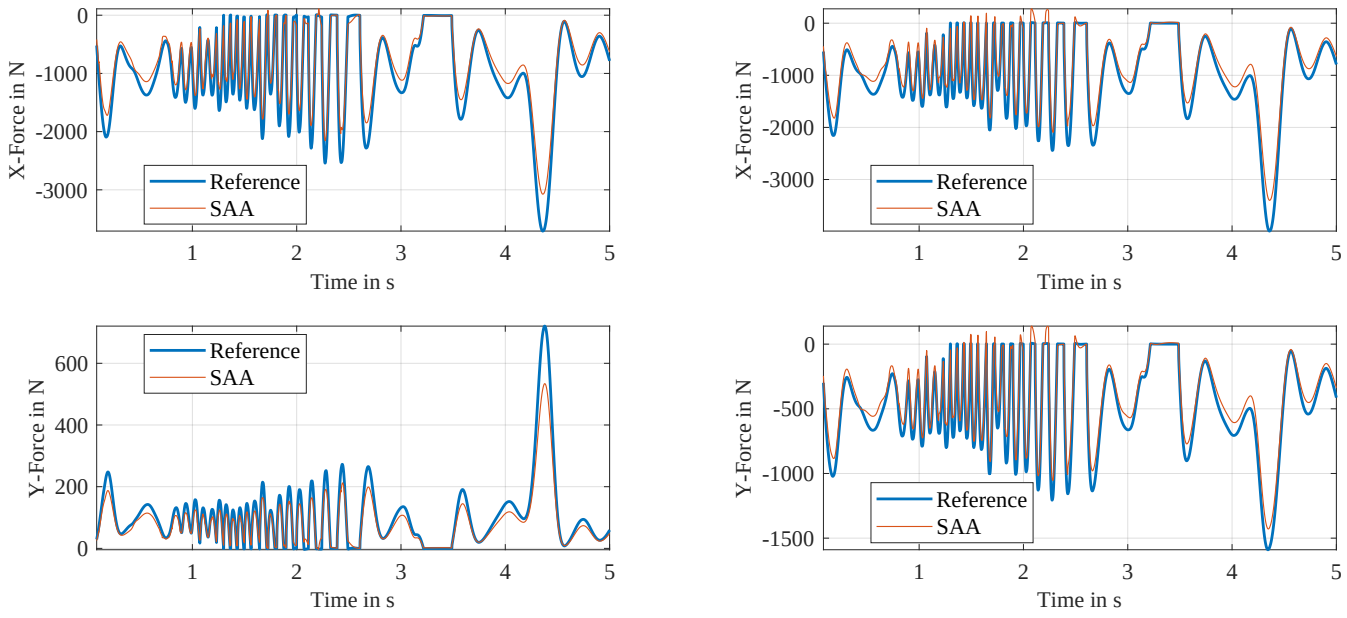
$$\mathrm{R}^2 = 1 - \frac{\sum_i (\mathrm{SAA}_i - \mathrm{Ref}_i)^2}{\sum_i (\mathrm{SAA}_i - \overline{\mathrm{SAA}}_i)^2} \tag{3}$$

2 Results

The following section discusses the performance of the four semi-analytical simulation models. The goal is to find a model that is able to reproduce the inner forces in the system based on the excitation loads measured in the reference drive. First, the force-time curves of the SAA results are compared with the loads of the reference drives. Furthermore, the introduced characteristic values RMSE, NRMSE, and R^2 are used to evaluate the accuracies of the simulations. At the excitation points, the forces in the SAA coincide exactly with the forces from the reference run and are therefore not considered in the evaluation of the agreement of the SAA with the reference data.

Hub constraints

Artificially constraining the bicycle systems using a locating-floating bearing leads in general to similar force-time curves between *fixed rear hub* and *fixed front hub*. This is particularly true at the validation points close to the rear hubs. Here, the force curves calculated in both SAA with hubs constraint show good agreement with the loads in the reference run. However, over the entire simulation time, lower absolute forces, in both the x- and y-axis, can be observed for the loads estimated by the SAA simulations. Figure 5 exemplarily shows the force-time curves of the *fixed rear hub* at the rear two validation points. In Figure 5a, the force comparison between the reference run and SAA is presented, divided into x- and y- axis, for the validation point between frame and chainstay. Figure 5b displays the force comparison at the validation point between the seat stay and lever.



(a) *fixed rear hub* forces between frame and chainstay

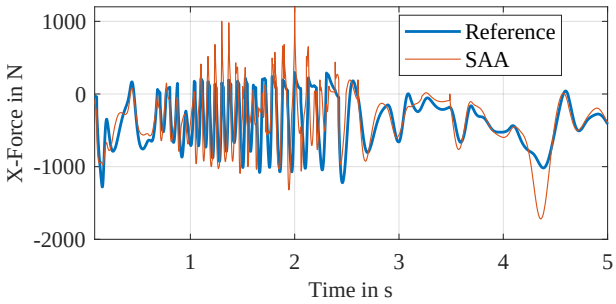
(b) *fixed rear hub* forces between seatstay and lever

Figure 5: Visualisation of force-time curves of the semi-analytical approach (SAA) model *fixed rear hub* as an exemplary display of the locating-floating bearing forces in the rear of the bicycle structure.

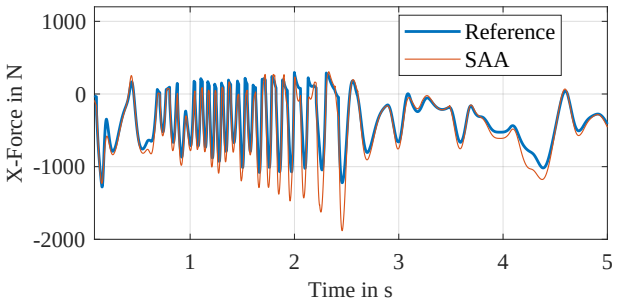
©2023 Bolk, J.& Corves, B published by TU Delft OPEN on behalf of the authors.
ISSN: 2667-2812

http://dx.doi.org/10.59490/6595820fa5398fcc65e8398a

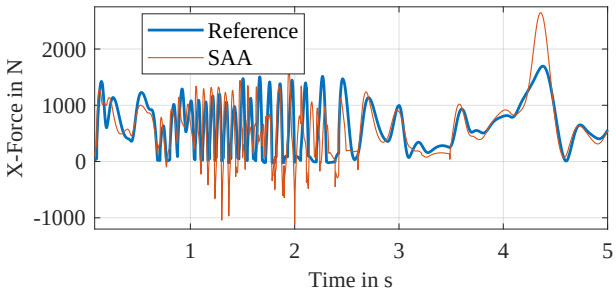
The underestimated forces by both SAA models may be explained due to the lack of active excitation forces at the hubs. The applied driver forces which are directed through the structure and supported at the hub constraints are therefore not capable of reproducing the original hub loads sufficiently. The evaluation based on the characteristic values is shown in Table 1 and Table 2. It can be seen that the accuracies at the rear validation points in *fixed front hub* are quite similar compared to *fixed rear hub*.
Clear differences between the simulation models can be seen in the front area of the bike. Figure 6 shows the forces in the fork mount for both simulation setups *fixed front hub* and *fixed rear hub*. Axial loads (y-axis) in the top fork are not shown in Figure 6a and b, as there is no constraint here and thus no forces arise. Axial movement is the only constraint at the bottom connection between fork and frame. The resulting forces are displayed in Figure 6c and d.



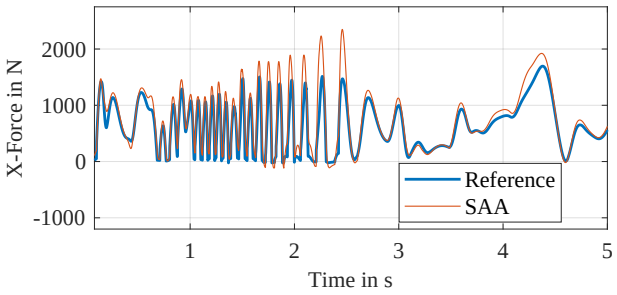
(a) *fixed front hub* forces between frame and fork top



(b) *fixed rear hub* forces between frame and fork top



(c) *fixed front hub* forces between frame and fork bottom



(d) *fixed rear hub* forces between frame and fork bottom

Figure 6: Visualisation of force-time curves of the semi-Analytical Simulation (SAA) setups *fixed rear hub* and *fixed front hub* at the connection points between the fork and the frame.

Visible in Figure 6c and d, forces in the axial fork direction (y-axis) can be reproduced relatively well for both SAA simulation models. This is also reflected in the characteristic values, where good agreement in the course of the curve (R^2) as well as in the root-mean-square error deviation (RMSE) can be observed, see Table 1 and Table 2. For both models, the accuracy of the axial forces is $\mathrm{NRMSE} < 10\,\%$ However, the radial forces show significant differences between the estimated forces by the SAA and the reference forces. The *fixed front hub* setup, shows a clear deviation between the reference forces and the calculated forces of the SAA in the fork mount as displayed in Figure 6a and c. The forces in the x-axis show a rather chaotic course, which is reflected in low R^2 value, see Table 1. A clear tendency cannot be determined, the forces are partly overestimated and partly underestimated. In comparison the *fixed rear hub* setup, shown in Figure 6b and d, shows consistently overestimated forces in the x-axis of the

©2023 Bolk, J.& Corves, B published by TU Delft OPEN on behalf of the authors.
ISSN: 2667-2812

 http://dx.doi.org/10.59490/6595820fa5398fcc65e8398a

frame-fork connection. Due to the floating bearing in *fixed rear hub*, horizontal forces induced at the handlebar cannot be supported by the front axle and are transmitted into the frame via a torque. Due to the setup of the constraints, this is reflected in increased forces in the x-axis of both fork frame constraints. The course of both curves shows good agreement for *fixed rear hub*, which is reflected in R^2 values close to one, see Table 2.

Table 1: Evaluation of the *fixed front hub* model

	x-axis			y-axis		
	RMSE	NRMSE	R^2	RMSE	NRMSE	R^2
frame − forktop	297.54	18.87	0.47	–	–	–
frame − forkbottom	373.57	21.76	0.5	92.99	6.54	0.85
frame − chainstay	236.94	6.37	0.98	36.17	5	0.99
seatstay − lever	210.74	5.27	0.99	84.72	5.31	0.99

Table 2: Evaluation of the *fixed rear hub* model

	x-axis			y-axis		
	RMSE	NRMSE	R^2	RMSE	NRMSE	R^2
frame − forktop	162.13	10.28	0.91	–	–	–
frame − forkbottom	217.39	12.67	0.91	73.22	5.15	0.9
frame − chainstay	214.48	5.76	0.99	36.39	5.03	1
seatstay − lever	217.81	5.44	0.99	90.13	5.64	0.99

Based on the characteristic values the *fixed rear hub* model (Table 2) shows slightly better results than *fixed front hub* model (see Table 1). However, further investigations have shown that this tendency is partly dependent on the test track and the resulting excitation. A general statement, on a prefernce of the approaches, can therefore not be made. At this point, it should also be noted that the implementation of the axial force excitation in the floating bearing can lead to a slight improvement in performance. However, the advantage of being able to perform the simulation independently of hub forces is lost in this scenario.

Frame constraints

Based on the same reference data, the results of the *fixed frame* and *guided frame* model are discussed below. The characteristic values determined at the validation points on the x- and y-axis are, respectively, listed in Table 3 and Table 4. Due to the consistently high accuracies of both simulation setups, a visual representation is omitted. Compared to the hub-constraint models presented so far, the *fixed frame* setup shows significantly more accurate results, both in absolute deviations (RMSE) and in the course (R^2), see Table 3. Although a slightly overestimated force can be observed in the load peaks. Based on the accuracy of these results, it can be confirmed that the neglect of the inertia loads of the bicycle system leads only to minor deviations in the calculated loads. The measurement of the center of gravity trajectory is therefore not mandatory to compute accurate results.

Table 3: Evaluation of the *fixed frame* model

	x-axis			y-axis		
	RMSE	NRMSE	R^2	RMSE	NRMSE	R^2
frame − forktop	30.66	1.94	1	–	–	–
frame − forkbottom	52.65	3.07	0.99	39.04	2.74	0.98
frame − chainstay	21.28	0.57	1	8.96	1.24	1
seatstay − lever	15.95	0.4	1	9.23	0.58	1

Compared to *fixed frame*, *guided frame* only shows negligible improvements in force accuracies. The reason for this is that only the inertia loads of the attachment components like fork, seatstay, and chainstay are reproduced by this setup. The inertia loads of the frame are directly supported by the artificial constraints to the fixed point. Accordingly, these do not contribute to the loads in the contact points between the bodies. Measured against the total weight of the rider-bike system, these components play an almost negligible role, which is reflected in the negligibly better simulation results, see Table 4.

©2023 Bolk, J.& Corves, B published by TU Delft OPEN on behalf of the authors.
ISSN: 2667-2812

 http://dx.doi.org/10.59490/6595820fa5398fcc65e8398a

Table 4: Evaluation of the *guided frame* model

	x-axis			y-axis		
	RMSE	NRMSE	R^2	RMSE	NRMSE	R^2
frame − forktop	30.65	1.94	1	–	–	–
frame − forkbottom	52.63	3.07	0.99	38.66	2.72	0.99
frame − chainstay	21.29	0.57	1	8.97	1.24	1
seatstay − lever	15.97	0.4	1	9.22	0.58	1

Although *fixed frame* and *guided frame* are straightforward to implement with rigid bodies, there are some challenges to overcome when it comes to the integration of elastic body properties of the frame. Such extensions of the MBS have a significant impact on the simulation results as shown in (Bolk et al., 2023). Constraining the frame results in constraints of single points on an elastic body. This leads to stress changes as loads are significantly higher at the constraint point and thus, natural deformation is restrained. Furthermore, the center of gravity of the frame, used in this work, is often not on the structure itself. A feasible solution could be, e.g., the implementation of a so-called rb3-element between the whole frame and the reference point. This is element is a common modeling element in finit-element-methods that distributes the load over many points on the structure.

3 Conclusion

The work presents and evaluates the performance of four approaches that allow a semi-analytical simulation of bicycles. It was shown that the approach of a locating-floating bearing setup is limited in its ability to reproduce internal system loads. This is especially true for maneuvers with horizontal loads. However, by constraining the frame, very high accuracies in the reproduced loads could be achieved. This was shown in the deviation as well as in the agreement of the course between the semi-analytical simulation loads and the reference loads at different points in the system. The hypothesis that for bicycles the neglection of inertia loads leads only to small deviations could be confirmed. This opens up the possibility of obtaining accurate results and numerically representing the internal system behavior without measuring the system trajectory. In the context of structural design, this allows for determining both the magnitude of peak loads and the number and amplitude of load changes.
Further research relates to the investigation of actively controlled compensation strategies. These strategies can provide the possibility to integrate elastic bodies, further enhancing the accuracy of numerically recreating loads in bicycle structures. Additionally, closed-loop stabilization approaches could allow an even more accurate representation of frame inertia forces if the center of gravity trajectory is known as well as the expansion and integration of torsional loads. In order to use this type of simulation, real measurement data must be available. However, it is unclear to what extent existing measurement data can be used when factors such as tires, rider, or frame geometry are changed. Unlike the invariant fully analytical simulation, the measurement data and therefore the semi-analytical simulation is partly dependent on the measurement system. Finally, the results need to be confirmed with real-life measurement inputs.

References

Blanchette, C., Boisvert, M., Joubert, N., Rancourt, D., and Desrochers, A. (2021). Dynamic input loads evaluation of a recreational vehicle frame using multibody dynamics hybrid modeling validated with experimental and full analytical modeling data. *Advances in Mechanical Engineering*, 13(8).

Bolk, J., Kiesewetter, M., and Corves, B. (2023). Establishment of a numerical test rig environment for bicycles by means of multi-body simulation. *9th IFToMM D-A-CH conference 2023: 16./17. March 2023, Univerity Basel*, 2023.

Bruni, S., Meijaard, J. P., Rill, G., and Schwab, A. L. (2020). State-of-the-art and challenges of railway and road vehicle dynamics with multibody dynamics approaches. *Multibody system dynamics*, 49(1):1–32.

DIN Standards Committee (2023). Cycles - Safety requirements for bicycles (ISO 4210-1:2023); German version EN ISO 4210:2023.

German Bicycle Industry Association (2023). 2022 market data - bicycles and e-bikes. *ZIV Zweirad-Industrie-Verband*.

Ingenlath, P. (2019). *Multibody simulation based bicycle design*. PhD thesis, RWTH Aachen Univercity.

©2023 Bolk, J.& Corves, B published by TU Delft OPEN on behalf of the authors.
ISSN: 2667-2812

Johannesson, P. and Speckert, M. (2014). *Guide to load analysis for durability in vehicle engineering*. Automotive series. Wiley, Chichester, West Sussex, 1 edition.

Joubert, N., Boisvert, M., Blanchette, C., St-Amant, Y., Desrochers, A., and Rancourt, D. (2020). Frame loads accuracy assessment of semianalytical multibody dynamic simulation methods of a recreational vehicle. *Multibody system dynamics*, 50(2):189–209.

Köhler, M., Jenne, S., Pötter, K., and Zenner, H. (2012). *Zählverfahren und Lastannahme in der Betriebsfestigkeit*. Springer, Berlin and Heidelberg.

Speckert, M., Ruf, N., and Dreßler, K. (2009). *Undesired drift of multibody models excited by measured accelerations or forces*, volume 162 of *Berichte des Fraunhofer-Instituts für Techno- und Wirtschaftsmathematik (ITWM Report)*. Fraunhofer-Institut für Techno- und Wirtschaftsmathematik, Fraunhofer (ITWM), Kaiserslautern.

Tebbe, J. C., Chidambaram, V., Kline, J. T., Scime, S., Shah, M. P., Tasci, M., and Zheng, D. (2006). Chassis loads prediction using measurements as input to an unconstrained multi-body dynamics model. *Load Simulation & Analysis in Automotive Engineering-SP-2038*.

©2023 Bolk, J.& Corves, B published by TU Delft OPEN on behalf of the authors.
ISSN: 2667-2812

The Evolving Scholar Vol. 3, 2023

http://dx.doi.org/10.59490/660179a06bf1082286458109

Bicycle and Motorcycle Dynamics 2023
Symposium on the Dynamics and Control of Single Track Vehicles
18–20 October 2023, Delft University of Technology, The Netherlands

Type of the Paper: Conference Paper

Revised

BRiM: A Modular Bicycle-Rider Modeling Framework
[version 2; peer reviewed]

Timótheüs J. Stienstra[1], Samuel G. Brockie[1], Jason K. Moore[1,*]

[1] Faculty of Mechanical, Maritime and Materials Engineering (3mE), Delft University of Technology, The Netherlands; j.k.moore@tudelft.nl, ORCID 0000-0002-8698-6143

[*] corresponding author

Name of Editor: Edwin De Vries
First published: 19/09/2023
Last published: 02/04/2024
Citation: Stienstra, T., Brockie, S. & Moore, J. (2024). BRiM: A Modular Bicycle-Rider Modeling Framework [version 2; peer reviewed]. The Evolving Scholar - BMD 2023, 5th Edition.
This work is licensed under a Creative Commons Attribution License (CC-BY).

Abstract:

The development of computationally efficient and validated single-track vehicle-rider models has traditionally required handcrafted one-off models. Here we introduce *BRiM*, a software package that facilitates building these models in a modular fashion while retaining access to the mathematical elements for handcrafted modeling when desired. We demonstrate the flexibility of the software by constructing the Carvallo-Whipple bicycle model with different numerical parameters representing different bicycles, modifying it with a front fork suspension travel model, and extending it with moving rider arms driven by joint torques at the elbows. Using these models we solve a lane-change optimal control problem for six different model variations which solve in mere seconds on a modern personal computer. Our tool enables flexible and rapid modeling of single-track vehicle-rider models that give precise results at high computational efficiency.

Keywords:

Bicycle Dynamics, Brim, Computational Modeling, Open-source, Sympy, Simulation, Trajectory Tracking Problem

©2023 Stienstra, T. J., Brockie, S. G., & Moore, J. K. published by TU Delft OPEN on behalf of the authors.
ISSN: 2667-2812

 http://dx.doi.org/10.59490/660179a06bf1082286458109

Introduction

Throughout the 200 year history of the bicycle, numerous researchers have developed mathematical models to investigate various aspects of bicycle dynamics and rider control (Schwab and Meijaard, 2013). These models have contributed valuably to our understanding of self-stability (Meijaard et al., 2011), active and passive rider control (Moore, 2012; Schwab et al., 2012; Sharp, 2008), and the identification of specific eigenmodes (Sharp, 1976). These insights have also informed the development of bicycles with improved stability, handling, and comfort (Plöchl et al., 2012).

Mathematical bicycle models have been created using both numeric and symbolic approaches, and a combination of the two. Furthermore, these have been facilitated by many different languages and software packages. For example, Meijaard et al. (2007) used the dynamics modeling software *SPACAR* (van Soest et al., 1992) to numerically derive the equations of motion (EoMs) for the Carvallo-Whipple bicycle model. The same thing has been done symbolically by Sharp (2008), who used Matlab's Symbolic Toolbox (The MathWorks Inc., 2023), and by Moore (2012) using both the symbolic dynamics package *AUTOLEV* (Levinson and Kane, 1990) and Python's computer algebra package *SymPy* (Meurer et al., 2017).

One commonality between these numeric and symbolic approaches is that they often handcraft the EoMs derivation. This approach is advantageous in that the implementer controls the choice of coordinates that are used, often optimizing the simplicity of the resulting EoMs. Indeed, handcrafted EoMs offer the highest reachable computational performance (Rosenthal and Sherman, 1986).

Many research grade software packages, like *SPACAR*, *Simbody* (Sherman et al., 2011), and *ADAMS* (Ryan, 1990), efficiently form the EoMs for a multibody system, but these resulting EoMs exist solely in the form of numeric computer code and lack accessibility to be interrogated. Modern physics engines, like *MuJoCo* (Todorov et al., 2012) and *Nimble* (Werling et al., 2021), also offer numerical computation of high-accuracy dynamics. However, these have not gained traction in bicycle dynamics research, perhaps due to the focus on general applicability with varying assumptions in contact dynamics. *FastBike* (Dynamotion, 2023) simulates single-track vehicles, but remains proprietary, and *JBike6* (Dressel, 2006) only calculates the eigenvalues of one model.

Symbolics offer transparency, allowing for a clear understanding of the underlying equations and enabling greater flexibility in manipulating and interpreting the resulting expressions. There is scope for a symbolic approach to result in more performant code through processes like term rewriting to minimize the number of expressions in the EoMs (Gowda et al., 2022). One downside is that model derivation is typically more expensive than with numeric approaches. However, for bicycle models this cost is often still only of the order of seconds and can be amortized if the resulting model is cached and reused.

Despite the extensive research, creating accurate and performant mathematical bicycle models remains a common challenge. As pointed out by Meijaard et al. (2007), numerous published models exhibit mistakes in their derivation. Nowadays, many researchers use the linearized Carvallo-Whipple model (Meijaard et al., 2007) as starting point and extend it to incorporate additional features such as tire models (Limebeer and Sharp, 2006; Plöchl et al., 2012; Schwab and Meijaard, 2013) or rider attachments (Moore, 2012). This approach is error prone (Schwab and Meijaard, 2013), time consuming, and hinders the development of more complex models. It also reduces research dissemination and reproducibility as models may not be compatible with one another due to the usage of different conventions and programming languages, or dependence on closed-source software.

BRiM targets two main user groups: researchers wanting to use accessible and validated bicycle-rider models ("*model users*"), and researchers developing their own modifications of, or extensions to, bicycle-rider models ("*model developers*"). To address the needs of the former group, *BRiM* provides a library of composable bicycle and bicycle-rider models that users can apply to their own research questions directly out of the box. Users can trust the accuracy of these as, where possible, they are prevalidated, in addition to the source code being open for review and critique. For the second user group, *BRiM* provides a framework for researchers to develop their own modular submodels and seamlessly integrate these into their bicycle and bicycle-rider models. Through the usage of *BRiM*, these extensions can more easily be shared between researchers due to the common tooling.

To summarize, our contributions are twofold. First is the development and release of the open-source package *BRiM* for bicycle-rider modeling, including its library of composable bicycle-rider models and frameworks for users to implement their own extensions, as well as utilities for parametrization, simulation, and visualization. Second is the demonstration of *BRiM* by formulating and solving multiple novel trajectory tracking optimization problems of bicycle and bicycle-rider models, including a comparison of the minimized steer torques required for a lane change maneuver for three different bicycle geometries, plus a comparison between a rigid fork and front suspension bike, and a comparison between the steering torque and elbow torques, for the same maneuver.

©2023 Stienstra, T. J., Brockie, S. G., & Moore, J. K. published by TU Delft OPEN on behalf of the authors.
ISSN: 2667-2812

 http://dx.doi.org/10.59490/660179a06bf1082286458109

Software Overview

BRiM is built on top of the `physics.mechanics` module of *SymPy*, a feature-rich and well-tested codebase for creating symbolic EoMs for complicated multibody systems. *BRiM*, via *SymPy*, uses Kane's method (Kane and Levinson, 1985) to form the EoMs of the system. Unlike classical methods for multibody dynamics, like Newton-Euler, Lagrange, and Hamilton, Kane's method leads directly to simpler EoMs for a system (Kane and Levinson, 1980; Rosenthal and Sherman, 1986). It was also designed to be systematic, making it easy to translate into a computational implementation. While other algorithms exist for efficiently computing a system's dynamics (Featherstone, 2008; Jain, 2010), these have been optimized for numerics. Consequently, Kane's method is a popular algorithm when deriving symbolic EoMs (Levinson and Kane, 1990).

BRiM provides three different levels of abstraction for constructing and interacting with bicycle-rider models. All three levels can be used interchangeably with one another, which is possible because they all either directly use, or abstract down to using, the symbolic building blocks defined with *SymPy*. At a high level, aimed predominantly at model users, *BRiM* offers a library of prebuilt modeling components that can be easily connected in a modular fashion to create a full bicycle or bicycle-rider model with minimal boilerplate code. At this level, the user is able to, for example, swap out a knife-edge wheel model for a toroidal wheel model in a single statement.

An intermediate-level interface allows the *SymPy* constructs for joints, bodies, and loads to be used directly to replace, extend, and augment models that do not exist at the component level. This level also allows model developers to readily transform these custom models into *BRiM* constructs that can then be used at the component level with an equally light interface as model components present within the package, thus making them suitable for sharing with, and use by, model users.

For advanced users, *BRiM* also allows direct manipulation of the *SymPy* equations, like the customization of the direction cosine matrices between reference frames. This enables modelers to make optimizations to the system's EoMs where their insight can simplify the model definition. It also allows the generated EoMs to be interrogated and transformed, which can be invaluable when debugging or optimizing custom models.

BRiM Core

BRiM has three types of components, models, connections, and load groups, with which a multibody dynamics system is described. A "*model*" is an object that represents a specific system within defined system boundaries. A model can be standalone or composed of multiple submodels. Each model encapsulates the relations and behaviors of the system, allowing for a modular and hierarchical tree representation where parent models do not know the details of their submodel children. Each subsystem is treated independently within its respective system boundary, which is simpler to model. Once the subsystems have been defined separately, they can be merged to form the complete system, with parents defining the interactions between their children. This modular approach not only simplifies the organization of the model but also promotes reusability and flexibility in system design.

A "*connection*" is a utility of a parent model to define relationships between two or more child submodels. Connections provide three key features. Firstly, connections enable parent models to define the interactions between their child submodels in a modular fashion. Secondly, connections enable the reuse of these possibly complex interactions. An example of both is the interaction between a wheel and the ground, where multiple complex descriptions of tire models are possible. Using connections these tire models can be defined once and then be reused in all bicycle models in *BRiM*. Lastly, connections allow new properties to be incorporated into a model. For example, when modeling a bicycle with a leaning rider, the axis should be defined about which the rider leans. However, if a bicycle is being modeled without a rider then this axis is not needed and so not considered.

A "*load group*" is a collection of related loads (forces and torques), which can be applied to an associated model or connection. Loads are separated from models because it is unlikely that a model will universally require specific loads in all circumstances. For example, consider a load group whose task is to provide the inputs to steer a bicycle model. The simplest option here would be to apply a simple time-varying torque actuator acting about the steering axis. If a rider model was also being used, a more complex load group could consist of two time-varying torque actuators acting one each at the rider's right and left elbows.

After a user has configured a model using submodels, connections, and loads, *BRiM* uses the following five-step algorithm to define the multibody system and establish all relationships required to form the system's EoMs. First, parent models associate their child submodels to their connections, which ensures that all connections have access to the information they require. Next, the "*define objects*" step creates objects such as symbols and reference frames, without defining any relationships between them. After this, the "*define kinematics*" step establishes relationships between the objects' orientations/positions, velocities, and accelerations. Next,

©2023 Stienstra, T. J., Brockie, S. G., & Moore, J. K. published by TU Delft OPEN on behalf of the authors.
ISSN: 2667-2812

 http://dx.doi.org/10.59490/660179a06bf1082286458109

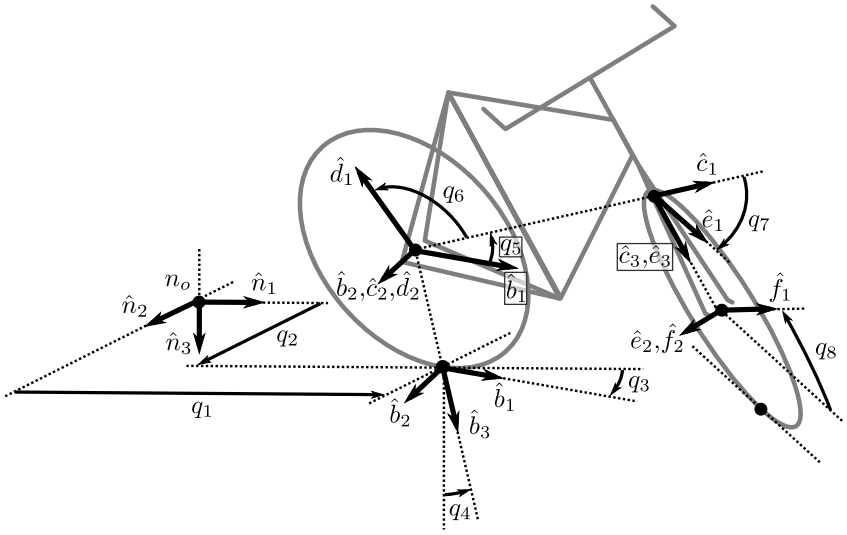


Figure 1. Configuration of the Carvallo-Whipple bicycle model following the convention from Moore (2012), where q_1 and q_2 are the perpendicular distances of the rear contact point in the ground plane, q_3, q_4, and q_5 are the yaw, roll, and pitch angles of the rear frame relative to the ground, q_7 is the steering rotation angle, and q_6 and q_8 are the rear and front wheel rotation angles.

the "*define loads*" step specifies the forces and torques acting on the system. Lastly, the "*define constraints*" step computes the holonomic and nonholonomic constraints on the system.

In each define step, a model first calls the define step for each of its submodels using a depth-first traversal, which is required because parent models may use properties of their submodels. Next, the model defines itself while triggering the define step of connections. These are initiated manually by the parent model because it is possible for there to be two-way dependence between parent models and their associated connections in a single define step. Finally, the model calls the define step for each of its associated load groups.

Upon completion of the above steps, all relationships within the model are defined. At this stage, the end-user can export the model to a `System` instance from the `physics.mechanics` module of *SymPy*, which can automatically form the EoMs.

BRiM Models

While it is possible to implement any bicycle model using *BRiM*, *BRiM* distributes a complete implementation of the Carvallo-Whipple bicycle model (Carvallo, 1899; Whipple, 1899) following the parameterization convention of Moore (2012). The Carvallo-Whipple bicycle is widely recognized as the lowest-order bicycle model to have been repeatedly validated by multiple authors (Kooijman et al., 2008; Schwab and Meijaard, 2013; Sharp, 2008). The parametrization convention of Moore, as shown in Figure 1, has been chosen due to its configuration independence, which is preferred when forming nonlinear EoMs of a bicycle, (Peterson, 2013). By default, the Carvallo-Whipple bicycle consists of a ground and four bodies: a rear wheel, a rear frame, a front frame, and a front wheel. Each body is assumed to be rigid and all bodies are attached using pin joints. The rear wheel's contact point is defined within the ground plane and the rear frame is oriented in yaw-roll-pitch rotation relative to the ground. The front wheel's contact point is constrained to the ground using a holonomic constraint, and nonholonomic constraints are applied to both wheels to enforce no-slip conditions. Further details of the Carvallo-Whipple bicycle model's definition are found in Moore (2012).

To facilitate the implementation of extensions, like toroidal-shaped wheels and tire models (Limebeer and Sharp, 2006; Schwab and Meijaard, 2013), to the Carvallo-Whipple bicycle in a modular fashion, *BRiM* splits the bicycle model into separate models for each body. This division results in a total of five submodels: ground, rear wheel, front wheel, rear frame, and front frame. The modularity of the tire models is achieved by using connections to describe the interaction between the ground and a wheel. A schematic overview is shown in Figure 2.

Published rider models tend to either fall into the category of upper-body models (Moore, 2012) or pedaling models (Park et al., 2022). To support varying complexities of both types of model, *BRiM* segments the rider into optional submodels and connections.

©2023 Stienstra, T. J., Brockie, S. G., & Moore, J. K. published by TU Delft OPEN on behalf of the authors.
ISSN: 2667-2812

 http://dx.doi.org/10.59490/660179a06bf1082286458109

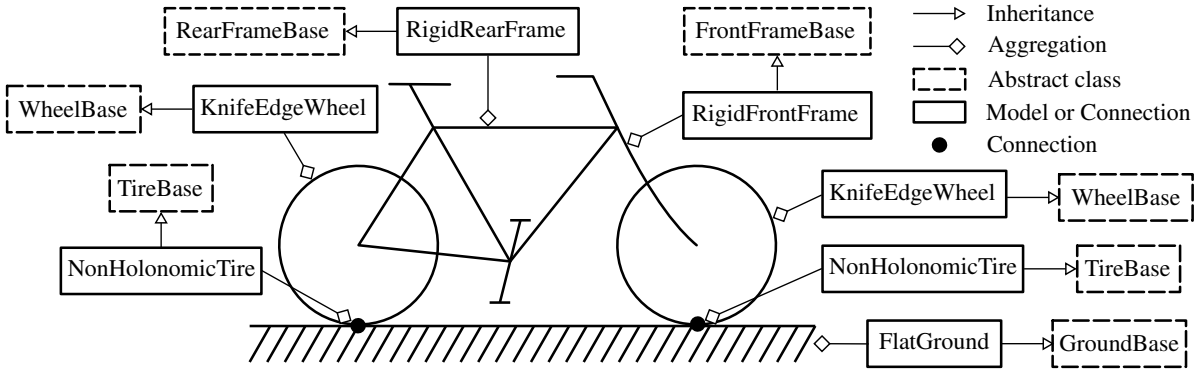


Figure 2. Schematic of the Carvallo-Whipple bicycle in *BRiM* aggregating from its constituent parts. The blueprint of these parts is described in abstract classes and is copied through inheritance.

The only mandatory submodel is the pelvis because it is shared by all rider models. The other five submodels forming the rider are the torso, left and right legs, and left and right arms. The relationships between these are described by five connections representing the various joints: the left and right hips, the left and right shoulders, and the sacrum connecting the torso to the pelvis. To extend a bicycle model with a rider, connections at the saddle, the handlebars, and the pedals are required.

Benchmarks

A convenient proxy for the computational performance of the derived EoMs is the number of floating point operations required to evaluate them. The output of *BRiM* has been compared to handcrafted EoMs of the Carvallo-Whipple bicycle by Moore (2012); Stienstra (2023a), both of which were also derived using *SymPy*. The version by Moore utilizes writing the equations as one might on paper to reduce the complexity resulting in 2198 operations. The version by Stienstra mainly utilized the intermediate-level interface in *SymPy* resulting in 2389 operations. *BRiM*'s output is in between the two containing 2291 operations, highlighting that *BRiM* is able to produce efficient EoMs on par with handcrafted derivations despite its modularity and user-friendly interface.

Demonstrations Methodology

To demonstrate the wide applicability, capabilities, and potential of *BRiM*, we solved a series of related trajectory tracking optimization problems for bicycle and bicycle-rider models. The goal here is to showcase the modularity and extensibility of *BRiM* with examples, and evidence that it can be readily used in novel applications, reducing the barriers to generating new results.

Bicycle and Bicycle-Rider Models

In the demonstrations, the same trajectory is tracked but the bicycle (or bicycle-rider) model involved differed. All six of these models were built entirely using *BRiM*. The specifics of the model used in each of the six optimization cases are outlined below.

- Optimization #1: This is the default Carvallo-Whipple bicycle model without the inertial effects of a rider. It uses the parameter values from a Batavus Browser Dutch style city bicycle (Moore, 2012), `"Browser"`. The constituent submodels used to create this instance are shown in Figure 2. The system's inputs are a torque applied to the rear wheel about the wheel hub axis (the "*propulsion/braking torque*") and a torque actuator applied between the handlebars and the rear frame such that they are actuated about the steering axis (the "*steering torque*").
- Optimization #2: This is the same as optimization #1 but with the parameter values from a Bianchi Pista steel frame track bicycle (Moore, 2012), `"Pista"`.
- Optimization #3: This is the same as optimization #1 but with the parameter values from a Gary Fisher hard-tail mountain bicycle (Moore, 2012), `"Fisher"`.

©2023 Stienstra, T. J., Brockie, S. G., & Moore, J. K. published by TU Delft OPEN on behalf of the authors.
ISSN: 2667-2812

- Optimization #4: This modifies optimization #3 by replacing the rigid front frame with a fork suspension on soft settings.
- Optimization #5: This is a bicycle-rider model. It extends optimization #1 by including the inertial effects of a rigidly attached rider including arms, where the shoulders are modeled to allow flexion and rotation, and the elbows are pin joints.
- Optimization #6: This modifies optimization #5 by replacing the "*steering torque*" with a pair of torque actuators at the elbows of the rider model (the "*elbow torques*").

Complete scripts for constructing these six models, plus formulating and running the trajectory tracking optimization problem, can be found in the GitHub repository for this paper: `github.com/mechmotum/brim-bmd-2023-paper`.

Equation Generation

BRiM automatically generates the EoMs of the system. For the base Carvallo-Whipple bicycle model (optimizations #1–3), which follows the convention of Moore (2012), *BRiM* produces a system defined in terms of eight generalized coordinates and eight generalized speeds. For the optimizations, we choose a set of seven ($Q = 7$) of the generalized coordinates ($\mathbf{q}_{ind}$) and three ($U = 3$) generalized speeds ($\mathbf{u}_{ind}$) to be independent. These are

$$\mathbf{q}_{ind} = [q_1, q_2, q_3, q_4, q_6, q_7, q_8] \ ,$$
$$\mathbf{u}_{ind} = [u_4, u_6, u_7] \ .$$

With these, we can formulate the 16 state equations that will enforce the system dynamics in the optimization problem. The first eight are the kinematic differential equations that map the time derivative of each generalized coordinate to the corresponding generalized speed

$$\dot{q}_i = u_i \qquad i \in \mathbb{N} \cap [1, 8] \ . \tag{1}$$

The next three are dynamic differential equations, each one corresponding to the time derivative of the three independent generalized speeds

$$\mathbf{M}\dot{\mathbf{u}}_{ind} - \mathbf{k} = \mathbf{0} \, , \tag{2}$$

where $\mathbf{M}$ is the 3×3 mass matrix of the bicycle model and $\mathbf{k}$ is its length-3 forcing column vector encompassing both externally applied forces and forces due to various velocity effects.

This is followed by a single differential algebraic equation that enforces the holonomic constraint to keep the front wheel in contact with the ground. Finally, four differential algebraic constraints, two each per wheel, enforce the nonholonomic constraints that provide the no-slip conditions for the front and rear wheels.

In optimization #4, one extra independent generalized coordinate (q_s) describing the suspension travel and one extra independent generalized speed (u_s) describing the suspension velocity are introduced. Consequently, $Q = 8$ and $U = 4$. This results in the addition of one extra kinematic differential equation involving $\dot{q}_s$ and one extra dynamic differential equation involving $\dot{u}_s$.

Optimizations #5–6, use the same base generalized coordinates and generalized speeds as optimizations #1–3. However, due to the addition of the rider, an additional six dependent generalized coordinates are introduced. For each of the two arms, two are for the flexion and rotation of the shoulder joint and one is for the flexion of the elbow joint. Additionally, each of these dependent generalized coordinates maps to a dependent generalized speed so an additional six of these are also required. Q and U are unchanged because no independent generalized coordinates or speeds are introduced. To keep the hands attached to the handlebar grips, six more holonomic constraints are used. In terms of additional state equations to enforce the dynamics, six additional kinematic differential equations are introduced, alongside six additional differential algebraic equations to enforce the holonomic constraints.

Let $\mathbf{r}$ be the vector of model inputs and R be its length. For optimizations #1–5, $R = 2$ and $\mathbf{r} = [T_p, T_s]$, where T_p and T_s are the propulsion/braking and steering torques respectively. For optimization #6, $\mathbf{r} = [T_p, T_l, T_r]$ and $R = 3$, where T_l and T_r are the left and right elbow torques respectively.

©2023 Stienstra, T. J., Brockie, S. G., & Moore, J. K. published by TU Delft OPEN on behalf of the authors.
ISSN: 2667-2812

Tracking Problem

In our trajectory tracking optimization problems, the task is to follow a target ground path representing a lane change. The path is defined by the equation

$$\bar{q}_2\left(q_1\right) = \begin{cases} 0\,, & q_1 < X_s \\ \frac{1}{2} X_2 \left(1 - \cos\left(\frac{q_1 - X_s}{X_1 - 2X_s}\pi\right)\right)\,, & X_s \leq q_1 \leq X_1 - X_s\,, \\ X_2\,, & X_1 - X_s < q_1 \end{cases} \tag{3}$$

where q_1 and q_2 are the states describing the longitudinal and lateral position of the rear wheel contact point in the Newtonian coordinate system respectively, $\bar{q}_2$ is the target lateral position as a function of q_1, X_1 and X_2 are the longitudinal length and lateral displacement of the target path respectively, and X_s is the length of straight at the beginning and end of the path.

The objective function J simultaneously minimizes both the tracking error and the input magnitudes, to find controls that minimize the approximated input energy used in the maneuver. It is defined as

$$J = \int_{t_0}^{t_F} (1 - w)\left(q_2 - \bar{q}_2\left(q_1\right)\right)^2 dt + w \sum_{i=1}^{R} \int_{t_0}^{t_F} r_i^2 dt\,, \tag{4}$$

where t_0 and t_F are the initial and final times, r_i is the ith input variable, and w is a weighting parameter between the squared tracking error and the sum of squared inputs. We selected $w = 2.5 \cdot 10^{-3}$, which aims to target a mean tracking error of $0.025\,\mathrm{m}$ for an approximate torque of $0.5\,\mathrm{N\,m}$.

We add constraints defining the initial and final state of the system's motion to be in the nominal configuration and at a nominal travel speed. In optimizations #1–6 we enforce

$$\begin{aligned} q_1\left(t_1\right) &= 0.0 & q_1\left(t_F\right) - X_1 &= 0.0 & q_6\left(t_1\right) &= 0.0 & \\ q_2\left(t_1\right) &= 0.0 & q_2\left(t_F\right) - X_2 &= 0.0 & q_7\left(t_1\right) &= 0.0 & q_7\left(t_F\right) &= 0.0 \\ q_3\left(t_1\right) &= 0.0 & q_3\left(t_F\right) &= 0.0 & q_8\left(t_1\right) &= 0.0 & \\ q_4\left(t_1\right) &= 0.0 & q_4\left(t_F\right) &= 0.0 & & & \end{aligned}$$

where the second node at t_1 is used for the initial state because the inputs do not affect the first node when using backward Euler discretization. Additionally, in optimization #4 the generalized coordinate and generalized speed for the suspension are constrained at t_1 such that the suspension compression and weight through the handlebars are in equilibrium.

Initial Guess

When solving an optimization problem using direct collocation, the initial guess provided can influence the convergence properties of the problem, or even whether the problem solves at all (Betts, 2010). For consistency between the six optimization cases, we used equivalent initial guesses, only accounting for the inclusion or exclusion of different states and inputs as decision variables.

The initial guess in each optimization was created using a forward simulation that aimed to simultaneously satisfy $\tilde{q}_1\left(t_0\right) = 0$, $\tilde{q}_2\left(t_0\right) = 0$, $\tilde{q}_1\left(t_F\right) = X_1$, and $\tilde{q}_2\left(t_F\right) = X_2$. The tilde above a variable denotes that this is the initial guess corresponding to that variable. The forward simulation from t_0 until t_F was conducted under null inputs ($\tilde{r}_i = 0, i \in \mathbb{N} \cap [1, R]$). Due to the null inputs, the initial state required modification such that the bicycle rides diagonally between the endpoints:

$$\tilde{q}_3\left(t_0\right) = \arctan\left(\frac{X_2}{X_1}\right) \qquad \tilde{u}_4\left(t_0\right) = 0 \qquad \tilde{u}_6\left(t_0\right) = -\frac{\sqrt{X_1^2 + X_2^2}}{r_R\left(t_F - t_0\right)} \qquad \tilde{u}_7\left(t_0\right) = 0\,.$$

As the system dynamics are defined as differential algebraic equations, the `IDA` differential algebraic equation solver (Gardner et al., 2022; Hindmarsh et al., 2005) from the *ODES* Scikit (Malengier et al., 2018) was used to conduct the forward simulation. The resulting initial guesses are dynamically feasible, with the only active instance constraint violations being

$$q_3\left(t_0\right) = \arctan\left(\frac{X_2}{X_1}\right) \neq 0 \qquad q_3\left(t_F\right) = \arctan\left(\frac{X_2}{X_1}\right) \neq 0\,.$$

©2023 Stienstra, T. J., Brockie, S. G., & Moore, J. K. published by TU Delft OPEN on behalf of the authors.
ISSN: 2667-2812

http://dx.doi.org/10.59490/660179a06bf1082286458109

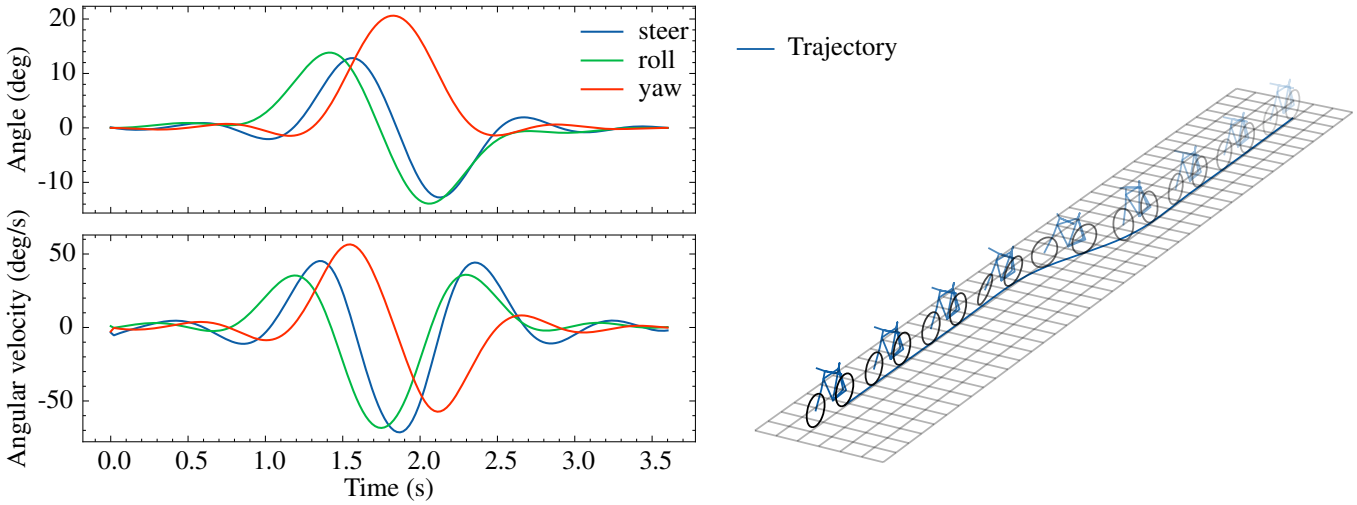


Figure 3. State plot and time-lapse of optimization #1 created using *SymMePlot* (Stienstra, 2023b).

Optimization

We solved each of the six trajectory tracking optimization problems using *opty* (Moore and van den Bogert, 2018), a Python package for solving optimization problems involving dynamic systems using direct collocation (Betts, 2010). *opty* is designed with *SymPy* in mind and thus interfaces seamlessly with *BRiM*. *opty* transcribes the optimization problem into a nonlinear programming problem, which is then solved numerically using the interior-point solver *Ipopt* (Biegler and Zavala, 2009). Each optimization problem was transcribed with 180 nodes, resulting in a node every $0.02\,\mathrm{s}$, and the dynamics were collocated using the backward Euler method. *Ipopt*'s default settings were used with the exception of enabling gradient-based scaling.

Results

All optimizations were successfully solved to the *Ipopt* converge tolerance from the stated initial guesses. Figure 3 shows the steer, roll, and yaw angle and angular velocity states for the optimal solution to optimization #1. Additionally, Figure 3 includes a sequence image of the Browser bicycle traversing the optimal trajectory. This was produced using *SymMePlot* (Stienstra, 2023b), a visualization library build on top of *SymPy*, which has been integrated with *BRiM*. A comparison of the optimal trajectories for all six optimizations is shown in Figure 4, along with comparisons of the optimal steer and roll angle states.

The optimal controls are shown in Figure 5. Comparisons are shown for the optimal propulsion/braking torque for all optimizations and optimal steering torque for optimizations #1–5. For optimization #6, where there was no steering torque, the optimal left and right elbow torques are included. A final subplot compares the tracking error of the optimal trajectory in each problem.

Figure 4 shows that all bicycles follow roughly the same trajectory. Optimizations #1–4, which were riderless, have consistent states and inputs, with the largest difference being seen in optimization #1 where the bicycle is the Batavus Browser. Optimization #5–6, which included the rider, exhibit trajectories with longer transitions and smoother states while also having an increased input cost. Comparing optimizations #5 and #6, it can be seen that the optimal torques in optimization #6 are of larger magnitude while resulting in almost the same trajectory and states.

Table 1 provides a range of metrics related to the optimization problem solves for each of the six optimization problems. These include the achieved optimal cost, and the tracking and input costs that contributed to these, along with the mean tracking error for each optimal trajectory. The number of iterations taken by *Ipopt* is provided to measure the convergence performance, and by association, the computational performance, in solving each problem.

©2023 Stienstra, T. J., Brockie, S. G., & Moore, J. K. published by TU Delft OPEN on behalf of the authors.
ISSN: 2667-2812

http://dx.doi.org/10.59490/660179a06bf1082286458109

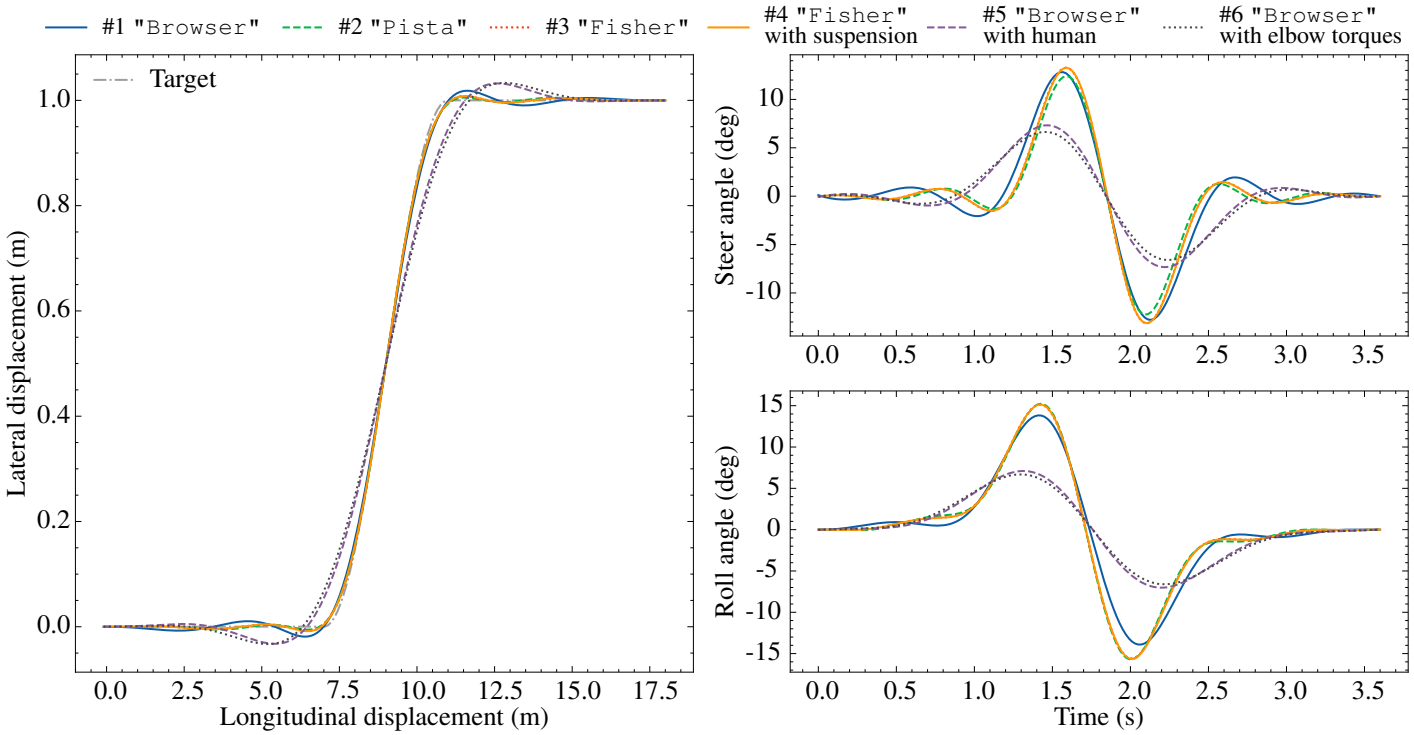


Figure 4. Comparison of the errors between the optimal and target trajectories, the optimal steer angles, and optimal roll angles for optimizations #1–6. Note that the trajectory plot has non-equal axes.

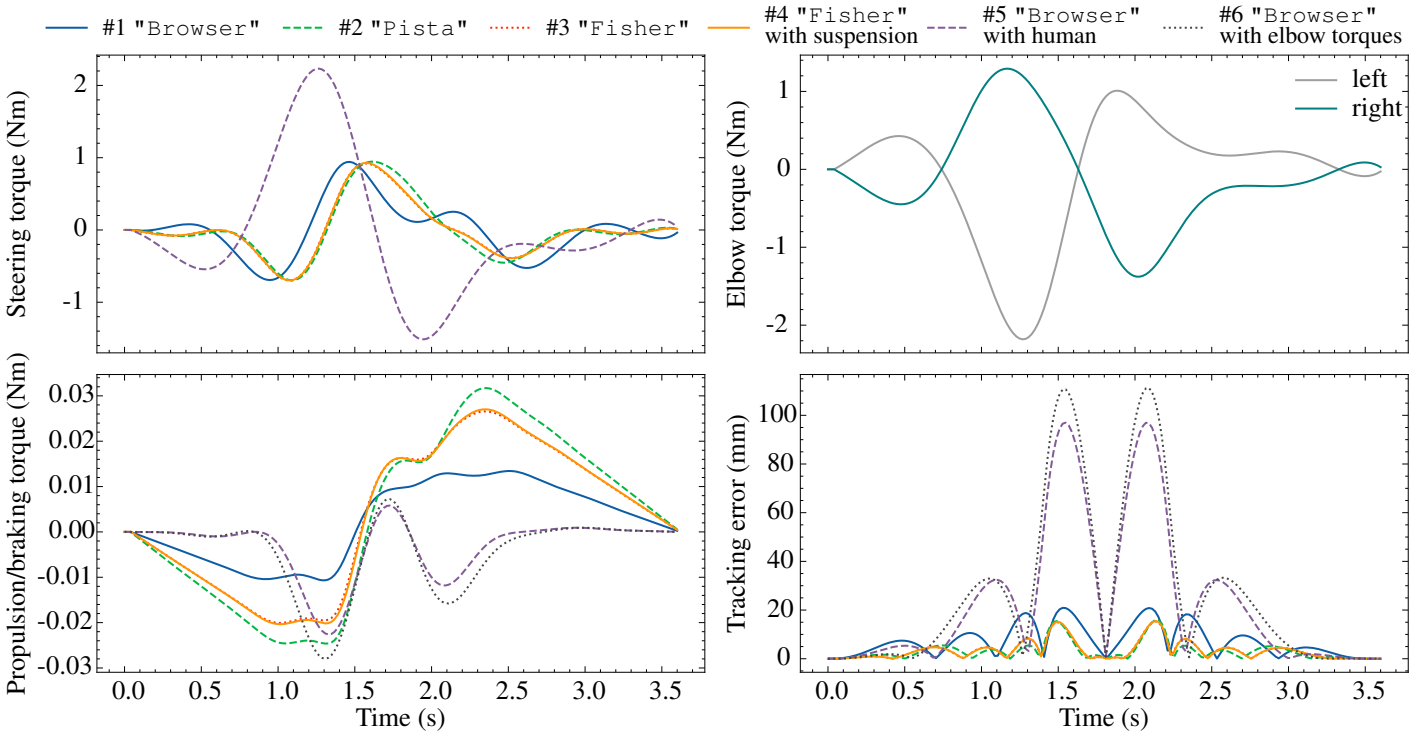


Figure 5. Comparison of the optimal inputs for optimizations #1–6. Note that #6 is missing in the steering torque graph because elbow torques are used.

©2023 Stienstra, T. J., Brockie, S. G., & Moore, J. K. published by TU Delft OPEN on behalf of the authors.
ISSN: 2667-2812

 http://dx.doi.org/10.59490/660179a06bf1082286458109

Optimization	Optimal cost	Tracking cost	Input cost	Mean tracking error (m)	# NLP iterations	Time in *Ipopt* (s)
#1	1.579×10^{-3}	3.267×10^{-4}	5.011×10^{-1}	9.526×10^{-3}	47	1.2
#2	1.434×10^{-3}	8.676×10^{-5}	5.392×10^{-1}	4.909×10^{-3}	76	2.3
#3	1.276×10^{-3}	9.468×10^{-5}	4.726×10^{-1}	5.128×10^{-3}	74	1.9
#4	1.288×10^{-3}	9.494×10^{-5}	4.772×10^{-1}	5.135×10^{-3}	77	2.4
#5	1.253×10^{-2}	5.175×10^{-3}	2.948	3.792×10^{-2}	25	3.5
#6	1.656×10^{-2}	6.864×10^{-3}	3.883	4.367×10^{-2}	23	2.5

Table 1. Solution and convergence metrics for optimization #1–6. Computational metrics were produced using an *Intel(R) Core(TM) i9-13900K CPU @ 3.00GHz*.

Discussion

In the optimal controls for all six problems, countersteering at the start acts to roll the bicycle toward the centerline of the target path while steering the bicycle away from it. This is to be expected as the mass center must be inside the wheels during a turn for the centrifugal forces and centripetal accelerations to balance the bicycle.

All optimal trajectories generally cross the target path in the middle. This can be explained by the target path's rotational symmetry and the periodicity constraints imposed at t_0 and t_F in all of the optimization problems. The propulsion/braking torque remains low in each optimization, as the path can mostly be followed without braking. The increased tracking error of optimization #1 compared to the other riderless optimization #2–4 can be explained by the lower agility of the Batavus Browser bicycle. It is designed to be a stable city bicycle and is almost twice as heavy as the Gary Fisher and Bianchi Pista bicycles.

The solutions to optimizations #3 and #4 are similar by multiple measures. Qualitatively, the optimal states (Figure 4) and inputs (Figure 5) appear nearly identical. As the target trajectory follows a path on flat ground, it should be expected that there will be very little to no travel in the suspension during the maneuver, and therefore the presence of suspension should have little effect on the results.

Comparing the solutions of optimizations #1 and #5, the shape of the optimal trajectories differs with much larger deviations from the target path at the transitions between the straights and the chicane being exhibited in optimization #5. This is to be expected as the addition of the rider results in a large increase in the mass and inertia of the system, and an increase in the height of the mass center. The optimal cost is approximately eight times as large in optimization #5, which can be attributed in equal parts to both the tracking and input costs.

The trajectories in optimizations #5 and #6 have the same shape, which is expected as the inertia is the same. Only the method of how the steering torque is applied differs. In optimization #6, the pair of elbow torques are relatively symmetrical to one another. It is more efficient in terms of the objective function for both elbow torques contribute equally to steering. Still, the combined magnitude of the elbow torques is relatively larger than the steering torque in optimization #5 because the efficiency of each arm is dependent on the steering angle.

Conclusion

This paper has presented *BRiM*, an open-source package for bicycle-rider modeling. *BRiM* enables model users to readily create bicycle and bicycle-rider models from its library of composable submodels. It also facilitates model developers to implement their own models and extensions, which can be used in tandem with all other aspects of the package. Additionally, benchmarking of the EoMs generated by *BRiM* shows that these are of comparable performance to handcrafted EoMs.

BRiM's functionality has been demonstrated by formulating and solving multiple novel trajectory tracking optimization problems of bicycle and bicycle-rider models. A comparison of the minimized steer torques required for a lane change maneuver for three different bicycle geometries has showcased how *BRiM* enables simple reparametrization of models. The modularity of *BRiM* has been illustrated by comparing a bicycle model with a rigid fork to one with suspension. By attaching a rider that can be actuated in a different way to a bicycle, *BRiM*'s models have been shown to be easily extended and modified.

A limitation of *BRiM* is that it forces model developers to use an existing interface for augmented model components. These

©2023 Stienstra, T. J., Brockie, S. G., & Moore, J. K. published by TU Delft OPEN on behalf of the authors.
ISSN: 2667-2812

interfaces can limit flexibility, especially if a component requires additional properties to be interacted with. While connections largely solve this problem, an over-usage of them can result in a cluttering of the implementation code.

Further development of *BRiM* continues. Work is currently underway to add further models to *BRiM*, improve the package's ability to interface with simulation and optimization tools like *opty*, and develop further teaching materials like a tutorial workshop. Examples of models currently under development include tire models and rider models actuated by musculotendons.

An obvious next step is for other researchers to use *BRiM* in their own work. This would provide valuable feedback, which could help guide the future development of the package. *BRiM*'s permissive open-source license also means that its source code can be reviewed and critiqued by others, ensuring the accuracy and validity of its models, which will benefit all users and their work. Our hope is that *BRiM* can become a foundational tool for bicycle dynamics research, improving the ease, speed, and accuracy of work done in this area, by helping researchers to develop and share their models in the future.

Acknowledgments

This project has been made possible in part by CZI grant CZIF2021-006198 and grant DOI https://doi.org/10.37921/240361looxoj from the Chan Zuckerberg Initiative Foundation (funder DOI 10.13039/100014989).

References

Betts, J. T. (2010). *Practical methods for optimal control and estimation using nonlinear programming*. SIAM.

Biegler, L. T. and Zavala, V. M. (2009). Large-scale nonlinear programming using IPOPT: An integrating framework for enterprise-wide dynamic optimization. *Computers & Chemical Engineering*, 33(3):575–582.

Carvallo, E. (1899). *Théorie du mouvement du monocycle et de la bicyclette.* Gauthier-Villars.

Dressel, A. E. (2006). The Benchmarked Linearized Equations of Motion for an Idealized Bicycle (Implemented in Software and Distributed via the Internet). Master Thesis, Cornell University.

Dynamotion (2023). Fastbike. https://www.dynamotion.it/en/software/fastbike-software/.

Featherstone, R. (2008). *Rigid Body Dynamics Algorithms*. Springer.

Gardner, D. J., Reynolds, D. R., Woodward, C. S., and Balos, C. J. (2022). Enabling new flexibility in the SUNDIALS suite of nonlinear and differential/algebraic equation solvers. *ACM Transactions on Mathematical Software*.

Gowda, S., Ma, Y., Cheli, A., Gwóźzdź, M., Shah, V. B., Edelman, A., and Rackauckas, C. (2022). High-performance symbolic-numerics via multiple dispatch. *ACM Communications in Computer Algebra*, 55(3):92–96.

Hindmarsh, A. C., Brown, P. N., Grant, K. E., Lee, S. L., Serban, R., Shumaker, D. E., and Woodward, C. S. (2005). SUNDIALS: Suite of nonlinear and differential/algebraic equation solvers. *ACM Transactions on Mathematical Software*, 31(3):363–396.

Jain, A. (2010). *Robot and multibody dynamics: analysis and algorithms*. Springer Science & Business Media.

Kane, T. R. and Levinson, D. A. (1980). Formulation of equations of motion for complex spacecraft. *Journal of Guidance and Control*, 3(2):99–112.

Kane, T. R. and Levinson, D. A. (1985). *Dynamics, theory and applications*. McGraw Hill.

Kooijman, J. D. G., Schwab, A. L., and Meijaard, J. P. (2008). Experimental validation of a model of an uncontrolled bicycle. *Multibody System Dynamics*, 19(1):115–132.

Levinson, D. A. and Kane, T. R. (1990). AUTOLEV—a new approach to multibody dynamics. In *Multibody Systems Handbook*, pages 81–102. Springer.

Limebeer, D. and Sharp, R. (2006). Bicycles, motorcycles, and models. *IEEE Control Systems Magazine*, 26(5):34–61.

©2023 Stienstra, T. J., Brockie, S. G., & Moore, J. K. published by TU Delft OPEN on behalf of the authors.
ISSN: 2667-2812

Malengier, B., Kišon, P., Tocknell, J., Abert, C., Bruckner, F., and Bisotti, M.-A. (2018). ODES: a high level interface to ODE and DAE solvers. *The Journal of Open Source Software*, 3(22):165.

Meijaard, J., Papadopoulos, J. M., Ruina, A., and Schwab, A. (2007). Linearized dynamics equations for the balance and steer of a bicycle: a benchmark and review. *Proceedings of the Royal Society A: Mathematical, Physical and Engineering Sciences*, 463(2084):1955–1982.

Meijaard, J. P., Papadopoulos, J. M., Ruina, A., and Schwab, A. L. (2011). History of thoughts about bicycle self-stability. Technical report, Cornell.

Meurer, A., Smith, C. P., Paprocki, M., Čertík, O., Kirpichev, S. B., Rocklin, M., Kumar, A., Ivanov, S., Moore, J. K., Singh, S., Rathnayake, T., Vig, S., Granger, B. E., Muller, R. P., Bonazzi, F., Gupta, H., Vats, S., Johansson, F., Pedregosa, F., Curry, M. J., Terrel, A. R., Roučka, v., Saboo, A., Fernando, I., Kulal, S., Cimrman, R., and Scopatz, A. (2017). SymPy: Symbolic computing in Python. *PeerJ Computer Science*, 3:e103.

Moore, J. K. (2012). *Human Control of a Bicycle*. PhD thesis, University of California, Davis.

Moore, J. K. and van den Bogert, A. J. (2018). opty: Software for trajectory optimization and parameter identification using direct collocation. *Journal of Open Source Software*.

Park, S., Caldwell, G. E., and Umberger, B. R. (2022). A direct collocation framework for optimal control simulation of pedaling using opensim. *Plos one*, 17(2):e0264346.

Peterson, L. (2013). *Bicycle dynamics: Modelling and experimental validation*. PhD thesis, University of California Davis.

Plöchl, M., Edelmann, J., Angrosch, B., and Ott, C. (2012). On the wobble mode of a bicycle. *Vehicle System Dynamics*, 50(3):415–429.

Rosenthal, D. and Sherman, M. (1986). High Performance Multibody Simulations via Symbolic Equation Manipulation and Kane's Method. *Journal of the Astronautical Sciences*, 34:223–239.

Ryan, R. (1990). ADAMS—multibody system analysis software. *Multibody Systems Handbook*, pages 361–402.

Schwab, A. L. and Meijaard, J. P. (2013). A review on bicycle dynamics and rider control. *Vehicle System Dynamics*, 51(7):1059–1090.

Schwab, A. L., Meijaard, J. P., and Kooijman, J. D. (2012). Lateral dynamics of a bicycle with a passive rider model: Stability and controllability. *Vehicle System Dynamics*, 50(8):1209–1224.

Sharp, R. S. (1976). The Dynamics of Single Track Vehicles. *Vehicle System Dynamics*, 5(1-2):67–77.

Sharp, R. S. (2008). On the Stability and Control of the Bicycle. *Applied Mechanics Reviews*, 61(6).

Sherman, M. A., Seth, A., and Delp, S. L. (2011). Simbody: Multibody dynamics for biomedical research. *Procedia Iutam*, 2:241–261.

Stienstra, T. J. (2023a). BRiM: A Modular Bicycle-Rider Modeling Framework. Master Thesis, Delft University of Technology.

Stienstra, T. J. (2023b). SymMePlot. https://github.com/tjstienstra/symmeplot.

The MathWorks Inc. (2023). Symbolic Toolbox. https://www.mathworks.com.

Todorov, E., Erez, T., and Tassa, Y. (2012). MuJoCo: A physics engine for model-based control. In *2012 IEEE/RSJ International Conference on Intelligent Robots and Systems*, pages 5026–5033. IEEE.

van Soest, A. J., Schwab, A. L., Bobbert, M. F., and van Ingen Schenau, G. J. (1992). SPACAR: a software subroutine package for simulation of the behavior of biomechanical systems. *Journal of biomechanics*, 25(10):1219–1226.

Werling, K., Omens, D., Lee, J., Exarchos, I., and Liu, C. K. (2021). Fast and Feature-Complete Differentiable Physics for Articulated Rigid Bodies with Contact. *arXiv*, page 15.

Whipple, F. J. (1899). The stability of the motion of a bicycle. *Quarterly Journal of Pure and Applied Mathematics*, 30(120):312–348.

©2023 Stienstra, T. J., Brockie, S. G., & Moore, J. K. published by TU Delft OPEN on behalf of the authors.
ISSN: 2667-2812

The Evolving Scholar Vol. 3, 2023 https://dx.doi.org/10.59490/65f89c8e269cb909bf53af3c

Bicycle and Motorcycle Dynamics 2023
Symposium on the Dynamics and Control of Single Track Vehicles
18 – 20 October 2023, Delft University of Technology, The Netherlands

Type of the Paper: Conference Paper

Revised

Development of a Hardware-in-the-Loop Test Bench for Validation of an Anti-lock Braking System on an E-Bike

[version 2; peer reviewed]

N. Ramosaj[1], C. Fusco[1,2], E. Viennet[1,*]

[1]School of Engineering and Architecture of Fribourg, HES-SO University of Applied Sciences and Arts Western Switzerland; nicolas.ramosaj@hefr.ch; christia.fusco@hes-so.ch; emmanuel.viennet@hefr.ch ORCID 0009-0004-0922-2934
[2]Dipartimento di Ingegneria Meccanica e Aerospaziale, Politecnico di Torino, Italy
*Corresponding author

Name of Editor: Jason Moore
First published: 27/09/2023
Last published: 08/05/2024
Citation: Ramosaj, N., Fusco, C. & Viennet, E. (2024). Development of a Hardware-in-the-Loop Test Bench for Validation of an Anti-lock Braking System on an E-Bike [version 2; peer reviewed]. The Evolving Scholar - BMD 2023, 5th Edition.
This work is licensed under a Creative Commons Attribution License (CC-BY).

Abstract

This article presents the development of a hardware-in-the-loop (HiL) test bench that can be used to validate an electric bicycle (e-bike) anti-lock braking system (ABS) in different test scenarios. The same e-bike can be used in a wide variety of loading conditions, such as with a child seat or panniers (mounted on the front or rear), and different types of tires. Therefore, validating the overall system—i.e., ABS and e-bike—over a wide range of parameters, such as the mass of the rider, load distribution, and tire characteristics, is challenging. The approach presented here involves interfacing a parameterizable virtual bicycle simulation model running on a real-time target machine with the physical ABS hardware under test. This article describes the derivation of an equation-based model that considers six degrees of freedom representing the in-plane longitudinal dynamics of an e-bike. The simulation model was experimentally validated against measurements made on an instrumented test bike. Tests carried out as part of this development show that the developed HiL test bench can be successfully interfaced with a commercially available ABS, enabling the overall behavior of the ABS and the e-bike to be tested and evaluated in a safe and reproducible way before testing begins on the track.

Keywords: bicycle, longitudinal dynamics, ABS, hardware-in-the-loop

©2023 Ramosaj N., Fusco C. & Viennet, E. published by TU Delft OPEN on behalf of the authors.
ISSN: 2667-2812

 http://dx.doi.org/10.59490/65f89c8e269cb909bf53af3c

1 Introduction

Although electrically assisted bicycles (e-bikes) are becoming increasingly popular and can facilitate active commuting, this comes at the cost of safety because e-bikers have a higher risk of traffic accidents than traditional cyclists (Haufe et al., 2022). However, the availability of on-board electric power is enabling the emergence of active safety systems, such as an anti-lock braking system (ABS), which could help reduce the accident rate in the same way as has been observed in recent decades for cars and motorcycles (Maier, 2018). ABS has been widely used on cars since the 1970s and on motorcycles since the 1990s, but it was not until the 2010s that this technology was adapted to bicycles (Enisz et al., 2012; Maier et al., 2015; Corno et al., 2018).

ABS is a mechatronic device involving multi-domain expertise—encompassing electronics, mechanics, and software—and the results from these specific domains need to be integrated into an overall system to be validated. In the context of product development, as defined by the Association of German Engineers (VDI, 2004), the validation task consists of iteratively checking that the system characteristics match the requirements. Depending on which stakeholder is performing the validation and the level of the development cycle, different quantitative requirements may be defined. For example, a bike manufacturer looking to test an ABS purchased from a supplier on the e-bike it is developing could define the braking distance and lock-up duration as quantitative requirements. The braking distance can be defined as the distance covered between the start of braking and the bike coming to a complete stop. The lock-up duration is the total time during which the front wheel speed is zero while the bicycle is still moving forward.

In all cases, validation of an ABS implies being able to carry out braking tests with an integrated ABS on an e-bike. However, hard braking on two-wheelers, particularly when the front wheel locks, is a safety-critical maneuver. Therefore, it is particularly risky to carry out the initial validation of an ABS using road tests. Furthermore, in the case of road braking tests carried out by a human, it is difficult to achieve a sufficient level of reproducibility, particularly with regard to the application of braking force and the position or movement of the rider on the e-bike. In such a situation, a hardware-in-the-loop (HiL) test procedure offers an interesting way to validate an ABS in a safe and reproducible manner.

HiL testing is a well-established method for the development of mechatronic systems in the automotive industry, but its use is seldom reported for bicycle systems, with the notable exception of work carried out since 2015 at the Pforzheim University of Applied Sciences (Pfeiffer et al., 2020). HiL testing enables the design of a component (unit under test) to be validated without complete system hardware and relies on a real-time plant simulator that acts as a digital twin of the missing parts of the system. Setting up an HiL test bench for the validation of an ABS device involves capturing the longitudinal dynamic behavior of an electric bicycle in a virtual model run on a real-time plant simulator. The virtual bike model and the ABS hardware under test are then interfaced and interacted within a real-time closed loop. Figure 1a) presents the operating principle of an HiL test setup, and Figure 1b) shows the necessary components used in a real-time plant simulator.

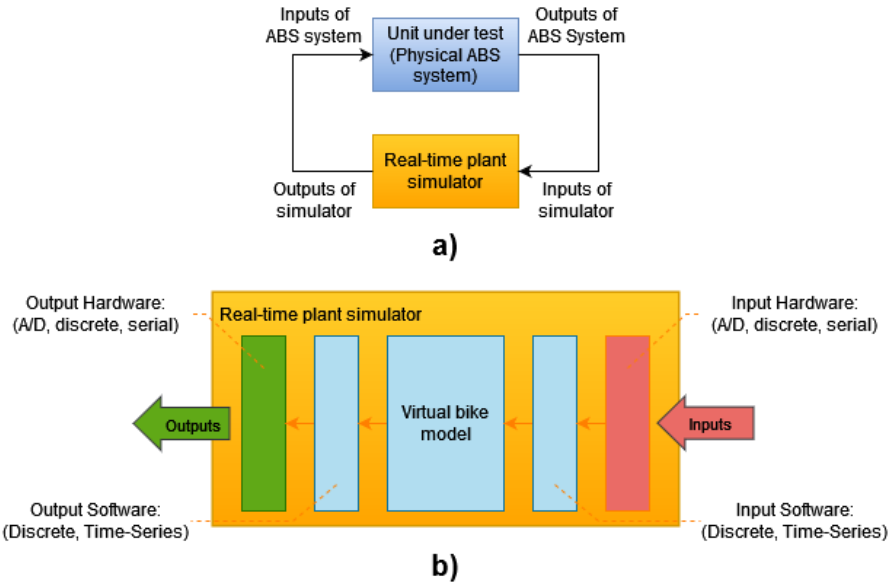


Figure 1. Operating principle of the hardware-in-the-loop test bench: a) unit under test and real-time plant simulator in closed loop; b) components of a real-time plant simulator (adapted from Gomez, 2001)

©2023 Ramosaj N., Fusco C. & Viennet, E. published by TU Delft OPEN on behalf of the authors.
ISSN: 2667-2812

 http://dx.doi.org/10.59490/65f89c8e269cb909bf53af3c

Inputs to the real-time plant simulator may be provided by the software or graphical user interface (input software) or by the unit under test (input hardware) and must be sampled at the test bench operating frequency to be interpreted by the virtual model. The outputs of the virtual model must also be conditioned so that they can be interpreted by the hardware (output software). The numerical solvers generally available for real-time operation require that the model be formulated mathematically without algebraic loops. In addition, the level of modeling must be carefully chosen to avoid overloading the simulator processor.

This paper presents the development of a HiL test bench that can be used to validate the overall behavior of an ABS and a bicycle over the wide range of operating conditions that an e-bike may encounter. The test bench enables parameters such as rider mass, load distribution on the bike or tire grip characteristics on the road to be varied. The point of view adopted is that of an e-bike manufacturer wishing to validate the performance and robustness of an ABS whose technical implementation details are unknown, which is typically the case when the ABS is purchased from a supplier. The derivation of a simulation model based on six-degrees-of-freedom equations representing the in-plane longitudinal dynamics of an e-bike is presented in Section 2. The mobile test apparatus used on the e-bike for the validation of the model and the specific measurements carried out to experimentally characterize its front suspension and tires are presented in Section 3. The validation of the virtual bike model is presented in Section 4. Finally, Section 5 describes the developed HiL test bench and illustrates how it can be used to evaluate the braking performance of an ABS being tested on a crossover bike.

2 Equation-Based Modeling of In-Plane Dynamics

In this section, a mechanical model describing the longitudinal in-plane dynamics of a semi-rigid e-bike (front suspension only) is described. The model consists of four rigid bodies: the main body (bicycle frame + rider), the lower part of the fork, and the rear and front wheels, see Figure 2. It is assumed that the rider does not move with respect to the bicycle frame; therefore, their masses and inertias are lumped together at a common center of gravity (CoG) G. The inertia of the lower part of the fork is neglected, as it plays only a limited role in the overall dynamics of the system. To capture the in-plane motion of the frame, the travel of the front suspension, and the possible slip of the wheels, a model with six degrees of freedom was chosen. The generalized coordinates are grouped in a column vector denoted q and given by Equation (1):

$$q = [x_G \;\; z_G \;\; \theta_G \;\; z_{FW} \;\; \delta_{FW} \;\; \delta_{RW}]^T, \tag{1}$$

where x_G and z_G are the longitudinal and vertical displacement of the main body CoG, θ_G is the main body pitch angle, z_{FW} is the vertical displacement of the front wheel and δ_{RW} and δ_{FW} are the angular positions of the rear and front wheels relative to the frame.

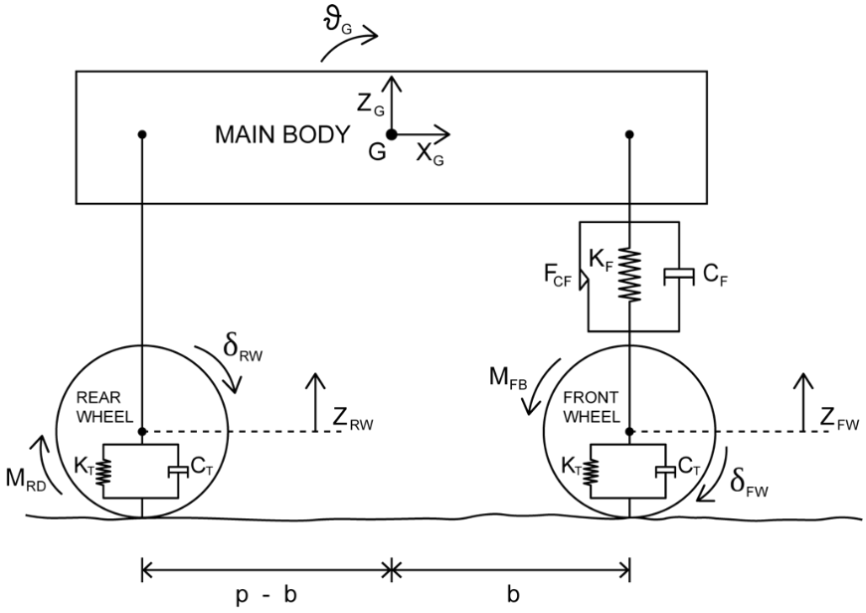


Figure 2. Bike model diagram

©2023 Ramosaj N., Fusco C. & Viennet, E. published by TU Delft OPEN on behalf of the authors.

ISSN: 2667-2812

 http://dx.doi.org/10.59490/65f89c8e269cb909bf53af3c

Although a typical front suspension is characterized by a caster angle ϵ, we chose to reduce this to an equivalent vertical suspension to simplify the analysis, as described by Cossalter (2006). The equivalent stiffness k_{F} and damping c_{F} of the suspension can be expressed in terms of the actual stiffness k and damping c. In addition, a Coulomb friction force F_{CF} was considered in the suspension. A hyperbolic tangent function, associated with a gain k and the maximum friction force F_{C}, was used to relate the Coulomb friction force to the sign of the relative velocity v_{rel} of the suspension as shown in Equation (2):

$$k_{\mathrm{F}} = \frac{k}{\cos^2 \epsilon} \ , c_{\mathrm{F}} = \frac{c}{\cos^2 \epsilon} \ , F_{\mathrm{CF}} = -F_{\mathrm{C}} \cdot \tanh(k \cdot v_{\mathrm{rel}}). \tag{2}$$

The contact between the tire and the ground was modeled with a linear spring in parallel with a viscous friction. The notations used are summarized in Table 1.

Table 1. List of parameters

Name	Title	Unit
$main\ body$	"Frame + rider"	-
m_{b}	Mass of "main body"	kg
$m_{\mathrm{FW}}, m_{\mathrm{RW}}$	Mass of the front and rear wheels	kg
I_{b}	Inertia of "main body"	kgm^2
I_{FW}, I_{RW}	Inertia of the front and rear wheels	kgm^2
p	Wheelbase	m
b	Horizontal length from the front wheel axis to the CoG	m
h	Height from the front wheel axis to the CoG at static equilibrium	m
R_{FW}, R_{RW}	Front and rear wheel radius at static equilibrium	m
x_{G}, z_{G}	Displacement of *G* along the *x*- and *z*-axes	m
θ_{G}	Pitch angle	rad
z_{FW}	Displacement of the front wheel along the *z*-axis	m
δ_{FW}, δ_{RW}	Angular position of the front and rear wheels	rad
k_{F}	Stiffness of the equivalent vertical front suspension	N/m
c_{F}	Damping of the equivalent vertical front suspension	Ns/m
F_{CF}	Coulomb friction in equivalent vertical suspension	N
k	Numerical gain for tanh function	m/Ns
k_{T}	Stiffness of the front and rear tires	N/m
c_{T}	Damping of the front and rear tires	Ns/m
M_{FB}	Brake torque on the front wheel	Nm
M_{RD}	Driving torque on the rear wheel	Nm

Note. Moments of inertia are expressed about each component's center of gravity.

For a six-degrees-of-freedom problem with generalized coordinates q_j and generalized velocities $\dot{q}_j$, it is possible to formulate the Lagragian $L = T - V$, where T is the kinetic energy and V is the potential energy. The Lagrange equation is given in Equation (3):

$$\frac{d}{dt}\left(\frac{\partial L}{\partial \dot{q}_j}\right) - \left(\frac{\partial L}{\partial q_j}\right) = Q_j, \tag{3}$$

where Q_j denotes the nonconservative generalized forces, with the conservative forces being considered in the potential energy V.

©2023 Ramosaj N., Fusco C. & Viennet, E. published by TU Delft OPEN on behalf of the authors.
ISSN: 2667-2812

 http://dx.doi.org/10.59490/65f89c8e269cb909bf53af3c

The generalized coordinates were measured from the static equilibrium position. Therefore, gravity is canceled by the initial spring forces and can be omitted from the potential energy. With a small angle approximation, the potential energy of the system can be expressed in Equation (4):

$$V = \frac{1}{2} \cdot k_{\mathrm{F}} \cdot (z_{\mathrm{G}} - \theta_{\mathrm{G}} \cdot b - z_{\mathrm{FW}})^2 + \frac{1}{2} \cdot k_{\mathrm{T}} \cdot z_{\mathrm{FW}}^2 + \frac{1}{2} \cdot k_{\mathrm{T}} \cdot \left(z_{\mathrm{G}} + \theta_{\mathrm{G}} \cdot (p - b)\right)^2. \tag{4}$$

The kinetic energy is given in Equation (5):

$$T = \frac{1}{2} \cdot m_{\mathrm{tot}} \cdot \dot{x}_{\mathrm{G}}^2 + \frac{1}{2} \cdot (m_{\mathrm{b}} + m_{\mathrm{RW}}) \cdot \dot{z}_{\mathrm{G}}^2 + \frac{1}{2} \cdot I_{\mathrm{tot}} \cdot \dot{\theta}_{\mathrm{G}}^2 + \frac{1}{2} \cdot I_{\mathrm{RW}} \cdot \dot{\delta}_{\mathrm{RW}}^2 + \frac{1}{2} \cdot m_{\mathrm{FW}} \cdot \dot{z}_{\mathrm{FW}}^2 + \frac{1}{2} \cdot I_{\mathrm{FW}} \cdot \dot{\delta}_{\mathrm{FW}}^2. \tag{5}$$

where m_{tot} and I_{tot} denote the total mass and inertia of the whole system, as expressed in Equation (6), with the approximation that the CoG of the whole system is identical to the CoG of the main body:

$$\begin{gathered} m_{\mathrm{tot}} = m_{\mathrm{b}} + m_{\mathrm{RW}} + m_{\mathrm{FW}} \\ I_{\mathrm{tot}} = I_{\mathrm{b}} + I_{\mathrm{RW}} + (h^2 + (p - b)^2) \cdot m_{\mathrm{RW}} + I_{\mathrm{FW}} + (h^2 + b^2) \cdot m_{\mathrm{FW}}. \end{gathered} \tag{6}$$

The generalized forces projected in the direction of each generalized coordinate are defined in Equation (7):

$$\begin{cases} Q_{x_{\mathrm{G}}} = -F_{x_{\mathrm{FW}}} - F_{x_{\mathrm{RW}}} \\ Q_{z_{\mathrm{G}}} = -\left((c_{\mathrm{F}} + c_{\mathrm{T}}) \cdot \dot{z}_{\mathrm{G}} + (c_{\mathrm{T}} \cdot (p - b) - c_{\mathrm{F}} \cdot b) \cdot \dot{\theta}_{\mathrm{G}} - c_{\mathrm{F}} \cdot \dot{z}_{\mathrm{FW}}\right) + F_{\mathrm{C}} \cdot tanh\left(k \cdot (\dot{z}_{\mathrm{FW}} + \dot{\theta}_{\mathrm{G}} \cdot b - \dot{z}_{\mathrm{G}})\right) \\ Q_{\theta_{\mathrm{G}}} = -((c_{\mathrm{T}} \cdot (p - b) - c_{\mathrm{F}} \cdot b) \cdot \dot{z}_{\mathrm{G}} + (c_{\mathrm{T}} \cdot (p - b)^2 + c_{\mathrm{F}} \cdot b^2) \cdot \dot{\theta}_{\mathrm{G}} - c_{\mathrm{F}} \cdot b \cdot \dot{z}_{\mathrm{FW}}) + \left(F_{x_{\mathrm{FW}}} + F_{x_{\mathrm{RW}}}\right) \cdot h \\ \qquad + F_{\mathrm{C}} \cdot tanh\left(k \cdot (\dot{z}_{\mathrm{G}} - \dot{\theta}_{\mathrm{G}} \cdot b - \dot{z}_{\mathrm{FW}})\right) \cdot b \\ Q_{z_{\mathrm{FW}}} = -\left(-c_{\mathrm{F}} \cdot \dot{z}_{\mathrm{G}} - c_{\mathrm{F}} \cdot b \cdot \dot{\theta}_{\mathrm{G}} + (c_{\mathrm{F}} + c_{\mathrm{T}}) \cdot \dot{z}_{\mathrm{FW}}\right) + F_{\mathrm{C}} \cdot tanh\left(k \cdot (\dot{z}_{\mathrm{G}} - \dot{\theta}_{\mathrm{G}} \cdot b - \dot{z}_{\mathrm{FW}})\right) \\ Q_{\delta_{\mathrm{FW}}} = F_{x_{\mathrm{FW}}} \cdot R_{\mathrm{FW}} - M_{\mathrm{FB}} \\ Q_{\delta_{\mathrm{RW}}} = M_{\mathrm{RD}} + F_{x_{\mathrm{RW}}} \cdot R_{\mathrm{RW}}. \end{cases} \tag{7}$$

By computing all the quantities and returning to Equation (3), the Lagrange equations can be expressed by the set of coupled ordinary differential equations in Equation (8):

$$\begin{cases} m_{\mathrm{tot}} \cdot \ddot{x}_{\mathrm{G}} = -F_{x_{\mathrm{RW}}} - F_{x_{\mathrm{FW}}} \\ \\ (m_{\mathrm{b}} + m_{\mathrm{RW}}) \cdot \ddot{z}_{\mathrm{G}} + (c_{\mathrm{F}} + c_{\mathrm{T}}) \cdot \dot{z}_{\mathrm{G}} - c_{\mathrm{F}} \cdot \dot{z}_{\mathrm{FW}} + (c_{\mathrm{T}} \cdot (p - b) - c_{\mathrm{F}} \cdot b) \cdot \dot{\theta}_{\mathrm{G}} \\ +(k_{\mathrm{F}} + k_{\mathrm{T}}) \cdot z_{\mathrm{G}} - k_{\mathrm{F}} \cdot z_{\mathrm{FW}} + (k_{\mathrm{T}} \cdot (p - b) - k_{\mathrm{F}} \cdot b) \cdot \theta_{\mathrm{G}} - F_{\mathrm{C}} \cdot tanh\left(k \cdot (\dot{z}_{\mathrm{FW}} + \dot{\theta}_{\mathrm{G}} \cdot b - \dot{z}_{\mathrm{G}})\right) = 0 \\ \\ \mathrm{I}_{\mathrm{tot}} \cdot \ddot{\theta}_{G} + (c_{\mathrm{F}} \cdot b^2 + c_{\mathrm{T}} \cdot (p - b)^2) \cdot \dot{\theta}_{\mathrm{G}} + (c_{\mathrm{T}} \cdot (p - b) - c_{\mathrm{F}} \cdot b) \cdot \dot{z}_{\mathrm{G}} + c_{\mathrm{F}} \cdot b \cdot \dot{z}_{\mathrm{FW}} \\ +(k_{\mathrm{F}} \cdot b^2 + k_{\mathrm{T}} \cdot (p - b)^2) \cdot \theta_{\mathrm{G}} + (k_{\mathrm{T}} \cdot (p - b) - k_{\mathrm{F}} \cdot b) \cdot z_{\mathrm{G}} + k_{\mathrm{F}} \cdot b \cdot z_{\mathrm{FW}} \\ -F_{\mathrm{C}} \cdot tanh\left(k \cdot (\dot{z}_{\mathrm{G}} - \dot{\theta}_{\mathrm{G}} \cdot b - \dot{z}_{\mathrm{FW}})\right) \cdot b = \left(F_{x_{\mathrm{RW}}} + F_{x_{\mathrm{FW}}}\right) \cdot h \\ \\ m_{\mathrm{FW}} \cdot \ddot{z}_{\mathrm{FW}} - c_{\mathrm{F}} \cdot \dot{z}_{\mathrm{G}} + c_{\mathrm{F}} \cdot b \cdot \dot{\theta}_{\mathrm{G}} + (c_{\mathrm{F}} + c_{\mathrm{T}}) \cdot \dot{z}_{\mathrm{FW}} - k_{\mathrm{F}} \cdot z_{\mathrm{G}} + k_{\mathrm{F}} \cdot b \cdot \theta_{\mathrm{G}} + (k_{\mathrm{F}} + k_{\mathrm{T}}) \cdot z_{\mathrm{FW}} \\ - F_{\mathrm{C}} \cdot tanh\left(k \cdot (\dot{z}_{\mathrm{G}} - \dot{\theta}_{\mathrm{G}} \cdot b - \dot{z}_{\mathrm{FW}})\right) = 0 \\ \\ I_{\mathrm{FW}} \cdot \ddot{\delta}_{\mathrm{FW}} = F_{x_{\mathrm{FW}}} \cdot R_{\mathrm{FW}} - M_{\mathrm{FB}} \\ \\ I_{\mathrm{RW}} \cdot \ddot{\delta}_{\mathrm{RW}} = F_{x_{\mathrm{RW}}} \cdot R_{\mathrm{RW}} + M_{\mathrm{RD}}, \end{cases} \tag{8}$$

©2023 Ramosaj N., Fusco C. & Viennet, E. published by TU Delft OPEN on behalf of the authors.

ISSN: 2667-2812

 http://dx.doi.org/10.59490/65f89c8e269cb909bf53af3c

where $F_{x_{\mathrm{FW}}}$ and $F_{x_{\mathrm{RW}}}$ are the friction forces due to the tire–road interaction, and they are computed using the Pacejka Magic Formula (Pacejka, 2005), with constant coefficients as expressed in Equation (9). The formula uses dimensionless coefficients *B*, *C*, *D*, and *E*, which depend on the road condition, the slip factor κ, and the vertical load F_z acting on the considered wheel.

$$F_x = F_z \cdot D \cdot sin\Big(C \cdot arctan\Big(B \cdot \kappa - E \cdot \big(B \cdot \kappa - arctan(B \cdot \kappa)\big)\Big)\Big), \tag{9}$$

where M_{FB} is the brake torque acting on the front wheel. It is modeled as a Coulomb friction and is computed as in Equation (10):

$$M_{\mathrm{FB}} = 2 \cdot F_{\mathrm{BP}} \cdot R_{\mathrm{disc}} \cdot \mu_{\mathrm{disc}} \cdot tanh\big(k \cdot \dot{\delta}_{\mathrm{FW}}\big), \tag{10}$$

where F_{BP} is the force acting on the brake pad, R_{disc} is the effective brake disc radius, and μ_{disc} is the friction coefficient. A hyperbolic tangent function and a gain k are used to relate the friction torque to the sign of the relative front wheel velocity $\dot{\delta}_{\mathrm{FW}}$. The factor 2 stands for the number of friction interfaces on the brake.

3 Description and Characterization of the Validation Bicycle

In this section, the mobile test apparatus implemented on the e-bike and the specific measurements conducted to experimentally characterize its front suspension and tire are presented.

Figure 3 shows a Flyer Goroc 2, a crossover-type bike that will serve as a reference for the validation of the virtual model. It was instrumented with various sensors (see

©2023 Ramosaj N., Fusco C. & Viennet, E. published by TU Delft OPEN on behalf of the authors.
ISSN: 2667-2812

 http://dx.doi.org/10.59490/65f89c8e269cb909bf53af3c

Table 2) to capture the in-plane dynamics of the bike during a strong braking maneuver with the front brake only.



Figure 3. Validation bicycle and equipment (different sensors used are circled)

The data logger, “AXX” (circled in dark green), recorded data from every channel and stored them on an external USB stick. It was mounted on the luggage rack and supplied by an external battery. The data acquisition system was also connected to a sensor switch, “AYY” (circled in red), which was able to collect data from four analog sensors and one frequency sensor. An inertial measurement unit (IMU) was directly included in the data logger; it measured accelerations and rotation rates in three directions. A force lever sensor, “A01” (circled in light green), was mounted on the front brake lever to measure the force applied by the rider when braking. The travel of the front suspension was logged using a linear potentiometer affixed parallel to the fork, “A02” (circled in purple).

©2023 Ramosaj N., Fusco C. & Viennet, E. published by TU Delft OPEN on behalf of the authors.

ISSN: 2667-2812

http://dx.doi.org/10.59490/65f89c8e269cb909bf53af3c

Table 2. Sensor characteristics

Measurand	Brake lever force	Fork displacement	Wheel speed	Acceleration/ rotation rate
Sensor name	2-D Debus Diebold SA-BS04-000	2-D Debus Diebold SA-LP150	2-D Debus Diebold SD-VI05-000	2-D Debus Diebold BC-3A4_3G500-000
Application	Brake lever	Fork	Front/rear wheels	Luggage rack
Principle	Strain gauge	Potentiometer	Inductive	Capacity effects/ Coriolis vibratory gyroscope
Range	0…500 N	0...150 mm	0...1,500 Hz	±4 g/±500 °/s
Accuracy	±0.5%	±1.5 mm	Depends on phonic wheel resolution	±1% /± 1%
Resolution	< 0.01 N	< 0.01 mm	Depends on data logger frequency	±0.00125 g/±0.02 °/s
Sampling rate	1 kHz	unlimited	< 50 kHz	1 kHz
Signaling	Voltage	Voltage	Voltage	CAN

The front wheel speed was recorded by an inductive sensor located near the front wheel axis, “A3X” (circled in yellow) and a phonic wheel with 60 ticks per revolution. It was used to measure the slip ratio of the front wheel during a braking maneuver. The rear wheel speed was measured in a similar way, “A03” (circled in blue), and only used as a bike speed reference. During the validation tests, only the front brake was used, so the slip ratio of the rear wheel could be neglected. Furthermore, the amount of braking force was kept in a range where no lift of the rear wheel could occur. All signals were logged with a sample frequency of 1 kHz.

While the force on the front brake pad could not be measured on the bike during tests, it was possible to experimentally determine the amplification factor between the force applied on the lever and the effective force on the brake caliper. For this reason, the brake system was removed from the bike, and an additional force sensor was mounted between the brake pads. This force sensor was a CLP/14kN used in conjunction with a CMD600 amplifier (both from HBM). Force steps were applied on the brake lever and the information delivered by both sensors was recorded. The measured points with the most significant population (steady state points) were averaged, while the points with the least significant population (transient points) were not considered. Finally, a function that went through the averaged points and interpolated linearly between them was designed (see Figure 4). With this function, it was possible to transform the force measured at the brake lever during the validation tests into a force at the front brake pad that served as an input to the virtual bike model. Interestingly, the interpolation function still provided good accuracy during transients.

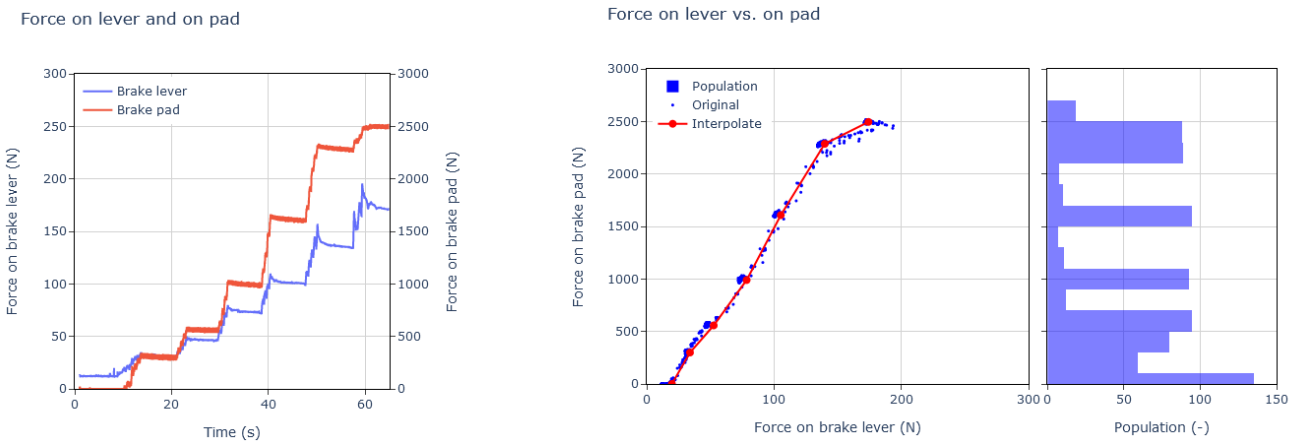


Figure 4. Interpolation function used to transform the force measured on the brake lever into a force at the brake pad: the measurements (left panel) and the correlation between measurements and the interpolation function (right panel)

©2023 Ramosaj N., Fusco C. & Viennet, E. published by TU Delft OPEN on behalf of the authors.

ISSN: 2667-2812

 http://dx.doi.org/10.59490/65f89c8e269cb909bf53af3c

For the experimental characterization of the front suspension, SR Suntour Raidon 34–120 mm, and the front tire, Maxxis Forekaster SilkShield 29 × 2.35, a servo-hydraulic double-rod test cylinder was used. It could test components statically with a force of ±25 kN and dynamically with a force of ±20 kN; the maximum displacement allowed was 150 mm (±75 mm) at a maximum speed of 1.8 m/s and a maximum frequency of 100 Hz. It was used to apply a displacement cycle as an input to the upper part of the fork.

Figure 5 shows the test setups used to identify the behavior of the front suspension and the tire. The rod of the hydraulic cylinder was equipped with a force sensor and a displacement sensor directly connected to the steerer tube. In the first test setup, a sinusoidal displacement was applied to the suspension alone, and the reaction force was measured for different amplitudes and frequencies. These measurements were used to identify suspension stiffness, damping, and Coulomb friction. In the second setup, the suspension was measured together with the front wheel and tire to determine the compression stiffness and damping of the tire at different inflation pressures. In this latter setup, a mount supported the wheel axis vertically (direction normal to the picture plane) to prevent any bending of the assembly under the test load.



Figure 5. Experimental setups on a dynamical test bench to characterize suspension and tire behavior: the setup with fork suspension alone (left panel) and the setup with both fork and front tire (right panel)

Based on the suspension measurements, constant friction, stiffness, and damping parameters—namely k_F, c_F, F_{CF}, k_T, c_T—could be estimated, and a good agreement was found for suspension travels up to a compression of approximately 70 mm and relative velocities up to 125 mm/s (see Figure 6, left panel). For further compression, the constant-parameter model did not reproduce the increasing stiffness of the suspension (see Figure 6, right panel). Although the maximum travel of the tested suspension model was approximately 120 mm, no measurements were available beyond a compression of 90 mm.

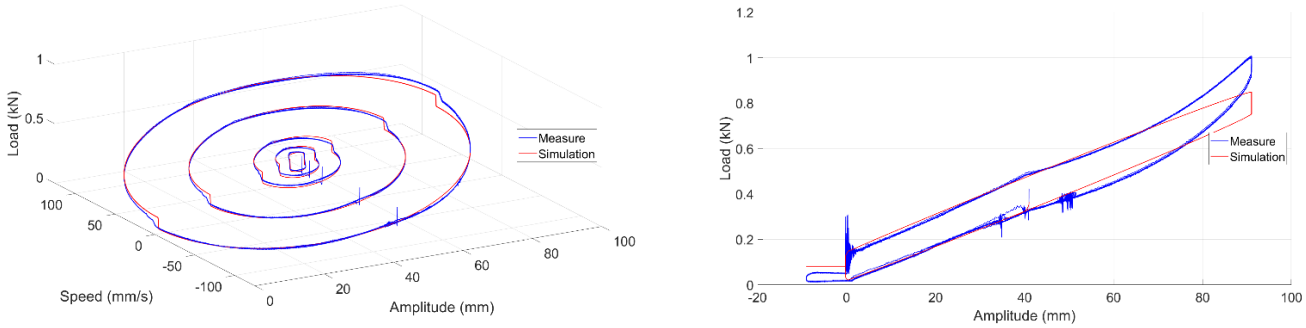


Figure 6. Validation of the suspension model in response to a sinusoidal displacement of different amplitudes displayed here at a frequency of 0.5 Hz with 0 mm corresponding to uncompressed suspension: amplitudes of ±2 mm, ±5 mm, ±10 mm, ±25 mm, ±40 mm (left panel); amplitude of ±50 mm showing increasing stiffness for a suspension travel beyond 70 mm (right panel)

©2023 Ramosaj N., Fusco C. & Viennet, E. published by TU Delft OPEN on behalf of the authors.

ISSN: 2667-2812

 http://dx.doi.org/10.59490/65f89c8e269cb909bf53af3c

4 Validation of the Simulation Model

In this section, the fidelity of the simulation model is assessed by comparing its results with measurements. The test scenario consisted of accelerating the e-bike on a flat road until reaching a speed of approximately 25 km/h, stabilizing the bike by ceasing pedaling for about 1 second, and braking strongly with the front brake until the bike came to a complete stop. Although the rider tried to remain immobile with respect to the bicycle frame during the braking phase, this was essentially impossible in the very late phase of braking. The tests were performed only on a clean, dry, high-grip surface so that any locking of the front wheel was made impossible and braking intensity was kept in a range where no lift of the rear wheel could occur.

The simulation model had only one input variable, namely the normal force applied at the front brake caliper, which was obtained from the measured force at the brake lever as detailed in Section 3. Numerical values of the parameters used for the presented simulation results are available in Ramosaj's (2023) GitLab repository. Mass distribution and inertias for the combined bike and rider were approximated from Moore's (2009) and Maier's (2018) data, while the Pacejka coefficients were identified from the friction measurements conducted on Schwalbe tour tires as presented in Klug's (2017) study.

Figure 7 compares the simulation results and the physical measurements of the bicycle based on the scenario described above. The agreement between the simulation and measurements was good for front wheel speed and longitudinal acceleration, the two most important quantities since they are the two inputs of the ABS. The overall deceleration of the front wheel speed was well reproduced by the model. However, the relatively high wheel slip measured at the start of braking was only partially visible in the simulation results. This may have been due to the use of a steady-state version of the magic formula for tire modeling, which is unable to account for transient effects. The measurement of longitudinal acceleration was rather noisy, mainly due to the irregularities of the road, which was not totally smooth, and the driver, whose movement was not totally negligible. However, the simulated acceleration corresponded well to the average of the measured signal, which validates the model. Interestingly, to compare the simulated longitudinal acceleration with the measured acceleration, it was necessary to take into account the terrestrial gravity component that appeared on the IMU measurement axis when the bike underwent a pitch angle, as this component could be significant even at small pitch angles.

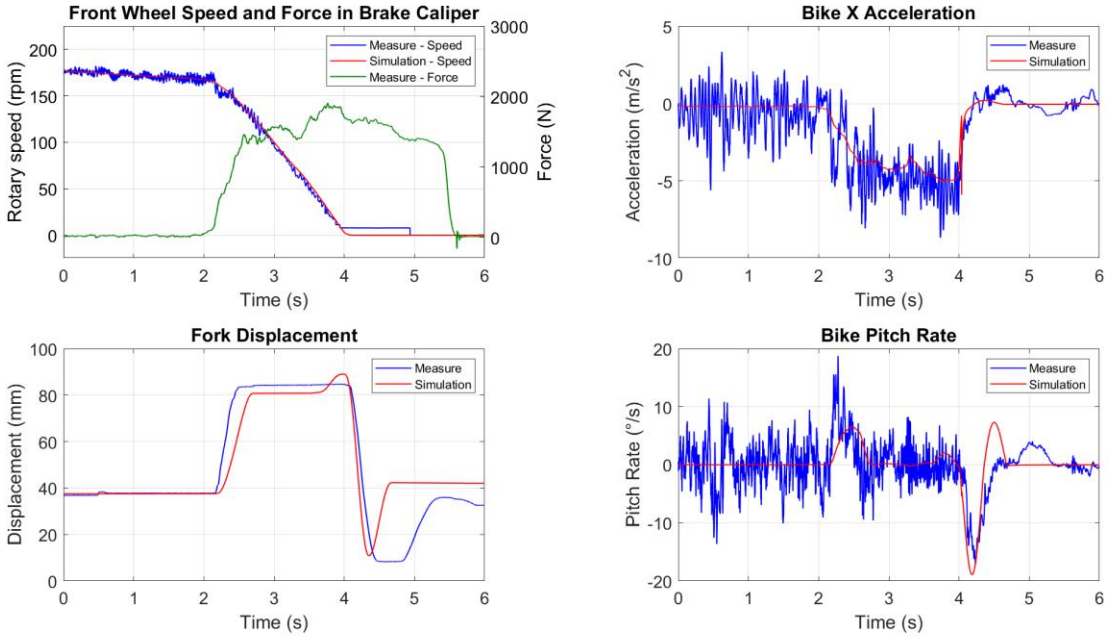


Figure 7. Comparison of the simulation model (red) and the physical bike (blue) when submitted to the same brake force input

A comparison of fork displacement and pitch velocity highlights certain weaknesses in the approach taken to suspension modeling. First, as shown in Figure 6, the actual suspension stiffness was not well captured by our constant-stiffness model, which resulted in a deviation between measured and simulated fork travel, especially for large compression values. Second, while the extension of the suspension model at the end of the braking phase occurred with a slightly too steeply decreasing slope, its compression at the

©2023 Ramosaj N., Fusco C. & Viennet, E. published by TU Delft OPEN on behalf of the authors.
ISSN: 2667-2812

 http://dx.doi.org/10.59490/65f89c8e269cb909bf53af3c

beginning of the braking phase was slower than in the measurements. In other words, the observed peak in pitch velocity during pitch-up was slightly overestimated, while the peak during nose dive was clearly underestimated compared to the measurement. One explanation is that the suspension may have had different damping in compression and extension, particularly at high relative speeds, which was not taken into account in the proposed suspension model.

5 Hardware-in-the-Loop Test Bench

In this section, the developed HiL test bench is presented, and its applicability to an ABS validation process is discussed. Figure 8 presents an overview of the installation, whose core part is the real-time target machine running the virtual bike model connected to the physical braking system of the bike.

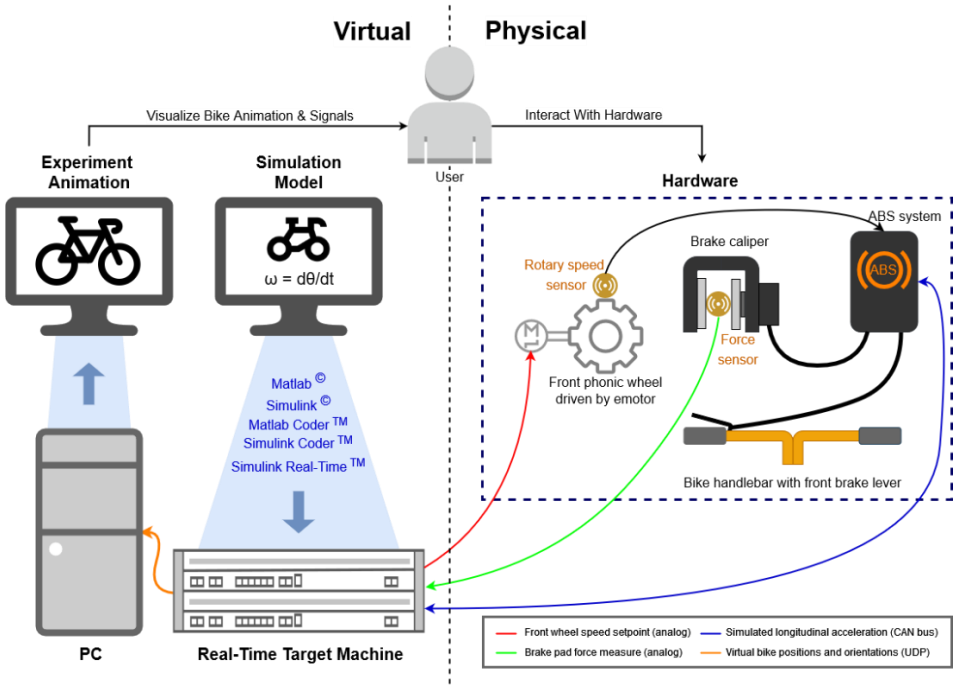


Figure 8. A complete overview of the hardware-in-the-loop test bench

The HiL test bench featured ergonomically positioned bicycle handlebars for use in real-life situations. The front brake lever was hydraulically connected to the ABS hydraulic module, which was, in turn, connected to the brake caliper. A force sensor (CLP/14kN from HBM) was placed between the brake pads and adjusted to the same thickness as a brake disc. The measured force was the input variable for the virtual bike model. A phonic wheel was driven by a fast-reacting DC motor whose speed set point was defined by the real-time simulation model. This emulated the rotation of the bike's front wheel so that the ABS speed sensor could be used to acquire the rotation speed signal as in the real world. The ABS under test also needed the bicycle's longitudinal acceleration as an input signal. In real-life operation, this acceleration is received from an on-board IMU, but in the HiL configuration, this acceleration was calculated by the simulation model and sent to the ABS control unit via a CAN bus.

Figure 9 illustrates the current installation of the HiL test bench. A pneumatic cylinder acts on the brake lever and can apply a force of up to 200 N. This makes it possible to run scenarios with different sets of parameters with good reproducibility. The entire HiL test bench was clocked at a frequency of 1 kHz. Simulink's fixed-step Extrapolation solver (ODE14x) was used to numerically integrate the ordinary differential equations of the virtual bicycle model. The integration time step must be chosen carefully to ensure correct convergence, even in the case of strong discontinuities in the inputs (e.g., sudden braking) or in the intrinsic behavior of the system (e.g., wheel locking). Although it is possible to reduce the time step to 0.2 ms without overloading the target machine's CPU in real time, a time step of 1 ms is sufficient in most cases.

©2023 Ramosaj N., Fusco C. & Viennet, E. published by TU Delft OPEN on behalf of the authors.

ISSN: 2667-2812

http://dx.doi.org/10.59490/65f89c8e269cb909bf53af3c



Figure 9. Developed HIL test bench: overview (left panel); handlebar, brake system, and ABS (right panel)

Figure 10 shows the typical results obtained for the following scenario: a large force is suddenly applied and held constant by the test bench's pneumatic cylinder. This force corresponds to a constant force of 1,000 N on the front brake pads without ABS intervention. The scenario tested considered a flat road with a low grip so that the braking torque applied exceeded the maximum friction force the tire could transmit to the road. When an excessive slip of the wheel was detected, the ABS triggered a pressure release in the hydraulic brake circuit, reducing the actual force measured at the front brake pad. When the slip of the front wheel was reduced, the pressure in the hydraulic brake circuit increased again, at first slowly and then with a steeper slope. The results show that, with the ABS, the wheel does not lock for a significant period of time. However, it reaches a speed close to zero for a short time, suggesting that ABS performance can be improved in these specific test conditions.

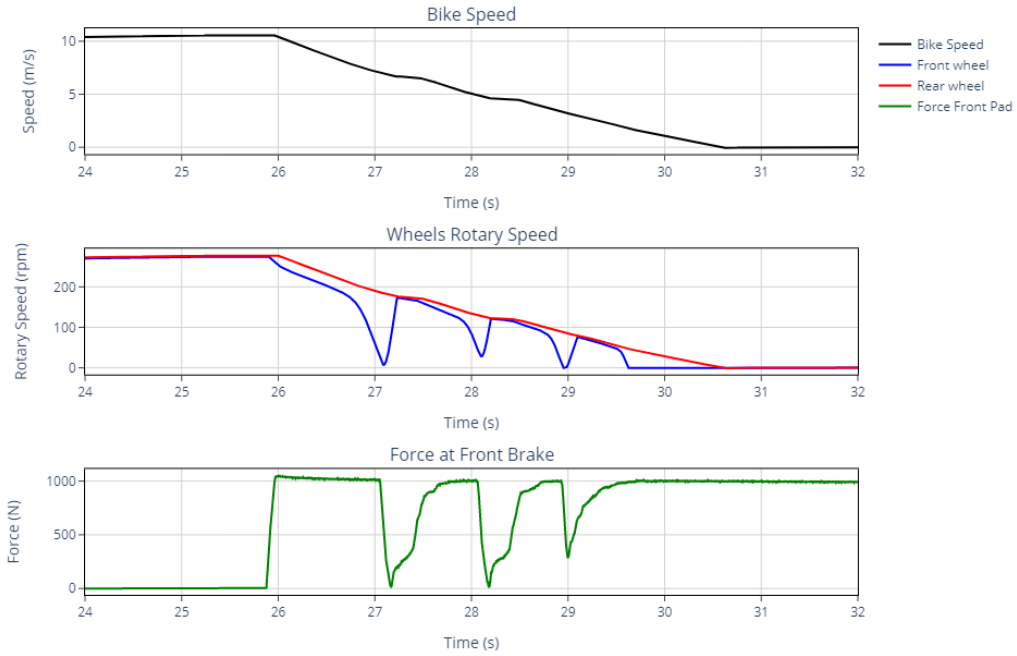


Figure 10. Example results obtained with the HiL test bench (the test scenario shows that ABS triggers a decrease of effective force at the front brake when an excessive slip condition is detected at the front wheel)

The HiL test bench presented here is based on a virtual bike model that has been validated for a specific load case but that is fully parameterizable, making it easy to simulate these different load cases by varying, for example, the position of the CoG, the rider's mass, or tire characteristics. In the current situation, the test bench is operational and can already provide useful information, for example, to an e-bike manufacturer wishing to validate the performance and robustness of an ABS on its bicycle.

©2023 Ramosaj N., Fusco C. & Viennet, E. published by TU Delft OPEN on behalf of the authors.

ISSN: 2667-2812

However, the discrepancies presented in Section 5 between the behavior of the virtual bike and the measurements should prompt one to draw cautious conclusions. In particular, as the wheel speed and longitudinal acceleration obtained from the virtual bike simulation model were relatively smooth, they did not allow us to test the ability of the ABS control logic to process the much noisier signals that would be acquired during real-life operation on the road.

One of the limitations of the test bench is the need to provide the ABS hardware under test with suitably conditioned inputs. In the case where the only input required by the ABS is the measurement of wheel speed, it is relatively simple to emulate the rotation of a phonic wheel and thus place the ABS sensor in operating conditions as close to reality as possible. However, if the ABS control logic requires acceleration information, it is not possible to have a device on the test bench that emulates this acceleration. This involves bypassing the IMU and sending the ABS control unit a signal representing the accelerations based on the simulation model. Ultimately, the disadvantage of this approach is that it makes interfacing between the virtual and physical worlds more complex, and it requires the cooperation of the ABS manufacturer to enable the control unit to receive an external signal.

6 Conclusions and Outlook

This paper presented the development of an HiL test bench that can be used to test the correct operation of an ABS on an e-bike. The HiL setup was based on a virtual bike model with six degrees of freedom, which was validated by on-road measurements on an instrumented bike and additional dynamic testing of the front suspension. Tests carried out as part of this development show that the developed test bench can be interfaced with an existing ABS and that it can easily be used to test different scenarios, such as emergency braking on a flat road with low grip, and different load cases, such as a child seat or panniers. The HiL test bench can be used by ABS manufacturers to improve their development processes using model-based design techniques or by e-bike manufacturers to validate the performance of a supplier's ABS in a quantitative, safe, and reproducible way. The simulation model proposed in this paper is adequate and sufficient, since it reproduces with good correlation the front wheel speed profile and the longitudinal acceleration profile, which are typically the two input quantities of an ABS. However, there is still room for improvement in reducing the discrepancies observed between measurements and simulation during strong braking. In particular, the nonlinear behavior of the suspension needs to be modeled in greater detail, and more complex tire models that can account for transient effects should be investigated.

7 References

Corno, M., D'Avico, L., & Savaresi, S. M. (2018). An anti-lock braking system for bicycles. *In 2018 IEEE Conference on Control Technology and Applications*, 834–839.

Cossalter, V. (2006). *Motorcycle dynamics*. LuLu.

Enisz, K., Szalay, I., Fodor, D., Nagy, K., & Jakab, R. (2012). Bicycle anti-lock braking system prototype development. *Acta Universitatis Sapientiae Electrical Mechanical Engineering, 4*, 45–57.

Gomez, M. (2001). Hardware-in-the-Loop Simulation. *Embedded Systems Design*, *14*(13), 38–49.

Haufe, S., Boeck, H. T., Häckl, S., Boyen, J., Kück, M., van Rhee, C. C., Graf von der Schulenburg, J.-M., Zeidler, J., Schmidt, T., Johannsen, H., Holzwart, D., Koch, A., & Tegtbur, U. (2022). Impact of electrically assisted bicycles on physical activity and traffic accident risk: a prospective observational study. *BMJ Open Sport & Exercise Medicine, 8(4)*, e001275.

Klug, S., Moia, A., Verhagen, A., Görges, D., & Savaresi, S. M. (2017). Effectiveness of actuating on rectilinear bicycle braking dynamics. *IFAC-PapersOnLine*, *50*(1), 972–979.

Maier, O., Pfeiffer, M., & Wrede, J. (2015). Development of a braking dynamics assistance system for electric bicycles: Design, implementation, and evaluation of road tests. *IEEE/ASME Transactions on Mechatronics*, *21*(3), 1671–1679.

Maier, O. (2018). *Modellbasierte Entwicklung eines aktiven Sicherheitssystems für elektrifizierte Fahrräder* [PhD thesis, Otto-von-Guericke-Universität Magdeburg].

Moore, J. K., Hubbard, M., Kooijman, J. D. G., & Schwab, A. L. (2009, January). A method for estimating physical properties of a combined bicycle and rider. In *International Design Engineering Technical Conferences and Computers and Information in Engineering Conference*: *Vol. 49019. Vehicle Systems and Tire Dynamics* (pp. 2011–2020). ASME. https://doi.org/10.1115/DETC2009-86947

Pacejka, H. (2005). *Tire and vehicle dynamics*. Elsevier.

Pfeiffer, M., Wrede, J., Steeb, S. (2020). Validation of a bicycle dynamics assistance system using hardware-in-the-loop simulation. *Proceedings of Bicycle and Motorcycle Dynamics 2019, Symposium on the Dynamics and Control of Single Track Vehicles, Italy*. https://doi.org/10.6084/m9.figshare.12363701.v1

Ramosaj, N. (2023). *BMD2023-ramosaj-fusco-viennet*. GitLab repository. https://gitlab.forge.hefr.ch/nicolas.ramosaj/bmd2023-ramosaj-fusco-viennet

VDI 2206. (2004). Design methodology for mechatronic systems. VDI 2206:2004–06.

©2023 Ramosaj N., Fusco C. & Viennet, E. published by TU Delft OPEN on behalf of the authors.

ISSN: 2667-2812

The Evolving Scholar Vol. 3, 2023

http://dx.doi.org/10.59490/65a5124da90ad4aecf0ab147

Bicycle and Motorcycle Dynamics 2023
Symposium on the Dynamics and Control of Single Track Vehicles
18–20 October 2023, Delft University of Technology, The Netherlands

Type of the Paper: Conference Paper

Revised

Essential Bicycle Dynamics for Microscopic Traffic Simulation: An Example Using the Social Force Model

[version 2; peer reviewed]

Christoph M. Schmidt[1,*], Azita Dabiri[1], Frederik Schulte[1], Riender Happee[1], Jason K. Moore[1]

[1] Delft University of Technology, The Netherlands; c.m.schmidt@tudelft.nl, ORCID 0000-0002-9405-6384, a.dabiri@tudelft.nl, ORCID 0000-0002-1296-7580, f.schulte@tudelft.nl, ORCID 0000-0003-3159-4393, r.happee@tudelft.nl, ORCID 0000-0001-5878-3472, j.k.moore@tudelft.nl, ORCID 0000-0002-8698-6143

[*] corresponding author

Name of Editor: Edwin De Vries
First published: 22/09/2023
Last published: 07/05/2024
Citation: Schmidt, C., Dabiri, A., Schulte, F., Happee, R. & Moore, J. (2024). Essential Bicycle Dynamics for Microscopic Traffic Simulation: An Example Using the Social Force Model [version 2; peer reviewed]. The Evolving Scholar - BMD 2023, 5th Edition.

This work is licensed under a Creative Commons Attribution License (CC-BY).

Abstract:

Microscopic simulation is an established tool in traffic engineering and research in which aggregated traffic performance measures are inferred from the simulation of individual agents. Measures describing the safety and efficiency of road user interactions gain importance for recent developments such as automated vehicles and urban cycling. However, current simulation frameworks model interactions including cyclists without considering the constraints of two-wheeler dynamics (mechanics of a bicycle in motion) that limit feasible maneuvers in a cycling conflict. To address this issue, we propose to bring bicycle dynamics to traffic simulation. We demonstrate that a novel reformulation of the social force framework can create input signals for a controlled inverted pendulum bicycle model and thereby enable more realistic two-dimensional open space simulation of cyclist interactions. The inverted pendulum model introduces the need to stabilize the bicycle as a constraint to the reactive behavior of simulated cyclists. Furthermore, it enables the simulation of countersteering and weaving for stabilization. Our cyclist social forces have anisotropic force fields with respect to relative interaction position and orientation to describe the varying interaction constellations in open space. With these models, we simulate the yaw angle step response and four test cases with up to three cyclists to show that the generated trajectories notably differ from results obtained from a 2D bicycle model without roll angle simulation. Measurements of the maximum lateral path deviation and post-encroachment time show that these differences are relevant for typical applications. Our work demonstrates the potential of introducing physics-based bicycle dynamics to the microscopic simulation of individual road user interactions and the fundamental capability of our reformulated cyclist social forces to do so. Going further, we plan to calibrate and validate our model based on naturalistic cycling data to support the initial results of this work.

Keywords:

Social Force Model, Microscopic Traffic Simulation, Cyclist Behaviour, Bicycle Dynamics, Bicycle Trajectories

©2023 Schmidt, C. M., Dabiri, A., Schulte, F., Happee, R. & Moore, J. K. published by TU Delft OPEN on behalf of the authors.
ISSN: 2667-2812

 http://dx.doi.org/10.59490/65a5124da90ad4aecf0ab147

Introduction

In traffic engineering and research, microscopic traffic simulation is a widespread tool to assess the impact of innovations in traffic control, road infrastructure, connectivity, automation, and other fields. Researchers and practitioners measure performance indicators for traffic efficiency and safety from the movements of individually simulated road users. Historically designed for cars, microscopic simulations use lane-based architectures, where lateral motion is limited to placement on the lane without considering vehicle dynamics. With this architecture, simulation environments struggle to accurately describe cyclists and their diverse motion patterns. Compared to cars, cyclists show less lane discipline and utilize legal and illegal options for the available infrastructure.

Previously, researchers have investigated several approaches to capture cycling behavior into models suitable for microscopic simulation. Kaths et al. (2021) and Kurtc and Treiber (2020) evaluate the adaptation of car-following models to bicycle behavior. While this successfully models some aggregated longitudinal characteristics, it does not capture the two-dimensional motion encountered in intersections and does not sufficiently enable lateral evasive maneuvers in conflicts. Popular approaches to enable two-dimensional motion are cyclist adaptions of the pedestrian social force model (Helbing and Molnár, 1995). In this paradigm, imaginary forces describe a person's motivation to act. Attractive forces draw road users to their intended destination, while repulsive forces prevent collisions with their environment. To capture the constraints of two-wheeler motion, researchers separate the social force acting on a cyclist into lateral and longitudinal components (Kaths, 2023). Other researchers improve the cycling characteristics by adding path-planning modules (Rinke et al., 2017) or anisotropic characteristics to the repulsive force fields of other road users (Yuan et al., 2019; Dias et al., 2018). Lastly, researchers add complex tactical layers to the social force model that explicitly model different behaviors and preferences depending on a cyclist's surroundings (Ni et al., 2023; Liang et al., 2018; Rinke et al., 2017). While all these innovations improve the capabilities of the social force model to simulate bicycling, we have not found work that introduces the physical constraints of riding a two-wheeled bicycle into the framework.

The inclusion of two-wheeler vehicle dynamics must consider two effects. Firstly, cyclists cannot accelerate laterally without longitudinal motion and steering. Direct lateral acceleration, however, is possible with the particle dynamics of the original pedestrian social force models. For cars, Huang et al. (2012) use the social force as input to a simple vehicle dynamics model to prevent unrealistic lateral acceleration. A similar application to bicycles is currently missing. Secondly, cyclists do not only steer to reach a destination but simultaneously need to stabilize the bicycle. This limits the set of feasible reactions without falling and thus impacts how cyclists react to their environment. One relevant effect is oscillating during stabilization. After disturbance or at low speeds, cyclist trajectories show lateral motions resulting from pedaling frequencies and stabilizing the bike. Another effect is countersteering, which requires cyclists to momentarily steer in the opposite direction of an intended turn to initiate an inward roll angle.

The simulation of safety is of increasing interest, specifically for cyclists and new forms of mobility like automated vehicles. For this, models must describe conflict mechanisms (Arun et al., 2021). The aforementioned effects directly impact the formation and development of cycling conflicts. For example, the need to countersteer limits feasible reaction times and amplitudes if a sudden evasive maneuver is required. Or, an overtaking car might collide with a cyclist when a temporal loss of stability requires weaving. Existing simulation frameworks do not consider these effects and thus do not sufficiently capture the causality of road user interactions. We propose to add physics-based road user models to microscopic simulation and hypothesize that this enables the creation of more meaningful conflicts in traffic simulation by improving the simulated causal chain of events. In an ongoing project, we are developing a cyclist social force model with realistic bicycle dynamics to validate this hypothesis. The present paper presents our first results of a reformulated social force coupled with controlled vehicle dynamic models. We use an inverted pendulum bicycle model, which enables us to simulate the countersteering effect, stabilizing oscillation, and minimum stable speeds. Similarly to Dias et al. (2018), we introduce a new version of anisotropic repulsive force fields depending on the relative position and relative orientation between cyclists. Additionally, we propose spline-based trajectory planning to calculate the destination force. Without loss of generality, we limit the scope of this paper to bicycle-bicycle interactions and do not yet consider repulsive forces from infrastructure boundaries. For a complete model, these components may be added in the future. We demonstrate the qualitative functionality of our approach with four different generic scenarios and discuss apparent benefits and shortcomings. Promising results pave the way for further development and full validation of a cyclist social force model that creates realistic safety-sensitive microscopic road user interactions. A software implementation of our model including experiments and all parameter values of this paper is available at https://github.com/chrismo-schmidt/cyclistsocialforce.

The remainder is structured as follows. First, we introduce the dynamic bicycle model, the cyclist social force model, and the control architecture. Then, we apply our model to four exemplary scenarios. Finally, we discuss the benefits and shortcomings of the results.

©2023 Schmidt, C. M., Dabiri, A., Schulte, F., Happee, R. & Moore, J. K. published by TU Delft OPEN on behalf of the authors.
ISSN: 2667-2812

 http://dx.doi.org/10.59490/65a5124da90ad4aecf0ab147

Method

To introduce realistic bicycle physics into the microscopic simulation, we add a bicycle dynamics model to the social force model. Figure 1 shows an overview of the proposed simulation system architecture. Following Kaths (2023), the magnitude and angle of the social force vectors are separated. In our architecture, individual dynamic models for speed and yaw then have the angle or magnitude as input and the updated bicycle state as output. Both models share the same state $\boldsymbol{z} = (x, y, v, \psi, \theta)^{\mathrm{T}}$. The following subsections explain the model building blocks in detail.

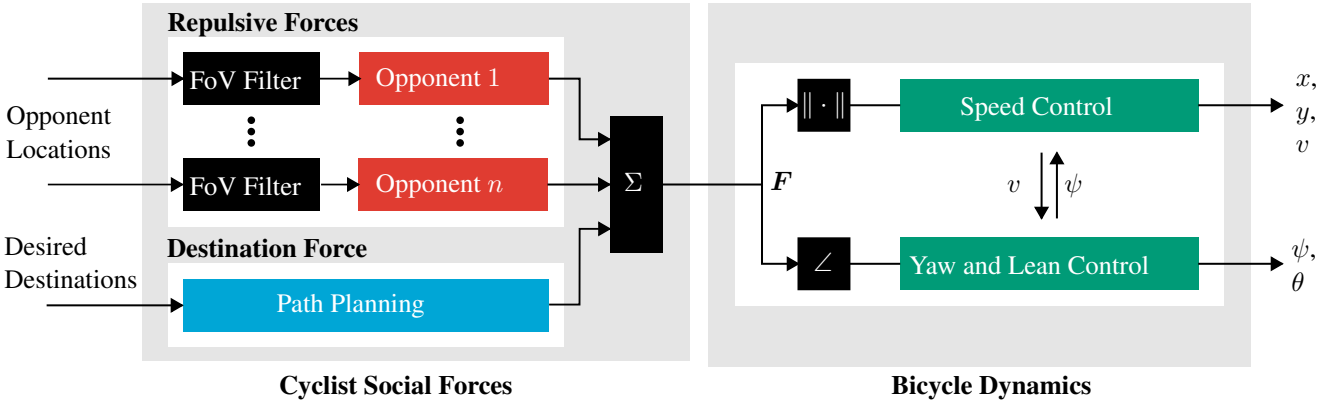


Figure 1. System overview of a cyclist with n opponents, experiencing the aggregated social forces $\boldsymbol{F}$ and controlling their speed v and yaw angle ψ accordingly. This also results in the bike's position x, y and roll angle θ.

Dynamic Bicycle Model

For our approach, we choose the linear inverted pendulum bicycle model (Karnopp, 2013, ch. 7). This simple model captures the desired effects of bicycle dynamics with minimal complexity. As a first approach for micro-simulation, we deem more complex effects like self-stabilization negligible. Figure 2 shows the inverted pendulum model. Each wheel is modeled as a point in the ground plane that is constrained to prevent relative lateral motion. The front wheel rotates about the vertical axis for steering. The bicycle and rider are modeled as an inverted compound pendulum that can roll about the line connecting the rear and front wheel points. The relative motion of the rider's body on the bicycle frame is neglected. At a constant longitudinal speed v, steering leads to lateral acceleration, which can be used to stabilize the pendulum.

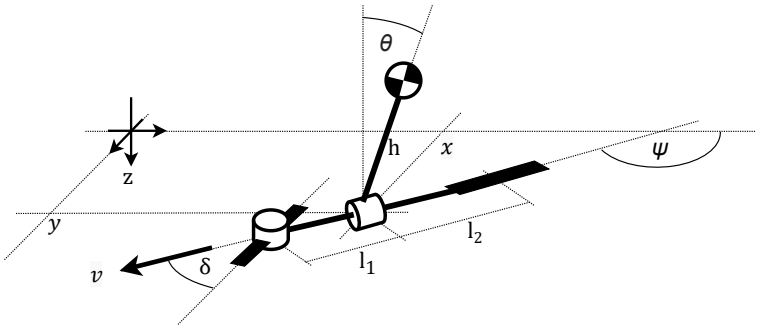


Figure 2. The inverted pendulum bicycle model.

As shown by Karnopp (2013, ch. 7), the transfer function relating the steer angle δ and the roll angle θ is

$$G_\theta(s) = \frac{\Theta(s)}{\Delta(s)} = -K\frac{\tau_2 s + 1}{\tau_1^2 s^2 - 1}, \tag{1}$$

©2023 Schmidt, C. M., Dabiri, A., Schulte, F., Happee, R. & Moore, J. K. published by TU Delft OPEN on behalf of the authors.
ISSN: 2667-2812

with $\tau_1^2 = \dfrac{I_\mathrm{b} + mh^2}{mgh}$, $\tau_2 = \dfrac{l_2}{v}$, $K = \dfrac{v^2}{gl}$, and $l = l_1 + l_2$, where I_b is the moment of inertia of the bike and rider around the roll axis, m is the combined mass of rider and bike, and g is the gravitational constant. We modify Karnopp's model by adding inertia and damping to the steering system, capturing the effects of resistance from tire friction and passive arm joint friction. The following transfer function describes dampened steering with the steering torque $T(s)$ as input.

$$G_\delta(s) = \frac{\Delta(s)}{T(s)} = \frac{1}{I_\mathrm{s} s^2 + cs}. \tag{2}$$

Here, I_s denotes the moment of inertia of the steering system around the steering axis and c the damping coefficient of the rotational motion. $G_\delta(s)$ is derived from the net torque equilibrium of the rotating steer column. The final yaw angle may be calculated from

$$G_\psi(s) = \frac{\Psi(s)}{\Delta(s)} = \frac{1}{\tau_3 s}, \tag{3}$$

derived from the geometric relationship while using a small angle approximation for δ and $\tau_3 = \frac{l}{v}$ (Moore, 2015).

Cyclist Social Forces

The original pedestrian model describes particles that can move in any direction. A superposition of repulsive and attractive psychosocial forces exerted on the individual by their intentions and environment acts as the driving force (Helbing and Molnár, 1995):

$$\boldsymbol{F}_a = \boldsymbol{F}_a^0 + \sum_b \boldsymbol{F}_{a,b} + \sum_B \boldsymbol{F}_{a,B} + \sum_i \boldsymbol{F}_{a,i} \tag{4}$$

Here, $\boldsymbol{F}_a = \frac{\mathrm{dv}}{\mathrm{dt}}$ is the social force experienced by a simulated pedestrian a. $\boldsymbol{F}_a^0$ is a social force that pulls a towards the intended destination. $\boldsymbol{F}_{a,b}$ are repulsive social forces between the individual a and other road users b, which prevents them from approaching each other closely. $\boldsymbol{F}_{a,B}$ are repulsive forces of delimiting infrastructure and $\boldsymbol{F}_{a,i}$ are attractive forces between persons that lead to group formation or draw people towards points of interest. For the scope of this publication, we only consider the destination force and repulsive forces of other road users. It is straightforward to add the other forces in future developments. Negative resulting forces are treated as 0.

The definition of the social force as an acceleration is suitable for particles that can be accelerated in all directions. The movement of a bicycle, however, is laterally constrained by its two-wheeler characteristics and the necessity to steer to achieve lateral acceleration. The social force can't move the bicycle directly. We, therefore, propose a reformulation of the social force that describes the intended velocity vector $\boldsymbol{v}_a$ rather than an acceleration. This may then be used as input for our controlled dynamic bicycle model.

$$\boldsymbol{F}_a := \boldsymbol{v}_a \tag{5}$$

As a result, the social *force* is now a velocity vector field. This weakens the original analogy with Newtonian forces. However, when used as the input of a controlled dynamic system, it retains its interpretability as the motivation to act. It is the desired quantity that the control system follows. To keep the reference to its origin, we retain the name *social force*. Zhao et al. (2023) have previously successfully applied similar velocity force fields as cost functions for the simulation of car interactions with optimal control.

Destination Force

Helbing and Molnár (1995) designed the destination force to point in the direction that corrects an agent's movement from its current velocity vector to the preferred velocity vector. Huang et al. (2012) use the same approach for their social force model for cars. This introduces a feedback loop that controls the agent to move in the direction of the desired destination. More complex dynamic models, however, may require dedicated tunable controllers to be stabilized and follow a desired trajectory. Hence, we propose to reformulate the destination force. To be used as an input for the controlled dynamic model, the destination force should directly point toward where the agent wants to go. This may either be a vector pointing at a desired location or a vector following a desired path. If the destination force directly points towards the desired destination, discontinuities occur when the bicycle has reached a destination and the force vector jumps to the next destination in the desired path or guideline proposed by Kaths (2023). These

©2023 Schmidt, C. M., Dabiri, A., Schulte, F., Happee, R. & Moore, J. K. published by TU Delft OPEN on behalf of the authors.
ISSN: 2667-2812

jumps can lead to instability of our dynamic model. Instead, we calculate the destination force based on a smooth spline connecting multiple intermediate locations. Let $\boldsymbol{p}_1^0$ ... $\boldsymbol{p}_i^0$ be a series of i consecutive destinations ahead of the cyclist and $\boldsymbol{p}_t^a$ the position of a cyclist a at time t. Then, $\boldsymbol{p}_1^{\mathrm{s}}$ ... $\boldsymbol{p}_j^{\mathrm{s}}$ are j points of a B-spline $\boldsymbol{\gamma}(t)$ through $\boldsymbol{p}_{t-\mu}^a, \boldsymbol{p}_t^a, \boldsymbol{p}_1^0$ ... $\boldsymbol{p}_i^0$. The look-back offset μ is a small multiple of the sampling time to include a previous location form the bike's trajectory, smoothing the spline at the bike's current orientation. The destination force then points in the direction

$$\boldsymbol{e}_{F0} = \frac{\boldsymbol{p}_{1+\nu}^{\mathrm{s}} - \boldsymbol{p}_1^{\mathrm{s}}}{\|\boldsymbol{p}_{1+\nu}^{\mathrm{s}} - \boldsymbol{p}_1^{\mathrm{s}}\|}, \tag{6}$$

where ν describes a look-ahead offset to compensate for the delay introduced by the dynamic bicycle model. While going straight, the magnitude of the destination force is given by the velocity v_{d} that the cyclist desires. For turns, we derive $\|\boldsymbol{F}^0\|$ from the curvature of the spline ahead of the cyclist, given as (Pressley, 2010, p. 31)

$$\kappa = \frac{\|\ddot{\boldsymbol{\gamma}} \times \dot{\boldsymbol{\gamma}}\|}{\|\dot{\boldsymbol{\gamma}}\|} = \frac{|\dot{\gamma}_{\mathrm{x}}\ddot{\gamma}_{\mathrm{y}} - \dot{\gamma}_{\mathrm{y}}\ddot{\gamma}_{\mathrm{x}}|}{\sqrt{\dot{\gamma}_{\mathrm{x}}^2 + \dot{\gamma}_{\mathrm{y}}^2}^3}, \tag{7}$$

where $\boldsymbol{\gamma}(t) = (\gamma_{\mathrm{x}}(t), \gamma_{\mathrm{y}}(t), 0)^{\mathrm{T}}$ is the spline in the xy-plane and a dot denotes the derivative $\frac{\mathrm{d}}{\mathrm{dt}}$. Interpreting the curvature as the inverse of the turn radius $R = \frac{1}{\kappa}$, we may then use the following relationship given by Karnopp (2013, p.152) to determine the radius of a turn at a constant speed and roll angle:

$$R = \frac{v^2}{g\theta_{\mathrm{ss}}}. \tag{8}$$

This is derived from the steady state roll angle θ_{ss} at a constant steer angle and the geometric relationship between steer angle and turn radius. Assuming that riders unconsciously choose a maximum comfortable roll angle $\theta_{\mathrm{c}} = \theta_{\mathrm{ss}}$ for their maneuvers, this gives the ideal speed for a turn of radius R. It serves as a turn-dependent upper limit to the destination force otherwise equaling the preferred cycling speed v_{d}. Additionally, we introduce a lower speed limit v_{s} that prevents the destination force from suggesting unstable speeds for small turn radii. The final expression of the destination force magnitude is:

$$\|\boldsymbol{F}^0\| = v(\kappa) = \begin{cases} v_{\mathrm{s}} & \text{if } \sqrt{g\frac{\theta_{\mathrm{c}}}{\kappa}} < v_{\mathrm{s}} \\ v_{\mathrm{d}} & \text{if } \sqrt{g\frac{\theta_{\mathrm{c}}}{\kappa}} > v_{\mathrm{d}} \\ \sqrt{g\frac{\theta_{\mathrm{c}}}{\kappa}} & \text{otherwise} \end{cases}. \tag{9}$$

Repulsive Forces

In the social force model, repulsive forces prevent road users from approaching each other closely. Generally, the magnitude of these forces describes how strong an opponent reacts, while the direction of the repulsive force describes the direction of any evasive maneuver. For a pair of cyclists, these realistic reactions depend on their relative position and relative orientation. For example, two cyclists going parallel to each other might be comfortable with a small lateral clearance that only requires minor evasive action, whereas encroaching maneuvers might require strong breaking and steering to prevent collisions. We directly tailor repulsive force fields $\boldsymbol{F}_{\mathrm{rep},a,b} = F_{\mathrm{rep},a,b} \cdot \boldsymbol{e}_{\mathrm{rep},a,b}$ to represent this anisotropy of cyclist interactions. For convenience, the relative position of two cyclists a and b is expressed in polar coordinates $(r_{a,b}, \varphi_{a,b})$ centered at a's position. $\psi_{a,b}$ is their relative heading. Similar to Helbing and Molnár, we base the contour lines of our force field on ellipses described by

$$r_{a,b}(\varphi_{a,b}) = \frac{\beta}{\sqrt{1 - (e(\psi_{a,b})\cos\varphi_{a,b})}}, \tag{10}$$

where β is the semi-minor axis of the ellipse and $e(\psi_{a,b})$ is an anisotropic eccentricity. Additionally, we introduce an anisotropic radial decay $\sigma(\varphi_{a,b}, \psi_{a,b})$. The magnitude of repulsive force then becomes

$$F_{\mathrm{rep},a,b}(r_{a,b}, \varphi_{a,b}) = F_0 \exp\left(-\frac{\beta}{\sigma(\varphi_{a,b}, \psi_{a,b})}\right) = F_0 \exp\left(-\frac{r_{a,b}\sqrt{1 - (e(\psi_{a,b})\cos\varphi_{a,b})}}{\sigma(\varphi_{a,b}, \psi_{a,b})}\right). \tag{11}$$

©2023 Schmidt, C. M., Dabiri, A., Schulte, F., Happee, R. & Moore, J. K. published by TU Delft OPEN on behalf of the authors.
ISSN: 2667-2812

 http://dx.doi.org/10.59490/65a5124da90ad4aecf0ab147

The direction of the repulsive force is perpendicular to the contour lines and hence equals the direction of the negative gradient:

$$\boldsymbol{e}_{\mathrm{rep},a,b} = -\frac{\nabla F_{\mathrm{rep},a,b}(r_{a,b}, \varphi_{a,b})}{\|\nabla F_{\mathrm{rep},a,b}(r_{a,b}, \varphi_{a,b})\|} \tag{12}$$

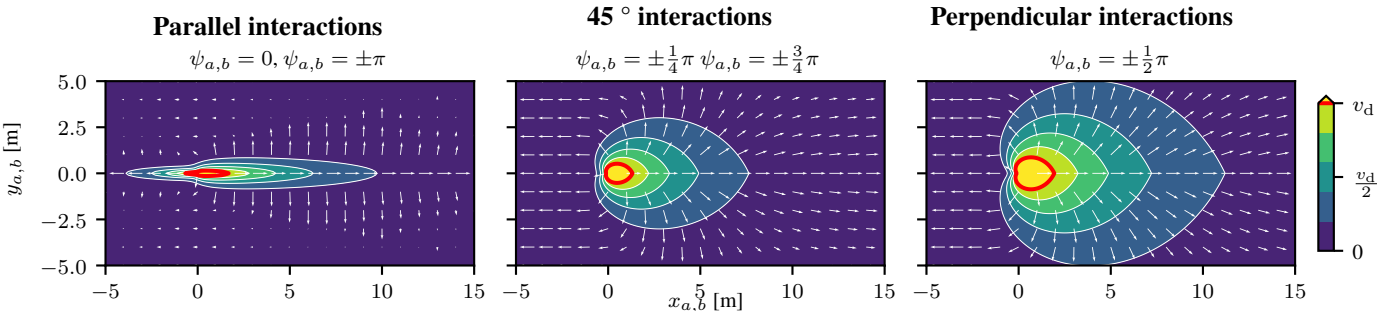


Figure 3. Repulsive force acting on a cyclist b interacting with a cyclist a (located at $(0, 0)$, riding in x-direction) for different relative orientations $\psi_{a,b}$ and positions $(x_{a,b}, y_{a,b})$. Colors indicate the magnitude of the force field as multiples of the desired velocity v_d of b. At the red line, the repulsive force equals the maximum of b's destination force. The force direction (black arrows) experienced by b is perpendicular to the contour lines. Parameter values: $F_0 = 7\ \frac{\mathrm{m}}{\mathrm{s}}$, $e_0 = 0.995$, $e_1 = 0.7$, $\sigma_0 = 0.5$ m, $\sigma_1 = 5.0$ m, $\sigma_2 = -0.3$ m, $\sigma_3 = -4.9$ m.

We introduce the two anisotropic properties to enable passing with small lateral clearances for parallel interactions and early braking for perpendicular interactions. In the first case, the contour lines of the force field should be elongated in the cyclist's direction of travel and narrowed perpendicular to this direction. In the second case, the contour lines must approach a circular shape and have a low radial decay to ensure early reaction. In both cases, the area in front of the cyclists must have strong repulsive forces with a small radial decay to prevent collisions. The area behind the cyclists may have large radial decay to allow others to follow closely. To achieve these properties, we modulate the eccentricity and decay as follows:

$$e(\psi_{a,b}) = e_0 - e_1 \sin^2 \psi_{a,b} \tag{13}$$

$$\sigma(\varphi_{a,b}, \psi_{a,b}) = \sigma_0 + \sigma_1 \sin^2 \psi_{a,b} + (\sigma_2 + \sigma_3 \sin^2 \psi_{a,b}) \left|\sin \frac{\varphi_{a,b}}{2}\right| \tag{14}$$

This introduces the tune-able parameters $0 < e_1 < e_0 < 1$, $\sigma_0, \sigma_1 > 0$, $\sigma_2 > -\sigma_0$, and $\sigma_3 > -\sigma_1$. Figure 3 shows the resulting almond-shaped force fields for different relative orientations between two cyclists a and b. We chose these modulation functions heuristically to create force fields with the properties described above. Hence, they are not unique and do not guarantee optimal performance.

Control Architecture

To make a simulated cyclist a execute the movement indicated by the overall social force $\boldsymbol{F}_a$, we introduce two separate control loops for speed and yaw (see Figure 1). The first system controls the speed v based on social force magnitude $v_\mathrm{d} = \|\boldsymbol{F}_a\|$ experienced by a. The second system controls the yaw angle ψ based on the desired yaw derived from the social force angle $\psi_\mathrm{d} = \angle \boldsymbol{F}_a$.

Roll and Yaw Angle Control

When riding a bicycle, humans try to reach their destination while also having to keep the bicycle stable. We describe this effort with a nested control loop for the roll angle $\theta(t)$ and yaw angle $\psi(t)$ (Figure 4). Firstly, a PI-controller derives the desired roll angle from the yaw error. The desired roll angle is the input for the inner loop, which consists of a D-controller that derives the torque $\tau(t)$ at the handlebar, the steer column dynamics $G_\delta(s)$, and the roll dynamics $G_\theta(s)$. Note that ideal D-characteristics are not realizable for physical systems. However, in our simulation scenario, the transfer function of the inner loop still retains a higher

©2023 Schmidt, C. M., Dabiri, A., Schulte, F., Happee, R. & Moore, J. K. published by TU Delft OPEN on behalf of the authors.
ISSN: 2667-2812

 http://dx.doi.org/10.59490/65a5124da90ad4aecf0ab147

degree denominator than numerator and hence is realizable as a whole. One may also interpret the inner loop as the combined human roll control dynamics and implement this for simulation. The inner loop transfer function with respect to the roll angle θ is

$$G_{\text{inner},\theta}(s) = \frac{\Theta(s)}{\Theta_\text{d}(s)} = \frac{G_{\text{R2}}(s)G_\delta(s)G_\theta(s)}{1 + G_{\text{R2}}(s)G_\delta(s)G_\theta(s)} = \frac{-KK_\text{D}\tau_2 s - KK_\text{D}}{I\tau_1^2 s^3 + c\tau_1 s^2 - (I + KK_\text{D}\tau_2)s - (c + KK_\text{D})}. \tag{15}$$

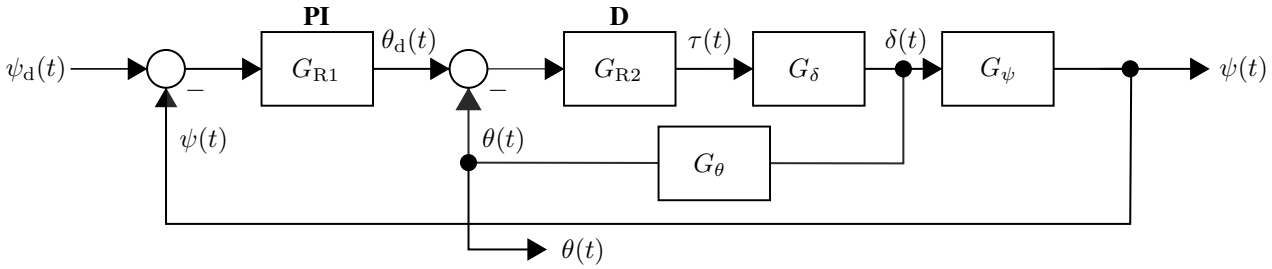


Figure 4. Nested control of steer $\delta(t)$ and yaw $\psi(t)$.

Using the Routh–Hurwitz stability criterion, four stability conditions for the inner loop can be derived:

$$(\text{A}_2)\quad K_\text{D} < -\frac{I_\text{s}}{K\tau_2} = -\frac{I_\text{s} gl}{l_2 v} \qquad (\text{A}_3)\quad K_\text{D} < -\frac{c}{K} = -\frac{cgl}{v^2} \qquad (\text{B}_{1\text{-}1})\quad K_\text{D} < 0 \qquad (\text{B}_{1\text{-}2})\quad v < \frac{cl_2}{I_\text{s}} \tag{16}$$

For a realistic moment of inertia $I_\text{s} < 1$ of the steering column, realistic steering dampening $c \gg 1$, bike dimensions $l_1 \approx 1$, and realistic speed $v < 15\frac{\text{m}}{\text{s}}$, (A_2) is dominated by (A_3) and $(\text{B}_{1\text{-}2})$ is always satisfied. The inverse dependency on the bicycle speed means that no bounded gain K_D will be able to stabilize the bicycle at all speeds. For very small speeds, the average cyclist has to step off the bike to prevent falling. This minimum speed for stability can be tuned by choosing a suitable K_D. We create an adaptive $K_\text{D}(v)$ that enables stability at low speeds while preventing unreasonably large controller outputs at higher speeds. With

$$K_\text{D}(v) = \frac{k_{\text{d}0}}{v + k_{\text{d}1}}, \tag{17}$$

instability of the inner loop occurs for $v < \frac{-cgl - \sqrt{(cgl)^2 - 4cglk_{\text{d}0}k_{\text{d}1}}}{2k_{\text{d}0}} \approx 0.98\frac{\text{m}}{\text{s}}$. Figure 5 shows (16) - (17) for the values of a common bike (Moore, 2015).

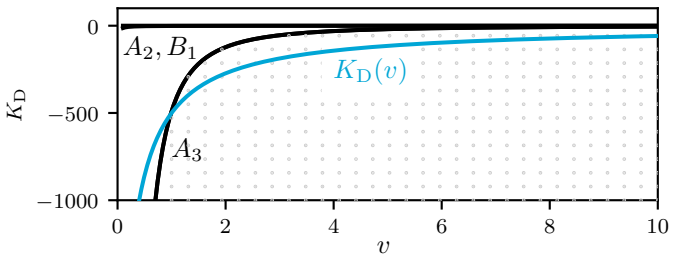


Figure 5. Stability limits (black lines) and stability region (gray dots) of the inner loop for $K_\text{D}(v)$ with $k_{\text{d}0} = -600$, $k_{\text{d}1} = 0.2$, $I_\text{s} = 0.07\ \text{kgm}^2$, $c = 50\ \text{Nms}$.

The outer loop takes the steer angle from the inner loop and passes it to the steer-yaw transfer function $G_\psi(s)$:

$$G_{\text{outer}}(s) = \frac{\Psi(s)}{\Psi_\text{d}(s)} = \frac{G_{\text{R1}}(s)G_{\text{inner},\delta}(s)G_\psi(s)}{1 + G_{\text{R1}}(s)G_{\text{inner},\delta}(s)G_\psi(s)} = \frac{b_2 s^3 + b_3 s^2 + b_4 s + b_5}{a_0 s^5 + a_1 s^4 + a_2 s^3 + a_3 s^2 + a_4 s + a_5}. \tag{18}$$

with $G_{\text{inner},\delta}(s) = \frac{\Delta(s)}{\Theta_\text{d}(s)} = \frac{G_{\text{inner},\theta}}{G_\theta(s)}$ and the parameters:

$$\begin{aligned} a_0 &= I\tau_1^2\tau_3 & a_2 &= (K_\text{P}K_\text{D}\tau_1^2 - (I + KK_\text{D}\tau_2)\tau_3) & a_4 &= -K_\text{P}K_\text{D} \\ a_1 &= c\tau_1^2\tau_3 & a_3 &= (K_\text{I}K_\text{D}\tau_1^2 - (c + KK_\text{D})\tau_3) & a_5 &= -K_\text{I}K_\text{D} \end{aligned} \tag{19}$$

©2023 Schmidt, C. M., Dabiri, A., Schulte, F., Happee, R. & Moore, J. K. published by TU Delft OPEN on behalf of the authors.
ISSN: 2667-2812

 http://dx.doi.org/10.59490/65a5124da90ad4aecf0ab147

$$b_2 = K_\mathrm{P} K_\mathrm{D} \tau_1^2 \qquad b_3 = K_\mathrm{I} K_\mathrm{D} \tau_1^2 \qquad b_4 = -K_\mathrm{P} K_\mathrm{D} \qquad b_5 = -K_\mathrm{I} K_\mathrm{D} \qquad (20)$$

Again, we evaluate the Routh–Hurwitz stability criterion to find limits for the gain parameters. The symbolic expressions of the stability conditions based on Routh coefficients of the fifth-order system are very long. For brevity, we only present their numerical solutions (Fig. 6) using the inner loop gain and bicycle parameters from above (Fig. 5).

Figure 6 illustrates that speed-adaptive outer loop gains have little effect on the stability range. We choose K_P and K_I to be constant to limit the number of model parameters. The minimum stable speed results from the intersection of the stability limit D_1 and the gain curves. Numerically, we determine $v_\mathrm{min} \approx 2.26 \frac{\mathrm{m}}{\mathrm{s}}$. This is notably higher then the minimum stable speed of the inner loop (Fig. 5). Within the scope of this paper, we intend to do experiments at normal riding speeds ($3 - 6 \frac{\mathrm{m}}{\mathrm{s}}$). Hence, the stability range is sufficient.

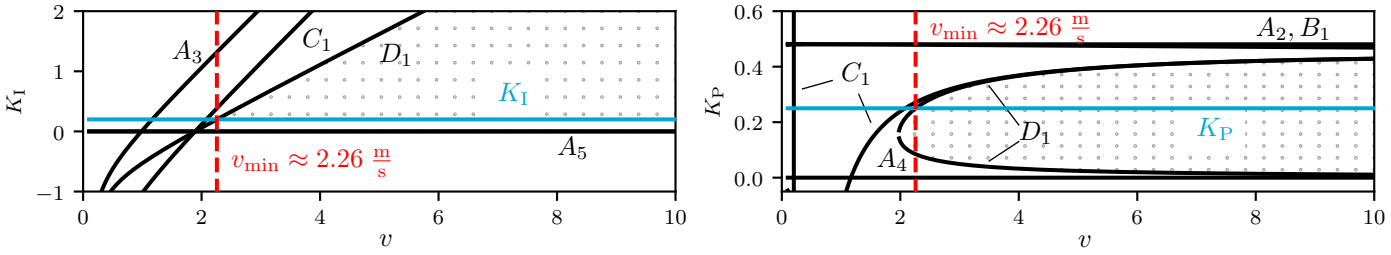


Figure 6. Stability limits (solid black) and stable area (gray dots) of the outer loop for the gains $K_\mathrm{P} = 0.25$ and $K_\mathrm{I} = 0.2$. Capital letters naming the constraints refer to the corresponding coefficients of the Routh table.

Speed

For simplification, the inverted pendulum bicycle model assumes constant speed. However, simulated cyclists need to adapt their speed $v(t)$ according to the magnitude of experienced social force $v_\mathrm{d}(t) = \|\boldsymbol{F}_a\|$. Hence, we introduce a second independent control loop for the speed. This loop (Figure 7) consists of a P-controller to derive an acceleration from the current speed error and an integrator to model the bicycle speed. For simplicity, this controller implicitly incorporates driving forces, friction, and drag. We set conservative limits ($-3 \frac{\mathrm{m}}{\mathrm{s}^2} \leq a(t) \leq 1 \frac{\mathrm{m}}{\mathrm{s}^2}$) to prevent unrealistically high acceleration. The resulting longitudinal speed variations violate the above-mentioned assumption of constant speed. However, for sufficiently small simulation time steps and accelerations, the speed variations per step are small as well and may be neglected. Furthermore, Limebeer and Sharma (2008) have previously determined that lateral bicycle dynamics are only little affected by small longitudinal accelerations. This further justifies treating our model as time-invariant. Empirically, we have not observed instability of the roll and yaw angle control due to speed variation.

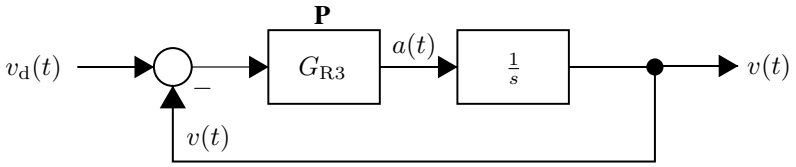


Figure 7. Speed control.

Simulation Results

To demonstrate our model with reformulated social forces and bicycle dynamics, we implement it in Python 3.11 (Python Software Foundation, Beaverton, USA) using the Python Control Systems Library (Fuller et al., 2021) and perform a series of tests. First, we present the desired yaw step response of a single cyclist. Then, we show simulations of multiple cyclist interactions. We compare the results for the inverted pendulum bicycle model and a traditional 2D bicycle model that consists only of a two-dimensional two-wheeler model in the ground plane without consideration of the roll angle (Corke, 2017, p. 101). In a simple control loop, a

©2023 Schmidt, C. M., Dabiri, A., Schulte, F., Happee, R. & Moore, J. K. published by TU Delft OPEN on behalf of the authors.
ISSN: 2667-2812

 http://dx.doi.org/10.59490/65a5124da90ad4aecf0ab147

P-controller aligns the steering angle with the desired yaw angle. Other than that, the 2D bicycle model shares the embedding of the inverted pendulum model into the cyclist social force model, including spline-based destination forces and repulsive force fields.

For this demonstration, we use the physical parameters of a standard bicycle, $l_1 = l_2 = 0.5$ m, $h = 1$ m, $m = 87$ kg, $I_\mathrm{b} = 3.28\ \frac{\mathrm{kg}}{\mathrm{m}^2}$, presented by Moore (2015). We tune the steer column dynamics heuristically to produce the expected outcome. The resulting values are $I_s = 0.07\ \mathrm{kgm}^2$ and $c = 50.0\ \mathrm{Nms}$. For full calibration, these values need to be experimentally confirmed. Similarly, we heuristically calibrate the cyclist social force and control parameters so that the simulation shows the expected effects. Figures 3, 5, and 6 list their values. We choose the comfortable roll as $\theta_\mathrm{c} = 10\ ^\circ$ and simulated cyclists ride at desired velocities of $3 - 6\ \frac{\mathrm{m}}{\mathrm{s}}$. A calibration based on naturalistic driving data was not possible due to the unavailability of suitable data at the current time.

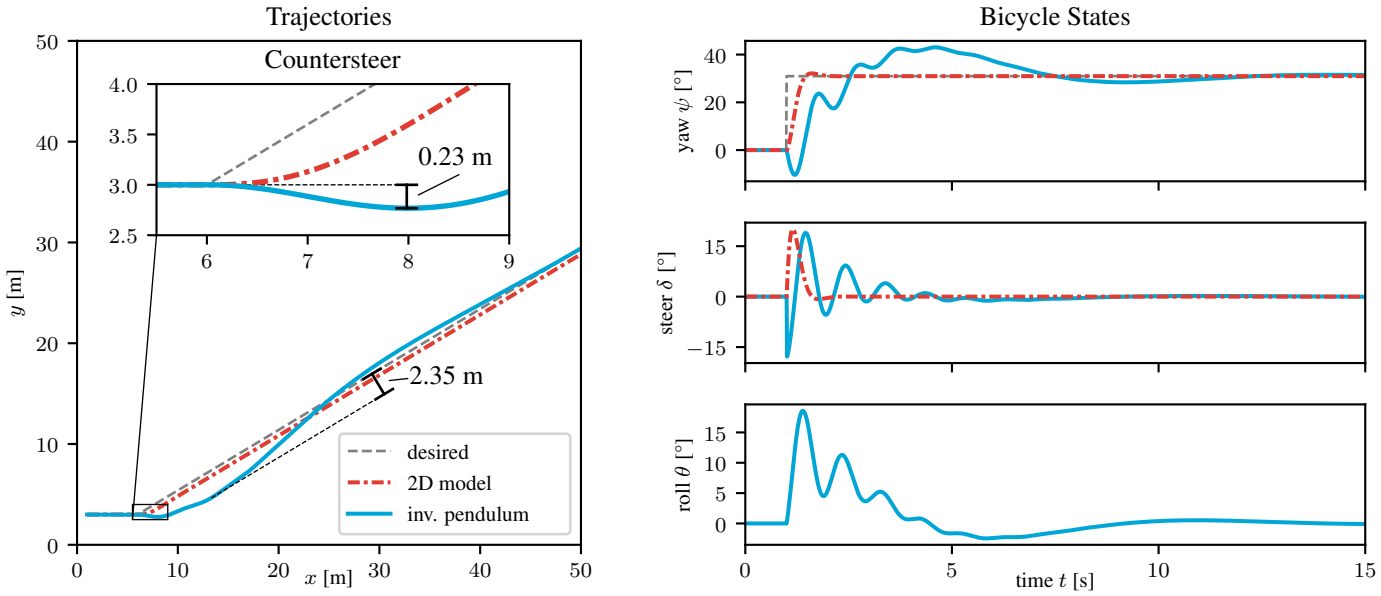


Figure 8. Yaw angle step response at constant speed. Comparison between the inverted pendulum bicycle dynamics (solid blue) and 2D bicycle dynamics (dash-dotted red). The left column shows the simulated trajectories with the reaction to a sudden change of the desired yaw angle. The right column shows the simulated bicycle states over time.

In the first experiment, we apply a step in the desired yaw angle to a cyclist traveling at constant speed. To get an undisturbed view of the yaw and roll dynamics, we disable path planning and adaptive speed for this scenario. Figure 8 shows the trajectories of an inverted pendulum and a 2D bicycle (left column) together with the corresponding yaw, steer, and roll angles over time (right column). The step of the desired yaw angle to the left leads to a steep rise of steer angle in the opposite direction to initiate the turn. Steering to the right makes the inverted pendulum cyclist (solid blue) fall left into the intended turn. With the roll angle in the right direction, the controller then quickly steers to the left to perform a left turn. This showcases the countersteering effect that is necessary to control a bicycle. An enlarged part of the trajectory plot focuses on the moment when the yaw angle step is applied to visualize the countersteering effect. The inverted pendulum cyclist notably swerves to the right, whereas the 2D cyclist directly steers left. This leads to a lateral displacement of approximately 23 cm (see inset of Figure 8). The maneuver also results in a delay between the desired and actual change of direction, which the inverted pendulum bike only slowly recovers from. At its maximum, it laterally diverts 2.35 m from the ideal step response trajectory. The oscillations of the yaw angle also show how the inverted pendulum cyclist has to use lateral motion to stabilize the bike while trying to execute the desired maneuver. On the other hand, the 2D bicycle (dash-dotted red) follows the sudden change in direction faster, without a swerve in the other direction and with a smaller lateral offset.

In a second experiment, we create four scenarios for our simulated cyclists. This time, the whole model pipeline is active, including path planning for destination force calculation and adaptive speeds. The model parameters in all four scenarios are identical to the first experiment. The left column of Figure 9 shows a snapshot of the simulation with one or more inverted pendulum cyclists. It visualizes the cyclists' trajectories up to that moment, the planned path, the social forces acting on the cyclist at that moment, and any intermediate destinations of the cyclist. The right column presents the final trajectories of the inverted pendulum bike (solid blue) and the 2D bike (dash-dotted red). In the 'parcours' scenario, a single cyclist has to travel to a series of destinations with lateral offset

©2023 Schmidt, C. M., Dabiri, A., Schulte, F., Happee, R. & Moore, J. K. published by TU Delft OPEN on behalf of the authors.
ISSN: 2667-2812

http://dx.doi.org/10.59490/65a5124da90ad4aecf0ab147

to demonstrate the model's agility. Both cyclist models execute the curves given by the intermediate destinations. Similar to the step response experiment, the inverted pendulum cyclist is lagging behind due to the delay introduced by the need to countersteer. Note that, in our simulation, the cyclists don't have to reach an intermediate destination fully. After a cyclist has approached a destination closer than the distance $d_{\min} = 2$ m, they switch to the next.

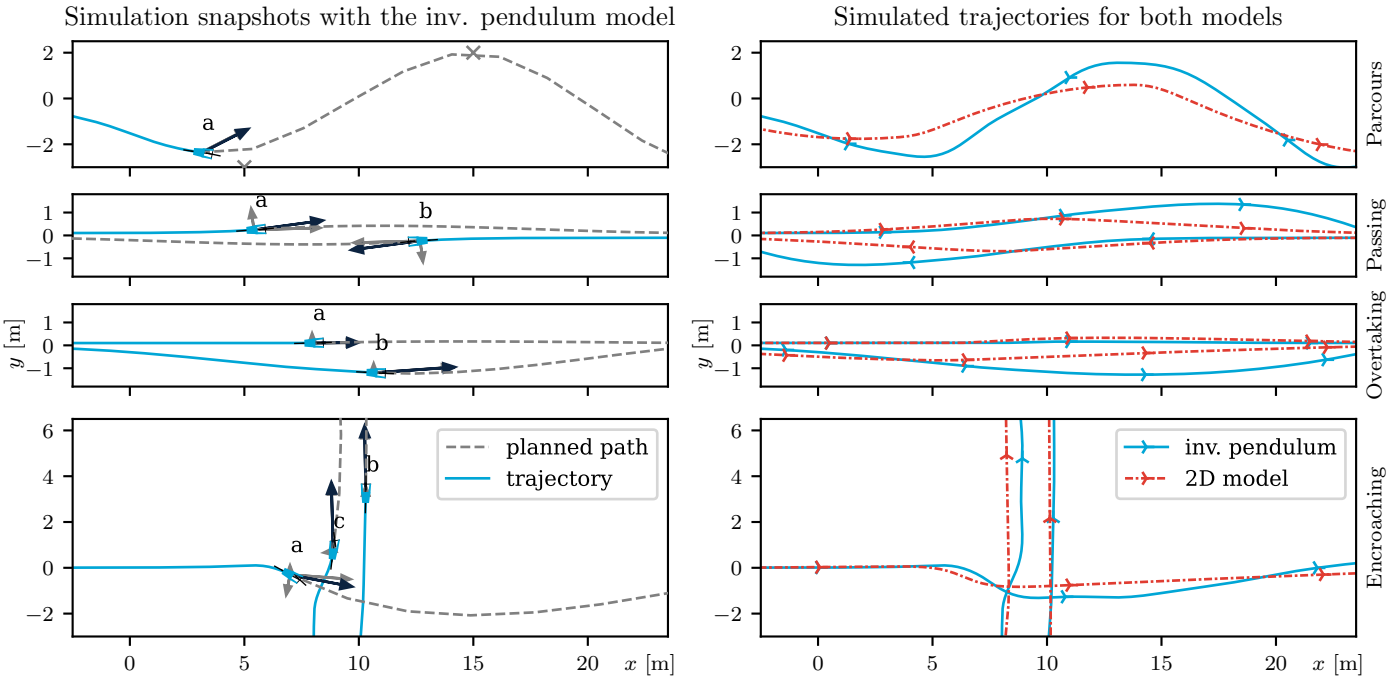


Figure 9. Simulations of interaction test scenarios (top to bottom: 'parcours', 'passing', 'overtaking', 'encroaching'). The left shows simulation snapshots of inverted pendulum bikes during interaction. Arrows indicate the individual social forces experienced by the cyclist (gray) and the resulting force (dark blue). The right compares the simulated trajectories of inverted pendulum bikes (solid blue) and 2D bikes (dash-dotted red).

The other three scenarios show simple interactions of multiple cyclists to demonstrate the general capability of our model to handle common interactions. In the 'passing' and 'overtaking' scenarios, two interactions are shown. Two cyclists evade each other smoothly and the trajectories of the 2D and inverted pendulum models show only small differences at the beginning of each maneuver. Again, countersteering causes a delay in the reaction of the inverted pendulum cyclists, but the effect is small because the desired course correction is only very minor. In the second half of the maneuvers, the two model variants differ more. In the absence of any repulsive forces after the cyclists have passed each other, the path-planning-based destination force is the only influencing factor. Re-planning the path to the destination in every time step amplifies the small lag of the inverted pendulum bicycle compared to the 2D bicycle. The return to a straight path becomes unrealistically wide and delayed. The fourth scenario ('encroachment') shows an interaction of three cyclists. In an evasive maneuver, the two cyclists traveling upwards slightly swerve to the right, while the single cyclist traveling right decelerates and performs a stronger evasive maneuver. Again, the inverted pendulum bikes show a small lag in their trajectory and small decaying oscillations after the initial evasive movement. Additionally, Figure 10 shows the lateral deviation of cyclist a from the undisturbed straight horizontal trajectory that both models were tasked with. The evasive maneuver of the inverted pendulum cyclist results in more than a 1 m bend to the right, whereas the 2D cyclist requires about 40 cm less lateral space. This puts into numbers how the additional need to stabilize the bike affects the space requirements.

Lastly, we report the Post-Encroachment Time (PET), which measures the time between the first bicycle leaving and the second bicycle entering the conflict area and is a surrogate safety indicator designed to assess the safety of road user interactions (Allen et al., 1978). For simplicity, we calculate the PET with respect to the intersection of the trajectories of the road user center points and do not consider their footprint. Table 1 shows a difference of more than 11% between the two models for the interaction of a and b. This shows that the inverted pendulum model notably affects typical performance measures used in traffic simulation and assessment.

©2023 Schmidt, C. M., Dabiri, A., Schulte, F., Happee, R. & Moore, J. K. published by TU Delft OPEN on behalf of the authors.
ISSN: 2667-2812

 http://dx.doi.org/10.59490/65a5124da90ad4aecf0ab147

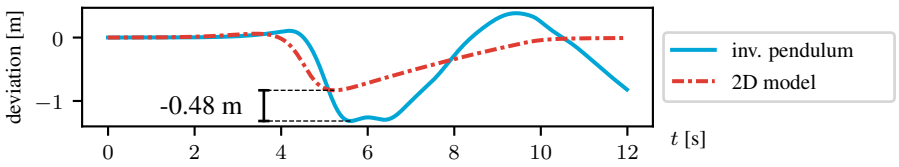


Figure 10. Deviation of cyclist a in the 'encroaching' scenario from it's undisturbed path.

Table 1. Post Encroachment Times (PET) in the 'encroaching' scenario of Figure 9 for both model types.

bike models	PET between a and b	PET between a and c
inv. pendulum	1.86 s	1.00 s
2D model	1.64 s	0.93 s

Discussion

The test scenarios show the general capability of the social force reformulation and the inverted pendulum model to describe cyclist interactions. Compared to established microscopic frameworks, this enables lane-free simulation of road user interactions. Additionally, the simulated trajectories of our model exhibit countersteering and lateral oscillation for stabilization. Compared to the 2D model without roll angle, these affect the relative positions, orientations, and speeds of the cyclists. The PET measurements demonstrate that this can result in notable differences of typical performance indicators and hence might lead to a different assessment of an interaction. Furthermore, we observe that the need to stabilize the bicycle leads to an increase in space requirements. For example, a lateral countersteering displacement of 23 cm corresponds to 10 % of the width of a unidirectional Dutch bicycle path (Veroude et al., 2022). Similarly, the lateral deviation difference between the inverted pendulum model and the 2D model is 48 cm or 20.1 % of the width of a Dutch bicycle lane (Veroude et al., 2022). These results show that the stabilization task impacts cyclists' reactions to disturbances in a way relevant to simulation applications like infrastructure design and safety assessment. Qualitatively, the underlying physics support the behavior of our model. Quantitatively, heuristic parameter value choice without calibration based on real-world data limits the interpretability of the observed effect magnitude. While we plan to perform calibration and validation in our next work, the presented simulations seem realistic. For example, the step response leads to a countersteering motion of about 2 m in length at a speed of 5 $\frac{\mathrm{m}}{\mathrm{s}}$, which equates to a countersteering duration of 0.4 s. Therefore, these first results strengthen our hypothesis that more realistic bicycle dynamics are significant for the micro-simulation of bicycle interactions.

Shortcomings of the model are apparent in the unrealistic course corrections after the interaction in the 'overtaking' and 'passing' scenarios. This effect is created by our spline-based path planning. More advanced path planners or predictive control may solve the issue. Other shortcomings relate to missing functionalities of a full interaction model. These are, for example, coming to a halt at a specific location or identifying a crash from large roll angles. For the first case, the model already creates a minimum speed at which the bicycle becomes unstable. To perform experiments in the critical speed range, tuning of the controller enables calibrating the slow-speed stability. The transition between riding and a safe and accurate stop is yet unsolved.

Conclusion

In this work, we present how physics-based bicycle dynamics may influence the microscopic simulation of cyclists. Firstly, our cyclists are constrained by the degrees of freedom available to a two-wheeler. Secondly, we add the simulation of the roll angle to the bicycle, which introduces countersteering and lateral oscillation for stabilization. In a comparison of simulated bicycle trajectories with and without roll angle, this notably impacts the simulated maneuvers in terms of lateral deviation and post-encroachment time. Hence, simulating bicycle dynamics may affect an assessment of interactions on a microscopic level and the aggregated performances on a macroscopic level.

To enable the coupling between the social force model and a bicycle dynamics model, we present a reformulation of the social force model. This interprets the social force as a desired velocity rather than an acceleration. The desired velocity vector then becomes the input of our controlled bicycle model. A new spline-based destination force pointing directly along the desired path decouples

©2023 Schmidt, C. M., Dabiri, A., Schulte, F., Happee, R. & Moore, J. K. published by TU Delft OPEN on behalf of the authors.
ISSN: 2667-2812

the social force model and the control of the bicycle dynamics. Additionally, we tailor anisotropic force fields to describe the largely anisotropic characteristics of bicycle traffic. We heuristically arrive at these design choices motivated by the creation of a model that showcases the known real-world effects described above. Going further, we plan to calibrate and validate our model based on real-world data to confirm the hypothesis that realistic bicycle dynamics are an important element of simulated interactions.

References

Allen, B. L., Shin, B. T., and Cooper, P. J. (1978). Analysis of traffic conflicts and collisions. *Transportation Research Record*, 667(1):67–74.

Arun, A., Haque, M. M., Bhaskar, A., Washington, S., and Sayed, T. (2021). A systematic mapping review of surrogate safety assessment using traffic conflict techniques. *Accident Analysis & Prevention*, 153:106016.

Corke, P. (2017). *Robotics, Vision and Control: Fundamental Algorithms In MATLAB®*, volume 118 of *Springer Tracts in Advanced Robotics*. Springer, Cham, 2nd edition.

Dias, C., Nishiuchi, H., Hyoudo, S., and Todoroki, T. (2018). Simulating interactions between pedestrians, segway riders and cyclists in shared spaces using social force model. *Transportation Research Procedia*, 34:91–98.

Fuller, S., Greiner, B., Moore, J., Murray, R., van Paassen, R., and Yorke, R. (2021). The python control systems library (python-control). In *60th IEEE Conference on Decision and Control (CDC)*, pages 4875–4881. IEEE.

Helbing, D. and Molnár, P. (1995). Social force model for pedestrian dynamics. *Physical Review E*, 51(5):4282–4286.

Huang, W., Fellendorf, M., and Schönauer, R. (2012). Social Force based Vehicle Model for 2-dimensional Spaces. In *Transportation Research Board 91st Annual Meeting*, Washington D.C. Transportation Research Board.

Karnopp, D. (2013). *Vehicle Dynamics, Stability and Control*. Mechanical Engineering. CRC Press, Boca Raton, 2nd edition.

Kaths, H. (2023). A movement and interaction model for cyclists and other non-lane-based road users. *Frontiers in Future Transportation*, 4.

Kaths, H., Keler, A., and Bogenberger, K. (2021). Calibrating the Wiedemann 99 Car-Following Model for Bicycle Traffic. *Sustainability*, 13(6):3487.

Kurtc, V. and Treiber, M. (2020). Simulating bicycle traffic by the intelligent-driver model-Reproducing the traffic-wave characteristics observed in a bicycle-following experiment. *Journal of Traffic and Transportation Engineering (English Edition)*, 7(1):19–29.

Liang, X., Xie, M., and Jia, X. (2018). New Microscopic Dynamic Model for Bicyclists' Riding Strategies. *Journal of Transportation Engineering, Part A: Systems*, 144(8):04018034.

Limebeer, D. J. N. and Sharma, A. (2008). The dynamics of the accelerating bicycle. In *2008 3rd International Symposium on Communications, Control and Signal Processing*, pages 237–242.

Moore, J. K. (2015). *Bicycle Control Design in Python/v3*. Plotly, Montreal, https://plotly.com/python/v3/ipython-notebooks/bicycle-control-design/.

Ni, Y., Li, Y., Yuan, Y., and Sun, J. (2023). An operational simulation framework for modelling the multi-interaction of two-wheelers on mixed-traffic road segments. *Physica A: Statistical Mechanics and its Applications*, 611:128441.

Pressley, A. (2010). *Elementary Differential Geometry*. Springer Undergraduate Mathematics Series (SUMS). Springer, 2 edition.

Rinke, N., Schiermeyer, C., Pascucci, F., Berkhahn, V., and Friedrich, B. (2017). A Multi-layer Social Force Approach to Model Interactions in Shared Spaces Using Collision Prediction. *Transportation Research Procedia*, 25(1):1249–1267.

Veroude, B., Gurp, M. v., and Boggelen, O. v. (2022). *Geactualiseerde aanbevelingen voor de breedte van fietspaden 2022*. Fietsberaad CROW, https://www.fietsberaad.nl/Kennisbank/Aanbevelingen-breedte-fietspaden-2022.

Yuan, Y., Goñi-Ros, B., van Oijen, T. P., Daamen, W., and Hoogendoorn, S. P. (2019). Social Force Model Describing Pedestrian and Cyclist Behaviour in Shared Spaces. In *Traffic and Granular Flow '17*, pages 477–486, Cham. Springer.

Zhao, J., Knoop, V. L., and Wang, M. (2023). Microscopic traffic modeling inside intersections: Interactions between drivers. *Transportation Science*, 57(1):135–155.

©2023 Schmidt, C. M., Dabiri, A., Schulte, F., Happee, R. & Moore, J. K. published by TU Delft OPEN on behalf of the authors.
ISSN: 2667-2812

The Evolving Scholar Vol. 3, 2023 https://dx.doi.org/10.59490/65ba4abfd6388d6fe70f4cb4

Bicycle and Motorcycle Dynamics 2023
Symposium on the Dynamics and Control of Single Track Vehicles
18 – 20 October 2023, Delft University of Technology, The Netherlands

Type of the Paper: Conference Paper

Revised

Evaluation of Lane Change Maneuvers on a Dynamic Motorcycle Riding Simulator Utilizing a Rider Leaning Input

[version 2; peer reviewed]

Raphael Pleß[1, *], Sebastian Will[1], Nora L. Merkel[1], Alexandra Neukum[1]

[1] Würzburger Institut für Verkehrswissenschaften GmbH, Germany; pless@wivw.de, ORCID 0009-0006-5984-6723; will@wivw.de, ORCID 0000-0003-0098-6212; merkel@wivw.de, ORCID 0000-0002-4865-368X; neukum@wivw.de

*corresponding author

Name of Editor: Jason Moore
First published: 03/10/2023
Last published: 27/03/2024
Citation: Pleß, R., Will, S., Merkel, N. & Neukum, A. (2024). Evaluation of Lane Change Maneuvers on a Dynamic Motorcycle Riding Simulator Utilizing a Rider Leaning Input [version 2; peer reviewed]. The Evolving Scholar - BMD 2023, 5th Edition.
This work is licensed under a Creative Commons Attribution License (CC-BY).

Abstract

Up until today, high fidelity dynamic motorcycle riding simulators (DMRS) lack behind the rideability and accessibility of real motorcycles. This is a limiting factor when it comes to the applicability of such simulators in the development processes of motorcycle manufacturers, suppliers and research institutes. Extensive training of the study participants can help to overcome issues with a simulator's rideability and accessibility and therefore enables valid studies. However, it decreases the test efficiency due to the timely effort and weakens the trust of managers and decision makers into the results gained on the simulator. One approach to increase the rideability of DMRS is to introduce a technology, that allows utilizing rider motion as an input to the simulation, instead of only implementing a steering input. This approach is called "Dual Loop Rider Control" (DLRC) and is realized on the DESMORI simulator by measuring the rider induced roll torque that takes any coupling torque between the rider and the motorcycle frame around the vehicle's longitudinal axis into account (Pleß, 2016).

The objective of the paper at hand is to discuss if and how the applicability and performance of DLRC in dynamic riding maneuvers can be rated. Scales and ratings known from literature, that are for example applied for the analysis of motorcycle handling, are not sufficient for this purpose. For instance, the Lane-Change-Roll Index will decrease when implementing DLRC and utilizing leaning (vs. riding with steering input only). Typically, such lower steer torque efforts would indicate improved handling ratings. But ultimately, they have no relevance in terms of rideability, accessibility and realism of the simulator, as these qualities cannot be boiled down to lower steering efforts. Thus, there is the need for new objective performance measures.

It is hypothesized that an increased rideability of the simulator is observable in a higher precision and repeatability when performing a lane change maneuver. A set of characteristic values describing this maneuver is presented to objectively evaluate the performance of the simulator. The values result from a curve fitting of the vehicle trajectory to a hyperbolic tangent function. In order to

©2023 Pleß, R., Will, S. Merkel, N. & Neukum, A. published by TU Delft OPEN on behalf of the authors.
ISSN: 2667-2812

 http://dx.doi.org/10.59490/65ba4abfd6388d6fe70f4cb4

investigate the effects of DLRC on these characteristic values, the lane change maneuver is tested at velocities between 30 km/h and 100 km/h in three different configurations: pure steering control, pure leaning control and DLRC. The collected data highlights the effectiveness of the added leaning input and indicates slight improvements in rideability of the lane change maneuver. However, the objective performance ratings still don’t suffice to draw a precise picture of the gain in rideability through DLRC.

Keywords: Motorcycle, Simulator, Lane-change

©2023 P**leß**, R., W**ill**, S. Merkel, N. & Neukum, A. published by TU Delft OPEN on behalf of the authors.

ISSN: 2667-2812

 http://dx.doi.org/10.59490/65ba4abfd6388d6fe70f4cb4

Introduction - Dual Loop Rider Control

One key difference between motorcycling and driving cars is the vehicle's response to rider/driver motion. The car driver may move around in the seat without any subjectively perceivable effect and without significant reactions in vehicle dynamics. The steering wheel can typically be considered as the only driver input to the vehicle's lateral dynamics. In contrast, motorcycles will not only react to a rider's steering inputs, but to lateral motion of the rider's center of gravity (CoG) as well. The effects of an eccentric rider CoG on the steady state behavior of a motorcycle are well known (Cossalter, 2006). While maintaining a constant velocity and curvature of the motorcycle trajectory, leaning the rider's body towards the center of a curve will for example decrease the motorcycle's geometric roll angle and steering torque. Furthermore, the rider motion generates dynamic effects on the motorcycle that can even suffice to follow a slightly curved trajectory without applying any torques to the handlebar at all. The relevant dynamic equations have been derived e.g. by (Åström, 2005) and result in the simplified transfer function shown in Equation (1):

$$G_{\text{lean}}(s) = \frac{\varphi_{\text{mcy}}(s)}{\varphi_{\text{rid}}(s)} = \frac{-b_1 s^2 + b_2}{a_1 s^2 + a_2(v)s + a_3(v^2, v)} \tag{1}$$

Where $b_{1,2}$ describe the rider's inertial properties and $a_{1,2,3}$ contain inertial and geometric properties of the motorcycle, with the latter two being subject to the current vehicle speed v. Figure 1 exemplarily shows the response of the vehicle roll angle φ_{mcy} to a sigmoid shaped rider lean angle excitation $\varphi_{\text{rid}} = 10° \left(1 - \cos\left(\frac{\pi t}{0.5\ s}\right)\right); 0 \leq t \leq 0.5$ s

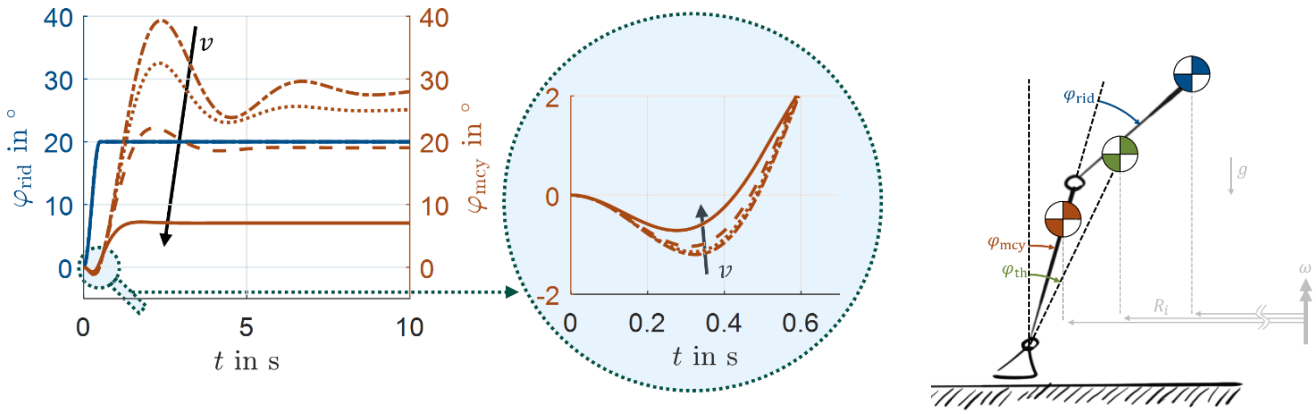


Figure 1. Exemplary response of the Lean-to-Roll transfer function (Pleß, 2023) derived from the model of (Åström, 2005)

It can be seen how a rider leaning sideways (blue line) will initially cause the motorcycle to lean in the opposite direction (red lines, magnified representation in the middle image of the figure) with decreasing amplitudes as the velocity increases. After a few oscillations, a new equilibrium results, which depends on the vehicle's speed.

Although the effects of rider motion on the lateral dynamics are well known, they have not been considered widely in the development of motorcycle riding simulators. Many static and dynamic motorcycle riding simulators rely on the steering as their only input to the lateral dynamics ("Single Loop Rider Control") and until today, the design of steering systems for motorcycle riding simulators is an open field of research, see e.g. (Werle, 2022). Of the better-known motorcycle riding simulators, the DIMEG Simulator at the University of Padua was the first to consider rider motion as an input by means of a vertical load measurement at the foot pegs (Cossalter, 2011). In the following, such systems will be referenced to as "Dual Loop Rider Control" (DLRC), as they not only utilize steering, but rider motion as an input to the vehicle dynamics model. The motorcycle riding simulators of BMW Motorrad (Guth, 2017) and Cruden (Westerhof, 2018) implemented optical measurement methods to track the rider's upper body. All abovementioned systems have in common, that they rely on rather specific input cues. For example, pressure sensitive foot pegs will not respond to body motion if the rider is supporting their weight through the simulator frame and handlebars rather than deliberately pressing down on a foot peg. Optical measurements on the other hand are limited to the motion of the observed body parts and will neglect all other motions. An approach for a holistic rider motion determination was presented with the DESMORI simulator (Pleß, 2016). It consists of a longitudinally mounted mechanical axis that allows for a rotation of the motorcycle frame relative to the motion platform. This rotation is however supported against a load cell and will not result in a perceptible movement.

©2023 Pleß, R., Will, S. Merkel, N. & Neukum, A. published by TU Delft OPEN on behalf of the authors.

ISSN: 2667-2812

http://dx.doi.org/10.59490/65ba4abfd6388d6fe70f4cb4

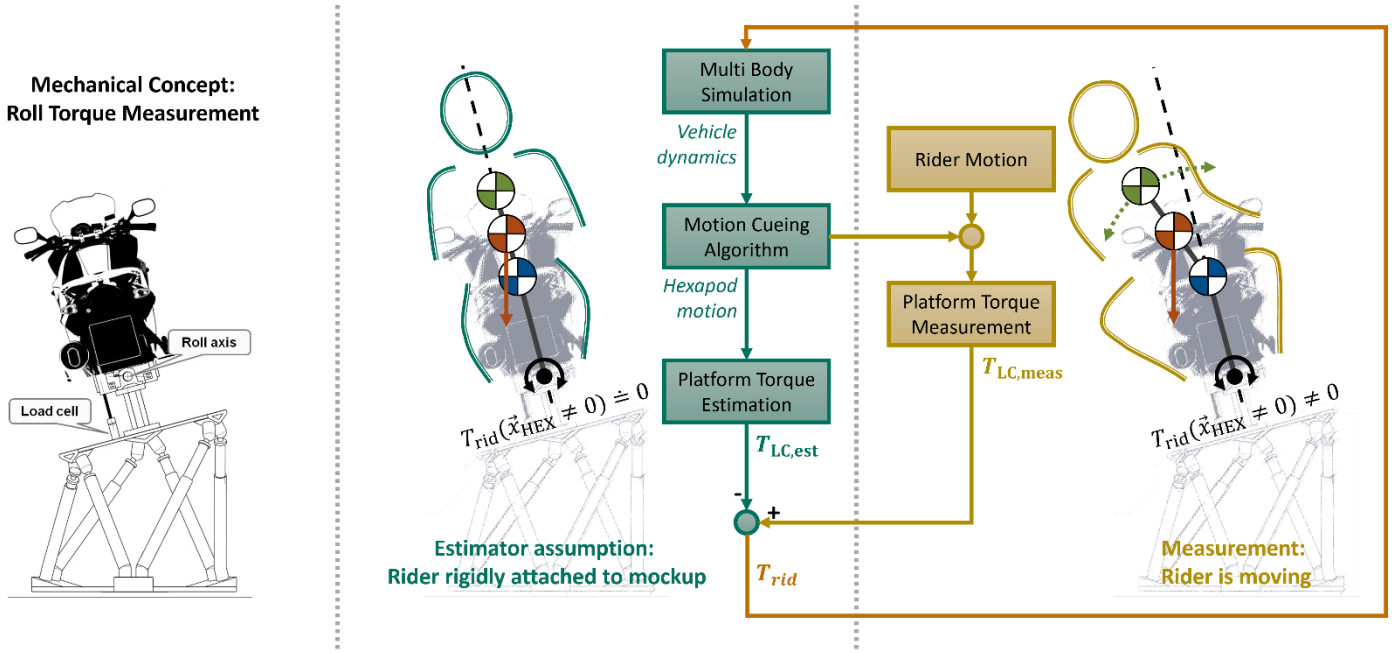


Figure 2. Measuring concept of the rider induced roll torque.

The concept is sketched in Figure 2. The measured torque $T_{\mathrm{LC,meas}}$ that is acting around the mechanical axis (yellow) contains effects from both rider motion and platform motion. The latter can be estimated by assuming that the rider is a stiff point-mass, as the inertial properties and motion cues of the system are known (green). The difference between the measured signal $T_{\mathrm{LC,meas}}$ and the estimated signal $T_{\mathrm{LC,est}}$ will therefore contain the torque that the rider applies on the motorcycle frame both actively (leaning) and passively (being an elastic and inert mass). This so called "rider induced roll torque" T_{rid} (red) is then used as input to the multi body simulation model of the motorcycle, which is built by using the commercially available software VI-grade Bike RealTime.

The described system will react to any rider body excitation, may it result from leaning to one side, shaking the head or stretching a leg. The precision of the system depends on the quality of the torque estimator as well as mechanical properties like the component's stiffnesses or bearing friction. The estimator was tested in various realistic motion scenarios, where it showed root mean square errors below 3 Nm while the rider induced torques range up to around ± 150 Nm (Pleß, 2023).

Scenario Description

The lane change experiment discussed in this paper was performed on a virtual test track that is based on a planar, straight, three-lane road. Cones were used to define the areas where the rider is supposed to enter, perform and exit the lane change maneuver. Figure 3 shows the track segments by means of a map view (top) and screenshots of the simulation environment SILAB® (bottom). The maneuver was repeated for ten times consecutively, before changing the target velocity or control configuration.

Firstly, the length l_{pre} allows the rider to control and adjust the target velocity as well as smoothly entering the segment l_{entry}, where the rider is forced into a 50 m long corridor with a limited lane width of 1.8 m. (leftmost picture). When passing the corridor, the rider will see the upcoming blocked middle lane. The traffic sign will show either a left or right arrow at the instance the rider exits the entry corridor. From this moment on, the rider has about 2.5 s to react and change the lane (second left picture). The exit segment is offset by 3 m and uses a 75 m long corridor of cones with a width of 1.8 m as before (second right picture). This is intended to urge the rider to come to a straight riding state at a rather well constrained lateral offset, rather than only passing and "corner cutting" alongside the obstacle on the middle lane. Lastly, in the segment l_{post}, the rider can smoothly transition back towards the next entry. The "pre" and "post" lengths are chosen such that the rider may take up to 7 seconds at the indicated target velocity to reach the entry.

©2023 Pleß, R., Will, S. Merkel, N. & Neukum, A. published by TU Delft OPEN on behalf of the authors.
ISSN: 2667-2812

http://dx.doi.org/10.59490/65ba4abfd6388d6fe70f4cb4

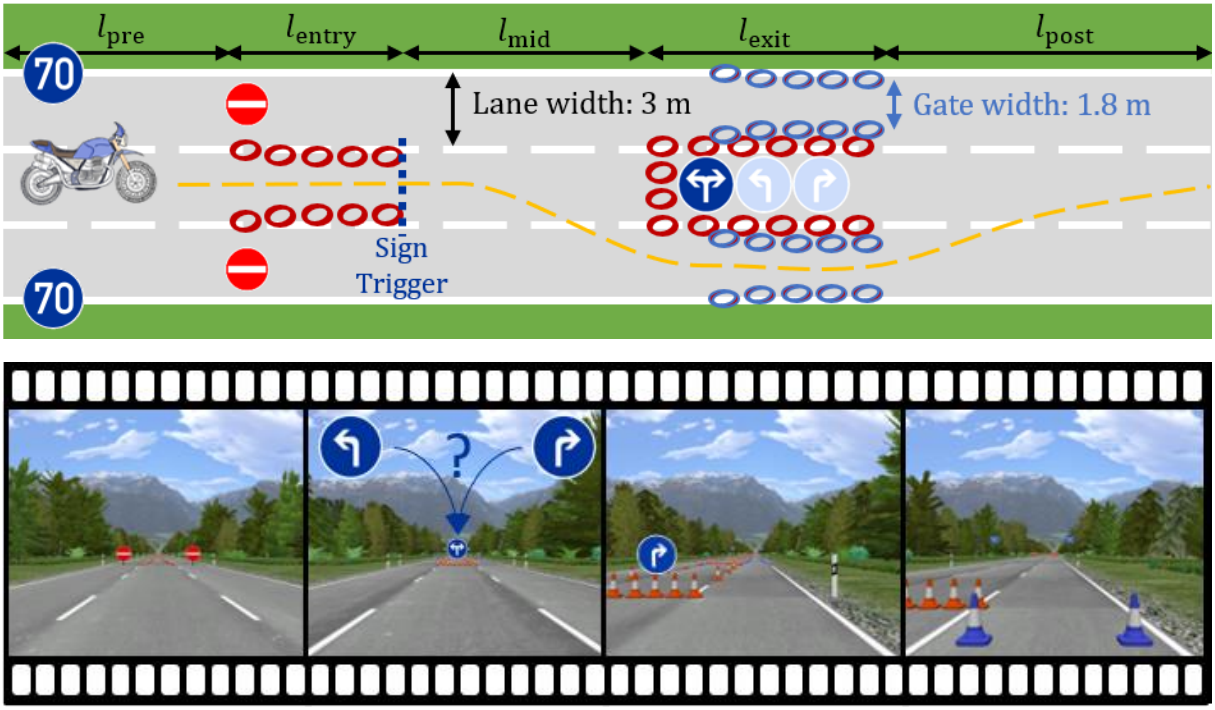


Figure 3. Map view of the lane change scenario (top) and sequence of events in the rider perspective (bottom).

The maneuver was performed in different control configurations. Each rider was either allowed to use the handlebar (H1) or not (H0), while activating (L1) or deactivating (L0) the leaning input. In the following discussions and figures, the lane change maneuver is indicated as "DL". This results in the configuration descriptors DL_{L0}^{H1}, DL_{L1}^{H0} & DL_{L1}^{H1}. Obviously, a DL_{L0}^{H0} variant would be impossible to perform, as no steering or leaning input exist. Both H1 configurations were tested at 30, 50, 70, 90 and 110 km/h. For the H0/L1 configuration – i.e. riding without hands – the test was performed at 50 and 80 km/h (set by a cruise control) while using the track geometries from the 70 and 110 km/h versions of the H1 configurations. This results in a total of twelve scenario configurations with ten repetitions. The test parameters are listed in Table 1:

Table 1. Lane Change Scenario Configurations.

DL_{L1}^{H1}	DL_{L0}^{H1}	DL_{L1}^{H0}	l_{pre}	l_{entry}	l_{mid}	Δy_{mid}	$\Delta t(DL_{Lx}^{H1})$	$\Delta t(DL_{Lx}^{H0})$	l_{exit}	l_{post}
km/h			m	m	m	m	s	s	m	m
110	110	80	150	50	80	3	2.6	3.6	75	60
90	90		125	50	65	3	2.6		75	50
70	70	50	100	50	50	3	2.6	3.6	75	40
50	50		70	50	35	3	2.5		75	30
30	30		42	50	20	3	2.4		75	17

The table highlights the l_{mid} section in blue. It can be seen, that the lateral offset Δy_{mid} is kept constant in all variations and the length is adjusted such that a duration about 2.5 seconds is achieved for the variation with steering control and a duration of 3.6 seconds without steering control. Only participants that were well trained on the motorcycle simulator performed the experiment. Each variation was repeated ten times before lowering the target velocity and eventually changing the control configuration.

©2023 Pleß, R., Will, S. Merkel, N. & Neukum, A. published by TU Delft OPEN on behalf of the authors.

ISSN: 2667-2812

 http://dx.doi.org/10.59490/65ba4abfd6388d6fe70f4cb4

Measurements

The results shown in the following sections contain data from the same rider. The data from two other riders showed no relevant differences and is therefore not further depicted or discussed here. For the following detailed discussions on the timeseries of dynamic quantities, the middle scenario of Table 1 was selected such that all plots are based on the same track geometry.

Figure 4 shows the front tire trajectories for the two configurations with active steering. Each blue line represents one of the ten repetitions that the rider performed. The left plot shows the configuration with a disabled roll torque input, whereas the right plot shows the configuration with DLRC, i.e. both steering and leaning inputs being active. The DL_{L1}^{H1} condition arguably shows smaller deviations in the entry and exit corridors as well as less amount of overshooting at the end of the lane change maneuver.

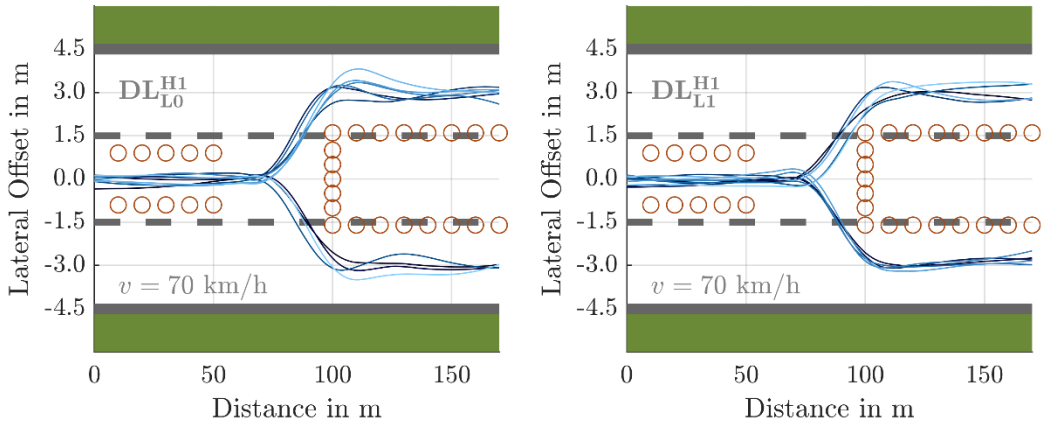


Figure 4. Trajectories of the front tire contact point during lane change without (left) and with (right) activated DLRC.

All correlation coefficients between each measurement per condition are greater than 99%. In the following it is therefore assumed that left- and right-hand lane changes can be evaluated as equal by mirroring the left-hand lane change data onto the right-hand data. The following plots show the relevant lateral-dynamic quantities of the same configurations as above. Figure 5 represents the left-hand data of Figure 4, where the rider could only use the steering as input, while Figure 6 represents the right-hand data, where DLRC was active and both steering and leaning of the rider affected the vehicle dynamics. Lastly, Figure 7 shows the remaining configuration, where only the leaning input was utilized. The dynamic quantities are discriminated by color. Blue indicates the roll angle and green the steer angle of the virtual motorcycle respectively, red indicates the rider induced roll torque and yellow the steering torque measured on the simulator. The thick lines depict the mean values of the ten repetitions, while the shaded areas span over one standard deviation. The angles are referenced on the left ordinate, torques on the right.

The DL_{L0}^{H1} condition shown in Figure 5 can be seen as the baseline condition, as it represents the state of the art of controlling a motorcycle simulator only by means of a steering input during a lane change maneuver. At a distance of approximately 60 m a rapid increase in the steer torque in the opposite direction of the lane change (negative sign) causes a counter steering motion. In consequence, a roll angle towards the direction of the lane change is building up, reaching it's maximum at around 75 m. At this point, the rider will apply a positively signed steer torque in order to quickly build up a roll angle that allows the rider to return to a straight direction of travelling again. The amplitudes of the roll and steer angles reach similar values both for entering and exiting the lane change. Tthe increasing roll angles at the end of the plot show how the rider is not able to find a straight running equilibrium but rather initiates the return to the center lane for the experiment's next repetition early within the exit corridor. As the speed is easily kept constant, and the target trajectory is rather constrained by the given cones, there is not really any room for choosing alternative lines in the mid-section of the scenario. Furthermore, any variation can only result from steering inputs as no other disturbances exist. Therefore, the data shows rather small standard deviations.

In Figure 6, the rider induced roll torque is added as an input (red line and shaded area). While the standard deviation of the roll angle increases slightly, the opposite is true for the steer torque and angle. When initiating the lane change, the rider induced roll torque points towards the direction of the lane change. This lean-in approach requires less steer torque and generates smaller counter steer angles. When exiting the lane change, the leaning motion results in a much smoother up-righting of the motorcycle, allowing to ride through the final corridor in a straighter line as before. The prominent peak in the roll torque signal at around 85 m can be traced back to a malfunction of the motion platform during one repetition and can be neglected here.

©2023 Pleß, R., Will, S. Merkel, N. & Neukum, A. published by TU Delft OPEN on behalf of the authors.
ISSN: 2667-2812

http://dx.doi.org/10.59490/65ba4abfd6388d6fe70f4cb4

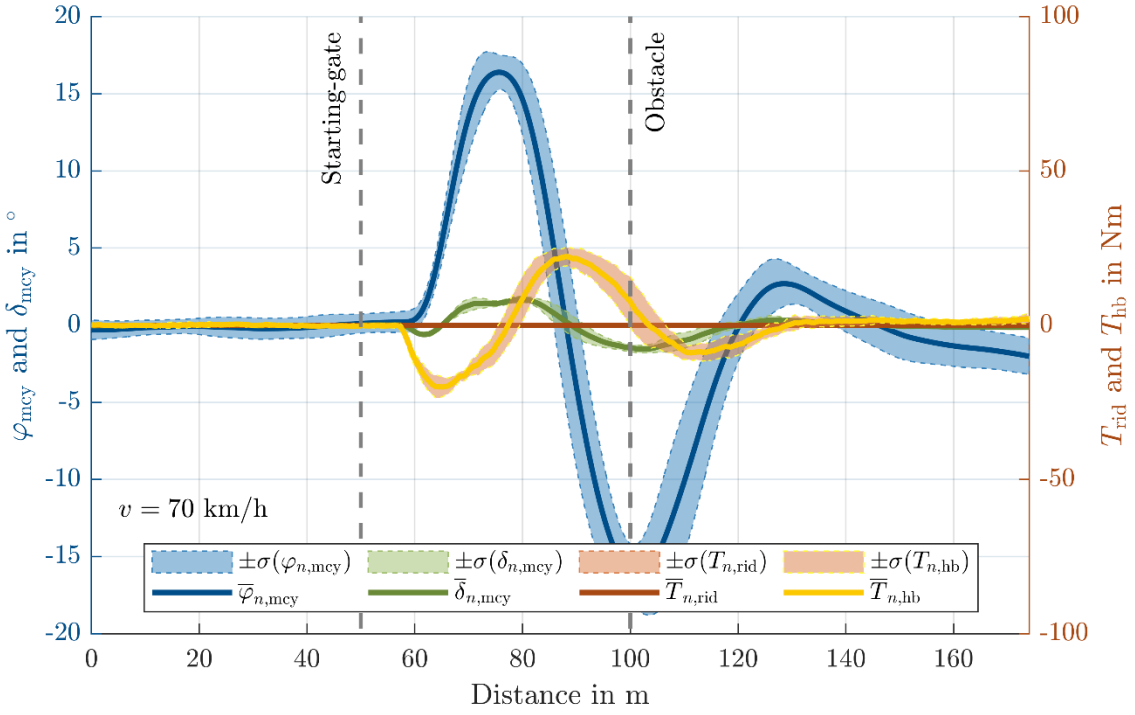


Figure 5: Average values and standard deviations of dynamic quantities in $\mathbf{DL}_{\mathbf{L0}}^{\mathbf{H1}}$ condition.

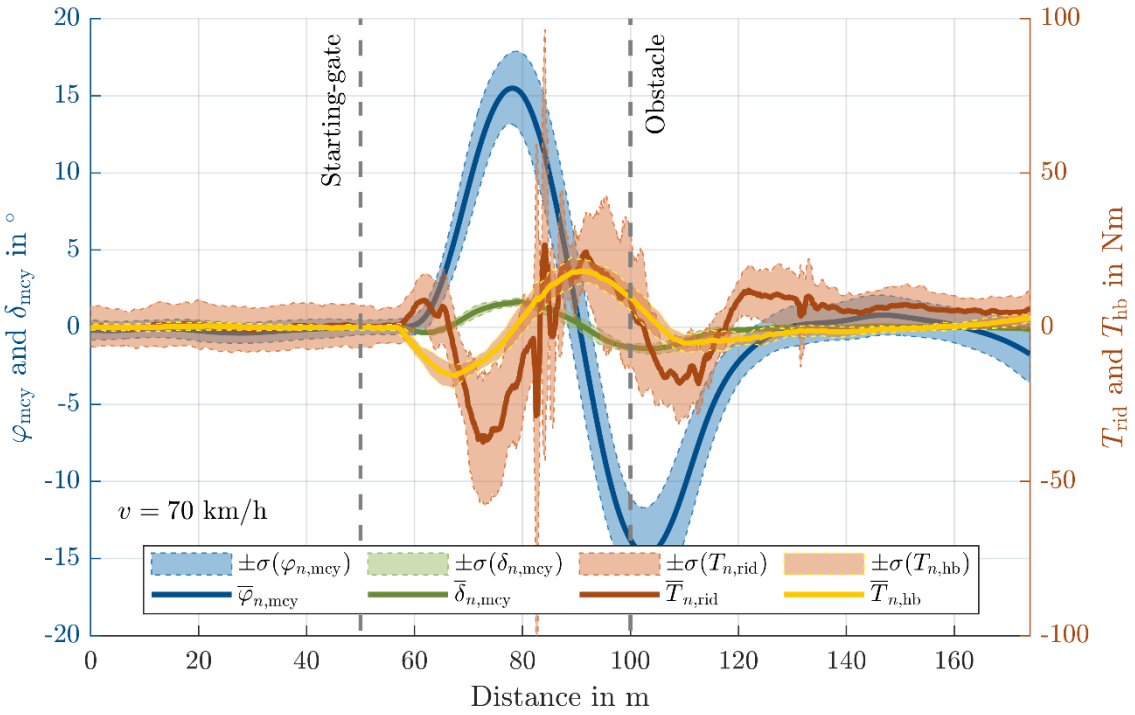


Figure 6. Average values and standard deviations of dynamic quantities in $\mathbf{DL}_{\mathbf{L1}}^{\mathbf{H1}}$ condition.

©2023 Pleß, R., Will, S. Merkel, N. & Neukum, A. published by TU Delft OPEN on behalf of the authors.
ISSN: 2667-2812

 http://dx.doi.org/10.59490/65ba4abfd6388d6fe70f4cb4

In the last condition DL_{L1}^{H0} the rider does not grip the handlebar and the velocity is set by a cruise control at 50 km/h while maintaining the same track geometry as before. Figure 7 shows an overall similar behavior of the roll and steer angle as before. However, it must be noted that in this case the counter steering angle is not the result of a steer torque. The initial rider leaning motion towards the direction of the lane change causes an opposing support torque in the motorcycle frame (i.e. as the rider moves right, the motorcycle frame wants to move to the left). This is observable in a small roll angle peak at about 62 m in the opposite direction of the lane change. This will in consequence cause a small steering angle in the same direction as well (see magnified representation in the top right corner). Only then, as the tilted front wheel causes sideslip and camber side forces, the roll motion towards the direction of the lane change will begin. After that, a similar process leads to returning the motorcycle to a straight riding.

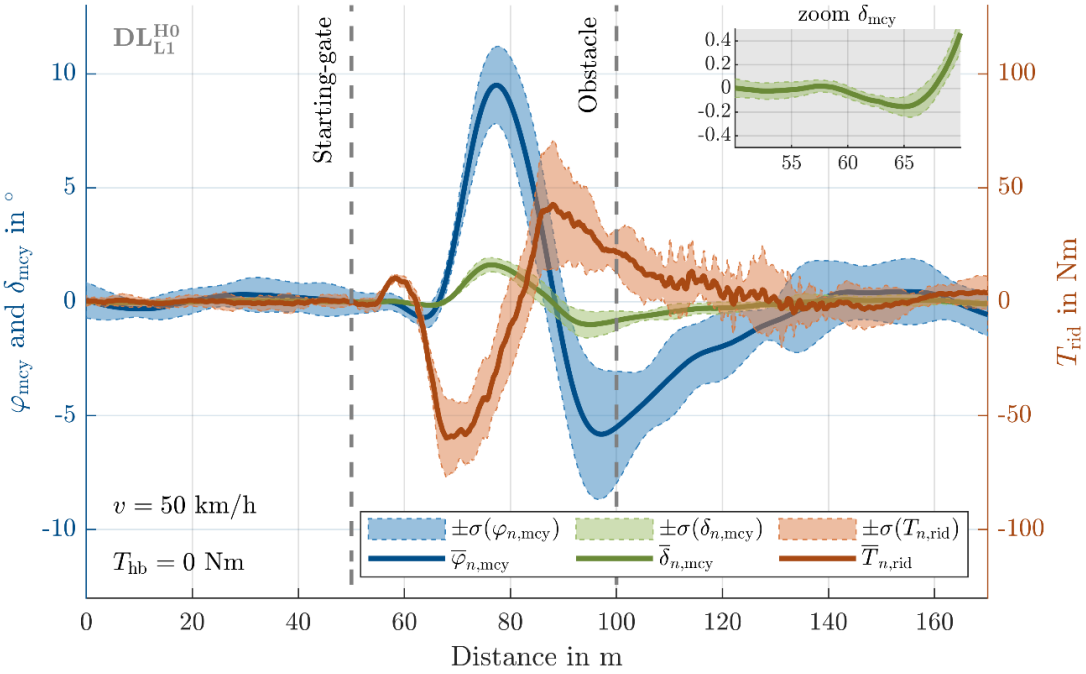


Figure 7. Average values and standard deviations of dynamic quantities in $\mathbf{DL_{L1}^{H0}}$ condition.

Results

The previous timeseries have shown that adding a control cue sensitive to rider motion can cause plausible vehicle reactions of the virtual motorcycle and even allow a rider to maneuver it without hands. The data shows, that the rider is applying a lean-in strategy to maneuver through the scenario. As known from literature, it is expected that lean-in should have a decreasing effect on the steer torque. To gather an overview about this effect, Figure 8 shows a statistical analysis of the Lane-Change-Roll Index Υ_{LC} (Cossalter, 2006) that relates the peak to peak steering torque $T_{hb,p-p}$ to the product of the mean velocity $\overline{v}$ and the peak to peak roll rate $\dot{\varphi}_{th,p-p}$. When comparing different vehicles or vehicle configurations, smaller values of the Lane-Change-Roll Index are considered superior to larger values, as the rider needs less effort to control the vehicle through the lane change, which arguably results in better "handling". As observed in Figure 8, all experiments at velocities above 50 km/h result in smaller Υ_{LC} for the DL_{L1}^{H1} condition. Only at 30 km/h, the index increases when adding the leaning input, which can be explained by higher steering efforts needed due to a decreasing vehicle stability at such speeds and the tendency to utilize lean-out. As there is no absolute rating possible for the Lane-Change-Roll Index, it is not sufficient to rating the performance of the DLRC.

Cheli (2011) investigates the rider's body influence in double lane change maneuvers. The results indicate, that the utilization of rider motion will result in a delay in the peak steer torques and steer angles with respect to the peak roll angles. Figure 9 shows the absolute locations (0 m indicating the start of l_{mid}) of peak values of multiple quantities on the left side and the relative distances between the peaks of different quantities on the right side. The data shows that the configuration with active DLRC results in little to no delay of the absolute locations of the roll angle peak $s(\hat{\varphi}_{BRT})$, steer torque peak $s(\hat{T}_{\delta,BRT})$ and steer angle peak $s(\hat{\delta}_{BRT})$. The relative delay from the roll angle peak to the steer angle peak $\Delta s_{\delta,\varphi}$ – if anything – decreases slightly.

©2023 Pleß, R., Will, S. Merkel, N. & Neukum, A. published by TU Delft OPEN on behalf of the authors.

ISSN: 2667-2812

 http://dx.doi.org/10.59490/65ba4abfd6388d6fe70f4cb4

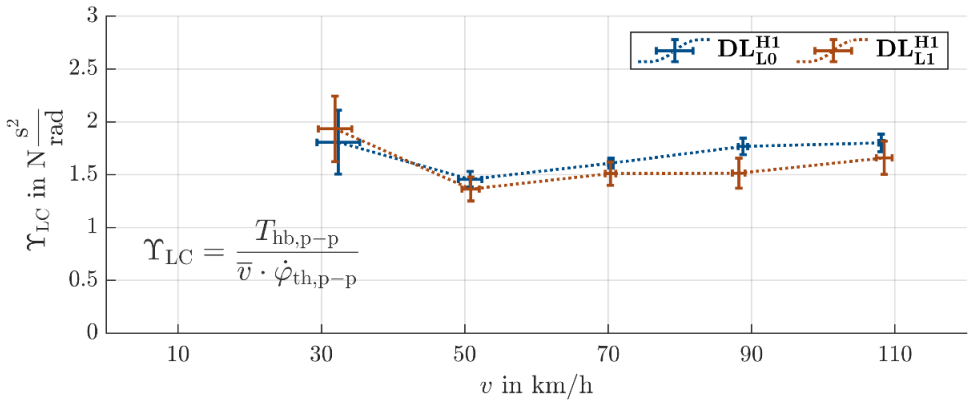


Figure 8. Lane-Change-Roll-Indexes for two configurations at different velocities.

The behavior described by (Cheli, 2011) could therefore not be reproduced. However, to the knowledge of the authors, there exists no definition of an ideal behavior in that regard. The delay or advance of the peak locations may vastly differ when utilizing lean-in or lean-out. But again, as there is no absolute reference available, this measure is not well suited to rate the performance of DLRC.

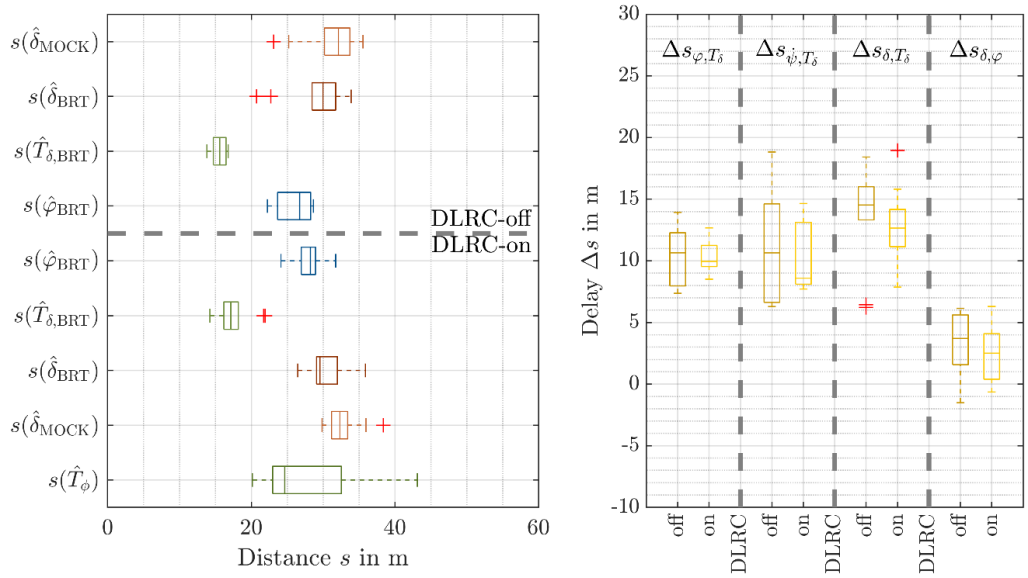


Figure 9. Locations of peak values and delays between the peaks of different quantities at lane change with 70 km/h.

Due to the described deficiencies of the known indexes, a new approach was developed and firstly described by Hammer (2021), that aims to compare the performance of a lane change by fitting a hyperbolic tangent function to the motorcycle trajectory by minimizing the loss function shown in Equation (2).

$$E_{\tanh} = RMS\left(\tilde{y}_0 + \frac{\Delta\tilde{y}}{2} \cdot \left(1 + \frac{\tanh(x_{\mathrm{CG}} - \tilde{x}_{\mathrm{mid}})}{\Delta\tilde{y}/\left(2 \cdot \max\left(\frac{\partial\tilde{y}}{\partial\tilde{x}}\right)\right)}\right) - y_{\mathrm{CG}}\right) \tag{2}$$

©2023 Pleß, R., Will, S. Merkel, N. & Neukum, A. published by TU Delft OPEN on behalf of the authors.

ISSN: 2667-2812

 http://dx.doi.org/10.59490/65ba4abfd6388d6fe70f4cb4

Therein, the hyperbolic tangent function is offset by $\tilde{x}_{\mathrm{mid}}$ and $\tilde{y}_0$ and scaled by the maximum offset rate $max(\frac{\partial \tilde{y}}{\partial \tilde{x}})$ and amplitude $\Delta\tilde{y}$. These four fitting parameters as well as the RMS value allow statements about the precision of the lane change maneuver. The initial offset $\tilde{y}_0$ should ideally be zero, and the amplitude $\Delta\tilde{y}$ should ideally match the width of the lane change maneuver. The maximum offset rate $max\ (\frac{\partial \tilde{y}}{\partial \tilde{x}})$ shows how quickly a rider performs the lateral transition and the RMS value rates the quality of the tanh-fitting. Small values will indicate a smooth, undistorted trajectory. Figure 10 (left) shows the trajectory of the motorcycle's CoG (blue) and the hyperbolic tangent that is fitted on this trajectory (green). The abovementioned parameters of this fitted trajectory define the green bubble in the righthand plot. The RMS value is depicted by the size of the bubble, the ordinate shows the lateral offset and the abscissa shows the maximum offset rate. Both latter variables have been normalized by the target offset.

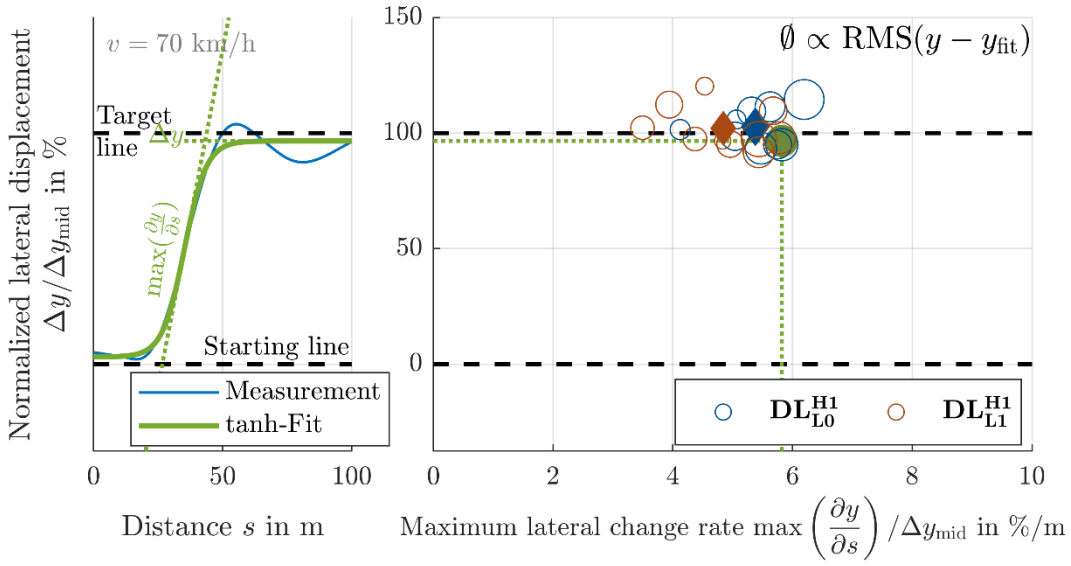


Figure 10. Development of the Bubble-Cluster Plot.

In this representation, an optimally performed lane change would result in a single point (rather than a large bubble) that is placed exactly at the 100% line, while the maximum lateral change rate depends on the length that is available to perform the lane change. During 10 repetitions, the resulting points should show a minimal scattering, indicating a good repeatability and therefore good controllability and ease of riding.

In the experiment we see differently sized bubbles that are scattered around a center. The red and blue color indicate the configuration of the simulator – red showing the DLRC condition. The diamonds represent the mean location and size of the bubbles of all ten repetitions. It can be seen from this example, that the maximum lateral change rate decreases, when DLRC is activated and the RMS error is slightly smaller compared to the configuration without the leaning input. However, no effect is visible for the reached lateral displacement.

Figure 11 shows the bubble clusters for all tested velocities with and without the use of DLRC. For a better comparability, the abscissa was additionally normalized by the length l_{mid}. Starting at high velocities (rightmost plot) it can be seen that the activation of DLRC causes a slight decrease of the RMS error and a shift of the cluster towards lower maximum lateral change rates. This indicates a smoother transition from the center lane to the outside lane. While this supports the previously shown results collected at 70 km/h, the picture is less clear when looking at the 90 km/h and 50 km/h data that show a less pronounced separation of the two clusters. At 30 km/h, the size of the bubbles increases clearly, indicating much larger deviations of the trajectory from the hyperbolic tangent function, which is plausible for the lesser amounts of self-stabilization given at this speed. With activated DLRC the overshooting of the target lateral offset decreases slightly.

©2023 Pleß, R., Will, S. Merkel, N. & Neukum, A. published by TU Delft OPEN on behalf of the authors.

ISSN: 2667-2812

http://dx.doi.org/10.59490/65ba4abfd6388d6fe70f4cb4

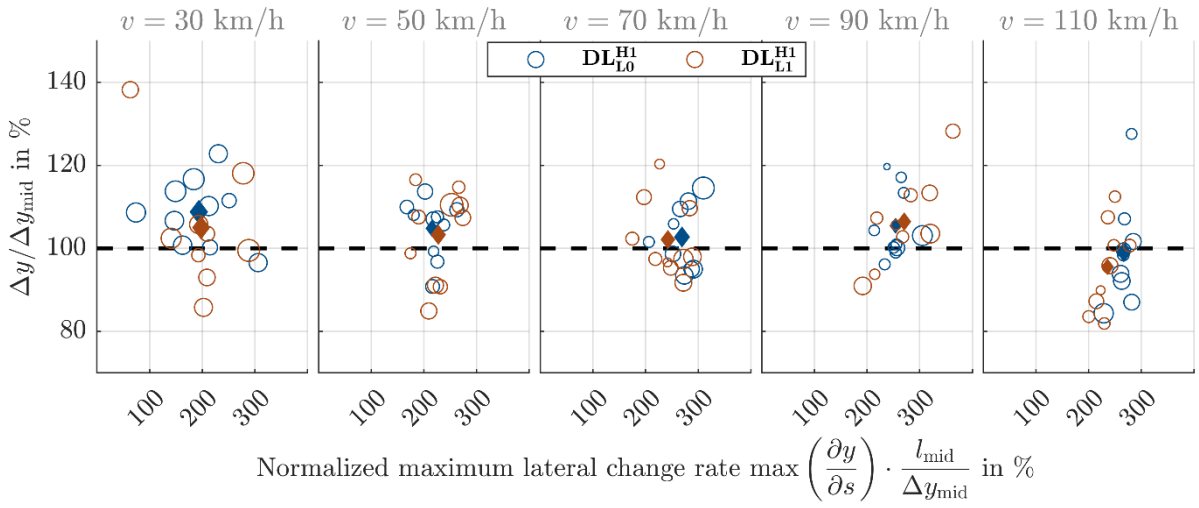


Figure 11. Comparison of bubble clusters in two configurations for different velocities.

Conclusion and Outlook

The described implementation of DLRC aims to increase the rideability of a dynamic motorcycle riding simulator, as it allows the rider to utilize behavioral patterns known from real life riding. The data shows, that the presented determination of the rider induced roll torque is an effective method to design a DLRC. The system is capable of provoking plausible vehicle reactions known from real life riding. In order to objectively rate the effectiveness of this method, known indices like the Lane-Change-Roll Index or the peak locations have been investigated. The results however show, that they are not really suited to rate the effect of DLRC on the rideability of the simulator. Therefore, another set of characteristic values was developed to try and gain insight on the lane change behavior. First results show small but noticeable differences in the measurements that indicate smoother lane transitions with less steer torque efforts and less scattering, when DLRC is activated. However, the amount of available data is yet too small to provide final results.

Therefore, in the next steps, more data of various participants should be collected to improve the statistical evidence. Furthermore, the newly defined characteristic values might need to be revised, by e.g., adjusting the fitting function from a hyperbolic tangent to a different sigmoid, or by investigating e.g., the tire trajectories rather than the CoG trajectory. In general, the method provides absolute values that could be used for comparison of different real and simulated vehicles in various lane change parametrizations. The shown representation of bubble clusters provides a quick overview of the data and allows for data clustering, such that it promises to be feasible for analytics of larger data bases as well.

References

Åström, K. J., Klein, R. E., & Lennartsson, A. (2005). Bicycle Dynamics and Control. *Control Systems Magazine*, 25(4), 26-47.

Cheli, F.; Pezzola, M.; Taroni, N.; Mazzoleni, P.; Zappa, E. (2011) Driver's movements influence on the lateral dynamic of a sport motorbike, *19th Mediterranean Conference on Control and Automation*

Cossalter V., (2006). *Motorcycle Dynamics*. Lulu, Raileigh

Cossalter, V.; Lot, R.; Massaro, M.; Sartori, R.: Development and validation of an advanced motorcycle riding simulator. *Proceedings of the Institution of Mechanical Engineers, Part D: Journal of Automobile Engineering (6)*, Issues 225, pp. 705–720, 2011

Guth, S. (2017) *Absicherungsmethode von Anzeigekonzepten zur Darstellung fahrfremder Informationen mittels eines Motorrad-Fahrsimulators*, Dissertation, TU Darmstadt

©2023 Pleß, R., Will, S. Merkel, N. & Neukum, A. published by TU Delft OPEN on behalf of the authors.

ISSN: 2667-2812

Hammer, T.; Pleß, R.; Will, S., et al. (Eds.) (2021). Anwendungsmöglichkeiten von Motorradsimulatoren, *Berichte der Bundesanstalt für Straßenwesen, Mensch und Sicherheit Heft 323*, Fachverlag NW in der Carl Schünemann Verlag GmbH, Bremen, Germany

Pleß, R. (2016). *Approach to a holistic input determination for a motorcycle riding simulator*. Proceedings of the Bicycle & Motorcycle Dynamics Symposium, Milwaukee, 2016

Pleß, R. (2023). *Dual Loop Rider Control of a Dynamic Motorcycle Riding Simulator*, Dissertation, TU Darmstadt

Werle, A., Diermeyer, F. (2022). An Approach for Steering Advancement in Motorcycle Riding Simulation. *Human Interaction & Emerging Technologies (IHIET-AI 2022)*

Westerhof, B. E. (2018). *Evaluation of the Cruden Motorcycle Simulator*, Master-Thesis, Delft University of Technology

©2023 P**leß**, R., W**ill**, S. Merkel, N. & Neukum, A. published by TU Delft OPEN on behalf of the authors.

ISSN: 2667-2812

The Evolving Scholar Vol. 3, 2023 https://dx.doi.org/10.59490/65ea2e57849efaac633d9392

Bicycle and Motorcycle Dynamics 2023
Symposium on the Dynamics and Control of Single Track Vehicles
18 – 20 October 2023, Delft University of Technology, The Netherlands

Type of the Paper: Conference Paper

Revised

Identification and Modeling of a Mountain Bike Front Suspension Subsystem Equipped with a Telescopic Fork and Tire Damping

[version 2; peer reviewed]

Noah Schoeneck[1*], James Sadauckas[2], and Mark Nagurka[3]

[1]Vehicle Measurements Group, Harley-Davidson Motor Company, Yucca AZ 86438, USA; noah.schoeneck@harley-davidson.com
[2]Trek Performance Research, Trek Bicycle Corporation, Waterloo, WI, 53594, USA; jim_sadauckas@trekbikes.com; ORCID 0000-0002-6055-9047
[3]Professor Emeritus, Department of Mechanical Engineering, Marquette University, Milwaukee, WI 53233, USA; mark.nagurka@marquette.edu

*corresponding author

Name of Editor: Jason Moore
First published: 25/09/2023
Last published: 08/04/2024
Citation: Schoeneck, N., Sadauckas, J. & Nagurka, M. (2024). Identification and Modeling of a Mountain Bike Front Suspension Subsystem Equipped with a Telescopic Fork and Tire Damping [version 2; peer reviewed]. The Evolving Scholar - BMD 2023, 5th Edition.
This work is licensed under a Creative Commons Attribution License (CC-BY).

Abstract:

A key component in the mountain bike industry is the telescopic front suspension, which offers performance advantages when traversing obstacles, rough terrain, and high impact landings. Despite the popularity of telescopic forks in the market, their modeling details and assumptions have received limited attention in the literature. This paper presents a system identification and modeling approach that promises a deeper understanding of the dynamic behavior of mountain bikes with telescopic front suspensions. The mountain bike front suspension subsystem is modelled initially using the classic quarter car model with the suspension and tire both included as second-order systems, each with spring and damper elements in a Kelvin-Voigt arrangement stacked in series. The boundary and initial conditions of the subsystem are modified from the classic quarter car model to capture the impact and loss of ground contact condition. The paper then incrementally increases the complexity of the quarter car model based on a parameterization study of the fork and tire. Simulation results are compared to data from an impact sled test of a telescopic mountain bike front suspension subsystem. The correlation between the quarter car model response and the test data varies with the complexity of the model and its parameters suggesting the importance of including key parameters in models of mountain bike front suspension subsystems.

Keywords: Mountain Bike Suspension, Tire Damping, System Identification, Quarter Car, Simulation

©2023 Schoeneck, N., Sadauckas, J. & Nagurka, M. published by TU Delft OPEN on behalf of the authors.
ISSN: 2667-2812

 https://dx.doi.org/10.59490/65ea2e57849efaac633d9392

Introduction

Modeling and simulation of vehicle suspension subsystems have been essential to the design of high performance vehicles. The automotive industry has used various versions of the quarter car model as a first approach in vehicle suspension design. Despite the similarities between automotive and mountain bike suspensions in function and utility, the mountain bike telescopic front suspension subsystem has received little attention in the literature at the subsystem level. Lumped parameter mass-spring-damper models for the mountain bike tire and for the mountain bike telescopic front suspension have been used as part of a broader full vehicle model with minimal focus spent on the complexity of the subsystem parameters.

Through the years the classic two degree-of-freedom quarter car model has been met with both criticism and praise in predicting vehicle suspension performance. One concern is the classic quarter car model used in automotive studies is a linear model. Automotive suspension springs can be represented as piecewise linear stiffnesses combining multiple linear spring rates (i.e., stiffnesses) or have nonlinear characteristics. Automotive suspension dampers often exhibit nonlinear behavior. Dedicated hydraulic circuits for compression and rebound damping can further be divided as having low and high speed behavior. A second concern with classic quarter car models from literature is their inability to model the system when the tire loses contact with the ground. Typically, the classic quarter car model predicts relatively low amplitude displacements from an equilibrium position, but this is inadequate for an impact study.

Pneumatic tires have complicated stiffness behaviors, typically represented by dynamic and static stiffnesses. A survey of automotive literature suggests a long-running debate on whether to include tire damping within the model. Those advocating for the exclusion of the effects of tire damping have purported, but not necessarily shown, that these effects have only a small influence on the overall system response and thus can be neglected. Those including it generally do so without particular attention to its measurement or estimation except for a few specific studies (Acosta, 2020, Mahr, 2011, Levitt, 1991). This paper demonstrates that for relatively flexible tires, such as those of a mountain bike with minimal carcass plys, limited tread rubber, and relatively low inflation pressures, encountering relatively large deformations with respect to their aspect ratio under impact, both dynamic stiffness and damping can influence system response.

A feature that is often included in mountain bike telescopic forks, whether coil or air sprung, is the ability to adjust the suspension preload. For a coil, the preload is the amount the spring is displaced when installed into the fork or shock plus any additional compression the user adds via the preload adjuster. The preload allows the equilibrium position of the suspension under the steady-state load of vehicle and rider, also known as sag, to be set independently from the spring rate chosen for ride characteristics. When properly set, the preload serves the important task of balancing the available suspension travel between compression, to resist bottoming at maximum stroke, and rebound, to avoid topping the suspension at full extension. Despite its practical implications, preload is not included in many classical quarter car models (Lot, 2021).

Suspension bottoming presents a variety of concerns. It can lead to significant loading with the road input directly transferred to the chassis and, from a structures and durability perspective, should be avoided. In addition, it can lead to large chassis accelerations that contribute to rider discomfort. For these reasons shock absorbers often include a “bump stop” or “jounce bumper”, i.e., a stiff elastomer in parallel to the main spring to ease the transition to end stroke. Topping events are of less concern as the loads transmitted to the chassis are lower, but such events may still affect vehicle road holding, diminish rider comfort, and possibly even damage suspension components. Motorcycle and mountain bike suspensions often include a top out spring to help prevent damage to the suspension internal components and provide a better riding experience. The top out spring also helps control the wheel and keeps the tire in contact with the ground. It is another suspension element that is not typically included in the classic quarter car model.

This paper investigates the parameters and accuracy of the quarter car model as applied to a mountain bike front telescopic suspension subsystem. It describes the experimental measurement of the stiffness and damping parameters of both the telescopic fork and the tire. Then, starting from a classic two degree-of-freedom linear quarter car model (denoted S1), a series of 14 simulations incrementally explore nonlinear stiffness (S2 & S3), additional spring parameters such as top out (S4 & S5) and preload S6 & S7), linear damping (S8), nonlinear damping (S9 & S10), as well as tire stiffness and damping (S11 through S14). Simulation results are compared to fork and tire subsystem test data collected using an impact test sled to help identify model elements that are critical for a given level of fidelity.

©2023 Schoeneck, N., Sadauckas, J. & Nagurka, M. published by TU Delft OPEN on behalf of the authors.

ISSN: 2667-2812

 https://dx.doi.org/10.59490/65ea2e57849efaac633d9392

Model

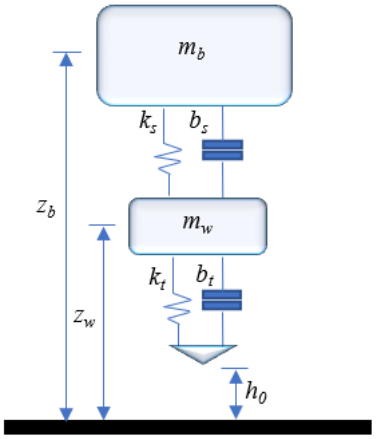


Figure 1. Quarter car model.

Figure 1 shows a lumped-parameter quarter car impact model, where m_b is the mass of the body, m_w is the mass of the wheel assembly, k_s and b_s are the stiffness and damping coefficients of the suspension, respectively, k_t and b_t are the stiffness and damping coefficients of the tire, respectively, z_w is wheel displacement, z_b is the body displacement, and h_0 is the initial drop height for impact. This height is used to calculate the velocity at impact, v_i, which combined with z_b and z_w represent the initial conditions of the model.

$$v_i = \sqrt{2gh_0} \tag{1}$$

The equations of motion for the model of Figure 1 are:

$$m_b\ddot{z}_b = k_s(z_w - z_b) + b_s(\dot{z}_w - \dot{z}_b) - m_b g \tag{2}$$

$$m_w\ddot{z}_w = -k_s(z_w - z_b) - b_s(\dot{z}_w - \dot{z}_b) + k_t z_w + b_t\dot{z}_w - m_w g \tag{3}$$

These coupled linear second-order equations are recast as state space equations that can be solved using MATLAB's ode23s solver given numerical parameters.

Test Setup

A test sled was fabricated using 2.5 x 2.5 cm (1x1 inch) 16-gauge square steel tubing. The sled attaches to intermediate rails at two locations on both sides of the fixture for a total of four mounting locations. The intermediate rails each slide on two linear bearings, four bearings total, which ride on bearing rails that are attached to outer fixture supports. This setup constrains the sled to translate only in the vertical direction.

The normal load is set by adding weights to each side of the test sled. The weights are placed onto a threaded rod and secured using a threaded nut. The masses of the weights used range from 1 kg to 15 kg. The mass of the wheel, m_w, is 2.3 kg and the mass of the body, m_b, including the fork assembly and additional weights, is 53.2 kg for a combined normal load for this test of 544.5 N which represents an 85 kg rider and an 11 kg bicycle with 58% front 42% rear weight distribution (as if descending a ledge).

A winch was installed to the outer fixture support to facilitate lifting the loaded sled to the desired drop height. Once at the desired height the sled was then connected to a snap shackle release and the rope from the winch was removed. The snap shackle opens rapidly to release the sled. The tire then lands on the bottom of the fixture where a removable insert was secured to allow the use of different frictional surfaces; 3M® Safety Walk was used for all data presented in this paper.

The test sled was designed to mimic a common impact event that a mountain bike and rider may experience while descending a trail. As such, the fork axis is aligned with the sled vertical axis. The sled is released from a nominal height of 95 mm. (By releasing from this height, the stroke of mid-priced coil fork used in this study achieves 80% of its available 120 mm of travel and the tire

©2023 Schoeneck, N., Sadauckas, J. & Nagurka, M. published by TU Delft OPEN on behalf of the authors.
ISSN: 2667-2812

 https://dx.doi.org/10.59490/65ea2e57849efaac633d9392

is displaced 40% of its maximum displacement.) After release, the tire fork system generally exhibits one bounce in which the tire leaves the ground in rebound and the fork experiences a topping event before regaining ground contact.

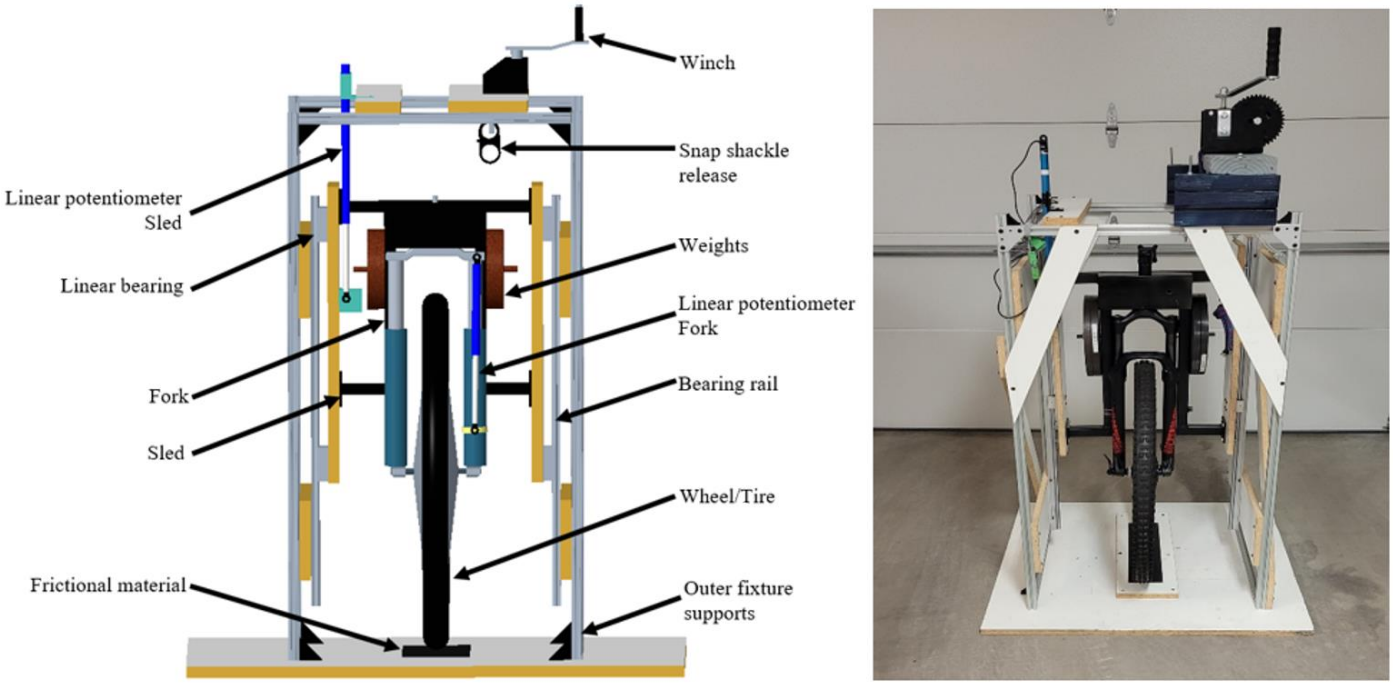


Figure 2. Test sled schematic (left) and actual test sled with front suspension subsystem installed (right).

A linear potentiometer is used to measure sled displacement with respect to the outer fixture support and zeroed when the sled is lifted such that the tire tread just contacts the ground. A second linear potentiometer is mounted on the fork to measure displacement of the fork and is zeroed with the fork at resting equilibrium with no weight. Tire displacement is calculated as the difference between the readings of the two potentiometers. The specifications of the potentiometers and data logger are as follows:

Linear potentiometers
- Range: 275 mm (Sled); 150 mm (Fork)
- Make: Penny & Giles
- Model: SLS190/0275/C/66/01/N (Sled); SLS190/0150/C/66/01/N (Fork)

Data logger
- Make: imc Dataworks
- Model: CRONOS-XT logger with uni-8 amplifier

Data is sampled at 1 kHz with an antialiasing filter applied and a 400 Hz roll-off frequency.

Parameter Identification and Simulation

Spring

The mountain bike telescopic front suspension was installed on a shock dynamometer to experimentally determine the stiffness and damping of the suspension. The suspension was stroked to the middle of the available travel before it was exercised. During the spring dynamometer test the fork was first compressed and then pulled in extension past both the main spring and top out spring. In this way, the top out spring rate was determined as the fork returned to zero on the compression stroke.

©2023 Schoeneck, N., Sadauckas, J. & Nagurka, M. published by TU Delft OPEN on behalf of the authors.

ISSN: 2667-2812

https://dx.doi.org/10.59490/65ea2e57849efaac633d9392

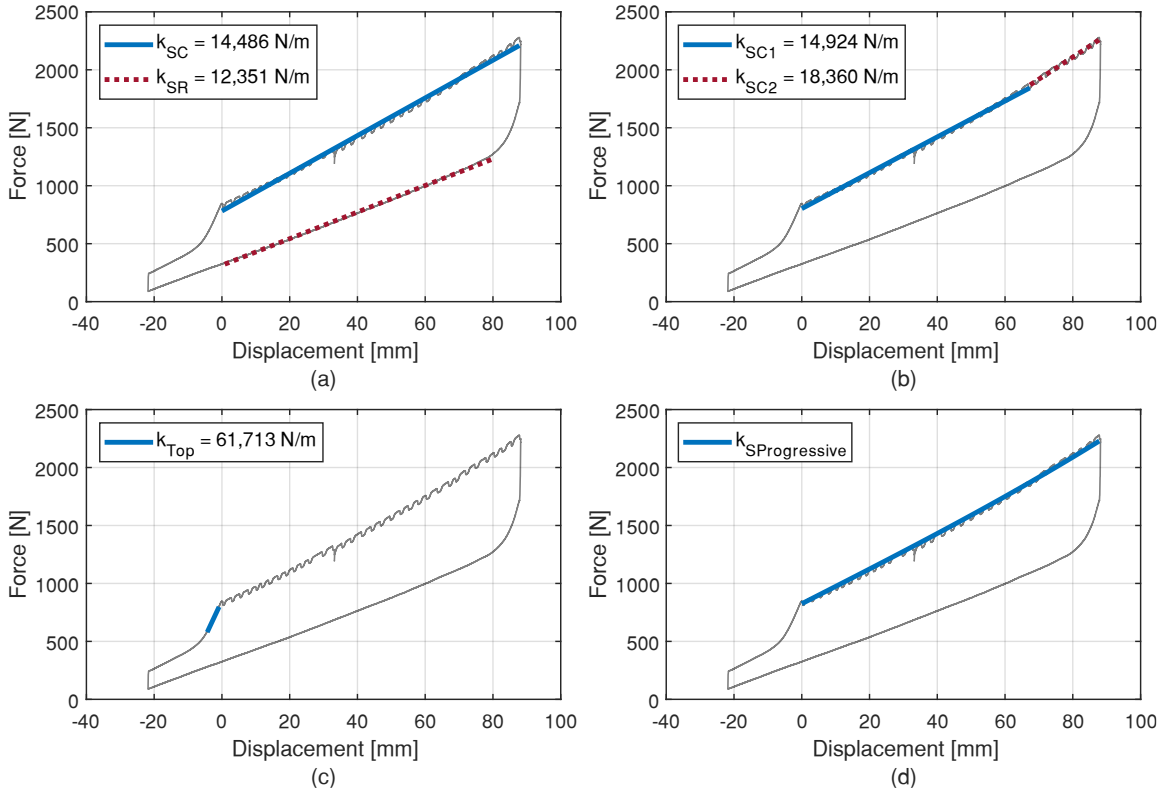


Figure 3. (a) Linear fit of fork compression and rebound spring rates, (b) bi-linear fit of fork compression spring rate, (c) linear fit of fork top out spring rate, (d) progressive fit of compression spring rate.

Figure 3 displays four different approaches for fitting the force versus displacement data to determine the fork spring rate. The fork displacement zero point is taken with the fork hanging in its equilibrium position with no external loads applied. From this reference point, the top out spring is exercised when the displacement is negative, and the main spring is exercised when the displacement is positive. Figure 3a shows the characteristic for the main spring compression (denoted subscript SC). and spring rebound (denoted subscript SR). The top curve is the compression stroke, and the bottom curve is the rebound stroke. Figure 3b depicts the compression stiffness with a bi-linear fit given by the piecewise function (with subscripts SC1 and SC2 for spring compression 1 and 2, respectively):

$$k_s = \begin{cases} k_{sc1}, & 0 < d_s < 67 \text{ mm} \\ k_{sc2}, & d_s \geq 67 \text{ mm} \end{cases} \tag{4}$$

Figure 3c indicates the characteristic stiffness of the top out spring. The slope is evident only when the suspension is extended, unloading the main spring as if the suspension is approaching a topping event.

Figure 3d shows the characteristic with a progressive fit to the compression stroke. To prevent bottoming events, a progressive suspension stiffness is often desirable for mountain bike suspensions. Air springs are used widely in mountain bikes as they allow the rider to adjust the spring rate and preload by adding air pressure and volume spacers. The suspension tested in this paper is a coil spring that exhibits a slightly progressive trend due to air trapped in both the spring and damper sides of the fork. The quarter car model is used to perform a parameterization study of the fork stiffness based on the values described above. For these first seven simulations (denoted S1 through S7), focused on spring parametrization, an average value for the fork damping coefficient and singular baseline (impact-only) values for the tire damping and spring rates were used (Sadauckas, 2023). The fork damping coefficient and tire parameters are investigated and discussed later in the paper.

©2023 Schoeneck, N., Sadauckas, J. & Nagurka, M. published by TU Delft OPEN on behalf of the authors.

ISSN: 2667-2812

https://dx.doi.org/10.59490/65ea2e57849efaac633d9392

Figure 4 shows the time histories of sled displacement, fork displacement, and tire displacement plotted for each simulation (blue lines) compared to the data measured on the sled (black dash-dot line). The tire impacts the ground at time zero and the fork and the tire compress as the sled continues to travel down on the bearing rails after impact. After the initial impact is absorbed by the system at Peak 1, the tire and fork begin to rebound with the tire eventually leaving the ground around 0.2s into the test. As the tire leaves the ground the suspension has a topping event after which the fork is fully extended (zero fork displacement). The sled then transitions back into freefall and the tire again impacts the ground leading to Peak 2 after which it remains in contact with the ground as the sled oscillates through Valley 1 and Peak 3 before eventually coming to rest.

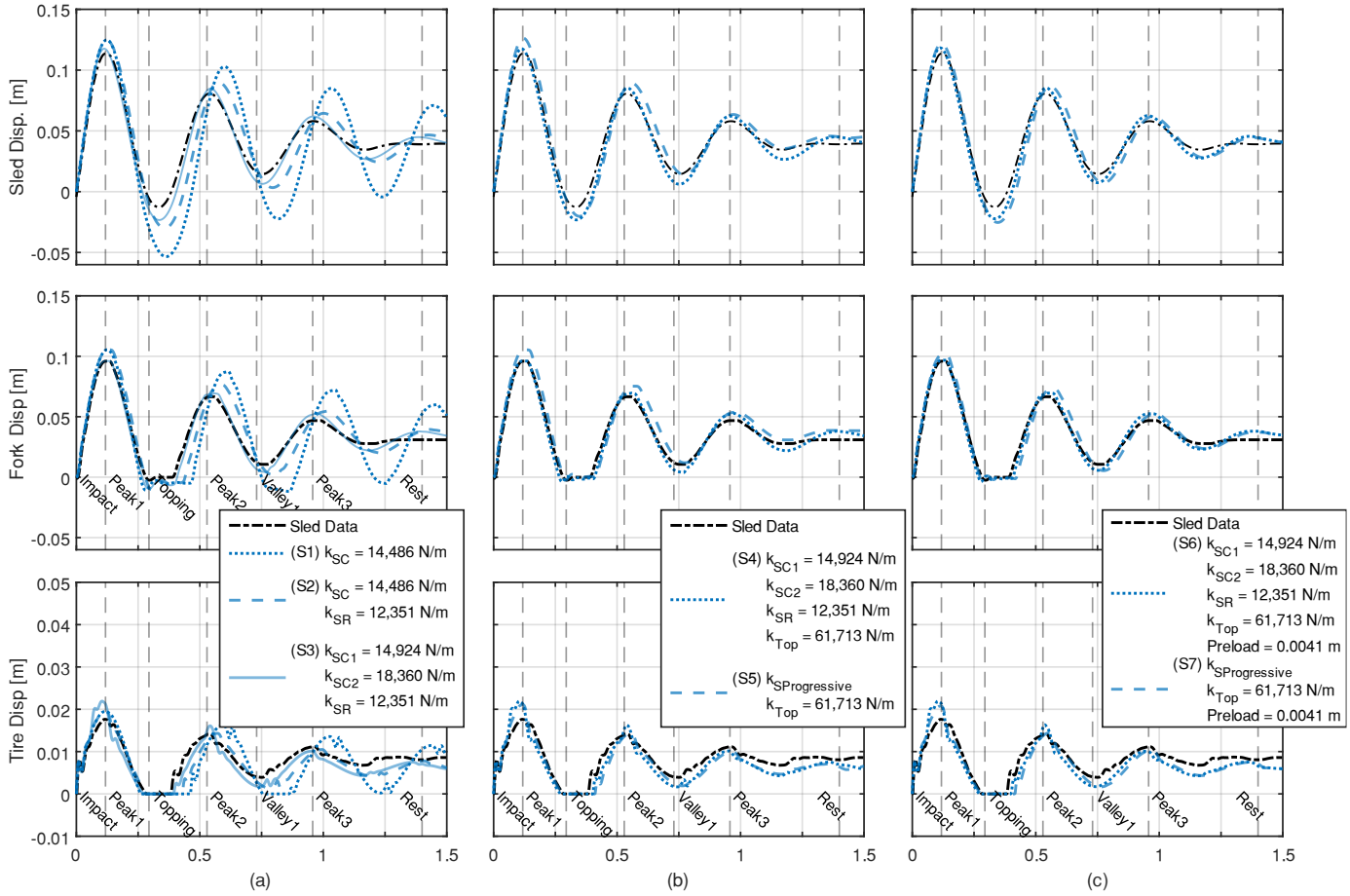


Figure 4. Mountain bike quarter car simulation results varying fork spring parameters overlaid on sled, fork, and tire drop test displacement data for (a) linear and bi-linear stiffnesses, (b) bi-linear and progressive stiffnesses both including a top out spring, (c) bi-linear and progressive stiffness with top out spring and preload force.

Examining Figure 4a, the first simulation, S1 (blue dotted line) models the fork spring stiffness using a single linear parameter for rebound and compression. When compared to the sled test data (black dash-dotted line), this simulation exhibits the most overshoot in the sled, fork, and tire displacement. This subsystem model does not come to rest and there is poor correlation of the top out event at Valley 1. Simulation S2, shown by the long-dashed blue line, uses separate compression and rebound spring rates resulting in a slightly more accurate subsystem model. Overshoot is reduced and the system damps more quickly. Simulation S3 (solid blue line) which contains the bi-linear compression spring rate (solid line) starts to match the test sled data more closely at Peaks 1, 2, and 3.

In Figure 4b, the top out spring is introduced to the quarter car model in combination with the separate compression and rebound spring rates from Figure 3a and the progressive spring rate fit shown previously in Figure 3d. Both simulations (S4 and S5) suggest the top-out spring greatly improves the model fidelity around the initial fork topping event (between Peaks 1 and 2). The return of tire to ground also changes subtly prior to Peak 2.

©2023 Schoeneck, N., Sadauckas, J. & Nagurka, M. published by TU Delft OPEN on behalf of the authors.

ISSN: 2667-2812

https://dx.doi.org/10.59490/65ea2e57849efaac633d9392

Finally, the fork spring stiffness simulation results (S6 & S7) shown in Figure 4c include a preload force in the quarter car model with the same spring stiffness values and top out spring used in the previous plot. The results suggest additional improvements in following the experimental data.

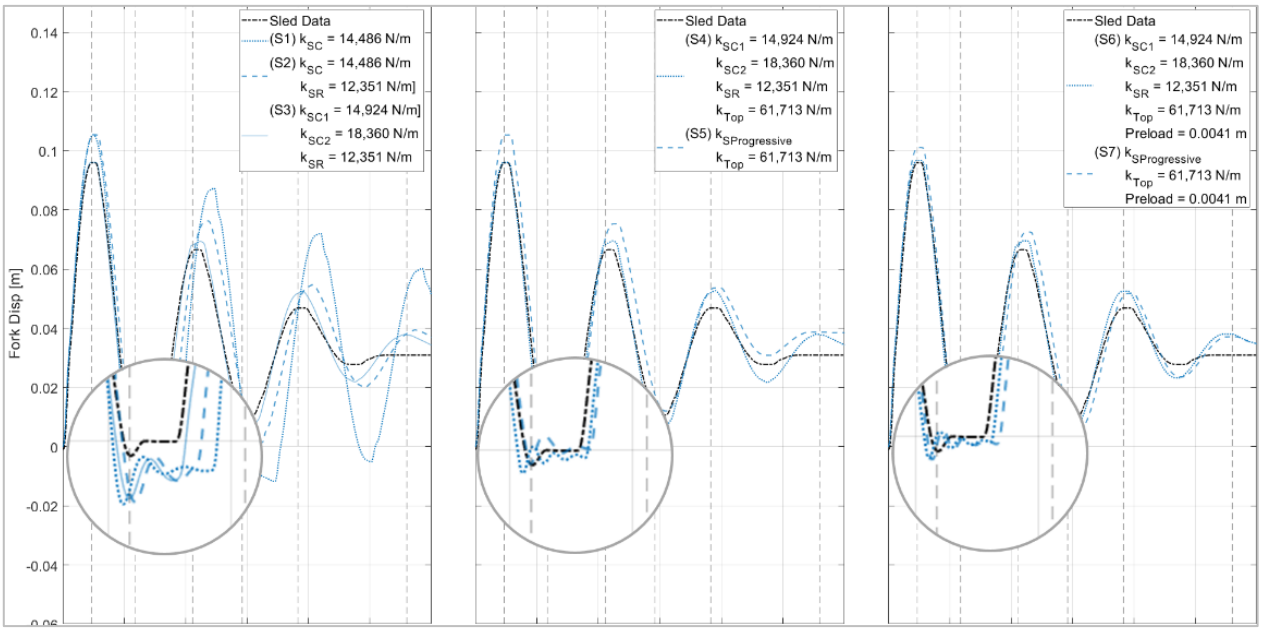


Figure 5. Mountain bike quarter car simulation results showing fork displacement with emphasis on topping event with various fork spring parameters.

Figure 5, focused on fork displacement, shows the benefits of increased fidelity of the fork stiffness parameterization (S2 & S3) as well as a top out spring (S4 & S5) and fork preload (S6 & S7) in greater detail. There is less overshoot in fork displacements at Peaks 1, 2, and 3 with the addition of the top out spring and preload parameters. The results shown in the zoomed area (circle) of the middle and right plots demonstrate the benefits of including the top out stiffness and preload in matching the topping event.

Damper

Figure 6 shows the fork damping force versus stroking velocity measured on the suspension dynamometer. From this data the damping coefficient can be approximated. The friction component can also be derived from the damping curves as evident by non-zero force values at the velocity origin. Various linear fits of damping coefficient for compression and rebound are shown. A single linear damping coefficient (green dotted line) was found taking an average of the compression and rebound coefficients. This single term average is often used in literature and textbooks. In this case it misses various nuances of the fork system measurements. As noted previously, this average damping value was used as the fork damping coefficient for all simulations in the fork spring rate parameterization study above.

©2023 Schoeneck, N., Sadauckas, J. & Nagurka, M. published by TU Delft OPEN on behalf of the authors.

ISSN: 2667-2812

https://dx.doi.org/10.59490/65ea2e57849efaac633d9392

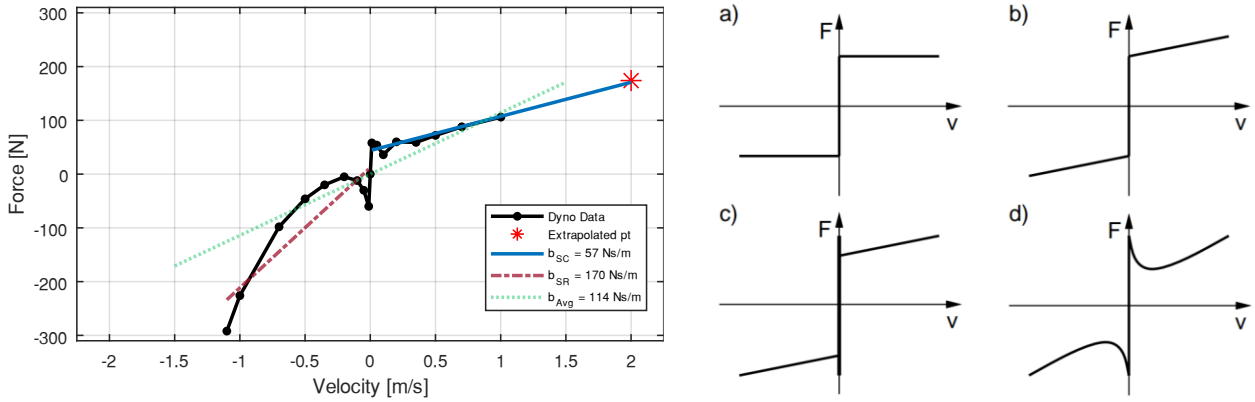


Figure 6. Left: Mountain bike front suspension fork damper peak force versus velocity. Dynamometer measurements are shown as black points, average linear fit shown as green dashed line, and bi-linear fits for compression and rebound blue solid and red dashed, respectively. Right: Force vs. velocity plots for four different friction models (Olsson, 1998).

Four friction models are shown in the right side of Figure 6: plot a) displays a Coulomb friction model, plot b) combines a Coulomb and viscous model, plot c) adds stiction to the Coulomb and viscous model, and plot d) shows a more realistic nonlinear friction model that captures the essence of plot c) (Olsson, 1998). A comparison between these friction models to the data collected on the shock dynamometer is shown for a deeper understanding of the type of friction forces (i.e., Coulomb, viscous, etc.) present in the fork. These classic friction models can be observed in the dynamometer damping data shown on the left of Figure 6. The rebound curve (negative sign convention) mimics the shape of plot d). The front suspension compression damping curve (positive sign convention) displays a similar shape to that in plot b). The ability to identify and model the friction forces acting in the telescopic fork plays an important role in modeling mountain bike longitudinal braking performance (Klug et al, 2019) and modeling impact events as shown in the following simulations.

The quarter car model was used to examine the parameterization of the fork damping. The simulation results for three different damping approximations are shown in Figure 7. The first of these simulations (S8) uses the average fork damping value (dotted red line), the second (S9) adopts the bi-linear approach with a separate fork damping coefficient for compression and for rebound (dashed red line), and the third simulation (S10) uses a lookup table (solid red line).

©2023 Schoeneck, N., Sadauckas, J. & Nagurka, M. published by TU Delft OPEN on behalf of the authors.

ISSN: 2667-2812

https://dx.doi.org/10.59490/65ea2e57849efaac633d9392

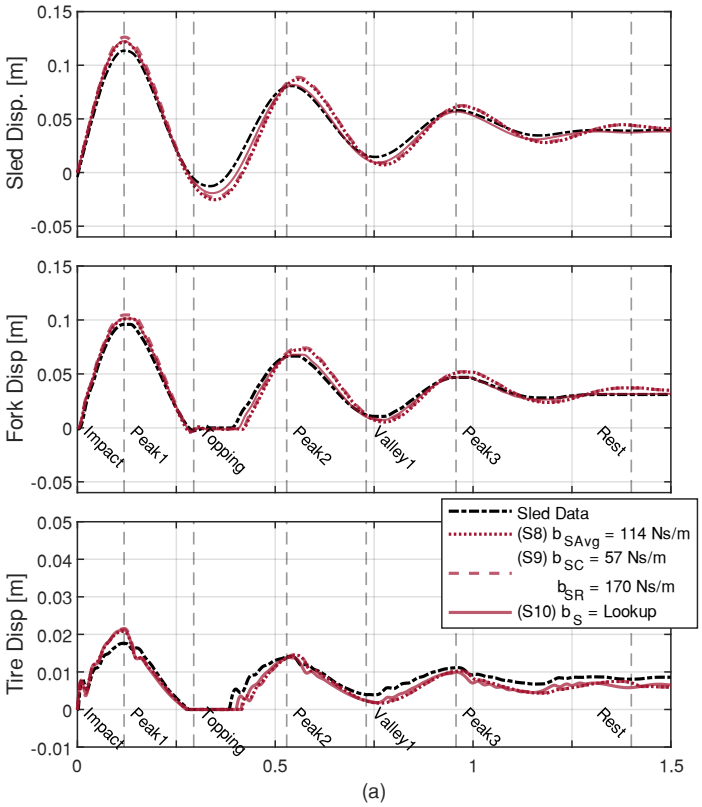


Figure 7. Quarter car model simulation results with varying fork damping and inclusion of fork friction.

Figure 7 suggests subtle differences in the displacement responses of the subsystem comparing the average fork damping (S8) and bi-linear damper (S9) simulations. The lookup table for damping which includes the frictional characteristics (S10) provides improvement in modeling the fork top out event and the displacement of the subsystem as it comes to a rest.

Figure 8 shows a more detailed view of the fork displacement from the fork damping parameterization study. The frictional force in the simulation with the fork damping coefficient lookup table (S10) reduces the ringing during the top out event (zoomed circle at left) and aides in better predicting the resting displacement (zoomed circle at right). In addition, there are improvements in the match of displacement responses at Peak 2, Valley 1 and Peak 3.

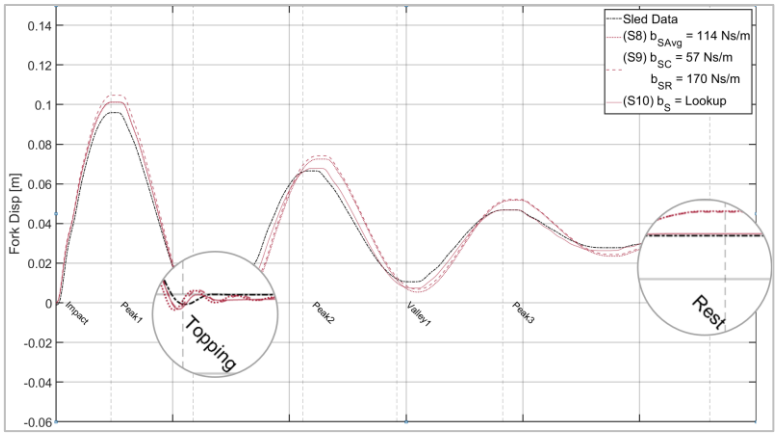


Figure 8. Fork displacement from Figure 7 with emphasis on top out and system coming to rest.

©2023 Schoeneck, N., Sadauckas, J. & Nagurka, M. published by TU Delft OPEN on behalf of the authors.
ISSN: 2667-2812

 https://dx.doi.org/10.59490/65ea2e57849efaac633d9392

Tire

The tire stiffness and damping coefficients used here are based on impact and measured using a coefficient of restitution method (Sadauckas, 2023). This method can be used to identify a dynamic tire stiffness and damping coefficient for both impact and in-contact oscillatory behavior. For these simulations the tire stiffness and damping can be divided into two piece-wise regions based on the system response. The impact stiffness and damping are used when the subsystem is in free fall through the initial impact event, i.e., Peak 1 through topping. The in-contact values are then applied in the region when the tire is in constant contact with the ground and may still be oscillating. Previous studies found the tire stiffness by applying a force to the tire and measuring the displacement. This tire stiffness value was used in the parameterization study as a comparison to the coefficient of restitution approach. (Dressel, 2020).

The quarter car model was utilized for a tire parameterization study. Four different simulations were performed. The tire parameter simulations included the progressive fork spring rate, fork top out spring rate, fork preload, and the use of the lookup table for the fork damping force. The first of the tire parameterization simulations (S11) used the tire impact dynamic stiffness and damping coefficient, the second (S12) used both the impact and in-contact values, the third simulation (S13) used the impact stiffness but with tire damping removed from the model (to test the hypothesis of some automotive papers), and the fourth tire simulation (S14) used the static tire stiffness (which is nearly 30% lower than its dynamic stiffness) with the impact dynamic damping coefficient.

Figure 9 shows the simulation results overlaid on the experimental data from the test sled. The first two simulations (S11 & S12) produce similar tire displacement during the impact region of the model. There is a noticeable improvement in predicting the resting displacement when the in-contact tire spring rate and damping coefficient are included (S12, green dashed). The simulation with no tire damping (S13, green solid) exhibits slight ringing seen in the tire displacement and in the fork displacement. Using the tire static spring rate (S14, green dash-dot) predicts large overshoots in tire displacement at Peaks 1, 2, and 3. In addition to the overshoots in the tire displacement, the subsystem response peaks are adversely affected regarding phasing and amplitude and the subsystem continues to oscillate.

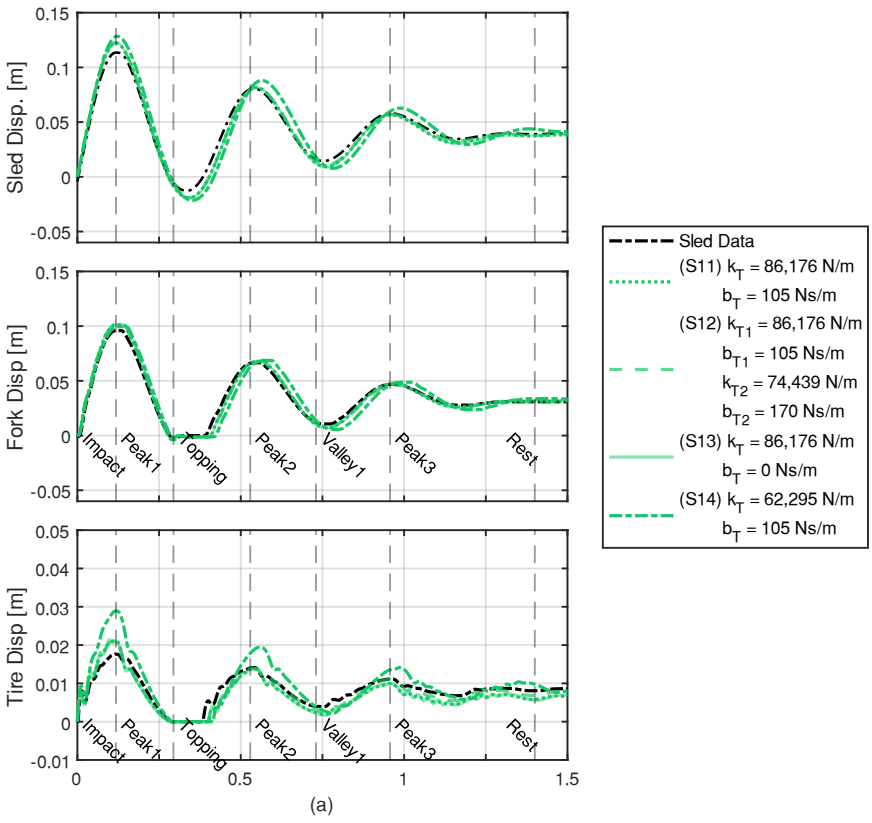


Figure 9. Quarter car model simulation results with varying tire spring rates and damping coefficients.

©2023 Schoeneck, N., Sadauckas, J. & Nagurka, M. published by TU Delft OPEN on behalf of the authors.

ISSN: 2667-2812

https://dx.doi.org/10.59490/65ea2e57849efaac633d9392

Discussion

The displacement of the peaks and valley from the parameter sweep simulations varying model complexity were compared to the test sled data and the differences in amplitude were calculated. The results of the amplitude errors are shown in Figure 10.

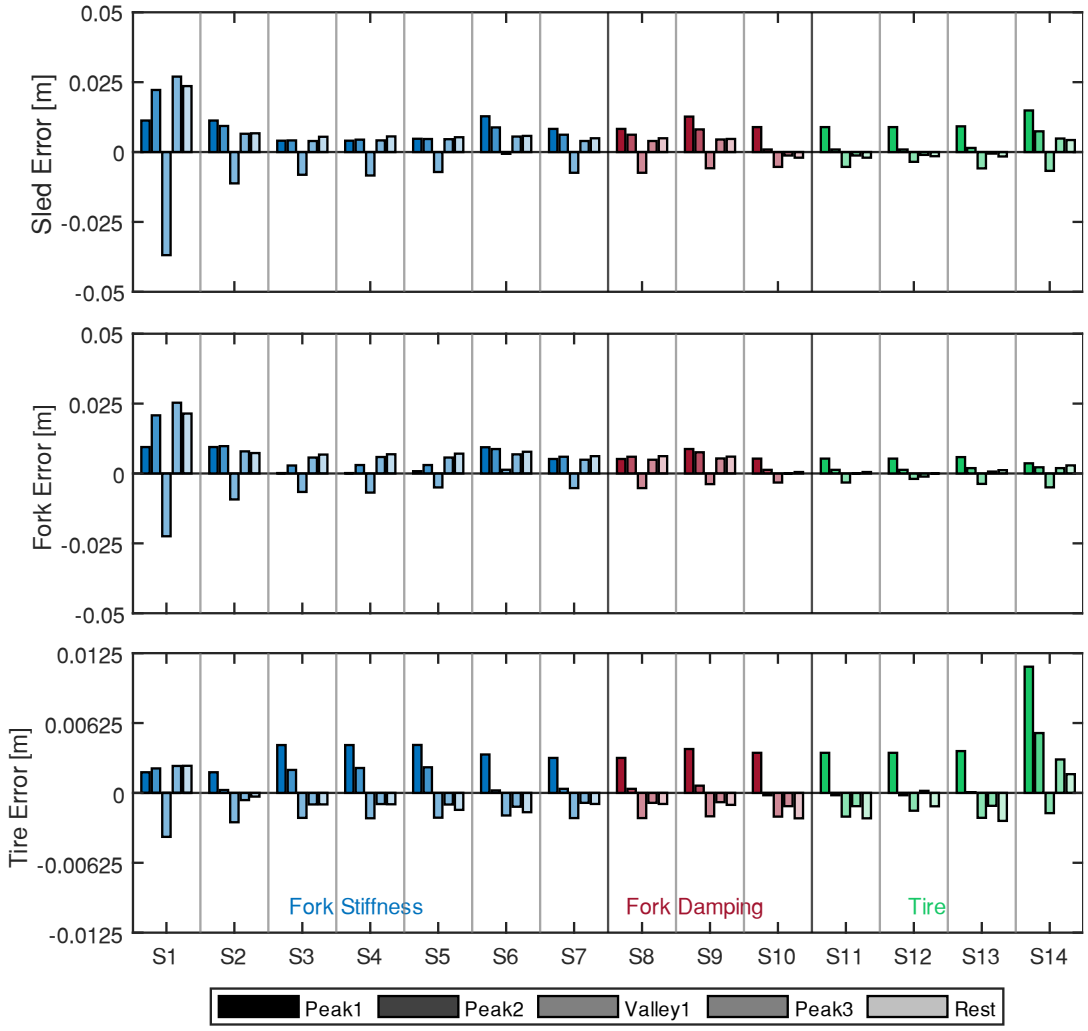


Figure 10. Sled, fork, and tire displacement amplitude errors. Each bar represents the error in predicting a key peak or valley in the response, with parameterization effects of fork stiffness (blue), damping (red), and tire parameterization (green) grouped accordingly. Positive error values overpredict the displacement; negative error values underpredict the displacement.

Regarding the fork spring parameterization, simulation S1 with a single linear rate for fork and tire spring rate and damping coefficients showed the most sled and fork displacement errors with displacement overshoot exceeding 25 mm in both directions. Incrementing across the fork spring rate simulations (S1 through S7) the sled and fork displacement errors decrease while the tire displacement errors increase as the parameterization fidelity of the fork spring stiffness increases. This highlights the tradeoffs of the different parameters within the subsystem. The incremental additions to fork stiffness (via the progressive rate and preload term) increase the force applied to the tire resulting in overshoot. This is most notable on the initial impact (see Peak 1 for simulations S3 through S7).

As for the fork damping coefficient parameterization study (S8 through S10), the largest reduction in error was seen in simulation S10 with the introduction of the fork damping lookup table (and frictional terms). The most significant improvement of this parameterization was seen in the fork and sled displacement error on Peak 2 and as the subsystem comes to rest.

©2023 Schoeneck, N., Sadauckas, J. & Nagurka, M. published by TU Delft OPEN on behalf of the authors.

ISSN: 2667-2812

Finally, in comparing tire parameterization (S11 through S14), simulation S14 the static tire spring rate (with nominal impact tire damping) exhibited the largest tire displacement error. The amplitude error at Peak 1 was four times higher than for the other three tire parameterizations. The increased tire error also has a negative effect on sled displacement error. Tire amplitude error is lower when using both the impact and in-contact dynamic spring rates (S12) and damping coefficients. The improvement was most notable when the tire remained in contact with the ground with amplitude error ranging from 0.1 mm to 1.5 mm compared to the error using only the impact dynamic stiffness and damping coefficient (S11) ranged from 1.0 mm to 2.2 mm. The exclusion of tire damping (S13) increased the tire error at Valley 1, Peak 3, and at rest and had a negative influence on the fork and sled displacements.

Conclusion

In this paper, the mountain bike telescopic front suspension subsystem was investigated using a quarter car model. Several methods were applied to identify the parameters for both the fork and tire ranging from linear, bi-linear, to nonlinear. Additionally, the model was extended to include other forces from a top out spring, preload forces, and friction forces in the fork. Predictions of fork displacement were more accurate using a bi-linear or progressive spring rate. Additionally, it was shown that including a top out spring in the model can have a positive effect for topping events and may be omitted if the subsystem being modeled does not leave the ground (or if the actual system being modelled is not equipped with this feature). The effects of friction on the fork were studied and shown to play an important role in modeling the fork displacement at low velocities as the subsystem is coming to rest and at topping events and helps to attenuate earlier peak overshoots. Tire stiffness and damping parameters were also studied. The model demonstrates that the use of an impact tire stiffness more closely matches the drop sled test data compared to simulations using the tire stiffness measured statically which produced large displacement amplitude error. Neglecting tire damping forces in the quarter car model resulted in an increase in displacement error and model stability of both the tire and the entire suspension subsystem response.

The lightweight, low load (relative to automotive, aerospace, or agriculture tires), and aggressive use case of mountain bikes, in conjunction with the sophistication of their suspension systems, make them particularly interesting to study in terms of in-plane dynamics. This paper builds on previous tire-only measurement and simulation studies by including measurement, modeling, and simulation of the front fork plus tire front suspension subsystem to quantify tradeoffs in the model parameterization for an impact use case.

Future work may consider adopting this subsystem-focused approach to parameter identification, model sensitivity analysis, and targeted parameterization based on use case prior to making broad assumptions about those constitutive elements within a larger, more complex vehicle or system model. This study was limited to a relatively simple coil sprung front suspension fork and can be extended to more performance-oriented fork specifications, settings, alternate tires, inflation pressures, test boundary conditions (such as drop height, rocks, or other terrain under the tire) and even a rolling wheel on a drum, treadmill, or otherwise.

References

Carabias Acosta, E., Castillo Aguilar, J.J., Cabrera Carrillo, J. A., Velasco Garcia, J.M., Fernandez, J.P., & Alcazar Vargas, M.G. (2020). Modeling of Tire Vertical Behavior Using a Test Bench. *IEEE Access, 8*, pp. 106531-106541.

Dixon, J.C. & Mech, F.I. (2007). *The Shock Absorber Handbook.* West Sussex: John Wiley & Sons, Ltd.

Dressel, A., & Sadauckas, J. (2020). Characterization and modeling of various sized mountain bike tires and the effects of tire tread knobs and inflation pressure. *Applied Sciences*, 10(9), 3156. https://doi.org/10.3390/app10093156.

Klug, S., Moia, A., & Schnabel, F. (2019). Influence of damper control on traction and wheelie of a full suspension eBike with anti-squat geometry. *Bicycle and Motorcycle Dynamics.* Padova.

Levitt, J.A., & Zorka, N.G. (1991). The Influence of Tire Damping in Quarter Car Active Suspension Models. *Journal of Dynamic Systems, Measurement, and Control*, 134-137.

Maher, D. & Young, P. (2011). An insight into linear quarter car model accuracy. *Vehicle System Dynamics, 49*(3), pp. 463-480.

Rill, G. & Arrieta Castro, A. (2020). *Road Vehicle Dynamics* (2nd ed). Boca Raton: CRC Press.

Sadauckas, J., Schoeneck, N., & Nagurka, M. (2023) Radial Stiffness and Damping of Mountain Bike Tires Subject to Impact Determined Using the Coefficient of Restitution. Bicycle and Motorcycle Dynamics 2023 Symposium on the Dynamics and Control of Single Track Vehicles 18-20 October 2023, Delft University of Technology The Netherlands.

Lot, R., & Sadauckas, J. (2021). *Motorcycle Design Vehicle Dynamics Concepts and Applications*

Olsson, H., Astrom, K., Canudas de Wit, C., Gafvert, M., & Lischinsky, P. (1998). Friction Models and Friction Compensation. *European Journal of Control, 4*(3), 176-195.

©2023 Schoeneck, N., Sadauckas, J. & Nagurka, M. published by TU Delft OPEN on behalf of the authors.

ISSN: 2667-2812

The Evolving Scholar Vol. 3, 2023 https://dx.doi.org/10.59490/65ba8dea64053c783f97f5b7

Bicycle and Motorcycle Dynamics 2023
Symposium on the Dynamics and Control of Single Track Vehicles
18 – 20 October 2023, Delft University of Technology, The Netherlands

Type of the Paper: Conference Paper

Revised

Improvement of Cycling Efficiency for Drivetrains with Elasticity

[version 2; peer reviewed]

Willem den Boer

Huron Cycling LLC, Brighton, Michigan, USA; willem@huroncycling.com, ORCID 0000-0001-9290-8320

Name of Editor: Jason Moore
First published: 07/09/2023
Last published: 27/03/2024
Citation: Den Boer, W. (2024). Improvement of Cycling Efficiency for Drivetrains with Elasticity [version 2; peer reviewed]. The Evolving Scholar - BMD 2023, 5th Edition.
This work is licensed under a Creative Commons Attribution License (CC-BY).

Abstract:

Test and modeling results are reported on a bicycle crankset with limited elasticity. Like record-breaking running shoes, the crank set has spring action which mitigates the effect of the dead zone during the pedal stroke. Fiber composite leaf springs are inserted inside the hollow carbon crank arms. The crank arms are not directly attached to the crank axle. Instead, sleeve bearings allow the crank arms to rotate by up to about five degrees relative to the crank axle. The rotation is counteracted by the springs and is proportional to applied torque at the pedals. The novel crank set and a conventional crank set with forged aluminum crank arms were both tested on a stationary bike. The ratio of effective speed to input power is used as a measure of cycling efficiency. Depending on the difference in torque during the downstroke and in the dead zone, this ratio is typically a few percent higher for the novel crankset than for a conventional crankset. Multiple tests show efficiency improvements in the range of 1 to 4% at power levels of 200 W and cadence of 71 rpm with average of around 2%. Details of a test with 2.3 % improvement are presented. This would translate, for example, into a one minute advantage in a 45 minute time trial.

In an attempt to understand the test results computer modeling of bicycle speed and crank arm angular velocity vs. time was performed for non-elastic and and elastic crank arms. It is difficult to explain the test results with computer modeling unless it is assumed that conventional crank sets introduce energy losses in the drivetrain from twisting of the crank arms and flexing of the bicycle frame under load at the pedals and that these energy losses are reduced for the crank set with built-in elasticity.

Keywords: Cycling Efficiency, Bicycle Drivetrain, Bicycle Crankset

©2023 den Boer, W., published by TU Delft OPEN on behalf of the authors.
ISSN: 2667-2812

 http://dx.doi.org/10.59490/65ba8dea64053c783f97f5b7

Introduction

It is well known that carbon fiber plates in running shoes provide a propulsive sensation which helps improve speed. Several brands of shoes have been using this technology to add a degree of elasticity in their state-of-the-art products. This has led to multiple world records in road and track running in recent years.

In the drivetrain of bicycles a limited degree of elasticity can be built in as well with beneficial effects, for example in the spider of the crank set (Hamamoto, 2019) or in the crank arms (den Boer, 2019-1 and Bastianelli *et al*, 2019). In figure 1 the method we adopted is shown. Fiber composite leaf springs are inserted inside the hollow carbon crank arms. The crank arms are not directly attached to the crank axle. Instead, sleeve bearings allow the crank arms to rotate by up to about five degrees relative to the crank axle. The rotation is counteracted by the leaf springs and is proportional to applied torque at the pedals. Since torque varies from a maximum during the downstroke to a minimum in the dead zone of the pedal stroke, the leaf springs inside the hollow crank arms bend and store energy during the downstroke and release this energy in the dead zone in the direction of rotation to contribute to effective torque.

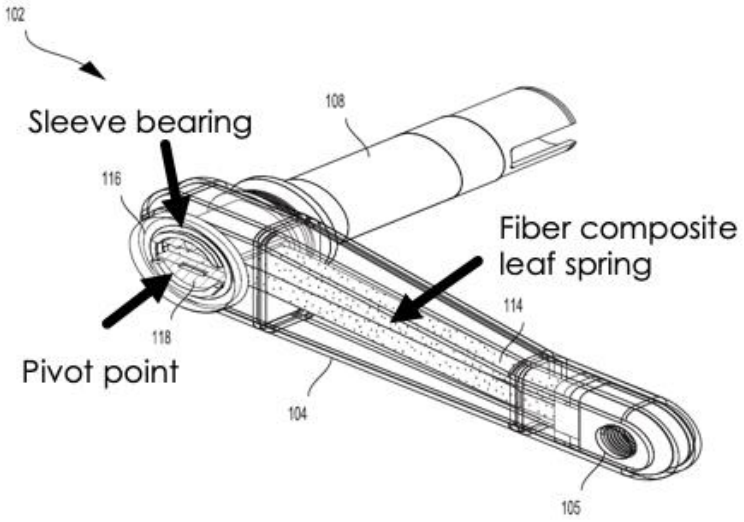


Figure 1. Cutaway view of crank arm and crank axle.

The angle of rotation θ of the crank arms relative to the crank axle is given by:

$$\theta = \frac{\tau}{k} = \frac{P}{\omega k} \tag{1}$$

where τ is the torque from the tangential force F_p applied at the pedals ($\tau = F_p * r$ with r the crank length). P is the applied power and ω is the angular velocity of the crank arms. k is a constant representing the degree of elasticity by bending of the leaf spring. For conventional cranksets without intentional elasticity the k value of the crank arms is high (Fairwheel Bikes, 2021), typically > 5000 Nm, so that θ is small. In our novel crankset k = 1000 Nm, resulting in θ = 0.07 rad (4 degrees) and a deflection at the pedals $D = \theta * r$ = 12.25 mm (0.48 inch) for a tangential force of 400 N (90 pounds). Leaf springs with different k values can be used depending on the power and skill of the cyclist.

Figure 2 shows a photograph of several crank sets based on the principle of internal leaf springs. In earlier prototypes we also used metal compression springs outside the crank arms (Bastianelli *et al*, 2019, www.huroncycling.com) for proof of concept. They are, however, too heavy for practical use.

©2023 den Boer, W. published by TU Delft OPEN on behalf of the authors.

ISSN: 2667-2812

 http://dx.doi.org/10.59490/65ba8dea64053c783f97f5b7



Figure 2. Photograph of crank sets based on the design of figure 1.

Although the principle of operation of limited elasticity in bicycle drivetrains is quite different from that in running shoes, testing shows a benefit in cycling as well.

Testing

The novel crankset was installed on a carbon frame bicycle and compared with a conventional crank set with forged aluminum crank arms, while keeping the gear ratio constant at 36/17 and the slope constant at 3 %. To eliminate wind drag factors and changing conditions the testing was performed indoors on a Tacx Neo smart trainer with two power meters (see figure 3):

1. A Powertap P1 pedal power meter at left and right pedals to measure input power
2. The internal power meter of the Tacx Neo to measure effective speed



Figure 3.Test setup

Data from the smart trainer was displayed and stored on the Tacx app on a smart phone via Bluetooth wireless protocol.
The input power was measured at the pedals, both left and right, with a Powertap P1 pedal-based power meter. This power is representative of the input power applied by the left and right legs to the pedals. The information was displayed and stored on a Garmin Edge 810 head unit via ANT+ wireless protocol.

©2023 den Boer, W. published by TU Delft OPEN on behalf of the authors.

ISSN: 2667-2812

 http://dx.doi.org/10.59490/65ba8dea64053c783f97f5b7

More than twenty sets of tests were performed of 15 or 30 minutes duration each with seven different prototypes of our novel crank set. To verify repeatability of the measurements each set of experiments consisted of at least two tests with the novel crankset with limited elasticity and at least two tests with the conventional crank set made of forged aluminum. All other conditions in a set of tests, such as speed target, slope setting, gear ratio) were kept identical. This allows a direct comparison of the two crank sets. Each test was performed at constant input power of around 200 W.

The speed-power ratio *SPR* was used as a measure for cycling efficiency. Percentage of change *Δ(%)* between the prototype novel crank set and the conventional crank set was defined as:

$$\Delta(\%) = \frac{SPR_{proto} - SPR_{conv}}{SPR_{conv}} \quad (2)$$

where SPR_{proto} and SPR_{conv} are the speed-power ratio for drivetrains with the prototype and conventional crank set, respectively. Table 1 shows the input conditions for a representative test of 15 minutes. The effective speed measured on the Tacx smart trainer is based on the number of rotations of the back wheel.

Table 1. Experimental setup and conditions of typical test

Test equipment	Tacx Neo smart bike trainer
Slope setting	3 %
Power target	200 W
Duration of tests	15 minutes
Gear ratio	36/17
Power meters	Tacx Neo (better than 0.5 % accuracy)
	Powertap P1 left and right pedal power meter
Control conventional crank set	FSA Gossamer BB30 175 mm crank length
Prototype novel crank set	Leaf springs with k=1000 Nm 175 mm crank length

The conventional crank set was an FSA Gossamer BB30 unit with forged aluminum crank arms. After the control testing, the conventional crank set was replaced with the novel crank set with embedded leaf springs. The slope on the Tacx Neo was set at 3 % to prevent any freewheeling during the tests. In each test the power was ramped up to 200 W before starting the measurement and was then maintained around 200 W for the remaining time of the test.
Test results for a typical 15 minute test are shown in Table 2. Repeatability of results was within 0.5 % for each crankset and the table shows the average of two identical tests for each crank set.

Table 2. Test results around 200 Watts on Tacx Neo at 3 % slope for 15 minutes

	Conventional crank set	Novel crank set
Average Speed Tacx (km/h)	19.4	19.4
Average Cadence Tacx (rpm)	71	71
Distance Tacx (km)	4.865	4.865
Average Power Powertap P1 (Watts)	200.5	196
Energy Powertap P1 (kJoule)	180.5	176.5

As seen in Table 2, for the novel crank set the speed-power ratio is higher than for the conventional crank set. The difference *Δ(%)*, as defined in equation (2) is 2.3 %. In other words: With the novel crankset the cyclist can go faster using the same power or maintain the same speed while exerting less power. This is confirmed by the energy in kJoule comparison, which gives the same percentage difference. It takes less energy to complete the same distance at the same speed for the novel drivetrain.
The twenty sets of experimental data for seven different prototypes with k = 1000 Nm show a range of improvement *Δ(%)* of 1 to 4% as compared to the conventional crankset with forged aluminum crank arms.
The lower power needed to maintain the same speed with the novel crank set may be explained by the reduced force on the pedals during the down stroke at 3 o'clock and 9 o'clock crank angles and the release of stored energy from the springs in the dead zone.

©2023 den Boer, W. published by TU Delft OPEN on behalf of the authors.
ISSN: 2667-2812

 http://dx.doi.org/10.59490/65ba8dea64053c783f97f5b7

A few tests were also performed at constant 200 W power for different cadence levels by changing the gear ratio to 36/19 and 36/15. In the range of 64 to 80 rpm the improvement with the novel drivetrain remains in the same range.
For constant cadence of about 72 rpm but lower power levels of 179 Watts (gear ratio 36/19) we still see similar improvement. When the power is further lowered to 162 Watts (gear ratio 36/21) at 72 rpm on the Tacx trainer, the improvement is reduced. This is to be expected as a result of the reduced force on the pedals and reduced torque on the crank and therefore reduced deflection at the pedals. The test results do not depend on the type of pedal-based power meter: For earlier testing a Garmin Vector power meter for left and right pedals was used with similar results as the Powertap P1.

Modeling

In an attempt to understand the effect of drivetrain elasticity on bicycle speed vs. input power, computer modeling was performed. Figure 4 shows the forces at work and the resulting speed of the bicycle. Torque τ on the pedals $\tau = F_p * r$, where r is the crank length and F_p is the tangential force on the pedal. This results in a force F_{bike} propelling the bicycle. $F_{counter}$ is the counterforce, such as wind drag or gravity going uphill. Torque varies by $\Delta\tau$ between a maximum during the downstroke and a minimum during the dead zone of the pedal stroke. $\Delta\tau$ depends on the rider style, but is typically high, even for skilled cyclists. The novel crank set makes a difference only if $\Delta\tau$ is nonzero, i.e. when the springs are alternatingly storing and releasing energy.

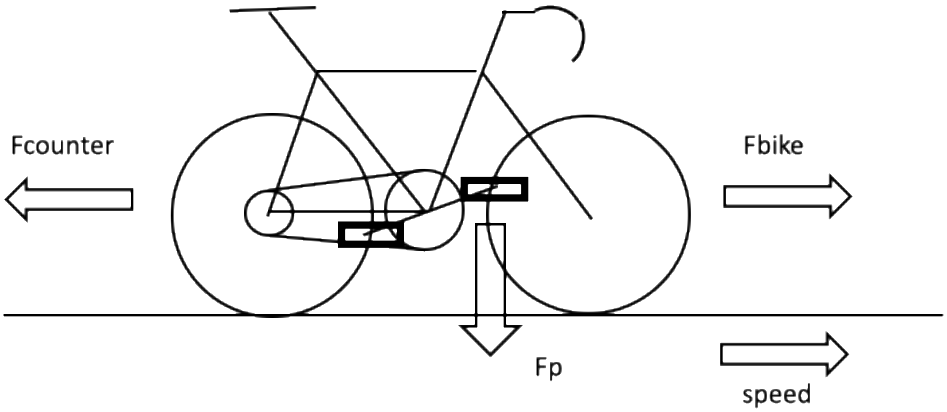


Figure 4. Forces at work on a bicycle

Measurements of torque vs crank angle by us (den Boer, 2019-2) and many power meter manufacturers show that the combined power P applied at left and right pedals is approximately sinusoidal with a frequency twice the crank rotation frequency. In the following P is assumed to vary between a maximum during the downstroke and zero at the dead spot:

$$P = P_0 (\sin \beta)^2 = P_0(1 - \cos(2\beta))/2 \tag{3}$$

where β is the crank angle and P_0 is the maximum power during the downstroke when β = 90 degrees. At $t = 0$ the crank angle is in the vertical position of one of the cranks. The torque τ on the crank axle is:

$$\tau = \frac{P}{\omega} \tag{4}$$

where ω is the angular velocity of the crank arms. The force propelling the bicycle is given by:

$$F_{bike} = \frac{P}{v} \tag{5}$$

The change in speed dv of the bicycle from a starting velocity of v_0 is given by Newton's law:

$$\mathrm{d}v = \frac{F_{net} * \mathrm{d}t}{m} \tag{6}$$

©2023 den Boer, W. published by TU Delft OPEN on behalf of the authors.

ISSN: 2667-2812

 http://dx.doi.org/10.59490/65ba8dea64053c783f97f5b7

where F_{net} is the net force on the bicycle ($F_{net} = F_{bike} - F_{counter}$), dt is the time step in the calculation and m is the combined mass of rider plus bike. In an iterative numerical calculation F_{bike} and v can be calculated vs time. The time step dt can be reduced to ensure it is small enough to not impact the calculated results.

In the following the counterforce is gravity on an uphill slope with angle α:

$$F_{counter} = mgsin\alpha \tag{7}$$

where g is the gravitational acceleration (g = 9.81 m/s^2)

Modeling of conventional drivetrain without elasticity

For a drivetrain without any elasticity the angular velocity of the crank arms and velocity of the bicycle are directly related to each other:

$$v = \omega * R * GR \tag{8}$$

where R is the rear wheel diameter and GR is the gear ratio between front chainring and back cog. The following is an example calculation for the following input parameters:

m = 70 [kg]
v_0 = 1 [m/s]
P_0 = 500 [W] for an average power of 250 W
R = 0.35 [m]
GR = 2
r = 0.175 m
Uphill slope α = 0.1 rad, corresponding to 5.72 degrees or 10 %

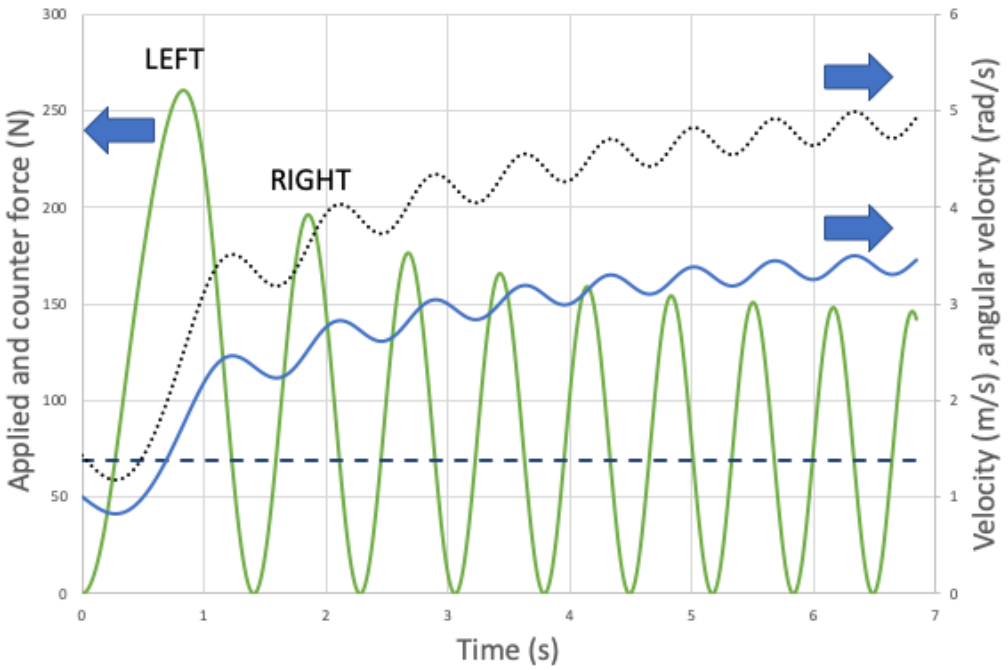


Figure 5. Example of calculated F_{bike}, $F_{counter}$ (dashed line) and velocity and angular velocity (dotted line) vs. time for a drivetrain without elasticity. LEFT and RIGHT represent alternatingly left and right pedal.

©2023 den Boer, W. published by TU Delft OPEN on behalf of the authors.
ISSN: 2667-2812

 http://dx.doi.org/10.59490/65ba8dea64053c783f97f5b7

In figure 5 the results are shown for the applied force F_{bike} to the bike and the resulting velocity of the bike and angular velocity of the cranks vs. time. $F_{counter}$ is constant at 68.5 N. Both F_{bike} and v oscillate. The velocity increases from 1 m/s to an average of about 3.65 m/s when the pace stabilizes. In the final steady state the average F_{bike} and $F_{counter}$ cancel each other out. After the pace settles to its final value, v still oscillates as a result of the varying torque on the crank axle. There is a phase delay of about 45 degrees between the maxima in angular velocity and applied force, because velocity continues to increase as long as net force is positive. This phase delay is well-documented in measurements of angular velocity profiles by power meters (see e.g. www.favero.com) and is the result of the varying torque applied by the rider at the pedals. For a perfectly rigid drivetrain without any elasticity the oscillations in bicycle velocity v are, percentagewise, the same as the oscillation in angular velocity of the crank arm, in agreement with equation (8). The amplitude of the velocity oscillations is proportional to the torque variation $\Delta\tau$ during the pedal stroke and inversely proportional to cadence (i.e. to average angular velocity at constant pace). The dependence on cadence is shown in figure 6 where the velocity oscillations in percent are defined as:

$$\Delta v\ (\%) = \frac{v_{max} - v_{min}}{v_{max} + v_{min}} \tag{9}$$

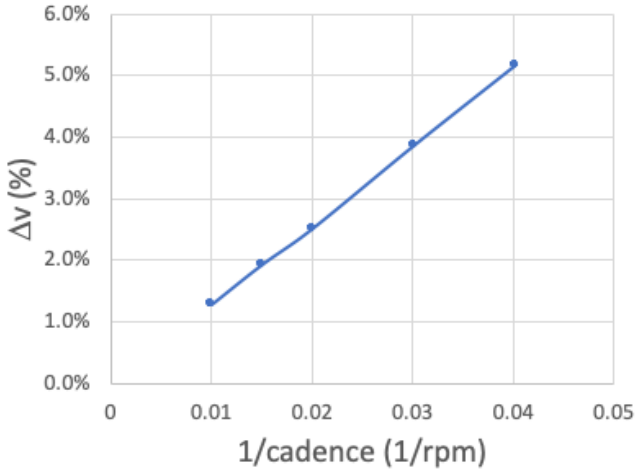


Figure 6. Dependence of velocity oscillations on cadence

It is well-known that the most energy-efficient way to travel is at constant velocity. If the velocity oscillates, the power required to maintain the average final speed of 3.65 m/s (the pace) increases, as a result of the quadratic dependence of kinetic energy on velocity. One of the purposes of the modeling was to find out if these velocity oscillations are reduced when there is elasticity in the drivetrain, since, if this is the case, this could explain the test results at least partially.

Modeling of drivetrain with elasticity

When the bicycle drivetrain has limited spring action, i.e. some degree of elasticity, equation (8) is no longer valid. Even when the gear ratio GR is fixed, the angular velocity of the cranks is not exactly proportional to the speed of the bicycle. In the case of the crank set of figure 1 limited elasticity is achieved by leaf springs inside the hollow crank arms. The angles of the left and right crank arms are no longer the same as the angle of the crank axle. During the downstroke energy is stored in the spring, which is then released in the dead spot in the direction of rotation. This contributes to torque on the crank axle close to the dead spot. The instantaneous applied power to the pedals is no longer equal to the power to propel the bike as a result of the temporary energy storage in the springs. Figure 7 shows the effect of the springs on the crank and crank arm angles

©2023 den Boer, W. published by TU Delft OPEN on behalf of the authors.
ISSN: 2667-2812

 http://dx.doi.org/10.59490/65ba8dea64053c783f97f5b7

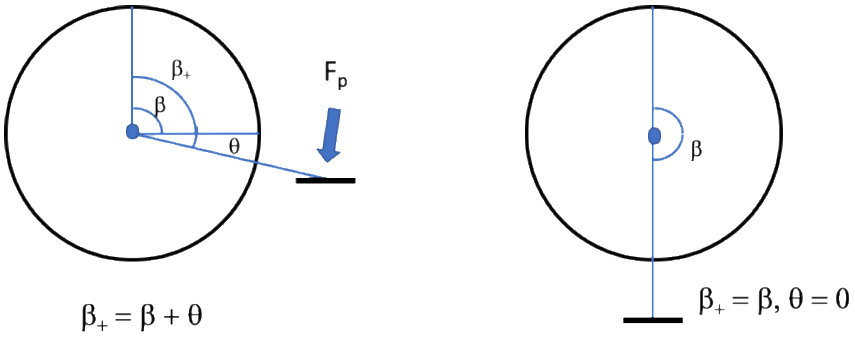


Figure 7. Deflection θ of the crank arm with elasticity, at left during the downstroke, at right in the dead spot

At applied torque τ at the pedals the crank arm deflects by an angle θ:

$$\tau = F_p * r = k\theta \tag{10}$$

where k is the spring constant of the fiber composite leaf spring inside the hollow crank arm and θ is the deflection angle of the crank arm at torque τ. As a result the angle β_+ of the crank arms is different from the angle of the crank axle β and is augmented with the deflection angle θ:

$$\beta_+ = \beta + \theta \tag{11}$$

In the dead spot the leaf spring releases its stored energy and the angle θ decreases to zero if the torque decreases to zero. The angular velocity ω_+ of the crank arm also becomes different from the angular velocity ω of the crank axle:

$$\omega_+ = \frac{d\beta_+}{dt} = \omega + \frac{d\theta}{dt} \tag{12}$$

The tangential pedal force F_p is now:

$$F_p = \frac{P}{\omega_+ r} \tag{13}$$

The energy E_{spring} stored in the spring is given by:

$$E_{spring} = \frac{1}{2} k\theta^2 \tag{14}$$

The power P_{spring} is added to P and is the negative derivative of E_{spring}. It is negative when the spring is loaded, i.e. when θ increases, and positive when the spring relaxes, i.e. when θ decreases:

$$P_{spring} = -\frac{dE_{spring}}{dt} = -k\theta \frac{d\theta}{dt} \tag{15}$$

The force F_{spring} exerted by the spring at the pedals is added to the force applied bythe cyclist:

$$F_{spring} = \frac{P_{spring}}{\omega_+ r} \tag{16}$$

©2023 den Boer, W. published by TU Delft OPEN on behalf of the authors.

ISSN: 2667-2812

 http://dx.doi.org/10.59490/65ba8dea64053c783f97f5b7

Using equations (3), (10), (15) and (16) it can be shown that:

$$F_{spring} = -F_p * \frac{P_0 \sin(2\beta)}{\omega_+ k} \tag{17}$$

The force F_{ax} applied to the crank axle is:

$$F_{ax} = F_p + F_{spring} = F_p(1 - \frac{P_0 \sin(2\beta)}{\omega_+ k}) \tag{18}$$

When only the crank arms have elasticity and the rest of the drivetrain is inelastic, the forward force applied to the bicycle, becomes:

$$F_{bike} = \frac{F_{ax} * r}{R * GR} \tag{19}$$

Very high values of k represent conventional crank sets with little elasticity, when F_{ax} is almost equal to F_p in equation (18). The difference between F_{ax} and F_p is small, even for elastic crank arms with k = 1000 Nm. However, the difference in the angular velocity fluctuations of the cranks is significant. For the conditions of the simulation listed earlier the angular velocity of, alternatingly, the left and right crank arms and the crank axle are actually out of phase with each other, as shown in figure 8. The speed of the bicycle and the crank axle angular velocity still track each other because there is no elasticity in the drivetrain between the crank axle and the rear wheel. F_p and F_{bike} no longer track each other exactly as a result of energy storage in the springs.

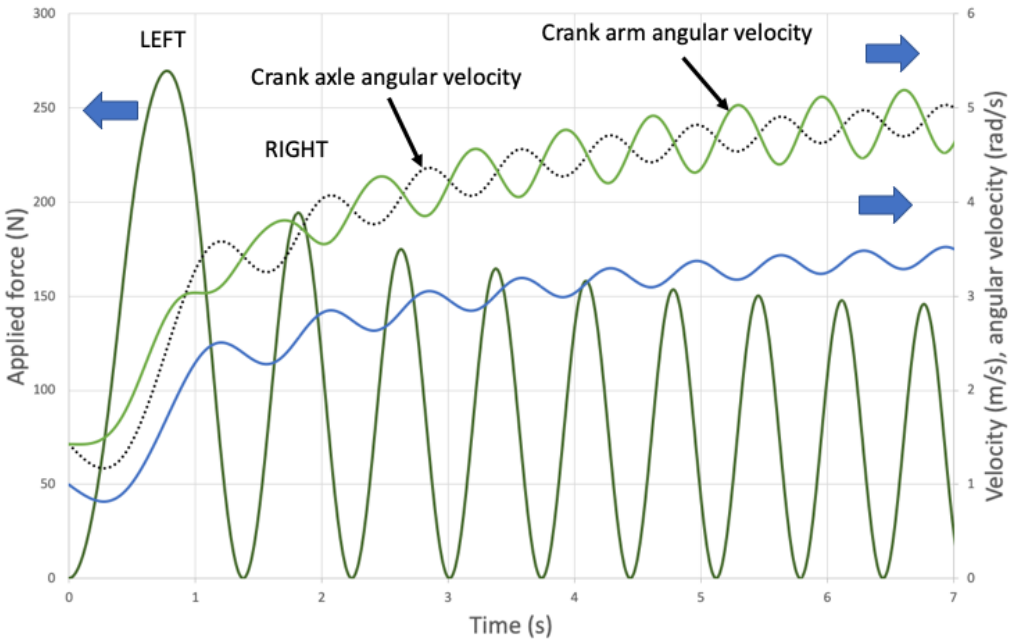


Figure 8. Calculated F_{bike}, velocity and angular velocities vs. time for the drivetrain with elasticity

Calculation of speed-power ratio

The ratio of average speed to input power was calculated at constant pace for inelastic and elastic drivetrains. Although the angular velocity profile of the crank arms changes significantly when elasticity is introduced, as shown in figure 8 , we do not see much change in the speed-power ratio at constant pace, certainly not enough to explain the experimental results. Bicycle velocity oscillations do not change much, when elasticity is introduced into the drivetrain. Therefore they cannot explain the observed test

©2023 den Boer, W. published by TU Delft OPEN on behalf of the authors.

ISSN: 2667-2812

results, unless there are significant delays in the energy release of the leaf springs. This was not considered yet, because the resonance frequency of the springs is much larger than the pedaling frequency. In the case of loss-free crank sets, only a large reduction of oscillations in the bicycle velocity would reduce power input. This large reduction is not seen in the modeling to date. More accurate modeling, considering the delay in reaction to forces on the springs, may give only slightly different results.

Losses in conventional crank sets

The modeling above shows that speed/power ratio does not significantly change when elasticity is introduced in the drivetrain. This is attributed here to the assumption that there are no losses in a conventional crankset. It is, however, well known that during large force on the pedals during the downstroke the bicycle frame can be flexed significantly in a lateral direction (ACT Lab, 2017). In the dead spot the frame flexes back but the energy used in flexing is not returned to effective torque on the crank axle and therefore lost for propulsion. Similarly, the load on the pedal several centimeters away from the crank arm causes twisting of the crank arms (ACT Lab, 2016) during the downstrokes. Again, the energy used for twisting is not recovered in the dead spot and therefore lost.

The strain energy losses from twisting in conventional crank arms can amount to more than 1.6 % at a cadence of 100 rpm (Fairwheel Bikes, 2021) and even more at lower cadence for the same power input. We argue that in our crank set with leaf springs the strain energy on the crank arms is mostly absorbed in the leaf springs before flexing the frame and twisting the crank arms. It is then returned without significant losses in the dead spot. Since the applied force and torque in figures 5 and 8 are not very different, twisting of the crank arms is a more likely cause.

Modeling of drivetrains with loss

To simplify modeling the flexing of the frame and twisting of the crank arms during the downstroke are combined in the degree of deformation D :

$$D = \frac{\tau}{q} \tag{20}$$

where τ is again the torque applied to the crank arms and q is the combined constant for flexing the frame and twisting the crank arms. The energy E_{def} stored during this deformation is, analogous to equation (14), given by:

$$E_{def} = \frac{1}{2} q D^2 \tag{21}$$

The total power applied to propel the bike, P_{bike} , is then:

$$P_{bike} = P + P_{spring} + P_{def} \tag{22}$$

When the strain on the frame and crank arms is reduced approaching the dead spot, P_{def} is zero, because this strain energy is not returned into effective torque on the crank axle:

$$P_{def} = -qD \frac{dD}{dt} \quad \text{if } dD/dt > 0 \tag{23}$$

$$P_{def} = 0 \quad \text{if } dD/dt < 0 \tag{24}$$

This means that P_{def} is always negative or zero and therefore reduces the power applied to propel the bike. We argue that the presence of the springs in the crank arms significantly reduces the flexing of the frame and the twisting of the crank arms, as compared to a conventional crank set. In other words, the deformation of the springs, which is reversible and contributes to propulsion in the dead spot, replaces, at least partially, the deformation of frame and crank arms. Irreversible losses are replaced by reversible losses.

For the conventional crankset $P_{spring} = 0$, so it does not have the elasticity to absorb the same losses. For example, if he deformation energy $½\ qD^2$, when using a conventional crankset is the same as the energy stored in the leaf springs $½k\theta^2$, the model shows that for the parameters listed above the pace at 250 W average input power is reduced from 3.65 to 3.5 m/s, for a 2.8 % reduction in speed/power ratio. In the novel crankset the deformation energy would be, at least partially, replaced by reversible energy loss in the leaf springs, keeping the pace closer to 3.65 m/s and the speed/power ratio higher.

©2023 den Boer, W. published by TU Delft OPEN on behalf of the authors.

ISSN: 2667-2812

 http://dx.doi.org/10.59490/65ba8dea64053c783f97f5b7

Conclusions

Test results have been presented indicating that a bicycle drivetrain with elasticity in the crank arms can improve cycling efficiency, as reported by others as well (Bastianelli *et al*., 2019). For the conditions used in one particular test, an increase of 2.3 % in the speed-power ratio of our bicycle with a crank set including leaf springs was measured. In a 45 minute time trial this would translate into more than one minute advantage, a large improvement compared with the more incremental benefits from aerodynamic optimization.

Our computer modeling to date cannot explain the test results unless energy losses are assumed in conventional crank sets from flexing the bicycle frame and twisting the crank arms during the downstroke. We argue that in a drivetrain with limited elasticity these irreversible losses during the downstroke are reduced and partially converted into reversible losses in the leaf springs. More testing is recommended on elastic drivetrains in general to verify and confirm our test results, as well as measurements of cranksets with elasticity in the spider (Hamamoto, 2019). Elasticity in the drivetrain can also be introduced by using stretchable drive belts instead of chains.

Other explanations than presented here are possible based on more advanced computer modeling. FEA modeling with all the material constants involved may be needed to obtain more quantitative results.

References

ACT Lab (2016), Crank Fatigue Test, https://www.youtube.com/watch?v=7rZ1L6brkNE

ACT Lab (2017), Frame Fatigue with Pedalling Forces Test, https://www.youtube.com/watch?v=8blo6O_KIAs

Bastianelli, B. M., Workman, A. & McGregor, S. (2019, June), Novel Crank with Elastomer Spring Improves Effective Power in Trained Cyclists and Triathletes, *Medicine & Science in Sports & Exercise*, Chicago, 2019, 51(6S):p 942-943, June 2019.

den Boer, W. (2019-1), US Patent 11,142,281, Cycle Crank Assembly, www.huroncycling.com

den Boer, W. (2019-2), White Paper IMPACT power meter August 2019: www.huroncycling.com

Fairwheel Bikes (2021), https://blog.fairwheelbikes.com/reviews-and-testing/road-bike-crank-testing/

Hamamoto, Y. (2019), US Patent 10,450,030, Rotational Apparatus and Bicycle provided with same, www.free-power.jp

©2023 den Boer, W. published by TU Delft OPEN on behalf of the authors.

ISSN: 2667-2812

The Evolving Scholar Vol. 3, 2023

http://dx.doi.org/10.59490/65b6fdb42ae3df4e3454736f

Bicycle and Motorcycle Dynamics 2023
Symposium on the Dynamics and Control of Single Track Vehicles
18–20 October 2023, Delft University of Technology, The Netherlands

Type of the Paper: Conference Paper

Revised

Influence of aerodynamic lift and centre of pressure position in motorcycle stability

[version 2; peer reviewed]

Benjamin E. Gonzalez[1,*], Felipe A. Vasquez[2]

[1] Department of Mechanical Engineering, University of Concepcion, Chile; bgonzalez2018@udec.cl, ORCID 0000-0001-6132-1367
[2] Department of Mechanical Engineering, University of Concepcion, Chile; fevasquez@udec.cl, ORCID 0000-0002-6385-237X
[*] corresponding author

Name of Editor: Jason Moore
First published: 19/09/2023
Last published: 27/03/2024
Citation: González, B. & Vasquez Stuardo, F. (2024). Influence of aerodynamic lift and centre of pressure position in motorcycle stability [version 2; peer reviewed]. The Evolving Scholar - BMD 2023, 5th Edition.
This work is licensed under a Creative Commons Attribution License (CC-BY).

Abstract:

Motorcycles are systems with complex dynamic behaviour that can become unstable under certain driving conditions. Avoiding such instabilities from the design stage is not trivial since they depend on various interrelated parameters, one of which is aerodynamics. Aerodynamic forces in a vehicle can be essentially described by its longitudinal (drag) and vertical (lift) components acting in a point known as the centre of pressure (CoP). Additionally, several authors explain that drag influences stability through four mechanisms: damping lateral motion and changing weight distribution, tire cornering stiffness, and rake geometry. On the other hand, the lift force, which has been used importantly in sports motorcycles in recent years, can also influence stability, however, its effect has not been described in the literature. Therefore the aim of this research is to analyse the influence of lift magnitude and CoP position on motorcycle stability in straight-running conditions. To this end, we develop a motorcycle stability model and perform an analysis on a motorcycle with several CoP and downforce values. We consider the CoP ahead, aligned, and behind the motorcycle centre of mass, together with multiple lift coefficients. Results showed that CoP towards the front end stabilises wobble mode, while rear CoP may cause instability on weave mode. The result contributes to the understanding of motorcycle aerodynamics providing new insights into how to use aerodynamics to enhance stability.

Keywords:

Weave, Wobble, Stability, Aerodynamics

©2023 Gonzalez, B. E., Vasquez, F. A. published by TU Delft OPEN on behalf of the authors.
ISSN: 2667-2812

 http://dx.doi.org/10.59490/65b6fdb42ae3df4e3454736f

1 Introduction

Motorcycle racing focuses on the pursuit of better lap times and enhancing efficiency. Reducing lap times follows two main strategies: Increasing top and cornering speed. To increase top speed, acceleration and power output needs to be maximised while aerodynamic and mechanic drag, minimised. To improve cornering speed, motorcycle grip needs to be maximised through progressive power delivery, suspension settings, and aerodynamics. However, the strategies are in conflict since increasing grip also increases mechanic drag and worsens the top speed. Therefore, it has been seen that the winning motorcycle is the one that finds the balance between cornering and top speed.

Large racing motorcycles, like the ones used in MotoGP, tend to *wheelie* in almost every corner exit. *Wheelie* is when the front wheel loses contact with the ground due to large load transfer to the rear wheel in strong acceleration. A recent solution to this problem is to counter the effect of load transfer using inverted wings in the front end of the motorcycle. Inverted wings generate negative lift, also known as downforce, which increase the normal load on the front tyre, reducing the tendency to wheelie. Consequently, the loads on the motorcycle are more balanced, which allows harder accelerations in corner exits.

However, motorcycle aerodynamics vary over time due to several factors. The movement of the rider interrupts air flow on some aerodynamic elements, changing their effect. Also, sports motorcycles have a more extended suspension travel compared to sports cars, which changes their pitch angle as a result of braking and accelerating manoeuvres. In conjunction with the previous factors, motorcycles lean for cornering, changing both geometry and airflow through their body. Consequently, the constantly changing aerodynamics of motorcycles make it more challenging to have an ideal setup.

In the early years of the studies of the aerodynamics of racing motorcycles, the main focus was to reduce the drag force to increase top speed. Large fairings used in early racing motorcycles were a solution to the problem. However, those fairings had a large lateral area, which caused instabilities when exposed to cross-winds. Therefore, safety regulations banned it and next generations fairings from 1960 were considerably smaller. This fairing shape continued its progressive evolution for almost six decades until the new aero-fairings appeared in 2018 changing the scene.

The main difference between the fairings with winglets from 2015 - 2016 and recent aero-fairings lies in the use of aerodynamic forces. While the former focuses only on downforce to counter "*wheelie*", the latter enhances overall performance. Thus, there have been seen several airflow-distribution devices to modify the cornering dynamics and the cooling of certain components.

The key part of aero-fairings, and the most relevant to the present work, are the inverted wings used in the front of the motorcycle. Those inverted wings are different among manufacturers, however, the average properties can be deduced from images available on the web. The main characteristics of inverted wings are the airfoil, the surface area and the angle of attack. Since in the present work wings will be considered perfectly rigid and the model does not consider pitch degree of freedom, the angle of attack will be constant. Whereas the airfoil is used to determine the lift coefficient (C_l) and the airfoil-induced drag coefficient (C_d) range.

To simplify the aerodynamic analysis, resulting forces are represented by the Centre of Pressure (CoP). From the literature, it is known that CoP needs to stay behind the Centre of Mass (CoM) to keep the system stable (Foale, 2002). Nevertheless, adding front wings on motorcycle fairing means the CoP will be in front of the CoM, which may compromise motorcycle stability.

The study of motorcycle stability encompasses several phenomena, with a primary focus on the crucial modes of vibration, which are Weave and Wobble. *Weave* mode is a low-frequency oscillation, from 0.5 to 5 [Hz], similar to a fishtail movement. On the other hand, the *Wobble* mode is an oscillatory movement from the motorcycle steering with a frequency between 5 and 10 [Hz]. Indeed, Lot and Sadauckas (2021) presents a mathematical model that predicts those modes of vibration with reasonable precision. Furthermore, it has been demonstrated that multiple factors affect those modes of vibration, such as frame stiffness, and tyre properties, among others.

However, there is no clarity about the influence of downforce in motorcycle stability, due to its recent inclusion in the sport. This generates a research gap about the influence of aerodynamic factors on the lateral stability of the motorcycle. Thus, the aim of this study is to analyse the influence of CoP position and aerodynamic lift on motorcycle stability. To this end, in this article we extend the Lot and Sadauckas (2021) stability model, considering longitudinal CoP position and adding downforce.

©2023 Gonzalez, B. E., Vasquez, F. A. published by TU Delft OPEN on behalf of the authors.
ISSN: 2667-2812

 http://dx.doi.org/10.59490/65b6fdb42ae3df4e3454736f

2 Stability model

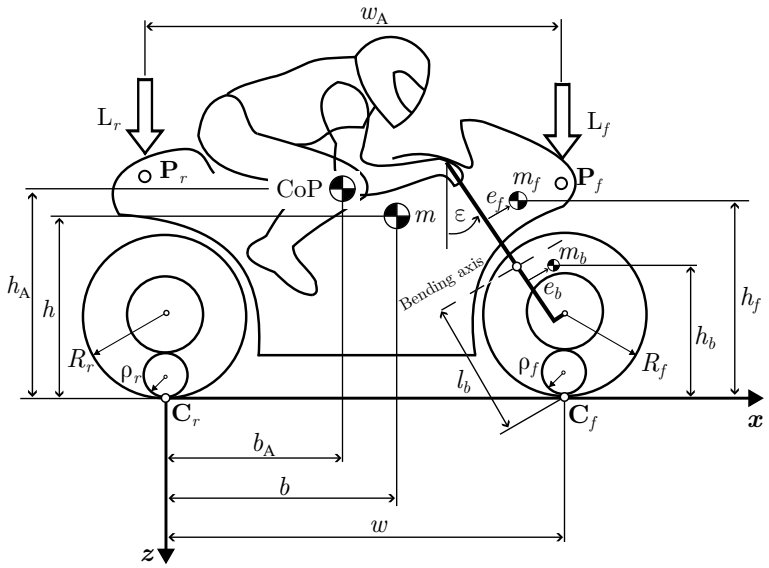


Figure 1. Motorcycle geometry.

The present work is an extension of the stability model from Lot and Sadauckas (2021). The main goal of the model is to predict the stability of the two well-known modes of vibration: *Weave* and *Wobble*. Here we consider four bodies: two wheels, a front and a rear chassis, which can be seen in Figure 1. Indeed, several geometrical parameters are self explanatory in Figure 1. Along with that, the model has five Degrees of Freedom (DoF), being the simplest one with reasonable results according to Lot and Sadauckas (2021). The DoF are roll (φ), yaw (ψ), steer angle (δ), fork bending (β) and lateral velocity of the chassis (V_y). Additionally, all equations were derived and revised using SymPy, finding and solving several inconsistencies (Gonzalez, 2023).

2.1 Kinematic equations

Since motorcycles have a complex geometry due to steering motion and caster angle (ε), it is necessary to establish some kinematical relations.

First, Lot and Sadauckas (2021) shows that the front wheel roll φ_f differs from roll measured at the chassis φ and are related by

$$\varphi_f = \gamma_f = \varphi + \delta \sin(\varepsilon) + \beta \cos(\varepsilon), \tag{1}$$

where δ is the steering angle measured at the handlebar, while β is the fork bending angle.

Similarly, the steering angle projected to the ground Δ is different to δ, and are related by

$$\Delta = \delta \cos(\varepsilon) - \beta \sin(\varepsilon). \tag{2}$$

It is important to note that Equations (1) and (2) are linearised due to small angles for roll and steering.

Regarding the angular velocity of the rear wheel ω_r and the velocity of the front wheel ω_f, they are defined as

$$\omega_r = V_x / R_r \tag{3a}$$

$$\omega_f = V_x / R_f. \tag{3b}$$

Besides, there is agreement that the practical sideslip is expressed as

©2023 Gonzalez, B. E., Vasquez, F. A. published by TU Delft OPEN on behalf of the authors.
ISSN: 2667-2812

 http://dx.doi.org/10.59490/65b6fdb42ae3df4e3454736f

$$\alpha_r = -\frac{V_y}{V_x} \tag{4a}$$

$$\alpha_f = \Delta + \frac{a_n\dot{\delta} - w\dot{\psi} - V_y + (l_b - \rho_f\cos(\varepsilon))\dot{\beta}}{V_x}, \tag{4b}$$

where a_n corresponds to mechanical trail, w is the wheelbase, l_b is the fork bending position measured from the ground and ρ_f is the toridal radius of the tyre as can be seen in Figure 1.

Lastly, the CoP longitudinal position is described introducing the new length between the position of the front and rear wings. Analogously to the wheelbase and position of the CoM, we define w_A and b_A as aerobase and position of the CoP respectively. To avoid misunderstandings, the position of the rear downforce $\mathbf{P}_r$ is aligned with the wheel contact point $\mathbf{C}_r$. Therefore, the equation is

$$b_A = \frac{L_f w_A}{L}, \tag{5}$$

where L is the total lift force on the motorcycle and L_f is the lift force generated by the front wings.

2.2 Forces description

The main interaction between the motorcycle and the environment is produced in the wheels. Therefore, the forces that acts on the tyres are the lateral forces Y, the normal forces N and the yaw torques M.

Firstly, this model captures the transient behaviour of the tyres using α', which is the contact patch sideslip in place of the practical sideslip α. Secondly, k_a and k_t are the normalised stiffness of aligning and twist torque respectively. Lastly, k_α and k_γ are the normalised sideslip and camber stiffness respectively. Then, lateral forces in both tyres are considered linear and according to Cossalter (2006) and Lot and Sadauckas (2021) it can be shown to be

$$Y_r = (k_{\alpha r}\alpha'_r + k_{\gamma r}\gamma_r)N_r \tag{6a}$$

$$Y_f = (k_{\alpha f}\alpha'_f + k_{\gamma f}\gamma_f)N_f. \tag{6b}$$

Normal forces including aerodynamic lift, load transfer due to aerodynamic drag and inertial forces and torques of the spinning wheels, results

$$N_r = \left(1 - \frac{b}{w}\right)mg + \frac{h_A}{w}F_{ad} + \frac{1}{w}\left(mh + \frac{I_{\omega r}}{R_r} + \frac{I_{\omega f}}{R_f}\right)a_x - \left(1 - \frac{b_A}{w_A}\right)L \tag{7a}$$

$$N_f = \frac{b}{w}mg - \frac{h_A}{w}F_{ad} - \frac{1}{w}\left(mh + \frac{I_{\omega r}}{R_r} + \frac{I_{\omega f}}{R_f}\right)a_x - \frac{b_A}{w_A}L, \tag{7b}$$

where $I_{\omega f}$ and $I_{\omega r}$ are the front and rear wheel spin inertia respectively.

Tyre yaw torques for front and rear tyres can be calculated as

$$M_{rz} = (k_{ar}\alpha'_r + k_{tr}\gamma_r)N_r \tag{8a}$$

$$M_{fz} = (k_{af}\alpha'_f + k_{tf}\gamma_f)N_f. \tag{8b}$$

To obtain downforce acting on the motorcycle, it is necessary to know the aerodynamic characteristics of the wings. Therefore, a brief analysis of sports motorcycles wings was performed, obtaining a range of possible values for C_l and angle of attack. To this end,

©2023 Gonzalez, B. E., Vasquez, F. A. published by TU Delft OPEN on behalf of the authors.
ISSN: 2667-2812

we use Lifting Line Theory (LLT) and the XFOIL software, using estimated inputs from detailed observation of MotoGP images. The former theory is based on the idea that the lift generated by a wing can be approximated by a series of lifting segments distributed along its span. While the latter is a computational tool used in aerodynamics to analyse airfoil characteristics and performance.

Thus, from LLT, the C_l at 10° was 1.09 and for 15° was 1.64. While the NACA 0012 airfoil tested in XFOIL gave a C_l of 1.2 at 10°. Besides that, the wingspan of each wing is set at 200 [mm], with a chord of 100 [mm]. Finally, the C_l used is -1.5 since sports motorcycles use non-symmetrical airfoils which have a greater C_l than symmetrical airfoils like the ones revised. Hence, downforce is calculated using negative lift coefficients in the classical lift equation that is given by

$$L = \frac{1}{2}\rho C_l S V_x^2, \tag{9}$$

where ρ is the air density, V_x is the longitudinal speed and S is the surface area of the wing.

The airfoil-induced drag coefficient from LLT is calculated by

$$C_d = C_{d0} + \frac{C_l^2}{e\pi AR}, \tag{10}$$

where AR is the area ratio given by the expression $AR = \frac{wingspan}{chord}$, considering the wingspan of a single wing, while e is the Oswald efficiency number, and C_{d0} is the minimum drag coefficient (Scott, 2004).

Lastly, airfoil-induced drag is added to the overall motorcycle drag equation resulting

$$F_{ad} = \frac{1}{2}\rho(C_D A + C_d S)V_x^2, \tag{11}$$

where C_D is the vehicle drag coefficient without wings, A is the frontal area of the motorcycle and C_d is the airfoil-induced drag coefficient.

2.3 Equations of motion

For this study, sum of forces in longitudinal axis x and vertical axis z can be neglected since there are no motion in these planes. For the remaining direction, the sum of forces in the y axis reads

$$m(\dot{V}_y + b\ddot{\psi} + h\ddot{\varphi} + V_x\dot{\psi}) + m_f e_f \ddot{\delta} - m_b z_b \ddot{\beta} = Y_r + Y_f + \Delta X_f, \tag{12}$$

where m_f is the mass of front assembly, e_f is the longitudinal position of the front assembly centre of mass, m_b is the bending mass and z_b is represents the position of the centre of mass of the bending body.

Similarly to the sum of forces, pitch is neglected in this model, which means no moments around y axis. Therefore, only the sum of moments in x and z axis are presented, which are Equations (13a) and (13b) respectively

$$\begin{aligned}(mbh - I_{xz})\ddot{\psi} + (mh^2 + I_{xx})\ddot{\varphi} + (m_f e_f h_f + I_{fzz}\sin(\varepsilon))\ddot{\delta} + (I_{bxx}\cos(\varepsilon) - m_b h_b z_b)\ddot{\beta} + mh(\dot{V}_y + V_x\dot{\psi}) = \\ [(a_n - \sin(\varepsilon)\rho_f)\delta + (l_b - \cos(\varepsilon)\rho_f)\beta - \rho_f\varphi]N_f - \rho_r\varphi N_r + mgh\varphi - m_b g z_b\beta + m_f g e_f\delta\end{aligned} \tag{13a}$$

$$\begin{aligned}(mb^2 + I_{zz})\ddot{\psi} + (mbh - I_{xz})\ddot{\varphi} + (m_f e_f b_f + I_{fzz}\cos(\varepsilon))\ddot{\delta} + (I_{bxx}\sin(\varepsilon) - m_b b_b z_b)\ddot{\beta} + \\ mb(\dot{V}_y + V_x\dot{\psi}) + (m_b z_b\beta - mh\varphi - m_f e_f\delta)\dot{V}_x - I_{\omega r}(\omega_r\dot{\varphi} + \dot{\omega}_r\varphi) - I_{\omega f}(\omega_f\dot{\varphi}_f + \dot{\omega}_f\varphi_f) = wY_f - \rho_r X_r\varphi + \\ h_A F_{ad}\varphi + M_{rz} + M_{fz} + [(a_n + \omega\cos(\varepsilon) - \rho_f\sin(\varepsilon))\delta - \rho_f\varphi + (l_b - \rho_f\cos(\varepsilon) - w\sin(\varepsilon))\beta]X_f + b_A L\varphi,\end{aligned} \tag{13b}$$

©2023 Gonzalez, B. E., Vasquez, F. A. published by TU Delft OPEN on behalf of the authors.
ISSN: 2667-2812

 http://dx.doi.org/10.59490/65b6fdb42ae3df4e3454736f

where I_{xx} and I_{xz} are the overall moments of inertia, while I_{fzz} and I_{bxx} are the front assembly and bending body moments of inertia respectively.

An additional DoF is the steering angle, for which the equation of motion is

$$(m_f e_f^2 + I_{fzz})\ddot{\delta} + (m_f e_f h_f + I_{fzz}\sin(\varepsilon))\ddot{\varphi} - m_b e_b z_b \ddot{\beta} + (m_f e_f b_f + I_{fzz}\cos(\varepsilon))\ddot{\psi} + m_f e_f(\dot{V}_y + V_x\dot{\psi} + \dot{V}_x\cos(\varepsilon)\delta) + I_{\omega f}\omega_f(\dot{\psi}\sin(\varepsilon) - \dot{\varphi}\cos(\varepsilon)) - I_{\omega f}(\omega_f\dot{\beta} + \dot{\omega}_f\beta) = M_\delta - a_n Y_f + M_{fz}\cos(\varepsilon) + [(l_b\cos(\varepsilon) + a_n\sin(\varepsilon))\beta + \rho_f\cos(\varepsilon)\gamma_f]X_f + + [(a_n - \rho_f\sin(\varepsilon))\gamma_f + (l_b\sin(\varepsilon) + a_n\cos(\varepsilon))\beta]N_f + (a_x\cos(\varepsilon) + g\sin(\varepsilon))(m_f e_f\delta - m_b z_b\beta) + g m_f e_f\varphi - c_\delta\dot{\delta}, \quad (14)$$

where M_δ is the rider input torque, and c_δ is the torque generated by steering bearings friction and the action of and steering damper if it exists.

Furthermore, one of the main contributions of Lot and Sadauckas (2021) model, is considering the fork bending. The importance is demonstrated in Cossalter et al. (2007), where it was concluded that flexible fork stabilises wobble mode at high-speed range. To include the lateral fork bending angle β, the equation of motion of this DoF is

$$-(m_b b_b z_b - I_{bxx}\sin(\varepsilon))\ddot{\psi} + (I_{bxx}\cos(\varepsilon) - m_b h_b z_b)\ddot{\varphi} - m_b e_b z_b\ddot{\delta} + (m_b z_b^2 + I_{bxx})\ddot{\beta} - m_b z_b(\dot{V}_y + V_x\dot{\psi}) + I_{\omega f}\omega_f(\dot{\varphi}_f + \dot{\psi}\cos(\varepsilon)) = - l_b Y_f - M_{fz}\sin(\varepsilon) + [(l_b - \rho_f\cos(\varepsilon))N_f + \rho_f\sin(\varepsilon)X_f]\gamma_f - k_\beta\beta + m_b z_b[a_x(\beta\sin(\varepsilon) - \delta\cos(\varepsilon)) - g\gamma_f], \quad (15)$$

where right-hand terms are moments generated with respect to the bending axis x_b, while k_β is the bending stiffness of the fork.

Moreover, the present work uses a model that captures the transient behaviour of the tyres. Since the contact patch of the tyre changes as a consequence of motorcycle roll, its sideslip is affected, generating the new component α'.

The relation between both sideslips is expressed by

$$\frac{k_{\alpha r}N_r}{k_{lr}}\frac{\dot{\alpha_r}'}{V_x} + \alpha_r' = \alpha_r + \frac{(1-k_{\gamma r})N_r}{k_{lr}}\frac{\dot{\gamma_r}}{V_x} \quad (16a)$$

$$\frac{k_{\alpha f}N_f}{k_{lf}}\frac{\dot{\alpha_f}'}{V_x} + \alpha_f' = \alpha_f + \frac{(1-k_{\gamma f})N_f}{k_{lf}}\frac{\dot{\gamma_f}}{V_x}. \quad (16b)$$

Finally, the stability of this system can be assessed by obtaining the eigenvalues from the space-state formulation. Here, the variables are collected into a state vector, which is a 10 x 1 matrix as can be seen in

$$\mathbf{x} = \begin{bmatrix} V_y & \dot{\psi} & \dot{\varphi} & \dot{\delta} & \dot{\beta} & \alpha_r' & \alpha_f' & \varphi & \delta & \beta \end{bmatrix}^T. \quad (17)$$

Then, the eigenvalue problem is defined as

$$\mathbf{E}\dot{\mathbf{x}} = \mathbf{A}\mathbf{x}, \quad (18)$$

where **A** and **E** are 10x10 matrices assembled from equations of motion previously detailed.

©2023 Gonzalez, B. E., Vasquez, F. A. published by TU Delft OPEN on behalf of the authors.
ISSN: 2667-2812

 http://dx.doi.org/10.59490/65b6fdb42ae3df4e3454736f

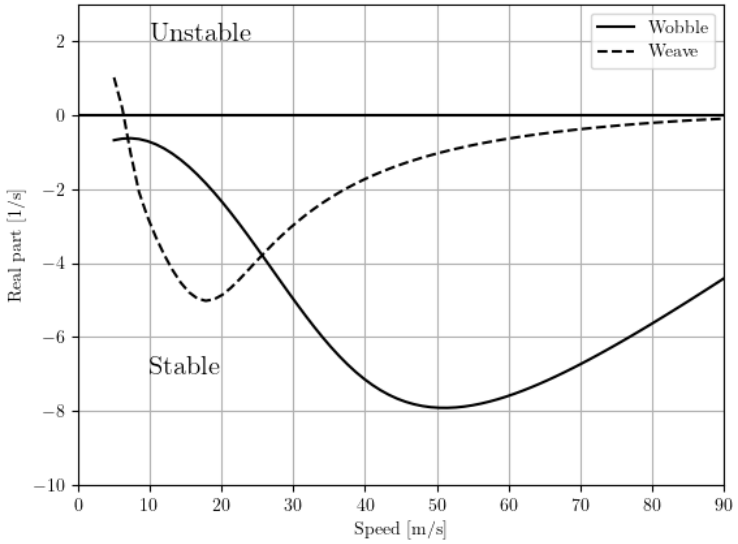


Figure 2. Influence of speed on motorcycle stability.

3 Results

From the numerical implementation of the model, we obtain plots of the influence of speed on motorcycle stability, where results for weave and wobble are shown together. Afterwards, we perform a sensitivity analysis using 3-dimensional plots, first considering constant C_l with variable CoP position, and then, constant CoP position with variable C_l. For this paper, original values of a sport touring motorcycle characteristics from Lot and Sadauckas (2021) are used. However, the range of speed is extended due to the effect of aerodynamics and is expected to become predominant over 45 [m/s]. Therefore, the range of speed used is from 5 [m/s] to 100 [m/s], which agrees with the values seen in top-class sports motorcycles.

First of all, results with zero downforce conditions are shown in Figure 2 as a reference. Both modes are stable at the considered range of speed, reaching maximum stability and decreasing its stability at high speeds. For weave mode, the maximum stability is achieved around 17 [m/s], with a decrease to an almost unstable zone at a top speed of 90 [m/s]. Whereas, wobble mode reaches its maximum stability at 50 [m/s], decreasing with an almost linear tendency, finishing in the stable zone. Evidently, the basic design of the motorcycle is stable in the range of speed tested, which is the reference for the following analysis. Additionally, sensitivity analysis showed continuous curves for both modes along the complete range, therefore, we only present the three main cases in each plot.

First, from Figures 3 and 4 it can be seen that downforce has an effect on stability, mainly at high speeds. Results exposed in Figure 3 consider the CoP aligned with the CoM, to show only the effect of adding downforce. Next, Figure 4 shows the changes on stability considering strong downforce (C_l = -1.5) in different CoP positions with respect to the CoM.

For weave mode, it reaches the unstable zone for both tested cases of downforce, mainly with greater C_l. The magnitude of C_l affects directly to the stability, generating instability at 81 [m/s] for the case of $C_l = -1.5$ Equally, it can be seen changes in stability depending on the position of the CoP with respect to the CoM as shown in Figure 4. While adding downforce turns weave mode unstable at high speeds, positioning the CoP towards the front end improves the behaviour, extending the stability up to 86 [m/s]. On the contrary, CoP towards the rear end worsens the stability, making the system unstable from 78 [m/s]. In outline, the downforce generates instability, while the CoP position may affect its stability range up to 8%.

By the same, an effect on wobble mode stability is shown in both plots. From Figure 3 it is seen an improvement of stability from 40 [m/s] when adding downforce. Again, the CoP position has a great effect, mainly stabilising the system when it is towards the front end. Overall, the wobble mode is modified significantly but remains stable for the complete speed range in all of the tested cases.

To sum up, the range of speed used is extended because aerodynamic forces play a significant role above 45 [m/s]. Consequently, the different effects are seen over this speed in both modes of vibration. Mainly in the weave mode, downforce changes its stability

©2023 Gonzalez, B. E., Vasquez, F. A. published by TU Delft OPEN on behalf of the authors.
ISSN: 2667-2812

 http://dx.doi.org/10.59490/65b6fdb42ae3df4e3454736f

in all of the considered cases. On the other hand, wobble mode is less sensitive to downforce, maintaining stable behaviour in the whole range of speed. Therefore, downforce towards the front end generates a stabilising effect on the system.

4 Conclusion

In this article, we have studied the effect of the CoP position and aerodynamic lift in motorcycle stability. To this end, we modified a relatively simple stability model which predicts weave and wobble mode. Results revealed that downforce generates a stabilising effect on the motorcycle.

On the whole, the effect of downforce is predominant in weave mode, while is almost negligible for wobble mode stability. Furthermore, with a CoP significantly to the rear, instability on weave mode can be worsened at high speeds. On the contrary, downforce stabilises wobble mode in any CoP position, however, the maximum stability is reached with the CoP towards the front end. This is a reasonable result since aerodynamic forces at low speeds are small.

However, to generalise conclusions about the influence of aerodynamics on motorcycle stability, it is necessary to perform an analysis in cornering conditions, where the effect may vary. We could expect variations due to the dynamics of the corner or the changes in aerodynamics due to rider movements in the manoeuvres. Additionally, analysing the effect of large pitching events from braking and acceleration may reveal new information. Finally, contrasting these results against experimental data would validate the results.

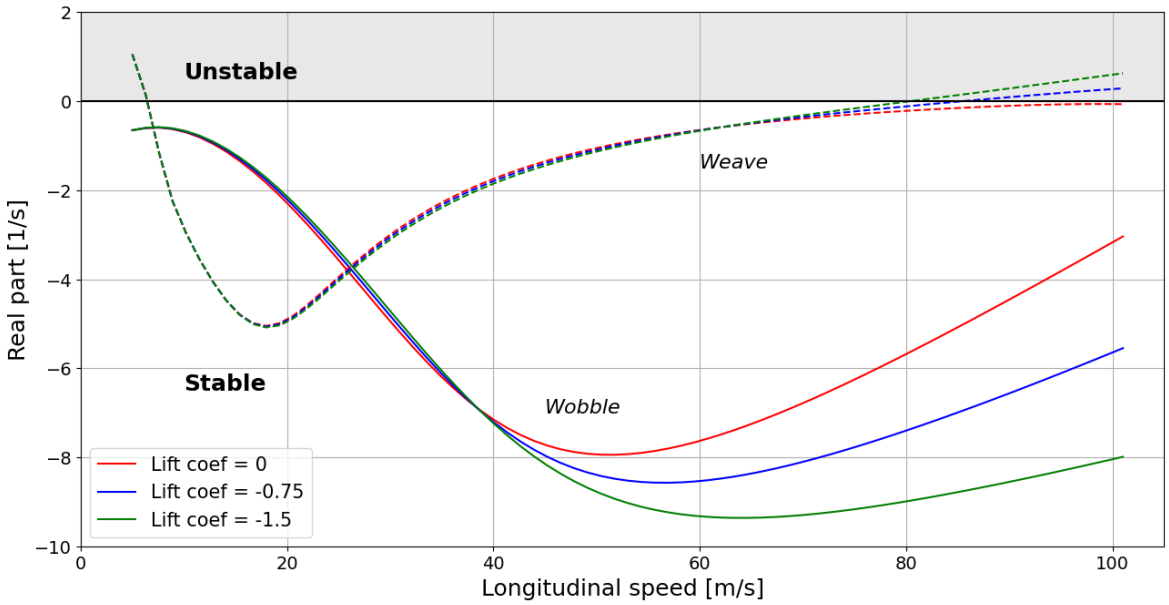


Figure 3. Influence of speed on motorcycle stability for multiple C_l.

©2023 Gonzalez, B. E., Vasquez, F. A. published by TU Delft OPEN on behalf of the authors.
ISSN: 2667-2812

http://dx.doi.org/10.59490/65b6fdb42ae3df4e3454736f

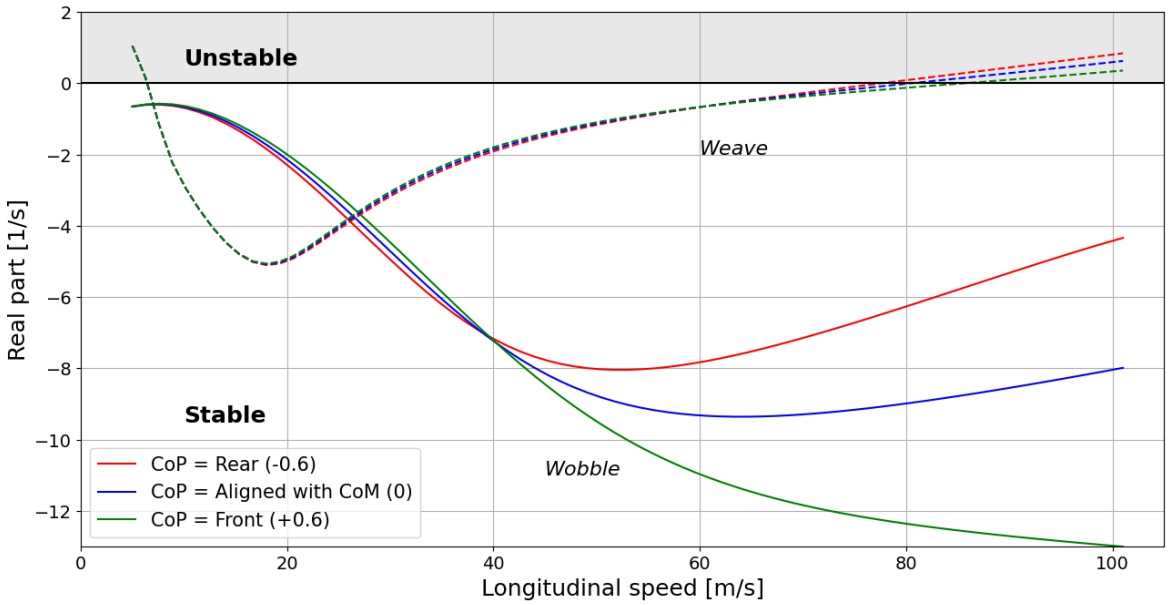


Figure 4. Influence of speed on motorcycle stability varying CoP position.

©2023 Gonzalez, B. E., Vasquez, F. A. published by TU Delft OPEN on behalf of the authors.
ISSN: 2667-2812

 http://dx.doi.org/10.59490/65b6fdb42ae3df4e3454736f

References

Cossalter, V. (2006). *Motorcycle Dynamics Second Edition*.

Cossalter, V., Lot, R., and Massaro, M. (2007). The influence of frame compliance and rider mobility on the scooter stability. *Vehicle System Dynamics*, 45:313–326.

Foale, T. (2002). *Motorcycle Handling and Chassis Design the art and science*.

Gonzalez, B. E. (2023). Implementación de un modelo matemático para estudiar la estabilidad de las motocicletas. Departamento ingeniería Mecánica, Universidad de Concepcion, Informe Proyecto de Ingeniería Mecánica.

Lot, R. and Sadauckas, J. (2021). *Motorcycle Design: Vehicle Dynamics, Concepts and Applications*. 1 edition.

Scott, J. (2004). Aerospaceweb.org - drag coefficient & lifting line theory. Accessed: 2023-07-24.

©2023 Gonzalez, B. E., Vasquez, F. A. published by TU Delft OPEN on behalf of the authors.
ISSN: 2667-2812

The Evolving Scholar Vol. 3, 2023 https://dx.doi.org/10.59490/660572d0bfc285d425a828c0

Bicycle and Motorcycle Dynamics 2023
Symposium on the Dynamics and Control of Single Track Vehicles
18 – 20 October 2023, Delft University of Technology, The Netherlands

Type of the Paper: Conference Paper

Revised

Influence of Available Rear Wheel Travel and Target Sag on Suspension Performance of a Cruiser Motorcycle

[version 2; peer reviewed]

K. Peck[1,*], and J. Sadauckas[2]

[1] Vehicle Dynamics Group, Harley-Davidson Motor Company, Milwaukee, WI, 53222, USA; kasey.peck@harley-davidson.com; ORCID 0009-0004-8497-7691
[2] Trek Performance Research, Trek Bicycle Corporation, Waterloo, WI, 53594, USA; jim_sadauckas@trekbikes.com; ORCID 0000-0002-6055-9047
*corresponding author

Name of Editor: Jason Moore
First published: 03/10/2023
Last published: 02/04/2024
Citation: Peck, K. & Sadauckas, J. (2024). Influence of Available Rear Wheel Travel and Target Sag on Suspension Performance of a Cruiser Motorcycle [version 2; peer reviewed]. The Evolving Scholar - BMD 2023, 5th Edition.
This work is licensed under a Creative Commons Attribution License (CC-BY).

Abstract:

The design and optimization of two-wheel vehicle suspension provides an exciting design challenge due to the multitude of potential layouts and interrelated variables to consider. Balancing these design factors to achieve the desired *comfort* and *road holding* performance while also ensuring the vehicle achieves the desired trim state under the various operating conditions, termed *chassis control* for the purposes of this paper, requires a deep level of technical understanding to execute successfully. Consequently, a specific area of two-wheel vehicle suspension development that has received little attention is defining the nominal vehicle trim state in terms of target sag and the associated proportion of vertical wheel travel to be used in compression versus that available for extension. For closed course racing vehicles, both on-road and off-road, the suspension travel and target sag are determined experimentally based on simulation or testing to obtain the primary objective of minimum lap time. However, for commercial on-road vehicles, suspension travel and target sag are often constrained by numerous vehicle design requirements such as aesthetics, seat height, and packaging limitations. These design constraints require production-intent suspension travel and target sag to be selected early in the product development cycle. Until now, limited literature has been published regarding nominal target sag and how best to proportion suspension travel between compression and extension, though a general guideline proposes ~33% target sag as the starting point. The intention of this paper is to provide a deeper technical understanding of suspension performance trade-offs between available suspension travel and target sag using physical vehicle testing and multibody simulations.

Keywords: Motorcycle, Two-wheeler, Sag, Rebound, Ride Quality, Road Holding, Chassis Control, Suspension, Preload

Introduction

Suspension travel, i.e., the available suspension displacement from a fully extended to fully compressed condition, is known to be a critical factor in overall suspension performance. However, suspension sag, defined here as the suspension displacement at ride height under steady-state operating conditions, is an important setup and tuning parameter, largely neglected in the available motorcycle research literature. This paper aims to provide foundational knowledge regarding the influence of suspension sag on vehicle *comfort*, *roadholding*, and *chassis control*.

©2023 Peck, K., Sadauckas, **J.** published by TU Delft OPEN on behalf of the authors.
ISSN: 2667-2812

 http://dx.doi.org/10.59490/660572d0bfc285d425a828c0

Within the motorcycle industry, optimal suspension sag is dependent on the specific performance the suspension must deliver but within scientific literature this topic has received very little attention. As a general guideline ~33% target sag has been proposed (Thede, 2010). Most motorcycle owner's manuals specify a preload adjuster setting to achieve a desired sag state depending on rider weight and vehicle load. For closed course racing vehicles, both on-road and off-road, the sole objective of the vehicle is to achieve the fastest possible lap time. As a result, optimal suspension sag is determined experimentally to achieve the desired vehicle trim state at specific areas on the racecourse to maximize traction, drive, cornering, or braking. Conversely, for commercially available road-going motorcycles, suspension travel and target sag are constrained by numerous vehicle-level design requirements including aesthetics, seat height, and packaging limitations. These design constraints require production-intent suspension ride-height, thus travel and target sag, to be selected early in the product development cycle. Fixing two of the key suspension variables prior to physical suspension tuning limits the engineer's ability to fully optimize the suspension performance of the vehicle. Additional foreknowledge regarding the relationship between suspension travel and target sag on the resultant suspension performance can better inform the production suspension layouts and offer the potential of improved suspension performance with no additional investment in part cost or damper technology.

This paper presents the results of physical testing of a cruiser motorcycle with three unique rear suspension layouts with variations in suspension travel, sag, and rebound damping. For each layout, qualitative suspension performance ratings were captured on selected closed-course suspension events by a professional motorcycle test rider, trained to articulate perceptible differences in suspension performance. At the same time, quantitative suspension data was collected on the vehicle including front fork and rear shock displacement and velocity, accelerations at the steer head and mid-frame, and the chassis pitch rate, as well as vehicle speed. Correlation analysis between the qualitative and quantitative data was conducted to identify suspension performance indices useful in the development of predictive multibody simulations.

After multibody model correlation was assessed, simulations were conducted to further understand the vehicle performance trends observed during physical testing. The simulation model closely represented the actual test vehicle and was fitted with the three unique rear suspension layouts as characterized on a suspension dynamometer. Simulation of the specific closed-course suspension events enabled calculation of tire normal load, and thereby the determination of *road holding*, which is difficult to measure during physical testing. Simulation further supplemented the physical test by examining additional variations in damper settings, vehicle speeds, and maneuver constraints.

Physical Testing

Test Setup

The test vehicle used for this research was a heavyweight cruiser motorcycle with front and rear suspension subsystems. The front suspension uses conventional telescopic forks with linear springs and bilinear damping characteristics (Lot, 2021). The rear suspension uses a direct acting hydraulic "mono-shock" shock absorber with linear springs and bilinear damping in both compression and rebound.

Three different rear suspension shock absorber setups, referred to as layouts, were tested. Each layout is a unique combination of travel, sag, and rebound damping. For each layout, the vehicle ride height and resultant seat height, remain unchanged. Layout #1 represents the production vehicle, with a moderate 86 mm of rear wheel travel and rear spring preload set to achieve 30% sag. Layout #2 increases the rear shock travel by 13 mm (a 26 mm increase in rear wheel displacement due to the kinematics of the swingarm) while maintaining the same rear shock damper characteristics and vehicle ride height as Layout #1. This is achieved by sagging the suspension deeper into its travel. Layout #3 is the same as Layout #2 with rebound damping reduced by 40% via changes to the piston architecture and hydraulic rebound damper shim stack. Table 1 outlines the rear suspension layouts tested.

©2023 Peck, K., Sadauckas, **J** published by TU Delft OPEN on behalf of the authors.
ISSN: 2667-2812

 http://dx.doi.org/10.59490/660572d0bfc285d425a828c0

Table 1. Detailed description of the rear suspension layouts tested.

	Layout #1	Layout #2	Layout #3
Rear Wheel Wheel Displacement [mm]	86	113	113
Rear Shock Travel [mm]	43	56	56
Target Sag [% Travel]	30%	47%	47%
Rear Shock Spring Rate [N/mm]	110	110	110
Rear Shock Preload Force @ 1G Sag [N]	3,300	3,300	3,300
Rebound Damping @ 0.5 m/s [N]	3,325	3,327	1,959 (40% Reduction)
Laden Seat Height [mm]	655.3	655.3	655.3
Rear Wheel Vertical Compression Travel [mm]	60.2	60.2	60.2
Rear Wheel Vertical Extension Stroke [mm]	25.8	52.8	52.8

Figure 1 shows overlays of both force versus velocity, at left, and shock spring force versus displacement information, at right, for the three rear suspension layouts tested as measured on a suspension dynamometer. The force versus velocity data shows the damping force between Layout #1 and Layout #2 are nearly identical, while Layout #3 achieves the desired 40% reduction in rebound damping. For Layout #3, changes to the hydraulic damping circuit required to achieve the reduced rebound damping resulted in slightly lower compression damping. The force versus displacement spring curves show all three rear suspension layouts use the same spring rate and jounce bumper, with the differences in available compression and extension displacement clearly labelled.

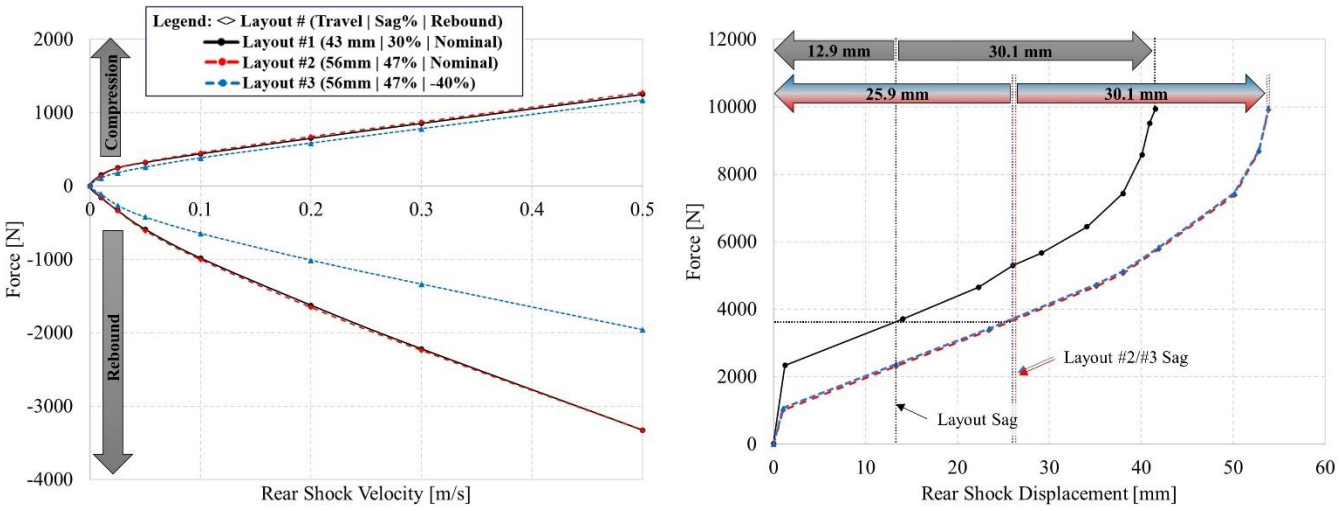


Figure 1. Force versus Velocity and Force versus Displacement comparisons for the rear suspension layouts tested.

The test vehicle was instrumented to quantify suspension performance differences between the three layouts as follows: vehicle speed via a GPS receiver, front fork and rear shock displacement via linear potentiometers, rear frame acceleration via a DC tri-axial accelerometer mounted under the rider's seat, and pitch rate via a pitch rate gyrometer also mounted under the rider's seat. The front fork and rear shock linear potentiometers were zeroed at full extension with positive suspension displacement and velocity

©2023 Peck, K., Sadauckas, **J** published by TU Delft OPEN on behalf of the authors.
ISSN: 2667-2812

indicating a compression event. The DC tri-axial accelerometer and pitch rate sensor were mounted under the rider's seat in the global orientation following the SAE sign convention (x-axis forward, y-axis to the right, and z-axis to the down) per SAE J670. The pitch rate sensor follows the right-hand rule with positive values indicating the front of the vehicle rotating upward while the rear of the vehicle tilts toward the ground.

Each rear suspension layout was tested over three specific suspension events: Pothole, Camel, and Threshold braking. The Pothole is a negative/downward event of roughly trapezoidal cross section with depth 0.10 m, length 0.91 m and 70-degree vertical slope, used in this paper to evaluate suspension *comfort*. The Pothole was tested at 24, 32, 40, and 48 kph. The Camel is a positive half-sinusoidal event with length 5.35 m and height 0.15 m and was used to evaluate both *chassis control* and *road holding*. Results from the Camel at 32 kph are described. The final event was a front-only threshold braking event from 100 kph to a full stop executed at the limit of front tire grip without skidding or ABS activation. This threshold braking maneuver was used as an initial attempt to further quantify *chassis control*.

As the Pothole and Camel are discrete transient bump events, road roughness and the corresponding *comfort* frequency analysis were of limited applicability (De Luca, 2007). Past research also showed that test rider comfort correlates to the highest peaks of acceleration (Strandemar, 2005). As a result, peak vertical acceleration at the mid-frame of the vehicle was the primary metric used to quantify suspension c*omfort* for this study. Further examination of *chassis control* considered the rear suspension extension rate over the Camel and during threshold braking, whereas *road holding* was gleaned from rear suspension displacement trends and further examined by considering simulated rear tire normal load.

Qualitative Evaluations

For each layout, qualitative suspension performance was evaluated on closed-course suspension events by a single professional motorcycle test rider. The test rider used for this research has been trained to articulate minute differences in suspension performance through years of motorcycle suspension testing and tuning experience. A single test rider was purposely used for this research to provide a direct performance comparison between the tested layouts. Multiple test rides would have provided a wider range of qualitative suspension performance feedback given differences in skill level and ride feel but would have provided less resolution on the performance differences between layouts. For this research, the test rider's suspension performance feedback was limited to the three events being studied. The specific suspension performance attributes that were evaluated for each event are outlined in Table 2.

Table 2. Suspension event and corresponding attribute for rider qualitative feedback.

Event	Performance Attribute	Definition
Pothole	Exit Abruptness	Magnitude of abruptness to rider when the suspension compresses on Pothole impact
Camel	Rear Rebound Rate	Magnitude of the rear suspension extension rate over the top of the Camel
	Rider-Vehicle Separation	Magnitude of separation between the rider and vehicle over the top of the Camel
Threshold Braking	Reaction to Brake Input	Magnitude of the vehicle pitch rate during the initial front brake input
	Maximum Pitch Angle	Maximum pitch angle achieved during threshold braking event

For each suspension layout, the rider took detailed notes on the subjective performance across the three events and speeds being studied and provided a subjective score of 1 through 7 for each performance attribute, with a rating of 1 indicating poor performance, 4 indicating acceptable performance and 7 being excellent performance. A subjective score change of 0.5 was defined as perceptible to a trained rider, while a subjective score change of 1 was defined as being perceptible to an average rider. After the three layouts were tested, rider qualitative feedback and subjective scores for all three layouts were compiled. Figure 2 outlines the subjective scores for each performance attribute.

©2023 Peck, K., Sadauckas, **J** published by TU Delft OPEN on behalf of the authors.

ISSN: 2667-2812

 http://dx.doi.org/10.59490/660572d0bfc285d425a828c0

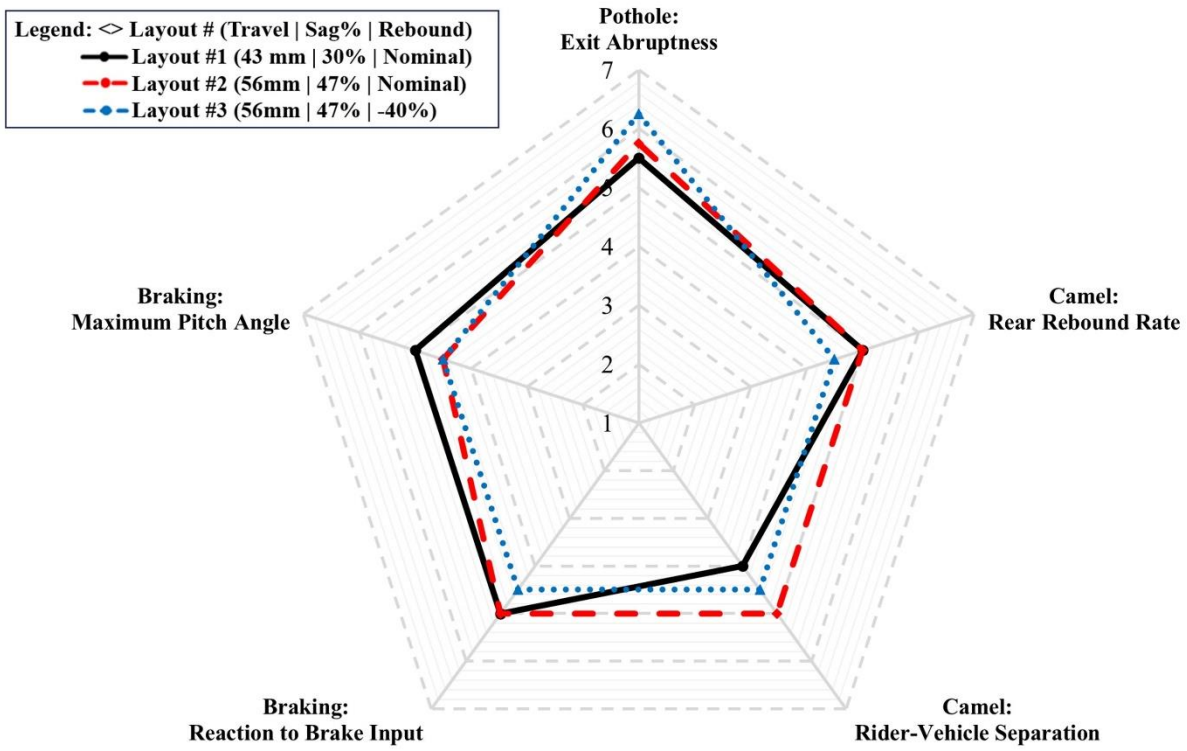


Figure 2. Summary of subjective ratings (from 1 = Poor to 7 = Good) of suspension performance for a cruiser motorcycle by trained test rider for three rear suspension layouts across five performance attributes over three test events (Pothole, Camel, Braking). Maximal enclosed area suggests best overall performance.

Over the Pothole, the rider noted discernable differences in the abruptness that resulted in differences in perceived *comfort*. Both Layout #2 and Layout #3 reduced the perceived impact and, thus, increased *comfort* at 40 kph and 48 kph specifically, with the increase in *comfort* from Layout #3 greater than Layout #2. At 24 kph and 32 kph, the level of perceived *comfort* was similar between the three rear suspension layouts.

The Camel at 32 kph also showed discernable performance differences between the three rear suspension layouts. Layout #1 provided adequate control of the stored spring energy during the initial rebound phase after cresting the Camel. However, the rear suspension reached full extension quickly with an audible noise during topping, defined here as full extension of the suspension, and the rider was momentarily separated from the seat. Layout #2 provided similar control of the stored spring energy during the initial rebound phase, but the rear shock did not reach full extension or separate the rider from the seat. The rebound control of Layout #3 was found to be insufficient and extended faster than the rider desired. Additionally, Layout #3 reached full extension with an audible topping noise and a very subtle separation of rider from the seat, the magnitude of both were smaller than Layout #1.

Threshold Braking events showed small differences in performance between the three rear suspension layouts. Layout #1 had an acceptable reaction to the initial brake input, providing the necessary *chassis control* to enable the rider to apply the brakes aggressively and achieve the desired brake dive (fork compression) rate and vehicle geometry. Additionally, the maximum pitch rate for Layout #1 was perceived to be acceptable. Layout #2 exhibited similar performance during initial brake application as Layout #1 but achieved higher maximum pitch angle at threshold. However, the increased pitch angle did not impact braking performance or *chassis control* and was not found to be objectionable by the rider. Layout #3 was found to be more sensitive to the initial brake application, with the rear suspension extending noticeably faster than Layouts #1 and #2. This increased pitch rate and rear suspension extension velocity during the initial brake application required more precise input from the rider to control the dive rate (of the front forks), hence load transfer, and was perceived as a degradation in *chassis control*. The maximum pitch rate perceived for Layout #3 was unchanged from Layout #2 and was not found to be objectionable.

©2023 Peck, K., Sadauckas, **J** published by TU Delft OPEN on behalf of the authors.

ISSN: 2667-2812

 http://dx.doi.org/10.59490/660572d0bfc285d425a828c0

Quantitative Data Analysis

The data collected from all three suspension layouts for the three test events was analyzed. Data analysis for each event was tailored to identify key system response parameters best correlated to the subjective rider feedback for each suspension performance attribute.

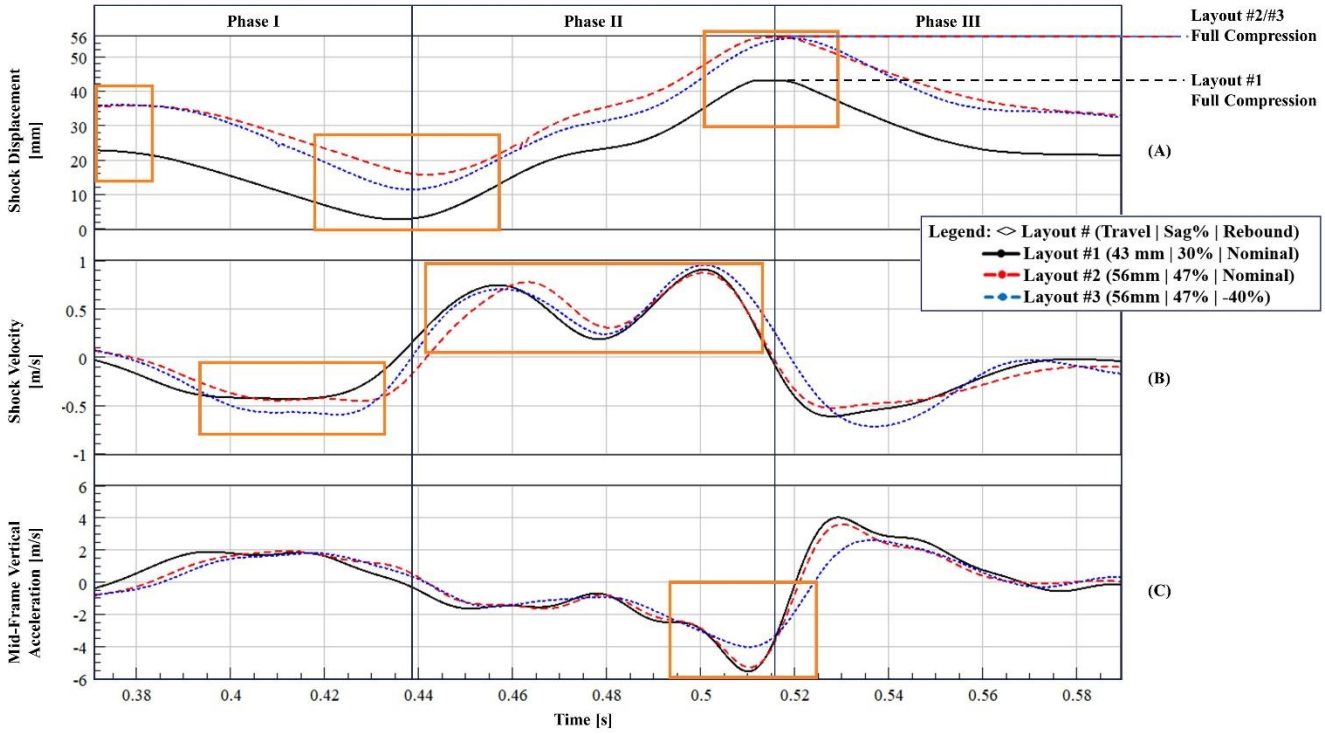


Figure 3. Pothole suspension test event for cruiser motorcycle with three rear suspension layouts, showing A) shock displacement, B) shock velocity and C) mid-frame vertical acceleration of the chassis.

Figure 3 shows the rear shock displacement, rear shock velocity, and mid-frame vertical acceleration through the Pothole at 32 kph. The plot is divided into three phases: In Phase I the rear shock extends into the pothole, during Phase II the rear shock compresses as the tire exits the Pothole, during Phase III the rear shock returns to sag. Phase II, containing the largest mid-frame vertical acceleration, was chosen to inform the analysis of suspension *comfort*. However, Phase I and Phase III also offer insights into rear suspension performance. In Phase I, differences in available extension travel from sag are prevalent between Layout #1 and Layouts #2 and #3. The extra extension travel (plot A) in Layout #2 and #3 provides more topping resistance than Layout #1, though none of the Layouts reach full extension in this specific example. In Phase 1, Layout #3 extends at a higher velocity (plot B) and achieves a greater total extension displacement than Layout #1 and #2 due to its reduced rebound damping. As the rear wheel enters Phase II, the magnitudes of peak shock compression velocity (plot B) for each of the three layouts remains similar. However, Layout #1, which has 43 mm of total shock travel, and Layout #2, which has 56 mm of shock travel, both reach full compression abruptly as indicated by the dwell at the peak in the shock displacement overlay (plot A). These abrupt bottoming events result in a similar peak amplitude of mid-frame vertical acceleration (plot C). Conversely, Layout #3, which started Phase II with more remaining compression travel due to its faster and greater extension in Phase 1, also reaches full compression (blue peak) but less abruptly. This reduction in bottoming abruptness yielded a 1.2 g reduction in peak mid-frame vertical acceleration for Layout #3 with respect to the other layout for this Pothole event at 32 kph, thus providing more *comfort*.

©2023 Peck, K., Sadauckas, **J** published by TU Delft OPEN on behalf of the authors.

ISSN: 2667-2812

http://dx.doi.org/10.59490/660572d0bfc285d425a828c0

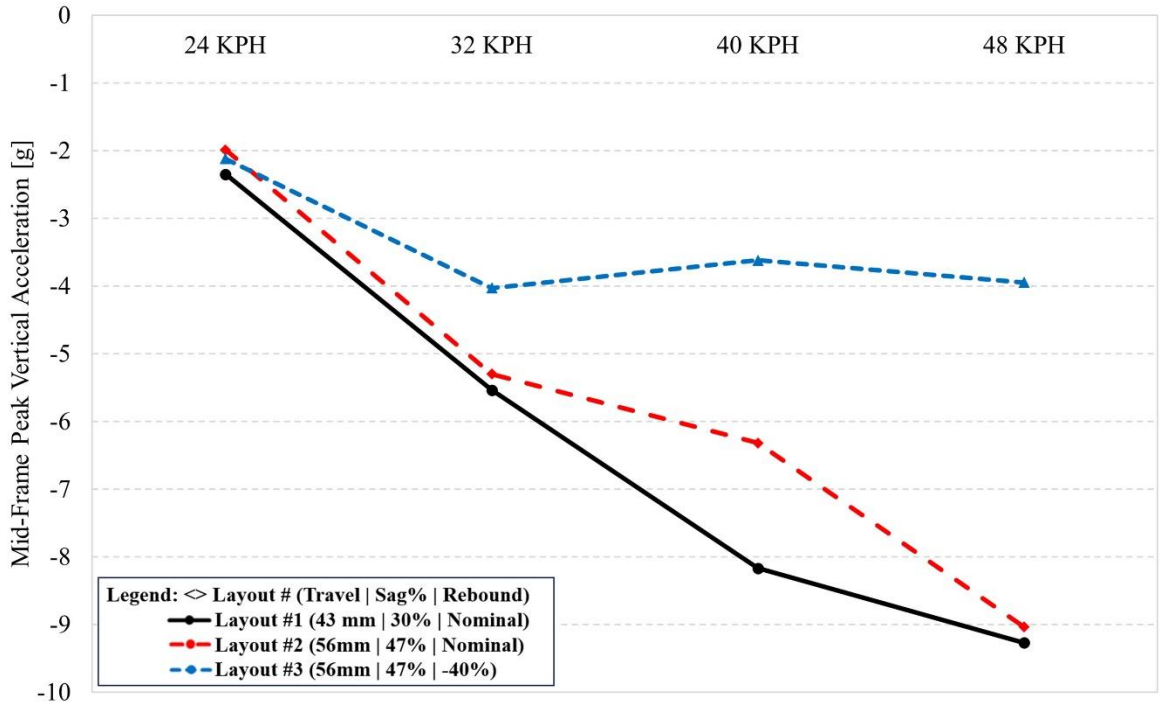


Figure 4. Peak mid-frame vertical acceleration during Pothole impact for three motorcycle cruiser rear suspension layouts plotted for four different test speed. Negative acceleration of the chassis is upward with respect to ground per SAE J670

Figure 4 shows the peak mid-frame vertical acceleration during Pothole impact for all three rear suspension layouts across all test speeds. For all three layouts, the peak mid-frame vertical accelerations at 24 kph are similar, and small in magnitude. The peak mid-frame vertical acceleration of Layouts #1 and #2 increase proportionally to the vehicle speed, reaching a peak mid-frame vertical acceleration of –9.0 g at 48 kph. Conversely, Layout #3 has a peak mid-frame vertical acceleration of –4.0 g at 32 kph and maintains a similar magnitude at both 40 and 48 kph. At 48 kph, Layout #3 achieves a 5 g (44%) reduction in magnitude of peak acceleration, and an associated improvement in *comfort* over Layout #1 and #2. This reduction in peak mid-frame vertical acceleration for Layout #3 is the result of an increase in the available compression travel due to Layout #3's faster rebound during Phase 1 of the Pothole. Performance of Layout #3 may also benefit from reduced seal friction within the damper since the setting generates less rebound force [Doria, 2009]

©2023 Peck, K., Sadauckas, **J** published by TU Delft OPEN on behalf of the authors.

ISSN: 2667-2812

 http://dx.doi.org/10.59490/660572d0bfc285d425a828c0

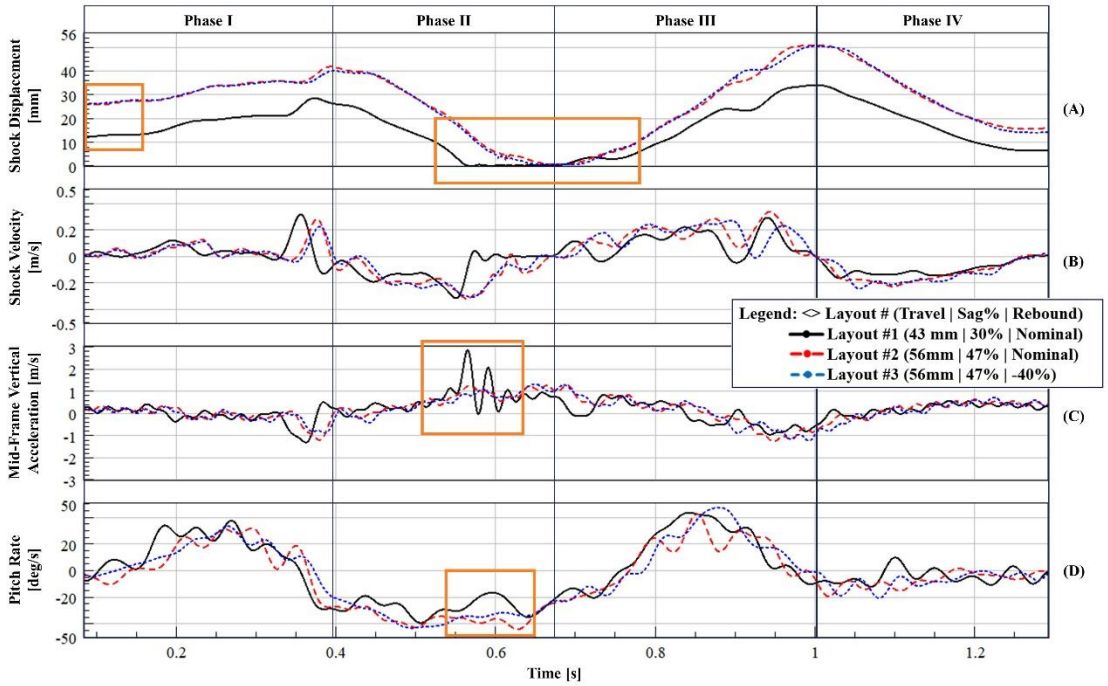


Figure 5. Camel (half-sinusoid) suspension test event for cruiser motorcycle with three rear suspension layouts, showing A) shock displacement, B) shock velocity, C) mid-frame vertical acceleration of the chassis, and D) pitch rate of the chassis.

Figure 5 shows rear shock displacement, rear shock velocity, mid-frame vertical acceleration, and pitch rate over the Camel at 32 kph. The plot is divided into four phases: In Phase I the rear suspension compresses as it encounters the Camel, in Phase II the rear suspension extends over the backside of the Camel, in Phase III the landing on the backside of the Camel occurs, and in Phase IV the rear suspension returns to sag. Early in Phase I the difference in target sag as well as the resulting difference in available extension travel between Layout #1 and Layouts #2/#3 is evident (plot A). During Phase II, Layout #1 reaches full extension quickly (plot A) and has an abrupt and prolonged topping event before eventually transitioning to Phase III where its compression is delayed with respect to the other layouts. The Layout #1 topping event corresponds to a spike in the mid-frame vertical acceleration (plot C) and a sharp reduction in the negative pitch rate (plot D) that is not present for Layouts #2 and #3. Conversely, Layout #2 during Phase II does not reach full extension which removes the abrupt topping event (plot A), subsequent mid-frame acceleration spike (plot C) or pitch rate change (plot D). Layout #3 through Phase II reaches full extension sooner than Layout #2, while its subtle topping corresponds to a similar magnitude mid-frame vertical acceleration (plot C). The reduction in topping abruptness for Layouts #2 and #3 is attributed to the increase in available extension travel and also to the reduced spring force near full extension (i.e., the lower installed spring preload force afforded by the deeper target sag state). Although suspension topping indicates reduced tire normal load, measuring normal load on a moving vehicle, especially over bump events, is difficult. As such, in a later section of this paper, simulation will be utilized to quantify rear tire normal load variation across the three rear suspension layouts as it relates to *road holding* performance.

Figure 6 shows a time series overlay of vehicle speed, front fork displacement, rear shock displacement, and pitch angle for all three rear layouts during a Threshold Braking event from ~100 kph. Layout #1 rear shock reaches full extension quickly (plot C) and sustains full extension for the duration of the braking event. It can also be observed that Layout #1 front fork nearly reaches full compression (plot B) during the Threshold Braking event. Conversely, the rear suspensions for both Layouts #2 and #3 never achieve full extension (plot C) during the Threshold Braking event and the front forks do not quite reach full compression (plot B). This additional margin to front fork full compression provides more suspension travel to absorb small road irregularities during threshold braking and having available rear shock travel before topping theoretically allows more rear brake to be applied, both of which can enable higher deceleration rates [Cossalter, 2004]. It is also hypothesized that for Layouts #2 and #3, the available shock extension displacement (plot C) during the threshold brake event provides a more consistent rear tire load, and thus additional (directional) stability under braking by inhibiting vehicle yaw. Again, multibody simulation will prove useful to quantify rear tire roadholding.

©2023 Peck, K., Sadauckas, **J** published by TU Delft OPEN on behalf of the authors.

ISSN: 2667-2812

 http://dx.doi.org/10.59490/660572d0bfc285d425a828c0

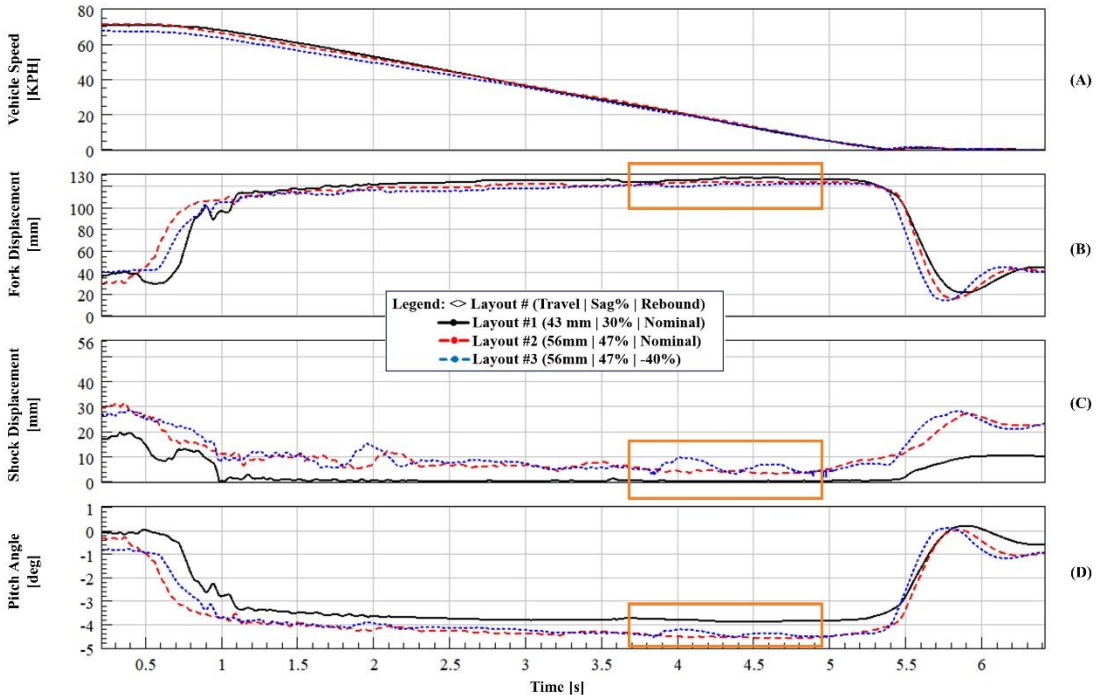


Figure 6. Threshold Braking test event of a cruiser motorcycle with three rear suspension layouts, showing A) vehicle speed, B) fork displacement, C) shock displacement and D) pitch angle of the chassis.

Qualitative vs. Quantitative Comparison

For the qualitative performance metric Exit Abruptness in the Pothole, Layout #3 achieved the best perceived rider comfort performance followed by Layout #2 and the difference in *comfort* was most noticeable at 40 kph and 48 kph. This qualitative performance directionally aligns with the peak mid-frame vertical acceleration measurement results (Figure 3). That data showed similar peak mid-frame vertical acceleration at the slower 24 kph and 32 kph speeds for all three layouts beyond which measured peak acceleration for Layout #1 and, to a lesser degree, Layout #2 increases linearly with vehicle speed, while Layout #3 maintains a reduced peak acceleration at 32 kph through 48 kph.

For the qualitative performance metric Rear Rebound Rate over the Camel, the rider noted the performance of Layouts #1 and #2 were very similar, while Layout #3 extended faster and was found to lack the desired *chassis control* by the rider. These perceived differences in rear suspension rebound performance can be observed within the quantitative data (Figure 5), with Layout #3 rear shock rebound velocity faster than both Layouts #1 and #2.

For the qualitative performance metric Rider-Vehicle Separation over the Camel, Layout #1 provided the largest rider-vehicle separation while Layout #2 provided none. Analysis of the Camel time series overlay (Figure 5) indicates that for Layout #1, a positive mid-frame vertical acceleration is generated when the suspension abruptly tops and is followed by a reduction in the negative pitch rate that slows the forward rotation of the vehicle. This change in pitch rate is hypothesized to cause the rider to momentarily separate from the vehicle. The rider, who is not rigidly attached to the rear sprung mass, maintains an initial, higher negative (forward) pitch rate from before the topping event even after the rear sprung mass pitch rate is reduced, thus causing separation through disparate rotational velocities. Conversely, as discussed for Figure 5, the peak mid-frame vertical acceleration for Layouts #2 and #3 does not indicate an abrupt topping event and the pitch rate of the chassis stays consistent (thus matched with that of the rider) during Phase 2 of the Camel.

For the qualitative performance metric Reaction to Brake Input during a Threshold Braking event, Layouts #1 and #2 provide similar perceived sensitivity to the initial brake input and were not found to be objectionable to the rider. However, Layout #3 was found to be more sensitive than desired, with the rear suspension extending quickly during the initial brake input and lacking the desired *chassis control*. However, after analyzing the Threshold Braking time series data (Figure 6), there is no clear indication in rear suspension displacement or in pitch angle that indicates Layout #3 performed deficiently. The lack of correlation between the

©2023 Peck, K., Sadauckas, **J** published by TU Delft OPEN on behalf of the authors.
ISSN: 2667-2812

 http://dx.doi.org/10.59490/660572d0bfc285d425a828c0

Threshold Braking qualitative and quantitative data is attributed to the manner in which the rider executed this specific event. Regardless of the suspension layout, the rider tried to perceptibly load the front tire before reaching maximum brake force. As a result, differences in rear suspension *chassis control* influence how the rider modulated the application of the front brake under these conditions. The rider was adapting their input and thus affecting measured vehicle response.

For the qualitative performance metric Maximum Pitch Angle during a Threshold Braking event, differences in perceived maximum pitch angle were noted between Layout #1 and Layouts #2 and #3, though none were found objectionable by the rider. Analysis of the Threshold Braking data (Figure 6) clearly shows a difference if maximum pitch angle between Layout #1 and Layouts #2 and #3 that directionally aligns with rider feedback. The differences in front fork compression and rear shock extension between Layout #1 and Layouts #2 and #3 were not mentioned as being perceptible by the rider. This omission is likely due to the smooth test surface, which would diminish the necessity of enhanced bump absorption, and by the usage of the front brake only, which foregoes potential improvements in deceleration from increased rear tire load if the rear brake was also being applied [Cossalter, 2004].

Multibody Simulation

Using FastBike (Cossalter, 2002), three multibody simulation models were developed based on physical measurements of the test vehicle and the measured rear suspension force versus velocity and force versus displacement characterization data (Figure 1). Each simulation model was tested over virtual events developed to match the Camel and Threshold Braking used during physical testing. The primary objective of this simulation was to enable of the calculation of tire normal load, for the determination of *road holding*, which is difficult to measure during physical testing due to cost and complexity associated with the required instrumentation.

Camel - Road Holding

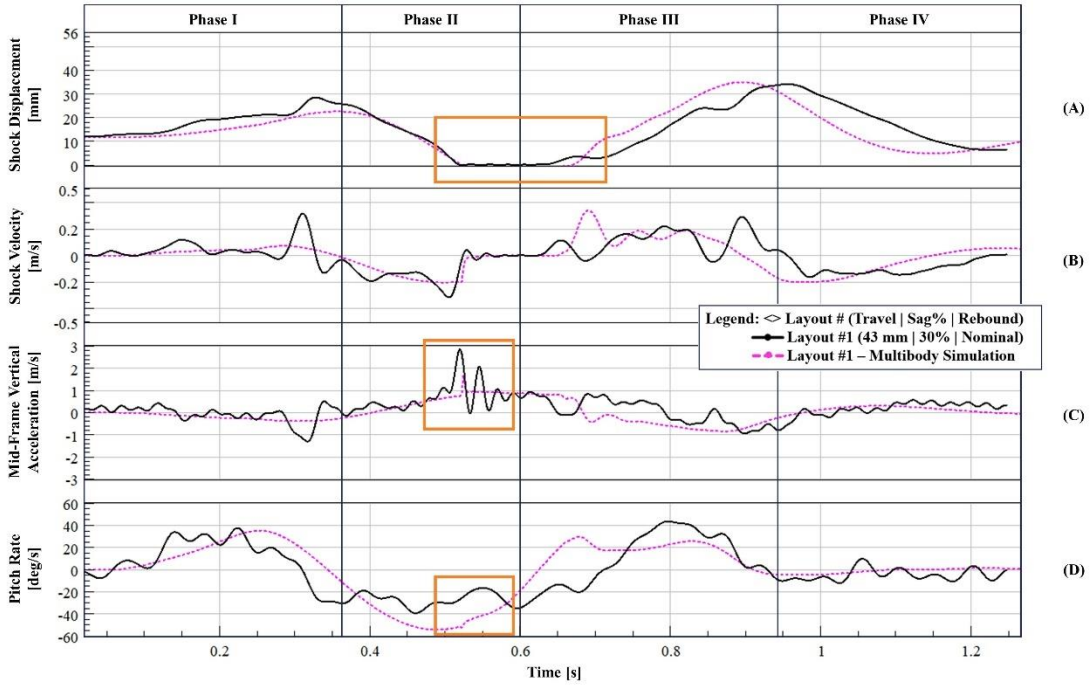


Figure 7. Test data (black/solid) and the simulation (pink/dotted) for cruiser motorcycle rear suspension Layout #1 (43mm rear shock travel | 30% sag | Nominal rear shock rebound damping) over Camel event, showing A) shock displacement, B) shock velocity and C) mid-frame vertical acceleration of the chassis and D) pitch rate of the chassis.

Figure 7 shows the rear shock displacement, rear shock velocity, mid-frame vertical acceleration, and pitch rate over the Camel at 32 kph for both Layout #1 physical test data (black/solid) and simulation (pink/dotted). The multibody simulation correlates well to the physical test data. In Phase II, both the test and simulation show a similar prolonged topping event (plot A) with corresponding

©2023 Peck, K., Sadauckas, **J** published by TU Delft OPEN on behalf of the authors.
ISSN: 2667-2812

 http://dx.doi.org/10.59490/660572d0bfc285d425a828c0

spike in mid-frame vertical acceleration (plot C). Additionally, both test and simulation show a change in pitch rate in conjunction with the topping event (plot D), though the magnitude of pitch rate change for the simulation is less than that of the physical test data. Similar correlation between test and simulation across the three Layouts is deemed sufficient to use their respective models to further study rear tire load, and *road holding*, for the Camel at 32 kph.

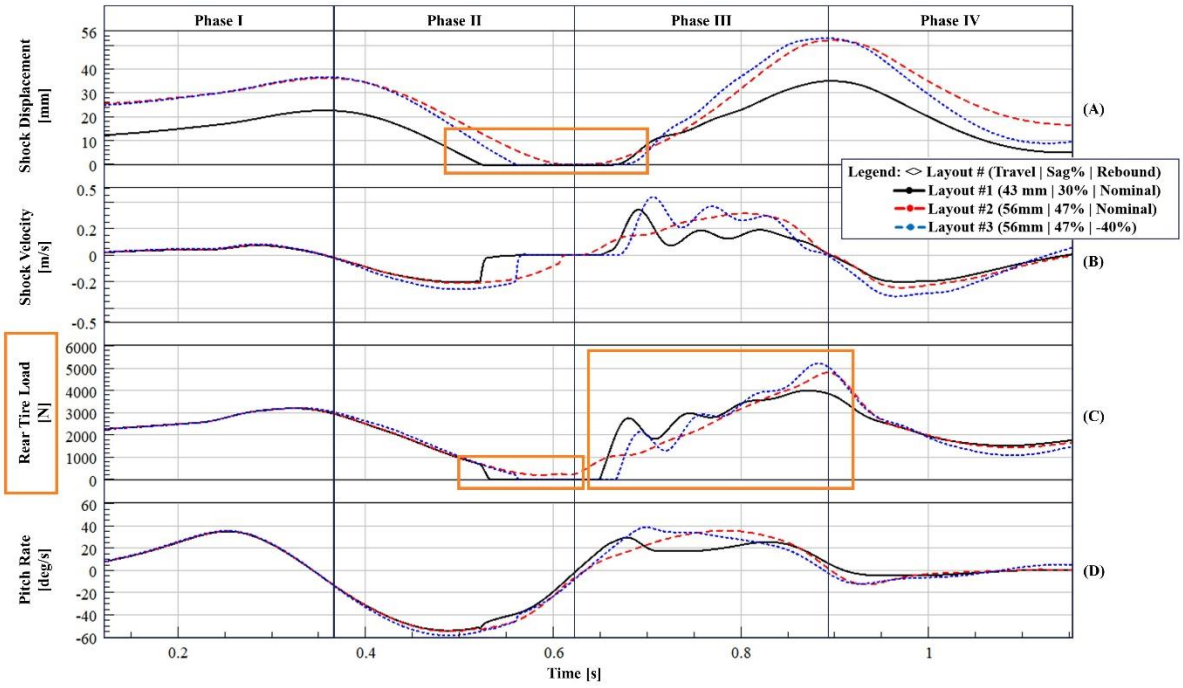


Figure 8. Simulation data for three rear suspension layouts on a cruiser motorcycle over the Camel event, showing A) shock displacement, B) shock velocity and C) rear tire normal load (label highlighted in orange) and D) pitch rate of the chassis.

Figure 8 shows simulated rear shock displacement, rear shock velocity, mid-frame vertical acceleration, and pitch rate over the Camel at 32 kph for each of the three rear suspension layouts. In Phase II, Layout #1 and Layout #3 have prolonged topping events (plot a) that corresponds to the rear tire load going to zero (plot C), indicating the rear tire is unloaded and potentially off the ground. As Layouts #1 and #3 move through Phase III and begin to compress, the rear tire load increases abruptly (plot C) as the tire regains contact with the ground, causing the tire load to oscillate momentarily. Conversely, Layout #2 does not have a prolonged topping event (plot A) and maintains a positive, albeit small, rear tire load. As Layout #2 begins to compress through Phase III, the tire load increases linearly until the Phase III compression event is complete. For Layout #1 and Layout #3, the momentarily null tire load in Phase II and the tire load variations in Phase III are not desired and have a negative impact on *road holding*.

Threshold Braking - Chassis Control and Road Holding

A virtual Threshold Braking event was simulated using the same three simulation models outlined above. Simulation model correlation across layouts was deemed acceptable, as alluded to in Figure 7. The virtual Threshold Braking event applies a front braking force to achieve a target deceleration rate of -0.72 g based on the track test average. During the physical Threshold Braking test (Figure 6), the rider modulated the front brake while monitoring the chassis pitch rate to achieve the desired load transfer to the front tire before applying maximum braking force. The virtual Threshold Braking maneuver achieves the desired deceleration but achieves it in a more consistent and abrupt manner.

©2023 Peck, K., Sadauckas, **J** published by TU Delft OPEN on behalf of the authors.

ISSN: 2667-2812

 http://dx.doi.org/10.59490/660572d0bfc285d425a828c0

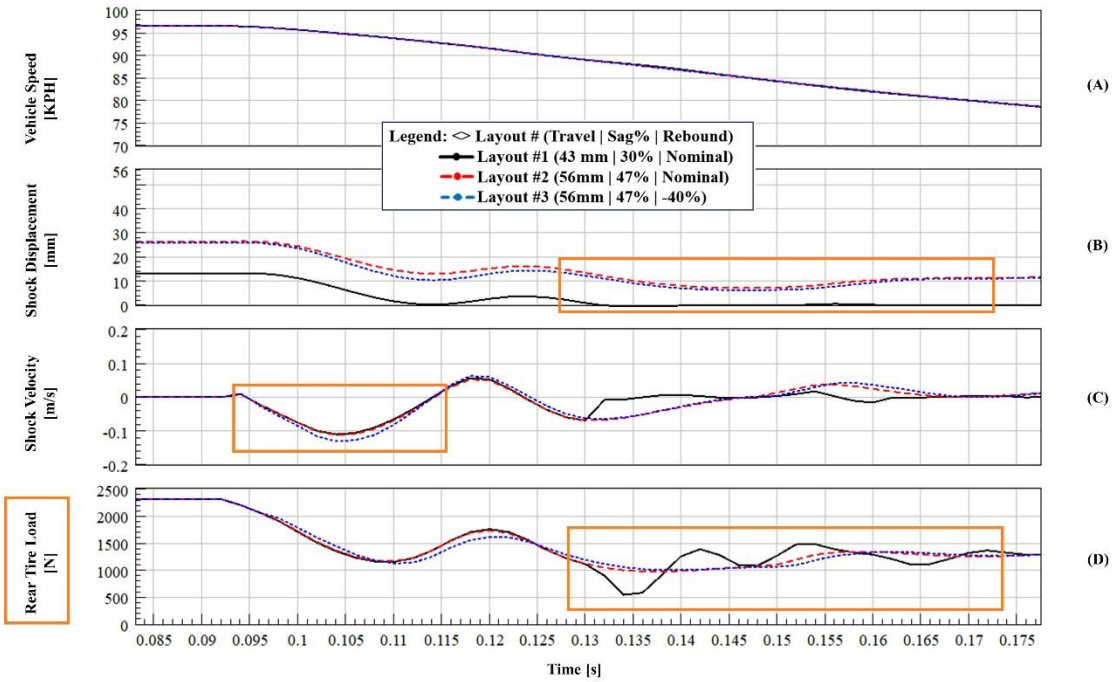


Figure 9. Simulation data for three rear suspension layouts on a cruiser motorcycle during Threshold Braking event, showing A) vehicle speed, B) shock displacement, C) shock velocity and D) rear tire normal load (label highlighted in orange).

Figure 9 shows the simulated time series results overlay of vehicle speed, front fork displacement, rear shock displacement, and rear tire normal load for all three rear suspension layouts during a Threshold Braking event from ~100 kph. Similar to test data shown in Figure 6, Layout #1 shock displacement (plot B) reaches full extension quickly after the Threshold Braking event begins. When the rear shock reaches full extension there is an abrupt reduction in rear tire load (plot D), though the rear tire load does not drop to zero likely because some normal load, due to the substantial unsprung mass, is still present. Additionally, the rear tire load (plot D) on Layout #1 oscillates through the remainder of the Threshold Braking simulated event, likely due to the stiffness and damping of the rear tire as the rear suspension remains at full extension. Conversely, Layouts #2 and #3 maintain a consistent rear tire normal load (plot D) at threshold, providing better *road holding* than Layout #1.

Figure 9 also shows a degradation in *chassis control* associated with Layout #3. During the initial virtual brake application, the shock velocity (plot C) for Layout #3 is higher than Layouts #1 or #2. This performance difference between layouts aligns with the qualitative feedback from the rider regarding Reaction to Brake Input, shown in Figure 2. Moreover, the fact that the simulation applies braking force in a consistent manner to achieve the prescribed deceleration allows the simulation to highlight differences in shock velocity that were masked in the instrumented test by the rider adapting their brake application to each layout. Thus, the simulation is better able to capture the degradation in *chassis control* of Layout#3 during Threshold Braking.

Conclusions

This research investigated the trade-offs of available suspension travel, target sag, and rebound damping on suspension performance in terms of *comfort*, *roadholding*, and *chassis control* for a cruiser motorcycle. Qualitative suspension performance ratings over specific on-road events were evaluated by a professional motorcycle test rider and correlated to quantitative data collected on the vehicle via instrumentation. All of the qualitative attributes noted by the rider were able to be extracted from the quantitative data through detailed analysis of the suspension displacement, stroking velocity, pitch rate, and pitch angle. These sensors and a commensurate data acquisition package are relatively common in industry and easily installed and removed from a test vehicle.

For a cruiser motorcycle with relatively limited rear suspension travel, improved *comfort* and *road holding* can be achieved by increasing the suspension travel and also increasing the target sag to maintain the original seat height, i.e., chassis trim. These suspension layout changes provide additional suspension travel from sag to full extension, resulting in an increase in topping resistance. Over the Camel event, the increased topping resistance of Layout #2 reduced both the measured and simulated peak

©2023 Peck, K., Sadauckas, **J** published by TU Delft OPEN on behalf of the authors.
ISSN: 2667-2812

mid-frame vertical acceleration and better maintained rear tire normal load (per simulation),thus providing improved *comfort* and *road holding* over the more conventional Layout #1. During Threshold Braking, the increased topping resistance of Layout #2 provided more consistent rear tire load further improving *road holding* over Layout #1, while also enabling a higher peak deceleration rate if combined front and rear braking were utilized.

As exemplified by Layout #3, increasing the suspension travel and target sag also enabled an improvement in *comfort*, achieved through a reduction in rebound damping. The reduction in rebound damping is feasible due to the increase in available extension travel between sag and full extension, which enables the suspension to extend faster and further without additional topping. For a negative event, such as the Pothole, where the road surface undulates downward, away from the vehicle, a rear suspension with reduced rebound damping is able better follow the road surface thereby extending further into the event. This additional extension allows for greater subsequent compression displacement over which to absorb the Pothole impact resulting in lower peak vertical acceleration. However, too much of a reduction in rear suspension rebound damping can adversely affect *chassis control*, allowing the suspension to extend faster than desired during certain large events and/or aggressive braking maneuvers. As demonstrated, the balance between *comfort, roadholding,* and *chassis control* is complex. Thankfully, through an appropriate combination of analysis, physical test, and multibody simulation, these tradeoffs can be understood and used to inform design.

Future research comparing qualitative versus quantitative suspension performance could focus on additional events, additional performance attributes, other motorcycle genres, alternate suspension parameter variants, and other test rider populations. Simulation model fidelity that includes bilinear spring and damping characteristics along with appropriately-adjusted spring preloads for setting sag, is crucial to obtaining realistic suspension behavior. Introduction of certain nonlinearities related to internal shock absorber friction and the verification of suspension parameters via subsystem identification and modelling has been shown to hold promise (Schoeneck, 2023). Finally, while directional indications of suspension response can be achieved by simulating generic bump events, correlation to test data requires a fairly accurate bump input profile.

References

Cossalter, V. (2006). Motorcycle Dynamics, 2nd ed. Lulu.com.

Cossalter, V., Lot, R., & Maggio, F. (2004). On the Braking Behavior of Motorcycles. SAE Transactions, 113, 1274–1280. http://www.jstor.org/stable/44724955

De Luca, P., & Doria, A. (2007). Setting of scooter suspensions to optimize comfort in the presence of road bumps. Ingegneria de Autoveicolo, 60.

Doria, A., Cossalter, V., Pegoraro, R., & Trombetta, L. (2009). On the non-linear behaviour of motorcycle shock absorbers. Journal of Automobile Engineering, 224j au. https://doi.org/10.1243/09544070JAUTO1273

Lot, R. & Sadauckas, J. (2021). Motorcycle Design: Vehicle Dynamics Concepts and Applications. Lulu.com.

SAE International Vehicle Dynamics Standards Committee, “Vehicle Dynamics Terminology,” SAE Standard J670, Rev. June 2022.

Schoeneck, N., Sadauckas, J., & Nagurka, M. (2023, Oct. 18-20). *Identification and modeling of a mountain bike front suspension subsystem equipped with a telescopic fork and tire damping*. Paper submitted, BMD2023, Delft University, Netherlands.

Strandemar, K. & Thorvald, B. (2005). The Ride Diagram - A Tool for Analysis of Vehicle Suspension Settings. The Dynamics of Vehicles on Roads and on Tracks, Italy.

Thede, P. & Parks, L. (2010). Race Tech's Motorcycle Suspension Bible. Motorbooks.

Cossalter, V & Lot, R. (2002). A Motorcycle Multi-Body Model for Real Time Simulations Based on the Natural Coordinates Approach, Vehicle System Dynamics, 37:6, 423-447, DOI: 10.1076/vesd.37.6.423.3523

©2023 Peck, K., Sadauckas, **J** published by TU Delft OPEN on behalf of the authors.

ISSN: 2667-2812

The Evolving Scholar Vol. 3, 2023 https://dx.doi.org/10.59490/65e596c8801ffd3afcd0f246

Bicycle and Motorcycle Dynamics 2023
Symposium on the Dynamics and Control of Single Track Vehicles
18 – 20 October 2023, Delft University of Technology, The Netherlands

Type of the Paper: Conference Paper

Revised

Instrumented Bicycle for Experimental Investigation of Braking Dynamics including Front Brake induced Rear Wheel Lift Up

[version 2; peer reviewed]

J. Skatulla[1,2,*], O. Maier[1], and S. Schmidt[2]

[1]Robert Bosch GmbH, Germany; johann.skatulla@de.bosch.com, ORCID 0009-0005-7653-2307; oliver.maier2@de.bosch.com
[2]University of Applied Science Merseburg, Germany; stephan.schmidt@hs-merseburg.de

*corresponding author

Name of Editor: Jason Moore
First published: 22/09/2023
Last published: 27/03/2024
Citation: Skatulla, J., Maier, O. & Schmidt, S. (2024). Instrumented Bicycle for Experimental Investigation of Braking Dynamics including Front Brake induced Rear Wheel Lift Up [version 2; peer reviewed]. The Evolving Scholar - BMD 2023, 5th Edition.
This work is licensed under a Creative Commons Attribution License (CC-BY).

Abstract:

Cyclists are usually afraid of using the front brake of their bicycles aggressively. They fear the danger of falling over the handlebar, sustaining serious neck or head injuries. Preventing this pitch-over can be addressed using electronic brake assistance. But little work is found on the dynamics involved, especially of the early phase were mitigating the pitch-over is still possible by brake pressure reduction. To address this, an instrumented bicycle equipped with sensors measuring variables of motion including absolute over ground velocity and attitude is presented. The need for a novel instrumented bicycle capable of capturing pitch-over dynamics and detecting when ground contact is lost, is pointed out. Needed sensors and their calibration is worked out, and the instrumented bicycle is built and tested. The capturing capabilities are shown, and robust jet precise methods of ground contact loss detection are presented.

Keywords: Bicycles, Vehicle Dynamics, Brakes, Pitch-over, Lift Up, Braking, Instrumented Bicycle

©2023 Skatulla, J., Maier, O., & Schmidt, S. published by TU Delft OPEN on behalf of the authors.
ISSN: 2667-2812

Introduction

When riding a bicycle, slowing it down is a safety relevant process. Various aspects can be investigated: Psychological questions, e.g., why, when, and how does the rider apply the brake? Or mechanical questions, e.g., how does the brake system deliver the stopping power. Or dynamical questions like: What are the dynamics of slowing a bicycle down?

Instrumented Bicycles

A promising way to investigate these and other related questions are instrumented bicycles (IB) because they enable in situ (outside of the laboratory) observations. Thus, using them for transport-related research has increased in popularity recently. A majority of the publications focus on behavioral and safety related studies (Gadsby & Watkins, 2020). Others deployed an IB to understand bicycle dynamics and cyclist behavior in real road scenarios (Dozza & Fernandez, 2014). As well as Kooijman, Schwab, and Meijaard (2008) validated a dynamic bicycle model using an unmanned IB.

Maier, Pfeiffer, and Wrede (2016b) presented an IB they use for closed loop testing a novel ABS system for bicycles. The IB included the following sensors: Brake pressure, wheel speed, inertial sensors, fork travel, and rear wheel lift up distance. Despite that, the braking was recorded with an external high-speed camera. For safety reasons, it allowed manned and unmanned testing. Due to this, a lot of additional mass was added, possibly influencing the bicycles handling and overall dynamics. Furthermore, there was no sensing of the bikes attitude including pitch and roll angle measurements and no rear wheel contact force measurement.

Bicycle dynamics

Bicycles exhibit complex dynamics that can be divided in two groups. (1) Longitudinal and vertical dynamics describe motions in the central plane of symmetry including rolling forward, stoppies, wheelies, and suspension activities. (2) Lateral dynamics take place out of the central plane of symmetry including balancing, leaning, steering, and turning.

Using the bicycles brake system can cause multiple motions. First and foremost, the bicycle is decelerated longitudinally when the brake is applied. If applied too strong on a low grip surface the wheels can start to skid, causing an out-of-plane slide sideways. Applying the front brake too strong on a high grip surface can cause an in-plane pitch-over motion. Even though pitch over accidents are a source of serious head and neck injuries (Bretting et al., 2010), little work can be found on brake induced pitch-over motion.

Another field of dynamics is crash testing. Bicycles typically have a high center of gravity (COG), combined with their short wheelbase makes them particularly prone to pitch over motion when colliding with an obstacle. Werner, Newberry, Fijan, and Winter (2001) performed a frontal collision of a bicycle with a rigid object. They observed the crash with cameras and compared the measured kinematics to a simulation. Bretting et al. (2010) crash tested bicycles in a controlled environment observing the motion extrinsically. They were taking external force measurements and track reference points like hip or head using photogrammetry. In both works the bicycles are not instrumented with sensors.

Although longitudinal bicycle and motorcycle dynamics are generally very similar, they are distinctively separated in two groups by the height of COG as well as the ratio between rider and machine mass. A modified motorcycle was fixed to a sledge and put under defined deceleration by Frank, Smith, Hansen, and Werner (2008). To the best of the authors' knowledge, there is no instrumented motorcycle used to investigate pitch-over motion in an in-situ over braking situation.

Theory of pitch-over motion

Using the standard ISO vehicle coordinate system (ISO 8855), pitch-over motion (also called "endo" or "stoppie") is defined as a rotation of the rider and his bicycle about the pitch axis of the bicycle. To provide greater understanding of the event and define a terminology used throughout this work, Figure 1 shows the pitch-over motion divided into three phases:

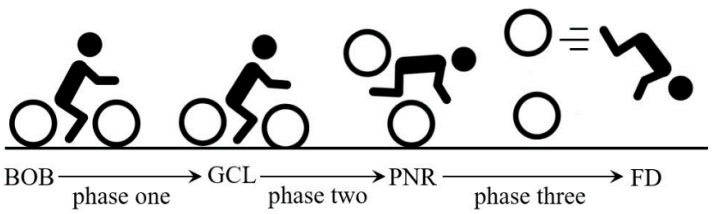


Figure 1. Phases of the pitch-over motion.

©2023 Skatulla, J., Maier, O., & Schmidt, S. published by TU Delft OPEN on behalf of the authors.

ISSN: 2667-2812

 http://dx.doi.org/10.59490/65e596c8801ffd3afcd0f246

The *first phase* is defined by the buildup of braking force and load transfer after the begin of braking (BOB). Applying the front brake too hard on a high grip surface will cause a significant load transfer towards the front wheel. During this phase, the rear wheel is still in contact with the road. There is no major movement present other than suspension movement and tire spring deflection.

If the brake force is further increased, at some point the rear wheel load vanishes. This marks the transition into *phase two*. Without the rear wheel pushing on the road the former completely constrained system becomes partly constrained (a mechanism rather than a structure), and the rear wheel experiences ground contact loss (GCL). If not acted upon swiftly, pitch angle and pitch rate increase until a point of no return (PNR) is surpassed. Even completely releasing the brake can no longer prevent a fall over the handlebars.

Phase three begins with the PNR. Bike and rider continue to pitch over, but the movement is non recoverable and will lead to a falling down of the rider (FD). Without ground contact or acting forces between rider and bicycle, both will follow a ballistic trajectory. This work does not consider phase three because the presented IB is not designed to crash.

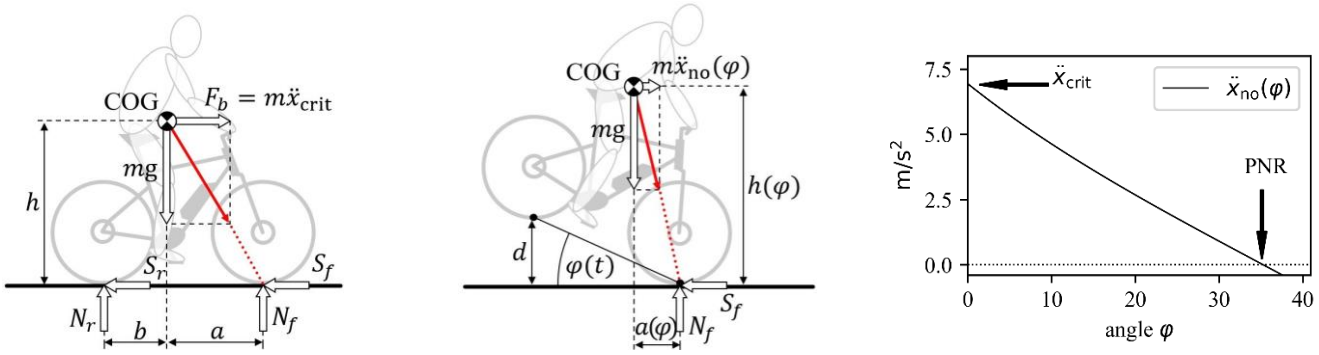


Figure 2. Load shift and point of no return calculations. (left) Load shifting before ground contact is lost. (middle) Forces acting during *phase two* of pitch-over. (right) Maximum possible deceleration $\ddot{x}_{\text{no}}$ over the pitch angle φ.

Previous work has looked at when ground contact is lost. Cossalter, Lot, and Maggio (2004) use a simplified motorcycle model to describe the load transfer needed for GCL to happen. The motorcycle and rider are modelled as single rigid body without suspension. Assuming a constant deceleration $\ddot{x}$, no road gradient, neglecting air drag and rolling resistance. The static equilibrium is defined by three equations:

$$\begin{aligned} S_f + S_r &= m\ddot{x} \\ mg - N_f - N_r &= 0 \\ N_f a - N_r b - (S_f + S_r)h &= 0 \end{aligned} \tag{1}$$

where m is the overall mass, h is the height of the COG, a and b are the distances from the front and rear wheel contact patch to the COG respectively, N_f and N_r are the front and rear tire loads, S_f and S_r are the front and rear braking forces, g is the acceleration due to gravity, and $\ddot{x}$ is the deceleration. The system is solved for the tire loads:

$$\begin{aligned} N_f &= mg\frac{b}{a+b} + m\ddot{x}\frac{h}{a+b} \\ N_r &= mg\frac{\mathrm{a}}{a+b} - m\ddot{x}\frac{h}{a+b} \end{aligned} \tag{2}$$

The equations show a counteracting, but linear influence the deceleration has on the tire loads. When decelerating, the load is shifted to the front, acceleration shifts load to the back. Forcing Nr to zero and solving for $\ddot{x}$ gives the value for which GCL occurs:

$$\ddot{x}_{\text{crit}} = \frac{a}{h} \cdot \mathrm{g} \tag{3}$$

with the critical deceleration $\ddot{x}_{\text{crit}}$ (Cossalter, Lot, & Maggio, 2004). Note that $\ddot{x}_{\text{crit}}$ is only dependent on the COG's position and not on the mass of bicycle or rider. Imagine the following geometric representation as an aid. When the combined vector of gravitational force and brake force surpasses the front wheel contact point, a GCL must occur (see Figure 2, left).

©2023 Skatulla, J., Maier, O., & Schmidt, S. published by TU Delft OPEN on behalf of the authors.

ISSN: 2667-2812

Maier, Pfeiffer, Scharpf, and Wrede (2016) tried the same approach for bicycles, giving identical findings. But they also presented a simplified dynamic model for *phase two* of the pitch-over motion. Considering moments of inertia as well as changes in geometry:

$$(J_{\mathrm{CG}} + m \cdot d^2) \cdot \ddot{\varphi}(t) = m \cdot \ddot{x}(t) \cdot h(\varphi) - m \cdot \mathrm{g} \cdot a(\varphi) \tag{4}$$

in addition to the previous variables, J_{CG} is the overall angular momentum and $\ddot{\varphi}$ is the rate of change of the pitch angle. Note that $h(\varphi)$ and $a(\varphi)$ are now varying with the pitch angle dependent position of the COG relative to the front wheel's contact point.

Simply assuming $\ddot{\varphi}$ equals zero, the minimal deceleration $\ddot{x}_{\mathrm{no}}(\varphi)$ for retaining pitch-over motion as a function of φ is found:

$$\ddot{x}_{\mathrm{no}}(\varphi) = \frac{a(\varphi)}{h(\varphi)} \cdot \mathrm{g} = f(\varphi) \ . \tag{5}$$

Their calculations show: $\ddot{x}_{\mathrm{no}}(\varphi)$ decreases with increasing pitch angle. I.e., the pitch-over motion has a self-amplification effect. This seems rather plausible considering the growing lever arm when pitch angle increases. Eventually, $\ddot{x}_{\mathrm{no}}(\varphi)$ becomes zero. This is the case when the COG is directly above the front wheels contact point and marks the PNR. This is also rather plausible because the brake does not have the opportunity to apply acceleration. Furthermore, it means that during *phase two* of a pitch-over motion, the deceleration $\ddot{x}(t)$ must be reduced below $\ddot{x}_{\mathrm{no}}(\varphi)$, in order to stop and reverse the pitch-over motion.

Contribution

Despite the many experimental work on crash testing covering *phase three* of a pitch-over motion, there are only few theoretic and no experimental work on *phase two*. But unlike with passenger cars, a bicycle is a rider-active vehicle in which the rider can control the behavior of the vehicle through changes in body position and is not "coupled" to the vehicle. Because the rider weighs significantly more than his bike, the influence that can be exerted is great. Thus, the modelling errors made by previous authors must be non-neglectable. This motivates doing experimental research on *phase two* of a pitch-over motion. Consequently, this work describes an IB designed to be used for investigation of *phase two* and its dynamics. It is equipped with sensors capable of detecting GCL in the beginning of *phase two*, and with sensors to observe how the bicycle behaves during *phase two*.

Method

As stated in the introduction, this work presents a novel IB that will be used to investigate the dynamics of *phase two* experimentally and facilitates testing of models against real world measurements. Figure 3 (left) shows the IB, it is an eBike equipped with Bosch drive unit, battery, and ABS system. It has a trekking bike frame geometry with front suspension only. Table 1 holds information about the relevant components used.

Mounted sensors

The bike is equipped with sensors with the aim of measuring all important signals that characterize a pitch-over motion. But also, the sensors should be kept small and lightweight in order not to disturb the measurement. A realistic riding experience was a priority because the rider must have confidence in the bike to do high but controlled lift-ups. All used sensors are summarized in Table 2, and Figure 3 (left) shows them mounted to the bike.

Core part of the instrumentation is a GL2400 datalogger from Vector Informatik GmbH. Key features are support of up to eight simultaneously logged CAN busses (four of which are CAN FD capable), four analog inputs, and support for the universal measurement and calibration protocol (XCP). This protocol enables capturing internal software signals from either the ABS system or the drive unit. This makes debugging new control algorithms much easier. All captured data is logged at a rate of 500 Hz onto a

Table 1. Components of the IB.

Component	Model	Setup
Frame	Bosch development frame	
Base brake front	Magura eStop 203mm	
ABS-System	Bosch eBike ABS Gen 2	
Fork	SR Suntour Aion, 100 mm, 29", axis 15x100 mm	Air spring pressure 70 psi, mid rebound setting, unloaded length 106 mm
Wheels	Schwalbe Marathon 28", 47-622	inflation pressure 2.0 bar

©2023 Skatulla, J., Maier, O., & Schmidt, S. published by TU Delft OPEN on behalf of the authors.

ISSN: 2667-2812

SD card. The logger and all other sensors are powered by the eBike's 36 Volt battery. A programmable 4.3-inch display is mounted on the handlebars. It displays live data to the rider, allowing an immediate check of the riding maneuver and comparing it to maneuver specification.

The most important signal source is the "Ellipse N" inertial navigation system (INS) consisting of an inertial measurement unit (IMU) mounted to the seat tube and an antenna to receive signals from the global navigation satellite system (GNSS) mounted in front of the head tube. The IMU measures accelerations and angular rates in three orthogonal axes, making it a 6-axis sensor. Integrated signal processing combines these IMU and GNSS measurements into a 9-axis navigation solution, including: velocity, orientation, and position. All measurements are sent via CAN bus to the logger. The INS is configured to give readings relative to the rear wheel contact point in the standard ISO vehicle coordinate system (ISO 8855) as seen in Figure 3 (right). Note that the navigation solution is an estimate not a real measurement, but with high accuracy though. The datasheet states a root mean square accuracy of 0.1° for roll and pitch and 0.03 m/s for the velocity (SBG Systems, 2020). The IMU's mounting orientation and position relative to the rear wheel contact point are important parameters that can be changed in the calibration software of the INS. They must be identified and calibrated with great care. The method presented in Rodrigo Marco, Kalkkuhl, Raisch, and Seel (2020) is used, resulting in v_z and v_y to be mean zero during a straight-line riding maneuver.

The front axle is not rigidly attached to the bike frame. Relative to the frame, it is rotated around the steering axis and moved longitudinally along the suspension axis. Furthermore, it is subject to elastic deformation under load, especially fork bending as discussed in Klug et al (2021) and Skatulla, Maier, and Schmidt (2023). In order to measure its dynamics, a second "Ellipse N" is mounted near the axle on the lower part of the fork. Here only the IMU is used in the integrated signal processing, resulting in a vertical reference unit (VRU). Without a GNSS antenna only pitch and roll can be estimated with an accuracy of 0.1° (SBG Systems, 2020).

To measure suspension movement a displacement transducer is mounted between the upper and lower part of the fork. The transducer is supplied from the logger with a constant reference voltage and outputs an analog voltage proportional to its position, measured by the logger. It was calibrated to read zero stroke when the fork is completely compressed to its end stops.

The bike is equipped with a Bosch eBike ABS generation 2. This system consists of three parts. An electronic control unit (ECU) together with a hydraulic actuator is put in one housing and mounted to the lower fork arms. Two external speed sensors are mounted on front and rear wheel with tone wheels mounted to the brake disks. A sensor inside the ECU measures the pressure applied to the brake caliper. The ABS system is put in a passive state not doing any pressure modulation and only outputs its measurements on the CAN bus for logging.

In order to also measure the pressure input to front and rear brake applied by the rider, two additional sensors are installed near the master cylinders. They are also supplied from the logger, measuring their analog outputs as well. The pressure sensors where calibrated to read 0 bar if no break input is applied.

Table 2. Sensors attached to the IB.

Sensor	**Brand, Model**	**Physical quantity**
Datalogger	Vector Informatik GmbH, GL2400	CAN bus and analog inputs
VRU fork	SBG Systems, Ellipse N	Acceleration, angular rate, pitch and roll
INS frame	SBG Systems, Ellipse N	Acceleration, angular rate, velocity, orientation, position
GNSS-Antenna	SBG Systems, TW7972	(Used for INS frame)
Linear potentiometer fork	2D Data, SA-LP	Distance
Wheel speed front	Bosch, eBike ABS	Rotational speed
Wheel speed rear	Bosch, eBike ABS	Rotational speed
Pressure front wheel caliper	Bosch, eBike ABS	Pressure
Pressure front master cylinder	Bosch, DS2	Pressure
Pressure rear master cylinder	Bosch, DS2	Pressure
Laser sensor liftup height	Kistler, CHFA-HF-500C	Distance
Rear wheel load	CSM GmbH, STG6 MM and DMS	Force

Note: Acceleration, angular rate, velocity, attitude, and position are three dimensional quantities.

©2023 Skatulla, J., Maier, O., & Schmidt, S. published by TU Delft OPEN on behalf of the authors.

ISSN: 2667-2812

 http://dx.doi.org/10.59490/65e596c8801ffd3afcd0f246

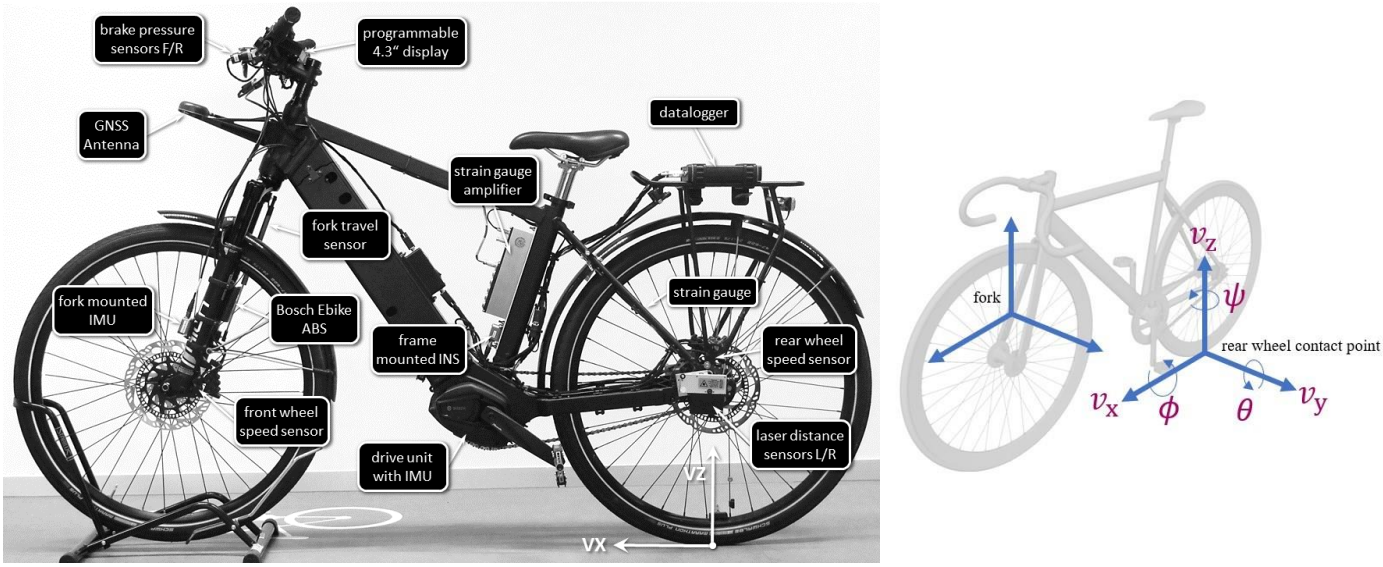


Figure 3. (left) Mounting position of sensors attached to the IB. (right) Coordinate system definition used for the IB according to ISO8855 and positioned at the rear wheel contact point.

During a pitch-over motion the ground contact loss of the rear wheel defines the transition between *phase one* and *phase two*. A method for direct measurement is needed. Important feature of the wheel is the elasticity of its tire, compared to the stiff road surface. But if properly inflated the tires elasticity is high and does not allow a lot of tire compression if loaded. Bicycle tire stiffness found in literature is about 100 N/mm (Klug, 2020; Knuit et al., 2015; Maier et al., 2018). With the 50th percentile rider (Maier et al., 2016) a load of 475 N is estimated at the rear wheel, this results in approx. 5 mm tire travel. This is not much and makes the GCL identifiable with a distance measurement. Three methods are proposed: First a distance measurement, second a force measurement and third a wheel speed based GCL detection.

GCL detection method 1: distance measurement

The goal is to measure the distance between tire and road. Because the tire rotates, the measurement device must be mounted to the frame. Since the tire has tangential road contact, the measurement device should be mounted normal to the contact point, this means mounting it at the height of the rear axle in the bikes x direction. Since a bicycle can lean over the roll axis, ideally the sensor must be placed in the middle of the axle. This is of course not possible. Therefore, two sensors are mounted on the right and left side of the rear wheel axle with identical distance to its middle. The mounting position can be seen in Figure 3 (left).

With this setup the roll angle induced elongation of the distance measured on one side is counteracted by shortening on the other side. Figure 4 left shows a cross section y-z-plane, the rear wheel is rolled with angle ϕ and is lifted up the ground by d. The reading of both sensors is l_L and l_R respectively. The measured lift-up distance m is calculated with:

$$m = \frac{l_\mathrm{L} + l_\mathrm{R}}{2} - m_0 \approx d\,. \tag{6}$$

With the length m_0, which is the distance in the symmetry plane of the undeformed tire between the axle and the undeformed outer perimeter. There is a measurement error e_ϕ that is made when the bike is rolled, it can be calculated with:

$$e_\phi = m - d = (r_\mathrm{T} + d)\left(\frac{1}{\cos(\phi)} - 1\right) \tag{7}$$

where r_T is the tire radius. Because pitch-over motion needs a high deceleration, high grip is needed. Any big roll angle would produce big side holding forces and therefore would capitalize on the bearable longitudinal force to much (traction circle). In a GCL scenario roll angle is usually rather small. For small angles the error vanishes.

©2023 Skatulla, J., Maier, O., & Schmidt, S. published by TU Delft OPEN on behalf of the authors.
ISSN: 2667-2812

http://dx.doi.org/10.59490/65e596c8801ffd3afcd0f246

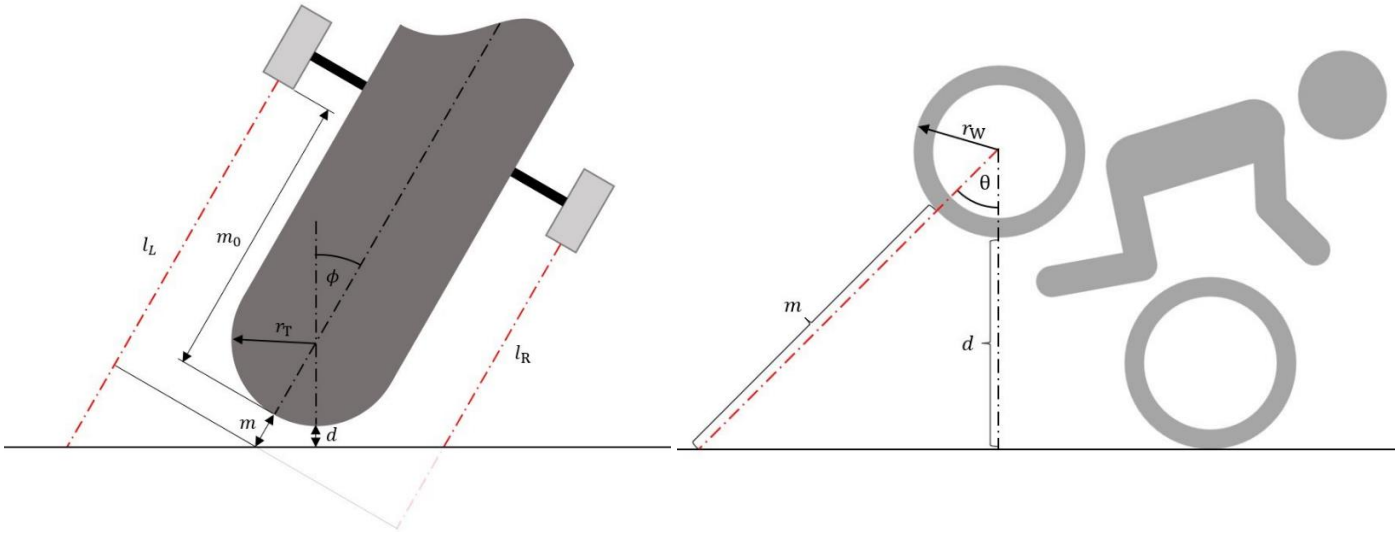


Figure 4. Geometric errors influencing laser distance sensor readings. (left) Error emerging from rolling the bicycle. (right) Error made from pitching the bike.

Figure 4 right shows a *phase two* of a pitch-over motion in the x-z-plane with large pitch angle. The measured lift-up distance m is not the same as the true value d, the error e_θ is calculated with:

$$e_\theta = m - d = l\,(\tan\theta - \sin\theta) + r_W\left(\frac{1}{\cos(\theta)} - 1\right). \tag{8}$$

where r_W is the wheel radius, l is the wheelbase, and θ is the pitch angle. This is a significant error for large pitch angles. Both error components, e_ϕ and e_θ, can be superimposed. The total measurement error caused by roll and pitch is $e = e_\phi + e_\theta$. Figure 5 (left) shows the evolving error over the pitch and roll angle using the IB's values. Up until a lift-up height of 0.2 m the error stays under 11 mm even with a roll angle of 20°. To gain perspective, the PNR of the IB (with 50th percentile rider) is used as maximum pitch angle in the graph, at roughly 35° or 0.7 m. At the PNR the error is already 0.25 m. But GCL usually occurs with zero pitch angle and very small roll angle, in this important situation the measurement is not geometrically falsified.

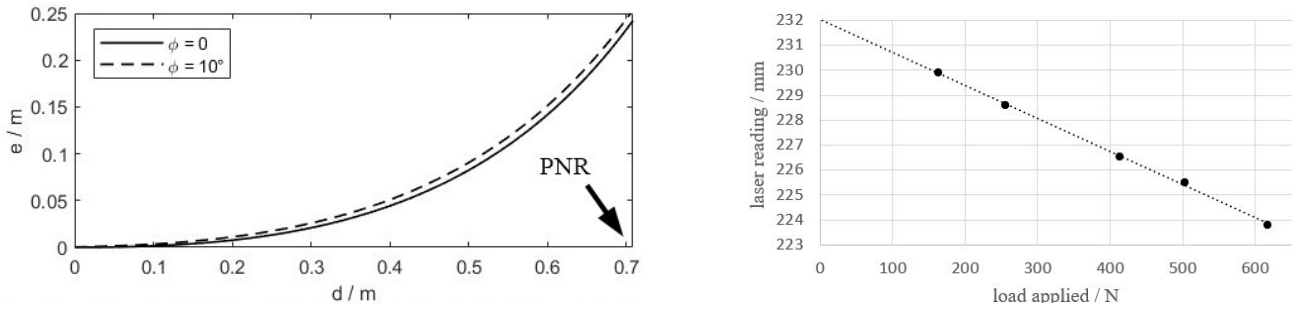


Figure 5. (left) Error evolving over roll angle and lift-up distance d. (right) Calibration of the distance m_0.

To calibrate m_0 needed to calculate m with Equation (6), the bike is placed upright on a level surface with negligible roll and pitch angle. The saddle is loaded with weights and the resulting rear wheel load is measured with a weighing scale. Simultaneously the measured distances from the lasers are noted. Figure 5 (right) showing the results, the readings are extrapolated using linear regression to obtain the reading for no load $m_0 = 232$ mm. With this calibration $m > 0$ indicates GCL.

GCL detection method 2: force measurement

A second direct method to measure the GCL is to measure the force applied from the wheel to the ground. It gives an indication of the load shift under braking and when the force completely vanishes the wheel has lost ground contact. A good position where to measure the load must be found, the most direct way of measuring the load would be by tire pressure. This poses firstly the challenge

©2023 Skatulla, J., Maier, O., & Schmidt, S. published by TU Delft OPEN on behalf of the authors.

ISSN: 2667-2812

of wirelessly transmitting the signal and secondly the change in tire pressure is in the following analyzed to be too small for measurement. A rough estimate of the pressure change under load can be calculated assuming isothermal volume change. The volume of the tire without load is approximated with a torus:

$$V_{\mathrm{noLoad}} = 2\pi^2 r^2 (R + r) \approx 3.64 \cdot 10^{-3}\ \mathrm{m}^3\ . \tag{9}$$

To calculate the loaded volume a rough estimate is to extrude the contact patch size with the tire springs travel. The wheels contact patch must withstand 475 N (50$^{\mathrm{th}}$ percentile rider) with an inflation pressure of 2.0 bar. This results in approximately $2.4 \cdot 10^{-3}\ \mathrm{m}^2$ contact patch size ($A = {}^{F}/_{p}$). Also, a tire travel of 5 mm was taken from Figure 5 right for extrusion, resulting in a displaced tire volume $V_{\mathrm{C}} = 0.12 \cdot 10^{-3}\ \mathrm{m}^3$. Assuming isothermal volume change, the following formula gives the change in tire pressure:

$$\frac{p_{\mathrm{noload}}}{p_{\mathrm{load}}} = \frac{V_{\mathrm{noload}} - V_{\mathrm{C}}}{V_{\mathrm{noload}}} \rightarrow \Delta p = p_{\mathrm{load}} \left(\frac{-V_{\mathrm{C}}}{V_{\mathrm{noload}}} \right). \tag{10}$$

With realistic parameters, taken from the IB, this results in a tire pressure change of -6.6 mbar. To get an accurate reading a tire pressure sensor with a resolution in the range 0.1 to 1 mbar is needed. Further requirements are a measurement frequency of at least 100 Hz and a formfactor that makes it mountable to the rotating wheel. No sensor fulfilling all of those requirements could be found. Thus, the tire pressure approach is pursued no further.



Figure 6. FEM results showing the bicycle frame deformation caused by A) normal load, B) braking forces, and C) acceleration.

Chosen solution is to use strain gauges to measure the strain induces by the rear tire load. Two main approaches emerge from literature. One direction is to construct and install custom made wheel hubs instrumented with strain gauges to measure the ground contact force (De Lorenzo & Hull, 1999; Drouet & Champoux, 2010). But this is very time consuming and complex, thus is not pursued further.

The other direction is to apply strain gauges to the load transferring elements of the bicycle frame (Manolova et al., 2015; Petrone et al., 2012; Pirnat et al., 2011). In order to find the best position to apply the strain gauges, a simulation of the IB's frame using the finite elements method (FEM) is consulted. Realistic loads are applied at the rear axle, namely: normal load, braking and acceleration.

FEM simulation results from each isolated load scenario are shown in Figure 6, revealing that the chain side seat tube is mostly loaded by normal load and less by braking or accelerating. A strain gauge is applied to the inner side of the chain seat tube, as marked in Figure 6. The STG6 MM module amplifies the signal from the strain gauge and transmits it via CAN bus. Its readings are calibrated using a weighing scale and various loads applied to the saddle of the bicycle as described above. Using linear regression, a calibration curve is fitted and stored to the amplifier.

The proposed normal load measurement with a strain gauge is a more indirect measurement compared to the tire inflation pressure approach. Interferences from braking and acceleration are attenuated but still present and dynamic loads from accelerating the wheels mass are present. This is a drawback of this method. But on the other hand, they can be mitigated by firstly not using the rear brake and secondly will the force reading only be analyzed in *phase one* before GCL. This means there is nearly no movement of the rear wheel and thus only small forces caused by its inertia.

©2023 Skatulla, J., Maier, O., & Schmidt, S. published by TU Delft OPEN on behalf of the authors.

ISSN: 2667-2812

 http://dx.doi.org/10.59490/65e596c8801ffd3afcd0f246

GCL detection method 3: rear wheel speed

During braking not only the kinetic energy of the rider and bicycle must be dissipated through the brakes, but also the stored rotational energy of the wheels. In case only the front brake is applied the rear wheel is slowed down from friction with the road. When GCL occurs, it is not braked any more and conserves its energy by spinning freely. This can be recognized by the rear speed signal separating from the front and moving sideways, producing a noticeable "kink". The rear brake must intentionally not be used for this method to work, making it unreliable. But, on the other hand this method is probably very precise.

Results

After building up the IB and doing a so-called shakedown test, making sure that every sensor is properly fixed to the frame, several calibration runs are done to ensure proper orientation of the Ellipse and that all other sensors read plausible values. With that done, a skilled rider is asked to perform four experiments with the goal to test the IB's ability to capture pitch-over motion and to detect GCL accurately.

First, he is asked to try braking as hard as possible without the rear wheel losing ground contact (threshold braking), there is no limit on the number of attempts, but the external high speed camera footage is used to exclude tries where ground contact loss occurred. After the experiment the attempt with the highest deceleration of all valid runs is selected and the results are plotted in Figure 7 (left). The rider applies the brake aggressively with a pressure gradient of approx. 500 bar/s up to 40 bar and holds it for a period of 1 sec, afterwards the brake is released with a gradient of 250 bar/s. The rear brake is not applied. Using the recorded speeds from front and rear wheel as well as the ellipse, an average deceleration during the pressure holding period of 6 m/s² is observed. The front wheel speed shows an initial slippage due to the front wheel load building up slowly and fork bending induced oscillations near the end of the braking. During brake apply the pitch angle increases around 2° to 3° and the fork suspension travels approx. 50 mm under load. Both look like smoothed replicas of the brake pressure.

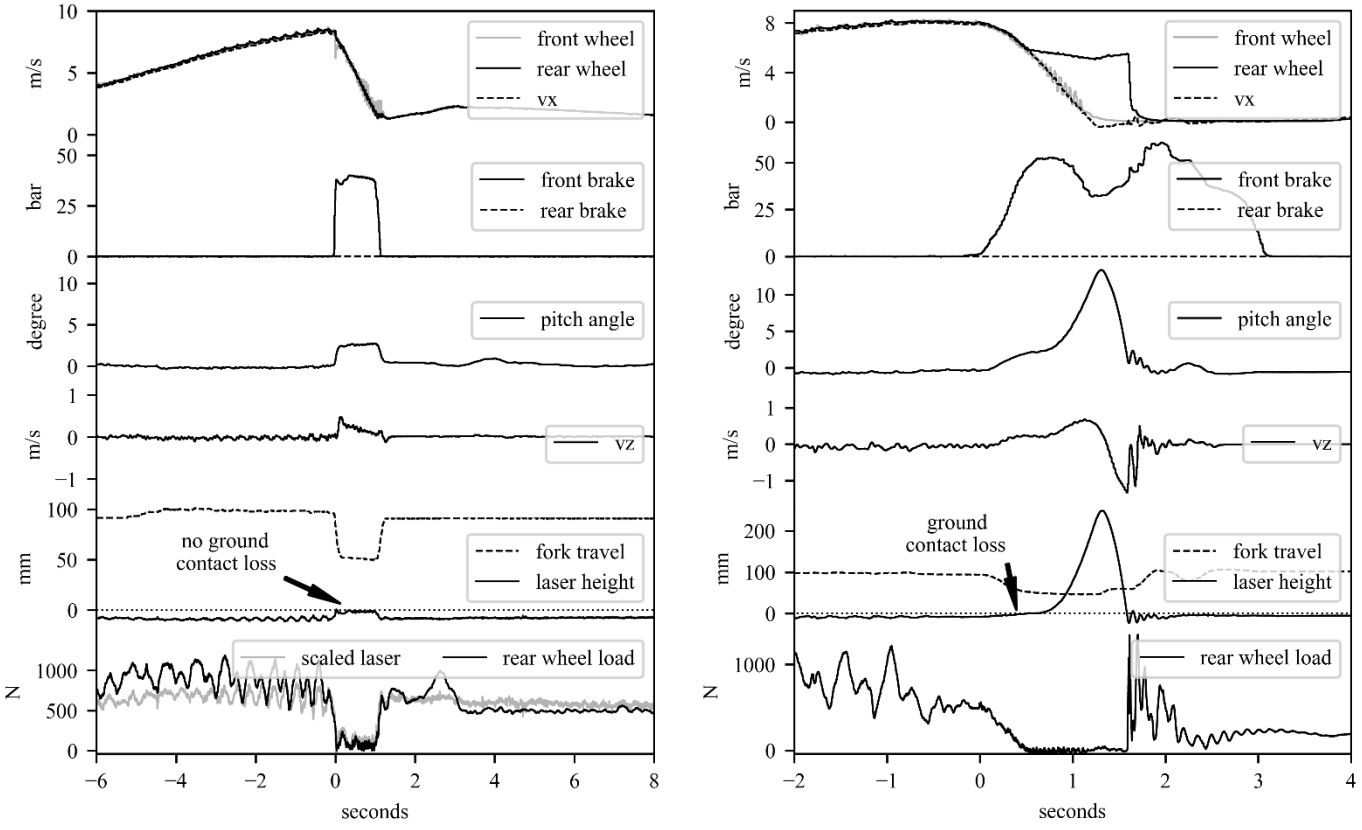


Figure 7. Measurement results taken from the IB. (left) Threshold braking without GCL. (right) Controlled higher lift-up until standstill.

©2023 Skatulla, J., Maier, O., & Schmidt, S. published by TU Delft OPEN on behalf of the authors.

ISSN: 2667-2812

http://dx.doi.org/10.59490/65e596c8801ffd3afcd0f246

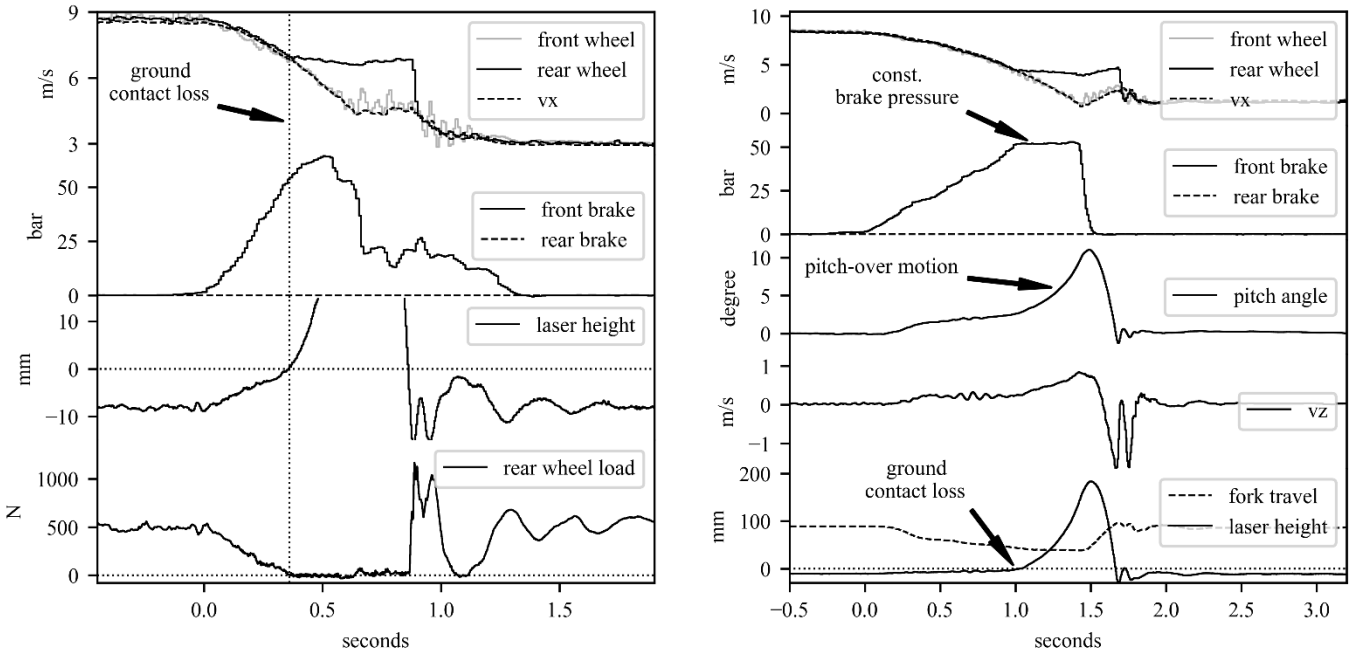


Figure 8. Measurement results taken from the IB. (left) Comparison of GCL detection methods. (right) Study of self-amplification.

Results of the *second* experiment shows Figure 7 (right). The rider is asked to perform a high lift-up scenario and hold the brake pressure until the bike comes to a full stop. At $t = 0.5$ sec the rear wheel speed shows a kink and progresses sideways, front wheel and ellipse speed continue to decrease. At this moment the brake pressure is 50 bar, the laser height is zero and the rear wheel load is also near zero. Consulting the high-speed camera footage, this moment is defined as GCL. The deceleration is approx. 6.5 m/s² at GCL. At $t = 0.5$ sec the wheel touches the ground again, causing big spikes in the load signal, followed by some bouncing.

The *third* experiment is about testing the precision of GCL detection, the results are shown in Figure 8 (left). The rider is instructed to increase the brake pressure until he feels pitch-over motion starting and release the brake gradually afterwards. A horizontal line marks the time when GCL is detected by the lasers. Brake pressure is 55 bar at that moment and rear wheel speed as well as rear wheel load show characteristic kinks. The deceleration is approx. 6.6 m/s² at GCL. Please note: The laser signal is clipped by the zoom, its maximum value is 84 mm.

Lastly, the rider is instructed for the *fourth* experiment (Figure 8, right) to slowly increase the brake pressure with a gradient of 50 bar/s. After one second, critical brake pressure of 50 bar is reached. A pitch-over motion starts, and the brake pressure is held constant by an end stop, mounted to the handlebar. The deceleration is approx. 6.4 m/s² at GCL. Pitch angle and rear wheel height increase progressively until t = 1.5 s when the brake is released, reaching maximum values of 10° and 200 mm respectively. Afterwards the bike starts to come down again, impacting on the surface followed by brief bouncing.

Discussion

The maximum achieved deceleration in all experiments is very similar (6, 6.5, 6.6, and 6.4 m/s²) and aligns with theoretic results: The combined COG of the IB with a 72 kg weighted driver is approx. 0.7 m behind the front wheel and 1 m off the ground, using Equation (3) a critical deceleration of 6.87 m/s² is calculated.

The ability of the IB's sensors to reliably distinguish between *phase one* and *phase two* is analyzed by comparing the *first* and *second* experiment (Figure 7, left and right). The rear wheel speed signal shows the "kink" only when GCL occurs. This is a binary information, meaning GCL can be detected precisely but there is no information about load shift in *phase one* or lift height in *phase two*. The wheel load on the other hand yields continuous information about the load shift in *phase one*, but no information about GCL and lift height in *phase two*. This is seen in the experiments: The measured deceleration is close to the critical deceleration and the measured wheel load in both is roughly zero. One can hardly tell the difference between end of *phase one* and GCL or *phase two*. Lastly, the laser height captures the most information. It strictly monotonically increases before and after GCL. Thus, giving continuous information in *phase one* and *phase two*. The laser measurement method is considered the most suitable for

©2023 Skatulla, J., Maier, O., & Schmidt, S. published by TU Delft OPEN on behalf of the authors.

ISSN: 2667-2812

evaluating pitch-over motion. It provides accurate and precise measurements, making it highly effective in this regard. On the other hand, the wheel speed method can also be used to detect ground contact loss (GCL), but it comes with a significant limitation – the rear wheel cannot be braked. However, in applications where cost is a crucial factor, this restriction may be deemed acceptable.

The wheel load measurement is not suited for robust GLC detection but can be used for load shift evaluation. It reveals that the load shift happens instantly and that there is no noticeable delay between brake actuation, load shift, and fork suspension movement. To validate the strain gauge readings, the laser height is scaled by the identified tire stiffness and shown next to the force measurement in Figure 7 (left). They agree nicely during braking, during acceleration before and after the braking the side effect of additional forces passing through the seat stay can be seen. Please note that the laser height and wheel load shown in Figure 8 (left) look very alike, they seem to be mirrored. With a known and calibrated tire stiffness the accurate laser height measurement could very well be used as a substitute for the wheel load measurement.

The temporal precision of the GCL detection methods is found to be very good with the *third* experiment. The laser height threshold is calibrated independently beforehand. It crosses the zero value just in the same moment the rear wheel load becomes zero (thus assuming GCL detection) and the "kink" of the rear wheel speed indicates GCL. The timing agreement of all three methods is below 30 ms in a post measurement analysis. Please note that wheel load and wheel speed based detections will have some delay compared to the distance based detections when used in real time applications. This is because they need multiple measurement values to detect a shape in the signal rather than comparing one value with a threshold.

Experiment *four* confirms the self-amplification effect described earlier. Because the brake pressure is held constant, also the brake force and deceleration are held constant. But because of the shortening of the lever arm lift-up height, angle, and speed increase progressively. Please note that the pitch-over motion is not reversed immediately after releasing the brake, there is a time delay caused by the time it takes gravity to counteract the stored potential energy (lift-up height) and angular energy (pitch-over rate).

Conclusion

The need for a novel IB capable of capturing pitch-over dynamics in detail is pointed out. Needed sensors and their calibration is worked out, and the IB is build and tested. The capturing capabilities and precision of GCL detection is presented. It enables future studies of GCL scenarios and flip-over motion. The IB's capability of providing a ground truth will be used in future work. New algorithms for rear wheel lift-up detection, only using standardly available sensors, will be developed, tested, and evaluated. Also, new control algorithms to mitigate flip-over motion using pressure modulation will be investigated with the bike.

Acknowledgements

The authors would like to acknowledge the help of Maximilian Wiendl in the design and build of the IB. We would also like to acknowledge the help of Florian Mangold with testing and validation.

References

Bretting, G. P., Jansen, H. P., Callahan, M., Bogler, J., & Prunckle, J. (2010). Analysis of Bicycle Pitch-Over in a Controlled Environment. *SAE International Journal of Passenger Cars - Mechanical Systems*, 3(1), 57–71. https://doi.org/10.4271/2010-01-0064

Cossalter, V., Lot, R., & Maggio, F. (2004). On the Braking Behavior of Motorcycles. *SAE Transactions*, 1274-1280. https://doi.org/10.4271/2004-32-0018

De Lorenzo, D. S., & Hull, M. L. (1999). A Hub Dynamometer for Measurement of Wheel Forces in Off-Road Bicycling. *Journal of Biomechanical Engineering*, 121(1), 132–137. https://doi.org/10.1115/1.2798034

Dozza, M., & Fernandez, A. (2014). Understanding Bicycle Dynamics and Cyclist Behavior From Naturalistic Field Data (November 2012). *IEEE Transactions on Intelligent Transportation Systems*, 15(1), 376–384. https://doi.org/10.1109/TITS.2013.2279687

Drouet, J.-M., & Champoux, Y. (2010). A novel dynamometric hubset design to measure wheel loads in road cycling. *Procedia Engineering*, 2(2), 2925–2930.

©2023 Skatulla, J., Maier, O., & Schmidt, S. published by TU Delft OPEN on behalf of the authors.

ISSN: 2667-2812

Frank, T. A., Smith, J. W., Hansen, D. C., & Werner, S. M. (2008). Motorcycle Rider Trajectory in Pitch-Over Brake Applications and Impacts. *SAE International Journal of Passenger Cars - Mechanical Systems*, 1(1), 31–42. https://doi.org/10.4271/2008-01-0164

Gadsby, A., & Watkins, K. (2020). Instrumented bikes and their use in studies on transportation behaviour, safety, and maintenance. *Transport Reviews*, 40(6), 774–795. https://doi.org/10.1080/01441647.2020.1769227

Klug, S. (2020). Modeling and Control of Bicycle Dynamics with Focus on Brake and Suspension Systems [PhD Thesis]. Technische Universität Kaiserslautern.

Klug, S., Moia, A., Verhagen, A., Görges, D., & Savaresi, S. (2021). The influence of bicycle fork bending on brake control. *Vehicle System Dynamics*, 59(3), 375–395.

Knuit, J., KoN, F., Raaphorst, P., & SpeN, A. (2015). Bicycle tire stiffness and damping [Bachelor Thesis]. TU Delft.

International Organization for Standardization. (2011). Road vehicles - Vehicle dynamics and road-holding ability - Vocabulary (ISO Standard No. 8855:2011). https://www.iso.org/standard/51180.html

Kooijman, J. D. G., Schwab, A. L., & Meijaard, J. P. (2008). Experimental validation of a model of an uncontrolled bicycle. *Multibody System Dynamics*, 19(1–2), 115–132. https://doi.org/10.1007/s11044-007-9050-x

Maier, O., Hillenbrand, S., Wrede, J., Freund, A., & Gauterin, F. (2018). Vertical and longitudinal characteristics of a bicycle tire. *Tire Science and Technology*, 46(3), 153–173.

Maier, O., Pfeiffer, M., Scharpf, S., & Wrede, J. (2016a). Conditions for nose-over and front wheel lockup of electric bicycles (pp. 219–224). *11th France-Japan & 9th Europe-Asia Congress on Mechatronics (MECATRONICS) /17th International Conference on Research and Education in Mechatronics (REM), IEEE*. https://doi.org/10.1109/MECATRONICS.2016.7547145

Maier, O., Pfeiffer, M., & Wrede, J. (2016b). Development of a Braking Dynamics Assistance System for Electric Bicycles: Design, Implementation, and Evaluation of Road Tests. *IEEE/ASME Transactions on Mechatronics*, 21(3), 1671–1679. https://doi.org/10.1109/TMECH.2015.2505186

Manolova, A., Crequy, S., Lestriez, P., Debraux, P., & Bertucci, W. (2015). Relationship between the Pedaling Biomechanics and Strain of Bicycle Frame during Submaximal Tests. *Sports*, 3(2), 87–102. https://doi.org/10.3390/sports3020087

Norgia, M., Boniolo, I., Tanelli, M., Savaresi, S. M., & Svelto, C. (2009). Optical Sensors for Real-Time Measurement of Motorcycle Tilt Angle. *IEEE Transactions on Instrumentation and Measurement*, 58(5), 1640–1649. https://doi.org/10.1109/TIM.2008.2009421

Petrone, N., Giubilato, F., Giro, A., & Mutinelli, N. (2012). Development of instrumented downhill bicycle components for field data collection. *Procedia Engineering*, *34*, 514–519. https://doi.org/10.1016/j.proeng.2012.04.088

Rodrigo Marco, V., Kalkkuhl, J., Raisch, J., & Seel, T. (2020). A novel IMU extrinsic calibration method for mass production land vehicles. *Sensors*, 21(1), 7.

SBG Systems SAS. (2020, November). *ELLIPSE SERIES High Performance, Miniature Inertial Sensors* [Hardware Manual]. https://support.sbg-systems.com/sc/el/files/latest/11240254/17990941/1/1617893855126/Ellipse+3+-+Hardware+Manual.pdf

Skatulla, J., Maier, O., & Schmidt, S. (2023). Fork bending self-oscillation on bicycles influencing braking performance. Presented at the 10 th Annual International Cycling Safety Conference, Technische Universität Dresden.

Werner, S., Newberry, W., Fijan, R., & Winter, M. (2001). Modeling of Bicycle Rider Collision Kinematics. https://doi.org/10.4271/2001-01-0765

©2023 Skatulla, J., Maier, O., & Schmidt, S. published by TU Delft OPEN on behalf of the authors.

ISSN: 2667-2812

The Evolving Scholar Vol. 3, 2023 https://doi.org/10.59490/660fcc0691b3c7eaff6c258a

Bicycle and Motorcycle Dynamics 2023
Symposium on the Dynamics and Control of Single Track Vehicles
18 – 20 October 2023, Delft University of Technology, The Netherlands

Type of the Paper: Conference Paper

Revised

Investigation of the Applicability of a Motorcyclist Model for Trajectory Prediction in Real Traffic

[version 2; peer reviewed]

Scherer, F.[1]* and Eschinger, M.[2]

[1]Technical University Darmstadt; florian.scherer@tu-darmstadt.de, ORCID 0009-0007-8234-3347
[2]Technical University Darmstadt, maximilian.eschinger@web.de
*corresponding author.

Name of Editor: Jason Moore
First published: 03/10/2023
Last published: 08/04/2024
Citation: Scherer, F. & Eschinger, M. (2024). Investigation of the Applicability of a Motorcyclist Model for Trajectory Prediction in Real Traffic [version 2; peer reviewed]. The Evolving Scholar - BMD 2023, 5th Edition.
This work is licensed under a Creative Commons Attribution License (CC-BY).

Abstract:

To develop advanced motorcycle assistance systems, the focus is shifting towards the rider's abilities. A model in (Scherer et al. 2022) predicts motorcycle dynamics influenced by riders without specific rider or vehicle parameters. It employs mathematical functions to describe speed and roll angle changes, revealing differences among riders. Unlike previous stochastic approaches, this model allows clear interpretation of measurement data with rider-specific parameters like correction amplitudes and trends, aiding critical maneuver identification.

The paper investigates applying this rider model to real traffic data. For this purpose, three riders (two experienced frequent riders and one inexperienced infrequent rider) on two different vehicles (Honda CBF 1000 and BMW K1200R Sport) were recorded and examined on a sample basis using a validated low-cost measurement technique with a total amount of n = 40 measurements. Taking into account evaluation curves suitable for proving the methodology, two consecutive country road curves were selected with a respective change in direction (equivalent to a yaw angle change of the vehicle between entering and exiting the curve) of approx. 180°. These were each driven through 6 times by all three riders under constant conditions in good, summer weather and road conditions. In addition, one of the riders drove through them in wintry and less than optimal road conditions at the beginning of the season.

Initial findings assess the model's transferability to real traffic. The investigation results show its applicability, with rider-specific riding styles and parameterization functions, as well as the need to repeat the study with a large number of samples.

The model accurately predicts future positions; the relative deviation between the calculated and measured trajectory in a lateral direction (to the direction of travel) is less than 2 m in 85% of cases. This corresponds to the measurement uncertainty of the system used over the distance travelled of 148 m. This demonstrates applicability under real conditions, confirming its efficacy beyond the closed terrain test in (Scherer et. al., 2022).

In the future, this model will enable rider-dependent trajectory predictions with uncertainty intervals in real traffic situations.

Keywords: Trajectory, Motorcycle, Modeling, Study, Real Traffic, Simulation, Dynamics, Riding Ability, Parameterisation

©2023 Scherer, F. & Eschinger, M. published by TU Delft OPEN on behalf of the authors.
ISSN: 2667-2812

Introduction

The accident statistics show that 33.7 % of all motorcycle accidents in 2020 can be classified as single-vehicle accidents. Motorcyclists between the ages of 15 and 24 are the most affected age group, accounting for more than one third of all riders involved in accidents. The most frequent cause of accidents involving motorbikes with registration plates was found to be "inappropriate speed" in 22.4 % of cases (Destatis, 2021). A study by the *Allgemeiner Deutscher Automobil-Club e.V.* (ADAC) from 2015, last updated in 2019, examined motorbike accident types in a more differentiated manner according to accident causes in combination with riding maneuver and identified "inappropriate speed in curves" as the cause of accidents in 21 % (Pschenitza, 2019).

Compared to passenger cars, the ability of motorbikes to negotiate curves depends to a large extent on the leaning angle built up. As a result, the rider's specific skills play a central role, both physically and mentally. For the further development of active safety systems, it is possible to predict the condition of one's own vehicle using riding dynamics measured variables and taking into account rider influences. On the basis of this prediction, it is possible, for example, to show motorcyclists an individual, optimal approach to a curve before entering it or to improve the skills of the riders with the help of a detailed riding analysis.

In this publication, based on the model presented in (Scherer et. al 2022) for the parameterisation of a motorcyclist's cornering, a first assessment of the applicability of the methodology in road traffic is made. For the modelling, parameterisable mathematical functions are used to describe the speed- and roll angle progression.

The manoeuvre primitives of cornering introduced in (Magiera 2020) are used for this purpose. Every cornering manoeuvre of a motorbike can be divided into a dynamic roll-in and roll-out phase and a quasi-stationary area, similar to a holding phase, when considering the roll angle progressions. The start and end condition of the overall manoeuvre is straight-ahead travel. Here the coefficients used in the nomenclature used in this paper, each lined up as a pair, stand for: R = Right, L = Left, I = In, O = Out.

A special case is the direct transition of a curve into the next curve, in which a right-hand curve goes directly into a left-hand curve, or vice versa, which can result in the combination RL or LR.

The curve combination considered in this paper, consisting of a series of right-hand curves with a transition to a left-hand curve, is shown as an example in Figure 1.

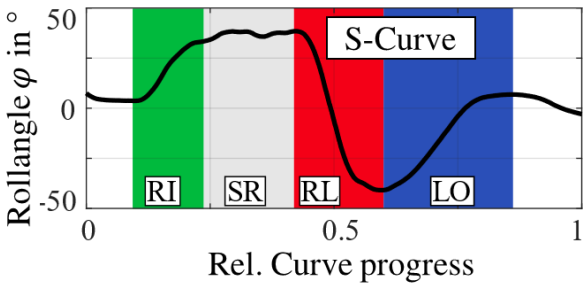


Figure 1 Relative Curve Progress and Maneuver Primitives

For comparability of the results in (Scherer et. al 2022) the so-called curve progression range was introduced. Here, each curve is divided into a start and end point based on the local relationship, and the distance travelled is normalized and distributed locally equidistantly in percentages from 0 to 100%.

The approach of the model used here is to collect measurement data of motorcyclists' riding dynamics, in particular roll angle and speed, which are then transferred into a parameter representation via mathematical approach functions and a curve fitting. The aim of this is making different riders comparable as well as the possibility of reverse transformation into the time domain for the use of the parameters for trajectory prediction. The approach provides that if a curve is passed sufficiently often, a future estimate for the passage of a similar curve can be made.

In (Scherer et. al 2022), two different approach functions for the dynamic and quasi-stationary part of the curve travel are presented. Central variables of consideration are the start and end bounds of the growth functions, the base and gradient values of the linear regression (stationary primitive) and the overlaid oscillations. The nomenclature according to formula (1) is used to separate the coefficients of the two approach functions and to clarify the respective variable.

©2023 Scherer, F. & Eschinger, M. published by TU Delft OPEN on behalf of the authors.

ISSN: 2667-2812

$$k_{\substack{i_1 \\ i_2}\, i_3} \tag{1}$$

Here *k* stands for the coefficient of the approach function. The index i_1 indicates the approximated measured variable (roll angle/ velocity) and the index i_2 contains the information about the considered primitive. If there are several values of the coefficient, this is indicated by the index, this is made clear by the index i_3. Table 1gives an overview of the meaning of the indices.

Table 1. Coefficient Matrice for the approximation functions (Scherer et. al. 2022)

Variable			**Meaning**
k	Coefficient of the approach function	vz	Direction of the growth function
		b	Exponent coefficient of the growth function
		$s_s = vz(a+d)$	Start bound of the growth function
		$s_e = vz(c+d)$	End bound of the growth function
		$base$	Basis of the linear regression
		g	Slope of the linear regression
		$\tilde{a}$	Amplitude of overlaid oscillation
		$\tilde{f}$	Frequency of overlaid oscillation
		$\tilde{l}$	Phase shift of overlaid oscillation
Index			**Meaning**
i_1	Approximated signal	roll	Roll angle signal
		vel	Speed signal
i_2	Primitive	LI/RI	Curve initiation (left/right curve)
		LO/RO	Curve exit (left/right curve)
		LR/RL	Direction change S-curve
		SL/SR	Stationary curve (left/right curve)
i_3	Expression	1	First overlaid oscillation
		2	Second overlaid oscillation
		s	Start (barrier)
		e	End (barrier)

Significant differences between different riders are thus visible in the test track investigations. In contrast to previous scientific approaches with stochastic evaluation of riding ability f.e. in (Magiera, 2020), with the model from (Scherer et. al., 2022) it is possible to interpret measurement data using clear rider-specific parameters, to approximate their course and to compare them across riders.

As in (Scherer et. al. 2022), the following equation (2) is also used in this paper to approximate the dynamic transitions. During the curve initiation, the roll angle is increased from a lower level to a higher level. A logistic growth function is used as an approach, which changes sign depending on the direction of the curve.

$$f(x) = vz \cdot \left(\frac{a \cdot c \cdot e^{b \cdot x}}{c + a \cdot (e^{b \cdot x} - 1)} + d \right) + \tilde{a} \cdot \sin\left(2\pi \cdot \tilde{f} \cdot \left(x + \tilde{l}\right)\right) \tag{2}$$

The constants a, b and c define the basic shape-influencing parameters of the logistic growth function. Since growth functions cannot map an offset in the solution data, the constant element d is additionally defined, which causes a vertical shift of the function.

The parameters $\tilde{a}$, $\tilde{f}$ and $\tilde{l}$ represent the amplitude, frequency and phase shift of the logistic growth function overlaid oscillation.

The stationary part of cornering typically shows a trend in the roll angle signal. This trend manifests itself in an increase/decrease of the roll angle. In (Scherer et. al. 2022) and also in the current paper a linear regression is used to map this trend. In addition to the trend, there are corrective oscillations, especially in the case of long stationary curves. To take these into account, the first-

©2023 Scherer, F. & Eschinger, M. published by TU Delft OPEN on behalf of the authors.

ISSN: 2667-2812

degree polynomial is superimposed with two sinusoidal oscillations. These represent the oscillations that occur. Formula (3) shows the approach of the used mathematical approximation, wherin the same nomenclature as in Table 1 provided is used:

$$f(x) = base + g \cdot x \ + \tilde{a}_1 \cdot \sin\left(2\pi \cdot \tilde{f}_1 \cdot \left(x + \tilde{l}_1\right)\right) + \tilde{a}_2 \cdot \sin\left(2\pi \cdot \tilde{f}_2 \cdot \left(x + \tilde{l}_2\right)\right) \quad (3)$$

To calculate the trajectory using the methodology presented in Scherer et.al. (2022), the approximated signals are transformed back into the time domain.

The transverse offset between the estimated and real (measured) trajectory serves as a quality criterion. The estimated trajectory results from the approximated measured data of the roll angle and speed signal, the correction factors due to stationary and dynamic cornering and the manoeuvre distribution. For a more detailed derivation, please refer to (Scherer et. al. 2022).

Methodology

To select suitable curves that match the reference curve presented in Scherer et. al. possible curves were analysed in a radius of 50 km around Frankfurt am Main, Germany.

For the definition of the evaluation curve to prove the transferability of the results from the closed-off test area to the real world, the relationship of the quasi-stationary state at constant cornering between vehicle speed v, curve radius R and the roll angle φ was used. This results in the following relationship, Formula (4:

$$R = -\frac{v^2}{\tan(\varphi) \cdot g} \quad (4)$$

For the evaluation of a motorcyclist's riding abilities, it must be possible under real, good conditions to complete a curve, taking into account the legal limitation, to the limits of riding dynamics. Taking into account the permissible maximum speed on German country roads of v=100 kmh and assuming a theoretical limit roll angle phi=45° at my=1, the following relationship thus results in Table 2:

Table 2. Values for the Reference Curve

Reference Curve Radius		
φ in °	v in km/h	R in m
45 °	40	12.6
	60	28.3
	80	50.3
	100	78.7

This results in a possible, reasonable curve radius between approx. R = 13 m and R = 79 m for German country roads. Curves with a much smaller radius are less suitable for the method presented here, as the low speeds here mean that the quasi-stable range of a typical motorcycle is approached too closely. Especially since it can be assumed that only a few percent of average motorcyclists drive through a curve with near phi =45 °. Additionally, the investigation on the closed track in (Scherer et. al. 2022) was performed with a curve radius of R = 12 m, what is the minimum requirement to the evaluate curve in the real traffic study.

The result of a real-world riding study from (Scherer et. al. 2021) serves as an example here, whereby 75 % of all lean angles are below 25 ° on a typical country road trip in Germany.

In addition to requirements on the curve radius for the particular suitability of the proof of methodology, an important criterion for such a curve is the change in direction that is completed within a curve. This is equivalent to the difference in the vehicle yaw angle between entering and exiting the curve, what can be described as in Formula (5).

$$\Delta\psi = \left|{}^{\mathrm{hor}}\psi_{0\%} - {}^{\mathrm{hor}}\psi_{100\%}\right| \quad (5)$$

©2023 Scherer, F. & Eschinger, M. published by TU Delft OPEN on behalf of the authors.

ISSN: 2667-2812

A change in direction of at least $\Delta\psi = 90\,°$ must be achieved. Preliminary tests on closed terrain have shown that with a smaller change in direction, the quasi-stationary part of the curve is only present for a very short time or not at all. For comparability with the tests on closed terrain, a $\Delta\psi = 180\,°$ is targeted, as this was the change in direction of the evaluation curve on the closed track in (Scherer et. al. 2022).

In order to be able to exclude vehicle-related influences on the verification, at least two different vehicles should be used in the real-world comparison. In addition, at least two different riding ability levels are necessary for the investigation of the rider's influence. In addition, the influence of external conditions is a focus of the investigation, therefore at least one test person must carry out the test ride several times on days with significantly different boundary conditions (as weather or street conditions).

Influences due to changes between the sterile test environment on the track and rides on the real road must be taken into account. Overall, care must be taken to ensure that the test conditions are as similar as possible, and in particular that the lane width of at least 3 m is maintained.

Measurement Equipment

A Honda CBF 1000 (Figure 2 left) and a BMW K1200 R Sport (Figure 2right) were used for the investigation. Both vehicles are in standard condition, without any modifications or conversions and comply with the German registration regulations.



Figure 2: Motorcycles used for Test Rides

The motorbikes used are clearly distinguished by different chassis concepts (Honda telescopic fork, BMW Duolever), the drive train (Honda chain, BMW cardan) and the power (Honda 98 hp, BMW 163 hp). This is to exclude differences due to the vehicle.

Two measuring devices were used to record the motorbike riding dynamics: a measuring device developed by a student and a WingMan Race from RideLink GmbH. Both devices were validated in advance against a high-precision measuring technique (Automotive Dynamic Motion Analyzer - ADMA from Genesys), whereby inaccuracies in the roll angle of $\varphi = 1°$, the speed $v = 0.5\ \mathrm{m/s}$ and the position in the lane of approx. 1 m must be taken into account when interpreting the results. Both devices have an Inertial Measuring Unit (IMU) including rotation rates, acceleration and magnetic field sensors with a measuring frequency of 100 Hz and a Global Navigation Satellite System signal with a sampling rate of 10 Hz. As visible in Figure 2, the measuring devices were attached to the rear seat of the vehicles and calibrated at the beginning of the measurement rides. The student device was used for validating the RideLink WingMan. The data shown in the following figures were measured through the RideLink WingMan device.

According to the criteria for the selection of an evaluation curve presented in the previous section, a curve combination was selected in the north of Frankfurt on the L3024, at the height of the Windeck parking lot. As shown in **Figure 3**, the curve is approached from the north (point (1) in **Figure 3**) and initially includes a right-hand curve with a radius R = 63 m and a $\Delta\psi = 135°$. At point

©2023 Scherer, F. & Eschinger, M. published by TU Delft OPEN on behalf of the authors.

ISSN: 2667-2812

(2) in **Figure 3**, this changes into a left-hand curve with R = 50 m and a change in direction $\Delta\psi = 110°$. up to point (3). Hereby both partial curves of the total S-combination fulfil the established conditions.

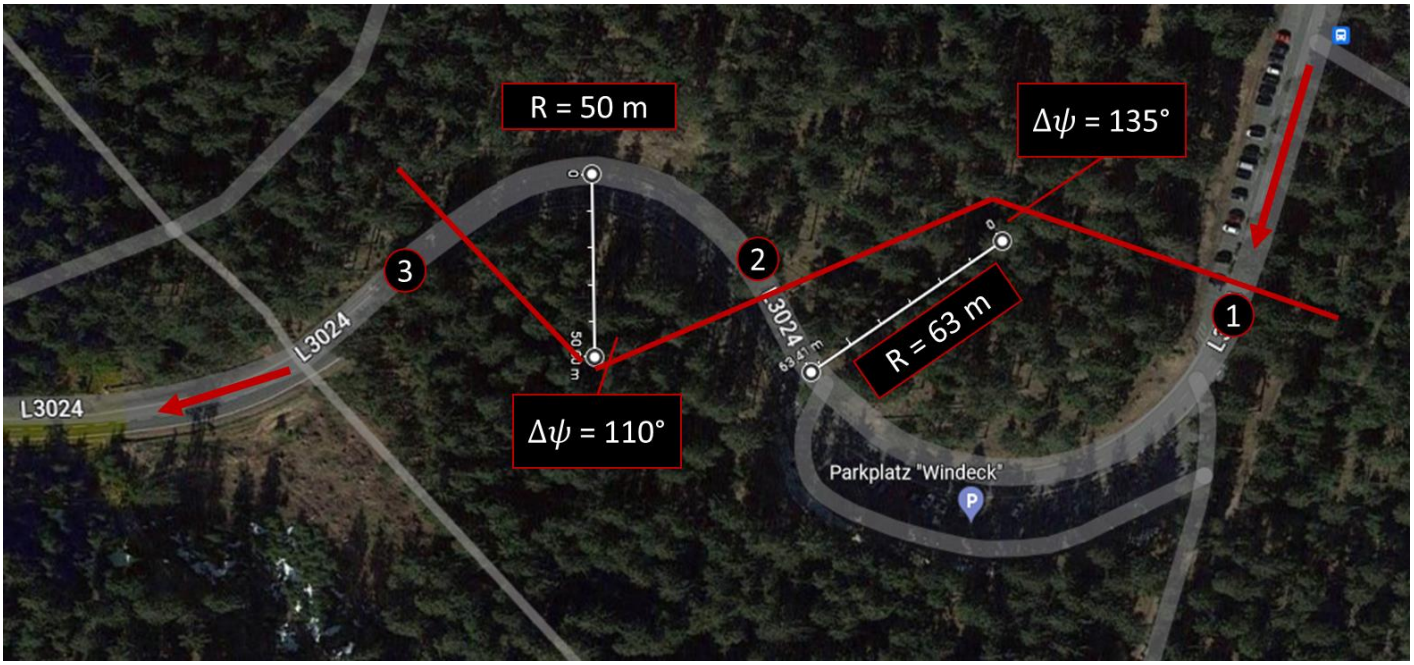


Figure 3. Evaluation Curves for the Real World Investigation

Experiments, Riding Study

The study was conducted on two different days with a total of 4 riders and three vehicles. Due to a faulty installation of the measurement equipment on the vehicle, one data set could not be used for the evaluation and is therefore not discussed further in this publication. Thus, four complete data sets are available for the first proof of the methodology, which does not correspond to any statistical robustness. However, this is not necessary for an initial, random investigation. Each data set contains 6 passes. The given route of a total of 5.2 km with 9 right-hand bends and 11 left-hand bends (one of which corresponds to the evaluation curve) was passed through 6 times in each direction. This results in a total number of n = 40 curve passages, which were used for the further results.

As with the comparison rides on closed track, riding through the entire route served to "familiarise" the riders with the vehicle and the surroundings. The riders did not know in advance what the focus of the study was or, in particular, which curves would be used for the evaluation. The riders were asked to ride within their comfort zone, i.e. not to provoke a particularly risky, but also not a particularly restrained riding style. In addition, the riders were instructed to pause their journey if they ran into other vehicles or if another vehicle appeared behind them, until it was possible to continue on their own again without being influenced by other road users. In addition, the riders were sent into the section of road at an appropriate distance from each other to avoid meeting each other.

The first measurement day was carried out in March 2022 (in the further course marked by the "M" behind the rider number) with the vehicle BMW K1200R (by the abbreviation "B") with rider 1. This part of the study aims to compare different environmental influences. On the day of the measurement, the outside temperature was 6°C, the road conditions were dry, the sky was overcast. The second measurement day on which all riders, i.e. rider 1 again, rider 2 and rider 3 drove the measurement routes for the first time was carried out in July 2022 with an outside temperature of 30°C, sunshine and very good and dry road conditions.

©2023 Scherer, F. & Eschinger, M. published by TU Delft OPEN on behalf of the authors.

ISSN: 2667-2812

Table 3: Riders Age, Yearly km and Experience for Real World Study

Rider					
Rider Nr.	Motorcycle	Age	Yearly km	Experience	Season
1MB	BMW	32	4000	Experienced	First Ride
1JB	BMW	32	4000	Experienced	Well Practice
2JH	HONDA	31	500	Beginner	First Ride
3JH	HONDA	29	5000	Experienced	Well Practice

Table 3 lists the characteristics of the riders and vehicles, as well as the respective seasonal influence. Rider 1 and rider 3 are experienced frequent riders with a high annual mileage, whereas rider 2 has riden less than 1000 km since receiving the riding licence and the last active trip was years ago.

Thus, the results in the comparison of rider 1 are representative for the investigability of seasonal differences, the comparison between rider 1 and rider 3 with otherwise similar riding behaviour for the influence of different vehicles and the difference between rider 1 or rider 3 and rider 2 for the influence by riding experience or also riding ability in general.

Results

For a first general impression, the complete roll angle and speed curves of all runs are first analysed. Figure 4 in the top left-hand corner shows the roll angle curves for each rider and also separately for the March (blue) and July (red) runs.

The roll angle remains relatively stable for a single rider across different experiments. However, it's clear that roll angles differ significantly between distinct riders, emphasizing the unique nature of each rider's control style.

©2023 Scherer, F. & Eschinger, M. published by TU Delft OPEN on behalf of the authors.

ISSN: 2667-2812

When riders share similar experience levels and practice under comparable seasonal conditions, their roll angle profiles closely align. This consistency highlights the role of both experience and seasonal practice in shaping roll angle patterns. Notably, riders with more experience tend to exhibit higher baseline roll angle values, visible in Figure 4, down left for the base values of the quasi-stationary right cornering phase. Seasonal variations lead to changes in total roll angle values, but the underlying patterns persist. This suggests that seasonal factors may affect the magnitude of roll angles while leaving the fundamental roll angle behaviour across riders largely intact.

Velocity profiles exhibit significant disparities between different riders, with noticeable differences emerging, especially at the beginning of curves, visible in Figure 4 on the right. This underscores the significant impact of individual rider preferences and control strategies on velocity changes. High levels of rider experience or training are associated with elevated velocity profiles. This finding suggests that seasoned riders navigate curves at higher speeds, reflecting their enhanced control and confidence. In the stationary curve segments of the velocity profiles, we observe striking similarity among riders with similar experience and training levels. This underscores how these factors contribute to maintaining consistent velocity during stable riding conditions.

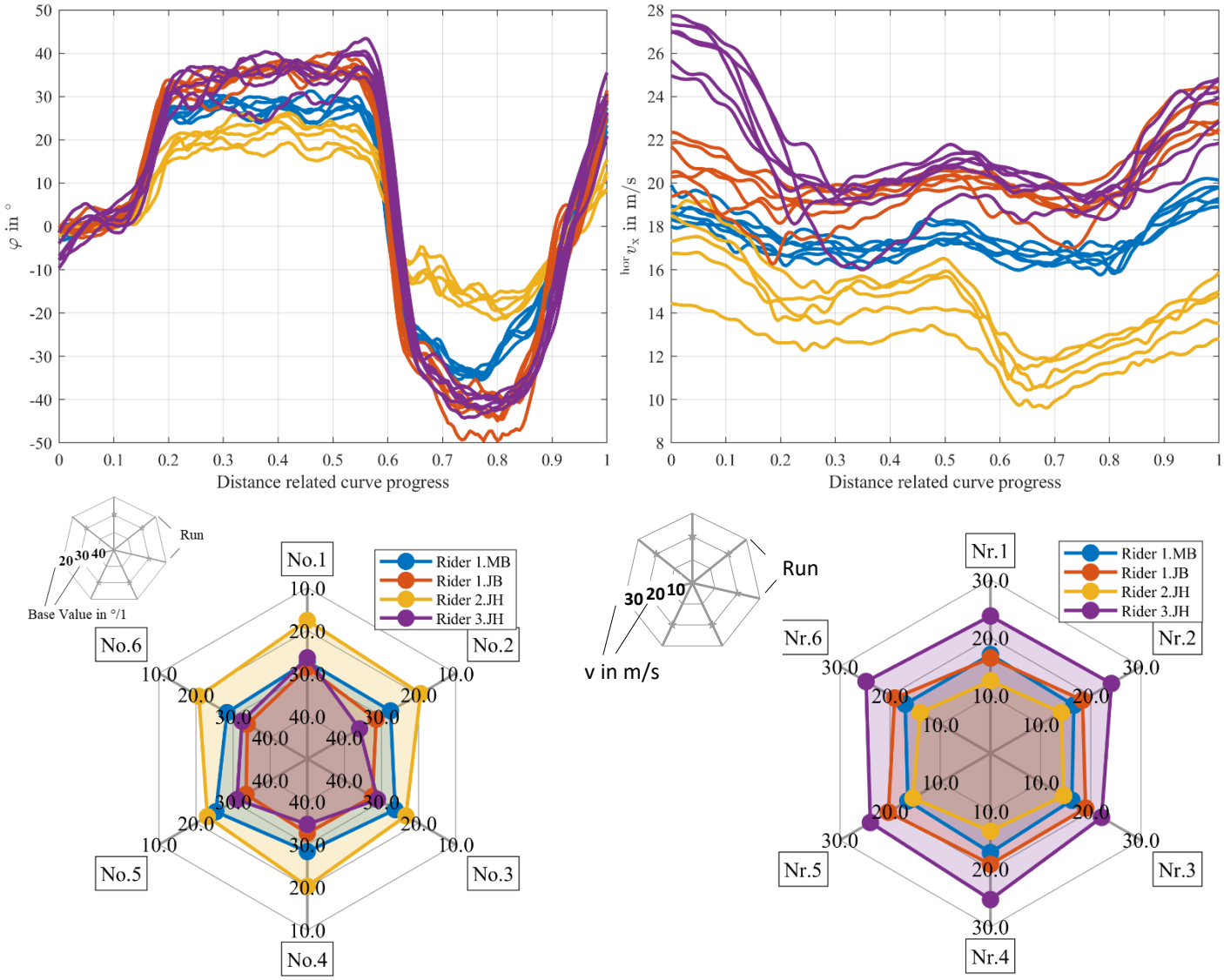


Figure 4. Top: left: roll-angle , right velocity over curve progress, down: left average roll angle in stationary right (SR), left in average velocity in stationary right (SR)

©2023 Scherer, F. & Eschinger, M. published by TU Delft OPEN on behalf of the authors.
ISSN: 2667-2812

Seasonal variations result in lower overall velocity values. However, the fundamental velocity patterns remain consistent, indicating that seasonal conditions may influence velocity magnitude without altering the underlying velocity trends.

Looking at the development of the roll angle gradient during the quasi-stationary right cornering, a slightly different pattern becomes visible in Figure 5.

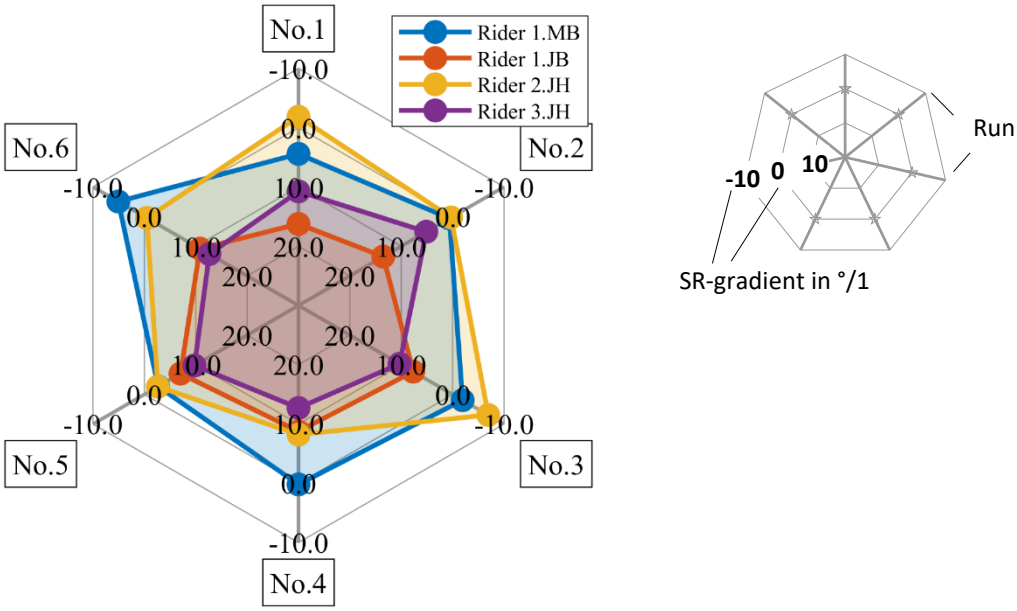


Figure 5. Filtered (LMSE) Stationary Right Gradient of all Riders, see formula 3

Here it is noticeable that the experienced rider 1 in March shows a similar behaviour in unfavourable weather and road conditions as the inexperienced rider 2 in very good conditions. A gradient close to zero or in the negative range stands here for very defensive cornering, a reduction in lean angle over the cornering course.

With the experienced riders 1.JB and 3.JH a quite similar behaviour is observed in good conditions. A build-up of lean angle over the course of the curve can be observed. However, the riders differ more on the first two runs than from the third run onwards. Here, for example, a kind of habituation effect to the curve may occur after repeated riding. It is noticeable that none of the riders constantly increases from pass to pass, which was a possible assumption at the beginning of the study.

As described in equation (3), the linear regressive part of the approximation is superimposed by two oscillation parts. In the current paper only the first superimposed oscillation is handled, as for the second one there are no significant insights visible.

©2023 Scherer, F. & Eschinger, M. published by TU Delft OPEN on behalf of the authors.

ISSN: 2667-2812

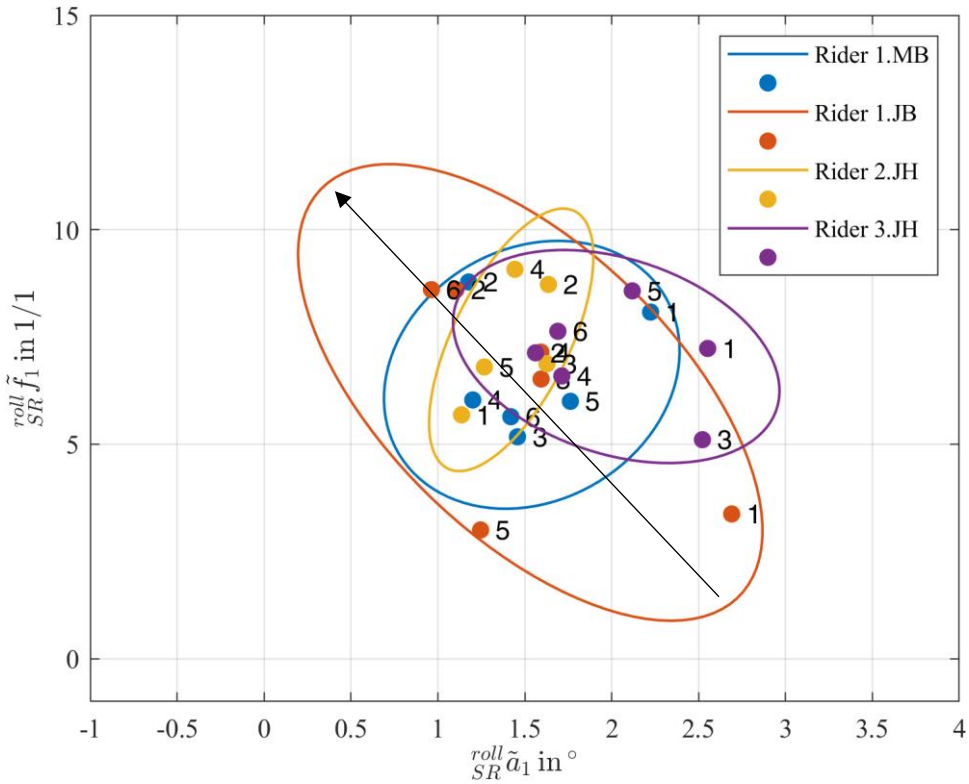


Figure 6. Pairing of Coefficients of Amplitude ($\tilde{\mathbf{a}}_1$) und frequency ($\tilde{\mathbf{f}}_1$) in a **90**% confidence intervall

The pairs of coefficients from the amplitude and frequency of the first superimposed oscillation, shown in Figure 6, give a sense of the way in which the lean angle is maintained or changed in a stable manner, for example in the quasi-stationary phase. During the tests on closed-off terrain, a correlation was found in particular between the alignment of the ellipses (shown here with a confidence interval of 90 %) and the riding skill. This cannot be demonstrated with the sample size shown here. A difference is visible, but cannot be attributed to any of the influencing variables.

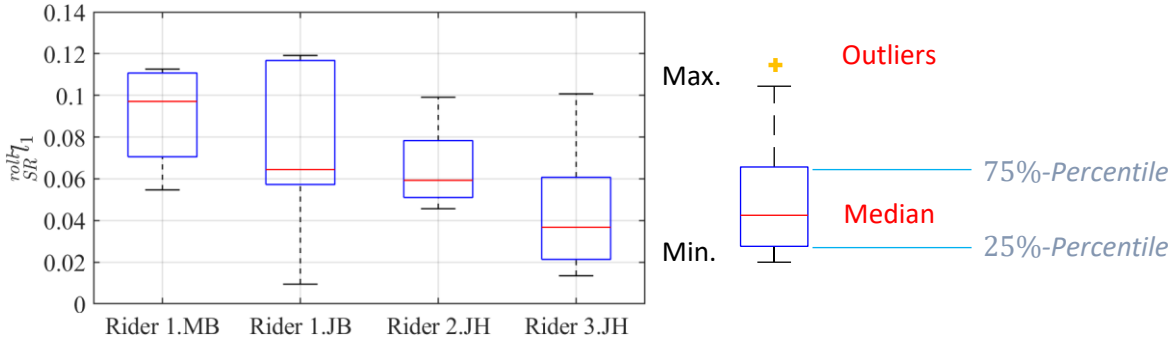


Figure 7. Phase shift of the first superimposed oscillation

The same applies to the phase shift of the first oscillation. Here, as can be seen in Figure 7, no distinction is possible between the three riders considered.

Due to the number of coefficients examined, the results of the remaining variables are summarised in the Table 4. The coefficients for the real world and closed track are valued in yes (verifiably for all drivers), partially (verifiable for some drivers) and no (not verifiable).

©2023 Scherer, F. & Eschinger, M. published by TU Delft OPEN on behalf of the authors.

ISSN: 2667-2812

Table 4. Comparison of all coefficients betweem real world and closed track investigation

Coefficient type	Curve	Primitivee	Coefficient	Realworld	Closed-Track
Roll angle coefficient	180°-right corner	SR-Primitive	Gradient	yes	yes
			Base Value	yes	yes
			Correction amplitude and frequency first overlaid vibration	yes	yes
			Phase displacement first overlaid vibration	no	no
			Correction amplitude and frequency second overlaid vibration	partially	yes
			Phase displacement second overlaid vibration	partially	partially
		RI-Primitive	Start borders	partially	yes (but LI-Primitive)
			End borders	yes	yes (but LI-Primitive)
			Exponent coefficient	no	yes
			Correction amplitude and frequency overlaid vibration	no	yes
		RO-Primitive	Start borders	yes	yes
			End borders	no	yes
			Exponent coefficient	no	yes
			Correction amplitude and frequency first overlaid vibration	no	no
	S-Curve	SL-Primitive	Gradient	no	not recorded
			Base value	partially	not recorded
			Correction amplitude and frequency first overlaid vibration	no	not recorded
		RL-Primitive	Correction amplitude and frequency overlaid vibration	no	not recorded
		LO-Primitive	Correction amplitude and frequency overlaid vibration	no	not recorded
Velocity coefficients	180°-Right corner	RI-Primitive	Start borders	yes	yes (but LI-Primitive)
			End borders	yes	yes (but LI-Primitive)
			Correction amplitude and frequency first overlaid vibration	no	yes (but LI-Primitive)
			Sign	no	partially (but LI-Primitive)
		SR-Primitive	Gradient	no	anders analysiert
			Base value	yes	not recorded
			Correction amplitude and frequency first overlaid vibration	no	no (but SL-Primitive)
			Correction amplitude and frequency first overlaid vibration und Base value	yes	yes (but SL-Primitive)
		RO-Primitive	Start borders	yes	yes (but LO-Primitive)
			End borders	yes	yes (but LO-Primitive)
			Exponent coefficient	yes	yes (but LO-Primitive)
			Sign	no	no (but LO-Primitive)
	S-Curve	SL-Primitive	Gradient	yes	not recorded
			Base value	yes	not recorded

As described in the introduction, with the help of the coefficients approximated in this study, a backward transformation into the time domain and, resulting from this, a future position of the motorbike can be estimated by calculating a yaw rate from the roll angle and speed characteristics. Corresponding trajectories were calculated for all three riders by using the mean values of the coefficients. As an example, the result of the estimation with the largest deviation is shown in Figure 8.

©2023 Scherer, F. & Eschinger, M. published by TU Delft OPEN on behalf of the authors.

ISSN: 2667-2812

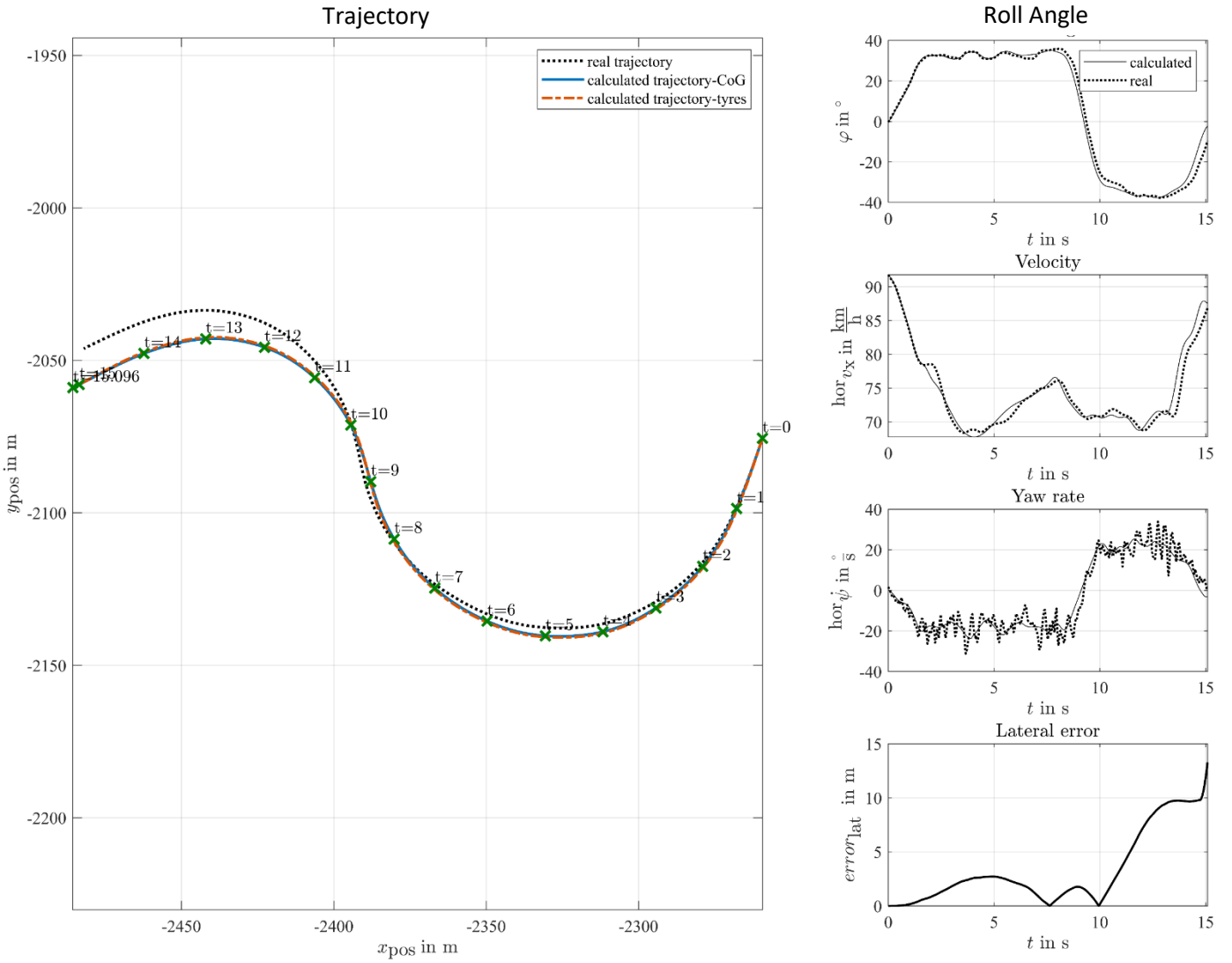


Figure 8. Trajectory prediction, comparing measurements and estimation, left x and y in a reference coordinate system, right from the top: roll angle, velocity, yaw rate and lateral error over time

The disparity between the estimated and measured trajectories reaches its peak, with a lateral deviation of 3 meters occurring at t = 5 seconds. This error gradually diminishes until the transition into the opposite curve, only to resurge and reach its maximum magnitude at t = 15 seconds, resulting in a lateral deviation of 12 meters. The largest estimation error occurs at the transition to the opposite curve. The model shows a high prediction accuracy for future positions, as the relative deviation between the calculated and measured trajectory in the lateral direction (to the direction of travel) is less than 2 m in 85 % of cases. This is due to the uncertainty of the measuring system over the distance travelled of 148 m. This affirms its effectiveness in real-world conditions, validating its utility beyond the closed terrain testing outlined in (Scherer, 2022).

The results of the curves in the opposite direction are comparable with the results shown. They are therefore not shown further. Particularly noteworthy is the phase following the completion of the first curve segment, where the estimated trajectory, accounting for the measurement inaccuracies of the GNSS system, falls within a range that allows us to distinguish between staying within the lane and successfully navigating the corner without incident.

©2023 Scherer, F. & Eschinger, M. published by TU Delft OPEN on behalf of the authors.

ISSN: 2667-2812

Discussion and Outlook

The aim of this study was the investigation of the applicability of a motorcycle rider model from a closed test track, with a particular focus on roll angle and velocity profiles and the usability for trajectory prediction. While the investigation was constrained by a limited number of measurements conducted on chosen evaluation curves involving three riders, it has yielded valuable insights. Notably, rider experience, training, and seasonal conditions play pivotal roles in shaping both roll angle behaviour in quasi-stationary phases and velocity trends. These insights underline the importance of considering individual rider characteristics in the development of motorcycle safety systems. However, it is worth noting that not all the observations of the closed-track tests could be unequivocally confirmed, especially regarding superimposed oscillations, which did not exhibit the same level of specificity as the other parameters. The accuracy refers to the described deviation between the measured and the calculated position signal on which the trajectory prediction shown is based. The requirement is that the deviation over the travelled distance of 148m is smaller than the tolerance in the measuring system. In this case in particular the GPS accuracy. The trajectory prediction performed by means of the back-transformed parameterised coefficients yielded an error in the form of the lateral deviation between measurement and estimation of less than 2m in more than 85% of all maneuver after the first curve passage. This is related to the total distance passed of 148m. This is equivalent to the uncertainty of the measuring system.

Looking ahead, there is significant potential for further exploration in this field. A crucial next step would involve a comprehensive statistical validation of the presented method. By expanding the dataset and employing robust statistical techniques, the reliability and generalizability of these findings could be approved. Furthermore, future research could explore the development of tailored motorcycle safety interventions based on the rider-specific insights gained in this study. These interventions could aim to enhance rider safety and reduce the risk of accidents by accounting for individual rider characteristics, experience levels, and seasonal conditions.

In summary, this study lays a foundation for a deeper understanding of motorcycle rider behaviour, opening the door to more effective safety measures. As the extension of knowledge in this domain continues, in the future tailored safety systems and interventions will contribute significantly to improving motorcycle safety on the road.

References

Destatis, (2021) Verkehrsunfälle, Statistisches Bundesamt, Germany

Magiera, N, (2020) Identifikation des Fahrfertigkeitsniveaus von Motorradfahrern in Kurvenfahrt im Realverkehr, *Dissertation*, TU Darmstadt, Germany

Pschenitza, M. (2019), Auswertung von Motorradunfällen: Konstellationen, Besonderheiten, Abhilfemaßnahmen. *Berichte der ADAC Unfallforschung*, Landsberg am Lech, Germany

Prokop, G., Hannawald, L., Köbe, M. (2017, April), Szenarien-basierte Plattform zur Inspektion automatisierter Fahrfunktionen - Eine Bewertungsmethodik zur Inspektion automatisierter Fahrfunktionen. *Proceedings, Symposium für Unfallforschung und Sicherheit im Straßenverkehr der ADAC Stiftung*, Munich, Germany, 115-127

Scherer, F., Basten, T. (2022, October 03-04), Development of a motorcyclist model for trajectory prediction. *Proceedings, 14th International Motorcycle Conference 2022*, Cologne, Germany, 265-299

Scherer, F.; Winner, H.; Pleß, R.; Will, S; Neukum, A.; Stanglmaier, M.; Bäumler, M.; Siebke; C.; Prokop, G.; (2021, November), Schräglagenangst. *Berichte der Bundesanstalt für Straßenwesen, F142*, Bergisch-Gladbach, Germany

©2023 Scherer, F. & Eschinger, M. published by TU Delft OPEN on behalf of the authors.

ISSN: 2667-2812

The Evolving Scholar Vol. 3, 2023

http://dx.doi.org/10.59490/6656d105744b7e9fc69bc5dc

Bicycle and Motorcycle Dynamics 2023
Symposium on the Dynamics and Control of Single Track Vehicles
18–20 October 2023, Delft University of Technology, The Netherlands

Type of the Paper: Conference Paper

Revised

Measuring vertical tyre stiffness of bicycle tyres
[version 3; peer reviewed]

Malte Rothhämel[1,*]

[1] KTH Vehicle Dynamics & Center for ECO2 Vehicle Design, Department of Engineering Mechanics, Royal Institute of Technology, Sweden; malter@kth.se, ORCID 0000-0002-2480-5554

[*] corresponding author

Name of Editor: Jason Moore
First published: 22/09/2023
Last published: 29/05/2024
Citation: Rothhämel, M. (2024). Measuring vertical tyre stiffness of bicycle tyres [version 3; peer reviewed]. The Evolving Scholar - BMD 2023, 5th Edition.
This work is licensed under a Creative Commons Attribution License (CC-BY).

Abstract:

This contribution presents an analysis of the vertical tyre stiffness of 20” bicycle tyres as usually mounted on bicycle carriers for the transport of children. The current research contributes to the science on bicycle comfort with the focus on the next generation cyclists. Two different methods to measure vertical or radial tyre stiffness of bicycle tyres are presented – a dynamic approach on a dynamic press and a static approach. Parameters modified are tyre inflation pressure and vertical load in the static experiment. In the dynamic experiment additionally dynamic load and frequency are varied. The dynamic experiments are performed on two different tyres. The same tyres are also used for the static experiments and completed with a third tyre, which is a clincher version of the narrow foldable tyre. The tyres are made for 406 mm rim diameter as usually for bicycle carriers since the comfort of children in bicycle transportation is the larger scope behind the experiments.

The main findings are as follows:

- The stiffness of the tyres is in a range of 31 N/mm to 147 N/mm. It must be considered that values below 50 N/mm are related to extremely low inflation pressure that probably do not work reliably because the rim will puncture the tube.
- Tyre inflation pressure is the main factor that controls the vertical stiffness.
- Type of tyre (balloon vs. narrow tyre) hardly affects the stiffness.
- The dynamic stiffness at 1 Hz is slightly higher than the static stiffness.
- With increasing excitation frequency the stiffness increases, however, this effect is non-linear and varies between 3.7% at high pressure in the narrow tyre and up to 20% at low pressure in the balloon tyre.
- Similarly, there is a trend to higher stiffness with increasing vertical load in a magnitude of 20% increase.

Keywords:

Bicycle tyre, Vertical tyre stiffness, Radial tyre stiffness, Tyre suspension, Dynamic stiffness, Static stiffness

©2023 Rothhämel, M. published by TU Delft OPEN on behalf of the authors.
ISSN: 2667-2812

 http://dx.doi.org/10.59490/6656d105744b7e9fc69bc5dc

Introduction

Studying bicycle carrier comfort is an important research topic for at least three reasons. First, it is closely related to sustainable mobility, as the problem of low-emission and (sub-)urban daily mobility is often planned to be solved through an increased use of bicycles. Second, bicycle as mode of transportation is more and more in focus even for simulation tools supporting planning of infrastructure. So, there is need for empirical data for the simulation of bicycles as means of transport. Third, child transportation in bicycle carriers and cargo bikes makes a significant fraction of child transportation by bike. However, there is lack of data about the vibration level and the experienced comfort.

In the realm of cycling, there is a trend toward adopting wider tyres, even in competitive racing. This contributes to a decrease of rolling resistance Rothhämel (2023). Simultaneously, there is a presumed increase in comfort associated with wider tyres; however, a comprehensive systematic demonstration of this comfort improvement is still pending. Regarding bicycle carriers wider tyres (balloon tyres) are often used in combination with lower inflation pressure to increase comfort. Anyhow, in previous experiments lower tyre inflation pressure did not automatically correspond to decreased level of acceleration i. e. increased comfort Rothhämel (2023).

However, ride comfort or the absence of discomfort are important motivation factors for utility cycling. Hagemeister and Schmidt (2003) found that good road surface quality and the absence of curbs has highest priority for cyclists in their route choice, which is strongly connected to ride comfort. One solution (A) is to improve the surface quality within bicycle infrastructure, another solution (B) is to make bicycles more robust against bad surface quality. In reality the choice will not be A or B only. In addition, both of them are embedded in compromises against other factors as also Hagemeister describes.

The tyre and its properties, specifically stiffness and eigenfrequencies, are important steps to improve the understanding of ride comfort on bicycles and in cycle carriers.

Earlier research

Several investigations were done for tyres on agriculture tractors. Lines and Murphy (1991) found that the radial stiffness increased linearly with the inflation pressure superposed by an offset of the carcass stiffness. However, they found rim diameter, tyre section width, tyre age, and inflation pressure to be the significant parameters affecting tyre stiffness. Therefore, they suggested to replace the conceptual model describing tyre stiffness by means of an equivalent spring and damper by means of an empirical formula including these factors.

Brassart and Wright (1993) measured vertical stiffness of agriculture tractor tyres on a test rigg in a static and a dynamic way. Next to the already known linear correlation between tyre inflation pressure and static stiffness, they found that the dynamic behaviour differs from the static. In spite of the fact that the excitation was sinusoidal, this result is in contrast to the findings by Zegelaar (1998).

In his thesis Zegelaar (1998) made comprehensive measurements of automotive tyres. He found that the vertical stiffness of rolling tyres differed from the stiffness of non-rolling tyres when excited randomly but hardly when excited sinusoidally.

In context with a multibody simulation of bicycles Waechter et al. (2002) measured tyre stiffness on two different bikes. The tyres were not specified in detail, however, the stiffness measured was 200 N/mm and 134 N/mm respectively.

Lepine et al. (2016) measured in-situ two different wheel sets (including different tyres) on system level and could distinguish the two wheel-sets.

Maier et al. (2018) investigated mainly longitudinal characteristics of a bicycle tyre but also measured vertical stiffness with 173 N/mm.

Doria et al. (2019) performed a modal analysis of complete utility bicycles and identified bounce and pitch modes in the range of 10-15 Hz based on tyre deformation. To verify some of their findings, they measured the static vertical tyre stiffness in an isolated setup. They found a certain non-linear behaviour at loads around 100 N but a quite linear behaviour at higher loads that are of more importance, however, no tyre modes were identified. In a later experiment Doria et al. (2021) tested a numerical method to predict

©2023 Rothhämel, M. published by TU Delft OPEN on behalf of the authors.
ISSN: 2667-2812

 http://dx.doi.org/10.59490/6656d105744b7e9fc69bc5dc

the comfort of a city bike and identified frequency response functions of the complete bicycle including the tyres. Most of the peaks were in a frequency range larger than 20 Hz.

In contrast, Rothhämel (2023); Rothhämel and Liu (2023) found when investigating the system comfort of children transported in a bicycle carrier, next to a dependency of speed and inflation pressure, peaks at 3.3 Hz and higher. Anyhow, cycle carriers have a different architecture that might influence how the tyre characteristics affects the results.

Scope

The scope of this publication is to contribute knowledge around the stiffness and eigenfrequencies of bicycle tyres and to improve the understanding of the parameters such as type of tyre, inflation pressure, static and dynamic vertical load. In addition, two different measurement methods are applied, once a static method, once a dynamic method, with the goal to verify each other or to understand differences in the tyre behaviour.

Method

Tyre setup

The wheel used for this investigation consisted of a 20" rim with 36 spokes. The tyres were a narrow one of the type Schwalbe Kojak in the ETRTO[1] dimension 35-406 once in a foldable, once in a non-foldable version and a balloon tyre of the type Schwalbe Big Apple in the dimension 60-406 non-foldable. The tyres were mounted with corresponding butyl rubber tubes. The tyre inflation pressure was varied between the tyre individual maximum and a fraction of the minimum specified on the tyre. The pressure was measured with a commercially available indicator that could unfortunately not be calibrated. However, the tyre pressure was measured before and after each series of experiments, which gave at least consistent results.

Static vertical tyre stiffness

The static vertical tyre stiffness ($k_{V,stat}$) was measured by means of scales and a metering rule. The tyres were mounted on a cycle carrier that was placed on three scales. The carrier was levelled by means of a lifting jack under the hitch, see Fig. 1. The tyre inflation pressure was set and thereafter load (steel plates of 10 kg each) was added bit by bit in the cycle carrier. For each combination of tyre inflation pressure and load the vertical deflection as well as the vertical force were measured. At six different levels of inflation pressure and nine sets of load measurements were taken (Fig. 2). The wheels did not rotate during the measurements.



Figure 1. Cycle carrier on scales for static vertical tyre stiffness measurements.

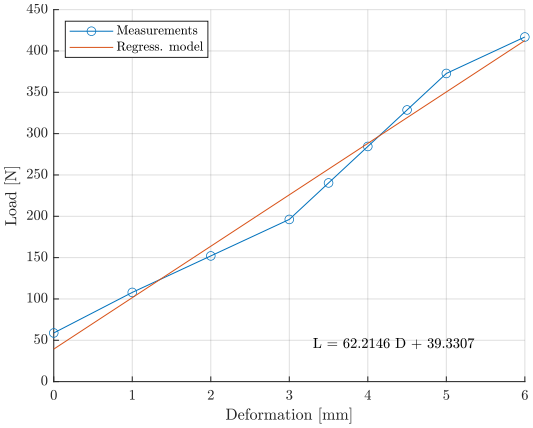


Figure 2. Load (L) over deformation (D) for the balloon tyre (60-406) at 150 kPa.

[1]European Tyre and Rim Technical Organisation: www.etrto.org

©2023 Rothhämel, M. published by TU Delft OPEN on behalf of the authors.
ISSN: 2667-2812

 http://dx.doi.org/10.59490/6656d105744b7e9fc69bc5dc

For each level of inflation pressure (p_{infl}) the corresponding vertical tyre stiffness was calculated by means of linear regression analysis. The coefficient describing the inclination was set as stiffness at this inflation pressure.

Dynamic vertical tyre stiffness

The static vertical tyre stiffness ($k_{V,dyn}$) was measured on a non-rotating wheel by means of a dynamic press as shown in Fig. 3.



Figure 3. Bicycle wheel in a dynamic press for vertical stiffness measurements (narrow tyre: 35-406).

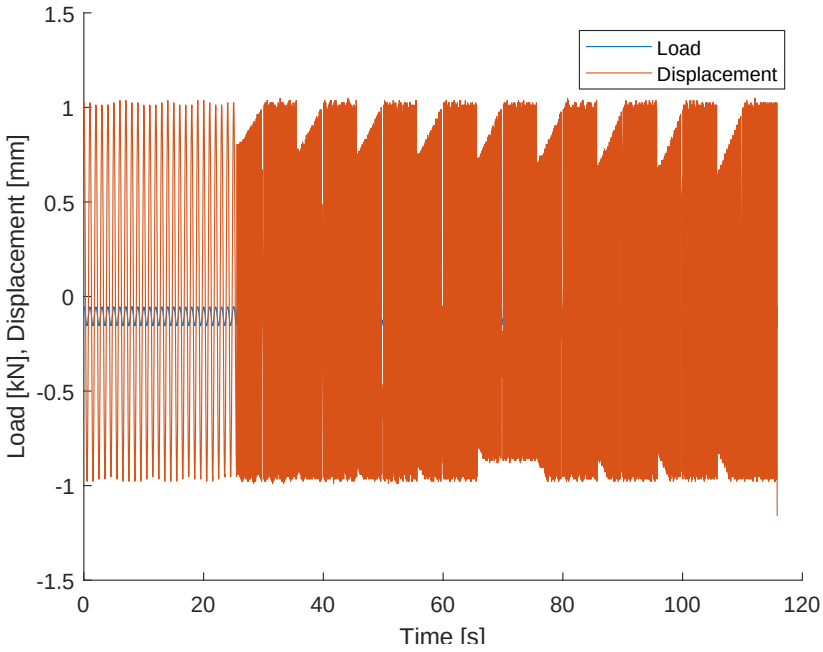


Figure 4. Load and displacement over time for the balloon tyre (60-406) at 400 kPa.

Adaptors were designed and manufactured to guarantee a planar surface. In addition, the surface was covered with abrasive paper with grain size P80 as usual in tyre testing to simulate a fine asphalt surface. The tyre was pressed in-between a piston and an overarm. This means that the tyre suspension took place two times, once on the upper contact patch and once on the lower contact patch. However, the force acting vertically is the same. This was considered in the evaluation by dividing the displacement by two.

The machine was controlled by displacement. Therefore, for each setting a static pre-test was performed to define the necessary displacement. Deviations of the force were accepted. A deviation of the results was not expected because corresponding force and displacement were measured simultaneously and evaluated accordingly.

For each setting the tyre pressure was measured first. Then, the tyre was loaded at a frequency of 1 Hz to avoid settlements during the measurements. After that, the pre-test was done to map the controller. This was done manually, increasing the force by means of the controller, reading the resulting displacement. The actual test was performed three times always beginning with a 1 Hz sine over a time span of 25 s followed by 10 s each at higher frequencies. In general, the frequency range from 1 Hz to 10 Hz was in focus. In earlier investigations FFT-analyses were performed on measurements taken with a bicycle carrier on the road Rothhämel (2023). These showed clearly that the most important frequencies were in the range up to 10 Hz. Only for driving on cobblestones at higher speed the range up to 20 Hz was of limited interest, too. In preliminary tests on this test bed the frequencies above 10 Hz did not show interesting results. In contrast, when testing frequencies between 1 Hz and 10 Hz (see first line Table 1) there was a clear peak around 7 Hz. Therefore, the focus was moved to a higher resolution of frequencies around 7 Hz, and a second set of frequencies was generated (see second line in Table 1).

©2023 Rothhämel, M. published by TU Delft OPEN on behalf of the authors.
ISSN: 2667-2812

 http://dx.doi.org/10.59490/6656d105744b7e9fc69bc5dc

Table 1. Frequencies for testing dynamic tyre stiffness.

1^{st} setting	1	1.7	2.2	2.8	3.6	4.7	6.0	7.8	10		Hz
2^{nd} setting	1	6	6.5	7	7.5	8	8.5	9	9.5	10	Hz

In some way unsatisfactorily was the fact that the higher the frequency was controlled, the higher was the deviation of the machine. The controller could obviously not adapt the hydraulics quick enough. Over time the regulator in the machine compensated for that, therefore only the latter part was used for evaluation (see Fig. 4).

Results

Static tyre stiffness results

The force and deflection characteristics were evaluated by means of a regression analysis as shown in Fig. 2. The gradient of the regression function was set as the stiffness value for each tyre inflation pressure. In a second regression analysis these characteristics were summarised as tyre stiffness over inflation pressure in coincidence with equation (1). The corresponding coefficients are shown in Table 2. In addition, the stiffness is visualised in Fig. 5.

$$k_{V,stat}(p_{infl}) = b_1 \cdot p_{infl} + b_2 \tag{1}$$

Table 2. Coefficient for Equation (1) including the 95% confidence intervals (CI).

Tyre	b_1 [(N/mm)/kPa] $\pm$ CI	b_2 [N/mm] $\pm$ CI
35-406 foldable	0.274 ± 0.092	5.983 ± 17.86
35-406 non-foldable	0.315 ± 0.132	0.891 ± 25.77
60-406 non-foldable	0.244 ± 0.185	22.34 ± 39.61

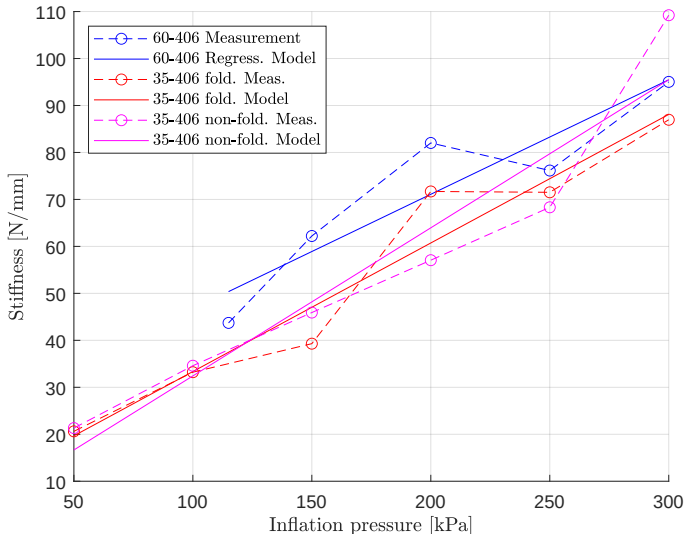


Figure 5. Vertical tyre stiffness over tyre inflation pressure for three types of tyres and the corresponding models based on regression analysis. The confidence intervals (not shown here) overlap widely.

According to Lines and Murphy (1991) b_2 in Equation (1) and Table 2 can be seen as the tyre's own carcass stiffness of $k_{V,stat,0}$ independent of inflation pressure. In contrast b_1 is the gradient of the graph that indicates how the stiffness increases over an inflation pressure range from 50 to 300 kPa. The b_2 coefficients indicate a higher tyre own stiffness for the wider tyre, which corresponds with the subjective impression when handling the tyres. However, the b_2 confidence intervals (not shown in the figure) for all tyres

©2023 Rothhämel, M. published by TU Delft OPEN on behalf of the authors.
ISSN: 2667-2812

 http://dx.doi.org/10.59490/6656d105744b7e9fc69bc5dc

include zero. Negative values are technically not meaningful. Anyhow, the tyres cannot be distinguished significantly with regard to their stiffness based on these measurements. This is valid for both of the coefficients.

Dynamic tyre stiffness results

The measurements as shown in Fig. 4 were evaluated in a script where the inclination of the mid 50% of the hysteresis loop where approximated by means of a linear function. An interim result is shown in Fig. 6. The measured frequency deviated from the set frequency by approximately 5%.

The results of several measurements were averaged for each setting consisting of inflation pressure, load (pre-load and dynamic load variation) and frequency. An example plot is given in Fig. 7.

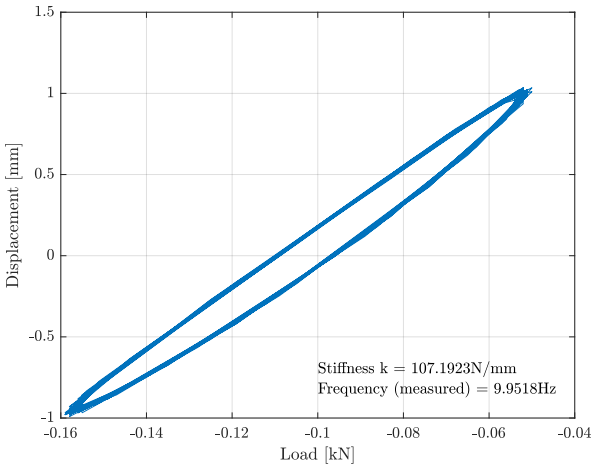


Figure 6. Single measurement of displacement over vertical load at 10 Hz and 400 kPa inflation pressure (tyre: 60-406).

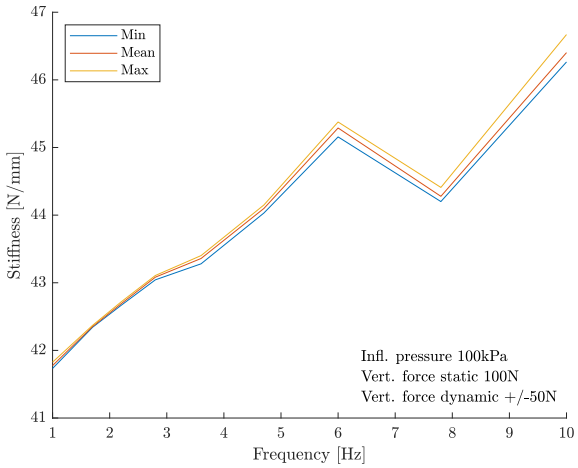


Figure 7. Dynamic vertical stiffness measurements at 100 kPa inflation pressure and 100 $\pm$ 50 Nm vertical load (tyre: 35-406).

The results show a general increase of stiffness over up to 12% from 1 Hz to 10 Hz. For very low tyre inflation pressure in the balloon tyre the increase can reach 20%. Independent of tyre pressure and load a clear local minimum was available at 7.8 Hz, which could be understood and during the experiment experienced as some kind of resonance. Therefore, further investigations focussed more on this frequency range using another setting of frequencies for testing (see second line in Table 1). A test for one setting with higher frequencies (10 – 30 Hz) did not show large changes and specifically not a certain trend. This triggered the decision to focus on the frequency range below 10 Hz only.

Fig. 8 and 9 show the results with focus on 6 – 10 Hz. The downwards peak at 7 Hz is much more distinct than in Fig. 7. In addition, it can be seen that there is a certain deviation e. g. 2% at 1 Hz in Fig. 8, which shows room for improvements within repeatability. When investigating Fig. 8 it must be noted that the inflation pressure is not equal to the desired 650 kPa. During the second measurement campaign a problem with the air pressure system occurred in the lab, which lead to this deviation.

Next to the experiments on the narrow tyre (see above), a balloon tyre was tested with about three times the air volume (see Table 3), where the tyre volume was approximated by means of the geometric figure of a torus. The results are shown in Fig. 10 and 11. Even in these experiments the downwards peak at 7 Hz is clearly visible. In a later test of the machine without the bicycle wheel, it could be shown that the machine has an eigenfrequency at 6.8 Hz! This means that a superposition of the tyre properties and the test machine must be assumed where the effects of the machine probably will overbalance.

Table 3. Comparison of narrow and balloon tyre.

Tyre	Volume
35-406 (non-)foldable	1.333 l
60-406 non-foldable	4.139 l

©2023 Rothhämel, M. published by TU Delft OPEN on behalf of the authors.
ISSN: 2667-2812

http://dx.doi.org/10.59490/6656d105744b7e9fc69bc5dc

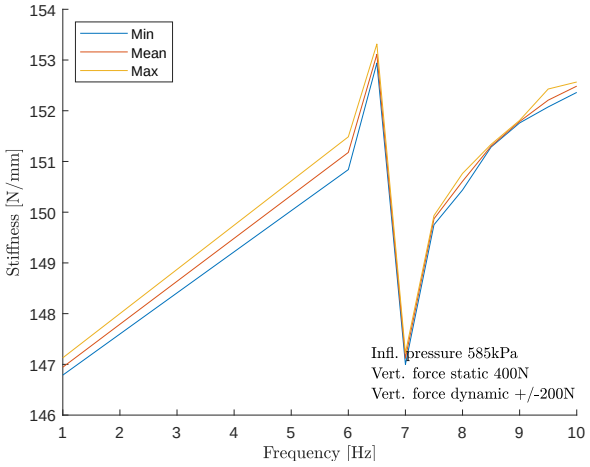


Figure 8. Dynamic vertical stiffness measurements with focus on 6 – 10 Hz at 585 kPa inflation pressure and 400 ± 200 Nm vertical load (tyre: 35-406).

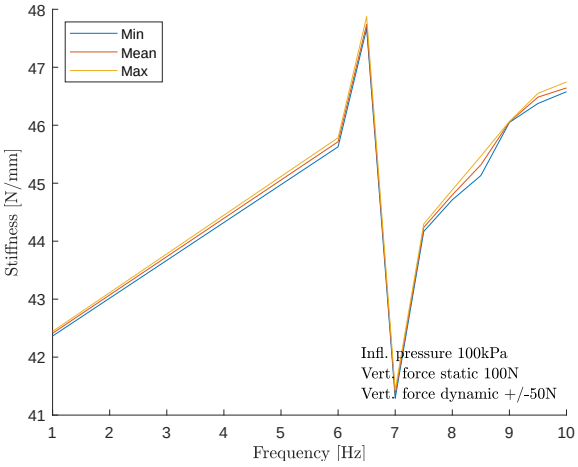


Figure 9. Dynamic vertical stiffness measurements with focus on 6 – 10 Hz at 100 kPa inflation pressure and 100 ± 50 Nm vertical load (tyre: 35-406).

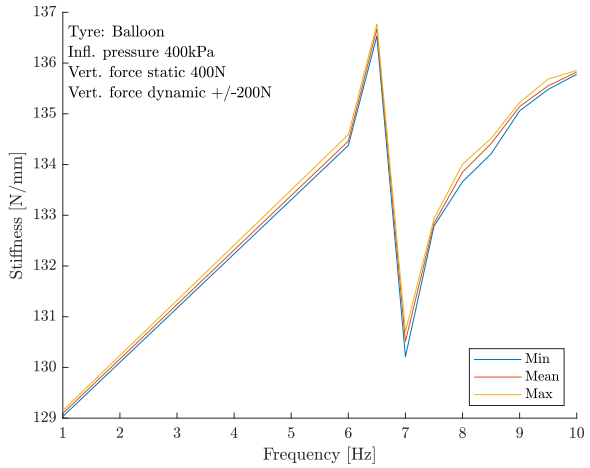


Figure 10. Dynamic vertical stiffness measurements with focus on 6 – 10 Hz at 400 kPa inflation pressure and 400 ± 200 Nm vertical load (tyre: 60-406).

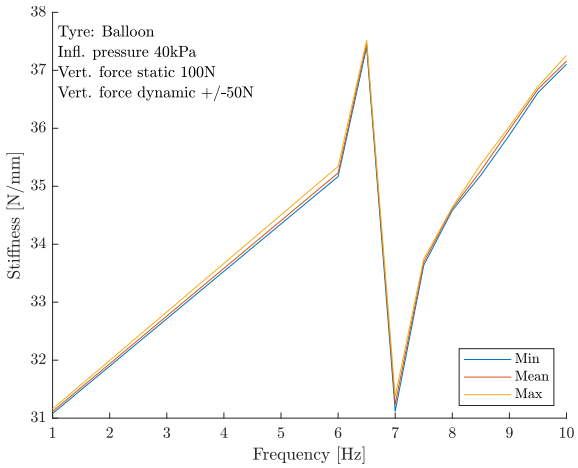


Figure 11. Dynamic vertical stiffness measurements with focus on 6 – 10 Hz at 40 kPa inflation pressure and 100 ± 50 Nm vertical load (tyre: 60-406).

Discussion

Two different methods to measure vertical or radial tyre stiffness of bicycle tyres were presented – a dynamic approach on a hydropuls machine and a static approach. Parameters modified were tyre inflation pressure and vertical load in the static experiment. In the dynamic experiment additionally dynamic load and frequency were varied. The dynamic experiments were performed on two different tyres. The same tyres were used for the static experiments and completed with a third tyre, which was a clincher version of the narrow foldable tyre. The tyres were made for 406 mm rim diameter as usual for bicycle carriers since the comfort of children in bicycle transportation was the larger scope behind the experiments.

The stiffness of the tyres was in a range of 31 N/mm to 147 N/mm in the dynamic measurements and in the range of 20 N/mm to 110 N/mm in the static measurements. The differences depend on different tyre pressure ranges. It must be considered that values below 50 N/mm are related to inflation pressure and tyre combinations that probably do not work reliably because the rim

©2023 Rothhämel, M. published by TU Delft OPEN on behalf of the authors.
ISSN: 2667-2812

 http://dx.doi.org/10.59490/6656d105744b7e9fc69bc5dc

will puncture the tube. This coincides with the values known from literature as e.g. by Waechter et al. (2002) who identified 200 N/mm on a recumbent bike and 134 N/mm on a special upride bike both with 20" wheels as in the present study, without any more specifications about type of tyre and inflation pressure. The tyre stiffness measured by Maier et al. (2018) is with 173 N/mm at 475 kPa inflation pressure significant higher. Two major differences to the present experiments are that Maier et al. tested a 28" tyre (42-622) and that they tested with higher load (up to 1500N). In their plot the stiffness at lower vertical load is obviously lower and closer to the here presented findings.

Considering the magnitude of the stiffness, the characteristics of the different tyres tested in this experiments, cannot be distinguished. The parameter with significant influence seems to the inflation pressure. This is also valid for the different measurement methods when considering the dynamic measurement at 1 Hz as nearly static. In contrast, with increasing excitation frequency the stiffness increases, however, this effect is non-linear and varies between 3.7% at high pressure in the narrow tyre and up to 20% at low pressure in the balloon tyre. Similarly, there is a trend to higher stiffness with increasing vertical load in a magnitude of 20% increase. This is in contrast to the findings of Doria et al. (2019) who found for a not in detail specified tyre with 300 kPa inflation pressure at low vertical load (< 100 N) a stiffness of 38 N/mm and at high vertical load (> 200 N) a stiffness of 91 N/mm, which corresponds to an increase of 140%.

All results of the dynamic tyre stiffness experiment are summarised presented in Fig. 12 for the balloon tyre and in Fig. 13 for the narrow tyre.

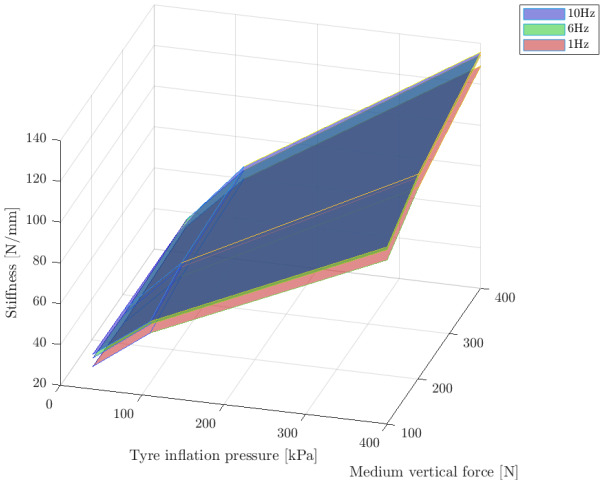


Figure 12. Dynamic vertical stiffness measurements over inflation pressure and vertical load at different excitation frequencies (tyre: 60-406).

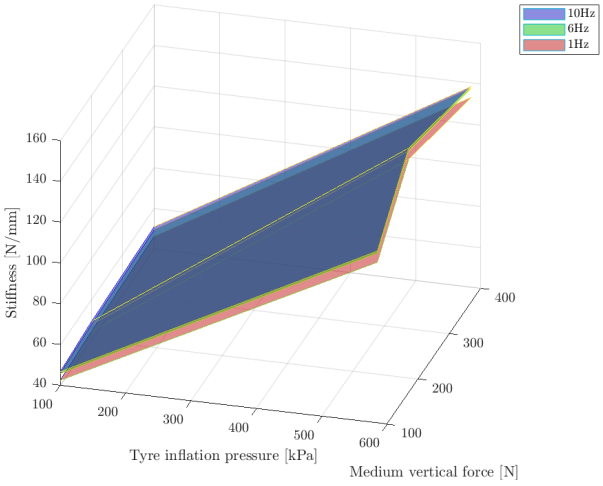


Figure 13. Dynamic vertical stiffness measurements over inflation pressure and vertical load at different excitation frequencies (tyre: 35-406).

Eigenfrequencies of the tyre were not investigated any longer after the superposed effect of the dynamic press and its dominating eigenfrequency around 6.8 Hz.

Conclusion

In this study, we investigated the dynamic stiffness characteristics of various types of tires under different conditions of excitation frequency and vertical load.

First, the most important factor for vertical tyre stiffness is the tyre inflation pressure. Second, dynamic measurements at 1 Hz cannot be interpreted as as static, specifically because of the uncertainty of the static measurements. In addition, in the dynamic measurements there is a small but clear increase in vertical tyre stiffness with increasing excitation frequency. Third, over increasing vertical load no clear stiffness characteristic could be identified.

This suggests that tire stiffness is slightly dependent on the excitation frequency and tire type, emphasizing the need for careful

©2023 Rothhämel, M. published by TU Delft OPEN on behalf of the authors.
ISSN: 2667-2812

 http://dx.doi.org/10.59490/6656d105744b7e9fc69bc5dc

consideration when designing tires for specific applications.

The advantage of the presented dynamic method is that it can be utilised in a machine that is available in many labs. The disadvantage is that the path of the vertical load does not correspond with the path when the wheel is mounted at a bicycle or bicycle carrier. A further study is suggested where the presented measuring method will be compared to a fork mounted wheel. In addition, a comparison to larger wheels 559 mm or 622 mm is recommended to clarify a generalisation of the results.

References

Brassart, F. P. and Wright, M. E. (1993). *A Machine to Study Vertical Tire Stiffness and Damping Coefficient*. SAE Technical Paper Series.

Doria, A., Marconi, E., and Cialoni, P. (2019). Modal analysis of a utility bicycle from the perspective of riding comfort. In *Proceedings of the ASME Design Engineering Technical Conference*, volume 3.

Doria, A., Marconi, E., Munoz, L., Polanco, A., and Suarez, D. (2021). An experimental-numerical method for the prediction of on-road comfort of city bicycles. *Vehicle system dynamics*, 59(9):1376–1396.

Hagemeister, C. and Schmidt, A. (2003). Which criteria own which level of importance for the choice of route for utility cyclists? (In German: Wie wichtig sind welche Kriterien für die Routenwahl von Alltagsradfahrern?). *Straßenverkehrstechnik*, 47(6):313–321.

Lepine, J., Champoux, Y., and Drouet, J. (2016). Test protocol for in-situ bicycle wheel dynamic comfort comparison. *Procedia Engineering*, 147:568–572.

Lines, J. A. and Murphy, K. (1991). The stiffness of agricultural tractor tyres. *Journal of terramechanics*, 28(1):49–64.

Maier, O., Hillenbrand, S., Wrede, J., Freund, A., and Gauterin, F. (2018). Vertical and longitudinal characteristics of a bicycle tire. *Tire Science and Technology*, 46(3):153–173.

Rothhämel, M. (2023). On rolling resistance of bicycle tyres with ambient temperature in focus. *Int. J. of Vehicle Systems Modelling and Testing*, 17(1):67–80.

Rothhämel, M. and Liu, Y. (2023). On comfort in cycle carriers for child transport. In *28th International Symposium on Vehicle System Dynamics, Ottawa, Canada*.

Rothhämel, M. (2023). Comfort and vibration level of children in cycle carriers. *PloS one*, 18(3):e0282778–.

Waechter, M., Riess, F., and Zacharias, N. (2002). A multibody model for the simulation of bicycle suspension systems. *Vehicle system dynamics*, 37(1):3–28.

Zegelaar, P. (1998). The dynamic response of tyres to brake torque variations and road unevennesses, Ph.D. thesis, TU Delft.

©2023 Rothhämel, M. published by TU Delft OPEN on behalf of the authors.
ISSN: 2667-2812

The Evolving Scholar Vol. 3, 2023

http://dx.doi.org/10.59490/65b7a66dc3bb2ea6dd4f2173

Bicycle and Motorcycle Dynamics 2023
Symposium on the Dynamics and Control of Single Track Vehicles
18–20 October 2023, Delft University of Technology, The Netherlands

Type of the Paper: Conference Paper

Revised

Modeling of a Bicycle Cargo Trailer with Magic Formula Tire Model for Vehicle Dynamics Simulation

[version 2; peer reviewed]

Marius Miller[1,*], Markus Pfeil[1], Ralph Kennel[2], Raphael Murri[3]

[1] Department of Electrical Engineering, Ravensburg-Weingarten University of Applied Sciences (RWU), Germany; marius.miller@rwu.de, ORCID 0000-0002-4574-608X; markus.pfeil@rwu.de
[2] School of Engineering and Design, Technical University of Munich (TUM), Germany; ralph.kennel@tum.de
[3] School of Engineering and Computer Science, Bern University of Applied Sciences (BFH), Switzerland; raphael.murri@bfh.ch
[*] corresponding author

Name of Editor: Jason Moore
First published: 25/09/2023
Last published: 15/02/2024
Citation: Miller, M., Pfeil, M., Kennel, R. & Murri, R. (2024). Modeling of a Bicycle Cargo Trailer with Magic Formula Tire Model for Vehicle Dynamics Simulation [version 2; peer reviewed]. The Evolving Scholar - BMD 2023, 5th Edition.
This work is licensed under a Creative Commons Attribution License (CC-BY).

Abstract:

In modern and sustainable concepts for supply chains, cargo bicycles, and cargo trailers can be a target-oriented solution in urban areas. However, drivers should be aware of the dynamics of these systems since, in the case of a loaded trailer, the trailer mass significantly exceeds the mass of the towing vehicle. However, the electrification of cargo trailers opens up the possibility of equipping these systems with an intelligent control system. This type of control system can be based on a model or tested using a model of the system. For this reason, the present research presents a single-track model of a bicycle-trailer system that considers longitudinal dynamics as well. In addition, a detailed tire model of a typical tire for cargo bikes is integrated. With the help of a prototype trailer, which forms the basis for the model's parameters, measurement data is collected and compared with the simulation results. Within the scope of the comparison, speed, acceleration in longitudinal and lateral direction, hitch force, yaw rate, and the angle between the towing vehicle and trailer are compared in a longitudinal and lateral dynamic case. The presented model shows a good agreement with the reality in the longitudinal dynamic investigation regarding the tested scenarios. In terms of lateral dynamics, the model can reproduce a significant part of the measured data but exhibits minor differences related to environmental conditions, limited degrees of freedom, measurement errors, and the implementation of a needed driver model in this setup, which represents the human component. In the future, the model can be used to investigate the driving characteristics of bicycle-trailer systems. Furthermore, adding a model of the trailer powertrain and its control to the simulation can enable simulation-based design and testing of the required vehicle dynamics controller before implementation on a prototype.

Keywords:

Cargo-trailer, Bicycle-trailer, Tire Modeling, Micromobility, Electrified Bicycle Trailer, Bicycle-trailer Model, Vehicle Dynamics

©2023 Miller, M., Pfeil, M., Kennel, R. & Murri, R. published by TU Delft OPEN on behalf of the authors.
ISSN: 2667-2812

 http://dx.doi.org/10.59490/65b7a66dc3bb2ea6dd4f2173

1 Introduction

Electrically assisted cargo trailers allow the transportation of heavy loads using a sustainable towing vehicle such as a conventional bicycle. However, this results in configurations in which the towing vehicle, consisting of bicycle and driver, has a significantly lower weight than the loaded trailer. In certain situations, the trailer dynamics can critically affect the towing vehicle. This results in unstable and dangerous conditions such as jackknifing and swaying of the trailer. If an electrified trailer is used in a bicycle-trailer system, the trailer powertrain and an appropriate vehicle dynamics control can contribute to the overall safety. Since testing such a vehicle dynamics control system can be dangerous for the test driver, Miller et al. (2023b) suggests testing with the help of a simulation and, in a more advanced sense, with a hardware-in-the-loop (HIL) system. In this context, the simulation is based on a simplified model, which can include different levels of detail. The advantage of using a HIL system is that it enables the integration of the controller's target hardware to test if it is interacting with the developed software. Furthermore, other control units can be integrated as hardware to test if the systems interact as required. However, this test method is based on a reliable model that is consistent with the real-world application. The same applies to a model-based control strategy, whose quality is defined, among other things, by a model that fits the system. For this reason, a model with three degrees of freedom (3DOF) is presented in the context of the present investigations, which can be used to represent the vehicle dynamics of a trailer attached to a bicycle. The current model does not consider an electric powertrain of the trailer. This basic model can be used to investigate various driving dynamic situations to identify under which conditions the system becomes unstable and critical situations can arise regarding user safety. Based on these identified driving maneuvers, the evaluation of a vehicle dynamics controller can be performed. Existing studies, according to Korayem et al. (2022) point out the so-called "snaking" and "jack-knifing" as particularly critical situations in trailer systems. The phenomenon of "snaking" describes the swaying of the trailer due to lateral forces, especially on slippery surfaces. If a vehicle-trailer system is braked in a curve and tire forces exceeding the saturation limit, the angle between the towing vehicle and the trailer can decrease significantly, resulting in a possible collision of the trailer with the towing vehicle, which is called "jack-knifing". In this context, Vempaty & He (2017) gives an overview of various approaches to stabilize tractor-trailer systems via the vehicle dynamics control of the tractor. Furthermore, the momentum of a fully loaded trailer can cause the comparatively light system of a bicycle and rider to be pushed by the trailer during braking.

The model of this research is based on the model presented by Korayem et al. (2022), but extended by a longitudinal dynamics model as can be seen in Miller et al. (2023b) and a detailed tire model. The tire model is based on a special tire for cargo bicycles measured and modeled according to Miller et al. (2023a), which is implemented as a magic formula (MF) model according to Pacejka & Besselink (2012).

The simulation results are then compared with the measured data of a prototype to evaluate whether the vehicle model corresponds to real-world conditions. Since there are no standardized test scenarios for driving dynamics testing of electrically powered bicycle trailers in Germany, two test scenarios are proposed to test the systems in simulation and in real-life testing. This involves comparing both a straight-ahead and an avoidance maneuver to allow the longitudinal and lateral behavior of the model to be evaluated. The trailer prototype used for comparison is a one-axle, all-wheel drive prototype with a system power of 2 kW. In addition to measuring acceleration and angular rates, a drawbar, according to Miller et al. (2021), enables direct measurement of the hitch force. In addition, an angle sensor is used to measure the angle between the bicycle and the trailer.

2 Bicycle and Trailer Model

Within the modeling framework, a mathematical description of the physical system behavior of the bicycle, rider, and trailer is carried out on a level that represents simplified real-world physical conditions. The bicycle-trailer model takes into account the forces acting on the system. The first part of the human driver is represented as a control system, which tries to follow a given speed trajectory by applying pedal force. The second part of the human driver is a predictive control system that tries to follow a given reference road trajectory by adjusting the steering angle. Modeling is carried out in Matlab SIMULINK. The vehicle model in the longitudinal and lateral direction is described first, followed by the tire model and concluding with the driver model.

©2023 Miller, M., Pfeil, M., Kennel, R. & Murri, R. published by TU Delft OPEN on behalf of the authors.
ISSN: 2667-2812

 http://dx.doi.org/10.59490/65b7a66dc3bb2ea6dd4f2173

2.1 Vehicle Model

In the scope of the present investigations, a vehicle model is presented to analyze the yaw stability of bicycle-trailer systems in micromobility. The model shown in this research is a single-track model, which combines the trailer's axle on one track. Since the bicycle's wheels are already on one track, there is no simplification regarding the axles, as it is usually done when considering multi-track systems such as a car. According to He & Ren (2013), pitch and roll motions are of minor importance for these investigations and are therefore neglected when the analysis is performed with dual-track vehicles. In contrast, it must be noted that bicycles are driven not only by a steering angle but also by tilting the system. Because of this, a restriction compared to reality arises in this case since this degree of freedom is not available in the presented model. The analysis of this research will evaluate whether the proposed model can simulate the behavior of a bicycle-trailer system with a reduced set of degrees of freedom in a target-oriented way. Furthermore, the presented model does not consider the elevation of the road and is therefore only valid on even road surfaces. In addition to the lateral dynamics, the model also considers the longitudinal dynamic behavior of the system. A detailed description of the longitudinal model can be found in Miller et al. (2023b). A schematic representation of the presented single-track model can be found in Figure 1.

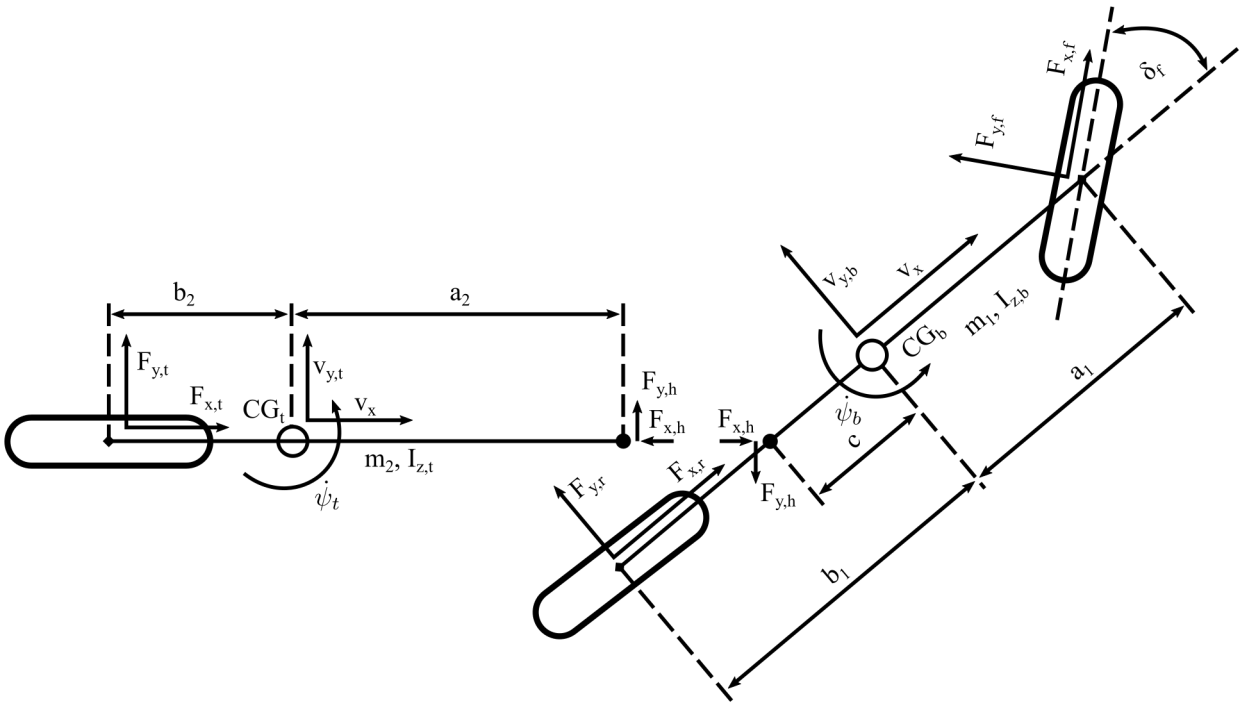


Figure 1. Bicycle Trailer Systems as a single track model.

As can be seen in Figure 1, the two subsystems consisting of bicycle and trailer can be coupled to each other via the hitch forces $F_{x,h}$ and $F_{y,h}$ acting in the x and y directions at the hitch. The resulting Equations of motion are given by Equation 1 to 4:

$$m_b(\dot{v}_{y,b} + v_x\dot{\psi}_b) = F_{y,f} + F_{y,r} - F_{y,h} \tag{1}$$

$$I_{z,b}\ddot{\psi}_b = a_1F_{y,f} - b_1F_{y,r} + cF_{y,h} \tag{2}$$

$$m_t(\dot{v}_{y,t} + v_x\dot{\psi}_t) = F_{y,t} + F_{y,h} \tag{3}$$

$$I_{z,t}\ddot{\psi}_t = -b_2F_{y,t} + a_2F_{y,h} \tag{4}$$

The forces $F_{y,f}$, $F_{y,r}$, and $F_{y,t}$ acting on the tire are no constant forces but describe complex interactions of the tire with the road. In the context of the presented work, these are modeled as a function of the respective slip angle of the wheel and its vertical force F_z. This model will be explained in more detail in the subsequent section.

©2023 Miller, M., Pfeil, M., Kennel, R. & Murri, R. published by TU Delft OPEN on behalf of the authors.
ISSN: 2667-2812

 http://dx.doi.org/10.59490/65b7a66dc3bb2ea6dd4f2173

2.2 Tire Model

The tire behavior of the bicycle and trailer is modeled using a generic form of the Magic Formula (MF) model according to Pacejka & Besselink (2012) and the results of Miller et al. (2023a). This model considers the tire characteristics in the longitudinal and lateral direction as a function of the slip κ as well as the slip angle α of the wheel and F_z, but under the assumption that no camber angles occur. Regarding the tire model, it is assumed that bicycle and trailer use 20 in wheels with the tires described in Miller et al. (2023a). While this is true for the trailer with one axle and two wheels when operated on an even surface, a bicycle can be driven with camber angles $\neq 0°$. At this point, the modeling differs from reality, as the presented three degrees of freedom (3DOF) model allows for motion in the xy plane as well as rotation about the z-axis but does not allow for rotation of the system around the x- or y-axis. In this research, the measured tire data from Miller et al. (2023a) is normalized using the F_z force. Afterwards, the coefficients of the generic MF are optimized using the non-linear least squares method so that the mathematical model fits the measured data as accurately as possible. The model generated this way becomes a function of κ or α and the vertical force F_z as described in Equation 5 and 6.

$$F_{x,i}(\kappa_i, F_z) = F_z((Dsin(Carctan(B\kappa_i - E(B\kappa_i - arctan(B\kappa_i))))))) \tag{5}$$

$$F_{y,i}(\alpha_i, F_z) = F_z((Dsin(Carctan(B\alpha_i - E(B\alpha_i - arctan(B\alpha_i))))))) \tag{6}$$

Where i represents the index for each tire position since the slip angles can differ from the respective axle and tire positions. The coefficients of the MF model determined by optimization are listed in Table 1 with the respective goodness of fit. The resulting tire

Table 1. Parameters - Normalized MF tire model.

	Value	SSE	R^2
B_x	0.1803	8.612	0.9807
C_x	1.469		
D_x	1.114		
E_x	0.7769		
B_y	0.1826	10.25	0.9944
C_y	1.533		
D_y	1.289		
E_y	0.7658		

models are visualized in figure 2.

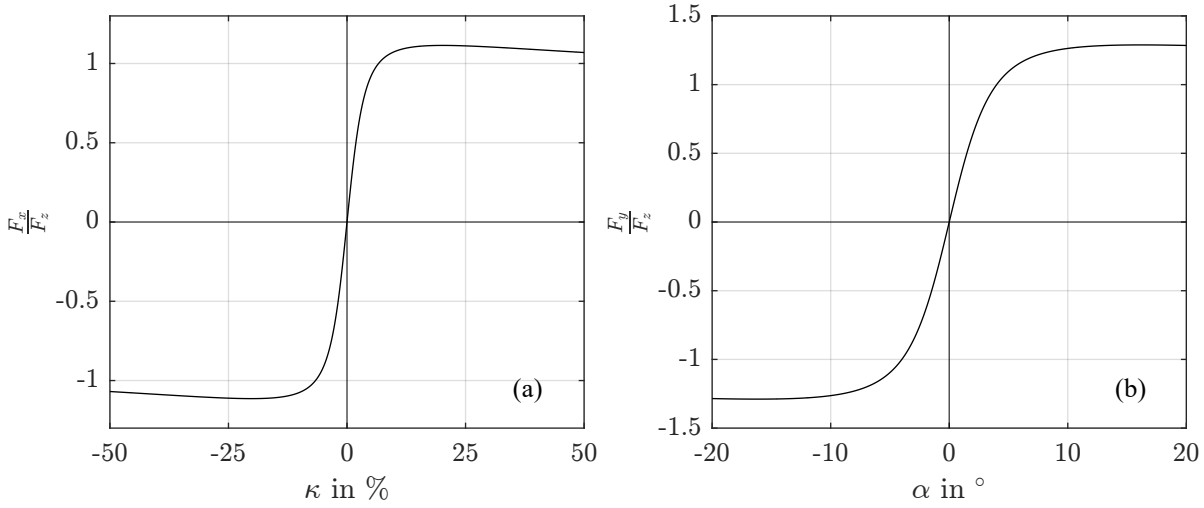


Figure 2. Normalized MF tire model of a Schwalbe Pick-Up 20 × 2.15 in tire at p = 3.5 bar where (a) shows the $F_x(\kappa)$ and (b) shows the $F_y(\alpha)$ relation.

©2023 Miller, M., Pfeil, M., Kennel, R. & Murri, R. published by TU Delft OPEN on behalf of the authors.
ISSN: 2667-2812

 http://dx.doi.org/10.59490/65b7a66dc3bb2ea6dd4f2173

In order to represent the lateral dynamics of the system, the respective slip angles of the associated wheels are required. Figure 3 shows the tire of a vehicle in the x_T-y_T tire fixed coordinate system. Where v_x is the longitudinal velocity vector that points in the vehicle's direction of movement. While $v_{x,T}$ and $v_{y,T}$ represent the longitudinal and lateral velocity vectors in the tire fixed coordinate system. Respectively, the slip angle is defined as the angle α between the center line of the tire and the longitudinal velocity vector v_x.

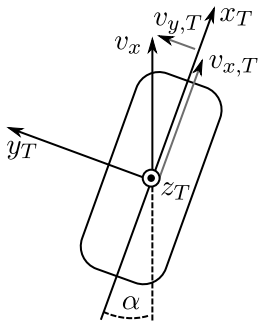


Figure 3. Slip angle definition in the tire-fixed coordinate system according to Ersoy & Gies (2017).

According to Chen & Tomizuka (1995), the slip angles at the front, rear, and trailer axles are defined by Equations 7 to 9.

$$\alpha_f = \delta_f - arctan\left(\frac{v_{y,b} + a_1\dot{\psi}_b}{v_x}\right) \tag{7}$$

$$\alpha_r = -arctan\left(\frac{v_{y,b} - b_1\dot{\psi}_b}{v_x}\right) \tag{8}$$

$$\alpha_t = -arctan\left(\frac{(v_{y,t} - c\dot{\psi}_b)cos(\psi_b - \psi_t) - \dot{\psi}_t(a_2 + b_2) + v_x sin(\psi_b - \psi_t)}{v_x cos(\psi_b - \psi_t) - (v_y - c\dot{\psi}_b)sin(\psi_b - \psi_t)}\right) \tag{9}$$

The steering angle δ_f impacts the front axle, while the unsteered rear axle is based solely on the angular relationship between v_x and $v_{y,b}$ as well as the yaw rate $\dot{\psi}_b$. Similar relations occur at the trailer axle, incorporating the hitch angle $\dot{\theta}$. Where according to Korayem et al. (2022), the relation for $\dot{\theta}$ is given in Equation 10.

$$\dot{\theta} = \dot{\psi}_t - \dot{\psi}_b \tag{10}$$

2.3 Driver Model

A driver model is required to drive and steer the vehicle model. The implementation follows the two control loops shown in Figure 4. A PI controller is used in the model to track the velocity reference trajectory which is defined as $v_{x,ref}(t)$. The error is calculated by comparing the given reference velocity $v_{x,ref}$ with the current longitudinal velocity v_x with respect to the body coordinate system of the towing vehicle. The proportional term of the PI controller multiplies the current error by a gain factor K_p. The second part of the PI controller consists of an integral term, which includes the time integration of the error and multiplies this part by the factor K_i. Normalization over the nominal velocity v_{nom} results in an output quantity of the system between zero and one as t_{gain}. This percentage output of the controller is then multiplied by a simulated maximum available driver torque. In an initial driver simulation, the results according to Korff et al. (2007) were adopted simplistically, resulting in a torque T_c at the crank by the driver of approx. 40 Nm, which is not constant but dependent on the position of the crank. For this reason, the torque curve is superimposed with an ideal sine to represent the described behavior in a simplified form. The frequency of the sine wave is 2.1 Hz, which results from the obtained cadence during the test drives. To avoid numerical problems, the superimposed sine wave is only applied at speed values higher than $2.5\frac{m}{s}$. In addition, high torques of up to 100 Nm are temporarily permitted for start-up, which can occur in real-world operation by standing pedal operation. The resulting torque is transferred to the bicycle-trailer system, where the movement is computed.

©2023 Miller, M., Pfeil, M., Kennel, R. & Murri, R. published by TU Delft OPEN on behalf of the authors.
ISSN: 2667-2812

 http://dx.doi.org/10.59490/65b7a66dc3bb2ea6dd4f2173

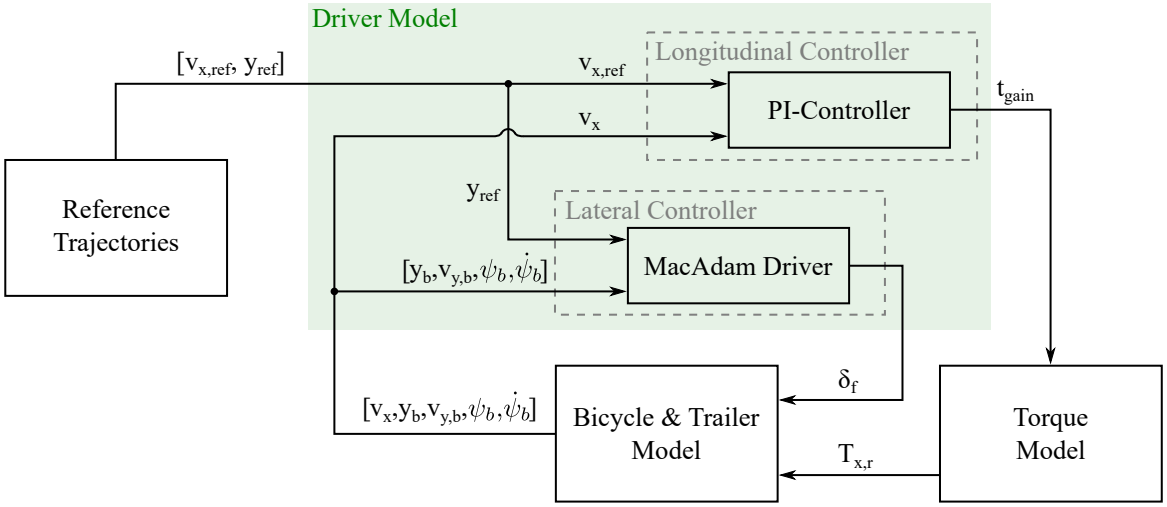


Figure 4. Driver Model and control scheme.

Bubb et al. (2015) describes the difficulties of mapping the behavior of a person driving a vehicle in a simulation, as humans have kinesthetic perception in addition to visual perception. Bubb et al. (2015) also lists complex cognitive human models, which are, however, too in-depth for many vehicle dynamics studies. Accordingly, control engineering approaches can be used to simulate the behavior of a human in certain areas. Therefore the steering controller is implemented according to MacAdam (1988) as an optimization based predictive controller. The goal of this approach is to track a given y_{ref} trajectory by using a built-in single-track state-space model of the system and optimizing the manipulated variable δ_f. Therefore the controller needs v_x, y_b, $v_{y,b}$, ψ_b and $\dot{\psi}_b$ as feedback values. By minimizing the quadratic cost function between the previewed path and the current lateral position in Equation 11 the optimal front wheel steering angle δ_f is computed.

$$J = \frac{1}{T} \int_{t}^{t+T} \left[f(\eta) - y(\eta) \right]^2 d\eta \tag{11}$$

With the previewed time window T calculated with the prediction distance P and the current longitudinal velocity v_x:

$$T = \frac{P}{v_x} \tag{12}$$

Furthermore the controller uses the delay function in Equation 13 to implement the response time of the driver τ_{resp}.

$$H(s) = \exp^{-s\tau_{resp}} \tag{13}$$

The final value of δ_f is set as an output for the bicycle and trailer system. With the applied value of δ_f the lateral movement of the system can be computed by the bicycle and trailer system in the simulation. According to MacAdam (1988), the driver behavior can be adjusted by the response time of the driver τ_{resp} and the prediction horizon P. For example, a long response time can be used to simulate a slow reacting driver. A long prediction horizon enables gentle steering movements because the goal position can be reached in longer time horizon, while a short prediction horizon can lead to aggressive steering movements depending on the system dynamics and the reference trajectory. The parameters for the driver model can be seen in Table 2. While the PI-controller parameters are adjusted by minimizing the error between v_{ref} and v_x, the lateral controller's parameter τ_{resp} was chosen with 0.4 s corresponding to a medium reaction time to an unintended collision avoidance maneuver. With a value of 0.35 m, the preview distance P has a small value, so an unforeseen avoidance maneuver is suggested to the simulated driver. A small preview distance corresponds to the real-world measurements since small traffic cones were used, which led to late recognition of the evasion point. It is important to note that a general replication of human driver behavior remains challenging since each driver has their own characteristics when it comes to accelerating, braking, and steering. Therefore, the presented parameters form a model of one driver type.

©2023 Miller, M., Pfeil, M., Kennel, R. & Murri, R. published by TU Delft OPEN on behalf of the authors.
ISSN: 2667-2812

 http://dx.doi.org/10.59490/65b7a66dc3bb2ea6dd4f2173

Table 2. Parameters for Driver Model.

Area	Parameter	Value
Longitudinal	K_p	13
Longitudinal	K_i	5
Longitudinal	v_{nom}	5
Lateral	τ_{resp}	0.4
Lateral	P	0.35

3 Measurement System and Prototype Trailer

The prototype trailer is a single-axle system with a wheel hub motor on each side. The main frame is made of aluminum profiles and offers cargo storage up to a length of 1.40 m and a width of 0.81 m. The trailer's hitch is placed in the center and attached to the bicycle with the help of a ball hitch. The values of the masses, mass inertias, drag coefficients, as well as the areas and dimensions of the trailer and an exemplary conventional bicycle are listed in Table 3. For subsequent control of the trailer, the system has sensors, a

Table 3. Parameters for Simulation.

Parameter	Value	Unit	Description
m_b	100.00	kg	Bicycle + Driver
$I_{z,b}$	3.73	kgm^2	Moore et al. (2009)
$c_{d,b}$	1.10		Chowdhury & Alam (2012)
$A_{f,b}$	0.50	m^2	Chowdhury & Alam (2012)
a_1	0.57	m	From CAD Model
b_1	0.41	m	From CAD Model
c	0.17	m	From CAD Model
m_t	112.60	kg	From CAD Model
$I_{z,t}$	45.17	kgm^2	From CAD Model
$c_{d,t}$	1.10		Chowdhury & Alam (2012)
$A_{f,t}$	0.85	m^2	From CAD Model
a_2	1.91	m	From CAD Model
b_2	0.13	m	From CAD Model

central vehicle dynamics control unit (VDCU), and an electric powertrain, which are visualized in the system layout in Figure 5. The powertrain consists of a 48V battery with 29.7Ah and two VESC 6 75 power electronics, which drive two 1kW wheel hub motors via field-oriented control using software developed by Vedder (2023). With the help of a DC/DC converter, all sensors, including the VDCU, are supplied with voltage. The sensorset includes the sensors listed in Table 4. In addition to the standard methods of

Table 4. Sensorset of prototype trailer.

Sensor	Measured Value(s)	Communication	Description
Load Cells	hitch force $F_{h,x}$	Analog Signal	BCM 169H
Hitch Angle Sensor	hitch angle θ	Analog Signal	Novotechnik RFD-4021
IMU	acceleration $\dot{v}_x$, $\dot{v}_y$ and yaw rate $\dot{\psi}_z$	CAN-Bus	Movella / Xsens MTi-630
Power Electronics	wheel speed right rpm_r, wheel speed left rpm_l and respectively v_r and v_l measurement	CAN-Bus	TRAMPA BOARDS VESC 6 75V

measuring speeds and accelerations, the trailer has a system for measuring the hitch force according to Miller et al. (2021), which is based on load cells. Furthermore, an angle sensor is used to measure the hitch angle between the trailer and the towing vehicle. The values of the sensor are sampled by the VDCU with 80 Hz. While the power electronics and the inertial measurement unit (IMU) communicate via CAN-Bus, the load cells and hitch angle sensor signals are analog signals processed directly by the VDCU. For post-processing and analysis of the measured data, a CAN-Bus logger is included in the system, which gets time synchronized values from the VDCU. The control of the power electronics is done via CAN-Bus by the VDCU, which is not used in the present investigations to ensure that both model and simulation are compared in the same setup without additional torque of the electric drives.

©2023 Miller, M., Pfeil, M., Kennel, R. & Murri, R. published by TU Delft OPEN on behalf of the authors.
ISSN: 2667-2812

 http://dx.doi.org/10.59490/65b7a66dc3bb2ea6dd4f2173

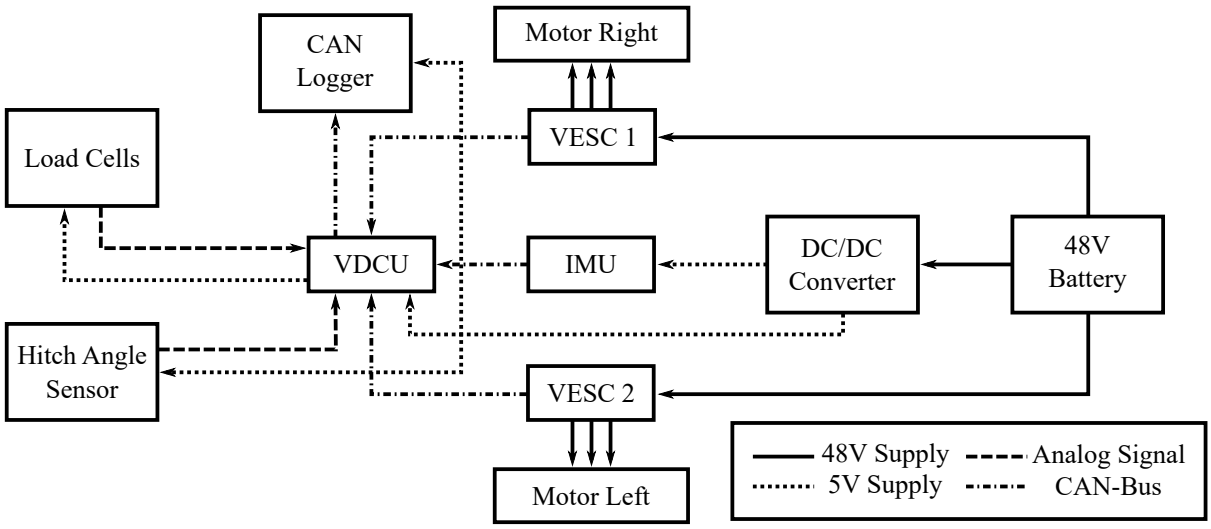


Figure 5. System layout - Prototype trailer.

The trailer prototype with the described measurement system attached to a bicycle is shown in Figure 6. Electrified bicycles such as pedelecs bring different torque characteristics to the system due to their drive, depending on the control scheme. The present tests are limited to investigating the human impact on the system and the ability to simulate this behavior. Therefore, in contrast to Figure 6, a conventional bicycle was used for the tests without any electric drive to change the torque characteristics of the rider. Apart from connecting the trailer via a conventional hitch and clamping the angle sensor to the seat post, no modifications were made to the bicycle.



Figure 6. Prototype trailer attached to a bicycle.

4 Test Cases

A comparative analysis with measurement data from test drives with the prototype is carried out to evaluate the model presented in this paper. Within the scope of these tests, both the longitudinal and the lateral dynamic behavior are to be evaluated. For this reason, a straight-line drive without steering intervention by the driver (longitudinal test case) and an avoidance maneuver (lateral test case) is performed with the prototype trailer and in the simulation. Regarding the longitudinal test case, acceleration is performed from 0 $\frac{m}{s}$ until a final speed of approx. 4 $\frac{m}{s}$ is reached. After a short constant travel of 4 $\frac{m}{s}$, a braking maneuver is performed until the vehicle comes down to a velocity of 0 $\frac{m}{s}$ again. The lateral test case also starts from 0 $\frac{m}{s}$, after acceleration up to a speed of approx. 4 $\frac{m}{s}$, the speed is kept constant for a short section before the collision avoidance is performed. The obstacle to avoid has a

©2023 Miller, M., Pfeil, M., Kennel, R. & Murri, R. published by TU Delft OPEN on behalf of the authors.
ISSN: 2667-2812

 http://dx.doi.org/10.59490/65b7a66dc3bb2ea6dd4f2173

lateral length of 1.5 m and is placed at a 1 m distance to the evasion point, resulting in a situation that should replicate an unexpected maneuver. Afterwards, the system is decelerated to 0 $\frac{m}{s}$ again.

5 Comparison of Measured and Simulated Data

In the first investigation, the longitudinal dynamic characteristics of the model are compared with the measured data. In this context, the velocity v_x and the acceleration $\dot{v}_x$ in the vehicle-fixed coordinate system as well as the measured hitch force $F_{x,h}$ in the drawbar are compared with each other. Figure 7 shows the measured and simulated data for the longitudinal test case. The indices "meas" represents data obtained with the prototype, while "sim" shows data generated during simulation with the presented model. The reference speed $v_{x,ref}$ as input for the driver model results from an average value of the left $v_{x,l,meas}$ and right $v_{x,r,meas}$ wheel speed, which was measured during the test drive. All measured values were smoothed using a moving average, with the sliding window for smoothing ranging from $k-2$ to $k+2$ samples starting from the current point k.

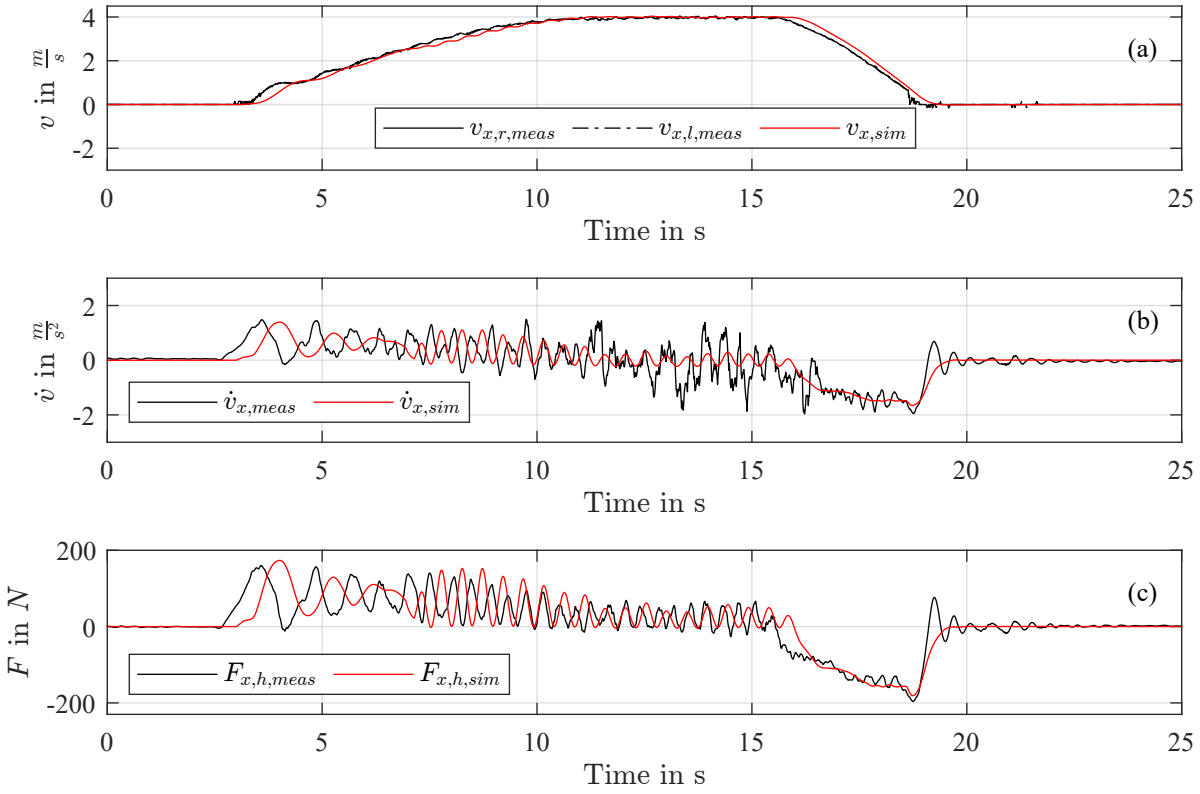


Figure 7. Longitudinal test case - Comparison of measured data and simulation results where (a) shows the velocity v_x, (b) shows the acceleration $\dot{v}_x$ and (c) shows the hitch force $F_{x,h}$.

As can be seen in Figure 7 (a), the simulated bicycle tries to follow the reference v_x signal given by the measured data. With a short delay of approx. 0.25 s, the model achieves to meet the required speed of approx. 4 $\frac{m}{s}$. The sinusoidal amplitudes of the $\dot{v}_{x,meas}$ signal result from the periodic torque output at the cyclist's crank. Despite sinusoidal modeling of the torque, the model's $\dot{v}_{x,sim}$ signal does not exactly reproduce the peaks of the acceleration amplitudes of the measured signal. One reason for this is the threshold value of 2.5$\frac{m}{s}$, which must be exceeded for the model to perform a sinusoidal torque superposition. Moreover, the pedal frequency of a cyclist varies depending on the situation, which cannot be represented by a fixed superposition frequency as used in the model. However, it is evident in the time domain that the frequencies of the sinusoidal waves of both systems are similar but show a phase shift. High similarity regarding the amplitudes can be seen by comparing $F_{x,h}$ of the model and measured data, whereas the simulated data exhibits the described lack of 0.25 s. During acceleration, a positive peak of 160.26 N is obtained in $F_{x,h,meas}$, which the model almost exactly meets with a value of 173.41 N. The same behavior can be seen during deceleration,

©2023 Miller, M., Pfeil, M., Kennel, R. & Murri, R. published by TU Delft OPEN on behalf of the authors.
ISSN: 2667-2812

http://dx.doi.org/10.59490/65b7a66dc3bb2ea6dd4f2173

where a negative peak of -196.32 N is obtained in $F_{x,h,meas}$. Whereas the simulation reaches a value of -181.05 N for $F_{x,h,sim}$, resulting in a difference of 15.27 N. In the second investigation, the lateral test case is compared. Figure 8 shows the measured and simulated data for the lateral test case.

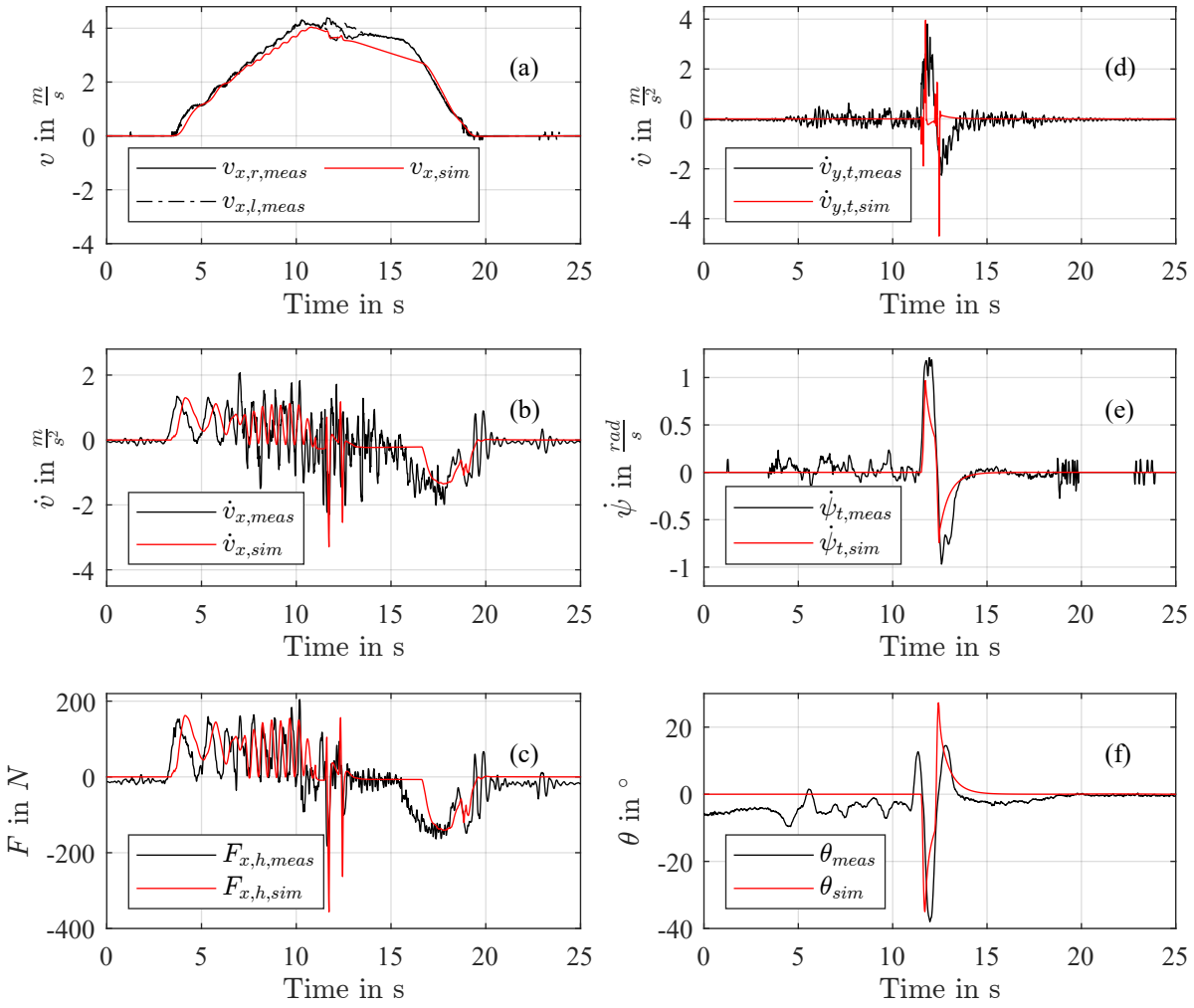


Figure 8. Lateral test case - Comparison of measured data and simulation results where (a) shows the velocity v_x, (b) shows the acceleration $\dot{v}_x$, (c) shows the hitch force $F_{x,h}$, (d) shows the acceleration $\dot{v}_y$, (e) shows the yaw rate $\dot{\psi}_t$ and (f) shows the hitch angle θ.

As in the longitudinal dynamic test case, the longitudinal velocity of the measured data is used as $v_{x,ref}$ signal for the simulation. The model's controller tracks the model's speed v_x and adjusts the torque so the given $v_{x,ref}$ curve can be followed with a slight delay. The periodic torque output, caused in real-world measurements by pedaling, can be seen in the $\dot{v}_x$ signal of the measured data during acceleration as a sinusoidal superposition of the signal. The simulation, which has a fixed simulated pedaling cadence, can reproduce this behavior to some extent, as can be seen from approx. 7.5 s to 11 s. The acceleration peaks occurring in this case are slightly higher in the measured data. During the real-world test, there was no active braking during the avoidance maneuver and no pedaling after the avoidance maneuver. For this reason, braking is only allowed for $t > 15\ s$, and pedaling is prevented in the simulation for $t > 15\ s$. As a result, the $\dot{v}_{x,sim}$ curve shows only a slightly negative signal in this period due to the speed falling from the driving resistances. As can be seen in Figure 8 (a), braking is initiated from 16.7 s, which can be seen in Figure 8 (c) with a pushing trailer and negative hitch force values in $F_{x,h,meas}$. The simulated signal $F_{x,h,sim}$ also shows this decrease and results in a negative peak value of -141.20 N, while $F_{x,h,meas}$ has a negative peak of -163.72 N. The resulting difference is therefore given as an absolute value of 22.52 N. From 11.25 s the avoidance maneuver takes place, which can be seen in the measurement data

©2023 Miller, M., Pfeil, M., Kennel, R. & Murri, R. published by TU Delft OPEN on behalf of the authors.
ISSN: 2667-2812

via a positive and a negative deflection in the signals of $\dot{v}_{y,t}$ and $\dot{\psi}_t$ in Figure 8 (d) and (e). The positive amplitude of $\dot{v}_{y,t,meas}$ with 3.81 $\frac{m}{s^2}$ is closely met by $\dot{v}_{y,t,sim}$ with a value of 3.96 $\frac{m}{s^2}$. Regarding the negative amplitude of $\dot{v}_{y,t,meas}$ with -2.26 $\frac{m}{s^2}$, the simulation is reaching a value of -4.69 $\frac{m}{s^2}$. For this purpose, it is assumed that the filter profile of the IMU leads to an attenuation of the measured amplitude so that the true value could be higher and closer to the simulation. The investigation of this assumption will be examined in the context of new measurements so that the deviation of the negative amplitude can be evaluated. Further, it must be mentioned that the measurements of the test drives were carried out on a concrete surface. The tire measurements, which serve to create the tire model, were carried out on asphalt. The resulting different slip values also influence the behavior of $\dot{v}_{y,t,meas}$. Regarding the angular velocity, shown in Figure 8 (e), it can be seen that the model can reproduce the data of the real test run with a small error. The positive peak of the measured data is at 1.18 $\frac{rad}{s}$, while the model shows a nearly identical maximum with 0.97 $\frac{rad}{s}$. The negative peak of the real data with -0.97 $\frac{rad}{s}$ can be reproduced by the model as well with -0.74 $\frac{rad}{s}$. In comparison with $\dot{\psi}_{t,meas}$, the shape of $\dot{\psi}_{t,sim}$ is more edged, which is caused by the steering characteristics of the simulated driver. Looking at θ in Fig. 8 (f), it is recognizable that the simulation data follows the measured data with a good fit after 10 s. With a peak of -34.99 °, θ_{sim} has a peak of almost the same size as θ_{meas}, which has a value of 37.98 °. The difference up to the time of 10 s results from a not exactly in-one-line standing trailer and bicycle at the start of the test drive. This offset improves in the course of approx. 15 s and settles at approx. -0.2 °, which results from the measurement inaccuracy of the sensor and the positioning error of the sensor on the bicycle.

6 Conclusion

In the present work, the modeling of a bicycle trailer was investigated using a single-track model with an additional longitudinal dynamics model. The model includes a nonlinear tire model based on the not linearized calculations of the slip angles. The normalized tire model is built on the research of Miller et al. (2023a) and is used in a lateral vehicle dynamics simulation for the first time. A combined driver model based on a longitudinal and lateral controller has been introduced to follow a reference longitudinal velocity and a lateral trajectory. With the help of a new trailer prototype, test drives were performed, and measurement data was collected. In the case of validating the proposed vehicle model, the measured data was compared to the simulation results. In this context, the measured velocity of the prototype and a defined test scenario serve as inputs for the simulation. While the longitudinal dynamics model shows a good alignment between simulated and measured data, there is a slight deviation in the model compared to reality in the context of lateral dynamics. Regarding this relation, the model's driver has a significant impact as this part affect the overall system's behavior. The steering trajectory from the MacAdam Driver model which is dependent on prediction distance and the drivers response time affects the turning behavior and lateral acceleration. The parameters of this part of the control structure have a corresponding weighting when comparing simulation data with measured data. Consequently, finding the proper prediction distance and the correct driver response time, which leads to a steering angle trajectory similar to the one in the measured case, is difficult. This result follows the findings of Bubb et al. (2015), who refers not only to visual perception but also to kinaesthetic perception. Therefore mapping the human behavior in this framework is one of the major difficulties, as no steering signal was measured from the cyclist. The parameters found for the MacAdam driver lead to a good agreement between the simulated and measured yaw rates $\dot{\psi}$ and hitch angles θ, meaning that the model behaves in accordance with reality in this aspect. To improve the agreement of the simulated and measured lateral accelerations $\dot{v}_y$, the MacAdam Driver parameters can be further optimized in the future by recording the real steering angle curve. Furthermore, the present tests were performed on a concrete surface, while the data for the tire model was measured on asphalt. Different friction values between the model and the real-world scenario can lead to varying values of the slip angle α, resulting in deviations of the lateral acceleration $\dot{v}_y$. On the other hand, measurement error can also lead to an error between the simulated and measured signals. Regarding this topic, the settings of the IMU can lead to deviations as well. The IMU is assumed to be responsible for the damping of occurring acceleration peaks by its internal filters. Despite the mentioned deviations, the presented model shows a target-oriented fit since rotating movements around the x- and y-axis, especially with the towing vehicle, are not considered in the model. Thus, the presented model can be used to investigate vehicle dynamic stability. Furthermore, the model can be supplemented by a powertrain simulation as presented in Miller et al. (2023b), allowing the control of an electrically driven trailer to be tested, for example, with a hardware-in-the-loop system before implementation on a prototype.

References

Bechtloff, J. (2017). *Schätzung des Schwimmwinkels und fahrdynamischer Parameter zur Verbesserung modellbasierter Fahrdynamikregelungen*. Technische Universität Darmstadt

©2023 Miller, M., Pfeil, M., Kennel, R. & Murri, R. published by TU Delft OPEN on behalf of the authors.
ISSN: 2667-2812

Bubb, H., Bengler, K., Grünen, R. E., Vollrath, M. (2015) *Automobilergonomie* ,. 1st ed.; Springer Vieweg: Wiesbaden, Germany.

Chen, C., Tomizuka, M. (1995), Dynamic Modeling of Tractor-Semitrailer Vehicles in Automated Highway Systems. California PATH Working Paper, UCB-ITS-PWP-95-8.

Chowdhury, H., Alam, F. (2012), Bicycle aerodynamics: an experimental evaluation methodology. Sports Eng (2012), 15. DOI 10.1007/s12283-012-0090-y

Ersoy, M., Gies, S. (2017) *Fahrwerkhandbuch - Grundlagen – Fahrdynamik – Fahrverhalten– Komponenten – Elektronische Systeme – Fahrerassistenz – Autonomes Fahren– Perspektiven*,. 5th ed.; Springer Vieweg: Wiesbaden, Germany.

He, Y. and Ren, J. (2013), A Comparative Study of Car-Trailer Dynamics Models. In SAE Int. J. Passeng. Cars - Mech. Syst. 6(1):177-186, https://doi.org/10.4271/2013-01-0695

Kiencke, U., Nielsen, L. (2005) *Automotive Control Systems - For Engine, Driveline, and Vehicle*,. 2nd ed.; Springer Berlin: Heidelberg, Germany.

Korayem, A.H., Khajepour, A., Fidan B. (2022), A Review on Vehicle-Trailer State and Parameter Estimation. In IEEE Transactions on Intelligent Transportation Systems, vol. 23, no. 7, pp. 5993-6010, July 2022, doi: 10.1109/TITS.2021.3074457

Korff, T., Romer, L. M., Mayhew, I.; Martin, J. C. (2007), Effect of Pedaling Technique on Mechanical Effectiveness and Efficiency in Cyclists. Medicine & Science in Sports & Exercise 39(6):p 991-995, June 2007. DOI: 10.1249/mss.0b013e318043a235

MacAdam, C. C. (1988), Development of Driver/Vehicle Steering Interaction Models for Dynamic Analysis. Final Technical Report UMTRI-88-53. Ann Arbor, Michigan: The University of Michigan Transportation Research Institute.

Miller, M., Kaufmann, A., Reick, B., & Pfeil, M. (2021), Intelligente Anhängerdeichsel für verschiedene Zugfahrzeuge. Hochschule Ravensburg-Weingarten, Weingarten

Miller, M., Pfeil, M., Reick, B., Murri, R., Stetter, R., & Kennel, R. (2023a), Measurement and Modeling of a Cargo Bicycle Tire for Vehicle Dynamics Simulation. Applied Sciences, 13(4), 2542. https://doi.org/10.3390/app13042542

Miller, M., Pfeil, M., & Kennel, R. (2023b), Trailer Electrification–A HIL Approach for MPC Powertrain Control to Ensure Driver Safety in Micromobility (No. 2023-24-0180). SAE Technical Paper, doi:10.4271/2023-24-0180

Moore, J., Kooijman, J., Hubbard, M. & Schwab, A. (2009), A Method For Estimating Physical Properties of a Combined Bicycle and Rider, *Proceedings of the ASME 2009 International Design Engineering Technical Conferences & Computers and Information in Engineering Conference IDETC/CIE 2009*, San Diego, California, USA

Pacejka, H.B., Besselink, I. (2012) *Tire and Vehicle Dynamics*, 3rd ed.; Butterworth-Heinemann: Oxford, UK.

Vedder, B. (2023), bldc. https://github.com/vedderb/bldc/ (Accessed on 05.09.2023)

Vempaty, S., He, Y., A Review of Car-Trailer Lateral Stability Control Approaches. SAE Technical Paper 2017-01-1580, 2017, https://doi.org/10.4271/2017-01-1580

©2023 Miller, M., Pfeil, M., Kennel, R. & Murri, R. published by TU Delft OPEN on behalf of the authors.
ISSN: 2667-2812

The Evolving Scholar Vol. 3, 2023 https://dx.doi.org/10.59490/665841de8a4558165d52bf58

Bicycle and Motorcycle Dynamics 2023
Symposium on the Dynamics and Control of Single Track Vehicles
18 – 20 October 2023, Delft University of Technology, The Netherlands

Type of the Paper: Conference Paper

Revised

Modelling, parameterizing and validating the motion of a tadpole style cargo tricycle with real world experiments

[version 3; peer reviewed]

Clemens Groß[1*], and Steffen Müller[2]

[1] Chair of Automotive Engineering, Technische Universität Berlin; email gross.1@tu-berlin.de; ORCID: 0000-0002-1606-3845
[2] Chair of Automotive Engineering, Technische Universität Berlin; email steffen.mueller@tu-berlin.de

*corresponding author

Name of Editor: Jason Moore
First published: 03/10/2023
Last published: 30/05/2024
Citation: Groß, C. & Müller, S. (2024). Modelling, parameterizing and validating the motion of a tadpole style cargo tricycle with real world experiments [version 3; peer reviewed]. The Evolving Scholar - BMD 2023, 5th Edition.
This work is licensed under a Creative Commons Attribution License (CC-BY).

Abstract:

In the past years, cargo bicycles in different configurations have gained popularity for many use cases. Their configurations differ substantially. Single-track cargo bicycles and their kinematics are linked closely to conventional bicycles. The kinematics of inverted tricycles, so-called tadpole trikes, are different. In this work, we model the motion for such a tadpole tricycle with articulated steering in order to predict the kinematic potential of such a vehicle.

A single-track model for vehicle kinematics is implemented and compared to a planar model that incorporates a term for the lean (or roll) angle. To do so, the connection between steering and lean angle is calculated by the help of wheel flop. This is validated by inversing the modelling process and optimizing the geometrical approach function with the help of naturalistic cycling studies. The tricycle used for this study is measured experimentally to find the parameters for the models. The cargo tricycle is then instrumented with measuring devices. We validate the two presented kinematic models for the motion of the tadpole tricycle with real world measuring data for given driving scenarios. These two models are impinged with data from our experimental driving maneuvers. It is shown that the two derived kinematic models hold reasonably well against the measurements for short term predictions during driving scenarios below the limits of driving dynamics. For the performed test scenarios, we compare the experimentally measured trajectory with the simulated ones and quantify the error. It is shown that a planar model that incorporates lean performs minimally better compared to a single-track model. We discuss model limitations as well as potential inaccuracies caused by the used measuring devices on our instrumented cargo tricycle.

With the help of the kinematic models, motion prediction of tadpole cargo tricycles can be undertaken. The range for which the implemented planar models are considered to be valid is depicted by the range of forward speeds until the liftoff condition. For motion prediction, a single-track model is considered feasible, as the more complicated planar model with lean does not substantially outperform it. For maneuvers at the limits of driving dynamics, more sophisticated dynamic models are needed, as the simple kinematic models presented in this work are not sufficient for this kind of tasks.

©2023 Groß, C & Müller, S. published by TU Delft OPEN on behalf of the authors.
ISSN: 2667-2812

 http://dx.doi.org/10.59490/665841de8a4558165d52bf58

Introduction

Dating as far back as 1899, bicycle dynamics have been from great interest in mechanical engineering. Recently, novel bicycle concepts are penetrating the market, in particular cargo vehicles which do not follow the conventional "one track, two wheels" (1T2W) bicycle layout. More and more of these cargo vehicles which feature two front and a single rear wheel, are encountered on city streets and their prevalence is considered to be growing even further (Behrensen & Sumer 2020). It is therefore crucial to understand the driving behavior of these so-called tadpole tricycles to improve infrastructure quality and planning, as well as for motion prediction and safety assessment of tadpole trikes. For these kinds of tasks, minimized models are used predominantly. For motorized vehicles, for example, the simplified single-track model is prevalent (Rajamani, 2012).

Overview of the Study

In this work, we simplify the motion of a tadpole style cargo tricycle. Firstly, we present a short literature overview on the kinematics of tricycles. In turn, the parameter identification for the cargo tricycle used in this study is discussed. Subsequently, we show how this tricycle is equipped with measurement technologies, to measure steering and lean angle, velocity and brake actuation, among others. Since our vehicle has an articulated steering, the connection between the steering and lean angle is derived in the next section, before we present our test maneuvers and experiments in the following section. Thereupon, we explain the two models used to depict the motion of tadpole tricycles in this work. The results, in terms of a comparison of model output when fed with the data from the described experiments, are presented in the following section. We discuss the obtained results thereinafter and discuss model validity by the help of the tip over condition before concluding the work in the last section.

State of the Art and Related Works

Models for the conventional concept of a two-wheeled bicycle are already available, just like for four-wheelers. Few works consider the specific needs of tricycles though. Even fewer studies focus on the specifics of tadpole tricycles, which are used commonly for cargo bicycles. With the exception of the works of Sponziello et al. (2008), Bartolozzi et al. (2008), and Wibowo et al. (2017), little attention has been drawn towards this topic. Sponziello et al. (2008) present a mathematical model of a tadpole-style motor scooter, respectively a MSC Adams model of it (Bartolozzi et al. 2008), and validate it against an instrumented scooter. Due to the differences in chassis design between this scooter and widespread concepts of cargo tricycles with articulated steering, their model cannot be used for the specifics of the latter. Wibowo et al. (2017) show a simplified, two-dimensional model of another type of tadpole-style scooter and discuss controller design for this vehicle without quantifying errors arising from this simplification. Similarly, the work of Sumarsono et al. (2020), discusses basic kinematics and the rollover stability of tadpole tricycles.

Geometry and Model Assumptions

A sketch of the tadpole cargo tricycle model is shown in Figure 1. It consists of five rigid bodies: the rear wheel (W), the rear frame (F), the front frame/cargo box assembly (B), as well as the front right (R) and front left (L) wheel. Note that we consider the tires to be rigid as well and furthermore assume that all wheels have ground contact at any time. We assume that the tire-ground contact is a knife-edge contact, which is especially important for the rear tire as it may tilt. Given our previous assumptions, the front/frame cargo box assembly (B) may not tilt, so that the front wheels are always perpendicular to the ground plane, which is considered to be a flat surface for our model derivation. All bodies are considered to be thin and, except for the front wheels, lie upon the vehicle middle axis when the steering angle is zero. For the single-track model, tire slip has to be zero.

Determination of Parameters

The geometrical parameters of the type of cargo tricycle that we have access to for this study are derived experimentally. An inverse photogrammetric measuring system is used and a 3D-CAD model of the tricycle is generated, from which the geometrical parameters of the cargo bike are then exported. These are shown in Table 1. Note that the sign of the angle of the steering axis is opposite from the sign of conventional bicycle, see Figure 1 for reference. Mass parameters are ascertained for future studies on the dynamic behavior of the tricycle and on rollover stability. These are measured by the help of scales. The center of gravity (COG) for the individual parts is determined as well as for the complete cargo tricycle, as it is needed for model discussion (see Eq. 9).

©2023 Groß, C & Müller, S. published by TU Delft OPEN on behalf of the authors.
ISSN: 2667-2812

 http://dx.doi.org/10.59490/665841de8a4558165d52bf58

Table 1. Geometrical parameters of the cargo tricycle

Parameter	Symbol	Unit	Value
wheel radius front	r_f	m	0.254
wheel radius rear	r_r	m	0.262
track width	w	m	0.88
wheelbase	l	m	1.35
trail	b	m	0.31
angle of steering axis / head tube angle	λ	°	9.2
distance of COG from ground plane along vertical axis	z_{COG}	m	-0.504
vehicle mass	m_V	kg	71.5

Instrumented Cargo Tricycle

To validate the kinematic model, and to undertake studies on driving safety, the previously presented cargo tricycle is equipped with measuring devices. Among others, a resistive displacement sensor is attached to the front frame and elongated (or clinched respectively) when a steering angle δ is applied between front frame and rear frame. The resulting lean (or roll) angle ϕ of the rear frame is measured by the help of an inertial measurement unit that is mounted on the rack above the rear wheel. Furthermore, speed and actuation of the brakes is measured. Data is recorded with a Raspberry Pi, mounted on the rear rack. Figure 2 shows the instrumented cargo tricycle.

Lean Angle of Rear Frame in Dependency from Steering Angle

For modelling the pure movement of the vehicle, without asking for dynamic forces, we model the lean angle that results from the tilted steering axis between the bodies F and B. Formally, the lean angle ϕ is the projection of the angle between F and a vertical, perpendicular axis (e.g. n_z) on the plane spanned by n_z and n_y. See Figure 1 for reference.

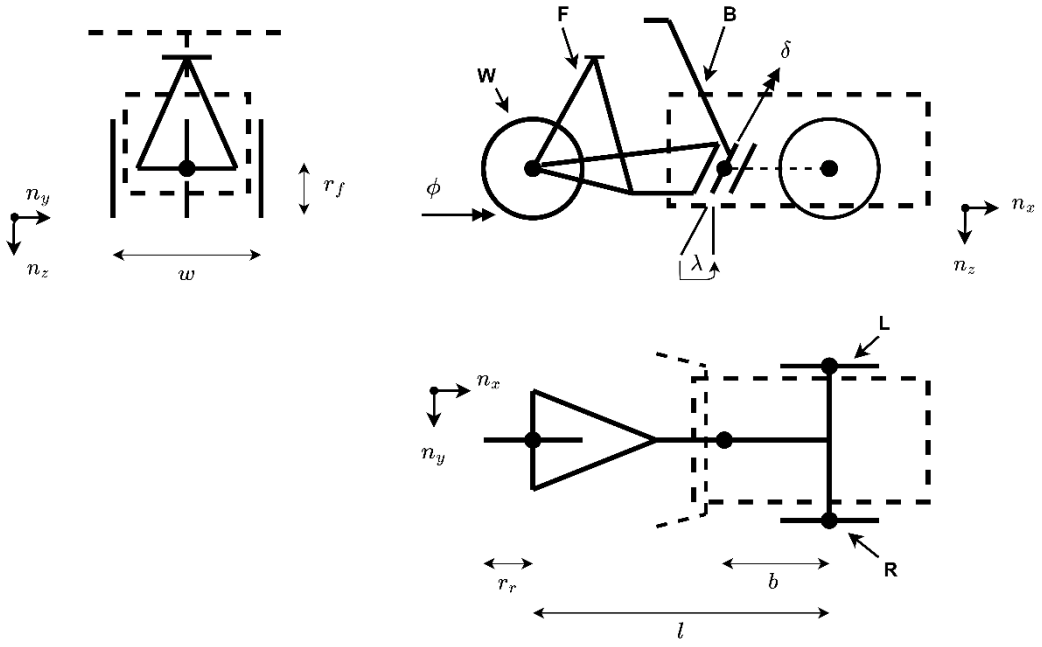


Figure 1. Schematic of the instrumented tadpole cargo tricycle

©2023 Groß, C & Müller, S. published by TU Delft OPEN on behalf of the authors.
ISSN: 2667-2812

 http://dx.doi.org/10.59490/665841de8a4558165d52bf58

Geometrically, it is subject to the tangent of the wheel flop (see e.g. Zinn, 2004) multiplied with the sine component of the handlebar steering angle δ and divided by the rear wheel radius, as we assume that the height of the front box B is constant. The lean angle ϕ can be determined as

$$\phi = \tan\frac{\sin(\delta)\, b \cos(2\pi - \lambda)\sin(2\pi - \lambda)}{r_r} = \tan\frac{-\sin(\delta)\, b \sin(2\lambda)}{2r_r}. \quad (1)$$

This is shown in Figure 3, which shows measurements for the lean angle ϕ with respect to the handlebar steering angle δ, measured between the front and rear frame, and the correlation shown in Equation (1). Figure 3b) shows the kinematic connection and data obtained during standing still. Figure 3a) shows this connection of lean and steering angle, as well as data collected with the instrumented cargo tricycle during naturalistic cycling studies. Note the large outliers in Figure 3a), which occur when the tricycle is about to tip over and which is not depicted in our model. Understandably, this did not occur during the steady state test. Based on all sample points shown in Figure 3a), we invert the modelling process by formulating an optimization problem that minimizes the sum of the Euclidean distances of the sample points from a curve to be fitted. As approach function, Eq. (1) is used. With the aim to find a value for λ, which is supposed to yield the headtube angle of the cargo tricycle, and making use of the analytically found approach function in Equation (1), the goal is to

$$\text{minimize} \sum_{i}^{n} \sqrt{\left(\phi_{i,c} - \phi_{i,m}\right)^2 + \left(\delta_{i,c} - \delta_{i,m}\right)^2}, \quad (2)$$

where $\phi_{i,m}$ is the i-th measured value for the lean angle with respect to the steering angle $\delta_{i,m}$. Likewise, $\phi_{i,c}$ is the i-th calculated value for the lean angle, according to Eq. (1). As δ is our independent variable for which we numerically solve the optimization problem, we can choose it freely. Choosing $\delta_{i,c} = \delta_{i,m}$ and substituting $\phi_{i,c}$ in Eq. (2) with the expression from Eq. (1) yields

$$\text{minimize} \sum_{i}^{n} \sqrt{\left(\tan\frac{\sin(\delta)\, b \cos(2\pi - \lambda)\sin(2\pi - \lambda)}{r_r} - \phi_{i,m}\right)^2}. \quad (3)$$

When doing so with data from the naturalistic cycling studies, the value found for λ_c is 6.9 degrees, compared to the measured 9.2 degrees as shown in Table 1. This discrepancy can be explained by the fact that all data points from the naturalistic cycling study were considered for the optimization problem. As discussed earlier, and as shown in Figure 3a), outliers (from near tip-over situations, where wheel lift on the front wheels occurred) have an influence on the result of the optimization.



Figure 2. The instrumented cargo tricycle

©2023 Groß, C & Müller, S. published by TU Delft OPEN on behalf of the authors.

ISSN: 2667-2812

 http://dx.doi.org/10.59490/665841de8a4558165d52bf58

Figure 3a) shows, next to the measured data points and the model depicted in Equation (1), the model fitted with our optimization approach as well. Applying the optimization algorithm to the data points from the stand still test only, a rounded value of 9.2 degrees for λ_c is calculated and the fitted model equals our theoretical model. It is thus not shown in Figure 3b).

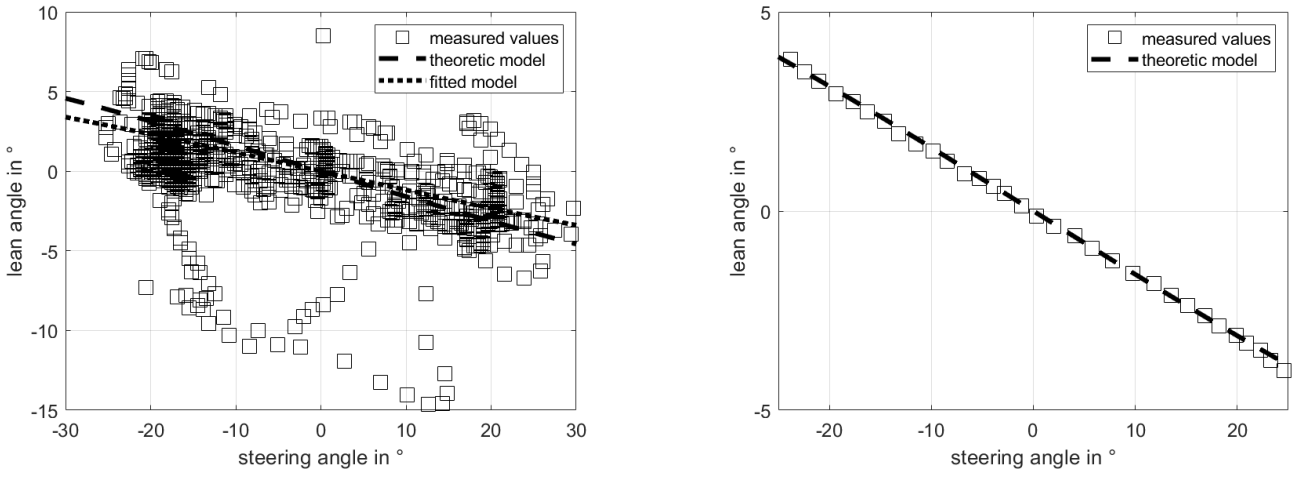
Test Maneuvers and Experiments

Two test maneuvers are performed in experiments and simulation to validate the kinematic equations. These are a slalom with a distance of 5 meters between the cones and as well as a steady-state circular test with a diameter of 10m. For both maneuvers, riders were instructed to ride as fast as they could without having to fear of tipping over. We present the results of three different riders, that did not, or only shortly, violated our model assumptions in Fig. 5. Several other riders experienced substantial wheel lift during the experiment and have therefore not been included in this study.

The mean velocity reached during the slalom ranged from 1.83 m/s to 2.84 m/s (6.59 km/h to 10.24 km/h). The difference in speed reached by the different riders explains for the outliers depicted in Figure 3 too, as some riders experienced wheel lift during their maneuvers. The mean velocity over an entire circle during the steady circular tests ranges from 2.46m/s to 3.08 m/s (8.85 to 11.12 km/h). Figure 4 shows the experimental set-up for the slalom maneuver. For the steady-state circular test, the position of the rear tire of the cargo tricycle is verified by the help of a chalk trace. During the slalom maneuver, the position of the cargo tricycle is recorded with a stationary LIDAR sensor and an object detection algorithm.

The experimental data is flattened making use of a moving average filter with heuristically defined window size. Instead of implementing a trajectory tracking controller, we use the flattened input from the human drivers during the experiments for the simulation. This way, the influence of the human driver does not need to be modelled, since we focus on modelling the cargo tricycle. Figure 5 shows in a)-c) three slalom maneuvers in experiment and the respective values of the velocity, lateral position, lean angle, and steering angle of the cargo tricycle. For the circular tests, Figure 5d) shows lean and steering angle. For the sake of clarity, the quasi-constant velocity and the lateral position are omitted here.

It can be seen that the dynamic forces acting on the bicycle cannot be neglected, especially during highly demanding dynamic maneuvers, such as our test cases. Several times during the experiment, wheel lift off on the front axle occurred (see e.g. Fig. 5a) at approx. 8s). The challenges of exploring aggressive 1T2W trajectories have been discussed in Hauser et al. (2004). For less demanding driving maneuvers, we consider the models presented in the following paragraph sufficient for a trajectory forecast.



a) Naturalistic cycling study b) Stand still test

Figure 3. Lean angle of the rear frame in dependency from steering angle

©2023 Groß, C & Müller, S. published by TU Delft OPEN on behalf of the authors.
ISSN: 2667-2812

 http://dx.doi.org/10.59490/665841de8a4558165d52bf58

Trajectory Models

For the trajectory forest, we implement two models (a single-track model and a planar model with lean) in Matlab/Simulink and impinge them with steering angles δ and speed v collected during the experiments. A sketch of the single-track model is shown in Figure 6a). It can be seen that the kinematic steering angle $\delta_{kin,b}$ around the instant center of rotation (ICR) of single-track model is determined by

$$\delta_{kin,b} = \delta = \tan^{-1}\left(\frac{l}{R}\right), \tag{4}$$

and equals the handlebar steering angle δ, as wheel slip is zero. See e.g. Rajamani (2012) for a concise explanation and Cossalter et al. (2014) for the difference between kinematic and handlebar steering angle.

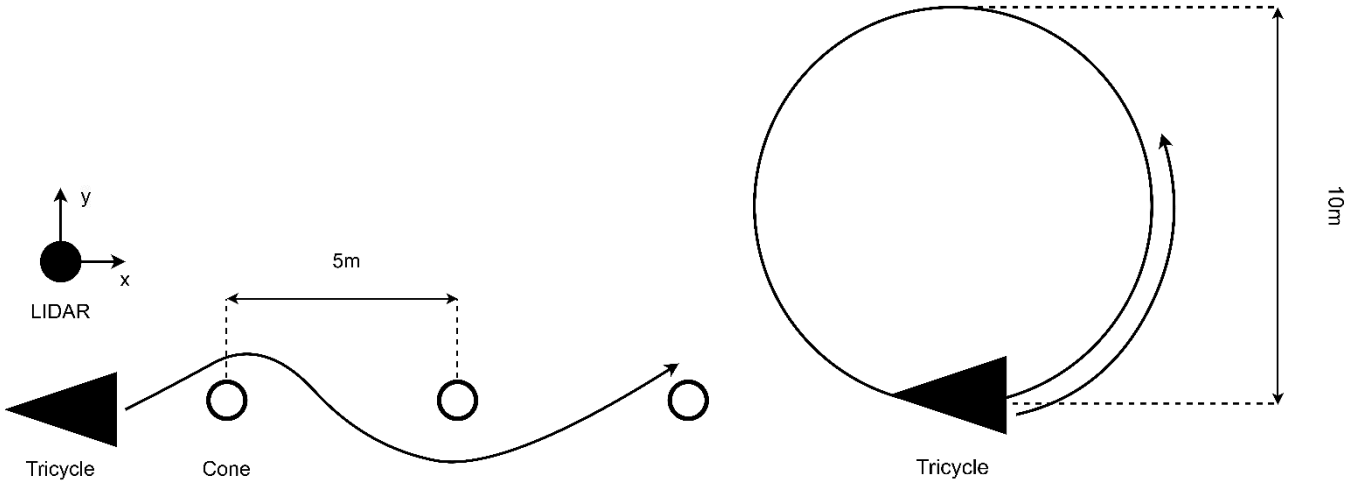
For the planar model with lean, we incorporate the connection between steering angle δ and lean angle ϕ which pushes the contact point of the rear tire is inwards (or: opposite when referring to the positive handlebar steering angle δ and a lever) by the sine component of the rear frame roll angle and the rear wheel radius - as it turns about the connecting line with the front frame and thus its center axis. Albeit small, a discrepancy Δ_{kin} between actual turning radius R and kinematic turning radius R_{kin} thus arises. Figure 6b) shows the idea behind this planar model with lean in exaggeration. While the handlebar steering angle δ is still measured with the same reference (the projection of the connection line from rear wheel center to steering axis on the longitudinal axis), which does not lean (see the dotted line in Fig. 6b)), the kinematic steering angle $\delta_{kin,l}$ for the model with lean is now determined by

$$\delta_{kin,l} = \tan^{-1}\left(\frac{l}{R_{kin}}\right) = \tan^{-1}\left(\frac{l}{R-\Delta_{kin}}\right), \tag{5}$$

where

$$\Delta_{kin} = \sin(\phi) r_r, \tag{6}$$

as it is the sine component of the lean angle about the rear wheel center axis and thus the radius of the rear wheel.



a) Slalom maneuver b) Steady state circular maneuver

Figure 4. Experimental set up for the slalom maneuver

©2023 Groß, C & Müller, S. published by TU Delft OPEN on behalf of the authors.

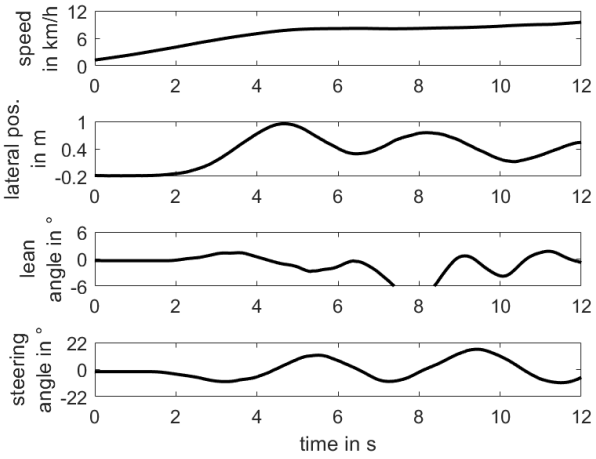
ISSN: 2667-2812

 http://dx.doi.org/10.59490/665841de8a4558165d52bf58

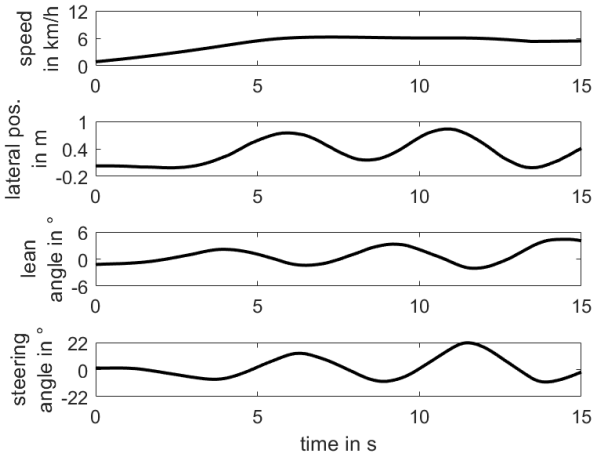
Note that formally the no slip condition is not fulfilled anymore, since kinematic angle and handlebar, and thus front wheel, angle differ. Since we only care about the kinematics of the tricycle, pure calculation of the tricycle's trajectory $\overrightarrow{r_m}$ is sufficient. Expressed in global coordinates, where x is the position of the tricycles COG along the unit vector n_x, and y along n_y respectively, this is given by

$$\overrightarrow{r_m} = \begin{bmatrix} x_m \\ y_m \end{bmatrix} = \begin{bmatrix} \int v \cos \delta_{kin} \\ \int v \sin \delta_{kin} \end{bmatrix} \tag{7}$$

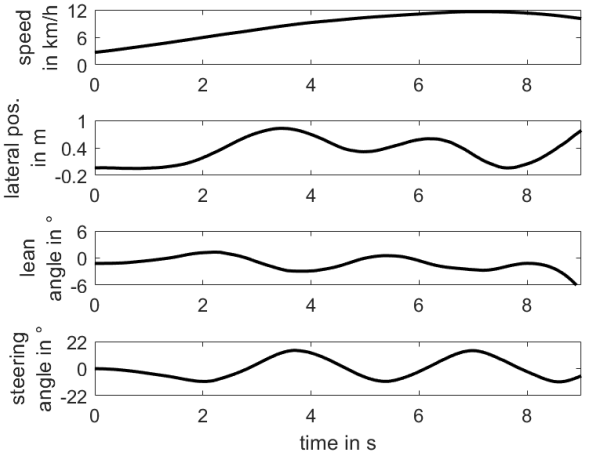
for the single-track model as well as for the planar model with lean. In Equation (6), ϕ is subject to Eq. (1), and δ_{kin} in Eq. (7) is given by Eq. (4) for the single-track model and Eq. (5) for the planar model with lean.



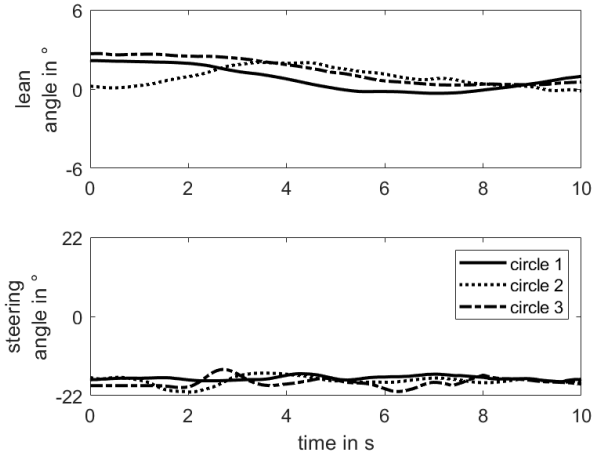
a) Slalom 1



b) Slalom 2



c) Slalom 3



d) Steady state circular tests

Figure 5. Measured values for the speed, lateral position, lean, and steering angle during the experiments

©2023 Groß, C & Müller, S. published by TU Delft OPEN on behalf of the authors.
ISSN: 2667-2812

 http://dx.doi.org/10.59490/665841de8a4558165d52bf58

Results

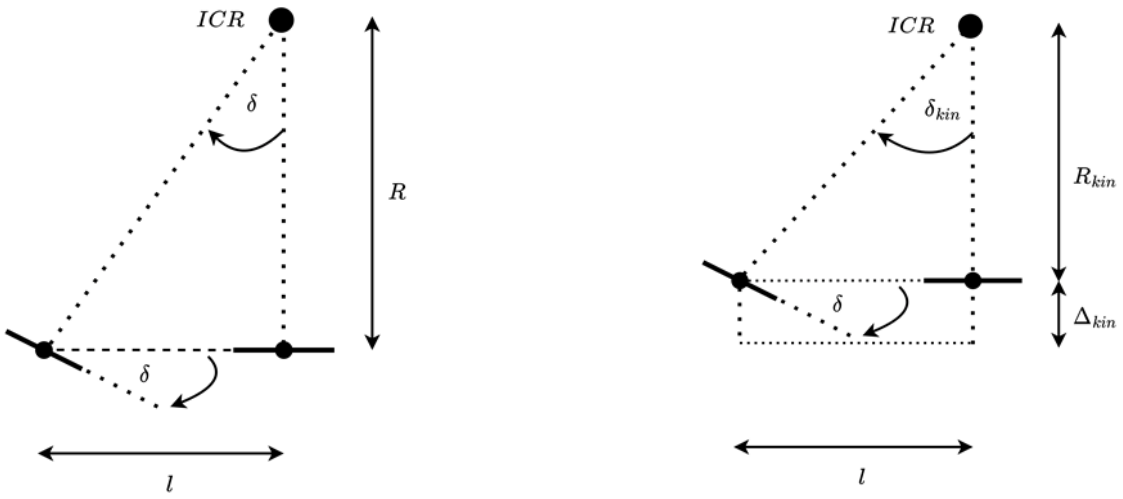
We impinge the two models with data from the experiments, as we did not include a trajectory tracking controller, or any other kind of controller for that matter, in our model.

For the given test maneuvers, the experimental and simulated trajectories are compared to each other. This is shown in Figure 7, where Fig. 7a) shows the three slalom maneuvers in experiment and Fig. 7b) shows a comparison between experiment and the two implemented models for the first deflection of a slalom maneuver. It can already be seen that the single-track model and the bicycle model with lean produce comparable results. We assess the error between the trajectories from the experiments and the model results by the help of a mean error over the first 10 meters of the maneuver

$$e_{ME,S} = \frac{1}{n}\sum_{i}^{n} |y_{e,i} - y_{m,i}|, \tag{8}$$

with $y_{e,i}$, the position from experiment at step i, $y_{m,i}$ the position from either model at the same step, and n the number of steps in the maneuver. Since our model is solved numerically, we set the respective x-coordinates so that $x_{e,i} = x_{m,i}$ and the longitudinal position is omitted in the error term in Eq. (8). The numerical solver is also the reason to not consider the entire maneuver length for the calculated error. As it can be seen from Fig. 7b) already, error grows the longer the simulation. This error arises mainly from the integration of the measured, thus noisy, input data for our model. Table 2 shows the error for three performed slalom maneuvers. Next to the discussed numerical integration, deviations between simulation and experiment can be traced back to e.g. measurement and filtering errors of the experimental data as well as model abstractions, such as neglecting tire behavior and the absence of dynamic reactions of the cargo tricycle and its rider.

For the second test scenario, the circular turning test, the mean value of the handlebar steering angle over the experiments is compared with the value for the handlebar steering angle for the single-track model and the planar model with lean. The difference between the angles derived by the models is neglectable and $\delta_{c,s} = \delta_{c,l}$ equals -15.3 degrees. The error e_c between the mean of the measured steering angle during the steady turn experiments $\delta_{e,mean} = -20.1$ degrees and the calculated values $\delta_{c,s}$ and $\delta_{c,l}$ is substantial though and reaches $e_c = |\delta_{e,mean}| - |\delta_c| = 4.8$ degrees for both models.



a) Single-track model

b) Planar model with lean

Figure 6. Schematic of the two models

©2023 Groß, C & Müller, S. published by TU Delft OPEN on behalf of the authors.

ISSN: 2667-2812

Table 2. Mean error for the slalom experiments, comparing single-track model and planar model with lean

	slalom 1	slalom 2	slalom 3
single-track model	0.025m	0.016m	0.026m
planar model with lean	0.023m	0.015m	0.026m

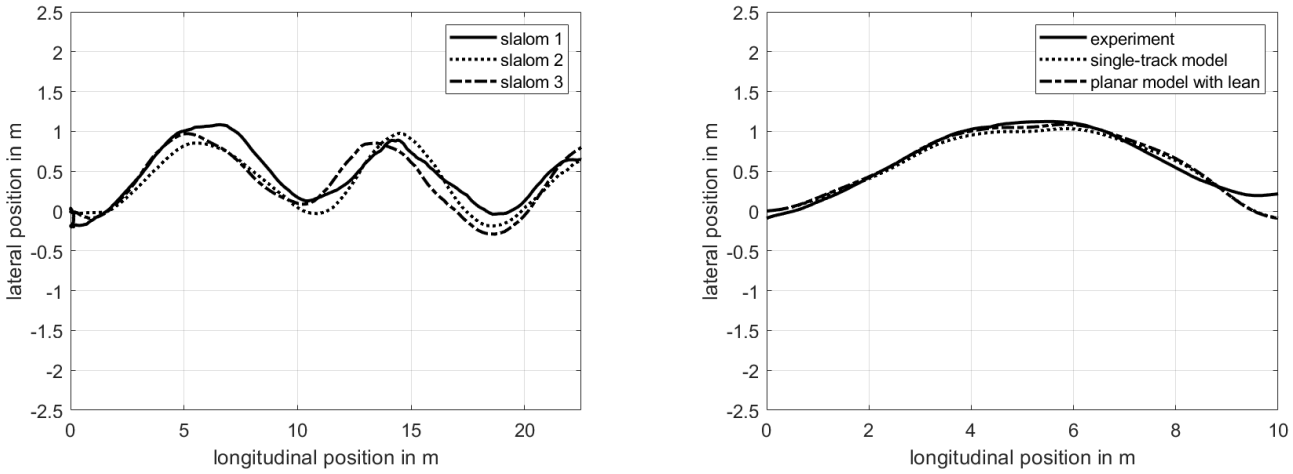
It has to be kept in mind though that lift of the inner front wheel did occur during the steady state turning tests. It is thus shown that driving maneuvers close to the stability bounds of the tricycle are not well depictable with the simple models discussed here. Note furthermore that the kinematic turning radius is larger than what is calculated by the help of the planar bicycle model, which calculates the handlebar steering angle in dependency of it. A substantial understeer of the cargo tricycle is observed. Shift of the COG due to rider lean is considered to have a huge impact on the error term, as our model assumption is that the roll of the front box is neglectable - which was shown to be not the case during highly dynamic driving scenarios.

Model Discussion, Validity and Steady-State Rollover Stability

From our experiments, the question of the validity of the models arises. The main model simplifications made are that the front box does not tilt and the neglection of the dynamic forces, which also results in non-consideration of the shift of the center of gravity, that is (also) subject to rider input. Especially the shift of COG, is considered to introduce a large error to the planar models discussed here. As the height of the COG is, for the unloaded, but especially for the loaded, cargo tricycle above the tilting axis, the lean angle results in lowering the COG and thus a lower risk of rollover, as given by Eq. (9). To specify clearer bounds for the validity of our models, we calculate the range of forward speeds for which the planar models are applicable with reasonable error as the speeds from zero to the lift off condition of the outer wheel (Sumarsono et al., 2020):

$$\left(0\frac{m}{s}, \sqrt{\frac{gRw}{2|z_{COG}|}}\right). \tag{9}$$

In Eq. (9), g is gravity, and R is the turning radius of the tadpole trike of 5m according to the steady turning experiment. Model validity is thus dependent on the actual driving maneuver. This results in a range from 0 to 6.54m/s (23.56 km/h), when parametrized according to Table 1. Note that this range is considerably larger than what was reached during the experiments. This is due to the fact that parameters in Table 1 denote an unloaded tricycle, while the tricycle during our tests was ridden by human riders.



a) Slalom experiments b) First deflection of slalom 1

Figure 7. Trajectories of the slalom experiments in experiment and model results

©2023 Groß, C & Müller, S. published by TU Delft OPEN on behalf of the authors.

ISSN: 2667-2812

For a bicycle with rider, properties can be found according to e.g. Moore et al. (2009) or Williams (2015). Using rider parameters and the relaxed seating position from Williams (2015), the height of the COG z_{COG} equals now 1.66m. Eq. (9) yields a range from 0 to 3.61 m/s (13km/h), which is comparable, albeit slightly higher, to the speeds reached during the steady turning test in the experiment. Within some distance from this range, defined by constants and geometric parameters of the tricycle as well as the ratio of the turning radius and the height of the center of gravity, trajectory deviations calculated according to Eq. (8) are small and acceptable for the needs of trajectory prediction as discussed in this work. One has to consider that the model assumptions for the planar model with lean are not that different from the assumptions made for the single-track model. Both models are therefore only valid for basic motion analyses, and not suitable for investigations at driving dynamics limits.

Conclusion

Both kinematic models hold reasonable errors for basic driving maneuvers, where our model assumptions are fulfilled. In these kinds of scenarios and for a short-term forecast, model error is within an acceptable range. Due to its low complexity, the use of the single-track model seems feasible. It can be used e.g., for trajectory prediction or the development of a controller for trajectory tracking. For more sophisticated studies, a more detailed driving dynamics model which incorporates the dynamic forces is from greater use and thus needed.

This could be the next step and lead to e.g., the implementation of a tire model as well. More so, the tadpole tricycle with articulated steering discussed in this work does not possess a tilting mechanism of the front wheels. Whether models with a tilting mechanism can be adequately modelled by the help of a single-track model is an open question as well. Studying this question could in turn also lead to a dynamic model of a tadpole tricycle which tilts.

References

Behrensen, A. & Sumer, A. (2020), *First European Cargo Bike Industry Survey*. Cyclelogistics.eu, Brussels/Berlin. Available online: http://cyclelogistics.eu/wp-content/uploads/2022/09/Survey_market_sitze_results.pdf

Bartolozzi, R., Frendo, F., Giuggiano, M., & Sponziello A. (2008). Comparison between experimental and numerical handling tests for a three-wheeled motorcycle. S*AE Int. J. Engines* 1(1): 1389-1395, doi: 10.4271/2008-32-0061.

Cossalter, V., Lot, R. & Massaro, M. (2014). Motorcycle Dynamics. In Tanelli,, M., Corno, M. & Savaresi, S. M. (Eds.), Modelling, Simulation and Control of Two-wheeled Vehicles. John Wiley & Sons Ltd, Chichester.

Hauser, J., Saccon, A. & Frezza, R. (2004, December 14-17). Achievable Motorcycle Trajectories. *43rd IEEE Conference on Decision and Control*, Atlantis, Paradise Island, Bahamas.

Moore, J. K., Hubbard, M., Kooijman, J. D. G. & Schwab, A. L. (2009, August 30 - September 2). A Method for Estimating Physical Properties of a Combined Bicycle and Rider. *Proceedings of the ASME 2009, Vol. 4*: *7th International Conference on Multibody Systems, Nonlinear Dynamics, and Control (IDETC/CIE 2009),* San Diego, California, USA.

Rajamani, R. (2012). *Vehicle Dynamics and Control.* Springer, New York, NY.

Sponziello, A., Frendo, F., & Giuggiano, M. (2008). Stability analysis of a three-wheeled motorcycle. S*AE Int. J. Engines* 1(1):1396-1401, doi: 10.4271/2008-32-0062.

Sumarsono, D. A., Jati, M. K. & Muiz, M. A. (2020). Modelling of Tilting and Steering Control System for a Tadpole Three-Wheeled Vehicle. *J. Phys.: Conf. Ser. 1519 012008,* doi:10.1088/1742-6596/1519/1/012008.

Wibowo, Lambang, L., Pratama, G. & Surojo, E. (2017, October 5-6). Simulation and Analysis of Three Wheeled Reverse Trike Vehicles with PID Controller. In Suwarno, V. S. Djanali, B. Pramujati & V. A. Yartys (Eds.), *Proceedings of the 3rd International Conference on Mechanical Engineering (ICOME 2017),* Surabaya, Indonesia.

Williams, T. A. (2015). Influence of Frame Stiffness and Rider Position on Bicycle Dynamics: An Analytical Study. *Theses and Dissertations. 985.* The University of Wisconsin Milwaukee. Available online: https://dc.uwm.edu/etd/985

Zinn, L. (2004). *Zinn's Cycling Primer: Maintenance Tips and Skill Building for Cyclists*. Velo Press, Boulder, CO.

©2023 Groß, C & Müller, S. published by TU Delft OPEN on behalf of the authors.

ISSN: 2667-2812

The Evolving Scholar Vol. 3, 2023

http://dx.doi.org/10.59490/65bbc2e6315708a53e169769

Bicycle and Motorcycle Dynamics 2023
Symposium on the Dynamics and Control of Single Track Vehicles
18–20 October 2023, Delft University of Technology, The Netherlands

Type of the Paper: Conference Paper

Revised

On the Development of a Path Tracking Controller by combining Optimal Preview Control and Pursuit Control Methods

[version 2; peer reviewed]

David Gabriel[1,*], Daniel Baumgärtner[1], Daniel Görges[2]

[1] Bosch eBike Systems, Robert Bosch GmbH, Germany; david.gabriel@de.bosch.com, ORCID 0000-0002-5339-4889
[2] Department of Electrical and Computer Engineering, RPTU Kaiserslautern-Landau, Germany; ORCID 0000-0001-5504-0972
[*] corresponding author

Name of Editor: Jason Moore
First published: 26/09/2023
Last published: 15/02/2024
Citation: Gabriel, D., Görges, D. & Baumgärtner, D. (2024). On the Development of a Path Tracking Controller by combining Optimal Preview Control and Pursuit Control Methods [version 2; peer reviewed]. The Evolving Scholar - BMD 2023, 5th Edition.
This work is licensed under a Creative Commons Attribution License (CC-BY).

Abstract:

Path tracking controllers are an important part when developing self-driving vehicles. When designing such a controller for a single-track vehicle, a major challenge is that the vehicle not only has to follow a predefined path but has to be stabilized at the same time. Especially if the vehicle has slow steering dynamics (e.g. $\tau > 1.5\,\mathrm{s}$) and the path contains tight corners which should not be cut (e.g. directional change of more than 90° in less than $2\,\mathrm{s}$), the design of a suitable path tracking controller can be difficult. In this work an optimal preview controller that stabilizes a bicycle and that can track a given yaw rate trajectory is combined with a quintic polynomial pursuit controller. With this approach, we can achieve good tracking performance for the predefined paths, which can be seen in the simulation and experimental results.

Keywords:

Control systems engineering, Vehicle engineering, Bicycle Dynamics, Stabilization, Optimal Preview Control, Path Tracking, Pursuit Control, Quintic Polynomials

©2023 Gabriel, D., Baumgärtner, D., Görges, D. published by TU Delft OPEN on behalf of the authors.
ISSN: 2667-2812

 http://dx.doi.org/10.59490/65bbc2e6315708a53e169769

Introduction

In the development of advanced rider assistance systems, a self-driving bicycle or motorcycle can be very helpful. Such a system is not only able to perform more reproducible measurements than a human but can also be used for safety-critical maneuvers. An important aspect when developing a self-driving single-track vehicle is the development of a controller that can stabilize the vehicle and can follow a desired roll angle, steer angle or yaw rate. When such a controller has been implemented, the next step is to develop a path tracking controller so that the vehicle can not only be operated remotely but can also follow a predefined path (important for reproducible measurements).

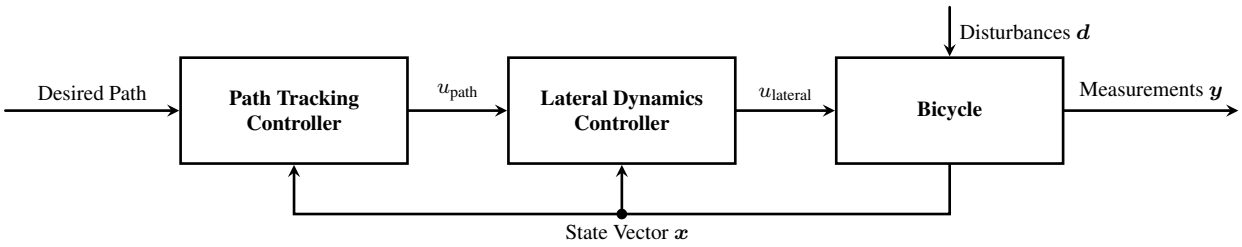


Figure 1. Cascaded control loop for combined stabilization and path tracking control.

A simplified cascaded control loop is shown in Fig. 1. For that control loop, it is assumed that the bicycle travels at a constant speed and that the bicycle states are measurable or that an observer exists, which estimates the bicycle state vector from the measured signals. When using a cascaded controller, the inner loop should be at least 3-4 times faster than the outer loop. Otherwise, performance problems and instabilities of the whole system can occur. As a result, with a slow lateral-dynamics controller, the path-tracking controller must be even slower. In (Gabriel et al., 2022) a lateral dynamics controller was presented, which is able to stabilize the bicycle and track a desired yaw rate of the bicycle. The closed loop has a time constant of $\tau \approx 1.5\,\mathrm{s}$, therefore the outer control loop must have a time constant of at least $4.5\,\mathrm{s}$.

There is a lot of literature dealing with stabilization and tracking control of single-track vehicles. A good overview can be found in (Kooijman and Schwab, 2013). However, most of this work is theoretical, and as far as we know, no one has implemented a path tracking controller on a bicycle that uses only steering actuation to stabilize the bicycle and works well at low speeds and for tight turns. A particular challenge is that the controllers must also work with real actuators (actuator limits, resonances, ...) and must allow easy implementation on a microcontroller.

A good overview on path tracking methods in general (not limited to single track vehicles) can be found in (Snider et al., 2009). These methods can be divided into two groups: On the one hand, there are geometric path tracking controllers such as the "Pure Pursuit Controller" and the "Stanley Controller", which completely neglect the dynamical behavior of the underlying system. Hence, it is important that the cascaded control loop rule is followed, otherwise the whole system can become unstable (Heredia and Ollero, 2007). On the other hand, there are linear and nonlinear model-based controllers that take the system dynamics into account and usually combine the path-tracking controller and the lateral dynamics controller in a single controller.

We have several requirements on the path-tracking controller, which none of the existing approaches can fulfill:

- The controller should ensure good tracking behavior despite the relatively slow steering dynamics of the lateral dynamics controller.
- Tight corners should not be cut. In particular, curves with a minimum radius associated with a bicycle roll angle of 15-20°, should be possible.
- The controller has to use little computing power so that it can be implemented on a microcontroller.

The problem with the geometric controllers is that they would require huge look-ahead distances to be stable. That would lead to

©2023 Gabriel, D., Baumgärtner, D., Görges, D. published by TU Delft OPEN on behalf of the authors.
ISSN: 2667-2812

 http://dx.doi.org/10.59490/65bbc2e6315708a53e169769



Figure 2. Experimental setup of the test bike

cutting corners. The nonlinear model-based approaches cannot be used because the algorithms usually require a lot of computing power. The linear model-based approaches such as in (Sharp, 2006) are very promising, but cannot be used due to the linear path model, which does not allow directional changes of more than $90°$ within the preview distance. To fulfill all our requirements, methods of the model-based controllers and the geometric controllers must be combined: Instead of using the Linear Quadratic Integral controller which was proposed in (Gabriel et al., 2022), an Optimal Preview controller with integral part is used as lateral-dynamics controller. This controller not only receives a reference yaw rate for the current time step but also a reference yaw rate trajectory for a specific preview time. By using a controller with preview, the inner loop becomes faster since it can react to setpoint changes in advance. The reference yaw rate trajectory must be generated by the path-tracking controller in the outer loop. Therefore, the path-tracking controller must first find an intermediate path which guides the bicycle from the current position back to a target point on the reference path. A reference yaw rate trajectory can be generated from that intermediate path. When the intermediate path is calculated it is important to ensure that the resulting reference yaw rate trajectory is realizable (continuous, without jumps) and that the target point is reached with the correct conditions for the following path. Therefore, not only the current position and the target position, but also the current yaw angle and yaw rate as well as the target yaw angle and yaw rate are taken into account when calculating the intermediate path. To calculate an intermediate path with the required boundary conditions quintic polynomials can be used.

This paper is structured as follows: First, the experimental setup of the test bicycle is described. Then the models used for simulation and controller design are described. In the next section, the inner loop controller, which is an Optimal Preview controller with integral part, is introduced. This controller uses the steer rate as a control signal and stabilizes the bicycle and tracks a given yaw rate trajectory. After that, the method used to generate the yaw rate trajectory which represents the outer loop of the controlled system is derived. This method is based on pursuit path tracking control and quintic polynomials. The results from simulations and experiments are then presented and discussed. Finally, an overview of the obtained results is given.

Experimental Setup

The proposed control methods have been tested on a prototype of a self-balancing bicycle which is shown in Fig. 2. This prototype is equipped with various sensors and actuators: The drive unit ① can be used for propulsion and contains a 9-axis IMU (3-axis accelerometer, 3-axis gyroscope, 3-axis magnetometer). Additionally, the bicycle is equipped with an automotive steer angle sensor ② and an ABS-system with two high-resolution wheel speed sensors ③. Localization of the prototype can be achieved using a differential GPS system ④. A steering motor ⑤ controlled by an electronic control unit ⑥ with speed control is used to stabilize the bicycle and for path following control. A dSpace MicroAutoBox real time computer for function prototyping ⑦, which is located on the bike's rack, has been used to implement various state estimation algorithms and the controllers presented here.

©2023 Gabriel, D., Baumgärtner, D., Görges, D. published by TU Delft OPEN on behalf of the authors.
ISSN: 2667-2812

 http://dx.doi.org/10.59490/65bbc2e6315708a53e169769

Models

For the work that is presented in this paper, two different models were used:

On the one hand, a detailed nonlinear simulation model is used, which is based on the Carvallo-Whipple model (Whipple, 1899; Carvallo, 1901). The nonlinear model equations were derived as in (Basu-Mandal, 2007) and then extended with an additional constraint that forces the bicycles steer rate to be equal to a (filtered) controller steer rate. Low-pass filtering of the controller steer rate is necessary to prevent jumps in the controller steer rate and thus infinite constraint torques. With this extension, the model can be used to simulate a steer rate-based controller. The simulation model also contains sensor models that are used to simulate accelerometer and gyroscope measurements including common sensor errors (noise, offset, scaling error). The state vector is then reconstructed from the simulated sensor values using the Kalman filter that was introduced in (Gabriel et al., 2023). This way, the simulation reflects the real system, since some states are not directly measurable.

On the other hand, a simplified and linearized point-mass model which is based on the nonlinear model in (Getz, 1995) is used for controller design:

$$\begin{bmatrix} \dot{\varphi} \\ \ddot{\varphi} \\ \dot{\delta} \end{bmatrix} = \underbrace{\begin{bmatrix} 0 & 1 & 0 \\ -\frac{g}{z_{\boldsymbol{T}}} & 0 & \frac{v^2}{l z_{\boldsymbol{T}}} \\ 0 & 0 & 0 \end{bmatrix}}_{\mathbf{A}} \begin{bmatrix} \varphi \\ \dot{\varphi} \\ \delta \end{bmatrix} + \underbrace{\begin{bmatrix} 0 \\ \frac{x_{\boldsymbol{T}} v}{l z_{\boldsymbol{T}}} \\ 1 \end{bmatrix}}_{\mathbf{B}} u_{\dot{\delta}}. \tag{1}$$

This model has three states: roll angle φ, roll rate $\dot{\varphi}$ and steer angle δ and four parameters: the longitudinal velocity v, the x-coordinate of the center of gravity $x_{\boldsymbol{T}}$, the z-coordinate of the center of gravity $z_{\boldsymbol{T}}$ and the wheelbase l. The input is defined as the steer rate $u_{\dot{\delta}}$, the output is the yaw rate $\dot{\psi}$, which can be approximated as follows:

$$\dot{\psi} \approx \frac{v}{l} \delta. \tag{2}$$

Optimal Preview Yaw Rate Controller

As described before, it can be difficult, to design a fast lateral dynamics controller for a bicycle that tracks a given yaw rate and at the same time stabilizes the bicycle. Most controllers can only track a given reference with a certain delay. The Linear Quadratic Regulator with integral part that was introduced in (Gabriel et al., 2022) stabilizes the bicycle well but has a high time constant of $\tau \approx 1.5\,\mathrm{s}$. If not only the current target yaw rate is known, but also a target yaw rate trajectory, tracking performance can be improved by incorporating these future target values in the controller. For this purpose, the system model has to be extended.

The linear discrete-time model of the plant is given as

$$\begin{aligned} \boldsymbol{x}[k+1] &= \mathbf{A}_d\, \boldsymbol{x}[k] + \mathbf{B}_d\, \boldsymbol{u}[k] \\ y[k] &= \mathbf{C}\, \boldsymbol{x}[k] \end{aligned} \tag{3}$$

with the control variable y (yaw rate), which is supposed to track a reference variable r. Assuming, that the reference variable is known N time steps in advance, the evolution of it can be modelled as a shift register. This yields the following preview model:

$$\underbrace{\begin{bmatrix} s_0[k+1] \\ s_1[k+1] \\ \vdots \\ s_N[k+1] \end{bmatrix}}_{\boldsymbol{s}[k+1]} = \underbrace{\begin{bmatrix} 0 & 1 & 0 & \cdots & 0 \\ \vdots & \ddots & \ddots & \ddots & \vdots \\ & & \ddots & \ddots & 0 \\ & & & \ddots & 1 \\ 0 & \cdots & \cdots & \cdots & 0 \end{bmatrix}}_{\mathbf{A}_s} \underbrace{\begin{bmatrix} s_0[k] \\ s_1[k] \\ \vdots \\ s_N[k] \end{bmatrix}}_{\boldsymbol{s}[k]} + \underbrace{\begin{bmatrix} 0 \\ \vdots \\ 0 \\ 1 \end{bmatrix}}_{\mathbf{B}_s} r[k+1+N]. \tag{4}$$

Every state $s_a[b]$ of this model corresponds to a (future) value of the reference variable:

$$s_a[b] \mathrel{\hat{=}} r[b+a]. \tag{5}$$

©2023 Gabriel, D., Baumgärtner, D., Görges, D. published by TU Delft OPEN on behalf of the authors.
ISSN: 2667-2812

 http://dx.doi.org/10.59490/65bbc2e6315708a53e169769

The plant model and the preview model of the reference variable can be combined, resulting in the following model:

$$\begin{aligned}\left[\begin{array}{c|c}\boldsymbol{x}[k+1]\\\hline\boldsymbol{s}[k+1]\end{array}\right] &= \left[\begin{array}{c|c}\mathbf{A}_d & \mathbf{0}\\\hline\mathbf{0} & \mathbf{A}_s\end{array}\right]\left[\begin{array}{c}\boldsymbol{x}[k]\\\hline\boldsymbol{s}[k]\end{array}\right] + \left[\begin{array}{c}\mathbf{B}_d\\\hline\mathbf{0}\end{array}\right]\boldsymbol{u}[k] + \left[\begin{array}{c}\mathbf{0}\\\hline\mathbf{B}_s\end{array}\right] r[k+N+1]\\ y[k] &= \left[\begin{array}{c|c}\mathbf{C} & \mathbf{0}\end{array}\right]\left[\begin{array}{c}\boldsymbol{x}[k]\\\hline\boldsymbol{s}[k]\end{array}\right].\end{aligned} \tag{6}$$

The last part of the model equation ($\left[\begin{array}{c}\vdots\\\end{array}\right] r[k+N+1]$) can be treated as a disturbance in the controller design and can therefore be ignored. If the model of the plant is controllable or stabilizable, the combined model will also be stabilizable since the preview model is stable and therefore no unstable modes are added by combining the two models. The combined model is then used to design a LQR controller. When designing this controller, it is important to choose the weighting matrix $\mathbf{Q}$ so that it penalizes a deviation from the reference variable. Therefore, the weighting matrix can be chosen as follows:

$$\begin{aligned}\mathbf{U} &= \left[\begin{array}{c|c}-\Delta t\mathbf{C} & \Delta t \quad 0\cdots 0\\\hline\cdots\cdots & \cdots\cdots\cdots\cdots\end{array}\right] \begin{array}{l}\text{control error } e\\\\\text{other states or combinations of states}\\\text{that should go to zero}\end{array}\\ \mathbf{Q} &= \mathbf{U}^\top \boldsymbol{q}\, \mathbf{U}.\end{aligned} \tag{7}$$

Each row in matrix $\mathbf{U}$ describes a state or a combination of states that should be controlled to zero. The entries of the vector $\boldsymbol{q} = \left[\begin{array}{ccc} q_e & \cdots \end{array}\right]$ are weights to penalize the deviations of these states / state combinations to zero.

In theory, to obtain optimal results, the preview interval must be infinitely long. Since this is not possible in most cases, the length of the preview interval can be limited depending on the controller gains, which depend on the weighting matrix. For example a high weight on the control error leads to high controller gains for the first elements of the reference trajectory and to smaller gains for those that are further away. Therefore, a shorter preview interval is possible. If the known reference trajectory is shorter than necessary, steady-state errors may occur.

To solve this problem and to increase the robustness to external disturbances at the same time, the model can be augmented with the integral of the control error $\xi(t) = \int_0^t e(\tau)d\tau$. The (discrete) extended system model is given by:

$$\begin{aligned}\left[\begin{array}{c|c|c}\boldsymbol{x}[k+1]\\\hline\boldsymbol{\xi}[k+1]\\\hline\boldsymbol{s}[k+1]\end{array}\right] &= \left[\begin{array}{c|c|c}\mathbf{A}_d & \mathbf{0} & \mathbf{0}\\\hline-\Delta t\mathbf{C} & 1 & \Delta t\ 0\ \cdots\ 0\\\hline\mathbf{0} & \mathbf{0} & \mathbf{A}_s\end{array}\right]\left[\begin{array}{c}\boldsymbol{x}[k]\\\hline\boldsymbol{\xi}[k]\\\hline\boldsymbol{s}[k]\end{array}\right] + \left[\begin{array}{c}\mathbf{B}_d\\\hline 0\\\hline\mathbf{0}\end{array}\right] u[k] + (\ldots)\\ y[k] &= \left[\begin{array}{c|c}\mathbf{C} & \mathbf{0}\end{array}\right]\left[\begin{array}{c}\boldsymbol{x}[k]\\\hline\boldsymbol{s}[k]\end{array}\right].\end{aligned} \tag{8}$$

If this extended model is used for (LQR) controller design, the integral part must also be taken into account in the weighting matrix. A feasible weighting matrix can be constructed as follows:

$$\begin{aligned}\mathbf{U} &= \left[\begin{array}{c|c|c}-\Delta t\mathbf{C} & 0 & \Delta t \quad 0\cdots 0\\\hline\mathbf{0} & 1 & \mathbf{0}\\\hline\cdots\cdots & \cdots & \cdots\cdots\cdots\cdots\end{array}\right] \begin{array}{l}\text{control error } e\\\text{integral of the control error } \xi\\\\\text{other states or combinations of states}\\\text{that should go to zero}\end{array}\\ \mathbf{Q} &= \mathbf{U}^\top \boldsymbol{q}\, \mathbf{U}\end{aligned} \tag{9}$$

with $\boldsymbol{q} = \left[\begin{array}{cccc} q_e & q_\xi & \cdots \end{array}\right]$. The result is an Optimal Preview controller with integral part (OPI controller).

To calculate the controller gains for the OPI controller, the combined and extended model has to be created. For this the model equations from (1) have to be discretized and then inserted into (8). In order to obtain the weight matrix, one has to specify which states and which combinations of states should go to zero. These are:

(a) The control error $e[k] = s_0[k] - \mathbf{C}\boldsymbol{x}[k]$,

©2023 Gabriel, D., Baumgärtner, D., Görges, D. published by TU Delft OPEN on behalf of the authors.
ISSN: 2667-2812

 http://dx.doi.org/10.59490/65bbc2e6315708a53e169769

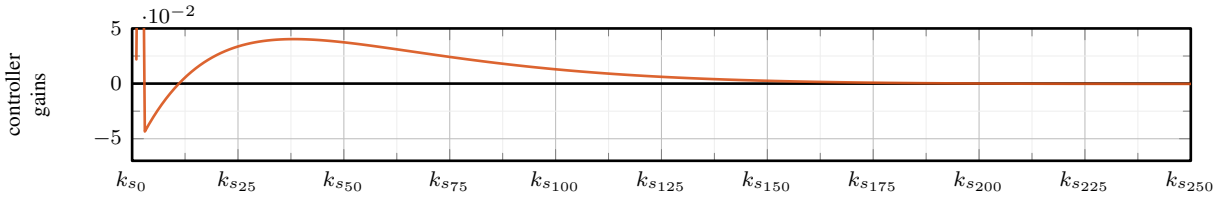


Figure 3. Controller gains of the preview-states $s_0 \dots s_{250}$ of the OPI controller.

(b) the integral of the control error $\xi[k]$,

(c) the difference between the roll angle associated with a yaw rate in a steady curve and the measured/estimated roll angle $\frac{v}{g}s_0[k] - \varphi[k]$

(d) the difference between a roll rate, calculated from the rate of change of the target yaw rate and the measured roll rate $\frac{v}{g\Delta t}(s_0[k] - s_1[k]) - \dot{\varphi}[k]$

One obtains the matrix $\mathbf{U}$ and the weight matrix $\mathbf{Q}$:

$$\mathbf{U} = \left[\begin{array}{cccc|cccc} 0 & 0 & -\frac{v}{l} & 0 & 1 & 0 & \cdots & 0 \\ \hline 0 & 0 & 0 & 1 & 0 & \cdots & & 0 \\ \hline -1 & 0 & 0 & 0 & \frac{v}{g} & 0 & \cdots & 0 \\ 0 & -1 & 0 & 0 & \frac{v}{g\Delta t} & -\frac{v}{g\Delta t} & 0 & \cdots 0 \\ \varphi & \dot{\varphi} & \delta & \xi & s_0 & s_1 & s_2 \cdots & s_N \end{array}\right] \begin{array}{l} \text{(a)} \\ \text{(b)} \\ \text{(c)} \\ \text{(d)} \end{array} \tag{10}$$

$$\boldsymbol{q} = \begin{bmatrix} q_a & q_b & q_c & q_d \end{bmatrix}^\top$$

$$\mathbf{Q} = \mathbf{U}^\top \boldsymbol{q}\, \mathbf{U}.$$

With the weight factors $q_a \dots q_d$ chosen as:

$$q_a = 2, \quad q_b = 0.5 + 2v, \quad q_c = 9, \quad q_d = 1. \tag{11}$$

For the calculations of the controller gains the weight matrix for the input(s) $\mathbf{R}$ also has to be defined which is chosen to be:

$$\mathbf{R} = 1. \tag{12}$$

Knowing the system matrices and the weight matrices, the controller gains can be calculated using LQR methods. In Figure 3 the controller gains of the preview states are shown. It can be seen that the controller gains converge to zero as the preview distance increases. Thus, reference values that are too far in the future can hardly be utilized by the controller and can therefore be neglected. As mentioned before, it is important to find a good trade-off between a short preview interval and good performance of the controller. If possible, the preview distance should be chosen such that at least 95-99 % of the area between the plot of the controller gains and the x-axis is included. This means that in our case a preview distance of 200 time steps ($\hat{=}2\,\mathrm{s}$) is sufficient.

Quintic Polynomial Pursuit Control

For the calculation of a reference yaw rate trajectory, already known methods from geometric path tracking are used. This approach does not require a vehicle model, and the vehicle's steering dynamics are neglected. By using quintic polynomials or two connected clothoids, it is possible to account for the fact that the steering angle and the yaw rate cannot change abruptly. Due to the lower computational complexity, quintic polynomials are preferred and, therefore, used to generate the target yaw rate trajectory. As with the pure pursuit controller, a target point on the following path is first determined for the calculation of the target yaw rate trajectory. Quintic polynomials are then computed that describe a path from the current vehicle position to the target point (rather than a circular path for the pure-pursuit controller). These polynomials are then used to generate the target trajectory.

The process for generating the reference yaw rate trajectory is illustrated in Figure 4 and includes the following steps:

©2023 Gabriel, D., Baumgärtner, D., Görges, D. published by TU Delft OPEN on behalf of the authors.
ISSN: 2667-2812

 http://dx.doi.org/10.59490/65bbc2e6315708a53e169769

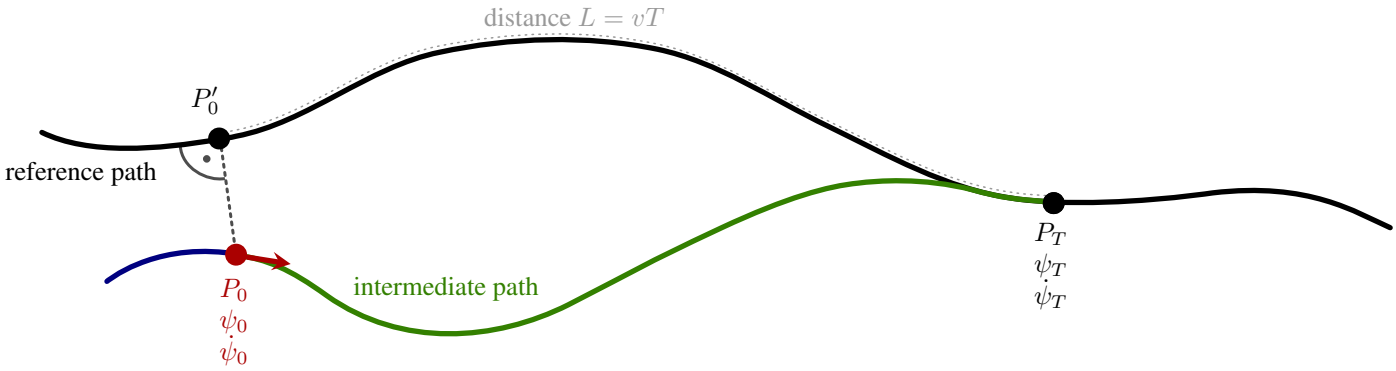


Figure 4. Generation of an intermediate path that leads back to the reference path

1. Find a goal point on the reference path:
   a) Determine the projection of the position of the vehicle P_0 onto the position on the reference path which is closest to the vehicle P_0'.
   b) Find the goal point P_T at a distance $L = vT$ (with preview time T) from P_0' along the path. Then determine the coordinates, yaw angle and yaw rate at the goal point.
2. Calculate quintic polynomials (intermediate path) from the current position P_0 of the vehicle to the goal point P_T, taking into account the start and target yaw angle (ψ_0, ψ_T) as well as the start and target yaw rate ($\dot{\psi}_0$, $\dot{\psi}_T$).
   a) Transform the target coordinates and the target yaw angle into the vehicle coordinate system.
   b) Calculate quintic order polynomials.
3. Derive the yaw rate trajectory from the previously calculated polynomials.
4. If the yaw rate trajectory is too short, it can be extended with additional target yaw rates that can be derived from the reference path behind the goal point.

The calculation of the polynomials will be explained in more detail below. For that the results from Amidi and Thorpe (1991) were used as basis. The goal is to get quintic order polynomials which represent x- and y-coordinates of the path from the current position to the target position in the vehicle coordinate system. The polynomials are given as a function of the scaled time variable $t \in [0, T]$. The time variable is scaled so that the goal point will be reached at time $T = 1$. The polynomials and their derivatives have the following form:

$$x(t) = a_0 + a_1 t + a_2 t^2 + a_3 t^3 + a_4 t^4 + a_5 t^5 \tag{13}$$
$$\dot{x}(t) = a_1 t + 2a_2 t + 3a_3 t^2 + 4a_4 t^3 + 5a_5 t^4 \tag{14}$$
$$\ddot{x}(t) = 2a_2 + 6a_3 t + 12a_4 t^2 + 20a_5 t^3 \tag{15}$$

$$y(t) = b_0 + b_1 t + b_2 t^2 + b_3 t^3 + b_4 t^4 + b_5 t^5 \tag{16}$$
$$\dot{y}(t) = b_1 t + 2b_2 t + 3b_3 t^2 + 4b_4 t^3 + 5b_5 t^4 \tag{17}$$
$$\ddot{y}(t) = 2b_2 + 6b_3 t + 12b_4 t^2 + 20b_5 t^3. \tag{18}$$

The travelled distance is represented by the position variable $s \in [0, L]$ with L being the total distance from the start to the target point along the path which is defined by the polynomials. It is assumed, that the vehicle travels with a constant speed v. Hence, the velocity can be calculated as

$$v = \frac{ds}{dt} = \frac{L}{T} = L. \tag{19}$$

It is important to note that the calculated velocity v and the yaw rate that is calculated below are scaled variables (because of the scaled time variable).

©2023 Gabriel, D., Baumgärtner, D., Görges, D. published by TU Delft OPEN on behalf of the authors.
ISSN: 2667-2812

 http://dx.doi.org/10.59490/65bbc2e6315708a53e169769

Due to the transformation of target point and target yaw angle into the vehicle coordinate system, the boundary conditions have the following simplified form:

$$x(0) = 0 \quad (20) \qquad x(T) = x_T \quad (24)$$
$$y(0) = 0 \quad (21) \qquad y(T) = y_T \quad (25)$$
$$\psi(0) = 0 \quad (22) \qquad \psi(T) = \psi_T \quad (26)$$
$$\sigma(0) = \sigma_0 = \dot{\psi}_0/v \quad (23) \qquad \sigma(T) = \sigma_T. \quad (27)$$

In these equations $\dot{\psi}_0$ describes the current yaw rate of the vehicle. Assuming that there is no wheel slip and therefore there is no lateral velocity at the rear wheel contact point, we get for $\dot{x}$ and $\dot{y}$:

$$\frac{dx}{dt} = \frac{dx}{ds}\frac{ds}{dt} = \cos\psi\, L \quad (28) \qquad \frac{dy}{dt} = \frac{dy}{ds}\frac{ds}{dt} = \sin\psi\, L\,. \quad (29)$$

Taking the derivative of those velocities with respect to time yields the accelerations

$$\frac{dx}{dt^2} = -\dot{\psi}\sin\psi\, v \quad (30) \qquad \frac{dy}{dt^2} = \dot{\psi}\cos\psi\, v. \quad (31)$$

The curvature of a path σ can be obtained from by taking the derivative of the yaw angle ψ with respect to the distance s.

$$\sigma = \frac{d\psi}{ds} = \frac{d\psi}{dt}\left(\frac{ds}{dt}\right)^{-1} = \frac{\dot{\psi}}{v} = \frac{\dot{\psi}}{L}. \quad (32)$$

The equations 13-32 can be combined to a set of 12 equations:

Boundary conditions at the start point:

$$\begin{aligned}
x(0) &= 0 && \Rightarrow && a_0 = 0\\
\dot{x}(0) &= \cos(0)\, v && \Rightarrow && a_1 =\\
\ddot{x}(0) &= -\dot{\psi}_0 \sin(0)\, v && \Rightarrow && a_2 = 0\\
y(0) &= 0 && \Rightarrow && b_0 = 0\\
\dot{y}(0) &= \sin(0)\, v && \Rightarrow && b_1 = 0\\
\ddot{y}(0) &= \dot{\psi}_0 \cos(0)\, v = \sigma_0 L^2 && \Rightarrow && b_2 = \sigma_0 L^2/2.
\end{aligned}$$

Boundary conditions at the goal point:

$$\begin{aligned}
x(T) &= x_T && \Rightarrow && a_3 + a_4 + a_5 = x_T - L\\
\dot{x}(T) &= \cos(\psi_T)\, L && \Rightarrow && 3a_3 + 4a_4 + 5a_5 = (\cos(\psi_T) - 1)L\\
\ddot{x}(T) &= -\dot{\psi}_T \sin(\psi_T)\, v = -\sigma_T L^2 \sin(\psi_T) && \Rightarrow && 6a_3 + 12a_4 + 20a_5 = -\sigma_T L^2 \sin(\psi_T)\\
y(T) &= y_T && \Rightarrow && b_3 + b_4 + b_5 = y_T - \sigma_0 L^2/2\\
\dot{y}(T) &= \sin(\psi_T)\, L && \Rightarrow && 3b_3 + 4b_4 + 5b_5 = \sin(\psi_T)\, L - \sigma_0 L^2\\
\ddot{y}(T) &= \dot{\psi}_T \cos(\psi_T)\, v = \sigma_T L^2 \cos(\psi_T) && \Rightarrow && 6b_3 + 12b_4 + 20b_5 = L^2(\cos(\psi_T)\, \sigma_T - \sigma_0).
\end{aligned} \quad (33)$$

These equations are linear in the coefficients $(a_0, ..., a_5, b_0, ...b_5)$ of the polynomials: In theory, solving them is straightforward, but the exact length L of the path that is represented by the polynomials is not known. Therefore, both the coefficients of the polynomials and the value of L must be computed iteratively.

©2023 Gabriel, D., Baumgärtner, D., Görges, D. published by TU Delft OPEN on behalf of the authors.
ISSN: 2667-2812

The polynomials can now be used to calculate the reference yaw rate trajectory. Using equations (28) and (29), the equation of yaw rates along the path can be derived as follows:

$$\tan\psi = \frac{\dot{y}}{\dot{x}} \qquad |dt \tag{34}$$

$$\Rightarrow \qquad \dot{\psi}(1+\tan^2\psi) = \frac{\ddot{y}}{\ddot{x}} \tag{35}$$

$$\overset{(34)}{\Leftrightarrow} \qquad \dot{\psi} = \frac{\dot{x}\ddot{y} - \dot{y}\ddot{x}}{\dot{x}^2 + \dot{y}^2}. \tag{36}$$

It is important to remember that the calculated yaw rates still represent scaled values. Hence, they must be converted to the original time base.

If the path, that is described by the polynomials, and consequently the calculated yaw rate trajectory, is too short for the OPI controller ($< 2\,\mathrm{s}$), additional yaw rate values can be obtained from the reference path and its curvature behind the target point.

Results

In the following section, the simulation results of the optimal preview controller and the simulation and experimental results of the combined path tracking and optimal preview controller are presented.

The simulations are performed using a complete bicycle model including sensors and state estimators. As a result, it can be ensured that there are no negative cross-effects between the different modules that are also used on the real bicycle.

A simplified localization algorithm is used for the experiments, which calculates the bicycle position and yaw angle by taking the integral of the velocity and the yaw rate. This approach can only be used for short experiments because there might be offsets in the yaw rate and the velocity which can lead to a drift of the calculated position and yaw angle.

Optimal Preview Yaw Rate Controller

The path tracking controller was designed in such a way that there are no jumps in the reference yaw rate. For this reason the underlying OPI controller is simulated with a sinusoidal reference signal. The results are presented together with the simulation results of the LQI controller that was introduced in (Gabriel et al., 2022) in Figure 5. The simulations of both controllers are performed with the following initial conditions: (constant) bicycle speed $v_0 = 2.5\,\mathrm{m/s}$, initial bicycle roll angle $\varphi_0 = 2°$, initial roll rate $\dot{\varphi}_0 = 0\,\mathrm{rad/s}$ and initial steering angle $\delta_0 = 0°$. The target yaw rate is zero at first and from time t_1 it follows a sinusoidal shape with an amplitude of $0.5\,\mathrm{rad/s}$ and a frequency of $1\,\mathrm{rad/s}$.

When comparing the results of the two controllers, it can be seen that the OPI controller tracks the reference yaw rate well without any delay. In contrast, the LQI controller only follows the given yaw rate with a delay of $\approx 1.5\,\mathrm{s}$. Both controllers have a slight deviation in the amplitude of the yaw rate signal. In the case of the OPI controller, the achieved yaw rate sometimes exceeds the desired yaw rate. The reason for this is that the yaw rate obtained from the steering angle and the resulting control error e (that are used for controller design) were not exactly modeled. During modeling, it was assumed that the yaw rate could be determined from the steering angle, the velocity, and the wheelbase. This is true for an upright bicycle, but as soon as the bicycle is leaning to one side, the steering head angle ε and the roll angle φ also affect the resulting yaw rate. The resulting amplitude of the yaw rate when using the LQI controller is slightly lower than the amplitude of the reference yaw rate. The reason for this is that the system controlled by the LQI controller has a low-pass-like behavior, which results in a slight suppression of fast changes in the setpoint.

Overall, the OPI controller produces very good results when the reference yaw rate trajectory is known some time in advance and when it has a smooth shape without jumps. Other simulations have shown that even if these conditions are not met, the results will still be at least as good as those of the LQI controller.

Quintic Polynomial Pursuit Control (+ underlying Optimal Preview Yaw Rate Controller)

The reference paths are defined as waypoints, which have a distance of $0.5\,\mathrm{m}$. In addition to the coordinates also the yaw angle and the curvature of the path are given for each waypoint. These quantities can also be calculated using the surrounding waypoints,

©2023 Gabriel, D., Baumgärtner, D., Görges, D. published by TU Delft OPEN on behalf of the authors.
ISSN: 2667-2812

 http://dx.doi.org/10.59490/65bbc2e6315708a53e169769

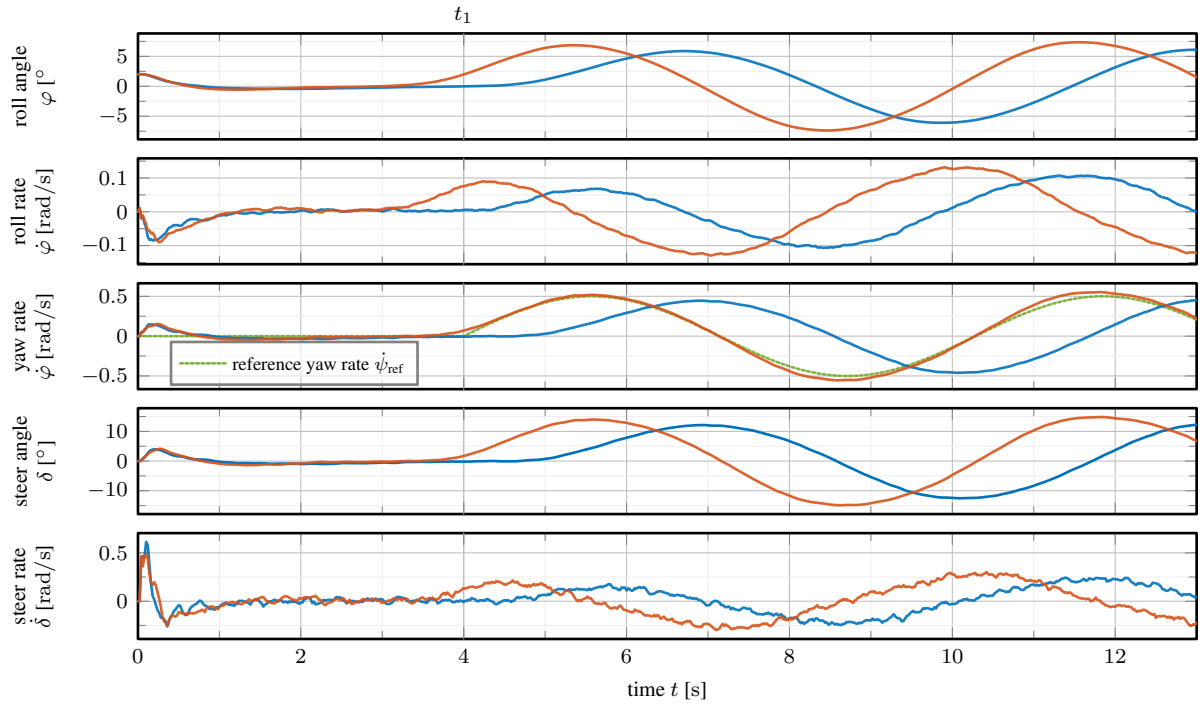


Figure 5. Simulative comparison of LQI controller (——) and OPI controller (——) with a sinusoidal reference signal.

but for simplicity they are already given with the path. The path tracking controller was tested with various reference paths. The following path, located inside an office building, was chosen to demonstrate the capabilities of the path tracking controller when the path has very tight turns. The path starts in a straight hallway, turning left after about 16 meters onto a larger area. The bike performs a U-turn on this area, and after another right turn, returns to the corridor. The path is illustrated in Figure 6.

Experiments and simulations were performed with a constant speed of $v = 2\,\mathrm{m/s}$, the results can be found in Figure 6 and Figure 7. For the measurements with the real system, the controller is activated at time t_0. Both, experimental and simulation results show, that the bicycle is able to follow the reference path. However, deviations from the desired path occur during both simulation and measurement. First, when the bicycle is moving on a straight path, these deviations are small but grow to a maximum of $\approx 0.3\,\mathrm{m}$ as the curve radius decreases. It can also be observed that in case of sudden changes in the curvature of the given trajectory (e.g. change from driving on a circle to driving on a straight line), larger deviations can occur. In addition, it can be seen that the driven path in the measurement (especially for the U-turn) differs significantly from the driven path in the simulation. There are various reasons for these observations:

- By using quintic polynomials to calculate the target yaw rate trajectory, the start and target positions, yaw angles, and yaw rates are taken into account, but not the yaw accelerations. This can sometimes make it difficult for the OPI controller to realize a requested yaw rate trajectory.

- The OPI controller does not accurately control specified target yaw rate trajectories and in the case of fast changes in the requested yaw rate, it is not fast enough (see Figure 5 at time t_1). As a result, deviations from the specified path occur, in particular in the case of sudden changes in curvature.

- When modeling the bicycle dynamics, a simplified wheel-road contact was assumed. The properties of the bicycle tire are not considered in the model. But in reality, there are forces on the tires, especially at large steering and lean angles, which also affect the steering and bicycle dynamics. In Figure 7 it can be seen that steering angles of up to $40°$ occur during the U-turn. The forces on the front wheel push it further into the curve (larger steering angle), so the radius of the curve becomes smaller. In order to achieve a better match between simulation and reality, the simulation model has to be extended by a tire model.

©2023 Gabriel, D., Baumgärtner, D., Görges, D. published by TU Delft OPEN on behalf of the authors.
ISSN: 2667-2812

http://dx.doi.org/10.59490/65bbc2e6315708a53e169769

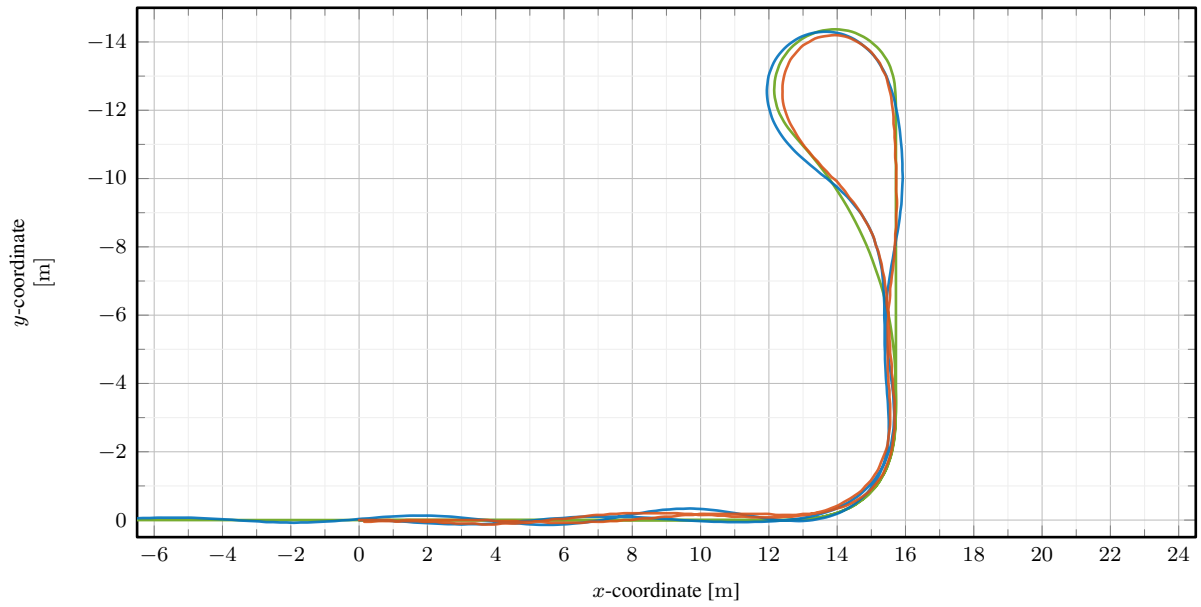


Figure 6. Experimental results (——) and simulation results (——) of the path tracking controller following a reference path (——).

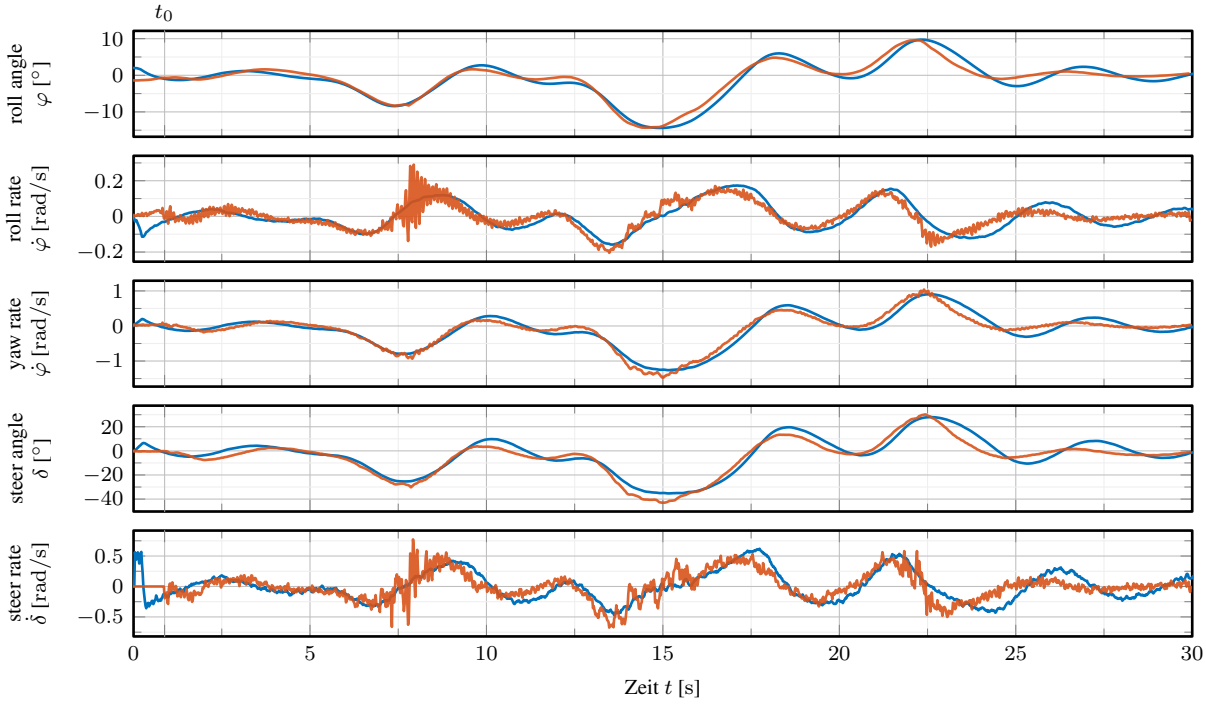


Figure 7. Experimental results (——) and simulation results (——) of the path tracking controller following a reference path.

©2023 Gabriel, D., Baumgärtner, D., Görges, D. published by TU Delft OPEN on behalf of the authors.
ISSN: 2667-2812

Figure 7 shows the signal traces of the state variables as the vehicle travels along the reference path. The signal traces of the simulation and the measurement look very similar. However, in the measurement the steering angle and yaw rate have higher values. This is caused by the unmodeled tire forces as described above. In addition, it is noticeable that there is significantly more noise / oscillations in the roll rate and the input variable (steer rate) in the measurement than in the simulation. This can have several causes: e.g. resonances in the transfer behavior of the bicycle frame or an excitation of the gyroscope by the Drive Unit and/or the speed controller.

The different experimental tests as well as the simulations have shown that the new path tracking controller works well and that only small deviations from the reference path occur.

Conclusion

A new method for path tracking control of single-track vehicles is proposed. The method which can also be applied to other vehicles where a sudden change in the steer angle is not possible, combines optimal preview control and geometric path tracking control in a cascaded control loop: The inner controller is an Optimal Preview controller with integral part that uses the steer rate as a control input. It stabilizes the bike and tracks a predicted (reference) yaw rate trajectory provided by the outer controller. The outer loop uses pursuit control methods and quintic polynomials to generate a smooth, continuous yaw rate trajectory that returns the bicycle to the reference path.

The path-tracking controller has been tested in simulations and experiments, yielding very good results; the requirements were fully met, and the bike was able to follow given paths with minimum radii smaller than $2\,\mathrm{m}$. However, there is still room for improvement, such as including yaw acceleration as a boundary condition in calculating the yaw rate trajectory. Additionally, the path tracking controller needs to be further investigated (robustness to uncertainties, disturbances).

References

Amidi, O. and Thorpe, C. (1991). Integrated mobile robot control. In *Proceedings of SPIE - The International Society for Optical Engineering*, volume 1388, pages 504 – 523.

Basu-Mandal, P. (2007). *Studies on the dynamics and stability of bicycles*. PhD thesis.

Carvallo, E. (1901). *Theorie de mouvement du monocycle et de la bycyclette*. J. Ec. Polytech. Paris.

Gabriel, D., Baumgärtner, D., and Görges, D. (2022). Development and Validation of a Remote-Controlled Test Platform for Bicycle Dynamics. In *International Cycling Safety Conference*.

Gabriel, D., Baumgärtner, D., and Görges, D. (2023). Accurate and robust state estimation for bicycles. *Vehicle System Dynamics*, 61(9):2338–2351.

Getz, N. H. (1995). *Dynamic inversion of nonlinear maps with applications to nonlinear control and robotics*. PhD thesis, University of California, Berkeley.

Heredia, G. and Ollero, A. (2007). Stability of autonomous vehicle path tracking with pure delays in the control loop. *Advanced Robotics*, 21(1-2):23–50.

Kooijman, J. D. G. and Schwab, A. L. (2013). A review on bicycle and motorcycle rider control with a perspective on handling qualities. *Vehicle System Dynamics*, 51(11):1722–1764.

Sharp, R. S. (2006). Motorcycle Steering Control by Road Preview. *Journal of Dynamic Systems, Measurement, and Control*, 129(4):373–381.

Snider, J. M. et al. (2009). Automatic steering methods for autonomous automobile path tracking. *Robotics Institute, Pittsburgh, PA, Tech. Rep. CMU-RITR-09-08*.

Whipple, F. J. W. (1899). The Stability of the Motion of a Bicycle. *The Quaterly Journal of Pure and Applied Mathematics*, 30:312–348.

©2023 Gabriel, D., Baumgärtner, D., Görges, D. published by TU Delft OPEN on behalf of the authors.
ISSN: 2667-2812

The Evolving Scholar Vol. 3 (2023)

https://doi.org/10.59490/66eb6542c598a23330635f06

Bicycle and Motorcycle Dynamics 2023
Symposium on the Dynamics and Control of Single Track Vehicles
18 – 20 October 2023, Delft University of Technology, The Netherlands

Type of the Paper: Conference Paper

Revised

Position Measuring System for a Motorcycle Using Quad Omnidirectional Cameras

[version 3; peer reviewed]

Junji Hirasawa[1,*]

[1] Ibaraki KOSEN, College of Technology, Japan; hirasawa@ss.ibaraki-ct.ac.jp, ORCID 0000-0001-9213-5831

*corresponding author

Name of Editor: Jason Moore
First published: 26/09/2023
Last published: 24/09/2024
Citation: Hirasawa, J. (2024). Position Measuring System for a Motorcycle Using Quad Omnidirectional Cameras [version 3; peer reviewed]. The Evolving Scholar - BMD 2023, 5th Edition.
This work is licensed under a Creative Commons Attribution License (CC-BY).

Abstract:

In this article, an improvement in a system for position measurement of a motorcycle is presented. Position measurement of a motorcycle when running presents a difficult problem because loading of measurement equipment would cause changes in the vehicle's mass and its moment of inertia. Therefore, this paper proposes a novel measurement method that uses omnidirectional cameras to acquire angles relative to fixed camera positions. The method is based on a general stereoscopic positioning approach. The results of previous research have shown that a simple measurement method using image processing techniques could be applied to the position measurement of a motorcycle when running on a figure-of-eight-shaped course around two omnidirectional cameras. The main weakness of this method using two omnidirectional cameras is the large error that occurs near the camera baseline (i.e., the line connecting the two cameras), particularly in the baseline direction. To improve position measurement precision, the author has added two more omnidirectional cameras to the system. Running tests of the proposed system using a real motorcycle were executed on a paved area. The experimental results showed that the proposed measurement method is sufficiently accurate to allow it to check the locus of a motorcycle running on a figure-of-eight-shaped course.

Keywords: Motorcycle, Position, Stereo Vision, Omnidirectional Camera

©2023 Hirasawa, J. published by TU Delft OPEN on behalf of the authors.
ISSN: 2667-2812

https://doi.org/10.59490/66eb6542c598a23330635f06

Bicycle and Motorcycle Dynamics 2023
Symposium on the Dynamics and Control of Single Track Vehicles
18 – 20 October 2023, Delft University of Technology, The Netherlands

Introduction

High-precision measurement techniques are essential to gain an understanding of the dynamics of a single track vehicle in full de - tail. Therefore, many researchers have tried previously to measure the required data from an actual motorcycle while it is running. During the period from the 1960s to the 1970s, which can be regarded as the dawn of the research into single-track vehicle dy - namics, several researchers tried to measure precise data using running vehicles. Fu tried to measure the steering angle and roll angle of a running motorcycle (Fu, 1965). The test vehicle was equipped with a recording device that used recording papers. Fu also attempted to measure the data using a running bicycle (Fu et al., 1978). The unmanned bicycle with the associated large-sized measurement equipment was towed by an automobile for the test. Kageyama described the difficulties of both experimental re - search and theoretical research on single track vehicles as long ago as the 1970s (Kageyama, K., 1977).

In the half-century that has passed since that time, compact-sized measurement devices have been developed especially for use with automobiles. These devices, which include data loggers and batteries, are designed to fit inside the luggage spaces of auto- mobiles. However, few of these devices are suitable for use with a motorcycle. Loading of the measurement devices changes both the mass and the moment of inertia of the test vehicle. These parameters are influential with respect to the dynamics of the motor - cycle (Kageyama, 2017) (Waegli, 2008).

Alternatively, motion capture systems have proven to be effective for measurement of the precise movements of humans. These systems only require some markers that are small in size and light in weight to be set on the object to be measured. This approach requires small changes to be detected for determination of the dynamics of the measurement object; therefore, to enable the mo - tion capture system to cover the entire running area of a motorcycle, huge numbers of specialized cameras would be needed (Na - kamura et al., 2013).

Figure 1 shows the predicted problems if existing measurement systems are applied to running tests of motorcycles. These are the main reasons why this paper proposes a novel measurement system for use with motorcycles.

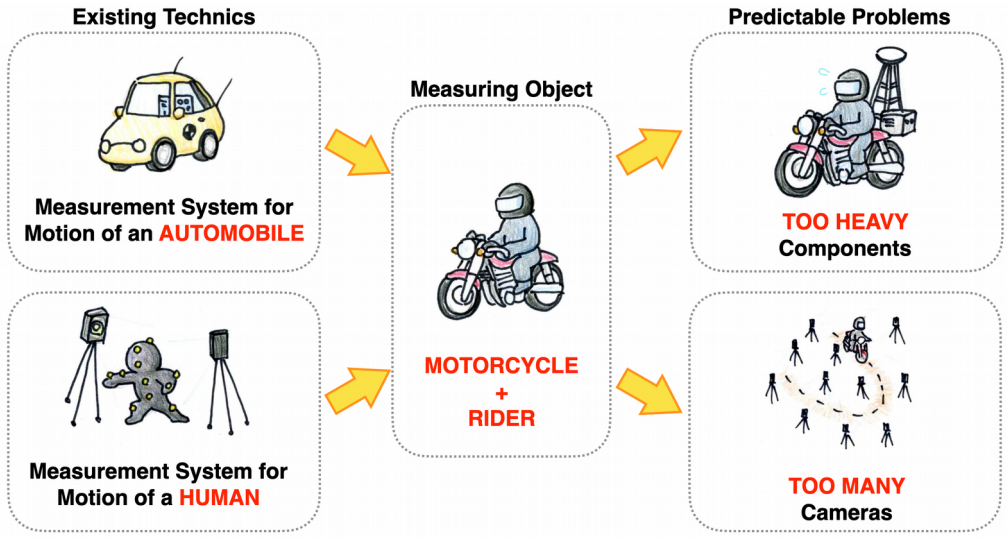


Figure 1. Predicted problems with measurement of motorcycle in the case where existing measurement systems are applied.

©2023 Hirasawa, J. published by TU Delft OPEN on behalf of the authors.
ISSN: 2667-2812

https://doi.org/10.59490/66eb6542c598a23330635f06

Bicycle and Motorcycle Dynamics 2023
Symposium on the Dynamics and Control of Single Track Vehicles
18 – 20 October 2023, Delft University of Technology, The Netherlands

Concept of the proposed system

The proposed measurement system is expected to be useful for both general users and researchers or developers. From the beginning of this research, the three design concepts listed below have been adopted to realize a simple measurement system:

(1) The motorcycle must be in its normal condition. The measurement system must have no mechanical connection with the vehicle.

(2) The measurement system must be composed of devices that are marketed widely at reasonable cost.

(3) The measured data can be visualized to aid all users in understanding of the measured phenomenon.

Therefore, the author selected the stereo vision method to measure the position of the object using omnidirectional cameras. Images acquired using an omnidirectional camera tend to show significant distortion and errors in terms of the object length. However, the omnidirectional images represent relative angles accurately (Hirasawa, 2021). In this study, the simple idea where the omnidirectional camera is mounted on a pylon is used. Figure 2 shows a concept image of the basic system design. The possible shooting distance of the omnidirectional camera determines the limit of the application range of the proposed system; therefore, running the motorcycle on a figure-of-eight-shaped course is suitable for this system.

In previous research, it was clarified that the downward direction is the most suitable orientation for the optical axis of the omnidirectional camera (Hirasawa, 2023).

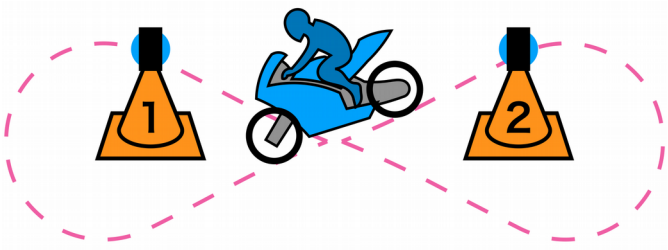


Figure 2. Concept image of the proposed measurement system.

Position measurement

The results of previous research showed that a simple measurement method combined with image processing techniques could be applied to the position measurement of a motorcycle running in a figure-of-eight-shaped course around two omnidirectional cameras. The omnidirectional camera images then provide information about the relative angles between the camera 's center and the measurement point.

However, the method based on use of two omnidirectional cameras has a weakness, represented by the presence of a significant error near the camera baseline (i.e., the line connecting the two cameras), particularly in the baseline direction.

In this research, two more omnidirectional cameras were added to the system in the orthogonal direction relative to the existing cameras. The relative positions of the quad omnidirectional cameras are shown in Figure 3. Camera 1 and camera 2 are attached to green and red pylons, respectively. The midpoint between these two cameras is set as the origin point for the coordinate system and is denoted by X_0-Y_0-Z_0. The two-dimensional positions of the measurement points can be calculated easily using the relative angles acquired from camera 1 and camera 2, as shown in Equation (1), in a manner similar to the principle of a stereo camera.

©2023 Hirasawa, J. published by TU Delft OPEN on behalf of the authors.
ISSN: 2667-2812

https://doi.org/10.59490/66eb6542c598a23330635f06

Bicycle and Motorcycle Dynamics 2023
Symposium on the Dynamics and Control of Single Track Vehicles
18 – 20 October 2023, Delft University of Technology, The Netherlands

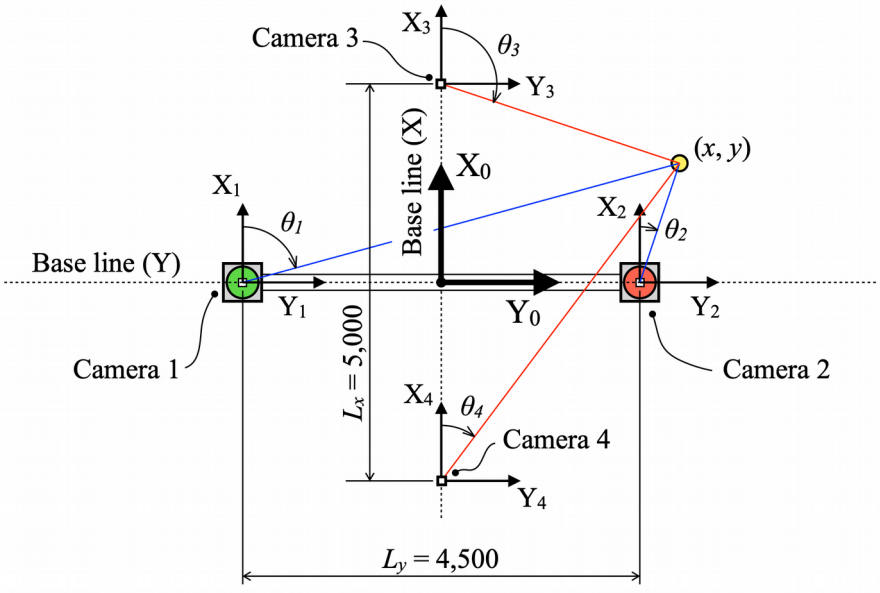


Figure 3. Disposition of the quad omnidirectional cameras for the position measurement system.

$$(x, y)=(L_y \frac{cos\theta_1 cos\theta_2}{sin(\theta_1-\theta_2)}, \frac{L_y}{2} \frac{sin(\theta_1+\theta_2)}{sin(\theta_1-\theta_2)}) \quad (1)$$

Here, L_y is the distance between camera 1 and 2 along the baseline (Y), and θ_1 and θ_2 are the relative angles from each camera, as shown in Figure 3.

Camera 3 and camera 4 are set to be orthogonal to the baseline formed by camera 1 and camera 2. The positions of the measure - ment points are calculated as shown in Equation (2) using the images from camera 3 and camera 4.

$$(x, y)=(\frac{L_x}{2} \frac{sin(\theta_3+\theta_4)}{sin(\theta_3-\theta_4)}, L_x \frac{sin\theta_3 sin\theta_4}{sin(\theta_3-\theta_4)}) \quad (2)$$

Here, L_x is the distance between cameras 3 and 4 along the baseline (X), θ_3 and θ_4 are the relative angles from each camera, as shown in Figure 3.

Figure 4 shows one example of the proposed measurement method. The four images have been rotated by small angles to align their relative positions accurately. The blue lines represent the relative angles from camera 1 and camera 2, therefore the crossing point of the blue lines represents the estimated position for the measurement object. In this case, it is the center of the helmet worn by the rider. The coordinates of this crossing point are equal to the values of x and y that were derived from Equation (1).

©2023 Hirasawa, J. published by TU Delft OPEN on behalf of the authors.
ISSN: 2667-2812

https://doi.org/10.59490/66eb6542c598a23330635f06

Bicycle and Motorcycle Dynamics 2023
Symposium on the Dynamics and Control of Single Track Vehicles
18 – 20 October 2023, Delft University of Technology, The Netherlands

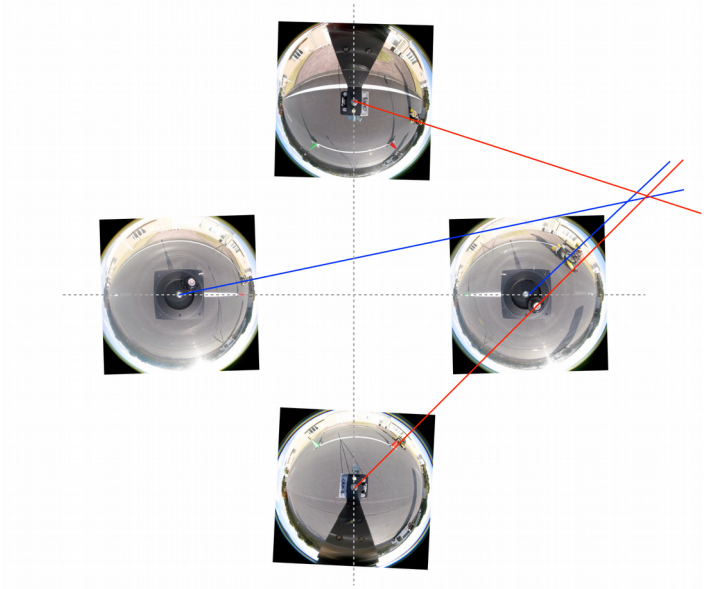


Figure 4. Example of the measurement method when using images from the quad omnidirectional cameras.

The omnidirectional images in the experiments, including the four images shown in Figure 4, were captured using commercially available Kodak PIXPRO 4KVR360 cameras. This camera type has a 235° dome lens and a 155° front lens. In this research, the dome lens side only was used in the experiments. The size of the captured images was 1,920 pixels squared.

Running experiment

Figures 5, 6, and 7 show the locus of a motorcycle that was measured while running around pylons in a figure-of-eight-shaped course. The running test with a real motorcycle was executed on a paved area at the Shirosato test center of the Japan Automobile Research Institute (JARI) in November 2022. The figures show the results for one lap of movement of the center of the helmet worn by the rider. The test vehicle used was an electric scooter, e-Vino, which is produced by the Yamaha Motor Co., Ltd. The blue crosses shown in Figure 5 were plotted at the positions that were calculated using Equation (1) every 1 s. The blue crosses shown in Figure 6 were plotted at the positions that were calculated using Equation (2) during the same period. The angles θ_1, θ_2, θ_3 and θ_4 were measured by hand and supported by GIMP software, an image processing freeware package, on the omnidirectional images. The black and grey circles in Figures 5, 6, and 7 are plotted at the positions of the omnidirectional cameras.

Figures 5 and 6 show significant position errors near the camera base line when compared with each other. Therefore, to restrict the measurement errors, in the case of points measured within 1 m of the baseline (Y), y values that are derived from Equation (2) (using θ_3 and θ_4) take priority. In other words, Figure 7 use the y values from Equation 2 only for the range $-1 < x < 1$. In contrast, in case of points measured within 1 m of the baseline (X), x values that are derived from Equation (1) (using θ_1 and θ_2) take priority. Figure 7 shows the revised positions based on these conditions. The asymmetrical shape of the locus shows the rider's personal abilities and immaturity.

©2023 Hirasawa, J. published by TU Delft OPEN on behalf of the authors.
ISSN: 2667-2812

https://doi.org/10.59490/66eb6542c598a23330635f06

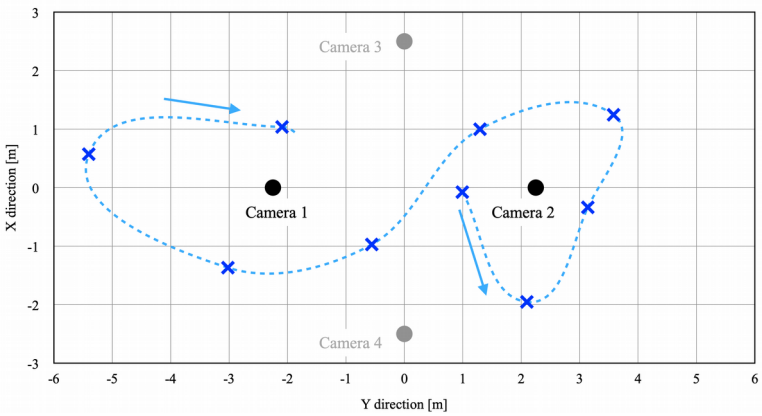


Figure 5. Locus of a motorcycle with a figure-of-eight-shaped course (using data from cameras 1 and 2 only).

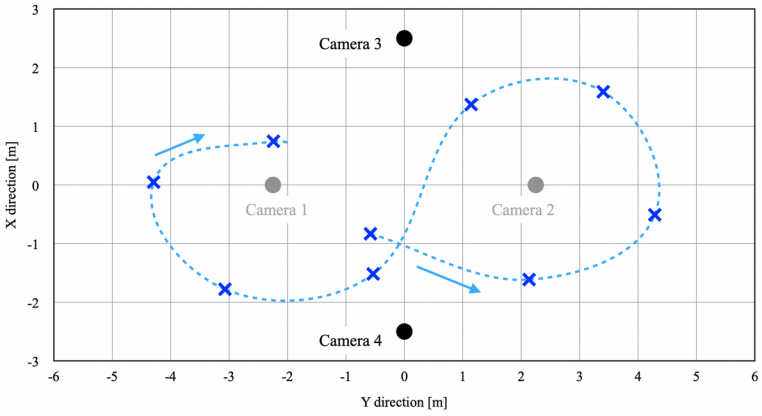


Figure 6. Locus of a motorcycle with a figure-of-eight-shaped course (using data from cameras 3 and 4 only).

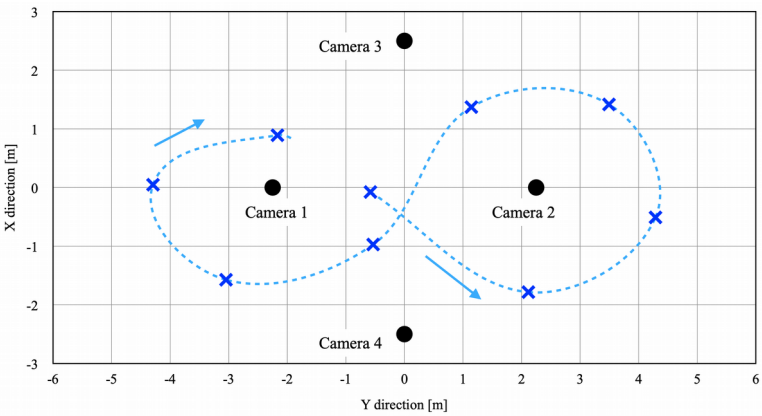


Figure 7. Locus of a motorcycle with a figure-of-eight-shaped course (using data from cameras 1, 2, 3, and 4).

©2023 Hirasawa, J. published by TU Delft OPEN on behalf of the authors.
ISSN: 2667-2812

https://doi.org/10.59490/66eb6542c598a23330635f06

Conclusion

A novel measurement system designed especially for a single track vehicle that includes omnidirectional cameras has been proposed in this work. The measurement results confirmed that the proposed method using quad omnidirectional cameras obtained the position data for a motorcycle with constant precision. The weak point of the proposed system is the necessity to treat the numerous image files generated by the four cameras in offline mode. In future work, a measurement technique must be established for multiple points on the vehicle, with the exception of the center point on the rider's helmet. Development of a sequential program that outputs the position data automatically is another issue that must be addressed urgently.

Acknowledgement

This work was supported by the Japan Keirin Autorace Foundation (JKA).

We thank David MacDonald, MSc, from Edanz (https://jp.edanz.com/ac) for editing a draft of this manuscript.

References

Fu, H. (1965). Fundamental Characteristics of Single-Track Vehicles in Steady Turning. *Transactions of Japan Society of Mechanical Engineers*, Vol.31, No.229, 1305-1314.

Fu, H., Shibahata, H., & Kikuchi, T., (1978). Stability Analysis of Uncontrolled Motion of Single-track Vehicles. *Transactions of Society of Automotive Engineers of Japan*, No.15, 51-58.

Hirasawa, J. (2021). Research on Motion Measurement for a Motorcycle Using Image Processing. *Proceedings of JSME Transportation and Logistics,* No.21-72, PS2-10.

Hirasawa, J. (2023). Using Omnidirectional Cameras to Measure Position of a Motorcycle. *Transactions of Society of Automotive Engineers of Japan*, Vol.54, No.1, 21-28.

Kageyama, I., et al. (2017). Study on Influence of Tire Characteristics on Motorcycles Behavior. *Proceedings of JSAE Congress* (*Spring*), 20175091.

Kageyama, K. (1977). Current Research on Two-wheel Vehicles in Historical Perspective. *Proceedings of JSAE Congress* (*Spring*), 20175091.

Nakamura, Y., Takao, K., Saguchi, T., & Matsuyama, T. (2013, November 11-13), New experimental method for evaluating the maneuverability of rider-bicycle system. *Proceedings, Bicycle and Motorcycle Dynamics 2013, Symposium on the Dynamics and Control of Single Track Vehicles,* Narashino, Japan, 3.2-3.

Waegli, A., Schorderet, A., Prongue, C. and Skaloud, J. (2008). Accurate Trajectory and Orientation of a Motorcycle derived from low-cost Satellite and Inertial Measurement Systems. *Proceedings of 7th ISEA conference, P42,* 1–6.

©2023 Hirasawa, J. published by TU Delft OPEN on behalf of the authors.
ISSN: 2667-2812

The Evolving Scholar Vol. 3, 2023 https://dx.doi.org/10.59490/65c5fb14c9fa9023b6a2e622

Bicycle and Motorcycle Dynamics 2023
Symposium on the Dynamics and Control of Single Track Vehicles
18 – 20 October 2023, Delft University of Technology, The Netherlands

Type of the Paper: Conference Paper

Revised

Simulator validation – a new methodological approach applied to motorcycle riding simulators

[version 2; peer reviewed]

Sebastian Will[1]*, Thomas Hammer[1], Raphael Pleß[1], Nora Leona Merkel[1], and Alexandra Neukum[1]

[1] Würzburger Institut für Verkehrswissenschaften (WIVW GmbH); will@wivw.de, https://orcid.org/0000-0003-0098-6212; hammer@wivw.de; pless@wivw.de, ORCID 0009-0006-5984-6723; merkel@wivw.de, ORCID 0000-0002-4865-368X; neukum@wivw.de

*corresponding author

Name of Editor: Jason Moore
First published: 26/09/2023
Last published: 22/03/2024
Citation: Will, S., Hammer, T., Pleß, R., Merkel, N. & Neukum, A. (2024). Simulator validation – a new methodological approach applied to motorcycle riding simulators [version 2; peer reviewed]. The Evolving Scholar - BMD 2023, 5th Edition.
This work is licensed under a Creative Commons Attribution License (CC-BY).

Abstract:

Whenever driving simulators are used in research and development, to a certain extent the generalizability of the gained results is subject to discussion. Typically, a simulator gets validated in a rather effortful and complex process to prove the adequacy of the use of this specific simulator as research tool for a given research question. Traditionally, there is a differentiation between a simulator's physical validity and its behavioral validity. Whilst the first focusses on the simulator's behavior and the presence of specific cues and operating elements, the latter focusses on the driver's perception and consequently behavior. Furthermore, the degree of accordance between vehicle and simulator forms a category of validity, namely, absolute, and relative validity. Whilst absolute validity describes an absolute numerical accordance of measurable dimensions between vehicle and simulator (e.g., certain forces, accelerations), relative validity describes a correlational accordance. Independent of the addressed dimension, simulator validation is a highly complex process, which is specific to the respective research question for which the simulator gets validated (e.g., training race riders vs. assessing distraction caused by human-machine interfaces, HMI). Regarding single-track vehicle simulator concepts for which there is less experience from previous research, a rather broad validation procedure would be a useful tool to assess a simulator's overall characteristics and therefore to assess its potential fields of application on a wider basis. This paper addresses this gap and presents such a methodological validation approach applied to motorcycle riding simulators. The main assumption of the method is that complex riding tasks can be divided into smaller units that allow for discrimination of specific rider input characteristics, the so-called minimal scenarios. These minimal scenarios are riding tasks such as 'starting from standstill' or 'initiating a curve at constant velocity'. Furthermore, it is assumed that minimal scenarios can be reorganized to more complex riding tasks. This is intended to describe the variety of potential applications with a necessary minimum of elementary tasks to reduce the validation effort for a global assessment of the simulator's capabilities. This more generic result can also be regarded as a limitation. The proposed empirical evidence from participant studies on a static, a dynamic motorcycle riding simulator as well as a reference ride on a real motorcycle suggests that the validation approach can be beneficial.

Keywords: Motorcycle, Powered Two-wheeler, Simulator, Methods, Validation

©2023 Will, S., Hammer, T., Pleß, R.; Merkel, N. L., & Neukum, A. published by TU Delft OPEN on behalf of the authors.
ISSN: 2667-2812

 http://dx.doi.org/10.59490/65c5fb14c9fa9023b6a2e622

Introduction

Driving simulators play an essential role for the investigation of safety relevant research topics in the passenger car sector. Ranging from usability and user experience research to the investigation of highly automated driving, simulators support the fast development in the passenger car domain. In recent years, the motorcycle sector has undergone a rapid change of technical developments as well. Yet, motorcycle simulators are in a rather early stage in this regard which poses the challenge to gain knowledge concerning their validity for specific use cases and therefore their applicability for different research questions at hand. Motorcycle simulators, especially those with a complex, high-fidelity setup are less common than passenger car simulators. Therefore, the overall experience regarding their application is at a rather early stage (e.g., Cossalter, Lot, Massaro, & Sartori, 2011; Grottoli, Mulder, & Happee, 2022; Hammer, Pleß, Will, Neukum, & Merkel, 2021; Westerhof, De Vries, Happee, & Schwab, 2020).

Especially the inherent instability of single-track vehicles needs to be considered. This major difference makes the simple transfer of knowledge of applications from the passenger car sector to the motorcycle sector almost impossible. In general, motorcycle simulators seem appropriate as a tool for research and development (R&D) as well as training purposes. Same as in the passenger car sector. Yet, this assumption needs to be proven before results gained on a simulator may be generalized to real riding. This process of simulator validation is typically limited to the specific field of application and therefore a complex and expensive process which implies the need for a validation study for every single use case. For instance, a simulator without motion base might be perfectly applicable to assess the effects caused by the interaction with a human-machine interface (HMI) while driving, if the workload caused by the driving task is comparable between simulator and reality. Yet, this specific static simulator might not be appropriate to investigate the effects caused by an autonomous emergency braking system as the participant does e.g., not feel the resulting vestibular cues of braking.

Another important aspect lies within the selection of the investigated parameters for validity assessment. A validation study aiming at distraction assessment will observe other parameters than a validation study aiming at the application of a suspension setup. Since the 1970s validity concepts that are specific for the field of driving simulation have been developed. Traditionally, there is a differentiation between a simulator's physical validity and behavioral validity. Whilst the first focusses on the simulator's behavior and the presence of specific cues and operating elements, the latter focusses on the driver's behavior. Yet, the idea of applying a more holistic and multidimensional validation approach is almost as old as the field of research itself. For instance, Blaauw (1982) proposed that simulator validation should involve objective riding parameters, subjective performance indicators, and rider workload.

Furthermore, the degree of accordance between vehicle and simulator forms a category of validity, namely, absolute, and relative validity. Whilst absolute validity describes a numerical accordance between vehicle and simulator, relative validity describes a correlational accordance (Allen & O'Hanlon, 1979; Blaauw, 1982; Blana, 1996). As absolute validity for all components of a simulator and all fields of application will probably remain unreachable, a focus on relative validity is recommended by different researchers (Blaauw, 1982; Caird & Horrey, 2011; Godley, Triggs, & Fildes, 2002). Depending on the intended purpose of simulator use, the focus on physical validity or behavioral validity might change. To take up the above-mentioned example again, a simulator that is used for suspension assessment is going to focus more on physical validity. Yet, it must be noted that even simulators with a complex motion system are always limited and cannot replicate all potentially relevant and highly dynamic scenarios. The simulator in use for distraction assessment will probably be validated regarding behavioral validity. For the latter, the driver or rider workload is then an important aspect to be considered (Espié, Gauriat, & Duraz, 2005). For human factors research questions, the workload caused by the primary riding task is of highest importance. This workload should be as close to normal driving on public roads as possible, if e.g., the effects of a warning shall be measured while driving. Any overstraining simulator control task may bias the observed reaction times as response to the warning.

The technical term of *simulator validation* contains different facets which will be described in the following sections. Firstly, a simulator's validity cannot be attributed to its components in an additive way. The question that must rather be posed is: which components are necessary to answer the respective research question (Caird & Horrey, 2011). Thus, providing specific sensory cues, such as certain vestibular feedback, can be seen as a necessary but not sufficient condition for a simulator's validity for a specific use case. An available but distorted presentation of a stimulus might even cause more unnatural behavior which in turn decreases validity (e.g., if a poorly implemented motion cueing feels unnatural while braking, participants may – voluntarily or not – avoid (stronger) braking). Furthermore, a change in a simulator's setup might change rider's perception regarding the simulator behavior fundamentally. As an example, a simulator's visualization system could be replaced from a front projection to a head-mounted display. By changing the presentation of the visualization also the rider's reference to his spatial orientation in the room changes (as nothing is visible except the presentation in the head-mounted display). Additionally, the perception of simulator motions (if available) might change by the alteration of visual presentation, as participants' expectations towards motion might

©2023 Will, S., Hammer, T., Pleß, R.; Merkel, N. L., & Neukum, A. published by TU Delft OPEN on behalf of the authors.
ISSN: 2667-2812

depend on visualization and vice versa. Therefore, strictly speaking, every significant change in a simulator's setup would need a repetition of the previously conducted validation studies.

Thus, established validation approaches do hardly seem feasible for simulator setups that are still in development and therefore underlie regular changes. To cope with this challenge, a new method was developed that shifts the focus from detailed validation studies to a broader assessment of a simulator for a predefined set of potential applications. The research question at hand was, whether it is possible to validate short generic maneuvers (so-called minimal scenarios) instead of complex and use case-specific riding tasks to gain a broader assessment of the simulator's validity. The validation metrics and categories of validity are still up to the researchers. Summarized, simulator validation is a highly effortful and complex process, which is specific to the respective use case that is validated. Especially regarding innovative simulator concepts for which there is less experience from previous research, a rather broad validation procedure could be a useful tool to assess a simulator's overall characteristics and therefore to assess its potential fields of application on a broad basis. The following paper presents a method that tries to assess simulator validity on a holistic and less detailed level than conventional validation methods do.

Methods

Following the above-mentioned research question, data was gathered from two fundamentally different motorcycle simulators and a ground truth in real riding. The aim was to identify whether the combined minimal scenarios lead to the same validity as more complex riding maneuvers and whether properties of the specific simulators are replicated with the new validation approach.

General methodology

The main assumption of the method is that complex riding tasks can be divided into smaller units that allow for discrimination of specific rider input characteristics. These minimal scenarios are riding tasks that are conducted only serially such as 'starting from standstill' or 'initiating a curve at constant velocity'. To identify relevant minimal scenarios for the respective simulator that should be investigated, the potential fields of application, for which a simulator is intended to be used, must be defined. Usually, a simulator is not suitable for all fields of application in the same way (e.g., a simple, static simulator which was built for training hazard perception can probably not be used to assess different suspension setups). For the general verification of this approach, the German system for accident classification was analyzed to retrieve a list of practically important rider behaviors, which should help avoiding the different accident types. This list was transferred into a list of minimal scenarios that fulfill the assumption of seriality and that reflect the most typical riding scenarios.

With that list at hand, a verification study with $N = 6$ experts (professional trainers, motorcycle researchers etc.) that understand the underlying vehicle dynamics principles was conducted. In this study, the different minimal scenarios were tested as isolated as possible (Figure 1) with varying levels of dynamics (i.e., different predefined speeds, different distances to achieve a certain speed etc.) and in all three test environments (static simulator, dynamic simulator, real motorcycle). The outcome was a matrix of objective and subjective parameters characterizing the different test environments.

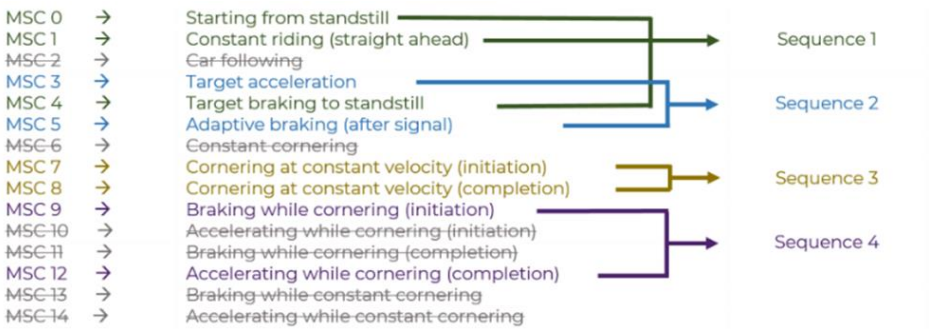


Figure 1. List of identified minimal scenarios with the selection made to be tested in the expert study.

In a next step, a participant study with $N = 15$ non-professional riders was conducted. The aim was to understand whether more natural and complex combinations of the different minimal scenarios still reflect the previously identified characteristics of the test environment. Further, this is intended to describe the variety of potential applications with a necessary minimum of elementary tasks in order to reduce the validation effort for a global assessment of the simulator's capabilities (Hammer et al., 2021).

©2023 Will, S., Hammer, T., Pleß, R.; Merkel, N. L., & Neukum, A. published by TU Delft OPEN on behalf of the authors.

ISSN: 2667-2812

Test environments

To investigate the applicability of the developed validation concept, a series of experiments has been conducted involving a measurement motorcycle to deliver some kind of ground truth and two motorcycle riding simulators.

Measurement motorcycle

A KTM 790 Duke was used as measurement motorcycle within the participant study (see Figure 2 left). The vehicle has a 799 cm^3 two-cylinder in-line engine with an engine power of 77 kW (103 HP). The series motorcycle is already equipped with state-of-the-art sensors and assistance systems, as for example an IMU (inertial measurement unit) and motorcycle stability control. Due to the rather low sitting height, the upright seated position, and the low weight of 187 kg, the vehicle is suitable for a wide range of participants. Additionally, the implemented measurement technology allows direct access to the onboard sensors which allows the recording of relevant riding parameters such as roll angle, brake pressure and velocity. The entire measurement technology was placed within a custom aluminum side case which is mounted at the left-hand side of the motorcycle. Most relevant parameters are supplied via CAN-Bus and recorded with an Intel NUC© and SILAB® as data logging software. The recording rate is at 60 Hz. Additionally, position data is recorded with a Navilock USB receiver with a sampling rate of 5 Hz. For acquisition and output of analog signals an Arduino© was installed. The power supply of the measuring technology is provided by a second battery with charging unit.

Motion-based dynamic motorcycle riding simulator DESMORI

The DESMORI dynamic motorcycle riding simulator at WIVW (see Figure 2 center) with the driving simulation software SILAB was used as high-fidelity simulator (2018 setup). For the studies a vi-grade BikeRealTime multi body simulation model was used. A BMW F 800 is used as mockup, which is mounted on a 6-dof motion platform. The velocity-dependent motion-cueing algorithm (MCA) divides the non-filtered calculated roll angle in a mechanical (approx. 1/3) and a visual part (approx. 2/3). Further, it is scaled to display max. 80% of the calculated roll angle. All rider controls such as throttle twist grip, front and rear brakes, 6-speed manual gear box including clutch operation are available. A curved projection screen with 4.5 m diameter and 2.9 m height enables 220° horizontal field-of-view. The two rear-mirrors are realized by 7-inch TFT-displays while the dashboard is displayed on a 10-inch TFT-touchscreen. The sound is provided via in-helmet speakers. A so-called g-vest provides forces to the rider torso simulating aerodynamical drag and acceleration. Steering torque is provided by an electric motor providing up to 80 Nm maximum torque.

Static motorcycle riding simulator

Opposed to the dynamic motorcycle riding simulator with so-called counter-steering control that results from the multi-body dynamics model, the static motorcycle riding simulator of WIVW was equipped with a simplified single-track vehicle model with positive steering (Figure 2 right). This means that riders steer in the direction they want to go as if riding a two-track quad bike. Visual cues are provided by three 55” LCD screens offering 180° horizontal field of view.



Figure 2. Measurement motorcycle in the participant study (left), dynamic motorcycle riding simulator DESMORI (center) and static motorcycle riding simulator (right) used for the validation study.

The MCA provides visual roll scaled with a degressive characteristic curve between 30% to 70% of the calculated roll angle. The instrument cluster is displayed on a 10” LCD screen and the two rear-mirrors via 7-inch TFT-screens. A KTM 1290 Super Adventure R was installed as mockup. The motorcycle simulator uses an automatic gear box. All relevant controls such as throttle twist grip, front and rear brake levers are implemented. As within the dynamic motorcycle riding simulator the simulation was provided by

©2023 Will, S., Hammer, T., Pleß, R.; Merkel, N. L., & Neukum, A. published by TU Delft OPEN on behalf of the authors.

ISSN: 2667-2812

SILAB simulation software. Data including all rider inputs was recorded at a frequency of 100 Hz. Acoustic cues come from in-helmet speakers. Haptic feedback on steering torque is provided by an electric motor that delivers a maximum torque of 50 Nm.

Procedure

The study was conducted using a within-subjects design. This means that all participants completed all tasks in all three test environments. The real riding investigation exemplarily described in this paper was performed on a closed test-track. In the beginning, all riders had time to familiarize with the measurement motorcycle as to their own needs. Same on both simulators, where all participants went through a training session in order to familiarize with the simulated riding. Every appointment started with a completion of an informed consent document and explanation of the study purpose. The participants completed different test rides as described more detailed in the report from Hammer et al. (2021). Questionnaires were filled in after each ride and a longer inquiry took place at the end of each appointment. For the test sequence described in this paper, the motorcyclists were instructed to ride on an oval-shaped test course with a constant velocity of 35 km/h. A visual signal in the dashboard indicated at short notice whether to perform an avoidance maneuver to the left, to the right (3 m lateral displacement within 15 m) or whether to continue the oval-shaped course without avoidance maneuver. The different trajectories were marked using colored gates with traffic cones. All tests were done clockwise and counter-clockwise.

Participant panels

For the expert study, N = 6 motorcyclists (aged m = 26.2 years, SD = 1.95; all male) with professional knowledge in the field of motorcycle dynamics participated. The average mileage ridden in the last 12 months was M = 7 667 km (min = 2 000 km; max = 20 000; SD = 6 574 km). In the participant study, N = 15 motorcyclists (aged m = 37 years, SD = 14; n_{female} = 1) with a valid license class A (motorcycle unlimited) were observed. The average mileage ridden in the last 12 months was M = 7 300 km (min = 1 000 km; max = 25 000; SD = 7 496 km).

Results

All experts and regular participants were able to complete all experimental conditions without loss of control or motion sickness. Below, selected results for experts and regular participants are presented.

Qualitative rider feedback

The riders rated the dynamic simulator as more realistic than the static motorcycle simulator in terms of steering and overall impression. The interaction with the dynamic simulator was also rated as being more natural. The stabilization of the dynamic simulator approaches the stabilization of the real motorcycle with increasing speed. Hence, the cornering stability is evaluated as too low for the dynamic motorcycle simulator. In the static simulation the stabilization is evaluated as too high. Visual and haptic/proprioceptive feedback of the vehicle dynamics is evaluated as too weak in both simulation environments. More of these subjective ratings were captured with questionnaires, e.g., on presence (Will, 2017), which provide important insights on the simulator acceptance, for instance.

Subjective questionnaire data

As an example, on how to deal with subjective measures, Figure 3 shows the subjectively experienced levels of workload while performing the different minimal scenarios in the expert study as a function of the test environment. The general pattern comparing the minimal scenarios seems stable across test environments. The demand posed by the minimal scenarios is on average allocated in the lower half of the workload scale. An offset towards higher perceived workload can be seen in the dynamic motorcycle riding simulator. A certain variation regarding the ratings between riders can be observed across all minimal scenarios and test environments.

©2023 Will, S., Hammer, T., Pleß, R.; Merkel, N. L., & Neukum, A. published by TU Delft OPEN on behalf of the authors.

ISSN: 2667-2812

 http://dx.doi.org/10.59490/65c5fb14c9fa9023b6a2e622

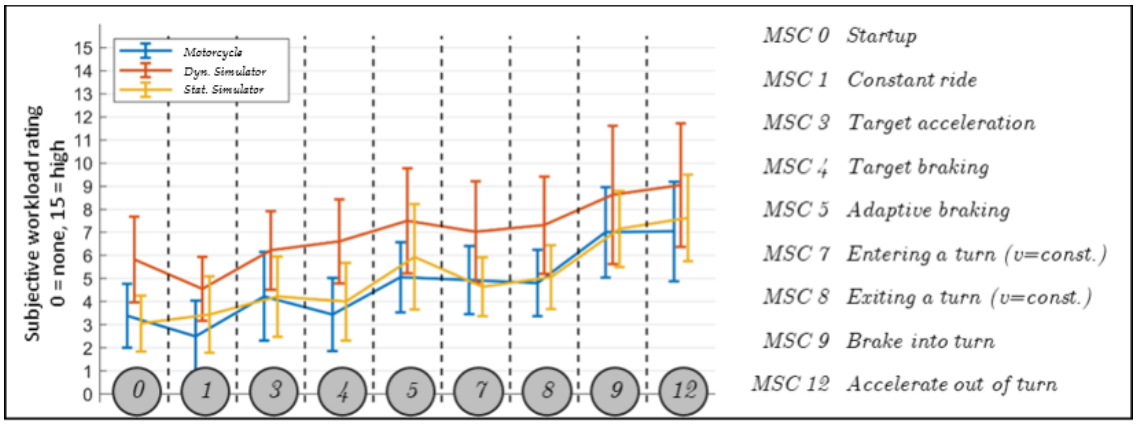


Figure 3. Experts' subjective workload ratings for the different investigated minimal scenarios (MSC) as a function of test environment. Average mean values and standard deviations are displayed, while the lines shall help identifying patterns between the test environments.

Objective vehicle dynamics data

An example dealing with objective metrics is given in Figure 4. This graph shows exemplary vehicle dynamics data from the test sequence 'avoidance maneuver', which consisted of three previously defined minimal scenarios 'constant riding', 'entering a turn (v = const.)' and 'exiting a turn (v = const.)'. Across all test environments, people manage to comparably follow the target speed instruction, which can be seen in the lower half of the figure. The roll angle over time shows a higher accordance between real riding and the dynamic motorcycle riding simulator, while the implemented vehicle dynamics model of the static simulator is not capable of replicating these effects. On a qualitative basis, it is obvious that the completion of the given minimal scenarios combined to an avoidance maneuver requires a roll angle sequence to the left and right – or vice versa – on the real motorcycle as well as the dynamic simulator. So, for the solid line in Figure 4, which shows an avoidance maneuver to the left, a roll angle to the left can be observed before the vehicle leans to the right to pass through the laterally offset gates ($Gate_2$ and $Gate_3$). In absolute numbers the median roll angle reaches between 7° and 10° maximum roll angle between the gates. In both environments, a certain variation can be seen between different runs and riders (shaded area). The dynamics data of the static motorcycle simulator differs from that pattern. Further the absolute roll angle medians reach 1° to 4° maximum and there is almost no variance in between runs and riders. Due to the limited space available for the test, riders did not go completely straight before and after the gates to follow the oval shaped test course.

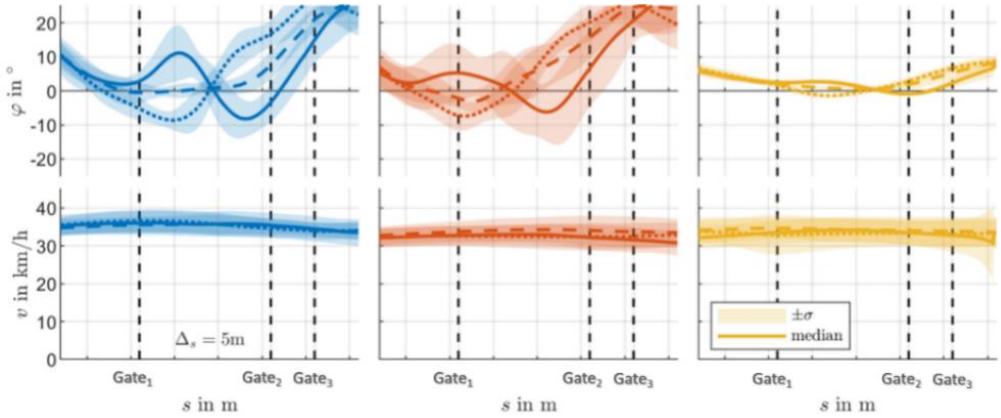


Figure 4. Roll angles and velocities for the avoidance maneuver in the environments test motorcycle (blue), dynamic motorcycle riding simulator (red) and static motorcycle riding simulator (yellow) from the participant study. The solid line indicates an avoidance maneuver to the left, the dotted line to the right and the dashed line shows the control maneuver going straight. Negative roll angles imply a lean angle to the right.

©2023 Will, S., Hammer, T., Pleß, R.; Merkel, N. L., & Neukum, A. published by TU Delft OPEN on behalf of the authors.

ISSN: 2667-2812

Conclusion

The paper proposed a simulator validation approach that complements existing methods. The main difference is the validation of sequential minimal scenarios instead of complex riding maneuvers. If vehicle as well as rider behavior in the minimal scenarios was comparable to their behavior in reality, the simulator seems capable of validly replicating this specific maneuver (e.g., constant riding requires the same workload on simulator A as in reality). Consequently, the simulator might be appropriate to answer research questions where rider workload while riding at constant speed is important (e.g., effects of secondary task engagement while riding on a highway with speed limit). The following section summarizes the exemplary validation results of two motorcycle riding simulators to evaluate the proposed validation method.

The qualitative feedback provides important information on which holistic impression the simulator creates. It can guide the direction of simulator optimization and provide first insights in potential fields of application for the given simulator. More directly related to the validation process itself is the quantitative subjective feedback. For instance, the different minimal scenarios vary as to their demand towards the rider. As an example, riding constantly requires less input and control than accelerating out of a turn. Therefore, it was expected to find this differentiation between the minimal scenarios in the subjectively experienced workload. This was true and the pattern between minimal scenarios was stable across all test environments, which is a good indicator for relative validity in this domain. Yet, the absolute level of perceived workload was constantly higher in the dynamic motorcycle riding simulator as compared to a good fit between static simulator and real motorcycle. This implies that riding the given dynamic simulator setup requires more resources than riding the static simulator or the real motorcycle. For research questions with a focus on rider workload (e.g., dual-task paradigm to investigate the distraction caused by the interaction with an HMI while riding), the static simulator might be a better fit as the amount of resources to deal with the secondary task is comparable between static simulator and real riding across all minimal scenarios. This would follow the arguments of Espié et al. (2005).

Opposed to the workload results the objective data has shown a more adequate representation of motorcycle dynamics for the dynamic motorcycle simulator compared to the static motorcycle simulator across the three minimal scenarios. This was shown both for steering characteristics as well as roll angle representation. Both, the measurement motorcycle, and the dynamic motorcycle simulator have shown variance in riders' behavior while the results for the static motorcycle simulator are rather homogeneous. Yet, the simulator properties might emphasize different strategies. For instance, the MSC entering a turn should start when passing $gate_1$. While the main roll angle increase is observed after passing the gate with the real motorcycle, participants on the dynamic motorcycle riding simulator seem to initiate entering the turn earlier and pass $gate_1$ already at a certain lean angle. This might, e.g., be because riders try to avoid higher roll rates in the dynamic simulator. The initiation of MSC exiting a turn (changing lean angle from one side to the other) seems to take place similarly and with a comparable roll angle progression on the real motorcycle and the dynamic simulator. Thus, besides the higher workload levels the dynamic motorcycle simulator appears to be more adequate to investigate research questions which involve a detailed representation of vehicle dynamics and the rider input provoking these dynamics as compared to the static simulator.

Based on the specific research question and the resulting relevance of physical or behavioral validity, the tested sequence of minimal scenarios can support the simulator's validity for different research questions. For instance, the example given above aims at validating an avoidance maneuver existing of three different minimal scenarios. If the results for the relevant concept of validity are positive, there is no need to conduct separate validation studies for different research questions involving the same relevant minimal scenarios. In this case, an investigation of a warning assistance system, which aims at triggering an avoidance maneuver could be investigated likewise to a hazard perception training, which includes avoiding a suddenly appearing threat, on that same simulator.

Still, what remains an issue of discussion is the definition of thresholds. How precisely must the observed parameters in the simulator and a real vehicle resemble each other to create a meaningful fit? Inferential test statistics are obviously a way to define this. Hence, depending on the data set this may not necessarily mark a meaningful correspondence. Further, the decision to start the validation process coming from accident scenarios resulted from the fact that the specific simulators under investigation were mainly designed to deal with research questions related to motorcycle safety. Also, the definition of the relevant range of vehicle dynamics resulted from that origin. Different minimal scenarios or at least vehicle dynamics ranges may result, if a simulator is meant to be used for other purposes, such as race rider training. Even if there remain limitations, certain degrees of freedom for the design of simulator validation studies and their interpretation, the benefits of using a validated simulator for a given research question may outweigh the disadvantages and challenges. Figure 5 proposes a decision tree that could guide towards one or the other test environment based on the specific research question, which follows Caird's (2011) idea of individual simulator setups based on the research question at hand.

©2023 Will, S., Hammer, T., Pleß, R.; Merkel, N. L., & Neukum, A. published by TU Delft OPEN on behalf of the authors.

ISSN: 2667-2812

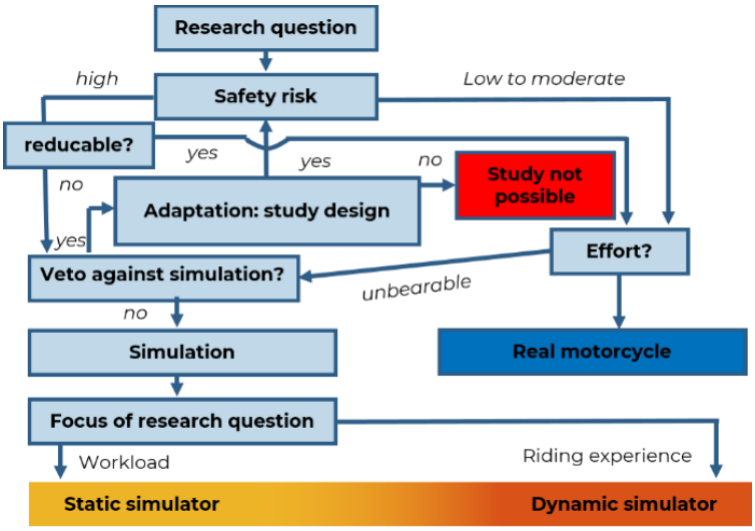


Figure 5. Decision tree for the selection of a research environment based on boundary conditions (Hammer et al., 2021, p.10).

In summary, the presented method does not try to substitute but complements established methodologies in the field of driving simulator validation. Further, the proposed concept of validating minimal scenarios that can be combined to different meaningful and more complex maneuvers needs more investigation. The proposed approach shall provide a method for a justified global assessment of a simulator's potential fields of application including objective dynamics data as well as subjective assessments. Additionally, the method shall help identifying potentials for optimizing a certain simulator setup. This is done with a defined set of minimal scenarios to which the established validation concepts shall be applied.

This method was developed to be applied to single-track vehicle simulators as these simulators are in a rather early stage compared to well-established passenger car simulators and a wider overview about the simulator's validity could be more helpful in the beginning than a statement about the simulator's validity for one specific research question. Yet, the approach is not limited to the field of single-track vehicles and may deliver interesting insights in potential down- and upsides of a simulator concept across all modes of transport.

Acknowledgements

This research was funded by the German Federal Highway Research Institute (Bundesanstalt für Straßenwesen, BASt) with the grant agreement number FE 82.0700/2017.

References

Allen, R., & O'Hanlon, J. (1979). Effects of roadway delineation and visibility conditions on driver steering performance. *Transportation research record, 739*, 5-8.

Blaauw, G. J. (1982). Driving experience and task demands in simulator and instrumented car: a validation study. *Human FActors, 24*(4), 473-486.

Blana, E. (1996). Driving Simulator Validation Studies: A Literature Review.

Caird, J. K., & Horrey, W. J. (2011). Twelve practical and useful questions about driving simulation. *Handbook of driving simulation for engineering, medicine, and psychology*, 5.1-5.16.

Cossalter, V., Lot, R., Massaro, M., & Sartori, R. (2011). Development and validation of an advanced motorcycle riding simulator. *Proceedings of the Institution of Mechanical Engineers, Part D: Journal of Automobile Engineering, 225*, 705-720. doi:10.1177/0954407010396006

Espié, S., Gauriat, P., & Duraz, M. (2005). *Driving simulators validation: The issue of transferability of results acquired on simulator.* Paper presented at the Driving Simulation Conference North-America (DSC-NA 2005), Orlondo, FL.

Godley, S. T., Triggs, T. J., & Fildes, B. N. (2002). Driving simulator validation for speed research. *Accident Analysis & Prevention, 34*(5), 589-600.

©2023 Will, S., Hammer, T., Pleß, R.; Merkel, N. L., & Neukum, A. published by TU Delft OPEN on behalf of the authors.

ISSN: 2667-2812

Grottoli, M., Mulder, M., & Happee, R. (2022). Motorcycle simulator subjective and objective validation for low speed maneuvering. *Proceedings of the Institution of Mechanical Engineers, Part D: Journal of Automobile Engineering*, 1-16. doi:10.1177/09544070221110

Hammer, T., Pleß, R., Will, S., Neukum, A., & Merkel, N. L. (2021). *Anwendungsmöglichkeiten von Motorradsimulatoren* (Bundesanstalt für Straßenwesen Ed. Vol. M323). Bremen: Carl Schünemann Verlag,.

Westerhof, B. E., De Vries, E. J., Happee, R., & Schwab, A. (2020). *Evaluation of a motorcycle simulator.* Paper presented at the Symposium on the Dynamics and Control of Single Track Vehicles, Padova, Italy.

Will, S. (2017). *Development of a presence model for driving simulators based on speed perception in a motorcycle riding simulator.* (PhD thesis), University of Wuerzburg, Wuerzburg.

©2023 Will, S., Hammer, T., Pleß, R.; Merkel, N. L., & Neukum, A. published by TU Delft OPEN on behalf of the authors.

ISSN: 2667-2812

The Evolving Scholar Vol. 3, 2023 https://dx.doi.org/10.59490/663dcf0465e90c80e41b78a9

Bicycle and Motorcycle Dynamics 2023
Symposium on the Dynamics and Control of Single Track Vehicles
18 – 20 October 2023, Delft University of Technology, The Netherlands

Type of the Paper: Conference Paper

Revised

Systematic Literature Review: Motorcycle Simulators

[version 3; peer reviewed]

Dorothea Wildner[1], Frank Diermeyer[2]

[1] Department of Automotive Engineering, TUM School of Engineering and Design, Technical University Munich, Germany; Dorothea.Wildner@tum.de, ORCID 0009-0006-0919-1917
[2] Department of Automotive Engineering, TUM School of Engineering and Design, Technical University Munich, Germany; Diermeyer@tum.de, ORCID 0000-0003-1441-5226

Name of Editor: Jason Moore
First published: 27/09/2023
Last published: 13/05/2024
Citation: Wildner, D. & Diermeyer, F. (2024). Systematic Literature Review: Motorcycle Simulators [version 3; peer reviewed]. The Evolving Scholar - BMD 2023, 5th Edition.
This work is licensed under a Creative Commons Attribution License (CC-BY).

Abstract:

An increasing number of researchers have started to focus on motorcyclists due to their increased risk of accidents, their vulnerability, and the limited possibilities to enhance their passive safety. An important tool hereby is the use of motorcycle simulators. They can be used to evaluate human-machine interfaces, design future advanced rider assistance systems like forward collision warnings, or determine an optimal ergonomic position to reduce mental loads and stress. However, compared to the automotive sector, only a few simulators exist, but they differ greatly. To the author's knowledge, no recent systematic overview of the existing motorcycle simulators exists. Therefore, this literature review provides an overview of the current state-of-the-art powered two-wheeler simulators based on 151 publications. The review describes these simulators in detail, including their prioritized research areas, conducted studies, strengths and limitations, development over the years, and validation.
A tabular overview of the simulators can be found in the supplementary materials or requested.

Keywords: Systematic Literature Review, Motorcycle Simulator, Motorcycle Research

©2023 Wildner, D., Diermeyer, F. published by TU Delft OPEN on behalf of the authors.
ISSN: 2667-2812

1 Introduction

Numerous articles related to motorcycle research state that the number of accidents and their severity is their motivation for further developments in this area (Huth et al., 2012; Benedetto et al., 2014; Will & Schmidt, 2015; Will, 2017; Bouaouni et al., 2021). Simulators are a popular tool for development and research in traffic and transport. They help to develop new technologies and consider the rider's behavior during the evaluation (Westerhof et al., 2020). However, they differ significantly concerning for example, Degrees of Freedom (DOF), motion platforms, human-machine Interface (HMI), software, simulation of forces, steering input and feedback, and validation status. Simulators will always offer a level of abstraction from the real world in which users can experience specific characteristics of a real system (Stedmon et al., 2009). Some applications of simulators are evaluating vehicle designs, developing safety regulations, human factors engineering research, or training and education. Those different purposes then pose different requirements for the simulators. For example, while a simple driver interface and low to no vehicle motions are sufficient for education purposes, the demands on vehicle motion simulation are high for development. Human factors research poses certain requirements on vehicle motions and the interface (Norfleet et al., 2009). To determine the optimal areas of applications for motorcycle simulators and to assess their strengths and limitations, it is crucial to provide a current state of the art. Using the overview of the existing simulators from this paper, new areas of applications can be found, and simulators that specifically target these can be created.

2 Methods

Search terms for the identification of all motorcycle simulators were: "Motorcycle simulator" OR "Motorcycle riding simulator" OR "Motorcycle training simulator". With them, corresponding papers in Google Scholar (817 articles), ScienceDirect (108 articles), Scopus (108 articles), and IEEE (8 articles) were identified in September 2023. These prioritized search words must be in the title or abstract or used as a keyword. After removing duplicates, the relevance of the found articles was identified: the titles and abstracts were revised, and studies mentioning man-in-the-loop motorcycle simulators providing a physical human-machine handlebar interface were selected. Only English or German articles were considered. After these steps, 151 articles are building the basis for this review. Simulators that were mentioned in three or more articles are described in detail. These simulators were then ordered chronologically and divided into the section "History of motorcycle simulators" if there was no information within the last 20 years about their use or development or into the section "Current motorcycle simulators." This time period was chosen due to the increase of new simulators within the last 20 years.

3 History of Motorcycle Simulators

Dahl handed the first patent for a motorcycle simulator in 1971. The primary purpose of this stationary simulator was to train novice motorcycle riders. Using the simulator, the rider could gather experience with starting, stopping, steering, braking, and shifting gears. However, there is no visualization of the environment (Dahl, 1971; Doz Nadal, 2014). In 1984, Dr. Karl-Peter Born started to develop a research simulator during his PhD. This simulator was built to investigate the behavior of the motorcyclists. It also included a visualization and a simulation of forces due to long-term accelerations (Born, 1989; Doz Nadal, 2014).

Often, the simulator conceived by Honda in 1988 is referred to as the first motorcycle simulator. The main goal of the simulator was to be able to study the stability and maneuverability of motorcycles. Seven moveable axes represented the five DOF: roll, yaw, pitch, lateral motions, and steering. A cradle-type swinging mechanism was applied to simulate the feeling of sustained acceleration. The corresponding linear simulation model had four DOF. Although the dynamic equations showed a good correlation to actual motorcycle behavior, the participants had difficulties controlling the simulator, especially in situations with low speeds and cornering. Furthermore, the participants tended to use positive-steering. This was probably due to the lack of centrifugal forces and differences in the roll acceleration (Miyamaru et al., 2002; Arioui et al., 2010; Nehaoua et al., 2007a,b, 2008, 2011b; Vieira et al., 2014; Lot and Cossalter, 2014).

Honda´s second Prototype followed a few years later and was first installed in 1991 at Japan's Suzuka traffic education center. This simulator was intended for safety training and used to verify the effectiveness of safe riding training. The DOF had been reduced to three (pitch, roll, and steer), and an empirical motorcycle model controlled the simulation. (Miyamaru et al., 2002; Arioui et al., 2010; Nehaoua et al., 2007a,b, 2008; Cossalter et al., 2011; Nehaoua et al., 2011b; Vieira et al., 2014). In 1996, a change was made to the Japanese Road Traffic Act, which required simulators in riding school lessons. Honda presented their mass-produced version of the second prototype in the same year. Controllability and easy riding were the main focus instead of recreating the actual dynamics. A roll axis at a height of 250mm improved the riding feeling. This simulator is still used in driving education centers (Chiyoda et al., 2002; Vidotto et al., 2008; Cossalter et al., 2009, 2011; Vieira et al., 2014; Lot and Cossalter, 2014).

In 1993, Colburn et al. investigated the influence of the legal alcohol limit on driving performance using a simulator with an interactive screen. Control of the throttle and brakes was very realistic, according to the authors (Colburn et al., 1993).

©2023 Wildner, D., Diermeyer, F. published by TU Delft OPEN on behalf of the authors.

ISSN: 2667-2812

The MORIS simulator was conceived as a tool to investigate and design motorcycle handling and stability in the early design stages in 1995. This simulator with a scooter mockup located at the PERCRO Laboratory in Pisa, Italy, had seven DOF and was also used to investigate rider control behavior (Ferrazzin et al., 2009). A good overall sense of realism without the symptoms of motion sickness was demonstrated in a subjective evaluation using 20 subjects (Grottoli, 2021)
In 2002, Honda´s third prototype with a six DOF parallel manipulator and a head-mounted display was developed. This simulator used a four DOF model for the lateral motorcycle dynamics and a one DOF model for the longitudinal dynamics (Chiyoda et al., 2002; Nehaoua et al., 2007a,b, 2008; Cossalter et al., 2009; Lot and Cossalter, 2014; Westerhof, 2018).

4 Current Motorcycle Simulators

Based on the systematic review process described in section 2, the motorcycle simulators referenced in at least three articles were identified. They are ordered by the year of their development, starting with the oldest. If the articles did not state a development year, the year of the first article referencing the simulator has been used. Other simulators are summarized in chapter 4.13.

4.1 DIMEG

In 2000, the development of the DIMEG (also referred to as UNIPD, or MDRG) at the University of Padua (ital. Padova) started. The first prototype was presented in 2003 and was used in the Projects SAFERIDER, 2BESafe, and Safebike. The DIMEG is considered one of the most advanced motorcycle simulators (Lot & Cossalter, 2014; Lobjois et al., 2016b). It aimed to study man-vehicle interactions in a safe environment. It was designed to test devices improving the rider's safety, like curve warning, speed alert, or frontal collision warning. The developed mechanical structure has five DOF (lateral, roll, pitch, yaw, and steering) and is actuated by five electric servomotors. This structure consists of a cubic cage with three different frames. The first one is responsible for the lateral displacement and yaw motion, the second controls roll motion, and the third enables the pitch movement. A specific washout filter design was developed for the platform motions. Sensors monitor the rider’s steering torque via strain gauges and input at the throttle, brakes, clutch, and gearbox. The rider’s body motion was not considered for the first version of this simulator. After improvements, the rider can also steer the motorcycle by leaning, which is indirectly calculated using sensorized footpegs and a sensorized seat. However, measuring the pressure exerted on the footpegs seemed to have a greater impact. Nowadays, it can also reproduce the effects of suspension and tire characteristics. The simulation model has 11 DOF and is optimized for real-time applications. Later, the model was enhanced to a non-linear 14 DOF model. The visual system consists of a 2mx2m screen and one projector, later replaced by a 180° widescreen. (Cossalter et al., 2004; Nehaoua et al., 2007a,b; Cossalter et al., 2008, 2011; Nehaoua et al., 2011b; Biral et al., 2012; Huth et al., 2012; Lot and Cossalter, 2014; Doz Nadal, 2014; Lot et al., 2016; Will, 2017; Bartolozzi et al., 2022; Pless, 2023).
Objective and subjective validations were carried out for the standard maneuvers acceleration, breaking, steady cornering, lane change, and slalom with 20 participants (Lot and Cossalter, 2014; Savino et al., 2016; Grottoli, 2021). Also, the speed, steering angle, and steering torque have been visually compared and deemed good. Only the roll angle overshoots the 35° of the motorcycle ride by 5° (Lot et al., 2016; Westerhof et al., 2020). With the DIMEG assessments of a new algorithm for the activation of airbag vests (Cossalter et al., 2011), a curve warning system (Huth et al., 2012; Buld et al., 2014), and the appropriate combination HMI elements, like a vibrating glove (Biral et al., 2012) have been done.
In 2011, a portable driving simulator using a fixed handlebar was also developed at the University of Padova. The primary purpose of this simulator is to train riders and conduct behavioral studies. Therefore, the simulator is also used at safety events and driving schools. The characteristic, like counter steering, of a motorcycle are implemented. The rider´s input at the handlebar, throttle, front, and rear brakes are monitored using torque sensors. A roll axis has been implemented to enhance the rider´s feeling of immersion. The total roll motion is split between the physical roll motion of the simulator and a visual roll motion depicted on the screens. However, the participants seem to have difficulties starting from a standstill or executing low-speed maneuvers (Massaro et al., 2013; Bartolozzi et al., 2022; Di Miceli et al., 2022).

4.2 Honda Riding Trainer

The Honda riding trainer is one of the most commonly used motorcycle simulators. It was developed in 2005 and is a compact and low-cost simulator made for rider safety training and can easily be transported. For this purpose, the riding trainer offers 16 courses with seven or eight scenarios with hazardous situations. The scenarios were identified using the "In-depth Analysis of Motorcycle Accidents" report by MAIDS (2004). This report analyzed 921 motorcycle accidents that occurred over three years. These provided scenarios cannot be altered, posing a weakness for research purposes. Several characteristics, like the engine size or light conditions, can be chosen, but the recorded data are not easily accessible. The simulator comprises a frame, a handlebar, pedal controls for clutch and braking, a seat, and a monitor. The rider can only steer the motorcycle using the handlebar. This simulator can represent

©2023 Wildner, D., Diermeyer, F. published by TU Delft OPEN on behalf of the authors.

ISSN: 2667-2812

the seating position of an automatic moped or manual geared motorcycle. (Vidotto et al., 2008; Gamberini et al., 2009; Nehaoua et al., 2011b; Symmons and Mulvihill, 2011; Vidotto et al., 2011; Stedmon et al., 2012; Tagliabue et al., 2013; Benedetto et al., 2014; Tagliabue and Sarlo, 2015; Tagliabue et al., 2017).
The Honda riding trainer is often used for studies related to safe riding, like hazard perception (Vidotto et al., 2011; Liu et al., 2009; Vidotto et al., 2008; Tagliabue et al., 2019), or effects of safety training with a simulator (Symmons & Mulvihill, 2011; Tagliabue et al., 2013; Tagliabue & Sarlo, 2015; Tagliabue et al., 2017). It has been validated for hazard perception training and training of riding skills (Tagliabue et al., 2013; Tagliabue & Sarlo, 2015; Vidotto et al., 2008, 2011; Gianfranchi et al., 2017).

4.3 INRETS Motorcycle Simulator

The INRETS motorcycle simulator was developed as part of the SIMACOM project by a collaboration of INRETS (formerly IFSTTAR), IBISC, and UPSUD Laboratories in France. The simulator was presented in 2007. An identical simulator is placed at the Hellenic Institute of Transport called CERTH-HIT. The two primary purposes of the simulator are training and behavioral studies. The aim was to provide a low-cost simulator with acceptable realism. A modified Yamaha YBR 125, including a steering column with handlebars, gas tank, seat, footrests, throttle, front and rear brakes, and gear shifting devices, is used as a mockup. The platform has three rotational DOF. These have been chosen to be able to reproduce realistic turns (roll) and longitudinal accelerations (pitch) and to simulate the slippage of the rear wheels in accident situations (yaw). Roll and pitch are reproduced by two legs, driven by brushless servomotors, at the front of the platform frame. The rolling angle is split between the tilting of the visual screen and the rolling of the platform. The height of the roll axis is adjustable. An optical encoder is used for the measurement of the steering angle. The simulation software is based on the SIM2 car simulation and uses a linear five DOF motorcycle model. The rider can operate the simulator using original command organs: left and right-hand control pods, accelerator, clutch, brake, pedal, and gearbox selector. Shifts of the rider's body weight can be detected via pressure transducers. The visualization of the scenarios is projected onto a 1,85mx1,24m white screen. The screen size was later adapted to 1,88mx2,4m, and two more screens were placed at the sides. Using three 42" TFT screens is also possible. Thus, a coverage of up to 180° horizontal field of view was achieved. Acoustic information is first provided using a 4.1 sound system and later by a 5.1 sound system. (Nehaoua et al., 2007a, 2008; Cossalter et al., 2009; Nehaoua et al., 2010; Arioui et al., 2010; Cossalter et al., 2011; Nehaoua et al., 2011b; Nehaoua and Arioui, 2008; Benedetto et al., 2014; Shahar et al., 2014; Vieira et al., 2014; Lobjois et al., 2016b; Will, 2017; Lobjois and Mars, 2020; Bougard et al., 2020; Michel et al., 2022; Pless, 2023). This simulator's unique feature is the handlebar's double haptic feedback. One is responsible for the inertial delay on the rider's upper body due to accelerations. This is done by creating an effort on the rider's arms by varying the distance between the saddle and the handlebar. The second force feedback system located at the handlebar simulates the torques resulting from the tire-road contract, the gyroscopic effects, and the front wheel trail (Nehaoua et al., 2007a,b; Nehaoua et al., 2010; Will, 2017; Bartolozzi et al., 2022; Michel et al., 2022; Pless, 2023). Therefore, the INRETS has five DOF.
Using this simulator, the influence of physical and visual roll motion was analyzed (Lobjois et al., 2016a). Another study examined the rider´s steering and gaze behavior and the impact of physical roll and reverse steering on the subjective experience (Lobjois & Mars, 2020). Also, the effects of sleepiness on riding performance have been analyzed (Bougard et al., 2020). Some open-loop tests were carried out to validate the actuation system's performance. These showed satisfactory results; therefore, it was concluded that the simulator fulfills the objectives for every day, dangerous, and extreme situations (Nehaoua et al., 2007a,b; Arioui et al., 2010; Nehaoua et al., 2011b). Nehaoua et al. (2011a) state that the results are "highly acceptable even at low speed".

4.4 NIHON

The simulator has been developed by the NIHON University in Japan to conduct experiments on the relation between the rider and the motorcycle. It has three DOF (roll, pitch, and steering) moved by three AC servo motors. A screen before the rider fills a horizontal field of view of 150°. The participants can steer the motorcycle using the handlebar and by body motion. Corresponding systems simulate sound and wind. Later, the steering torque and attitude angle around the x-axis were inputs. Furthermore, a driving sense simulator provides reaction forces to the handlebar for feedback (Kageyama & Tagami, 2002; Kishida and Kageyama, 2007; Watanabe et al., 2012; Lobjois et al., 2016b). The NIHON has been used to investigate the effects of visual roll on the subject's behavior (Lobjois et al., 2016b).

4.6 Static Motorcycle Simulators at the WIVW

In 2010, the first motorcycle riding simulator at the WIVW was developed. This simulator is equipped with a full-size BMW R100S. The rider can use all physical control interfaces, and the data, like acceleration or steering, can be logged. It is rotatable and fixed at its longitudinal axis, allowing for a passive roll motion due to the rider's movements. A 2mx1.7m screen for the projector is positioned directly in front of the mockup and over a field of view of 60° horizontal and 42° vertical. A 2.0 stereo system provided

©2023 Wildner, D., Diermeyer, F. published by TU Delft OPEN on behalf of the authors.

ISSN: 2667-2812

the sound. Initially, counter-steering was implemented. However, the participants failed to steer the motorcycle, so they changed to positive steering. Data from a real motorcycle ride doing different maneuvers have been used to validate the motorcycle simulator's acceleration, brake pressure, and pitch angle (Will and Schmidt, 2009; Buld et al., 2014; Will and Schmidt, 2015; Will, 2017). This motorcycle simulator was, for example, used to assess the rider's workload (Will, 2017). In 2014, it was substituted by a new static simulator with a BMW R1200RT and a KTM1290 Super Adventure Bike as mockups. Further updates to the simulator include the coverage of a horizontal field of view of 180° using three 55" flat screens. Two 7" TFT displays are used as rearview mirrors, and a 10" touch screen is used as a cockpit. Body shakers imitate haptic feedback of the engine vibrations, and an electrical actuator produces a steering torque at the handlebar, like before the positive steering concept is implemented (Will, 2017, 2018; Hammer et al., 2021; Sevarin et al., 2020). Studies like assessing visual and haptic HMI or concepts for hazard warnings have been conducted (Sevarin et al., 2020). The latest update to this static simulator is an adaptable mockup. The handlebar, seat, and foot pegs can be positioned for model-specific research (Muehlbacher et al., 2023).

4.5 MotorcycleSim

This simulator is based at Nottingham University. It was designed to investigate human factors research and human-machine interactions. It consists of a fully equipped Triumph Daytona 675 (except the motor and drive train) mounted on a parallel platform. The rider input on the throttle, brake lever, brake pedal, gear selector, and clutch lever are recorded and fed into the commercially available "STISIM-Drive" Software. Two pairs of pneumatic actuators allow for a leaning motion. They work in reciprocal pairs and can be operated in a static (pressure of approximately 10bar) or dynamic mode. In the latter mode, the leaning angle can change from -25° to +25° in less than two seconds and has a sampling of 40 Hz. Thus, the rider has to balance his weight. The rolling axis is located at the base of the wheels. The simulator can be used in four modes: Static simulation with 'STISIM-Drive'; cornering/leaning training with and without 'STISIM-Drive'; And an advanced dynamic model with 'STISIM-Drive'. The leaning, acceleration, and deceleration are visually represented on a 285cm×228cm flat screen via tilting or pitching the scenery. At the bottom of the screen, a speedometer, tachometer, gear selection, and view of the road behind are presented. The breaks are connected, and the pressure is distributed 75% at the front and 25% at the rear brake. For wet scenarios, the pressure is equally distributed. It is possible to use either a counter- or positive-steering concept. However, it must be defined for each ride and cannot be changed during rides. This is planned for further development. The sound is provided using 5.1 surround sound speakers (Stedmon et al., 2011a,c,b; Benedetto et al., 2014; Buld et al., 2014; Stedmon et al., 2011b; Crundall et al., 2012; Stedmon et al., 2012; Crundall et al., 2014; Nugent et al., 2019). Therefore, the MotorcycleSim can investigate motorcycle design, rider equipment, rider behavior, road safety, and training (Stedmon et al., 2011b). Exemplary studies investigate rider behavior and the effect of experience (Crundall et al., 2012, 2014) or the behavior when approaching hazardous situations (Crundall et al., 2013).

4.7 MUARC Advanced Driving Simulator

The interactive Monash University Accident Research Centre (MUARC) riding simulator uses a real Honda NSR 150 as a mockup. The mockup is fixed statically and cannot replicate dynamic movements. The participant can control the motorcycle using the handlebar (steering angle), throttle, and both brakes. The dynamics of the simulator are calculated using the software Carsim, and the visualization is projected onto a curved projection screen, which provides a 180° horizontal and 40° vertical field of view (Filtness et al., 2013; Filtness & Rudin-Brown, 2012; Nugent et al., 2019). Some modifications have been made to improve the simulator's fidelity: Counter-steering was implemented for a more realistic riding feeling. Now, counter- as well as positive-steering are possible. The steering assembly was attached to the frame using two pre-loaded helical springs to achieve a roll angle for the lateral motion cues. The mockup was mounted on a three DOF motion base to reproduce yaw, pitch, and roll motions. The motion is only made physically; the visualization on three forward-surround screens does not tilt (Savino et al., 2016; Nugent et al., 2019). As validation, the simulator was subjectively evaluated in terms of fidelity. It was rated as reasonable and realistic, and 11 out of 12 participants rated the steering control as acceptable to very good. Additionally, the steering torques were compared to real-world and simulated values. While the steering torques were generally higher, the speed variations and signs of the input were consistent (Savino et al., 2016; Nugent et al., 2019).

4.8 CAVE Motorcycle Simulator

The CAVE Motorcycle simulator was built at Keio University as a part of Kenichiro Ito's doctoral thesis. The aim was an evaluation of a Head-Up-Display for motorcycles (Ito, 2017). The mockup is a scooter-type simulator but is adaptable to represent the positions of a naked, sports, or roadster bike. The rider´s input on the handle (steering angle), accelerator, and brakes are measured using potentiometers. The simulation software has car dynamics, so counter-steering is not implemented. The CAVE system consists of

©2023 Wildner, D., Diermeyer, F. published by TU Delft OPEN on behalf of the authors.

ISSN: 2667-2812

three screens, which are placed on the sides and front of the rider, as well as one additional screen on the floor (Ito, 2017; Ito et al., 2015, 2013; Ogi, 2015). So far, no objective validation has been shown, but the measurement of an eye-tracking device shows similar viewpoint movements for the two evaluated subjects (Ito, 2017).

4.9 Postura Motergo

In 2014, the ergonomic motorcycle test rig, Postura Motergo, was developed at the Motorcycle Engineering Technology Lab of the University Teknologi MARA in Malaysia. It has been designed to investigate motorcycle ergonomics and can cater to four riding postures based on the Riding Posture Classification RIPOC. The mockup is custom-made and consists of a handlebar, an adjustable tank cover, the seat, and footpegs. The handlebar, seat, foot-peg length, and height positions can be adjusted. It has semiautomated equipment and electronic devices to include the HMI in the simulation. Initially, the Postura Motergo had two DOF, using springs and two rotational shafts to replicate the movement. The initial setup used only a flat screen in front of the rider for the visualization (Azhar, 2014; Fauzi et al., 2015a,b; Rashid et al., 2017). Further developments of the test rig include synchronizing the handlebar and foot-pegs adjustment and adding one more DOF: now rolling, pitching, and steering are possible. The roll and pitch motion were enabled using a DC motor. To improve the visualization, a 180° curved screen was designed. Using potentiometers to measure the rider's input, the simulator can be controlled using the steering (angle), throttle, front and rear brake, clutch, and gear inputs. The simulator also includes sound, vibrations, and wind simulation (Fauzi et al., 2015b; Wan Fauzi et al., 2017).

4.10 DESMORI Simulators (at WIVW and at BMW)

There are two DESMORI simulators, sometimes referred to as twin simulators. One is located in Munich at BMW, and the other is in Würzburg at WIVW. They use the same vehicle dynamics model (VI-grade BikeRealTime). Both simulators use standard interfaces regarding handlebar, throttle, clutch, brakes, and gear shifter, and 7" TFT displays as rearview mirrors. Their main difference is how they measure the rider-induced torques and their steering feedback (Delgado Ojeda, 2019; Pless et al., 2016; Will et al., 2016). Additionally, they have developed differently over the past years.
A BMW K1600GT was initially used as a mockup for the BMW DESMORI simulator, mounted on a six DOF motion platform. The rider can manipulate the virtual motorcycle using the steering angle, front and rear brake, clutch, shift, and body position. The rider's motions are captured using a camera tracking system, which tracks two labels on the rider's back. A 4mx3m screen was used for the visualization. A 4.1 sound system provides sound. By manipulating the BUS system, the instrument cluster shows the information on speed or engine revolutions. An electric drive can reproduce steering torques up to 35Nm. A so-called G-vest can be used to simulate the feeling of a long-term acceleration. Two small fans simulate the cooling effect of airflow, which increases proportionally with the longitudinal speed (Doz Nadal, 2014; Guth et al., 2016; Will et al., 2016; Will, 2017; Delgado Ojeda, 2019; Werle & Diermeyer, 2021). More recent studies using this simulator use a static mode (Werle & Diermeyer, 2021). This simulator has been used to measure human processing by analyzing the mean glance duration and determine the importance of realistic steering feedback (Guth et al., 2016; Savino et al., 2016). After the DESMORI project, the simulator was further developed, and a new curved screen was built, covering a 310° horizontal field of view. Additionally, the steering input was changed to the steering torque. The WIVW DESMORI is in the center of a cylindrical projection screen with a horizontal field of view of 220°. Additionally, a floor with a projection screen has been built at the height of the road surface to enhance the simulation. The virtual environment is simulated using SILAB, a WIVW in-house software. The frame, fairing, and controls of a BMW F800S are mounted on a six DOF steward platform. The rider can interact with the motorcycle using the handlebar, gear selector, clutch, brake pedal/lever, and changing the center of gravity by leaning. The change of the mass distribution due to the rider's motion is detected via a load cell measuring the induced roll torque. This system is positioned between the mockup and the motion platform and builds a longitudinal axis relative to the motion platform. However, the rotational movement is prohibited by the torque sensor. An 80Nm steering torque can be generated via an electric actuator to rotate the handlebar accordingly to the virtual motorcycle. The sound system is integrated into a helmet with headphones. A customized airbag west with a rope mechanism is used to cue proprioception of the accelerations and wind forces and can generate forces up to 300N. To simulate the vibrations a shaker is placed beneath the seat (Pless, 2023; Ghafarian et al., 2023; Pless et al., 2016; Will et al., 2016; Delgado Ojeda, 2019; Merkel et al., 2019; Scherer et al., 2020; Westerhof et al., 2020; Grottoli, 2021; Hammer et al., 2021; Will et al., 2022; Merkel et al., 2022). This simulator has been developed to investigate human-machine interfaces on motorcycles (Scherer et al., 2020). For example, it has been used to rate a new HMI concept or to analyze the rider´s effort and distraction using it (Pless, 2023; Will et al., 2022). The WIVW DESMORI simulator was validated for speed perception and workload, presence, as well as rider behavior in different minimal scenarios (Will 2017, Hammer et al. 2021).

©2023 Wildner, D., Diermeyer, F. published by TU Delft OPEN on behalf of the authors.

ISSN: 2667-2812

4.11 MOTORIST

The MOTORIST is a scooter simulator designed by TU Delft and Simens in 2016. The primary use of the simulator is riding training. They use a Piaggio Beverly 350cc as a mockup, mounted on a six DOF hexapod platform by MOOG. A traditional washout filter is used for the movement cueing. The axis of the rolling motion is located at approximately the height of the rider's head. The rider can steer the simulator using the handlebar (steering angle), throttle, and front and rear brakes. The head-mounted display Oculus Rift Developer Kit 2 is used for the visualization. The sound is provided via headphones integrated into the helmet. The steering works with the counter-steering principle, and a steering-torque motor provides haptic force feedback. The Motorcycle is stabilized when standing still, and the roll dynamics are augmented for low speeds (up to 3m/s). For safety reasons, the rider can be secured using a harness (Will, 2017; Kovacsova et al., 2020; Grottoli, 2021; Grottoli et al., 2023; Ghafarian et al., 2023).
The MOTORIST simulator model has been validated for accelerating, braking, and turning. The model data was compared with data collected on an instrumented motorcycle. Also, the subjective validation showed good levels of simulator presence (Grottoli et al., 2019). It was also validated with a focus on low speeds of 0m/s and 10m/s. The results showed comparable velocities and positions for the maneuvers accelerating, breaking, and turning (Grottoli et al., 2023).

4.12 Cruden Simulator

Cruden is a company that specializes in developing simulators. Their motorcycle simulator uses a Ducati Panigale as their mockup, mounted on a six DOF platform. For the movement simulation, a classical washout filter design is used. Besides the actual motorcycle suspensions, a virtual roll spring facilitates the take-off from a standing position with a stiffness of 100kN/rad. This gradually fades out to zero above a velocity of 3m/s. Cruden developed a software called Panthera to integrate vehicle dynamics, vision, audio, and motion platform control into one application. This software uses an adapted model of the one developed and validated by Sharp and Alsted. The rider movements are captured using two Intel RealSense SR300´s cameras. This allows both pitch and roll rider-induced torques to be considered in the vehicle dynamics simulation. The camera system uses natural markers like facial features and shapes. The Oculus Rift is used as a head-mounted display for visualization and can trek the rider's head movements. The acoustic feedback is provided using a surround system (Westerhof, 2018; Delgado Ojeda, 2019; Westerhof et al., 2020; Pless, 2023; Grottoli, 2021; Ghafarian et al., 2023).
A subjective evaluation of the speed perception and path following with velocities between 50 and 120 km/h was conducted. Their assessment of the benefits of the motion platform showed an increase in performance and subjective evaluation. However, at the end of this experiment, not all participants could identify the rides with motion from those without. The authors concluded that the simulator can be used for research and development (Westerhof, 2018; Westerhof et al., 2020; Grottoli, 2021).

4.13 Further Motorcycle Simulators

In addition to the presented simulators, further simulators are listed in this section for completeness. At the University of Tokyo, a hexapod-based simulator with six DOF was built (Pless, 2023; Ferrazzin et al., 2002). Wu et al. constructed a motorcycle simulator for training patients with spinal cord injuries (Wu et al., 2011). The University of Florence developed a low-cost motorcycle riding simulator called MOVING (Pinelli et al., 2018; Di Miceli et al., 2022). The Southampton Simulator is an adjustable motorcycle mockup that can vary the distance between the seat and the handlebar by 221mm (Thomas et al., 2017). At the Nanyang Technological University Transportation Laboratory, a static Scooter simulator was used to study hazard response times (Wong, 2019). A riding simulator was developed in 2020 in Vietnam to research rider behavior (Vu et al., 2020). In 2022, a low-complexity simulator was designed to investigate similarities in steering control (Bartolozzi et al., 2022).
Commercial simulators are, for example, the California Superbike School (Stedmon et al., 2011c), the IFZ (Stedmon et al., 2012), the EF-Bike (Pless, 2023), the Kawasaki (Nehaoua et al., 2011b; Hosokawa et al., 2022) or the VR Project Simulator (Will, 2017).

5 Conclusion

All described simulators are primarily used for human factor research, especially focusing on display and safety concepts, and no exclusive focus on vehicle development was found. Possible reasons are the unique dynamics of a single-track vehicle and the limited possibility of increasing passive safety. For motorcyclists, improvements in active safety offer considerable potential, and human-in-the-loop studies are needed to investigate the interaction with the new safety system. In the current state of motorcycle research, this area offers great potential when working with a simulator. Thus, ergonomics and human behavior are significant topics in motorcycle simulator research. For example, the question of motorcycle geometry affecting ergonomics is not yet determined, even though simulators like the Postura Motergo or the static WIVW simulator try to consider the different motorcycle

©2023 Wildner, D., Diermeyer, F. published by TU Delft OPEN on behalf of the authors.

ISSN: 2667-2812

geometries. While ergonomics affects the rider, their stress, reactions, and safety greatly (Stoffregen, 2010), a detailed analysis of the needed methods and requirements regarding the simulator for these human factors experiments has not yet been conducted. Also, the different validation studies of the simulators are interesting for developing validation designs for motorcycle simulators. A standard process for the validation would also offer great potential for improvements in this research area.

Acknowledgements

As the first author, Dorothea Wildner initiated the research and conducted the literature review. Frank Diermeyer revised the content of this work critically and made an essential contribution to the conception. This research was funded by BMW Motorrad.

References

Arioui, H., Nehaoua, L., Hima, S., Seguy, N., & Espie, S. (2010). Mechatronics, design, and modeling of a motorcycle riding simulator. IEEE/ASME Transactions on Mechatronics, 15(5):805–818.

Azhar, M. F. (2014). Structural analysis of an ergonomic motorcycle test rig using finite element analysis (fea).

Bartolozzi, M., Berzi, L., Meli, E., and Savino, G. (2022). Similarities in steering control between cars and motorcycles: application to a low-complexity riding simulator. Meccanica, 57(11):2863–2883.

Benedetto, S., Lobjois, R., Faure, V., Dang, N.-T., Pedrotti, M., and Caro, S. (2014). A comparison of immersive and interactive motorcycle simulator configurations. Transportation research part F: Traffic psychology and behaviour, 23:88–100.

Biral, F., Lot, R., Rota, S., Fontana, M., and Huth, V. (2012). Intersection support system for powered two-wheeled vehicles: Threat assessment based on a receding horizon approach. IEEE Transactions on Intelligent Transportation Systems, 13(2):805–816.

Born, K.-P. (1989). Entwurf und Aufbau eines Motorradfahrsimulators unter Verwendung eines digitalen Aussensichtsystems und Untersuchung seiner verkehrssicherheitstechnischen Anwendungsmöglichkeiten. PhD thesis, Bergische Universitat Wuppertal.

Bouaouni, M. Y., Yahia, R. A. A., and Boubezoul, A. (2021). Driving-pattern identification and event detection based on an unsupervised learning framework: Case of a motorcycle-riding simulator. IEEE Access, 9:158456–158469.

Bougard, C., VanBeers, P., Sauvet, F., Drogou, C., Guillard, M., Dorey, R., Gomez-Merino, D., Dauguet, J., Takillah, S., Espie, S., et al. (2020). Motorcycling performance and sleepiness during an extended ride on a dynamic simulator: relationship with stress biomarkers. Physiological measurement, 41(10):104004.

Buld, S., Will, S., Kaussner, A., and Kruger, H.-P. (2014). Entwicklung eines Verfahrens zur Erfassung der Fahrerbeanspruchung beim Motorradfahren.

Chiyoda, S., Yoshimoto, K., Kawasaki, D., Murakami, Y., and Sugimoto, T. (2002). Development of a motorcycle simulator using parallel manipulator and head mounted display. In The Proceedings of the International Conference on Motion and Vibration Control 6.1, pages 599–602. The Japan Society of Mechanical Engineers.

Colburn, N., Meyer, R. D., Wrigley, M., & Bradley, E. L. (1993). Should motorcycles be operated within the legal alcohol limits for automobiles. The Journal of Trauma, 35(2):183–186.

Cossalter, V., Alberto, D., and Lot, R. (2004). Development and validation of a motorcycle riding simulator. FISITA F.

Cossalter, V., Lot, R., Massaro, M., and Sartori, R. (2009). Development and testing of assistant rider systems with the unipd motorcycle riding simulator. In XIX Congresso Aimeta Associazone Italiana di Meccanica Teorica e Applicata, Italy, page 24.

Cossalter, V., Lot, R., Massaro, M., and Sartori, R. (2011). Development and validation of an advanced motorcycle riding simulator. Proceedings of the Institution of Mechanical Engineers, Part D: Journal of Automobile Engineering, 225(6):705–720.

Cossalter, V., Lot, R., Sartori, R., Massaro, R., et al. (2008). A motorcycle riding simulator for the improvement of the rider safety. FISITA F, pages 11–015.

Crundall, D., Stedmon, A.W., Crundall, E., & Saikayasit, R. (2014). The role of experience and advanced training on performance in a motorcycle simulator. Accident Analysis & Prevention, 73:81–90.

Crundall, E., Crundall, D., & Stedmon, A. W. (2012). Negotiating left-hand and right-hand bends: A motorcycle simulator study to investigate experiential and behaviour differences across rider groups. PLoS One, 7(1):e29978.

Crundall, E., Stedmon, A. W., Saikayasit, R., & Crundall, D. (2013). A simulator study investigating how motorcyclists approach side-road hazards. Accident Analysis & Prevention, 51:42–50.

Dahl, C. W. (1971). Motorcycle riding simulator. US Patent 3686776A.

©2023 Wildner, D., Diermeyer, F. published by TU Delft OPEN on behalf of the authors.

ISSN: 2667-2812

Delgado Ojeda, R. J. (2019). Design of a motorcycle mount with integrated roll-and-pitch-torque measurement on a motorcycle simulator. Master's thesis, Universitat Politecnica de Catalunya.

Di Miceli, D., Bartolozzi, M., Berzi, L., and Savino, G. (2022). Sensibilization of a motorcycle simulator to the effects of the roll motion: Modelling and experimental validation. Proceedings of the Institution of Mechanical Engineers, Part D: Journal of Automobile Engineering, page 09544070221136613.

Doz Nadal, A. (2014). Evaluation of acceleration sensation induced by proprioception on a motorcycle simulator.

Fauzi, W., Omar, A., Jaafar, R., Ma'arof, M., Rashid, H., and Fauzi, W. (2015a). Adjustable tank cover for Postura Motergo™ utilizing rib and spine chassis (risctm). Procedia Manufacturing, 3:2635–2641.

Fauzi, W. M. S. W., Omar, A. R., Jaafar, R., Ma'arof, M. I. N., and Rashid, H. (2015b). A review on enhancing human machine environment interface for Postura Motergo™. Jurnal Teknologi, 76(11):21–25.

Ferrazzin, D.; Salsedo, F.; Barbagli, F.; Avizzano, C. A.; Di Pietro, G.; Brogni, A. et al. (2009): The MORIS Motorcycle Simulator: An Overview. In: Dustin Williams, Jace Allen und Ramadev Hukkeri (Hg.): Electronic control module network and data link development and validation using hardware in the loop systems. 400 Commonwealth Drive, Warrendale, PA, United States. [Warrendale, PA]: SAE International (SAE technical paper series).

Marcacci, M., et al. (2002). The Moris motorcycle simulator: an overview. SAE Transactions, pages 199–210.

Filtness, A. & Rudin-Brown, C. M. (2012). Drinking and riding: Is subjective workload related to performance? In Proceedings of the Australasian Road Safety Research, Policing and Education Conference 2012, pages 1–10. Australasian College of Road Safety (ACRS).

Filtness, A. J., Rudin-Brown, C. M., Mulvihill, C. M., & Lenne, M. G. (2013). Impairment of simulated motorcycle riding performance under low dose alcohol. Accident Analysis & Prevention, 50:608–615.

Gamberini, L., Spagnolli, A., Furlan, S., Chalambalakis, A., Bertoli, L., Scottini, R., and Turra, P. (2009). Users performance with a riding simulator: The role of the social setting.

Ghafarian, M., Watson, M., Mohajer, N., Nahavandi, D., Kebria, P. M., and Mohamed, S. (2023). A review of dynamic vehicular motion simulators: Systems and algorithms. IEEE Access.

Gianfranchi, E., Spoto, A., and Tagliabue, M. (2017). Risk profiles in novice road users: relation between moped riding simulator performance, on-road aberrant behaviors and dangerous driving. Transportation research part F: Traffic psychology and behaviour, 49:132–144.

Grottoli, M. (2021). Development and evaluation of a motorcycle riding simulator for low speed maneuvering. PhD thesis, Delft University of Technology Delft, The Netherlands.

Grottoli, M., Celiberti, F., van der Heide, A., Lemmens, Y., and Happee, R. (2019). Motorcycle multibody model validation for human-in-the-loop simulation. In Driving simulation & virtual reality conference & exhibition.

Grottoli, M., Mulder, M., and Happee, R. (2023). Motorcycle simulator subjective and objective validation for low speed maneuvering. Proceedings of the Institution of Mechanical Engineers, Part D: Journal of Automobile Engineering, 237(9):2175–2189.

Guth, S., Geiger, M., Parduzi, A., Will, S., Pless, R., and Winner, H. (2016). Method to assess the processing of optical information by non-primary riding tasks while riding a motorcycle. Proceedings, Bicycle and Motorcycle Dynamics 2016.

Hammer, T., Pless, R., Will, S., Neukum, A., and Merkel, N. L. (2021). Anwendungsmöglichkeiten von Motorradsimulatoren. Berichte der Bundesanstalt fur Strasenwesen. Unterreihe Mensch und Sicherheit, (323).

Hosokawa, S., Nagasaka, K., and Watanabe, H. (2022). Development of evaluation technology for motorcycle advanced rider assistance systems. Technical report, SAE Technical Paper.

Huth, V., Biral, F., Martin, O., & Lot, R. (2012). Comparison of two warning concepts of an intelligent curve warning system for motorcyclists in a simulator study. Accident Analysis & Prevention, 44(1):118–125.

Ito, K. (2017). Design in immersive virtual reality environment for information presentation of motorcycle head-up display. PhD thesis, Keio University.

Ito, K., Nishimura, H., and Ogi, T. (2015). Head-up display for motorcycle navigation. In SIGGRAPH Asia 2015 Head-Up Displays and their Applications, pages 1–3.

Ito, K., Tateyama, Y., Lee, H., Nishimura, H., & Ogi, T. (2013). Development of head-up display for motorcycle navigation system. In Asia-Pasific Conference on Systems Engineering (APCOSEC), No. TS–05–2.

©2023 Wildner, D., Diermeyer, F. published by TU Delft OPEN on behalf of the authors.

ISSN: 2667-2812

Kageyama, I. and Tagami, N. (2002). Development of a riding simulator for two-wheeled vehicles. JSAE review, 23(3):347–352.

Kishida, T. & Kageyama, I. (2007). A study on riding simulator for motorcycle. In Driving Simulation Conference, North America 2007 (DSC-NA 2007) Ford Motor CompanyNational Highway Traffic Safety AdministrationUniversity of Iowa, Iowa CityTransportation Research Board.

Kovacsova, N., Grottoli, M., Celiberti, F., Lemmens, Y., Happee, R., Hagenzieker, M. P., and de Winter, J. C. (2020). Emergency braking at intersections: A motion-base motorcycle simulator study. Applied ergonomics, 82:102970.

Liu, C. C., Hosking, S. G., and Lenne, M. G. (2009). Hazard perception abilities of experienced and novice motorcyclists: An interactive simulator experiment. Transportation research part F: Traffic psychology and behaviour, 12(4):325–334.

Lobjois, R., Dagonneau, V., and Isableu, B. (2016a). The contribution of visual and proprioceptive information to the perception of leaning in a dynamic motorcycle simulator. Ergonomics, 59(11):1428–1441.

Lobjois, R. and Mars, F. (2020). Effects of motorcycle simulator configurations on steering control and gaze behavior in bends. Journal of experimental psychology: applied, 26(1):108.

Lobjois, R., Siegler, I. A., and Mars, F. (2016b). Effects of visual roll on steering control and gaze behavior in a motorcycle simulator. Transportation research part F: Traffic psychology and behaviour, 38:55–66.

Lot, R. and Cossalter, V. (2014). A virtual-reality framework for the hardware-in-the-loop motorcycle simulation. Modeling, Simulation and Control of Two-Wheeled Vehicles, pages 183–195.

Lot, R., Massaro, M., Cossalter, V., and Sadauckas, J. (2016). Using simulators for the assessment of handling of motorcycles.

MAIDS, A. (2004). In-depth investigation of accidents involving powered two-wheelers. Final report 1.2. Brussels: Association of European Motorcycle Manufacturers (ACEM).

Massaro, M., Cossalter, V., Lot, R., Rota, S., Ferrari, M., Sartori, R., and Formentini, M. (2013). A portable driving simulator for single-track vehicles. In 2013 IEEE International Conference on Mechatronics (ICM), pages 364–369. IEEE.

Merkel, N. L., Pless, R.,Winner, H., Hammer, T., Norbert, S., andWill, S. (2019). Tolerability of unexpected autonomous emergency braking maneuvers on motorcycles-a methodology for experimental investigation. In National Highway Traffic Safety Administration (Ed.), The 26th ESV Conference Proceedings. International Technical Conference on the Enhanced Safety of Vehicles (ESV), Eindhoven, The Netherlands.

Merkel, N. L., Pless, R.,Winner, H., Hammer, T., Schneider, N., andWill, S. (2022). Automatische Notbremssysteme für Motorräder.

Michel, P., Bouaziz, S., Delgehier, F., and Espie, S. (2022). Rider in the loop dynamic motorcycle simulator: An instrumentation strategy focused on human acceptability. Electronics, 11(17):2690.

Miyamaru, Y., Yamasaki, G., and Aoki, K. (2002). Development of a motorcycle riding simulator. JSAE review, 23(1):121–126.

Muehlbacher, D., Will, S., Merkel, N., Perterer, N., Mlakar, S., Haller, M., and Perterer, M. (2023). Compliance to eco-riding recommendations on an e-scooter: Effects on energy consumption and user acceptance. Transportation Research Interdisciplinary Perspectives, 20:100831.

Nehaoua, L. and Arioui, H. (2008). Parameters identification for motorcycle simulator's platform characterization. In AIP Conference Proceedings, volume 1019, pages 133–138. American Institute of Physics.

Nehaoua, L., Arioui, H., & Fridman, L. (2011a). Force feedback control based on vgsta for single track riding simulator. In 2011 50th IEEE Conference on Decision and Control and European Control Conference, pages 8243–8248. IEEE.

Nehaoua, L., Arioui, H., & Mammar, S. (2011b). Review on single track vehicle and motorcycle simulators. In 2011 19th Mediterranean Conference on Control & Automation (MED), pages 940–945. IEEE.

Nehaoua, L., Hima, S., Arioui, H., & Seguy, N. (2008). A new motorcycle simulator platform: Mechatronics design, dynamics modeling and control. IFAC Proceedings Volumes, 41(2):4452–4457.

Nehaoua, L., Hima, S., Arioui, H., Seguy, N., & Espie, S. (2007a). Design and modeling of a new motorcycle riding simulator. In 2007 American Control Conference, pages 176–181. IEEE.

Nehaoua, L., Hima, S., Arioui, H., Seguy, N., & Espie, S. (2007b). Open-loop test and validation of a new two-wheeled vehicle riding simulator. In 2007 European Control Conference (ECC), pages 4911–4916. IEEE.

Nehaoua, L., Khettat, A., Arioui, H., Imine, H., and Espie, S. (2010). Rider steer torque estimation for motorcycle riding simulator. IFAC Proceedings Volumes, 43(18):505–510.

©2023 Wildner, D., Diermeyer, F. published by TU Delft OPEN on behalf of the authors.

ISSN: 2667-2812

Norfleet, D., Wagner, J., Alexander, K., & Pidgeon, P. (2009). Automotive driving simulators: research, education, and entertainment. SAE International Journal of Passenger Cars-Electronic and Electrical Systems, 2(2009-01-0533):186–193.

Nugent, M., Savino, G., Mulvihill, C., Lenne, M., and Fitzharris, M. (2019). Evaluating rider steering responses to an unexpected collision hazard using a motorcycle riding simulator. Transportation research part F: Traffic psychology and behaviour, 66:292–309.

Ogi, T. (2015). Design and evaluation of hud for motorcycle using immersive simulator. In SIGGRAPH Asia Head-Up Displays and their Applications, pages 5–1.

Pinelli, G., Rajan, P., Berzi, L., Savino, G., et al. (2018). The influence of body lean on the realism of a motorcycle riding simulator adopting counter-steering approach. AIAS–Associazione italiana per l'analisi delle sollecitazioni, 47.

Pless, R., Will, S., Guth, S., Hofmann, M., and Winner, H. (2016). Approach to a holistic rider input determination for a dynamic motorcycle riding simulator. In Proceedings of the Bicycle and Motorcycle Dynamics Conference, Milwaukee, WI, USA, pages 21–23.

Pless, R. A. M. (2023). Dual loop rider control of a dynamic motorcycle riding simulator.

Rashid, H., Omar, A. R., Ahmad, I. N., Mohamed, Z., Wan Fauzi, W. M. S., Mahmud, Z., and Haron, R. (2017). Motorcyclists'prolonged riding simulation: The setup and procedures. Journal of Mechanical Engineering (JMechE), (5):197–208.

Savino, G., Pierini, M., and Lenne, M. G. (2016). Development of a low-cost motorcycle riding simulator for emergency scenarios involving swerving. Proceedings of the Institution of Mechanical Engineers, Part D: Journal of Automobile Engineering, 230(14):1891–1903.

Scherer, F., Pless, R., and Winner, H. (2020). Identification of rider-vehicle coupling on motorcycles and riding simulators. Symposium on the Dynamics and Control of Single Track Vehicles.

Sevarin, A.,Will, S., Mikschofsky, N., Menato, L., Hammer, T., Schneider, N., and Mark, C. (2020). Assessment of visual and haptic HMI concepts for hazard warning of powered two-wheeler riders. Proceedings of the 13th International Motorcycle Conference.

Shahar, A., Dagonneau, V., Caro, S., Israel, I., and Lobjois, R. (2014). Towards identifying the roll motion parameters of a motorcycle simulator. Applied ergonomics, 45(3):734–740.

Stedmon, A., Brickell, E., Hancox, M., Noble, J., & Rice, D. (2012). MotorcycleSim: a user-centred approach in developing a simulator for motorcycle ergonomics and rider human factors research. Advances in Transportation Studies, (27).

Stedmon, A., Crundall, D., Crundall, E., Irune, A., Saikayasit, R., Van Loon, E., Ward, P., and Greig, N. (2011a). Investigating motorcycle rider behaviour: developing an integrated experiment approach. Advances in Transportation Studies: Special,(2010), pages 63–78.

Stedmon, A., Young, M., and Hasseldine, B. (2009). Keeping it real or faking it: The trials and tribulations of real road studies and simulators in transport research. In Contemporary Ergonomics 2009: Proceedings of the International Conference on Contemporary Ergonomics 2009, volume 21. CRC Press.

Stedmon, A. W., Crundall, D., Crundall, E., Saikayasit, R., van Loon, E., Irune, A., Ward, P., & Greig, N. (2011b). 'STIsimdrive ' meets 'motorcycleSim': Using driving simulation software to develop a unique motorcycle simulator for rider behavior research. In HCI International 2011–Posters' Extended Abstracts: International Conference, HCI International 2011, Orlando, FL, USA, July 9-14, 2011, Proceedings, Part II 14, pages 76–80. Springer.

Stedmon, A. W., Hasseldine, B., Rice, D., Young, M., Markham, S., Hancox, M., Brickell, E., and Noble, J. (2011c). 'motorcyclesim: an evaluation of rider interaction with an innovative motorcycle simulator. The Computer Journal, 54(7):1010–1025.

Stoffregen, Jürgen (2010): Motorradtechnik. Grundlagen und Konzepte von Motor, Antrieb und Fahrwerk. Wiesbaden: Springer Fachmedien.

Symmons, M. and Mulvihill, C. (2011). A simulator comparison of riding performance between new, returned and continuing motorcycle riders. In Driving Assessment Conference, volume 6. University of Iowa.

Tagliabue, M., Da Pos, O., Spoto, A., and Vidotto, G. (2013). The contribution of attention in virtual moped riding training of teenagers. Accident Analysis & Prevention, 57:10–16.

Tagliabue, M., Gianfranchi, E., and Sarlo, M. (2017). A first step toward the understanding of implicit learning of hazard anticipation in inexperienced road users through a moped-riding simulator. Frontiers in Psychology, 8:768.

©2023 Wildner, D., Diermeyer, F. published by TU Delft OPEN on behalf of the authors.

ISSN: 2667-2812

Tagliabue, M. and Sarlo, M. (2015). Affective components in training to ride safely using a moped simulator. Transportation research part F: Traffic psychology and behaviour, 35:132–138.

Tagliabue, M., Sarlo, M., and Gianfranchi, E. (2019). How can on-road hazard perception and anticipation be improved? Evidence from the body. Frontiers in Psychology, 10:167.

Thomas, L., Lot, R., et al. (2017). A new test rig for motorcycle rider impedance measurement. In Proceeding of the 15th European Automotive Congress, Madrid, Spain.

Vidotto, G., Bastianelli, A., Spoto, A., and Sergeys, F. (2011). Enhancing hazard avoidance in teen-novice riders. Accident Analysis & Prevention, 43(1):247–252.

Vidotto, G., Bastianelli, A., Spoto, A., Torre, E., Sergeys, F., et al. (2008). Using a riding trainer as a tool to improve hazard perception and awareness in teenagers. Adv. Transp. Stud. Int. J. B, 16:51–60.

Vieira, R., Steidle, M., Vieira, A., and Santos, R. A. P. (2014). Conceptual architecture of motorcycle simulators for the training of novice riders. In Proceedings of the 10th International Motorcycle Conference, Cologne, Germany.

Vu, A. T., Nguyen, M. T., Nguyen, D. V. M., and Khuat, V. H. (2020). Investigating the effect of blood alcohol concentration on motorcyclist's riding performance using an advanced motorcycle simulator. Transportation research part F: Traffic psychology and behaviour, 73:1–14.

Wan Fauzi, W. M. S., Omar, A. R., and Rashid, H. (2017). Enhancement of Postura Motergo^{TM}: From an ergonomic motorcycle test rig to a full-scale simulator. Journal of Mechanical Engineering (JMechE), (4):43–59.

Watanabe, A., Kageyama, I., and Kuriyagawa, Y. (2012). Construction of riding simulator for two-wheeled vehicle.

Werle, A. and Diermeyer, F. (2021). An investigation of smart glasses for motorcyclists as a head-up-display device-performed on a riding simulator. In International Conference on Applied Human Factors and Ergonomics, pages 226–237. Springer.

Westerhof, B. (2018). Evaluation of the Cruden motorcycle simulator.

Westerhof, B., De Vries, E., Happee, R., and Schwab, A. (2020). Evaluation of a motorcycle simulator. Symposium on the Dynamics and Control of Single Track Vehicles.

Will, S. (2017). Development of a presence model for driving simulators based on speed perception in a motorcycle riding simulator. PhD thesis, Universitat Wurzburg.

Will, S. (2018). A new approach to investigate powered two wheelers' interactions with passenger car drivers: the motorcycle–car-multi-driver simulation. UR: BAN Human Factors in Traffic: Approaches for Safe, Efficient and Stress-free Urban Traffic, pages 393–402.

Will, S., Pless, R., and Guth, S. (2016). Bringing single track vehicle dynamics to motorcycle riding simulators–results of a pilot study. Proceedings, Bicycle and Motorcycle Dynamics 2016.

Will, S. and Schmidt, E. A. (2009). Workload assessment for motorcycle riders. Wuerzburg Institute for Traffic Sciences (WIVW). Veitshoechheim, Germany.

Will, S. and Schmidt, E. A. (2015). Powered two wheelers' workload assessment with various methods using a motorcycle simulator. IET intelligent transport systems, 9(7):702–709.

Will, S., Wehner, T., Hammer, T., Merkel, N., Werle, A., Umlauf, I., and Neukum, A. (2022). Assessment of data glasses for motorcycle riders in a simulated lane change test. Transportation research part F: Traffic psychology and behaviour, 89:467–477.

Wong, G. M. E. (2019). Motorcycle rider perception response times to abrupt and gradual-onset hazards in a simulator.

Wu, S.-Y., Sung,W.-H., Tsai, Y.-A., Cheng, H., and Chen, J.-J. (2011). The effects of using a modified motorcycle simulator training for the spinal cord injury patients.

©2023 Wildner, D., Diermeyer, F. published by TU Delft OPEN on behalf of the authors.

ISSN: 2667-2812

The Evolving Scholar Vol. 3, 2023 https://dx.doi.org/10.59490/662e39b33ea21e1276135969

Bicycle and Motorcycle Dynamics 2023
Symposium on the Dynamics and Control of Single Track Vehicles
18 – 20 October 2023, Delft University of Technology, The Netherlands

Type of the Paper: Keynote Paper

Revised

The History of Two-wheeled Vehicle Dynamics in Japan and Subsequent Trends

[version 2; peer reviewed]

Ichiro Kageyama[1]

[1] Professor Emeritus of Nihon University, Japan; kageyama.ichiro@nihon-u.ac.jp

Name of Editor: Jason Moore
First published: 19/09/2023
Last published: 13/05/2024
Citation: Kageyama, I. (2024). The History of Two-wheeled Vehicle Dynamics in Japan and Subsequent Trends [version 2; peer reviewed]. The Evolving Scholar - BMD 2023, 5th Edition.
This work is licensed under a Creative Commons Attribution License (CC-BY).

Abstract:

The purpose of this paper is to review research related to motorcycling conducted in post-war Japan, a country that was somewhat closed both linguistically and regionally. After World War II, many aeronautical engineers worldwide lost their jobs and moved on to other fields of study, especially in Japan, where aeronautical engineer jobs, including research, were banned and many aeronautical engineers shifted their research focus on transportation machinery, especially automotive engineering. Against this background, Japanese two-wheeled vehicles-related research has developed in its own unique way, while retaining a strong influence from aeronautical engineering. Because of the wide base of research on motorcycle kinematics, we first presented the literature for each study in the same line of research together. They are summarized in the following four areas：

(1) Experimental studies dealing with motorcycle motion and problem extraction.
(2) Research dealing with theoretical aspects such as the construction of equations of motion to solve experimental problems and to look at motion from the aspect of characteristics estimation.
(3) Research on various human-related issues, such as human control behavior modeling, vibration characteristics of the human body, HMI, and so on.
(4) Research on motorcycles as control objects and research focused on control systems.

Although there are many studies that straddle these two categories, they were generally grouped into one or the other.

Keywords: Two-wheeled Vehicles, History, Dynamics

©2023 Kageyama, I. published by TU Delft OPEN on behalf of the author.
ISSN: 2667-2812

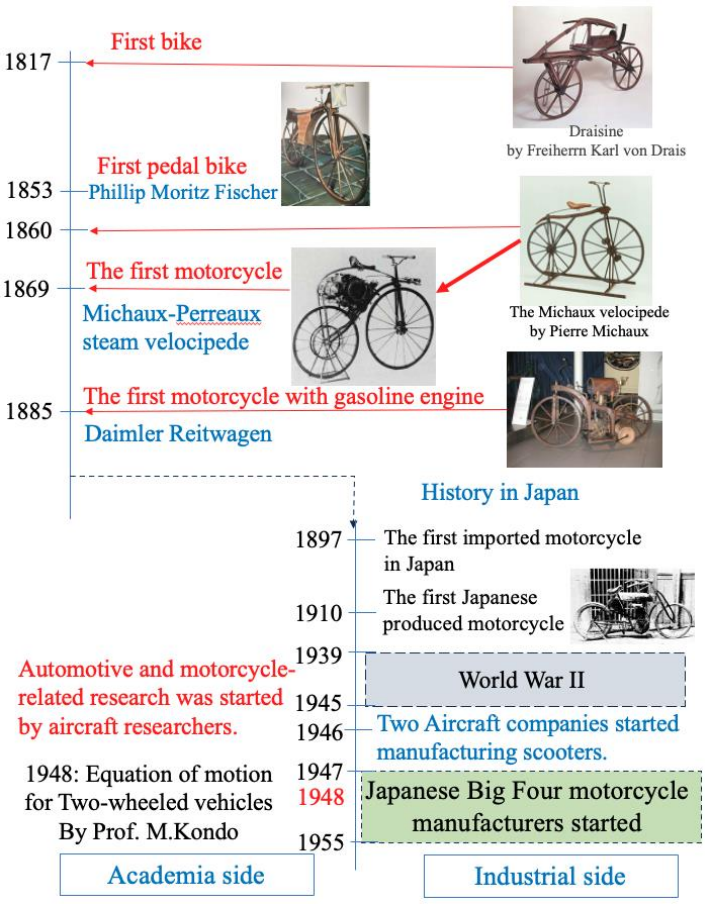
 http://dx.doi.org/10.59490/662e39b33ea21e1276135969

1. Introduction

Since Japan was closed off from the rest of the world for about 220 years until 170 years ago, various academic disciplines developed independently. For example, in the field of mathematics, famous mathematician Ko-wa Seki used ``Wasan" which is Japanese way of Mathematics to derive solutions to simultaneous equations using the process of elimination, 70 years earlier than in Europe. He also showed that pi could be calculated to 26 digits in the 1600s. Furthermore, there are references that use derivatives for analysis, although the method of expression is different. Thus, a unique academic culture developed in Japan, but it was a system of study by a very small number of scholars who constituted a school and was not open for many ordinary peoples. Therefore, while these Japanese historical research materials on “Wasan" have attracted attention in Japan, their results have not received much attention because they were written in the old Japanese script, and in recent years many people have focused on the academic systems established in Western countries. In recent years, Japan's education system has undergone major changes and is becoming increasingly Westernized. However, from the perspective of spreading education widely, most subjects can be studied in Japanese up to higher education, such as graduate school, and when a new academic field starts overseas, such as modern control theory or AI technology, its literature is translated into Japanese at an early stage and specialized books in the field are also published in Japanese. This creates an environment where new and original research is discussed in Japanese and published as papers in Japanese. In recent years, this trend has been greatly improved, and many young researchers have become active abroad and presented their own research results at international conferences, etc. International exchange has progressed, but the fact remains that few academic papers from the early days of vehicle dynamics, including motorcycles, are known abroad.

To turn our attention to the field of two-wheeled vehicles, we focus on history of global technological trends and the relationship between these trends in Japan. It is extremely difficult to accurately determine the history, and it is extremely difficult to accurately determine the starting point of the vehicles in this case about two-wheeled vehicles because of the various factors involved. Therefore, the generally accepted history of two-wheeled vehicles is summarized in Fig. 1. This figure shows the rough sketch that led to the history of motorcycles in Japan.

The history of two-wheeled vehicles began in 1817 with the invention of the Draisine by Freiherrn Karl von Drais. This vehicle was driven by a person riding on it and kicking the ground with their left and right feet, but even if the standing stability of such a vehicle was a little low, it could be stabilized by placing your feet on it. A separate drivetrain had to be considered for humans to remain in the vehicle for long periods of time, and in 1853, pedals were installed on the front tires. In other words, it seems that numerous innovations for standing stability were made at this time to some extent. Later, the Michaux-style bicycle, introduced around 1860, became widely popular. In 1869, a steam engine was installed under the seat of this Michaud-style bicycle, creating the first motorcycle with rear-wheel drive. Later, in 1885, a two-wheeled vehicle with a gasoline engine and auxiliary wheels was built by Daimler, which some researchers call the first motorcycle. The history of Japanese motorcycles begins in 1897, when records remain of the first motorcycle being imported to Japan. The first purely domestic motorcycle was a 4-stroke, single-cylinder, 400 cc vehicle built by Narazo Shimazu in 1909. After this, companies were established to manufacture foreign knockdown motorcycles as well as their own vehicles, supplying motorcycles to the market. However, there was little to see in terms of vehicle dynamics during this period. A major historical turning point in this trend was World War II, around which time aeronautical engineering made major advances worldwide, especially in the areas of stability and maneuverability. However, after the end of World War II, many aeronautical engineers and researchers worldwide lost their jobs, especially in Japan,



©2023 Kageyama, I. published by TU Delft OPEN on behalf of the authors.
ISSN: 2667-2812

where they were banned from research as well as production of aeronautical engineers, and they had to change direction to other vehicles, especially the automotive field. Therefore, it was introduced scientific perspectives to the two-wheeled and four-wheeled vehicles that had been built empirically. Turning to the flow of motorcycles in Japan, two aircraft manufacturers began prototype production of scooters fitted with airplane tailwheels, which were commercialized in 1946. However, several kinematic problems arose during this development process, and aeronautical researchers initiated various studies to solve these problems. Therefore, the first equation of motion for two-wheeled vehicles was constructed by Prof. M.Kondo and it was published in 1948. This was the starting point for research on the kinematics of two-wheeled vehicles in Japan. In addition, the "Big Four" companies in the Japanese motorcycle industry were successively established between 1947 and 1955. Therefore, when looking at the history of motorcycle research in Japan, it is necessary to consider the year 1948 as a starting point. Therefore, the following chapters will examine the details of the subsequent motorcycle-related studies and provide an overview of them.

2. Classification of Two-wheeled Vehicle Dynamics Research

Previous papers on two-wheeled vehicle motion and control need to be categorized to follow the flow. Although this classification needs to be considered from various perspectives, the following approach is used here to classify as broadly as possible. In addition, some papers in the past literature fall into more than one category, so they will be used in duplicate in their respective descriptions.

The first research (Category 1) on the dynamics of two-wheeled vehicles is based on the peculiarities of their motion, and the first studies started by extracting the problem experimentally. When understanding the motion of motorcycles theoretically, certain types of motion may be hidden due to the limitation of degrees of freedom based on various assumptions, and experiments using actual vehicles are very important to clarify various issues. Therefore, we consider one category of research that pioneering researchers have focused on, which is the experimental clarification of the identification of problems that occur in real vehicles.

The next category (Category 2) is theoretical analysis, which is a tool that can be used not only to describe vehicle motion using models, but also to predict vehicle behavior for example at extremely high speeds behavior. Furthermore, it is also important to construct a model for use in control such as stabilization control during stoppage. In addition, multibody dynamics software (hereinafter MBD), which have been used by many engineers in recent years, can be seen as an experiment using a computer, but these softwares use various kinds of models, and it is important to analyze motion in virtual space. Therefore, it is necessary to include this category in the theoretical analysis because it uses a model built based on certain assumptions.

The next category (Category 3) would be as a human-machine system. This classification encompasses a very broad range, including those that focus on the characteristics of the human body itself, those that focus on mental aspects, and even the role of the human controller as a control system. This classification should also be widely considered in papers that examine the evaluation of two-wheeled vehicle dynamics, for example, to evaluate the handling level of each vehicle or to evaluate riding comfort, papers that consider the human body as a dynamic element and examine its effect on two-wheeled vehicle dynamics, papers that examine the role of humans as controllers and their use in autopilot, as well as the construction of rider models for use in software such as CAE, and so on.

The last category (Category 4) is control systems. The role of humans as controllers is placed in the category of human-machine systems, and the construction of systems that directly control vehicle motion, such as upright stability control, etc., are classified in this control system category.

In general, classification by direction of motion axis (horizontal, vertical, up and down, etc.) is often used, but here I classify them as follows according to the above. The next chapter summarizes the main topic, the flow of research on two-wheeled vehicle dynamics in Japan.

3. History of Two-wheeled Vehicle Dynamics Research in Japan

Many studies on two-wheeled vehicles have been conducted in the past in terms of improving their characteristics, but as mentioned above, it was not until aeronautical engineers entered this field after World War II that they began to take shape in the literature. This does not mean to deny the studies conducted prior to World War II, but since there are almost no documents available, this study was conducted based on the results of the literature survey conducted after this period.

3.1 Experimental Approaches

Although an experimental approach is not necessarily the best way to identify and evaluate problems in an object, various filters have been used before various things have been constructed and become commonplace, so the evaluation of products formed at that

©2023 Kageyama, I. published by TU Delft OPEN on behalf of the authors.

ISSN: 2667-2812

 http://dx.doi.org/10.59490/662e39b33ea21e1276135969

stage makes sense. This is also true in the direction of the method on Genetic Algorithms, one method of optimization. Numerous studies have been conducted to experimentally evaluate such two-wheeled vehicles and to identify their kinematic problems.

In 1948, "Dynamics of two-wheeled vehicles (2nd Report) - On the stability of two-wheeled vehicles under free control and in steady state turning" by Masaichi Kondo et al. was presented at the Japan Society of Mechanical Engineer, Conference on Applied Mechanics. The society was founded in 1897 and is a prestigious organization in Japan, but due to the period of confusion at the time, I was unable to locate the publication itself, although I could not find that it had been published. Furthermore, since this is the second report, there should have been a first report, but I could not find it. However, these were eventually compiled into an experimental study on the stability and handling on two-wheeled vehicles, and submitted as a journal paper in 1955, so we can know the contents. A very difficult problem in experiments on motorcycles is the measurement of their motion. Today, with the widespread use of various lightweight sensors, data loggers, etc., and especially gyro-sensors using MEMS, it has become relatively easy to record driving data. However, at that time, gyros and other devices were too large and expensive to be used for such experiments. Therefore, Kondo et al. constructed a device in which the front wheel was placed on a drum and rotated, and the rear wheel could rotate in the yawing direction around the position of wheel axle center and was restrained only in the longitudinal and lateral directions. In order to incorporate human elements, a new wooden dummy, the first of its kind in Japan, consisting of six body parts, was made and fixed to the seat as shown in Fig. 2. In this state, the vehicle body could not be maintained in an upright position, springs were placed above the rear axle to prevent collapse, and also to ensure restoring torque in front of the rear wheel, the other springs ware set. These spring settings was very important but were determined based on the relationship between restoring moment and upright moment. With such a device, it was possible to create a simulated running condition for motorcycles, and measurements could be easily made. The experiment shows the results of the free control condition shown in the figure, and the experiment itself was conducted with varying speeds, caster angles and trails. In addition, the paper also showed the results of a running experiment in which the steering angle and force measurement device developed for this research was set to a real vehicle. In addition, the steering angle and steering force measurement device developed in this study was set up on an actual vehicle, and a steady circle turning test using this device was used to show that there are many vehicles that oversteer[2]. In addition, the Lemniscate experimental method, which is necessary to manipulate constant change, was also performed. The results of these experiments were very significant and had a tremendous impact on subsequent research in this field.

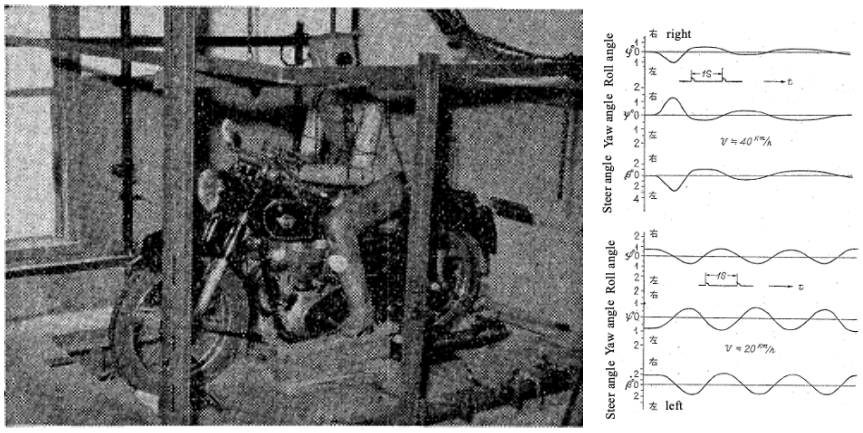


Fig.2 Experimental equipment for motorcycle running and the results of

In 1961, K. Kageyama et al. conducted an analysis using an experimental apparatus with a motorcycle on a rotating belt to confirm the effects of center-of-gravity height, front wheel design parameters, and other factors. In addition, this device was used to study the effects of shimmy by a trail that occurs when running straight ahead[4]. These results had a major impact on motorcycle design at the time. In particular, the results discussed the importance of the geometric relationship of the front-wheel system of a two-wheeled vehicle to the stability and advanced the study as information for design specifications [6].

M. Kondo's focus on steady-state gains (steady-state turning characteristics) led to research on steady-state circular turning characteristics of motorcycles, which in turn led to research on rider's riding posture (lean-in, lean-with, lean-out) by K. Kageyama et al.[3], H. Fu [7, 14], and others[20], and then to test method standards for motorcycles such as JASO-T011 'Standard Test Method for Motorcycles'. Furthermore, for the ordinary riders who use a motorcycle in the speed range up to about 120 km/h, the main criteria for evaluating motorcycles are steady-state gain and immediate response. Therefore, the possibility of using these steady-state characteristics for motorcycle evaluation has been investigated as the subject of JSAE Technical Committee on Motorcycles. It was later compiled and presented by I. Kageyama et al[32,33].

Since motorcycles are usually driven with an upper limit of about 120 km/h, except in Europe and on racetracks and so on, the steady-state gain and response mentioned earlier are problems, but another major issue is the shimmy that usually occurs in the handlebar system at 80 km/h. This is a vibration that generally appears as a vibration of 6 to 8 Hz in a very narrow speed band around 80 km/h. The solution has been to include friction or oil dampers around the steering shaft, but the effects of these dampers

©2023 Kageyama, I. published by TU Delft OPEN on behalf of the authors.
ISSN: 2667-2812

http://dx.doi.org/10.59490/662e39b33ea21e1276135969

can appear as a problem at high speeds. A description of this vibration can be found in the Reference (2) on the first experiment shown here. Systematic verification of this vibration problem had to wait until the systematic experiments conducted by I. Kageyama et al. in 1995[49),50)]. In this study, the frequency, amplitude, and other parameters at the steering system were measured against changes in speed by running on a proving ground and on a drum-type bench-top test apparatus. As a result, it was confirmed that this vibration with low stability appears around 80 km/h. It was also confirmed that the cause of this vibration was approximately the same frequency as that generated when an impact was applied to the handlebar while stopped, and it was clear that this vibration was related to the lateral rigidity of the front tire. Furthermore, in this study, a new model of the steering system that considered the lateral stiffness of the front tires was constructed, and its vibration modes were described using characteristic root loci, showing that the stability of the system was most reduced at around 80 km/h as shown in Fig.3. In 2010, the results of incorporating this tire model into a full vehicle model were presented, showing the importance of considering the lateral stiffness of the front wheels in vehicle model constructing[64)].

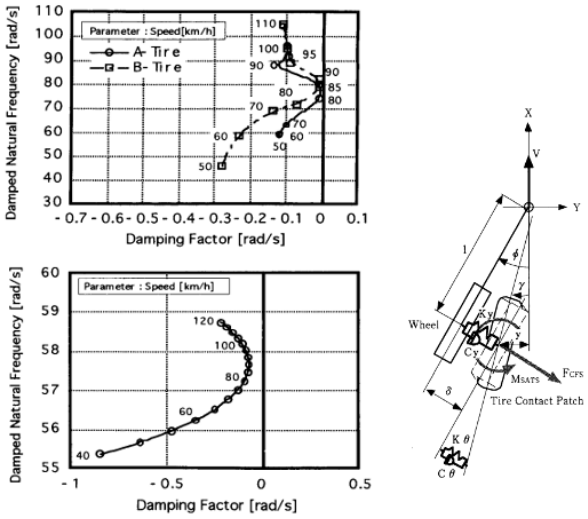


Fig.3 Experimental data and model output[46)]

An important point in research on two-wheeled vehicles is to find and analyze problems based on actual vehicle behavior. But unfortunately, two-wheeled vehicles have limited space for measuring instruments, and in each paper our predecessors have shown how to measure characteristics under such limited space[2),4),7),14),41),27),28),35)]. Furthermore, it is very difficult to obtain fundamental data such as the center of gravity, moment of inertia, individual human characteristics, tire characteristics, and so on in the human-motorcycle system. There are still several papers that have boldly attempted to obtain these data, but due to space limitations, I just described to confirm them with references[9),11),29),76),78),80),82),83)].

3.2 Theoretical Approaches

Theoretical research is as important as experimental research in mechanical systems. Particular attention needs to be paid to the modeling of two-wheeled vehicles and the results of such modeling, as the use of equations of motion and other approaches are important for the prediction of possible phenomena. However, the biggest problem in theoretical studies is that the equations of motion for high degrees of freedom cannot be solved directly, and even if the equations of motion can be constructed, their solutions cannot be obtained. The solution to these problems was greatly advanced by the personal computer, which was developed in the 1970s and became popular in the 1980s. These digital computer techniques have made it possible to obtain the equations of motion for these multiple degrees of freedom using approximate numerical analysis methods. Because such tools were not available in the late 1940s, when the equations of motion for two-wheeled vehicles were constructed, researchers have primarily used mechanical calculators and analog computers as well as huge digital computers to perform the analysis.

As mentioned above, aeronautical engineers and researchers contributed greatly to the theoretical study of two-wheeled vehicles, and the equations of motion for motorcycles were constructed by Prof. M. Kondo in 1948 based on their method of describing the dynamics of the vehicles[39),40),41)]. In using a dynamic coordinate system to analyze vehicles, they adopted the coordinate system used in aircraft in both US and Japan (called the SAE coordinate system in Japan) to construct the equations of motion for not only four-wheeled vehicles but also two-wheeled vehicles. Fortunately, this coordinate system was a convenient way to describe motorcycles because their basic motion is to roll inward in a turn, just like an aircraft. As an aside, afterward, in the analysis of the motion of a four-wheeled vehicle, a coordinate system is then used by the ISO with the z-axis facing up, oriented to the characteristics of the vehicle. Next, the equations of motion for this two-wheeled vehicles are described. The degrees of freedom are around the y-axis, x-axis (roll motion), z-axis (yawing motion), and steering axis, and the

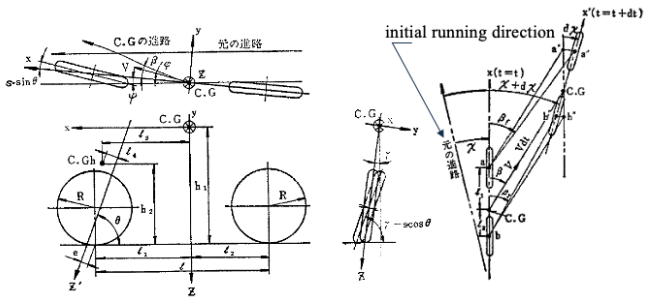


Fig. 4 Two-wheeled vehicle model[37),38)]

©2023 Kageyama, I. published by TU Delft OPEN on behalf of the authors.

ISSN: 2667-2812

equations were derived for a hands-off state with constant speed and fixed rider body as shown in Fig.4. The forces to be considered, including inertia forces, were (1) cornering force for each tire due to the angle of lateral slip, (2) camber thrust for each tire, (3) running resistance and driving force, (4) road reaction forces on the front and rear wheels, (5) weight of the steering system, (6) centrifugal force, (7) gyro moment, (8) related to yawing angular acceleration, (9) related to rolling angular acceleration, (10) related to steering angular acceleration, (11) aerodynamic forces and moments. The first half of the paper calculated a time series analysis from the induced equations of motion, while the second half obtained a sixth-order characteristic equation, from which periodic (conjugate complex roots) and non-periodic (real roots) oscillations were obtained as period and 1/10 damping time with respect to velocity. Furthermore, analysis was conducted on the differences between the six different specifications to determine which specification was preferred, up to 120 km/h, the practical speed range at the time. The time series analysis shows that divergent motion appears in the steering wheel system at 120 km/h, indicating the presence of the currently discussed wobble oscillation. Fig. 5 is a partial excerpt of the results of this time response. It follows that the equations of motion presented until 1963 are the results of the four-degree-of-freedom equations of motion that are in common use today, and this is the excellence of this study.

Subsequent dynamics research can be divided into two directions. One is to increase the number of degrees of freedom to take into account frame stiffness and other human considerations, and the other is to examine ways to find the causes of low instability.

One such analysis was conducted by N. Tsuta et al. in 1996, in which they constructed a model with 10 degrees of freedom for the vehicle system, including frame stiffness, and 2 degrees of freedom for the human body, for a total of 12 degrees of freedom, and analyzed their coupled motions as shown in Fig.6[88]. The equations of motion were induced using the Lagrange equations, and eigenvalue analysis was performed using the obtained equations of motion. The results of the weave and wobble analysis were relatively well represented by the experimental results, and the parameters of the human arm were examined to find that the stability limit could be improved at high speeds. Regarding the effect of frame stiffness, a separate study on straight running was conducted by Aoki et al. and these effects were examined as eigenvalue and eigenvector analyses[48),49),50)].

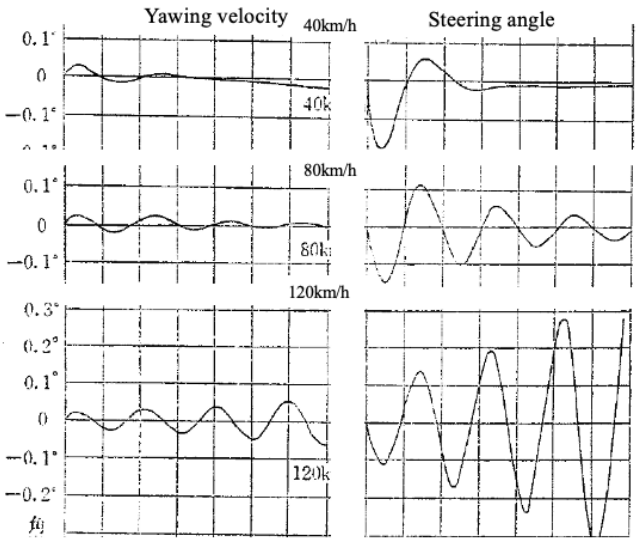


Fig. 5 Response of the model[40),41)]

In general, the analysis of multi-degree-of-freedom systems is mostly done by parameter studies, since it is not possible to identify the cause of instability by direct mathematical analysis, and the same approach is used in the above[37)]. In contrast, Katayama et al. proposed in Ref. 45) to verify destabilization by examining the energy flow to each response using the energy flow method. It has been used in subsequent papers because of its effectiveness in this type of analysis[65),69)].

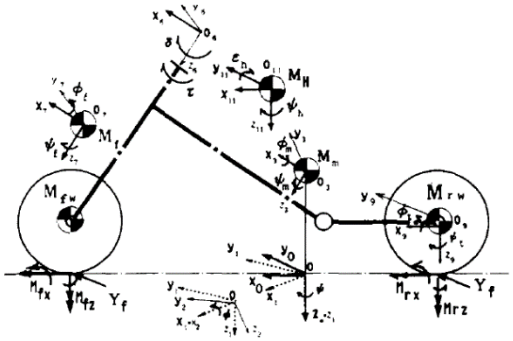


Fig. 6 12 degrees of freedom model [88)]

Next, since this classification also includes considerations using MBD, papers in that area are described. In the late 1980s, MBDs were developed around the world and used for analysis in many fields. When constructing equations of motion for motorcycles, four degrees of freedom has been the minimum, and various attempts have been made to describe more than four degrees of freedom, but the use of MBD has become widely used in development because it is easy to analyze nonlinear multi-degree-of-freedom systems. Its effectiveness has been demonstrated in the analysis of human-motorcycle systems, which have multiple degrees of freedom, in 1997, Imaizumi et al. modeled the human-motorcycle system and conducted a series of subsequent analyses[90),92),95),96),97),98)]. Through these series of analyses, an overview of the influence of various design parameters on dynamics, the influence of frame stiffness, the influence of raider and payload, the influence of vibration control, and the analysis of rider's behavior was obtained.

3.3 Human-Vehicle systems

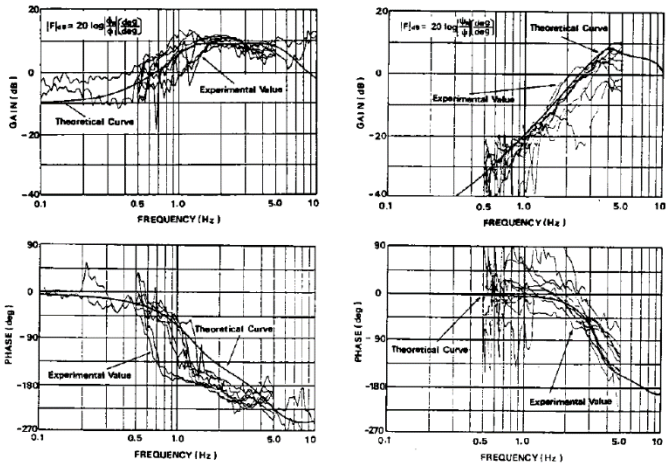
©2023 Kageyama, I. published by TU Delft OPEN on behalf of the authors.

ISSN: 2667-2812

 http://dx.doi.org/10.59490/662e39b33ea21e1276135969

As noted in the classification, human-motorcycle systems research has been studied from various aspects, but first the rider model as the controller of the control system is focused on. The modeling of humans manually controlling an object was analyzed using transfer functions by Arnold Tustin, a British electrical engineer during World War II. Therefore, many human operator studies since then have been described in terms of transfer functions. However, operator models that use such transfer function representations to human-vehicle system are not always easy to use in terms of understanding their algorithms. Therefore, in 1958, the creation of a model that based on such an algorithm construction was proposed by M. Kondo[71]. The inspiration for this model is said to have come from the field of aeronautical research, as it is said to have originated from the behavior of pilots during dogfights with fighters. The algorithm of this model, called the preview model, which uses forward information to steer, was proposed as a driver model for 4-wheeled vehicles. The basic idea is to steer according to the deviation between the target course at the gazing point and the extension of the vehicle center. The distance to the position where the driver gazes is called the gazing distance, and the deviation of that position from the target course is called the preview model because it is directly visible. The tracking performance changes according to the preview distance, which is consistent with ordinary driver behavior, and thus has become widely used in Japan. Later, a new model was proposed by K. Yoshimoto in 1982 to address the shortcomings of this model, which could not be corrected for steady state disturbances[75]. This model was a modification of Kondo's preview model, which used a method of determining the deviation from the current vehicle motion to the vehicle's position in the gazing point using up to a quadratic prediction term of Taylor expansion, rather than corrective action for the direction the vehicle was facing. Because the model involves predictive behavior, it is called the preview-prediction model and has been used in many subsequent studies of human-vehicle systems. This model was adopted for motorcycle riders by Katayama et al[91]. In this case, Katayama et al. divided the rider's upper and lower bodies and adopted a model in which the upper body performs lean motion, and the lower body performs lateral motion. The basic control algorithm was the quadratic prediction model described above, but Gaussian distributed weight coefficient with the gazing point as the peak position was introduced. The results showed that the model represents the rider's control behavior well. These rider preview and second-order prediction models have since been used in models for CAE and for autonomous motorcycles. In 1995, Y. Owada et al. used neural networks (hereafter NNS) to model what kind of information a person controlling a motorcycle obtains from the environment and how it leads to driving behavior[87]. The results of experiments on straight lines and curves were used for sufficient learning, and it was confirmed that the results were almost the same as the rider output. Using the trained NNS, they followed the flow of neurons from the input layer to the output layer one by one and performed factor analysis on the output values by each input to conclude which input was dominant for steering torque. Similarly, in 2004, S.Fujii et al. used a genetic algorithm (hereafter GA) to construct a model of motorcycle maneuvering. In this model, a preview model was used, and GA was used to identify the optimal parameters for deviation at the gazing point and rider's input[101]. The resulting model was used to simulate arbitrary course running in the speed range of 1-15 m/s, and stable results were achieved. A similar approach was implemented in 2007 by Inoue et al. as other-input, multiple-output adjustment of motorcycles using Fuzzy logic[108]. As a result, it was possible to incorporate the knowledge of a human expert and showed that it was suited to control motorcycles.

Similarly, humans exert various influences on motorcycles, which can be not only a disturbance but also an input to the control of the motorcycle. Therefore, it is necessary to clarify the relationship between human behavior and vehicle response. An early study focusing on these responses and others was conducted by Katayama et al. in 1985[80]. In this paper, a 2-DOF lean model and a 2-DOF yaw model of the rider's body were constructed and examined, including how they were modeled. In order to study these effects, a vibration measurement device in the form of a motorcycle was constructed to confirm these from the frequency characteristics as shown in Fig.6. From these, they finally examined how the rider's body affects the motion of the motorcycle, and the results showed that the transverse direction of the lower body and the lean angle of the upper body had a significant effect. This was shown as the input to the motorcycle given by the rider. A similar experiment using an actual motorcycle was conducted by I. Kageyama et al. in 1989[83]. They fabricated a device to fix the rider's body to the chassis, restrained all movements, and then opened it up one by one for frequency analysis based on the pulse response test results. The results showed that the largest effect of the response by the human body was the lean angle, followed by the yaw motion of the human body in the frequency band around 1 Hz, which had a significant effect on the motorcycle motion. From these results, the inputs that the rider provides to the motorcycles were identified. In 1984, Tomita et al. analyzed a man two-wheeled vehicle integrated movement



Roll angle excitation results (output: upper body lean angle)

Yaw angle excitation results (output: upper body yaw angle)

Fig. 7 Response of the model[80]

©2023 Kageyama, I. published by TU Delft OPEN on behalf of the authors.

ISSN: 2667-2812

used in trial competitions: jumping over a projection on a flat surface[77]. Since this is not a common movement, this section is limited to description only.

The next section deals with the information recognition ability of humans operating motorcycles. This is called Human Machine Interface (hereafter HMI) and is a study of the extent to which humans can acquire information, including meters and alarms. Such studies have been conducted as one of the various items to be considered for motorcycles. Although there have not been many such studies, this is an important characteristic as vehicles become more information oriented.

Finally, we focus on the results of the study of the relationship between elements of the human body and motorcycles. In 1985, T. Katayama et.al. conducted measurements on the center of gravity and moment of inertia of riders[79]. These obtained the human parameters that were the basic data to be used in the human-motorcycle system to be used in the future. In 1984, Kageyama et al. measured the frequency characteristics of the human arm using vibrations received from the handlebars. This analysis was used to identify the equivalent mass of the human arm (the mass of the arm that moves with the handlebar), the equivalent damping factor, and the equivalent spring constant that are given to the steering system[76),78]. In addition, the effects of human grip force and pushing on the handle were examined, and the mechanical equivalent of these factors was studied. Finally, the degree to which these mechanical factors affected the motion of a motorcycle was shown by the characteristic root locus using a 4-DOF model.

3.3 Control Technology

As a final section, control techniques are summarized. Although the introduction of control systems has been slower for two-wheeled vehicles than for four-wheeled vehicles, research has been conducted to introduce support systems and for experiments and other purposes.

The first such control was presented by Nagai in 1983 for upright control of a lightweight bicycle[116]. Since lightweight sensors such as MEMS and lightweight controllers were not available in this era, a belt-driven road surface was fabricated, on which a small bicycle was mounted and controlled by a wire. Control was performed by steering, and lateral and upright directional control was examined, while front/rear directional control was performed with restraints on the belt. As a result, it was confirmed that upright stability and directional stability were maintained on the belt. A similar study on self-supporting systems was developed by S. Miyagishi et al. in 2003[123]. The system was constructed for autonomous driving and used a video camera called “rider robot” to recognize the road ahead with camera and second order prediction model[124),126),127]. Furthermore, the arms were constructed with a spring and damper system set up based on the equivalent dynamic elements of the rider constructed in references 76) and 78), and the system was designed to steer with this system. The system was constructed for test operation during the development of new vehicles or when a new support system is built. As shown in Fig. 8, the robot was able to drive a two-wheeled vehicle autonomously. Similarly, a self-supporting system using a model motorcycle was constructed by H. Sato et.al. in 2006, showing self-supporting running results[125]. Furthermore, in 2011, E. Tsujii et al. constructed a system with front and rear wheel steering system to ensure stability, including autonomy in a stopped state[135].



Fig. 8 Rider Robot

In 1990, a reverse control system for motorcycles was introduced by A. Ota et al.[120] This was a control system that verified the conditions of large motorcycles when reversing and was incorporated to enable stable reversing. Other control system research has been presented as a support system and is expected to spread in the future[128),129),130),131),133),134),136].

4.Postscript

Summarizing the research conducted in Japan on bicycling relations, Japan’s uniqueness and other characteristics that were initially pointed out have not necessarily been maintained in recent years, that the problems of interaction with other countries and language are being resolved mainly by young researchers, and that these interactions have recently begun to influence each other internationally and move toward similar research topics. The total number of references listed here is 136, but I am sure I have missed quite a few. The majority of these 136 references are written in Japanese, and from viewpoint of an overseas researchers,

©2023 Kageyama, I. published by TU Delft OPEN on behalf of the authors.

ISSN: 2667-2812

the research environment may still be considered closed. Since there are not so many motorcycle researchers in the world, I hope that they will take advantage of these BMD opportunities to gradually eliminate the language barrier and interact with each other.

References

Experimental Approaches (Category 1)

1) Masaichi Kondo et.al.: Dynamics of Two-wheeled vehicles (2nd Report) – On the stability of two-wheeled vehicles under free control and in steady state turning (in Japanese) , the Japan Society of Mechanical Engineer, Conference on Applied Mechanics, 1948.11

2) Masaichi Kondo et.al.: Experimental study of stability and maneuverability of two-wheeled vehicles (in Japanese), Journal of the JSME, Vol.58, No.442, (1955), pp.5-11

3) Katsumi Kageyama et.al.: Experiments on the effects of maneuverability, especially lean-in and lean-out, on steady-state turning of two-wheeled vehicles (in Japanese), Journal of JSAE No. 13, No.10, (1959) , pp.41-45

4) Katsumi Kageyama et.al.: Experimental study of the stability of two-wheeled vehicles (in Japanese), Journal of JSME, Vol.64, No. 508, 1961-05, pp.746-753

5) Katsumi Kageyama et.al.: A prototype towing force gauge for motorcycles and its two or three applications (in Japanese), Journal of JSAE, Vol. 16, No.10, (1962)

6) Katsumi Kageyama et.al.: Geometry of the front wheel system of a two-wheeled vehicle (in Japanese), Journal of JSAE, Vol. 18, No.11, (1964)

7) Hiroyasu Fu (Nagae): Basic Characteristics of Motorcycles in Steady State Turning (in Japanese), Transaction of JSME (Category1), Vol.31, No. 229 (1965), pp.1305-1314

8) Katsumi Kageyama et.al.: A prototype flat tire tester and a couple of experiments (in Japanese), Journal of JSAE, Vol. 20, No.5, (1966), pp.426-430

9) Hideo Sakai: Cornering characteristics of motorcycle tires (in Japanese), Journal of JSAE, Vol. 21, No.11,(1967), pp.1115-1121

10) Keigo Yoshida et.al.: Stability and Handling on Motorcycles (in Japanese), Journal of JSAE, Vol. 26, No.7,(1972), pp.866-872

11) Seichi Motomiya et.al.: The mechanical properties of the components of motorcycles (3rd report: Tire characteristics) (in Japanese), Proceedings of JSAE, No.772, (1972), pp.577-580

12) Y. Watanabe et.al.: Motorcycle handling performance for obstacle avoidance, Second International Congress on Automotive Safety, Paper No. 73033, (1973), pp.101-123

13) Hiroyasu Fu (Nagae): Research on Motorcycle Dynamics (in Japanese), Doctoral Thesis at Nihon University, (1976), pp.1-306

14) Hiroyasu Fu (Nagae): Steer moment of motorcycle in steady state turning (in Japanese), Transaction of JSME, Vol.43, No.367, (1977), pp.46-54

15) Katsumi Kageyama et.al.: Motorcycle Dynamics (in Japanese), IATSS Review, Vol. 3, No.1, (1977), pp.15-21

16) Keigo Yoshida: Motorcycle maneuverability and stability tests (in Japanese), Journal of JSAE, Vol. 31, No.5,(1977), pp.385-390

17) Akira Aoki et.al.: Basic characteristics of motorcycles (in Japanese), JARI Research Journal, No.62, (1977), pp.1-36

18) Akira Aoki et.al.: Aerodynamic characteristics of motorcycles (in Japanese), JARI Research Journal, No.63, (1977), pp.1-36

19) Hiroyasu Fu (Nagae): Analysis of two-wheeled vehicles on free control (in Japanese), Transaction of JSAE, No.5, (1978), pp.51-58

20) Akira Hasegawa: Characteristics of Motion of Motorcycles (in Japanese), Journal of JSAE, Vol. 32, No.4,(1978), pp.300-304

21) Akira Aoki et.al.: Steer Dynamics of Motorcycle Tires (in Japanese), Automotive Research, Vol.2, No.6 (1980), pp.167-171

22) Hiroyasu Fu (Nagae) et.al.: Inertia Equivalent Mass of Engine and Driving System of Motorcycle -Estimation Result from Gyro Effect during Steady State Turning- (in Japanese), Transaction of JSAE, No.22, (1981), pp.51-56

23) Hiroyasu Fu (Nagae): Stability and Handling on Two-wheeled Vehicles - Turning Characteristics of Motorcycles - (in Japanese), Journal of JSAE, Vol. 36, No.3, (1982), pp.298-304

24) Hiroyasu Nagae: Stability and Handling on Two-wheeled Vehicles (in Japanese), IATSS Review, Vol.8, No.2, (1982), pp.45-52

25) Tadashi Kikuchi: Motorcycle behavior and tire characteristics (in Japanese), Journal of JSAE, Vol. 38, No.3,(1984), pp.332-336

26) Akira Aoki et.al.: On Directional Stability of Motorcycles (in Japanese), Journal of JSAE, Vol. 40, No.3,(1986), pp.305-310

27) Ichiro Kageyama: On a Testing Method for Two Wheeled Vehicle Handling, Technical Papers of SETC '93,Vol.2, No.931554,(1993) pp.679-684

28) Tomoo Nisimi et.al.: Cross wind characteristics of Motorcycles (in Japanese), Journal of JSAE, Vol. 48, No.12,(1994), pp.59-65

29) Akira Aoki et.al.: Measurement of motorcycle frame stiffness (in Japanese), Automotive Research, Vol.19, No.9 (1997), pp.362-367

30) Tsuyoshi Katayama et.al.: Influence of Frame Stiffness on Wobble Mode of Motorcycle - Analysis by Eigenvector Method-. Automotive Research, Vol.20, No.9 (1998), pp.404-407

31) Akira Aoki et.al.: Analysis on Influence of Frame Stiffness on Straight-running Stability of Motorcycles (in Japanese), Transaction of JSME (Category C), Vol.64, No.625 (1998), pp.3555-3562

32) Akira Aoki et.al.: Investigation of the validity of the basic motion model for motorcycles (in Japanese), Transaction of JSME (Category C), Vol.65, No.636 (1999), pp.3142-3148

33) Akira Aoki: Study on Motorcycle Dynamics (in Japanese), Doctoral Thesis at Nihon University (2000), pp.1-199

34) Eichi Yagi: Research on the kinematic characteristics of motorcycles (in Japanese), Doctoral Thesis at Osaka University (2005)

35) Ichiro Kageyama el.al.: Study on Evaluation Method of Motorcycle using Steady-State Characteristics (in Japanese), Transaction of

©2023 Kageyama, I. published by TU Delft OPEN on behalf of the authors.

ISSN: 2667-2812

JSAE, Vol.41, No.6, (2010), pp.1225-1230
36) Ichiro Kageyama el.al.: Steady-state turning characteristics of motorcycles considering equivalent compliance (in Japanese), Transaction of JSAE, Vol.50, No.5, (2019), pp.1402-1408
37) Ichiro Kageyama el.al.: Study on Motorcycle Dynamics at Extremely Low Speeds (in Japanese), Transaction of JSAE, Vol.51, No.2, (2020), pp.385-391
38) Akinori Shinagawa etl.al.: Development and application of simple measurement and analysis techniques for motorcycle motion (in Japanese), Yamaha Motor Technical Review (2021-12), pp.131-136

Theoretical Approaches (Category 2)
39) Masaichi Kondo et.al.: Fundamental Equations of Motion for Two-wheeled Vehicle Running Stability and Their Application to Bicycles (in Japanese) , JSME Meeting, 1948.11
40) Masaichi Kondo et.al.: Theoretical Study on Two-wheeled Vehicle Stability (in Japanese) , Journal of JSAE, Vol.17, No.1,(1963), pp.8-18
41) Masaichi Kondo: Mechanics of motorcycles (bicycles, mopeds, scooters, motorcycles) (in Japanese) , Bicycle Production Technology, No.93-94 (1975), pp.1-94
42) Hiroyasu Fu (Nagae): Study on Motorcycle Dynamics (in Japanese), Doctoral Thesis at Nihon University (1976), pp.1-306
43) Ichiro Kageyama et.al.: The human element in the hand system of motorcycles (in Japanese), Transaction of JSME (Category C), No.458 (1984), pp.2037-2045
44) Takao Tomita et.al.: Measurement and simulation of rider/motorcycle system jump behavior (in Japanese), Journal of JSAE, Vol. 38, No.12, (1984), pp.1463-1471
45) Ichiro Kageyama et.al.: Human Factors in the Steering System of Two-wheeled vehicle, Bulletin of the JSME,Vol.28,No.240, (1985)
46) Akira Hasegawa: Prediction Technology and CAE for Motorcycle Stability and Handling (in Japanese), Journal of JSAE, Vol.40, No.3,(1986), pp.324-330
47) Nobuyasu Endo etl.al.: Study on Dynamics of motorcycles at running-Equations of motion in finite motion (in Japanese), Yamaguchi University Faculty of Engineering Research Report, Vol.39, No.1 (1988), pp.169-175
48) Tsuyoshi Katayama et.al.: Energy flow method for the study of motorcycle wobble mode, Vehicle System Dynamics No.19, (1990), pp.151-175
49) Ichiro Kageyama el.al.: Study on shimmy Phenomenon on motorcycles (in Japanese), Transaction of JSME (Category C), Vol.61, No.582, (1995), pp.227-232
50) Ichiro Kageyama el.al.: On a Modeling of Shimmy Phenomenon for Two Wheeled Vehicle, Proceedings of SETC'95, USA (1995), pp.387-392
51) Tsuyoshi Katayama et.al.: Analysis of wobble modes of motorcycles using eigenvectors (in Japanese), Automotive Research, Vol.20, No.4 (1998), pp.137-140
52) Hiroyasu Nagae: Turning Behavior of Motorcycles - Actual Riding Based on Calculation- (in Japanese), Motor Ring (JSAE), Vol. 9 (1999), pp.4-5
53) Tsuyoshi Katayama: On Equation of Motion for Stability Analysis on Two-wheeled Vehicle(in Japanese), Bicycle Technical Information, No.77 (2000), pp.1-16
54) Yoshitaka Tezuka et.al.: Application of the Magic Formula Tire Model to Motorcycle Dynamic Performance Analysis (in Japanese), Honda R & D Technical Review, Vol.12, No.1 (2000), pp.145-150
55) Tsuyoshi Katayama: Weave Mode Analysis of Motorcycles (Report 1) (in Japanese), Automotive Research, Vol.23, No.10 (2001), pp.538-541
56) Yoshitaka Marumo et.al.: Weave Mode Analysis of Motorcycles (Report 2) (in Japanese), Automotive Research, Vol.24, No.2 (2002), pp.63-66
57) Ichiro Kageyama et.al.: A Study on tire modeling for camber thrust and camber torque, JSAE Review Vol.23, No.3, (2002), pp.325-331
58) Yoshitaka Marumo et.al.: Analysis on Influence of Frame Stiffness on Weave Mode of Motorcycles (in Japanese), Transaction of JSME (Category C), Vol.69,No.684, (2003), pp.2142-2149
59) Eiich Yagi: Research on the kinematic characteristics of motorcycles (in Japanese), Doctoral Thesis at Osaka University 乙No.9035 (2005)
60) Tetsuya Kubota et.al.: Analysis of Turning Characteristics of Motorcycles Using Multi-body Dynamics Language (in Japanese), Transaction of JSAE, Vol.38, No.2, (2007), pp.31-35
61) Shu Shoho et.al.: Motion Analysis of Motorcycles Using Multibody Dynamics Theory (in Japanese), Transaction of JSME (Category C), Vol.73, No.728, (2007), pp.1067-1074
62) Ichiro Kageyama et.al.: Influence of Braking Force on Motorcycle Turning Performance (in Japanese), Transaction of JSAE, Vol.40, No.6, (2009), pp.1411-1416
63) Ichiro Kageyama et.al.: Study on Motorcycle Behavior at Braking using Quasi Steady State Method, Proc. of IAVSD'09 (Stockholm) (2009)
64) Yuya Aikawa et.al.: Study on Dynamic Characteristics of Motorcycles Considering Tire Degree of Freedom (in Japanese), Proceedings of the 19th the Transportation and Logistics JSME (2010), pp.117-120
65) Yoshitaka Marumo et.al.: Analysis on Motorcycle Weave Mode by Using Energy Flow Method (in Japanese), Transaction of JSME (Category C), Vol.77, No.781, (2011), pp.287-298
66) Ichiro Kageyama et.al.: Study on stability of motorcycles at standstill and at extremely low speeds (in Japanese), Transaction of JSAE,

©2023 Kageyama, I. published by TU Delft OPEN on behalf of the authors.

ISSN: 2667-2812

Vol.50, No.3, (2019), pp.789-795
67) Sharad Shinghania et.al.: Study on Low-Speed Stability of a Motorcycle, Applied Sciences (2019)
68) Takahiko Yoshino et.al.: Compatibility issues between weave and wobble modes for motorcycles (in Japanese), Kurume Institute of Technology Research Report No.41,(2019), pp.59-64
69) Takahiko Yoshino et.al.: Energy flow method for the study of motorcycle wobble mode (in Japanese), Transaction of JSAE, Vol.50,No.5, (2019), pp.1372-1376
70) Ichiro Kageyama et.al.: Study on Tire Model for Motorcycle Motion Analysis (in Japanese), Transaction of JSAE, Vol.52, No.1, (2021), pp.43-50

Human-Vehicle systems (Category 3)
71) Masaichi Kondo: Fundamental relationship that exists between vehicle steering and motion. (in Japanese), Transaction of JSAE, No.5,(1958), pp.40-43
72) Masaichi Iguchi: Dynamics of Two-Wheeled Vehicles (1) - Analysis of Basic Characteristics by Linear Theory (in Japanese), Mechanical Research, Vol.14, No.7, (1962), pp.890-894
73) Masaichi Iguchi: Dynamics of Two-Wheeled Vehicles (2) - Analysis of Basic Characteristics by Linear Theory (in Japanese), Mechanical Research, Vol.14, No.8,(1962), pp.1009-1017
74) Tadataka Kobayashi: Man-Motorcycle Dynamics (in Japanese), Journal of JSAE, Vol. 28, No.4,(1974), pp.310-314
75) Ken-ichi Yoshimoto: Modeling the driving behaviors of an automobile driver, Human Factors Vol.18, No.6 (1982), pp.301-305
76) Ichiro Kageyama et.al.: The rider's element in the handlebar system of motorcycles (in Japanese), Transaction of JSME (Category C), No.458, (1984), pp.2037-2045
77) Takao Tomita et.al.: Measurement and simulation of rider/motorcycle system jump behavior (in Japanese), Journal of JSAE, Vol. 38, No.12, (1984), pp.1463-1471
78) Ichiro Kageyama et.al.: Human Factors in the Steering System of Two Wheeled vehicle, Bulletin of the JSME,Vol.28,No.240, (1985)
79) Tsuyoshi Katayama et.al.: Measurement of Rider's Center of Gravity and Moment of Inertia (in Japanese), Automotive Research, Vol.7, No.12 (1985), pp.519-522
80) Tsuyoshi Katayama et.al.: Measurement of Rider Vibration Characteristics (in Japanese), Automotive Research, Vol.7, No.1 (1985), pp.422-425
81) Masanori Motoki: Motorcycle Rider's Eye Range (in Japanese), Automotive Research, Vol.8, No.1 (1986), pp.15-18
82) Tsuyoshi Katayama et.al.: Measurement of Rider Vibration Characteristics (in Japanese), Transaction of JSAE, No.35, (1987),pp.147-153
83) Ichiro Kageyama et.al.: Kinematic characteristics of human-motorcycle systems and various control inputs (in Japanese), Report from CIT, Nihon University, Vol.22, No.2 (1989), pp.7-15
84) Tsuyoshi Katayama et.al.: Steer characteristics of motorcycle rider during lane change (in Japanese), Transaction of JSAE, No.41, (1989), pp.45-50
85) Motomu Yokomori et.al.: Steering characteristics with motorcycle rider during low-speed straight running (in Japanese), Transaction of JSME (Category C), Vol.57, No.535, (1991), pp.2621-2626
86) Ichiro Kageyama: The relationship between rider and two-wheeled vehicle, IATSS Research, Vol.19, No.1 (1995)
87) Katsuyuki Owada et.al.: An Analysis of A riding Control Algorithm for Two Wheeled Vehicle Using a Neural Network Modeling, 14th IAVSD Symposium (1995)
88) Norio Tsuta et.al.: Analysis of high-speed running stability of coupled human-motorcycle systems (in Japanese), Transaction of JSME (Category C), Vol.62, No.593, (1996), pp.76-82
89) Ichiro Kageyama, et. al.: On Development of Two Wheeled Vehicle Riding Simulator, SETC'97(1997)
90) Hirohide Imaizumi et.al.: Study on Motorcycle-Rider System Dynamics using Multi-body Dynamics Language: Effects of Frame Stiffness and Tire Characteristics on Weave, Transactions of JSAE, Vol. 28, No. 3, (1997), pp.131-136
91) Tsuyoshi Katayama et.al.: Simulation model for motorcycle rider maneuvering behavior (in Japanese), Transaction of JSAE, Vol.28, No.3 (1997), pp.137-142
92) Hirohide Imaizumi et.al.: Study on Motorcycle-Rider System Dynamics using Multi-body Dynamics Language (2nd report): Analysis of Parameter Effects on Wobble Motion Characteristics by Running Experiments and Simulations (in Japanese), Transactions of JSAE, Vol. 28, No. 3, (1997), pp.131-136
93) Hajime Uchiyama et.al.: Riding Simulator for Two-wheeled Vehicle Handling, Proc. of AVEC '98, (1998), pp.349～354
94) Akira Aoki et.al.: Effects of Rider's Vibrational Characteristics on Straight-Running Stability of Motorcycles (in Japanese), Transaction of JSME (Category C), Vol.65, No.634, (1999), pp.134-141
95) Hirohide Imaizumi et.al.: Study on Motorcycle-Rider System Dynamics using Multi-body Dynamics Language (3rd report): Analysis of the Influence of Loaded Weight and Rider on Motorcycle Dynamics and its Vibration Damping Method (in Japanese), Transactions of JSAE, Vol. 30, No. 3, (1999), pp.99-104
96) Hirohide Imaizumi et.al.: Study on Motorcycle-Rider System Dynamics using Multi-body Dynamics Language (4th report): Analysis of Rider's Maneuvering Behavior and Motorcycle Kinematics (in Japanese), Transactions of JSAE, Vol. 30, No. 3, (1999), pp.99-104
97) Hirohide Imaizumi et.al.: Study on Motorcycle-Rider System Dynamics using Multi-body Dynamics Language (6th report): Analysis of Motorcycle-Rider System Kinematics Using Parametric Model (in Japanese), Preprint of JSAE, (2000)
98) Hirohide Imaizumi et.al.: Study on Motorcycle-Rider System Dynamics using Multi-body Dynamics Language (7th report): Motorcycle Stability and Handling Analysis (in Japanese), Preprint of JSAE, (2001)

©2023 Kageyama, I. published by TU Delft OPEN on behalf of the authors.

ISSN: 2667-2812

99) N.Tagami et.al.: Development of a riding simulator for two-wheeled vehicles, Elsevier, JSAE Review Vol.23,No.3,(2002), pp.347-352
100) Yoshitaka Marumo et.al.: Analysis of Influence on Rider Vibration Characteristics on Motorcycle Weave Modes (in Japanese), Transaction of JSME (Category C), Vol.70, No.699, (2004), pp.3001-3008
101) Shigeru Fujii et.al.: A Model for Motorcycle Rider Operation Based on Genetic Algorithms (in Japanese), Yamaha Motor Technical Review (2008-08)
102) Yoshitaka Marumo et.al.: Examination of Influence of Tandem Riding on Weave Mode in Motorcycles (in Japanese), Transaction of JSAE, Vol.36 No.6, (2005), pp.199-204
103) Eichi Yagi et.al.: Acceleration and Jump Motion Analysis of Motorcycles and Human Systems (in Japanese), Transaction of JSME (Category C), Vol.72, No.715, (2006), pp.816-822
104) Shuhei Kawasaki et.al.: Directional control by weight shift of motorcycle rider including vehicle speed control (in Japanese), Transaction of JSAE, Vol.37 No.5, (2006), pp.45-50
105) T. Kishida et.al.: Development of riding Simulator for two wheeled vehicles and fundamental study on HMI for advanced safety vehicle, Proc. of Driving Saturation Conference (2007)
106) M.Kusakari et.al.: Fundamental Study on HMI for Advanced Safety Vehicles: Information Presentation Method for Active Safety of Motorcycles (in Japanese), Transaction of JSAE, Vol.38 No.2, (2007), pp.237-242
107) Shu, Shoho et.al.: Modeling of a Rider-Motorcycle System and Optimal Motion Control for Lane Change (in Japanese), The 50th Automatic Control Union Lecture Meeting, (2007), pp.785-790
108) Genta Inoue: Proposal of an intelligent multi-input, multi-output control scheme for motorcycles, The 28th Fuzzy Workshop (2007), pp.65-68
109) Shu, Shoho et.al.: Rider assisted control for optimum steering and obstacle avoidance (in Japanese), JSAE Annual Conference 2009, 2009-05
110) Ichiro Kageyama: Motorcycle Rider's Behavior from a viewpoint of rider robot design, AVEC-Workshop'09
111) Hiroshi Daimoto et.al.: Case studies on Ergonomic Methos based on Human Centered Design for Motorcycles, IATSS Review Vol. 36, No.1 (2011), pp.14-23
112) Atsushi Watanabe et.al.: Construction of Riding Simulator for Two-wheeled Vehicle Handling, Proc. of DSC 2012 (2012)
113) Atsushi Watanabe et.al.: Study on Construction of Riding Simulator with Stereoscopic Vision for Two-Wheeled Vehicle (in Japanese), Transaction of JSME (Category C), Vol.79, No.806, (2013), pp.343-352
114) Wataru Ishii et.al.: Development of Measuring method for Riding Motion of Motorcycles during Actual Riding, Yamaha Motor Technical Review No.53, (2017), pp.102-109
115) Ichiro Kageyama et.al.: Study on Motorcycle Dynamics at Extremely Low Speeds (2nd Report) -Influence of rider's body-, Transaction of JSAE, Vol.52, No.1, (2021), pp.154-159

Control Technology (Category 4)
116) Masao Nagai et.al.: Analysis of Rider and Single-Track-Vehicle System, its Application to Computer- Controlled Bicycle, Automatica, Vol.19, No.6, (1983), pp.737-740
117) Masakazu Iguchi et.al.: Fundamental Study on the Stability of Two-Wheeled Vehicles with Front and Rear Wheel Steering (in Japanese), Transaction of JSAE, No.32, (1986), pp.106-112
118) Masao Nagai: Control on motorcycle running at low speeds (in Japanese), Transaction of JSAE, No.32, (1986), pp.113-118
119) Atsushi Matsuda et.al.: Introduction of the application of front and rear wheel steering systems to motorcycle (in Japanese), Journal of JSAE, Vol.41, No.3, (1987), pp.411-417
120) Atsurou Ohta et.al.: Reverse control system for motorcycles (in Japanese), HONDA R&D Technical Review Vol.2 (1990), pp.49-58
121) Takio Ohya et.al.: Stability control circuit for motorcycle driving (in Japanese), Transaction of JSME (Category C), Vol.69, No.688, (2003), pp.3191-3197
122) Yutaka Kamata et.al.: System identification and front-wheel steering control of motorcycles (in Japanese), Transaction of JSME (Category C), Vol.69, No.688, (2003), pp.3191-3197
123) Shun-ichi Miyagishi et.al.: Study on construction of a rider robot for two-wheeled vehicle, JSAE Review Vol.24, No.3, (2003), pp.321-326
124) Ichiro Kageyama et.al.: Construction of robot to control two-wheeled vehicles (in Japanese), Journal of JSAE, Vol.58, No.5, (2004)
125) Takumi Sato et.al.: Modeling and Robust Attitude Control of Self-Sustaining Motorcycles at Standstill (in Japanese), Transaction of JSME (Category C), Vol.72, No.719, (2006), pp.2130-2136
126) K.Kuriyama et.al.: Construction of Rider Robot System for Two-Wheeled Vehicle, Proc. of AVEC'06 (2006)
127) S.Suzuki et.al.: Study on construction of Rider Robot for Motorcycles, Proc. of AVEC'08,(2008)
128) Shu, Shoho: Analysis of cornering characteristics and stabilized control for two-wheeled vehicles (in Japanese), JSME D&D Conference (2009)
129) Nozomi Katagiri et.al.: Evaluation of Lane-Keeping Assistance System for Motorcycles using Rider Control Model (in Japanese), Transaction of JSAE, Vol.40, No.3, (2009), pp.635-640
130) Shintaro Murakami: Design of a rider assist control system for motorcycles during braking (in Japanese), Keio Associated Repository of Academic resources, (2009) Doctoral Thesis
131) Genta Inoue et.al.: An Intelligent Two-wheeled Vehicle Driving Support System Based on Operation Knowledge of Skilled Rider (in Japanese), Intelligence and Information, Vol. 21, No.1 (2009), pp.24-31
132) Shu Shoho et.al.: Model-based design of front-steering assist control system for motorcycles (in Japanese), Keio Associated Repository

©2023 Kageyama, I. published by TU Delft OPEN on behalf of the authors.

ISSN: 2667-2812

of Academic resources, (2009) Doctoral Thesis
133) Hidekazu Nishimura: Cornering characteristics and stabilization control of two-wheeled vehicles (in Japanese), Journal of JSAE), Vol. 64, No.2, (2010-12), pp.241-246
134) Shintaro Murakami: Validation of Front-Wheel Steering Assist Control for Motorcycles (Simulation considering nonlinearity of cornering force) (in Japanese), Journal of JSAE), Vol. 64, No.2, (2010-12), pp.241-246
135) Eichiro Tsujii et.al.: Development of a two-wheel steering system (evaluation of stability of motorcycles at low speeds) (in Japanese), Yamaha Motor Technical Review, No.47 (2011), pp.67-73
136) S.Shinghania et.al.: Steering control to balance a motorcycle at low speeds based on riders' input, I Mech E Part D: J. of Automobile Engineering, (2021), pp.1-13

Acknowledgement

I would like to express my gratitude to the editor and the reviewers. They pointed out several mistakes and problems with the formatting of the references. I have made corrections to the paper according to their suggestions.

©2023 Kageyama, I. published by TU Delft OPEN on behalf of the authors.

ISSN: 2667-2812

The Evolving Scholar Vol. 3, 2023 https://dx.doi.org/10.59490/66664f995777b675f57fe3c0

Bicycle and Motorcycle Dynamics 2023
Symposium on the Dynamics and Control of Single Track Vehicles
18 – 20 October 2023, Delft University of Technology, The Netherlands

Type of the Paper: Conference Paper

Revised

Trajectory Forecasting for Powered Two Wheelers by Roll Angle Prediction with an LSTM Network

[version 3; peer reviewed]

Karl Ludwig Stolle[1,*], Anja Wahl[1], and Stephan Schmidt[2]

[1] Robert Bosch GmbH, Germany; karlludwig.stolle@bosch.com, ORCID 0000-0002-6535-1894
[2] University of Applied Science Merseburg, Germany

*corresponding author

Name of Editor: Jason Moore
First published: 07/09/2023
Last published: 09/09/2024
Citation: Stolle, K., Wahl, A. & Schmidt, S. (2024). Trajectory Forecasting for Powered Two Wheelers by Roll Angle Prediction with an LSTM Network [version 3; peer reviewed]. The Evolving Scholar - BMD 2023, 5th Edition.
This work is licensed under a Creative Commons Attribution License (CC-BY).

Abstract:

Active safety systems for powered two wheelers (PTWs) are considered a key pillar to further reduce the number of accidents and thus of injured riders and fatalities. Enhanced awareness for the current riding situation is required to improve the performance of current systems as well as to enable new ones; this includes the detection of the rider's intention – the action that is planned by the rider for the short-term future. The prediction of a continuous trajectory for the upcoming seconds of the ride is one way to express rider intention. Our work pursues the prediction of the PTW lateral dynamic state by means of a roll angle trajectory over the upcoming 4 s of riding. It thus considers the special vehicle dynamics characteristics of single-track vehicles that negotiate bends at a roll angle compared to cars. A deep learning (DL) prediction model that is based on a Long-Short Term Memory (LSTM) layer is optimized and trained for this task using a broad on-road riding dataset that focuses on the rural road environment. Inputs to the prediction model are PTW internal signals only, that are measurements of vehicle dynamics, rider inputs, and rider behavior. The latter two groups of signals are non-common for current series production PTWs and were especially added to our test bike before gathering the riding data set. The prediction performance of the optimized DL model is compared to a simple heuristic algorithm using multiple metrics in the roll angle and position trajectory domain. Evaluation on a representative test data set shows a significantly improved detection of rider intention by the DL model in all metrics. Reasonable lateral trajectory accuracy is achieved for at least 2 s of the total 4 s prediction horizon in 99 % of all test cases, given the chosen model architecture and input features. Furthermore, the feature importance of the especially added non-common measurement signals of steering and rider behavior is investigated in an ablation study. It reveals the importance of steering signals in the first second of the prediction horizon whereas the rider behavior signals aid trajectory prediction performance for up to 2.5 s.

Keywords: Deep Learning, Trajectory Prediction, Powered Two Wheeler, Rider Behavior, Riding Intention

©2023 Stolle, K. L., Wahl, A. & Schmidt, S. published by TU Delft OPEN on behalf of the authors.
ISSN: 2667-2812

 http://dx.doi.org/10.59490/66664f995777b675f57fe3c0

Introduction

Three quarter of all PTW accidents in Europe are non-single accidents (Brown et al., 2021). Riders are especially prone to heavy injuries or fatalities in case of collision due to the inherently low passive safety of PTWs. Riding gear including airbags, that offer an additional cushioning space in case of an accident, are an ongoing trend that increases passive safety on PTWs, but their benefit in the field is not investigated yet (Tissot, Ballester, & Honoré, 2022). So, accident avoidance and mitigation by the help of active safety systems are objective of research and development in the field of PTWs.

The overall active safety systems landscape for PTWs can be differentiated into three levels as illustrated in Figure 1. On a first level, we find stabilization systems like Antilock Braking System (ABS) and Motorcycle Stability Control (MSC) that help avoiding accidents by intervening into the longitudinal dynamics of PTWs when instabilities are occurring, e.g., preventing the wheels from slipping or locking (Lich, Block, Prashanth, & Heiler, 2016). Stabilization systems successfully found their way into series PTWs for decades, reaching a broad spread nowadays. On a second level of active safety systems, Advanced Rider Assistance Systems (ARAS) are emerging in PTWs since a few years (Savino et al., 2020). Continuously assisting the riding task (e.g., distance-controlled cruise control ACC) and predictive warning ahead of critical situations (e.g., forward collision warning FCW) can reduce riding errors and thus help to lower the chance of accidents, being it single accidents or collisions with other traffic participants. ARAS systems rely on sensors that are on-board the PTWs capturing its environment. The third level of active safety systems utilizes connectivity to receive information about the environment from a backend or exchange information with other vehicles. The latter case is developed under the term Cooperative Intelligent Transport Systems (C-ITS), where traffic participants share their driving intentions with each other (Connected Motorcycle Consortium (CMC), 2023). By warning the rider and drivers of surrounding vehicles in case of an imminent risk of collision, such systems are suited to reach better collision avoidance potential than ARAS systems; they are yet not available in production.

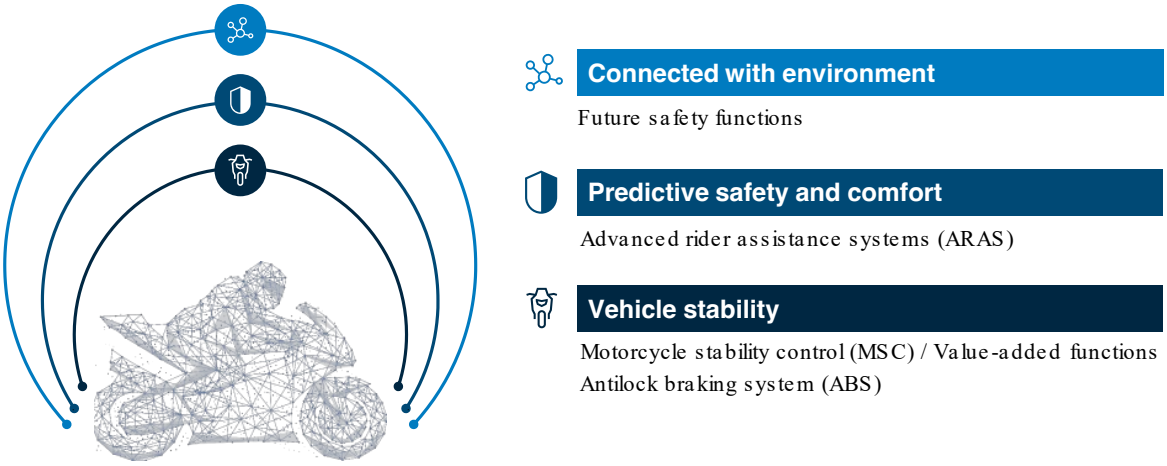


Figure 1. Three levels of active safety systems for powered two wheelers with exemplary functions.

Beside the mentioned collisions, single vehicle accidents make up of a quarter of PTW accidents with fatalities or serious injured riders in Europe, while 64 % of them occur during cornering (Brown et al., 2021). Most single accidents are primarily caused by rider error and could therefore be avoided (Biral, Bosetti, & Lot, 2014). A prominent scenario of a single accident during cornering is known as ‘undercornering’ where a rider fails to follow the lane and leaves the curve towards its outside. It is hereby important to mention that undercornering is not caused by reaching the physical limit in most cases – e.g., the maximum roll angle for the given road conditions – but riders fail to increase the roll angle by their own error, e.g., due to corner fear (Scherer et al., 2021).

Future safety systems for PTWs, being it ARAS or C-ITS or a combination of both, strongly require information about the ego rider intention, either to share it with other traffic participants (C-ITS) and identify collision critical situations, or to identify riding errors. A performant detection of the rider intention will enable a multitude of functions that warn the rider or intervene in the controls to enhance riding safety. This challenging task is therefore the subject of current research. As an example for the required look-ahead time of a rider intention detection, the Connected Motorcycle Consortium (CMC) states that 6.5 s time before a collision (TTC) is needed to properly process and display a warning to riders for the left turn collision assistance system (CMC, 2023).

Recent work in the field of vehicle behavior prediction is introduced in the first section of this paper. Some investigations regarding rider behavior and intention detection for PTWs are presented as well. The specific problem statement and our approach to it are

©2023 Stolle, K. L., Wahl, A. & Schmidt, S. published by TU Delft OPEN on behalf of the authors.

ISSN: 2667-2812

explained in a second section. Following is the description of the riding data used for training and testing a deep learning (DL) trajectory prediction model. Afterwards, the chosen DL prediction model architecture is described, and metrics used for model training and testing are explained. As first part of the results, the prediction performance of our DL model is contextualized by comparison to a heuristic approach. Secondly, the findings of our ablation study on the feature importance of the non-common measurement signals of rider steering inputs and rider behavior are presented.

Related work

Early research on vehicle behavior prediction was mostly concerned with physics-based approaches like filters (Lefèvre, Vasquez, & Laugier, 2014). These are not regarded as state-of-the-art anymore in the current research, which is mainly driven by autonomous driving applications (Mozaffari, Al-Jarrah, Dianati, Jennings, & Mouzakitis, 2022). Instead, DL based models are incorporated to predict intended behavior of traffic participants surrounding an autonomous agent that needs the information to plan and act in a safe and comfortable way. These surrounding vehicles are mostly cars due to their high share of representation in the available public datasets. Prediction of vehicle behavior can either be understood as classification problem where the output is a maneuver intention (high-level), or it is understood as regression problem where a continuous trajectory is output of the prediction model (Mozaffari et al., 2022). Either problem setting comes with advantages and disadvantages. Prediction of maneuver intention provides high-level understanding of the traffic scene but is restricted to a-priori defined maneuver classes. Whereas the biggest benefit of continuous trajectory prediction lies in its universality to traffic scenarios and the explicit statement of future vehicle states. The latter is very useful input to the downstream planning tasks. But the universality of regression may be of theoretical nature as specific model approaches are narrowing the problem statement down again to certain maneuvers or behaviors.

Recent examples of vehicle behavior prediction algorithms use information coming from environmental sensors of the ego vehicle or on infrastructure side as inputs, as they are mostly predicting the behavior of surrounding vehicles. Some approaches directly use the processed information of relative positions, velocities (or similar) of the surrounding that is assumed observable from the raw sensor data. As driver behavior is not assumed to fulfill the first-order Markov assumption, it is necessary to feed a time history of measurements instead of current state information only to any prediction model. Information about the road infrastructure like lanes and traffic rules are incorporated as additional inputs in some approaches (Mozaffari et al., 2022). In contrast, information that is assumed to contain valuable cues about the driving intention, like detailed measurements of vehicle dynamics and driver inputs, is not used in autonomous driving applications, because it is only available in the ego-trajectory prediction use case. Therefore, the transferability of the current state-of-the-art algorithms to the ego-trajectory prediction for PTW must be proven in our study.

Beside the classification type of behavior prediction model, Mozaffari et al. (2022) cluster regression models according to the number of predicted behavior modes (unimodal vs. multimodal) and differentiate whether the prediction model incorporates maneuver information (maneuver intention awareness). The latter type of approach can be seen as a combination of high-level maneuver classification and trajectory regression problem in a single model. So, a distinct split into classification and regression models is not applicable to a variety of more complex model types that incorporate both. A high share of DL based trajectory prediction models is based on Recurrent Neural Networks (RNN) because they are very powerful in extracting temporal information from time-series data (Mozaffari et al., 2022).

There is some related work available that aims directly on the behavior prediction of PTWs. Scherer and Basten (2022) present a heuristic algorithm in the form of a parameterizable mathematical model for the calculation of rider- and curve-individual roll angle trajectories. Their approach relies on the hypothesis that an individual rides through a specific curve in a repeatable way. Any explicit measurements on rider inputs or rider behavior are not incorporated in their work. The algorithm is presented for a single curve on an enclosed test track that was ridden multiple times by the participants of a riding study. A current whitepaper of CMC discusses the need for trajectory prediction for PTWs (CMC, 2023). They investigate the position trajectory prediction capability of simple algorithms that rely on current vehicle dynamic state information only; in summary, those algorithms assume either ‘constant heading’ or ‘constant curvature’ over the prediction horizon. Different turning maneuvers in an intersection scenario are simulated using a motorcycle multi-body model. A metric called evaluation index (EI) is introduced that is the maximum look-ahead time in the current riding state that can be predicted without the lateral distance error between the algorithm’s prediction and the ground truth trajectory getting larger than 2 m. The investigation shows insufficient prediction accuracy of all approaches tested as the EI metric declines to only about 1 s during the course of any turning maneuvers tested. Additionally, small in-lane corrections of the simulated rider during ‘going straight’ scenarios cause the EI to fall to 2-3 s already. Based on those results, the authors motivate the necessity of detecting rider intention and predicting the behavior based on the riding history to improve the accuracy, e.g., using machine learning techniques. The authors are not aware of any such research activities on trajectory prediction of PTW using machine-learned algorithms.

©2023 Stolle, K. L., Wahl, A. & Schmidt, S. published by TU Delft OPEN on behalf of the authors.

ISSN: 2667-2812

 http://dx.doi.org/10.59490/66664f995777b675f57fe3c0

Approach

Our research approach on rider intention detection by roll angle trajectory prediction has been outlined in an extended abstract earlier (Stolle, Wahl, & Schmidt, 2023). The following describes it in greater detail. We aim for predicting cornering of PTW, as it is the case for the two PTW references presented above; thus, the future lateral dynamic state is predicted, not the longitudinal dynamics, e.g., forward velocity. We choose a machine learning approach by training a DL neural network on the prediction task as we are aiming to utilize typical rider intention patterns in riding data. Any prediction approach based on a physical model is limited to the time delay between rider inputs and the lateral dynamic vehicle states. A previous study revealed that the time delay between a steer torque rider input and the roll angle state ranges between 0.45 s and 2 s for the given test motorcycle, dependent on velocity (Stolle, Wahl, & Schmidt, 2022a). Consequently, empirical methods need to be applied to achieve further predictions. Upon reviewing the on-road riding data to be used in this work, which is highly variable in road and rider, it became apparent that the effort required to develop a heuristic model – like Scherer and Basten (2022) – that generalizes on the highly variable set of situations in the data set is unforeseeable high, coupled with uncertain chances of success. Therefore, it was decided to use the exploratory capability of a deep learning (DL) model to investigate the possibilities in predicting the rider cornering behavior.

The scope of our prediction algorithm is to use only internal PTW signals and no environmental sensing as input features, which means there is no information about road infrastructure or surrounding traffic participants. We can access a broad variety of vehicle dynamics signals and have special measurement signals of steering and rider behavior available; those are explained in more detail in the following section about the dataset. The decision to disregard any environmental information is made for multiple reasons. We focus on the rural road riding environment, especially as most single riding accidents occur there, where any infrastructure-based information is not expected to be available in the future. There is also no incorporation of surrounding vehicle information captured by on-board sensors as it is of minor importance for the rural road use case and single accidents. We also forgo to use any course information (e.g., from maps) as input for the rider intention detection for two main reasons. First, PTWs show a high variety of position within the own lane compared to non-single-track vehicles due to their narrow size; this makes their trajectories less tied to the course and thus poses challenges to localization. Secondly, using course information as input would hinder any prediction model to address riding errors where the course of the road is left, like the undercornering use case. Any learned algorithm would very likely not predict such a behavior as we fortunately don't have major riding errors in the data set.

The task of detecting the rider intention for lateral dynamics is broken down to a regression problem. A DL model based on RNN layers is predicting the future trajectory of the roll angle state which strongly correlates with the lateral dynamics of a PTW – except for tilted roads, side wind or uneven loading of the PTW. Maximum prediction time, that is referred to as length of the prediction horizon, is defined to be 4 s. This lies in the range of other use cases in literature, and it is also expected to cover the maximum available performance that is feasible with the given input data. The detailed design of the DL model is introduced in the model section. Three research questions are to be answered using the developed trajectory prediction model for PTWs:

> How much is the prediction improving over a simple benchmark algorithm when using a machine learning approach?
>
> What is the importance of the especially added steering and rider behavior measurement signals?
>
> Which prediction horizon is feasible with the developed DL model given the chosen input signals?

Riding data

A KTM 1290 Super Adventure motorcycle is equipped with data logging and several additional sensors for gathering vehicle dynamics, rider input and rider behavior data. Not all the measured signals are used as input features of the DL model, but a set of influential features is experimentally identified during model development. Table 1 provides an overview of the set of 16 signals and their respective sensor or source that are used as input features in the final prediction model.

Three 'steering signals' are measured at the steering system of the motorcycle that are non-common for series-production PTW. A linear potentiometer measures steering angle, an additional Inertial Measurement Unit (IMU) reads steering rate, and strain gauges applied to the handlebar measure the rider's steering torque input. Furthermore, rider upper body and head movements are captured by a camera-based measurement system that was introduced by the authors for previous tests and is described in (Stolle, Wahl, & Schmidt, 2022b); those signals are referred to as 'rider behavior' measurements. Lateral upper body position is described by the two variables of relative lean angle between rider and motorcycle and a lateral offset of the hip point from the motorcycle center plane. Head movement is given as the rotational angle of the rider's helmet around the vertical axis in the motorcycle's frame coordinate system.

©2023 Stolle, K. L., Wahl, A. & Schmidt, S. published by TU Delft OPEN on behalf of the authors.
ISSN: 2667-2812

http://dx.doi.org/10.59490/66664f995777b675f57fe3c0

Table 1. List of measurements signals that are input features of the best DL prediction model and their source. Abbreviations: IMU, Inertial Measurement Unit; MSC, Motorcycle Stability Control algorithm.

Signal name	Sensor / Source	Signal name	Sensor / Source
Roll angle	Estimate (MSC)	Forward velocity	Estimate (MSC)
Roll rate	IMU	Front brake pressure	Pressure sensor
Pitch angle	Estimate (MSC)	Steering torque	Strain gauges
Pitch rate	IMU	Steering angle	Linear potentiometer
Yaw rate	IMU	Steering rate	Steering IMU & IMU
Longitudinal accel.	IMU	Rider upper body lean angle	Rider camera
Lateral accel.	IMU	Rider upper body lateral offset	Rider camera
Vertical accel.	IMU	Rider head yaw angle	Rider camera

The usage of on-road measurement data poses additional challenges to any prediction model due to noise and disturbances in comparison to synthetically created data sets. Especially the steering torque signal suffers due to a low signal to noise ratio; one finds it to be smaller than unity in straight riding and also in most constant cornering situations. Filtering was addressed during model development with the ultimate result that the DL model's best performance is with unfiltered data, which is probably due to the time delay that is added by the filtering process.

The on-road riding data set was gathered on various routes all over Southwest Germany and with a major focus on rural roads, which are typical for the sports/leisure use-case of PTWs in Europe; but still riding through towns, small cities, and on highway is also present to some extent. Having different routes for each ride ensures that a machine learning approach is not misled to learn course information. Overall, it comprises more than 70 h of riding by 21 riders of different riding experience, skills, and style. During data preparation, it is ensured that only riding with a velocity > 30 km/h is regarded for the prediction task to ensure the motorcycle is in the stable regime: this leaves ~ 65 h of data remaining. Besides, the data needs further preparation as one finds a strong bias towards straight riding in the data set due to its high appearance in real-world road design. Such a bias affects any learning based unimodal prediction model negatively. We are thus reducing straight riding by deleting 90 % of all data samples that are pure straight riding. This condenses the overall amount of data to ~ 49 h used for training, validation, and test of the DL model. The split into the latter three categories is chosen to be 75 %, 18 %, and 7 %.

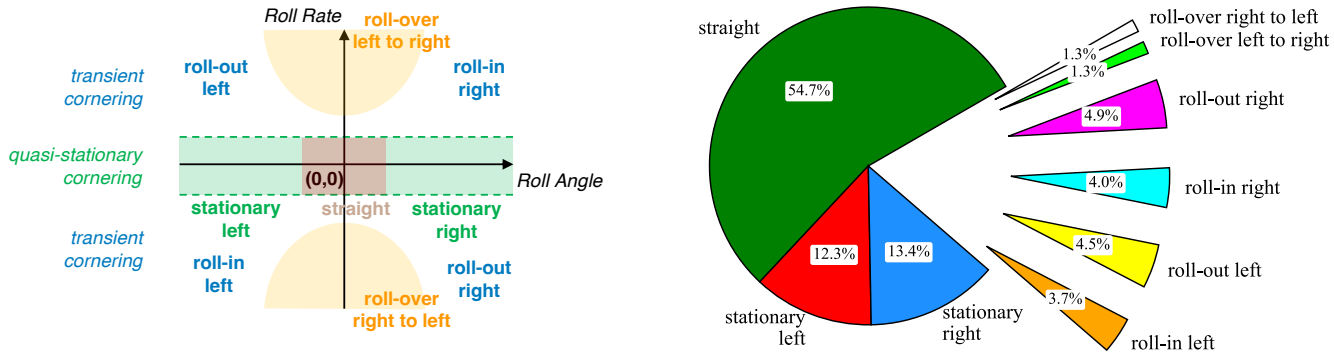


Figure 2. Left: definition of maneuver segments based on the lateral dynamic state (roll angle and roll rate) of a powered two-wheeler. Right: share of the lateral dynamic maneuver segments in overall prepared data (training, validation & test).

The composition of the remaining prepared data set is further analyzed by assigning maneuver segment labels. The idea of labeling a PTW ride with maneuver segments according to the lateral dynamic states of roll angle and roll rate is taken from Magiera (2020); nine different maneuver segment classes are defined based on the PTW roll dynamic, those are illustrated in the left of Figure 2. The maneuver segment labeling process is realized with a state machine that distinguishes six transient from three quasi-stationary maneuver segments, mainly by the parameter roll rate. Quasi-stationary segments of straight riding and stationary cornering are separated by the roll angle state. Thresholds, hystereses, and other conditions of the state machine are chosen by expert knowledge with the objective of creating reasonable labels during cornering, i.e., a single corner without major riding line corrections should consist of a stationary cornering phase that is surrounded by roll-in and roll-out phase that start and end in straight riding. The

©2023 Stolle, K. L., Wahl, A. & Schmidt, S. published by TU Delft OPEN on behalf of the authors.

ISSN: 2667-2812

 http://dx.doi.org/10.59490/66664f995777b675f57fe3c0

distribution of maneuver segments over the whole prepared data set is presented in the pie chart on the right of Figure 2. One still notices a high share of straight riding which is caused by the length of samples (the sampling process is described in the 'model & metrics' section). Only samples with pure straight riding classification were deleted during data preparation. Samples that feature multiple maneuver segments over time still contain a high share of straight riding.

Model & Metrics

According to the previously described approach to rider intention detection, the specific trajectory prediction task of the DL model is introduced. Figure 3 illustrates the following description schematically. At a current point in time t_i, a regression type DL model predicts future roll angle values P up to a certain maximum prediction time t_{i+P} at multiple discrete points that are evenly spaced along the prediction horizon with T_P. Input to the model at time t_i is a time series of n features F_n from $t_{i\text{-}H}$ in the past up to the current point in time t_i, evenly sampled at discrete points with T_H. The number and choice of the input features, input sampling time, and length of the input time series are all subject of hyperparameter optimization, whereas the prediction horizon length and output sampling time are preset to 4 s and 0.2 s each. The riding data is sliced into so-called samples during data preparation, where each sample ranges from $t_{i\text{-}H}$ to t_{i+P} and contains all input features F_n and the desired ground truth output P. One sample is created every 0.2 s, so samples are overlapping each other.

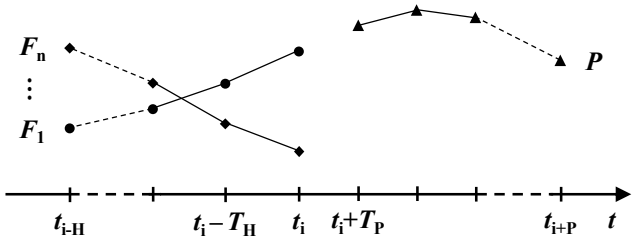


Figure 3. Illustration of the DL models prediction task at single time point t_i. Discrete time series data of n features $\boldsymbol{F}_n$ is input to the DL model. Its output is a prediction P at multiple discrete time points over a given prediction horizon.

The DL model architecture consists of one long short-term memory (LSTM) layer that is followed by a multilayer perceptron (MLP), which is a common neural network architecture for time-series prediction (Altche & De La Fortelle, 2017). The LSTM layer is a specific type of RNN, and it interprets the time-series of all input features into a hidden state. After processing the whole input time series, the LSTM's final hidden state is fed into the MLP, which is a serial sequence of fully connected linear layers in our model. Definition of the network's architecture is realized by hyperparameter optimization with the Python library Optuna. The following parameters were altered: size/number of LSTM layers, size/number of layers in the MLP, and the model's training parameters of learning rate, batch size, weight initialization, and regularization. Optimization resulted in a single LSTM layer featuring 64 cells and two hidden linear layers of 64 and 32 neurons in the MLP before the output layer. All linear layers use the ReLU (Rectified Linear Unit) activation function.

Multiple metrics are used to evaluate the prediction model performance in training and testing, they are introduced hereinafter. The Mean Squared Error (MSE) of all predicted roll angle values along the prediction horizon is used as the DL model's cost function during training; in combination with the Adam adaptive gradient descent learning strategy, this is a common choice for regression models (Bianchi, Maiorino, Kampffmeyer, Rizzi, & Jenssen, 2017). Calculating its root generates the 'overall RMSE', a more descriptive metric for model testing. In addition to a single cumulative RMSE value for the whole prediction, the roll angle error calculation is unraveled over the prediction horizon and the 'RMSE over prediction horizon' is analyzed for each of the 20 prediction points along the 4 s prediction horizon separately in testing. Furthermore, the prediction model's performance will be compared to the results of the CMC investigations (CMC, 2023). This requires calculation of the EI metric that was mentioned in the related work. The roll angle trajectory output of our prediction model as well as the ground truth roll angle trajectory need to be transformed into position trajectories for this. A lateral position offset is then calculated based on these two position trajectories, which serves as basis for the EI.

Transforming a roll angle into a position trajectory means that we leave the lateral only domain as it requires the assumption of longitudinal velocity over the prediction horizon. We are using the ground truth future velocities for the transformation of the ground truth roll angles, and a constant velocity assumption for the transformation of the DL model's predictions. First step of the transformation itself is the calculation of curvature, where a simple 'single wheel' model is used; it considers the width of the wheels

©2023 Stolle, K. L., Wahl, A. & Schmidt, S. published by TU Delft OPEN on behalf of the authors.
ISSN: 2667-2812

http://dx.doi.org/10.59490/66664f995777b675f57fe3c0

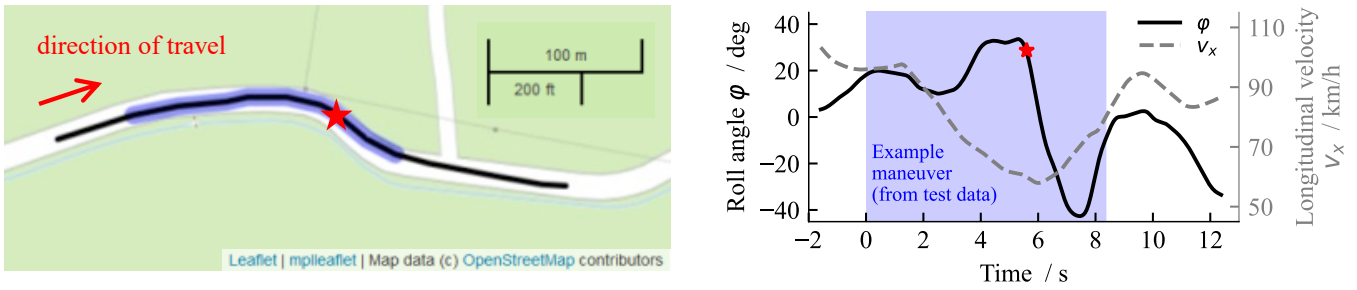


Figure 4. Example curve riding maneuver on rural roads. The prediction is analyzed in the marked blue section of 8.4 s length. Additional 1.6 s of riding history at the beginning and 4 s of prediction horizon at the end are displayed. A single situation of interest is marked with red star at 5.6 s.

as well as the center of gravity height of the PTW. The curvature is then propagated constantly between the 20 discrete point along the prediction horizon and relative positions (x, y) are calculated accordingly. The RMSE of lateral distance between ground truth and predicted trajectory is evaluated at each point along the prediction horizon separately and the EI is calculated for each sample with a lateral error threshold of 2 m as in the CMC reference (CMC, 2023). The longitudinal distance error along the predicted relative position trajectory is not evaluated as the focus lies on lateral prediction.

The procedure from roll angle prediction to EI metric shall be demonstrated for a single exemplary maneuver from the test data set to establish understanding of the just described. Figure 4 shows the course of the example cornering maneuver on rural roads in the map and the corresponding plots of roll angle and velocity. Data points that are underlined in blue are subject of the evaluation while the attachments at the beginning and end illustrate the DL model's input history in the first and prediction horizon in the last test data point. The maneuver is a right-left S-curve that is already approached in a slight right turn. The following left curve can already be seen in the prediction horizon at the end of the maneuver.

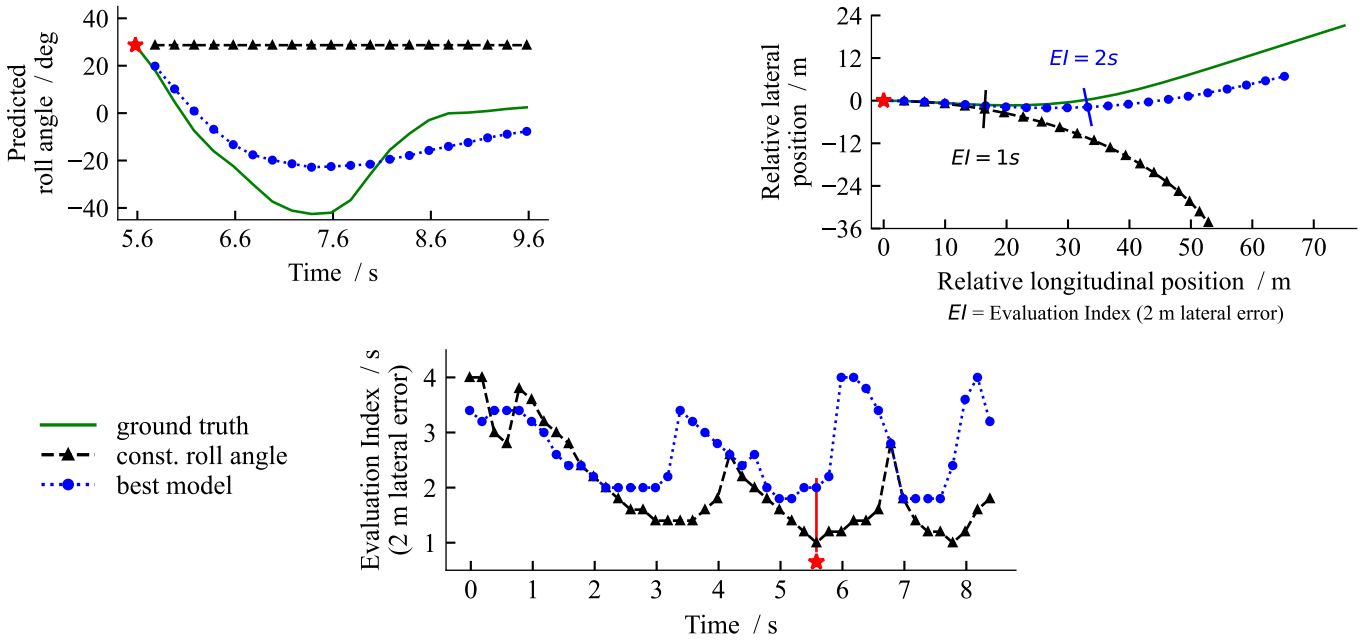


Figure 5. Top: predictions at a single point of interest from the example curve riding situation, marked with red start in Figure 4, in further analysis. Top left: Roll angle prediction of machine learning (ML) model ('best model') compared to ground truth future roll angle and constant roll angle assumption. Top right: Relative position trajectories calculated from roll angle and velocity. EI metric with 2 m lateral distance error threshold marked. Bottom: EI metric evaluated over the whole example curve riding maneuver of Figure 4.

©2023 Stolle, K. L., Wahl, A. & Schmidt, S. published by TU Delft OPEN on behalf of the authors.
ISSN: 2667-2812

 http://dx.doi.org/10.59490/66664f995777b675f57fe3c0

The red star in Figure 4 marks a single point of interest at time 5.6 s for which the concrete predictions are presented in the upper two diagrams of Figure 5. Herein, the top left plot shows the ground truth roll angle over the 4 s prediction horizon beside the DL model's prediction, denoted as 'best model', and a simple constant roll angle algorithm, that is equivalent to the assumption of constant curvature. Transformation into position trajectories results in longitudinal and lateral positions relative to the current state. Those trajectories are presented in the top right plot in Figure 5. Lateral distance errors are calculated by determining the distance of predictions perpendicular to the ground truth and the EI metrics for the black and blue trajectories in this single point in time are labelled in the plot too. The DL model reaches a prediction time of 2 s without the lateral distance error being larger than 2 m, while the simple assumption achieves 1 s only. The lower plot in Figure 5 shows the EI evaluated at each point of the exemplary test manoeuvre of Figure 4, where our best prediction model never goes below 1.8 s while the simple algorithm drops to 1 s in minimum.

Trajectory prediction compared to simple heuristic approach

The prediction performance of the optimized DL trajectory prediction model is presented in the following and is denoted as 'best model' in all graphics. This model has the 16 variables presented in Table 1 as inputs, sampled with a T_H of 20 ms over a signal history of 1.6 s. Its performance is compared to the simple heuristic algorithm of constant roll angle; this assumption equals a constant curvature logic which is presented as baseline in related work. Both predictions are evaluated on the same test data set that was drawn randomly before any DL training or optimization.

The left plot in Figure 6 shows the 'RMSE over prediction horizon' calculated for the roll angle predictions. One sees an advantage for the DL model over the simple approach for the whole prediction horizon as the gap between dotted blue and dashed black curve is ever increasing, while the biggest improvement, i.e., the strongest build-up of the gap, occurs within the first second of prediction. The 'overall RMSE' of roll angle is 56 % higher for the constant roll angle logic compared to the best model. Transforming roll angle into position trajectories, using the constant velocity assumption for both models, results in the lateral distance 'RMSE over prediction horizon' that is presented in the right plot in Figure 6. The gap between DL model and simple algorithm increases progressively as the transformation is integrating in nature. The constant roll angle algorithm is 83 % worse than the best model in 'overall RMSE' of lateral distance.

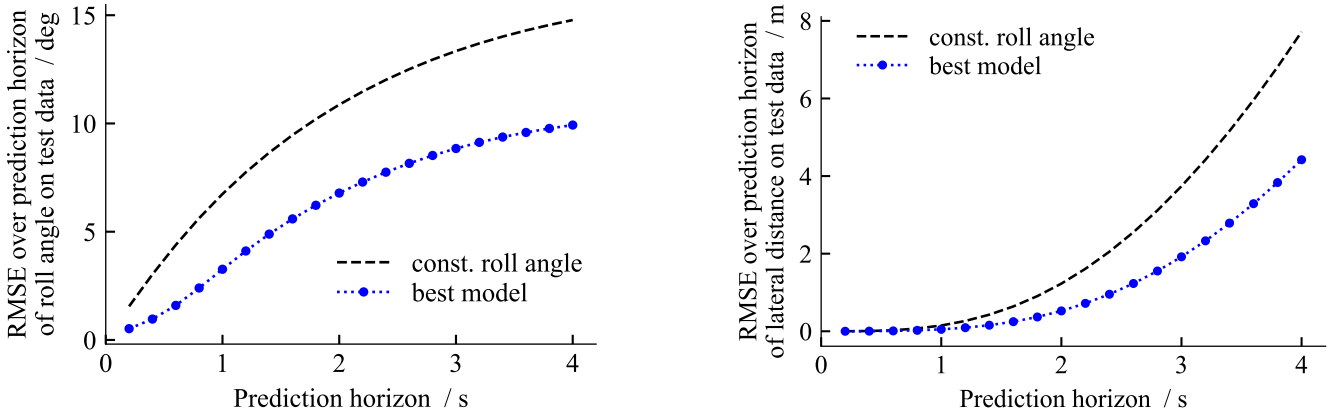


Figure 6. 'RMSE over prediction horizon' metric evaluated on test data for the best deep learning prediction model (blue dots) and the simple constant roll angle model (black). Left: roll angle predictions. Right: lateral distance evaluated after transforming roll angle into relative position trajectories.

Evaluating the EI metric for each sample of the test data set shows smallest occurring EIs of 1 s for the simple constant roll angle algorithm and 1.4 s for the best model. Comparing the occurrence of EIs in the histogram in Figure 7 reveals a distinct improvement of EI for the DL model in blue. Coming from the grey striped constant roll angle baseline, the number of test samples with EI smaller than 2 s decreases by 91 %, whereas the samples with an EI greater or equal 3 s increase by 26 %. In absolute numbers, the best model achieves at least 2 s of EI for 99.1 % of all test samples and for 80.5 % of all test samples an EI of 3 s or more is realized.

©2023 Stolle, K. L., Wahl, A. & Schmidt, S. published by TU Delft OPEN on behalf of the authors.

ISSN: 2667-2812

http://dx.doi.org/10.59490/66664f995777b675f57fe3c0

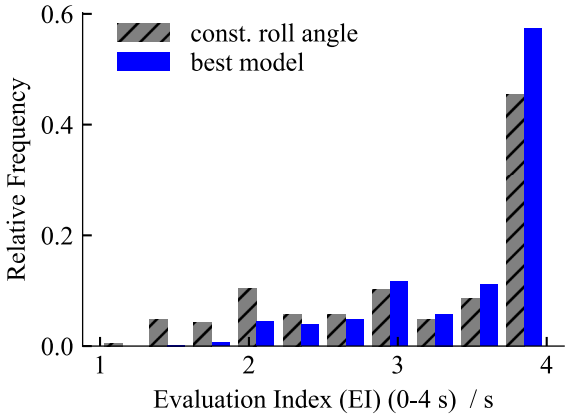


Figure 7. Relative frequency of Evaluation Index (EI) metric evaluated for each sample of the test data set with a lateral error threshold of 2 m. Best deep learning prediction model displayed in blue and simple constant roll angle model in striped grey.

Ablation study of non-common measurement signals

An ablation study on the importance of the non-common measurement signals as input features for the DL model is carried out. Ablation models are trained without specific input signals and are then compared to the best model for this. The results of three ablation models, where groups of input signals were removed, are illustrated in three individual diagrams in Figure 8. Each diagram shows the 'RMSE over prediction horizon' curves of the roll angle predictions for the ablation model and the best model in comparison. The difference between those two curves is shown separately as a dashed line with dots to aid interpretation. A performance degradation caused by the removal of input features is visible for all three configurations that were tested. Those were the ablation of: a) steering signals (steering angle, rate & torque), b) rider behavior signals (rider head yaw angle, rider upper body lean angle & lateral offset of the hip point) and c) both steering and rider behavior signals. The observed effects are described in more detail below.

Removing the steering signals causes the 'overall RMSE' of roll angle to increase by 1 % (3.5 % in 'overall RMSE' of lateral distance) compared to the best model. One can see the green curve of the ablated model moving upwards away from the blue curve towards larger errors right at the beginning of the prediction horizon in Figure 8a. The dashed curve, showing the difference between both models, reaches its maximum at a prediction horizon of 0.8 s. For the further prediction horizon, the difference in prediction performance is decreasing again and is almost identical from 3 s onwards. This means that the ablated model can almost make up for the disadvantage it suffered between 0.2 and 0.8 s due to the absence of steering signals. We conclude from the observation, that the distance between the error curves of both models only increases in the range from 0.2 to 0.8 s, that the steering signals contain valuable information for prediction only for this time horizon.

Removing the rider behavior features leads to a 5 % increase in 'overall RMSE' of roll angle (6.2 % in 'overall RMSE' of lateral distance) compared to the best model. Following the same line of argumentation as for the steering signals, the behavior of the 'RMSE over prediction horizon' curves in Figure 8b reveals that rider behavior signals contain valuable information for the roll angle trajectory prediction in between 0.4 and ~2.5 s of the prediction horizon. Interestingly, there is even a slight improvement from 0.2 to 0.4 s without the mentioned signals, but this has no significant influence on the 'overall RMSE'. Unlike before, the performance disadvantage cannot be recovered before reaching the maximum prediction horizon of 4 s.

A roll angle trajectory prediction model without the steering system and rider behavior signals has only common measurement signals (regarding state-of-the-art PTWs) remaining. It's performance difference compared to the best model is shown in Figure 8c where the gap between ablated and best model builds up between 0.2 and ~1.9 s of the prediction horizon. Having only the standard signals causes the highest degradation of prediction performance of all three configurations tested. The 'overall RMSE' of roll angle increases by 6.6 % (11.1 % in 'overall RMSE' of lateral distance) which is even a bit more than the sum of the single ablation effects presented before.

©2023 Stolle, K. L., Wahl, A. & Schmidt, S. published by TU Delft OPEN on behalf of the authors.

ISSN: 2667-2812

http://dx.doi.org/10.59490/66664f995777b675f57fe3c0

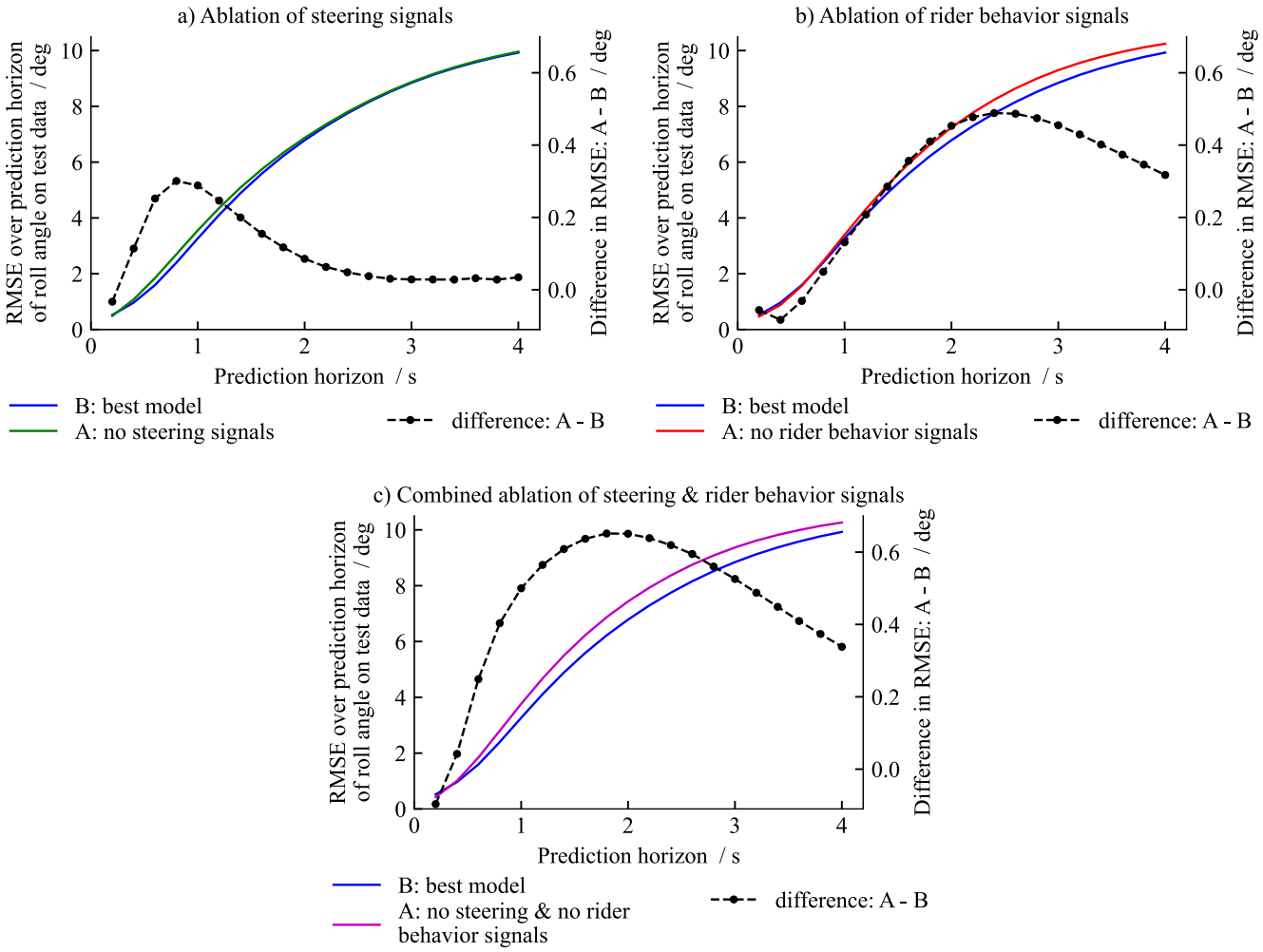


Figure 8. Ablation study on the importance of the non-common measurement signals of steering and rider behavior. RMSE over prediction horizon of roll angle is presented for the best and an ablated model that has a) no steering signals, b) no rider behavior signals or c) no steering and no rider behavior signals as input features.

Conclusion

Research on PTW active safety systems aims for an improved detection of rider intention, with this work focusing on cornering. Prediction of the lateral dynamic state of roll angle over 4 s of future riding is realized by optimization of a DL model based on a LSTM layer. A diverse and broad riding data set, that focuses on the rural road environment, is used for development and testing. Only PTW internal measurements of vehicle dynamics and especially added signals of steering and rider behavior are applied as features to the DL model. The performance of the developed prediction model is evaluated using different metrics in the roll angle as well as position trajectory domain and is compared to a simple heuristic algorithm assuming constant roll angle. An ablation study on the importance of the especially added measurements is performed as well, to find answer to the research questions posed.

How much is the prediction improving over a simple benchmark algorithm when using a machine learning approach?

Testing on a representative 7 % of all riding data available reveals strong improvements of the DL model over the simple heuristic of constant roll angle that are visible in all metrics evaluated. E.g., the occurrence of riding situations that have less than 2 s of feasible look-ahead time (EI metric) – defined by a lateral trajectory offset < 2 m – is lowered by over 90 %. In total numbers, an EI of at least 2 s is achieved in 99.1 % of all test cases.

What is the importance of the especially added steering and rider behavior measurement signals?

©2023 Stolle, K. L., Wahl, A. & Schmidt, S. published by TU Delft OPEN on behalf of the authors.

ISSN: 2667-2812

The results of the ablation study reveal the importance of the non-common input features of steering and rider behavior signals. The three signals of steering torque, angle, and rate do only benefit in first second of prediction, their overall effect is thus small. Removing rider head yaw angle, rider upper body lean angle and lateral offset of the hip point from the set of input features has a stronger effect on prediction performance as those signals incorporate valuable information for trajectory prediction up to a prediction horizon of 2.5 s. Removing all non-common signals causes the biggest deterioration of prediction performance of 11 % in overall lateral distance error.

Which prediction horizon is feasible with the developed DL model given the chosen input signals?

The distribution of the EI metric over all test samples as well as the ablation study give indications on the prediction horizon that is feasible with reasonable accuracy. The EI shows that a minimum of 2 s of prediction horizon without a lateral distance error > 2 m is achievable in most cornering situations as 99 % of all test samples achieve this value. Similarly, the ablation study indicates that there is valuable information in the rider behavior input features for a prediction horizon of up to 2.5 s.

In summary, the LSTM based DL model predicting a roll angle trajectory is a promising approach for the detection of the rider intention regarding lateral dynamics. The method demonstrates that there is information in the history of the time-series vehicle dynamics and rider behavior measurement signals of a PTW that is valuable for the prediction of cornering. It significantly improves over simple heuristic approaches that only take the current state of the PTW into account. However, the method presented did not consider longitudinal dynamics, for which the simple assumption of constant velocity was made. It remains to investigate the subsequent drawback in the metrics under consideration. In addition, the extension of the method to include prediction of the longitudinal dynamics will be tested. Future work on the DL trajectory prediction model will also investigate in detail how different maneuvers and riding styles affect the prediction.

References

Altche, F., & De La Fortelle, A. (2017). An LSTM network for highway trajectory prediction. In *IEEE 20th International Conference on Intelligent Transportation Systems (ITSC)* (pp. 353–359). IEEE.

Bianchi, F. M., Maiorino, E., Kampffmeyer, M. C., Rizzi, A., & Jenssen, R. (2017). *Recurrent neural networks for short-term load forecasting: An overview and comparative analysis. SpringerBriefs in computer science.* Springer.

Biral, F., Bosetti, P., & Lot, R. (2014). Experimental evaluation of a system for assisting motorcyclists to safely ride road bends. *European Transport Research Review, 6*(4), 411–423. https://doi.org/10.1007/s12544-014-0140-6

Brown, L., Morris, A., Thomas, P., Ekambaram, K., Margaritis, D., Davidse, R., Usami, D. S., Robibaro, M., Persia, L., Buttler, I., Ziakopoulos, A., Theofilatos, A., Yannis, G., Martin, A., & Wadji, F. (2021). Investigation of accidents involving powered two wheelers and bicycles - A European in-depth study. *Journal of Safety Research, 76*, 135–145. https://doi.org/10.1016/j.jsr.2020.12.015

Connected Motorcycle Consortium. (2023, April 7). *Path Prediction for PTWs: CMC Whitepaper.* https://www.cmc-info.net/uploads/1/2/1/4/121453783/whitepaper_path_prediction.pdf

Lefèvre, S., Vasquez, D., & Laugier, C. (2014). A survey on motion prediction and risk assessment for intelligent vehicles. *ROBOMECH Journal, 1*(1). https://doi.org/10.1186/s40648-014-0001-z

Lich, T., Block, W. G., Prashanth, S. N., & Heiler, B. (2016). Motorcycle Stability Control - The Next Generation of Motorcycle Safety and Riding Dynamics. *SAE International Journal of Engines, 9*(1), 491–498. https://doi.org/10.4271/2015-32-0834

Magiera, N. (2020). *Identifikation des Fahrfertigkeitsniveaus von Motorradfahrern in Kurvenfahrt im Realverkehr*, Technische Universität Darmstadt. 10.25534/tuprints-00014011.

Mozaffari, S., Al-Jarrah, O. Y., Dianati, M., Jennings, P., & Mouzakitis, A. (2022). Deep Learning-Based Vehicle Behavior Prediction for Autonomous Driving Applications: A Review. *IEEE Transactions on Intelligent Transportation Systems, 23*(1), 33–47. https://doi.org/10.1109/TITS.2020.3012034

Savino, G., Lot, R., Massaro, M., Rizzi, M., Symeonidis, I., Will, S., & Brown, J. (2020). Active safety systems for powered two-wheelers: A systematic review. *Traffic Injury Prevention, 21*(1), 78–86. https://doi.org/10.1080/15389588.2019.1700408

©2023 Stolle, K. L., Wahl, A. & Schmidt, S. published by TU Delft OPEN on behalf of the authors.

ISSN: 2667-2812

Scherer, F., & Basten, T. (2022). Entwicklung eines Motorradfahrendenmodells zur Trajektorienprädiktion. In Insitut für Zweiradsicherheit (ifz) e.V. (Ed.), *ifz-Research Publication Series: Nr. 20, Sicherheit - Umwelt - Zukunft XIV: Tagungsband der 14. Internationalen Motorradkonferenz 2022* (pp. 265–299). Institut für Zweiradsicherheit.

Scherer, F., Winner, H., Pleß, R., Will, S., Neukum, A., Stanglmaier, M., Bäumler, M., Siebke, C., & Prokop, G. (Eds.). (2021). *Berichte der Bundesanstalt für Straßenwesen F, Fahrzeugtechnik: Heft 142. Schräglagenangst: = Corner fear.* Fachverlag NW in Carl Ed. Schünemann KG. https://bast.opus.hbz-nrw.de

Stolle, K. L., Wahl, A., & Schmidt, S. (2022a). Importance of motorcycle rider upper body movement for rider intention detection and motorcycle state prediction. In Insitut für Zweiradsicherheit (ifz) e.V. (Ed*.), ifz-Research Publication Series: Nr. 20, Sicherheit - Umwelt - Zukunft XIV: Tagungsband der 14. Internationalen Motorradkonferenz 2022* (pp. 32–41). Institut für Zweiradsicherheit.

Stolle, K. L., Wahl, A., & Schmidt, S. (2022b). Motorcycle rider posture measurement for on-road experiments on rider intention detection. In *2022 IEEE 1st International Conference on Cognitive Mobility (CogMob)* (pp. 51–56). IEEE. https://doi.org/10.1109/CogMob55547.2022.10118004

Stolle, K. L., Wahl, A., & Schmidt, S. (2023). Trajectory Prediction for Powered Two Wheelers with Deep Learning. The Evolving Scholar - BMD 2023, 5th Edition. https://doi.org/10.24404/63fdc49b743b257fd7f65c53

Tissot, P.-F., Ballester, O. C., & Honoré, V. (2022). Smart wearable airbags: Benefits for users and remaining challenges after 60 million kilometres and 3000 accidents. In Insitut für Zweiradsicherheit (ifz) e.V. (Ed*.), ifz-Research Publication Series: Nr. 20, Sicherheit - Umwelt - Zukunft XIV: Tagungsband der 14. Internationalen Motorradkonferenz 2022* (pp. 202–207). Institut für Zweiradsicherheit.

©2023 Stolle, K. L., Wahl, A. & Schmidt, S. published by TU Delft OPEN on behalf of the authors.

ISSN: 2667-2812

The Evolving Scholar (2023)

https://doi.org/10.59490/65ba5e88bfab2a7d6973cd85

Bicycle and Motorcycle Dynamics 2023
Symposium on the Dynamics and Control of Single Track Vehicles
18 – 20 October 2023, Delft University of Technology, The Netherlands

Type of the Paper: Conference Paper

Revised

Validation of a bicycle simulator based on objective criteria

[version 2; peer reviewed]

Donaji Martinez Garcia[1]*, Kilian Gröne[1], Martin Fischer[1], Min Zhao[1] and Melina Bergen[1]

[1]German Aerospace Center - DLR; Donaji.MartinezGarcia@dlr.de, ORCID 0000-0002-0839-0627; Kilian.Groene@dlr.de, ORCID 0000-0001-9035-4440; Ma.Fischer@dlr.de, ORCID 0000-0001-8435-4321; Min.Zhao@dlr.de, ORCID 0000-0002-0485-5255; Melina.Bergen@dlr.de, ORCID 0009-0009-0727-0218
*corresponding author.

Name of Editor: Jason Moore
First published: 03/10/2023
Last published: 27/03/2024
Citation: Martinez Garcia, D., Gröne, K., Fischer, M., Zhao, M. & Bergen, M. (2024). Validation of a bicycle simulator based on objective criteria [version 2; peer reviewed]. The Evolving Scholar - BMD 2023, 5th Edition.
This work is licensed under a Creative Commons Attribution License (CC-BY).

Abstract:

Statistics show, that bicycles become more and more popular as transportation method, e.g. 25% increase in Germany between 2019 and 2021 (Sinus, 2021). To ensure the safety of bicycle riders as vulnerable road users (VRUs), analysing critical traffic situations is essential (Wendel, 2020). To be able to explore such situations in a safe environment, a bicycle simulator was built at DLR that can be used stand-alone or in combination with other simulators in order to integrate other traffic participants such as pedestrians or car drivers (Fischer et al., 2022; Martinez Garcia, 2021). This work describes the development of the simulator with the goal of creating a realistic and therefore immersive cycling experience (Jacobi, 2022; Janssen, 2022). A detailed description of the implementation of the recent improvements is provided as well as an objective evaluation for validation of the simulator.

Keywords: Bicycle Simulator, Vr, Bicycle Dynamics, Validation, Objective Criteria

© 2023 Martinez Garcia, D., Gröne, K., Fischer, M., Zhao, M. & Bergen, M. published by TU Delft OPEN on behalf of the authors.
ISSN: 2667-2812

Introduction

Simulator studies are valid if they produce results that can be generalized to real-world situations, and if the occurrence of unwanted symptoms, such as simulator sickness, doesn´t affect the results (Shoman & Imine, 2021). Hence, to accomplish this goal, the aim of simulator design is to evoke realistic cycling behaviour. In this context, it is still an open question how much physical validity, e.g. realistic simulation of bicycle dynamics, is necessary to support behavioural validity, which is a measure of how realistic the participants feel and behave when using the simulator. However, the main goal is to enhance behavioural validity for the use of bicycle simulators in traffic interaction research studies. A realistic perception of the environment is crucial to elicit valid and reliable behaviour. This includes the infrastructure, other road users, and the overall experience of cycling. To evaluate behavioural validity, performance measures of a simulator can be compared with those of a real bicycle on the road (O'Hern et al., 2017).

The study presented in this paper aimed to evaluate a new control logic together with hardware changes done to the DLR bicycle simulator and to identify in which areas it is possible to fine-tune the simulator so that it allows for a more realistic behaviour. For this purpose, two different set-ups of the simulator will be compared based on objective criteria first in a simulator study and then to data obtained with an equipped research bicycle. A parameterization of the simulator based on real-life information enables the delivery of realistic feedback to the users by adjusting the dynamic model, motion cueing and hardware modules. These initial steps are used as a basis for the process of obtaining an immersive and realistic cycling behaviour and motion perception. This should help to improve the bicycle simulator to represent real traffic situations in a virtual scenario and create an immersive environment.

Experimental set-up

With the goal of improving the cycling sensation and on the basis of previous evaluations (Martinez Garcia, 2022), a series of developmental changes were performed to the simulator. For the validation of the simulator data, an e-bike was instrumented with sensors with the main purpose of measuring the steering angle, leaning angle and cycling velocity with the goal of comparing this data to the controllable elements of the simulator. The final set-up of both the simulator and the real bicycle are described below.

Bicycle simulator

The dynamic simulator setup is depicted in Figure 1. The main objective is to achieve a high quality of the simulator and therefore provide a realistic experience. To achieve this, the force feedback modules and the real-time simulation of the bicycle must have a corresponding performance. The right fine-tuning is crucial for creating a highly immersive driving experience.



Figure 1. Bicycle simulator at the MoSAIC-VRU-Lab from the German Aerospace Center (DLR)

Two different versions, V1.1 and V2.0, of the DLR bicycle simulator (Martinez Garcia et al., 2023; Martínez García et al., 2022) were tested in different scenarios (s. Table 1).

For the lateral dynamics on V1.1, the force feedback of the steering motor was calculated by a modified steering force simulation based on motorized vehicles, whereas on V2.0 it was calculated based on the Whipple-bicycle physics model (Meijaard et al., 2007). The lean angle behaviour was controlled either by the force of the body (V1.1) or by the position of the steering angle (V2.0). For the longitudinal dynamics, on V2.0 the measurement of cycling velocity and braking was performed with an incremental encoder that has higher resolution and lower latency than the bicycle trainer used in V 1.1. In addition, the wind simulator was configured to deliver wind dynamically (depending on cycling velocity), whereas in V1.1 it was static and constantly delivered the same amount of air for all velocities. Within the next paragraphs, the underlying formulas and mechanical set-ups for both versions are described in more detail.

© 2023 Martinez Garcia, D., Gröne, K., Fischer, M., Zhao, M. & Bergen, M. published by TU Delft OPEN on behalf of the authors.
ISSN: 2667-2812

Table 1. Features of both versions of the bicycle simulator concerning lateral and longitudinal behaviour

	Feature	V1.1	V2.0
Lateral	**Steering**	Look-up table with adapted vehicle dynamics steering forces	Whipple-bicycle physics model
	Leaning	Force control	Position control
Longitudi	**Acceleration**	Bike trainer	Incremental encoder
	Braking	Disc brake + bike trainer signal	Disc brake + incremental encoder signal
	Wind	Static	Dynamic

Visualization - The visualization was developed by using Unreal Engine 4. The visual system, which generates visual stimuli by displaying a virtual reality (VR), is implemented in two different ways. One possibility for visualizing the driving environment is transmission on a single monitor and another is the use of a head mounted display (HMD). Through the interaction of internal and external sensors, the position and orientation of the VR goggles in space can be detected. In contrast to the monitor, it is thus possible to adopt a 360° viewing angle independent of the direction of travel. For the presented study, only the VR googles were used.

Haptics - With the use of haptic gloves, the movements and position of the hands are tracked and displayed in the visualization, which is displayed as part of the virtual environment.

Bike trainer - To create adjustable resistance when pedalling, a Tacx® FLUX 2 Smart trainer is used to replace the rear wheel. This system provides a measurement of the driving velocity which was first utilized for the visualization for V1.1. Due to abrupt changes in the perceived movements in the visualization, a more precise measuring method was implemented for V2.0. An optical incremental encoder (Kübler Automation 8.KIH40.5462.2048) was placed on the shaft of the bike trainer, which allows a maximal resolution of 250 ppr with a maximal pulse frequency of 250 kHz. Figure 2 shows the assembly of the incremental encoder and a disc brake to the shaft of the bike trainer (Jacobi, 2022).

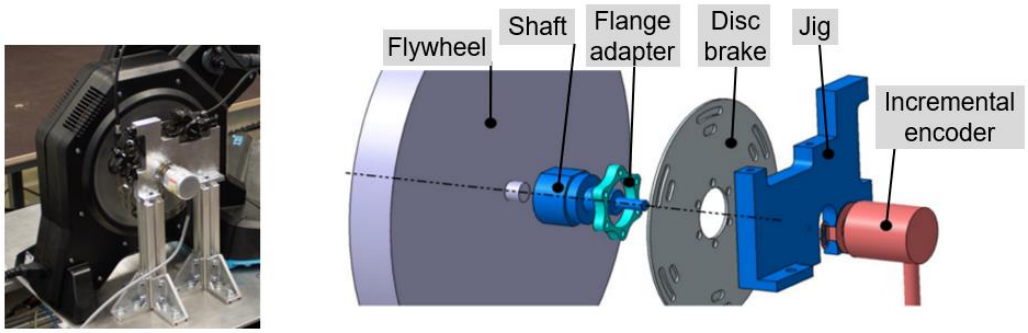


Figure 2. Assembly of the incremental encoder and disc brake

To calculate the velocity value for V2.0, the number of measured increments is recorded in a specific time interval. The calculation for the virtual cycling velocity $\boldsymbol{v_{virtual}}$ is based on a bicycle with a wheel radius $\boldsymbol{r_{wheel}}$ of 28 ":

$$\boldsymbol{v_{virtual} = r_{wheel} \cdot \omega_{wheel}} \quad \boldsymbol{with\ \omega_{wheel} = 2 \cdot \pi \cdot n_{pinion}} \tag{1}$$

The internal transmission ratio of the roller trainer $\boldsymbol{i}$ considering the rotational speed of the pinion $\boldsymbol{n_{pinion}}$ and the flywheel $\boldsymbol{n_{flywheel}}$ is:

$$\boldsymbol{i = \frac{z_{out}}{z_{in}} = \frac{1}{7} = \frac{n_{pinion}}{n_{flywheel}}} \tag{2}$$

This now allows the rotation velocity of the flywheel $\boldsymbol{n_{flywheel}}$ to be determined considering the resolution of the incremental encoder:

© 2023 Martinez Garcia, D., Gröne, K., Fischer, M., Zhao, M. & Bergen, M. published by TU Delft OPEN on behalf of the authors.
ISSN: 2667-2812

$$n_{flywheel} = \frac{rotations}{\Delta t} = \frac{\frac{\Delta increments}{resolution}}{t_{now} - t_{end}} \tag{3}$$

By substituting (2) and (3) in the basic formula (1), we can now calculate the cycling velocity $v_{virtual}$:

$$v_{virtual} = \frac{r_{wheel} \cdot 2 \cdot \pi \cdot \Delta increments}{7 \cdot (t_{now} - t_{end}) \cdot resolution} \tag{4}$$

Wind - A WAHOO® KICKR Headwind Simulator is used to aid immersion and reduce motion sickness. This device is capable of providing velocity-based airflow by communicating with the bike trainer via Bluetooth Low Energy (BLE). For V1.1 only static wind was used, whereas for V2.0 the Headwind Simulator provides wind with a factorized velocity depending on the cycling velocity.

Steering motor - A servomotor (Schneider Electric BSH1003P31A2A) is used to control the steering behaviour. Direct coupling with the handlebar creates a haptic steering system which, in conjunction with the dynamics model, provides a steering-angle-dependent resistance torque. Where V1.1 used a simple lookup-table with adapted vehicle dynamics steering forces, a new approach for the dynamics model based on the Whipple-bicycle physics model (Meijaard et al., 2007) was developed (Janssen, 2022) for V2.0. The mathematical model of Schwab and Recuero, based on the findings of Meijaard et al. was used to calculate the force feedback T_f for the handlebars. Considering mass matrix M, damping matrix C, and stiffness matrix K, and depending on the bicycle lean angle ϕ and steer angle δ (Schwab & Recuero, 2013), the basic formula for the counter moment is:

$$M\ddot{q} + C\dot{q} + Kq = M\ddot{q} + vC_1\dot{q} + (gK_0 + v^2K_2)q = f$$
$$\text{with the time-varying quantities: } q = (\phi, \delta)^T \text{ and } f = (T_\phi, T_\delta)^T \tag{5}$$

From this basic equation and its matrix form, the counter torque of the handlebar or the force feedback T_f can be calculated:

$$T_f = -(M_{\delta\phi}\ddot{\phi} + C_{\delta\phi}\dot{\phi} + C_{\delta\delta}\dot{\delta} + K_{\delta\phi}\phi + K_{\delta\delta}\delta) \tag{6}$$

The calculations for the individual matrix values were performed by using the values given by Meijaard et al., 2007 and compared to the determined values for the counter torque or force feedback T_f according to Schwab and Recuero, 2013. A further factor for the counter-torque has been included, which serves as compensation for the fine-tuning between the servomotor and the rectifier.

Platform – The simulator is assembled on top of a 2-DOF motion platform (pitch and roll) that allows for leaning behaviour and additionally stimulates the vestibular sensory system during incline and acceleration. The leaning angle is measured on the base of the platform. For V1.1, the platform is controlled by a force/torque application from the cyclist (force control). In addition, the motion platform pushes the rider back to the centre with a spring force, which can lead to a pendulum motion and a safety risk when the rider is involved. This setting is also extremely dependent on the height and weight of the riders. Therefore, a position control approach was designed for V2.0 in which the leaning angle is dependent on the steering angle and the driving velocity to provide more safety to the rides while counteracting the platform to build up a pendulum moment (Janssen, 2022). The basic formula for the leaning behaviour considering the heading of the bicycle ψ and the steer axis tilt λ is as follows (Meijaard et al., 2007):

$$-m_T\ddot{y}_P z_T + I_{T_{XX}}\ddot{\phi} + I_{T_{XZ}}\ddot{\psi} + I_{A_{\lambda X}}\ddot{\delta} + \dot{\psi}vS_T + \dot{\delta}vS_F\cos\lambda = T_{B_\phi} - gm_T z_T\phi + gS_A\delta$$
$$with\ \dot{\psi} = \left(\frac{v\delta + c\dot{\delta}}{w}\right)\cos\lambda \rightarrow \ddot{\psi} = \left(\frac{v\dot{\delta} + c\ddot{\delta}}{w}\right)\cos\lambda \quad and\ \ddot{y}_P = \left(\frac{v^2\delta + vc\dot{\delta}}{w}\right)\cos\lambda \tag{7}$$

The 2-DOF motion platform used did not include a sensor system to measure the applied leaning moment of the driver T_{B_ϕ} which would provide feedback for the calculation basis. Therefore, a different approach was developed to ensure the control of the platform. The calculation was created as a function of velocity and steering angle for the deflection acceleration $\ddot{y}_P$ at the rear contact point *P*. Figure 3 illustrates the development of the concept (adapted from Astrom et al., 2005; Meijaard et al., 2007).

© 2023 Martinez Garcia, D., Gröne, K., Fischer, M., Zhao, M. & Bergen, M. published by TU Delft OPEN on behalf of the authors.
ISSN: 2667-2812

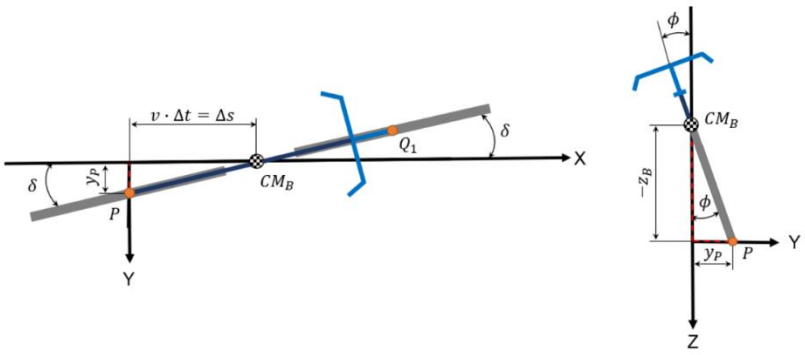


Figure 3. Concept of the leaning behaviour (adapted from Astrom et al., 2005; Meijaard et al., 2007)

For the calculation of the lean angle ϕ, first the displacement $\boldsymbol{y_P}$ of the rear contact point *P* is determined as follows:

$$\sin \delta = \frac{y_P}{\Delta s} = \frac{y_P}{v \cdot \Delta t} \rightarrow y_P = \sin \delta \cdot v \cdot \Delta t \tag{8}$$

Finally, based on (8), the lean angle ϕ can be determined in the next step:

$$\tan \phi = \frac{y_P}{-z_B} \rightarrow \phi = \arctan\left(\frac{y_P}{-z_B}\right) \tag{9}$$

To compensate for the displacement $\boldsymbol{y_P}$, a "bleeding" factor is set in the calculation, which resets an occurrence of errors in the integral and differential calculation and thus allows the platform to move smoother. Furthermore, the inputs of the steering angle δ and the measured cycling velocity v were parameterized to allow for later adjustment for an even finer or smoother leaning behaviour. Likewise, a range for the steering angle δ was set by a trial in order not to move the platform at the smallest angle changes. This also applies to the travel velocity v. The limits for this are ±0.05 rad or approx. ±3° and above 2.5 m/s. Additionally, the maximum lean angle ϕ was limited to ±15° and the velocity of the platform was reduced to prevent a pendulum motion as in the previous setup.

Research bicycle

The real-world study aimed to gather validation data with a 28” e-bike, shown in Figure 4.



Figure 4. Research bicycle instrumented with sensors

The bicycle is equipped with an Elipse-D sensor that includes a 9-DOF Inertial Measurement Unit (IMU) with GNSS receiver with which we measured the leaning angle, position and velocity of the bicycle. The IMU was placed under the seat of the bicycle and is connected to a Raspberry Pi. An incremental encoder (Bourns EMS22D) with 512 pulses per revolution was attached to the handlebar and was used to measure the steering angle. It is read out by an Arduino Mega Board via digital inputs. The Arduino counts the increments and calculates the increment velocity. Afterwards, it is sent to the Raspberry via the serial output. All values (incremental encoder and the IMU) run together and are logged in Node-RED.

© 2023 Martinez Garcia, D., Gröne, K., Fischer, M., Zhao, M. & Bergen, M. published by TU Delft OPEN on behalf of the authors.
ISSN: 2667-2812

Study design

Study participants were recruited via the online tool “Probandenpool” (pool of subjects) of the Institute of Transportation Systems. The study was approved by the "Research Ethics" office at the German Aerospace Center.

The combination of a simulator study and a real-world study was designed to answer the following research questions:

- RQ1: Does the mechanical structure and control of the bicycle simulator allow the feeling of riding on a real bicycle?
- RQ2: Is the data collected from the bicycle simulator similar to the data of a real bicycle?
- RQ3: Which of the simulator set-ups is better suited in terms of RQ1 and RQ2?

To answer these questions, the following hypotheses were evaluated:

- H1: The mechanical and algorithmic changes made to the simulator will deliver a more realistic steering behaviour.
- H2: The mechanical and algorithmic changes made to the simulator will deliver a more realistic leaning behaviour.
- H3: The cycling velocity choice will be more realistic with V2.0.

Simulator study design

The simulator study was performed in September 2022. Both versions of the simulator set-up were successfully tested by 27 participants (5 female, 22 male, mean age 29.4 years) in a within-subject study design. 8 participants could not finish the study due to simulator sickness or not being able to control the simulator. After a training on the simulator, 6 scenarios with different tasks (s. Table 2) were conducted. The participants answered questionnaires on simulator sickness, presence, acceptance and realism. Simulation data on driving velocity, steer angle, and lean angle was collected to evaluate the differences between the simulator set-ups (V1.1 and V2.0).

Table 2. Scenarios of the evaluation study

Scenario	Task
A	Stop at a traffic light and go around a construction site
B	Slalom
C	Double left turn at intersection
D	Interaction with pedestrian + Right turn
E	Overtaking an E-Scooter + Left turn
F	Turning area



Figure 5. Scenario A (left), B (middle) and F (right)

The scenarios took place on 2 different tracks depending on the task. Most of the scenarios of the main experiment (A, C, D, E) were performed on a virtual replication of the research intersection in Braunschweig, Germany, whereas scenarios B and F were performed on road sections of the city Cremlingen, Germany (Figure 5). The tasks performed on each scenario were chosen to be realistic and comparable with data from the real track.

© 2023 Martinez Garcia, D., Gröne, K., Fischer, M., Zhao, M. & Bergen, M. published by TU Delft OPEN on behalf of the authors.
ISSN: 2667-2812

More details about the simulator setup are presented by (Fischer et al., 2022) and (Martínez García et al., 2022). Additional analyses of the subjective evaluation of the two simulator set-ups can be found in (Martínez García et al., 2023).

Real-world study design

The study was performed in August 2023 with 11 participants (2 female, 9 male, mean age 34 years). The main goal of the study was to collect data about the driving velocity, steer angle and lean angle to compare it with the simulator data on a between-subject design. Scenarios A, C, D and E were performed at the research intersection in Braunschweig (Figure 6, left). Although these scenarios were identical in terms of route, there were many variables concerning the traffic conditions that could not be controlled or simulated. These conditions include the state of traffic lights, other road users and their behaviours, weather conditions and sirens of ambulances or police. For scenario D there was no instructed pedestrian to cross at the intersection and in scenario E there was no instructed E-Scooter. Therefore, these scenarios consisted only on turning to the right or to the left. Scenarios B and F were recreated in a space with no other road users (Figure 6, right). Due to space limitations, the measurements used in the simulation could not be replicated in real life. For scenario B (Slalom) the cones on the real track were placed with 4 meters of separation between each other, whereas in the simulation, the cones had a separation of 9 meters. Furthermore, on the real track there were 8 cones, whereas on the simulation there were 11. Due to asphalt space limitations the turning area in scenario F had a diameter of only 12 meters on the real track and not 20 meters as in the simulation.



Figure 6. Real world study. Image of the research intersection (left) and slalom course of scenario B (right)

Results

Even though the simulator study was carried out in a balanced order design, due to the drop outs, in the end one group with 16 test subjects experienced V1.1 first and V2.0 afterwards, whereas the second group with the reversed order of simulator set-ups contained only 11 subjects. Since some order effects in the subjective ratings could be found (s. Martinez Garcia, 2023), this limits the expressiveness of the results. However, the objective analysis does not reveal similar order effects and thus the results seem to be trustworthy nevertheless. During the real-world study some major technical problems occurred, so that only a few data sets were usable for the analysis (between 2-4 depending on the scenario). Especially the steering recordings showed a strong drift, which made quantitative conclusions impossible. Thus, the steering angle is only analysed comparing the two simulator set-ups. The validation hence focuses on the driving velocity and the leaning angle.

A multivariate analysis of variance (MANOVA) was conducted, in which the differences in means between the profiles were compared for the three dependent variables (leaning angle, steering angle and velocity) together. The data of many participants in the real-world study was not usable, so that the remaining data is not sufficient to base reliable conclusions on. Therefore, only the simulator data was included in the statistical analysis. Furtherly, the analysis only includes datapoints where the velocity is greater than 1 m/s in order to eliminate the data produced when standing waiting at a traffic light. The multivariate test results for scenario A indicate that there are significant differences among the profiles when considering all dependent variables together. The p-values are very close to zero, suggesting a highly significant effect (Wilks' Lambda = 0.1951, $F(2, 46 = 63.2775$, $p < 0.001$). Similarly, the MANOVA showed significant effects of the profile on the dependent variables for scenario D (Wilks' Lambda = 0.5786, $F(3, 46) = 11.1661$, $p < 0.001$), scenario E (Wilks' Lambda = 0.6856, $F(3, 46) = 7.0308$, $p < 0.001$) and scenario F (Wilks' Lambda 0.3498, $F(3, 46) = 28.5019$, $p < 0.001$). Pairwise comparisons were carried out to examine how the two profiles individually affected lean angle, steer angle and speed.

Steering behaviour

In the simulator study, no clear differences could be found in the steering behaviour of both versions. Figure 7 shows the frequency density of the steering angle of all the participants across all scenarios combined. This information is consistent with the analysis of individual scenarios.

© 2023 Martinez Garcia, D., Gröne, K., Fischer, M., Zhao, M. & Bergen, M. published by TU Delft OPEN on behalf of the authors.
ISSN: 2667-2812

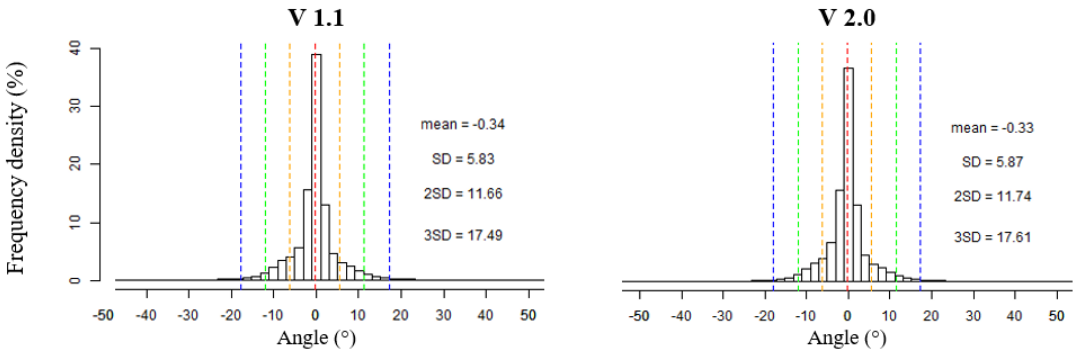


Figure 7. Distribution of leaning angle for the simulator study

As the data of the incremental encoder used during the real-world study cannot be trusted (see above) the data was excluded from the further analysis.

Leaning behaviour

The analysis of the leaning angle shows significant differences between V1.1 and V2.0 in all scenarios (Table 3).

Table 3 . Post-hoc pairwise comparison of V1.1 and V2.0 for leaning angle

Scenario	Mean V1.1	Mean V2.0	se	T	df	p-val
A	1.843	0.870	0.073	13.330	44.848	< 0.001
B	2.110	1.728	0.157	2.430	36.054	0.020
C	1.959	1.615	0.150	2.299	42.548	0.026
D	1.847	1.231	0.111	5.573	46.980	< 0.001
E	1.941	1.488	0.107	4.249	37.959	< 0.001
F	1.953	3.478	0.180	-8.462	46.814	< 0.001

A more controlled steering behaviour and a more even distribution of leaning angles (Figure 8, bottom) was observed with V2.0. A small offset (between 1.5° and 2°) was often observed on V1.1, which means that the participants were not precisely cycling with 0° while being in upright position (Figure 8, top). This effect was not present in V2.0 due to the control mechanism of the platform, which did not allow this to happen.

Comparing the simulator data to the real-world data, we find that there is greater variation in the leaning angle in the real-world condition compared to simulator runs. Figure 9 displays the distribution of the leaning angle for the slalom (B) and the turning area (F). The absolute values of the leaning angles were used, as we are interested in how much the participants were leaning rather than the direction of the leaning. For both scenarios the plots show a large number of outliers for simulator version V1.1, which may be an indication that the participants were less steady in their leaning movements. For V2.0 the leaning angle is smaller than in the real-world condition, however the variance is more similar to the real data. The deviation in the leaning angle might be related to the differences in cone distances and turning area diameter (see above), which does not allow for a real validation in this context.

However, to get a better impression of the distribution of the leaning angle, Figure 10 shows the leaning angle per participant over distance for the slalom. The plots support the notion that the leaning behaviour was more unstable in V1.1 condition, compared to the V2.0 condition.

© 2023 Martinez Garcia, D., Gröne, K., Fischer, M., Zhao, M. & Bergen, M. published by TU Delft OPEN on behalf of the authors.
ISSN: 2667-2812

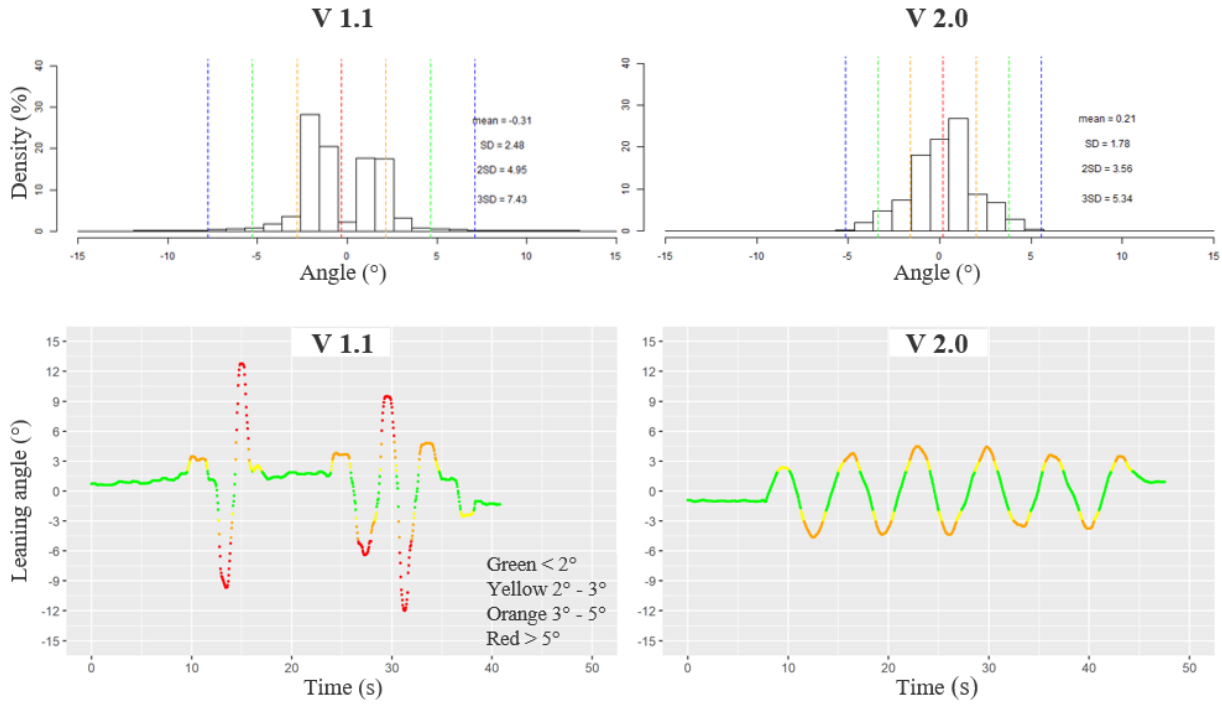


Figure 8. Leaning angle on a slalom course. Distribution for all participants (top) and timeline of a single participant (bottom)

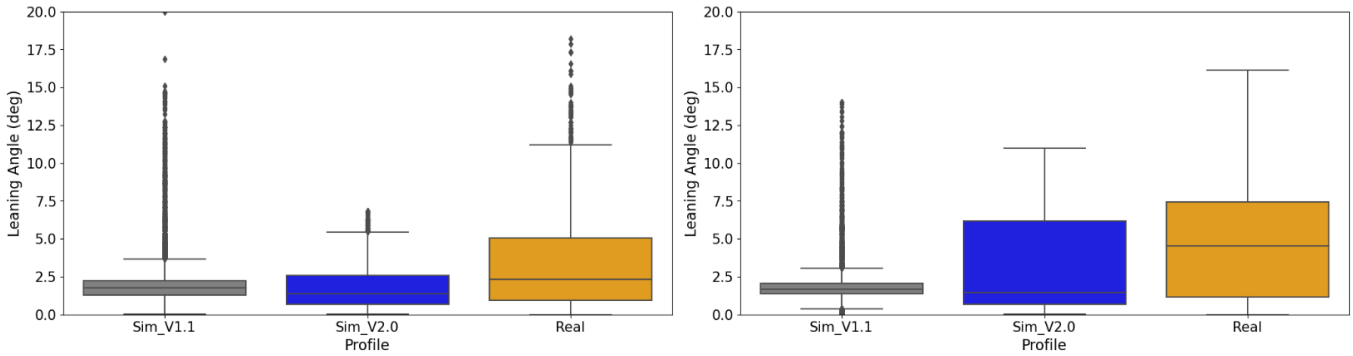


Figure 9. Boxplot of leaning angles for simulator version V1.1, V2.0 and real-world study for scenario B (slalom, right) and scenario F (turning area, left)

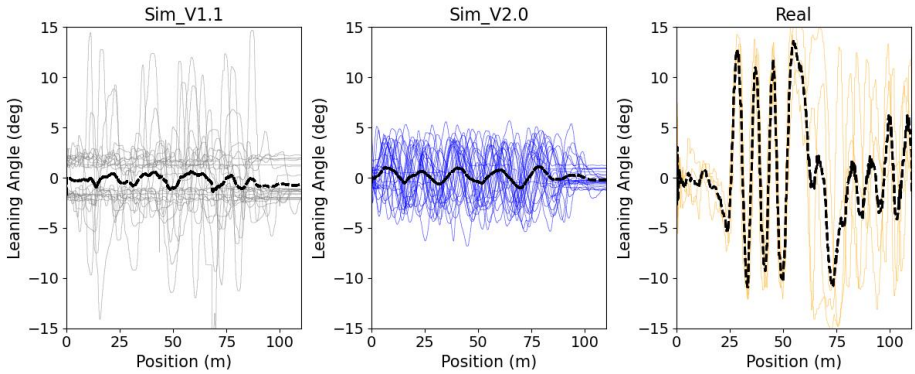


Figure 10. Leaning angle over distance for simulator version V1.1, V2.0 and real-world study for slalom scenario B. Data for all participants with mean (black, dotted line)

© 2023 Martinez Garcia, D., Gröne, K., Fischer, M., Zhao, M. & Bergen, M. published by TU Delft OPEN on behalf of the authors.
ISSN: 2667-2812

Figure 11 shows the leaning angle over distance for the turning area. The simulator version V2.0 produces a smoother leaning pattern, which has a greater resemblance to the real-world data than V1.1, even though that the leaning into the curve seems to happen more gradually in simulation than in the real-world trial.

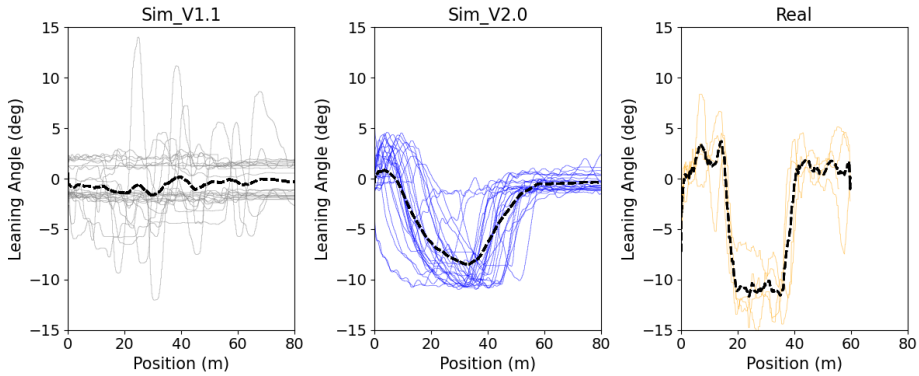


Figure 11. Leaning angle over distance for simulator version V1.1, V2.0 and real-world study for turning area scenario F. Data for all participants with mean (black, dotted line)

Cycling velocity

The cycling velocity of the participants was evaluated to solve H3. Overall, no significant differences were found between V1.1 and V2.0 regarding the velocity for any of the scenarios. Figure 12 illustrates the distribution of velocity per profile across scenarios. The velocity in the simulator was on average roughly 0.5 m/s higher than in the real-world condition. In addition, the variance in velocity is slightly smaller in the V2.0 condition than in the V1.1 condition.

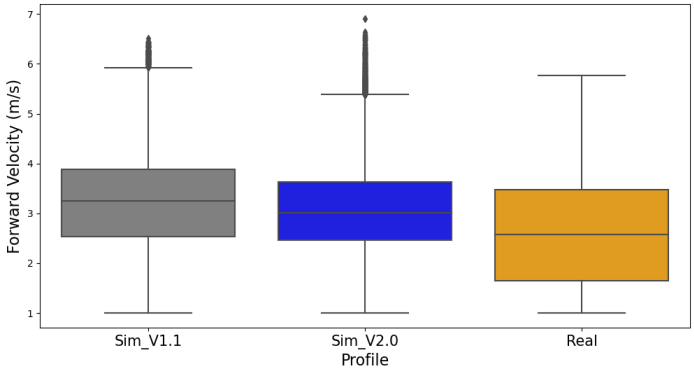


Figure 12. Boxplot of velocity for simulator version V1.1, V2.0 and real-world study based on data from all scenarios

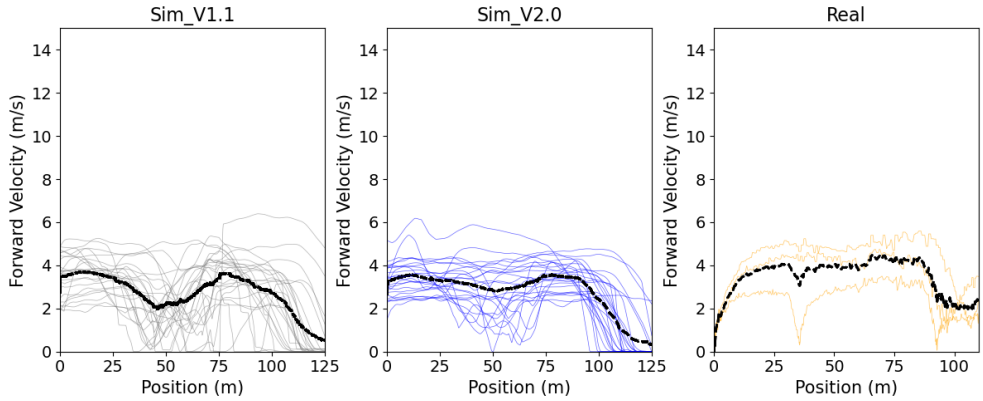


Figure 13: Driving velocity over distance for simulator version V1.1, V2.0 and real-world study for scenario D. Distribution for all participants with mean (black, dotted line)

Figure 13 compares the velocity for scenario D, turning right and interaction with pedestrian, for both simulation set-ups and the real-world study. The velocity keeping seems to be less steady and on average the breaking behaviour shows stronger deceleration for V1.1 than for V2.0. The same effect can be observed looking at individual data sets.

© 2023 Martinez Garcia, D., Gröne, K., Fischer, M., Zhao, M. & Bergen, M. published by TU Delft OPEN on behalf of the authors.
ISSN: 2667-2812

Subjective ratings

The expectation, that higher acceptance can be reached with V2.0, could not be supported with the subjective ratings of the participants. However, the analysis of the perceived realism after each trial showed that wind effects and braking were evaluated as significantly better while riding with V2.0. Hence, the longitudinal enhancements were clearly preferred by the participants. This could not equally be observed for the lateral dynamics.

Summary, discussion and conclusion

The studies performed in this paper provide insight into the realism of the simulator in comparison to a real bicycle. The adaptations to the configuration of the simulator were presented. The analyses of two different versions of the simulator were displayed and the resemblance to real-world data gathered with a bicycle while cycling in the same scenarios was examined. The study aimed to evaluate a new control logic and hardware changes in the DLR bicycle simulator. The version V2.0 was therefore compared to the older V1.1 version of the simulator set-up.

The analysis of the subjective ratings collected within the presented study (Martinez Garcia et al., 2023) showed, that the mechanical set-up and control algorithms of the bicycle simulator to some extend support the feeling of riding a real bicycle. Aspects related to the longitudinal cycling behaviour, thus braking, accelerating and wind effects, were rated more realistic in V2.0 than in V1.1. With regard to the lateral behaviour, namely the steering and leaning, no significant differences were found in the subjective rating of the participants.

This study aimed to compare the objective simulator data to real-world data. In order to do that, participants were asked to ride similar scenarios as in simulator on a real bicycle at the research intersection in Braunschweig. Unfortunately, due to major technical problems a lot of the data was not usable, so that the comparisons can be seen as a first indication, but no solid conclusions can be drawn from the real-world data. For the analysis, it must be noted that the scenarios did not have the same dimensions and number of cones on the slalom, which may affect the comparison of the results. The steering angle data from the real-world condition was not usable due to strong drifts in the data. Therefore, *H1*, the assumption that the mechanical and algorithmic changes made to the simulator deliver a more realistic steering behaviour, cannot be answered conclusively. Comparing the steering data of V1.1 and V2.0 revealed no significant differences between the two versions. With respect to the leaning behaviour, we found a steadier behaviour in V2.0, which more closely resembled to the leaning behaviour observed in the real-world condition. These findings support the hypothesis *H2*, that the changes made to simulator promote a more realistic leaning behaviour. However, the subjective ratings of the lateral behaviour in V2.0 was not significantly better than the rating for V1.1. Regarding the longitudinal behaviour we found that even though the mean velocity does not significantly differ between the simulator versions, the velocity was steadier in V2.0. Further, we observed stronger, more abrupt decelerations for V1.1 than for V2.0. The notion, that V2.0 allowed for a smoother and steadier longitudinal behaviour was supported by the subjective ratings of the participants, which showed significantly higher ratings for V2.0 compared to V1.1. Given these results, we can see a small indication that the cycling velocity choice is more realistic with V2.0 (*H3*). However, further research will be needed to confirm this indication.

Some limitations of this study include that too many changes were performed on the simulator in parallel and therefore, it is partly difficult to evaluate them individually and identify the differences between both versions. For this reason, more specific research will be performed on each feature which requires further fine-tuning. As the steering angle analysis of the changes performed on the simulator delivered no clear results and the measurements of the steering angle during the real study were not precise due to a drift of the sensor, a more precise analysis should be performed to evaluate this behaviour. Another important consideration is that in the simulator study, a within design was used, whereas between the real bicycle and the simulator a between design was used. The data gathered with the real bicycle was not highly dynamic since the participants had to wait long times at the red traffic lights. Also, there were a lot more road users and aspects we couldn't control as in the simulation. Furthermore, the results of the data recorded with the real bicycle were extremely limited since the sensors didn't work properly and many datasets had to be dismissed. The findings from these analyses will be incorporated into the further development of the simulator.

This study provided valuable insights into the behaviour of persons riding the DLR bicycle simulator (V2.0) compared to real-world cycling and in contrast to the previous simulator set-up (V1.1). Even though technical issues prevent definitive conclusions in some aspects, the findings suggest some promising improvements in the simulator's performance. Specifically, for the longitudinal behaviour version V2.0 demonstrated smoother velocity profiles and less abrupt decelerations. Additionally, indications could be found that V2.0 exhibits a more realistic leaning behaviour although subjective ratings did not show significant differences in lateral behaviour compared to V1.1. However, it is essential to acknowledge the study's limitations, including the challenges in data collection, the need for more fine-tuned studies of individual simulator features, and the differences in scenario design between the simulator and real-world experiments. Hence, this research serves as a foundation for further refinement and development of the DLR bicycle simulator. Future studies will focus on isolating specific simulator features for improvement and conducting more precise analyses, especially regarding the comparison to real-world data, e.g. by using non-public test tracks for gathering real-world data. By addressing these limitations and building upon the current findings, enhancing the simulator's ability to replicate real-world cycling experiences will be continued, ultimately contributing to safer and more effective bicycle research and training.

© 2023 Martinez Garcia, D., Gröne, K., Fischer, M., Zhao, M. & Bergen, M. published by TU Delft OPEN on behalf of the authors.
ISSN: 2667-2812

References

Astrom, K. J., Klein, R. E., & Lennartsson, A. (2005). Bicycle Dynamics and Control: Adapted Bicycles for Education and Research. *IEEE Control Systems*, *25*(4), 26–47. https://doi.org/10.1109/MCS.2005.1499389

Fischer, M., Temme, G., Gröne, K., Martinez Garcia, D., Grolms, G., & Rehm, J. (2022). A VRU-simulator for the evaluation of pedestrian- and cyclist-vehicle interaction – Design criteria and implementation. *Proceedings of the Driving Simulation Conference*, 153–160.

Jacobi, D. (2022). *Konzeptentwicklung, Umsetzung und Evaluation der Längsdynamik eines Fahrradsimulators für eine realitätsnahe, interaktive Simulation*. Bachelor thesis, DIPLOMA Hochschule.

Janssen, V. (2022). *Konzeptentwicklung, Umsetzung und Evaluation der Querdynamik eines Fahrradsimulators für eine realitätsnahe, interaktive Simulation*. Bachelor thesis, DIPLOMA Hochschule.

Martinez Garcia, D. (2021). *Construction, parameterization and evaluation of a bicycle simulator for a realistic and interactive simulation environment.* Master thesis, Technische Universität Braunschweig.

Martinez Garcia, D., Gröne, K., Janssen, V., Jacobi, D., Ackermann, S., Zhao, M., Nicolay, E., Bergen, M., & Fischer, M. (2023). Technical adjustments of a bicycle simulator . Impact on simulator sickness , presence , acceptance and realism. *Proceedings of the Driving Simulation Conference 2023 Europe*, *2023*, 201–203.

Martínez García, D., Gröne, K., Quante, L., Fischer, M., Thal, S., & Henze, R. (2022). *Parameter tuning of a bicycle simulator for a realistic riding behaviour and motion perception*. *Proceedings of the Driving Simulation Conference 2022 Europe*, Driving Simulation Association, Strasbourg, France, 1–2.

Meijaard, J. P., Papadopoulos, J. M., Ruina, A., & Schwab, A. L. (2007). Linearized Dynamics Equations for the Balance and Steer of a Bicycle: A Benchmark and Review. *Proceedings of the Royal Society A: Mathematical, Physical and Engineering Sciences*, *463*, 1955–1982. https://doi.org/10.1098/rspa.2007.1857

O'Hern, S., Oxley, J., & Stevenson, M. (2017). Validation of a bicycle simulator for road safety research. *Accident Analysis and Prevention*, *100*, 53–58. https://doi.org/10.1016/j.aap.2017.01.002

Schwab, A. L., & Recuero, A. M. (2013). Design and experimental validation of a haptic steering interface for the control input of a bicycle simulator. *Proceedings of the ECCOMAS Thematic Conference on Multibody Dynamics 2013*, 103–110.

Shoman, M. M., & Imine, H. (2021). Bicycle Simulator Improvement and Validation. *IEEE Access*, *9*, 55063–55076. https://doi.org/10.1109/ACCESS.2021.3071214

Sinus-Studie (2021). Fahrrad-Monitor Deutschland 2021 - Ergebnisse einer repräsentativen Online-Befragung. https://www.bmdv.bund.de/SharedDocs/DE/Artikel/StV/Radverkehr/fahrradmonitor-2019.html, Nov. 2021

Wendel, K. D. (2020). *Bicycle-rider control identification*. Technische Universiteit Delft.

© 2023 Martinez Garcia, D., Gröne, K., Fischer, M., Zhao, M. & Bergen, M. published by TU Delft OPEN on behalf of the authors.
ISSN: 2667-2812

Proceedings of the 5th Symposium on the Dynamics and Control of Single-Track Vehicles

Bicycle and Motorcycle Dynamics 2023, October 18-20, Delft, The Netherlands

Jason K. Moore, Edwin de Vries, Andrew Dressel, Leila Alizadehsaravi



Jason K. Moore, PhD
Delft University of Technology I Mechanical Engineering

Jason K. Moore is an Assistant Professor of BioMechanical Engineering at Delft University of Technology. He leads the TU Delft Bicycle Lab (http://bicycle.tudelft.nl) that focuses on a broad set of bicycle related engineering topics. His primary research interest is the human operated control of single-track vehicles but his work also spans various topics in sports engineering, computational optimal control, bicycle traffic safety, and engineering education. He teaches topics in dynamics, control, and engineering computation. He is a past Fulbright Scholar and his graduate degrees are from the University of California, Davis where he was also an assistant professor of teaching from 2015-2020.

BICYCLE & MOTORCYCLE DYNAMICS 2023

@ 2024 TU Delft OPEN Publishing
ISBN 978-94-6366-958-0
DOI: https://doi.org/10.59490/mg.121

BOOKS.OPEN.TUDELFT.NL

TU Delft OPEN